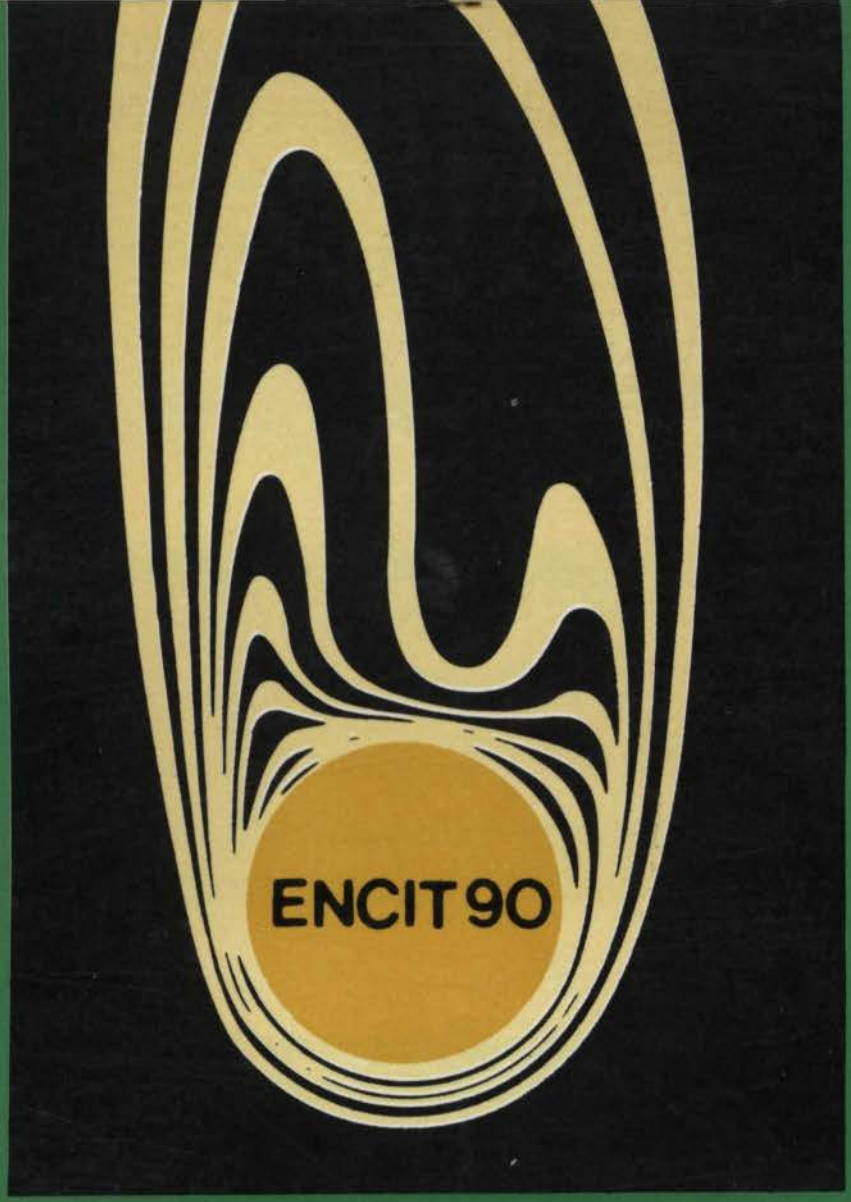

III ENCONTRO NACIONAL DE CIÊNCIAS TÉRMICAS

3rd BRAZILIAN THERMAL SCIENCE MEETING

VOLUME I

ANAIS
PROCEEDINGS

ANAIS
PROCEEDINGS

VOLUME I

III ENCONTRO NACIONAL DE CIÊNCIAS TÉRMICAS
3rd BRAZILIAN THERMAL SCIENCE MEETING

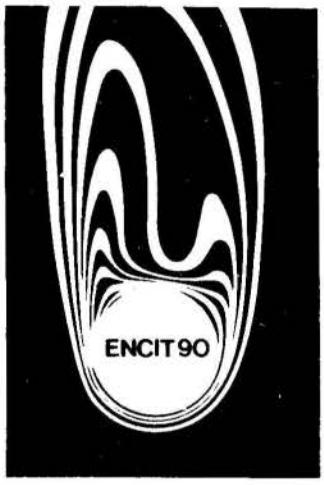

Editores
Edited by

C. R. Maliska, C. Melo, A.T. Prata

DEPARTAMENTO DE ENGENHARIA MECÂNICA
UNIVERSIDADE FEDERAL DE SANTA CATARINA
ITAPEMA - SC
10 a 12 de Dezembro de 1990

Embraco
Empresa Brasileira de Compressores S.A.

GOVERNO DO ESTADO DE
SANTA CATARINA
SECRETARIA DA CIÊNCIA E TECNOLOGIA

TUPY

TUPY TERMOTÉCNICA
ISOLAMENTOS LTDA.

IBM
IBM Brasil

Consul
A marca da gente

Springer Carrier

CNPq
CONSELHO NACIONAL
DE DESENVOLVIMENTO
CIENTÍFICO E TECNOLÓGICO

finep

BRASTEMP

PROMOÇÃO
(PROMOTED BY)

ASSOCIAÇÃO BRASILEIRA DE CIÊNCIAS MECÂNICAS
(BRAZILIAN SOCIETY OF MECHANICAL SCIENCES)

ABRAVA

ASSOCIAÇÃO BRASILEIRA DE REFRIGERAÇÃO, AR CONDICIONADO VENTILAÇÃO E AQUECIMENTO
(BRAZILIAN ASSOCIATION OF REFRIGERATION, AR CONDITIONING, VENTILATION AND HEATING)

DEPARTAMENTO DE ENGENHARIA MECÂNICA
(DEPARTMENT OF MECHANICAL ENGINEERING)
UNIVERSIDADE FEDERAL DE SANTA CATARINA
(FEDERAL UNIVERSITY OF SANTA CATARINA)

ASSOCIAÇÃO BRASILEIRA DE CIÊNCIAS MECÂNICAS
(BRAZILIAN SOCIETY OF MECHANICAL SCIENCES)

Diretoria:
(Board of Directors)

Presidente: **SIDNEY STUCKENBRUCK**
Vice-Presidente: **LUIS BEVILACQUA**
Secretário Geral: **ELOI FERNANDEZ Y FERNANDEZ**
Secretário: **OSWALDO A. PEDROSA JR.**
Diretor de Patrimônio: **ANTONIO MAC DOWELL DE FIGUEIREDO**
Secretária Executiva: **SIMONE MARIA FRADE**

III ENCONTRO NACIONAL DE CIÊNCIAS TÉRMICAS
3rd BRAZILIAN THERMAL SCIENCE MEETING

Comissão Organizadora
(Organizing Committee)

ÁLVARO T. PRATA – UFSC – Coordenação Geral
CLÁUDIO MELO – UFSC – Coordenação Geral
CLÓVIS R. MALISKA – UFSC – Coordenação Geral
LEONARDO GOLDSTEIN JR. – UNICAMP
MIGUEL H. HIRATA – COPPE
PAULO R. DE SOUZA MENDES – PUC/RJ
RENATO M. COTTA – COPPE

International Representative for ENCIT 90
DR. RAMESH K. SHAH
(HARRISON RADIATOR DIVISION - GENERAL MOTORS CORPORATION)

COORDENADORES TÉCNICOS

(TECHNICAL COMMITTEE)

- **AERODINÂMICA**

Paulo Afonso de Oliveira Soviero - ITA/CTA

- **ANÁLISE EXERGÉTICA**

Luiz Fernando Milanez - UNICAMP

- **CAMADA LIMITE E TURBULÊNCIA**

Átila Pantaleão Freire - COPPE/UFRJ

- **COMBUSTÃO**

Demétrio Bastos Neto

- **COMPORTAMENTO TÉRMICO DE AMBIENTES**

Paulo César Philippi - UFSC

- **CONDUÇÃO TÉRMICA**

Eduardo Cleto Pires - USP/São Carlos

- **CONVECÇÃO FORÇADA**

Carlos Alberto Carrasco Altemani - UNICAMP

- **CONVECÇÃO NATURAL**

Genésio José Menon - EFEI

- **ESCOAMENTO BIFÍSICO**

Mário Roberto Granziera - IPT

- **ESCOAMENTO DE FLUIDOS E TRANSFERÊNCIA DE CALOR E DE MASSA EM EXPLOTAÇÃO E PRODUÇÃO DE PETRÓLEO**

Kelson V. Serra - UNICAMP

- **ESCOAMENTO E TRANSFERÊNCIA DE CALOR EM ALTAS VELOCIDADES**

Paulo Moraer Jr. - IAE/CTA

- **ESCOAMENTO E TRANSFERÊNCIA DE CALOR EM PROCESSOS METALÚRGICOS**

Eloi Fernandez y Fernandez - PUC/RJ

- **EQUIPAMENTOS TÉRMICOS: TROCADORES DE CALOR, CALDEIRAS E FONOS**

Nísio C. L. Brum - COPPE/UFRJ

- **FENÔMENOS DE TRANSPORTE EM SANEAMENTO E SISTEMAS DE CONSERVAÇÃO AMBIENTAL**

Marcius F. Giorgetti - USP/So Carlos

- **FONTES ALTERNATIVAS DE ENERGIA**

Everaldo A.N. Feitosa - UFPe

- **HIDRODINÂMICA E ESCOAMENTOS POTENCIAIS**

Antônio Francisco Parentes Fortes - UnB

- **INSTRUMENTAÇÃO E TÉCNICAS EXPERIMENTAIS**

Luís Fernando Alzuguir Azevedo - PUC/RJ

- **INTENSIFICAÇÃO DE TRANSFERÊNCIA DE CALOR**

Francisco M. Saboya - PUC/RJ

- **LUBRIFICAÇÃO**

Carlos Roberto Ribeiro - UFU

- **MÁQUINAS TÊRMICAS: TURBINAS, MOTORES E COMPRESSORES**

José Alberto dos Reis Parisi - PUC/RJ

- **MEIOS POROSOS**

Osvair Vidal Trevisan - UNICAMP

- **MÉTODOS ANALÍTICOS**

Sérgio Colle - UFSC

- **MÉTODOS COMPUTACIONAIS**

Ângela Ourivio Nieckele - PUC/RJ

- **PLANEJAMENTO ENERGÉTICO**

Sérgio Valdir Bajay - UNICAMP

- **PROPRIEDADES TERMOFLUIDODINÂMICAS**

Joaquim de Sylos Cintra Filho - UFSC

- **PROPULSÃO**

Nivaldo J. N. Hinckel - INPE

- **RADIAÇÃO EM MEIOS PARTICIPANTES E NÃO PARTICIPANTES**

Pedro Carajilescov - PUC/RJ

- **REFRIGERÇÃO, AR CONDICIONADO E BOMBAS DE CALOR**

Rogéro Tadeu da Silva Ferreira - UFSC

- **REOLOGIA**

Marco Van Hombeeck - CENPES/Petrobrás

- **SISTEMAS E EQUIPAMENTOS HIDRÁULICOS E MÁQUINAS DE FLUXO**

Vilson C. da S. Ferreira - UFRGS

- **TERMOHIDRÁULICA DE REATORES**

Marcelo José dos Santos Lemos - ITA/CTA

- **TRANSFERNCIA DE CARLOS EM SISTEMAS REATIVOS**

José Teixeira Freire - UFSCar

- **TRANSFERNCIA DE CALOR COM MUDANÇA DE FASE**

José Maria Saiz Jabardo - USP/So Carlos

- **TRANSFERNCIA DE MASSA**

Theo Guenter Keickbusch - UNICAMP

REVISORES
(REFEREES)

Alberto Luis de Andrade – FEQ/UNICAMP
Alcir de Faro Orlando – PUC/RJ
Alfredo de Almeida Vitali – ITA/CTA
Álvaro Toubes Prata – UFSC
André Luiz Seixlack – UNESP
Ângela Ourivio Nieckele – PUC/RJ
Antônio Cândido Faleiros – ITA/CTA
Antônio Cláudio de França Corrêa – UNICAMP
Antônio Fábio Carvalho da Silva – UFSC
Antônio José de A. Meirelles – FEA/UNICAMP
Antônio Mac Dowell de Figueiredo – COPPE/UFRJ
Antônio Santos Vargas – PUC/RJ
Átila Pantaleão Silva Freire – COPPE/UFRJ
Augusto César Galeão – LNCC
Bernadino Pereira Neto – UFPa
Carl Herrman Weis – ITA/CTA
Carlos Alberto de Almeida – PUC/RJ
Carlos Alberto Ferrari – UNICAMP
Carlos Alberto Gaspareto – FEA/UNICAMP
Caros Edilson Maneschy – PUC/RJ
Carlos Valois Maciel Braga – PUC/RJ
Cesar Santana - UNICAMP
Cirus Macedo Hackenberg – COPPE/UFRJ
Cláudio Melo – UFSC
Clóvis Raimundo Maliska – UFSC
Darcy das Neves Nobre – INPE/IME
David Zylbersztajn – USP
Douglas Lauria – EEM
Durval Henriques da Silva Filho – EMBRAER
Edson Luiz Zaparoli – ITA/CTA
Eduardo A. Gomes Pereira – SICOM
Eduardo Mach Queiroz – UFRJ
Emanuel Rocha Woiski – UNESP
Euclides Carvalho Fernandes – ITA/CTA
Eugênio Spano Rosa – UNICAMP
Evaristo Chalbaud B. Júnior – COPPE/UFRJ
Fred Nitzsche – EMBRAER
Francisco Domingues Alves de Souza – IPT
Francisco Eduardo Mourão Saboya – PUC/RJ
Geraldo Lombardi – EESC/USP
Giulio Massarani – COPPE/UFRJ
Gordiano Faria Alvim Filho – ITA/CTA
Harry Edmar Schulz – EESC/USP
Heraldo da Silva Couto – INPE
Jacek Piotr Gorecki – ITA/CTA
Jayme Pinto Ortiz – EPUSP
Jerônimo dos Santos Travelho – INPE
Jesus A. Costa Jr. – PUC/RJ
Jerzy Tadeusz Sielawa – INPE
João Andrade de Carvalho Júnior – INPE
João Augusto Ribeiro Fontoura – PROMON
João Francisco Escobedo – UNESP
João Luiz Filgueiras de Azevedo – IAE/CTA
Jorge Isaias Llagostera Beltrán - UNICAMP
José Alberto dos Reis Parise – PUC/RJ
José de Anchieta Rodrigues – UFSCar
José Faria Telles – ITA/CTA
José Gobbo Ferreira
José Maurício Gurgel - UFPb
José Ricardo Figueiredo – UNICAMP
José Roberto D. Finzer = DEQ/UFU
José Teixeira Freire – DEQ/UFSCar
Júlio César Passos – COPPE/UFRJ
Kamal A. R. Ismail - UNICAMP
Leonardo Goldstein Júnior – UNICAMP
Luís Augusto Barbosa – UNICAMP
Luís Felipe Mendes de Moura – FEM/UNICAMP
Luís Fernando Alzuguir Azevedo – PUC/RJ
M. Fabbri – INPE
Maher Nars Bismarck Nars – EMBRAER
Marcelo J. S. de Lemos – ITA/CTA
Márcio José do Prado Schmidt – ITA/CTA
Marco Antônio Guglielmo Cechini – ITA/CTA
Marco Aurélio Ferreira – INPE
Marcos Aurélio Ortega – ITA/CTA
Marcus A. V. Duarte – UFU
Marcos M. Pimenta – EPUSP
Maria Ângela De A. M. Petenate – FEA/UNICAMP
Maria Elisa Helene – USP
Mauri Fortes – UFMG
Maurício Pazini Brandão – ITA/CTA
Miguel Hiroo Hirata – COPPE/UFRJ
Nide G.C.R. Fico Júnior – CTA
Nehemias Lima Lacerda – ITA/CTA
Nilton Mori – UNICAMP
Nisio de Carvalho Lobo Brum – COPPE/UFRJ
Nivaldo Hinckel – INPE
Paulo Cesar de Camargo – UFSCar
Paulo César Philippi – UFSC
Paulo de Barros Correia – UNICAMP
Paulo Magalhães Filho – FEG/UNESP
Paulo Murillo de Souza Araújo – PUC/RJ
Paulo Moraes Júnior – IAE/CTA
Paulo Roberto de Souza Mendes – PUC/RJ
Pedro Carajilescov – PUC/RJ
Philemon de Mello Cunha – PUC/RJ
Renato Machado Cotta – COPPE/UFRJ
Roberaldo Carvalho de Souza – UFAL
Roberto Lamberts – UFSC
Roberto D.M. Garcia – CTA
Roberto da Mota Girardi – ITA/CTA
Rogério Klüppel – UFPb
Rogério Martins Saldanha da Gama – LNCC
Rogério Tadeu da Silva Ferreira – UFSC
Sérgio Braga – PUC/RJ
Sérgio Leal Braga – PUC/RJ
Sérgio Mourão Saboya – ITA/CTA
Sérgio V. Möller – COPPE/UFRJ
Sidney Lage Nogueira – CTA
Sidney Paciornik
Silvia Azucena Nebra de Perez – UNICAMP
Sílvio Carlos Anibal de Almeida – UFRJ
Sinclair Mallet-Guy Guerra – UNICAMP
Theo Guenter Kieckbusch – UNICAMP
Toshio Hattori – ITA/CTA
Toshiaki Yoshino – CTA/IAE
Vilson Carlos da Silva Ferreira – UFRGS
Washington Braga Filho – PUC/RJ
Wilson Sérgio Venturini – EESC/USP
Woodrow Nelson Lopes Roma – EESC/USP

ACKNOWLEDGEMENTS

We are grateful to the area coordinators for their work in taking care of the revision process and for the reviewers in selecting the papers and making suggestions for improvements. We also acknowledge the professional help of the International Representative, Dr. Ramesh K. Shah, for announcing ENCIT 90 outside Brazil.

Special thanks are due to our guests for their invited lectures and short courses.

- **Invited Lectures**

  "Biological Applications of Fluid Mechanics"
  Sir James Lighthill – University College of London

  "Transport Phenomena in Metals Processing"
  Professor Julian Szekely – MIT

  "Recent Advances in Thermal Comfort"
  Dr. Bjarme W. Olesen – Bruel & Kjaer

- **Short Courses**

  "Some Recent Advances in Computational Heat Transfer and Fluid Flow"
  Professor B. R. Baliga – McGill University

  "CFC's – Perspectives and Alternatives"
  Dr. David Didion – National Bureau of Standards

  "Design and Analysis of Heat Exchangers"
  Dr. Ramesh K. Shah – General Motors Co.

  "Introduction to Vector Processing"
  Dr. Rad Olson – IBM

We greatly appreciate the financial support provided by ours sponsors: Federal University of Santa Catarina, State Secretary of Science and Technology of Santa Catarina, CNPq, FINEP, BRASTEMP, CONSUL, EMBRACO, IBM, SPRINGER-CARRIER and TUPY.

Finally, our thanks go to the staff and students of the Mechanical Engineering Department of the Federal University of Santa Catarina for their help.

Organizing Committee

EDITORIAL

In December of 1985, during the Brazilian Congress of Mechanical Engineering (COBEM), held in São José dos Campos, SP, the brazilian thermal science community decided to organize a separate meeting in the thermal science area. The motivation to have an event in this area was that the COBEM, the main forum used so far, had become too large do allow a close interaction among participants. The expectation was that with a smaller meeting it would be possible to promote deeper discussions on scientific and engineering problems related to the area, and to identify trends to be pursued by our community.

In this spirit, the first Brazilian Thermal Sciences Meeting (Encontro Nacional de Ciências Térmicas) was held in Rio de Janeiro in December 1986. Sixty one refereed research papers were presented and published in the proceedings. The event fulfilled the original expectation, and in a general assembly, it was decided to constitute the Thermal Sciences Committee of the Brazilian Society of Mechanical Sciences, which from then on has been very active. Additionally, it was also decided that a thermal sciences meeting was to be organized every other year. The ENCIT 88 was then held during December 6-8 in Águas de Lindóia, SP. Ninety four papers were presented and published in the conference proceedings. This represented a substancial growth and encouraged those engaged in promoting the fields of thermal and fluid sciences and engineering.

The papers included in these two volumes were presented at ENCIT 90, held in Itapema, SC, during December 9-12. For this meeting an approach different than that employed in the first two events was adopted. In order to have an event covering a broad scope in the thermal and fluid fields, and to bring together engineers and scientist from branches other than mechanical engineering, thirty five areas were selected. These areas were coordinated by leading scientists having chemical, petroleum, environmental, food science, aerospace, nuclear and civil engineering background. Additionally, an internacional representative was chosen to promote ENCIT 90 outside Brazil. A joint effort of the coordinators and of the international representative resulted in 216 accepted papers, a number well beyond our original expectation. Around 25 per cent of the papers came from abroad, indicating that the event has started its way in becoming an international congress.

ÍNDICE / CONTENTS

CONDUÇÃO DE CALOR
HEAT CONDUCTION

RADIAÇÃO TÉRMICA
THERMAL RADIATION

CONVECÇÃO NATURAL
NATURAL CONVECTION

CONVECÇÃO FORÇADA
FORCED CONVECTION.

AERODINÂMICA
AERODYNAMICS

ESCOAMENTO E TRANSFERÊNCIA DE CALOR A ALTAS VELOCIDADES
HIGH SPEED FLUID AND HEAT TRANSFER

ESCOAMENTO E TRANSFERÊNCIA DE CALOR EM REGIME TURBULENTO
TURBULENT FLUID FLOW AND HEAT TRANSFER

CAMADA LIMITE TURBULENTA
TURBULENT BOUNDARY LAYER

MÉTODOS ANALÍTICOS
ANALYTICAL METHODS

VOLUMES FINITOS EM ESCOAMENTOS DE FLUIDOS E TRANSFERÊNCIA DE CALOR
FINITE VOLUME METHODS IN FLUID FLOW AND HEAT TRANSFER

ELEMENTOS FINITOS E ELEMENTOS DE CONTORNO EM ESCOAMENTO DE FLUIDOS E TRANSFERÊNCIA DE CALOR
FINITE AND BOUNDARY ELEMENT METHODS IN FLUID FLOW AND HEAT TRANSFER

INSTRUMENTAÇÃO E TÉCNICAS EXPERIMENTAIS
INSTRUMENTATION AND EXPERIMENTAL TECHNIQUES

REOLOGIA
RHEOLOGY

LUBRIFICAÇÃO
LUBRICATION

TRANSFERÊNCIA DE MASSA
MASS TRANSFER

TRANSFERÊNCIA DE CALOR EM SISTEMAS BIFÁSICOS
HEAT TRANSFER IN TWO-PHASE FLOW

MEIOS POROSOS
POROUS MEDIA

TUBOS DE CALOR
HEAT PIPES

TRANSFERÊNCIA DE CALOR COM MUDANÇA DE FASE
PHASE CHANGE HEAT TRANSFER

TRANSFERÊNCIA DE CALOR EM LEITOS FIXOS
HEAT TRANSFER IN PACKED BEDS

ESCOAMENTO E TRANSFERÊNCIA DE CALOR EM LEITOS MÓVEIS
FLUID FLOW AND HEAT TRANSFER IN FLUIDIZED BEDS.

COMBUSTÃO
COMBUSTION

MOTORES DE COMBUSTÃO INTERNA
INTERNAL COMBUSTION ENGINES

PROPULSÃO
PROPULSION

REFRIGERAÇÃO E AR CONDICIONADO
REFRIGERATION AND AIR CONDITIONING

SISTEMAS TÉRMICOS
THERMAL SYSTEMS

TROCADORES DE CALOR
HEAT EXCHANGERS

COMPORTAMENTO TÉRMICO DE EDIFICAÇÔES
THERMAL BEHAVIOUR OF BUILDINGS

PLANEJAMENTO ENERGÉTICO
ENERGY PLANNING

ENERGIA SOLAR
SOLAR ENERGY

ANÁLISE EXERGÉTICA
EXERGY ANALYSIS

FENÔMENOS DE TRANSPORTE EM SISTEMAS DE SANEAMENTO AMBIENTAL
TRANSPORT PHENOMENA IN ENVIRONMENTAL SYSTEMS

ESCOAMENTO DE FLUIDOS E TRANSFERÊNCIA DE CALOR EM ENGENHARIA DE PETRÓLEO
FLUID FLOW AND HEAT TRANSFER IN PETROLEUM ENGINNERING

TÓPICOS ESPECIAIS EM ENGENHARIA E CIÊNCIAS TÉRMICAS E DE FLUIDOS

SPECIAL TOPICS IN THERMAL AND FLUID SCIENCE AND ENGINEERING

AUTORES / AUTHORS

D

E

F

G

H

I

J

K

L

M

N

O

P

Q

R

S

T

V

W

X

Z

III ENCIT – Itapema, SC (Dezembro 1990)

HEAT TRANSFER IN FINS WITH A PERIODIC SOURCE

E. MEDINA, F. MENDEZ AND C. TREVIÑO
Depto. Fluidos y Térmica
Facultad de Ingeniería, UNAM
México, D. F., 04510
MEXICO

ABSTRACT

The non-linear transient response of a quasi one-dimensional model for heat transfer in fins with a periodic source is analyzed in this paper using both asymptotic techniques as well as numerical methods based in spectral techniques. In the asymptotic analysis, a perturbation method is employed using the inverse of the non-dimensional frequency of the heat source as the small parameter of expansion. An asymptotic solution is obtained for the heat flux at the fin base using the Green function. In the numerical part, the Chebyshev orthogonal polynomials are employed and the non-linear terms are calculated using the Fast Fourier Transform routine.

INTRODUCTION

The transient response of fins is of importance in many applications in heat transfer equipment. For thin fins, the heat transfer process in the upper and lower surfaces can be modelled in the energy equations with a sink proportional to the local temperature elevated to some power. The transient response for a convecting fin (linear dependence) has been analyzed in several works [1-4]. The exponent may take values of 0.75, 1, 1.25, 3.0 and 4 when the fin is cooled by film boiling, natural convection, forced convection, nucleate boiling and radiation [5].

In order to solve the non-linear equations, several approaches have been undertaken. Finite-difference methods as well finite element methods have been used in several works [6, 7]. Perturbation as well as other approximate techniques have been also introduced in the analysis of the heat transfer processes in thin fins [4,8,9]. Aziz and Na [8] used a perturbation technique in the study of the heat transfer process of periodic temperature at the fin base and variable thermal properties. The amplitude of the temperature oscillations are assumed to be small with the mean value at the fin base. Aziz and Na [4] used a coordinate expansion technique in order to study the transient response of thin fins for small values of the non-dimensional times. Chang et al. [9] used the linear approximation of the non-linear equations with the aid of variational methods.

The main objective of the present paper is to obtain an approximate solution for the heat flux at the fin base with a periodic source using both asymptotic techniques for large frequency of the heating source and spectral techniques.

ANALYSIS

We consider the pseudo-one dimensional heat conduction process in a thin straight fin of uniform thickness and finite length. At time t=0, the temperature at the base of the fin changes abruptly from the ambient temperature to a higher temperature oscillating around a mean value with a known amplitude and frequency. It has been assumed that the heat transfer rates at the lower and upper surfaces of the fin can be modelled with a power law type of dependence on the temperature [1, 9]. The non-dimensional energy equation takes the form

$$\partial^2\Theta/\partial x^2 - D\,\Theta^{\beta} = \partial\Theta/\partial\tau \qquad (1)$$

where the parameter D and the non-dimensional variables can be defined in different forms depending on the dominant heat transfer mechanism assumed in both surfaces of the fin [1-4, 9]. The value for the exponent β also changes depending on this heat transfer mechanism. In equation (1), Θ represents the non-dimensional temperature and is assumed to be proportional to the temperature diference with the ambient., x is the normalized longitudinal coordinate, with x=0 being the fin base. τ corresponds to the non-dimensional time. The initial and boundary conditions are given by

$$\Theta(0,\tau)=1+\alpha\ \mathrm{Sin}(\omega\tau),\quad \Theta(x,0)=\Theta(1,\tau)=0 \qquad (2)$$

The solution to eqs. (1) and (2) can be obtained after splitting the final steady-state and oscillatory parts as

$$\Theta = \Theta_e(x) + \phi\ (x,\tau) \qquad (3)$$

The energy balance equation (1) then takes the form

$$d^2\Theta_e/dx^2 - D\,\Theta_e^{\beta} = 0 \qquad (4)$$

$$\partial^2\phi/\partial x^2 - D\,[(\Theta_e+\phi)^{\beta} - \Theta_e^{\beta}] = \partial\phi/\partial\tau \qquad (5)$$

with the initial and boundary conditions

$$\Theta_e(0) = 1;\ \Theta_e(1) = 0 \qquad (6)$$

$$\phi(x,0)=-\Theta_e(x);\ \phi(1,\tau)=0;\ \phi(0,\tau) = \alpha\ \mathrm{Sin}\ (\omega\tau) \qquad (7)$$

For large values of D, that is for semi-infinite fins, the solution of eqs. (3) and (6) is given by

$$\Theta_e = [1+(\beta-1)\ \sqrt{D/2(\beta+1)}\,x]^{-2/(\beta-1)},\ \text{for}\ \beta>1 \qquad (8)$$

$$\Theta_e = \exp\ (-\sqrt{D}\ x),\ \text{for}\ \beta=1$$

Introducing the following variables

$$\sigma = \omega\,\tau;\quad \xi = \sqrt{\omega}\ x \qquad (9)$$

The energy equation for the oscillatory part (5) transforms to

$$\partial^2\phi/\partial\xi^2 - \partial\phi/\partial\sigma = \varepsilon\ [(\Theta_e+\phi)^{\beta} - \Theta_e^{\beta}] \qquad (10)$$

where $\varepsilon = D/\omega$. In the following section we solve eq. (10) using a perturbation technique for the case of a heating source with large non-dimensional frequency.

ASYMPTOTIC SOLUTION FOR $\varepsilon \ll 1$

We assume a solution of eq. (10) of the form

$$\phi(\xi,\sigma) = \sum_{j=0}^{\infty} \varepsilon^j \phi_j(\xi,\sigma) \qquad (11)$$

Introducing the relation (11) into eq. (10), we obtain the following set of equations:

$$\text{Order } \varepsilon^0 \qquad L(\phi_o) = 0 \qquad (12)$$

$$\text{Order } \varepsilon^1 \qquad L(\phi_1) = (1+\phi_o)^{\beta} - 1 \qquad (13)$$

$$\text{Order } \varepsilon^2 \qquad L(\phi_2) = \beta\sqrt{2/(\beta+1)}\ \xi\ [1 - 1(1+\phi_o)^{\beta-1}] \qquad (14)$$

etc. Here L corresponds to the linear differential operator defined by

$$L[\ ] = \partial^2/\partial\xi^2 - \partial/\partial\sigma$$

with the initial and boundary conditions given by

$$\phi_o(\xi,0) = -\Theta_e(\xi);\ \phi_j(\xi,0) = 0 \text{ for } j > 0$$

$$\phi_o(0,\sigma) = \cos(\sigma);\ \phi_j(0,\sigma) = 0 \text{ for } j > 0 \qquad (15)$$

$$\phi_j(\infty,\sigma) = 0 \text{ for all } j$$

The solution of eq. (10) together with the appropriate initial and boundary conditions, is given by

$$\phi_o = -\mathrm{erf}(\xi/\sqrt{2\sigma}) + \alpha\ \mathrm{Re}\{\exp[i\sigma - (1+i)/\sqrt{2}\ \xi]\} \qquad (16)$$

where Re denotes the real part and i corresponds to the imaginary component, $i=\sqrt{-1}$. We are interested in the stationary oscillations of the non-dimensional temperature for large values of the non-dimensional time σ. In this case,

$$\phi_o \sim \alpha \exp(-\xi/\sqrt{2})\ \cos\ (\sigma - \xi/\sqrt{2}),\ \text{for } \sigma \to \infty \qquad (17)$$

The solution to eq. (13) with the corresponding boundary conditions can be given by

$$\phi_1 = -\int_o^{\sigma} d\sigma' \int_o^{\infty} G(\xi,\sigma|\xi',\sigma')\, g(\xi',\sigma')\, d\xi' \qquad (18)$$

where G correspond to the Green function

$$G(\xi,\sigma|\xi',\sigma') = \frac{1}{\sqrt{4\pi(\sigma-\sigma')}}\ \{\exp[-\frac{(\xi-\xi')^2}{4(\sigma-\sigma')}] - \exp[-\frac{(\xi+\xi')^2}{4(\sigma-\sigma')}]\} \qquad (19)$$

and g to the function

$$g(\xi'.\sigma') = \mathrm{Re}\{1+\alpha\ \exp[i\sigma' - (1+i)/\sqrt{2}\ \xi']\}^{\beta} - 1 \qquad (20)$$

The most important parameter to be obtained corresponds to the non-dimensional heat flux at the base fin given by

$$q = \partial\Theta/\partial x\big|_{x=0} = d\Theta_e/dx\big|_{x=0} + \sqrt{\omega}\ \partial\phi_o/\partial\xi\big|_{\xi=o}$$
$$+ D/\sqrt{\omega}\ \partial\phi_1/\partial\xi\big|_{\xi=o} + D^{3/2}/\omega\partial\phi_2/\partial\xi\big|_{\xi=o} + \ldots \qquad (21)$$

Therefore it is necessary to obtain the spatial derivative of the non-dimensional temperature evaluated at the fin base. After derivating eq. (18) with respect to ξ, at ξ=o, we obtain

$$\partial\phi_1/\partial\xi\big|_{\xi=o} = -\frac{1}{\sqrt{\pi}} \int_o^{\sigma} \frac{d\sigma'}{(\sigma-\sigma')^{3/2}} \int_o^{\infty} \xi' \exp[-\frac{\xi'^2}{4\pi(\sigma-\sigma')}]$$
$$[\{1+\alpha\ \exp[i\sigma' - (1+i)/\sqrt{2}\ \xi']\}^{\beta} - 1]\ d\xi' \qquad (22)$$

where the real part is implicit. For integer values of β, the binomial form is expressed by a number of finite terms involving the different powers. For simplicity, we take in the following lines a value of β= 2. Any extention to different integer values is straight forward. In this case, eq. (22) takes the form

$$\partial\phi_1/\partial\xi\big|_{\xi=o} = -\frac{\alpha}{\sqrt{\pi}} \int_o^{\sigma} \frac{d\sigma'}{(\sigma-\sigma')^{3/2}} \{2\exp[i\sigma] \int_o^{\infty} \chi\ \exp[-\chi^2/k - \chi(1+i)]\, d\chi$$
$$+ \alpha\ \exp[2i\sigma] \int_o^{\infty} \exp[-\chi^2/k - 2\chi(1+i)]\, d\chi\} \qquad (23)$$

Here, $\chi = \xi'/\sqrt{2}$ and $k = 2(\sigma-\sigma')$. After some manipulations, the asymptotic solution for large non-dimensional times of eq. (23) is given by

$$\partial\phi_1/\partial\xi\big|_{\xi=o} = -\alpha\ \cos(\sigma - \pi/4) - \alpha^2(1+\sqrt{9/2})\cos(2\sigma - \pi/4),\ \text{as } \sigma \to \infty \qquad (24)$$

Therefore, up to this approximation, the non-dimensional heat flux at the fin base is given by

$$q/\sqrt{\omega} = -\alpha\cos(\sigma+\pi/4) - \sqrt{2(\beta+1)}\sqrt{\varepsilon} - \alpha[\cos(\sigma - \pi/4)$$
$$+ \alpha(1+\sqrt{9/2})\cos[2(\sigma - \pi/2)]\varepsilon + 0(\varepsilon)^{3/2} \qquad (25)$$

NUMERICAL SOLUTION

In order to obtain the numerical solution of eqs. (1) and (2) using spectral techniques, we follow the guidelines given elsewhere [10]. We assume a solution of the form

$$\Theta(\eta,\tau) = \sum_{m=o}^{M} a_m(\tau)\ T_m(\eta) \qquad (26)$$

where $\eta = 2x - 1$, and T_m are the Chebyshev polynomials defined by

$$T_m(\eta) = \cos\ (m\alpha),\ \alpha = \cos^{-1}(\eta) \qquad (27)$$

and M is the maximum number of modes taken into account. The boundary conditions then take the form

$$\Theta(-1,\tau) = 1 + \alpha\sin(\omega\tau) \to \sum_{m=o}^{M} a_m(\tau) T_m(-1) = \sum_{m=o}^{M} a_m(\tau)(-1)^m = 1 + \alpha\sin(\omega\tau) \qquad (28)$$

$$\Theta(1,\tau) = 0 \to \sum_{m=o}^{M} a_m(\tau) T_m(1) = \sum_{m=o}^{M} a_m(\tau) = 0 \qquad (29)$$

Taking into account only N=M-2 modes and the two extra modes are used only to satisfy the boundary conditions as

$$a_{N+1} = 1/2 + \alpha/2\ \sin\ (\omega\tau) - \sum_{n=o}^{(N-1)/2} a_{2n}$$

$$a_{N+2} = -1/2 - \alpha/2\ \sin\ (\omega\tau) - \sum_{n=o}^{(N-1)/2} a_{2n+1} \qquad (30)$$

With these relationships, the energy equation then take the form

$$da_m/d\tau = 4/c_m \{ \sum_{\substack{p=m+2 \\ p+m \text{ even}}}^{N} p(p^2-m^2) a_p$$
$$+ (N+L+[(N+L)^2 - m\ ][(3/2-L) - \sum_{n=o}^{(N-1)/2} a_{2n+L-1}]\} - 2D\bar{\theta}_m^{\beta}/\pi c_m \qquad (31)$$

where c_o=2 and c_m=1 for m<0, L=1 for m even and L=2 for m odd. The last term in eq. (31) can be written as

$$\bar{\theta}_m^{\beta} = \int_{-1}^{1} \theta^{\beta} T_m (1-\eta^2)^{-1/2} d\eta = 2\pi \int_{o}^{1/2} \theta^{\beta} \cos(2\pi m\alpha)\, d\alpha \qquad (32)$$

The integral in eq. (32) is the Cosine Fourier transform of θ^{β}. Using finite difference for the time, eq. (31) takes the form

$$a_m(k+1) - 2\Delta\tau/c_m \sum_{\substack{p=m+2 \\ p+m \text{ even}}}^{N} p(p^2-m^2) a_p(k+1)$$

$$+2\Delta\tau/c_m (N+L)[(N+L)^2-m^2] \sum_{n=o}^{n-1/2} a_{2n+L-1}(k+1)$$

$$= 2\Delta\tau/c_m \sum_{\substack{p=m+2 \\ p+m \text{ even}}}^{N} p(p^2-m^2) a_p(k) + 4\Delta\tau (N+L) c_m [(N+L)^2-m^2]$$

$$x[(3/2-L) - \sum_{n=o} a_{2n+L-1}(k)/2] + a_m(k) - 2\Delta\tau D\bar{\theta}_m^{\beta}/\pi c_m \qquad (33)$$

In eq. (33) the index k and k+1 represents the solution at two different consecutive time steps. Eq. (33) represents a set of algebraic linear equations given by a full matrix. The non-linear term can be obtained through the Fast Fourier Transform routine. The most important parameter in this type of processes is the heat flux at the fin base. In non-dimensional variables is given by

$$\partial\theta/\partial x]_{\eta=-1} = 2\partial\theta/\partial\eta]_{\eta=-1} = 4 \sum_{m=o}^{M} T_m(-1)/c_m \sum_{\substack{p=m+1 \\ p+m \text{ odd}}}^{N} p a_p \qquad (34)$$

RESULTS

Fig. 1 different nondimensional temperature profiles for the case of a step change in the temperature at the fin base. The parameters used in these calculations are D=25 and β=2. The number of modes taken into account were 32. For larger number of modes the solution oscillates, indicating that some modes achieve the quasi steady-state behavior. Fig. 2 shows the nondimensional heat flux at the fin base as a function of the nondimensional time. Here, it is shown how the heat flux reaches asymptotically the steady-state condition. Practically this steady-state condition is achieved for values of τ of order of 10^{-1}. These results show that the spectral techniques are appropriate for the analysis of this type of heat transfer problems.

Fig. 3 and 4 show the temperature profiles and the non-dimensional heat flux at the fin base, respectively, for a representative case of α=0.1 and ω=10. More calculations have to be done in order to scan the parametric space. However, the main objective of this paper is to present some results using spectral techniques.

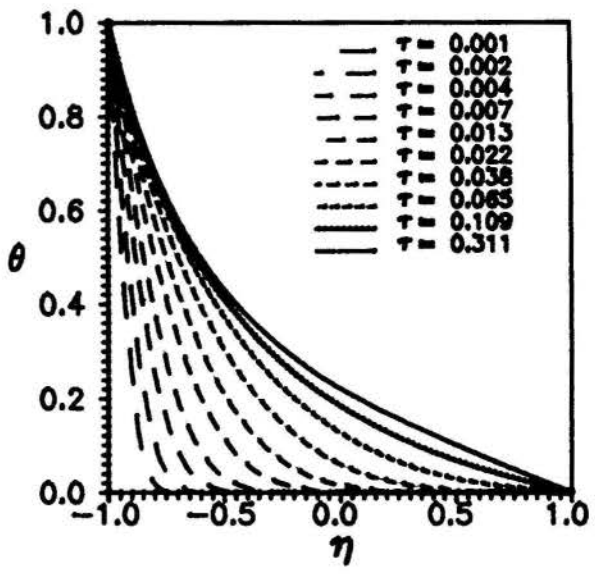

Fig. 1 Non-dimensional temperature profiles as a function of τ for β=2.

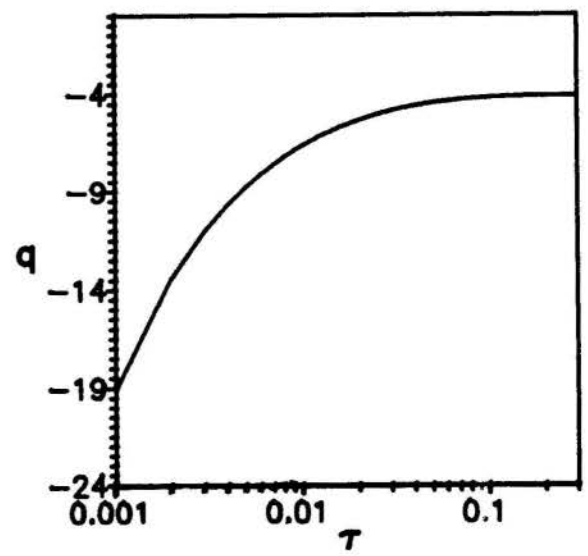

Fig. 2 Non-dimensional heat flux as a function of τ for β=2.

REFERENCES

1. A.B. Donaldson and A.R. Shouman, Unsteady-state temperature distribution in convecting fin of constant area. Appl. Sci. Res., 26, 75-85, 1972.
2. A.J. Chapman, Transient heat Conduction in annular fins of uniform thickness. Chem. Eng. Symp. Series, 55, 195-201, 1959.
3. N.V. Suryanarayana, Transient response of fins, J. Heat Transfer, 97C, 417-423, 1975.
4. A.Asiz and T.Y. Na. Trasient response of fins by coordinate perturbation expansion, Intern. Journal Heat Mass Transfer, 23, 1695-1698, 1980.
5. K.W. Haley and J.W. Westward, Boiling Heat Transfer from Single Fins, Proceedings of the International Heat Transfer Conference, 3, 245-253, 1966.
6. N.V. Suryanarayana, Two dimensional effects on the heat transfer Rates from an Array of Straight Fins. ASME Journal of Heat Transfer, 99, 129-132, 1977.
7. P.R. Stones. Ph. Thesis, Leeds University, England, 1980.
8. A. Aziz and T.Y. Na, Periodic Heat Transfer in Fins with Variable Thermal Parameters, Int. J. Heat and Mass Transfer, 24, 1397-1401, 1981.
9. Y.M. Chang. C.K. Chen and J.W. Cleaver, Transient Response of Fins by Optical Linearization and Variational Embedding Methods, ASME J. Heat Transfer, 104, 813-815, 1982.
10. D. Gottileb and S. Orszag, Numerical Analysis of Spectral Mehtods, SIAM, Philadelphia, USA. 1977.

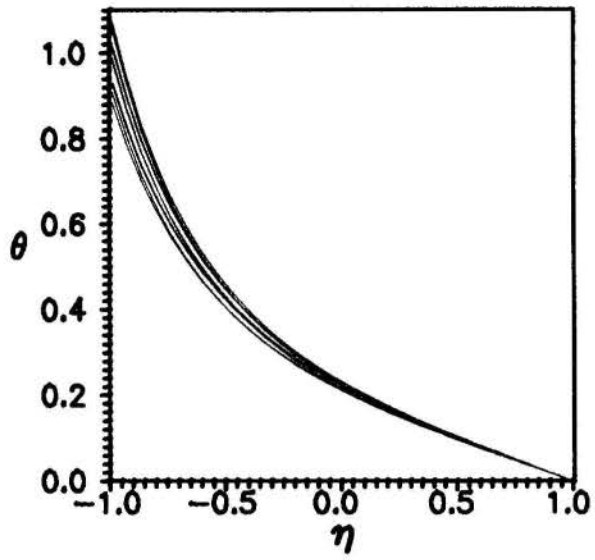

Fig. 3 Non-dimensional temperature profiles as a function of τ for α=.1 and ω=10.

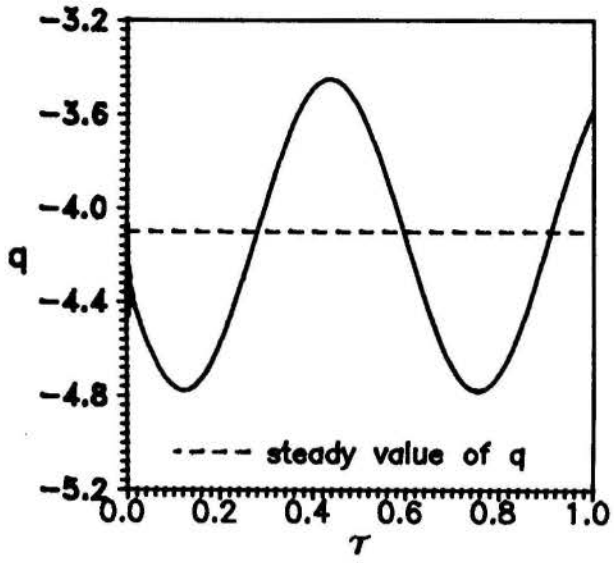

Fig. 4 Non-dimensional heat flux as a function of τ for α=.1 and ω=10.

III ENCIT – Itapema, SC (Dezembro 1990)

OTIMIZAÇÃO TERMODINÂMICA DE ALETA PINADA EXPOSTA A ESCOAMENTOS CRUZADOS

CEZAR OTAVIANO RIBEIRO NEGRÃO E SERGIO COLLE
Departamento de Engenharia Mecânica - UFSC
Caixa Postal 476
88049 - Florianópolis - SC

RESUMO

O presente trabalho propõe uma extensão da formulação de otimização termodinâmica de aletas tipo pino cilíndrico expostas a escoamentos cruzados, através da minimização da geração de entropia associada ao processo de transferência de calor, tendo como restrição o volume de material fixo. São apresentados resultados numéricos que ilustram a presente análise para valores numéricos de relações de aspecto para os quais a teoria de aleta é valida.

INTRODUÇÃO

Aletas como elementos promotores do aumento da transferência de calor entre uma superfície sólida e um escoamento de fluido, podem também provocar um significativo arrasto.

Portanto, as irreversibilidades inerentes ao processo de transferência de calor em aletas ocorrem tanto devido à diferença de temperatura entre a aleta e o fluido quanto a forças viscosas. Poulikakos e Bejan [2] apresentam a equação de geração de entropia dessas irreversibilidades como função do diâmetro e comprimento de aletas do tipo pino cilíndrico. Otimizaram (minimizaram) então a função objetiva da geração de entropia em relação ao diâmetro da aleta para um dado comprimento fixo, e vice-versa, ou seja, restrigem espaço físico disponível, quando fixam comprimento ou diâmetro.

Uma formulação alternativa consiste em considerar o volume de material consumido na fabricação da aleta constante. Sob o ponto de vista econômico, em escala maior, esta alternativa é equivalente a determinar as dimensões da aleta cilíndrica que minimize o custo operacional, este expresso por uma função de geração de entropia adequada, com custo de capital fixo.

Como será apresentado neste breve trabalho, o processo de otimização com restrição de volume constante tem como caso limite ótimo o ponto de ótimo absoluto determinado em [2], para cada valor numérico de parâmetro de projeto fixo.

FORMULAÇÃO

A entropia gerada pela presença de uma aleta em um escoamento é dividida em duas parcelas, a primeira das quais devida à irreversibilidade da transferência de calor e a outra devida à irreversibilidade da perturbação do escoamento.

A geração de entropia é expressa então pela equação:

$$\dot{S}gen = (\dot{S}gen)_{tf} + (\dot{S}gen)_{af} \qquad (1)$$

Fixando-se o fluxo de calor Q_B na base da aleta, pode-se provar que [2]:

$$\dot{S}gen = \frac{Q_B^2}{\pi/2\ T_\infty^2\ k\ D^2\ (\frac{h}{kD})^{1/2}\ tgh(g)} + \frac{\rho\ U_\infty^2\ L\ D\ C_D}{2\ T_\infty} \qquad (2)$$

onde, $g = 2\ (\frac{h}{kD})^{1/2}\ L$

cuja forma adimensional é a seguinte,

$$Ns = \frac{\dot{S}gen}{(Q_B^2 U_\infty / k\nu T_\infty^2)} = \frac{(k/\lambda)^{1/2}}{\pi/2\ Nu^{1/2}\ Re_D\ tgh(m)} + \frac{1}{2}\ B\ C_D\ Re_L\ Re_D \qquad (3)$$

onde, $m = 2\ Nu^{1/2}\ (\lambda/k)^{1/2}\ Re_L/Re_D$ e $B = \rho\nu^3 k T_\infty / Q_B^2$ é o parâmetro de projeto que avalia a importância relativa da irreversibilidade devido ao atrito sobre a irreversibilidade devida à transferência de calor.

Se o pino é esbelto (L/D > 5), o número de Nusselt e o coeficiente de arrasto para um cilindro exposto a escoamento transversal podem ser expressos respectivamente pelas correlações,

$$Nu = a\ Re_D^b\ Pr^{1/3} \qquad (4)$$

$$C_D = c\ Re_D^d \qquad (5)$$

onde, as constantes a, b, c e d são especificadas para diferentes faixas de Re_D [2].

Substituindo (4) e (5) em (3) tem-se:

$$Ns(Re_D, Re_L) = \frac{(k/\lambda)^{1/2}}{\pi/2\ a^{1/2}\ Re_D^{b/2+1}\ Pr^{1/6}\ tgh(f)} + \frac{1}{2}\ B\ c\ Re_D^{d+1}\ Re_L \qquad (6)$$

onde, $f = 2\ a^{1/2}\ Re_D^{b/2-1}\ Pr^{1/6}\ (\frac{\lambda}{k})^{1/2}\ Re_L$

A otimização proposta em [2], consiste em minimizar a equação (6) com relação a Re_D ou Re_L.

O volume da aleta expresso por,

$$V = \frac{\pi}{4}\ D^2\ L \qquad (7)$$

pode ser adimensionalizado na forma,

$$\alpha = \frac{V\ \nu^3}{\nu_\infty^3} = \frac{\pi}{4}\ Re_D^2\ Re_L \qquad (8)$$

Introduzindo agora o parâmetro α na equação (6) resulta,

$$Ns(Re_D, \alpha) = \frac{M/a^{1/2}}{\pi/2\ Re_D^{b/2+1}\ tgh(\eta)} + \frac{2}{\pi}\ c\ B\ Re_D^{d-1}\ \alpha \qquad (9)$$

onde, $M = \dfrac{(k/\lambda)^{1/2}}{Pr^{1/6}}$

$$\eta = \frac{8}{\pi}\ \frac{a^{1/2}}{M}\ Re^{b/2-3}\ \alpha$$

Através desta expressão pode-se ver que é possível a minimização do número de Reynolds referente ao diâmetro, para um dado α (volume adimensional) fixo ou alternativamente, em relação ao volume para um dado número de Reynolds fixo.

A derivação parcial da equação (9) relativamente a α, para cada Re_D fixo, resulta uma equação não-linear, que resolvida numericamente fornece uma raiz para α. Alternativamente, fixando-se α e derivando-se a equação (8) relativamente a Re_D, tem-se uma equação para a variável Re_D

RESULTADOS

Resultados ilustrativos são apresentados na figura (1). Esta figura mostra que a função Ns possui um mínimo em relação ao diâmetro da aleta, para volume e parâmetros referentes a propriedades físicas do ar e aleta e referentes ao processo de transferência de calor (M,B) fixos.

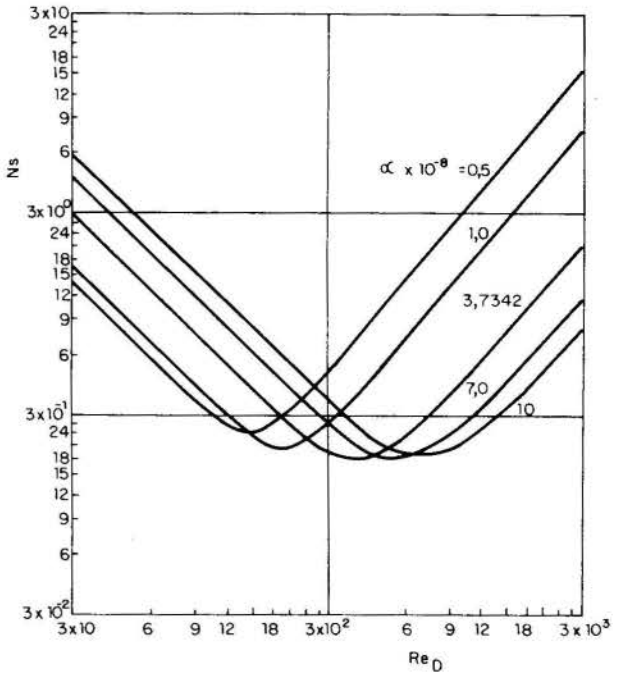

Fig. 1 Número de geração de entropia (Ns) em função do Re_D, para M = 100 e B = 10^{-7}. Valor de α ótimo igual a $3,7342 \times 10^{8}$

Na tabela (1) são apresentados parâmetros de ótimo absoluto para a geração de entropia Ns, onde os valores de Re_L foram obtidos da equação (8) para Re_D e α ótimos especificados. Como era esperado, existe um valor de α ótimo fixo que corresponde ao valor ótimo calculado em [2]. Para valores de α distintos de α ótimo (vide figura (1)), $Re_{D,ot}$ e Re_L não coincidem com os valores calculados em [2].

Ainda da tabela (1) pode-se ver que Ns cresce com o aumento de B.

Tabela 1. Valores ótimos para Re_D, α, Re_L, Ns e L/D para vários valores de B (M=100).

B	$Re_{D,ot}$	$\alpha_{ot} \times 10^{-5}$	Re_D	Ns	L/D
10^{-9}	2021,4	381627	11892	0,0300602	5,88
10^{-8}	876,09	37750,1	6262,3	0,0842765	7,15
10^{-7}	379,70	3734,20	3297,8	0,2362755	8,68
10^{-6}	164,56	369,384	1736,8	0,6624117	10,6
10^{-5}	71,322	36,5391	914,58	1,8571320	12,8
10^{-4}	27,785	3,02535	498,96	5,1454920	18,0

A presente teoria é válida para a relação L/D maiores que 5. Nem todos os valores de α são compatíveis com este limite. Os valores de α máximos abaixo dos quais L/D > 5,0, são apresentados na tabela (2), para M=100 e vários valores de parâmetro de projeto B.

Tabela 2. Valores máximos para α correspondentes a L/D=5 e $Re_{D,ot}$ para este α fixo com M=100.

B	$\alpha_{max} \times 10^{-6}$	$Re_{D,ot}$
10^{-14}	95100000	28929
10^{-13}	33500000	20432
10^{-12}	7860000	12602
10^{-11}	1515700	7280,8
10^{-10}	263800	4065,1
10^{-9}	47324	2292,7
10^{-8}	5906,2	1145,7
10^{-7}	723,08	568,90
10^{-6}	87,36	281,24
10^{-5}	10,457	138,60
10^{-4}	1,2435	68,156

CONCLUSÃO

Os resultados aqui apresentados ilustram o caso particular de otimização termodinâmica com restrição de volume fixo. A otimização sem restrições como aquela relatada em [2], fornece o valor do volume adimensional como resultado secundário. A otimização a volume constante aqui apresentada inclui a otimização absoluta como caso particular.

O parâmetro B representativo do peso da irreversibilidade devida à viscosidade em relação ao peso da irreversibilidade devida a transferência de calor deve ter o menor valor possível, para que o valor ótimo da geração de entropia seja pequeno. Em outras palavras, a diminuição da irreversibilidade viscosa e/ou aumento do fluxo térmico, contribuem para diminuir a geração de entropia ótima.

NOMENCLATURA

- B - $\rho\nu^3 kT\infty/Q_B^2$
- C_D - Coeficiente de arrasto (= $F_D/(1/2\rho U\infty^2 DL)$)
- D - Diâmetro da aleta
- F_D - Força de arrasto na aleta
- h - Coeficiente convectivo de transferência de calor entre aleta e fluido
- k - Condutividade térmica do fluido
- L - Comprimento da aleta.
- M - $(k/\lambda)^{1/2} / Pr^{1/6}$
- Ns - Número de geração de entropia (= $\dot{S}gen/(Q_B^2 U\infty/k\nu T\infty^2)$)
- Nu - Número de Nusselt (= hD/k)
- Pr - Número de Prandtl
- Q_B - Calor transferido através da base da aleta
- Re_D - Número de Reynolds referente ao diâmetro da aleta (= $U\infty D/\nu$)
- $Re_{D,ot}$ - Número de Reynolds ótimo referente ao diâmetro da aleta
- Re_L - Número de Reynolds referente ao comprimento da aleta (= $U\infty L/\nu$)
- $Re_{L,ot}$ - Número de Reynolds ótimo referente ao comprimento da aleta
- $\dot{S}gen$ - Geração de entropia
- $(\dot{S}gen)_{af}$ - Geração de entropia devida ao arrasto
- $(\dot{S}gen)_{tf}$ - Geração de entropia devido a transferência de calor
- $T\infty$ - Temperatura do fluido
- $U\infty$ - Velocidade do fluido
- V - Volume da aleta (= $\pi D^2 L/4$)
- α - Volume adimensional da aleta (= $V\nu^3/U\infty^3$)
- λ - Condutividade térmica do material da aleta
- ν - Viscosidade cinématica do fluido
- ρ - massa específica do fludo

REFERÊNCIAS

[1] Bejan, A., "Entropy Generation Through Heat and Fluid Flow", John Wiley & Sons, 1982.

[2] Poulikakos, D., Bejan, A., "Fin Geometry for Minimum Entropy Generation in Forced Convection," ASME Journal of Heat Transfer, vol. 104, pp. 616-623, 1982

ABSTRACT

This work reports the optimization of a cylindrical pin of constant volume exposed to a cross turbulent flow. The entropy generation is expressed as a sum of the entropy generation due to the heat transfer and driving force as usual. There is an optimum volume, which is the limit-point of the optimum found, when the diameter and the lenght of the pin are considered as independent optimization parameters.

III ENCIT – Itapema, SC (Dezembro 1990)

AN INVERSE METHOD APPLIED TO THERMAL CONDUCTIVITY MEASUREMENT OF COMPOSITE MATERIALS

MICHELE CALI, VALTER GIARETTO and GIUSEPPE RUSCICA
Dipartimento di Energetica del Politecnico di Torino
C.so Duca degli Abruzzi, 24
10124 - Torino - Italy

SUMMARY

The paper aims to study the behaviour of very low density materials to heat transmission due to rapid aging treatment and in extreme conditions of use, identifyng conductivity as a parameter of degradation. The experimental data are analyzed with an inverse method.

INTRODUCTION

Low density insulating materials, widely used in many sectors, are particularly suitable for use in the aeronautic and spatial industry due to low values of $\rho \cdot \lambda$ (a parameter which take account volume mass and heat transfer).

Nonetheless, all material used in space, including insulating materials used to protect the outer structure, are subject to particularly heavy stresses, above all if used in transport vehicles which pass from the earth's atmosphere to extremely hostile environments on repeated occasions during their lifetime and almost always with rapid temperature changes, reaching extreme conditions of use for a few minutes at a time.

The thermal characterisation of insulating materials following degradation in relation to the number of missions accomplished is one of the most important engineering assessment elements for their correct use; in fact the maintenance costs and the achievement of the project conditions, both in terms of temperature and in terms of thermal flows exchanged with the space environment, partly depend on them.

Since the studied phenomenon is cyclic, the most characteristic parameter is thermal conductivity; the problem of its experimental assessment in extreme conditions of use within relatively rapid time limits, and without damaging materials, remains to be solved. For this reason, stationary methods have been rejected in favour of transitory methods which can give the same information within a sufficiently short time, provided the appropriate methodology is identified.

The materials examined are not homogeneous and in general show a high degree of porosity; the use of local measuring methods, such as hot wire or flash methods (see [3]) are not thought suitable, since they would give rise to local assessments of thermal conductivity and give a false idea of the overall characteristics of the material.

The proposed method is based on Vernotte's idea (1937) of the "mirror image" realised by Beatty et al. (1960) as reported in [6]. It consists in recording the transient temperature on a plate placed between two identical flat, and even large size, test specimens which receive heat through their other two faces from a thermal source at a constant temperature.

The accuracy of experimental results essentially depends on the control of edge losses from the test specimens and from the heat sink. A methodology has been elaborated for the analysis and interpretation of results which we consider will enable us to overcome the above mentioned difficulties by realising a very simple experimental device using a guarded hot plate apparatus (GHP), built according to ISO/STANDARD DIS 8302 [4], that has also been used for a European standardisation programme, [7], and replacing the hot plate with a copper plate.

METHODOLOGY

A physical phenomenon may be considered well known if all necessary and sufficient quantities have been identified on the basis of existing knowledge on the subject to characterise it fully, and if these quantities can be correlated in a "**model**", that is a set of analytical relations which allows the phenomenon to be explained in the context of the theories and basic laws of physics.

All there physical quantities, which are correlated with one another in the model, are called "**parameters of the model**" in the following text. They may be classified into two main groups, one which includes all that "physically observable", namely those which can be directly measured, $<\mathbf{y}>$, and the other which includes all the others, $<\mathbf{b}>$ (see [1]).

If the term "solution of the model" is used to mean the mathematical procedures with which some parameters are obtained in relation to others, "**direct solutions**" are those procedures which allow some measurable quantities to be obtained in relation to others. "**Inverse solutions**", on the contrary, are the procedures which allow some of those quantities which are not directly observable, to be obtained in relation to all the others.

In the majority of the cases, the inverse solution is easy to obtain only in very simple geometric situations and configurations. For this reason, from an experimental point of view, it is necessary to elaborate procedures and apparatus in order to reproduce as far as possible the configurations for which simple solutions can be found, and concentrate attention on effective measurements.

For example, in the present case, which is aimed at the laboratory measurement of the thermal conductivity of a given material, the model comprises a basic equation of conduction in unsteady state conditions represented by a differential equation to partial derivatives and the relative boundary conditions.

The use of this model in the above experimental problem, with all the limits that this may entail, represents the ground on which all subsequent experimental activity is based, from the conception of the measuring procedure, to the design and testing of the equipment, and to the measuring process itself.

In this type of model the measurable quantities are normally the temperatures in some parts of the body, whereas non-measurable parameters are almost always the thermophysical characteristics of materials, the edge losses and the temperature distribution over the entire body.

In this study, we describe the use of a slightly different method of inquiry, based on the theory of Inverse Problems, as expounded in [1] and [2]. A rigourous mathematical treatment based on statistical calculations allows some of the approximations needed to resolve the model can be eliminated using more complex calculation procedures and paying special attention to the treatment of measuring errors; it is possible to reduce the complexity of the experimental procedure.

THE EXPERIMENTAL APPARATUS AND THE CALCULATION METHOD

The apparatus used is shown in Fig. 1. Two identical samples of the material, M, of 500 x 500 x 50 mm, are packaged with the copper plate R between them. When the package is placed in the cavity C, it is enclosed between the two plates L, maintained at a constant temperature T_1 by a fluid-controlled thermostatic system. The two samples are separated by a copper plate R, the package is enclosed in a cavity C, in which a thermostatic control system enables the temperature to be kept at a value of T_C.

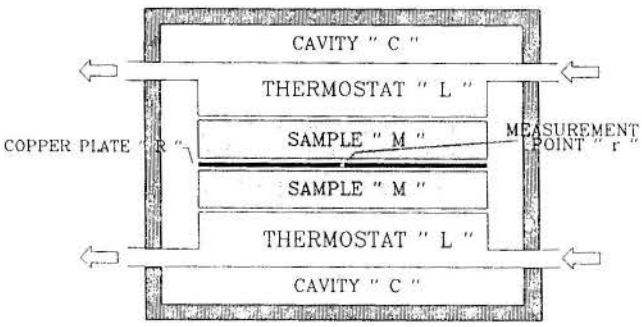

Fig. 1 - Experimental apparatus

For the tests the package is first brought to the ambient temperature T_0 in an environment in which it is kept for sufficient time to ensure a perfect spatial uniformity. When this condition is reached, it is rapidly transferred in the cavity C then producing a temperature step on the boundaries. The quantity measured is the temperature at point r of Fig. 1, recorded by an automatic data collection system.

The model was formulated, taking into account the symmetry of the apparatus, starting from the heat conduction equation with boundary conditions of equivalent convection (corresponding to convection + linearized radiation), and introducing the following simplified hypotheses:

a. The temperatures of plates L and cavity C are constant over time, whereas the starting temperature of the samples is uniform in every point.
b. The test material is isotropic.
c. Thermal conductivity can be considered independent from the temperature.
d. The thermal capacities are all concentrated in two points, m and r, which are representative of the samples and of the copper plate (so-called "lumped capacity" method).
e. The heat flow rate density exchanged by equivalent convection along the borders is described by an empirical relation of the type:

$$q = h \cdot (T - T_c) \qquad (1)$$

The heat transfer coefficient by equivalent convection and radiation is defined by:

$$h = m \cdot (T - T_c)^n \qquad (2)$$

where $<m>$ and $<n>$ are two constant parameters to be determined and T_C is the cavity temperature which is known a priori.

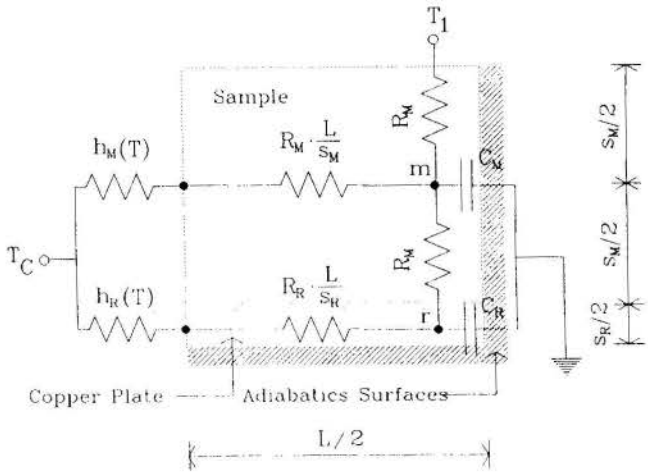

Fig. 2 - Analog model

The equivalent electric network is shown in Fig. 2. The direct model is represented by the set of ordinary differential equations (the bold letters means vectors and matrices):

$$\frac{d\mathbf{T}}{dt} = \mathbf{A} \cdot \mathbf{T} + \mathbf{B} \qquad (3)$$

A more detailed expression of (3) is given in Appendix A. The solutions of eq. (3) gives the temperatures versus time at points m and r for fixed values of thermal conductivity, of the heat capacity of materials, of their geometric dimensions, and of the temperatures of the thermostatic-controlled plates and the cavity.

The integration has been carried out using a numeric "predictor-corrector" method, which allows the values of temperatures at points m and r to be calculated at the generic i-th instant of time, in relation to the values of temperatures at the previous instances and to values assumed by parameters, thus obtaining a recursive expression of the type:

$$\mathbf{T}_i = \mathbf{T}_{i-1} + g_i(T_0, \mathbf{T}_1, \cdots, \mathbf{T}_{i-1}, \mathbf{b}) = f_i(T_0, \mathbf{T}_1, \cdots, \mathbf{T}_{i-1}, \mathbf{b}) \qquad (4)$$

where **T** is the vector of temperatures of points m and r.

We assume that **Y** and **T** are two vectors whose N elements are respectively the measured and calculated temperatures in the time during the experiment; **b** is the vector of the parameter to be determined. Vector **e** is the error defined by the equation:

$$\mathbf{e}_i(\mathbf{b}) = Y_i - T_i(\mathbf{b}) \qquad \forall i = [1, \ldots, N] \qquad (5)$$

From the theory of inverse problems it is known that the best possible estimate of parameters is that which maximises the probability distribution of the parameters and minimises the expression (vectorial notation):

$$S = \mathbf{e}^T(\mathbf{b}) \cdot \mathbf{W}^{-1} \cdot \mathbf{e}(\mathbf{b}) \qquad (6)$$

Where **W** is the co-variance matrix of experimental data, dimensions (NxN), whose terms on the diagonal contain the squares of the errors of measurements.

The temperature calculated by equation (4) is a non-linear function of the parameters to be assessed so it is necessary to use an iterating algorithm for the solution. It can be seen that, if an estimated value of parameters $\mathbf{b}^{(k)}$ is known, equation (4) can be developed in Taylor's series around this value, stopping at the first term; the following is then obtained:

$$T^{(k+1)} = T^{(k)} + X(b^{(k)}) \cdot (b^{(k+1)} - b^{(k)}) \qquad (7)$$

X is the gradient or "sensitivity" matrix, likewise a non-linear function of the parameters.

Differentiating (6) in relation to the parameters, and taking into account (4) which is equal to zero, after a few steps we obtain:

$$b^{(k+1)} = b^{(k)} + P^{(k)} \cdot H^{(k)} \qquad (8)$$

Where:

$$P^{(k)} = X^T(b^{(k)}) \cdot W^{-1} \cdot X(b^{(k)}) \qquad (9)$$

$$H^{(k)} = X^T(b^{(k)}) \cdot W^{-1} \cdot [Y - T(b^{(k)})] \qquad (10)$$

The new values of the parameters can be calculated iteratively by relations from (8) to (10), until the norm of the differences is within a preestablished value.

At the end of the iterative procedure, it is possible to estimate the average standard deviation of each parameter with the relation:

$$\sigma_p = \sqrt{P_{pp}} \qquad (11)$$

EXPERIMENTAL RESULTS

The measured values are the temperatures at point r in Fig. 1. Four different materials were tested, indicated as A, B, C, and D, their main physical characteristics are shown in Tables Ia ÷ Ic (Appendix B).

Material A, which did not undergo aging cycles, was used as a reference to control the validity of the mathematical model and of the parameter estimation method. Since the value of conductivity was measured with a high accuracy in the steady state conditions in a comparative experiment between different European laboratories (see [3]), it was possible to estimate coefficients $<m>$ and $<n>$ of equation (2) as parameters.

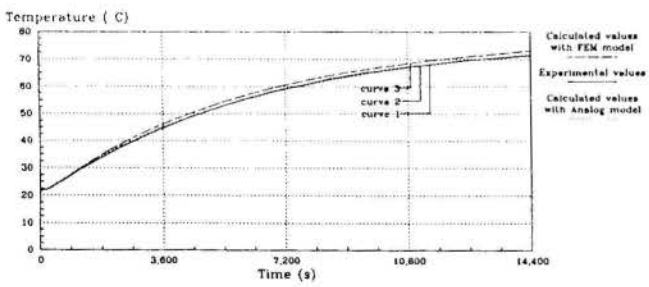

Fig. 3 - Comparison between experimental and calculated values

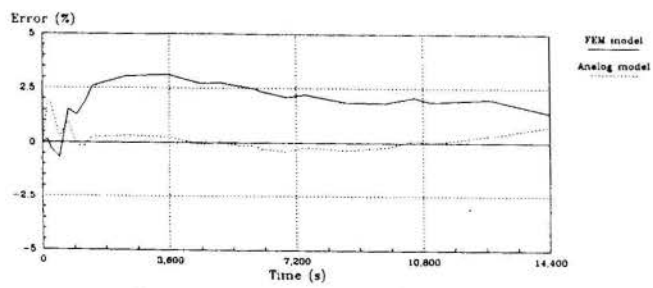

Fig. 4 - Errors of the simulation models

Fig. 3 shows for this materials the temperatures respectively measured (curve 1), calculated by the lumped parameter model (curve 2) and calculated by a FEM programme (curve 3), with the known $<m>$ and $<n>$ parameters as boundary conditions.

The Fig. 4 shows the percentage deviation in both cases between the calculated and measured values. Table II (Appendix A) shows the parameters values $<m>$ and $<n>$, obtained using the same procedure, for materials B, C and D, on the basis of known values at cycle 0 of the average steady state thermal conductivity in the interval 20 ÷ 80 °C.

The materials were subjected to repeated accelerated aging cycles, each of which involves heating and cooling, and humidification and drying operations, starting from the original conditions according to procedure III, Aggravated, of regulations [5]. At the end of each cycle, the samples were heated to a temperature of 105 °C, then brought back to room temperature before being placed in the testing apparatus to measure conductivity using the procedure described above.

Calculations, of thermal conductivity, were performed using the above procedure in two phases. In the first, the error of experimental apparatus was assessed as:

$$\sigma_\lambda = 6.25 \cdot 10^{-2} \quad °C \qquad (12)$$

thus obtaining matrix **W**. The results obtained for the different cycles are reported in Table III (Appendix A).

In order to extrapolate the results at a different number of cycles to that effectively performed, conductivity values for each material were represented by a simple regression equation which is valid only for integers values of the cycle index number j:

$$\lambda_j = \lambda_0 + \Delta\lambda \cdot \exp\left(-\frac{\alpha}{j}\right) \qquad (13)$$

where λ_0 is the thermal conductivity measured before carrying out the aging cycles, $\Delta\lambda$ and α are two constants to be determined by the best fitting with the least square technique.

The values of $\Delta\lambda$ in Table IV also represent the estimated degradation undergone by the materials for an infinite number of cycles.

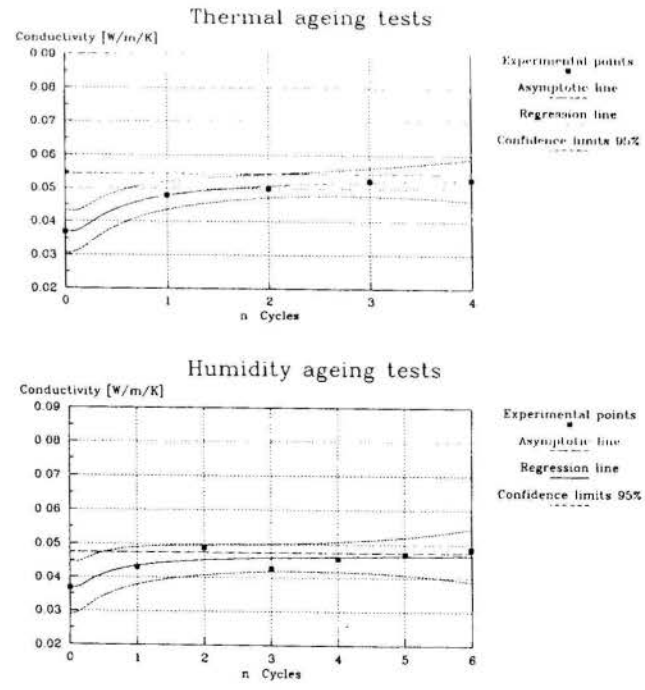

Fig. 5 - SAMPLE B: Thermal conductivity degradation

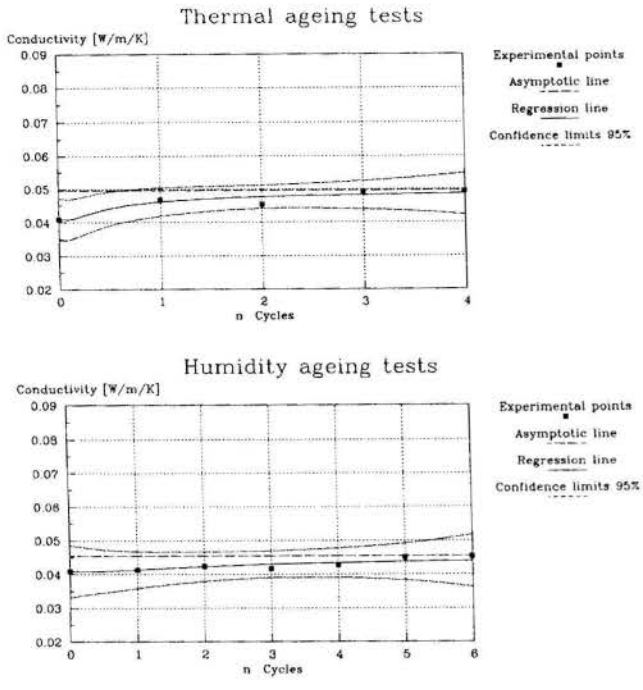

Fig. 6 - SAMPLE C: Thermal conductivity degradation

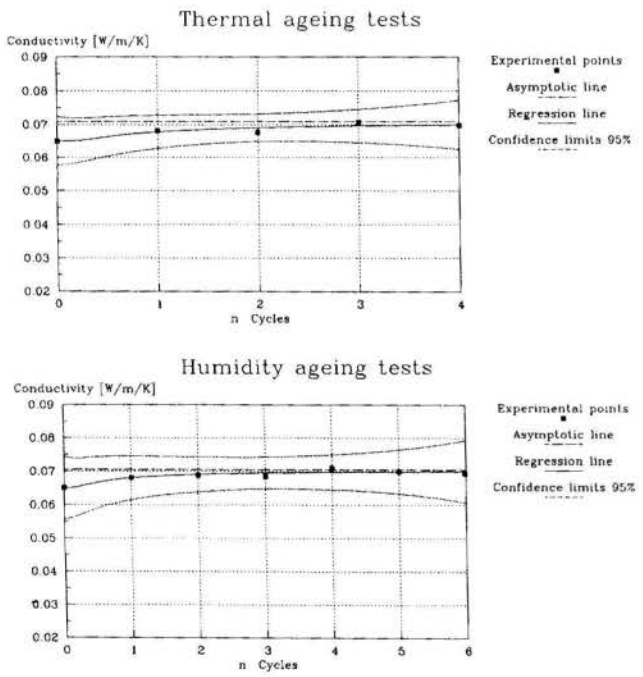

Fig. 7 - SAMPLE D: Thermal conductivity degradation

In figs. 5 ÷ 7 are shown the estimated conductivity values, the best fit curves obtained with (13) and the 95% confidence limits assessed using Student's t distribution according to the relation:

$$\lambda = \lambda_j \pm t_{1-a/2} \cdot (N-2) \cdot s_\lambda \qquad (14)$$

where a = 5%, N is the observations number and s_λ the standard error of the estimate.

Where compatible with the size of the statistical sample and in relation to the established confidence interval, it is possible to conclude that the regressions obtained are significant: in fact, it can be seen that all the estimated points fall within the confidence range. It follows that the expected behaviour of the materials in the aging tests is reliable.

CONCLUSIONS

The results show that the power of the use of the inverse method of thermal conductivity measurement of some materials is interesting for the pupose of this study, but it is necessary to stress three points:

a. The method allowed the parameter estimation $<m>$ and $<n>$ for boundary heat transfer starting from a steady state measurement value of thermal conductivity for each material.
b. The temperature range of measurement is not dangerous for the materials investigated.
c. The transient duration of temperature variation is too long.

The last two aspect involve the type of the thermostatic fluid and the design of the apparatus that we used, beside the data acquisition system and accuracy of this. The method validation suggested our choice for the apparatus and the ancillary equipment.

The first aspect, on the contrary, puts in evidence the need to have some more informations on the phenomenon for the contemporary estimation of the thermal conductivity and the boundary parameters: for example another measure point in the test specimens.

The work purpose is the overcoming of these difficulties.

REFERENCES

[1] Tarantola A., *Inverse Problem Theory*, Elsevier 1987.
[2] Beck J.V., Arnold K.J., *Parameter Estimation in Engineering and Science*, J.Wiley 1977.
[3] *Compendium of Thermophysical Property Measurement Methods*, ed. Maglic et Al., vol. I, p. 221, Plenum Press, New York and London, 1984.
[4] *Thermal Insulation Determination of Steady State Areal Thermal Resistance and related Properties, Guarded Hot Plate Method*, ISO/DIS 8302, 87/09/03.
[5] MIL-STD-810D, *Environmental Tests Methods and Engineering Guidlines, method 507.2*, 19 July 1983
[6] Beatty K.O., Armstrong A.A., and Schoenborn E.M., (1950). Ind. Eng. Chem., 42, 1527.
[7] Ruscica G., Bertoglio F., *Comparative measurements of the Thermal Conductivity of non-metallic solid materials*, Atti del Congresso Nazionale A.T.I. (1979), Vol. 2, p. 321.

APPENDIX A

Equation (3) can be written in an expanded form:

$$\begin{vmatrix} \frac{dT_m}{dt} \\ \frac{dT_r}{dt} \end{vmatrix} = \begin{vmatrix} a_{M,M} & a_{M,R} \\ a_{R,M} & a_{R,R} \end{vmatrix} \begin{vmatrix} T_m \\ T_r \end{vmatrix} + \begin{vmatrix} b_M \\ b_R \end{vmatrix}$$

where C is the heat capacity of the materials, s and L are respectively the thickness and width of each of the two samples and h the heat transfer coefficient, thus giving:

$$a_{M,M} = -(2 \cdot d_{1,M} + d_{2,M}) \quad a_{M,r} = d_{1,M}$$

$$a_{R,M} = d_{1,R} \quad a_{R,R} = -(d_{1,R} + d_{2,R})$$

$$b_M = T_0 \cdot (d_{1,M} + d_{2,M}) \quad b_R = T_0 \cdot d_{2,R}$$

$$d_{1,M} = 2 \cdot \frac{L^2}{C_M \cdot R_M} \qquad d_{2,M} = \frac{s_M^2}{C_M \cdot \left(\frac{s_M}{L} + \frac{h_M \cdot R_M}{2} \right)}$$

$$d_{1,R} = 2 \cdot \frac{L^2}{C_M \cdot R_R} \qquad d_{2,R} = \frac{s_R^2}{C_R \cdot \left(\frac{s_R}{L} + \frac{h_R \cdot R_R}{2} \right)}$$

APPENDIX B

Table Ia - RM64-BCR Reference material characteristics

Material	Composition	Nominal Density [kg/m^3]	Measur. Density [kg/m^3]	Thickness [mm]
A	Glass fiber resine bonded	88.0	86.0	34.5

Table Ib - Materials characteristics for humidity ageing tests

Material	Composition	Nominal Density [kg/m^3]	Measur. Density [kg/m^3]	Thickness [mm]
B	Melamine foam	11.0	9.5	50.0
C	Glass fiber resine bonded	9.6	10.0	49.5
D	Polymide foam	8.0	9.3	50.2

Table Ic - Materials characteristics for thermal ageing tests

Material	Composition	Nominal Density [kg/m^3]	Measur. Density [kg/m^3]	Thickness [mm]
B	Melamine foam	11.0	9.4	50.1
C	Glass fiber resine bonded	9.6	9.5	49.5
D	Polymide foam	8.0	9.1	50.1

Table II - <m> and <n> parameters

Material	m	n
B	2.0012	0.7847
C	5.0341	0.4667
D	1.0007	0.7667

Table III - Measured thermal conductivity with estimated errors

Cycle	Specimen	Thermal ageing $10^2 \cdot \lambda$ [W/(m K)]	Humidity ageing $10^2 \cdot \lambda$ [W/(m K)]
0	B	$3.68_6 \pm 0.08$	$3.68_6 \pm 0.08$
	C	$4.08_4 \pm 0.08$	$4.08_4 \pm 0.08$
	D	$6.50_1 \pm 0.10$	$6.50_0 \pm 0.10$
1	B	$4.79_4 \pm 0.11$	$4.30_9 \pm 0.10$
	C	$4.67_7 \pm 0.09$	$4.13_4 \pm 0.08$
	D	$6.80_7 \pm 0.10$	$6.81_7 \pm 0.10$
2	B	$4.99_9 \pm 0.11$	$4.88_8 \pm 0.10$
	C	$4.53_8 \pm 0.08$	$4.23_7 \pm 0.08$
	D	$6.77_3 \pm 0.10$	$6.88_7 \pm 0.10$
3	B	$5.22_2 \pm 0.11$	$4.27_6 \pm 0.10$
	C	$4.91_3 \pm 0.09$	$4.17_2 \pm 0.08$
	D	$7.08_5 \pm 0.10$	$6.85_8 \pm 0.10$
4	B	$5.26_8 \pm 0.11$	$4.56_8 \pm 0.10$
	C	$4.97_1 \pm 0.09$	$4.27_8 \pm 0.08$
	D	$7.00_2 \pm 0.11$	$7.09_5 \pm 0.10$
5	B	-	$4.69_9 \pm 0.10$
	C	-	$4.49_9 \pm 0.09$
	D	-	$7.00_5 \pm 0.11$
6	B	-	$4.79_6 \pm 0.10$
	C	-	$4.59_9 \pm 0.09$
	D	-	$6.99_5 \pm 0.10$

Table IV - Thermal conductivity degradation

Specimen	Thermal ageing $10^2 \cdot \Delta\lambda$ [W/(m K)]	Humidity ageing $10^2 \cdot \Delta\lambda$ [W/(m K)]
B	1.06_7	1.75_8
C	0.45_7	0.86_1
D	0.55_2	0.58_3

III ENCIT – Itapema, SC (Dezembro 1990)

ANÁLISE COMPARATIVA DE PROCEDIMENTOS EXPERIMENTAIS PARA DETERMINAÇÃO DA CONDUTÂNCIA TÉRMICA DE JUNÇÕES APARAFUSADAS

Marcia Barbosa Henriques Mantelli

Instituto de Pesquisas Espaciais
Av.dos Astronautas, 1758 - Jardim da Granja
12201 - São José dos Campos, SP - Brasil

RESUMO

Por ser um dado de suma importância no projeto térmico de satélites, as juntas aparafusadas do primeiro satélite brasileiro foram simuladas experimentalmente no INPE. Este trabalho apresenta os resultados obtidos para as duas últimas séries de testes, e uma análise comparativa dos procedimentos adotados, de onde surgem conclusões importantes a cerca do seu comportamento térmico destas junções e procedimentos de isolamento térmico, que mantenham as perdas térmicas em níveis adequados.

INTRODUÇÃO

A condutância térmica de juntas aparafusadas é um dado de suma importância em diversos projetos mecânicos, dentre os quais, o projeto térmico de satélites. Seu valor teórico é difícil de ser obtido, já que este depende de uma série de fatores, muitas vezes desconhecidos, tais como: tipo de parafuso e torque de aperto, material e número de arruelas, acabamento final de superfícies em contato, propriedades físicas dos materiais, resistência térmica de contatos entre os diversos componentes da junção, etc. Um procedimento bastante comum, é a determinação experimental desta condutância. O grupo de controle térmico de satélites do Instituto de Pesquisas Espaciais (INPE), tem adotado este procedimento; para isto as junções aparafusadas do primeiro satélite de coleta de dados da MECB foram simuladas no Laboratório de Controle Térmico de Satélites, e testadas em câmara vácuo- térmica de simulação espacial. Diversas séries de ensaios foram realizadas, sempre aprimorando os procedimentos, de forma a obter resultados cada vez mais confiáveis. Neste trabalho, as duas últimas séries são descritas criticamente, seus resultados apresentados e comparados, estabelecendo-se procedimentos experimentais adequados ao estudo da condutância térmica de junções aparafusadas.

SIMULAÇÃO EXPERIMENTAL

Descrição da Junção do Satélite. As juntas aparafusadas em estudo situam-se entre os painéis estruturais (tipo colméia) laterais e horizontais do primeiro satélite brasileiro. São encontrados dois tipos de junções: a primeira possui inserto fixo e parafuso ℓ10; a segunda possui inserto móvel e parafuso ℓ8. O material do parafuso é titânio , as chapas são de alumínio 2024 e os insertos são de aço inox. As arruelas tem duas funções específicas : satisfazer as condições estruturais (garantindo dimensões, torques de aperto, etc.) e satifazer o projeto térmico do satélite. Com o objetivo de isolar termicamente os painéis entre si , utiliza-se arruelas fabricadas de epoxi e fibra de vidro (material usado na confecção de placas PCB). Estas são intercaladas com arruelas de aço inox para garantir as propriedades mecânicas da junção. A arruela que se encontra em contato com a cabeça do parafuso é de alumínio. Note-se que o parafuso está fixando superfícies de alumínio pertencentes ao painel tipo colméia à uma superfície de aço inox , pertencente ao inserto.

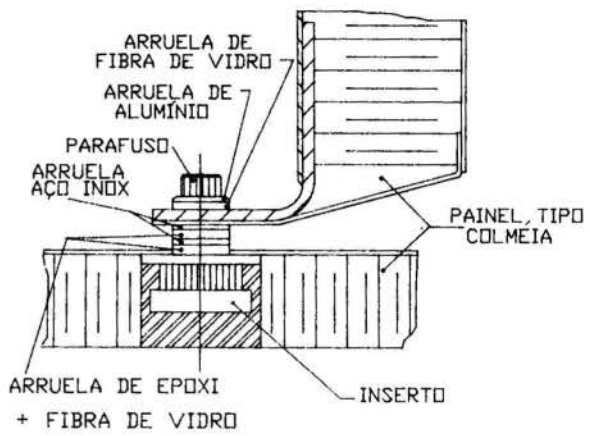

Figura 1. Junta aparafusada do satélite.

Montagem Experimental. Foram realizados estudos experimentais para os dois tipos de junções descritos na seção anterior. Para cada caso foram feitas dez montagems iguais, a fim de possibilitar um tratamento estatístico dos dados. A Figura 2 mostra um esquema dos aparatos experimentais construídos. Nas montagems experimentais adotadas, as superfícies de alumínio foram substituídas por aquecedores planos e circulares, e as superfícies dos insertos por resfriadores. Cada aquecedor consiste de um "sanduíche" formado por duas chapas de alumínio circulares, planas e finas (com espessuras de 1 e 1,5 mm e 80 mm de diâmetro), e por um fio roliço resistivo de Níquel-Cromo de resistividade de 30 Ohms por metro, enrolado em espiral plana, situado entre as chapas de alumínio. Para isolamento elétrico entre o fio resistivo a as chapas, foram colocados filmes de Polyester (Therphane, fabricado pela Rhodia do Brasil) de 25 microns de espessura. A resistência elétrica obtida em cada aquecedor varia entre 15.5 e 19.0 Ohms. As espessuras das chapas de alumínio do aquecedor foram escolhidas de forma que a sua soma fosse próxima à soma das chapas do painel estrutural.

O resfriador foi projetado e construído de forma a manter, dentro do possível, as características físicas e térmicas do inserto. Este foi feito de aço inox nas mesmas dimensões do inserto, possuindo uma base circular de 60 mm de diâmetro e 2mm de espessura para facilitar a perda de calor para o ambiente de teste. A

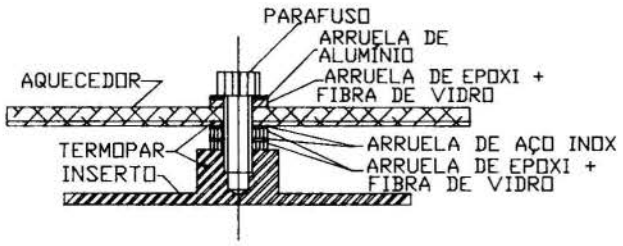

Figura 2. Aparato experimental.

altura total do resfriador é de 9.5 mm e o diâmetro de seu corpo principal é de 14,2 mm para a junção que possui inserto fixo e 17,4 mm para a junção com inserto móvel. Foram feitas roscas nos centros dos resfriadores de modo a alojar parafusos ℓ10 para os insertos fixos e ℓ8 para os insertos móveis.

Entre os aquecedores e resfriadores encontram-se duas arruelas de epoxi e fibra de vidro intercaladas por duas arruelas de aço inox nas dimensões de 1,6 e 0.4 mm de espessura respectivamente, e 10 mm de diâmetro , especialmente fabricadas para uso neste satélite. Uma arruela de alumínio e uma de fibra de vidro estão localizadas sob a cabeça do parafuso.Os diâmetros internos das arruelas dependem do parafuso da junção.

Como na época da realização do experimento não havia parafusos de titânio disponíveis, estes foram substituídos por parafusos de aço de alta liga, facilmente encontrados no mercado. Estes parafusos comprimem os elementos descritos acima, com torques iguais aos das junções reais.

Os vinte aparatos resultantes foram colacados lado a lado em quatro fileiras de cinco espécimens instalados em uma mesa de celeron (material isolante térmico). Para monitorar as temperaturas dos aquecedores, foram instalados, nas suas faces internas, termopares tipo T (cobre-constantan), bitola AWG 36, revestidos de teflon. A temperatura dos resfriadores foram monitoradas através de termopares semelhantes, instalados no centro dos cilindros principais para os insertos fixos e nas superfícies externas para os insertos móveis.

A resistência térmica da junta é obtida dividindo-se a diferença de temperatura entre o aquecedor e o inserto pelo fluxo de calor que atravessa a junção. Para forçar que o calor gerado flua pelas arruelas e parafuso, a face externa da chapa circular do resfriador e o cilindro principal do inserto foram pintadas de preto. Estas superfícies apresentam uma emissividade de 0.85 a 0.90, conforme medidas do laboratório ótico do INPE. Também foram instalados, na parte externa dos aquecedores, superisolantes multicamadas (MLI) formados por 8 folhas de polyester aluminizadas em ambas as faces, separadas entre si por redes de nylon.

Os testes foram realizados em câmara vácuo-térmica, pertencente ao laboratório de controle térmico de satélites. Esta câmara opera em alto vácuo (10-7 torr) e possui uma camisa refrigerada por nitrogênio líquido (LN2), atingindo temperaturas por volta de -190°C, simulando desta forma o ambiente espacial.

DESCRIÇÃO DAS DUAS SÉRIES DE TESTES

As duas séries de testes analisadas neste trabalho são muito semelhantes, já que ambas foram realizadas no mesmo aparato experimental descrito anteriormente. Após o tratamento dos dados da primeira série, observou-se que as perdas térmicas estavam extremamente elevadas, alcançando em alguns casos cerca de 50% da potência total fornecida, tornando os resultados finais bastante imprecisos (ver Tabelas 2 e 5). Para aumentar a confiabilidade dos dados, foi preciso minimizar estas perdas. A segunda série corresponde à reedição da primeira, porém com a adoção de técnicas de isolamento térmico mais refinadas. Para isto as juntas foram desmontadas e, ao remontá-las, foi tomado o cuidado de se manter exatamente os mesmos componentes e a mesma ordem original destes em cada junta (como, por exemplo, as mesmas arruelas, na mesma ordem), de forma que fosse possível uma análise crítica e comparativa das séries de testes.

Diferenças Entre as Duas Séries de Testes. Originalmente, a face do aquecedor voltada para o resfriador (ver Figura 2), foi revestida por uma fita de aluminio polido, de forma a manter a sua emissividade superficial baixa, resultando no isolamento térmico do aquecedor. Tal medida não se mostrou eficiente, e na segunda série foi inserido sobre esta superfície, superisolantes multicamadas compostos de 10 folhas de filmes de polyester aluminizados. Note-se que, desta forma, o aquecedor passou a ter ambas as faces isoladas por MLI. Este procedimento reduziu estas perdas térmicas entre o aquecedor e resfriador, e aquecedor e câmara térmica, em cerca de 50%. Porém, a maior fonte de perda de calor foi através dos fios de potência elétrica, revestidos por PVC, que possuem alta emissividade térmica. Para minimizar estas perdas, estes fios, assim como os fios de termopar, foram revestidos por filmes de polyester aluminizados, de forma a reduzir drasticamente as suas emissividades superficiais. Este procedimento provocou uma redução de cerca de 90% do calor transferido através de fios de potência e termopares, tornando as perdas por termopares desprezíveis. Por serem muito pequenas, as demais fontes de perda de calor não receberam, na segunda série, técnicas de isolamento especiais, uma vez que as adotadas para a primeira série se mostraram suficientes.

Note-se que, quando o aparato foi montado para a segunda série, alguns termopares defeituosos foram trocados. Também foram realizadas medidas em mais dois patamares diferentes de temperatura (na primeira série foram adotados três patamares, e na segunda, cinco).

A Tabela 1 apresenta um resumo das principais diferenças entre as duas séries analisadas.

Tabela 1. Diferenças Entre as Séries de Testes

	PRIMEIRA SÉRIE	SEGUNDA SÉRIE	RED.PERDA
No.NÍVEIS TEMPERATURA	FITA DE ALUMIN. POLIDO	FITA DE ALUMIN. +MLI 10 CAMADAS	50 %
FACE AQUEC. VOLTADA RESF.	PVC	PVC+FILME DE POLYESTER ALUM.	90 %
FIOS DE POT. ELÉTRICA	TEFLON	TEFLON+FILME DE POLYESTER ALUM.	90 %

RESULTADOS EXPERIMENTAIS

A Tabela 2 apresenta os resultados obtidos para as duas séries de testes para junções com inserto móvel, e a Tabela 3 para com insertos fixos. Estas tabelas relacionam as temperaturas do aquecedor e do resfriador com as perdas totais, com a potência total fornecida ao aquecedor, com a resistência térmica da junção (objetivo principal deste trabalho), e com as incertezas associadas: ao cálculo das perdas de potência elétrica, às medidas experimentais, e ao erro padrão apresentado pela variação das resistências térmicas das montagens iguais para cada caso. O erro padrão é equivalente à incerteza da média das resistências térmicas, sendo dado por [1]:

$$\text{erro padrão} = \frac{\text{desvio padrão}}{\text{raiz quadr. número aparatos iguais}} .$$

Tabela 2. Resultados para Insertos Móveis

	TEMPERATURA		POTÊNCIA TOTAL DISSIP.	PERDAS TOTAIS	RESIST. TÉRMICA	INCERTEZAS		
	AQUEC.	RESF.				PERDAS	EXPERIM.	RESIST.
PRIM.	68.036	-11.702	1.947230	0.479975	54.521	0.123519	4.62565	3.0373
SÉRIE	14.065	-40.173	1.089811	0.249681	64.791	0.069998	5.46463	3.4566
	-13.179	-54.941	0.730549	0.166290	74.227	0.046824	6.17419	3.2786
	35.125	-33.754	1.465544	0.076810	49.709	0.028018	1.10542	3.8758
SEG.	10.444	-42.996	0.998672	0.049583	56.402	0.018549	1.21648	4.4556
SÉRIE	-1.705	-48.380	0.813601	0.042047	81.901	0.016601	2.51465	6.5456
	-29.168	-65.433	0.346546	0.026235	113.477	0.012231	4.51509	8.9343
	-61.907	-87.272	0.083864	0.014048	364.682	0.010398	54.56923	28.3706

Tabela 3. Resultados para Insertos Fixos

	TEMPERATURA		POTÊNCIA TOTAL DISSIP.	PERDAS TOTAIS	RESIST. TÉRMICA	INCERTEZAS		
	AQUEC.	RESF.				PERDAS	EXPERIM.	RESIST.
PRIM.	69.222	8.084	1.839201	0.513024	46.312	0.114841	4.08110	1.9777
SÉRIE	13.447	-25.102	1.028562	0.259940	50.211	0.062307	4.09765	1.7303
	-13.907	-42.474	0.689253	0.169030	55.044	0.042198	4.47708	2.3844
	32.277	-14.467	1.424113	0.077424	34.831	0.025614	0.90729	4.9978
SEG.	8.409	-27.594	0.970439	0.048580	39.141	0.016488	0.99769	5.2692
SÉRIE	-9.581	-37.915	0.696254	0.037584	54.138	0.013823	1.82015	7.1526
	-59.013	-53.708	0.336749	0.025863	77.157	0.010471	3.52077	11.6907
	-124.93	-79.778	0.081493	0.013638	250.479	0.007281	36.60355	42.8491

Em cada um dos níveis de temperatura, as medidas foram efetuadas após os espécimens atingirem regime permanente. Os aparatos foram mantidos em temperatura e dissipação constante por um sistema eletrônico de aquisição e controle de dados. Para permitir a verificação do estado de regime permanente, e para o cálculo preciso das incertezas experimentais assim como das incertezas das perdas, foram tomadas cerca de 150 medidas para cada temperatura. A potência dissipada foi determinada através da medida da resistência elétrica de cada aquecedor e da voltagem correspondente. A incerteza dos valores obtidos está associada à metade da menor divisão da escala utilizada nos instrumentos de medição. O procedimento adotado para a determinação destas incertezas está detalhado na Referência [2].

É importante notar que não foi possível coletar e/ou aproveitar todos os dados gerados por uma série de fatores tais como: rompimento de termopares, mal contato de cabos de extenção com o sistema de aquisição de dados, junções de termopares que se deslocaram das suas posições originais, etc. Desta forma as médias finais não foram calculadas com os dez espécimens testados.

COMPARAÇÃO DOS RESULTADOS

Através das Tabelas 1, 2, e 3, é possível observar o efeito, em todo o experimento, dos procedimentos de isolamento térmico, que diferenciam as duas séries de testes. Na Tabela 1 está mostrada a redução percentual das perdas térmicas particularizadas para cada uma das fontes que foram modificadas. As Tabelas 2 e 3 apresentam valores globais, onde se observa que, na segunda série, as perdas totais são sempre inferiores às primeiras. A Figura 3 apresenta graficamente as incertezas experimentais (barras verticais), associadas aos valores de resistência térmica em função da temperatura média entre aquecedor e resfriador, para os quatro casos estudados (dois tipos de insertos, e duas séries de testes). Note-se que, para a primeira série, as incertezas são praticamente constantes e quase não variam com a temperatura. Já para a segunda série, além das incertezas serem sistematicamente inferiores às da primeira série, elas variam sensivelmente com a temperatura, tornando-se desprezíveis para altas temperaturas. Note-se também que as incertezas equivalentes às temperaturas mais baixas na segunda série, inserto móvel e fixo, não foram plotadas porque, como suas resistências e incertezas são bastantes altas, a inclusão destes pontos tornariam o gráfico de difícil vizualização.

Perdas Térmicas. Para o cálculo cuidadoso das perdas térmicas, algumas hipóteses foram adotadas,e estão descritas a seguir. O cálculo das perdas através dos termopares e fios de potência elétrica foi feito considerando-os aletas radiativas finitas ou infinitas dependendo deles atingirem ou não a temperatura ambiente. Para a determinação das perdas pelos MLIs, multiplicou-se a condutividade efetiva do MLI pela diferença entre as temperaturas das suas camadas internas e externas . O cálculo das perdas por radiação do aquecedor para o resfriador e ambiente foi feito numericamente, através de programa de diferenças finitas, desenvolvido no INPE.

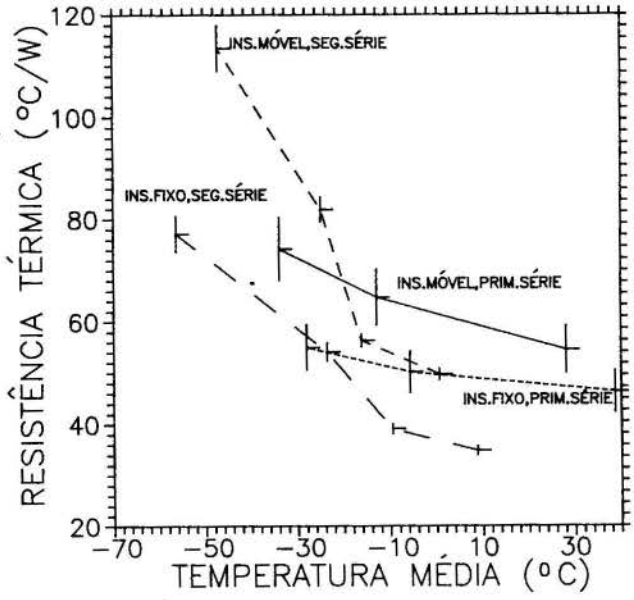

Figura 3. Incertezas experimentais.

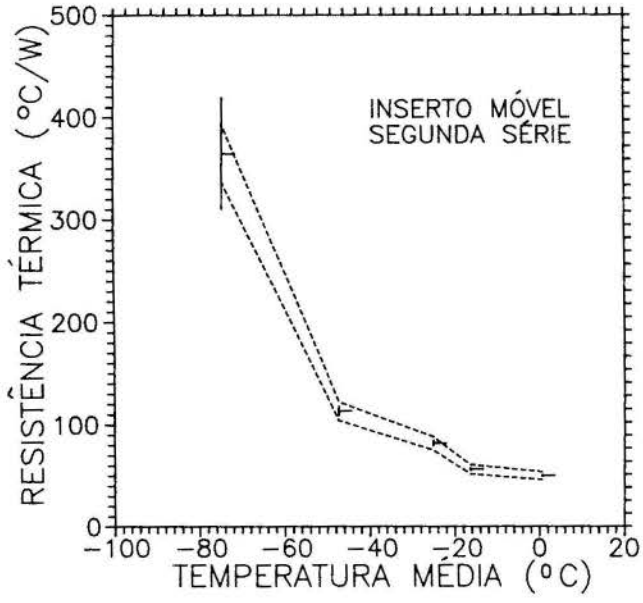

Figura 5. Erros experimentais e erros padrão para segunda série, inserto móvel.

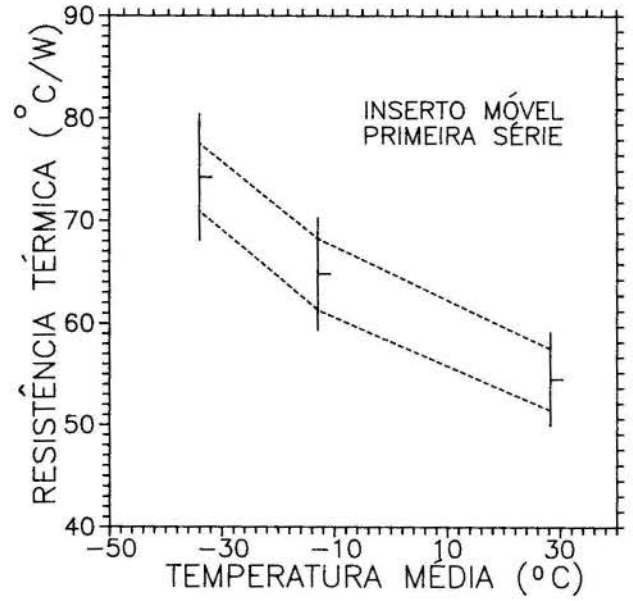

Figura 4. Erros experimentais e erros padrão para a primeira série, inserto móvel.

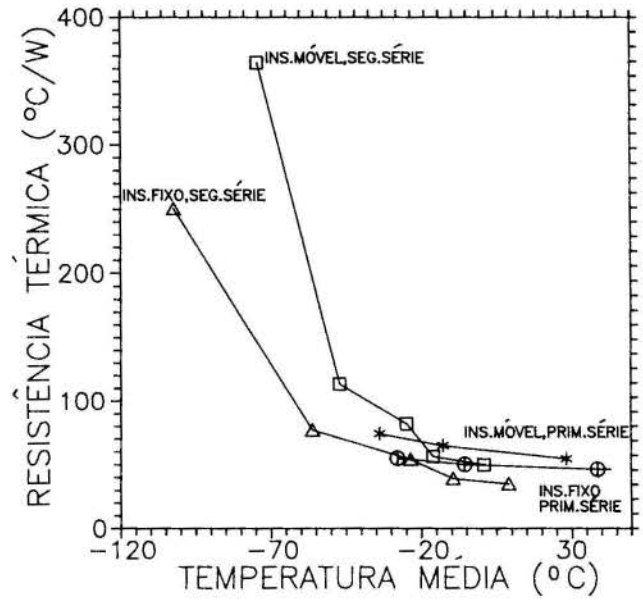

Figura 6. Compilação de todos os dados obtidos.

As Figuras 4 e 5 apresentam uma comparação entre a incerteza das medidas experimentais (barras verticais) e a incerteza baseada na dispersão (erro padrão) das resistências térmicas dentre os dez aparatos idênticos testados simultaneamente (curvas tracejadas), para a primeira e segunda série de testes, respectivamente. Na primeira série, as incertezas experimentais foram superiores ao erro padrão encontrado, mostrando que os dez aparatos testados simultaneamente não aumentaram a precisão dos resultados finais. Isto não ocorre na Figura 5, indicando que o procedimento adotado foi correto, excessão feita ao dado correspondente à baixa temperatura. Estas curvas (Figuras 4 e 5) são muito semelhantes às obtidas para o inserto fixo, que não serão apresentadas aqui.

A Figura 6 apresenta todos os dados obtidos, onde se verifica que a resistência térmica é altamente dependente da temperatura. A questão que surge é: porque existe tal dependência? Na realidade, à medida em que a temperatura cai, as propriedades térmicas dos materiais das junções se modificam, provocando: queda da condutividade térmica e contração diferencial. A contração diferencial dos materiais provoca sensível alívio na pressão de contato entre os componentes da junta, diminuindo a resistência de contatos (ver gráficos na Referência [3]). A diminuição da condutividade térmica, assim como o aumento da resistência térmica de contatos, provocam a variação da resistência térmica total com a temperatura. Este efeito justifica a variação da incerteza experimental com a temperatura, observados nas Figuras 3 e 5, da seguinte maneira: as trocas de calor por radiação,

principal mecanismo de perda de calor, quase não são afetadas pela variação de temperatura. Assim, aumentando a resistência térmica da junção, é de se esperar que mais calor flua através dos mecanismos de perdas, que permaneceram quase constantes. Como a grande fonte de incerteza experimental está na determinação das perdas térmicas, aumentando-se sua proporção em relação a dissipação total, a incerteza da resistência térmica da junção deve aumentar.

COMENTÁRIOS GERAIS

Da análise dos dados obtidos, algumas observações interessantes podem ser feitas:

- a resistência térmica é sempre maior para insertos móveis, como é possível observar nas Figuras 3 e 6. Isto se justifica pelo fato de que o inserto móvel tem componentes não rígidos, permitindo o movimento relativo de, por exemplo, parafusos em relação aos painéis estruturais. Desta forma há um maior número de superfícies em contato, aumentando a resistência,

- na Figura 6 observa-se que há uma diferença quase constante entre as resistências térmicas dos mesmos tipos de insertos da primeira e segunda séries de testes. Isto significa que quando as juntas foram montadas na primeira vez, ocorreram transformações plásticas nos materiais. Como na segunda montagem manteve-se a mesma ordem dos componentes das juntas, estes já estavam acomodados entre si, melhorando o seu contato físico, reduzindo a resistência térmica de contatos, e portanto a resistência térmica total. Desta forma não se recomenda a remontagem de partes estruturais do satélite, utilizando os mesmos componentes originais,

- com esta sensível variação da resistência térmica da junção com a temperatura, é possível utilizar junções aparafusadas como controle ativo de satélites,

- quando se desejar em experimentos distintos reproduzir as mesmas junções, deve-se sempre procurar usar arruelas não testadas, escolhidas aleatoriamente dentro de um universo grande de arruelas (Referência [1]),

- foi apenas verificado, neste experimento, o efeito da variação da resistência térmica com a temperatura. Para sua melhor compreensão serão necessários novos estudos experimentais concentrando as medidas na região do "cotovelo" observado nas Figuras 5 e 6.

CONCLUSÃO

O procedimento adotado na primeira série de testes é inconveniente por apresentar erros de medidas experimentais extremamente grandes, e por conter um número desnecessário de aparatos iguais, aumentando o custo do experimento, sem aumentar a precisão dos resultados finais. Já o procedimento adotado na segunda série mostrou ser satisfatório, apresentando resultados com precisão adequada às necessidades de projetos térmicos de satélites. Desta forma, para este tipo de experimento, deve-se adotar as técnicas aqui descritas de isolamento térmico.

REFERÊNCIAS

[1] Cox,D.R., "Planning of Experiments", John Wiley & Sons Inc., New York, 1958.

[2] Moffat, R.J., "Describing the Uncertainties in Experimental Results", Experimental Thermal and Heat Science, Vol. 1, pp. 3-17, 1988.

[3] Mantelli, M.B.H., "Comparação de Métodos para o Cálculo da Resistência Térmica de Contatos do Primeiro Satélite Brasileiro", Tese de Mestrado, Instituto de Pesquisas Espaciais, São José dos Campos, SP, Brasil, 1985.

III ENCIT – Itapema, SC (Dezembro 1990)

INTENSIFICAÇÃO DA CONDUTIVIDADE TÉRMICA DE LEITOS GRANULARES ATRAVÉS DE MISTURAS BIDISPERSAS E DE INSERÇÕES DE ESPONJAS METÁLICAS

José Maurício Gurgel

Laboratório de Energia Solar
Universidade Federal da Paraíba
58.000 - João Pessoa - PB

Francis Meunier
J.J.Guilleminot
LIMSI-CNRS
B.P. 30, F 91406
Orsay-(France)

Foram testadas duas possibilidades de intensificação da condutividade térmica de leitos granulares através de misturas bidispersas homogêneas e de inserções metálicas. As medições foram realizadas por um método transiente. Usou-se amostras de esferas de zeolita, vidro e aço e os resultados obtidos mostram uma forte dependência da porosidade no valor da condutividade das misturas bimodais. Os melhores resultados obtidas foram através da introdução das esponjas no leito, com aumentos entre 60 e 120%

INTRODUÇÃO

A análise das trocas térmicas em bombas de calor e máquinas frigoríficas a sorção sólida faz aparecer um efeito limitador ao desempenho de tais sistemas: a baixa condutividade térmica do leito poroso do qual são formados seus adsorbedouros.

Em alguns estudos realizados para bomba de calor (1) e para um refrigerador solar (2), o C.O.P. foi calculado em função de parâmetros caracterizando as aletas, onde são mostrados um aumento de desempenho em função da intensificação das propriedades de transferência térmica: não somente da condutividade térmica como também do coeficiente de transferência parede/leito granular.

Este trabalho avalia algumas das possibilidades de aumento da condutividade térmica de leitos porosos com a experimentação de alguns casos.

A condutividade térmica do leito poroso é influenciada por vários parâmetros (3-4) entre os quais os mais importantes são: a condutividade térmica dos grãos, a natureza do gás e a porosidade. A condutividade da fase sólida e gasosa são determinadas pelas propriedades termo-físicas do par utilisado (carvão ativado-metanol, zeolita-água, silica gel-água, etc). Diante disto, algumas das possíveis possibilidades de aumento da condutividade térmica do leito granular poderão ocorrer através de:

-diminuição da porosidade do leito granular, através de um condicionamento bimodal

-preenchimento dos espaços entre os grãos com um pó metálico de boa condutividade.

-inserção dentro de leito granular de elementos condutores tendo a forma geométrica de agulhas, fios, fibras, etc.

-inserção de esponjas metálicas dentro do leito granular.

Os fenômenos físicos associados a essas possibilidades de aumento da condutividade térmica são basicamente dois:

-A diminuição da porosidade através de uma mistura de grãos tendo diferentes dimensões, permite aumentar a condutividade térmica devido ao aumento da proporção da fase sólida maior condutora que a fase gasosa.

-A introdução de esponjas, inserções metálicas, etc, visa a criar uma condutividade em paralelo com o leito poroso: o objetivo consiste em fazer uma distribuição de "aletas" de uma maneira homogênea dentro do leito fixo granular.

MODELO PREDITIVO

Entre os modelos desenvolvidos para predição da condutividade de leitos granulares monodispersos , tem-se o de M.Okasaki(5) e o de Bauer-Schlünder (6) que foram extendidos para os casos de leitos bidispersos. Este último foi escolhido para confrontação com os resultados experimentais apresentados neste trabalho pela sua flexibilidade e confiabilidade (4). O modelo de Bauer-Sshlünder (BS) é baseado na tranferência de calor dentro de uma célula unitária formado por duas partículas em contato (fig.1). Dentro desta célula, é assumido um fluxo de calor unidimensional entre as partículas que têm a forma geométrica deformável. Esta deformação é obtida supondo-se que a interface solida-gasosa é de revolução em torno de um eixo paralelo au gradiente térmico (eixo dos z) e tem como equação:

$$r^2 + \frac{z^2}{[B - (B - 1)\, z]^2} = 1 \qquad (1)$$

B é um parâmetro dependente de um fator de forma Cforma, do valor ξ da distribuição granulométrica e de porosidade ε do leito. BS dão para B a seguinte expressão:

$$B = C_{forma}\,[(1-\varepsilon)/\varepsilon]^{10/9}(1+3\xi) \qquad (2)$$

O valor de B depende da forma geométrica da partícula utilizada dentro da célula elementar (Cforma = 1 para grãos esféricos) e do valor do coeficiente de dispesão granulométrica ξ .

Este modelo é apresentado para o caso de um leito monodisperso em (7). Maiores detalhes podem ser encontrados em (3,4,6,8,9).

Dentro de um leito bidisperso, a utilização de uma mistura de partículas de diferentes dimensões permite a diminuição da porosidade com um consequênte aumento dos pontos de contato entre as particulas. Como a maior parte da transferência de calor se efetua na vizinhança destes pontos de contato, tem-se em consequência a intensificação da condutividade térmica do leito granular. Para

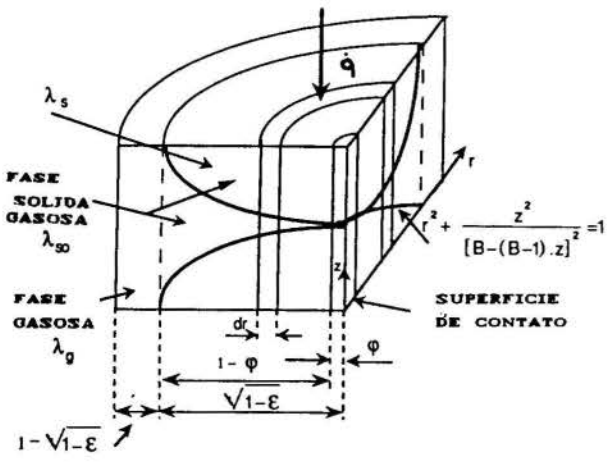

Fig.1 Célula elementar usada para o calculo da condutividade térmica do leito granular.

levar em consideração estes efeitos, BS utilisam o mesmo modelo proposto para o caso monodisperso mas causando uma deformação na partícula elementar que represente o leito bidisperso. BS propõem, para uma mistura bimodal de partículas de mesma forma geométrica, a seguinte expressão:

$$\xi = \left[\frac{DD_g + (1 - DD_g)\, r}{DD_g + (1 - DD_g)\, r^2} - 1 \right]^{1/2} \qquad (3)$$

onde DD_g é a proporção volumétrica das maiores partículas presentes na mistura (Ex: $DD_g = 1$ leito formado com 100% das maiores partículas de diâmetro D_g, $DD_g=0$ leito formado com as menores partículas de diâmetro D_p), $r = D_g/D_p$, relação entre diâmetros equivalentes das partículas.

Enfim para uma mistura bimodal, a distância característica D é dada por:

$$D = \frac{1}{\frac{DD_g}{D_g} + \frac{1 - DD_g}{D_p}} \qquad (4)$$

APARELHAGEM

As medidas foram realizadas em um reator cilindrico de aço inoxidável (fig. 2) tendo um diâmetro de 250 mm e altura de 250 mm. A amostra granular ocupa a parte central do reator e é limitada lateralmente por uma parede isolante de "teflon". A relação entre o diâmetro do leito granular pela sua altura é superior a 4 que permite uma redução das interferências sobre o campo térmico no centro (10) (local de medida), causado pelas perdas térmicas laterais. Isto também foi verificado através de uma análise numérica bidimensional do problema.

Quatro sondas de temperatura são colocadas dentro da amostra e regularmente espaçadas de 10 mm e estão presas sobre dois fios de aço muito fino extendidos por molas. A primeira sonda é colocada junto a uma placa de cobre de 5 mm de espessura que constitue o fundo do coletor. Uma resistência elétrica plana com a forma de um disco é colada sob esta placa de cobre para a dissipação de um fluxo de calor uniforme.

As sondas de temperatura são de platina de 100 Ω montadas pelo método de quatro fios. O diâmetro é de 0.9 mm e comprimento 10 mm e apresentam precisão absoluta de 0.3 °C. Após

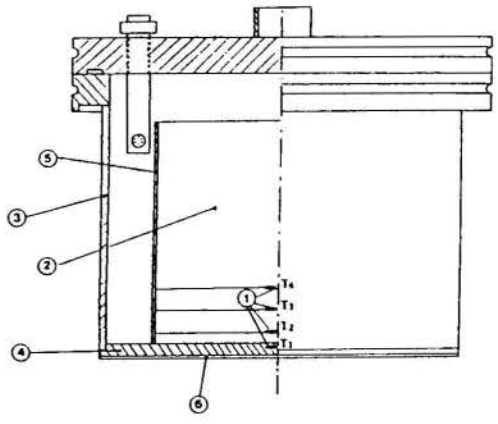

Fig. 2 - Reator utilizado para as medições. (1) sondas de temperatura, (2) amostra a ser estudada, (3) parede do aparelho em aço inoxidavel, (4) disco em cobre, (5) cilindro de "teflon", (6) resistência elétrica.

as aferições, a precisão relativa das medidas de temperatura é inferior a 0.01 °C. Un sistema de aquisição de dados HP 3421a ligado a um micro-computador compatível PC-IBM permitiu periodicamente à leitura e registro de temperaturas (intervalos de 5 segundos) com uma reprodutividade de 0.01 °C.

MÉTODO DE MEDIÇÃO

É utilizado um método transitório que permite medições rápidas e a utilização de pequenas amostras de material. Neste método, a amostra recebe um impulso térmico e em seguida registra-se o histórico de temperatura, que permite calcular a condutividade térmica indiretamente através da difusividade térmica obtida por identificação, através da comparação com a solução de Fourrier.

Conhecendo-se a capacidade térmica efetiva C_e e a massa volumétrica ρ da amostra, a condutividade térmica é identificada a partir da solução de:

$$\lambda_l \frac{\partial^2 T}{\partial y^2} = \rho\, C_e \frac{\partial T}{\partial \Theta} \qquad (5)$$

A condição inicial é o campo de temperatura uniforme dentro da amostra.

$$T(y,\Theta) = T_i \qquad p/ \quad \Theta = 0 \qquad (6)$$

As condições aos limites para a temperatura são do tipo "Dirichlet": conhecimento da temperatura em função do tempo. São utilizados os termogramas obtidos experimentalmente com as sondas 2 e 4 que se encontram sobre uma mesma linha de fluxo (fig.2). No caso tem-se:

$$T(y_2,\Theta) = f2(\Theta) \qquad (7)$$

$$T(y_4,\Theta) = f4(\Theta) \qquad (8)$$

É utilizado um método numérico a diferenças finitas para a resolução do problema. A identificação da condutividade é feita utilisando-se uma routina de otimização com um critério de erro dos mínimos quadrados entre o termograma experimental da sonda 3 com os respectivos valores calculados obtidos com a solução numérica do problema.

Este método também permite avaliar o valor do coeficiente térmico de contato (h_{pl}) na interface leito granular/parede. Para isto, utiliza-se como condições aos limites os termogramas experimentais obtidos com as

sondas 1 e 3:

$$\lambda_l(\partial T/\partial y)\Big|_{y=o} = h_{pl}\ (T_1 - T_p) \qquad (9)$$

$$T(y_3,\Theta) = f3(\Theta) \qquad (10)$$

T_p, é a temperatura extrapolada do gradiente térmico do leito granular até a interface parede/leito, calculada com a solução numérica. A identificação deste coeficiente é realizada igualmenta como foi para a condutividade térmica, utilizando-se a comparação do termograma experimental fornecido pela sonda 2 com os respectivos valores calculados.

Um exemplo típico de uma experiência com os termogramas experimentais de cada sonda é mostrado na fig. 3. Para se evitar os problemas ligados a dependência de grandezas termo-fisicas com à temperatura, foram utilizados para as identificações as temperaturas adquiridas durante os primeiros 15-30 mn, tempo no qual o gradiente térmico entre as sondas de medida é inferior a 15 °C.

O intervalo de tempo obtido entre duas experiências é da ordem de três horas, que corresponde ao tempo de resfriamento do reator, necessário para um novo estado de homogeneidade de temperatura dentro da amostra.

A precisão para o valor da condutividade térmica calculada por este método, depende das incertezas do conhecimento da massa volumétrica e capacidade térmica da amostra e sobre a difusividade térmica, calculada por um método numérico, que é sensível ao posicionamento das sondas. É estimada uma precisão absoluta da ordem de 10% sobre as medições da condutividade térmica do leito, valor que foi confirmado através de ensaios de reprodutividade (3).

A porosidade intergranular foi determinada dentro de uma proveta de grandes dimensões utilizando-se um líquido para o cálculo do volume entre os grãos. Ela também pode ser estimada pela seguinte expressão:

$$\varepsilon = 1 - \rho l/\rho s \qquad (11)$$

onde ρl e ρs são respectivamente as massas volumétricas do leito granular e de um grão.

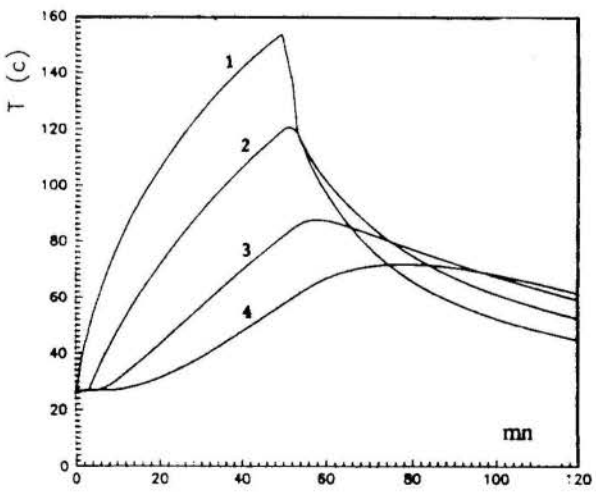

Fig. 3 - Exemplo típico de uma experiência: evolução das temperaturas das quatro sondas em função do tempo com aquecimento seguido de resfriamento brusco.

Para os leitos porosos monodispersos de partículas esféricas, foram medidos entre todos os casos estudados, uma porosidade compreendida entre 0.37 e 0.39. A variação é proveniente da forma de preenchimento do leito granular e de erros experimentais. Para misturas bidispersas, as incertezas são da ordem de 10% do valor medido.

As misturas bimodais foram efetuadas diretamente dentro do reator e para ficarem com uma boa homogeneidade, foram fabricadas através da colocação de camadas alternadas sucessivas de grandes e pequenas esferas, com o carregamento feito sempre de uma altura da ordem de 3 centímetros. Após a realização de cada camada o leito era acomodado através de suaves batidas sobre a parede externa do reator.

MISTURAS BIDISPERSAS COM GRÃOS DE MESMA NATUREZA.

Foram utilizados amostras de esferas de zeolita, vidro e aço. As respectivas propriedades são dadas na tab. 1. As experiências foram realizadas, misturando-se materiais homogêneos de diferentes diâmetros e variando-se a cada vez a proporção das maiores particulas (DD_g) em 25%. Para cada mistura feita, é medida a condutividade térmica na presença de hélio ou Argon a pressão atmosférica (1 bar) e a baixa pressão (5 mbar). Os resultados obtidos são mostrados nas figuras 4-6.

Em todos estes casos, são observados aumentos entre 25 e 100% da condutividade térmica do leito granular bidisperso em relação ao monodisperso, e são sistematicamente associados a menor porosidade do leito granular, que corresponde a uma proporção compreendida entre 70 e 80% das maiores partículas presentes na mistura. Esta intensificação da condutividade térmica é atribuida ao aumento do número de pontos de contato entre as partículas e pela substituição parcial de uma fase fluida pouco condutora por outra sólida de boa condutividade.

Os resultados obtidos com o gás a uma pressão de 5 mbar sofreram interferência do régime de Knudsen na condutividade da fase gasosa; no caso as distâncias intergranulares são da mesma ordem de grandeza que o livre percurso médio das moleculas de gás e consequentemente a condutividade do gás depende fortemente da pressão. Verificou-se um exagerado aumento da condutividade térmica em leitos monodispersas de grãos de 10 mm em relação a leitos idênticos de mesma natureza, formado com grãos de menores dimensões. Mesmo levando-se em consideração a radiação térmica (proporcional as dimensões dos grãos) e possíveis interferências devido ao regime de Knudsen, é provável que a origem deste grande aumento seja proveniente de um problema experimental sistemático ligado ao valor da

Tabela 1. - Propriedades fisicas dos materiais utilizados (3) (17).

Esferas	Aço	Vidro	Zeolita
Dg (mm)	10.2	10	4
Dp (mm)	2	1.5	0.5
C (J/kg K)	386	750	800
ρ (kg/m)	4850	1530	620
λ_s (W/m K)	20	0.9	0.19

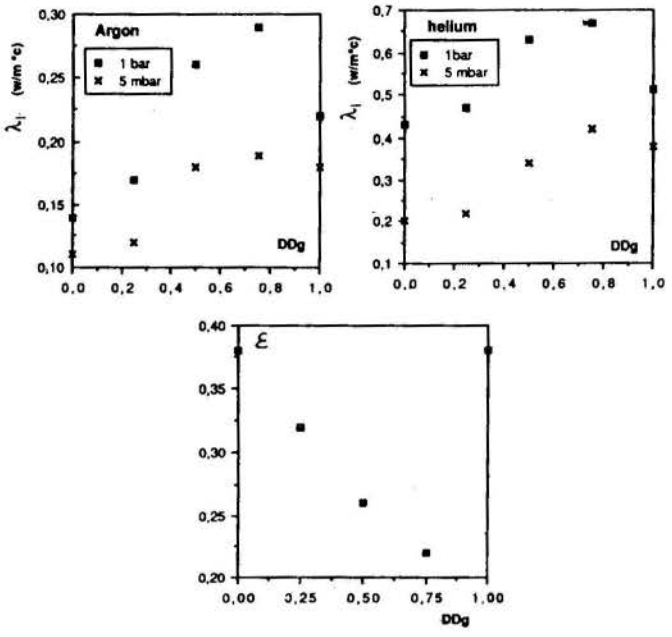

Fig.4- Condutividade térmica e porosidade (figura inferior) de leitos granulares formados de misturas de esferas de vidro, em função da fração volumétrica (DDg) ocupada pelas maiores partículas. D_G=10 mm e D_P=1.5 mm.

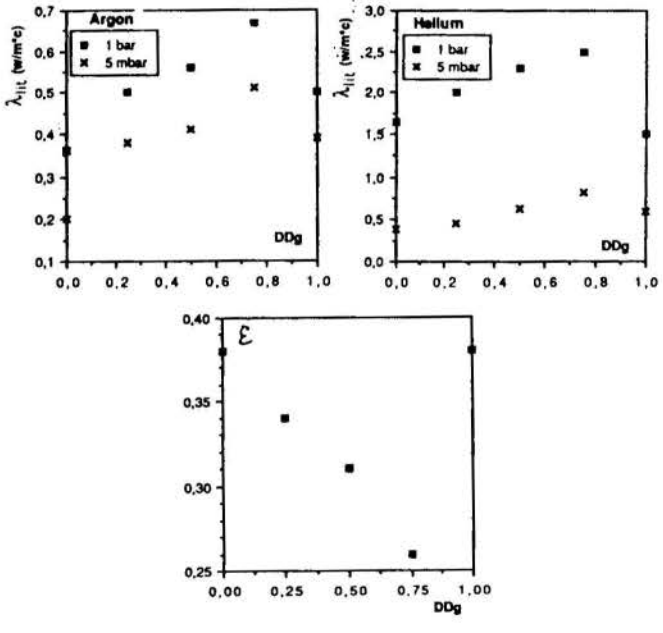

Fig.5- Condutividade térmica e porosidade (figura inferior) de leitos granulares formados de misturas de esferas de aço, em função da fração volumétrica (DDg) ocupada pelas maiores partículas. D_G=10.2 mm e D_P=1.05 mm.

porosidade local (8) que pode ter se agravado com o leito formado pelas esferas de 10 mm de diâmetro, interferindo assim no valor da porosidade da região da sonda 2 (fig. 2), localizada a apenas 10 mm da parede do reator.

No caso dos leitos formados com grãos de menores dimensões ou de misturas com presença de pequenas partículas, este problema é

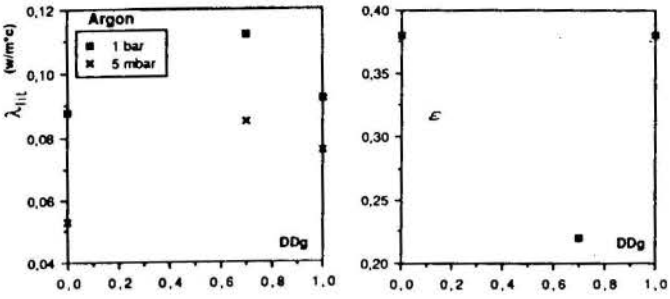

Fig.6- Condutividade térmica e porosidade (figura inferior) de leitos granulares formados de misturas de esferas de zeolita, em função da fração volumétrica (DDg) ocupada pelas maiores partículas. D_G=4 mm e D_P=0.5mm.

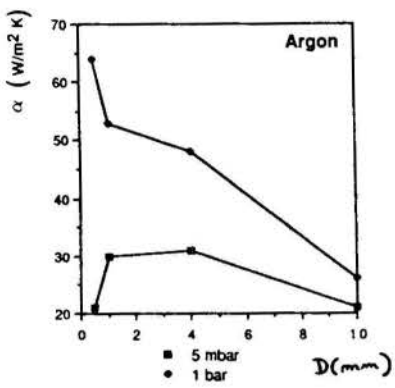

Fig. 7 - Coeficiente de Tranferência térmica α (W/m^2K), na interface leito/parede, em função do diâmetro dos grãos.

minimizado pois a porosidade assume um valor mais homogêneo logo nas primeiras camadas subsequentes a parede do reator. São mostrados na fig.7 a variação do coeficiente de transferência térmica na interface parede/leito em função das dimensões dos grãos.

Observa-se à pressão atmosférica, que este coeficiente aumenta com a diminuição das dimensões dos grãos, consequente do aumento do número de pontos em contato com a parede. A baixa pressão (5mbar), este coeficiente sofre a confrontação do número de pontos de contato com a parede, que depende das dimensões das partículas, com o efeito de Knudsen que limita a condutividade térmica da fase gasosa. Observa-se uma maximização deste coeficiente, situada para grãos tendo dimensão da ordem de 4 mm de diâmetro. Este ponto é de grande importância para as aplicações tecnológicas.

Os resultados experimentais da condutividade térmica das misturas bidispersas são confrontados com respectivos valores calculados com o modelo de Bauer-Schlünder, com uma modificação proposta por Tsotsas (considerar o parâmetro de distribuição granulométrica, ξ = 0), como para o caso monodisperso (13)(3).

Para estes cálculos, são necessários o conhecimento de parâmetros termo-físicos do leito granular. Foram utilisados 0.9 e 0.36 como valores (8) para o coeficiente de acomodação para os gases utilizados: Argon e hélio. A temperatura média para todos os casos

Tabela 2 - Parâmetros utilizados para o cálculo da condutividade térmica de leitos granulares usando o modelo de Bauer-Schlünder.

Material	Dg (mm)	Dp (mm)	DDg (mm)	ε	λ_s	ρ^2
Zeolita	4	0.5	0.7	0.22	0.22	0.0015
Vidro	10	1.5	0.25 0.50 0.75	0.32 0.26 0.22	0.9	0.0017
Aço	10.2	2	0.25 0.50 0.75	0.32 0.31 0.26	20	0.00035

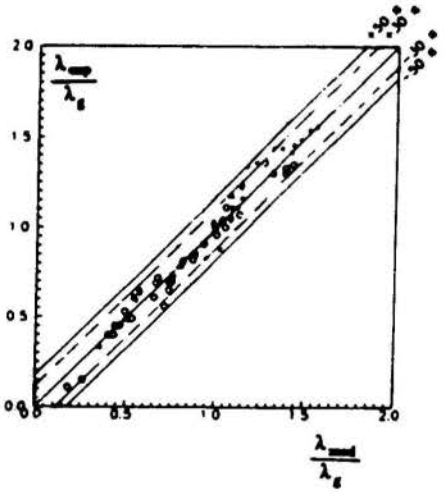

Fig. 8 - Comparação entre os resultados experimentais obtidos e os respectivos calculados com o modelo de Bauer-Schlünder.

o: Leitos monodispersados, $\varepsilon \simeq 0.38$ (aço, vidro e zeolita)

*: zeolita, D_g/D_p = 4/0.5, DD_g = 75%
□ : Vidro, D_g/D_p = 10/1.5, DD_g = 25%
Δ : Vidro, D_g/D_p = 10/1.5, DD_g = 50%
◇ : Vidro, D_g/D_p = 10/1.5, DD_g = 75%
+: Aço, D_g/D_p = 10.2/2, DD_g = 25%
x: Aço, D_g/D_p = 10.2/2, DD_g = 50%
*: Aço, D_g/D_p = 10.2/2, DD_g = 75%

estudados foi de 308 K. Os outros parâmetros utilizados estão na tabela 2. Os resultados são mostrados, na fig. 8.

Nesta figura a ordenada de cada ponto corresponde ao valor experimental e a abscissa ao respectivo valor calculado. A diagonal (traço contínuo) corresponde aos valores coincidentes entre a experiência e modelo preditivo (erro zero).

Entre todos os resultados medidos da condutividade térmica obtidos sobre leitos monodispersos, pode-se observar um bom acordo entre os valores medidos e calculados, com 96% das medições apresentando erro inferior a 30% (linhas pontilhadas)

Para as misturas, a confrontação entre as medições e os resultados calculados com o modelo apresenta 86% das medições efetuadas com erro inferior a 30% e todos os resultados com desvios inferiores a 50%.

Uma análise estatística mais significativa necessitaria de um maior números de experiências.

INSERÇÃO DE ESPONJAS METÁLICAS DENTRO DO LEITO GRANULAR.

A inserção de fibras, fios, etc, dentro do leito granular com o objetivo de intensificar de sua condutividade térmica, já foi estudado por M. Barki (14) e G. Antonini (15), que detectaram aumentos relativos da condutividade da ordem de 20 a 40%.

A realização dessas misturas é muito delicada devido as dificuldades práticas de orientar estas partículas na direção do fluxo térmico para que possam contribuir de uma forma eficaz na transferência de calor dentro do leito granular .

Afim de eliminar estes incovenientes de ordem prática, foram utilizadas esponjas metálicas (Cobre e Níquel) de baixa densidade volumétrica (100 kg/m^3) permitindo a introdução de grãos tendo diâmetro de 0.5 mm com grande facilidade.

O leito foi então formado através de algumas camadas de esponja (cada camada tinha 5 mm de espessura) sobrepostas quando finalmente os grãos eram derramados de uma altura de cerca de 3 centimetros sobre elas. Para permitir um melhor preenchimento dos espaços vazios dentro das esponjas, foiprovocado um pouco de vibração no reator, através de batidas na parede exterior. Foram obtidos com este procedimento, valores de densidade em relação a um leito monodisperso, de 0.9 com a introdução de esferas de 0.5 mm de vidro e de 0.8 com particulas de zeolita de 0.5mm.

Os resultados experimentais obtidos da condutividade térmica em leitos granulares monodispersos e em leitos misturados com as espejas são mostrados na tabela 3.

Tabela 3. - Condutividade térmica λ_l(W/m K) de leitos granulares (monodispersados e misturados com esponjas)

Gás	Argon		Hélio	
Pressão	1bar	5 mb	1bar	5 mb
Esferas de Vidro (EV)	0.12	0.06	0.41	0.12
EV + Esponja Niquel	0.20	0.13	0.57	0.21
EV + Esponja Cobre	0.23	0.12	0.72	0.25
Esferas de Zeolite(EZ)	0.09	0.05	-	-
EZ + Esponja Niquel	0.16	0.12	-	-
EZ + Esponja Cobre	0.17	0.14	-	-

Estes resultados mostram uma intensificação média da condutividade térmica da ordem de 60 a 120%, em relação ao leito monodisperso, conseguida com a introdução das esponjas metálicas (16). As esponjas contribuem para a condutividade efetiva equivalente do leitogranular permitindo adicionar uma condutividade térmica em paralelo. As medidas realizadas com Argon, a contribuição das esponjas é da ordem de 0.07 a 0.11 W/mK junto ao leito. Com o Hélio é constatado nas medidas realizadas com o leito de esferas de vidro, uma contribuição da ordem de 0.1 a 0.3 W/mK. O fato de que a condutividade equivalente das esponjas dependem da natureza do gás, é consequência da

resistência térmica de contato entre as diversas camadas.

Estes resultados são animadores e poderão ser melhoradosdesde que estas esponjas possam ser fornecidas em blocos de grande espessura.

É preciso ser prudente para o caso de utilização destas misturas a baixas pressões devido a forçosa utilização de pequenas partículas dentro das esponjas. Apesar do aumento global da condutividade devido as esponjas as pequenas dimensões dos grãos penalisam o valor da condutividade térmica do leito granular em consequência da presença dos efeitos de Knuden.

CONCLUSÃO

Os resultados experimentais obtidos com os leitos formados de misturas bidispersas homogêneas, apresentaram aumento da condutividade térmica em relação aos respectivos leitos monodispersos, da ordem de 40 a 100%. Esta intensificação esteve sistematicamente associada a menor porosidade do leito (proporção da ordem de 75% das maiores partículas).

O modelo de Bauer-Schlünder para a predição da condutividade térmica, foi utilizado com uma modificação proposta por Tsotsas e mostrou-se coerente com os resultados obtidos com leitos bidispersos.

As inserções de esponjas metálicas dentro do leito granular permitiu a obtenção dos melhores resultados da intensificação da condutividade térmica com aumentos entre 60 e 120%.

Para as aplicações tecnológicas (máquinas frigoríficas a adsorção sólida), as misturas homogêneas bidispersas apresentam grandes dificuldades de ordem prática para a elaboração de uma mistura homogênea. Por outro lado, a utilização de esponjas, permitem uma fácil fabricação das misturas com um leito granular e mostraram aumentos da condutividade mesmo a baixas pressões.

AGRADECIMENTOS

O primeiro autor agradece a bolsa dada pela CAPES e ao LIMSI-CNRS (Laboratoire d'Informtique pour la Mécanique et les Sciences de l'Ingénieur), Orsay-França, pela realização deste trabalho.

REFÊRENCIAS

[1] N. Douss, F. Meunier. "Effet of Operation Temperatures on the Coefficient of Performance of active Charbon Methanol Systems", J. heat Recovery Systems V8,N5 (1988).
[2] J.J.Guilleminot, F. Meunier and J.Paklesa, "Heat and Mass Transfer in non-isothermal fixed bed solid adsorbent reacteur:a uniform pressure non-uniform temperature case." Int. J. Mass Transfer,30 (1987)2225-2245.
[3] J.M.Gurgel "Contribution a l'étude experimentale de la conductivité thermique de milieux granulaires (mono ou bidisperses avec ou sans adsorption", tese de doutorado apresentado a Universidade Paris VI - LIMSI, dez. 1989.
[4] E.Tsotsas and H.Martin, "Thermal conductivity of packed beds: A review", Chem. Eng. Process, 22, 19-37 (1987).
[5] M.Okasaki, T.Yamasaki, S.Gordonand R.Toci, "Effective thermal conductivity for granular beds of various bimodal mixtures", J. Chem.Eng. Jpn 14 (1981) 183-189.
[6] R.Bauer and E.U.Schlünder, "Effective radial thermal conductivity of packing in gaz flow. Part II. Thermal conductivity of the packing fraction without gaz flow", Int. Chem. Eng, 18, N°2 (1978).
[7] J.M.Gurgel e Ph.Grenier, "medição da condutividade térmica do carvão ativado AC 35 em presença de gases inertes e de diferentes concentrações de metanol adsorvido", proposto ao ENCIT 90.
[8]E. U. Schlünder and T.Tsotsas, Wärmeübertragung in Festbetten, Durch Schüttgü-ter und Wirberlschichten. Edition: G.Thiene verlag Stuttgart-N.York (1988).
[9]J.M.Gurgel et Ph.Grenier, "Mesure de la Conductivité Thermique du Charbon Actif AC-35 en Presence de Gaz", The Chemical Engineering Journal, 44 (1990) 43-50.
[10] P.Dumez, "La conductivité thermique des materiaux pulvérulents et granulaires et ses méthodes de mesure en régime établi, 1° partie, R.G.T. N° 54. Juin 1966.
[11]J.A. Currie, "Gaseous diffusion in porous, Part I. A non steady state method, Dry granular materials", Int.J.M.Transfer, 20 (1977) 711-723.
[12] D. Kunii, J.M. Smith, "Heat transfer characteristics of porous recks", A.I.Ch.E.J., 6, 71-78 (1960).
[13] Tsotsas, comunicação privada.
[14] M.K.Barcik,"effetcs of bomodal particle and metaliic fiber on thermal conductivity in a solid adsorbent bed heat pump application, ME8501: Special problems in mechanical engineering, georgia Tech Scholl of Mechanical Engineering, december 1988.
[15] G.Antonini et J.P.Pain "Etudes en dynamique ed pompes à chaleur à adsorption solide" Contrat CEE/GRADIENT n° EN3E-0099-F(CD), Juin (1987).
[16] J.J.Guilleminot and J.M.Gurgel, "heat transfert intensification in adsorbent beds of adsorption thermal devices", Int. Solar Energy Conf. ASME, avril 1990, Miami, Florida.
[17] H.Sahnoune, "Mesure de la conductivité thermique d'une zéolite supportée". tese de doutorado apresentada a E.N.S.A.M, Paris, 1988.

SUMMARY

This work shows two possibilities intensification of heat transfer in pellet beds: binary mixtures of different size pellets and mixture of pellets with metallic foam. The measurements of the thermal conductivity and the wall/bed resistance are conducted using a transient method. Measurements were made in zeolite, glass and ateel beads. Experiments show a strong dependence on the porosity for the conductivity of a bidispersed bed. The increase in conductance for a two sizes mixtures lies between a factor of 1.2 and 2. The use of metallic foam in the bed increases the conductivity by a factor between 1.6 and 2.2. The experimental results for binary-mixtures, show a good agreement with the Bauer-Schlünder model predictions.

II ENCIT – Itapema, C (Dezembro 1990)

ANÁLISE DA DISTRIBUIÇÃO DE TEMPERATURA DURANTE A SOLDAGEM AUTOMÁTICA EM PLACAS

FRANCISCO RICARDO DA CUNHA *
VALMOR FERNANDES DE ALMEIDA
DEPARTAMENTO DE ENGENHARIA MECÂNICA
UNIVERSIDADE DE BRASÍLIA - CEP: 70.910

RESUMO

Uma solução numérica baseada no método de diferenças finitas com formulação de volumes de controle é desenvolvida com o objetivo de simular a distribuição transiente de temperatura, como uma função do tempo e da posição, durante um processo de soldagem automático em placas. A variação da condutividade térmica do metal com a temperatura é considerada e uma avaliação mais rigorosa do coeficiente de convecção é feita. Os resultados numéricos são comparados com a solução analítica do problema e uma boa concordância é observada.

INTRODUÇÃO

O estudo de transferência de calor em processos de soldagem vem ganhando nos últimos anos grande interesse por parte dos pesquisadores [1,2,3]. Fatores que eram considerados secundários ou não eram conhecidos, tornaram-se cada vez mais importantes. Entre esses fatores, a distribuição de temperatura durante a soldagem é particularmente importante em vista das mudanças estruturais e tensões termomecânicas que elas originam e que estão inteiramente ligadas às características físico-químicas e mecânicas dos materiais a serem unidos.

A soldagem por fusão implica no calor propagando-se pela peça e dissipando-se para o meio ambiente. A variação de temperatura desta propagação afeta a fusão e a solidificação de metais puros ou "ligados". A taxa de crescimento da fase sólida é controlada por intermédio da velocidade com o qual o calor latente é liberado e pode ser conduzido para a vizinhança. A taxa de crescimento do volume de líquido é controlada pelo fluxo de calor fornecido ao sistema pelo eletrodo (efeito Joule). Como uma primeira aproximação, conhecimentos sobre o campo de temperatura na estrutura da peça a ser soldada é de muita utilidade na avaliação preliminar de curvas de resfriamento e na análise de tensões térmicas resultantes.

Dentro desta perspectiva é desenvolvido um procedimento numérico para simulação do transiente térmico em placas delgadas sujeitos a um processo de soldagem automático. Na elaboração do programa utiliza-se o método de diferenças finitas com formulação de volume de controle, desenvolvido por Patankar [4]. A variação da condutividade térmica do material da placa com a temperatura e uma avaliação mais rigorosa do coeficiente global de transferência por convecção é considerada conforme [3]. O presente trabalho determina também, a distribuição de temperatura analiticamente com base nos estudos de transferência de calor com fonte móvel disponíveis em [5].

Comparações dos resultados analíticos e numéricos são feitas mostrando uma boa concordância. Assim, com o programa numérico dispõe-se de uma ferramenta concreta para simulação de diversas situações relacionadas aos principais parâmetros de soldagem.

FORMULAÇÃO FÍSICA E MATEMÁTICA

Considere uma placa plana de largura "2a", comprimento "b" e espessura δ onde é depositado material fundente ao longo do eixo de simetria através de um processo de soldagem como mostrado na figura 1. O domínio solução considerando a simetria do problema é: $0 \leq x \leq b$ e $0 \leq y \leq a$.

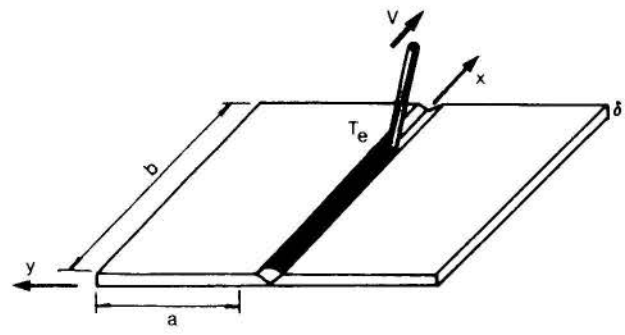

Figura 1 - Problema analisado.

O problema aqui analisado é do tipo condução de calor. Desta maneira, o comportamento térmico durante o processo de soldagem é governado pela equação da energia escrita como,

$$\rho \frac{\partial \varepsilon}{\partial t} = -\mathrm{div}(-k\,\mathrm{grad}T) + S \qquad (1)$$

onde ρ, k são respectivamente a densidade e condutividade térmica do material da placa, ε a energia interna específica, T a distribuição de temperatura, S o termo de geração de energia por unidade de volume e t o tempo.

Hipóteses Simplificativas. Para simplificações no presente modelo, as seguintes hipóteses são consideradas:

a) O problema é considerado quasi-bidimensional;
b) A fonte de calor é considerada pontual no domínio de solução;
c) As placas são rígidas, homogêneas e isotrópicas;
d) A velocidade de deslocamento do eletrodo é assumida constante durante todo o processo de soldagem;
e) A variação da condutividade térmica é atribuída apenas à variação do campo de temperatura nas placas;
f) Despreza-se os efeitos de transferência de calor por radiação para o ambiente e os efeitos de mudança de fase;
g) Os efeitos de transferência de calor por convecção serão considerados no termo de fonte, S, da equação de energia (1).

* Membro da ABCM

Portanto, para condução de calor quasi-bidimensional transiente, incluindo os efeitos de perdas de calor por convecção no termo de fonte, pode-se reescrever a equação (1) como:

$$\frac{\partial}{\partial x}\left(k\,\frac{\partial T}{\partial x}\right)+\frac{\partial}{\partial y}\left(k\,\frac{\partial T}{\partial y}\right)-\frac{2\bar{h}}{\delta}(T-T_a)=\rho c\,\frac{\partial T}{\partial t} \quad (2)$$

onde $\bar{h}$ é o coeficiente global de convecção, T_a a temperatura ambiente e c o calor específico do material da placa.

Condições de Contorno. Para condições de contorno do problema utiliza-se condições adiabáticas e de simetria, exceto para o ponto onde localiza-se o eletrodo. Neste ponto, pode-se especificar a temperatura ou o fluxo de calor por unidade de comprimento "$\dot{q}_o$". Deta maneira, as condições de contorno do problema são expressas matematicamente por,

$$\frac{\partial T}{\partial x}=0 \text{ em } x=0 \text{ para } 0\leq y\leq a \quad (3)$$

$$\frac{\partial T}{\partial x}=0 \text{ em } x=b \text{ para } 0< y\leq a \quad (4)$$

$$\frac{\partial T}{\partial y}=0 \text{ em } y=0 \text{ para } x\neq vt \quad (5)$$

$$-K\,\frac{\partial T}{\partial y}=\dot{q}_o/2 \text{ em } y=0 \text{ para } x=vt \quad (6)$$

v é a velocidade do eletrodo.

Como condição inicial:

$$T(x,y,0)=T_a \text{ (constante)} \quad (7)$$

O valor do fluxo de calor, $\dot{q}_o$, é obtido experimentalmente conhecendo-se a tensão (V) e a corrente de soldagem (I). Deve-se considerar um rendimento de soldagem "n" relacionado com as perdas de calor para o meio ambiente [2]. Quando utiliza-se a condição de contorno de temperatura especificada, T_f, esta deve ser considerada como sendo igual a temperatura de fusão do material [6].

SOLUÇÃO ANALÍTICA

O problema apresentado pode ser comparado ao problema de deslocamento de uma fonte de calor, movendo-se a uma velocidade constante em uma placa infinita. Neste problema, é identificado o que se chama regime quasi-estacionário. Neste caso, um observador que se desloca junto à fonte de calor notará que a configuração de isotermas não se modifica com o tempo. Portanto, voltando-se ao tamanho da placa finita, deseja-se saber quando o regime estacionário ocorre, levando-se em conta as bordas finitas da placa. O problema em regime transiente pode ser transformado para regime permanente, através de uma simples mudança de referencial, tendo em vista que a fonte móvel desloca-se com velocidade constante.

A solução analítica da equação (2) despreza as variações de condutividade térmica com a temperatura e considera um valor do coeficiente de convecção constante.

Da equação (2), fazendo-se $\Theta = T-T_a$ obtém-se,

$$\frac{\partial^2\Theta}{\partial x^2}+\frac{\partial^2\Theta}{\partial y^2}-\frac{\bar{h}\Theta}{k\delta}=\frac{1}{\alpha}\,\frac{\partial\Theta}{\partial t} \quad (8)$$

onde α é a difusidade térmica do material.

Definindo x, y como as coordenadas de um sistema absoluto e ξ, y como coordenadas do sistema móvel, onde se consegue o regime quasi-estacionário, pode-se verificar facilmente a seguinte relação de coordenadas,

$$\xi = x-vt \quad e \quad t=t' \quad (9)$$

No sistema de coordenadas absoluto o campo de temperatura deve satisfazer a equação (8). Deve-se obter então, a equação diferencial no sistema de coordenadas móveis. Das equações (09) verifica-se que:

$$\frac{\partial\Theta}{\partial x}=\frac{\partial\Theta}{\partial\xi}\;;\;\frac{\partial\Theta}{\partial t}=-v\,\frac{\partial\Theta}{\partial\xi}+\frac{\partial\Theta}{\partial t'} \quad (10)$$

ou ainda,

$$\frac{\partial^2\Theta}{\partial x^2}=\frac{\partial^2\Theta}{\partial\xi^2} \quad e \quad \frac{\partial\Theta}{\partial t}=-v\,\frac{\partial\Theta}{\partial\xi}, \text{ já que } \frac{\partial\Theta}{\partial t'}=0$$

no sistema de coordenadas móveis.

Assim, a equação diferencial que rege o problema no sistema de coordenadas móveis é dada por,

$$\frac{\partial^2\Theta}{\partial\xi^2}+\frac{\partial^2\Theta}{\partial y^2}-\frac{h\Theta}{k\delta}=\frac{1}{\alpha}\,v\,\frac{\partial\Theta}{\partial\xi} \quad (11)$$

A solução de (11) é da forma,

$$\Theta(\xi,y)=\exp(-v\xi/2\alpha)\,f(\xi,y) \quad (12)$$

logo de (11) e (12) obtém-se,

$$\frac{\partial^2 f}{\partial\xi^2}+\frac{\partial^2 f}{\partial y^2}-\left[h/k\delta+(v/2\alpha)^2\right]f=0 \quad (13)$$

Fazendo uma transformação do sistema de coordenadas móveis (ξ,y) para um sistema de coordenadas cilíndricas móveis (r,ϕ), onde:

$$r^2=\xi^2+y^2 \quad e \quad \phi=\operatorname{arctg}(y/\xi) \quad (14)$$

obtém-se uma nova equação em "f" dada por,

$$\frac{\partial^2 f}{\partial r^2}+(1/r)\,\frac{\partial f}{\partial r}+(1/r^2)\,\frac{\partial^2 f}{\partial\phi^2}-\eta f=0 \quad (15)$$

onde,

$$\eta=\frac{h}{k\delta}+\left(\frac{v}{2\alpha}\right)^2 \quad (16)$$

Entretanto desde que o sistema é simétrico com respeito a ϕ pode-se assumir que $\frac{\partial^2 f}{\partial\phi^2}=0$, logo de (13) tem-se,

$$r^2\,\frac{d^2 f}{dr^2}+\frac{1}{r}\,\frac{df}{dr}-\eta r f=0 \quad (17)$$

A solução de (18) é da forma,

$$f(r)=C_1 I_o(r)+C_2 K_o(r) \quad (18)$$

onde C_1 e C_2 são constantes e I_o, K_o são respectivamente as funções de Bessel de primeira e segunda espécie modificadas de ordem "o". As funções I_o e K_o foram aproximadas por ajustes polinomiais conforme [7].

Utilizando as condições de contorno do problema:

$$\text{em } r\to\infty \;,\; \Theta=0 \quad e \quad f=0 \quad (19)$$

$$\text{em } r=0,\; -2\pi rk\,\frac{\partial\Theta}{\partial r}=q_o \quad (20)$$

determina-se C_1 e C_2 dadas por,

$$C_1=0 \quad e \quad C_2=q_o/2\pi k \quad (21)$$

Portanto a solução analítica do problema requer que,

$$T(x,y,t)=T_a+\frac{q_o}{2\pi k}\left\{\exp\left[-v(x-vt)/2\alpha\right]\,K_o\left\{\sqrt{\eta\left[(x-v\Theta)^2+y^2\right]}\right\}\right\} \quad (22)$$

SOLUÇÃO NUMÉRICA

O problema é resolvido numericamente através da discretização da equação (2), utilizando diferenças centradas, com formulação implícita para o tempo. A equação (2) discretizada é obtida a partir do método variocional "fraco", cuja função peso é considerada a unidade |4|. Integrando a equação governante no volume de controle finito mostrado na figura (2), tem-se:

$$\int_t^{t+\Delta t}\int_w^e\int_s^n \frac{\partial}{\partial x}\left(k\,\frac{\partial T}{\partial x}\right)\,dx\,dy\,dt + \int_t^{t+\Delta t}\int_w^e\int_s^n \frac{\partial}{\partial y}\left(k\,\frac{\partial T}{\partial y}\right)\,dx\,dy\,dt - \int_t^{t+\Delta t}\int_w^e\int_s^n \frac{2\bar{h}}{\delta}(T-T_a)\,dx\,dy\,dt = \int_t^{t+\Delta t}\int_w^e\int_s^n \rho c\,\frac{\partial T}{\partial t}\,dx\,dy\,dt \quad (23)$$

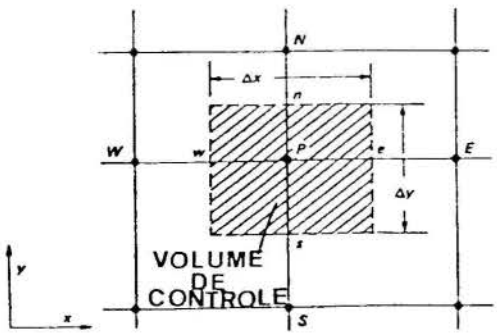

Figura 2 - Discretização por volume de controle

Assumindo um perfil linear de temperatura entre os pontos nodais, após desenvolvimentos algébricos em (23), obtém-se a equação final de discretização do problema dada por:

$$a_P T_P = a_W T_W + a_E T_E + a_N T_N + a_S T_S \quad (24)$$

onde: $a_E = \frac{k_e \Delta y}{(\delta x)_e}$; $a_W = \frac{k_w \Delta y}{(\delta x)_w}$; $a_N = \frac{k_n \Delta x}{(\delta y)_n}$;

$$a_S = \frac{k_s \Delta x}{(\delta y)_s} \; ; \quad b = S_C \Delta x \Delta y + a_P^o T_P^o \; ;$$

$$a_P = a_W + a_E + a_N + a_S + a_P^o - S_P \Delta x \Delta y \; ; \quad (25)$$

$$a_P^o = \frac{\rho c \Delta x \Delta y}{\Delta t} ; \quad S_C = \frac{2\bar{h}}{\delta} T_a \; ; \quad S_P = -\left(\frac{2\bar{h}}{\delta} + \frac{\rho c}{\Delta t}\right) .$$

O sistema de equações algébricas, obtido após o processo de discretização do domínio solução, é resolvido através do método TDMA linha-à-linha descrito em |4|, com o seguinte critério de convergência:

$$\left\| T_{i,j}^{k} - T_{i,j}^{k+1} \right\|_{máx} \leq 0{,}5^{o}C \quad (26)$$

O intervalo de tempo utilizado é tal que o eletrodo coincidia com um ponto nodal para cada tempo analisado. Foi utilizada uma malha uniforme de 22 x 22 pontos nodais, igualmente espaçados, para um domínio de a = 0,06m e b= 0,1m.

Uma avaliação mais apurada do coeficiente de transferência de calor por convecção, $\bar{h}$, é considerada. O cálculo de $\bar{h}$ é obtido da equação:

$$\bar{h} = 2\,k_{ar}\,C'(\bar{G}r_f \bar{P}r_f)^m \;/\; (b+a) \quad (27)$$

onde $\bar{G}r_f$ é o número de Grashof, $\bar{P}r_f$ é o número de Prandtl, k_{ar} é a condutividade térmica do ar e C', m são obtidos de |8|.

$$\bar{G}r_f = \frac{g\beta_f(\bar{T}_p - T_a)\left(\frac{b+a}{2}\right)}{\nu_f^2} \quad (28)$$

$$\bar{P}r_f = \frac{c_p \mu_f}{k_{ar}} \quad (29)$$

As condições de película de ar próxima a placa, tais como β_f, ν_f, ρ_{ar} e c_{par} são avaliadas através de aproximações polinomiais em função da temperatura de filme definida por:

$$T_f = \frac{T_a + \bar{T}_p}{2} \quad (30)$$

A temperatura média da placa, $\bar{T}_p$, é sempre avaliada durante as evoluções de temperatura nos tempos computacionais.

RESULTADOS

O estudo foi desenvolvido com a finalidade de obtenção da distribuição transiente de temperatura em uma placa de aço carbono de 5mm de espessura, 100mm de comprimento e 60mm de largura. As propriedades termofísicas do aço foram levadas em consideração. Enquanto na solução analítica a condutividade térmica é considerada constante, os resultados numéricos consideram a variação desta propriedade com a temperatura. O coeficiente de transferência de calor por convecção foi considerado como sendo de 10W/m²°c (valor constante) para solução analítica e avaliado de uma forma mais rigorosa, através da equação (27), quando utilizada a simulação numérica. A temperatura ambiente T_a foi de 25°c.Os resultados foram obtidos para velocidades do eletrodo de 2,4 e 8mm/s.

As figuras 3,4 e 5 representam a configuração de isotermas na placa obtidas com velocidades do eletrodo de 2,4 e 8mm/s, para as duas soluções. Observa-se que para velocidades de avanço maiores tem-se um gradiente térmico maior à frente do eletrodo e também uma deformação das isotermas em relação ao eixo x, implicando numa diminuição da extensão da zona termicamente afetada. Este fato diminui a probabilidade de aparecimento de trincas na junta soldada. O comportamento qualitativo levantado foi verificado em ambas as soluções.

Observa-se uma defazagem dos resultados obtidos nas soluções numéricas e analíticas em torno de 15%. Isto decorre da formulação analítica, pois existe uma singularidade no ponto onde encontra-se o eletrodo ($T \to \infty$) influenciando as temperaturas dos pontos vizinhos a estes. Além disso, as hipóteses simplificativas utilizadas para solução analítica não são totalmente compatíveis com as consideradas na simulação numérica. A formulação numérica está mais próxima ao fenômeno real.

Na figura 6 são mostrados os ciclos térmicos relativos as velocidades de 2,4 e 8mm/s para as duas análises desenvolvidas. Nota-se uma boa concordância entre as duas análises, tanto no aquecimento como no resfriamento de um ponto da placa. As discrepâncias apresentadas estão relacionados com o citado anteriormente.

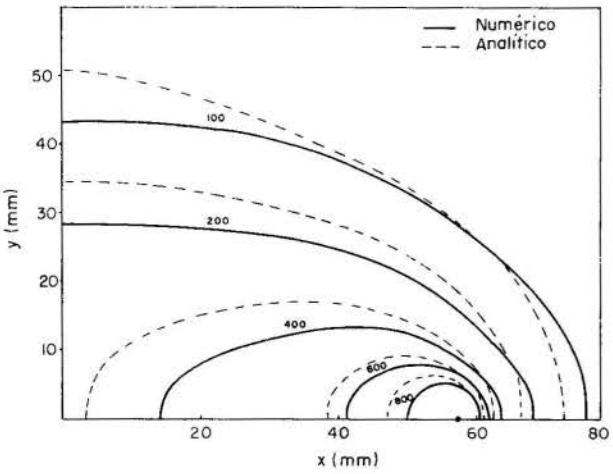

Figura 3 - Configuração de Isotermas para v=2mm/s, t= 30s.

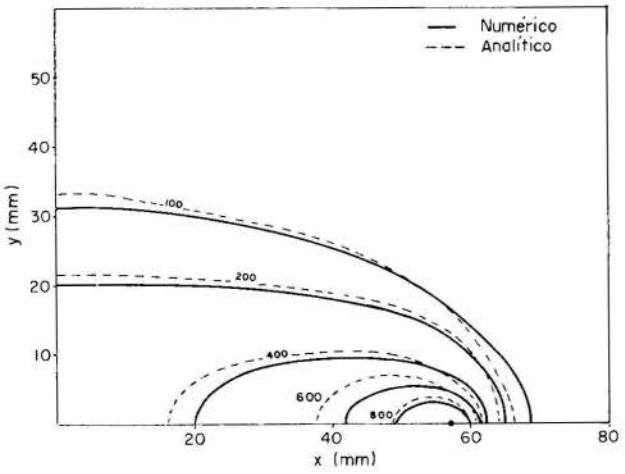

Figura 4- Configuração de isotermas para v=4mm/s, t= 15s.

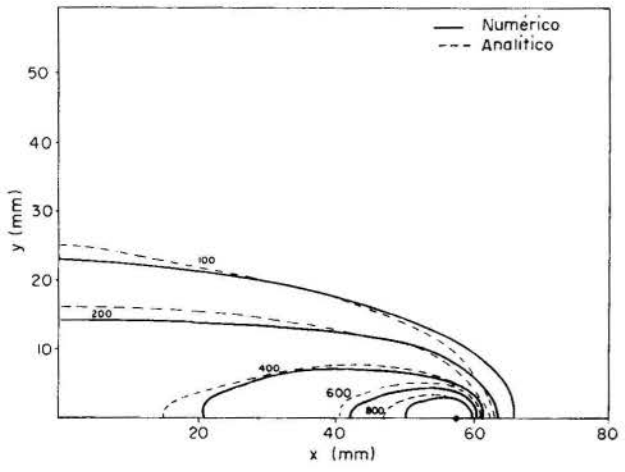

Figura 5- Configuração de isotermas para v=8mm/s, t= 7,5s.

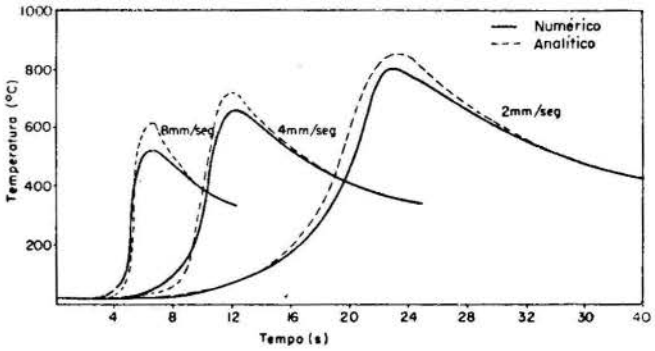

Figura 6- Ciclos térmicos de um ponto da chapa para três velocidades do eletrodo. Ponto: x= 42,5mm e y= 4,5mm.

CONCLUSÃO

1) A simulação numérica desenvolvida é capaz de determinar a temperatura como uma função do tempo para qualquer localização de um ponto da placa durante um processo de soldagem automática. Este modelo também poderia ser aplicado para qualquer outro metal onde suas propriedades físicas sejam conhecidas e incluídas no modelo. As hipóteses simplificativas utilizadas no modelo numérico o aproximam mais do processo real que o modelo analítico. Cabe observar, que dependendo do material do metal as discrepâncias entre os resultados analíticos e numéricos podem aumentar. Isto porque na simulação numérica considera-se a variação das propriedades do mesmo com a temperatura.

2) Os resultados mostram que existe uma velocidade ótima de soldagem que proporciona uma pequena zona termicamente afetada num tempo suficiente para que ocorra a fusão do metal de base. Assim, pode-se pensar em otimizar um processo de soldagem através do controle da velocidade do eletrodo, minimizando os efeitos de tensões térmicas que ocasionam defeitos no cordão de solda.

3) O presente trabalho tem uma aplicação importante na avaliação preliminar da zona termicamente afetada, tendo em vista que uma montagem experimental seria inviável para fornecer um campo de temperatura satisfatório. Através dos ciclos térmicos obtidos no atual estudo, pode-se prever a taxa de resfriamento e aquecimento do metal de base, que conjuntamente com ensaios micrográficos determina-se a qualidade da junta soldada do ponto de vista mecânico.

REFERÊNCIAS

[1] Zacharia, T., Eraslan, A.H., Aidun, D.K.,"Modeling of Non-Autogenous Welding". Welding Research Suplement, pp. 18s-27s (1988).

[2] Han, Z., Orozco, J., Indacochea, J.E., Chen, C.H., "Resistance Spot Welding: A heat transfer study" - Welding Research Suplement, pp. 363s - 371s (1989).

[3] Proença, R., Sobral, F., Cunha, F.R., Bracarense, A.Q., "Campo de Temperatura na Soldagem por Pontos em Placas". XV Congresso Brasileiro de Soldagem, São Paulo, SP, 1989. Anais da ABS 89, 2: pp. 807 - 820 (1989).

[4] Patankar, S.V., Numerical Heat Transfer and Fluid Flow. Ed. McGran Hill, 1ª edition, N.Y. (1982).

[5] Schneider, P.J., Conduction Heat Transfer. Addison W. Publishing Company - Reading, Machachusets, 2ª ed. (1957).

[6] Houldcroft, P.T., Tecnologia de los Processos de Soldadura. Ed CEAC SA - Espanha, 2ª ed. (1986).

[7] Abramowitz, M., Stegun, I. A., Handbook of Mathematical Functions. Dover Publications, N.Y., 8ª ed. (1972).

[8] Holman, J.P., Heat Transfer. McGran Hill London (1981).

ABSTRACT

During the automatic welding process the temperature distribution in the metal varies from position to position and locally with time. To simulate this process a finite difference method - Control Volume Simulation - is used in this work. The variation of the metal thermal conductivity with temperature was taken into account in the simulation. A good agreement is observed between the numerical result and the analitical solution in this heat transfer problem.

III ENCIT – Itapema, SC (Dezembro 1990)

SIMULAÇÃO DO PROCESSO DE SOLDAGEM POR PONTOS EM PLACAS

Francisco Ricardo da Cunha*
Departamento de Engenharia Mecânica - UnB
Alexandre Queiroz Bracarense**
Departamento de Engenharia Mecânica - CEFET -MG

RESUMO

Este trabalho apresenta uma simulação numérica para determinação da distribuição transiente de temperatura em placas durante o processo de soldagem por resistência elétrica por pontos. Utilizando o programa com condições de soldagem reais pré-estabelecidas é possível simular ciclos térmicos dos pontos de solda, mantendo as temperaturas máximas constantes e iguais à do primeiro ponto. Este controle das temperaturas dos pontos é possível a partir da redução do tempo de soldagem, visível nos resultados, que na prática implica em economia de energia elétrica.

INTRODUÇÃO

O estudo de transferência de calor na soldagem por resistência por ponto tem sido abordado tanto a nível teórico quanto a nível experimental nos últimos anos [1-3].

A soldagem por resistência elétrica por pontos é um processo versátil e tem-se apresentado com um excelente potencial produtivo, principalmente para soldagens de placas em juntas sobrepostas [4-7].

Na soldagem por pontos sucessivos, quando a distância entre os pontos de soldagem é tal que o tempo de passagem de um ponto para outro (Tempo de pausa) é menor que o tempo de difusão de calor gerado em um ponto até a região seguinte, os pontos serão realizados todos à mesma temperatura. Neste caso, desconsiderando os problemas inerentes do processo, os pontos serão iguais ou terão as mesmas características microestruturais.

Entretanto, quando um ponto pré-aquece o seguinte, mantidos os parâmetros de soldagem constantes, seguramente suas características serão diferentes. Desta forma, surgem duas possibilidades a fim de otimizar o processo de soldagem por pontos.

A primeira é, mantidos os parâmetros de soldagem constantes, diminuir a distância entre pontos ou aumentar o tempo de pausa, dentro de certos limites. Assim, consegue-se que a difusão de calor pelas placas promova o pré-aquecimento dos pontos de solda subsequentes. Por outro lado, esta medida aumentaria o consumo de energia e/ou o tempo de soldagem total o que acarretaria uma diminuição da produtividade.

A segunda é avaliar a influência do pré-aquecimento nas características dos pontos e controlar os parâmetros de soldagem (corrente, tempo e pressão), principalmente o tempo de soldagem a fim de obter pontos com as mesmas propriedades.

Um modelo computacional foi desenvolvido em [1] para simular o transiente térmico em placas delgadas sujeitas ao processo de soldagem por pontos. Na elaboração do programa utilizou-se o método de diferenças finitas com formulação de volume de controle, conforme [8]. Comparações dos resultados experimentais e numéricos, obtidos em [1], apresentaram uma boa concordância conforme pode ser visto na figura 1. Cabe ressaltar que o efeito da fonte externa de calor, responsável pela taxa de energia que produz a solda, foi modelado sob a forma de uma temperatura pré-escrita e como uma condição de contorno que especifica esta taxa de energia no ponto durante o tempo de soldagem.

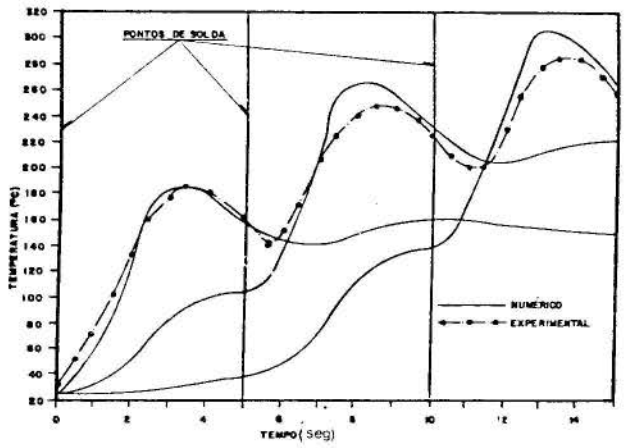

(a)

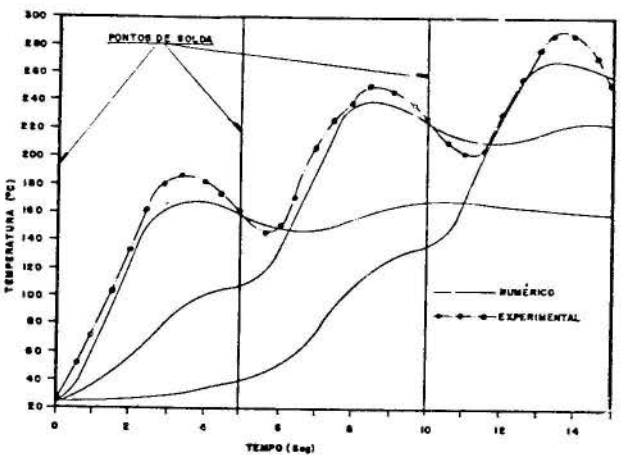

(b)

Figura 1 - Ciclos térmicos para três pontos à 10mm do ponto de solda. a) Fluxo de calor especificado e b) Temperatura especificada [1].

Utilizando nas investigações experimentais um sistema composto de: (1) Máquina de soldagem por pontos;

* Membro da ABCM/ABS
** Membro da ABS/AWS

(2) Amplificador de sinal de termopar; (3) Registrador potenciométrico; (4) Fonte de corrente e tensão calibrada; (5) Voltímetro digital e (6) Termopares tipo K (cromel-alumel) devidamente calibrados, conforme mostrado na figura 2, foi validado o programa.

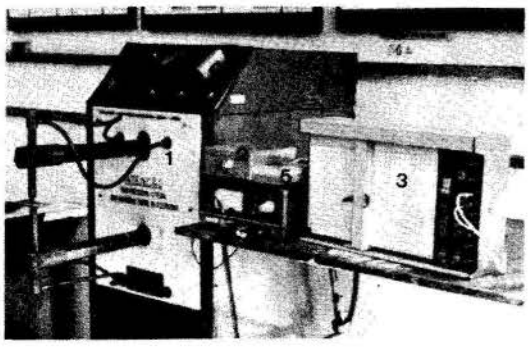

Figura 2 - Montagem Experimental [1].

Dentro deste contexto, avalia-se neste trabalho a influência do tempo de soldagem na temperatura de pré-aquecimento dos pontos. Busca-se assim a obtenção de uma curva base aproximadamente constante, descrita pelos picos de temperatura dos ciclos térmicos, a fim de que os pontos tenham as mesmas características e somado a isto, tenha-se economia de energia.

Com objetivo de visualização do pré-aquecimento dos pontos durante a soldagem, mostra-se também a configuração de isotermas na placa, tanto para um tempo de soldagem constante quanto para um tempo de soldagem variável durante o processo.

FORMULAÇÃO MATEMÁTICA

Sejam duas placas delgadas sobrepostas no domínio $0 \leq x \leq L$ e $0 \leq y \leq l/2$ e espessura "δ", sujeitas a um processo de soldagem por pontos ao longo do eixo de simetria longitudinal (x), tal como está esquematizado na figura 3.

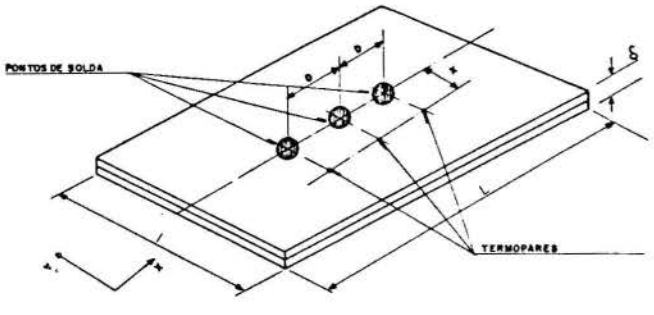

Figura 3 - Problema analisado

O problema aqui analisado é do tipo condução de calor. Desta maneira, o comportamento térmico durante o processo de soldagem é governado pela seguinte equação

$$\frac{\partial}{\partial x}\left(k\,\frac{\partial T}{\partial x}\right) + \frac{\partial}{\partial y}\left(k\,\frac{\partial T}{\partial y}\right) - \frac{2\bar{h}}{\delta}(T-Ta) = \rho c\,\frac{\partial T}{\partial t} \qquad (1)$$

Onde T é a distribuição de temperatura, $\bar{h}$ é o coeficiente de transferência de calor por convecção, Ta é a temperatura ambiente, t é o tempo e k, ρ e c são respectivamente a condutividade térmica, densidade e o calor específico do material das placas avaliados como função da temperatura através de ajustes polinomiais.

Uma avaliação mais rigorosa de $\bar{h}$ foi considerada, conforme pode ser visto em [1]. Deste modo considerou-se um valor de $\bar{h}$ mais real, pois avalia-se o mesmo durante as evoluções do campo de temperatura com o tempo, obtidas no próprio programa computacional.

Hipóteses Simplificativas. A formulação do problema baseia-se nas seguintes hipóteses:

1. O problema é considerado quasi-bidimensional;
2. A fonte de calor externa é considerada uma fonte pontual no domínio de solução;
3. As placas são rígidas, homogêneas e isotrópicas. Não introduz-se não-linearidade no comportamento do material devido a irregularidades nas placas;
4. A velocidade de deslocamento do eletrodo ou placa durante o tempo de pausa é assumida constante;
5. Despreza-se os efeitos de transferência de calor por radiação e os efeitos de mudança de fase localizada;
6. Os efeitos de transferência de calor por convecção serão considerados como termo de fonte na equação 1.

Condições Iniciais e de Contorno. A condição inicial do problema varia a cada ponto de solda que é realizado. No início, antes da ocorrência do primeiro ponto, a distribuição de temperatura é considerada igual à ambiente. Nos instantes posteriores, imediatamente antes da realização de novos pontos de solda, considera-se sempre um novo problema com condição inicial igual ao campo de temperatura obtido no tempo anterior a realização dos pontos. Isto pode ser expresso matematicamente como:

i) Condição inicial antes do primeiro ponto de solda.

$$T(x,y,0) = Ta \qquad (2)$$

ii) Condição inicial antes da realização dos pontos seguintes.

$$T(x,y,to) = T^*(x,y) \qquad (3)$$

Como condições de contorno do problema tem-se:

i) Durante o tempo de soldagem

$$\text{em } x=0,\ \frac{\partial T}{\partial x} = 0 \qquad (4)$$

$$\text{em } x=L,\ \frac{\partial T}{\partial x} = 0 \qquad (5)$$

em y=0, para fluxo de calor especificado

$$\frac{\partial T}{\partial y} = \begin{cases} 0 & \text{para pontos que não são de solda} \quad (6) \\ \dfrac{-q}{2\,kA} & \text{para pontos de solda} \quad (7) \end{cases}$$

onde A = área do volume de controle

para temperatura especificada

$$\frac{\partial T}{\partial y} = 0 \quad \text{para pontos que não são de solda} \qquad (8)$$

$$T = T_f \quad \text{para pontos de solda} \qquad (9)$$

o valor da taxa de transferência de calor, q, é obtido através de:

$$q = \eta\, VI \qquad (10)$$

onde η é a eficiência de soldagem estimada, V a tensão e I é a corrente de soldagem avaliados experimentalmente.

A temperatura especificada, T_f, é tomada como igual ou maior a temperatura de fusão do material [9].

ii) Durante o tempo de pausa

$$\text{em } x=0,\ \frac{\partial T}{\partial x} = 0 \qquad (11)$$

$$\text{em } x=L,\ \frac{\partial T}{\partial x} = 0 \qquad (12)$$

$$\text{em } y = 0, \quad \frac{\partial T}{\partial y} = 0 \qquad (13)$$

$$\text{em } y = 1/2, \quad \frac{\partial T}{\partial y} = 0 \qquad (14)$$

Com a especificação das condições de contorno, fica claro que a simulação é dividida em duas situações: A primeira onde tem-se a presença de uma fonte de calor (Tempo de soldagem) e a segunda descreve um problema onde não há presença da fonte de calor (tempo de pausa).

METODO NUMERICO

O problema é resolvido numericamente através da discretização da equação 1, utilizando o método dos resíduos ponderados, cuja função peso é considerada a unidade, com formulação implícita no tempo [8] . O sistema de equações algébricas obtido após o processo de discretização do domínio solução foi resolvido através do método TDMA linha a linha conforme [8]. O critério de convergência utilizado foi:

$$\left\| T_{i,i}^{K} - T_{i,i}^{K+1} \right\|_{Max} \leq 0{,}5^{\circ}C \qquad (15)$$

O tempo computacional para evolução do campo de temperatura é obtido conhecendo-se o tempo de soldagem e o tempo de pausa do processo. Foi utilizada uma malha de 70x14 pontos nodais.

A equação final de discretização do problema é do tipo:

$$a_P T_P = a_W T_W + a_E T_E + a_N T_N + a_S T_S + b \qquad (16)$$

onde os parâmetros definidos são os coeficientes de discretização da equação governante e são descritos em [1].

RESULTADOS E DISCUSSAO

A tabela 1 apresenta alguns parâmetros experimentais e numéricos utilizados na simulação.

Tabela 1 - Parâmetros experimentais e numéricos

Material das Placas: Aço 1020
Temperatura Especificada (T_f): 2800°c
Largura das Placas (l): $4{,}0\times10^{-2}$ m
Comprimento das Placas (L): $1{,}0\times10^{-1}$ m
Espessura das Placas (δ): $2{,}6\times10^{-3}$ m
Distância entre Pontos de Solda (D): 1×10^{-2} m
Tempo de Soldagem (ts): 2,0 seg
Tempo de Pausa (tp): 3,0 seg
Temperatura Ambiente (Ta): 24°c
Corrente de Soldagem (I): 18700 Amperes
Tensão de Soldagem (V): 0,8 a 1,0 Volts

A figura 4 apresenta a configuração de ciclos térmicos, a partir da simulação numérica, de 04 (quatro) pontos na placa, equidistantes entre si e à 3,57mm dos respectivos pontos de solda. Estes resultados foram obtidos considerando o tempo de soldagem de 2,0 seg e tempo de pausa de 3,0 seg, constantes durante a evolução do problema.

Conforme pode-se observar ocorre um pré-aquecimento entre os pontos refletido pela curva base formada pelos picos dos ciclos térmicos. Este Resultado confirma que, devido ao pré-aquecimento, os pontos estão alcançando temperaturas diferentes, o que não garante a homogenidade de suas características metalúrgicas. Além disto, excessivos gradientes de temperatura podem resultar em expulsão de material, cavitação e ruptura, reduzindo as propriedades mecânicas do material.

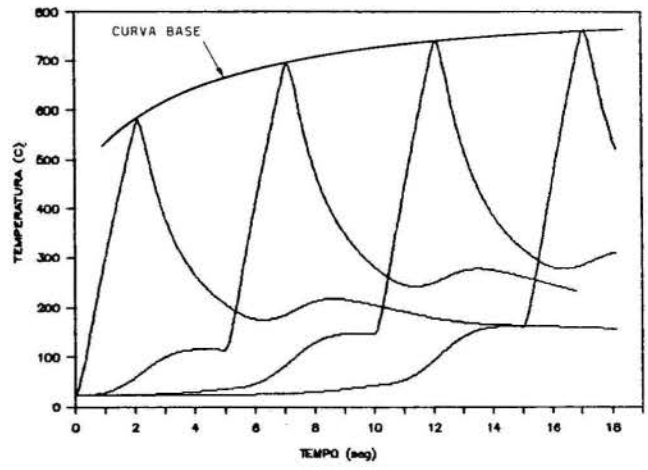

Figura 4 - Configuração de ciclos térmicos simulados para 04 (quatro) pontos de solda com tempo de soldagem CONSTANTE de 2,0 segundos.

A figura 5 mostra os ciclos térmicos nos mesmos pontos analisados na figura 4. Esta nova configuração foi obtida com tempo de soldagem variável e apresenta uma curva base aproximadamente constante para os picos dos ciclos térmicos.

Pode-se observar que os pontos alcançam a mesma temperatura máxima, o que na prática, deve garantir a homogenidade das características metalúrgicas e mecânicas dos pontos de solda. Vale ressaltar que a diminuição do tempo de soldagem implica em economia de energia.

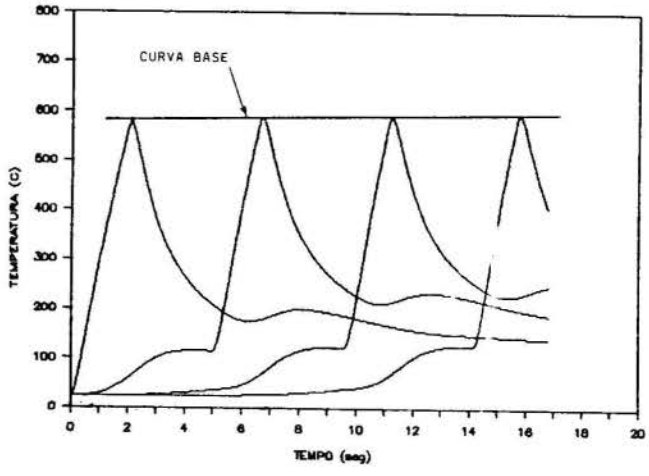

Figura 5 - Configuração de ciclos térmicos simulados para 04 (quatro) pontos de solda com tempo de soldagem VARIÁVEL.

A título de visualização da difusão de calor pela chapa, responsável pelo pré-aquecimento, apresenta-se na figura 6 a configuração de isotermas para as duas situações discutidas anteriormente.

Através das configurações, observa-se o pré-aquecimento de um ponto sobre o outro pela distorção das isotermas nos fins dos tempos de pausa.

Com relação a comparação das isotermas para as duas situações, nota-se que para um tempo de soldagem variável a difusão de calor na placa é mais lenta que para um tempo de soldagem constante. Observa-se também maiores gradientes de temperatura, nas vizinhanças de pontos de solda, em configurações de tempo de soldagem constante.

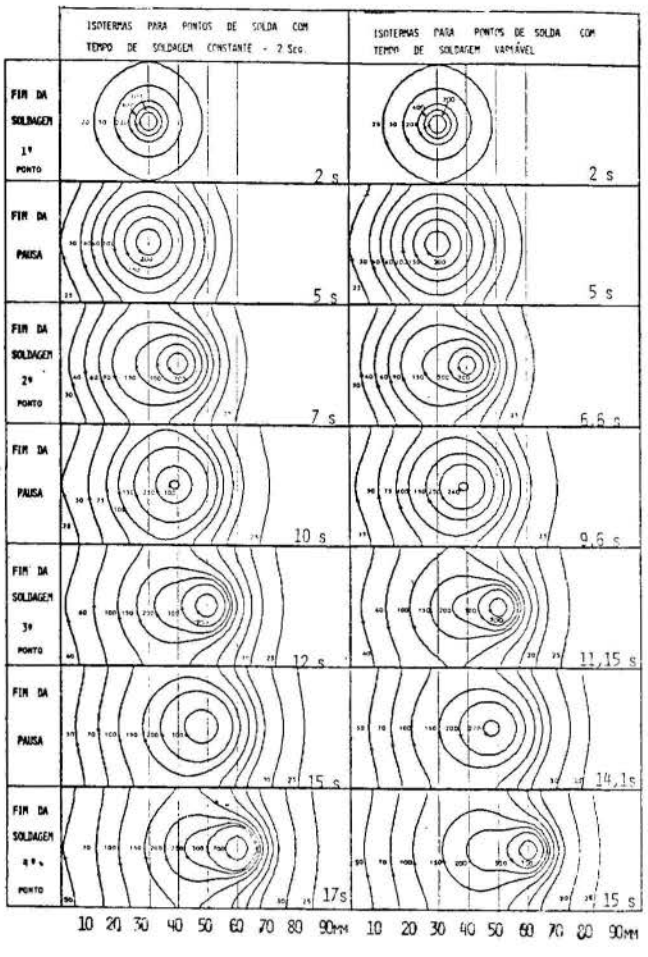

Figura 6 - Configuração de Isotermas (Tempo de pausa constante - 3 seg).

CONCLUSOES

Considerando os resultados obtidos com a simulação numérica pode-se concluir que:

1. Tem-se agora uma ferramenta muito forte para a automação do processo de soldagem por resistência elétrica por pontos;

2. Fica possível controlar a regulagem da máquina de soldagem estimando o tempo de soldagem para se ter pré-aquecimento entre os pontos mantendo as temperaturas máximas dos picos constantes e iguais à do primeiro ponto;

3. Com as temperaturas de pré-aquecimento controladas ocorre diminuição do tempo de soldagem o que leva a economia de energia elétrica. No caso do procedimento de soldagem apresentado nas figuras 4 e 5 esta economia foi em média de 16%.

REFERENCIAS BIBLIOGRAFICAS

[1] Proença, R.;Sobral, F.; Cunha,F.R.e Bracarense, A. Q.; "Campo de Temperatura na Soldagem por Pontos em Placas". Anais do XV Encontro Nacional de Tecnologia da Soldagem, São Paulo, S.P., Nov. 1989, pp. 807-820.

[2] Han, Z.; Orozco, J.; Indacochea, J.E. e Chen,C.H.; "Resistance Spot Welding: A Heat Transfer Study"; Welding Journal, Sept 1989, pp.363s-371s.

[3] Da Gama, R.M.S. e La Marca, B.; "Um Método Aproximado para a Simulação do Transiente Térmico em Placas, Durante Processos de Soldagem"; Anais do IX Congresso Brasileiro de Engenharia Mecânica, Florianópolis, SC, Dez 1987, pp.1-7.

[4]Recommended Practices For Resistance Welding - AWS (c1.1) - American Welding Society.

[5]Dickinson, D.W. et Alli; "Characterization of Spot Welding Behaviour by Dynamic Electrical Parameter Monitoring", Welding Journal, Jun 1980, pp.170s-176s

[6]Savage, W.F.; "Dynamic Contact Resistance of Series Spot Welds"; Welding Journal; Fev 1978, pp.435-505.

[7]Paes, M.T.P. e Outros; "Curvas de Soldabilidade e Características Mecânicas de Soldas por Pontos de Chapas Finas de Aço Carbono", Soldagem e Materiais-ABS, Jan/Mar 89, pp.32-36.

[8]"Numerical Heat Transfer and Fluid Flow", S.V. Patankar, 1ª Edition, 1982, Ed. McGranhill, NY-EUA.

[9]"Tecnologia de Los Processos de Soldadura"; P.T. Houdcroft, 2ª Edição, 1986, Ed. CEAC S/A, Espanha.

ABSTRACT

In this work a numerical solution is carried out for the transient temperature field in spot welding, process of flat plats. Making use of a program with real welding pre defined conditions it is possible to simulate termic cicles of the maximus temperature and equal to the first spot. This control of spot temperatures is possible from the reduction of the welding time, shown on the results, wich in practice implies in electric energy economy.

III ENCIT – Itapema, SC (Dezembro 1990)

PERFIL DE TEMPERATURA EM REGIME TRANSITÓRIO EM UMA REGIÃO PRÓXIMA A UM CENTRO CATALÍTICO ATIVO

A. MENDES *, J. BRITO **
*UFPE/DEMEC - Caixa Postal 7813
**UFPE/DES - Caixa Postal 7800
50741 - RECIFE - PE

SUMÁRIO

Em alguns tipos de reatores catalíticos, são encontrados centros catalíticos sobre a superfície do material suporte, devido a um processo de impregnação. Neste trabalho, procurou-se estimar o aumento de temperatura nas vizinhanças de um centro catalítico, quando da ocorrência de reações exotérmicas. O problema foi resolvido mediante a solução da equação geral de condução de calor. Da análise dos dados, conclui-se que o aumento de temperatura obtido não prejudica a atividade do catalisador.

INTRODUÇÃO

Os reatores catalíticos de leito fixo são os tipos mais comuns de reatores químicos, utilizados principalmente para reações altamente exotérmicas. O suporte do catalisador é geralmente uma substância porosa, de grande área superficial, como por exemplo, um material cerâmico. O uso de um suporte de melhor condutividade térmica, como um pó metálico, pode contribuir para um resfriamento mais efetivo do reator. Nos processos de impregnação, a substância catalítica encontra-se dispersa sobre o material poroso (suporte), formando concentrações de material catalítico (centros catalíticos) de dimensões microscópicas. A uma determinada temperatura, esses centros tornam-se ativos e reagem com o gás, produzindo o elemento final da reação. Desvios dessa temperatura de trabalho podem chegar a desativar o catalisador ou favorecer o surgimento de elementos indesejados. O objetivo deste trabalho é determinar teoricamente o perfil de temperatura em regime transitório, junto a um centro catalítico ativo, quando da ocorrência de reações exotérmicas.

ABORDAGEM DO PROBLEMA

Grão do Leito Catalítico. Neste trabalho, analizou-se um grão do material poroso, com um centro catalítico sobre sua superfície. Para reações exotérmicas, o centro catalítico atua como fonte de calor. Como as dimensões da superfície do centro catalítico são muito menores que as dimensões da superfície do grão do material suporte, o problema pode ser resumido à análise da transferência de calor de uma fonte pontual, localizada na superfície de um corpo semi-infinito [1]. A Fig.(1) mostra o modelo proposto.

Mecanismos de Transferência de Calor. Dos mecanismos de transferência de calor envolvidos, consideram-se apenas a condução através do grão. Em condições normais de funcionamento, a temperatura no centro catalítico, bem como na sua vizinhança, é maior que a temperatura do meio. Neste caso, a convecção contribui para a retirada de calor da superfície do grão. Trocas radiativas entre superfícies também contribuem para a retirada de calor do grão, uma vez que grãos adjacentes, destituídos de centros catalíticos, encontram-se a uma temperatura mais baixa. Com a exclusão no problema desses dois mecanismos de transferência de calor, procurou-se garantir a situação mais desfavorável, sob o ponto de vista da elevação de temperatura no grão. O caso mais desfavorável à retirada de calor do centro ativo ocorre quando não há troca de calor através da superfície do corpo (superfície isolada).

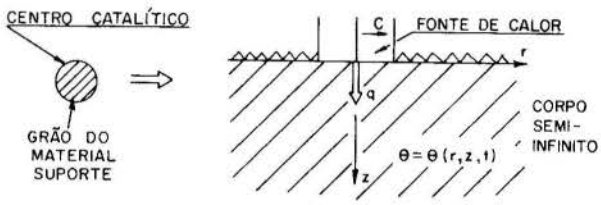

Fig. 1: Representação do modelo utilizado.

Liberação do Calor Provindo da Célula Catalítica. Sabe-se que a atividade do catalisador pode ser influenciada, dentre outros, pela temperatura. Nas condições normais de funcionamento do reator, para reações exotérmicas, é liberada uma determinada quantidade de calor, com a ocorrência da reação. Caso a temperatura na região onde está localizado o catalisador exceda um determinado valor, esse pode ter sua atividade suspensa. Ocorrendo resfriamento, o centro catalítico pode ter recuperada a sua atividade. Desta maneira são caracterizados pulsos que definem os períodos de atividade e inatividade do catalisador. Para simplificação do problema, foi tomado um valor médio para tais pulsos, admitindo-se assim que a liberação de calor seja contínua. Na realidade, uma liberação contínua de calor requereria um nível de refrigeração que viesse a impedir a elevação da temperatura acima da temperatura limite para ocorrência da reação. Para determinar-se um valor para a intensidade da fonte de raio "c", tomou-se como base a quantidade de calor liberada por

reação, a área da superfície do material suporte e dados de reatores típicos [2].

Equações do Modelo. Com base no modelo apresentado na Fig.(1) e nas simplificações já descritas, o problema da determinação do perfil de temperatura resume-se à solução da equação de condução de calor

$$\frac{1}{a}\frac{\partial\theta}{\partial t} = \nabla^2\theta + \frac{\dot{q}}{k} \qquad (1)$$

sujeita a condições de contorno específicas e a uma condição inicial.

A primeira condição de contorno representa a liberação de calor no centro ativo:

$$-k\left[\frac{\partial\theta}{\partial z}\right]_{z=+0} = q \quad , \quad 0 \leq r \leq c. \qquad (2)$$

A segunda condição de contorno diz respeito ao isolamento da superfície:

$$-k\left[\frac{\partial\theta}{\partial z}\right]_{z=+0} = 0 \quad , \quad r > c. \qquad (3)$$

A condição inicial é dada por:

$$\theta_0 = 0 \quad , \quad t = 0 \qquad (4)$$

para todos os pontos ($r \geq 0$, $z \geq 0$).

A solução da Eq.(1), sujeita às condições de contorno representadas pelas Eqs.(2) e (3), e sujeita à condição inicial Eq.(4), encontrada por Carslaw e Jaeger [3], tem a seguinte forma:

$$\theta(r,z,t) = \frac{cq}{2k}\int_0^\infty J_0(xr)J_1(xc)\ast$$

$$\left\{e^{-xz}\,\mathrm{erfc}\left[\frac{z}{2(at)^{1/2}} - x(at)^{1/2}\right] -\right.$$

$$\left. e^{xz}\,\mathrm{erfc}\left[\frac{z}{2(at)^{1/2}} + x(at)^{1/2}\right]\right\}\frac{dx}{x} \qquad (5)$$

sendo "θ" a temperatura (°C), "c" o raio da fonte de calor (m), "q" a densidade de fluxo de calor (W/m^2), "k" o coeficiente de condutividade térmica (W/mK), "r" e "z" coordenadas (m), "a" o coeficiente de difusibilidade térmica (m^2/s), "t" o tempo(s), "J_0" e "J_1" funções de Bessel de ordem zero e de primeira ordem, respectivamente, "erfc" a função erro complementar e "x" a variável de integração.

Esta equação foi resolvida numericamente, utilizando-se a subrotina DCADRE (integração pelo método de Romberg) da IMSL-Library (VAX), tomando-se os limites da integral como sendo (10^{-9}, 10^{-7}).

O programa de computador que calcula o perfil de temperatura bidimensional em regime transitório $\theta(r,z,t)$ apresenta como variáveis de entrada a intensidade da fonte "Q" (W) e o seu raio "c" (m).

O perfil de temperatura em regime permanente foi obtido tomando-se $t \to \infty$ na Eq.(5). A solução da equação resultante, como uma função de séries hiperbólicas e funções gama, pode ser encontrada em Watson [4].

RESULTADOS E CONCLUSÕES

Foram realizadas simulações para dois tipos de materiais utilizados como suporte, de condutividades térmicas distintas (suporte metálico: k = 17 W/mK e suporte cerâmico: k=0,81W/mK) e para duas reações exotérmicas (síntese da amônia e combustão do metano). Os resultados encontram-se representados em gráficos do tipo log (θ) versus log (t) para vários pontos do corpo semi-infinito, Figs.(2-4).

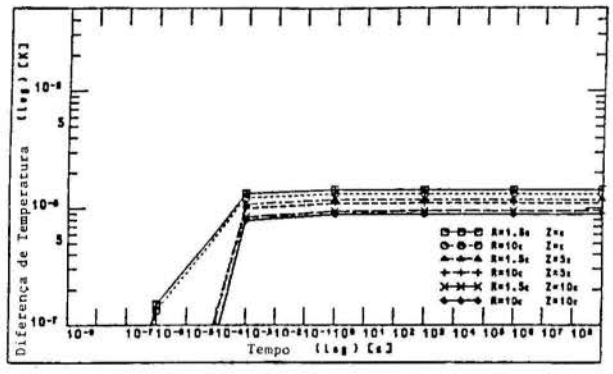

Fig. 2: Perfil de temperatura em regime transitório, para um corpo semi infinito (metálico, k = 17 W/mK), devido à presença de uma fonte de calor superficial (q = 510 W/m^2, c = 1,0x10^{-6} m). Reação: síntese da amônia.

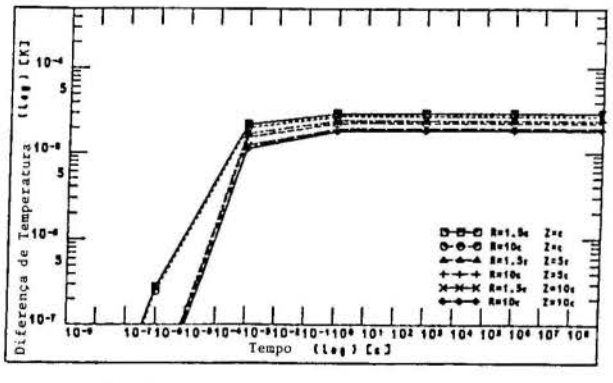

Fig. 3: Perfil de temperatura em regime transitório, para um corpo semi-infinito (cerâmico, k = 0,81 W/mK), devido à presença de uma fonte de calor superficial (q = 510 W/m^2, c = 1,0x10^{-6} m). Reação: síntese da amônia.

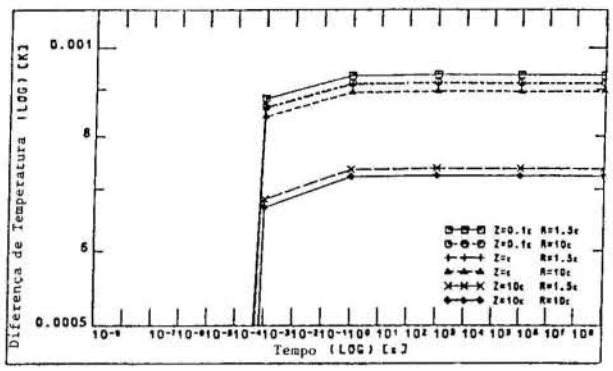

Fig. 4: Perfil de temperatura em regime transitório, para um corpo semi-infinito (metálico, K = 17 W/mK), devido à presença de uma fonte de calor superficial (q= $1,3x10^{+6}$ W/m^2, c = $0,5x10^{-6}$ m). Reação: combustão do metano.

Os resultados mais significativos das simulações em regime permanente, podem ser encontrados nas Figs.(5 e 6).

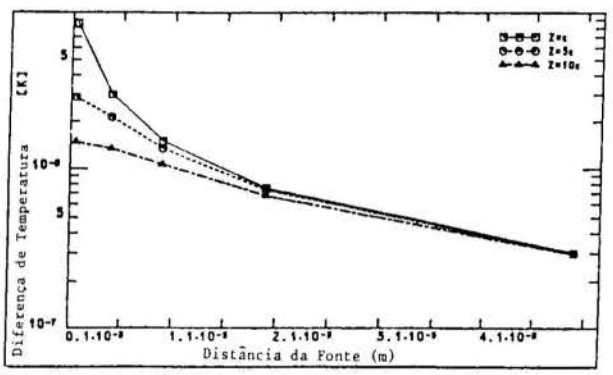

Fig 5: Elevação de temperatura em regime permanente para um corpo semi-infinito (metálico, K = 17 W/mK), devido à presença de uma fonte de calor superficial (q= 510 W/m^2, c = $1,0x10^{-6}$ m). Reação: síntese da amônia.

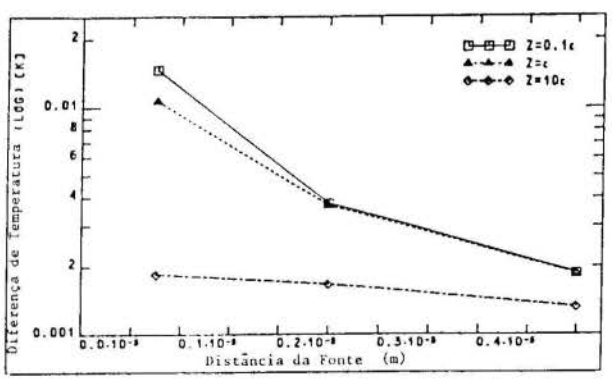

Fig. 6: Perfil de temperatura em regime permanente para um corpo semi-infinito (metálico, K = 17 W/mK), devido à presença de uma fonte de calor superficial (q = $1,3x10^{+6}$ W/m^2 c = $0,5x10^{-6}$ m). Reação: combustão do metano.

Como pode ser visto através das Figs. (2) e (3), por apresentar uma condutividade térmica mais elevada, o material metálico apresenta uma temperatura menor nas proximidades da célula catalítica, quando comparada com o material cerâmico.

Observa-se ainda que, para reações de síntese da amônia, a elevação de temperatura obtida foi de cerca de $0,1x10^{-5}$K, para suportes metálicos, e $0,3x10^{-4}$K para suportes cerâmicos. Para as reações de combustão do metano, trabalhou-se com uma maior concentração da fonte (q=$1,3x10^{+6}$ W/m^2, c=$0,5x10^{+6}$m), o que levou a um aumento de temperatura de até 0,001 K.

Da análise dos dados obtidos nas simulações (Figs.(2-6)), pode-se concluir que a atividade do catalisador não será afetada pelo aumento de temperatura produzido no centro ativo, para as duas reações consideradas. Este fato sugere que não é justificável que se promova a troca de um material cerâmico, de baixa condutividade, por um material metálico, de melhor condutividade, como tentativa de intensificar a retirada de calor do leito do reator.

REFERÊNCIAS

[1] Powell, R.W., "Thermal Conductivity Determination by Thermal Comparator Methods", Thermal Conductivity, Vol. 2, Academic Press, 1969.

[2] Mendes Primo Brito, A.R., "Wärmeübertragung in einem porösen Reaktionsbett", Zulassungsarbeit, IKE - Universität Stuttgart, Abril 1988.

[3] Carslaw, H.S., Jaeger, J.C., "Conduction of Heat in Solids" Oxford University Press, Segunda Edição, 1959.

[4] Watson, G.N., "Theory of Bessel Functions", Cambridge University Press, Segunda Edição, 1962.

ABSTRACT

In some types of fixed bed catalytical reactors, the bed can be impregnated with catalytically active substances. In this case, microscopical amounts of catalytic material (catalytic centers) can be found on the surface of the support grains. There is an optimal temperature for every reaction. Deviations from this working temperature can damage the catalytic material or generate undesirable products. To investigate the temperature increase nearby a catalytic active center, one has analyzed the effects produced on a grain of the bed due to a catalytic center on its surface. The problem has been solved by means of the well known formulation for conduction heat transfer in a semi-infinite medium (the support) subjected to a heat supply distributed over a small circular area (catalytic center), on its surface. Simulations have been carried out with data from two exothermic reactions (ammonia synthesis, methane combustion) and two types of supports (ceramic, metallic). An analysis of the data indicated that the increase on grain temperature was too small to reduce the activity of the catalyzer.

III ENCIT — Itapema, SC (Dezembro 1990)

NATURAL COOLING USING GEOMETRICAL SHADING

V. CUOMO*, G.V. FRACASTORO*, M. MACCHIATO**, E. NINO*, V. TRAMUTOLI*
*Istituto di Fisica dell'Università della Basilicata
Via Nazario Sauro, 85 - 85100 Potenza - Italy
**Dipartimento di Scienze Fisiche dell'Università di Napoli
Piazzale Tecchio, 80100 Napoli - Italy

SUMMARY

Infrared re-radiation appears as a promising method to realize natural cooling of surfaces facing the sky. During the day, however, there is a need to prevent solar radiation to reach the roof plate. This can be accomplished using geometrical shading. This paper presents a theoretical study of a geometrical shading technique consisting in a rank of parallel vertical fins placed over a flat horizontal roof. Results show that noticeable amounts of thermal power (up to 10 - 15 W/m²) can be emitted from a roof even with strong insolation, when this technique is adopted.

INTRODUCTION

As an alternative to the use of selective surfaces (see Bartoli et al.) natural cooling may be realized preventing the effect of solar radiation by means of geometrical shading techniques. This paper presents an analysis of these methods, coupled to a selective treatment of the shading device. On the opposite, the roof surface will be considered a grey surface with high absorptivity (α = 0.98).

The most common geometrical technique consists in installing a rank of parallel fins on the top of the roof. As a first approach, the effect of parallel, vertical fins on a flat, horizontal roof has been studied.

It should be noticed that any device interposed between the roof plate and the sky will also reduce the amount of infrared radiation emitted by the roof towards the sky. Moreover, any device, heated by solar radiation, will reach a temperature somewhat higher than ambient temperature, thus contributing with an infrared radiation flux to heat the roof plate.

A qualitative analysis of the optical characteristics of the fin surfaces shows that, in principle, they should be as "black" as possible on the sun facing side, in order to absorb all the incoming solar radiation, eventually dissipated by natural or forced convection to the air. Therefore, their shortwave emissivity should be as high as possible. On the other hand, in order to reduce the infrared exchanges between the fins and the roof plate, longwave emissivity should be as low as possible.

The influence of height and distance between fins will be investigated: it has been shown that the performance of this device is only influenced by the ratio between height and distance. The effect of the length of the fins, due to side effects, will also be analysed.

Further developments of this study will be in the direction of adopting tilted fins, which may probably lead to higher emitted powers, because they allow to increase the shape factor between roof plate and the sky, while still preventing direct solar radiation to reach the roof.

TEMPERATURE DISTRIBUTION IN THE FINS

In order to deal with infrared radiative exchanges, some hypotheses must be made about the temperature distribution in the fins. The upper part of the fin is lighted by the sun; due to the high shortwave absorptivity of the fin, solar radiation contributes to heat the upper part of the fin. A longitudinal conduction heat flow takes also place, contributing to heat also the shaded part of it. In order to determine the longitudinal temperature distribution the following hypotheses have been made:

- surface heat transfer coefficient and thermal conductivity are constant
- the transversal temperature distribution is uniform
- fin to air heat transfer occurs by natural convection
- heat flow at the fin tips is negligible

The geometrical features of the fin are shown in fig. 1.

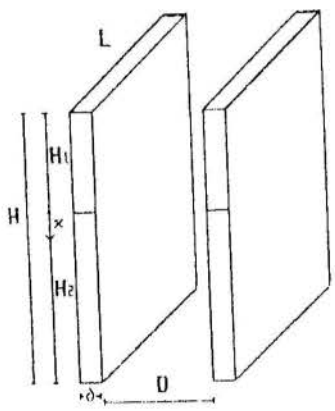

Fig. 1 - Geometrical features of the fin.

In the shaded part of the fin (from x = 0 to $x = H_2$) the temperature distribution is given by the equation:

$$\frac{d^2\Theta}{dx^2} - m^2\Theta = 0 \qquad (1)$$

where

$\Theta = T - T_a$

x = length of the fin (in the vertical direction)

$m^2 = hp/kA$

with

h = surface heat transfer coefficient

p = perimeter of the cross section of the fin = $2(L + \delta)$

k = thermal conductivity of the fin

A = cross section area of the fin = $L \cdot \delta$

The boundary conditions are:

$$\begin{aligned} x &= 0 \quad \Theta = \Theta_o = T_o - T_a \\ x &= H_2 \quad Q/A = -k \cdot (dT/dx)_{x=H_2} = 0 \end{aligned} \tag{2}$$

It should be noticed that Θ_o is at present an unknown. Integration of equation (1) with boundary conditions (2) yields the well known solution:

$$\Theta = \Theta_o \cdot \frac{ch[m(H_2 - x)]}{ch(mH_2)} \tag{3}$$

In the lighted part of the fin (from $x = -H_1$ to $x = 0$) the temperature distribution is given by the equation:

$$\frac{d^2\Theta}{dx^2} - m^2\Theta + n = 0 \tag{4}$$

where

$$n = \alpha \cdot I \cdot L/(k \cdot A \cdot \delta) = \alpha \cdot I/(k \cdot \delta)$$

with

α = shortwave absorptivity

I = solar radiation intensity, W/m^2

L = length of the fin

The boundary conditions are:

$$\begin{aligned} x &= 0 \quad \Theta = \Theta_o = T_o - T_a \\ x &= H_1 \quad Q/A = -k \cdot (dT/dx)_{x=-H_1} = 0 \end{aligned} \tag{5}$$

Integration yields:

$$\frac{\Theta - n/m^2}{\Theta_o - n/m^2} = \Theta_o \cdot \frac{ch[m(H_1 + x)]}{ch(mH_1)} \tag{6}$$

The unknown Θ_o may be found imposing the equality of heat fluxes at x = 0. In fact:

$$(Q/A)_{x=0} = k \cdot m \cdot \Theta_o \cdot \tanh(mH_2) \tag{7}$$

on the shaded part, and

$$(Q/A)_{x=0} = -k \cdot m(\Theta_o - n/m^2) \cdot \tanh(mH_1) \tag{8}$$

on the sunlit part. Equalling expressions (7) and (8) one obtains

$$\Theta_o = \frac{n/m^2 \cdot \tanh(mH_1)}{\tanh(mH_1) + \tanh(mH_2)} \tag{9}$$

As an example, fig. 2 shows the temperature distribution on a fin assuming $H_1 = H_2$, h = 5 W/m^2K, $\alpha \cdot I$ = 500 W/m^2, δ = 0.002 m, for the two cases of k = 50 W/m·K (e g, steel fin) or 0.5 W/m·K (e g, PVC fin), i e

m^2 = 100 or 10000 m^{-2}

n = 5000 or 500,000 $K \cdot m^{-2}$

and

n/m^2 = 50 K in both cases

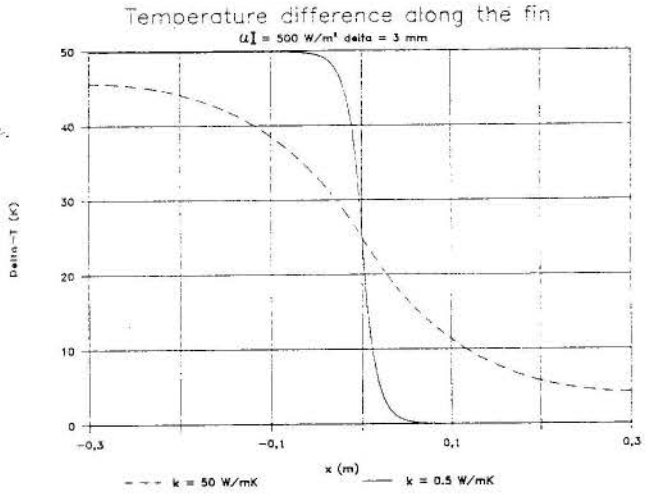

Fig. 2 - Temperature distribution along the fin.

It can be immediately seen that the temperature drop between the lighted and the shaded part is much more abrupt for the low conductivity fin, and it may be also seen that the temperature drop between the two parts increases with decreasing thickness (δ) of the fin.

In order to reduce infrared heat transfer to the roof plate, the lower part or the fin (having a higher shape factor to the roof plate) should be as cold as possible. By adopting thin, low conductivity fins, it may be therefore assumed without large errors that the lighted part of the fin has a uniform temperature equal to $T_a + n/m^2$, while the shaded part has a uniform temperature equal to T_a. Under this instance conduction along the fin may be neglected.

CALCULATION MODEL

As a first step it was necessary to make clear the heat transfer mechanism between the fin, the roof, and the sky.

In order to solve the problem the system has been divided in six elements (see fig. 3):

1 - roof plate between two adjacent fins

2 - lower part of shaded fin

3 - upper part of shaded fin

4 - sky

5 - upper part of sunlit fin

6 - lower part of sunlit fin

It has been assumed that heat was exchanged between the six elements only by infrared and diffuse solar radiation. This means that conductive heat transfer along the fin (as seen in the previous paragraph) has been neglected and that the air layer between the fins has been considered a heat sink, so that convective heat

transfer from one element to the air does not influence the temperature of the other elements. The roof (between two adjacent fin), the upper and lower part of the lighted side of the fin, and the upper and lower part of the shaded side of the fin are nonblackbodies, while the sky is a blackbody. Under these conditions it is possible to calculate the radiative heat transfer solving the equivalent electric circuit (see fig. 4).

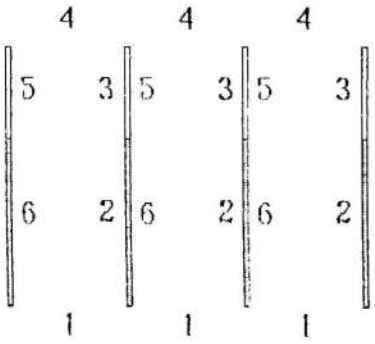

Fig. 3 - Schematic representation of fins geometry.

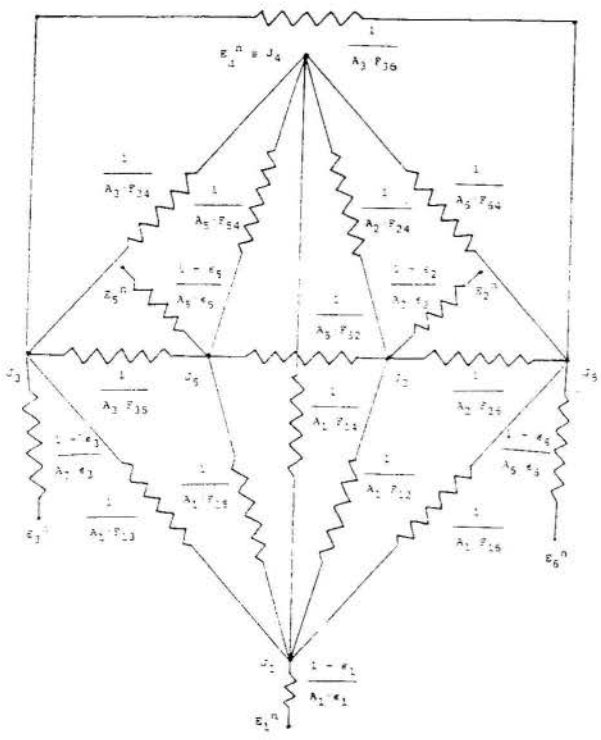

Fig. 4 - Equivalent electrical network for radiative heat transfer solution.

The first part of the program calculates the net solar irradiance incident on the fin, the diffuse solar radiation, and the geometric shape factors (F_{ij}) among the six elements (roof, fins and sky). The shape factor to the sky includes the lateral free space shape factor between two adjacent fins.

The second part of the program is made of two different steps.

In the first step the temperature of the six elements are fixed in this way: the temperature of element 4 (sky) is a fixed value, the temperature of elements 1 (roof), 2 and 6 is equal to the ambient temperature, the temperature of elements 3 and 5 is the equilibrium temperature calculated through the thermal balance between the incoming solar heat flux in element 5, and the outgoing convective heat in elements 3 and 5. Now it is possible to determine the radiative heat exchange among the six elements solving the system of five equations for the solution of the equivalent electric circuit for the heat exchange among five nonblackbodies and one blackbody (see, e g, Holman, 1976).

The system of equations is the following:

$$E_1^n \cdot \epsilon_1/(1-\epsilon_1) - J_1 \cdot (\epsilon_1/(1-\epsilon_1) + F_{12}+F_{13}+F_{14}+F_{15}+F_{16}) + J_2 \cdot F_{12} + J_3 \cdot F_{13} + J_4 \cdot F_{14} + J_5 \cdot F_{15} + J_6 \cdot F_{16} = 0$$

$$E_2^n \cdot \epsilon_2/(1-\epsilon_2) - J_2 \cdot (\epsilon_2/(1-\epsilon_2) + F_{21}+F_{24}+F_{25}+F_{26}) + J_1 \cdot F_{21} + J_4 \cdot F_{24} + J_5 \cdot F_{25} + J_6 \cdot F_{26} = 0$$

$$E_3^n \cdot \epsilon_3/(1-\epsilon_3) - J_3 \cdot (\epsilon_3/(1-\epsilon_3) + F_{31}+F_{34}+F_{35}+F_{36}) + J_1 \cdot F_{31} + J_4 \cdot F_{34} + J_5 \cdot F_{35} + J_6 \cdot F_{36} = 0$$

$$E_5^n \cdot \epsilon_5/(1-\epsilon_5) - J_5 \cdot (\epsilon_5/(1-\epsilon_5) + F_{51}+F_{52}+F_{53}+F_{54}) + J_1 \cdot F_{51} + J_2 \cdot F_{52} + J_3 \cdot F_{53} + J_4 \cdot F_{54} = 0$$

$$E_6^n \cdot \epsilon_6/(1-\epsilon_6) - J_6 \cdot (\epsilon_6/(1-\epsilon_6) + F_{61}+F_{62}+F_{63}+F_{64}) + J_1 \cdot F_{61} + J_2 \cdot F_{62} + J_3 \cdot F_{63} + J_4 \cdot F_{64} = 0 \qquad (10)$$

where:

E_i^n is the blackbody emissive power of element i
J_i is the radiosity, i e, the total radiation which leaves surface i per unit time and per unit area
ϵ_i is the emissivity of surface i
F_{ij} is the geometric shape factor between surface i and j

The radiosities are the unknowns of the system of equations, except for J_4 which coincides with the blackbody emissive power of the sky, a fixed datum in this analysis. With these values it is possible to calculate the radiative (incoming or outgoing) power for all elements with the following equation:

$$q_i = \frac{E_i^n - J_i}{(1 - \epsilon_i)/A \cdot \epsilon_i} \qquad (11)$$

In the second step the new equilibrium temperature of elements 3 and 5 subject to natural convection to the air, solar radiation, and to the just calculated infrared power q_3 and q_5 is determined. Using q_2 and q_6 plus convection the temperatures of elements 2 and 6 are also recalculated. By adopting these new temperatures the system of equations (10) for radiation heat transfer is solved again, until convergence is attained. The criterium for convergence is that the new calculated temperature is different from the old one by less than 3%.

The output of the program are the equilibrium temperatures and the emitted powers of all elements, in particular q_1 (the outgoing power from the roof).

It is possible to run the program in batch mode and to obtain the output for different geometric conditions (different ratio H/D and length L of the fins), for different optical properties (ϵ and α) of the fin and for different ambient conditions, in order to find the most favourable conditions to increase heat emission from the roof.

PARAMETRIC ANALYSIS: HYPOTHESES AND RESULTS

A parametric analysis has been performed to identify the effect of different geometric designs of the fins on the thermal behaviour of the system.

The following meteorologic characteristics have been fixed:

- "effective sky temperature" T_{sky} = 274 K

- zenith angle of the sun z = 20 °

- clear sky conditions (month of May)

Direct and diffuse solar radiation has been determined using the well known model described by ASHRAE (1980) for clear sky conditions.

The following radiative properties of the surfaces have been adopted:

- emissivity of the roof plate ϵ_p = 0.98

- emissivity of the fins ϵ_f = 0.1

- shortwave reflectivity of the fins = 0.95

The two geometrical features of the fins which have been varied are:

- height over distance ratio between the fins H/D

- length of the fins L

Moreover, the ambient temperature has been varied in the range 295 - 305 K, corresponding to a temperature difference between air and sky of 21 to 31 K.

The height of the fin has always been chosen greater than the sunlit part height, so that there is no direct sunshine on the horizontal roof plate.

Before analysing the results of the calculations, some considerations should be made: increasing the height of the fins or decreasing the distance between the fins (i e, increasing the ratio H/D) leads to a decrease of the shape factor between the horizontal plate and the sky, and simultaneously to a decrease of the shape factor from the plate to the sunlit area. This implies two conflicting effects:

- a decrease of infrared radiation emitted by the roofplate towards the (colder) sky, and

- a decrease of infrared power emitted by the warmer part of the fins onto the roof plate.

Only the calculations will show which of the two effects will prevail, but it is clear from the beginning that the first effect will increase with the increase of temperature difference between air and sky.

The calculations show (see fig. 5) that there is an optimal value of H/D at which the emitted power is maximum. The optimal H/D increases in its turn with the decrease ambient temperature. Other calculations not reported here for brevity show that the phenomenon depends on the temperature difference (ΔT) between the air and the sky, rather than on the individual values of the two temperatures. Of course, the maximum value increases with the increase of ΔT.

For higher values of H/D the emitted power tends to zero in all cases (as the shape factor between the shaded part of the fin and the roof plate tends to unity).

For an ambient temperature of 300 K (ΔT = 26 K), the optimal H/D value is around 10, and the corresponding maximum emitted power is about 6 W/m². With a ΔT of 31 K the maximum emitted power reaches 13 W/m² at H/D ≈ 6, while for a ΔT of 11 K, the optimal H/D becomes very large (around 14 - 16), and the corresponding emitted power becomes less than 2 W/m².

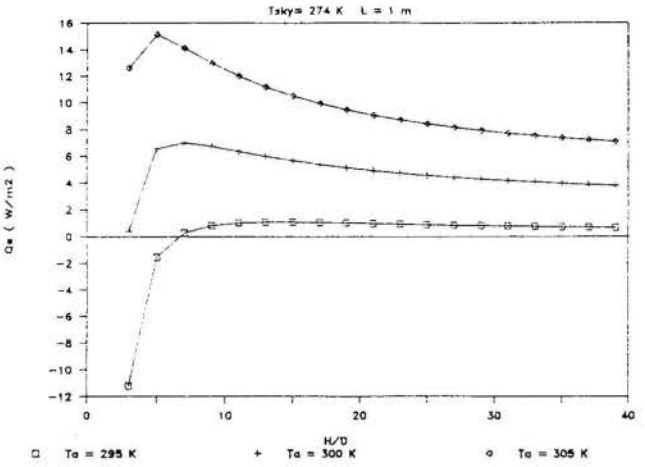

Fig. 5 - Emitted power for different H/D and Ta (L = 1 m)

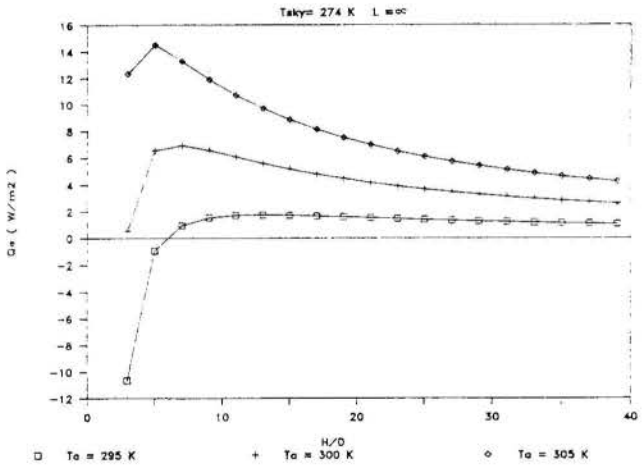

Fig. 6 - Emitted power for different H/D and Ta (L = ∞).

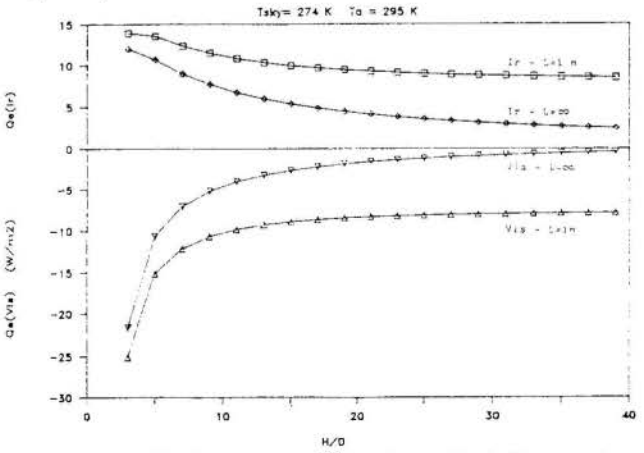

Fig. 7 - Visible and infrared emitted fluxes for L = 1 m and L = ∞.

It can be observed that convergence to zero becomes more rapid with increasing length of the fin (see fig. 6), due to the decrease of lateral shape factors, but this does not influence the optimal H/D value, although the maximum emitted

power shows a slight decrease.

Fig. 7 reports the disaggregated (visible and infrared) fluxes for the two lengths L = 1 m and L = ∞. It can be seen that both diffuse (visible) and infrared radiation tend to zero more rapidly for large values of L.

CONCLUSIONS

Although the calculations performed are referred only to a specific -- very conservative -- situation (clear sky, zenith angle of the sun equal to 20 °), some conclusions of more general validity can already be drawn.

In fact, geometrical shading of a roof using a rank of vertical absorbing fins seems to be an interesting alternative to the use of selective covers not only to prevent direct solar radiation to reach a flat horizontal roof, but also to allow the removal of small amounts of heat by re-radiation from the roof to the sky.

The calculations show that there is an optimal value of the ratio H/D between height and distance of the fins at which the net emitted power is maximum. Both the optimal H/D and the maximum emitted power depend upon the temperature difference between ambient and sky and probably also upon the reference data assumed for the analysis. Therefore the results cannot at this stage be generalized. However, when the equivalent sky temperature is about 25 K lower than ambient temperature the optimal H/D ratio is around 10 and the corresponding emitted power is about 6 W/m^2.

Optimization of such a device should be performed adopting the meteorological data of a typical reference season, including data of solar and atmospheric radiation.

Further developments of this research will be in the direction of a theoretical analysis of this kind, extended to different geometries of the fins (tilted parallel fins), and to "real" materials and dyes with their optical data.

An experimental study of the problem is also planned.

REFERENCES

ASHRAE, Handbook of Fundamentals, American Society of Heating, Refrigerating and Air Conditioning Engineers. New York, 1980.

Bartoli, B., Cuomo, V., Silvestrini, V., and Troise, G., Natural Cooling using Selective Surfaces. III Brazilian Thermal Science Meeting. Itapema - SC - Brazil - December 1990.

Holman, J.P., Heat Transfer, McGraw-Hill Book Company. 1976.

III ENCIT – Itapema, SC (Dezembro 1990)

NATURAL COOLING USING SELECTIVE SURFACES

V. CUOMO
Istituto di Fisica - Università della Basilicata
Via N.Sauro, 85 - 85100 Potenza - Italy

B. BARTOLI, V. SILVESTRINI, G. TROISE
Dipart. di Fisica-Università di Napoli Piazzale Tecchio-Napoli-Italy

SUMMARY

Since earth's atmosphere has a transparency window (8 - 13 μm), a blackbody placed at earth surface can interact with "cold" sky in clear nights and undergo a sizeable cooling effect if convective and conductive heat exchanges are removed or deeply reduced. Such effect is strongly enhanced if selective radiators are used with an emissivity matched with the atmospheric window. In this paper we analyze theoretically the phenomenon and present some experimental results which demonstrate the feasibility and the potential of this technique.

INTRODUCTION

It is well known that extra-atmospheric space can be considered as a thermal sink at a temperature of few kelvin. Since earth's atmosphere has a transparency window in the band from 8 to 13 μm black bodies exposed to clear sky during the night can undergo a remarkable cooling effect if conductive and convective heat exchange are removed or deeply reduced.

Such effect can be strongly [1,2] enhanced if selective radiators are used. These radiators must exhibit optical properties matched to infrared atmospheric window : i.e. spectral emissivity $\epsilon(\lambda) = 1$ in the atmospheric window and spectral reflectivity $r(\lambda) = 1 - \epsilon(\lambda) = 1$ out of the window.

In practice it is impossible to achieve these results so that generally $\epsilon(\lambda)$ ranges around 0.8 - 0.9 in the thermal band and around 0.1 - 0.2 out of it. Consequently the net radiated power looks as shown in fig. 1 when plotted against the temperature difference ΔT between the radiator and ambient temperature.

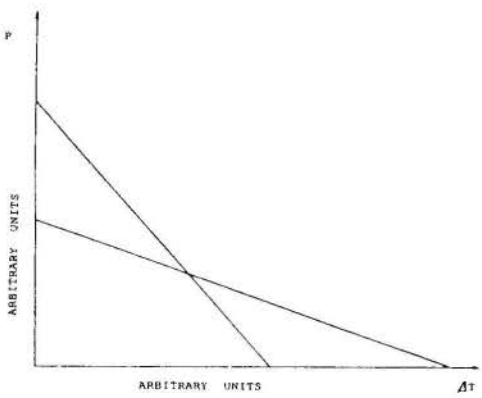

Fig. 1. Emitted power as a function of temperature difference ΔT between the radiator and ambient.

In typical atmospheric conditions at Italian latitudes and at sea level the net power emitted at $\Delta T = 0$ is around 100 W/m² depending on meteorological conditions which strongly affect atmospheric window. In any case these fluxes are about one order of magnitude less than solar radiation, so that radiative cooling is completely cancelled out by solar radiation effect during daytime. Of course, such a problem occurs in the case of black radiators, but is still present also in the case of selective ones. In fact a reflectivity of 0.1 is sufficient for the selective radiator to collect a solar power comparable to the net radiated power, and in all practical applications such a value of reflectivity represents a limit case. Consequently such a device can work during daytime only if it is shaded from solar radiation.

In principle, shading can be achieved mainly in two ways:

a) using selective covers which are transparent to infrared radiation but opaque to solar radiation;

b) using geometric structures able to stop incoming solar radiation without affecting emitted radiation.

In this paper we will briefly discuss the first approach, while the second is dealt in [3].

THE CASE OF SELECTIVE COVERS

In previous papers [4,5] it has been shown that the best way to obtain selective covers suitable to our purposes (i.e. transparent to infrared radiation and opaque to solar radiation) is the case of plastic films trasparent to thermal radiation, changing their optical properties in the solar band with some dyes.

If the radiator is selective, i.e. reflecting in the visible region, the best choice is to couple together two different films, the first one reflecting and the second absorbing in the solar band. In this case the cover must show the reflecting side to the sun and the black one to the selective radiator which has a low absorptance to solar spectrum.

Consequently we obtain that only a little fraction f of the incoming radiation Φ crosses the cover; moreover most of $(f \cdot \Phi)$ is then reflected by the radiator and absorbed by the cover. In practice only a very little part of the incoming solar radiation is absorbed by the radiator and the device can operate also during daytime.

The net radiated power in this case can be written as [5]:

$$P = W_o - \beta \cdot \tau - V \cdot \Phi \qquad (1)$$

where

$$W_o = \int W(\lambda, T_a) \cdot \delta(\lambda) \cdot [\, \chi(\lambda) + \zeta(\lambda) \,] \cdot d\lambda \qquad (2)$$

$$V = \int \Phi(\lambda) \cdot [\, \chi(\lambda) + \zeta(\lambda) \,] \cdot d\lambda \qquad (3)$$

$$\beta = [1-\varrho] \cdot h_{cr} + \int \left. \frac{\partial W}{\partial T} \right|_{T=Ta} \frac{\chi(\lambda)}{\tau(\lambda)} \cdot [1-r_2(\lambda)-\varrho \cdot \epsilon_2(\lambda)] \cdot d\lambda \qquad (4)$$

with

$I(\lambda)$: incoming solar radiation;

$$\chi(\lambda) = \frac{\alpha(\lambda) \cdot \tau(\lambda)}{1 - r_2(\lambda) \cdot [1 - \alpha(\lambda)]} \qquad (7)$$

$$\zeta(\lambda) = \varrho \cdot \{\epsilon_1(\lambda) + \epsilon_2(\lambda) \cdot \frac{1 - \alpha(\lambda)}{1-r_2(\lambda) \cdot [1 - \alpha(\lambda)]} \cdot \tau(\lambda)\} \qquad (8)$$

$$\delta(\lambda) = 1 - a(\lambda) \qquad (9)$$

$a(\lambda)$: spectral emissivity of the sky;

$\tau(\lambda)$: transparency of cover;

$r_1(\lambda)$, $r_2(\lambda)$, $\epsilon_1(\lambda)$, $\epsilon_2(\lambda)$: reflectance and emissivity of the upper (1) and lower (2) side of the cover;

$\alpha(\lambda)$: emissivity of the radiator;

$$\varrho = \frac{K_1}{K_2} \qquad (10)$$

$$K_1 = h_{cr} + \int \left. \frac{\partial W}{\partial T} \right|_{T=Ta} \cdot \frac{\alpha(\lambda) \cdot \epsilon_2(\lambda)}{1-r_2(\lambda) \cdot [1-\alpha(\lambda)]} \cdot d\lambda \qquad (11)$$

$$K_2 = h_{ca} + h_{cr} + \int \left. \frac{\partial W}{\partial T} \right|_{T=Ta} \cdot [\epsilon_1(\lambda)+\epsilon_2(\lambda) - \frac{[1-\alpha(\lambda)] \cdot \epsilon_2^{\,2}(\lambda)}{1-r_2(\lambda) \cdot [1-\alpha(\lambda)]}] \cdot d\lambda \qquad (12)$$

$W(\lambda, T)$: black body spectrum at temperature T;

T_a : ambient temperature;

T_c, T_r : cover and radiator temperature;

h_{cr}, h_{ca} : conductances between radiator and cover, and between cover and ambient (due to conduction and convection only).

It is quite interesting to analyze the properties of cooling panels in terms of solar radiation absorbed by the radiator (P) and by the cover (Q):

$$\frac{P}{\Phi} = \frac{\tau \cdot \alpha}{1 - (1 - \alpha) \cdot r_2} \qquad (13)$$

$$\frac{Q}{\Phi} = 1 - r_1 - \tau \cdot \frac{\alpha + \tau \cdot (1 - \alpha)}{1 - (1 - \alpha) \cdot r_2} \qquad (14)$$

where r_1, r_2, α, and τ are considered in the solar band.

It can be seen that P/Φ decreases for decreasing values of τ, α and r_2.

A fraction of solar power absorbed by the radiator is re-radiated in the thermal infrared; consequently it is useful to calculate α_{eff}, the fraction of the incoming solar power which heats the radiator.

It can be shown that the best values of α_{eff} are obtained for τ and r_2 tending to 0 and r_1 tending to 1.

This condition represents exactly the behaviour of a two faces film fully reflecting on the upper side and fully absorbing on the lower one.

RESULTS

Using a two face film of poliethylene plastic charged with TiO_2 on the upper side and black carbon on the lower side the following optical properties are obtained:

τ	transparency to solar radiation:	0.09
r_1	solar reflectivity (upper side):	0.67
r_2	solar reflectivity (lower side):	0.10
α	solar absorptance:	0.20

These values of τ, r_1 and r_2 allowed to obtain that f drops down to 0.05. The transparency in the atmospheric window was 0.75.

Using cooling panels (see fig. 2) based on this principle, a full scale warehouse (2.5 · 5 m², 2 m high) and an "inverse greenhouse" (≈ 100 m²) was built.

Fig. 2. Schematic drawing of an experimental natural emitter. C, cover,transparent to IR radiation; R, radiator; B, insulating box.

In fig. 3 the difference between internal temperature and ambient air temperature was reported as a function of the hour of the day. It is evident that results are satisfactory.

Nevertheless it should be stressed that satisfactory results can be obtained simply by shading the radiator from direct solar radiation. In this case the cover does not need any more to be selective.

Geometric shading is very simple in the case of small radiators (fig. 4) while for large scale devices suitable geometries must be chosen.

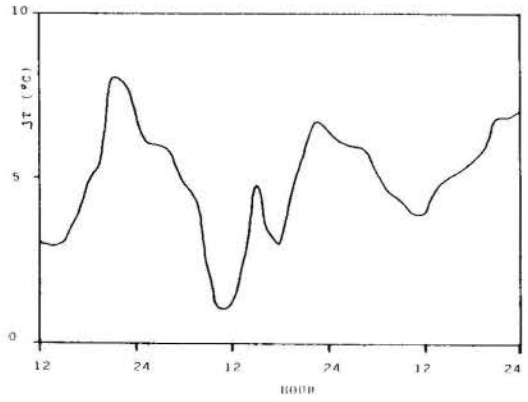

(a)

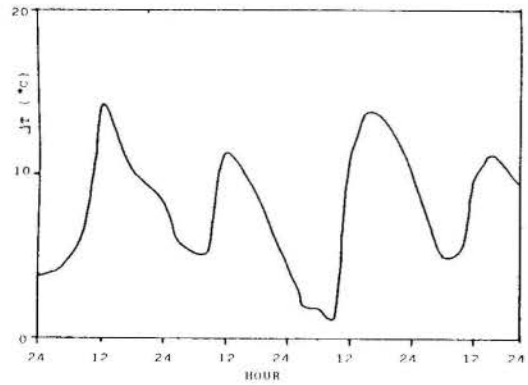

(b)

Fig. 3. (a) the case of inverse greenhouse. (b) the case of warehouse.

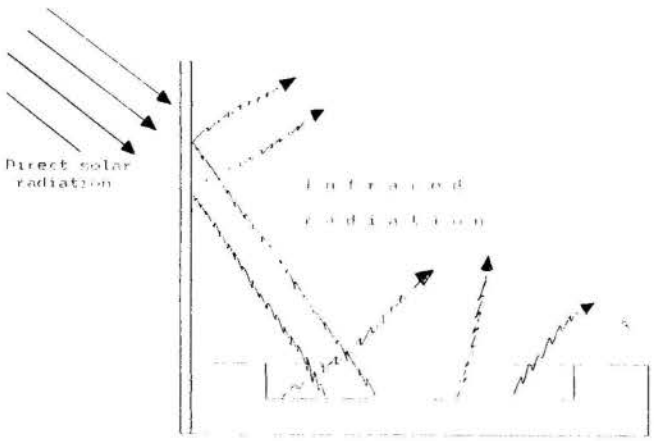

Fig. 4. Shading a small natural cooling device from direct solar radiation.

In fig. 5 the comparison of power radiated during daytime and night-time are reported in the case of geometric shading shown in fig. 4.

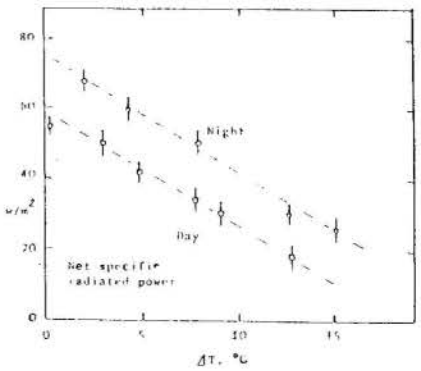

Fig. 5. Experimental performance of a natural cooling device with geometric shading from direct solar radiation. T is the temperature difference between radiator and external ambient.

Results appear much more satisfactory if one takes into account that they were we obtained in Naples, where the difference between ambient temperature and sky temperature is quite low because of polluted and humid air.

CONCLUSIONS

In this paper we have briefly resumed some results concerning radiative cooling.

It has been shown that radiative cooling can occur also during daytime if the radiator is shaded against solar radiation.

This effect can be performed both using selective covers or geometric shading. Results concerning large scale experimental setups have been reported.

It has been shown that satisfactory results can be obtained using two faces films with the upper side reflecting to solar radiation and the lower one absorbing. The main problem about this solution regards durability of plastic films used for the cover while there is no problem about maintenance of the selective radiator.

We have briefly resumed also some results concerning simple shading geometries which can be used only in the case of small radiators.

In this case of course there are no durability problems, so that it is worthwhile to analyze suitable geometries which can be used also in large scale setups.

This approach is analyzed in paper [3].

REFERENCES

[1] Catalanotti, S., Cuomo, V., Piro, G., Ruggi, D., Silvestrini, V., and Troise, G.: Solar Energy, 17, 83 - 89, 1975.

[2] Bartoli, B., Catalanotti, S., Coluzzi, B., Cuomo, V., Silvestrini, V., and Troise, G.,: Applied Energy, 3, 269 - 284, 1977.

[3] Cuomo, V., Fracastoro, G.V., Macchiato, M., Nino, E., Tramutoli, V., Natural cooling using geometrical shading, III Brazilian Thermal Science Meeting. Itapema - SC - Brasil, December 1990.

[4] Addeo, A., Bartoli, B., Silvestrini V., and Troise, G. : Nuovo Cimento, 1C, 419 - 420, 1978.

[5] Andretta, A., Bartoli, B., Coluzzi, B., and Cuomo, V. : Journal de Physique, Colloque C1, 42, C1423 - C1429, 1981.

III ENCIT – Itapema, SC (Dezembro 1990)

TEMPERATURE DISTRIBUTION IN A GRAY CIRCULAR PLATE, INDUCED BY A PUNCTUAL THERMAL RADIANT SOURCE

ROGERIO MARTINS SALDANHA DA GAMA
Laboratório Nacional de Computação Científica
Rua Lauro Müller 455
22290 - Rio de Janeiro - Brazil

SUMMARY

In this paper the energy transfer phenomenon in a gray circular plate, heated by an external (black) radiant source, is considered. The radiant source is modelled as a spherical black body with constant heat generation. A mathematical model is constructed, assuming that the heat transfer from/to the body takes place by thermal radiation. It is presented a functional whose minimum occurs for the solution to the considered problem. Some particular cases are simulated.

INTRODUCTION

The radiant interchange is an energy transfer mechanism which is always present when two bodies are separated by a nonopaque medium. Nevertheless, the radiative transfer is neglected in most of energy transfer phenomena considered for engineering calculations.

However, at high temperature levels and/or in a rarefied atmosphere, the radiative interchange plays the main role in the energy transfer process and can not be neglected.

Usually the radiative interchange is considered under very restrictive assumptions in order to reduce (drastically) the mathematical complexity of the problem. The most common assumption consists of assuming uniform temperature for the considered bodies, approximating a partial differential equation (subjected to nonlinear boundary conditions) by an algebric equation.

The subject of this work is the energy transfer process involving a black radiant source and a circular plate , as it is shown in figure 1. The source will be modelled as a spherical black body, with a constant heat generation rate Q and radius a (a→0) while the plate will be assumed to be rigid, opaque and gray, possessing constant emittance ε and constant thermal conductivity k. It will be also assumed that there exist no atmosphere, in such a way that the heat transfer from/to the plate takes place only by thermal radiation.

The circular plate will be represented by the open set Ω, with boundary $\partial\Omega$, given by

$$\Omega \equiv \{ (x,y,z) \text{ such that } x^2+y^2<R^2,\ -1<z<0 \} \qquad (1)$$

while the radiant source will be represented by the neighborhood Γ, with boundary $\partial\Gamma$, given by

$$\Gamma \equiv \{(x,y,z) \text{ such that } x^2+y^2+(z-H)^2<a^2,\ a<<H \} \qquad (2)$$

It will be assumed that the subset of $\partial\Omega$ given by $x^2+y^2=R^2$ is insulated.

The objective of this work is the mathematical modelling and the simulation of the above mentioned phenomenon. The mathematical model will be represented by a partial differential equation (governing the conduction heat transfer inside the plate) subjected to nonlinear boundary conditions (which represent the coupling between the radiative transfer and the conduction heat transfer on body boundary). This model, based on Classical Theories, will be modified (taking into account the physical reality) in order to give rise to a more adequated mathematical description, that have an equivalent minimum principle. This minimum principle will be employed for simulating some particular cases using a finite element approximation.

MODELLING THE THERMAL RADIANT SOURCE

The thermal radiant source will be regarded as a spherical black body which dissipates heat at a constant rate Q and is not affected by the presence of the plate. This black body is represented by the set Γ, with isothermal boundary $\partial\Gamma$, in which it is assumed that a<<H.

Since the source is a black body, the emitted thermal radiant energy is diffusely distributed [1]. Hence, the amount of energy that, leaving $\partial\Gamma$, reaches a given subset $\partial\Omega^*$ ($\partial\Omega^* \subset \partial\Omega$) is given by

$$S = \int_{Y\in\partial\Gamma} \left(\int_{X\in\partial\Omega^*} \sigma\, T_s^4\, K\, dA \right) dA \qquad (3)$$

$$K = \hat{K}(X,Y) = \frac{[(X-Y)\cdot m]\,[(Y-X)\cdot n]}{\pi\,[(X-Y)\cdot(X-Y)]^2}\ ,$$

if the points $X\in\partial\Omega$ and $Y\in\partial\Gamma$ can be connected by a straight line that does not intersect Γ or Ω.

$$K = \hat{K}(X,Y) = 0 \qquad \text{otherwise} \qquad (4)$$

in which n is the unit outward normal at $X \in \partial\Omega$, m is the unit outward normal at $Y \in \partial\Gamma$ and T_s is the temperature on $\partial\Gamma$ (constant).

Since $\partial\Omega^*$ is an arbitrary subset, we define the field s as follows

$$s=\hat{s}(X)=\int_{Y\in\partial\Gamma} \sigma T_s^4 \hat{K}(X,Y)\,dA \ , \quad \text{for all } X\in\partial\Omega \qquad (5)$$

The field $s=\hat{s}(X)$ represents the incident thermal radiant energy, per unit time and unit area, at the point $X\in\partial\Omega$.

In order to obtain an explicit relation for s, we shall carry out the above integral (under the assumption $a<<H$). Aiming to this, let us define a new rectangular cartesian system (x',y',z'), with an associated orthonormal basis [i',j',k'] such that

$$k' = \frac{xi + yj + Hk}{(x^2+y^2+H^2)^{1/2}}$$

$$j'\cdot n=0 \ , \ j'\cdot k'=0 \text{ and } i'=k' \times i' \qquad (6)$$

in which [i,j,k] is the orthonormal basis associated to the rectangular cartesian system (x,y,z).

Considering the following spherical coordinate system (associated to (x',y',z'))

$$\begin{aligned} x' &= \rho \cos\phi \sin\lambda \\ y' &= \rho \sin\phi \sin\lambda \\ z' &= \rho \cos\lambda \end{aligned} \qquad (7)$$

$$0\le\rho<\infty \ , \ 0\le\lambda\le\pi \ , \ 0\le\phi\le 2\pi$$

we have the vector fields n, m, X and Y given as follows

$$X = (H^2+r^2)^{1/2} k' \text{, in which } r=(x^2+y^2)^{1/2} \qquad (8)$$

$$Y = a\cos\phi \sin\lambda\, i' + a \sin\phi \sin\lambda\, j' + a\cos\lambda\, k' \qquad (9)$$

$$n = \cos\psi\, i' - \sin\psi\, j' \text{, in which } \sin\psi = H/(H^2+r^2)^{1/2} \qquad (10)$$

$$m = \cos\phi \sin\lambda\, i' + \sin\phi \sin\lambda\, j' + \cos\lambda\, k' \qquad (11)$$

Hence,

$$\frac{[(X-Y)\cdot n][(X-Y)\cdot m]}{\pi[(X-Y)\cdot(X-Y)]^2} = \left((H^2+r^2)^{1/2}\cos\lambda - a\right) \times$$

$$\times \frac{a\cos\psi\cos\phi\sin\lambda - a\sin\psi\cos\lambda + (H^2+r^2)^{1/2}\sin\psi}{\pi\left((a\sin\lambda)^2 + [a\cos\lambda - (H^2+r^2)^{1/2}]^2\right)^2} \qquad (12)$$

$$dA = a^2 \sin\lambda\, d\phi\, d\lambda \qquad (13)$$

Taking into account the restrictions (4), we have that

$$\hat{K}(X,Y) = 0 \ , \text{ for } \pi - \arccos\left(a(H^2+r^2)^{-1/2}\right) \le \lambda \le \pi \text{ or } z<0 \qquad (14)$$

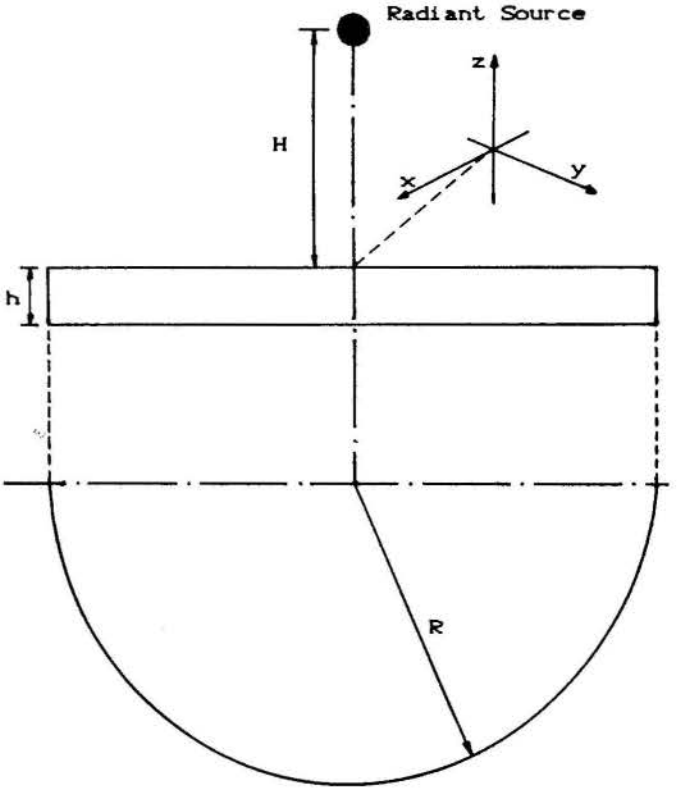

Figure 1 - Scheme for the studied phenomenon.

Consequently the field s, when $a<<H$, will be given as follows

$$s=\int_0^{2\pi}\int_0^{\pi/2} \sigma T_s^4 \left[\frac{H\,a^2}{\pi(H^2+r^2)^{1/2}}\right] \sin\lambda\cos\lambda\, d\lambda\, d\phi =$$

$$= \sigma T_s^4 \left[\frac{H\,a^2}{(H^2+r^2)^{3/2}}\right] \ , \quad \text{for } z=0 \qquad (15)$$

Denoting by Q the heat generation (per unit time) and taking into account that the source is a black body we have (from Stefan-Boltzmann Law)

$$Q = \sigma\, T_s^4\, 4\,\pi\, a^2 \qquad (16)$$

and, therefore, equation (15) may be written as follows

$$s = \frac{Q}{4\pi}\left[\frac{H}{(H^2+r^2)^{3/2}}\right], \ r=(x^2+y^2)^{1/2}, \ z=0 \qquad (17)$$

MODELLING THE HEAT TRANSFER IN THE PLATE

Since the plate is assumed to be rigid and opaque, the energy transfer mechanism, inside Ω, is the conduction heat transfer. Hence, the steady-state energy transfer in Ω will be governed by [2]

$$\Delta T = 0 \quad \text{in } \Omega \qquad (18)$$

in which "Δ" denotes the "Laplacian" and the field T represents the absolute temperature [3].

Taking into account the axial symmetry, equation (18) may be expressed as

$$\frac{1}{r}\frac{\partial}{\partial r}\left(r\,\frac{\partial T}{\partial r}\right) + \frac{\partial^2 T}{\partial z^2} = 0\ ,\quad 0\le r<R\ ,\quad -h<z<0 \qquad (19)$$

in which

$$r = (x^2+y^2)^{1/2} \qquad (20)$$

Since the surface $x^2+y^2=R^2$ is insulated, we have

$$\frac{\partial T}{\partial r} = 0 \qquad \text{at} \quad r=R \qquad (21)$$

The boundary condition on the surface z=-h arises when the conduction heat flux is imposed to be equal to the radiative heat flux. This boundary condition is mathematically represented by

$$k\,\frac{\partial T}{\partial z} = \varepsilon\,\sigma\,T^4 \qquad \text{at} \quad z=-h \qquad (22)$$

in which k is the thermal conductivity, ε ($0<\varepsilon\le 1$) is the emittance and σ is the Stefan-Boltzmann constant [1].

On the surface z=0 we must take into account the effect of the source modelled in the previous section. The heat loss, per unit time and unit area, will be given by the difference between the emitted and the absorbed thermal radiant energy (denoted here by $\bar{s}$).

Since the plate is assumed to be gray we have [4]

$$\bar{s} = \varepsilon\, s = \frac{\varepsilon Q}{4\pi}\left(\frac{H}{(H^2+r^2)^{3/2}}\right) > 0 \qquad (23)$$

and, consequently, at z=0

$$-k\frac{\partial T}{\partial z} = \varepsilon\sigma T^4 - \frac{\varepsilon Q}{4\pi}\left(\frac{H}{(H^2+r^2)^{3/2}}\right) \quad \text{at } z=0 \qquad (24)$$

Combining (19),(21),(22) and (24) we have the mathematical model for describing the considered phenomenon.

AN INDISPENSABLE CAUTION

When Q=0 it is easy to see that the problem (19)+(21)+(22)+(24) admits only the trivial solution (T≡0). It is physically plausible that, when Q>0, the solution T will be a nonnegative valued field.

Although physically expected, this reality is assured only if, together with (19)+(21)+(22)+(24), the following inequality is imposed

$$T \ge 0 \qquad -h\le z\le 0\ ,\ 0\le r\le R \qquad (25)$$

Aiming to ilustrate the necessity of imposing (25), let us consider the following (limit) case

$$Q = 68\,\pi\,H^2\,\sigma\ ,\qquad H\to\infty \qquad (26)$$

In such situation, when ε=1 and σ=k we have

$$\begin{aligned}
&\frac{1}{r}\frac{\partial}{\partial r}\left(r\,\frac{\partial T}{\partial r}\right) + \frac{\partial^2 T}{\partial z^2} = 0 \qquad -1<z<0\ ,\ 0\le r<R\\
&\frac{\partial T}{\partial r} = 0 \qquad \text{at} \quad r=R\\
&\sigma\,\frac{\partial T}{\partial z} = \sigma\,T^4 \qquad \text{at} \quad z=-1\\
&-\sigma\,\frac{\partial T}{\partial z} = \sigma\,T^4 - 17\,\sigma \qquad \text{at} \quad z=0
\end{aligned} \qquad (27)$$

When regarded under a strictly mathematical point of view, the above problem admits the following (real) solutions

$$(a) \rightarrow T = z + 2\ ,\quad -1\le z\le 0\ ,\ 0\le r\le R \qquad (28)$$

$$(b) \rightarrow T = 3.2697\,z + 1.9250\ ,\quad -1\le z\le 0\ ,\ 0\le r\le R \qquad (29)$$

The solution (a) is admissible, because T≥0 in the considered domain, while the solution (b) is not admissible, because T assumes negative values in the considered domain.

Solving (27), together with the restriction (25), we have only the admissible solution given by (28).

In order to preserve the physical meaning of the mathematical model, we shall work with the following mathematical problem

$$\begin{aligned}
&\frac{1}{r}\frac{\partial}{\partial r}\left(r\,\frac{\partial T}{\partial r}\right) + \frac{\partial^2 T}{\partial z^2} = 0,\ 0\le r<R\ ,\ -h<z<0\\
&\frac{\partial T}{\partial r} = 0 \qquad \text{at} \quad r=R\\
&k\,\frac{\partial T}{\partial z} = \varepsilon\,\sigma\,T^4 \qquad \text{at} \quad z=-h\\
&-k\,\frac{\partial T}{\partial z} = \varepsilon\,\sigma\,T^4 - \frac{\varepsilon Q}{4\pi}\left(\frac{H}{(H^2+r^2)^{3/2}}\right) \qquad \text{at} \quad z=0\\
&T \ge 0\ ,\quad 0\le r\le r\ ,\quad -h\le z\le 0
\end{aligned} \qquad (30)$$

SOLUTION'S UNIQUENESS FOR (30)

In order to prove that the solution ($T\ge 0$) to (30) is unique, let us assume that T_1 ($T_1\ge 0$) and T_2 ($T_2\ge 0$) are two solutions to (30).

Hence, the difference (T_1-T_2) satisfies the Laplace equation and, consequently, will assume its maximum and its minimum on the boundary $\partial\Omega$ [5]. In addition, since $\partial T/\partial n=0$ at r=R, the maximum and the minimum occur at z=-h or at z=0. At a point of $\partial\Omega$, in which (T_1-T_2) assumes its minimum, we must have a nonpositive exterior normal derivative. Thus, at this point

$$\frac{\partial}{\partial n}(T_1-T_2)\le 0 \Leftrightarrow \varepsilon\sigma(T_1^4-T_2^4)\ge 0\ ,\ T_1\ge 0\ ,\ T_2\ge 0 \qquad (31)$$

and, at a point of $\partial\Omega$ in which (T_1-T_2) assumes its maximum, we must have a nonnegative exterior normal derivative. Thus, at this point

$$\frac{\partial}{\partial n}(T_1-T_2)\geq 0 \Leftrightarrow \varepsilon\sigma(T_1^4-T_2^4)\leq 0 \ , \ T_1\geq 0 \ , \ T_2\geq 0 \quad (32)$$

From (31) we conclude that the minimum of (T_1-T_2) is nonnegative and, from (32), we conclude that the maximum of (T_1-T_2) is nonpositive. Consequently, we must have $T_1\equiv T_2$ and, therefore, the solution to (30) is unique.

VARIATIONAL FORMULATION

The field T which satisfies (30) is the one that minimizes the following functional

$$I[\tilde{T}] = \frac{1}{2}\int_0^R \int_{-h}^0 k\left[\left(\frac{\partial\tilde{T}}{\partial r}\right)^2+\left(\frac{\partial\tilde{T}}{\partial z}\right)^2\right] r\,dz\,dr + \\ + \frac{1}{5}\varepsilon\sigma\left(\int_0^R |\tilde{T}|^5 r\,dr\right)_{z=0} + \\ + \frac{1}{5}\varepsilon\sigma\left(\int_0^R |\tilde{T}|^5 r\,dr\right)_{z=-h} - \\ - \frac{\varepsilon Q}{4\pi}\left(\int_0^R \frac{H}{(H^2+r^2)^{3/2}}\tilde{T}\,r\,dr\right)_{z=0} \quad (33)$$

The Euler-Lagrange equation and the Natural boundary conditions associated to the above functional are given by

$$\frac{1}{r}\frac{\partial}{\partial r}\left(r\frac{\partial T}{\partial r}\right)+\frac{\partial^2 T}{\partial z^2}=0 \qquad 0\leq r<R \ , \ -h<z<0$$
$$\frac{\partial T}{\partial r}=0 \qquad \text{at} \quad r=R \quad (34)$$
$$k\frac{\partial T}{\partial z}=\varepsilon\sigma|T|^3T \qquad \text{at} \quad z=-h$$
$$-k\frac{\partial T}{\partial z}=\varepsilon\sigma|T|^3T-\frac{\varepsilon Q}{4\pi}\left(\frac{H}{(H^2+r^2)^{3/2}}\right) \qquad \text{at} \quad z=0$$

In order to demonstrate that (34) and (30) are equivalent, let us take into account that T reaches its minimum at z=0 or at z=-h. Hence, one of the following assertions must hold

(a) $\frac{\partial T}{\partial z}\leq 0$,
at the point r in which $T=T_{min}$, at $z=0$

(b) $\frac{\partial T}{\partial z}\geq 0$,
at the point r in which $T=T_{min}$, at $z=-h$ (35)

If (b) holds we conclude, from the boundary condition at $z=-h$, that $T\geq 0$ at $z=-h$ and, therefore, $T\geq 0$ in $\bar{\Omega}$. On the other hand, if (a) holds, we conclude, from the boundary condition at $z=0$, that $T>0$ at $z=0$ (once that $Q>0$) and, therefore, $T\geq 0$ in $\bar{\Omega}$. Hence, the field T is everywhere nonnegative and, thus,

$$|T|^3T \equiv T^4 \qquad \text{at} \quad z=0 \text{ and at } z=-h \quad (36)$$

Consequently, a solution to (34) is also a solution to (30).

Taking into account that (30) admits only one solution, we conclude that the field T, which makes extremum the functional I, is the solution to (30).

Since I is a convex functional, the above mentioned extremum is a minimum [6].

THE UNIFORM TEMPERATURE APPROXIMATION

The uniform temperature approximation is an usual assumption in engineering calculations and will be used here for posterior comparisons with other approximations.

The uniform temperature approximation may be obtained from the functional I. Aiming to this, we shall assume that

$$\tilde{T}=\bar{A}=\text{constant} \ , \ 0\leq r\leq R \ , \ -h\leq z\leq 0 \quad (37)$$

Considering (37) the functional I becomes

$$I[\tilde{T}] = f(\bar{A}) = \frac{1}{5}\varepsilon\sigma(2|\bar{A}|^5)\int_0^R r\,dr - \\ - \frac{\varepsilon Q}{4\pi}H\bar{A}\int_0^R \frac{1}{(H^2+r^2)^{3/2}}r\,dr \quad (38)$$

and, hence, the constant $\bar{A}$ is the (unique) solution to

$$\frac{df}{d\bar{A}}=0 \Leftrightarrow \varepsilon\sigma|\bar{A}|^3\bar{A}R^2+\frac{\varepsilon Q}{4\pi}\left(\frac{H}{(H^2+R^2)^{1/2}}-1\right)=0 \quad (39)$$

being given as follows

$$\bar{A}=\left(\frac{Q}{4\pi\sigma R^2}\right)^{1/4}\left(1-\frac{1}{(1+(R/H)^2)^{1/2}}\right)^{1/4} \quad (40)$$

DIMENSIONLESS FORMULATION

Defining $\alpha,\beta,\gamma,\xi,\eta$ and θ as follows

$$\alpha=\frac{k}{\varepsilon\sigma h}\left(\frac{Q}{4\pi\sigma R^2}\right)^{-3/4} \ , \ \beta=\frac{R}{H} \ , \ \gamma=\frac{R}{h} \quad (41)$$

$$\xi=\frac{r}{h} \ , \ \eta=\frac{z}{h} \quad (42)$$

$$\theta=T\left(\frac{Q}{4\pi\sigma R^2}\right)^{-1/4} \quad (43)$$

we may write problem (34) as follows

$$\frac{1}{\xi}\frac{\partial}{\partial\xi}\left(\xi\frac{\partial\theta}{\partial\xi}\right)+\frac{\partial^2\theta}{\partial\eta^2}=0 \ , \ 0\leq\xi<\gamma \ , \ -1<\eta<0$$
$$\frac{\partial\theta}{\partial\xi}=0 \qquad \text{at} \quad \xi=\gamma \quad (44)$$
$$\alpha\frac{\partial\theta}{\partial\eta}=|\theta|^3\theta \qquad \text{at} \quad \eta=-1$$
$$-\alpha\frac{\partial\theta}{\partial\eta}=|\theta|^3\theta-\left(\frac{\beta^2}{(1+\xi^2(\beta/\gamma)^2)^{3/2}}\right) \qquad \text{at} \quad \eta=0$$

and express the functional I as

$$I[\tilde{\theta}] = \frac{\alpha}{2}\int_{-1}^{0}\int_{0}^{\gamma}\left[\left(\frac{\partial\tilde{\theta}}{\partial\xi}\right)^2+\left(\frac{\partial\tilde{\theta}}{\partial\eta}\right)^2\right]\xi\,d\xi\,d\eta +$$

$$+\frac{1}{5}\left(\int_0^{\gamma}|\tilde{\theta}|^5\,\xi\,d\xi\right)_{\eta=0} +$$

$$+\frac{1}{5}\left(\int_0^{\gamma}|\tilde{\theta}|^5\,\xi\,d\xi\right)_{\eta=-1} -$$

$$-\left(\int_0^{\gamma}\frac{\beta^2}{(1+\xi^2(\beta/\gamma)^2)^{3/2}}\tilde{\theta}\,\xi\,d\xi\right)_{\eta=0} \quad (45)$$

A COMPARISON AMONG SOME PRELIMINAR APPROXIMATIONS

In order to ilustrate the employment of functional I for obtaining approximations for problem (44), let us consider the following approximations for the field θ

(a)→ $\tilde{\theta} = A$ (uniform temperature approximation) , $-1\le\eta\le0$, $0\le\xi\le\gamma$ (46)

(b)→ $\tilde{\theta} = A + B\eta$ (uniform surface temperature) , $-1\le\eta\le0$, $0\le\xi\le\gamma$ (47)

(c)→ $\tilde{\theta} = A + B\eta + C\eta^2$, $-1\le\eta\le0$, $0\le\xi\le\gamma$ (48)

(d)→ $\tilde{\theta} = A + B\eta + C\eta^2 + D\xi^2$, $-1\le\eta\le0$, $0\le\xi\le\gamma$ (49)

(e)→ $\tilde{\theta} = A\xi + B\eta + C$, $-\xi/\gamma\le\eta\le0$, $0\le\xi\le\gamma$

$\tilde{\theta} = (A+(D-B)/\gamma)\xi + D\eta + C$, $-1\le\eta\le-\xi/\gamma$, $0\le\xi\le\gamma$ (50)

With the above proposed approximations, the functional I gives rise to the following functions

(a)→ $$f_1(A) = \frac{\gamma^2}{5}|A|^5 - \gamma^2 A\left[1-(1+\beta^2)^{-1/2}\right] \quad (51)$$

(b)→ $$f_2(A,B) = \frac{\alpha\gamma^2}{4}B^2 + \frac{\gamma^2}{10}\left(|A|^5+|A-B|^5\right) - \gamma^2 A\left[1-(1+\beta^2)^{-1/2}\right] \quad (52)$$

(c)→ $$f_3(A,B,C) = \frac{\alpha\gamma^2}{4}(B^2-2BC+4C^2/3) + \frac{\gamma^2}{10}\left(|A|^5+|A-B+C|^5\right) - \gamma^2 A\left[1-(1+\beta^2)^{-1/2}\right] \quad (53)$$

(d)→ $$f_4(A,B,C,D) = \frac{\alpha\gamma^2}{4}(B^2-2BC+4C^2/3) + \frac{\alpha\gamma^4}{2}D^2 + \frac{1}{600}\left[|A+D\gamma^2|^5(A+D\gamma^2) - |A|^5 A + |A-B+C+D\gamma^2|^5(A-B+C+D\gamma^2) - |A-B+C|^5(A-B+C)\right] - \gamma^2 A(1-(1+\beta^2)^{-1/2}) - \frac{2\gamma^4 D}{\beta^2}((1+\beta^2)^{1/2}-1) + \gamma^4 D(1+\beta^2)^{-1/2} \quad (54)$$

(e)→ $$f_5(A,B,C,D) =$$

$$= \frac{\alpha\gamma^2}{6}(A^2+B^2) + \frac{\alpha}{12}((A\gamma^2-B+D)^2 + D^2\gamma^2) +$$

$$+\gamma^2((A\gamma+C)(1+\beta^2)^{-1/2}-C) -$$

$$-\frac{\gamma^3 A}{\beta}\mathrm{Ln}(\beta+(1+\beta^2)^{1/2}) +$$

$$+\frac{1}{5A^2}\left(\frac{|A\gamma+C|^7-|C|^7}{7} - \frac{|A\gamma+C|^5(A\gamma+C)-|C|^5 C}{6}C\right) +$$

$$+\left(\frac{\gamma/5}{A\gamma-B+D}\right)^2\left(\frac{|A\gamma-B+C|^7-|C-D|^7}{7} - \frac{|A\gamma-B+C|^5(A\gamma-B+C)-|C-D|^5(C-D)}{6}(C-D)\right) \quad (55)$$

The minimization of each of the above functions provides the coeficients for the approximations (a),(b),(c),(d) and (e).

The following equations present the results obtained with $\alpha=0.1$, $\beta=1.0$ and $\gamma=100.0$.

(a)→ $\theta = 0.736$, $-1\le\eta\le0$, $0\le\xi\le100$ (56)

(b)→ $\theta = 0.409\,\eta + 0.859$, $-1\le\eta\le0$, $0\le\xi\le100$ (57)

(c)→ $\theta = 0.409\,\eta + 0.859$, $-1\le\eta\le0$, $0\le\xi\le100$ (58)

(d)→ $\theta = -0.0000212\,\xi^2 + 0.414\,\eta + 0.958$, $-1\le\eta\le0$, $0\le\xi\le100$ (59)

(e)→ $\theta = -0.00264\,\xi + 0.364\,\eta + 1.029$, $-\xi/100\le\eta\le0$, $0\le\xi\le100$

$\theta = -0.00136\,\xi + 0.493\,\eta + 1.029$, $-1\le\eta\le-\xi/100$, $0\le\xi\le100$ (60)

It is to be noticed that the coeficient C, in approximations (c) and (d), is identically zero.

SIMULATION OF SOME PARTICULAR CASES (USING FINITE ELEMENTS)

In order to present some typical results, we shall approximate the field θ by the following linear field

$$\tilde{\theta} = (\theta_{2j+1}-\theta_{2j-1})\left(\frac{\xi-\xi_{2j-1}}{\Delta\xi}\right) - (\theta_{2j+2}-\theta_{2j+1})\eta + \theta_{2j-1} \text{ , for}$$

$$\xi_{2j-1}\le\xi\le\xi_{2j+1} \text{ , } \left(\frac{\xi-\xi_{2j-1}}{\Delta\xi}\right)\le\eta\le0$$

$$\tilde{\theta} = (\theta_{2j+2}-\theta_{2j})\left(\frac{\xi-\xi_{2j-1}}{\Delta\xi}\right) - (\theta_{2j}-\theta_{2j-1})\eta + \theta_{2j-1} \text{ , for}$$

$$\xi_{2j-1}\le\xi\le\xi_{2j+1} \text{ , } -1\le\eta\le\left(\frac{\xi-\xi_{2j-1}}{\Delta\xi}\right)$$

$$j=1,2,3,4,5,6,\ldots,N/2-1 \quad (61)$$

in which N is the number of nodes, θ_i is the

approximation (for θ) at the node i and

$$\xi_{2j-1}=\xi_{2j}=(j-1)\Delta\xi,\quad j=1,2,3,\ \ldots\ ,(N-2)/2 \qquad (62)$$

$$\Delta\xi = \xi_3 = (\xi_{2j+1} - \xi_{2j-1}) = (\xi_{2j+2} - \xi_{2j}) = 2\gamma/(N-2) \qquad (63)$$

Inserting (61) into (45) and carrying out the integrations, the functional I becomes a function of $\theta_1,\theta_2,\theta_3,\ \ldots\ ,\theta_N$.

The minimum of this function is reached when $\theta_1,\theta_2,\theta_3,\ \ldots,\ \theta_N$ are the roots of the following nonlinear system of equations

$$\frac{\partial f}{\partial \theta_i} = 0\ ,\quad i=1,2,3,4,5,\ldots,N \qquad (64)$$

in which f is the considered function.

SOME RESULTS

Figures 2 and 3 present results obtained with 50 finite elements (M=50, N=102). In the above mentioned figures it is also presented the uniform temperature approximation (dashed line).

In all the situations, system (64) was solved employing a Newton-Raphson scheme [7].

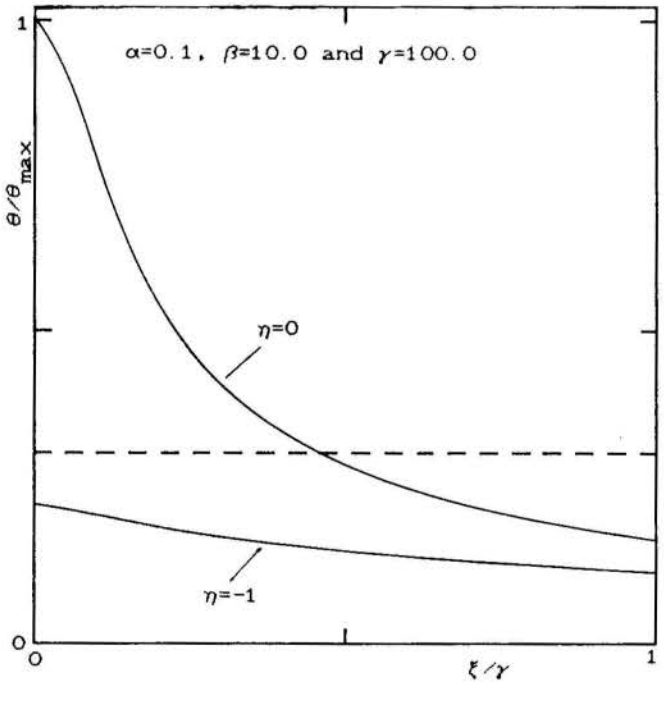

Figure 2 - The ratio θ/θ_{max} versus dimensionless radial position, at $\eta=-1$ and at $\eta=0$.

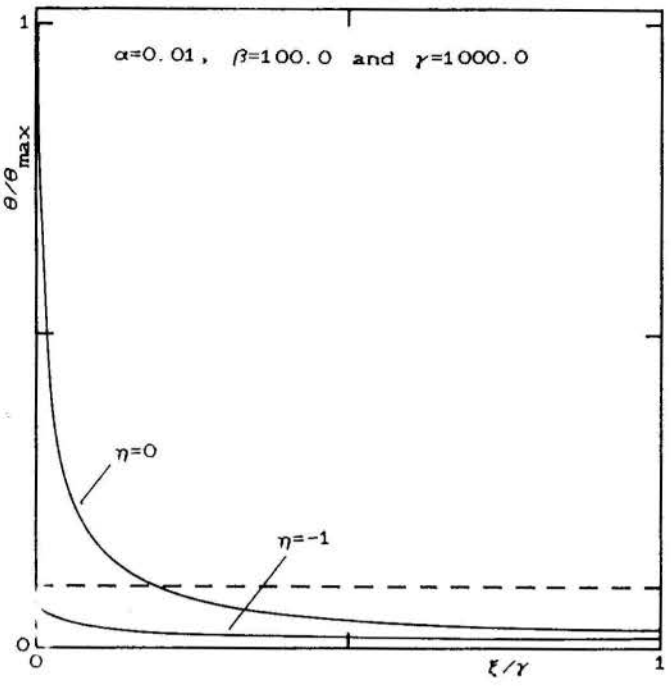

Figure 3 - The ratio θ/θ_{max} versus dimensionless radial position, at $\eta=-1$ and at $\eta=0$.

FINAL REMARKS

The considered phenomenon is motivated by the practical situations in which a small body, at very high temperature, is placed near another body.

The obtained results show that usual approximations, like constant temperature, may give rise to results very far from the reality.

This work is the first one which presents a local simulation of a conduction/radiation heat transfer phenomenon from the minimization of a functional, employing finite elements.

The presented approach is mathematically accurate and provides approximations only in the physically admissible range.

REFERENCES

[1] Sparrow, E.M. and Cess, E.M. , "Radiation Heat Transfer", McGraw-Hill, Washington, 1978.

[2] Holman, J.P. , "Heat Transfer", McGraw-Hill Kogakusha, 1976.

[3] Callen, H.B. , "Thermodynamics" , John Wiley & Sons, New York, 1960.

[4] Saldanha da Gama, R.M. , "A Note on the Solutions of Thermal Radiant Interchange Problems", Journal of Heat Transfer , vol. 110, no. 4A, pp. 1014-1016, 1988.

[5] John, F. , " Partial Differential Equations " , Springer-Verlag, New York, 1982.

[6] Brezis, H. , "Analyse Fonctionnelle", Masson, Paris, 1983.

[7] Ciarlet, P.G., "Introduction a l'Analyse Numerique Matricielle et a l'Optimisation" , Masson, Paris, 1982.

III ENCIT – Itapema, SC (Dezembro 1990)

TRANSIENT TEMPERATURE FIELD IN A SPHERICAL PARTICLE INCLUDING NONUNIFORM RADIANT ABSORPTION

P. L. C. LAGE and C. M. HACKENBERG
Chemical Engineering Department - COPPE - UFRJ
21945 - Rio de Janeiro, RJ - C.P. 68502 - Brazil
Fax No. (from overseas) : 55 21 290-6626

SUMMARY

A simplified model is proposed for the nonhomogeneous radiant absorption field inside a sphere. This model can be applied for both front and back-concentrated radiant absorption. It is used to calculated the radiant feedback from flames to non-vaporizing droplets in simplified combustor configurations, where large droplet limit permits some simplification in wavelength integration. The results show that non-uniform radiant absorption is the main source of fuel droplet heating and leads to highly asymmetric temperature field inside the sphere.

INTRODUCTION

The theory of fuel spray vaporization and combustion is fundamental tool for combustor modeling and improved design. Much progress has been made in this theory as few recent reviews [1,2] show. Vaporization models consist of the heat transfer analysis of the liquid phase (droplets) and the heat and mass transfer analysis of the gas phase. The droplet analysis are developed through the classical d^2-law, infinite conductivity, conduction limit and vortex models [3]. The former do not consider the droplet heating; the second considers homogeneous liquid temperature; the third is the spherically symmetric liquid heating model and the later takes into account the droplet internal circulation. This vortex model has been developed by Prakash and Sirignano [4,5] and Tong and Sirignano [6-8]. As pointed out by Sirignano [9], there is a increasing need for simple, yet accurate, vaporization models to be used in spray combustion calculations. This way, Abramzon and Sirignano [10,11] have recently developed a approximate droplet vaporization model modifying the classical gas phase model and accounting for transient droplet heating by an spherically symmetric effective conductivity model. This has been shown to agree very well with the more complex models whose computational time is very long.

The role of radiation absorption, in spray combustion models, has been considered in a simplified manner by Harpole [12]. Recently, Tuntomo et al. [13] shows that the radiation absorption by a sphere, from a radiating source, is highly non-uniform. They identified three regimes of absorption depending on the size parameter and the complex refractive index of the particle. Rangel [14] suggested that the radiation absorption should be included in droplet models by a volumetric source term, and that the spherical symmetric model, with an effective conductivity, is the simplest to be used.

In the present study, it is proposed a simplified model for non-uniform radiant heat absorption inside a droplet for the region before the flame zone, which will be called the preheating zone. This model is used to determine the influence of radiation absorption in the transient heating of a non-vaporizing droplet. In order to use the results of Tuntomo et al. [13], the flame front is regarded as a gray source emitting an unpolarized planar wave. The flame temperature and emissivity are determined from a simplified heat balance and a homogeneous non-gray model analysis, including gas and soot radiation.

DROPLET TEMPERATURE FIELD : DOUBLE-REGION SOURCE

The three main absorption regimes devised by Tuntomo et al. [13] are the uniform, the back concentrated and the front concentrated. The size parameter $\rho = 2\pi a/\lambda$ (a is the sphere radius and λ is the wavelength) and the complex refractive index $m = n - ik$ determine the absorption regime. Graphics of the local distribution of radiative energy absorption for various combinations of n, k and ρ were represented. Outside the transition regimes, these graphics indicate that the internal absorption could be simplified by assuming two regions with different local absorption constants. If one takes this assumption into consideration, the droplet temperature field may be analytically determined. This simplification permits to write the dimensionless heat conduction equation with a nonhomogeneous term due to the radiation absorption in an axisymmetric sphere as

$$\frac{1}{\eta^2}\frac{\partial\Theta}{\partial\eta}\left(\eta^2\frac{\partial\Theta}{\partial\eta}\right) + \frac{1}{\eta^2}\frac{\partial\Theta}{\partial\mu}\left((1-\mu^2)\frac{\partial\Theta}{\partial\mu}\right) + G = \frac{\partial\Theta}{\partial\tau} \qquad (1)$$

$$\frac{\partial\Theta}{\partial\eta} + Bi\,\Theta = 0, \quad \eta = 1 \qquad (2)$$

$$\Theta = 1, \quad \tau = 0 \qquad (3)$$

$$G(\eta,\mu) = \begin{cases} G_1, & \text{in region } R_1 \\ G_2, & \text{in region } R_2 \end{cases} \qquad (4)$$

where

$$\Theta(\eta,\mu,\tau) = (T - T_a)/(T_o - T_a) \qquad (5)$$

$$\eta = r/a \qquad (6)$$

$$\tau = \alpha t/a^2 \qquad (7)$$

$$Bi = ha/k \qquad (8)$$

$$G = \frac{Q\,a^2}{k(T_o - T_a)} \qquad (9)$$

and r is the radial coordinate, $\mu = \cos\phi$, ϕ the polar coordinate, t is the time, T, T_a and T_o are the local, ambient and initial temperature, respectively, α is the thermal diffusivity, k is the thermal conductivity, h

is the gas-droplet heat transfer coefficient and Q is the local volumetric radiant absorption constant.

Utilizing Green's function, Özişik [15], the solution for the temperature field can be written in the form

$$\Theta(\eta,\mu,\tau) = \sum_{p=0} A_{0p} \exp\left(- \beta_{0p}^2 \tau \right) j_0\left(\beta_{0p} \eta \right) +$$

$$\Delta G \sum_{n=0} \sum_{p=0} \frac{B_{np}}{\beta_{np}^2} \left[1 - \exp\left(- \beta_{np}^2 \tau \right) \right] j_n\left(\beta_{np} \eta \right) P_n(\mu) +$$

$$G_1 \sum_{p=0} \frac{A_{0p}}{\beta_{0p}^2} \left[1 - \exp\left(- \beta_{0p}^2 \tau \right) \right] j_0\left(\beta_{0p} \eta \right) \qquad (10)$$

where $\Delta G = G_2 - G_1$ and

$$A_{0p} = \frac{8\beta_{0p}}{4(Bi - 0.5)^2 + 4\beta_{0p}^2 - 1} \frac{j_1(\beta_{0p})}{j_0^2(\beta_{op})} \qquad (11)$$

$$B_{np} = \frac{1}{N(n)\ N(\beta_{np})} \iint_{R2} \eta^2\ j_n(\beta_{np}\eta)\ P_n(\mu)\ d\eta\ d\mu \qquad (12)$$

$$N(n) = 2/(2n + 1) \qquad (13)$$

$$N(\beta_{np}) = 0.5 \left[\frac{(Bi-0.5)^2}{\beta_{np}^2} + 1 - \frac{(n+0.5)^2}{\beta_{np}^2} \right] j_n(\beta_{np}^2) \qquad (14)$$

and the characteristic values, β_{np}, are the roots of

$$\beta_{np}\ j_{n-1}(\beta_{np}) + (Bi - n - 1)\ j_n(\beta_{np}) = 0 \qquad (15)$$

where j_n is the spherical Bessel function of the first kind and nth order and P_n is the Legendre polynomial of nth degree.

The two regions for the back concentrated absorption regime are : R2, the one inside a small eccentric sphere of radius c whose center is located at a distance b backwards from the center of the droplet, and R1, the remaining volume of the particle. Geometrically, we have, using the dimensionless distances B=b/a and C=c/a :

R2 : $(B - C) \le \eta \le (B + C)$ and $E(\eta) \le \mu \le 1$

where $C \le B \le 1$ and

$$E(\eta) = (\eta^2 + B^2 - C^2)/(2B\eta) \qquad (16)$$

In the case of front concentrated absorption we assume that the two regions are separated by the intersection with a larger eccentric sphere of radius c whose center is located at a distance b backwards the center of the droplet. In this case $C \ge B$, using the same definitions as before. The second region is given by

R2 : $-1 \le \mu \le \mu_o$ and $\eta_o \le \eta \le 1$

$$\mu_o = (1 + B^2 - C^2)/(2B) \qquad (17)$$

$$\eta_o = B \left[\mu + \sqrt{(C/B)^2 - 1 + \mu^2} \right] \qquad (18)$$

Recalling that in the solution given by equation (10), the volume integral due to radiant absorption, in both regions, has been written in terms of the coefficients B_{np}, which depends solely on the integral of region R2, the double integral given by equation (12) can be evaluated analytically to yield the following expressions

back-concentrated absorption :

$$B_{np} = \frac{1}{2N(\beta_{np})} \int_{B-C}^{B+C} \eta^2 j_n(\beta_{np}\eta) \left\{ \delta_{n0} + P_{n-1}[E(\eta)] - P_{n+1}[E(\eta)] \right\} d\eta \qquad (19)$$

where $\delta_{n0} = 1$ if $n = 0$ and is 0 for $n \ne 0$.

front-concentrated absorption :

$$B_{np} = \frac{1}{N(n)\ N(\beta_{np})} \int_{-1}^{\mu_o} P_n(\mu) \int_{\eta_o(\mu)}^{1} \eta^2 j_n(\beta_{np}\eta)\ d\eta\ d\mu \qquad (20)$$

where, using $y = \beta_{np}\eta$, we have

$$\int \eta^2 j_n(\beta_{np}\eta)\ d\eta =$$

$$\frac{1}{\beta_{np}^3} \sum_{m=0}^{n/2} \left\{ \prod_{i=0}^{m-1} [(n + 0.5)^2 - (0.5 - 2i)^2] + \delta_{m0} \right\} \left[y^{2-2m} j_{n+1}(y) - (n + 2m)\ y^{1-2m} j_n(y) \right]$$

for $n \ge 0$, n even and

$$\frac{1}{\beta_{np}^3} \left\{ - \prod_{i=0}^{(n+1)/2-1} [(n + 0.5)^2 - (0.5 - 2i)^2]\ y^{-n+1} j_{n-1}(y) + \sum_{m=0}^{(n+1)/2-1} \left\{ \prod_{i=0}^{m-1} [(n + 0.5)^2 - (0.5 - 2i)^2] + \delta_{m0} \right\} \left[y^{2-2m} j_{n+1}(y) - (n + 2m)\ y^{1-2m} j_n(y) \right] \right.$$

for $n \ge 1$, n odd (21)

These expressions for B_{np} have been numerically evaluated by Gauss-Legendre quadrature. The numerical integration procedure has been tested by comparison to B_{0p} analytical result.

One should notice that further simplification would be possible for the front-concentrated regime, where the first absorption constant, G_1, is approximately equal to zero. Therefore $\Delta G \cong G_2$.

Radiant heat absorption. The heat absorbed, Q, of equation (9) is the wavelength integrated spectral local radiant heat absorbed given by Tuntomo et al [13]

$$Q = \int_0 Q_\lambda\ d\lambda \qquad (22)$$

$$Q_\lambda = 4\pi nk\ S_\lambda(\eta,\mu)\ \frac{I_{\lambda o}}{\lambda} \qquad (23)$$

where $4\pi nk\ S_\lambda(\eta,\mu)$ is the normalized source function and $I_{\lambda o}$ is the incident radiant intensity. For a region R with volume V_R the mean local spectral volumetric heat absorption is

$$\bar{Q}_\lambda = \frac{1}{V_R} 2\pi \int_R\int Q_\lambda(\eta,\mu)\ \eta^2\ d\eta\ d\mu \qquad (24)$$

The mean absorption constants for the two regions R1 and R2 can be calculated using equations (22) to (24). However, here it is adopted a simplified calculation scheme, based on the dimensionless absorption cross-section, $\mathcal{C}$, defined by Tuntomo et al. [13] :

$$\mathcal{C} = \frac{\lambda C_a}{V} = \frac{6\pi nk}{a^3} \int_{-1}^{1}\int_0^1 S_\lambda(\eta,\mu)\ \eta^2\ d\eta\ d\mu \qquad (25)$$

where V is the droplet volume and C_a is the dimensional absorption cross-section.

If we consider that there is absorption only in region R2 the integrals in equation (24) and (25) lead to the same result, and the mean local spectral absorption can be written as

$$\bar{Q}_{\lambda 2} = f(B,C)\ \mathcal{C}\ \frac{I_{\lambda o}}{\lambda} \qquad (26)$$

where $f(B,C)$ is the total volume of the droplet divided by the volume of region R2. For the front concentrated absorption regime, it is given by

$$f(B,C) = \left[\frac{1 + B^2 - C^2}{4B} + 0.5 - \frac{1}{16B} - \frac{C^2 - B^2}{8B} + \frac{(C - B)^4}{16B} + \frac{(C^2 - B^2)(C - B)^2}{8B} \right]^{-1} \qquad (27)$$

This form is suitable for calculations, especially when the dimensionless absorption cross-section could be expressed in a simple form. This is the case in the limit of large particles where that coefficient is primarily a function of the size parameter, ρ, and with only a small dependence on the complex refractive index (mainly through its imaginary part, k). In the range of k between 0.01 and 1, and for size parameters around 100, from Figure 11 (Tuntomo et al. [13]) the dimensionless absorption cross-section is roughly

$$\mathcal{C} \cong 450/\rho \qquad \text{for} \quad \rho > 50 \qquad (28)$$

This equation will be considered here to hold to values of ρ up to 500. This expression is devised to simplify the integration in wavelength to obtain the mean total heat absorption in region R2 using equation (22). It should be noted that for $\rho > 50$ and $k > 0.01$ we have mainly the front concentrated absorption regime, where the assumption of absorption in only one region is justified. For back concentrated absorption it is necessary to use equations (22) to (24) to determine the mean local heat absorption in each region, and therefore, equation (28) can not be applied.

The final expression for the local heat absorption constants for the front concentrated regime is obtained assuming a gray incident radiation intensity

$$\bar{Q}_1 = 0 \qquad (29)$$

$$\bar{Q}_2 = f(B,C)\ \frac{225}{\pi a}\ I_o \qquad (30)$$

Combustor modeling. A simplified combustor configuration is adopted in order to determine its flame radiant intensity. Let us suppose that the flame consists of a cylindrical region with diameter D and length L. Also, let us consider L_p the distance between the combustor nozzle and the cylindrical flame. Therefore, this length is responsible for the droplet preheating zone.

A simple energy balance, considering the total enthalpy change in combustion and the energy lost only by radiation, is utilized to determine the flame temperature for a known stoichiometry.

Assuming flame homogeneity, Edwards [15] wide band model for gas radiation (with correction for overlapping bands of water and carbon dioxide in 2.7 and 15 micra regions) may be combined with the assumption of soot particles in the Rayleigh limit for soot radiation, to determine the flame emissivity. In order to accomplish this, it is assumed the soot complex refractive index given by Lee and Tien [17] based on their dispersion model. Following Tien and Lee [18], it has been used a homogeneous non-gray model for flame emissivity, which, after spatial integration of the radiative heat transfer equation, gives the emissivity as

$$\varepsilon = \varepsilon_s + \sum_{\substack{\text{gas}\\ i}} \sum_{\substack{\text{band}\\ j}} \frac{\bar{E}b_{\lambda ij}}{\sigma T^4}\ \bar{\tau}_{sij}\ A_{ij} - \sum_{\substack{\text{overlap}\\ \text{region}\ k}} \bar{\tau}_{sk}\ \Delta\varepsilon_k \qquad (31)$$

where A is the total band absorptance, $\Delta\varepsilon$ is the overlap correction, σ is the Stefan-Boltzmann constant, $\bar{E}b\lambda$ is the mean spectral blackbody emissivity power within the gas band range and ε_s and $\bar{\tau}_s$ are the total emissivity and the mean spectral transmissivity of the soot cloud within the gas band range. These parameters are calculated from

$$\varepsilon_s = 1 - \frac{15}{\pi^4}\ \psi^{(3)}\left[1 + \frac{\bar{C}_o\ fv\ T\ L}{C_2} \right] \qquad (32)$$

$$\tau_s = \exp\left(- C_o(n,k)\ fv\ \frac{L}{\lambda} \right) \qquad (33)$$

$$C_o(n,k) = \frac{36\pi\ nk}{(n^2 - k^2 + 2)^2 + 4\ n^2k^2} \qquad (34)$$

where $\psi^{(3)}$ is the pentagamma function, L is the given length, $\bar{C}_o$ is C_o evaluated at the wavelength of maximum blackbody function and C_2 is the second radiation constant.

The mean beam-length concept is used to determine the flame temperature. Therefore, the heat loss by radiation from a gas body of volume V_g irradiating to all its surface area A_g, in a cold enclosure, is given by

$$Q_r = \varepsilon(L_{mb})\ A_g\ \sigma T^4 \qquad (35)$$

$$L_{mb} = 3.6\ V_g/A_g \qquad (36)$$

The intensity of radiation incident upon a droplet in the preheating zone is determined by the emissivity based on the total flame length, L. Thus,

$$I_o = \varepsilon(L)\ \sigma T^4/\pi \qquad (37)$$

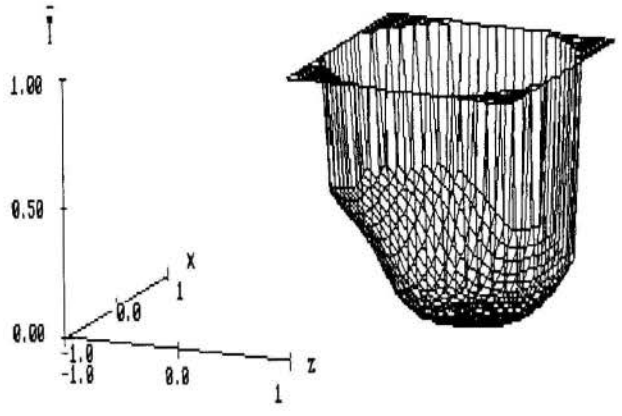

Fig. 1. Time dependent droplet temperature profile (τ = 0.04, y = 0)

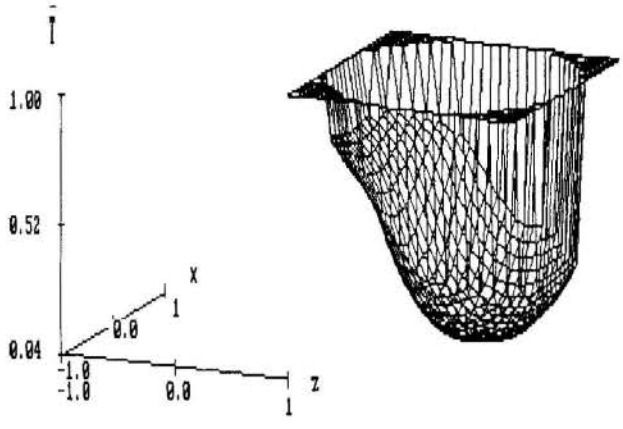

Fig. 2. Time dependent droplet temperature profile (τ = 0.08, y = 0)

Since the flame emissivity is a function of the flame temperature, an iterative procedure combined with the simple energy balance mentioned previously will suffice for their determination.

DROPLET TRANSIENT TEMPERATURE FIELD

Two combustor sizes, as well as three ambient temperatures for the preheating zone, and two droplet radius of 50 and 100 micra are used in the simulations. Reynolds numbers of 50 and 100 have been assumed for the smaller and the larger droplets, respectively. Since vaporization is neglected in the preheating zone, the Frossling correlation [19] may be utilized to estimate the Bi number (which appears in equation (8)) for air flowing past a sphere

$$\frac{2ah}{k_f} = 2.0 + 0.558\ Re_f^{1/2}\ Pr_f^{1/3}. \qquad (38)$$

In this equation, f indicates air properties evaluated at film temperature for non-vaporizing droplets with surface temperature considered as being the initial temperature as a first approximation, $T_f = (T_o + T_a)/2$.

Table 1. Combustor characteristics

Combustor	1	2
L (m)	0.5	1.0
D (m)	0.12	0.25
L_a (m)	0.08	0.15
m_{fuel} (10^{-3}kg/s)	2.5	1.0
m_{air} (10^{-3}kg/s)	15.78	63.14
v_{gases} (m/s)	28.2	25.3
T_{flame} (K)	1492	1452
$fv \times 10^6$	0.11	0.12
$\varepsilon(L_{mb})$	0.065	0.118
$\varepsilon(L)$	0.224	0.357
I_o (10^4 W/m^{2}sr)	1.95	2.86
λ_{max} (μm)	1.94	2.00

Moreover, isoctane is chosen as the burning fuel, for which Bard and Pagni [20] have determined a carbon conversion of 3.1% to soot (in a pool fire). Despite the differences in configurations, this conversion has been used to prevent inclusion of complex chemical kinetic models in this simplified analysis. The amorphous carbon density is also used as soot density.

The reactants for the combustion are fed at normal ambient conditions (1 atm and 298 K), with no excess air for the combustion stoichiometry. The characteristics of the two combustor sizes are given in Table 1. The soot volumetric fraction, f_v, is determined in a fairly close agreement with the value determined by Bard and Pagni [20], that is 0.46×10^{-6}. For the 3.1% soot conversion, the calculated flame temperature is about 400 K lower than the adiabatic flame temperature of 1860 K. The determined gases velocities are in the expected combustor range. It should be noticed that soot is the main factor responsible for the flame emissivity. Since the flame temperature is increased as its emissivity decreases, it turns out that the resulting intensity, I_o, which is a function of both flame parameters, is much less dependent on the soot volumetric fraction and on gas concentrations than its emissivity.

The parameters of the proposed model are given in Table 1 for both combustors, where B = 0.75 and C = 1.25 for the absorption model. Since the simulated temperature behavior is similar for both combustors, only the first combustor results will be presented here. The preheating zone temperatures of 400, 600 and 800 K are used in the simulations.

The transient temperature field for the first combustor simulation with a preheating zone temperature of 600 K and a droplet radius of 50 μm is presented in figures 1 to 4. These figures show the instantaneous temperature field ($\bar{T} = 1 - \Theta = (T - T_o)/(T_a - T_o)$) at 20, 40, 80 and 100% of the preheating zone residence time, t_r, reported in Table 2. The dimensionless cartesian coordinates (x,y,z) represent the normalized distance inside the droplet for the radius a. The highly asymmetric temperature field shows the importance of non-uniform radiant absorption in droplet internal heating. In the range of Bi numbers considered, the heat absorbed by radiation is surely the main heat source in droplet preheating. It should also be noticed that the energy blackbody fraction for $\rho > 50\ \mu m$ is greater than 0.90, which confirms the approximation of front concentrated absorption throughout the whole spectrum.

In Table 2 it is also shown the calculated time necessary for the droplet surface temperature to reach the isoctane boiling temperature (t_b). Since t_b varies from 0.13 to 2.0 ms, in a range of residence time variation from 1.3 to 6.5 ms, for the preheating zone of a combustor, one is led to recognize that droplet evaporation must be considered in the analysis.

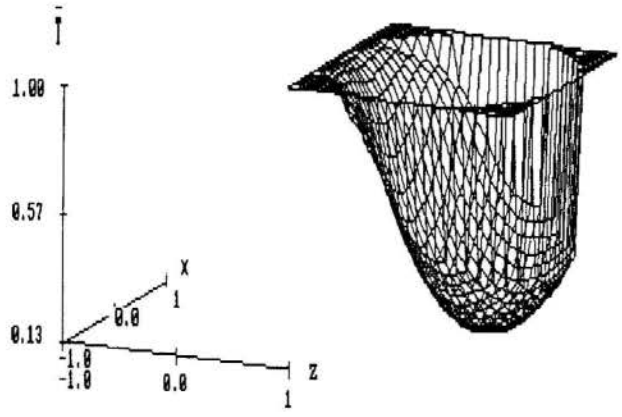

Fig. 3. Time dependent droplet temperature profile (τ = 0.12, y = 0)

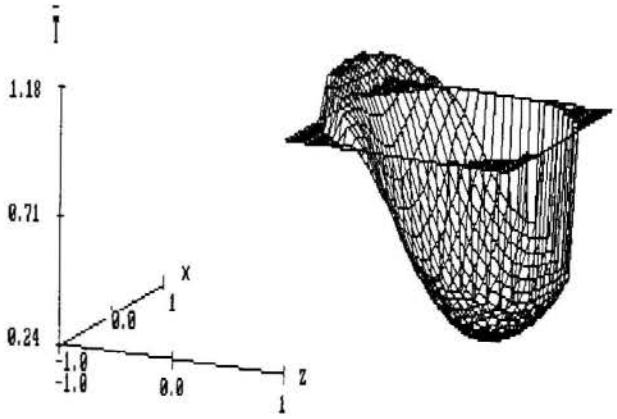

Fig. 4. Time dependent droplet temperature profile (τ = 0.16, y = 0)

CONCLUSIONS

Despite the simplified characteristics of the present work, one may verify that radiant absorption is the main heat source in droplet preheating. Since the initial droplets radius are usually in the range of 50-100 μm, and flame temperatures are about 1500 K, it is also shown that the radiant absorption, in the preheating zone of spray combustion systems, occurs mainly in the front concentrated absorption regime.

The proposed model enables a great deal of simplification on the analysis, which has permitted an analytical solution to the present problem. Even though the droplet heating model has not been tested with respect to the exact numerical solution using electromagnetic theory, the radiant energy absorption effect is found to be very important in droplet preheating.

Droplet preheating is responsible for fuel vapor mass fraction and droplet radius in the flame front. Since this, in turn, controls the flame propagation and the following diffusion-controled combustion processes, the radiation absorption has to be taken into account in the modeling of spray combustion systems.

REFERENCES

[1] Sirignano, W. A., "Fuel Droplet Vaporization and Spray Combustion Theory", *Prog. Energy Combust. Sci.* **9**, 291-322, 1983.

[2] Law, C. K., "Recent Advances in Droplet Vaporization and Combustion", *Prog. Energy Combust. Sci.* **8**, 171-201, 1982.

Table 2. Parameters for combustor 1

a (μm)	50			100		
ρ_{max}	162			324		
$\mathcal{F}_{front}$	0.90			0.98		
Ta (K)	400	600	800	400	600	800
t_r (ms)	4.5	6.5	1.3	4.5	6.5	1.3
τ_r	0.11	0.16	0.33	0.028	0.040	0.082
Bi	0.88	1.06	1.24	1.11	1.34	1.57
$-G_2$	24.5	8.27	4.98	49.0	16.5	9.95
t_b (ms)	1.1	0.59	0.13	2.3	1.3	0.31

[3] Aggarwal, S. K., Tong, A. Y. and Sirignano, W. A., "A Comparison of Vaporization Models in Spray Calculations", *AIAA J.* **22**, 1448-1457, 1984.

[4] Prakash, S. and Sirignano, W. A., "Liquid Fuel Droplet Heating with Internal Circulation", *Int. J. Heat Mass Transfer* **21**, 885-895, 1978.

[5] Prakash, S. and Sirignano, W. A., "Theory of Convective Droplet Vaporization with Unsteady Heat Transfer in the Circulating Liquid Phase", *Int. J. Heat Mass Transfer* **23**, 253-268, 1980.

[6] Tong, A. Y. and Sirignano, W. A., "Analytical Solution for Diffusion and Circulation in a Vaporizing Droplet", *19th Symposium (Int.) on Combustion*, The Combustion Institute, 1007-1020, 1982.

[7] Tong, A. Y. and Sirignano, W. A., "Analysis of Vaporizing Droplet with Slip, Internal Circulation and Unsteady Liquid-phase and Quasi-steady Gas-phase Heat Transfer", *JSME - ASME Thermal Engng Joint Conf. Proc.*, vol. 2, 481-487, 1983.

[8] Tong, A. Y. and Sirignano, W. A., "Transient Thermal Boundary Layer in Heating of Droplet with Internal Circulation : Evaluation of Assumption", *Combust. Sci Technol.* **11**, 1982.

[9] Sirignano, W. A., "An Integrated Approach to Spray Combustion Model Development", *Combust. Sci. Technol.* **58**, 231-251, 1988.

[10] Abramzon, B. and Sirignano, W. A., "Approximate Theory of Single Droplet Vaporization in a Convective Field : Effects of Variable Properties, Stefan Flow and Transient Liquid Heating", *Proc. 2nd ASME-JSME Thermal Engng. Joint. Conf.*, vol. 1, 11-18, 1987.

[11] Abramzon, B. and Sirignano, W. A., "Droplet Vaporization Model for Spray Combustion Calculations", *Int. J. Heat Mass Transfer* **32**, 1605-1618, 1989.

[12] Harpole, G. M., "Radiative absorption by evaporating droplets", *Int. J. Heat Mass Transfer* **23**, 17-26, 1980.

[13] Tuntomo, A., Park, S. H. and Tien, C. L., "Internal Field of Radiant Absorption in a Spherical Particle", to be presented in the 1990 ASME-AIAA Thermophysics and Heat Transfer Conference, Seattle, Washington, June 1990.

[14] Rangel, R. H., "Heat Transfer in The Vortically-Enhanced Mixing of Vaporizing Droplet Sprays", in Annual Review of Heat Transfer, vol. IV, Ed. C. L. Tien, 1990.

[15] Özişik, M. N., "Heat Conduction", John Wiley & Sons, 1980.

[16] Edwards, D. K., "Molecular Gas Band Radiation", in Advances in Heat Transfer, vol. 12, 115-193, 1976.

[17] Lee, S. C. and Tien, C. L., "Optical Constants of Soot in Hydrocarbon Flames", 18*th Symposium (Int.) on Combustion*, The Combustion Institute, 1981.

[18] Tien, C. L. and Lee S. C., "Flame Radiation", *Prog. Energy Combust. Sci.* **8**, 41-59, 1982.

[19] Bird, R. B., Stewart, W. E. and Lightfoot, E. N., "Transport Phenomena", John Wiley & Sons, 1960.

[20] Bard, S. and Pagni, P. J., "Carbon Particulate in Small Pool Fire Flames", *J. Heat Transfer* **103**, 357-362, 1981.

III ENCIT – Itapema, SC (Dezembro 1990)

ANÁLISE TÉRMICA DA REGIÃO DE BASE DE VEÍCULOS ESPACIAIS DURANTE A PARTIDA E VÔO PROPULSADO A GRANDES ALTITUDES

T.M. B. Carvalho e R. M. Cotta
Programa de Engenharia Mecânica - COPPE/UFRJ
J. B. Pessoa Filho
Instituto de Atividades Espaciais
Centro Técnico Aeroespacial - São José dos Campos - SP

RESUMO

É apresentado o trabalho conjunto desenvolvido pelo grupo de aerotérmica do IAE/CTA e o Programa de Engenharia Mecânica da COPPE/UFRJ, no sentido de desenvolver modelos teóricos que permitam avaliar os níveis de aquecimento na região de base de um veículo espacial. São analisadas as situações referentes à decolagem e ao vôo propulsado a grandes altitudes. O modelo proposto para a primeira situação é formalmente apresentado e resultados típicos para a fase propulsada são discutidos.

INTRODUÇÃO

A análise térmica da estrutura de veículos espaciais é uma tarefa de grande importância no projeto de tais veículos. É sabido que os primeiros veículos das séries Atlas e Júpiter tiveram suas missões comprometidas devido ao superaquecimento estrutural. Por essa razão uma das fases do projeto do Veículo Lançador de Satélites (VLS), desenvolvido pelo IAE/CTA como parte da Missão Espacial Completa Brasileira (MECB), Figura 1, consiste em se identificar as principais fontes de aquecimento externo e, posteriormente, desenvolver modelos teóricos e experimentais que permitam avaliar, quantitativamente, os níveis de aquecimento sobre regiões críticas do veículo, tais como a ogiva e a região de base. Neste contexto, pode-se identificar as principais fontes de aquecimento, como sendo:

- Aquecimento aerodinâmico (cinético);
- Aquecimento convectivo e radiativo devido aos gases de exaustão a elevadas temperaturas, na plataforma de lançamento (Figura 2);
- Aquecimento radiativo devido à energia emitida pelas partículas sólidas de Al_2O_3 existentes nos produtos de combustão (Figura 6);
- Recirculação de gases quentes sobre a região de base, devido à interação da plumagem com o escoamento externo.

A teoria, bem como o modelo desenvolvido para o cálculo do aquecimento cinético sobre a ogiva do VLS são apresentados na Ref. [3]. O desenvolvimento de um modelo teórico que permita avaliar o coeficiente de convecção, entre a região de base e os gases quentes de recirculação, durante a fase propulsada, está longe de ser alcançado, pois envolve a solução das equações de Navier-Stokes tanto para o escoamento externo como para o escoamento bifásico gás e partículas sólidas, no interior da plumagem. A solução adotada, neste caso, foi a utilização de coeficientes de convecção obtidos experimentalmente para uma configuração que se assemelha à do VLS, Ref. [4]. O presente trabalho trata, portanto, do aquecimento causado pelos produtos de combustão de um motor-foguete a propelente sólido em altitudes superiores a 33 km. Além disso, propõe um modelo conservativo que permite avaliar o aquecimento durante a partida do veículo.

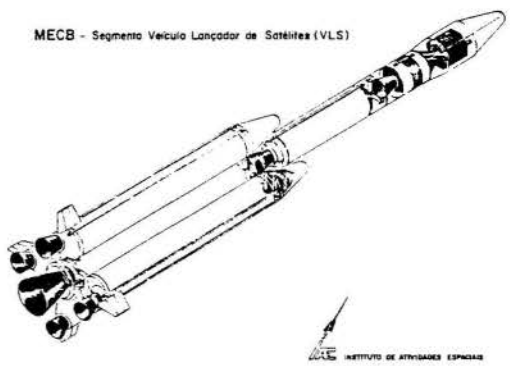

Figura 1: Configuração básica do VLS

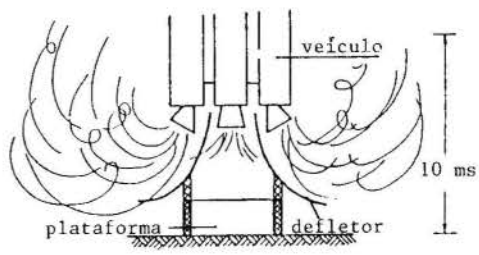

Figura 2: Veículo sobre a plataforma de lançamento

DECOLAGEM

Por ocasião do lançamento, o veículo estará montado sobre uma plataforma, conforme ilustra a Figura 2. Para evitar que os gases expelidos pelos 4 propulsores do 1º estágio incidam sobre o solo e retornem ao veículo, serão instalados defletores de jato. Entretanto, deve-se considerar a hipótese de que parte desses gases retornem ao veículo fazendo com que sua região de base fique por cerca de 3 s, tempo necessário para que o veículo atinja uma altitude de 10 m, em contato com esses gases. Considerando-se que nessa região estão localizados diversos componentes

eletrônicos, bem como o sistema de separação de estágios, deve-se avaliar, cuidadosamente, a condição de aquecimento da região de base.

A formulação desenvolvida considera a ocorrência simultânea dos três processos de transferência de calor, mas dada relevância a formulação do problema radiativo devido à sua predominância no processo, bem como sua natureza matemática mais complexa.

Seja a cavidade formada pelas superfícies mostradas na Figura 3. Considere-se ainda as seguintes hipóteses simplificadoras:

- Superfícies 1 e 2 cinzentas e opacas;
- Cavidade preenchida por um meio não participante;
- Emissão e reflexão difusas;
- Tubeira alinhada com a direção longitudinal do veículo;
- Superfície 3 negra, emitindo à temperatura do gás (T_g).

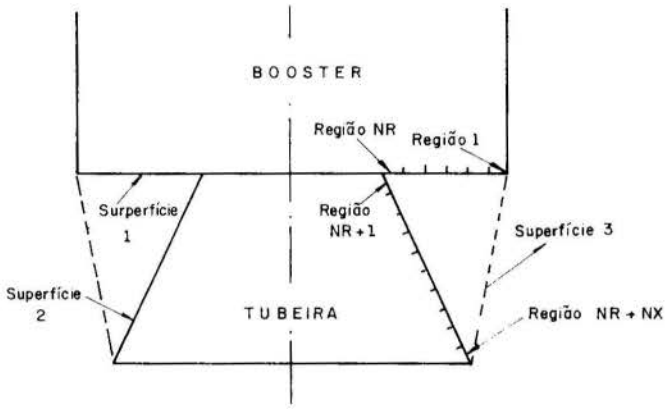

Figura 3: Configuração da cavidade a ser estudada

A análise consiste em se dividir as superfícies 1 e 2 em várias regiões, nas quais a radiosidade possa ser considerada uniforme.

As expressões para as radiosidades são dadas por:

Superfície 1:

$$R_i = \varepsilon_1 \sigma T_i^4 + (1 - \varepsilon_1)\left[\sum_{j=NR+1}^{NR+NX} F_{i\to j} R_j + F_{i\to 3} \sigma T_g^4 \right],$$

$$i = 1, \ldots, NR \qquad (1)$$

Superfície 2:

$$R_i = \varepsilon_2 \sigma T_i^4 + (1 - \varepsilon_2)\left[\sum_{j=1}^{NR} F_{i\to j} R_j + F_{i\to 3} \sigma T_g^4 \right],$$

$$i = NR+1, \ldots, NR+NX \qquad (2)$$

Para os fluxos de calor, tem-se:

Superfície 1:

$$q_i = R_i - \left[\sum_{j=NR+1}^{NR+NX} F_{i\to j} R_j + F_{i\to 3} \sigma T_g^4 \right],$$

$$i = 1, \ldots, NR \qquad (3.a)$$

ou

$$q_i = R_i - \left[\frac{R_i \sigma T_i^4}{(1 - \varepsilon_1)} \right], \quad i = 1, \ldots, NR \qquad (3.b)$$

Superfície 2:

$$q_i = R_i - \left[\sum_{j=1}^{NR} F_{i\to j} R_j + F_{i\to 3} \sigma T_g^4 \right],$$

$$i = NR+1, \ldots, NR+NX \qquad (4.a)$$

ou

$$q_i = R_i - \left[\frac{R_i \sigma T_i^4}{(1 - \varepsilon_2)} \right],$$

$$i = NR+1, \ldots, NR+NX \qquad (4.b)$$

O cálculo dos diversos fatores de forma foi feito a partir de expressões, já existentes na literatura (Refs. [5] e [6]), para o fator de forma entre um elemento de área infinitesimal, localizado sobre a superfície 1, dA_1, e a superfície cônica 2, $A_2(x)$, ou seja, $F_{dA_1 \to A_2}$. Vale contudo ressaltar que as expressões apresentadas nas Refs. [5] e [6], apresentam incorreções, conforme mostrado em [7].

Pela álgebra de fatores de forma:

$$F_{dA_1 \to \Delta A_2} = F_{dA_1 \to A_2(x+dx)} - F_{dA_1 \to A_2(x)}, \qquad (5)$$

onde ΔA_2 é a área do anel sobre a superfície 2.

Deseja-se, contudo, o fator de forma entre dois anéis finitos, ou seja, $F_{\Delta A_1 \to \Delta A_2}$. O mesmo é dado pela expressão:

$$F_{\Delta A_1 \to \Delta A_2} = \frac{1}{\Delta A_1} \int_{\Delta A_1} F_{dA_1 \to \Delta A_2} \, dA_1, \qquad (6)$$

A integração em cada anel ΔA_1, foi feita numericamente empregando-se a fórmula de Newton-Cotes, com sete pontos.

O cálculo dos demais fatores, $F_{\Delta A_1 \to A_3}$, $F_{\Delta A_2 \to \Delta A_1}$, $F_{\Delta A_1 \to A_3}$ é feito utilizando-se as expressões anterio-

res, juntamente com a relação de reciprocidade de fatores de forma.

Obtida a solução para o problema radiativo resta fazer o acoplamento com os problemas de condução e convecção. Neste caso, o coeficiente de convecção foi considerado constante e conhecido. O problema de condução é formulado considerando-se que seja transiente e unidimensional, na direção perpendicular às espessuras (esp_1 e esp_2). As propriedades dos materiais são admitidas não variarem com a temperatura. Além disso, os últimos anéis de cada superfície são considerados isolados. A solução do problema condutivo foi obtida utilizando-se o método das diferenças finitas com formulação explícita. Dessa forma, fazendo-se um balanço de energia sobre cada um dos elementos de volume considerados, Figura 4, obtem-se:

Para a região de base (superfície 1):

$$V_i\ \rho_1\ Cp_1\ \frac{dT_i}{dt} = h\ A_i(T_g - T_i) - q_{i,r}A_i + \frac{(T_{i-1} - T_i)}{\bar{R}_{i-1,i}} + \frac{(T_{i+1} - T_i)}{\bar{R}_{i,i+1}}, \qquad (7)$$

onde:

V_i: Volume do elemento considerado;

ρ_1: Massa especifica do material 1;

k_1: Condutividade térmica do material 1;

Cp_1: Calor especifico do material 1;

h: Coeficiente de convecção de calor;

T_g: Temperatura do gás;

$q_{i,r}$: Fluxo de calor por radiação;

A_i: Área do anel i;

$$\bar{R}_{i-1,i} = \frac{\Delta r}{2\ \pi\ k_1\ \bar{r}_i\ e_1}, \quad \bar{r}_i = \frac{r_{i-1} + r_i}{2}, \qquad (8)$$

$$\bar{R}_{i,i+1} = \frac{\Delta r}{2\ \pi\ k_1\ \bar{r}_i\ e_1}, \quad \bar{r}_i = \frac{r_{i+1} + r_i}{2}, \qquad (9)$$

$$i = 1, \ldots, NR$$

Para a região do divergente (superfície 2):

$$V_i\ \rho_2\ Cp_2\ \frac{dT_i}{dt} = h\ A_i(T_g - T_i) - q_{i,r}A_i + \frac{(T_{i-1} - T_i)}{\bar{R}_{i-1,i}} + \frac{(T_{i+1} - T_i)}{\bar{R}_{i,i+1}}, \qquad (10)$$

onde:

$$\bar{R}_{i-1,i} = \frac{\Delta x/\cos\beta}{k_2\ \pi\ \left[\ r_{ex}^2(x) - r_{in}^2(x)\ \right]_{x-dx/2}}, \qquad (11)$$

onde:

$r_{ex}(x)$: raio externo do divergente;

$r_{in}(x)$: raio interno do divergente.

$$\bar{R}_{i,i+1} = \frac{\Delta x/\cos\beta}{k_2\ \pi\ \left[\ r_{ex}^2(x) - r_{in}^2(x)\ \right]_{x+dx/2}}, \qquad (12)$$

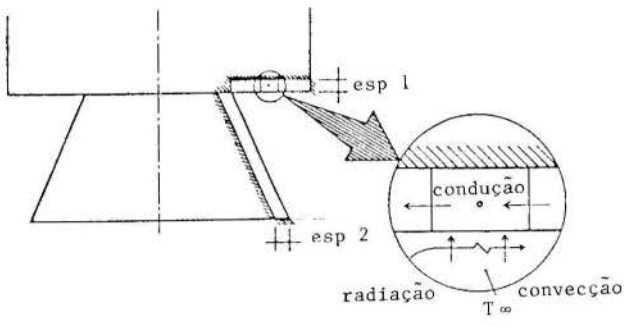

Figura 4: Balanço de energia num elemento de volume

Uma validação preliminar desta formulação pode ser feita, considerando-se apenas a transferência de calor por radiação (h=0), e $\varepsilon_2 = 1$. Dessa forma, obtem-se a seguinte expressão para a radiosidade:

$$R_i = \sigma T_i^4\ \left[\ \varepsilon_1 + (1 - \varepsilon_1)\ F_{dA_i \to A_2}\right] + (1 - \varepsilon_1)\ \sigma\ T_g^4\ F_{i \to 3}, \quad i=1,\ldots,NR \qquad (13)$$

RESULTADOS

Uma vez que uma expressão analítica é conhecida para $F_{dA_1 \to A_2}$ [5], a equação (13) representa uma solução exata para a radiosidade sobre a superfície 1. Assim, resolvendo-se as equações (1) e (2) para um número de 20 regiões (NR=NX=20), obtem-se os resultados apresentados na Tabela 1, com boa concordância.

Tabela 1: Resultados para a radiosidade sobre a sup. 1

($\varepsilon_1 = 0,8$; $\beta = 15^\circ$; $T_g = 1000$ K e $T_2 = 700$ K)

R [m]	RADIOSIDADE [W/m^2]	
	solução exata	solução numérica
0,4152	17.069,75	17.212,77
0,4218	17.334,16	17.498,99
0,4660	18.099,19	18.304,12
0,5014	18.476,51	18.698,96
0,5788	19.101,98	19.353,32

Uma vez validado o programa, é possível avaliar

os níveis de temperatura sobre as duas superfícies consideradas e, dessa forma, especificar o tipo e quantidade de materiais que devem ser utilizados como proteção térmica. Para o exemplo apresentado neste trabalho considerou-se, como material isolante, a cortiça, cujas propriedades de interesse são : ρ = 480 kg/m^3, k = 0,025 W/m^2 e α = 2,6x10^{-8} m^2/s, sendo α a difusividade térmica.

A Figura 5 apresenta a distribuição de temperatura em função do tempo. Observa-se que o seu crescimento dá-se de forma extremamente rápida. Isso se explica pelo fato de que há, para o exemplo dado, predominância da transferência de calor por radiação.

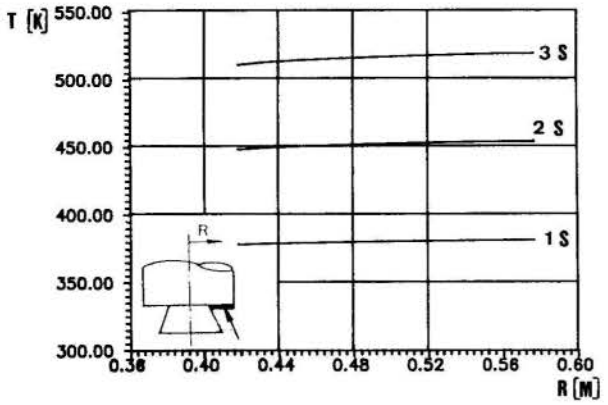

Figura 5: Distribuição de temperatura em função do tempo

A Figura 6 apresenta a distribuição de temperatura, ao longo da superfície 1, considerando-se várias espessuras de cortiça. Observa-se que apesar do pequeno intervalo de tempo considerado, já se verifica uma grande elevação nos níveis de temperatura do isolante. Este resultado pode ser usado para avaliar a espessura de material a ser utilizado, de modo a garantir que condições críticas de temperatura não se estabeleçam sobre a estrutura do veículo. Vale ressaltar, contudo, que a temperatura sobre a estrutura do veículo pode não ser a condição determinante da espessura do isolante, haja visto que, acima de uma determinada temperatura o isolamento térmico pode sofrer grandes variações nas suas propriedades físicas podendo, inclusive, mudar de

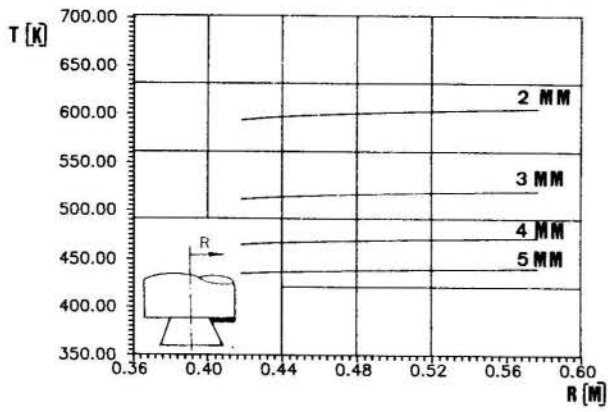

Figura 6: Distribuição de temperatura ao longo da superfície 1.

fase. Além disso, pode ocorrer que a cola utilizada para aderir o isolamento à estrutura não mantenha sua aderência acima de uma determinada faixa de temperatura. Para avaliar cada um desses fatores, devem ser realizadas medidas experimentais a fim de verificar os limites de temperatura tanto do material como do adesivo. Ao se comparar dois materiais distintos, outro fator que deve entrar na análise é o peso. Eventualmente, um determinado material que apresente melhores propriedades térmicas, notadamente baixa difusividade térmica, pode apresentar uma elevada massa específica inviabilizando, assim, sua utilização.

A Figura 7 ilustra para uma dada situação a influência da emissividade superficial. Quando se analisa a alteração da emissividade superficial, investiga-se a possibilidade de se revestir o material isolante com um filme com alta refletividade. Pelo fato de que se está considerando um coeficiente de convecção elevado, 300 W/m^{2}K, a emissividade da superfície não alterou significativamente a distribuição de temperatura.

Vale ressaltar que, para cada uma das situções analisadas, efetuaram-se testes de modo a garantir a convergência da solução numérica. Por exemplo, para os resultados apresentados neste trabalho adotou-se um incremento temporal de 0,002 s, e um número de 10 anéis em cada superfície. A temperatura do gás foi assumida constante e igual a 1000 K. A condição inicial de temperatura da estrutura foi de 300 K. Os valores de emissividade e espessura de isolante foram 0,8 e 3,0 mm, respectivamente. Em todas as simulações, a cortiça foi o material utilizado.

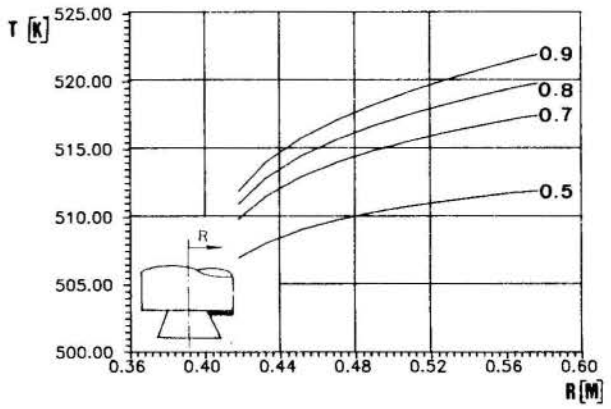

Figura 7: Influência da emissividade da superfície

VÔO PROPULSADO

Durante o vôo propulsado de um veículo espacial, o mesmo fica exposto, durante um intervalo de tempo relativamente grande (60 s no caso do VLS) à radiação emitida pelos produtos de combustão do seu propulsor, como ilustra equematicamente a Figura 8. Nos veículos que utilizam motores a propelente sólido, este problema torna-se mais crítico uma vez que existe uma quantidade significativa de partículas de Óxido de Alumínio (28 %, em massa) as quais, durante o processo de expansão que ocorre no divergente, não diminuem sua temperatura tão rapidamente como o fazem os gases. Dessa forma, mesmo a altitudes elevadas tem-se nos produtos de combustão desses motores, partículas sólidas a elevadas temperaturas emitindo radiação térmica. Adicionalmente, essas partículas (com diâmetro variando de 0.5 a 10.0 μm) espalham energia radiante. Tal fato faz com que a plumagem se torne um meio no qual se tem emissão, absorção e espalhamento de energia radiante. A solução de tal problema constitui, por si só, uma laboriosa tarefa, entretanto, acoplado ao problema radiati-

vo existe o problema convectivo. Dessa forma, a solução do problema do aquecimento da região de base de veículos espaciais a propelente sólido, compreende três fases distintas, quais sejam:

- Cálculo do fluxo de calor emitido pela pluma;
- Cálculo da fração de energia emitida pela pluma que atinge a superfície do veículo;
- Determinação dos níveis de temperatura sobre essas superfícies.

O modelo desenvolvido para calcular o fluxo de calor emitido pela plumagem, não será aqui discutido uma vez que as Refs. [1] e [2] tratam detalhadamente desse problema, ou seja, apresentam um modelo aonde a equação de transferência radiante é resolvida, juntamente com o problema convectivo. O cálculo da fração de energia emitida pela plumagem que atinge a superfície externa do veículo, notadamente a região de base é feita utilizando-se os fatores de forma propostos na Ref. [6].

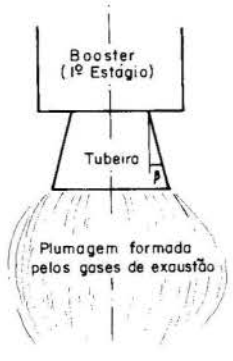

Figura 8: Representação esquemática da transferência de calor da plumagem para a região de base do veículo

A Figura 9 ilustra um resultado típico obtido para o fluxo de calor incidente sobre a região de base do 3º estágio do VLS. Apresenta-se os resultados para o fluxo de calor incidente sobre vários planos de base. Para Y1 = 1,49 m (coincidente com o plano de descarga dos gases) o fluxo máximo se dá em X2/Re =1, diminuindo à medida que afasta-se deste ponto. Para Y1 = 1,35 m, verifica-se que o fluxo máximo se dá para X2/Re ligeiramente maior que 1. Para Y1 = 1,00 m observa-se comportamento semelhante ao anterior diferindo, porém, no valor de X2/Re onde ocorre o fluxo máximo, em torno de X2/Re = 1,5. O deslocamento do ponto no qual se dá o fluxo de calor máximo é atribuído basicamente a dois fatores. São eles: proteção devido ao divergente e aumento da distância do plano de interesse, relativamente à pluma.

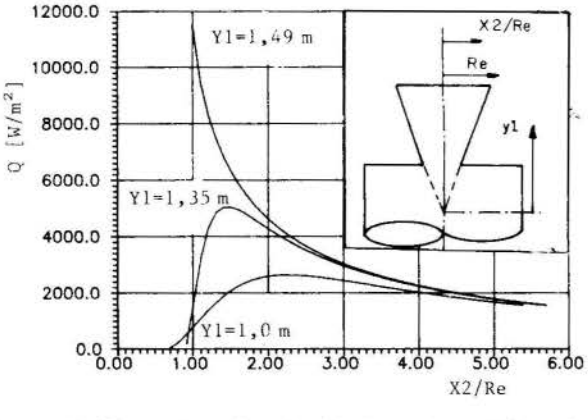

Figura 9: Fluxo de calor incidente sobre vários planos de base

Uma vez avaliado o fluxo de calor incidente, é possível resolver o problema de condução na proteção térmica utilizando-se as mesmas hipóteses anteriores, ou seja, utilizando-se a equação (7), com h=0. Observou-se que mesmo ocorrendo por um período prolongado, cerca de 60 s, o problema de aquecimento não é crítico. A explicação para este fenômeno deve-se ao fato de que o fluxo de calor incidente é muito baixo (vide curva da Figura 9 para y1 = 1,0 m). Dessa forma, o aumento de temperatura nessa região é extremamente baixo.

CONCLUSÕES

Foi apresentado um modelo teórico que permite avaliar o aquecimento da região de base de veículos espaciais durante a decolagem. O modelo desenvolvido possibilita, ainda numa fase preliminar do projeto, o dimensionamento de proteções térmicas sobre essas regiões. Os resultados aqui apresentados são importantes, no sentido de que auxiliam a identificar situações (ou regiões) críticas. Foi também avaliada a condição de aquecimento quando do vôo propulsado a grandes altitudes. Dos resultados apresentados, para o fluxo de calor incidente e para a distribuição de temperatura ao longo da região de base, concluiu-se que que tal aquecimento não é crítico.

REFERÊNCIAS BIBLIOGRÁFICAS

[1] Pessoa Filho, J. B. e Cotta, R. M. "Radiação Térmica Proveniente da Pluma de Foguetes a Propelente Sólido", Anais do III Workshop de Combustão e Propulsão, pp. 51-62, Lorena-SP, 1989.

[2] Pessoa Filho, J. B. e Cotta, R. M. "Analytical Models for Radiative Heat Transfer from Solid Propellant Rocket Exhaust Plumes", Anais do X Congresso Brasileiro de Engenharia Mecânica, pp. 313-316, Rio de Janeiro-RJ, 1989.

[3] Toro, P. G. P., "Determinação do Fluxo de Calor em Escoamento Supersônico Utilizando a Teoria de Aquecimento Cinético de Van Driest", trabalho a ser apresentado no III Encontro Naciona de Ciências Térmicas, Itapema, SC, 1990.

[4] Lourme, D. "Firing Tests of Models of Several Ariane 4 Launch Vehicle Configurations", Acta Astronautica, 15(1):17-28, 1987.

[5] Urquhart, J. B., "View Factor from Conical Surface by Contour integration", AIAA Journal, 7(11):2157-8 1987.

[6] Bobco, R. P., "Radiation from Conical Surface with Nonuniform Radiosity", AIAA Journal, 4(3):544-6, 1966.

[7] Pessoa Filho, J. B. "Análise do Aquecimento por Radiação e Circulação de Gases sobre Veículos Lançadores de Satélites - Revisão Bibliográfica". Relatório Interno da Divisão de Projetos - Instituto de Atividades Espaciais, Abril, 1988.

ABSTRACT

This work decribes the activities developed by the Aerothermal group (IAE/CTA) and the Mechanical Engineering Program (COPPE/UFRJ) in order to develop theoretical models to establish the heating level on the base region of a space vehicle during its lift off as well as during flight at high altitudes. In the first situation the developed model is formally presented and typical results for the second phase are discussed.

III ENCIT – Itapema, SC (Dezembro 1990)

ANDISORD: A COMPUTER PROGRAM FOR ATMOSPHERIC AND ENGINEERING RADIATIVE TRANSFER APPLICATIONS

ALEJO SANCHEZ A. and WITOLD F. KRAJEWSKI.

Iowa Institute of Hydraulic Research
The University of Iowa
Iowa City, Iowa 52242-1585 - U.S.A.

SUMMARY

In this paper, a radiation transfer algorithm for the solution of the equation of radiative transfer based on a finite difference implementation of the discrete-ordinates method is presented. Given the finite difference formulation of the resulting computer program, (ANDISORD), extension of the current 1-D version to 2-D or 3-D situations is straight forward. The program can handle a wide variety of boundary conditions, it has built-in anisotropic capability, it allows for thermal sources, and it can interact effortlessly with other modes of heat transfer. These characteristics make ANDISORD an excellent tool in engineering applications. Results obtained from benchmarking tests in both atmospheric and engineering applications are given.

INTRODUCTION

Rainfall over the tropics and oceans is one of the most important variables that needs to be estimated in order to properly calibrate the performance of the global circulation models. Given the spatial and temporal variability of rainfall, satellites represent the only viable alternative for obtaining such estimates. At the core of any satellite rainfall retrieval scheme remains the problem of solving, efficiently, the inverse radiation problem which in turn relies on a radiative transfer algorithm.

It is of interest to develop a general model for the solution of the radiative transfer equation in multidimensional, anisotropic, inhomogeneous medium [1]. As a first step in this direction, a radiation transfer algorithm for the solution of the equation of radiative transfer based on a finite difference implementation of the discrete-ordinates method is presented. Given the finite difference formulation of the resulting computer program, (ANDISORD), extension of the current 1D version to 2D or 3D situations is straight forward. The model contains all the procedures necessary to evaluate the optical properties of polydispersions. These polydispersions can be directly related to rainfall through a Marshall-Palmer type of relationship.

The model can handle a wide variety of boundary conditions, it has built-in anisotropic capability, it allows for thermal sources, it has the capability to evaluate the optical properties of particulated media, and it can interact effortlessly with general application programs for the solution of the conservative equations of momentum, mass and energy. These characteristics make ANDISORD an excellent tool in engineering applications.

Results obtained from benchmarking tests in both atmospheric and engineering applications are given in the following sections. Comparisons with other algorithms show the great flexibility and accuracy of ANDISORD.

THE GENERAL EQUATIONS

The ultimate objective of the described work is to develop a radiative transfer model that could be applied to cloudy and rainy atmospheres. This implies that the method used to solve the problem should account for: 1) multiple dimensions (3D); 2) anisotropic scattering (including water droplets); 3) compatibility with other modes of heat transfer; 4) inhomogeneities; 5) real gas; 6) computational efficiency; and 7) accuracy and stability.

The first five conditions are desirable due to the geometry, composition, and radiative properties of clouds themselves. For the sixth condition, computational efficiency, high speed is required because it is foreseen that the method will be applied to the interpretation of satellite data. As for the last condition, accuracy and stability, it is understood that the extra effort necessary to achieve "exact" solutions, although desirable in some situations, is not justified in this type of atmospheric problem due to the inexact knowledge of cloud constituents or their vertical distribution [2]. Hence, good, stable approximations rather than "exact" solutions are sought.

Subject to the boundary conditions of the particular problem at hand, the system of equations governing the problem are:

Energy Conservation Within the Medium. The well known form of the general energy conservation equation follows [3]:

$$\rho C_p \frac{DT}{Dt} = \beta_c T \frac{DP}{Dt} + \nabla\cdot(k\,\nabla T - q_r) + \dot{q} + \Phi' \qquad (1)$$

The left hand side of equation (1) represents the convection and transient energy storage while the terms on the right hand side are, in order, compression work, conduction, net radiative energy gained per unit volume, local heat generation, and viscous dissipation.

The divergence of the heat flux vector. In terms of radiative intensities, the divergence of the heat flux vector is expressed as:

$$\nabla\cdot q_r = \int_0^\infty \int_0^{4\pi} \left(\frac{\partial I_\lambda}{\partial x}\mu + \frac{\partial I_\lambda}{\partial y}\delta + \frac{\partial I_\lambda}{\partial z}\gamma \right) d\omega\, d\lambda \qquad (2)$$

where ω denotes solid angle; and μ, δ, and γ are the cosines of the angle between the direction of I (the intensity) and the x, y, and z axis, respectively, and I_λ is the monochromatic intensity at wavelength λ.

The monochromatic intensity. The monochromatic intensity is expressed as:

$$\frac{dI_\lambda}{d\zeta} = -(a_\lambda + s_\lambda) I_\lambda(\zeta) + a_\lambda I_{b\lambda}(\zeta) + \frac{s_\lambda}{4\pi} \int_0^{4\pi} I_\lambda(\zeta,\omega_i)\, \Phi(\lambda,\omega,\omega_i)\, d\omega_i \qquad (3)$$

where I is the radiant intensity, β is the extinction coefficient, I_b is the blackbody intensity, ζ is the line of sight of incident radiation, ω and ω_i are, respectively, the outgoing and the incident solid angle, and Φ is the scattering phase function. The left hand side of equation (3) is the variation of the monochromatic intensity along the line of sight direction (LSD). The three terms on the right hand side are, respectively, the attenuation of monochromatic intensity along the LSD due to the absorption and outward scattering characteristics of the

medium, augmentation of monochromatic intensity into the LSD due to emission in the medium, and the augmentation of monochromatic intensity due to inward scattering of the incoming radiant energy into the LSD. The monochromatic absorption and scattering coefficients are a_λ and s_λ respectively.

SOLUTION OF THE GENERAL EQUATIONS

Selection of a Method. A comparison among the different methods to solve the radiative transfer equation (RTE) is tabulated in Byun [4]. He classifies the various methods into four categories: flux (subdivided into flux, P-N or differential approximation, and S-N or discrete ordinates), integral, Monte Carlo, and zone methods. For three dimensional, emitting, absorbing and anisotropically scattering media the P-N and the S-N methods may be selected as those that better satisfy the needs expressed above.

Although the P-N method (in particular P-3) has been formulated and applied to 3D radiation transfer problems with anisotropic scattering conditions [5,6], the results seem to be very poor and questionable [7]. On the other hand, the use of the P-3 method for 2D geometries is claimed to be already too cumbersome. This leaves the S-N method as the best choice for the problem.

In situations where scattering is important, which is the case in the presence of raindrops and cloud water, the discrete ordinates method (S-N) is reported to work very well [8]. Very good agreement is reported [7, 9] between the S-N method (for N equal to or greater than 4) and the zone method for 3D problems with isotropic scattering.

The discrete ordinates method [7, 9, 10] is, therefore, selected as the working tool. The pros and cons for the use of the discrete ordinates method in atmospheric applications are discussed in detail in Lenoble [11] and Siegfrid [12].

The Discrete Ordinates Method. The general formulation as well as the description of the numerical implementation of the discrete ordinates method in three dimensional, anisotropically scattering radiative heat transfer problems is readily available elsewhere [7, 9, 10]. Some modifications have, however, been introduced here in order to make the scheme more applicable to atmospheric problems. In particular: parallel beam radiation (solar beam) and isotropic radiation on the boundaries (background radiation) have been included.

For the control volume depicted in Figure 1 the face intensities are related to the volume-center intensity throughout a spatial interpolation of the form:

$$I_i^p = \alpha\, I_i^{xe} + (1-\alpha)\, I_i^{xr} = \alpha\, I_i^{ye} + (1-\alpha)\, I_i^{yr} = \alpha\, I_i^{ze} + (1-\alpha)\, I_i^{zr} \qquad (4)$$

where α is a weight factor ($0.5 \le \alpha \le 1$) and the superscripts "r" and "e" denote reference and end-face (to indicate where the energy originates and where it arrives) for the indicated coordinate direction.

Equation (3) is discretized and rewritten as:

$$I_i^p = \frac{|\mu_i| A_{n,s} I_i^{xr} + |\delta_i| A_{e,w} I_i^{yr} + |\gamma_i| A_{f,b} I_i^{zr} + \alpha\,(S_1+S_2+S_3)\Delta V_p}{|\mu_i| A_{n,s} + |\delta_i| A_{e,w} + |\gamma_i| A_{f,b} + \alpha\beta\Delta V_p} \qquad (5)$$

where μ_i, δ_i, and γ_i are the direction cosines for the discrete direction i, and where the face areas (A), and the source terms (S_1, S_2, and S_3) for a differential volume ($\Delta V_p = \Delta x\, \Delta y\, \Delta z$) are given by the expressions:

$$A_{n,s} = \Delta y\, \Delta z \qquad \text{north/south faces}$$

$$A_{e,w} = \Delta x\, \Delta z \qquad \text{east/west faces}$$

$$A_{f,b} = \Delta y\, \Delta x \qquad \text{front/back faces}$$

$$S_1 = (1 - \Omega)\, \beta\, I_b^p \quad \Rightarrow \quad S_1 = a I_b^p \qquad (6)$$

$$S_2 = \frac{s}{4\pi} \sum_j w_j\, I_j^p\, \Phi_{ij} \qquad (7)$$

$$S_3 = \frac{s}{4\pi}\, F_o^p\, \Phi_{io} \qquad (8)$$

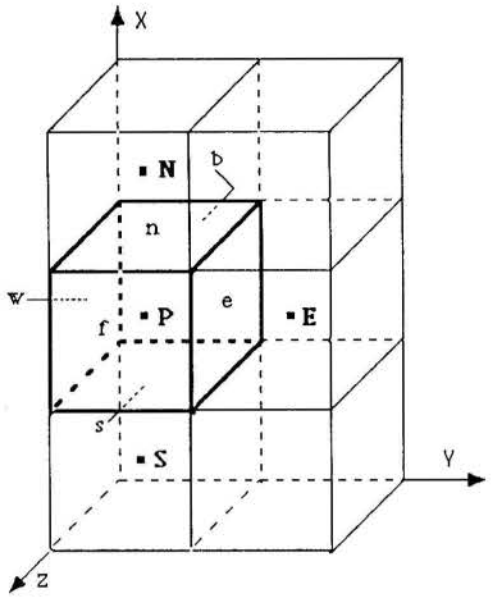

Fig. 1. Three-dimensional Control Volume.

In Equations (6-8) Ω is the scattering albedo; w are the weights for the quadrature procedure; F_o is the external flux for a parallel beam in direction μ_o, δ_o, and γ_o; and Φ_{ij} is the phase function.

The phase function is represented by:

$$\Phi_{ij} = \sum_{n=0}^{N} (2n+1)\, b_n\, P_n(\mu_i\mu_j, \delta_i\delta_j, \gamma_i\gamma_j) \qquad (9)$$

where b_n are coefficients for the series expansion of the phase function in terms of Legendre polynomials of order n (P_n).

When the surface bounding the enclosure is gray, opaque, and emits and reflects diffusively, the boundary conditions for equation (5) are

$$\begin{aligned}
&\text{at} \quad x = 0 && I_i = \varepsilon I_b + \frac{(1-\varepsilon)}{\pi} \sum_{\mu_j < 0} w_j\, |\mu_j|\, I_j && \text{for } \mu_i > 0 \\
&\text{at} \quad x = L_x && I_i = \varepsilon I_b + \frac{(1-\varepsilon)}{\pi} \sum_{\mu_j > 0} w_j\, \mu_j\, I_j && \text{for } \mu_i < 0 \\
&\text{at} \quad y = 0 && I_i = \varepsilon I_b + \frac{(1-\varepsilon)}{\pi} \sum_{\delta_j < 0} w_j\, |\delta_j|\, I_j && \text{for } \delta_i > 0 \\
&\text{at} \quad y = L_y && I_i = \varepsilon I_b + \frac{(1-\varepsilon)}{\pi} \sum_{\delta_j > 0} w_j\, \delta_j\, I_j && \text{for } \delta_i < 0 \\
&\text{at} \quad z = 0 && I_i = \varepsilon I_b + \frac{(1-\varepsilon)}{\pi} \sum_{\gamma_j < 0} w_j\, |\gamma_j|\, I_j && \text{for } \gamma_i > 0 \\
&\text{at} \quad z = L_z && I_i = \varepsilon I_b + \frac{(1-\varepsilon)}{\pi} \sum_{\gamma_j > 0} w_j\, \gamma_j\, I_j && \text{for } \gamma_i < 0
\end{aligned} \qquad (10)$$

where ε is the surface emissivity and L_i is the total length of the domain in the direction i.

If an external intensity I_s is incident on any of the surfaces, the term I_s should be added to the boundary condition at that surface.

Solution Procedure. If the temperature distribution throughout the computational domain is known, the terms S_1 as well as the optical properties of the medium can be evaluated as needed and the system of equations (4-10) can be solved independently of the energy equation. Normally, this is not the case and the radiative transfer equation has to be solved iteratively with the energy equation (*global iterations*) in order to find the needed temperatures.

For steady state, the energy equation (equation (1)) for a moving continuum can be written in the following general form:

$$C(T) = D(T) + S(T) \tag{11}$$

where C(T) is the convective term, D(T) the diffusion term, and S(T) the source term.

The source term can include compression work, viscous dissipation, heat generation and a radiation source. Whatever the other constituents of the source might be, the radiant source, if present, has to be found.

The radiant source is evaluated at each control volume (p) as:

$$(\nabla . q_r)_p = a\left(4\pi I_b^p - \sum_{j=1}^{n} w_j I_j\right) \tag{12}$$

Equation (11) is normally non-linear and must be solved iteratively by a numerical procedure [13]. Applications involving complete *global iterations* are not commonly found in the literature. In most cases, conduction and convection are assumed negligible and the source is considered to be either a radiation source alone ($\nabla . q_r = 0$) or radiation plus generation sources ($\nabla . q_r = q$).

In order to solve for a general energy equation, an iterative procedure between equations (4-10) and equations (11-12) has to be applied.

It is out of the scope of this paper to describe the details or to give examples of problems involving global iterations. However, given the importance of this type of problems in engineering, the interested reader is referred to Sánchez. et al. [14] were an example of the procedure for global iterations in a two-dimensional geometry is given.

THE ONE DIMENSIONAL IMPLEMENTATION

As a first step toward the full solution of the problem, a one-dimensional, parallel layers version of the procedure described previously was implemented. The geometry solved by the program is shown in Figure 2.

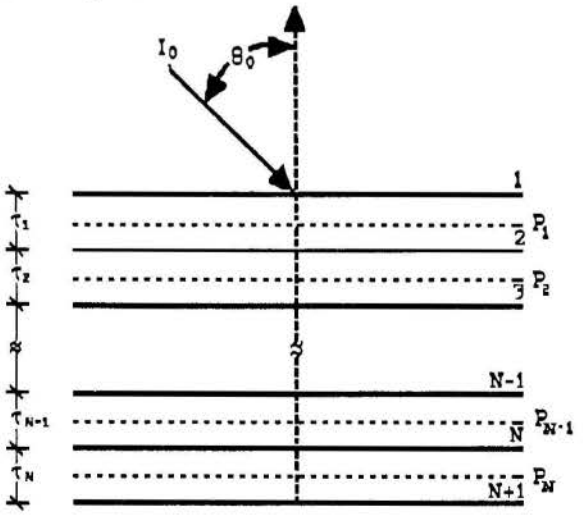

Fig. 2. Parallel Plates Geometry

The main characteristics of the program (called ANDISORD, and written in FORTRAN 77) are:

Sources. The program allows for any combination of parallel beam radiation at any angle θ_0, isotropic background radiation, and thermal sources.

Homogeneity. The layers are considered homogeneous in the horizontal direction, but they can be inhomogeneous in the vertical direction. i.e., the optical thickness (τ), the scattering albedo (ω_0) and the phase function can vary from layer to layer.

Scattering. The program allows for isotropic, anisotropic by similarity, Mie, or Henyey-Greenstein scattering.

Quadrature scheme. The code uses a Gaussian quadrature scheme to solve the integrals.

Azimuthal distribution. The program solves for azimuthally independent radiation. No effort was made in order to implement the azimuthal distribution of radiances, since this would require a Fourier expansion of the intensities. In the future, when the three-dimensional quadrature points are implemented, the azimuthal distribution will be obtained without extra effort due to the spatial distribution of the direction cosines.

Output. The program evaluates the radiances at any level and at any polar angle; the heat fluxes in and out of each inter-layer plane, discriminating between direct and diffuse fluxes; the irradiation at each inter-layer; and the transmissivity, reflectivity, and absorptivity of the whole "atmosphere".

The optical properties. Of primary importance for the application of ANDISORD to the problem of rainfall retrieval is the determination of the optical properties of polydispersions. To this effect, a companion program was written (POLY) that allows for the evaluation of those optical properties based on the following formulas [15, 16]:

$$\beta = \int_{r_{min}}^{r_{max}} \sigma_{ext}(r) \frac{dn(r)}{dr}\, dr \tag{13}$$

$$s = \int_{r_{min}}^{r_{max}} \sigma_{sca}(r) \frac{dn(r)}{dr}\, dr \tag{14}$$

$$\Phi(\theta) = \frac{1}{s} \int_{r_{min}}^{r_{max}} \sigma_{sca}(r)\, \Phi(\theta,r) \frac{dn(r)}{dr}\, dr \tag{15}$$

$$\frac{dn(r)}{dr} = 16000 e^{-\Lambda r} \ [m^{-3}\, mm^{-1}] \tag{16}$$

where σ_{ext}, and σ_{sca} are, respectively, the extinction and scattering cross-sections for a single sphere; β is the extinction coefficient (a + s) for the polydispersion; r is the drop radius; n(r) is the drop size distribution; θ is the scattering angle and Λ is:

$$\Lambda = 8.2\, R^{-0.21} \ [mm^{-1}] \tag{17}$$

R being the rainfall rate in [mm hr^{-1}]. Equations (16-17) imply a classic Marshall and Palmer type drop distribution.

The extinction (σ_{ext}) and scattering (σ_{sca}) cross-sections are evaluated from the exact Mie calculations, for a single hydrometeor of radius r, using wavelength dependent index of refractions tabulated from Kondratyev [17] and the computational procedure of Dave [18]. Expansion of the phase function in a series of Legendre polynomials – to find the b_n terms in equation (9) – is performed by means of a procedure similar to that described by Kumar [19].

RESULTS AND DISCUSSION

In order to benchmark the program (ANDISORD), several tests were executed. Due to space limitations, only some representative results are presented here.

Test 1. A set of six problems: three involving haze, two related to thicker clouds and one concerned with a more realistic atmosphere (including aerosols, etc.) were proposed to the scientific community by the Radiation Commission [11]. ANDISORD was used to solve the first two cases. Results from "case 2" follow.

The characteristics of the problem are: homogeneous plane-parallel atmosphere with total thickness $\tau = 1$ and albedo for single scattering $\omega_o = 0.9$; black, non-emitting ground; incident solar beam from direction $(\mu_o,0) = (-1,0)$ and flux $\pi F = \pi$ $(F = 1)$; anisotropic scattering with the coefficients for the expansion of the phase function into Legendre polynomials given.

Tables 1 and 2 present the result of the computations for comparison with other methods.

In all cases, ANDISORD was run with only six layers (τ = 0.05, 0.05, 0.1, 0.3, 0.25, 0.25) and with 32 streams (16 up and 16 down), while the phase function was approximated with a series of 31 Legendre polynomials (some of the other programs used up to 50) of orders 1 to 31.

ANDISORD provided excellent results. The error in the integrated quantities (fluxes) was always less than 0.1 percent, while for the discretized intensities the maximum error was in the order of 4 percent. Increasing the number of layers and streams would diminish these errors further.

Table 1. Radiance * 10: Haze L

τ	μ	spher. harmo.	Discr. Ord.	FN method	Monte Carlo	Current ANDISORD
0	1	0.2788	0.2784	0.2795	0.283	0.2665
	0.8	0.3139	0.3143	0.3144	0.323	0.3124
	0.2	0.6701	0.6702	0.6696	0.703	0.6715
	0	0.5196	0.5177	0.5175	0.475	0.5255
0.5	1	0.1371	0.1369	0.1374	0.136	0.1317
	0.8	0.1607	0.1609	0.1609	0.163	0.1599
	0.2	0.6676	0.6673	0.6671	0.680	0.6845
	0	0.9410	0.9399	0.9401	1.13	0.9283
	-0.2	0.9168	0.9155	0.9160	0.948	0.9208
	-0.8	2.385	2.385	2.385	2.38	2.3854
	-1	22.48	22.40	22.40	22.4	22.492
1.0	0	0.7962	0.7991	0.7932	0.749	0.8022
	-0.2	1.243	1.242	1.242	1.30	1.2425
	-0.8	3.870	3.870	3.869	3.91	3.8730
	-1	29.77	29.67	29.67	29.8	29.791

Table 2. Flux Case 2: Haze L.

Method	Diffuse Flux		Net Flux			
	$F^+(0)$	$F^-(\tau 1)$	τ=0	τ=0.1	τ=0.5	τ=1
Spheric harm. D	0.1236	0.1516	3.0180	2.9832	2.8418	2.6712
Discrete Ord. L	0.1243	1.537	3.0178	---	---	2.6714
FN Method	0.1237	1.5155	3.0179	2.9831	2.8418	2.6713
Doubling	0.1237	1.5155	3.0179	2.9831	2.8418	2.6713
Finite differ.	0.1233	1.1557	3.0182	2.9835	2.8425	2.6714
Monte Carlo.P	0.1230	1.516	3.019	2.985	2.837	2.672
Delta Eddi. W	0.1471	1.4998	2.9945	2.9601	2.8225	2.6555
2Stream Standard	0.0999	---	3.0417	3.0066	2.6569	---
"exact" value	---	---	3.018	2.9832	2.8418	2.6713
ANDISORD	0.1235	1.5190	3.0181	2.9834	2.8439	2.6748

Test 2. The ability of the program to handle different angles of incidence for the solar beam was tested by evaluation of reflection and transmission (direct plus diffuse) for two "atmospheres" with optical thicknesses of 0.25 and 1.0 respectively. Non conservative scattering (ω_o = 0.8) and Henyey-Greenstein scattering with asymmetry factor (g) of 0.75 was considered. In Table 3 results are compared with those tabulated in Liou [20]. These latest results were obtained with the use of a Discrete Ordinates Method (DOM) with 2, 4, 8, and 16 streams and by the Doubling Method. ANDISORD was run with 16 streams and 10 layers for optical thickness of 0.25, and 16 streams and 16 layers for the optical thickness of 1.0.

Table 3. Reflection and Transmission

		Reflection		Transmission	
τ_1	$\mu_o \Rightarrow$ Method$\Downarrow$	0.1	0.9	0.1	0.9
0.25	DOM, 2	0.31802	-0.01125	0.46566	0.95403
	4	0.30269	0.01746	0.46032	0.92623
	8	0.29599	0.01473	0.44354	0.92728
	16	0.29406	0.01558	0.43120	0.92679
	Doubling	0.28961	0.01547	0.43017	0.92669
	ANDISORD	0.2897	0.0155	0.4310	0.9267
1.0	DOM, 2	0.37519	-0.00064	0.29023	0.76333
	4	0.37646	0.05425	0.22724	0.72003
	8	0.36938	0.04901	0.20192	0.71702
	16	0.36071	0.04942	0.20416	0.71784
	Doubling	0.35487	0.04929	0.20556	0.71772
	ANDISORD	0.3559	0.0493	0.2073	0.7179

Test 3. The purpose of this test was to compare the results provided by ANDISORD with those from the "exact" zone method in an anisotropicaly scattering media [21,22]. The problem involves a layer of total optical thickness (τ), black walls, conservative scattering, and linearly anisotropic media with the phase function $P(\theta) = 1 + 3g\theta$. Results are given in table 4.

Table 4. Hemispherical Reflectivity of the Slab

g	References	τ 0.1	τ 1.0	τ 10.0
-1.0	Byun & Smith [21]	0.1048	0.5138	0.9092
	ANDISORD	0.1061	0.5138	0.9096
-0.7	Dayan & Tien [23]	0.099	0.495	--
	Yuen & Tien [24]	0.099	0.495	--
	Byun & Smith	0.0987	0.4954	0.9026
	ANDISORD	0.1001	0.4954	0.9030
0.0	Bleach et. al [25]	0.0843	0.4466	0.8833
	Busbrige et. al [26]	--	0.4466	0.8833
	Dayan et al	0.084	0.447	0.891
	Ozisik & Yener [27]	--	0.4466	--
	Sutton & Ozisik [28]	--	--	--
	Byun & Smith	0.0843	0.4465	0.8828
	Fiveland (S-6) [29]	--	0.4475	0.8842
	ANDISORD	0.0857	0.4465	0.8832
0.7	Dayan et al	0.069	0.389	--
	Byun & Smith	0.0694	0.3872	0.8529
	ANDISORD	0.0708	0.3872	0.8533
1.0	Busbrige et. al.	--	0.3577	0.8351
	Byun & Smith	0.0628	0.3577	0.8348
	Fiveland (S-6)	--	0.3583	0.8330
	ANDISORD	0.0643	0.3576	0.8351

Test 4. Figure 3 shows the excellent agreement between the dimensionless blackbody emissive power results obtained using ANDISORD and the zone method [22] for the solution of an absorbing, emitting and isotropically scattering medium enclosed by black walls. In this problem, the equation:

$$(-\nabla \cdot q_r)_p = a\left(\sum_{j=1}^{n} w_j I_j - 4\pi I_b^p\right) \qquad (12)$$

is solved for $(-\nabla \cdot q_r)_p = 0.0$ (radiative equilibrium)

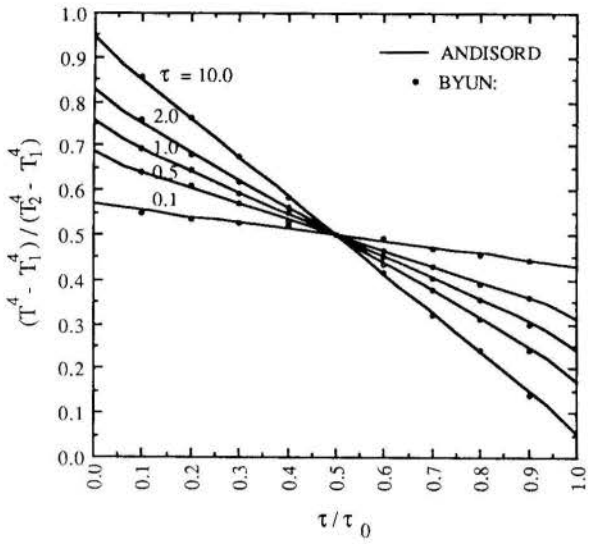

Figure 3. Dimensionless Emissive Power.

Test 5. Wiscombe et al.[30] (see also [31]) provide a series of tests for their computer program DISORD. Some of these tests were run to bench mark ANDISORD. The different "cases'" are named as in the original reference.

Table 5 compares results for cases 8A to 8C. These cases involve two inhomogeneous layers (denoted by the subindexes 01 and 02). The source of energy is isotropic radiation of intensity XISO=0.31831 incident on the upper surface and the scattering is isotropic.

TABLE 5. Intensities for two inhomogeneous layers.

						Intensities at μ =	
	At τ =	τ_{01}	τ_{02}	ω_{01}	ω_{02}	-1.0	1.0
		Case 8A					
Method		0.25	0.25	0.5	0.3		
DISORD	0.00					0.31831	0.019442
ANDISORD						0.31830	0.019472
DISORD	0.25					0.262711	0.005519
ANDISORD						0.262728	0.005514
DISORD	0.50					0.210014	0.000000
ANDISORD						0.209978	0.000000
		Case 8B					
		0.25	0.25	0.8	0.95		
DISORD	0.00					0.318310	0.049558
ANDISORD						0.31830	0.049542
DISORD	0.25					0.277499	0.025058
ANDISORD						0.277265	0.024978
DISORD	0.50					0.240731	0.000000
ANDISORD						0.240736	0.000000
		Case 8C					
		1.00	2.00	0.8	0.95		
DISORD	0.00					0.318310	0.104766
ANDISORD						0.31830	0.104748
DISORD	1.00					0.189020	0.065445
ANDISORD						0.188999	0.065383
DISORD	3.00					0.068476	0.000000
ANDISORD						0.068384	0.000000

TABLE 6. Fluxes for two inhomogeneous layers.

						Fluxes	
	At τ =	τ_{01}	τ_{02}	ω_{01}	ω_{02}	Down diffuse	Up diffuse
		Case 8A					
Method		0.25	0.25	0.5	0.3		
DISORD	0.00					1.000000	0.092963
ANDISORD						0.99997	0.093183
DISORD	0.25					0.722235	0.027895
ANDISORD						0.72122	0.027907
DISORD	0.50					0.513132	9.09E-18
ANDISORD						0.51214	0.00000
		Case 8B					
		0.25	0.25	0.8	0.95		
DISORD	0.00					1.000000	0.225136
ANDISORD						0.99997	0.22516
DISORD	0.25					0.795332	0.126349
ANDISORD						0.79494	0.12627
DISORD	0.50					0.650417	2.20E-16
ANDISORD						0.65010	0.00000
		Case 8C					
		1.00	2.00	0.8	0.95		
DISORD	0.00					1.000000	0.378578
ANDISORD						0.99997	0.37849
DISORD	1.00					0.486157	0.243397
ANDISORD						0.48580	0.24319
DISORD	3.00					0.159984	1.19E-17
ANDISORD						0.15972	0.00000

CONCLUSIONS AND RECOMMENDATIONS

Development of a 3D radiation transfer model accounting for hydrometeor scattering, real gas participation and all the boundary conditions appropriate for problems related to atmospheric radiation and satellite rainfall retrieval is an important objective of satellite remote sensing.

As a first step in the fulfillment of the goal, a 1D computer program (ANDISORD) was developed and implemented on a personal computer. The program, based on the finite difference version of the discrete ordinates method, was tested in a variety of situations with excellent results.

Although the program was not timed, it can be said that in all the cases tested, the required wall clock time was only a few seconds.

Future testing of ANDISORD, in its 1D version, as well as POLY – the companion program for the determination of the optical properties of polydispersions– will include thicker atmospheres and interaction with conduction and convective heat transfer. These are applications for which the program is already designed. In the near future, the 1D version will be enhanced to account for non-lambertian ground.

In addition to atmospheric remote sensing, the program can be readily applied to a wide variety of engineering problems. A recently developed 2D version of the program was applied to the problem of combined natural convection and radiation in a rectangular enclosure [14].

ANDISORD is available, upon request, to qualified users.

ACKNOWLEDGMENTS

The described investigations were partially supported by the grant NA89AA-D-AC195 from the National Oceanic and Atmospheric Administration: Global Change Program. These authors are thankful for this support.

The first author would also like to acknowledge the financial support received from Universidad de los Andes and Fundación Gran Mariscal de Ayacucho, both from the Republic of Venezuela.

REFERENCES

[1] Sánchez, A., Krajewski, W. and Smith, T. F., "Statistical Framework for Validation of Satellite-Based Global Precipitation Stimation; Part I: An Atmospheric Radiation Model — The Plane Layer Case," Progress report prepared for Grant NA89AA-D-AC195 for National Oceanic and Atmos. Admin., U.S.A.,1990.

[2] Kummerow, C., "Documentation for EDDGTON, a radiative transfer program using the Eddington approximation for multi-layered plane-parallel medium", NASA, Goddard Space Flight Center, 1989.

[3] Siegel, R. and Howell, J. R., "Thermal Radiation Heat Transfer", Hemisphere Publishing Corporation, New York., 1981.

[4] Byun, K., "Heat Transfer For Flow of an Absorbing, Emitting and Isotropically Scattering Medium in a Gray Diffuse Wall Duct," Ph. D. Thesis, The University of Iowa, U.S.A., 1987.

[5] Condiff, D. W., "Anisotropic Scattering in Three Dimensional Differential Approximation of Radiation Heat Transfer," Fundamental and Applications of Radiation Heat Transfer, Eds. A. M. Smith and T. F. Smith, HTD-Vol. 72, ASME, pp. 19-27, 1987.

[6] Menguc, M. P. and Viskanta, R., "Radiative Transfer in Three Dimensional Rectangular Enclosures Containing Inhomogeneous, Anisotropic Scattering Media," Quant. Spectrosc. Radiant. Transfer, Vol. 33, No. 6, pp. 533-549, 1985.

[7] Truelove, J. S., "Three-Dimensional Radiation in Absorbing-Emitting-Scattering Media Using the Discrete-Ordinate Approximation," Quant. Spectrosc. Radiant. Transfer, Vol. 39, No. 1, pp. 27-31, 1988.

[8] Tan, Z., "Radiative Heat Transfer in Multidimensional Emitting, Absorbing, and Anisotropic Scattering Media-Mathematical Formulation and Numerical Method," J. of Heat Transfer, Vol. 111, pp. 141-147, 1989.

[9] Fiveland, W. A., "Three-Dimensional Radiative Heat Transfer Solutions by the Discrete-Ordinates Method," J. Thermophysics Vol. 2, No. 4, pp. 309-316, 1988.

[10] Fiveland, W. A. and Jamaluddin, A. S., "Three Dimensional Spectral Heat Transfer Solutions by The Discrete-Ordinates Method," The 1989 National Heat Transfer Conference. Heat Transfer Phenomena in Radiation, Combustion, and Fires, Ed. R. K. Shah, ASME, HTD-Vol. 106, pp. 43-48, Pennsylvania, 1989.

[11] Lenoble, J., "Radiative Transfer in Scattering and Absorbing Atmospheres: Standard Computational Procedures", Ed. J. Lenoble, Deepack Publishing, Virginia, 1985.

[12] Siegfrid, A. W. G. and Zardecki, A., "Discrete-Ordinates Finite-Element Method for Atmospheric Radiative Transfer and Remote Sensing," Applied Optics, Vol. 24,No. 1, pp. 81-93, 1985.

[13] Patankar, S. V., "Numerical Heat Transfer and Fluid Flow", Hemisphere, Washington, 1980.

[14] Sánchez, A., House, J. and Smith, T. F., "Combined Natural Convection and Radiation in a Rectangular Enclosure in the Presence of a Polydispersion and a Non-Participating Gas," To be presented at the 3rd. Brazilian Thermal Science Meeting, Itapema, Brazil, 1990.

[15] Kummerow, C., "Microwave Radiances from Horizontally Finite, Vertically Structured Precipitating Clouds," Ph.D. Thesis, University of Minnesota, 1987.

[16] Savage, R. C., "The Radiative Properties of Hydrometeors at Microwave Frequencies," Journal of Applied Meteorology, Vol. 17, pp. 904-911, 1978.

[17] Kondratyev, K. Y., "Radiation in the Atmosphere", Academic Press, New York, 1969.

[18] Dave, J. V., Report # 320-3237, IBM Scientific Center , Palo Alto, California, 1968.

[19] Kumar, S., "Radiative Transport in an Absorbing/ Anisotropically Scattering Medium Exposed to a Collimated Incident Flux – an Analytical Solution by the Method of Singular Eigenfunction Expansions," Ms. Thesis, The State University of New York, Buffalo, 1984.

[20] Liou, K. N., "An Introduction to Atmospheric Radiation", International Geophysics Series, Academic Press, New York, 1980

[21] Byun, K. H. and Smith, T. F., "Application of the Zone Method to Linear Anisotropically Scattering Media Enclosed in a Plane Layer", Technical report ME-TFS-88-002, Department of Mechanical Engineering, The University of Iowa, Iowa, 1988.

[22] Byun, K. H. and Smith, T. F., "Development of the Zone Method for Linearly-Anisotropic Scattering Media," J. Quant. Spectrosc. Radiat. Transfer, Vol. 40, No. 5, pp. 591-604, 1988.

[23] Dayan, A. and Tien, C. L., "Heat Transfer in a Gray Planar Medium with Linear Anisotropic Scattering," J. of Heat Transfer, Vol. 97, pp. 391-396, 1975.

[24] Yuen, W. W. and Tien, C. L., "A Succesive Approximation Approach to Problems in Radiative Transfer with a Differential Formulation," J. Heat Transfer, Vol. 102, pp. 86-91, 1980.

[25] Bleach, H. L., Özisik M. N. and Siewert, C. E., "Radiative Transfer in Linearly Anisotropic Scattering Conservative and Non-Conservative Slabs with Reflective Boundaries," Int. J. of Heat and Mass Transfer, Vol. 14, pp. 1551-1565, 1971.

[26] Busbridge, I. W. and Orchard, S. E., "Reflection and Transmission of Light by a Thick Atmosphere According to a Phase Function: 1+ xcos(θ)," Journal of Astrophysics, Vol. 149, pp. 655-664, 1967.

[27] Özisik, M. N. and Yener, Y., "The Galerkin Method for Solving Radiation Transfer in Plane Parallel Participating Medium," J. of Heat Transfer, Vol. 104, pp. 351-354, 1982.

[28] Sutton, W. H. and Özisik, M. N., "An Iterative Solution for Anisotropic Radiative Transfer in a Slab," J. of Heat Transfer, Vol. 101, pp. 695-698, 1979.

[29] Fiveland, W. A., "Discrete Ordinates Methods for Radiative Heat Transfer in Isotropically Scattering Media," J. Heat Transfer , Vol. 109, pp. 809-812, 1987.

[30] Wiscombe, W., Stamnes, K., Tsay, S., Freidenreich, S. and Laszlo, I., "Documentation for DISORT, a radiative transfer program using the discrete ordinates method for multi-layered plane-parallel medium," NASA, Goddard Space Flight Center, 1988.

[31] Stamnes, K., Tsay, S., Wiscombe, W. and Jayaweera, K., "Numerically Stable Algorith for the Discrete-Ordinate-Method Radiative Transfer in Multiple Scattering and Emitting Layered Media," Applied Optics, Vol. 27, No. 12, pp. 2502-2509, 1988.

III ENCIT – Itapema, SC (Dezembro 1990)

INDUCED TRANSIENT TEMPERATURE DISTRIBUTION IN LARGE WATER BODIES FROM THERMAL RADIATION

Alejandro F. Romero-López, Professor
Crisanto Mendoza-Covarrubias, Graduate Student
División de Estudios de Posgrado Facultad de Ingeniería
Universidad Nacional Autónoma de México
P.O Box 70-270, 04510 México, D.F.

ABSTRACT

Incident solar radiation upon oceans and generally, large water bodies is reflected, transmitted to greater depths and absorbed by the fluid mass (Viskanta and Toor, 1973, 1978). There are presently several commercial systems that operate under these circumstances, such as solar-saline water ponds, solar collectors with descending film, pools, etc. The main objective of this paper is to obtain the transient temperature induced by thermal radiation in large water bodies, by use of the finite element method to discretize the space and finite differences to discretize the time variation.

NOMENCLATURE.

Cp	specific heat of water	kJ/kgK
$g(x)$	local radiation absorption rate,	W/m^3
$H_{D,k}$	incident direct solar radiation,	W/m^2
$H_{d,k}$	diffuse solar radiation,	W/m^2
K_k	water absorption coefficient as a wave length function.	
k	thermal conductivity of water,	W/mK
k_T	molecular thermal diffusivity	m^2/s
s	parameter in Fresnel's equation	
$T(x,t)$	temperature distribution in water	
Ta	ambient air temperature, K	
Ts	surface temperature, K	
t	time, s	
v	approximation function from v to T	
x	space variable, m	
$T'C'$	$\partial T/\partial x$	
C^2	$\partial^2 T/\partial x^2$	
ε	belonging sign, "belongs to..."	
Ω	vectorial space under study	
$T\varepsilon\bar{K}^*$	temperature belonging to a sub-region of Ω	
$\bar{K}$	sub-region of the space under study	
$H\varepsilon$	weight parameter	
ε	any value within the weight parameter	
λ	wave length, m, μm	
n	refraction index (1.333 for solar ponds)	
θ	angle	
μ	$\cos\theta$	
μi	incident angle	
ρ	density kg/m^3	
ρa	Fresnell reflectivity of air	
μ'	Snell's law, $(1-n^2(1-\mu^2)^2)^{1/2}$	
ϕn	solar radiation absorbed by surface	W/m^2
ϕsn	net radiation in surface,	W/m^2
ϕan	atmospheric radiation incident in the surface=$5.18\times10^{-4}(Ta+273)^6(1+0.17C^2)$,	W/m^2
ϕbr	Surface black body radiation	
ϕe	heat flow due to evaporation, $\rho aLvf(Wz)(es - ex)$	
$f(Wx)$	wind velocity at the height x	
W_2	wind velocity at 2m height	
Lv	evaporation enthalpy of water, J/kg	
es	saturated vapor pressure at Ts, mbar	
ex	vapor pressure at the height x, mbar	
C	clear or cloudy sky factor	
ρo	reference density kg/m^3	
ε	emissivity	
σ	Stefan-Boltzmann constant	W/m^2K^4
ϕc	conduction heat transfer, $0.255f(Wx)(Ts-Ta)$	

INTRODUCTION

The temperature distribution for shallow depths of water ponds or similar systems is a solved problem in the literature (Viskanta and Toor, 1978, Cengel and Özisik, 1984), among others, however very few or no attempts at all (Romero and Riesco, 1987), have been made to describe the radiation induced transient temperature distribution of oceans or large water bodies, like lakes, dam reservoirs, etc.

This paper presents an algorithm to predict the behaviour induced by solar radiation in large water bodies (see Fig. 1 & 2). The model assumes an initial temperature distribution and considers very large but finite depths. The results are then compared with available experimental data from authors like (Viskanta and Toor, 1973, and Behnia and Viskanta, 1979). The initial conditions can also be varied to suit actual distributions present in natural water bodies.

ANALYSIS.

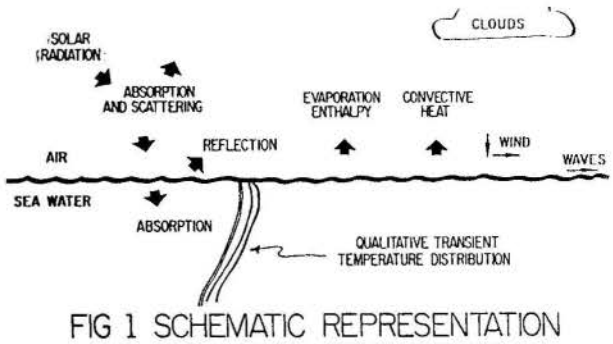

FIG 1 SCHEMATIC REPRESENTATION OF THE PHYSICAL MODEL

The energy equation for the thermal behaviour in water, considering simultaneously conduction and radiation is given by (Özisik, 1973)

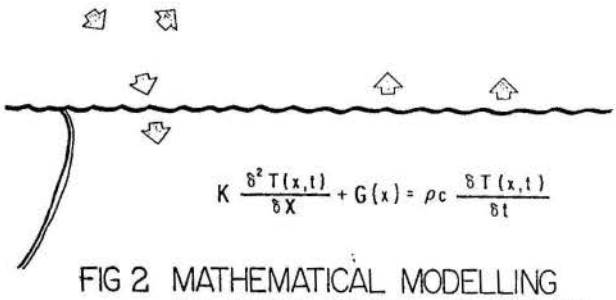

FIG 2 MATHEMATICAL MODELLING OF THE PHYSICAL BEHAVIOUR

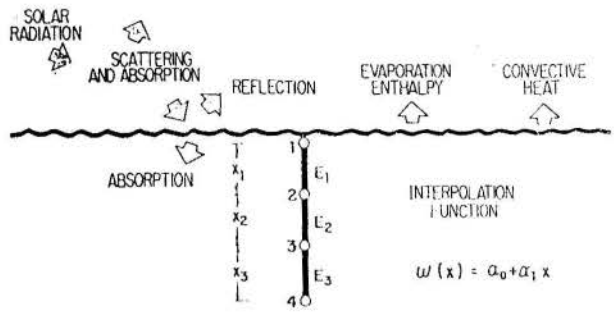

FIG 3 FINITE ELEMENTS DISCRETIZATION

$$k\frac{\partial^2 T(x,t)}{\partial x^2} + g(x) = \rho C_p \frac{\partial T(x,t)}{\partial t} \qquad (1)$$

where g(x) is the source term and represents the solar absorption rate per unit volume at a depth "x", measured from the surface.

In (1), the following assumptions have been made:

1) The water body is a semi-infinite onedimensional system

2) Air-water interface is flat (no transversal waves are present).

3) Refraction angle follows the Snell's law.

4) Thermal radiation within the water is negligible in the infrared spectrum ($\lambda > 3\ \mu m$).

5) Solar incident radiation on the water surface is composed of direct (H_D) and diffuse (H_d) components.

The boundary and initial conditions for (1) are given by (Atkinson, 1983):

$$k_T \frac{\partial T}{\partial x} = \phi_n \quad \text{at} \quad x = 0 \quad \text{for all } t$$

$$T \geq 278\ K \quad \text{for} \quad x \to \infty \quad \text{for all } t \qquad (2)$$

$$T = T_o \quad \text{for} \quad t = 0 \quad \text{for all } x$$

The term g(x) is defined as follows:

$$g_R(x) = K_R \left\{ \left[1 - \rho_a(\mu_i) \right] \frac{H_{D,k}}{\mu_r} e^{-k\mu x/\mu_r} + 2\, n^2 H_{d,k} \int_{\mu_r}^{1} \left[1 - \rho_a(\mu') \right] e^{-kx/\mu} d\mu \right\} \qquad (3)$$

FORMULATION OF THE FINITE ELEMENT METHOD.

In principle, the variational problem of (1) has to be obtained, that is to find T such that $T \in C'((0,T), C^2(\Omega))$, (see Fig. 3)

$$\begin{aligned} &T \geq 280 \quad \text{in } \Omega \times J \\ &k\,\Delta T + G = \rho\, C_p T' \quad \text{in } \Omega \times J \\ &U(0) = U_o \quad \text{in } \Omega \end{aligned} \qquad (4)$$

The first condition (2) has to be satisfied over $\partial\,\Omega \times J$, that is rising a Newman's type problem:

$$K = \left\{ v \in c' \left[(0,T),\ c'(\Omega) \right] :\ 0 < v(t) \leq 278 \text{ in } \Omega,\ t \in J \right\}$$

where **K** represents the set of admisible temperatures. The following equation can then be written:

$$\int_\Omega (K\,\Delta T + G) v\, d\Omega = \int_\Omega \rho\, C_p\, T'\, v\, d\Omega \qquad (5)$$

Expression (5) can be transformed through application of Green's theorem:

$$-\int_\Omega k\, \nabla T \circ \nabla v\, d\Omega = -\int_{\partial\Omega} k \frac{\partial T}{\partial x}\, v\, d\Omega - \int_\Omega \rho C_p T' v\, d\Omega \qquad (6)$$

So that the problem reduces to determine $T \in \tilde{K}$:

$$-\int_B X_\varepsilon \left\{ \rho C_p T' v \right\} dB - \int_B (K \nabla T \circ \nabla v)\, dB \geq \phi_n(0) v(0) - \int_B G v\, dB \qquad (7)$$

valid for all $\mathbf{v} \in K^*$, where:

$$K^* = \left\{ v \in \bar{k} :\ v(\bar{L}) \leq 0 \right\} \qquad (8)$$

Then the variational problem of (1) is to find $\mathbf{T} \in \mathbf{K}$:

$$-\int_B H_\varepsilon(t) \left\{ \rho C_p T' v \right\} dB - \int_B (K\, \nabla T \cdot \nabla\, v)\, dB = \phi_n(0)/k_t\, v(0) - \int_B G v\, dB \qquad \forall\ v \in \tilde{K}^* \qquad (9)$$

The limits are set as follows:

$$H_\varepsilon(t) = \begin{cases} 0, & T \leq 0 \\ T/\varepsilon, & 0 \leq T \leq \varepsilon \\ 1, & T \geq \varepsilon \end{cases}$$

In such a way that (9) leads to the solution of a matrix problem:

$$\underset{\sim}{H}(t)\alpha'(t) + k\alpha(t) = f(x) \qquad (10)$$

The space is then divided by finite one-dimensional elements, from which three different matrixes are developed, **k**, **H** and **f**, the first one being a band matrix, the second a diagonal matrix and the third one, a column matrix, whose representation is not presented here due to space limitations, (see Figs. 4 & 5)

Time discretization is made with finite differences (Bathe and Wilson, 1976) from the matrix problem (9), and the utilized interpolation functions corresponds to first degree polynomials of the form:

$$\omega(x) = \alpha_0 + \alpha_1 x, \qquad x \in E \qquad (11)$$

with (11), the interpolation functions are generated on each finite element E.

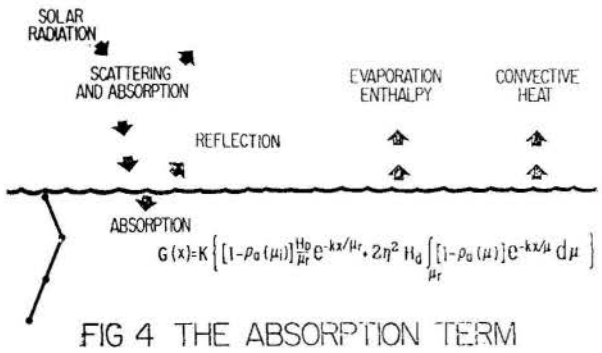

FIG 4 THE ABSORPTION TERM

By combining (9) and (11), the matrix problem is formally stated (matrix representations are omited here for the sake of space limitations, see Figs. 5 & 6, too). In order to discretize time, the method of forward finite differences is used (Bathe and Wilson, 1976), such that equation (9) can be written as:

$$(1/\Delta T)\underset{\sim}{H}(t)\alpha(t+\Delta t)= f(x)+ +\left[\underset{\approx}{k} + 1/\Delta t)\underset{\sim}{H}(t)\right]\alpha(\Delta t) \qquad (12)$$

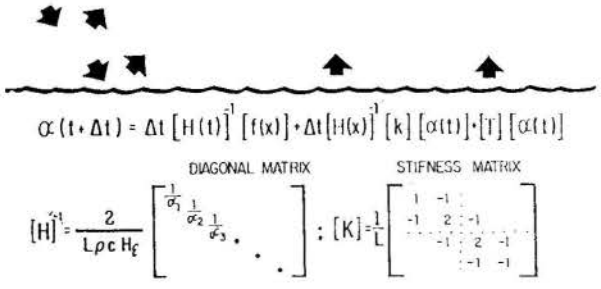

FIG 5 MATRIX EQUATION AND TYPES

For the solution of equation (12) a computer algorithm was implemented for which the finite elements were taken of the same length and for 40 nodal points. The temperature profiles were then calculated for some values of the solar radiation at different incident angles.

RESULTS

The figures 7 & 8, represent the temperature distribution as a function of time and depth for several time increments and three incident angles (0, 45 and 75°). Each curve corresponds to an overall time change of 30 minutes or 1800 sec, the qualitative behaviour agrees reasonably with some experimental values from other authors (Behnia and Viskanta 1979). The asymptotic approach to the cold temperature of greater depths ($z \geq 25$ m) agrees with temperature distributions found in the oceans.

In the determination of the absorption function $G(x)$, direct and diffuse radiation values were taken as 800 and 200 W/m^2, respectively, however in natural environments they must be a funcion of incident angle. Water absorption coefficients, were assumed to be equal to those of fresh water, and was taken from (Cengel and Özisik, 1984)

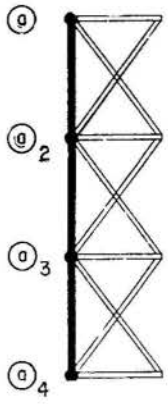

FIG 6 BASE FUNCTIONS IN THE ELEMENTS

CONCLUSIONS

1. The present model reproduces some of the features that are present in natural water bodies.

2. Like any numerical model it has some limitations for the exact reproduction of natural phenomena, however the results can be reasonably used for some preliminary studies of ecological nature or even, by modification of the source term, could be possibly used to predict temperature distribution under the effects of large thermal discharges in addition to the solar radiation effect.

3) An initial linear temperature distribution was imposed for the few computer runs. The induced transient temperature, as predicted by the model, approaches the same linear distribution as the depth increases, however, near the surface a temperature peak is detected, consistent with some stratification that occurs in nature. For all practical purposes, the total mass of the water body can easily be regarded as inifinity, it is therefore natural that at some depth, the water reaches the initial imposed temperature distribution.

4) A more realistic initial temperature distribution, can of course be imposed on the model, however, this requires a careful determination of some actual temperature distribution in a large natural water reservoir. Due to the nature of thermal radiation, this implies serious field difficulties, at the most this could be instantaneously achieved and the data so obtained fed to the computer.

5) It is evident that additional work has to be done in order to include not only a reliable data field measurement, but of course to consider the turbidity and salinity effects, in order to attain future improvements of the model.

REFERENCES.

Özisik. M.N., 1973 "Radiative Transfer", John Wiley & Sons, Inc., New York.

Viskanta, R. and Toor, J.S., 1973 "Effects of Multiple Scattering on Radiant Energy Transfer in Waters", J. Geophys Res., Vol. 78, pp. 3538-3542

Bathe, K.J. and Wilson, E.I., 1976 "Numerical Methods in Finite Element Analysis", Prentice-Hall, Inc.

Viskanta, R. and Toor, J.S., 1978 "Absorption of Solar

Radiation in Ponds", Solar Energy, Vol. 21, pp. 17-25.

Behnia, M. and Viskanta, R., 1979 "Laboratory Study of Flow and Thermal Structures in Heated and/or Cooled Layers of Water", Purdue University, West Lafayette, IN

Atkinson, J.F., 1983 "A Wind-mixed Layer Model for Solar Ponds", Solar Energy, Vol. 31, pp 243-259,

Cengel, Y.A. and Özisik, M.N., 1984 "Solar Radiation Absorption in Solar Ponds", Solar Energy, vol. 33, No. 6, pp. 581-591

Romero, A.F. and Riesco, J.M., 1987 "Absorción de Energía Radiante en Cuerpos de Agua", Proc. 13th Congress of the National Academy of Engineering of Mexico, Guadalajara, pp 18-22

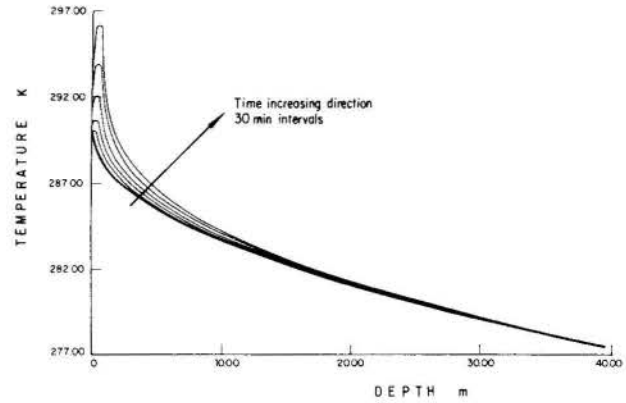

FIG. 9 TEMPERATURE EVOLUTION OF SEA WATER AS A FUNCTION OF DEPTH FOR AN INCIDENT ANGLE OF 75°

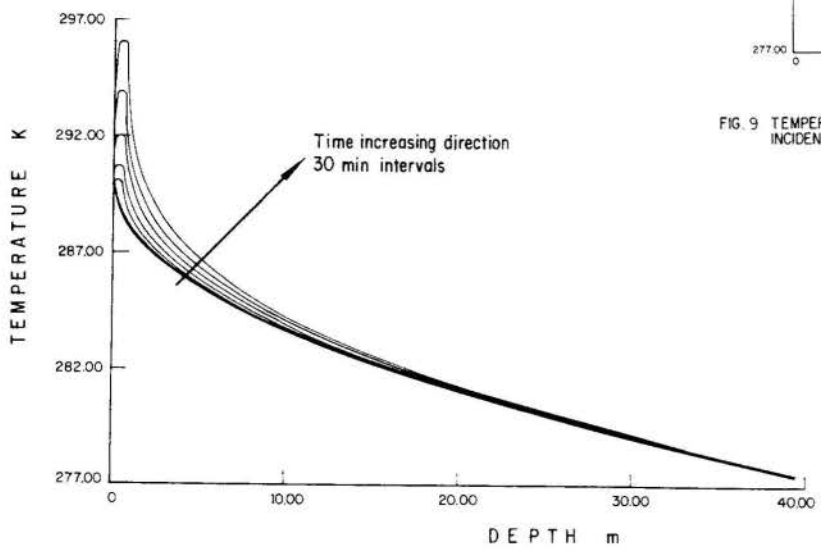

FIG 7 TEMPERATURE EVOLUTION OF SEA WATER AS A FUNCTION OF DEPTH FOR AN INCIDENT ANGLE OF 0°

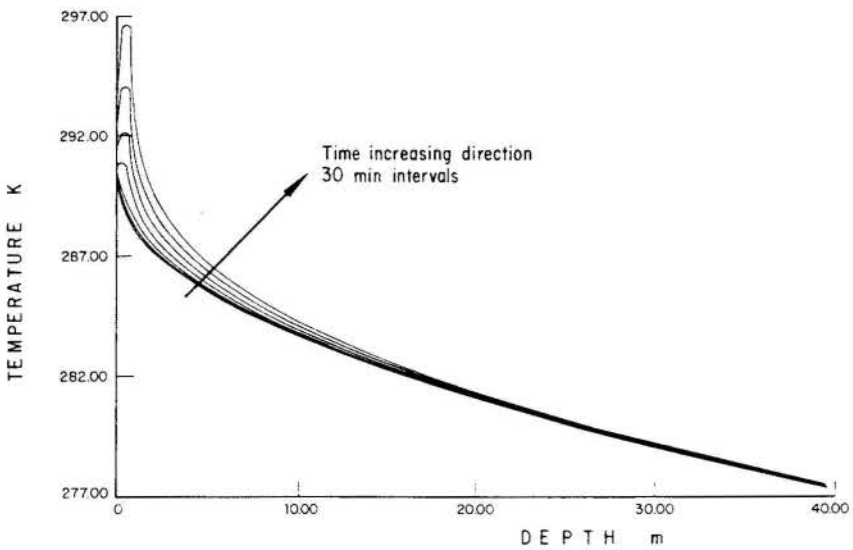

FIG 8 TEMPERATURE EVOLUTION OF SEA WATER AS A FUNCTION OF DEPTH FOR AN INCIDENT ANGLE OF 45°

III ENCIT – Itapema, SC (Dezembro 1990)

EFEITOS CONVECTIVOS NA TRANSFERÊNCIA DE CALOR RADIANTE EM MEIOS PARTICIPANTES ENTRE SUPERFÍCIES PARALELAS

C.O.M.M.TEIXEIRA e C.M.HACKENBERG
PROGRAMA DE ENGENHARIA QUÍMICA
COPPE/UFRJ - C.P. 68502
21945 - RJ - BRASIL

RESUMO

Este trabalho analisa os efeitos convectivos na estudo do mecanismo combinado condutivo convectivo radiante de transferência de calor em meios absorvedores e emissores. A investigação concentra se na avaliação do fenômeno para meios participantes contidos entre superfícies planas paralelas com temperaturas conhecidas. A solução matemática é obtida através do método das colocações ortogonais seguindo a linha de abordagem anteriormente adotada pelos autores na discussão do modelo condutivo radiante.

INTRODUÇÃO

O estudo do fenômeno de transferência de calor em meios participantes (absorvedores e emissores) constitui aspecto fundamental no dimensionamento de câmaras de combustão, em razão da necessidade imediata de utilização de modelos físicos mais abrangentes e precisos, que substituam os procedimentos simplificados ainda hoje adotados no projeto de fornos e caldeiras industriais, e minimizem as perdas de energia decorrentes da análise destes equipamentos através de metodologias limitadas.

Entretanto, apenas recentemente, a comunidade científica iniciou a pesquisa integrada dos mecanismos condutivo, convectivo e radiante de transporte de energia, observada a complexidade inerente a este tipo de problema, mesmo em situações onde é possível admitir certas hipóteses simplificadoras relativas às propriedades do meio e à geometria em questão. De uma forma geral, os trabalhos teóricos e experimentais eram desenvolvidos com o pressuposto da simultaneidade de apenas dois modos de transmissão de calor : condução e radiação, ou convecção e radiação.

Na linha de estudo do mecanismo condutivo-radiante, estes autores apresentaram trabalhos anteriores [1,2], onde determina-se o perfil de temperatura e calcula-se o fluxo térmico total (e suas parcelas condutiva e radiante) em meios absorvedores e emissores com geometria plana, bem como avalia-se a influência das principais propriedades do meio sobre a definição da importância relativa entre os dois mecanismos. A validade do formalismo matemático adotado e da técnica numérica usada foi verificada através da comparação com alguns resultados da literatura [3,4,5].

A segunda categoria de problemas (convecção e radiação) vem recebendo mais atenção a partir da intensificação dos empreendimentos aeroespaciais, notadamente os projetos de sistemas de propulsão de foguetes, e os textos de referência mais importantes para o acompanhamento deste assunto podem ser encontrados na documentação periodicamente publicada pela NASA.

O trabalho em pauta apresenta o desenvolvimento do modelo condutivo-convectivo-radiante para a obtenção do perfil de temperatura e do fluxo térmico total, pelo cômputo de suas parcelas, em meios participantes contidos entre superfícies planas paralelas. Evidencia ainda a aplicação do método das colocações ortogonais para a implantação de um código computacional que traduza o algoritmo representativo do modelo e facilite a análise da influência dos principais parâmetros envolvidos no problema.

Ratificando a adequação da modelagem aqui apresentada, os arquivos de saída (gráficos e tabulares) da rotina computacional, estruturada em FORTRAN para microcomputadores do tipo IBM-PC compatível, são objeto de uma análise comparativa com informações da literatura, através da determinação do perfil de temperatura em alguns casos práticos de interesse.

Na seqüência deste trabalho, os resultados do modelo em questão serão confrontados com aqueles originários da investigação do modelo condutivo-radiante [1], visando destacar o limite de relevância dos efeitos convectivos e avaliar os erros derivados da hipótese que considera o gás como um meio estacionário, de forma imprópria, em algumas situações.

MODELO CONDUTIVO-CONVECTIVO-RADIANTE

A forma diferencial genérica da equação da energia para o escoamento laminar de um fluido compressível considerado como um meio participante é dada por [6] :

$$\rho\, C_v \frac{DT}{Dt} = \mathrm{div}(K_c\, \mathrm{grad}\, T) - \mathrm{div}\, q_r - P\, \mathrm{div}\, U + \mu\, \Phi \qquad (1)$$

onde ρ, μ, C_v e K_c são a densidade, a viscosidade dinâmica, o calor específico e a condutividade térmica do fluido, T e P são a temperatura e a pressão do meio, U é o vetor velocidade do fluido, q_r é o vetor fluxo térmico radiante e Φ é a função dissipação de Rayleigh.

Esta expressão é obtida através da análise da primeira lei da Termodinâmica para um volume de controle do fluido, admitindo as seguintes hipóteses simplificadoras :

a) a existência do contínuo ;
b) a ocorrência de equilíbrio termodinâmico local ;
c) a energia interna do fluido é apenas função da temperatura ;
d) não há termo de geração de energia ;
e) o efeito da pressão radiante é desprezível ;
f) as propriedades físicas do fluido são constantes.

A partir do conceito de entalpia , da equação da continuidade e de algumas relações termodinâmicas auxiliares, é possível deduzir uma forma alternativa para a equação (1), ficando evidente a separação dos termos referentes aos mecanismos condutivo e radiante

de transferência de calor, aos efeitos de compressibilidade e aos efeitos viscosos :

$$\rho\, C_p \frac{DT}{Dt} = \mathrm{div}(K_c\ \mathrm{grad}\ T) - \mathrm{div}\ q_r + \beta\, T \frac{DP}{Dt} + \mu\, \Phi \qquad (2)$$

onde β é o coeficiente de expansão térmica do fluido.

Supondo pouco relevantes os efeitos de compressibilidade e os efeitos viscosos (número de Eckert bastante inferior à unidade) quando comparados com os demais termos da expressão da conservação da energia para um meio isotrópico, resulta da equação (2):

$$\rho\, C_p \frac{DT}{Dt} = K_c\, \nabla^2 T - \mathrm{div}\ q_r \qquad (3)$$

Para o escoamento bidimensional (x é a direção axial e y é a direção transversa) em regime permanente, vem que

$$\rho.C_p.\left(u\frac{\delta T}{\delta x} + v\frac{\delta T}{\delta y}\right) = K_c.\left(\frac{\delta^2 T}{\delta x^2} + \frac{\delta^2 T}{\delta y^2}\right) - \left(\frac{\delta q_{rx}}{\delta x} + \frac{\delta q_{ry}}{\delta y}\right) \qquad (4)$$

onde u e v são os componentes do vetor velocidade , e q_{rx} e q_{ry} são os componentes do vetor fluxo térmico radiante.

Considerando que é válido negligenciar a condução (número de Peclet elevado) e a radiação na direção axial, face à magnitude do fenômeno térmico na direção transversa :

$$u\frac{\delta T}{\delta x} + v\frac{\delta T}{\delta y} = \alpha.\frac{\delta^2 T}{\delta y^2} - \frac{1}{\rho.C_p}\frac{\delta q_{ry}}{\delta y} \qquad (5)$$

onde α é a difusividade térmica do fluido.

Concentrando o estudo no escoamento desenvolvido, ou seja, sabendo que o perfil de velocidade não varia na direção axial, em uma região onde os efeitos de entrada são desprezados, a equação (5) reduz-se a :

$$u\frac{\delta T}{\delta x} = \alpha.\frac{\delta^2 T}{\delta y^2} - \frac{1}{\rho.C_p}\frac{\delta q_{ry}}{\delta y} \qquad (6)$$

Ainda fazendo valer a consideração do escoamento desenvolvido, é possível aproximar o gradiente axial de temperatura pela seguinte expressão [7] :

$$\frac{\delta T}{\delta x} = \frac{T_w - T}{T_w - T_b}\left[\frac{2.q_w}{\rho.C_p.u_m.L}\right] \qquad (7)$$

onde T_w é a temperatura da parede do duto, T_b é a temperatura bulk do fluido, u_m é a velocidade média do fluido e L é a distância entre as paredes do duto na direção transversa.

Na equação (7) , q_w é o fluxo térmico na parede do duto, dado pela composição de suas parcelas condutiva e radiante :

$$q_w = -K_c \frac{\delta T}{\delta y}\Big|_{y=0} + q_{ry}\Big|_{y=0} \qquad (8)$$

Desenvolvendo esta expressão através da investigação detalhada do fluxo radiante na parede do duto e introduzindo o conceito de espessura ótica (τ), resulta que :

$$q_w = -K_c K \frac{\delta T}{\delta \tau}\Big|_{\tau=0} + 2\sigma T_w^4 (1 - E_3(\tau_o)) - 2\sigma \int_0^{\tau_o} T^4(t)\, E_2(t)\, dt \qquad (9)$$

onde σ é a constante de Stefan-Boltzmann, K é o coeficiente de absorção do meio, τ_o é a espessura ótica total e E_n são as funções exponenciais integrais de ordem n.

Uma vez que a configuração do duto consiste de duas placas planas, paralelas, infinitas, pretas e isotérmicas, e o meio é cinza e não defletor, o termo radiante da equação (6) é dado por [8] :

$$-\frac{dq_{ry}}{d\tau} = 2\sigma T_w^4 E_2(\tau) + 2\sigma T_w^4 E_2(\tau_o - \tau) + 2\sigma \int_0^{\tau_o} T^4(t)\, E_1(|\tau - t|)dt - 4\sigma T^4(\tau) \qquad (10)$$

Neste ponto, admite-se a validade da adoção de um perfil parabólico de velocidade para a descrição do escoamento de Poiseuille desenvolvido pelo fluido em questão. Com isto :

$$u = 6\, u_m \left(\frac{y}{L} - \frac{y^2}{L^2}\right) \qquad (11)$$

Reunindo as equações (7), (10) e (11), transforma-se a equação da energia (6) em :

$$2N\frac{d^2\theta}{d\tau^2} - \frac{6\psi}{\tau_o}\left(\frac{\tau}{\tau_o} - \frac{\tau^2}{\tau_o^2}\right)\left(\frac{1-\theta}{1-\theta_b}\right) = -E_2(\tau) - E_2(\tau_o - \tau) - \int_0^{\tau_o} \theta^4(t)\, E_1(|\tau - t|)dt + 2\theta^4(\tau) \qquad (12)$$

onde foram utilizados os adimensionais $N = \frac{K_c K}{4\sigma T_w^3}$, $\theta = \frac{T}{T_w}$, $\theta_b = \frac{T_b}{T_w}$ e $\psi = \frac{q_w}{\sigma T_w^4}$. O parâmetro ψ é resultante da modificação da equação (9), através do uso dos mesmos adimensionais apresentados anteriormente:

$$\psi = -4N \left.\frac{d\theta}{d\tau}\right|_{\tau=0} + 2\,(1-E_3(\tau_0)) - 2\int_0^{\tau_0} \theta^4(t)\,E_2(t)dt \qquad (13)$$

Para a composição final do modelo, resta ainda estabelecer as condições de contorno necessárias para a solução das equações (12) e (13) :

$$\tau = 0 \quad \Rightarrow \quad \theta = 1 \qquad (14)$$
$$\tau = \tau_0 \quad \Rightarrow \quad \theta = 1 \qquad (15)$$

A equação integro-diferencial assim obtida, derivada da modelagem do fenômeno térmico em questão, é não linear e de segunda ordem, caracterizando-se como um problema de complexa solução analítica.

Também com base na equação (13), define-se o número de Nusselt para o problema em questão :

$$Nu = \frac{2.\tau_0.\psi}{N.(1-\theta_b)} \qquad (16)$$

que é um adimensional de grande utilidade na avaliação comparativa para a determinação do mecanismo predominante no processo de transferência de calor. Nos exemplos onde o transporte de energia ocorre apenas por condução e convecção (valores extremamente elevados de N), a combinação das equações (13) e (16) mostra que o número de Nusselt reduz-se à sua forma convencional. Prosseguindo na análise destas duas equações, observa-se a possibilidade de reescrever o número de Nusselt da expressão (16) como a soma de um número de Nusselt devido à convecção (Nu_c) e outro devido à radiação (Nu_r).

FORMALISMO MATEMÁTICO

O grau de complexidade das expressões anteriores permite concluir que a solução da equação da energia, mesmo para situações físicas relativamente simples, é extremamente difícil. Na verdade, a equação integro-diferencial gerada na construção do modelo condutivo-convectivo-radiante não apresenta solução na forma fechada e, em consequência, é necessário recorrer a procedimentos numéricos.

A maior parte dos trabalhos encontrados na literatura especializada aponta para as técnicas iterativas de solução, principalmente quando não se tem em mente a linearização da variável dependente : a equação (12) pode ser prontamente convertida em uma equação integral não linear para posterior aplicação de uma adequada rotina computacional iterativa.

Alternativamente, como visto em [9], a referida equação pode ser resolvida com base na expansão da variável dependente em uma série de Taylor : a equação da energia assume a forma de uma equação diferencial não linear, fato que, apesar da aproximação introduzida pelo truncamento da série em questão, simplifica acentuadamente o tratamento matemático do problema. A abordagem que se segue envolve o método de Newton-Raphson e conduz à determinação do perfil de temperatura no meio, satisfeitas as condições de contorno (14) e (15), e a tolerância pré-estabelecida para a convergência.

No presente trabalho, optou-se pela utilização do método das colocações ortogonais após a linearização da variável dependente, seguindo a linha adotada por estes autores na resolução das equações oriundas do desenvolvimento do modelo condutivo-radiante [1].

A expressão final a ser avaliada pelo algoritmo numérico, após uma sequência de operações algébricas aqui omitidas pela sua extensão, apresenta a seguinte forma genérica :

$$\frac{d^2\theta}{du^2} + Co.fo(u).\theta(u) + C_1 \int_0^1 \theta(u').f_1(u,u').du' + C_2.f_2(u).(1-\theta(u)).\int_0^1 \theta(u').f_3(u').du' = C_3 + C_4.f_4(u) + C_5.f_5(u) + C_6 \int_0^1 f_1(u,u').du' \qquad (17)$$

onde C_i são constantes do modelo, f_i são funções resultantes do formalismo matemático adotado e u tem como origem uma conveniente mudança de variável ($\tau = \tau_0.u$).

O código computacional para a obtenção dos resultados do modelo condutivo-convectivo-radiante, estruturado em linguagem FORTRAN, contém, além das rotinas de entrada e saída de dados, outras rotinas integradas:

- cálculo dos zeros e derivadas dos polinômios de Jacobi ;
- interpolação através do polinômio de Lagrange ;
- determinação das derivadas dos pesos da interpolação de Lagrange e dos pesos da quadratura gaussiana ;
- solução de sistemas lineares (eliminação gaussiana com pivotamento parcial) ;
- cálculo dos pesos da quadratura de Radau e Lobatto (previsão da inclusão dos extremos) .

ANÁLISE DE RESULTADOS

A solução do modelo condutivo-convectivo-radiante, através da metodologia proposta neste trabalho, mostrou-se compatível com os resultados presentes na literatura [9]. As figuras 1 e 2 apresentam o confronto entre os perfis de temperatura obtidos pela referência em questão e pelo método das colocações ortogonais, destacando a semelhança entre as curvas para diferentes valores do parâmetro condutivo-radiante N. As aproximações consideradas no desenvolvimento do modelo tornam-se mais evidentes para os casos em que o valor de N está próximo de zero (condução nula), uma vez que não há previsão de um salto de temperatura na parede do duto : o gradiente de temperatura nesta posição, apesar de impreciso, não compromete a determinação da distribuição de temperatura para toda a faixa de espessura ótica.

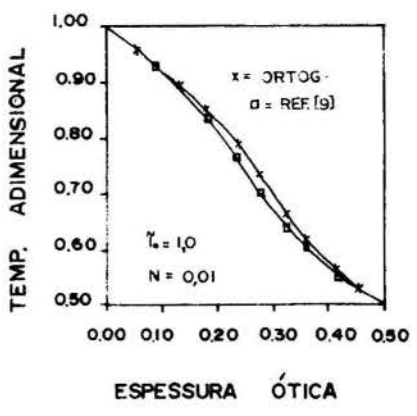

FIG. 1 - COMPARAÇÃO DE RESULTADOS

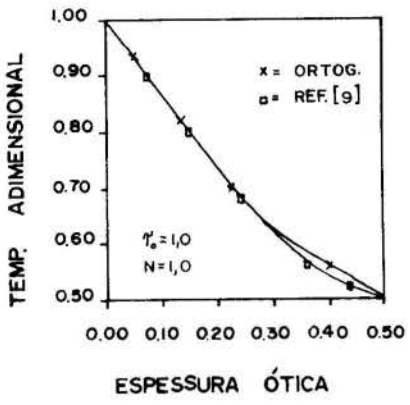

FIG·2 - COMPARAÇÃO DE RESULTADOS

A figura 3 mostra uma família de curvas que possibilita o estudo do mecanismo combinado condutivo-convectivo-radiante, a exemplo do que já foi feito em [1] para o modelo condutivo-radiante. A análise abrange um amplo espectro de valores de N, considerando desde o caso do limite convectivo-radiante (onde N = 0) até o extremo condutivo-convectivo (quando N tende para valores extremamente elevados). É interessante ressaltar que o predomínio do mecanismo condutivo manifesta-se mesmo para moderados valores de N (já a partir de N = 1), o que pode ser observado na figura 3 pela tendência de superposição com a curva do extremo condutivo-convectivo. Esta característica apenas deixa de ser registrada com a diminuição do parâmetro condutivo-radiante e a aproximação do caso puramente radiante (na figura em questão, N = 0).

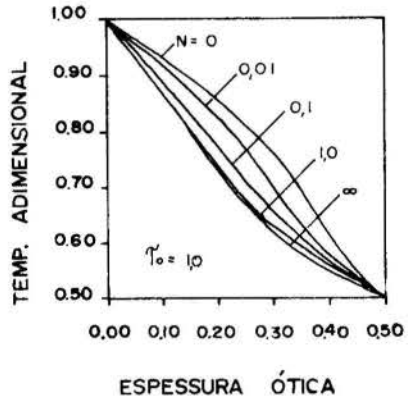

FIG. 3 - EFEITO DO PARAMETRO N

(COLOC. ORTOGONAL)

CONCLUSÕES

A validade do formalismo matemático empregado neste trabalho foi verificada através da comparação dos resultados encontrados pela rotina computacional, desenvolvida para o modelo condutivo-convectivo-radiante, com as informações extraídas da literatura. Este aspecto, aliado ao êxito já obtido na análise do modelo condutivo-radiante [1], permite concluir pela perfeita adequação do método das colocações ortogonais nos problemas de transferência de calor em meios absorvedores e emissores.

De imediato, é possível admitir que os cálculos do perfil de temperatura e do fluxo térmico total podem ser utilizados no dimensionamento de equipamentos térmicos industriais, desde que sejam avaliadas as hipóteses simplificadoras do modelo para uma dada aplicação. Além disso, já consolidada a estrutura do código computacional, torna-se viável a elaboração de um estudo de sensibilidade dos diversos parâmetros relevantes na investigação do fenômeno físico em foco (propriedades físicas e espectrais do gás, velocidade do meio, temperatura da parede do duto, etc.).

REFERÊNCIAS

[1] Teixeira, C.O.M.M., Oliveira, S.L. e Hackenberg, C.M., "Transferência de Calor em Meios Absorvedores e Emissores entre Superfícies Paralelas", Anais do X Congresso Brasileiro de Engenharia Mecânica, Rio de Janeiro, Brasil, 1989.

[2] Teixeira, C.O.M.M. e Hackenberg, C.M., "Análise Paramétrica em Câmaras de Combustão com Geometria Plana", Anais do Seminário PETROBRÁS de Recuperação e Transferência de Calor, Rio de Janeiro, Brasil, 1990.

[3] Viskanta, R. e Grosh, R.J., "Heat Transfer by Simultaneous Conduction and Radiation in an Absorbing Medium", Journal of Heat Transfer, vol.84, pp. 63-72, 1962.

[4] Yuen, W.W. e Takara, E.E., "Analysis of Combined Conductive-Radiative Heat Transfer in a Two-Dimensional Rectangular Enclosure with a Gray Medium", Journal of Heat Transfer, vol.110, pp. 468-474, 1988.

[5] Kim, T.K. e Smith, T.F., "Radiative and Conductive Transfer for a Real Gas in a Cylindrical Enclosure with Gray Walls", Int. Journal Heat Mass Transfer, vol.28 (12), pp. 2269-2277, 1985.

[6] Rohsenow, W.M. e Choi, H., "Heat, Mass and Momentum Transfer", Prentice-Hall, New Jersey, 1961.

[7] Seban, R.A. e Shimazaki, T.T., "Heat Transfer to a Fluid Flowing Turbulently in a Smooth Pipe with Walls at Constant Temperature", Trans. ASME, vol.73, pp. 803-809, 1951.

[8] Sparrow, E.M. e Cess, R.D., "Radiation Heat Transfer", Brooks/Cole Publishing Co., California, 1970.

[9] Viskanta, R., "Interaction of Heat Transfer by Conduction, Convection, and Radiation in a Radiating Fluid", Journal of Heat Transfer, vol.85, pp. 318-328, 1963.

ABSTRACT

This work presents the analysis of a conductive-convective-radiant model in order to explain the thermal behavior of an absorbing and emitting media, in a fully developed laminar flow, limited by isothermal parallel surfaces a finite distance apart. The resulting integro-differential equation is solved numerically by the orthogonal collocation method, allowing for the determination of the relative importance between the heat transfer mechanisms.

III ENCIT – Itapema, SC (Dezembro 1990)

COMPARISON OF FREE CONVECTIVE HEAT TRANSFER FROM A HEATED VERTICAL PLATE IN DIFFERENT MEDIA

HARRIS IMADOJEMU
PENNSYLVANIA STATE UNIVERSITY AT HARRISBURG
RICHARD JOHNSON
NORTH CAROLINA STATE UNIVERSITY

SUMMARY

Heat transfer of a plate embedded in water or in a water-saturated porous medium are described. Experiments included flow visualization of the boundary layer flow. Free convection heat transfer in a pure fluid, as expressed by the power law relationship between the Nusselt number and Rayleigh number, $Nu=0.89Ra^{0.2}$ is adequate for $10^4 < Ra < 10^{13}$. The expression, $Nu=ARa^n$ is not as effective for free convection in the porous medium as it is for a pure fluid. A, and n varies from one heat flux to another. Close to the leading edge of the plate the effects of wall channelling are important.

INTRODUCTION

Lorenz [1] was the first to carry out an experimental investigation on natural convection from a vertical plate in liquid. In 1934, he measured the mean heat loss from a 12cm high plate in oil. A good review through 1964 is given by A.J. Ede [2], and by Imadojemu [3]. Considerable research has been done on the study of convention between a vertical impermeable flat surface and a surrounding viscous fluid, or saturated porous medium. The studies are often theoretical, however, a few of the studies, involve experimental work, but no studies are reported for a comparison for the different media in the literature.

From an extensive review of literature it is seen that much of the previous attention has been devoted to the analytical and theoretical studies of convection, with relatively little emphasis on experimentation. This situation is most pronounced for convection in a porous medium. The sparsity of experimental studies is most probably due to the difficulties in measuring and obtaining the right flow, temperature and visualization of the flow in the presence of the porous matrix.

Ping Cheng [4,5], and M.A. Combarnous and S.A. Bories [6] give good reviews of analysis efforts in the area of free convection in porous media. H. Darcy [7] was the first to report any experimental work on porous media and he summarized his findings in a mathematical equation called the Darcy's law. Since then many theoretical studies have assumed that in Darcy's law, that the area-averaged fluid velocity through a column of porous medium is directly proportional to the pressure gradient established along the columns, applies. Subsequent experiments, however, show that the area-averaged velocity is also inversely proportional to the viscosity (μ) of the saturating fluid. Darcy's law may be written as:

$$U=\frac{-K}{\mu}\frac{dP}{dX} \qquad (1)$$

for one-dimensional forced flow. K is the permeability and P is pressure.

G.H. Evans and O.A. Plumb[8] carried out an experimental study to verify the similarity solutions of P. Cheng and W.J. Minkowycz [9] for a vertical heated porous layer adjacent to a vertical, heated, isothermal plate. They placed a heated flat aluminum plate vertically at one end of a box. The box was filled with glass beads. Ping Cheng and Minkowycz [9] report a Nusselt number (Nu) given by

$$Nu=0.772\ Ra^{0.3333} \qquad (2)$$

Where Ra is the modified Rayleigh number based on constant heat flux

$$Ra=\frac{K\,g\beta\,Y^2\,Q''}{k\alpha\,\nu} \qquad (3)$$

K is permeability, g is gravitational acceleration, β is co-efficient of thermal expansion Q" is Mean heat transfer per unit area W/m^2, k is effective thermal conductivity, α is thermal diffusivity and ν is kinematic viscosity.

Their experimental results fell slightly below the similarity solution for Rayleigh numbers less than 300 and this was due to the conduction error in the temperature measurement by the traversing probe. For the higher Rayleigh numbers the data fell above the values predicted by the similarity solution. Most importantly, they found that for particle Rayleigh numbers on the order of unity (Darcy flow regime), and a modified Rayleigh number of about 400, measured temperatures within the boundary layer were periodic. The periodicity indicates the appearance of a secondary flow, for which the similarity solution is not adequate.

No experimental investigation has been done for a semi-infinite vertical plate imbedded in a water saturated natural porous medium with a constant heat flux at the boundary, with the Darcy number greater than unity.

In order to better understand the heat transfer phenomenon we experimentally investigated the free, and mixed convection about a heated vertical plate with a constant heat flux, in water and in water saturated porous media. In this paper a comparison of the free convection for the three different conditions will be reported. The plate was submersed and tested in a homogeneous pure fluid (water), and then in water saturated porous media such as glass beads and gravel. The temperature profile was measured with thermocouples and the velocity profile by the electro-chemical formation of dye technique.

EXPERIMENTAL PROCEDURE

Apparatus. The apparatus employed in this investigation is depicted schematically in Fig. 1. The apparatus consists of a heated vertical plate imbedded in a porous material. The plate and material form a

test cell and are contained in a rectangular glass tank 91.4cm x 30.5cm x 58.4cm. The test tank is placed within a bigger 121.9cm x 45.7cm x 61.0cm glass tank to form a water jacket. The 25.4cm x 30.5cm x 58.4cm (length, breadth and height) test cell is partitioned from the filter material with a stainless steel screen. The screen allows free movement of water through the test cell, while keeping the beads in place.

The vertical plate is constructed out of two brass plates each 50.8cm x 25.4cm and 0.32 cm thick. Three strip heaters placed in series are sandwiched between the two plates and bonded together with a silicone paste. The heaters cover the entire surface of the plate and supply a constant heat flux per unit area to the plates. The leading edge of the plate is located about 5cm from the floor of the box. Holes housing the thermocouple beads are located at 0.0254m intervals on the vertical centerline and in the horizontal line mid-height of the inside of each brass plate. The thermocouple leads lay in narrow horizontal and vertical slots on each side of plate, which are filled with epoxy. The thermocouple locations are shown in Fig. 2. The thermocouples are used to determine the spatial variation of the wall temperature.

Fluid temperatures close to the plate surface are measured with thermocouple probes. The probes are supported by a narrow strip of brass 7.6cm from the plate. The first thermocouple is placed at 0.224cm away from the plate surface and the other two are equally spaced at 0.64cm intervals. This form 3 x 3 array of thermocouples as shown in Fig. 3. All thermocouples are copper-constantan T-type thermocouples.

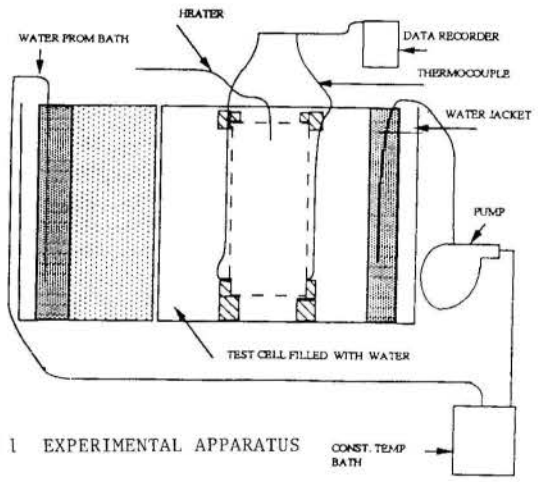

FIGURE 1 EXPERIMENTAL APPARATUS

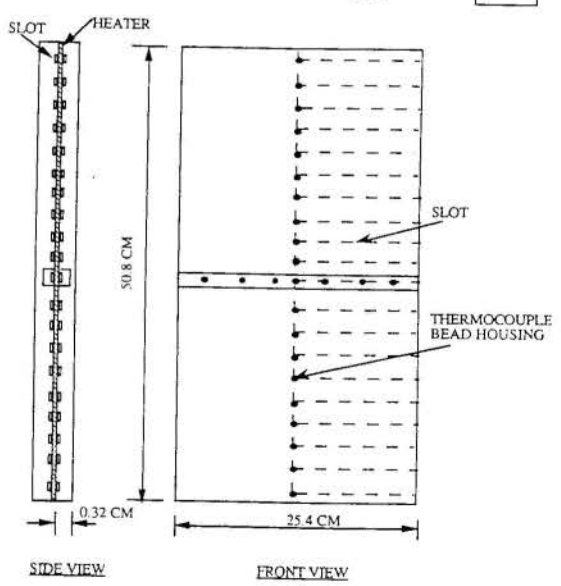

FIGURE 2 HEATED TEST PLATE SHOWING SANDWICHED CONSTRUCTION AND THERMOCOUPLE LOCATION

The thermocouple leads are connected to a 100 channel ACUREX autodata digital strip TEN/5 data recorder.

The first step in the main experiment is ensuring that the temperature of the saturating fluid in the tank is uniform, by thoroughly mixing or agitating the fluid. The bulk temperature is read from the thermocouples placed near the end of the tank. The sensing beads of the thermocouple is dipped in a silicone paste to prevent reaction with the matrix and the fluid, and the leads in the water are protected to prevent electrical leakage by hard varnish coating.

The water is deaerated by allowing it to sit for some time and thoroughly stirring it. This will get rid of the air bubbles that might form in the tank or especially in the porous matrix. Keeping the surface covered except during the experimental run can keep the water sufficiently deaerated for several days.

Some time is needed for the apparatus to reach steady state whenever the power is turned on or changed, this will be determined by monitoring the plate temperatures and determining the heat flux of the plate by measuring the heating strip resistance and current or voltage from the voltmeter. Calibration of the thermocouples provided accuracy to within $\pm$ 0.04°C. It took approximately 3 hours to reach steady state the temperature varied only to within $\pm$ 0.1°C.

To keep the bulk fluid temperature constant, it was necessary to circulate water from a constant temperature bath through the outer glass tank which served as a water jacket. By this arrangement we were also able to reduce thermal stratification. Temperatures were measured at 60 sec intervals. The fluid properties β, k, ν, ρ, and cp were evaluated at the average temperatures between the bulk fluid temperature and the heated wall temperature at any given vertical location.

The flow is made visible by local changes of color of the fluid itself. The color changes result from changes in pH (acidic to base). Arrangements were made for these color changes to occur both at the surface of the vertical plate and within the boundary layer. This enhanced the visualization of the three dimensional character of the flow. The flow visualization technique was originally described by Baker [10]. Thymol blue, a pH indicator, was added to the water in an amount 0.01% by weight, or about 0.1 gms/liter, and the solution was then titrated to end point (pH=8) with sodium chloride (NaC). Addition of hydrochloric acid (HCl) made the solution acidic and yellow-orange (tea color) in color. A small dc voltage (10-20V) from a dry cell source impressed between two wire electrodes inserted within this tea colored fluid produces a proton transfer reaction at the negative electrode. This results in a change in pH balance of the fluid (acidic to base) at the surface of the negative electrode with a corresponding change in color from the tea color to deep blue.

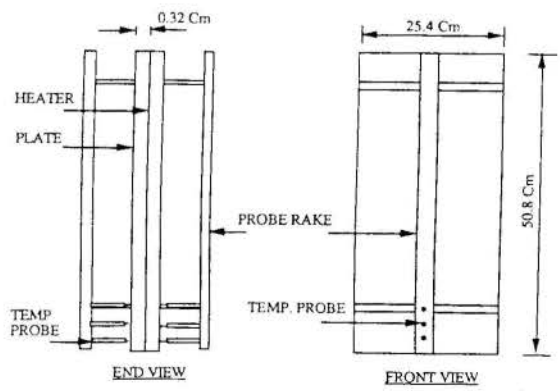

FIGURE 3 THERMOCOUPLE PROBE AND PLATE

The gravel is characterized by having a small, irregular particle size and shape with a porosity of 0.48 and a permeability of 4.8×10^{-8} m^2. The beads are characterized by having spherical particles of size 14.6mm with a porosity of 0.43 and a permeability of 4.5×10^{-7} m^2. The porosity may imply an uncertainty of about 4.0%. The effective stagnant thermal conductivity for the gravel/water medium was determined to be 2.37 W/m-K and for the glass/water medium the experimental conductivity is 3.9 W/m-K. The effective thermal conductivity of the porous material is a complex function of the materials packing geometry, and particle shape, and there was no resolution between the experimental and predicted value. An uncertainty in the experimental data mainly from the conductivity measurements were estimated at about 10% which was quite reasonable.

The details of the experimental set-up and procedure, flow visualization as well as the determination of the physical properties are reported in Imadojemu [3].

RESULTS AND DISCUSSION

Parameter non-dimensionalization. As is normal in free convection studies, results are presented in unified non-dimensionalized parameters. For free convection in water, the dimensionless parameters are:

1. LENGTH $$L^* = \frac{Y}{L} \tag{4}$$

2. TEMPERATURE $$\theta = \frac{(T_w(Y) - T_\infty)}{(T_w(Y) - T_\infty)_{max}} \tag{5}$$

3. HEAT TRANSFER $$Nu(Y) = \frac{h\,Y}{k} = \frac{Q''\,Y}{k\,(T_w(Y) - T_\infty)} \tag{6}$$

$$Ra = \frac{g\,\beta\,Y^4\,Q''}{(\alpha \nu\, k)} \tag{7}$$

The non-dimensional parameters that are used to characterize free convection in a porous medium are:

1. LENGTH $$L^* = \frac{Y}{L} \tag{8}$$

$$\zeta = \frac{Y}{K^{1/2}} \tag{9}$$

2. TEMPERATURE $$\theta = \frac{(T_w(Y) - T_\infty)}{(T_w(Y) - T_\infty)_{max}} \tag{10}$$

3. HEAT TRANSFER $$Nu_Y = \frac{h\,Y}{k} = \frac{Q''\,Y}{k\,(T_w(Y) - T)} \tag{11}$$

$$Ra = \frac{K\,g\,\beta\,Y^2\,Q''}{\alpha \nu\, k} \tag{12}$$

$$Ra_T = \frac{\rho\,g\,Y\,K\,\beta\,\Delta T}{\alpha \mu} \tag{13}$$

where $$\alpha = \frac{k_{eff}}{\rho c_p} \tag{14}$$

$$Re_p = \frac{K\,g\,\beta\,\Delta T}{\nu} \tag{15}$$

$$Gr_p = \frac{K\,g\,\beta\,\lambda\,\Delta T}{\nu^2} \tag{16}$$

Gr is Grashof number, h is convective heat transfer coefficient, Ra is Rayleigh number, Ra_T is Rayleigh number based on constant wall temperature, Ra_Y* is New or modified Rayleigh number, Re is Reynold's number, Re_p is porous Reynold's number, δ is Boundary layer thickness, λ is Forchheimer's constant, ζ is Dimensionless Length, θ is Dimensionless temperature, ρ is Density and Gr_p is the porous Grashof numbers respectively. Re_p, Gr_p are an indication of the deviation from Darcian flow.

In Fig. 4 we can see that for the same heat flux the gravel has the greatest temperature difference at the wall while water has the smallest. This is due to a combination of the particle shape, porosity, and thermal conductivity. For the porous material there is more restriction to flow and the heat exchange between the heated plate and porous particles is slower than the water alone. The symbols used in Fig. 4 are explained in Table 1 and Table 2 gives the correlations for the temperature variation.

TABLE 1. HEAT RATES

	RUN	HEAT FLUX (W/m^2)	
WATER	1	558.00	Lower Q"
	3	1116.00	Higher Q"
BEADS	1	527.00	Lower Q"
	3	1178.50	Higher Q"
GRAVEL	1	558.00	Lower Q"
	3	1178.50	Higher Q"

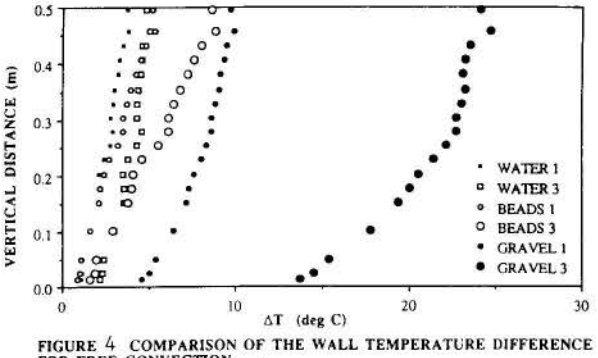

FIGURE 4 COMPARISON OF THE WALL TEMPERATURE DIFFERENCE FOR FREE CONVECTION.

TABLE 2 $= A\,Y^n$

	WATER		BEADS		GRAVEL	
RUN	A	n	A	n	A	n
1	4.386	0.377	6.543	0.315	11.15	0.235
3	5.669	0.252	10.939	0.264	27.32	0.182

There is a difference in value but no difference in the character of the temperature response between each medium at the lower heat flux at mid height in the horizontal coordinate of the plate as shown in Fig. 5. As the heat flux in increased, we notice the sinusoidal nature of a temperature wave. The wave has the most definable peaks and valleys for the experiments with beads. Although the temperatures at the wall for the gravel medium are higher the sine wave is less well defined. The sine wave is a function of the impressed heat flux and the porous material. We can further see the higher temperature response of the gravel medium and Reynold's number establish the fact that the constants A and n in the equation $Nu = A\,Ra^n$ differ for each heat flux and material. See Table 3 for the different values of the constants.

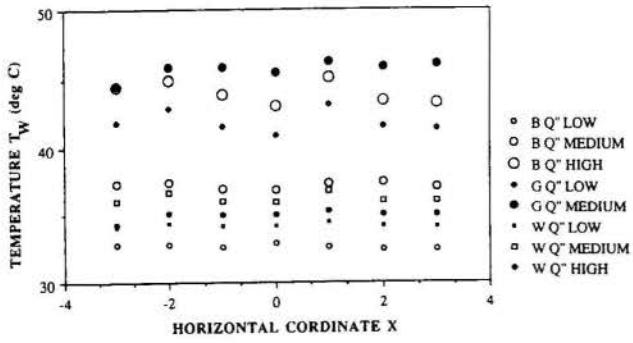

FIG 5 COMPARISON OF TEMPERATURE VARIATION WITH X COORDINATE AT PLATE MID HEIGHT FOR FREE CONVECTION.

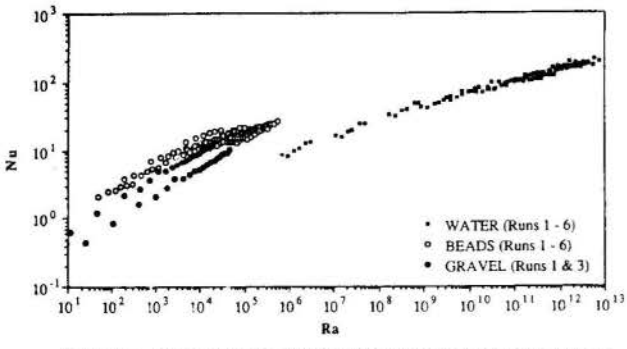

FIGURE 6 COMPARISON OF THE NUSSELT NUMBER VS RAYLEIGH NUMBER FOR ALL HEAT FLUXES FOR FREE CONVECTION.

Fig. 6 compares the result for all the water and beads experiments for each of the six different heat fluxes. The data for the porous material experiments are clustered at the lower Rayleigh number because of their lower heat transfer characteristics. See Table 3 for a comparison of the different values for the gravel and beads. For the water experiments we found a fairly good fit of

$$Nu = 0.89\ Ra^{0.2}$$

TABLE 3 $Nu = A\ Ra^n$

MEDIUM	Q"	$(Nu = Ra^n)$		$(Nu = A\ Ra_T^n)$	
	W/m^2	A	n	A	n
BEADS	527	1.28	0.228	1.38	0.29
	1178.5	1.36	0.222	1.47	0.28
GRAVEL	558	0.136	0.400	0.13	0.62
	1178.5	0.270	0.400	0.04	0.67

In Fig. 7 we compare the heat transfer parameter $Nu/\sqrt{Ra_T}$ for the two porous media tests, beads and gravel. At the leading edge the slope of the curve for the beads matrix is seen to be steeper than that for the gravel matrix. This is due to the fact that for the beads, the wall channelling effect is more felt, because of the bead size, and because porosity at the wall is almost unity. Especially at the leading edge, where the boundary layer is thinner than a typical void, the wall channelling effects the flow directly than it would in a homogeneous porous medium. The resistance to flow is less for the beads than the gravel and this means the fluid in the bead matrix will have a higher velocity. This leads to the fluid particles picking up more energy along the plate. Therefore the wall heat transfer for the beads is more enhanced when compared to the gravel. The wall effect is smaller for smaller permeability.

In Fig. 7 we can see the flow regimes: non-Darcian flow, the transition to Forchheimer's flow. The critical numbers of each flow regime is material and heat flux dependent.

Fig. 8 shows the variation of the heat transfer coefficients with the plate vertical distance. The gravel medium has the lowest coefficients while the water has the highest values. Again notice the overlapping and similar profile of the water and bead medium at the leading edge of the plate.

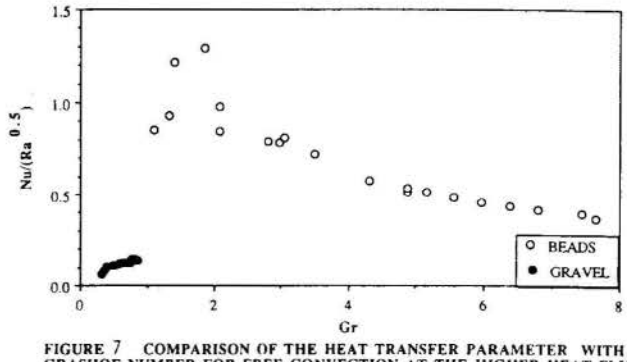

FIGURE 7 COMPARISON OF THE HEAT TRANSFER PARAMETER WITH GRASHOF NUMBER FOR FREE CONVECTION AT THE HIGHER HEAT FLUX.

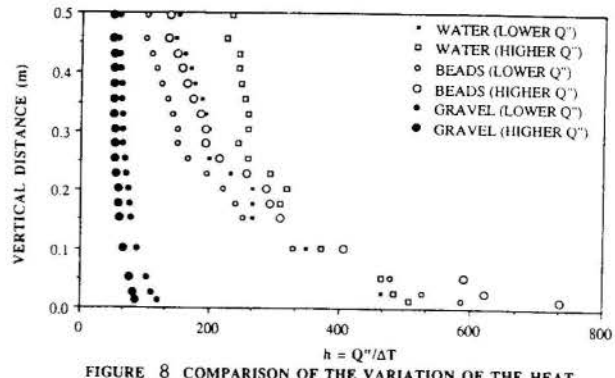

FIGURE 8 COMPARISON OF THE VARIATION OF THE HEAT TRANSFER CO-EFFICIENT FOR FREE CONVECTION.

Flow Visualization. Figure 9 shows the heat transfer mechanisms for the plate in pure water. The marker or tracer fluid (dark blue in color) which blankets the lower portion of the plate surface, is moving slowly parallel to, and up the surface of the plate. Up to a certain height on the plate, the flow is stable and fully laminar. At 0.338m, from the leading edge a faint two dimensional tracer fluid accumulation begins to appear. This is as a result of small disturbances entering the laminar flow regime from the surrounding fluid outside the boundary level. These are sent as the darker tracer fluid, immediately after the uneventful blanket of the tracer fluid on the plate.

The disturbances mark the end of the stable and fully laminar flow regime and the start of a very long and complex regime called transition regime. Notice that the tracer fluid is about sinusoidal in form, across the width of the plate at about 0.335m. These waves are formed in a random manner, with no discrete amplitude peaks, nor discrete wavelength. These are referred to as the Tollmien-Schlicting waves (T - S waves) in laminar forced boundary layer flows over a flat plate (Blasius flow). The T - S waves travel in the mean flow direction. We measured the wavelength which is the horizontal distance between peaks, approximately as 0.0254m. Because of the natural way the waves are formed, a portion of a wave moving downstream could be partially or completely engulfed by a second wave started at a slighly higher vertical location. In addition, there is also a spanwise motion very close to the plate's surface that help sweep the tracer fluid outwards.

Further up the plate there are tracer streaks from two or more adjacent wave fronts which is a result of a secondary twisting of the tracer fluid near the surface of the plate, giving rise to the formation of secondary mean flows or secondary instability. The waves appear as successive wave fronts, with an array of ordered spike-like peaks and valleys in the streamwise direction. These 'peak-valley' like waves are produced intermittently in the boundary layer. Up to this regime the flow is still considered laminar but not stable. Beyond this point, the transition process begins. Transition is fundamentally a non-linear process, and it is a result of the uncontrolled growth of the unstable 3-dimensional waves. The growth is a result of non-linear interactions of the 3-dimensional waves with the basic 2-dimensional instabilities. This 3-dimensional instability, which is the growth of the secondary instability, is attributed to a spanwise variation and differential amplification of the T-S waves through corrugations of the boundary layer, that eventually lead to a spanwise alternating of the peaks and valleys. This means an alternating enhancement and reduction of the wave amplitude.

The orginial mean momentum and thermal energy of the 3-dimensional disturbance lies with the free stream. This energy is redistributed both in the spanwise and normal directions including alternate spanwise concentration of the high shear layer. A shear layer within this unstable region has the capability to amplify slight 3-dimensional disturbances present in any natural convection spectrum [3]. The onset of these peaks-valleys can be clearly observed between locations 0.216m, and 0.229m. At this location the wave pattern is somewhat broken due to energy amplification. This results in a weak 3-dimensional displacement of the tracer fluid particles and the formation of stream wise vortices.

Vortices are formed with the rolling up of the tracer fluid. Sometimes this occurs just following the formation of the initial T - S waves. The roll-up process produces highly concentrated (very dark) spots for single streaks, or thick lines for several streaks. When formed, the vortices are mainly 2-dimensional, but soon after, they exhibit 3-dimensional characteristics. During this development the vortices begin to form a vortex loop as can be seen in the top portion of the plate. This precedes the formation of a turbulent burst.

FIGURE 9 SPANWISE VORTICITY AND 3-D VORTEX BREAKDOWN

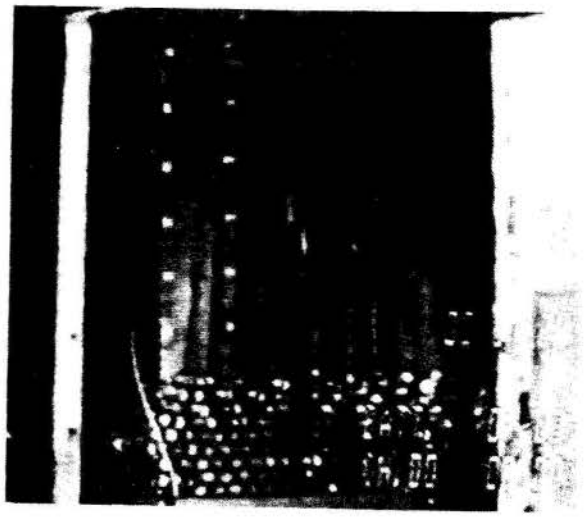

FIGURE 10 BEADS IN TEST CELL UP TO 0.127 m OF THE PLATE

The last process, is the formation of the turbulence burst, or Emmons spot. Emmons spots are sporadic turbulent spots and they are the final breakdown, rather than a growth to turbulence. In our experiments the plate was not high enough for the given heat fluxes to observe the complete transition to turbulence. The later part of this regime is the first real sign of turbulence commencement. The change to turbulence is not a sudden spatial phenomenon, but rather a sequence of complex mechanisms that are beyond the scope of this investigation. We observed the vortices being stretched and then beginning to disintegrate, into a highly random motion. In this regime intense local fluctuations occur at random times and location in the shear layer. Turbulent bursts emerge and grow downstream into turbulent spots.

Fig. 10 is the corresponding mechanism for a vertical plate embedded in water saturated bead porous medium and it shows the flow with the beads in the test cell up to a height of 0.127m. We observed that at the leading edge of the plate, the tracer fluid begins to form and move up the plate just like would without a porous medium. This can also be seen in the temperature measurement in Fig. 9. The temperature profile near the leading edge for the pure water is similar to that for the beads in water. Soon after the leading edge the tracer fluid begins to disperse laterally all across the plate's lower region and begins a slow movement outward into the bead matrix The fluid forms longitudinal streaks that move with fast speed towards the top of the bead level. The flatness of the plate straightens out the streaks. Once the boundary layer has grown to the order of one bead size, then the outward motion of the tracer fluid into the porous matrix is slowed. The fast moving long streaks move up the plate and soon form vortices, and further downstream start to behave as turbulent flows. The porous matrix acts like a trip and results in a quick formation of turbulence. Near the leading edge of the plate we can see how the dispersion of the fluid takes place, and the tortuous path the fluid particles take in the porous matrix.

CONCLUSION

From experiments with porous media it is conclude that the power law used to describe the variation of th Nusselt number with Rayleigh number for free convection $Nu = A\ Ra^n$ is not as effective as was found for heat transfer in a pure fluid. There are two features present in the data that need to be considered. The first is a variation of coefficients A and n for the heat flux. The second involves the apparent difference in coefficient n for Rayleigh numbers below 10^4 and for

Rayleigh numbers above 5 x 10^5.

From Table 3 the value of n can be approximated as a constant for the gravel, whereas both A and n vary with heat flux for the beads. This variation has its origin in the plots of Nusselt number against Rayleigh number. The experimental data clearly indicates two regions of behavior. One region for $Ra < 10^4$ and another for $Ra > 10^4$. The region for $Ra < 10^4$ includes a portion of the plate from the leading edge to a location a distance up the plate. From the data we conclude that heat transfer in this region behaves like free convection heat transfer for a pure fluid. Beyond this location Ra is greater than 5 x 10^4 and the heat transfer appears to be different, and more like that seen in the experiments with the gravel.

Close to the leading edge of the plate the effects of wall channelling appear to be important. Wall channelling effects are due to the non-homogeneous nature of the packing of the porous matrix and porosity in the neighborhood of a fixed boundary. For spherical particles the porosity is almost unity at the wall but approaches the bulk porosity at a distance of a particle size from the wall. Therefore near the leading edge a thin boundary can form that is similar to that in a pure fluid (porosity = 1). This boundary layer development may be evident for the vertical distance up the plate corresponding to the distance it takes the boundary layer to grow to a thickness of one particle size. At this location the ratio of thermal and momentum boundary layer thicknesses are close to one. This also appears to correspond to the location where Ra is approximately equal to 10^4 for the beads. Calculation of the boundary layer thickness is complicated by hydrodynamic dispersion due to flow around individual particles. Hydrodynamic dispersion produces a further thickening of the momentum boundary layer over and above the molecular diffusion. It also produces higher heat transfer rates because of the carrying of heat out into the flow. The significance of the region for $Ra < 10^4$ for the beads and not for the gravel is therefore attributed to the bead size (boundary layer thickness) and the particle shape (spherical beads have porosity of one at the wall, whereas the irregular shaped gravel has a porosity of less than one at the wall).

REFERENCES

[1] Lorenz, Ann. Phy. Lpz., 13 582 (1881), (REF 21).

[2] Ede, A.J., "Advances in Free Convection", in: ADVANCES IN HEAT TRANSFER; Vol. 14 (ed.) T.F. Irvine Jr. and J.P. Harnett, Academic Press, New York, NY, 1967. 1-64.

[3] Imadojemu, H.E., "Convective Heat Transfer from a Heated Vertical Plate Surrounded by a Saturated Porous Medium," Ph.D. Thesis, North Carolina State University, Raleigh, N.C. 1989.

[4] Cheng, P.,"'Natural Convection in Porous Medium': Fundamentals and Application" Ed.S. Kakac, W. Aung, R. Viskanta, Hemisphere 431-441 1986.

[5] Cheng, P., "Heat Transfer in Geothermal System", ADVANCES IN HEAT TRANSFER; Vol. 14 (ed.) T.F. Irvine Jr. and J.P. Harnett, Academic Press, New York, NY, 1979.

[6] Combarnous, M.A. and Bories, S.A., in "Hydrothermal Convection in Saturated Porous Media", ADVANCES IN HYDROSCIENCE; Vo. 10 Edited by Ven Te Chow.. 231-307 (1975).

[7] Darcy, H., 'Les Fontaines Puliques De La Ville De Dijon', Victor Damont, Paris (1856).

[8] Evans, G.H. and Plumb, O.A., "Natural Convection From A Vertical Isothermal Surface Imbedded In A Saturated Porous Medium," ASME CONFERENCE Paper # 78-HT-55 (1978).

[9] Cheng, P. and Minkowycz, W.J., "Free Convection About A Vertical Flat Plate Embedded In A Porous Medium With Application To A Dike", J. of Geophysics Research, 82, 2040-2044 (1975).

[10] Baker, D.J., "A Technique For the Precise Measurement of Small Velocities", J. of Fluid Mech., vol. 26 573-575 (1966).

III ENCIT – Itapema, SC (Dezembro 1990)

ASYMPTOTIC ANALYSIS OF THE DEVELOPING LAMINAR MIXED CONVECTION BETWEEN TWO VERTICAL FLAT PLATES

A.J. DA SILVA and K.GERSTEN
Institut für Thermo– und Fluiddynamik
Ruhr–Universität Bochum – IB 6
4630 Bochum – West Germany

SUMMARY

An asymptotic investigation of the developing laminar mixed convection momentum and heat transfer in vertical channels with symmetric heating is presented. The behavior of the ratio Nu/Nu_{forc} was investigated for two different values of the buoyancy parameter $M=Gr/Re$. Results obtained by an asymptotic solution are compared with a numerical solution, that reaches the fully developed flow.

Introduction

The laminar mixed convection has been investigated by several authors. The practical applications of this flow reach from the loss of cooling accident(LOCA) of nuclear reactors to electronic cooling. Generally speaking, laminar mixed convection occurs when the mass flow rate is sufficiently low to make buoyancy effects important. In the heat transfer literature , one finds analytical, numerical and experimental works, with different geometries and flow conditions(see Ref.(1 to 16)).

The object of the present study is to provide additional insight into the asymptotic characteristics of the developing laminar mixed convection between two vertical flat plates with uniform heat fluxes at the walls and a parabolic velocity profile at the beginning of the heated section. A schematic description is presented in Figure 1. The pure forced convection for this initial flow configuration has been already analyzed from an asymptotic point of view by Worsøe–Schmidt(17) as a special case of an annular flow. Here, we extend his asymptotic analysis to account for the buoyancy effects on the momentum and heat transfer.

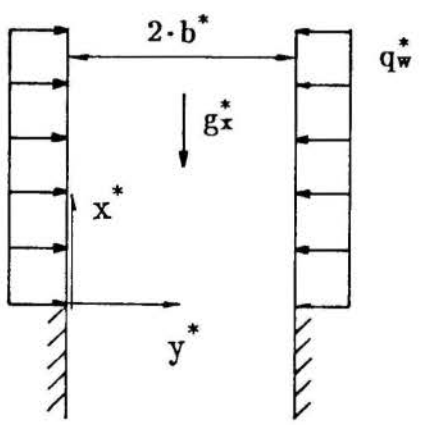

Fig. 1 – Schematic of the physical situation

Analysis

For simplicity we assume

(a) Incompressible, steady, two–dimensional laminar flow

(b) No pressure gradients perpendicular to flow direction

(c) The initial velocity profile is parabolic.

(d)constant fluid properties, except for the density change with temperature in the body force term.

We also assume, that the fluid satisfies the approximation

$$\rho^* = \rho_0^* \cdot \left[1 - \beta^* \cdot (T^* - T_0^*)\right] \qquad (1)$$

where * characterizes dimensional variables and parameters. The initially chosen dimensionless variables and parameters are

$$X \doteq \frac{x^*}{2 \cdot b \cdot Pe} \quad ; \quad y \doteq \frac{y^*}{2 \cdot b}$$

$$u \doteq \frac{u^*}{u_m^*} \quad ; \quad V \doteq \frac{v^*}{u_m^*} \cdot Pe \quad ; \quad \theta \doteq \frac{(T^* - T_0^*) \cdot \lambda^*}{2 \cdot q_w^* \cdot b^*}$$

$$p \doteq \frac{(p^* - p_0^*)}{\rho_0^* \cdot u_m^{*2}} \quad ; \quad Pe \doteq Re \cdot Pr \quad ; \quad Re \doteq \frac{2 \cdot b^* \cdot u_m^*}{\nu^*}$$

$$Pr \doteq \frac{\eta^* \cdot c_p^*}{\lambda^*} \quad ; \quad Gr \doteq \frac{g_x^* \beta^* q_w^* \cdot (2b^*)^4}{\nu^{*2} \cdot \lambda^*}$$

$$u_m^* \doteq \frac{1}{2b} \int_0^{2b} u^*(\xi) \cdot d\xi \quad ; \quad M \doteq \frac{Gr}{Re}$$

The corresponding governing equations are:

$$\frac{\partial u}{\partial X} + \frac{\partial V}{\partial y} \tag{2}$$

$$u \cdot \frac{\partial u}{\partial X} + V \cdot \frac{\partial u}{\partial y} = -\frac{dp}{dX} + Pr \cdot \frac{\partial^2 u}{\partial y^2} + Pr \cdot M \cdot \theta \tag{3}$$

$$u \cdot \frac{\partial \theta}{\partial X} + V \cdot \frac{\partial \theta}{\partial y} = \frac{\partial^2 \theta}{\partial y^2} \tag{4}$$

With the boundary and initial conditions

$$u(0,y) = 6(y - y^2) \quad ; \quad u(X,0) = u(X,1) = 0$$

$$\theta(0,y) = 0 \quad ; \quad p(0) = 0$$

$$\frac{\partial \theta}{\partial y}(X,0) = -1 \quad ; \quad \frac{\partial \theta}{\partial y}(X,1) = 1$$

For very small X–values we can divide the flow into two regions: the first one contains the developing thermal boundary layers near the walls. The second one is an isothermal region in the center of the channel. The direct buoyancy effects are restricted to the first region and the heat transfer can be understood as a perturbation of the isothermal regime. We formulate this with help of the following transformation:

$$(X,y) \rightarrow (\varepsilon,y) \; ; \; \varepsilon \doteq \left[\frac{3}{2}X\right]^{1/3} \ll 1 \tag{5}$$

The dimensionless equations become:

$$\frac{\partial u}{\partial \epsilon} + 2\varepsilon^2 \cdot \frac{\partial V}{\partial y} = 0 \tag{6}$$

$$u \cdot \frac{\partial u}{\partial \epsilon} + 2\varepsilon^2 \cdot V \cdot \frac{\partial u}{\partial y} = -\frac{dp}{d\epsilon} + 2\varepsilon^2 \cdot Pr \cdot \frac{\partial^2 u}{\partial y^2} + 2\varepsilon^2 \cdot Pr \cdot M \cdot T \tag{7}$$

$$u \cdot \frac{\partial T}{\partial \epsilon} + 2\varepsilon^2 \cdot V \cdot \frac{\partial T}{\partial y} = 2\varepsilon^2 \cdot \frac{\partial^2 T}{\partial y^2} \tag{8}$$

We assume now, that the the solution of the central region can be expanded in the form:

$$u(\varepsilon,y) = U_0(y) + \varepsilon \cdot U_1(y) + \varepsilon^2 U_2(y) + ..$$

$$V(\varepsilon,y) = \varepsilon \cdot V_1(y) + \varepsilon^2 \cdot V_2(y) + ...$$

$$\theta(\varepsilon,y) = \Theta_0(y) + \varepsilon \cdot \Theta_1(y) + \varepsilon^2 \cdot \Theta_2(y) ...$$

$$p(\varepsilon) = P_0 + \varepsilon \cdot P_1 + \varepsilon^2 \cdot P_2 + \varepsilon^3 \cdot P_3 + \varepsilon^4 \cdot P_4 + ... \tag{9}$$

One obtains as the solution for the first terms, that are necessary for the matching with the inner solution:

$$u_0(y) = 6(y - y^2) \; ; \; \Theta_0(y) = 0$$

$$P_0 = 0 \; ; \; P_1 = 0 \; ; \; P_2 = 0 \; ; \; P_3 = -12Pr \tag{10}$$

We introduce the Lévêque–Transformation for the formulation of the near wall region:

$$(\varepsilon,y) \rightarrow (\varepsilon,\eta) \quad ; \quad \eta \doteq \frac{y}{\varepsilon} \tag{11}$$

One substitutes the eq.(11) into the eqs.(6 to 8) to obtain:

$$\left[\eta \cdot u_\eta - \varepsilon \cdot u_\varepsilon - 2\varepsilon^2 \cdot V_\eta\right] = 0 \tag{12}$$

$$\frac{1}{2}\left[-\eta \cdot u_\eta - \varepsilon \cdot u_\varepsilon\right] \cdot u + \varepsilon^2 \cdot V \cdot u_\eta = \frac{1}{2}\eta \cdot P_\eta + \varepsilon \cdot Pr \cdot u_{\eta\eta} +$$

$$+ \varepsilon^2 \cdot Pr \cdot M \cdot \theta \tag{13}$$

$$\frac{1}{2}\left[\varepsilon \cdot \theta_\varepsilon - \eta \cdot \theta_\eta\right] \cdot u + \varepsilon^2 \cdot V \cdot \theta_\eta = \varepsilon \cdot \theta_{\eta\eta} \tag{14}$$

We assume again that the solution can be expanded in powers of ε:

$$u = \varepsilon \cdot u_0(\eta) + \varepsilon^2 \cdot u_1(\eta) + \varepsilon^3 \cdot u_2(\eta) + ...$$

$$V = \varepsilon \cdot v_1(\eta) + \varepsilon^2 \cdot v_2(\eta) + ...$$

$$p = \varepsilon^3 \cdot P_3 + \varepsilon^4 \cdot P_4 + ...$$

$$-\frac{\theta}{\varepsilon} \doteq \overline{\theta} = \overline{\theta}_0(\eta) + \varepsilon \cdot \overline{\theta}_1(\eta) + \varepsilon^2 \cdot \overline{\theta}_2(\eta) + ... \tag{15}$$

By substitution of eqs.(15) into the eqs.(12 to 14) and by ordering in powers of ε we obtain the problems:

(a) – Lévêque–Problem or 1st. Worsøe–Schmidt's problem (problem in ε^0):

$$\left[u_0 - \eta \cdot u_{0\eta}\right] = 0$$

$$\frac{1}{2}\left[u_0^2 - \eta \cdot u_0 u_0\right] = Pr \cdot u_{0\eta\eta}$$

$$\frac{1}{2}\left[\bar{\theta}_0 - \eta \cdot \bar{\theta}_{0\eta}\right] \cdot u_0 = \bar{\theta}_{0\eta\eta} \tag{16}$$

with the boundary and matching conditions:

$$u_0(0) = 0 \; ; \; \lim_{\eta \to \infty} u_0 = 6\eta \,(\text{matching})$$

$$\bar{\theta}_{0\eta}(0) = -1 \; ; \; \lim_{\eta \to \infty} \bar{\theta}_0 = 0 (\text{matching}) \tag{17}$$

or already solved for the velocity :

$$u_0(\eta) = 6\eta$$

$$\bar{\theta}_{0\eta\eta} + 3\eta^2 - 3\eta\bar{\theta}_0 = 0 \tag{18}$$

$$\bar{\theta}_{0\eta}(0) = -1 \; ; \; \lim_{\eta \to \infty} \bar{\theta}_0(\eta) = 0 \tag{19}$$

This problem corresponds to the pure forced convection with a linear velocity profile.

(b) – 1st correction to the Lévêque–solution or 2nd Worsøe–Schmidt's problem (problem in ε^1):

$$2u_1 - \eta \cdot u_1 = 0$$

$$3u_0u_1 - \eta(u_0u_{1_\eta} + u_{0_\eta}u_1) = -3 \cdot P_3$$

$$2u_0\bar{\theta}_1 + u_1\bar{\theta} - \eta(u_0\bar{\theta}_{1_\eta} + u_1\bar{\theta}_{0_\eta}) = 2 \cdot \bar{\theta}_{1_{\eta\eta}} \qquad (20)$$

with the boundary and matching conditions:

$$u_1(0) = 0 \;\; ; \;\; \lim_{\eta\to\infty} u_1(\eta) = -6\eta^2$$

$$\bar{\theta}_{1_\eta}(0) = 0 \;\; ; \;\; \lim_{\eta\to\infty} \bar{\theta}_1(\eta) = 0 \qquad (21)$$

or already solved for the velocity:

$$u_1(\eta) = -6\eta^2 \;\; ; \;\; P_3 = -12Pr$$

$$\bar{\theta}_{1_{\eta\eta}} + 3\eta^2 \cdot \bar{\theta}_{1_\eta} - 6\eta \cdot \bar{\theta}_1 = 3\eta^3 \cdot \bar{\theta}_{0_\eta} - 3\eta^2 \cdot \bar{\theta}_0$$

$$\bar{\theta}_{1_\eta}(0) = 0 \;\; ; \;\; \lim_{\eta\to\infty} \bar{\theta}_1(\eta) = 0 \qquad (22)$$

The equations(22) are the formulation of a correction for the pure forced convection due the quadratic term from the parabolic velocity profile and a pressure term, that appears for the first time.

(c) – 3rd correction of the Lévêque–solution with the **buoyancy effects** (problem in ε^2):

$$2 \cdot v_{1_\eta} + 3u_2 - \eta \cdot u_{2_\eta} = 0$$

$$Pr \cdot u_{2_{\eta\eta}} + 3\eta^2 \cdot u_{2_\eta} - 9\eta \cdot u_2 - 6v_1 = -Pr \cdot M \cdot \bar{\theta}_0 + 2P_4$$

$$\bar{\theta}_{2_{\eta\eta}} + 3\eta^2 \cdot \bar{\theta}_{2_\eta} - 9\eta \cdot \bar{\theta}_2 = 3\eta^3 \cdot \bar{\theta}_{1_\eta} - 3\eta^2 \cdot \bar{\theta}_1 + \frac{1}{2}\bar{u}_2\bar{\theta}_{0_\eta} + v_1\bar{\theta}_{0_\eta} - \frac{1}{2}\eta\bar{u}_2\bar{\theta}_{0_\eta} \qquad (23)$$

with the boundary and matching conditions:

$$u_2(0) = 0 \;\; ; \;\; \lim_{\eta\to\infty} u_2(\eta) = 0$$

$$\bar{\theta}_{2_\eta}(0) = 0 \;\; ; \;\; \lim_{\eta\to\infty} \bar{\theta}_2(\eta) = 0 \qquad (24)$$

The last three terms on the right side of the set of eqs.(23) take into account the buoyancy effects. They disappear for vanishing values of the parameter $M(=Gr/Re)$, while $\bar{\theta}_2$ converges to the asymptotic 2nd correction of the pure forced convection solution (3rd Worsøe–Schmidt's problem), $\bar{\theta}_{2forc}$. For finite values of M, however, there is a non–trivial solution for the corrections $v_1(\eta)$ and $u_2(\eta)$ together with a departure of $\bar{\theta}_2$ from $\bar{\theta}_{2forc}$.

These 3 sets of equations(problems (a), (b) and (c)) were solved numerically, in block, by means of a 4th order Runge–Kutta method(an analytical solution for the problem(a) was indicated by Worsøe–Schmidt(17). The problem (c) is linear in M and needs to be solved just for two values of this parameter, for instance, M=0 and M=1. We are specially concerned with the values of u_{2_η}, $\bar{\theta}_0$, $\bar{\theta}_1$ and $\bar{\theta}_2$ at the wall, which determine the momentum and heat transfer. The values listed in Table 1 are independent of the parameter M, u_{0_η}, u_{1_η}, $\bar{\theta}_0$ and $\bar{\theta}_1$ are also valid for the pure forced convection and are not influenced by the buoyancy effects or the Prandtl–number. The values of u_{2_η} and $\bar{\theta}_2$ at the wall were calculated for two values of Pr.

Table 1 – Values on the wall

$u_{0_\eta}(0)$	12	
$u_{1_\eta}(0)$	0	
$u_{2_\eta}(0)/M$	0.1245[a]	0.2055[b]
P_4/M	0.0645[a]	0.2400[b]
$\bar{\theta}_0(0)$	0.73849	
$\bar{\theta}_1(0)$	0.09635	
$\bar{\theta}_{2forc}(0)$	0.04004	
$(\bar{\theta}_2 - \bar{\theta}_{2forc})_w/M$	–0.00186[a]	–0.00399[b]

a: Pr = 0.7
b: Pr = 7.0

Friction factor c_f – We define the friction factor

$$c_f = -\frac{2\tau_w^*}{\rho_0^*\bar{u}^{*2}} = \frac{2\nu^*}{u_m^{*2}} \cdot \left.\frac{\partial u^*}{\partial y^*}\right|_w = \frac{2}{Re} \cdot \left.\frac{\partial u}{\partial y}\right|_w \qquad (25)$$

With help of the equations(15) one obtains:

$$c_f \cdot Re \cong 2\left[\frac{du_0}{d\eta} + \varepsilon \cdot \frac{du_1}{d\eta} + \varepsilon^2 \cdot \frac{du_2}{d\eta}\right]_{\eta=0}$$

$$c_f \cdot Re = \overbrace{12}^{c_{f0} \cdot Re} + 2 \cdot \varepsilon^2 \cdot K_f(Pr) \cdot M + O(\varepsilon^3) + \ldots$$

$$\frac{c_f}{c_{f0}} = 1 + \frac{1}{6} \cdot \varepsilon^2 \cdot K_f(Pr) \cdot M \qquad (26)$$

where $K_f(Pr) = u_{2_\eta}(0)/M$ (see table 1)

Nusselt–number – The definition of the Nu–number is

$$Nu \doteq \frac{2 \cdot q_w^* \cdot b}{\lambda^*(T_w^* - T_b^*)} = \frac{2}{(\theta_w - \theta_b)} \qquad (27)$$

For the bulk temperature results

$$\theta_b(X) = 2X = 2 \cdot \left(\frac{2}{3} \cdot \varepsilon^3\right) = \frac{4}{3} \cdot \varepsilon^3 \qquad (28)$$

and from the asymptotic series for $\overline{\theta}(\eta) = \frac{\theta(\eta)}{\varepsilon}$ one obtains

$$\theta_w \cong \varepsilon \cdot \overline{\theta}_0(0) + \varepsilon^2 \cdot \overline{\theta}_1(0) + \varepsilon^3 \cdot \overline{\theta}_{2forc}(0) + \\ + \varepsilon^3 \cdot \left[\overline{\theta}_2(0) - \overline{\theta}_{2forc}(0)\right] + \ldots \qquad (29)$$

It follows

$$\frac{2}{Nu} = \overbrace{\varepsilon \cdot \overline{\theta}_0(0) + \varepsilon^2 \cdot \overline{\theta}_1(0) + \varepsilon^3 \cdot \overline{\theta}_{2forc}(0) - \varepsilon^3 \cdot \frac{4}{3}}^{2/Nu_{forc}} + \\ + \varepsilon^3 \cdot \left[\overline{\theta}_2(0) - \overline{\theta}_{2forc}(0)\right] + \ldots \qquad (30)$$

We finally have

$$\frac{Nu_{forc}}{Nu} \cong 1 + \frac{Nu_{forc}}{2} \cdot \varepsilon^3 \cdot K_{Nu}(Pr) \cdot M \qquad (31)$$

where $K_{Nu}(Pr) = \frac{1}{M} \cdot \left[\overline{\theta}_2(0) - \overline{\theta}_{2forc}(0)\right]$ (see Table 1)

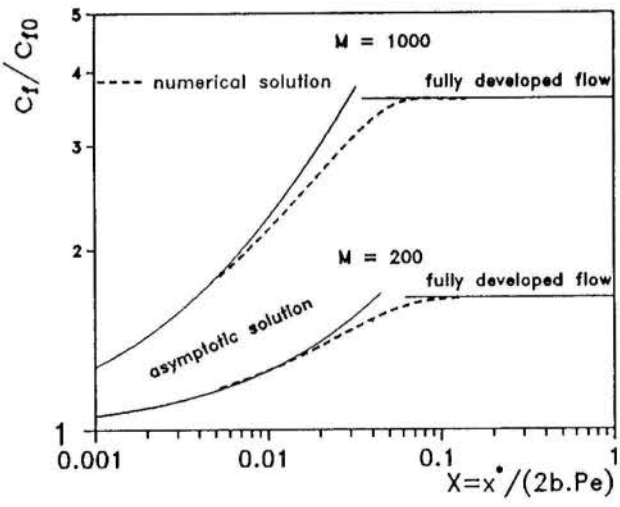

Fig. 2 – Friction factor c_f ; Pr = 0.7

The equations(26 and 31) are illustrated in the Figures 2 and 3 for Pr=0.7(air) together with a numerical solution and the values of the fully developed flow(for details of these last two solutions see ref.(18)) for two values of the parameter **M**. The asymptotic solution is in good agreement with the numerical solution for X < 0,01. These results were obtained with the first term of the asymptotic expansions, that takes into account the buoyancy effects. We expect, that additional terms would increase the agreement for greater values of **M** and X.

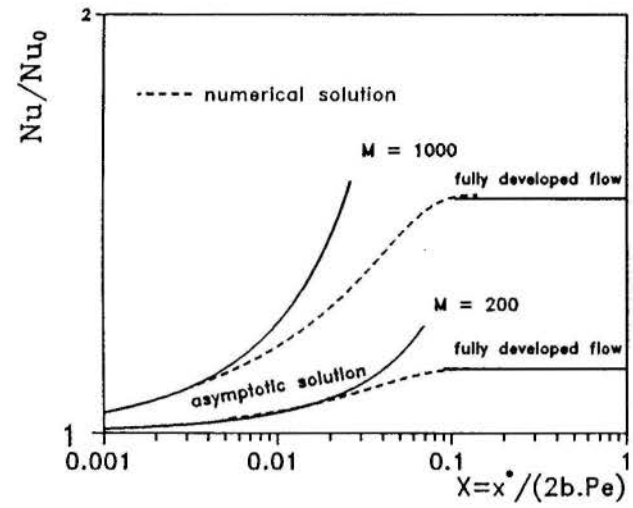

Fig. 3 – Heat transfer: Pr = 0.7

For moderate values of the parameter M(as M < 200), the asymptotic solution gives a good approximation for nearly all the developing flow region.

Concluding Remarks

The analysis of Worsøe–Schmidt(17) was extended to take into account the buoyancy effects of the two dimensional laminar mixed convection in a vertical flow between two flat plates. The present analysis has demonstrated the usefulness of an asymptotic formulation for computing the momentum and heat transfer rates in the region of developing flow. The results are corrections for the friction factor c_f and the Nusselt–number of the pure forced convection depending on the buoyancy parameter M=Gr/Re and on the Pr–number.The solution was compared with a numerical procedure.

REFERENCES

1 – TAO, L.N.: On Combined Free and Forced Convection in Channels.
J. Heat Transfer, Vol. 82, pp.233–238, Aug.(1960)

2 – ROSEN, E.M. and HANRATTY, T.J.: Use of Boundary Layer Theory to predict the Effect of Heat Transfer on the Laminar Flow field in a Vertical Tube with constant Wall Temperature.
AIChE Journal, Vol. 7, pp.112–123 (1961)

3 – BODOIA, J.R. and ORSTELE, J.F.: The Development of Free Convection between heated Vertical Plates.
J. Heat Transfer, Vol. 84, pp.40–44 (1962)

4 – LAWRENCE, W.T. and CHATO, J.C.: Heat Transfer Effects on the Developing Laminar Flow inside Vertical Tubes.
J Heat Transfer, Vol. 88, pp 214–222 (1966)

5 – LAUNDER, T.S. and WELCH, A.U.: Natural Convection Between Vertical Flat Plates with Uniform Heat Flux.
Proc. of 3rd Int. Heat Transfer Conf., Vol. II, pp.126–131 (1966)

6 – MARNER, W.J. and McMILLAN, H.K.: Combined Free and Forced Laminar Convection in a Vertical Tube with Constant Wall Temperature.
J. Heat Transfer, Vol. 92, pp. 559–562 (1970)

7 – SAVKAR, S.D.: Developing Forced and Free Convection Between Two Semi–infinite Parallel Plates.
Proc. of 4th Int. Heat Trans. Conf., Vol.IV, NC 3.8 (1970)

8 – AIHARA, T.: Effects of Inlet Boundary–conditions on Numerical Solutions of Free Convection Between Vertical Parallel Plates.
Rep. Inst. High Speed Mech., Vol. 28, pp. 1–27 (1973)

9 – AUNG, W.: Fully Developed Laminar Free Convection Between Vertical Plates Heated Asymmetrically.
Int. J. Heat Mass Trans., Vol. 15, pp. 1577–1580 (1972)

10 – AUNG, W. FLETSCHER, L.S. and SERNAS, V.: Developing Laminar Free Convection Between Vertical Flat Plates with Asymmetric Heating.
Int. J. Heat Mass Transfer, Vol. 15, pp. 2293–2308 (1972)

11 – ZELDIN, B. and SCHMIDT, F.W.: Developing with Combined Forced Free Convection in an Isothermal Vertical Tube.
J. Heat Transfer, Vol. 94, pp. 211–223 (1972)

12 – OOSTHUIZEN, P.H.: A Numerical Study of Laminar Combined Convective Flow Over Flat Plates.
J. Heat Transfer, Vol. 95, pp. 60–63 (1973)

13 – QUINTIERE, J., MÜLLER, W.K.: An Analysis of Laminar Free and Forced Convection between Finite Vertical Parallel Plates.
J.Heat Transfer, Vol. 95, pp. 53–59 (1973)

14 – YAO, L.S.: Free and Forced Convection in the Entry Region of a Heated Vertical Channel.
Int. J. Heat Mass Transfer, Vol. 26, pp.65–72 (1983)

15 – CAMPO, A. and PEREZ, C.: Numerical Analysis for Developing Laminar Flow in Vertical Ducts Applied to Combined Convection: Comparison with Experiments.
VIII COBEM–S.J.Campos, (1985)

16 – AUNG, W. and WORKU, G.: Theory of Fully Developed, Combined Convection Including Flow Reversal.
J. Heat Transfer, Vol.108. pp.485–488 (1986)

17 – WORSØE–SCHMIDT, P.M.: Heat Transfer in the Thermal Entrance Region of Circular Tubes and Annular Passages with Fully Developed Laminar Flow
Int. J. Heat Mass Transfer, Vol. 10, pp. 541–551, (1967)

18 – DA SILVA, A. : "Gemischte Konvektion in vertikalen Kanal– und Rohrströmungen bei hohen Reynolds–Zahlen"
Dr.–Ing. – Dissertation
Ruhr Universität Bochum 1990
(to be published)

III ENCIT – Itapema, SC (Dezembro 1990)

INCREMENTO DE LA TRANSMISION DE CALOR POR CONVECCION NATURAL ENTRE PLACAS PARALELAS VERTICALES CALENTADAS PARCIALMENTE.

Cinzia Simonis y Ulises Lacoa
Universidad Simón Bolívar. Caracas-Venezuela.
Antonio Campo
Florida International University, Miami, Fl, USA.

RESUMEN

Este trabajo presenta un estudio numérico sobre la convección natural en un conducto formado por dos placas paralelas en posición vertical. La región inferior de las placas se calienta a una temperatura uniforme, mientras que la región superior se conserva aislada. La discretización de las ecuaciones diferenciales que gobiernan el fenómeno se realizó en la dirección transversal solamente, utilizando el método de las líneas combinado con el método de los volúmenes de control (MOLCV). Los resultados del análisis se muestran en términos de las distorsiones de las distribuciones de la velocidad axial y de la temperatura a lo largo del canal.

INTRODUCCION

El tema de la transferencia de calor por convección natural en ductos verticales constituye un problema de gran trascendencia en algunas aplicaciones térmicas relacionadas a flujos internos. La aplicación más difundida es la de enfriadores compactos de equipos electrónicos [8]. Está aplicación ha motivado a un grupo substancial de investigadores a estudiar la convección natural en ductos verticales [1-5]; pero todavía, aspectos muy importantes permanecen sin resolver.

Numerosos investigadores se han dedicado a realizar estudios experimentales y numéricos sobre la convección libre en ductos verticales o placas paralelas, por ejemplo: Carpenter y Wassell [6], Elenbass [1] y Bodoia y Osterle [2]. Este último trabajo muestra estudios numéricos y experimentales sobre la convección libre en placas verticales totalmente calentadas. Quintiere y Mueller [7] realizaron un trabajo sobre la convección libre y forzada en placas verticales proporcionando un aporte significativo en cuanto a la condición de presión a la entrada del canal. También se ha contemplado la condición de flujo de calor en las paredes del canal, tanto simétrica como asimétricamente. Cabe mencionar: Dyer [9] y Wjrtz y Stutzman [10]. Por otro lado, un trabajo que muestra un estudio numérico de flujo laminar en convección libre a través de un ducto vertical parcialmente calentado, es el presentado por Oosthuizen [11], concluyendo que el incremento en la transferencia de calor está relacionado con la adición de una sección de pared adiabática sobre la sección calentada del ducto. Recientemente, Azevedo y Sparrow [12]; Sparrow, Ruiz y Azevedo [13] y Sparrow y Ruiz [14] han trabajado la convección libre en canales inclinados.

Habiendo investigado y analizado las referencias mencionadas anteriormente, en el presente estudio se propone examinar si es posible incrementar la transferencia de calor en un canal formado por placas paralelas, el cual tiene una sección inferior de pared calentada a una temperatura uniforme y una sección superior de pared adiabática. La discretización del conjunto de ecuaciones diferenciales que gobiernan el fenómeno físico se hizo mediante la utilización del método de las líneas combinado con el método de los volúmenes de control (MOLCV), que muestra una solución alternativa para problemas parabólicos asociados al flujo del tipo de capa límite. Este método propone un procedimiento de discretización de cada una de las ecuaciones diferenciales, obteniendo un sistema de ecuaciones diferenciales ordinarias que se resuelve por alguna técnica de integración analítica o numérica. El método MOLCV ha sido aplicado en otros problemas de una manera exitosa [16].

FORMULACION DEL PROBLEMA

Considérese el proceso de convección natural de aire en un canal vertical formado por placas paralelas. En la Fig.1 se dibuja la situación que caracteriza el fenómeno físico del presente trabajo.

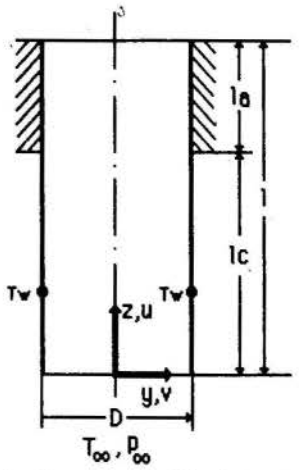

Fig. 1.- Esquema del fenómeno.

El canal está conformado por una sección inferior de paredes calentadas a una temperatura uniforme Tw que

es mayor que la temperatura del aire que circula a lo largo del canal, y una sección superior en la cual las paredes se mantienen adiabáticas. La temperatura y presión del aire circundante están caracterizadas por T_∞ y p_∞, respectivamente. Para realizar el análisis del presente problema se dispone de la ecuación de continuidad, de cantidad de movimiento, de energía y de continuidad integral. La formulación del problema se simplifica ya que los gradientes de presión serán únicamente importantes en la dirección del flujo.

Las suposiciones hechas en el modelaje y resolución de las ecuaciones fueron: fluído newtoniano, flujo laminar y uniforme, simetría térmica e hidrodinámica, propiedades termofísicas del fluído constantes excepto la densidad, ecuaciones del tipo de capa límite, no existe inversión en el campo de velocidad axial, utilización de la aproximación de Boussinesq para expresar la variación de la densidad con la temperatura y el perfil de velocidad uniforme a la entrada del ducto (u_e).

Al aplicar las suposiciones mencionadas anteriormente y despreciando los términos de disipación viscosa, difusión axial y la contribución de calor por radiación, el sistema de ecuaciones adimensional formado por la ecuación de continuidad, cantidad de movimiento, energía y continuidad integral, se puede escribir como:

$$\frac{\partial U}{\partial Z} + \frac{\partial V}{\partial Y} = 0 \qquad (1)$$

$$U\frac{\partial U}{\partial Z} + V\frac{\partial U}{\partial Y} = -\frac{dP}{dZ} + \frac{2}{Re}\frac{\partial^2 U}{\partial Y^2} + 4\frac{Gr}{Re^2}\theta \qquad (2)$$

$$U\frac{\partial \theta}{\partial Z} + V\frac{\partial \theta}{\partial Y} = \frac{2}{Re\,Pr}\frac{\partial^2 \theta}{\partial Y^2} \qquad (3)$$

$$\bar{M} = \frac{\bar{m}}{\rho\, u_m D} = \int_0^{1/2} U\, dY = 1 \qquad (4)$$

donde las variables participantes han sido definidas como:

$$Y = \frac{y}{D} \qquad Z = \frac{z}{D} \qquad U = \frac{u}{u_e} \qquad V = \frac{v}{u_e}$$

$$\theta = \frac{T - T_\infty}{T_w - T_\infty} \qquad P = \frac{p^* - p_\infty}{\rho_\infty u_e^2} \qquad Re = \frac{\rho\, u\, (2D)}{\mu} \qquad (5)$$

$$Pr = \frac{C_p\, \mu}{k} \qquad Gr = \frac{\beta\, g\, (T_w - T_\infty)\, D^3}{\gamma^2}$$

Las condiciones de borde asociadas a las ecuaciones (1)-(4) son las siguientes:

Para Z=0

$$U = 1 \qquad (6)$$

$$\theta = 0 \qquad (7)$$

$$P = -1/2 \qquad (8)$$

Para $Z \leq Z_C$

En Y=1/2

$$\theta = 1 \qquad (9)$$

Para $Z > Z_C$

En Y=1/2

$$\frac{d\theta}{dY} = 0 \qquad (10)$$

Para $Z \leq Z_1$

En Y=0

$$\frac{\partial U}{\partial Y} = 0 \qquad (11)$$

$$\frac{\partial \theta}{\partial Y} = 0 \qquad (12)$$

$$V = 0 \qquad (13)$$

En Y=1/2

$$U = 0 \qquad (14)$$

$$V = 0 \qquad (15)$$

Para $Z = Z_1$

$$P = 0 \qquad (16)$$

La resolución de las ecuaciones (1)-(4) unidas a sus condiciones de borde permiten obtener el campo hidrodinámico y térmico del fluído. Esta información sirve de punto de partida para calcular los siguientes parámetros de interés:

Flujo volumétrico:

$$Q = \frac{q}{U_m D} = 2\int_0^{1/2} U\, dY = U_m = 1 \qquad (17)$$

Temperatura volumétrica media:

$$\theta_b = \frac{T_b - T_\infty}{T_w - T_\infty} = 2\int_0^{1/2} U\,\theta\, dY \qquad (18)$$

Flujo de calor:

$$H = \frac{2\,h}{\mu\, C_p\, (T_w - T_\infty)} = 2\,Re\int_0^{1/2} U\,\theta\, dY = \theta_b\, Re \qquad (19)$$

METODO DE SOLUCION NUMERICA

El método MOLCV combina el método de los volúmenes de control (CV) con el método de las líneas (MOL). Básicamente la idea consiste en integrar el lado derecho de la ecuación (20) empleando el método de los volúmenes de control, mientras se mantiene continua la derivada del lado izquierdo de dicha ecuación.

La secuencia de cálculo se inicia con la introducción del Número de Grashof (Gr), el Número de Reynolds (Re), el Número de Prandtl (Pr) y la longitud de calentamiento adimensional (Zc). El algoritmo proporciona los parámetros de interés tales como: el flujo volumétrico, la temperatura volumétrica media y el flujo de calor. Es importante destacar el hecho de que la longitud de las placas se determina en forma indirecta. La solución se obtiene estableciendo una distancia axial lo suficientemente grande, en donde la longitud especifica de las placas se determina ubicando la posición axial para la cual la presión es cero (P=0). La ventaja de aplicar esta metodología radica en el hecho que evita el tener que realizar un proceso de ensayo y error para satisfacer la condición de presión (P=0) a la salida del canal. Esto ocurre cuando de antemano se especifica la longitud de las placas. El algoritmo utilizado es de propósito múltiple, que resuelve en general ecuaciones del tipo:

$$\frac{\partial(\rho u\phi)}{\partial x} + \frac{\partial(\rho v\phi)}{\partial y} = \frac{\partial}{\partial x}\left(\Gamma \frac{\partial \phi}{\partial x}\right) + \frac{\partial}{\partial y}\left(\Gamma \frac{\partial \phi}{\partial y}\right) + S_\phi \quad (20)$$

los términos de difusividad (Γ) y de fuentes (S_ϕ) se especifican para cada variable ϕ.

Tabla 1.- Términos de difusividad y de fuentes.

Ecuación	ϕ	Γ	S
Continuidad	1	0	0
Cantidad de movimiento	U	$\frac{2}{Re}$	$-\frac{dP}{dZ} + 4\frac{Gr}{Re^2}\theta$
Energia	θ	$\frac{2}{Re\ Pr}$	0

En la Tabla 1 se muestran los términos de difusividad y de fuentes particularizados para el presente estudio.

RESULTADOS Y DISCUSION

Los resultados numéricos obtenidos son para aire (Pr=0.7) con 6000 < Gr < 100000 y 50 < Re < 1000. La malla utilizada fue de 21 volúmenes de control de igual tamaño (malla uniforme) asegurando independencia con el número de volúmenes de control empleados. A continuación se presentan resultados representativos. Para más detalle se remite al lector a la referencia [17].

Las comparaciones presentadas en las Figs. 2 y 3, con los resultados de Bodoia y Osterle [2] y los de Oosthuizen [11], para el flujo volumétrico en placas paralelas totalmente calentadas, muestran una excelente concordancia, demostrando que la metodología numérica es capaz de predecir el fenómeno de convección natural en placas paralelas parcialmente calentadas.

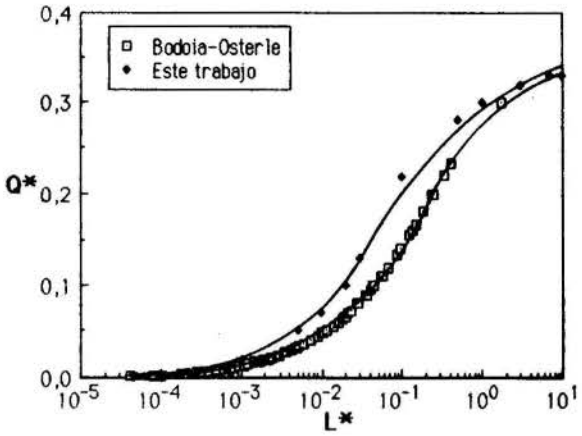

Fig. 2.- Comparación para el flujo volumétrico con los resultados de Bodoia y Osterle [2].

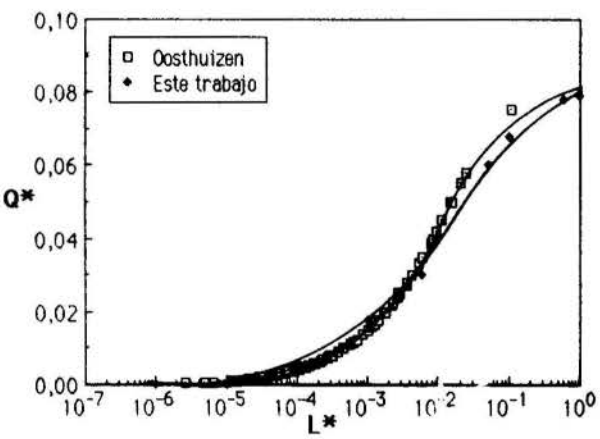

Fig. 3.- Comparación para el flujo volumétrico con los resultados de Oosthuizen [11].

En la Fig. 4 se observa la variación del flujo de calor y del Número de Reynolds en funcion de la longitud adimensional del ducto para Zc=2.24 y Gr=75000. En la Fig. 5 se observa la misma variación pero con Zc=5. Se aprecia que para mayores longitudes de ducto, el Reynolds que se impone es mayor. Desde el punto de vista físico este fenómeno corresponde al hecho que al colocar paredes adiabáticas sobre la longitud calentada se obtiene un incremento en el flujo volumétrico. En cuanto a la transferencia de calor, a medida que el ducto es más largo, o en otras palabras, cuando el Número de Reynolds aumenta, el calor transferido es mayor. Este aumento es originado por el incremento del flujo volumétrico inducido en las placas.

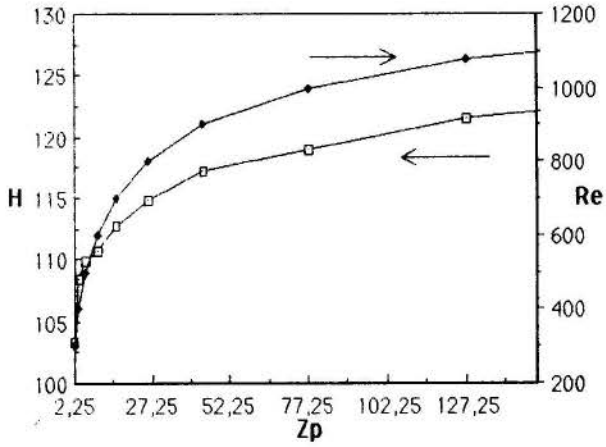

Fig. 4.- Variación de H y Re en función de Zp para Gr=75000 y Zc=2.25.

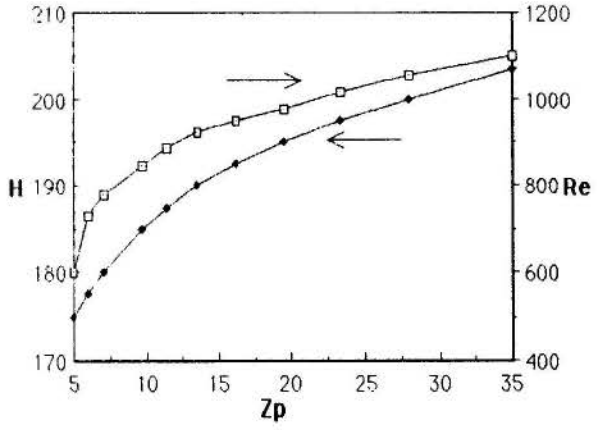

Fig. 5.- Variación de H y Re en función de Zp para Gr=75000 y Zc=5.

En la Fig. 6 se aprecia el desarrollo de los perfiles de temperatura a lo largo del ducto para Zc=2.25 y Gr=75000. Se observa que para el ducto parcialmente calentado, el perfil de temperatura se desarrolla hasta mostrar una pendiente horizontal en la pared (adiabática). También se aprecia como el perfil tiende a uniformizarse al valor de la temperatura volumétrica media. En la Fig. 7 se aprecia el desarrollo del perfil de velocidad a lo largo del canal para la mismas condiciones mencionadas anteriormente. Se aprecia claramente el efecto de la convección natural ya que la velocidad en el centro no llega a ser máxima (distorsión del perfil).

Una conclusion resaltante del presente estudio es que la adición de longitudes de pared adiabática contribuye a incrementar la transferencia de calor en el canal. Este incremento viene acompañado por un aumento del flujo volumetrico a través del ducto, y es este mismo incremento el que determina el aumento del Número de Reynolds que se impone en el canal y por ende la transferencia de calor.

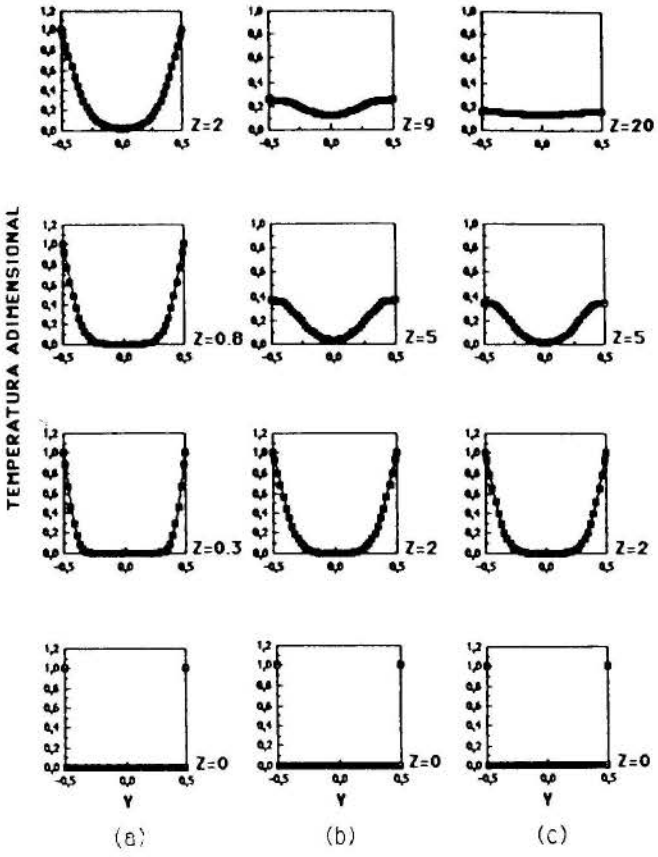

Fig. 6.- Desarrollo de los perfiles de temperatura para ductos con Zc=2.25 y Gr=75000. Totalmente calentado Zp=2.25 (a), parcialmente calentado Zp=9.49 (b) y Zp=26.06 (c).

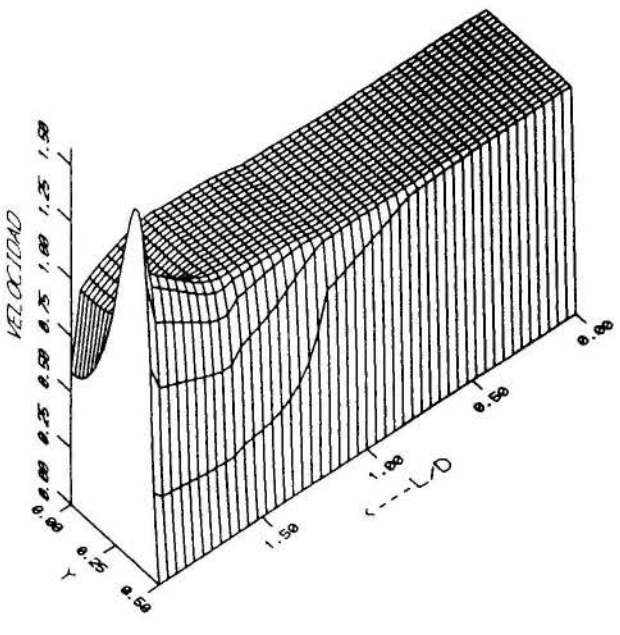

Fig. 7.- Desarrollo del perfil de velocidad para un ducto totalmente calentado, Zp=Zc=2.25 y Gr=75000.

REFERENCIAS

[1] Elenbass, W. : "Heat dissipation of parallel plates by free convection", Physica, Vol. 9, pp 865-874, 1942.

[2] Bodoia, J. R. and Osterle, F. J. : "The development of free convection between heated vertical plates", ASME, J. Heat of Transfer, Vol. 84, pp. 40-44, 1962.

[3] Currie, I. G. and Newman, W. A. : "Natural convection between isothermal vertical surfaces", Proc. of the fourth Int. Heat Transfer Conference, Vol. IX, NC27, 1970.

[4] Aung, W. : "Fully developed laminar free convection between vertical plates heated asymmetrically", Journal Heat Mass Transfer, Vol. 15, pp. 1577-1580, 1972.

[5] Aung, W., Fletcher, L. S. and Sernas, V. : "Developing laminar free convection between vertical flat plates with uniform heat flux", Proc of the third Int. Heat Conference, Vol. II, pp. 126-131, 1972.

[6] Carpenter, L. G. and Wassell, H. C. : "The loss of heat by natural convection from parallel vertical plates in air", Proc. Insts. Mech. Engrs, Vol.128, pp. 1439-457, 1934.

[7] Quintiere, J. and Mueller, W. K. : "An analysis of laminar free and forced convection between finite vertical parallel plates" , J. of Heat Transfer, pp. 53-59, 1973.

[8] Aung, W.; Kessler, T. J. and Beitin, K. I. : "Free convection cooling of electronic systems", IEEE Trans Parts-Hybrids, Vol. PHP9, pp. 74-86, 1973.

[9] Dyer, J. R. : "The development of laminar natural-convective flow in a vertical uniform heat flux duct", Int. J. Heat Mass Transfer, Vol. 18, pp. 1455-1465, 1975.

[10] Wirtz, R. A. and Stutzman R. J. : "Experiments on free convection between vertical plates with symmetric heating", Journal of Heat Transfer ASME, Vol. 104, pp. 501-507, 1982.

[11] Oosthuizen, P. H. : "A numerical study of laminar free convective flow through a vertical open partially heated plane duct", Fundamentals of Natural Convection and Electronic Equipment cooling, Vol. 32, pp. 41-47, 1984.

[12] Azevedo, L. F. and Sparrow, E. M. : "Natural convection in open-ended inclined channels", Journal of Heat Transfer.ASME, Vol. 107, pp. 893-901, 1985.

[13] Sparrow, E. M.; Ruiz, R. and Azevedo, L. F. : "Experimental and numerical investigation of natural convection in convergent vertical channels", Int. Journal Heat Mass Transfer, Vol. 31, No. 5, pp.907-915, 1988.

[14] Sparrow, E. M.; Ruiz, R. and Azevedo, L. F. : "Experiments on natural convection in divergent vertical channels and correlation of divergent, convergent and parallel channel Nusselt numbers", Int. Journal Heat Mass Transfer, Vol. 31, No. 11, pp. 2197-2205, 1988.

[15] Lauber, T. S. and Welch, A. V. : "Natural convection heat transfer between vertical flat plates with uniform heat flux", Proc. of the third Int. Heat Transfer Conference, Vol. II, pp 126-131, 1966.

[16] Morales, J. C.; Campo, A. y Lacoa, U. : "Calculation of turbulent forced convection in the thermal entry region of pipes by the method of lines and control volumes (MOLCV)", PCH Physico Chemical Hydrodynamics, Vol. 10, No. 1, pp. 65-76, 1988.

[17] Simonis, Cinzia: "Estudio del incremento de la transferencia de calor en placas paralelas parcialmente calentadas". Enero 1990. Universidad Simón Bolívar. Tesis de pregrado.

ABSTRACT

A numerical study of laminar natural convective flow between vertical plates partially heated has been conducted. The lower section of walls is heated to a uniform temperature and the upper section is insulated. The basic governing equations are continuity, momentum and energy. The discretization of these equations is performed in the transversal direction only using the combination of the methods of lines and control volumes (MOLCV). This method represents another step in the development of control volume methodology. This hybrid procedure shows a reformulation using a system of ordinary differential equations of first order. A selected group of results including the temperature and velocity profiles are presented. In all cases, the addition of the adiabatic section has increased the heat transfer rate and that this increase is associated with an increase in the volume flow rate. A comparison is made between the results of this theorical investigation and the works of Bodoia & Osterle and Oosthuizen.

III ENCIT – Itapema, SC (Dezembro 1990)

APPROXIMATE ANALYSIS OF FREE CONVECTIVE HEAT TRANSFER FROM A HEATED VERTICAL PLATE

F.L. BELLO-OCHENDE
Department of Mechanical Engineering
Faculty of Engineering and Technology
University of Ilorin, Ilorin, Nigeria.

SUMMARY

The effects of polynomial approximations, in one space coordinate, for the velocity and temperature profiles on predicted heat transfer coefficients due to laminar natural convection are investigated for a vertically suspended flat plate heated isothermally in some fluid media. A computer code is used to automatically compute heat transfer coefficients for any desired pairs of velocity and temperature profiles. For the best pairs of profiles, computed heat transfer results, which compare well with known empirical correlations, are presented graphically.

INTRODUCTION

The problem of natural convection heat transfer from a heated vertical surface is of considerable interest in several technological applications, particularly in electronic circuitory and some manufacturing systems.

Approximate analytical methods are available in heat transfer literatures [1 - 8] for the determination of laminar natural convection heat transfer from a vertically suspended heated flat plate. One of such approximate analytical methods, which is considered in this work, involves the use of polynomial approximations in one space coordinate for the local velocity and temperature profiles to solve the coupled momentum and energy transport equations.

In this work a total of nine possible pairs of velocity and temperature profiles which rigorously satisfy prescribed boundary and asymptotic conditions are considered. For each pair of profiles, percentage deviations of the present results from those obtained using an empirical correlation are computed for each fluid medium. Hence, a computer code is designed to facilitate quick computations of heat transfer coefficients for any desired pairs of velocity and temperature profiles. The best pairs of profiles for which the heat transfer coefficients compare well with empirical correlations in Wong [9] are determined for low and high Prandtl (Pr) numbers. The choice of fluids has been restricted to air, water, carbondioxide and unused engine oil because they are easy to procure for students' use.

For low Prandtl numbers (Pr = 0.689) less than unity, a pair of parabolic velocity and parabolic temperature profiles yields the best estimates of local heat transfer coefficients. The maximum deviation from empirical value is 1.70 percent. For Prandtl numbers (Pr = 2.22) greater than unity, the parabolic velocity profile and a cubic temperature profile constitute the best pair with a deviation of 0.37 percent from the empirical results. Also, for very high Prandtl numbers (Pr = 1050), the best result is obtained when a cubic velocity profile is paired with a parabolic temperature profile. The recorded deviation from the empirical correlation result is 1.40 percent. However, over the entire range of Pr, the best two alternative pairs of temperature and velocity profiles are:

(a) the pair of parabolic velocity and cubic temperature profiles and
(2) the pair of quartic velocity and parabolic temperature profiles.

These two pairs of velocity and temperature profiles will respectively give average deviations in heat transfer results of 6.0 and 4.0 percent from the empirical correlation for the parameter space $0.689 \leq Pr \leq 1050$.

To ensure that the laminar range is not overshot, the local Grashof number, Gr_x is computed a priori for each Pr and compared with the transition-to-turbulence value before computing the heat transfer coefficient. For brevity, some optimum heat transfer results are presented graphically to show comparisons of present results with those obtained using the empirical correlation in Wong.

The advantage of the present method is the simplicity of its presentation. The approach is easier than the similarity transformation technique which converts the coupled partial differential equations to a system of coupled ordinary differential equations. The solution of these coupled equations is difficult and often involves the use of special numerical techniques such as the shooting and the Runge-Kutta methods whose computer codes are robust and difficult to comprehend for an average undergraduate student.

ANALYSIS

The physical model, coordinate system, some boundary and asymptotic conditions are shown in Fig.1. The fluid is Newtonian and the Boussinesq approximation applies. Hence the governing equations of continuity, momentum and energy transports for the laminar flow, cast in primitive variables, are respectively:

$$\frac{\partial u}{\partial x} + \frac{\partial v}{\partial y} = 0 \tag{1}$$

$$u\frac{\partial u}{\partial x} + v\frac{\partial u}{\partial y} = g\beta(T-T_\infty) + \nu\frac{\partial^2 u}{\partial y^2} \tag{2}$$

$$u\frac{\partial T}{\partial x} + v\frac{\partial T}{\partial y} = \alpha\frac{\partial^2 T}{\partial y^2} \tag{3}$$

where u, v are the velocity components in the x- and y- directions respectively, T is the local temperature, g the acceleration due to gravity, β the volumetric coefficient of expansion, ν the kinematic viscosity and α the thermal diffusivity of fluid. The corresponding boundary and asymptotic conditions are respectively:

(a) At $y = 0$:

$$u = 0; \quad \frac{\partial^2 u}{\partial y^2} = -g\beta(T_w - T_\infty)/\nu \tag{4a}$$

$$T = T_w; \quad \frac{\partial^2 T}{\partial y^2} = 0. \tag{4b}$$

(b) As $y \to \delta$,

$$u \to 0; \quad \frac{\partial u}{\partial y} \to 0 \text{ (zero shear stress at the edge of the boundary layer)}$$

$$\frac{\partial^2 u}{\partial y^2} \to 0; \tag{5}$$

$$T \to T_\infty ; \quad \frac{\partial T}{\partial y} \to 0,$$

where T_w is the wall temperature and T_∞ is the ambient or quiescent fluid temperature.

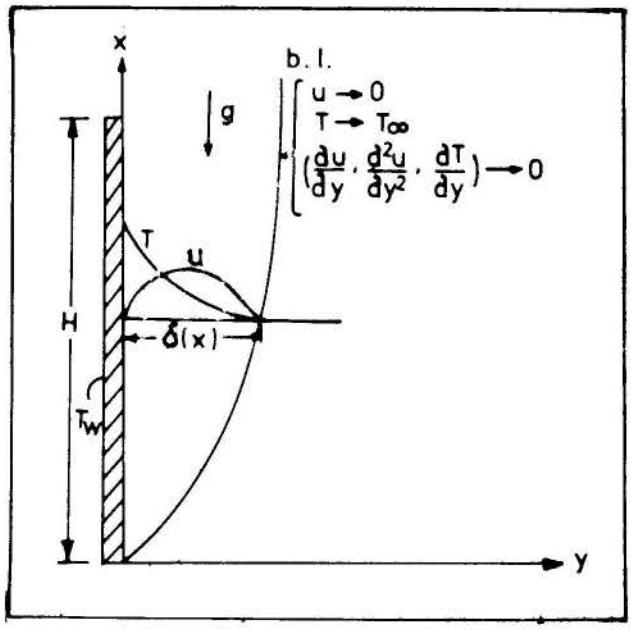

Fig.1 Physical model, coordinate system and some boundary and asymptotic conditions.

To solve the problem, the local velocity, u and the local boundary layer thickness, δ are postulated in the following generalized forms, respectively:

$$\begin{aligned} u_i &= \phi_i(x)\, \phi_i^*(y) \\ \phi_i(x) &= C_i x^{m_i} \\ \delta_i &= J_i x^{n_i} \end{aligned} \tag{6}$$

$\phi_i(x)$, $\phi_i^*(y)$ are functions of x and y only and C_i, J_i, m_i, and n_i are undetermined constants, where $i = 2,3,4$ denote parabolic, cubic and quartic velocity profiles, respectively. The assumed generalised local temperature, T is:

$$T_j = T_j(y) \tag{7}$$

where $j = 1,2,3$ denote linear, parabolic and cubic temperature profiles, respectively.

Typical Computational Technique. Consider a typical pair of quartic velocity profile (i=4) and cubic temperature profile (j=3). The corresponding polynomial representations deduced from Eqs. (6) and (7) are:

$$u_4 = \phi_4(x)\, \phi_4^*(y)$$

where,

$$\phi_4(x) = C_4 x^{m_4} \tag{8}$$

$$\phi_4^*(y) = a_4^* + b_4^* y + c_4^* y^2 + d_4^* y^3 + e_4^* y^4 \tag{9}$$

and

$$T_3 = a_3 + b_3 y + c_3 y^2 + d_3 y^3. \tag{10}$$

The boundary conditions applicable to Eqs. (9) and (10) are obtained form Eqs. (4) and (5). Thus the local coefficients in Eqs. (9) and (10) are:

$$\begin{aligned} a_4^* &= 0 \\ b_4^* &= g\beta(T_w - T_\infty)/6\nu\phi_4(x) \\ c_4^* &= g\beta(T_w - T_\infty)/2\nu\phi_4(x) \\ d_4^* &= g\beta(T_w - T_\infty)/2\nu\delta_4\phi_4(x) \\ e_4^* &= g\beta(T_w - T_\infty)/6\nu\delta_4^2\phi_4(x) \end{aligned} \tag{11}$$

and,

$$\begin{aligned} a_3 &= T_w \\ b_3 &= -3(T_w - T_\infty)/2\delta_4 \\ c_3 &= 0 \\ d_3 &= (T_w - T_\infty)/2\delta_4^2. \end{aligned} \tag{12}$$

From dimensional considerations, the quantity, $\beta g(T_w - T_\infty)/6\nu\phi_4(x)[=] L^{-2}$, where L is a characteristic linear dimension. Since the effect of buoyancy is predominantly felt within the δ- region, then by implication, $\beta g(T_w - T_\infty)/6\nu\phi(x)\,[=]\,\delta_4^{-2}$. Incorporating this into Eqs. (11), we have, except a_4^*, the following modified local coefficients to be:

$$\begin{aligned} a_4^{**} &= a_4^* = 0 \\ b_4^{**} &= 1/\delta_4^2 ; \quad c_4^{**} = 3/\delta_4^2 \\ d_4^{**} &= 3/\delta_4^3 ; \quad e_4^{**} = 1/\delta_4^4. \end{aligned} \tag{13}$$

The local velocity field becomes:

$$u_4 = y/\delta_4 (1 - y/\delta_4)^3 \tag{14}$$

where $\delta_4 = J_4 x^{n_4}$. (15)

Substituting these local coefficients in Eq. (12) into the temperature Eq. (10) and normalising, gives:

$$\theta_{3/\theta_w} = 1 - \frac{3}{2}(y/\delta_4) + \frac{1}{2}(y/\delta_4)^3 \tag{16}$$

where $\theta = (T - T_\infty)/(T_w - T_\infty)$.

The assumed forms of u_4 and θ_3 are now substituted into the governing equations and integral analysis carried out for the momentum and energy transport equations. Also, utilizing the expressions for δ_4 and $\phi_4(x)$ yields, after simplification:

$$\begin{aligned} m_4 &= 1/2 \\ c_4 &= 5.29\nu(10/27 + \nu/\alpha)^{-1/2}(g\beta\theta_w/\nu^2)^{1/2} \end{aligned} \tag{17}$$

and

$$\begin{aligned} n_4 &= 1/4 \\ J_4 &= 3.76(10/27 + \nu/\alpha)^{1/4}(g\beta\theta_w)^{1/4}(\nu/\alpha)^{-1/2}. \end{aligned} \tag{18}$$

Hence,

$$\delta_{4/x} = 3.76\, Pr^{-1/2}(0.370 + Pr)^{1/4} Gr_x^{-1/4} \tag{19}$$

where $Pr = \nu/\alpha$ and $Gr_x = g\beta\theta_w x^3/\nu^2$, is the local Grashof number.

Local Nusselt Number. In order to compute the local Nusselt number, Nu_x, we proceed as follows. The local surface film heat transfer coefficient, h_x is given by:

$$h_x = q/\theta_w \tag{20}$$

where q is the local heat flux at wall and

$$q = k\theta_w/\delta_4 \tag{21}$$

where k is the thermal conductivity of the fluid. Therefore,

$$h_x = k/\delta_4. \tag{22}$$

From Eq. (19),

$$h_x = Pr^{\frac{1}{2}} Gr_x^{1/4}/3.76(0.370 + Pr)^{1/4}.$$

Hence,

$$Nu_x = \frac{h_x x}{k} = 0.399\ Pr^{\frac{1}{2}} Gr_x^{1/4}(0.370 + Pr)^{-1/4}. \tag{23}$$

The above procedure is repeated for other pairs of velocity and temperature profiles. The average heat transfer coefficient over a vertical plate of height H is given by

$$Nu_{0-H} = \frac{4}{3} Nu(x = H). \tag{24}$$

RESULTS AND DISCUSSION

Listed below are the results for the local Nusselt numbers for the stipulated pairs of velocity and temperature profiles. In general, the transition-to-turbulence Grashof number, Gr_x^* varies from 8.13×10^8 to 9.76×10^8.

1. Velocity Profile: Parabolic
   Temperature Profile: Linear

$$Nu_x = 0.420\ Pr^{\frac{1}{2}} Gr_x^{1/4}(0.667 + Pr)^{-1/4}. \tag{24}$$

2. Velocity Profile: Parabolic
   Temperature Profile: Parabolic

$$Nu_x = 0.562\ Pr^{\frac{1}{2}} Gr_x^{1/4}(2.220 + Pr)^{-1/4}. \tag{25}$$

3. Velocity Profile: Parabolic
   Temperature Profile: Cubic

$$Nu_x = 0.485\ Pr^{\frac{1}{2}} Gr_x^{1/4}(1.429 + Pr)^{-1/4}. \tag{26}$$

4. Velocity Profile: Cubic
   Temperature Profile: Linear

$$Nu_x = 0.370\ Pr^{\frac{1}{2}} Gr_x^{1/4}(0.317 + Pr)^{-1/4}. \tag{27}$$

5. Velocity Profile: Cubic
   Temperature Profile: Parabolic

$$Nu_x = 0.508\ Pr^{\frac{1}{2}} Gr_x^{1/4}(0.952 + Pr)^{-1/4}. \tag{28}$$

6. Velocity Profile: Cubic
   Temperature Profile: Cubic

$$Nu_x = 0.436\ Pr^{\frac{1}{2}} Gr_x^{1/4}(0.625 + Pr)^{-1/4}. \tag{29}$$

7. Velocity Profile: Quartic
   Temperature Profile: Linear

$$Nu_x = 0.334\ Pr^{\frac{1}{2}} Gr_x^{1/4}(0.196 + Pr)^{-1/4}. \tag{30}$$

8. Velocity Profile: Quartic
   Temperature Profile: Parabolic

$$Nu_x = 0.467\ Pr^{\frac{1}{2}} Gr_x^{1/4}(0.556 + Pr)^{-1/4}. \tag{31}$$

9. Velocity Profile: Quartic
   Temperature Profile: Cubic

$$Nu_x = 0.399\ Pr^{\frac{1}{2}} Gr_x^{1/4}(0.370 + Pr)^{-1/4}. \tag{32}$$

The empirical correlation of Wong is given by

$$Nu_x = 0.600\ (Gr_x\ Pr)^{1/4}[1 + (1+Pr^{-\frac{1}{2}})^2]^{-1/4}. \tag{33}$$

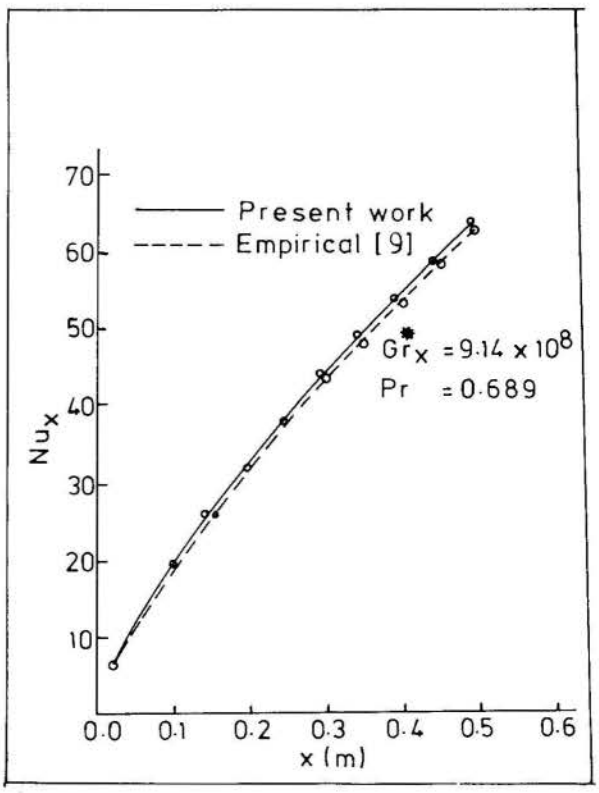

Fig. 2 Nu_x Vs. x(m) for parabolic velocity and temperature profiles for Air.

In Figs. 2-5, the plots of local Nusselt numbers for the best pairs of velocity and temperature profiles are shown together with that of empirical correlation in Wong. Fig. 2 illustrates the case of Prandtl numbers less than unity. Fig.3 shows the case for water whose Pr = 2.220. Figs. 4-5 represent the different pairs of velocity-temperature profiles for unused engine oil whose Prandtl number is 1050.

It can be seen from the figures that although the deviations of the computed local Nusselt numbers from those obtained from empirical correlations increases as Gr_x increases, the percentage deviations remain practically constant. Results also show that the best pairs of temperature-velocity profiles is significantly dependent on the heat transfer fluid considered. For example, while the best temperature-velocity profiles pair for low Pr, such as air and carbon dioxide, is parabolic-parabolic, the best pair for very high Pr, such as engine oil, is parabolic temperature and cubic velocity profiles.

However, if the general idea is to have a pair(s)

of profiles which will give a deviation which is less than 10% for a wide range of Prandtl numbers i.e., $0.689 \leq Pr \leq 1050$, Eqs. (28) and (31) will satisfy this requirement.

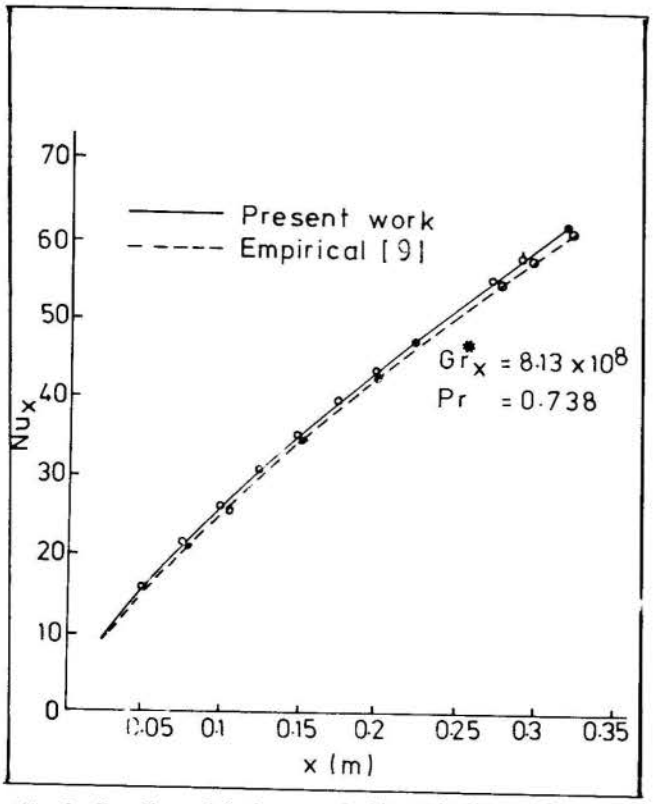

Fig.3 Nu_x Vs. x(m) for parabolic velocity and temperature profiles for CO_2.

To validate the results of the present work, we compute the two Pr limits of interest for the best pair of profiles. In the present case the best pair of profiles is as stipulated for Eq. (28).

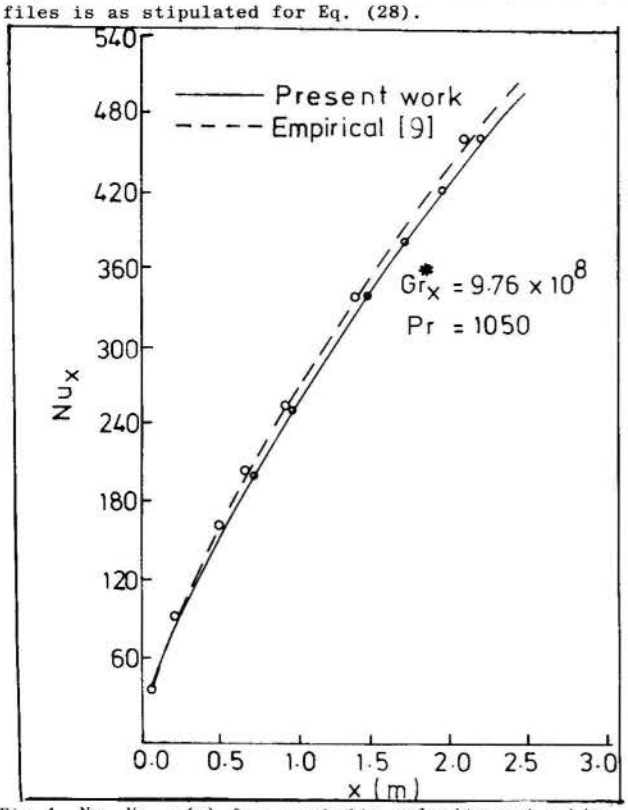

Fig.4 Nu_x Vs. x(m) for parabolic velocity and cubic temperature profiles for unused engine oil.

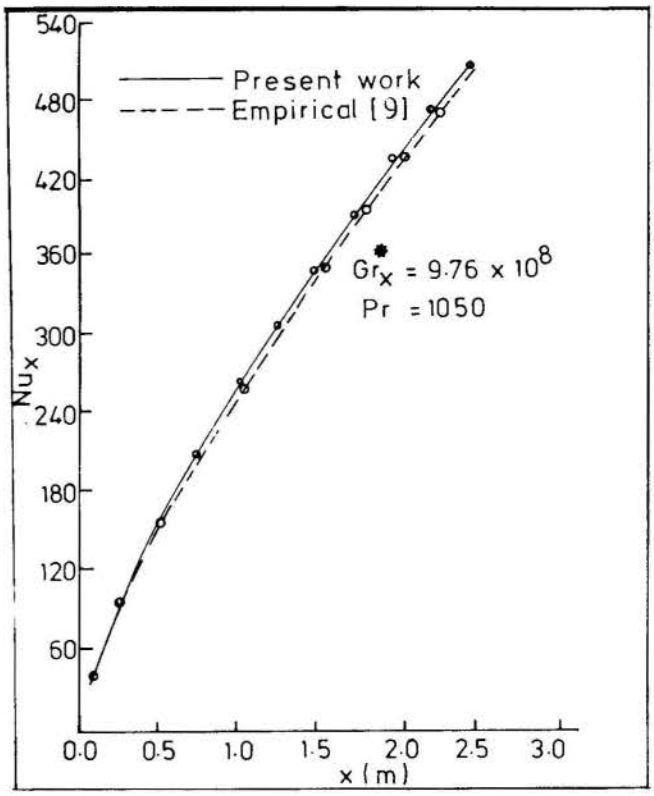

Fig.5 Nu_x Vs. x(m) for cubic velocity profile and parabolic temperature profile for unused engine oil.

For $Pr \to 0$, the asymptotic local Nusselt number is given by $0.514\,(Pr\,Ra_x)^{1/4}$. The dimensionless group, $Pr\,Ra_x = Bo_x$, is the Boussinesq number. For $Pr \to \infty$, the asymptotic Nusselt number is $0.508\,Ra_x^{1/4}$, where Ra_x is the Rayleigh number, $Pr\,Gr_x$.

The governing non-dimensional groups for the two Pr limits are in agreement with the scale analysis of Bejan. The asymptotic local Nusselt numbers compare well with those of Lefevre [10] as quoted by Bejan and recast here appropriately for ease of reference. Thus,

$$Nu_x = 0.6(Ra_x\,Pr)^{1/4} \quad \text{as} \quad Pr \to 0 \tag{34}$$

$$Nu_x = 0.503(Ra_x)^{1/4} \quad \text{as} \quad Pr \to \infty. \tag{35}$$

It is clear that the $Pr \to \infty$ limit results of Lefevre and the present work are very much in agreement. However, the $Pr \to 0$ results show a disparity of about 14% between the present analysis and that of Lefevre. We conclude that the polynomial approximation approach is not only simple but yields results that are as accurate as the similarity and empirical correlation results.

ACKNOWLEDGEMENT

The author wishes to acknowledge the assistance of Mr. N.I. Yusuf who carried out the numerical computations on the computer.

REFERENCES

[1] Jaluria, Y., "Buoyancy-induced flow due to isolated thermal sources on a vertical surface." ASME Journal of Heat Transfer, Vol.104, pp. 223-227, 1982.

[2] Jaluria, Y. and Gebhart, B., "Buoyancy-induced flow arising from a line thermal source on an

adiabatic vertical surface." International Journal of Heat, Mass Transfer, Vol.20, pp. 153-157, 1977.

[3] Sparrow, E.M. and Faghri, M., "Natural convection heat transfer from the upper plate of a colinear, separated pair of vertical plates." ASME Journal of Heat Transfer, Vol.102, pp. 623-629, 1980.

[4] Hardwick, N.E. and Levy, E.K., "Steady laminar free convection wake above an isothermal vertical plate." ASME Journal of Heat Transfer, Vol.95, pp. 289-294, 1973.

[5] Yang, K.T. and Jerger, E.W., "First-order perturbations of laminar free-convection boundary layers on a vertical plate." ASME Journal of Heat Transfer, Vol.86, pp. 107-115, 1964.

[6] Kelleher, M., "Free convection from a vertical plate with discontinuous wall temperature." ASME Journal of Heat Transfer, Vol.93, pp. 349-356, 1971.

[7] Carey, V.P., "A heat transfer correlation for natural convection from a vertical surface in cold water." ASME Journal of Heat Transfer, Vol.105, pp. 658-660, 1983.

[8] Bejan, A., "Convection Heat Transfer." John Wiley and Sons.

[9] Wong, H.Y., "Handbook of Essential Formula and Data on Heat Transfer for Engineers." 3rd Ed.

[10] Lefevre, E.J., "Laminar free convection from a vertical plane surface." Nineth International Congress of Applied Mechanics, Brussels, 1956.

III ENCIT – Itapema, SC (Dezembro 1990)

COMBINED NATURAL CONVECTION AND RADIATION HEAT TRANSFER IN A RECTANGULAR ENCLOSURE IN THE PRESENCE OF A POLYDISPERSION AND A NON-PARTICIPATING GAS

A. SANCHEZ A., J. M. HOUSE, and T. F. SMITH

Department of Mechanical Engineering
The University of Iowa
Iowa City, Iowa 52242-1585, USA

SUMMARY

In this investigation, combined heat transfer due to natural convection and radiation in a vertical rectangular enclosure containing a fluid with a polydispersion is studied. The four walls are assumed to be gray, and diffusely emitting and reflecting. The fluid within the enclosure walls consists of a radiatively transparent gas with water droplets. The water droplets absorb, emit, and scatter radiation. A finite control volume formulation and a two-dimensional discrete ordinates method were used to solve the governing equations. Results are presented to illustrate the effects of radiative heat transfer on the natural convection flow pattern within the enclosure and the heat transfer across the vertical walls.

INTRODUCTION

The problem of combined convection and radiation heat transfer in the presence of polydispersions has received particular attention in applications related to the cooling system of fast reactors, combustion chambers, and environmental processes. Recently, the need to cool electronic equipment in sealed enclosures has added interest to the field.

A similarity relationship was derived by Close and Sheridan [1] for the study of natural convection in enclosures filled with a saturated gas-vapor mixture in the presence of a polydispersion of fine water droplets (a fog). Radiation, however, was not included in that study.

Recent studies of combined natural convection and radiation in rectangular cavities show that the topics of interaction of surface radiation and gray gas participation with natural convection in the absence of scattering have been fairly covered [2-6]. Although it is known to over predict the interaction of natural convection and radiation, most of the work done has been based on the P-1 approximation [4, 7-11]. In one case, a one-dimensional radiation model [5] was used. In only a few cases, the effects of isotropic scattering and non-gray gas (using different spectral techniques) have been examined (mainly CO_2) [7-12]. The method of discrete ordinates has seldom been used in these types of problems [6]. A recent method [13] has yet to be fully tested in situations involving convection-radiation problems. To the best of our knowledge, the complete problem of interaction of natural convection with radiation in rectangular enclosures in the presence of an anisotropically scattering medium remains an unsolved problem. Furthermore, the discrete ordinates method (more accurate than the P-1 approximation) has only been used, in these type of problems, to solve the basic case of participating gray media.

It is of interest to study the effect, normally neglected, of the polydispersion in the overall heat transfer process when radiation is considered. In this paper, the combined effect of natural convection and radiation heat transfer is studied for a two-dimensional rectangular enclosure containing a non-participating gas that is saturated with a Mie-anisotropically scattering polydispersion. Following the work of Close and Sheridan, the equations of conservation of mass, momentum, and energy are rewritten in a form similar to those for a single component. After discretization of the control volume, the resulting elliptic problem is solved by means of an iteration procedure involving a finite control volume analysis and a two-dimensional radiation analysis using the discrete ordinates method. The radiative properties of the droplet cloud are calculated using the Mie theory.

Results showing the relative effects of considering convection alone, combined radiation and convection, and the presence or not of a radiatively participating medium are presented.

ENCLOSURE DESCRIPTION

The system under study is shown in Fig. 1 and consists of a square enclosure with sides of length L. The vertical walls are isothermal at temperatures T_h and T_c, where $T_h > T_c$, and the horizontal walls are adiabatic. The enclosure walls are gray and diffusely emitting and reflecting. The fluid within the enclosure consists of a saturated air-water vapor mixture that is assumed to be radiatively transparent gas and water droplets. The water droplets absorb, emit, and scatter radiation, where the scattering is anisotropic. The flow is laminar, and gravitational acceleration acts parallel to the isothermal walls. Except for the mixture density in the buoyancy term, the mixture properties are assumed to be constant, and the Boussinesq approximation applies. At a given spatial location, the mixture and water droplets are assumed to have the same velocity and temperature. The characteristics of the water droplets are described later.

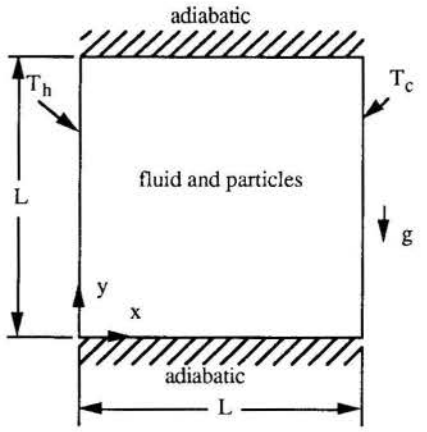

Fig. 1 Schematic of enclosure.

CONSERVATION EQUATIONS

Conservation Equations for a Single Component Fluid. The steady-state conservation equations for a single component fluid in dimensionless form are as follows [14]:

Continuity:

$$\frac{\partial}{\partial \xi}\left(\bar{u}\right) + \frac{\partial}{\partial \eta}\left(\bar{v}\right) = 0 \qquad (1)$$

x-momentum:

$$\frac{\partial}{\partial \xi}\left(\bar{u}\,\bar{u}\right) + \frac{\partial}{\partial \eta}\left(\bar{u}\,\bar{v}\right) = \Pr\left[\frac{\partial}{\partial \xi}\left(\frac{\partial \bar{u}}{\partial \xi}\right) + \frac{\partial}{\partial \eta}\left(\frac{\partial \bar{u}}{\partial \eta}\right)\right] - \frac{\partial \bar{P}}{\partial \xi} \qquad (2)$$

y-momentum:

$$\frac{\partial}{\partial\xi}\left(\bar{v}\,\bar{u}\right)+\frac{\partial}{\partial\eta}\left(\bar{v}\,\bar{v}\right)=\Pr\left[\frac{\partial}{\partial\xi}\left(\frac{\partial\bar{v}}{\partial\xi}\right)+\frac{\partial}{\partial\eta}\left(\frac{\partial\bar{v}}{\partial\eta}\right)\right]-\frac{\partial\bar{P}}{\partial\eta}$$

$$+\,\mathrm{Ra}\,\Pr\,\theta \quad (3)$$

Energy:

$$\frac{\partial}{\partial\xi}\left(\bar{u}\,\theta\right)+\frac{\partial}{\partial\eta}\left(\bar{v}\,\theta\right)=\frac{\partial}{\partial\xi}\left(\frac{\partial\theta}{\partial\xi}\right)+\frac{\partial}{\partial\eta}\left(\frac{\partial\theta}{\partial\eta}\right)-\frac{\bar{Q}}{\bar{N}\,(\psi_h\,-\,1)} \quad (4)$$

where ξ and η are dimensionless distances in the x and y directions, respectively; the velocities are normalized with α/L; the pressure is normalized with $\rho\,\alpha^2/L^2$; θ is given by $(T - T_c)/(T_h - T_c)$; Pr is the Prandtl number, Ra is the Rayleigh number; $\bar{N}$ is the conduction to radiation ratio $(k/L\,\sigma\,T_c^3)$; and $\psi = T/T_c$. The fluid properties are denoted by ρ for density, α for thermal diffusivity, and k for thermal conductivity. T is the temperature of the fluid. In Eq. (4), the dimensionless divergence of the radiative heat flux is represented by $\bar{Q}$ $(= L\,\nabla\cdot q_r/\sigma\,T_c^4)$, where q_r is the radiative heat flux vector and σ is the Stefan-Boltzmann constant.

The flow boundary conditions are zero velocities at all surfaces. The thermal boundary conditions become at

$$\xi = 0,\ \theta = 1\ ;\ \xi = 1,\ \theta = 0 \quad (5)$$

$$\eta = 0,\ \frac{\partial\theta}{\partial\eta}=\frac{\bar{q}_r(0)}{\bar{N}\,(\psi_h\,-\,1)}\ ;\ \eta = 1,\ -\frac{\partial\theta}{\partial\eta}=\frac{\bar{q}_r(1)}{\bar{N}\,(\psi_h\,-\,1)} \quad (6)$$

where the dimensionless radiant surface flux is $\bar{q}_r$ $(= L\,q_r/\sigma\,T_c^4)$.

Conservation Equations for the Mixture. The same equations presented for a single component fluid apply to the mixture provided that saturated conditions exist throughout the cavity, that the cloud of droplets (with the characteristics of a fog) circulates within the gas, and that the effect of the liquid droplets on density and viscosity is negligible. Under these circumstances, the properties and dimensionless groups of the equivalent single component fluid are evaluated as [1,15,16]:

Thermal conductivity: $$k = k_m + \rho_m(1+m)\,D\,h_{fg}\frac{d}{dT}\left(\frac{m}{1+m}\right) \quad (7)$$

Specific heat: $$C = \frac{dh_m}{dT} - h_l\frac{dm}{dT} + \frac{\rho_l}{\rho_d}\frac{dh_l}{dT} \quad (8)$$

Thermal expansion coefficient: $$\frac{\chi}{\chi_m}=\left[1-\frac{m\,(M_v - M_d)}{1+m}\,\frac{h_{fg}}{R\,T}\right] \quad (9)$$

where subscripts m, l, d, and v denote mixture without mass transfer, liquid, non-condensing component, and vapor, respectively; m is the mass ratio of vapor to non-condensing component; D is the diffusivity of gas-vapor mixture; h_{fg} is the enthalpy of vaporization; M stands for molecular weight; and R is the universal gas constant.

Prandtl number: $$\Pr = \frac{\rho_d\,C\,\nu_m}{k} \quad (10)$$

where ν is the kinematic viscosity.

Rayleigh number: $$\mathrm{Ra} = \frac{g\,\chi\,\Delta T\,L^3}{\nu_m\,\alpha} \quad (11)$$

The properties for the mixture were evaluated using the mass ratio and the individual properties of the vapor and the non-condensing component.

Heat Transfer. The overall heat transfer across the enclosure is expressed in terms of the overall Nusselt number defined by

$$\mathrm{Nu_t} = \mathrm{Nu_c} + \mathrm{Nu_r} \quad (12)$$

The average Nusselt number for natural convection is expressed by

$$\mathrm{Nu_c} = -\int_0^1 \left.\frac{\partial\theta}{\partial\xi}\right|_{\xi=0} d\eta \quad (13)$$

and the average radiation Nusselt number is evaluated from

$$\mathrm{Nu_r} = \frac{1}{\bar{N}\,(\psi_h\,-\,1)}\int_0^1 \bar{q}_r(\eta)\,d\eta \quad (14)$$

At the cold wall, the minus sign is omitted for the natural convection relation and inserted for the radiation relation. By conservation of energy across the cavity, the overall Nusselt numbers at the hot and cold walls must be equal. Note that although an attempt has been made to separate the overall Nusselt number contributions due to natural convection and radiation, $\mathrm{Nu_c}$ is nonetheless dependent on $\mathrm{Nu_r}$, that is, radiant exchange within the enclosure affects the temperature of the adiabatic walls and, therefore, the velocity fields. In turn, the velocity fields affect the temperature gradients at the isothermal walls that are used in the calculation of $\mathrm{Nu_c}$.

RADIATION MODEL

One of the motivations of this paper is to study the influence of a cloud of particles, namely, a fog of water droplets, on the overall heat transfer processes that take place in the enclosure when radiative transfer and natural convection are considered simultaneously. For this purpose, the gas mixture is considered non-participating and, therefore, all the radiation effects are due to surface radiation and to the presence of the polydispersion. The radiation problem to be solved is a two-dimensional problem in the presence of an absorbing, emitting, and anisotropically scattering media surrounded by gray, diffuesely emitting and reflecting walls.

The monochromatic problem. The governing equation of monochromatic radiative transfer is [17]

$$\mu\frac{dI}{dx}+\delta\frac{dI}{dy}+\gamma\frac{dI}{dz}=-\beta\,I+(1-\omega_o)\,\beta\,I_b + \frac{\omega_o\,\beta}{4\pi}\int_0^{4\pi} I(\zeta,\omega_i)\,\Phi(\lambda,\omega,\omega_i)\,d\omega_i \quad (15)$$

where μ, δ, and γ are direction cosines; I is the radiant intensity; β is the extinction coefficient; I_b is the blackbody intensity; ω_o is the single scattering albedo; ζ is the line of sight of incident radiation; ω_i is the incident solid angle; and Φ is the scattering phase function. Unless otherwise noted, all radiant energy and property quantities are understood to be monochromatic. The discrete ordinates method [18-20] was used to solve Eq. (15) for the intensity. For this method, Eq. (15) is discretized and rewritten, for two-dimensions, as:

$$I_i^p = \frac{|\mu_i|\,A_{n,s}\,I_i^{xr} + |\delta_i|\,A_{e,w}\,I_i^{yr} + a_r\,(S_1+S_2)\,\Delta V_p}{|\mu_i|\,A_{n,s} + |\delta_i|\,A_{e,w} + a_r\,\beta\,\Delta V_p} \quad (16)$$

subject to:
$$I_i^p = a_r\,I_i^{xe} + (1-a_r)\,I_i^{xr} = a_r\,I_i^{xe} + (1-a_r)\,I_i^{yr} = a_r\,I_i^{ze} + (1-a_r)\,I_i^{zr} \quad (17)$$

where: $$S_1 = (1-\omega_o)\,\beta\,I_b^p \quad \Rightarrow \quad S_1 = a\,I_b^p \quad (18)$$

$$S_2 = \frac{s}{4\pi} \sum_j w_j I_i^p \Phi_{ij} \qquad (19)$$

In Eqs. (16) to (19), s is the scattering coefficient; a is the absorption coefficient (= β - s); a_r is the spatial interpolating weight; w_j are the weights for the integration procedure; $A_{n,s}$, $A_{e,w}$, and ΔV_p are, respectively, the north-south and east-west areas and the volume of the grid element, where Eq. (16) is being applied; I_i^p is the outgoing intensity in the discrete direction i at the center (p) of that grid element; and superscripts xr and xe indicate reference (where energy originates) and end (where energy arrives) faces for the coordinate direction x.

The phase function is represented in terms of Legendre polynomials of order k:

$$\Phi_{ij} = \sum_{k=0}^{N} (2n+1)\, b_k\, P_k(\mu_i\mu_j, \delta_i\delta_j, \gamma_i\gamma_j) \qquad (20)$$

where b_k are coefficients for the series expansion of the phase function in terms of Legendre polynomials P_k and N is the number of terms.

The boundary conditions for Eq. (16) are at

$$x = 0 \qquad I_i = \varepsilon I_b + \frac{(1-\varepsilon)}{\pi} \sum_{\mu_j < 0} w_j |\mu_j| I_j \qquad \text{for } \mu_i > 0 \qquad (21a)$$

$$x = L \qquad I_i = \varepsilon I_b + \frac{(1-\varepsilon)}{\pi} \sum_{\mu_j > 0} w_j \mu_j I_j \qquad \text{for } \mu_i < 0 \qquad (21b)$$

$$y = 0 \qquad I_i = \varepsilon I_b + \frac{(1-\varepsilon)}{\pi} \sum_{\delta_j < 0} w_j |\delta_j| I_j \qquad \text{for } \delta_i > 0 \qquad (21c)$$

$$y = L \qquad I_i = \varepsilon I_b + \frac{(1-\varepsilon)}{\pi} \sum_{\delta_j > 0} w_j \delta_j I_j \qquad \text{for } \delta_i < 0 \qquad (21d)$$

where ε is the surface emittance. The summations in Eq. (21) are performed over the incoming directions for each surface.

The net radiation fluxes leaving the enclosure walls are evaluated at

$$x = 0 \text{ and } x = L \qquad q_{r,x} = \sum_j w_j \mu_j I_j \qquad (22a)$$

$$y = 0 \text{ and } y = L \qquad q_{r,y} = \sum_j w_j \delta_j I_j \qquad (22b)$$

The divergence of the radiative flux for each control volume is calculated from

$$\nabla \cdot q_r = a\left(4\pi I_b^p - \sum_j w_j I_j\right) \qquad (23)$$

The spectral integration problem. Equation (16) is formulated for a single wavelength (or a gray media). In order to account for the spectral variation of optical properties, an integration of Eq. (16) over the entire spectrum is needed. To this effect, the spectrum was divided into M rectangular wavelength bands, where the radiative properties, evaluated at the wavelength (λ) corresponding to the center of each band, are assumed constant over each band. Integrated quantities are found as the summation over all bands of the individual contributions for each band. Equations (22) and (23) become at

$$x = 0 \text{ and } x = L \qquad q_r(y) = \sum_{\lambda=1}^{M} \left(\sum_j w_j \mu_j I_j\right)_\lambda \qquad (24a)$$

$$y = 0 \text{ and } y = L \qquad q_r(x) = \sum_{\lambda=1}^{M} \left(\sum_j w_j \delta_j I_j\right)_\lambda \qquad (24b)$$

The boundary conditions in Eq. (24) are combined with those in Eq. (6) to evaluate the temperature distribution along the horizontal walls. The total divergence of the radiative flux is calculated from summing Eq. (23) over all bands to yield

$$\nabla \cdot q_r = \sum_\lambda \left[a\left(4\pi I_p^b - \sum_j w_j I_j\right)\right]_\lambda \qquad (25)$$

A computer program (an S-4 implementation of the discrete ordinates method) was written to solve Eqs. (16) to (23) subject to the boundary conditions given by Eq. (21) and to perform the spectral integration.

WATER DROPLET PROPERTIES

Number distribution. The cloud of droplets is assumed to have the number distribution characteristics shown in Fig. 2, where n is the number of particles of radius r, N is the total number of particles per unit volume, and w is is the water content. The particle number density is given by the following relation:

$$n = 3.52\, r^3\, e^{-2r/3} \qquad (26)$$

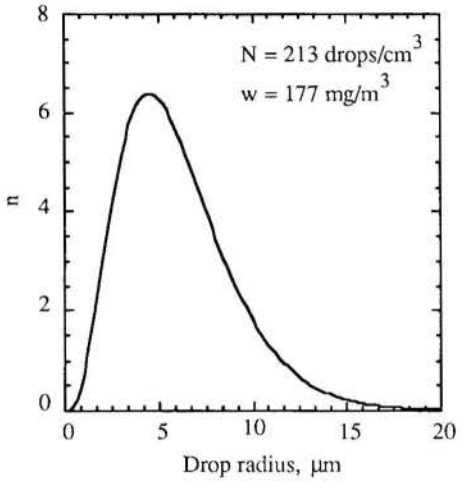

Fig. 2 Characteristics of the polydispersion.

Table 1. Spectral Data

Wavenumber Range, cm^{-1}			Scattering Coefficient, m^{-1}	Extinction Coefficient, m^{-1}
0→	189	0.0	0.0	
189	→	211	0.00726	0.02394
211	→	236	0.00815	0.02442
236	→	268	0.00957	0.02575
268	→	310	0.01246	0.02915
310	→	367	0.01557	0.03382
367	→	450	0.01790	0.03816
450	→	583	0.01939	0.04071
583	→	833	0.01418	0.03401
833	→	1500	0.02050	0.03069
1500	→	2500	0.03214	0.03903
500	→	∞	0.0	0.0

Under this conditions, the polydispersion has characteristics similar to those of a fog [21].

Optical properties and wavelength discretization. The spectrum was subdivided into twelve bands as shown in Table 1 (M = 12). Detailed calculations were performed for ten of those bands, concentrated in the region between 5 and 50 μm, where most of the radiant energy is concentrated. For each one of these bands, and for the polydispersion represented in Fig. 2, the parameters of interest are calculated from the following relations:

$$\beta = \int_{r_{min}}^{r_{max}} \sigma_{ext}(r) \frac{dn(r)}{dr} dr \quad (27)$$

$$s = \int_{r_{min}}^{r_{max}} \sigma_{sca}(r) \frac{dn(r)}{dr} dr \quad (28)$$

$$\Phi(\theta) = \frac{1}{s} \int_{r_{min}}^{r_{max}} \sigma_{sca}(r)\, \Phi(\theta,r) \frac{dn(r)}{dr} dr \quad (29)$$

The extinction (σ_{ext}) and scattering (σ_{sca}) cross-sections were evaluated from the exact Mie calculations, for a single water droplet of radius r, using wavelength dependent refractive and absorpive

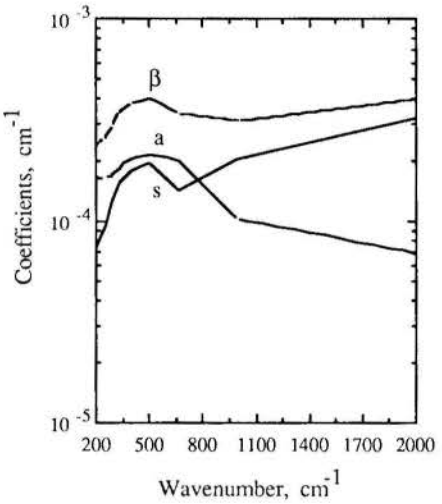

Fig. 3 Volume extinction, absorption, and scattering coefficients for the polydispersion.

indices tabulated by Kondratyev [22] and the computational procedure of Dave [23]. Expansion of the phase function in a series of Legendre polynomials to find the b_k terms in Eq. (20) was performed by means of a procedure similar to that described by Kumar [24].

Results of applying Eqs. (27) to (29) to the polydispersion presented in Fig. 2 are shown in Fig. 3 and Table 1. A qualitative comparison with similar results evaluated by Curran [25] for a C-1 cloud shows excellent agreement.

NUMERICAL PROCEDURE

Numerical solutions for the fluid flow and temperature patterns were obtained using the control-volume formulation and the SIMPLER algorithm described by Patankar [26]. The distribution of the control volumes were skewed along all surfaces in order to resolve accurately large velocity and temperature gradients. The control volumes for the flow and radiation models were identical. Convergence of the numerical solution was checked by performing overall mass and energy balance.

With the exception of the radiation model, where the divergence of the radiative flux given by Eq. (25) is treated as a heat sink term, the code is identical to that used by House, et al. [14]. The accuracy of the calculations for mixture velocities and temperatures is identical to that reported in the cited literature, and is not repeated here.

The resulting computer code for the radiation model was tested, where possible, against known results from other authors [13, 27-29]. With the exception of cases involving highly reflecting wall, where the code (as reported for other S-4 discrete ordinates implementations [27]) tends to over predict irradiations, the results obtained were always very good. Constant wall emittances of 0.8 are used in the present work and, therefore, very good results for both heat fluxes and irradiations can be expected. As an example of the accuracy of the radiation model, representative results for the nondimensional heat transfer rate at the hot surface are displayed in Fig. 4 for an square enclosure containing an isotropically scattering, non-absorbing medium. For the two cases presented (black and gray walls) the emissive power is one for the hot wall and zero for the other walls. The notation of ANDISORD refers to the current radiation model. Tests were performed to check the correct coding of the spectral problem. For these tests, results from a single band problem were compared with the results obtained after subdividing the single band into several rectangular partial bands and integrating. The results were in good agreement.

Convective Nusselt numbers, under the effects of radiation, at the hot and cold wall of a black square enclosure containing a non-scattering gray medium have been recently reported by Kassemi [30]. The combined radiation-natural convection code used in this study was tested against Kassemi [30]. The results of these tests show discrepancies, particularly for the convective Nusselt numbers at the cold wall. These discrepancies accentuate, and become significant, as radiation becomes the dominant mode of heat transfer. Unfortunately, Kassemi does not report radiation Nusselt numbers, and, therefore, energy conservation can not be verified. In all the cases tested with the present model, conservation of energy was satisfied.

Although not required to be, the grids for the flow and radiation models are identical. The results reported were produced using a nonuniform grid with 40 control volumes in each of the x- and y-directions. The grid generation algorithm placed a greater number of control volumes nearer to the surfaces where large gradients occur.

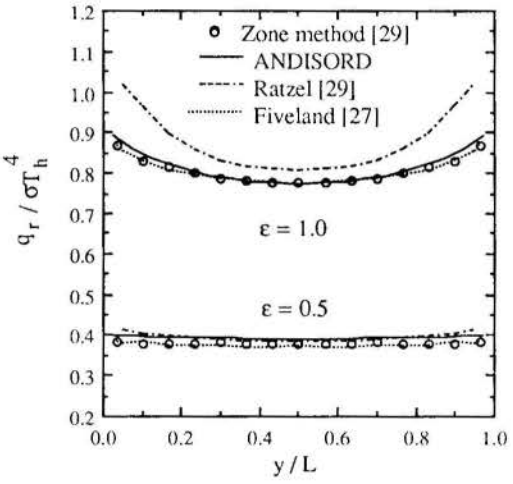

Fig. 4 Radiation model comparisons.

The computations were performed on an ENCORE computer system.

RESULTS AND DISCUSSION

Cases. Two sets of problems were solved, each set consisting of four cases: convection only for pure air, convection only for the mixture air-vapor, convection plus wall radiation for the mixture, and convection plus radiation with the mixture as a participating medium. For both set of problems the length of the cavity was 0.15 m, the average temperature was 300 and 350 K for sets I and II respectively, and the temperature difference between the hot and the cold wall was 5 K. The other properties are given in Table 3.

Table 3. Properties*.

	Air			Mixture		
Set	Pr	Ra, 10^6	k_d, 10^{-3}	Pr	Ra, 10^5	k
I	0.707	1.54	26.3	1.284	15.27	0.1304
II	0.700	1.08	30.0	0.404	8.48	1.8680

* Units for k are W/m-K

Streamlines and isotherms. Figures 5–8 show the streamlines and isotherms obtained from the solution of the two sets of problems

described above. For both convection plus wall radiation for the mixture, and convection plus radiation with the mixture as a participating medium, the streamlines and isotherms are similar, and therefore, only one set is presented. The streamlines and isotherms for air alone are available elsewhere [14] and are not repeated here.

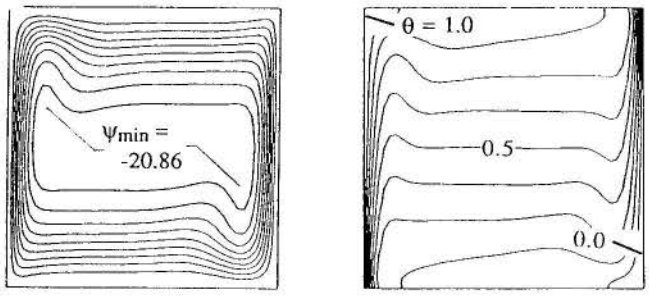

(a) Streamlines (b) Isotherms

Fig. 5 Set I. Mixture. Natural convection alone.

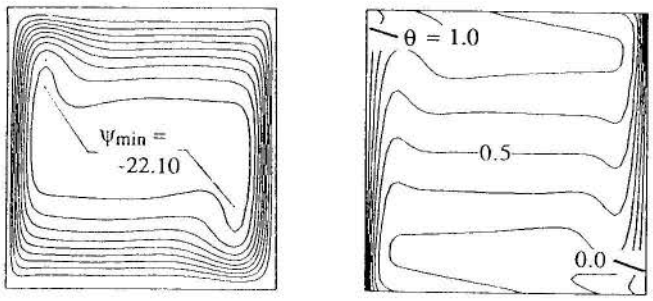

(a) Streamlines (b) Isotherms

Fig. 6 Set I. Mixture. Natural convection–surface radiation.

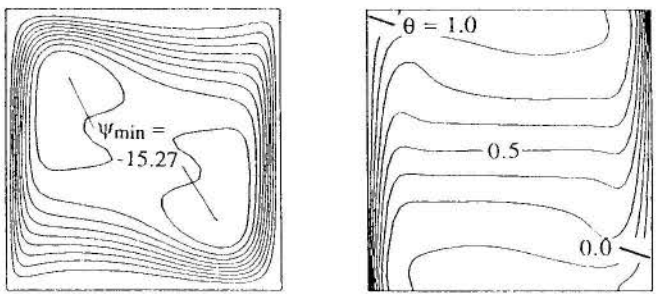

(a) Streamlines (b) Isotherms

Fig. 7 Set II. Mixture. Natural convection alone.

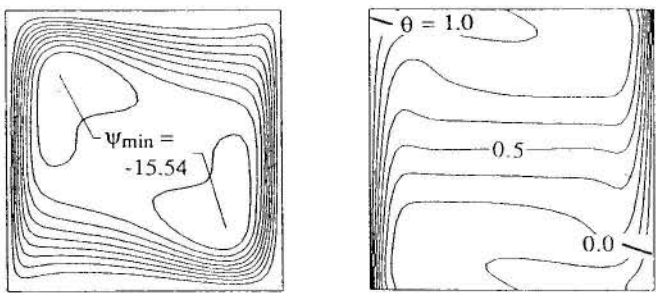

(a) Streamlines (b) Isotherms

Fig. 8 Set II. Mixture. Natural convection–surface radiation.

In Figures 5-8, Ψ_{min} is the minimum stream function value. Eleven equally spaced isotherms or stream functions are shown in each plot. In all the cases presented, the temperature and flow fields show symmetry and boundary layer characteristics. These results are due to the weak absorbing characteristics of the mixture, the small temperature difference, and the assumption of constant properties throughout the enclosure. When surface radiation is present, (Figures 6 and 8), the characteristic "s" curves appear as a consequence of the radiation exchange at the insulated walls.

Nusselt numbers. Tables 4 and 5 show the Nusselt numbers obtained from the solution of the two sets of problems given in Table 3. Results of applying Eq. (31) (a commonly used correlation [31] for problems involving natural convection alone), are given , for comparison purposes, in Table 4. Recalling the sharp difference in thermal conductivity between air and mixture shown in Table 3, it can be inferred from table 4, that the presence of the mixture produces a drastic improvement in the heat transfer by natural convection.

$$Nu_c = 0.18\left(\frac{Pr}{0.2 + Pr}\,Ra\right)^{0.29} \qquad (31)$$

Table 4. Nusselt numbers for natural convection alone.

	Air		Mixture	
Set	Eq. (31)	This study.	Eq.(31)	This study.
I	10.43	9.97	10.72	10.21
II	9.40	9.03	8.392	8.09

Table 5. Nusselt numbers for the mixture.

Set	With surface radiation.			With surface radiation and participating media		
	Nu_c	Nu_r	Nu_t	Nu_c	Nu_r	Nu_t
	Hot wall					
I	9.498	3.543	13.04	9.502	3.547	13.05
II	7.962	0.395	8.357	7.963	0.395	8.359
	Cold wall					
I	9.522	3.519	13.04	9.532	3.516	13.05
II	7.965	0.393	8.357	7.966	0.392	8.359

As reported by other authors [12], Nu_c at the cold wall is always higher than Nu_c at the hot wall when radiation is present. Tables 4 and 5 show that Nu_c at the hot wall, for combined radiation-natural convection, is always smaller than Nu_c for natural convection alone. This result has been reported previously [12] for gray gases, and for the range of Rayleigh numbers used in this study.

For the first set of problems (I), radiation accounts for approximately 27% of the total heat exchange, while for the second set of problems (II), the contribution of radiation to the total heat exchange is less than 5%. This relatively small influence of the radiation on the overall heat exchange [8,12] is due to the temperature difference ratio (Ψ_h -1) which, in set I, is in the order of 0.017 and in set II, in the order of 0.014.

It can be seen in Table 5 that the influence of the participating medium (polydispersion) in the overall heat exchange is negligible. This is due to the small water content (177 mg/m^3) and insignificant optical thickness for the problems under consideration. Similar behavior has been reported [32] for sodium droplets in the same domain of optical thickness and droplet distribution.

That energy is conserved in the numerical procedure can be verified from total Nusselt numbers at the hot and cold walls.

CONCLUSIONS

In this paper, the combined effect of natural convection and radiation heat transfer were studied for a two-dimensional rectangular enclosure containing a non-participating gas that is saturated with a Mie-anisotropically scattering polydispersion. Following the work of Close and Sheridan, limitations were imposed on temperature difference and liquid water content and the equations of conservation of mass, momentum, and energy were rewritten in a form similar to those for a single component. A finite control volume analysis and a two-dimensional radiation model using the discrete ordinates method were used to solve the governing equations. The radiative properties of the droplet cloud were calculated using the Mie theory.

The results of this study show that natural convection is highly enhanced when the mixture is present; the contribution of radiation to the overall heat exchange decreases rapidly with increasing average

temperature (for the imposed temperature difference of 5 K, surface radiation accounts for less than 30% of the total heat transfer when the average temperature is 300 K and less than 5% when the average temperature is 350 K); for the water content and droplet size distribution required for this study, the polydispersion has negligible influence on the radiation process.

Flow and temperature patterns, as well as Nusselt numbers, show qualitative agreement with other studies. Quantitative comparisons with similar studies are impossible at this point, due to the lack of published work in this area.

The methodology and computer codes described in this work represent a powerful tool for the study of combined radiation-natural convection heat transfer in the presence of particulate media.

ACKNOWLEDGMENTS

The first author would like to acknowledge the financial support received from Universidad de los Andes and Fundación Gran Mariscal de Ayacucho, both from the Republic of Venezuela.

REFERENCES

[1] Close, D. J. and J. Sheridan, "Natural Convection in Enclosures Filled with a Vapor and a Non-Condensing Gas," Int. J. Heat Transfer, Vol.32, pp. 855-862, 1989.

[2] Kim, D. M. and R. Viskanta, "Effect of Wall Conduction and Radiation on Natural Convection in a Rectangular Cavity," Numerical Heat Transfer, Vol. 7, pp. 449-470, 1984.

[3] Kurosaki, Y., H. Mishina, and T. Kashiwagi, "Heat Transfer Combined with Radiation and Natural Convection in a Rectangular Enclosure," 7th. Int. Heat Transfer Conf., Vol. 2, pp. 215-220, 1982.

[4] Lauriat, G., "Combined Radiation-Convection in Gray Fluids Enclosed in Vertical Cavities," J. of Heat Transfer, Vol. 104, pp. 609-615, 1982.

[5] Webb, B. W. and R. Viskanta, "Analysis of Radiation-Induced Natural Convection in Rectangular Enclosures," J. Thermophysics and Heat Transfer, Vol. 1, pp. 146-153, 1987.

[6] Yucel, A., S. Acharya, and M. L. Williams, "Combined Natural Convection and Radiation in Square Enclosures," ASME Proceedings of the 1988 National, Heat Transfer Conf., ed. H. R. Jacobs, HTD-Vol. 96, pp. 209-218, 1988

[7] Desrayaud, G., "Radiative Influence on the Stability of Fluids Enclosed in Vertical Cavities," Int. J. Heat Mass Transfer, Vol. 31, pp. 1035-1048, 1988.

[8] Fusegi, T. and B. Farouk, "Radiation-Convection Interactions in Asymmetrically Heated Square Enclosures," Numerical Methods in Heat Transfer, eds. J. L. S. Chen and K. Vafai, ASME HTD-Vol. 62, pp. 81-88, 1986.

[9] Fusegi, T. and B. Farouk, "Interaction Analysis of Natural Convection and Surface/Gas Radiation in Square Cavity," Num. Methods in Thermal Prob, Vol. VI, part A, pp. 588-599, 1989.

[10] Fusegi, T. and B. Farouk, "Laminar and Turbulent Natural Convection-Radiation Interactions in a Square Enclosure Filled with a Nongray Gas," Numerical Heat Transfer, Vol. 15, part A, pp. 303-322, 1989.

[11] Lauriat, G., "Numerical Study of the Interaction of Natural Convection with Radiation in Nongray Gases in a Narrow Vertical Cavity," 7th. Int. Heat Transfer Conf., Vol. 2, pp. 153-158, 1982.

[12] Zhong, Z. Y., K. Y. Yang and J. R. Lloyd, "Variable-Property Natural Convection in Tilted Enclosures with Thermal Radiation," Numerical Methods in Heat Transfer, ed. Lewis, R. W.,Vol. III, pp. 195-214, Wiley, New York,1985.

[13] Raithby, G. D. and E. H. Chui, "A Finite-Volume Method for Predicting a Radiant Heat Transfer in Enclosures with Participating Media," J. of Heat Transfer, Vol. 112, pp. 415-423, 1990.

[14] House, J. M., C. Beckermann, and T. F. Smith, "Effect of a Centered Conducting Body on Natural Convection Heat Transfer in an Enclosure," accepted for publication in Numerical Heat Transfer, Part A, 1990.

[15] Close, D. J., "Natural Convection with Coupled Mass Transfer in Porous Media," Int. Comm. Heat Mass Transfer, Vol. 10, pp. 465-476, 1983.

[16] Close, D. J. and M. K. Peck, "Experimental Determination of the Behavior of Wet Porous Beds in which Natural Convection Occurs," Int. J. Heat Mass Transfer, Vol. 29, pp. 1531-1541, 1986.

[17] Siegel, R. and J. R. Howell, "Thermal Radiation Heat Transfer", Hemisphere Publishing Corporation, New York, 1981.

[18] Fiveland, W. A., "Discrete Ordinates Methods for Radiative Heat Transfer in Isotropically and Anisotropically Scattering Media," J. Heat Transfer, Vol. 109, pp. 809-812, 1987.

[19] Sánchez, A., W. Krajewski and T. F. Smith, "Statistical Framework for Validation of Satellite-Based Global Precipitation Simulation; Part I: An Atmospheric Radiation Model — The Plane Layer Case", Progress report prepared for Grant NA89AA-D-AC195 for National Oceanic and Atmos. Admin., 1990.

[20] Truelove, J. S., "Three-Dimensional Radiation in Absorbing-Emitting-Scattering Media Using the Discrete-Ordinate Approximation," J. Quant. Spectrosc. Radiat. Transfer, Vol. 19, pp. 27-31, 1988.

[21] Jiusto, J. E., "Fog Structure," Clouds, their Formation, Optical Properties, and Effects, Hobbs and Deepak ed. Academic Press, New York, 1981.

[22] Kondratyev, K. Y., "Radiation in the Atmosphere", Academic Press, New York, 1969.

[23] Dave, J. V., Report # 320-3237, IBM Scientific Center , Palo Alto, California, 1968.

[24] Kumar, S., "Radiative Transport in an Absorbing/Anisotropically Scattering Medium Exposed to a Collimated Incident Flux – an Analytical Solution by the Method of Singular Eigenfunction Expansions", Ms. Thesis, The State University of New York, Buffalo, 1984.

[25] Curran, R. J., "Variation of Cloud Emissivity in the Infrared," Conference in Atmospheric Radiation, Amer. Met. Soc., pp. 103-107, 1972.

[26] Patankar, S. V., "Numerical Heat Transfer and Fluid Flow", Hemisphere, Washington, 1980.

[27] Fiveland, W. A., "Discrete-Ordinates Solutions of the Radiative Transport Equation for Rectangular Enclosures," J. of Heat Transfer, Vol. 106, pp. 699-706, 1984.

[28] Kim, T.-K. and H. Lee, "Two-Dimensional Radiative Transfer in Mie-Anisotropic Scattering Media: S-N Discrete Ordinates Solution," Symposium on Heat and Mass Transfer in Honor of B. T. Chao. University of Illinois, pp. 369-376, 1987.

[29] Ratzel III, A. C. and J. R. Howell, "Two-Dimensional Radiation in Absorbing-Emitting-Scattering Media Using the P-N Approximation," ASME Paper No. 82-HT-19, 1982.

[30] Kassemi, M. and Naraghi, M. H. N., "Analysis of Radiation-Natural Convection Interactions in 1-G and Low-G Environments Using the Discrete Exchange Factor Method," Radiation Heat Transfer: Fundamentals and Applications, eds. T. F. Smith, M. F. Modest, A. M. Smith, and S. T. Thynell, ASME HTD. Vol. 137, pp. 189-197, 1990.

[31] Catton, I., "Natural Convection in Enclosures," Proc. 6th. . Heat Transfer Conference, Vol. 1, pp. 13-31, 1978.

[32] Truelove, J. S., "Radiant Heat Transfer Through the Cover Gas of a Sodium-Cooled Fast Reactor," Int. J. Heat Mass Transfer, Vol. 27, No. 11,pp. 2085-2093, 1984.

III ENCIT – Itapema, SC (Dezembro 1990)

PRANDTL NUMBER EFFECT ON TRANSITION IN NATURAL CONVECTION IN AN ENCLOSURE

JOSÉ L. LAGE AND ADRIAN BEJAN
Department of Mechanical Engineering
and Materials Science
Duke University
Durham, NC 27706 - U.S.A.

SUMMARY

A set of numerical experiments covering the Prandtl number range 0.01-10 and Rayleigh number range 10^2-10^{11} is performed in a rectangular enclosure. The results show that the onset of inertia sustained fluctuations occurs at lower Rayleigh numbers when the Prandtl number decreases. The qualitative trend is compared with experimental observations of transition to turbulent natural convection and with the "local Reynolds number" criterion of transition to turbulence recommended by the buckling theory of turbulent flow. Final considerations show that is the Grashof number of order 10^9 and not the Rayleigh number of order 10^9 that pinpoints correctly the transition to turbulence.

INTRODUCTION

Despite the large volume of research dedicated already to natural convection in enclosures, there is a lack of information on low Prandtl number fluids, especially at high Rayleigh numbers [1]. Particularly absent in this low Pr / high Ra range are numerical simulations of the flow and associated heat transfer phenomenon. In the literature, this observation was stressed recently by Wolff et al. [2], who reported an experimental study complemented by numerical simulations based on the steady-state form of the governing equations.

In order to shed new light on the phenomenon of natural convection in enclosures filled with low Pr fluids, we designed a series of numerical simulations that place an emphasis on the detection of unsteadiness (fluctuations) in the flow field. This numerical approach was used recently by Henkes and Hoogendoorn [3], who relied on the unsteady two-dimensional Navies Stokes equations in the study of the beginning of fluctuations in a square cavity filled with air or water.

In the present study, the emphasis is placed on the Prandtl number effect. Indeed, the numerical results described in this paper show that the Prandtl number has a strong influence on the Rayleigh number above which fluctuations tend to persist. We find that the highest Rayleigh number of the present laminar flow solutions decreases dramatically as Pr decreases. This trend explains the lack of numerical results in the low Pr / high Ra domain. It suggests also that the transition to turbulence in low-Pr fluids occurs at Rayleigh numbers that are much lower than the often-mentioned order of magnitude $Ra \sim 10^9$ [4].

MATHEMATICAL FORMULATION

The two-dimensional rectangular enclosure model is presented in Fig. 1. The fluid is treated as Newtonian and Boussinesq-incompressible, with constant transport properties (ν,k,α) and coefficient of thermal expansion. The enclosure is initially occupied by motionless fluid the temperature of which is uniform and equal to the enclosure average $(T_h + T_c)/2$. Beginning with the time $t = 0$, the temperatures of the side walls are set equal to the new levels T_h and T_c, where $T_h > T_c$. The imposed temperature difference induces symmetric boundary layer flows near the two side walls and, in time, these flows merge into a circulation that covers the entire enclosure.

The anticipated time-dependent flow is described by the equations for mass, momentum and energy conservation, in which the time-derivative terms have been retained

$$\frac{\partial U}{\partial X} + \frac{\partial V}{\partial Y} = 0 \tag{1}$$

$$\frac{\partial U}{\partial \tau} + U\frac{\partial U}{\partial X} + V\frac{\partial U}{\partial Y} = -\frac{\partial P}{\partial X} + \left(\frac{Pr}{Ra}\right)^{1/2}.\nabla^2 U \tag{2}$$

$$\frac{\partial V}{\partial \tau} + U\frac{\partial V}{\partial X} + V\frac{\partial V}{\partial Y} = -\frac{\partial P}{\partial Y} + \left(\frac{Pr}{Ra}\right)^{1/2}.\nabla^2 V + \theta \tag{3}$$

$$\frac{\partial \theta}{\partial \tau} + U\frac{\partial \theta}{\partial X} + V\frac{\partial \theta}{\partial Y} = \frac{1}{(RaPr)^{1/2}}.\nabla^2\theta \tag{4}$$

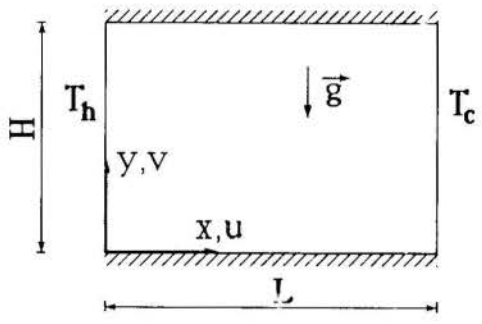

Fig. 1 Two-dimensional enclosure.

These equations have been nondimensionalized by using the height H as length scale, and defining the variables

$$(X,Y) = \frac{(x,y)}{H} \quad , \quad (U,V) = \frac{(u,v)}{(\alpha/H)(RaPr)^{1/2}} \tag{5}$$

$$\tau = \frac{\alpha (RaPr)^{1/2}}{H^2} t \quad , \quad \theta = \frac{T - (T_h + T_c)/2}{T_h - T_c} \tag{6}$$

$$P = \frac{H^2}{\rho\alpha^2}\frac{p + \rho g y}{RaPr} \quad , \tag{7}$$

where x, y, u, v and T are the physical variables defined in Fig. 1, t and p stands for time and pressure. The Rayleigh and Prandtl numbers have been defined in the usual way,

$$Ra = \frac{g\beta H^3 (T_h - T_c)}{\rho \alpha} \quad , \quad Pr = \frac{\nu}{\alpha} \tag{8}$$

The dimensionless boundary and initial conditions that correspond to Fig. 1 are (note that the top and bottom walls are adiabatic):

$$\begin{aligned} &U = V = 0 && \text{on all four walls} \\ &\theta = 0.5 && \text{at } X = 0, \\ &\theta = -0.5 && \text{at } X = L/H, \\ &\frac{\partial \theta}{\partial Y} = 0 && \text{at } Y = 0 \text{ and } Y = 1 \\ &U = V = \theta = 0 && \text{at } \tau = 0 \end{aligned} \tag{9}$$

NUMERICAL METHOD

The preceding problem was solved numerically using the control volume method described by Patankar [5].

The grid was selected as a trade-off between numerical accuracy, stability and computational time. The nonuniformity of the grid is described by the relation

$$s_{i+1} = s_i + \alpha_s^i \Delta \tag{10}$$

in which s_i represents the spatial location of the gridline, Δ the step size, and α_s the rate of grid stretching. Equation (10) prescribes a grid the density of which is higher near the solid walls of the enclosure, where sharp gradients of velocity and temperature are expected.

The fineness of the grid was determined based on accuracy tests of type illustrated in Fig. 2. The instantaneous, height-averaged Nusselt number is defined as

$$Nu = \frac{q''_{avg} H}{k (T_h - T_c)} = - \int_0^1 \left(\frac{\partial \theta}{\partial X} \right)_{X=0} dY \tag{11}$$

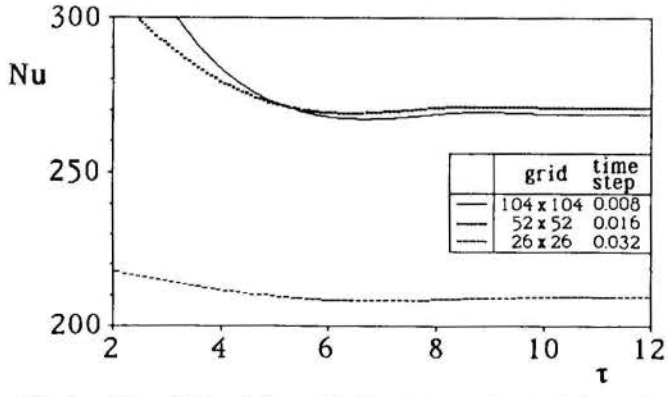

Fig. 2 The effect of the grid fineness on the evolution of the overall side-wall Nusselt number (Pr = 10, Ra = 10^{11}, L/H = 1).

It is evident that the act of increasing the number of control volumes continues to have an effect on the Nu(τ) curve in the $\tau \to 0$ limit, because, theoretically, Nu(0) = ∞. The 52 × 52 grid with $\alpha_s = 1.117$ and $\Delta = 0.004$ was adopted for $Ra = 10^{11}$ and all the lower Ra cases documented in this study.

Convergence at each time step was achieved when the relative discrepancy between two consecutive values of the overall Nusselt number was less than 10^{-6}.

The numerical work was performed on the IBM 3090-600E vector computer of the Cornell National Supercomputer Facility (CNSF). The need for supercomputer use was determined based on preliminary calculations conducted on slower machines.

SQUARE ENCLOSURES

The strategy used in the selection of the (Ra,Pr) cases chosen for complete, time-dependent simulation, consisted of first fixing the Prandtl number, and simulating flows of increasingly higher Rayleigh numbers. The Rayleigh number was increased to the point where inertial effects (fluctuations) in the flow and the excessively long computational time needed for a true steady-state solution became prohibitive. In this way, we searched for the approximate upper boundary Ra(Pr) above which we could no longer simulate steady laminar flows. To the shape and location of this boundary we return in Fig. 11 and 12.

Two examples of how oscillations proliferate as Ra increases at constant Pr are displayed in Fig. 3. In both graphs, the uppermost curve corresponds to the highest Ra value for which we were able to obtain steady-state results. Another interesting effect is the dependence of the oscillation amplitude on the Prandtl number. In relative terms, the amplitude increases as Pr decreases. This effect is explained by the fact that, as Pr decreases, inertia increasingly outweighs friction in the momentum balance of the vertical boundary layer.

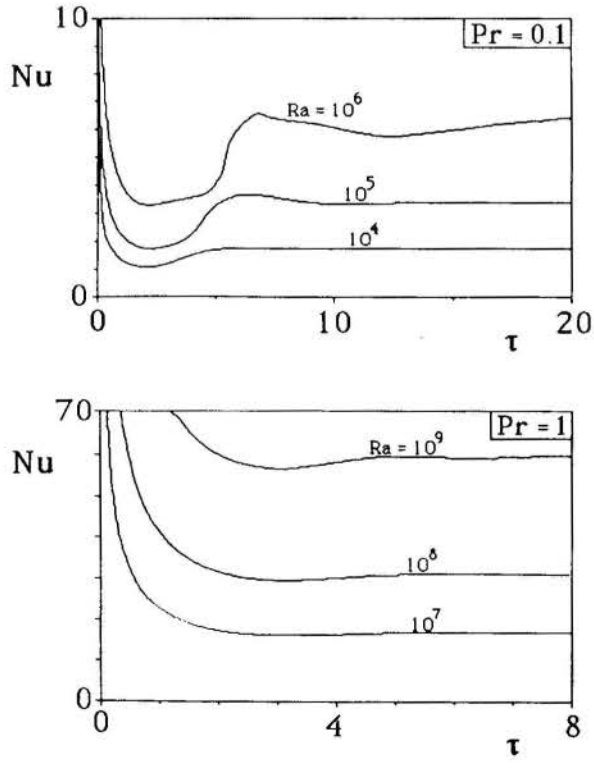

Fig. 3 The effect of Pr and Ra on the Nusselt number oscillations en route to steady state (L/H = 1).

Figure 4 shows for Pr = 0.01 not only the side-wall Nusselt number Nu of Eq. (11), but also the midplane Nusselt number

$$Nu_m = \frac{q_m}{k\,(T_h - T_c)} = \int_0^1 \left[(RaPr)^{1/2} U\theta - \frac{\partial \theta}{\partial X} \right]_{X=L/2H} dY \quad (12)$$

The figure shows that in the beginning of the differential heating process the midplane Nusselt number is much smaller than the side-wall Nu. This feature is explained by the $\tau = 0.6$ frame of streamlines and isotherms of Fig. 5, which show that the thermal boundary layers have not extended to the center of the cavity, and that not all the

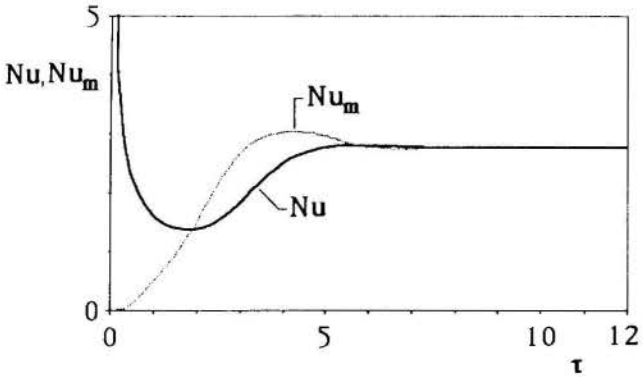

Fig. 4 The evolution of the side-wall and midplane Nusselt numbers in a low Prandtl number fluid (Pr = 0.01, Ra = 10^5, L/H = 1).

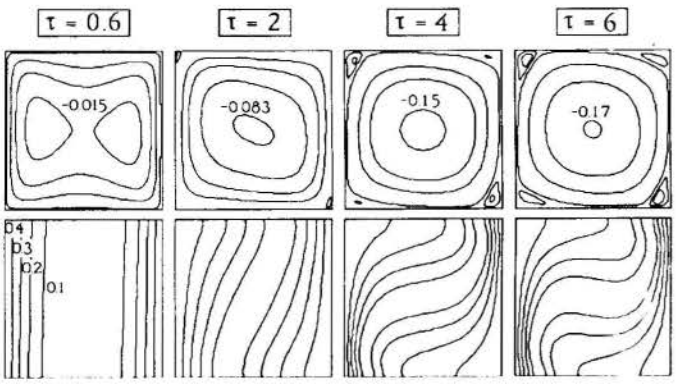

Fig. 5 The development of the flow and temperature fields in a low Prandtl number fluid (Pr = 0.01, Ra = 10^5, L/H = 1).

fluid that is driven by the side walls manages to cross the midplane of the cavity.

The Nu(τ) and $Nu_m(\tau)$ curves intersect around the time $\tau = 2$, when according to the second frame of Fig. 5 one large clockwise roll dominates the circulation pattern. In the same frame, we note the appearance of two small counterclockwise rolls in the upper-left and lower-right corners. These are the corners where the two side-wall boundary layers "arrive".

The Nu(τ) and $Nu_m(\tau)$ curves cross at least twice more as they reach their common steady state value of 2.77 at time τ of approximately 8. The streamline patterns of Fig. 5 show the formation of two additional counterclockwise rolls, this time in the "starting" corners of the side-wall boundary layers. These rolls are considerably weaker than the rolls housed by the corners discussed in the preceding paragraph.

Small cells in all four corners were observed also by Wolff et al. [2], in numerical simulations covering the range Pr = 0.011-0.0208, and Ra = (1.682)10^5 - (6.727)10^5. A direct quantitative comparison cannot be made because, of the different Pr value, and because unlike the present calculations, Wolff et al.'s were performed based on the steady-state version of the governing equations.

The development of the circulation pattern is quite different at higher Prandtl numbers. Figures 6-8 show the run made for Pr = 10 at the highest Rayleigh number of 10^{11}, for which the simulation proved too lengthy to permit the calculation of a true steady state solution. Although the side-wall Nusselt number reaches a steady value around $\tau \approx 120$, the midplane Nusselt Nu_m number oscillates appreciably about the steady Nu value (Fig. 6). The oscillation is almost periodic after $\tau \approx 100$, and its amplitude decays very slowly.

The earliest phase in the development of the Nu and Nu_m curves is illustrated in the four frames of Fig. 7. The vertical wall jets driven by the differentially heated side walls continue over the horizontal boundaries, as horizontal jets. The latter induce local clockwise rolls in the neighboring core fluid. These rolls travel the length of the horizontal boundaries, and at a time of approximately $\tau \approx 45$ they rebound against the opposing vertical wall. One by-product of this rebound is the creation of two counterclockwise cells further into the core fluid, as shown in the last frame of Fig. 7. These counterclockwise core cells are responsible for the severe drop exhibited by the midplane Nusselt number around $\tau \approx 45$ in Fig. 6.

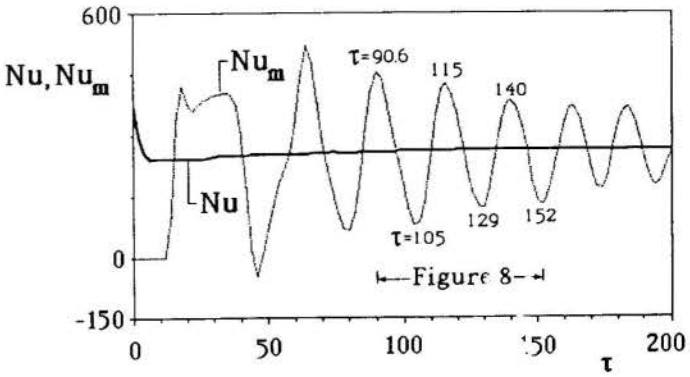

Fig. 6 The evolution of the side-wall and midplane Nusselt numbers in a high Prandtl number fluid (Pr = 10, Ra = 10^{11}, L/H = 1).

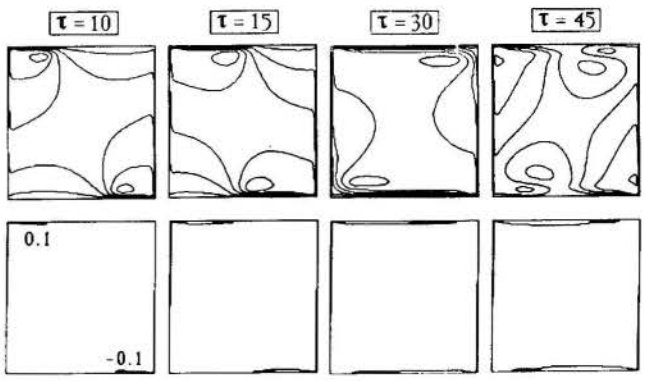

Fig. 7 The development of horizontal jets in a high Prandtl number fluid (Pr = 10, Ra = 10^{11}, L/H = 1).

The bottom three frames of Fig. 8 show the flows that correspond to three consecutive minima of the $Nu_m(\tau)$ curve of Fig. 6. The minimum midplane Nusselt number is due to the intermittent presence of a practically motionless core fluid in the vertical midplane of the cavity.

The upper row of Fig. 8 shows the streamline patterns at the in-between moments when Nu_m is maximum, namely at $\tau \equiv 90.6$, 115 and 140. At these times, the core fluid is dominated by two clockwise cells positioned in the upper-left and lower-right quadrants.

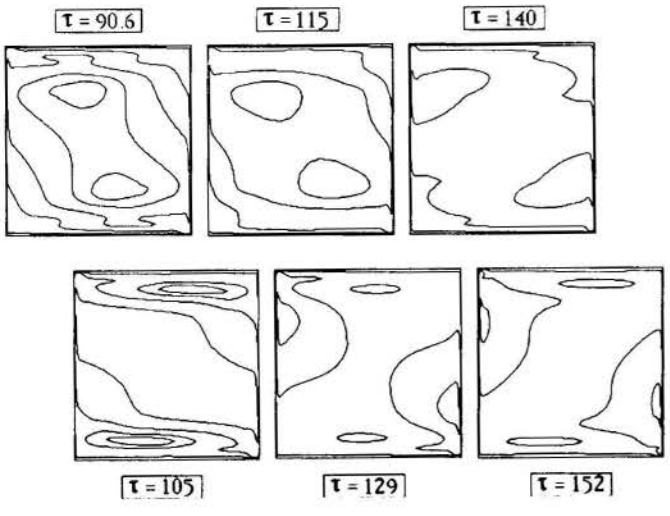

Fig. 8 Common features of the streamline patterns corresponding to the Nu_m maxima and minima indicated in Fig. 6 (Pr = 10, Ra = 10^{11}, L/H = 1).

TALL ENCLOSURES

Additional numerical runs were made in order to study the effect of the geometric aspect ration L/H, while the Rayleigh and Prandtl numbers are held fixed. Accuracy tests for each new L/H run preceded the numerical solutions that are reported in this section. These runs and their corresponding steady state Nusselt numbers are summarized in Table 1.

Table 1. The effect of the geometric aspect ratio L/H on the overall Nusselt number

Pr	Ra	L/H	Nu
0.01	10^5	1	2.77
		0.5	3.07
		0.25	4.14
0.1	10^6	1	5.62
		0.5	8.06
		0.25	7.80

Figure 9 shows the effect of L/H on the oscillations exhibited by $Nu(\tau)$ and $Nu_m(\tau)$ in a low Prandtl number fluid (Pr = 0.01, Ra = 10^5). This figure can be compared directly with Fig. 4, which dealt with the same case in a square enclosure. Worth noting is that the abscissa of Fig. 9 covers only the early part of the time-dependent natural convection process, when the Nu and Nu_m oscillations are most pronounced. It is clear that the amplitude of these oscillations decreases as L/H decreases, or as the differentially heated side-walls approach one another. In the case of L/H = 0.25, for example, the Nu and Nu_m curves coincide as early as $\tau \approx 1$ even though both curves continue to undulate until $\tau \approx 6$.

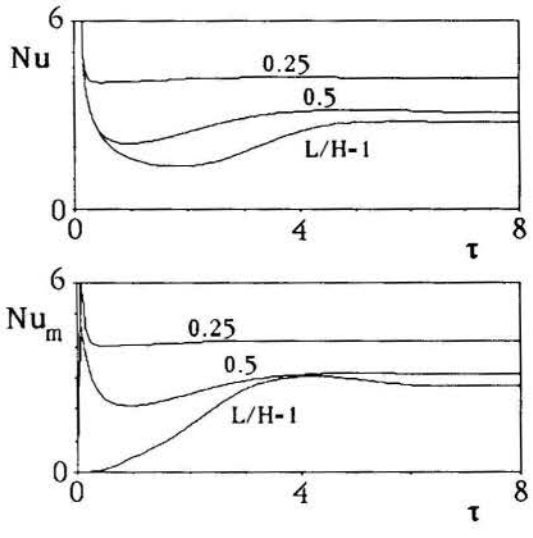

Fig. 9 The evolution of the side-wall and midplane Nusselt numbers in tall enclosures (Pr = 0.01, Ra = 10^5).

STEADY STATE HEAT TRANSFER RESULTS

Figure 10 summarizes the main heat transfer conclusions for steady laminar natural convection in square cavities. The Nu(Ra) curve is displaced downward as Pr decreases. Near the high-Ra end of each curve, Nu is proportional to approximately $Ra^{0.28}$. The fact that in the boundary layer regime the Ra exponent is slightly larger than 1/4 agrees with previous correlations of overall heat transfer in enclosures (see, for example, Catton's review [6]).

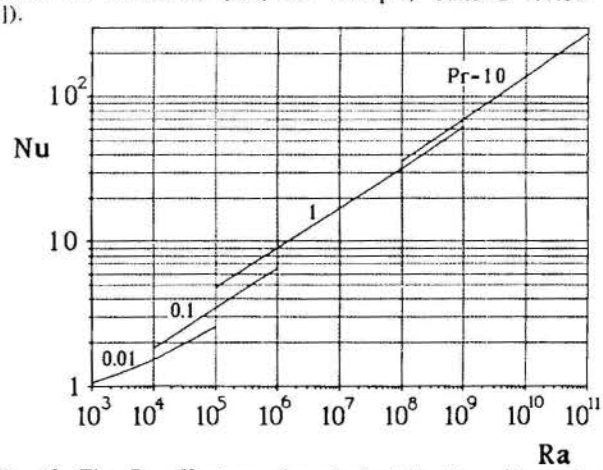

Fig. 10. The Pr effect on the steady-state Nusselt number for natural convection in square enclosures.

CONCLUSIONS

One interesting feature of the preceding numerical experiments is that the Prandtl number has a significant effect on the highest Rayleigh number of the laminar steady-state solutions. This effect is indicated by the white squares in Fig. 11, which represent the highest Ra runs. Throughout the Pr range 0.01 - 10, the highest Rayleigh number decreases appreciably as Pr decreases.

It is also interesting that the highest Rayleigh number of the Pr = 1 solution, Ra = 10^9, agrees with the widely recognized Ra order of magnitude for the transition to turbulence [4]. This agreement is not surprising, because the inertial effects that sustain the fluctuations that eventually limited our search for steady-state laminar

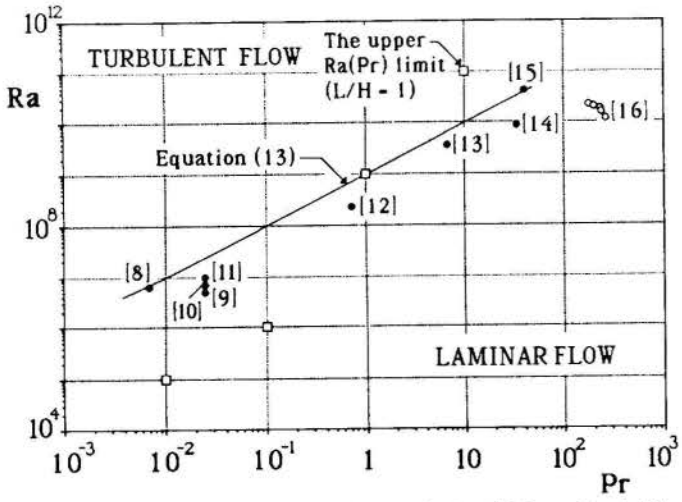

Fig. 11. Experimental observations of the highest Rayleigh number for laminar boundary layer flow along a vertical wall.

solutions are the same effects that in a real flow lead to the sinuous deformation of the bouyant wall jet.

Surprising is the apparent monotonic relationship between the Ra and Pr values of the white squares in Fig. 11, because the recommended Ra criterion for transition in natural convection vertical boundary layer flow ($Ra \approx 10^9$, Ref. [4]) is independent of the Prandtl number. In a first attempt to clarify this conflict [7], we reviewed the transition observations reported in nine experimental studies [8-16]. The Ra(Pr) points of the observed transitions are represented by black circles in Fig. 11. The observations reported by Mahajan and Gebhart [12] and Godaux and Gebhart [13] agree qualitatively with Henkes and Hoogendoorn's numerical simulations [3], which showed that in water fluctuations develop at a higher Rayleigh number than in air. In their experiments with oils, Farmer and McKie [16] observed only laminar flows, therefore the transition Rayleigh number is somewhere above the white circles plotted on the right side of Fig. 11.

The experimental data assembled in Fig. 11 recommend the relation [7]

$$Ra \approx 10^9 Pr \qquad (13)$$

as an empirical criterion for transition. In other words, it is Grashof number of order 10^9 that marks the transition in the entire Pr range 0.01 - 100, and not the often mentioned Rayleigh number of order 10^9.

It remains to provide a theoretical basis for the Ra(Pr) trend of the experimental and numerical data (transition boundary) of Fig. 11. One way to proceed is by invoking the time scale comparison [17,18] that led to the general conclusion that any straight flow ceases to be laminar when its local Reynolds number exceeds the order of magnitude 10^2,

$$\frac{v D}{\nu} \sim 10^2 \qquad (14)$$

The local Reynolds number vD/ν is based on the local longitudinal velocity scale (v), and the local transversal length scale of the flow (D). The transition criterion of Eq. (14) has been tested extensively [17]. The same criterion was derived based on a different theoretical argument by Mikic [18], who also demonstrated its power to predict the transition in turbulent flows.

In order to apply the local Reynolds number criterion, Eq. (14), to boundary layer natural convection in an enclosure heated form the side, it is important to first recognize the proper velocity and length scales of the flow. These scales depend on the Prandtl number range; furthermore, the velocity boundary layer has two length scales (cf. Ref. [17], p. 120):

	Pr < 1	Pr > 1
longitudinal velocity (v)	$\frac{\alpha}{H}(RaPr)^{1/2}$	$\frac{\alpha}{H}Ra^{1/2}$
distance from wall to velocity peak	$HGr^{-1/4}$	$HRa^{-1/4}$
outer thickness of wall jet	$H(RaPr)^{-1/4}$	$HRa^{-1/4}Pr^{1/2}$

A third transversal length scale that is eligible as D in Eq. (14) is the horizontal half-width of the enclosure, L/2. This last scale is the correct scale when it is smaller than the calculated outer thickness listed in the above table.

Low Pr fluids. Consider first the range Pr < 1, in which the longitudinal velocity scale is $v \sim (\alpha/H)(RaPr)^{1/2}$. If D is the outer thickness of the wall jet, then the criterion (14) reads

$$Ra \sim 10^8 Pr^3 \qquad (15)$$

On the other hand, if the enclosure is narrow enough to interfere with this outer thickness,

$$\frac{L}{2} < H(RaPr)^{-1/4} \qquad (16)$$

we set D ~ L/2, and the criterion (14) becomes

$$Ra \sim 10^4\left(\frac{H}{L/2}\right)^2 Pr \qquad (17)$$

For a fixed ratio H/L, equations (15) and (17) describe the Ra(Pr) boundary that limits from above the laminar flow domain, Fig. 12. The choice of using Eq. (17) instead of equation (15) is based on the inequality (16). In other words, the "knee" in the Ra(Pr) boundary described by Eqs. (15) and (17) occurs at the (Ra,Pr) point where the two sides of Eq. (16) are equal.

High Pr fluids. In the range Pr > 1, the longitudinal velocity scale is $v \sim (\alpha/H)Ra^{1/2}$. If the role of D is played by the outer thickness of the wall jet, then the criterion (14) becomes

$$Ra \sim 10^8 Pr^2 \qquad (18)$$

On the other hand, if D ~ L/2, we obtain

$$Ra \sim 10^4 \left(\frac{H}{L/2}\right)^2 Pr^2 \qquad (19)$$

The latter is valid when the enclosure is norrow enough so that

$$\frac{L}{2} < H Ra^{-1/4} Pr^{1/2} \qquad (20)$$

This inequality can be rewritten as

$$Ra < \left(\frac{H}{L/2}\right)^4 Pr^2 \qquad (21)$$

which in combination with equation (19) states that the criterion (19) prevails over the criterion (18) only when

$$\frac{H}{L/2} > 10^2 \qquad (22)$$

This finding is reported graphically in the Pr > 1 half of Fig. 12, where the criterion (19) generates a family of parallel lines, one line for each ratio H/L. In sufficiently wide enclosures where the inequality (22) fails, the Ra(Pr) transition is described by Eq. (18), and is no longer influenced by H/L.

It is instructive to compare now the empirical information of Fig. 11 with the broken-line theoretical boundary constructed in Fig. 12. When the aspect ratio H/L is fixed, the theoretical Ra(Pr) boundary of the laminar domain has the same general position and orientation as the string of data assembled in Fig. 11. Of course, the laminar flow is stabilized ("straightened") and the Ra(Pr) boundary is pushed to higher Ra values as the enclosure becomes narrower. The geometric aspect ratio H/L has a more significant and complicated effect on the Ra(Pr) boundary in the case of low Pr fluids.

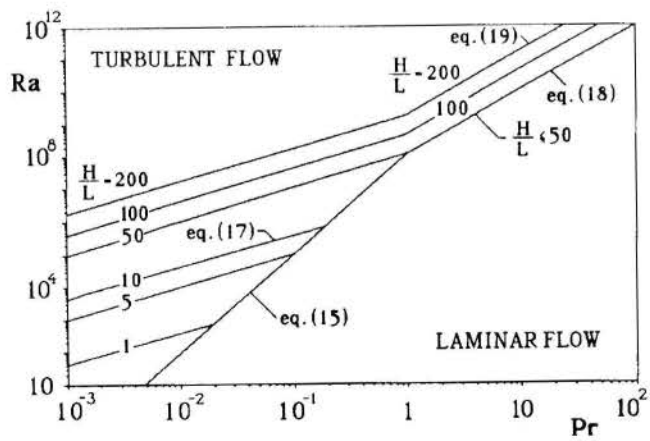

Fig. 12. Theoretical Ra(Pr, H/L) boundary of the laminar flow domain.

Acknowledgement. The numerical work was conducted using the Cornell National Supercomputer Facility, a resource of the Center for Theory and Simulations in Science and Engineering (Cornell Theory Center), which receives major funding from the National Science Foundation and IBM corporation, with additional support from New York State and members of the Corporate Research Institute.

J. L. Lage acknowledges with gratitude the support received from CAPES- The Brazilian Post-Graduate Education Federal Agency (Process no. 5943/87-2).

REFERENCES

[1] I. Catton, A. Bejan, R. Greif and K.G.T. Hollands, "Natural Convection in Enclosures," Proceedings of a Workshop on Natural Convection, K.T. Yang and J.R. Lloyd, Eds. University of Notre Dame, Notre Dame, IN, 24-35 (1983).

[2] F. Wolff, C. Beckermann and R. Viskanta, "Natural Convection of Liquid Metals in Vertical Cavities," Experimental Thermal and Fluid Science, vol. 1, pp. 83-91, 1988.

[3] R.A.W.M. Henkes and C.J. Hoogendoorn, "On the Stability of the Natural Convection Flow in a Square Cavity Heated from the Side," Appl. Sci. Res., 1989, in press.

[4] F.P. Incropera and D.P. DeWitt, "Fundamentals of Heat and Mass Transfer," second edition, Wiley, New York, p. 427, 1985.

[5] S.V. Patankar, "Numerical Heat Transfer and Fluid Flow," Hemisphere, Washington, DC, 1980.

[6] I. Catton, "Natural Convection in Enclosures," Heat Transfer 1978, Hemisphere, Washington, DC, vol. 6, pp. 13-43, 1978.

[7] A. Bejan and J.L. Lage, "The Prandtl Number Effect on the Transition in Natural Convection along a Vertical Surface," Journal of Heat Transfer, vol. 112, 1990, accepted for publication.

[8] N. Sheriff and N.W. Davies, "Sodium Natural Convection from a Vertical Plate," Heat Transfer 1978, Hemisphere, Washington, DC, vol. 5, pp. 131-136, 1978.

[9] W.W. Humphreys and J.R. Welty, "Natural Convection with Mercury in a Uniformly Heated Vertical Channel during Unstable Laminar and Transitional Flow," AIChE Journal, vol. 21, pp. 268-274, 1975.

[10] M. Uotani, "Natural Convection Heat Transfer in Thermally Stratified Liquid Metal," J. Nuclear Science and Technology , vol. 24 (6), pp. 442-451, 1987.

[11] P.S. Lykoudis, Private Communication, 1989.

[12] R.L. Mahajan and B. Gebhart, "An Experimental Determination of Transition Limits in a Vertical Natural Convection Flow Adjacent to a Surface," J. Fluid Mechanics, vol. 91, pp. 131-154, 1979.

[13] R. Godaux and B. Gebhart, "An Experimental Study of the Transition of Natural Convection Flow Adjacent to a Vertical Surface," Int. J. Heat Mass Transfer, vol. 17, pp. 93-107, 1974.

[14] T. Fujii, "Experimental Studies of Free Convection Heat Transfer," Bulletin JSME, vol. 2(8), pp. 555-558, 1959.

[15] Y.S. Touloukian, G.A. Hawkins and M. Jakob, "Heat Transfer by Free Convection from Heated Vertical Surfaces to Liquids," Trans. ASME, vol. 70, pp. 13-23, 1948.

[16] W.P. Farmer and W.T. McKie, "Natural Convection from a Vertical Isothermal Surface in Oil," ASME Paper No. 64-WA/HT-12.

[17] A. Bejan, "Convection Heat Transfer," Wiley, New York, 1984.

[18] B.B. Mikic, "On Destabilization of Shear Flows: Concept of Admissible System Pertubations," Int. Comm. Heat Mass Transfer, vol. 15, pp. 799-811, 1988.

III ENCIT – Itapema, SC (Dezembro 1990)

CONVECÇÃO NATURAL EM CAVIDADE RETANGULAR INCLINADA COM PARTIÇÕES LIGADAS À PAREDE FRIA

SEBASTIÃO FERNANDES
Departamento de Matemática e Computação - EFEI
GENÉSIO JOSÉ MENON
Departamento de Engenharia Mecânica - EFEI

RESUMO

Analisa-se numericamente a convecção natural laminar bidimensional numa cavidade retangular inclinada, através de um método de diferenças finitas explícito. A cavidade é constituida de uma superfície isotérmica fria, uma superfície isotérmica quente e duas superfícies isoladas termicamente. Partições finas, diatérmicas e igualmente espaçadas são ligadas à parede isotérmica fria. Consideram-se número de Rayleigh variando de 10^3 a 10^6, número de Prandtl 0,71, ângulos de inclinação 0^0, 30^0, 45^0 e 60^0, razões de aspecto 1 a 5 e número de partições de 1 a 3.

INTRODUÇÃO

O estudo da convecção natural de fluidos confinados no interior de cavidades de seção retangular tem sido tratado com muito interesse nos últimos anos, dada a sua importância para a engenharia.

Mais recentemente têm sido publicados alguns trabalhos acerca da redução nas perdas de calor por convecção devido à colocação de partições no interior da cavidade. A maior parte dos trabalhos sobre cavidades de geometria complexa trata de partições adaptadas às paredes isoladas e geralmente se verificam que as velocidades, a função corrente e os números de Nusselt locais ou médios diminuem com relação ao caso de cavidades não divididas, para um número de Rayleigh mantido constante. Já as cavidades com partições ligadas às suas paredes isotérmicas têm sido pouco citadas, constituindo-se assim objeto de estudo deste trabalho.

Weber [1], em 1980, estudou experimentalmente o campo de temperatura e a transferência de calor numa geometria tridimensional dividida, usando Freon-12 como fluido. Foi verificado que a transferência de calor é mais influenciada pela altura que pela largura da abertura retangular da partição.

Winters [3], em 1982, usou o método de elementos finitos para determinar a transferência de calor e as distribuições de temperatura e da função corrente para cavidade retangular dividida por uma partição. Foi considerado Ra entre 10^4 e 10^6.

Nansteel e Greif [2], em 1981, estudaram a convecção natural numa cavidade retangular com partições fixadas na parede isolada. Foram apresentados resultados do número de Nusselt e das distribuições da função corrente e da temperatura para $2{,}3\text{x}10^{10} \leq Ra \leq 1{,}1\text{x}10^{11}$ e razão de aspecto 0,5.

Lin e Bejan [4], em 1983, realizaram investigações analíticas e experimentais para convecção natural em cavidade retangular com uma divisão parcial semelhante ao tipo estudado em [2], porém com razão de aspecto 0,3.

Nansteel e Greif [5], em 1984, investigaram experimentalmente a transferência de calor por convecção natural em cavidade retangular dividida por uma partição vertical adiabática. Foram consideradas partições bi e tridimensionais e em ambos os casos as partições eram acopladas às paredes isoladas da cavidade e paralelas às paredes verticais isotérmicas. Os experimentos, no caso bidimensional, foram realizados para $2{,}25\text{x}10^{10} \leq Ra \leq 1{,}14\text{x}10^{11}$, $3 \leq Pr \leq 4{,}5$ e razão de aspecto 0,5. No caso de partição tridimensional, os experimentos foram feitos com $2{,}4\text{x}10^{10} \leq Ra \leq 1{,}1\text{x}10^{11}$, $3 \leq Pr \leq 4{,}3$ e razão de aspecto 0,5.

Acharya e Tsang [6], em 1985, investigaram a convecção natural numa cavidade inclinada com uma partição ligando as paredes isoladas. Os resultados foram obtidos usando o método de diferenças finitas para cavidades com razão de aspecto 1 e 2, com Ra variando até 10^7 e com ângulos de inclinação da parede quente com relação à horizontal de 30^0, 45^0, 60^0 e 90^0.

Nishimura e outros [7], em 1988, investigaram numericamente e experimentalmente a transferência de calor por convecção natural em uma cavidade retangular com múltiplas partições verticais igualmente espaçadas unindo as paredes adiabáticas. Nas investigações experimentais o número de partições foi variando de 1 a 4, com $10^6 \leq Ra < 10^8$, Pr=6 e razão de aspecto 4. Na solução numérica foi utilizado o método de elementos finitos, onde foram mantidos constantes o número de Prandtl e a razão de aspecto, enquanto o número de Rayleigh variou no intervalo $10^4 < Ra < 10^7$ com 2 e 3 partições.

Frederick [8, 9], em 1989, investigou numericamente o efeito da colocação de uma partição diatérmica na parede fria de uma cavidade quadrada inclinada. Analisou-se os efeitos do número de Rayleigh, do ângulo de inclinação e do comprimento da partição sobre o escoamento e a transferência de calor. As equações de conservação foram resolvidas pelo método de diferenças finitas considerando Pr=0,71, $10^3 \leq Ra \leq 10^5$ e ângulo de inclinação na parede quente com relação à horizontal entre 45^0 e 90^0. Verificou-se que a presença da partição era responsável por uma redução de até 47% na transferência de calor com relação aos resultados obtidos sem partição.

Neste trabalho estuda-se a convecção natural numa cavidade retangular inclinada com relação à horizontal e com partições colocadas junto à parede fria, conforme a Figura 1.

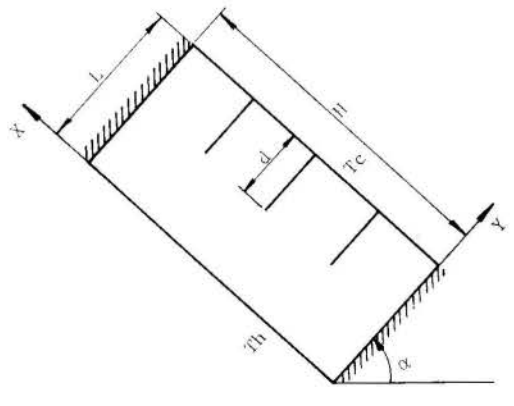

Fig. 1. Geometria da Cavidade.

Considera-se que duas superfícies são mantidas isotérmicas nas temperaturas fria Tc e quente Th, respectivamente, e que as outras duas superfícies são isoladas.

Para verificar a validade do procedimento numérico, comparou-se os resultados do presente trabalho com aqueles para cavidades sem partição obtidos por De Vahl Davis [10] e com uma partição obtido por Frederick [8, 9], encontrando excelente concordância.

São apresentados resultados do número de Nusselt médio (Nu) para número de Rayleigh (Ra) entre 10^3 e 10^6, número de Prandtl (Pr) 0,71, ângulos de inclinação (α) 0^0, 30^0, 45^0 e 60^0, razão de aspecto (R) 1, 2, 3, 4 e 5, partições com comprimentos adimensionais (d/L) 0,25, 0,5 e 0,75, número de partições 1, 2 e 3.

FORMULAÇÃO DO PROBLEMA

Considera-se o escoamento em regime laminar, permanente, bidimensional e incompressível, sem dissipação viscosa e sem efeitos de compressibilidade, as propriedades físicas são constantes, exceto a densidade que segue a relação de Boussinesq. Considera-se ainda que as partições são adiabáticas e têm espessura desprezível. As equações de conservação da massa, quantidade de movimento e energia podem ser escritas na seguinte forma adimensional:

$$\frac{\partial U}{\partial X} + \frac{\partial V}{\partial Y} = 0 \quad , \tag{1}$$

$$\frac{\partial \omega}{\partial t} + \frac{\partial (U\omega)}{\partial Y} + \frac{\partial (V\omega)}{\partial Y} = Pr\nabla^2\omega - RaPr\cos\alpha\frac{\partial \theta}{\partial Y} + RaPr\,\mathrm{sen}\alpha\frac{\partial \theta}{\partial X} \quad , \tag{2}$$

$$\frac{\partial \theta}{\partial t} + \frac{\partial (U\theta)}{\partial X} + \frac{\partial (V\theta)}{\partial Y} = \nabla^2\theta \quad , \tag{3}$$

$$\omega = \nabla^2\psi \quad , \tag{4}$$

onde os parâmetros adimensionais são definidos como:

$$R = \frac{H}{L} \ , \quad X = \frac{x}{L} \ , \quad Y = \frac{y}{L} \ , \quad U = \frac{u}{\overline{\alpha}/L} \ , \quad V = \frac{v}{\overline{\alpha}/L} \ ,$$

$$P = \frac{p}{\rho(\overline{\alpha}/L)^2} \ , \quad \theta = \frac{T-Tc}{Th-Tc} \ , \quad t = \frac{\tau}{L^2/\overline{\alpha}} \ , \quad Pr = \frac{\nu}{\overline{\alpha}} \ ,$$

$$Ra = \frac{g\beta(Th-Tc)L^3}{\nu\overline{\alpha}} \ , \quad \omega = \frac{\partial V}{\partial X} - \frac{\partial U}{\partial Y} \ , \quad U = -\frac{\partial \psi}{\partial Y} \quad e$$

$$V = \frac{\partial \psi}{\partial X} \ . \tag{5}$$

As equações (1) a (4) estão sujeitas às seguintes condições iniciais e de contorno:

Condições iniciais:

$$\omega(X,Y,0) = \psi(X,Y,0) = 0 \ \text{ e } \ \theta(X,Y,0) = 0{,}5 \ , \tag{6a}$$

Condições de contorno:

$$\psi(X,0,t) = \frac{\partial \psi}{\partial Y}(X,0,t) = 0 \ \text{ e } \ \theta(X,0,t) = 1 \ , \tag{6b}$$

$$\psi(X,1,t) = \frac{\partial \psi}{\partial Y}(X,1,t) = \theta(X,1,t) = 0 \ , \tag{6c}$$

$$\psi(0,Y,t) = \frac{\partial \psi}{\partial X}(0,Y,t) = \frac{\partial \theta}{\partial X}(0,Y,t) = 0 \ , \tag{6d}$$

$$\psi(R,Y,t) = \frac{\partial \psi}{\partial X}(R,Y,t) = \frac{\partial \psi}{\partial X}(R,Y,t) = 0 \ . \tag{6e}$$

MÉTODO DE SOLUÇÃO

Foi utilizado um método explícito de diferenças finitas para resolver o sistema formado pelas equações (1) a (4), juntamente com as condições (6a) a (6e).

As equações de (1) a (3) foram resolvidas através de um esquema numérico de diferenças finitas explícito apresentado em [11]. A equação (4) foi resolvida utilizando o método de sobre-relaxação com o seguinte critério de convergência:

$$\frac{\sum_{I,J} \left| \psi^{n+1}(I,J) - \psi^{n}(I,J) \right|}{\sum_{I,J} \left| \psi^{n+1}(I,J) \right|} \leq 10^{-6} \ , \tag{7}$$

onde n representa o número de iteração.

Para se resolver o sistema de equações de (1) a (4), foi utilizada a sequência discutida a seguir. Primeiramente resolveu-se a equação (2), obtendo a distribuição de ω, depois resolveu-se a equação (3) para se obter a distribuição de temperatura θ. Finalmente foi resolvida a equação (4) para se obter a distribuição de ψ.

Após determinar a distribuição de temperatura, o número de Nusselt médio pode ser calculado para cada iteração, pela seguinte equação:

$$Nu = \frac{1}{R}\int_0^R -\left(\frac{\partial \theta}{\partial Y}\right)_{Y=0} dX \tag{8}$$

O processo de cálculo é repetido até que se tenha convergência do número de Nusselt médio ou o número máximo de iterações seja atingido.

RESULTADOS E CONCLUSÕES

A tabela 1 apresenta os números de Nusselt médios e os respectivos desvios com relação aos resultados obtidos por De Vahl Davis [10]. Nota-se que existe uma boa concordância não apenas com os resultados de De Vahl Davis [10], como também em relação àqueles obtidos por Frederick [9].

Tabela 1. Comparação de resultados do número de Nusselt. Os valores entre parêntesis representam os desvios com relação à solução de De Vahl Davis [10] (Pr=0,71; R=1; α=0).

	Malha	Presente Trabalho	Frederick [9]	De Vahl Davis [10]
$Ra=10^3$	20x20	1,123(0,45)	1,120(0,36)	1,118
	40x40	1,119(0,09)		
$Ra=10^4$	20x20	2,315(3,2)	2,277(1,56)	2,243
	40x40	2,262(0,85)		
$Ra=10^5$	20x20	4,943(9,4)		4,519
	40x40	4,647(2,8)		
$Ra=10^6$	40x40	9,520(8,2)		8,799

Na tabela 2 são mostrados os números de Nusselt obtidos para cavidades com razão de aspecto 1 a 5 e d/L=0,25, 0,5 e 0,75, número de Rayleigh 10^4 e 10^5, com Pr=0,71 e ângulo de inclinação $\alpha=60^0$. Observa-se da tabela 2 que o menor número de Nusselt para $Ra=10^4$ ocorre quando a cavidade é quadrada (R=1). Para $Ra=10^5$, o menor número de Nusselt ocorre quando a cavidade possui razão de aspecto R=5, exceto para o caso d/L=0,75

Tabela 2. Valores do número de Nusselt para $\alpha=60^0$, Pr=0,71 e com uma partição.

	d/L=0,25		d/L=0,5		d/L=0,75	
	$Ra=10^4$	$Ra=10^5$	$Ra=10^4$	$Ra=10^5$	$Ra=10^4$	$Ra=10^5$
R=1	1,940	3,952	1,469	4,273	1,270	3,807
R=2	2,143	3,929	2,171	3,881	2,216	4,135
R=3	2,079	3,747	2,277	3,855	2,298	4,117
R=4	2,432	3,566	2,236	3,826	2,233	3,988
R=5	2,364	3,408	2,239	3,756	2,144	3,863

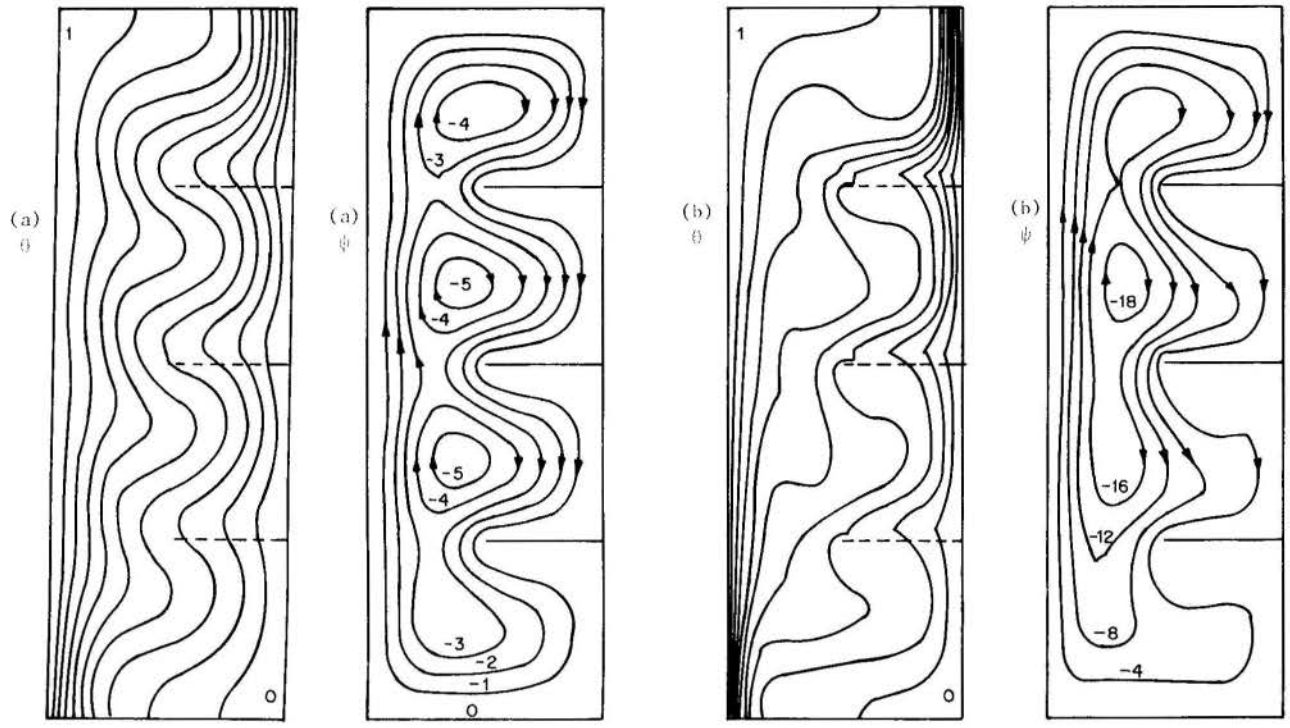

Fig. 2. Distribuições de θ e ψ para R=3, Pr=0,71, $\alpha=90^0$, 3 partições. (a) $Ra=10^4$, (b) $Ra=10^5$.

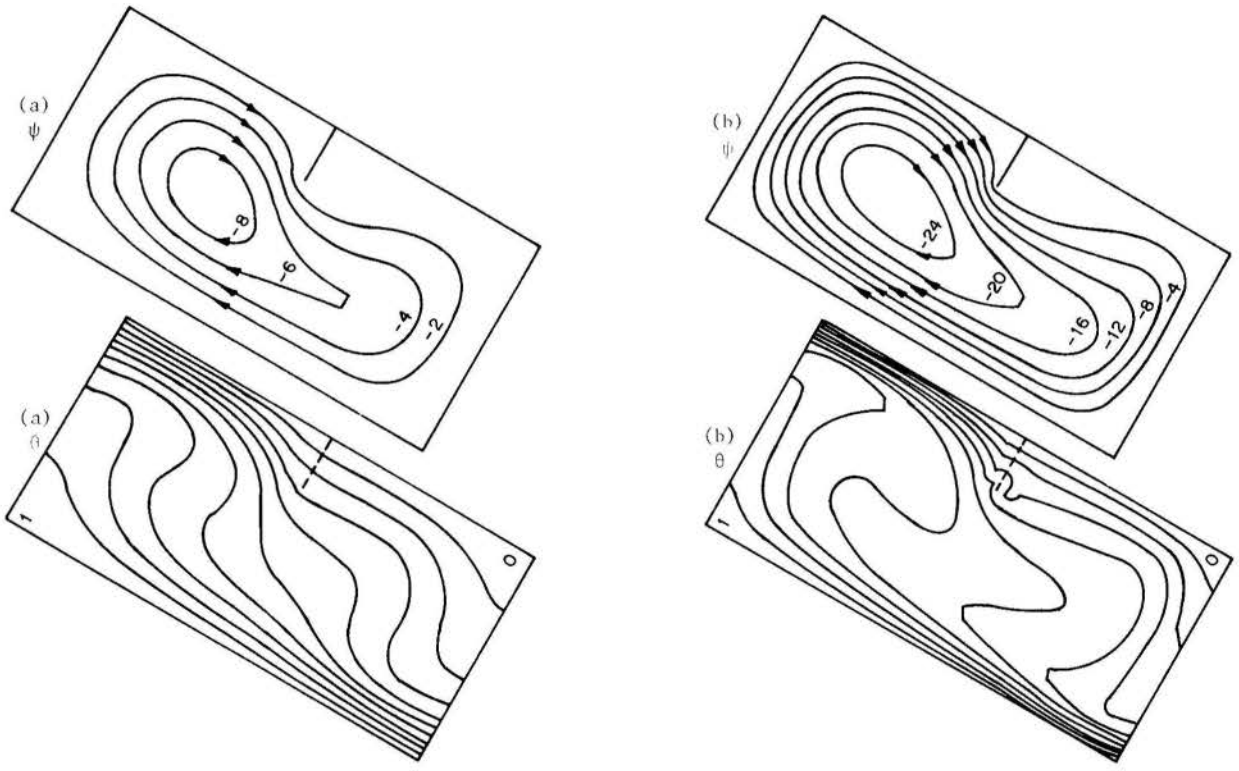

Fig. 3. Distribuições de ψ e θ para R=2, Pr=0,71, $\alpha=60^0$, 1 partição. (a) $Ra=10^4$, (b) $Ra=10^5$.

onde o menor valor ocorre para R=1. Na tabela 2, para razões de aspecto 1, 2, 3, 4 e 5 foram usadas, respectivamente, malhas 20x20, 20x40, 20x60 e 20x100.

As figuras 2 (a) e (b) mostram as distribuições de temperatura adimensional (θ) e da função corrente (ψ), para razão de aspecto R=3, número de Prandtl Pr=0,71, ângulo de inclinação $\alpha=90^0$, 3 partições. No caso (a) tem-se $Ra=10^4$ e no caso (b), $Ra=10^5$.

Nas figuras 2 (a) e (b), se observa que o escoamento apresenta várias células de convecção. Notando-se que no caso (b) os valores de ψ, em módulo, são maiores que em (a), o que justifica uma troca de calor por convecção mais intensa.

As figuras 3 (a) e (b), também mostram as distribuições de θ e ψ para R=2, Pr=0,71, $\alpha=60^0$, 1 partição. No caso (a), $Ra=10^4$ e no caso (b), $Ra=10^5$. Se observa das figuras 3 (a) e (b) que o escoamento tem apenas uma célula de convecção.

A tabela 3 apresenta resultados do número de Nusselt médio para cavidade sem partição (d/L=0) e com uma partição (d/L=0,25 e d/L=0,5), com ângulos de inclinação (α) 0^0, 30^0 e 45^0 e para diversos valores de Rayleigh. Considerou-se cavidade com razão de aspecto unitária e número de Prandtl 0,71. Os resultados mostram uma diminuição no número de Nusselt médio com a colocação de uma partição ligada à parede fria da cavidade.

Tabela 3. Número de Nusselt para Pr=0,71, R=1, sem partição (d/L=0) e com uma partição (d/L=0,25 e d/L=0,5).

		Número de Rayleigh (Ra)					
α	d/L	10^3	$5x10^3$	10^4	$5x10^4$	$7x10^4$	10^5
0^0	0	1,119	1,800	2,266	3,754	4,176	4,677
	0,25	1,042	1,427	1,788	3,122	3,517	3,992
	0,5	1,007	1,141	1,401	2,860	3,297	3,809
30^0	0	1,129	1,988	2,493	3,926	4,312	4,772
	0,25	1,039	1,516	1,934	3,249	3,606	4,028
	0,5	1,006	1,154	1,506	3,262	3,727	4,251
45^0	0	1,108	2,004	2,502	3,874	4,236	4,659
	0,25	1,030	1,509	1,929	3,153	3,479	3,862
	0,5	1,004	1,130	1,490	3,266	3,711	4,203

A tabela 4 apresenta os valores de Nusselt médios para o caso de cavidade com razão de aspecto R=3, contendo 1, 2 e 3 partições, com ângulos de inclinação $\alpha=0^0$, 30^0 e 60^0, comprimentos adimensionais d/L=0,25, 0,5 e 0,75 e Pr=0,71, para diversos números de Rayleigh. Os resultados mostram que o número de Nusselt tende a diminuir com o aumento do número de partições, para o mesmo valor de Rayleigh. A única exceção na tabela 4 ocorre para o caso de 3 partições, com $Ra=10^5$, $\alpha=60^0$ e d/L=0,5 onde o Nusselt calculado foi um pouco maior que aquele obtido com 2 partições, mas ainda menor que para o caso de apenas 1 partição.

Tabela 4. Valores do número de Nusselt para Pr=0,71, R=3 e malha 20x60.

		1 Partição		2 Partições		3 Partições	
α	d/L	$Ra=10^4$	$Ra=10^5$	$Ra=10^4$	$Ra=10^5$	$Ra=10^4$	$Ra=10^5$
0^0	0,25	2,162	4,104	2,018	3,907	1,890	3,707
	0,5	2,185	4,044	1,974	3,796	1,702	3,523
	0,75	2,258	4,279	2,045	4,066	1,728	3,811
30^0	0,25	2,211	4,110	2,045	3,888	1,912	3,670
	0,5	2,311	4,060	2,084	3,766	1,784	3,488
	0,75	2,377	4,388	2,179	4,184	1,859	3,920
60^0	0,25	2,079	3,747	1,898	3,504	1,748	3,287
	0,5	2,277	3,855	2,033	3,540	1,709	3,717
	0,75	2,298	4,117	2,100	3,914	1,771	3,541

A figura 4 mostra a redução relativa em porcentagem do número de Nusselt (Nu) para o caso onde se considera 1 partição, relativamente ao caso sem partição (Nuo), onde se mantém fixados todos os outros parâmetros envolvidos. Nota-se que para a situação analisada a redução máxima ocorre para Ra entre $2x10^3$ e 10^4. Observa-se da figura 4 que as reduções são maiores quando d/L=0,50, isto é, maiores comprimentos das partições, exceto para o caso onde $\alpha=45^0$ e $Ra>3x10^4$.

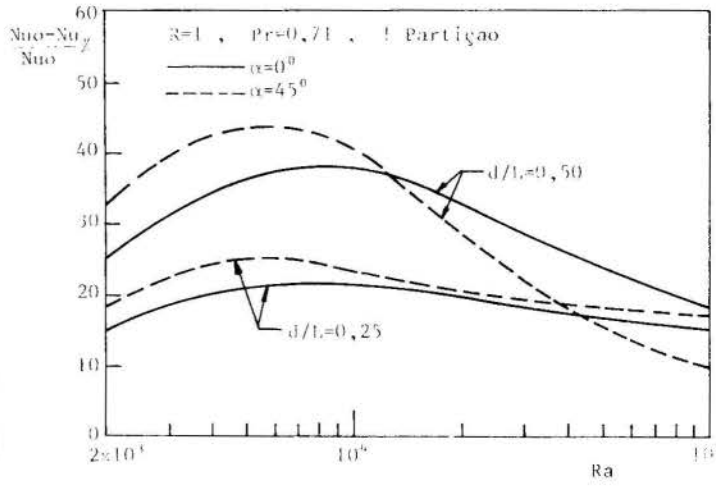

Fig. 4. Redução relativa das perdas em % versus Ra.

A colocação de partições modificam a estrutura do escoamento no interior da cavidade, reduzindo as perdas de calor por convecção relativamente ao caso sem partição em até 45%, dependendo dos vários parâmetros geométricos e térmicos. Contudo, para $Ra>10^4$, em geral se observa que a redução nas perdas de calor decrescem com o aumento do número de Rayleigh quando se mantém fixos os outros parâmetros envolvidos.

BIBLIOGRAFIA

[1] Weber, D.D., Similitude Modeling of Natural Convection Heat Transfer Through an Aperture in Passive Solar Heated Buildings, Ph.D. Thesis, Department of Physics, University of Idaho, Moscow, Idaho, 1980.

[2] Nansteel, M.W. e Greif. R., Natural Convection in Undivided and Partially Divided Rectangular Enclosures, J. Heat Transfer, Vol. 103, pp. 623-629, 1981.

[3] Winters, K.H., The Effect of Conducting Divisions on the Natural Convection of Air in a Rectangular Cavity With Heated Side Walls, Proc. 3rd Joint AIAA/ASME. Thermophysics, Fluids, Plasma and Heat Transfer Conf., St. Louis, 1982.

[4] Lin, N.N. e Bejan, A., Natural Convection in a Partially Divided Enclosure, Int. J. Heat Mass Transfer, Vol. 26, pp. 1867-1878, 1983

[5] Nansteel, M.W. e Greif, R., An Investigation of Natural Convection in Enclosures With Two and Three-Dimensional Partitions, Int. J. Heat Mass Transfer, Vol. 27, Nº 4, pp. 561-571, 1984.

[6] Acharya, S. e Tsang, C.H., Natural Convection in a Fully Partitioned, Inclined Enclosure, Numerical Heat Transfer, Vol. 8, pp. 407-423, 1985.

[7] Nishimura, T., Shiraishi, M., Nagasawa, F. e Kawamura, U., Natural Convection Heat Transfer in Enclosures With Multiple Vertical Partitions, Int. J. Heat Mass Transfer, Vol. 31, Nº 8, pp. 1679-1686, 1988.

[8] Frederick, R.L., Natural Convection in an Inclined Square Enclosure With a Partition Attached to its Cold Wall, Int. J. Heat Mass Transfer, Vol. 32, Nº 1, pp. 87-94, 1989.

[9] Frederick, R.L., Catalán, C., Natural Convection in Square Cavities With Partitions, Anais do II Congresso Latinoamericano de Transferência de Calor e Matéria, São Paulo, Nº 1, pp. 86-97, 1986.

[10] De Vahl Davis, G., Natural Convection of Air in a Square Cavity: a Bench Mark Numerical Solution , International Journal for Numerical Methods in Fluids, Vol. 3, pp. 249-264, 1983.

[11] Briggs, D.G., A Finite Difference Scheme for the Incompressible Advection - Diffusion Equation , Computer Methods in Applied Mechanics and Engineering, Vol. 6, pp. 233-241, 1975.

ABSTRACT

Natural convection in a bidimensional, rectangular and inclined cavity with diathermal partitions on its cold wall is numerically studied. A explicit method of finite differences was used to solve the conservation equations. The partitions causes heat transfer reductions relative to the undivided cavity at same Rayleight number.

III ENCIT – Itapema, SC (Dezembro 1990)

EXPERIMENT OF NATURAL CONVECTION IN A HEMISPHERICAL CAVITY WITH DISCRETE THERMAL SOURCE

L.C.Lima and E.P. Parreira
Department of Mechanical Engineering
Universidade Federal de Uberlândia
38400 - Uberlândia - MG - Brazil

SUMMARY

The natural convection heat transfer inside a hemispherical enclosure with discrete heat source at the center of its base was studied and observed that the results and the consequent correlation were close to similar cases correlations in the literature. It was also made an analogy between the effect of sensitivity variation from a pyranometer and the heat transfer coefficients variation inside the dome from that instrument.

INTRODUCTION

In the last three decades, there has been a growing awareness that natural convention phenomena are of interest and significance in many fields of science and technology, such meteorology, geophysics, astrophysics,nuclear reactor, processes, fire control, chemical, food and metallurgical industries [1].

The study of the effect of natural convection within a hemispherical cavity, precisely, inside the dome of a pyranometer and the effective cooling from electronic components necessaries to meet the growing electrical power dissipation and density on printed circuit board are very important topics that demand more researches. Characteristics from nyranometer such dynamic responses and variation of sensitivity when it is operated in tilted position, heat transfer in spherical segments occuring in small structures such geodesics,spherical heat storages, industrial and physical situation where there are buoyancy-driven fluid flow are studies that have relation with the present work.

Although buoyancy-driven fluid flow and heat transfer in a differentially heated horizontal and vertical cavities have been investigated extensively, most of the studies consider only fully heated walls. A detailed review of literature indicates that very few efforts have been made to study natural convection from either an isolated heat source or an array of distributed heat sources on a horizontal or vertical wall of an enclosure [2]. In the present case the black painted sensor of the pyranometer can be seen as a discrete heat source in a hemispherical enclosure.

Anderson [3] realized studies of convective heat transfer within the domes of several solarimeters and showed that when increasing the overall heat transfer coefficient for a given type of thermopile element, by altering the gaseous content or the casing dimensions, will decrease sensitivity and linearity of response, increase the temperature coefficient and decrease the response time and decreasing the thermal capacity of the element will decrease response time and increase sensitivity from those instruments.

Cabelli [4] obtained a numerical solution of the three-dimensional equations which describes the convective motion inside a hemispherical cavity. The effect of inclination on the rate of heat transfer was also examined and the relevance of that work to some aspects of the calibration of pyranometers was shown After Cabelli, in the calibration of pyranometers in inclined positions, discrepancies relative to readings obtained with the instrument held horizontally have been attributed in the past to the convective effects which take place within the hemispherical glass envelope and which affect the uniformity of the temperature of the air near the annular cold junction. It was shown in that work that convective losses themselves are a function of the inclination and would necessitate a calibration correction irrespective to the distribution of the temperature at the cold junction.

The purpose of this work is to experimentally study the natural thermal convection in a hemispherical cavity as shown in the Fig. 1, where a discrete thermal source is in a base, to find a correlation $Nu = C.Ra^n$ that represents the heat transfer on this process, compare with the literature and to bring some questions about the role from the natural heat convection inside the dome of pyranometers in the sensitivity of these instruments.

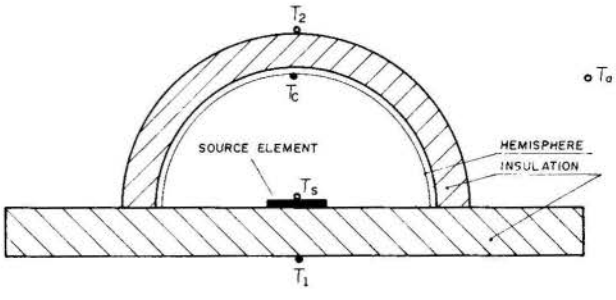

Fig. 1 - Experimental apparatus

EXPERIMENTAL APPARATUS AND PROCEDURE

The experimental apparatus, as shown in Fig. 1, consists of a glass hemisphere with 3.5cm inner radius and 0.5mm thick. That hemisphere was accomodated above a polystyrene plate of 20cm x 20cm and 5cm thick, with the external surface covered by an insulation of 5 cm thick.

At the base center from the hemisphere it was installed over a phenolite substrate a nickel resistive film as heat source, forming an uniformily heated squared area of $2.10^{-4} m^2$. As shown in Fig. 1, 30 gauge copper-constantan thermocouples were placed up on the internal surface from the insulation, in the lower side from the insulation base plate and externally monitoring the ambient temperature. The experimental assembly was installed in a room of approximately 2.5m wide, 3m high and 4m long, with ambient temperature controlled during the experimentation time. The temperature of the source element was determined by the knowledge of the variation of its electrical resistance due to the introduction of electric energy, VI, and by the film thermal coefficient of resistance α. Air was used as the working fluid inside the dome.

The source element was connected to a DC power supplier with variable control and 3 hours was the time necessary to attain steady state for the beginning of measurements.

UNCERTAINTY ANALYSIS

The thermocouples outputs were measured by a Robert Shaw milivoltimeter to 10μV, which results in ±0.25ºC sensitivity. The voltage and current inputs to the source element was measured with an accuracy of ±0.3percent, using a FLUKE 8050A digital multimeter. The power input to the source element was then calculated by using the measured voltage and current across the element. This procedure resulted in an uncertainty of ±1 percent in the calculated power inputs. The uncertainty associated with the length scale used in the data reduction was ±0.5mm. Based on the observed variation in the reported values in the literature the thermophysical properties of the air were assigned an uncertainty of ±2 percent

The overall uncertainty in the Nusselt and Rayleigh numbers varies with the power dissipated on the source element. Smaller power input results in a larger uncertainty due to the lower difference of temperature between the source element and the internal surface of the dome and the energy lost by conduction. The estimated uncertainties in the Nu and R_a numbers were in average of 5 and 7 percent, respectively.

DATA REDUCTION

The values of all thermophysical properties of the air were obtained in thermodynamics tables at the averaged temperature between that of the source element and that up in the internal surface of the dome.

The heat transfer coefficient for the source element was calculated as

$$h = (Q - Q_{rad} - Q_{cond})/A_s(T_s - T_c) \quad (1)$$

where Q is the power input to the source element, Q_{rad} heat lost by radiation which at the situation of greater temperature difference was of 2% percent of the total dissipated energy, Q_{cond} is the substrate and insulation heat transfer which at the situation of lower temperature difference was of 8% percent and at that of greater temperature difference was of 2% percent of the total dissipated energy, A_s the surface area of the source element and $(T_s - T_c)$ represents the temperature difference between the source element and the dome.

The temperature T_s of the thermoresistive source element was determined by the relationship

$$R_s = R_a[1 + \alpha(T_s - T_a)] \quad (2)$$

where R_s is the resistance of the source element at the temperature T_s, T_a the ambient temperature and α the thermal coefficient of resistance.

The Nusselt and Rayleigh numbers were defined as

$$Nu = hR/K \quad (3)$$

$$Ra = g\beta(T_s - T_c)R^3.Pr/\nu^2 \quad (4)$$

being K the air thermal conductivity, R inner radius of the hemisphere, g acceleration due to gravity, β thermal expansion coefficient, ν kinematic viscosity of the air inside the hemisphere and Pr the Prandtl number.

RESULTS AND DISCUSSION

Figure 2 presents the Nusselt number plotted against the Rayleigh number. A typical correlation for the Nusselt number in natural convection inside enclosure is in the form

$$Nu = C.Ra^n \quad (5)$$

being C and n dependents upon the enclosure geometric configuration, determined by the least-square fitting. In natural convection inside enclosures although in the literature it is common practice to use several values for n, in this work it was attributed the value of 0.25 for n.

By this way it was found the following correlation which represents the majority of the experimental values

$$Nu = 0.198.Ra^{0.25} \quad (6)$$

Applying all the data to the equation (6) it was reached the deviation range from -4% to +6%, being the deviation defined by

$$Deviation = [Nu_{cor} - Nu_{exp}]/Nu_{exp} \quad (7)$$

where Nu_{cor} and Nu_{exp} are the correlation and experimental Nusselt number, respectively.

As mentioned earlier, the subject from this study is to understand the natural heat convection inside a hemispherical cavity such that used as domes in pyranometers, at horizontal situation, with a discrete heat source located at the center of that hemisphere base. Keyhani et al. [2] and Ravine and Richards [5, 6], in recent publications, studied experimentally the problem of natural convection in vertical cavities with discrete heat sources and although those studies have different geometrical aspect as the present work the correlations found by the authors are not so divergent from the correlation found here. Here it is intended to compare the results with some studies of heat convection inside domes of solarimeters, trying to make some questions about the fact that the majority of these works attributes the sensitivity alteration of tilted pyranometers to the accentuated con

vective process on the instrument's sensor.

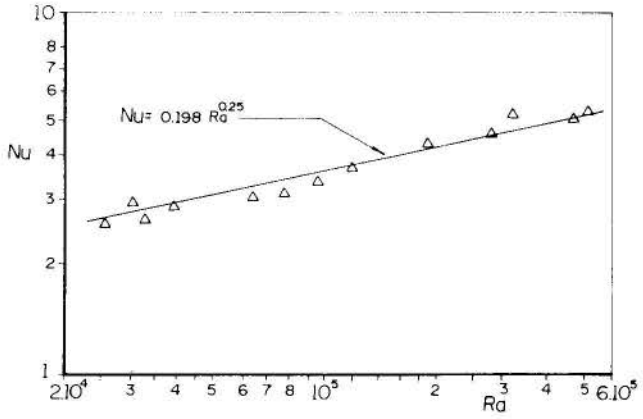

Fig. 2 - Correlation for heat transfer

Anderson |3|, realizing studies about role of the heat transfer in the design and performance of solarimeters, presented a experimental correlation in the form

$$Nu = 0.085.Ra^{0.32} \qquad (8)$$

The same doesn't happen to the correlation presented by Mikheyev |9| representing natural convection inside cavities with several geometrical aspects, calling an equivalent convective heat transfer, in the form

$$\varepsilon_c = 0.18.Ra^{0.25} \qquad (9)$$

which, when compared to the present study correlation, maintains a constant deviation of 10% along the entire range of Rayleigh number as shown in Table 1.

TABLE 1

Ra	Lima & Parreira	Mikheyev	Δ%	Anderson	Δ%
10^4	1.98	1.80	+10	1.62	+22
10^5	3.52	3.20	+10	3.39	+3.8
10^6	6.26	5.69	+10	7.07	-11

Trying to realize an analogy between the heat transfer inside a hemispherical cavity and the sensitivity alteration of a pyranometer, Sesso and Lima |10| studied the effect of tilting a instrument as shown by the figure 3. The literature about the effect of tilting pyranometer testifies deviation of up 7% in the sensitivity due to convective processes inside the domes.

By the Fig. 3, like other studies, that specific pyranometer has showed a maximum deviation of 3.5 percent from the ideal response when operated in tilted position.

The argument that the sensitivity variation of pyranometers operated in tilted position is related to the convective processes inside the domes although intuitively correct it is difficult to demonstrate because of uncertainties in the experimental determination of heat transfer coefficient.

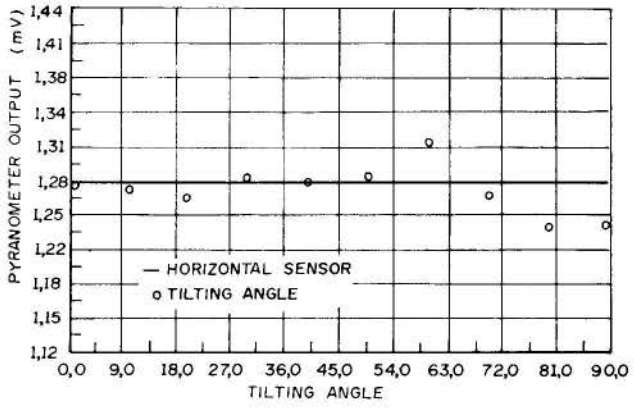

Fig.3 - Effect of tilting pyranometer |10|

CONCLUSION

In this paper the problem of natural convection in a hemispherical cavity, with discrete heat source at the center of a base, was studied. A good agreement between the results and the correlations in the literature was obtained.

The argument that the sensitivity variation of pyranometers operated in tilted position is related to the convectives processes inside the domes although intuitively correct, it is difficult to demonstrate because the uncertainty in the experimental determination of heat transfer coefficient is greater than the percentual deviation of sensitivity in that instrument.

REFERENCES

|1| Ostrach, S., 1988, "Natural convection in enclosures", ASME Journal of Heat Transfer, Vol. 110, pp. 1175-1190.

|2| Keyhani, M., Prasad, V and Cox, R., 1988, "An experimental study of natural convection in a vertical cavity with discrete heat sources", ASME Journal of Heat Transfer, Vol. 110, pp. 616-624.

|3| Anderson, M.C., 1967, "The role of heat transfer in the design and performance of solarimeters", Journal of Applied Meteorology, Vol. 6, pp. 941-947.

|4| Cabelli, A., 1977, "Natural convection in inclined hemispherical cavities - an application in pyranometry", Second Australasian Conference on Heat and Mass Transfer, The University of Sidney, pp. 257-264.

|5| Ravine, T.L. and Richards, D.E., 1988, "Natural convection heat transfer from a discrete thermal source on a channel wall", ASME Journal of Heat Transfer, Vol. 110, pp. 1004-1006.

|6| Ravine, T.L. and Richards,D.E., 1988, "Natural convection heat transfer from a discrete thermal source on a vertical surface" ASME Journal of Heat Transfer, Vol. 110,pp. 1007-1009.

|7| Norris, D.J., 1974, "Calibration of pyranometer in inclined and inverted positions", Solar Energy, Vol. 16, pp. 53-55.

|8| Hammer, T.M., 1984, "Calibration of tilted Eppley pyranometers under solar radiation", Solar Energy, Vol. 32, pp. 139-140.

|9| Mikheyev, M.A., 1964, "Fundamentals of Heat Transfer", MIR, Moscow, USSR.

|10|Sesso, M.G.V. and Lima, L.C., 1990, "A portable pyranometer", submitted to II PACAM, Valparaiso, Chile.

III ENCIT – Itapema, SC (Dezembro 1990)

3-D NUMERICAL SIMULATION OF PERIODIC NATURAL CONVECTION IN A DIFFERENTIALLY HEATED CUBICAL ENCLOSURE

TORU FUSEGI[1], JAE MIN HYUN[2], KUNIO KUWAHARA[3] AND BAKHTIER FAROUK[4]
[1] Institute of Computational Fluid Dynamics
1-22-3 Haramachi, Meguro, Tokyo 152, Japan
[2] Department of Mechanical Engineering
Korea Advanced Institute of Science and Technology
Chong Ryang, Seoul 131, Korea
[3] Institute of Space and Astronautical Science
3-1-1 Yoshinodai, Sagamihara, Kanagawa 229, Japan
[4] Department of Mechanical Engineering and Mechanics
Drexel University
Philadelphia, Pennsylvania 19104, U. S. A.

SUMMARY

A high-resolution, finite-difference numerical study is performed on three-dimensional steady periodic natural convection of air in a cubical enclosure at the Rayleigh number of 8.5 x 10^6. The enclosure is subjected to differential heating at the two vertical side walls. A linear temperature profile is specified for the horizontal walls. The oscillation frequency is in close agreement with the previous experimental and two-dimensional numerical investigations. The three-dimensionality of the mean flow fields is observed to be confined into narrow regions near the end walls.

INTRODUCTION

Natural convection in a rectangular enclosure, whose one vertical wall is heated and the opposing side cooled, is a basic model for a variety of thermal engineering systems. These include solar energy collectors, electronic device cooling and compartment fire problems. Analyses on the differentially heated enclosures with a square cross section are numerous; numerical studies have been performed for the two-dimensional geometry (square channels) [1-5] and for three-dimensional boxes [6-8], to cite a few. Experiments have been conducted for media whose Prandtl number ranges from 0.7 (air) to 6000 (glycerin) [9-15].

In the majority of the works mentioned above, the thermal boundary condition for the horizontal walls is adiabatic. This idealized situation does not fully represent the actual engineering applications and is difficult to realize in experiments. Despite much effort to completely insulate the horizontal walls, the heat transfer from the surfaces cannot be avoided, as seen in the temperature field measurements [9-11].

Cases for conducting horizontal walls have been studied to reveal the effect of the heat transfer on the field structure while the enclosures are heated differentially at the vertical walls. Lee and Sernas [1] used the isothermal condition on the horizontal walls for two-dimensional square cavities filled with air. In their computational analysis, the floor was cooled and the ceiling was heated at the same temperatures that were specified for the vertical walls. This boundary condition was found to stabilize the flow. Experimentally, Kirkpatrick and Bohn [13] constructed a water-filled cubical enclosure whose surfaces could be maintained independently at different temperatures in order to investigate the effect of differential heating at both the vertical and horizontal directions at a high Rayleigh number of around 10^{12}.

It has been observed that for small aspect ratios (less than 10, say), if the horizontal walls are conducting, the flow is destabilized at lower Rayleigh numbers than for the cases of the insulated condition. Le Quere and Alziary [5] obtained a stability diagram for two-dimensional air-filled rectangular enclosures over the aspect ratio range between 1 and 10. For the two-dimensional square enclosure in the case of the conducting horizontal wall, the critical Rayleigh number, beyond which periodic regular oscillations appeared in the fields, was found to be 2.2 x 10^6. This was obtained by solving the transient Navier-Stokes equations numerically [5]. The period of oscillation was in good agreement with the result based on the lowest Hopf bifurcation point, which was determined by a two-dimensional linear stability analysis [16]. However, no oscillations were observed for the insulated horizontal walls at this aspect ratio [15].

Experiments in a cubical box with the conducting horizontal walls have been conducted by Briggs and Jones [11]. Over the Rayleigh number range of 2.5 x $10^6 \le Ra \le$ 1.2 x 10^7, in which steady periodic oscillations were observed, the frequencies of the oscillations were determined from velocity fluctuations measured by laser Doppler techniques. They were found to take discrete values and two stable modes existed over certain Rayleigh number ranges. In their experiments, the frequency acquired at a given Rayleigh number depended on whether the Rayleigh number was approached from lower or higher values. Additional Schlieren temperature field measurements were made for the same geometry by Jones and Briggs [14]. Local velocity and velocity-temperature correlations were found to be characterized by the behavior of thermals formed in the enclosure. Two-dimensional numerical calculations were also performed as part of the analysis [14] for selected Rayleigh numbers. The frequencies of the steady periodic oscillations were in good agreement with the measurements.

Although the experiments [11, 14] were conducted in a nearly cubic enclosure, the three-dimensional characteristics of the fields were not investigated. When the measurements on the mid-symmetry plane (z = 0.5) were compared with the two-dimensional computations, the numerical results overpredicted the peak values of the horizontal velocity by nearly 20 % of the experimental data. The critical Rayleigh number, Ra_c, for periodic oscillations was 3.2 x 10^6, which was determined from the three-dimensional experiment; however, Ra_c appeared to take a lower value, 2.1 x 10^6, in the two-dimensional computations. These discrepancies were attributed to some unknown three-dimensional effects that were present in the experiment. This issue may be better illuminated by full three-dimensional calculations in a box with the conducting horizontal walls.

In the present paper, a numerical study is reported on three-dimensional natural convection in a cubical enclosure, whose thermal boundary condition is identical to that employed in Ref. [11]. As shown in *Figure* 1, the length of the cube is L_o, and the right vertical wall is heated isothermally at a temperature of T_H, while that in the left side is cooled at a temperature of T_C. The linear temperature profile is imposed over the horizontal walls. The planes located at $z = 0$ and L_o (hereafter referred to as the *end walls*) are considered to be thermally insulated. Computations are made for air at the Prandtl number of 0.71. In order to closely simulate the experimental condition [11, 14], the overall temperature difference of the problem, $T_H - T_C$, is set equal to one-tenth of the film temperature, $(T_C + T_H) / 2$, which is used as the reference temperature, T_o. Time averaged as well as instantaneous field characteristics are examined in detail by transient computations carried out on an extremely fine finite difference grid network of 62^3. This enables us to attain sufficient resolution of the local field characteristics. The numerical resolution of the present transient computations is comparable to the maximum accuracies that have been achieved in the previous two-dimensional situations [2]. The finite difference mesh is non-uniformly distributed to handle steep gradients of the field variables near the solid surfaces.

The primary objective of this study is to present complete three-dimensional pictures of the gross features of time-evolving convective

flow patterns in a cubical enclosure. At a high Rayleigh number, it is anticipated that the distinct boundary layers are present near the walls; in the bulk of the interior, a near-stagnant core will be a salient feature. The present paper clearly captures these prominent transient three-dimensional characteristics by use of the state-of-the-art computer simulation techniques. The field characteristics of the transient natural convection inside the enclosure are examined by elaborate three-dimensional numerical visualizations of the results. Time-dependent changes in the flow characteristics and heat transfer rate in the enclosure are scrutinized.

The three-dimensional numerical results of the present study provide useful and systematic data for this fundamental flow model; examination of the data permits closer analyses of unsteady three-dimensional features.

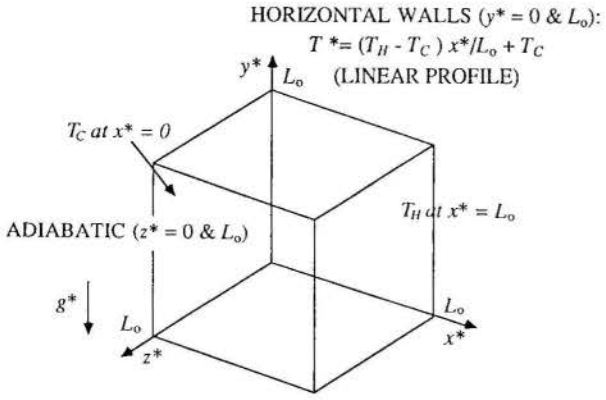

Figure 1 The geometry and the boundary conditions of the cubical enclosure

MATHEMATICAL MODEL

The flow is governed by the unsteady, incompressible Navier-Stokes and energy equations. The Boussinesq approximation is invoked for the fluid properties. The non-dimensionalized form of the governing equations can be expressed in tensor notation as:

$$\frac{\partial u_j}{\partial x_j} = 0 \tag{1}$$

$$\frac{\partial u_i}{\partial t} + \frac{\partial}{\partial x_j}(u_j u_i) = -\frac{\partial p}{\partial x_i} + \frac{1}{\mathrm{Re}}\frac{\partial^2 u_i}{\partial x_j \partial x_j} + \delta_{i2}\frac{T-1}{\mathrm{Fr}} \tag{2}$$

$$\frac{\partial T}{\partial t} + \frac{\partial}{\partial x_j}(u_j T) = \frac{1}{\mathrm{Re\,Pr}}\frac{\partial^2 T}{\partial x_j \partial x_j} \tag{3}$$

where x_i denotes the Cartesian coordinates, u_i represents the velocity components, t is the time, p is the pressure, T is the temperature, and δ_{ij} is the Kronecker delta ($\delta_{ij} = 1$ if $i = j$, and $\delta_{ij} = 0$ otherwise). The viscous dissipation and the pressure work terms are neglected in the energy equation.

The physical quantities are non-dimensionalized in the following manner:

$$(x, y, z) = (x^*, y^*, z^*) / L_o,\ (u, v, w) = (u^*, v^*, w^*) / u_o,$$

$$t = t^* u_o / L_o,\ p = (p^* - p_o) / \rho^* u_o^2,\ T = T^* / T_o$$

where the asterisk (*) denotes dimensional values and ρ is the density. The reference scales (with the subscript '$_o$') for length, velocity, time, pressure and temperature are the enclosure height (L_o), the convective velocity ($u_o = [g^*\beta^* L_o (T_H - T_C)]^{1/2}$, where g is the gravitational acceleration and β is the thermal expansion coefficient), the convective time ($t_o = [g^*\beta^*(T_H - T_C) / L_o]^{-1/2} = N^{-1}$, where N is the Brunt-Väisälä frequency), the hydrostatic pressure (p_o) and the film temperature ($T_o = (T_C + T_H)/2$), respectively.

The definitions for the non-dimensional parameters are:

Froude number: $\mathrm{Fr} = u_o^2 / g^* L_o$
Prandtl number: $\mathrm{Pr} = c_p^* \mu^* / k^*$
Reynolds number: $\mathrm{Re} = \rho^* u_o L_o / \mu^*$

where c_p is the specific heat, μ is the viscosity, k is the thermal conductivity. The Rayleigh number, Ra ($= g^* \beta^* c_p^* \rho^{*2} L_o^3 (T_H - T_C) / \mu^* k^*$), is related to the Reynolds number as $Ra = Re^2$ in the present analysis.

The following boundary conditions are specified:

$$u = v = w = 0 \quad \text{on all the walls} \tag{4}$$

$$T = (2 - \delta)/2 \ \text{ at } x = 0,\ T = (2 + \delta)/2 \ \text{ at } x = 1,$$
$$T = (x - 1/2)\,\delta + 1 \ \text{ at } y = 0 \text{ and } 1,$$
$$\text{and } \partial T / \partial n = 0 \ \text{ at } z = 0 \text{ and } 1 \tag{5}$$

where δ is the overheat ratio, $(T_H - T_C)/T_o$, which is set equal to 0.1 in the present study, and n represents the coordinate normal to the surface.

SOLUTION METHOD

A discretized form of the governing equations (1) - (3) are obtained through a control-volume based finite difference procedure. Numerical solutions are acquired by an iterative method, together with the pressure correction algorithm, SIMPLE [17]. The present technique employs the *S*trongly *Imp*licit Scheme [18] to accelerate convergence characteristics of the solutions. SIP is applied to the planes of constant z in order to determine simultaneously the dependent variables in the x and y directions on each plane.

The convection terms in the momentum equation (2) are treated by the QUICK methodology modified for non-uniform grids [19], while those in the energy equation (3) are dealt with by a hybrid scheme [17]. The QUICK scheme involves a third-order accurate upwind differencing, which possesses the stability of the first-order upwind formula and is free from substantial numerical diffusion experienced with the usual first-order techniques.

The entire enclosure constitutes the full computational domain. The number of grid points for computations is 62 x 62 x 62. Variable grid spacing is introduced to resolve steep gradients of the velocity and the temperature near the walls. The configuration of non-uniform grid system is determined from the results of three-dimensional computations which considered the thermally insulated horizontal walls [20]. Changes less than 2 % and 0.2 % of the peak velocity and the overall Nusselt number, respectively, took place when the number of the grid points was doubled in the x-direction. The minimum grid distance is approximately 0.015 in the non-dimensional length unit.

The fully implicit scheme is used for marching in time. The non-dimensional time step value is set equal to 0.01, which is sufficiently small compared to the period of oscillations in the fields, as discussed in the section that follows.

Convergence of computations at each time step is declared when the following convergence criterion is satisfied:

$$\frac{|\phi_n - \phi_{n-1}|}{|\phi_n|_{maximum}} \le 10^{-4} \quad \text{for all } \phi \tag{6}$$

where ϕ denotes any dependent variable, and n refers to the value of ϕ at the n-th iteration level.

The initial condition for the present study is an instantaneous solution of the two-dimensional computation at the same Rayleigh number. Starting from this state, the three-dimensional calculation is continued far beyond a time instant at which the influence of the initial condition on the result becomes negligible.

RESULTS AND DISCUSSION

Computations were performed on a HITACHI S-820/80 supercomputer system at the Institute of Computational Fluid Dynamics (ICFD) in Tokyo, Japan. The system has a maximum CPU speed of 3 GFLOPS and a maximum incore memory of 512 MB. The total CPU time for the three-dimensional computation required approximately 44 hours with 16000 time steps (160 non-dimensional time instants) and 100 MB of the memory. The results of the last 40 non-dimensional time steps, which were free from the effect of the initial condition, were used for the present discussion.

Regular periodic oscillations appeared at the computed Rayleigh number of 8.5×10^6. In the present section, the characteristics of the time-averaged fields are examined first to describe the overall field structure. The fluctuating field characteristics will be considered next, including a comparison of the results with the measurements [11, 14] and the two-dimensional numerical computations [5, 14].

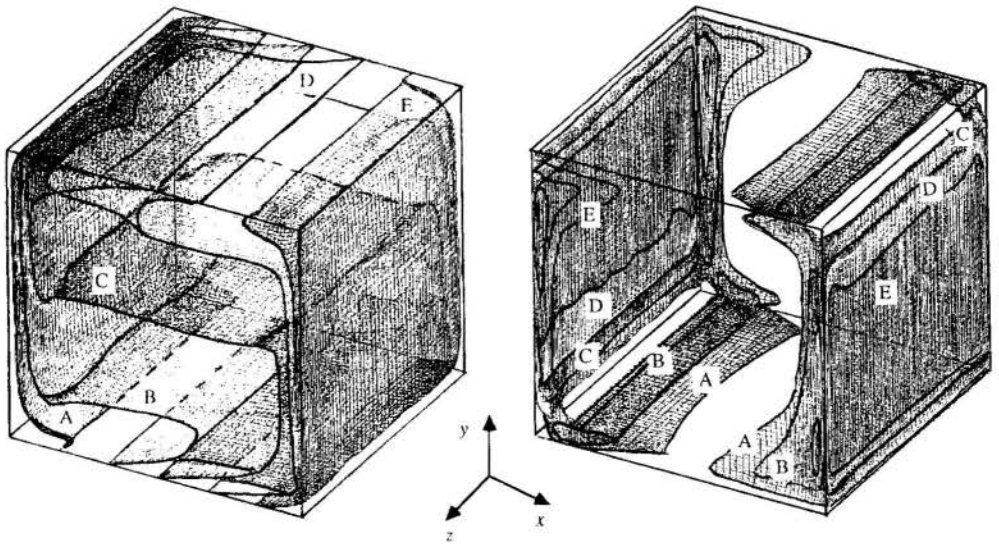

(a) ISOTHERMS (b) ISOVORTICITY SURFACES

Figure 2 The time-averaged isotherms and isosurfaces of the absolute values of the vorticity [contour levels: (a) 0.9667 (A), 0.9833 (B), 1.0 (C), 1.017 (D), 1.033 (E); (b) 5 (A), 10 (B), 15 (C), 20 (D), 25 (E)]

The Characteristics of the Time-Averaged Fields

The obtained field data are averaged over a non-dimensional time interval of 20, which is sufficiently large compared to the time scale of the flow. *Figure* 2 illustrates perspective views of the mean temperature and flow fields, represented by the isotherms and the isosurfaces of the absolute values of the vorticity (the magnitude of the vorticity vector). The fields exhibit centro-symmetry with respect to the plane located at $z = 0.5$ (hereafter referred to as the *symmetry plane*). At this Rayleigh number, the fields can be characterized as the boundary layer-stagnant core structure; thin thermal and hydrodynamic boundary layers develop along the isothermal walls, while the flow is nearly stagnant in the central region of the enclosure. The temperature field is seen to be stratified in the near-stagnant core. Due to the linear distribution of the temperature over the horizontal walls, the isotherms are strongly bent in the proximity of these surfaces. A dent is seen in the isotherm patterns near the symmetry plane. Examination of instantaneous isotherms reveals that a pair of dents is formed at locations which are symmetric with respect to the mid-plane ($z = 0.5$). They vacillate in the z-direction as the mirror images and merge into one on the symmetry plane. Two dents are observed in the isotherm in the vicinity of the bottom edge near the heated vertical wall. The period of these motions is seen to be much longer than that of the quasi-steady field oscillations. Actually, it is longer than the time interval used in the present computation. No description was given concerning this three-dimensional behavior of the temperature field in the experimental investigations [11, 14].

Except for this local phenomenon, the two-dimensional structure prevails over the major portion of the temperature field due to the uniform temperature distribution imposed in the z-direction on the horizontal and vertical walls. The vorticity is mostly concentrated within very narrow regions near the isothermal walls. Three-dimensional variation is not discernible in the flow field except for the regions in the proximity of the end-walls. The flow patterns that are associated with the motion of the isotherm dents are not apparent in the time-averaged vorticity field. The three-dimensional graphics were produced by an interactive graphic software [21], which runs on a FUJITSU VP-200 supercomputer system at the ICFD.

In order to closely examine the three-dimensionality of the time-averaged flow field structure, the velocity profiles near the horizontal and vertical walls in various planes of constant z are presented in *Figure* 3. The results of the two-dimensional computation of the present study are also shown for comparison. The velocity distribution in the symmetry plane located at $z = 0.5$ agrees very well with the two-dimensional case. Both the locations and the magnitude of the peak velocities are in close agreement. The slopes of the two-dimensional velocity components are slightly steeper than those of the three-dimensional results in the symmetry plane ($z = 0.5$). The velocity profiles for the three-dimensional computation at various z locations do not differ significantly from those in the symmetry plane.

The Characteristics of the Fluctuating Fields

The characteristics of the steady periodic fluctuations of the fields are discussed in this subsection. *Figure* 4 displays the variations of the temperature at a representative internal point and of the overall Nusselt number at the isothermal cold wall, which is defined as

$$Nu_{\text{mean}}(z) = \int_0^1 \frac{\partial T(y,z)}{\partial x}\Big|_{x=0} dy \quad \left(= \int_0^1 Nu_{\text{local}}(y,z)\ dy \right) \quad (7)$$

$$Nu_{\text{overall}} = \int_0^1 Nu_{\text{mean}}(z)\ dz \quad (8)$$

The frequencies of the periodic fluctuations that are apparent in the figure for the two quantities measured at these different locations turned out to be the same. The normalized frequency, f_{ND}, made dimensionless with the Brunt-Väisälä frequency, is found to be 0.33. In addition, velocity fluctuations detected at the same locations as the temperature shown are in phase with these oscillations. At this Rayleigh number ($Ra = 8.5 \times 10^6$), Briggs and Jones [11] reported that in their experiments in a cubical enclosure, two frequencies were possible: $f_{ND} = 0.25$ and 0.321. The latter value is within 5 % of the frequency detected in the present three-dimensional computation. In a two-dimensional calculation at $Ra = 9 \times 10^6$, Jones and Briggs [14] obtained $f_{ND} = 0.32$, which agreed very well with their measured value [11]. Another two-dimensional numerical analysis conducted independently [5] predicted f_{ND} to be 0.26 at $Ra = 2.2 \times 10^6$, which is again in close agreement with the frequency obtained [11].

The instantaneous maxima and minima of the velocity at given locations in the symmetry plane ($z = 0.5$) are plotted in *Figure* 5 as the velocity envelopes. They are compared with the experimental data [11], which are also shown in the same figure. For the horizontal velocity (u), the measurements attain generally higher values than the numerical predictions. The trend is reversed for the vertical velocity (v). In both cases, the locations of the peaks in the boundary layers near the walls agree well among the measurements and computations. The distinct boundary layers and near-stagnant interior core structure are inferred from the figure.

CONCLUSIONS

Three-dimensional natural convection in a differentially heated cubical enclosure with the conducting horizontal walls is investigated numerically at the Rayleigh number of 8.5×10^6. Steady periodic oscillations are observed in the fields. The period of the oscillations is in close agreement with the experimental measurements [11, 14] and the previous two-dimensional computations [5, 14]. This result is supportive of the two-dimensional assumption used in these prior investigations. According to the experiments [11, 14], two oscillation periods were obtained at this Rayleigh number, depending on whether

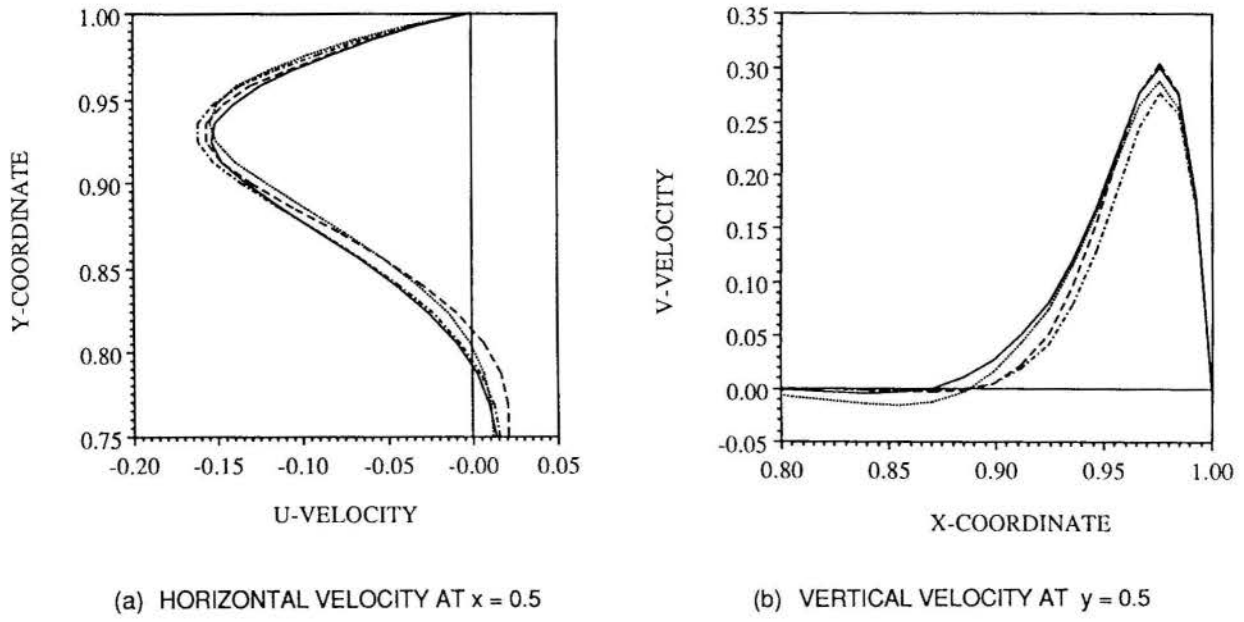

(a) HORIZONTAL VELOCITY AT x = 0.5

(b) VERTICAL VELOCITY AT y = 0.5

Figure 3 Time-averaged velocity profiles in the various planes of z = constant [———, at $z = 0.5$; — – — , $z = 0.3$; ·····, $z = 0.1$; - - - - - , two-dimensional results]

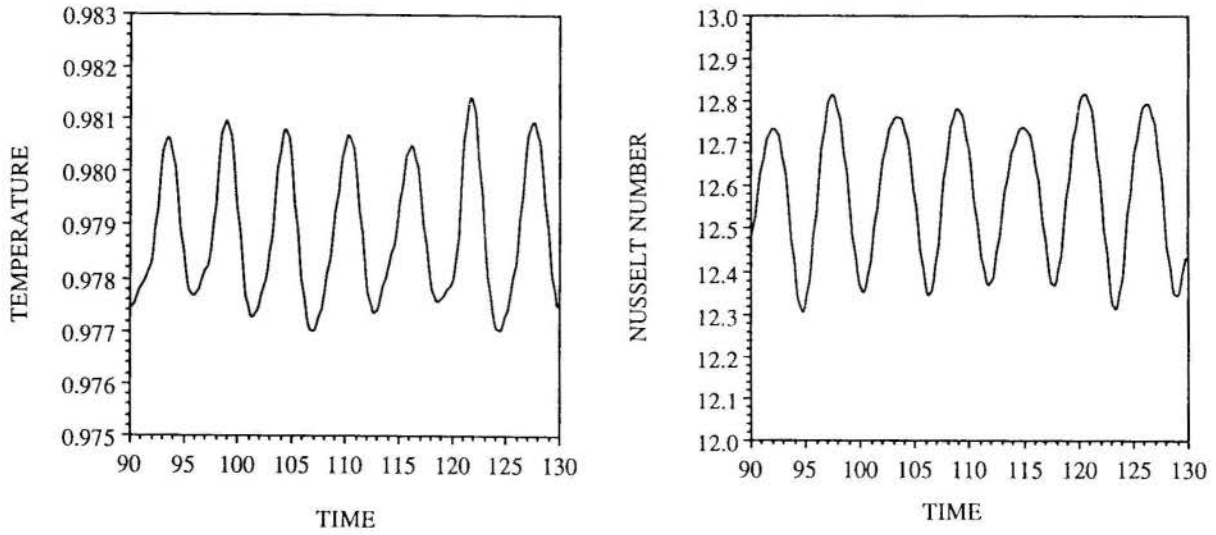

(a) TEMPERATURE AT
(x, y, z) = (0.186, 0.082, 0.5)

(b) OVERALL NUSSELT NUMBER
AT THE COOLED WALL

Figure 4 Periodic fluctuations of the local temperature and the overall Nusselt number

the particular *Ra* was approached from lower or higher values. In the present computation, the higher frequency was captured. Because of the limitation of the available CPU time, it was not possible to study the effects of the initial condition on the final solutions.

Another aspect of the present problem is the effects of the boundary condition at the end walls ($z = 0$ and 1). This has not been previously studied for the present geometry. Imperfectly insulated surfaces appear to give rise to the pronounced three-dimensionalities. Analyses of these effects are left as the subjects of future investigations.

Under the present boundary conditions at the end walls, the z-variations of the overall field structures are significant in the instantaneous local characteristics. In the time-averaged fields, the three-dimensionalities are less eminent, and the two-dimensional assumption appears to be reasonable to portray the gross features of the flow.

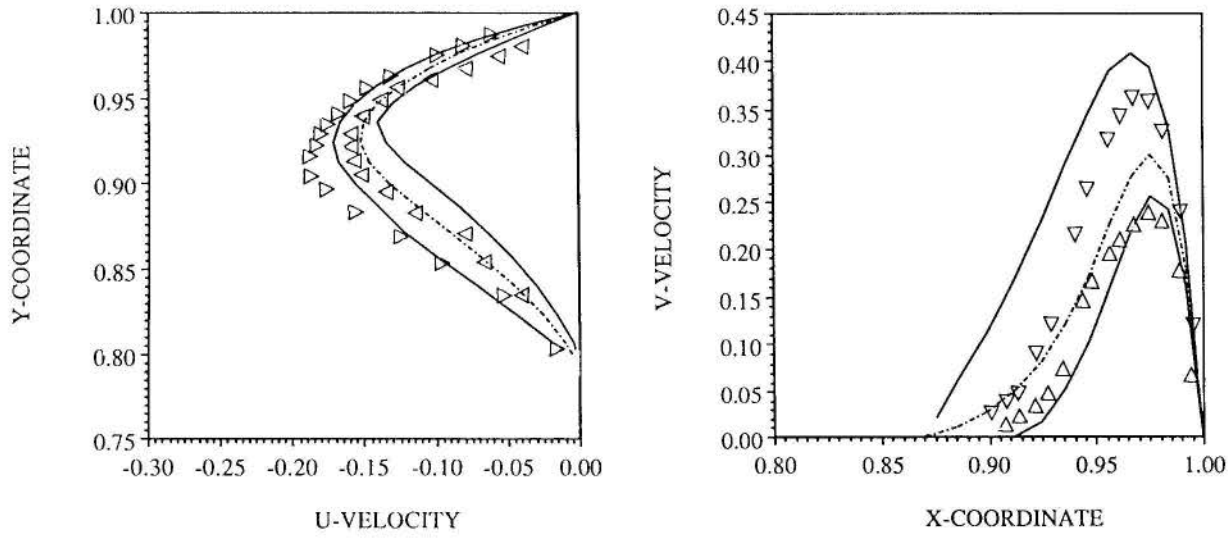

(a) HORIZONTAL VELOCITY AT x = 0.5

(b) VERTICAL VELOCITY AT y = 0.5

Figure 5 Velocity envelopes in the symmetry plane located at $z = 0.5$ [——— , the minimum and maximum velocity at each location; — — — , time-averaged velocity; symbols denote measured velocity envelopes[11]]

REFERENCES

1. Lee, E. I., and Sernas, V., "Numerical Study of Heat Transfer in Rectangular Air Enclosure of Aspect Ratio Less Than One," ASME Winter Annual Meeting, Chicago, Illinois, Paper No. 80-WA/HT-43, 1980.
2. de Vahl Davis, G., "Natural Convection of Air in a Square Cavity: a Bench Mark Numerical Solution," *International Journal for Numerical Methods in Fluids*, Vol. 3, pp. 249-264, 1983.
3. Markatos, N. C., and Pericleous, K. A., "Laminar and Turbulent Natural Convection in an Enclosed Cavity," *International Journal of Heat and Mass Transfer*, Vol. 27, pp. 755-772, 1984.
4. Ozoe, H., Mouri, A., Ohmura, M., Churchill, S. W., and Lior, N., "Numerical Calculations of Laminar and Turbulent Natural Convection in Water in Rectangular Channels Heated and Cooled Isothermally on the Opposing Vertical Walls," *International Journal of Heat and Mass Transfer*, Vol. 28, pp. 125 - 138, 1985.
5. Le Quere, P., and Alziary de Roquefort, T., "Transition to Unsteady Natural Convection of Air in Differentially Heated Vertical Cavities," *Significant Questions in Buoyancy Affected Enclosure or Cavity Flows*, ASME HTD-Vol. 60, pp. 29-36, 1986.
6. Mallinson, G. D., and de Vahl Davis, G., "Three-Dimensional Natural Convection in a Box: a Numerical Study," *Journal of Fluid Mechanics*, Vol. 83, pp. 1-31, 1977.
7. Lankhorst, A. M., and Hoogendoorn, C. J., "Three-Dimensional Numerical Calculations of High Rayleigh Number Natural Convective Flows in Enclosed Cavities," *Proceedings, 1988 National Heat Transfer Conference*, Houston, ASME HTD-96, Vol. 3, pp. 463-470, 1988.
8. Lee, T. S., Son, G. H., and Lee, J. S., "Numerical Predictions of Three-Dimensional Natural Convection in a Box," *Proceedings, 1st KSME-JSME Thermal and Fluids Engineering Conference*, Seoul, Korea, Vol. 2, pp. 278-283, 1988.
9. Bajorek, S. M., and Lloyd, J. R., "Experimental Investigation of Natural Convection in Partitioned Enclosures, " *Journal of Heat Transfer*, Vol. 104, pp. 527-532, 1982.
10. Krane, R. J., and Jessee, J., "Some Detailed Field Measurements for a Natural Convection Flow in a Vertical Square Enclosure, " *Proceedings, 1st ASME-JSME Thermal Engineering Joint Conference*, Vol. 1, pp. 323-329, 1983.
11. Briggs, D. G., and Jones, D. N., "Two-Dimensional Periodic Natural Convection in a Rectangular Enclosure of Aspect Ratio One," *Journal of Heat Transfer*, Vol. 107, pp. 850-854, 1985.
12. Bilski, S. M., Lloyd, J. R., and Yang, K. T., "An Experimental Investigation of the Laminar Natural Convection Velocity in Square and Partitioned Enclosures," *Proceedings, 8th International Heat Transfer Conference*, Hemisphere Publishing Corp., Washington, DC, Vol. 4, pp. 1513-1518, 1986.
13. Kirkpatrick, A. T., and Bohn, M., "An Experimental Investigation of Mixed Cavity Natural Convection in the High Rayleigh Number Regime," *International Journal of Heat and Mass Transfer*, Vol. 29, pp. 69-82, 1986.
14. Jones, D. N., and Briggs, D. G., "Periodic Two-Dimensional Cavity Flow: Effect of Linear Horizontal Thermal Boundary Condition,"*Journal of Heat Transfer*, Vol. 111, pp. 86-91, 1989.
15. Hiller, W. J., Koch, S., Kowalewski, T. A., de Vahl Davis, G., and Behnia, M., "Experimental and Numerical Investigation of Natural Convection in a Cube with Two Heated Side Walls," *Proceedings, International Union of Theoretical and Applied Mechanics Symposium*, Cambridge University Press, Cambridge, U. K., pp. 717-726, 1990.
16. Winter, K. H., "Hopf Bifurcation in the Double-Glazing Problem with Conducting Boundaries," *Journal of Heat Transfer*, Vol. 109, pp. 894-898, 1987.
17. Patankar, S. V., *Numerical Heat Transfer and Fluid Flow*, Hemisphere Publishing Corp., Washington, DC, Chap. 6, 1980.
18. Stone, H. L., "Iterative Solution of Implicit Approximations of Multi-Dimensional Partial Differential Equations," *Journal of Numerical Analysis*, Vol. 5, pp. 530-558, 1968.
19. Freitas, C. J., Street, R. L., Findikakis, A. N., and Koseff, J. R., "Numerical Simulation of Three-Dimensional Flow in a Cavity," *International Journal for Numerical Methods in Fluids*, Vol. 5, pp. 561-575, 1985.
20. Fusegi, T., Hyun, J. M., Kuwahara, K., and Farouk, B., "A Numerical Study of 3-D Natural Convection in Differentially Heated Cubical Enclosure", *International Journal of Heat and Mass Transfer* (submitted for publication), 1990.
21. Shirayama, S., and Kuwahara, K., "Patterns of Three-Dimensional Boundary Layer Separation, 25th Aerospace Sciences Meeting," Reno, AIAA Paper 87-0461, 1987.

III ENCIT – Itapema, SC (Dezembro 1990)

ANÁLISE E SIMULAÇÃO DO RESFRIAMENTO DE FILAMENTOS DE POLIÉSTER DURANTE A FIAÇÃO

MARIA APARECIDA LÓRA, M.S., Gerência de Processo, Departamento Textil
GGEG - Rhodia S.A., Santo André - 09000 - SP.
MARCOS M.PIMENTA, Ph.D., Departamento de Engenharia Mecânica - EPUSP
Cxa.Postal, 8174 - São Paulo - SP.

RESUMO

O processo de fiação de filamentos de poliester em fieiras é analisado. Simulação dos escoamentos e transferência de calor calcula perfis de velocidade e temperatura. O modelo considera o processo de resfriamento não isotérmico devido à corrente transversal de ar, à deformação axial dos fios estirados e propriedades variáveis com a temperatura. Efeitos de gravidade, inércia e arraste sôbre o fio são analisados. Balanços de massa, quantidade de movimento e energia aplicados a células infinitesimais incluem efeitos de aquecimento e da direção da trajetória do ar de resfriamento. Balanços de forças analisam as deflexões dos fios sob ação do ar. Resultados numéricos são apresentados.

INTRODUÇÃO

A fig.1.1 mostra esquematicamente o processo de fiação de fibras sintéticas. O polímero fundido é extrudado através de uma fieira, onde são formados os filamentos, que são resfriados por uma corrente transversal de ar. Uma vez resfriados os filamentos se solidificam, e são reunidos, formando um único fio que é então enrolado em bobinas.

A velocidade de enrolamento é consideravelmente maior do que a velocidade de extrusão, ocorrendo assim o estiramento do fio. Este processo de estiramento produz uma variação de secção transversal do filamento e uma maior orientação molecular quando de sua solidificação e cristalização. O esforço mecânico alinha as macro-moléculas resultantesda polimerização. Este grau de orientação molecular controla as propriedades físicas do produto final (módulo de elasticidade, elongamento, afinidade tintorial no tingimento) e é principalmente governado pela tensão atuante no fio no chamado ponto de transição vítria (T = 67°C no caso de fibras de poliéster). Esta tensão depende das variáveis do processo de fiação: temperatura de extrusão, velocidade de enrolamento, vazão em massa do polímero, temperatura e velocidade do ar de resfriamento.

Para o processo industrial, a homogeneidade entre os filamentos de um mesmo fio é uma qualidade importante do produto. As variáveis: temperatura de extrusão, velocidade de enrolamento e vazão em massa do polímero são normalmente controlados. Daí ser necessário um melhor conhecimento e controle do resfriamento. Sabe-se que nos sistemas produtivos atuais a corrente de ar é unidirecional, e se aquece ao resfriar as diversas correias de filamentos. Conclui-se que as diferentes carreiras de filamentos requererão tempos distintos para se solidificarem, e existirão diferentes graus de orientação molecular entre os filamentos de um mesmo fio.

Trabalhos experimentais de visualização do processo mostram que a qualidade do produto pode depender tanto da deflexão da corrente de ar como do feixe de filamentos. O ar fica mais aquecido na vizinhança da fieira, ficando sujeito ao empuxo, e também é arrastado pelos filamentos. A deflexão do feixe pode ocasionar que alguns filamentos se toquem entre si.

A simulação do processo de fiação que leve em consideração estes efeitos é importante para o projeto e aperfeiçoamento das fieiras, e ao controle de sua operação. Na literatura podem ser identificados alguns trabalhos neste assunto.

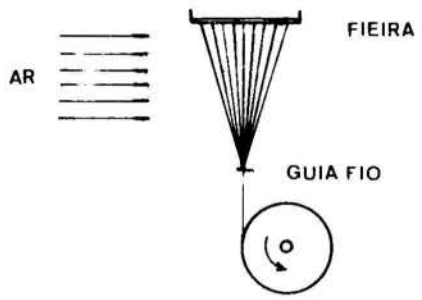

Fig.1.1- Sistema de fiação.

Dutta e Nadkarni [1], Kase e Msyduo [2] formularam modelos matemáticos de simulação baseados na hipótese de força constante ao longo do filamento. Recentemente, George [3] verificou que esta hipótese só é válida para baixas velocidades de enrolamento. Sabe-se, no entanto, que em fieiras de produção industrial e suas velocidades de operação, a força varia ao longo do filamento devido a efeitos de aceleração, gravidade e arrasto do ar sôbre o fio.

Yasuda, Yshihara e Yanagawa [4] propuseram um modelo bi-dimensional de simulação que inclui a força variável para vários filamentos. Paralelamente, balanços de massa e energia permitem o cálculo da velocidade e aquecimento do ar.

Lora [5] desenvolveu um modelo bi-dimensioanl de simulação que inclui os efeitos de: várias carreiras de filamentos no feixe; força variável ao longo do filamento; deflexão e não uniformidade do fluxo de ar; deflexão do fio.

Este trabalho apresenta alguns resultados desta simulação e analisa o efeito relativo dos diferentes fatores.

ANÁLISE DE UM FILAMENTO

Sob algumas hipóteses simplificadoras, o escoamento de um só filamento resfriado durante o processo da fiação envolve uma deformação uniaxial não-isotérmica com propriedades físicas dependentes da temperatura.

A fig.2.1 mostra esquematicamente o processo e as condições de contorno do problema analisado. A_1 é a secção transversal do filamento logo à saída da fieira e T_2 é a temperatura do filamento na região de cristalização. x = 0 corresponde à saída de fieira e x=L onde ocorre a transição vítrea.

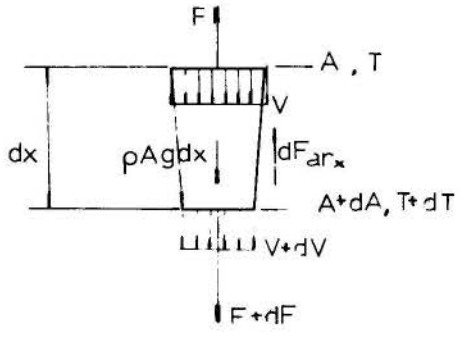

Fig.2.1- Esquema de um filamento.

T_A e V_A são a temperatura e velocidade do ar de resfriamento. Segue:

Balanço de massa

$$G = \rho.V.A. = \rho.(V+dV).(A+dA) \qquad (2.1)$$

Balanço de quantidade de movimento

$$\frac{dF}{dx} = \frac{-G^2}{\rho A^2} \cdot \frac{dA}{dx} - \rho.A.g + \frac{dF\ ar_x}{dx} \qquad (2.2)$$

Balanço de energia

$$G.C_p.dT = 2h.\sqrt{\pi A}.dx.\ (T-T_A) \qquad (2.3)$$

Tensão axial no filamento

$$\tau = 3\,\eta_o \cdot \frac{dV}{dx} \qquad (2.4)$$

Lora [5] substitui as relações experimentais para as propriedades físicas do poliéster e obtém as equações para a temperatura, força axial e área da secção do fio (sistema SI de unidades):

$$\frac{dT}{dx} = \frac{-1,512\ A^{1/6}}{G(995+3,875T)} \cdot (T-T_A).\left[\left(\frac{G/A}{1375-0,75T}\right)^2+(8V_A)^2\right]^{1/6} \qquad (2.5)$$

$$\frac{dF}{dx} = \frac{-G^2}{1375-0,75T}\,\frac{dA}{A^2dx} - (1375-0,75T)Ag + $$

$$+9,922\times10^{-4}.A^{-1,195}.(1375-0,75T)^{-1,39}\ G^{1,39} \qquad (2.6)$$

$$\frac{dA}{dx} = \frac{-(1375-0,75T).F.A.}{2,93\times10^{-2}.G.0,611^{5,2893}.\exp(6923,7/(T+273))} \qquad (2.7)$$

Este sistema de três equações acopladas pode ser resolvido numericamente com as condições de contôrno

$$T(x=0) = T_1 \qquad A(x=0) = A_1$$
$$T(x=L) = T_2 \qquad A(x=L) = A_2$$

Como a condição de contôrno para a força do fio não é conhecida, adota-se inicialmente a hipótese simplificadora de força constante. O valor desta força inicial é dado por

$$F_o = \frac{-1,512\ .\ G^{1/6}\ \int_{V_1}^{V_2}\ [(V^2+(8V_A)^2)]^{1/6}.V^{-7/6}.dV}{\int_{T_1}^{T_2}\ (\rho^{7/6}.C_p/[3.\eta_o.(T-T_A)]).\ dT} \qquad (2.8)$$

obtido das eqs.(2.1),(2.3)e(2.2)com F=constante.

ANÁLISE PARA VÁRIOS FILAMENTOS

Uma fieira é normalmente composta de aproximadamente 100 furos, distribuídos em círculo num arranjo quadrado ou triangular. Para se levar em consideração os efeitos das variações de temperatura e de velocidade do ar de resfriamento nas propriedades do filamento toma-se uma divisão bi-dimensional dos filamentos em células infinitesimais. A fig.3.1 mostra as células onde são realizados os balanços de massa, quantidade de movimento e energia

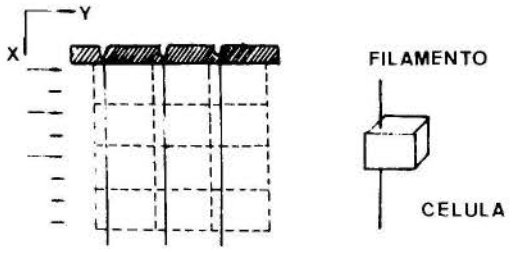

Fig.3.1- Células para os filamentos.

A fig.3.2 mostra esquematicamente a configuração de cada célula. Em contraste com a fig.2.1, neste diagrama estão incluídos a força de arraste sobre o fio F_{ar}, V_x e V_y componentes da velocidade do ar de resfriamento, V_a velocidade média do ar arrastado pelo fio, A_c área da secção de ar que é arrastado pelo fio que passa pela célula.

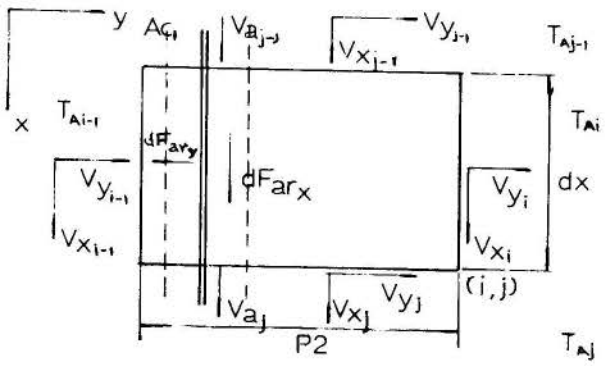

Fig.3.2- Esquema de uma célula.

O modelo a ser empregado para o cálculo de vários filamentos utiliza basicamente o modelo empregado anteriormente no cálculo de um único filamento. A cada passo a temperatura, a área e a força do filamento são calculados com as características do ar a montante. Uma vez tendo sido calculadas as variáveis do filamento, pode-se calcular o efeito do aquecimento e mudança de direção de velocidade do ar em cada célula.

O ar ao atravessar a célula se aquece com o calor cedido pelo filamento. Como o filamento atravessa a célula ar acaba sendo arrastado pelo filamento. Devido às forças atuantes na célula: arraste na direção horizontal e vertical, empuxo resultante das elevadas temperaturas do ar, as linhas de corrente do ar que atravessa a célula são curvas.

Lora [5] mostra que os balanços de massa, quantidade de movimento e energia são:

$$(Va_j.Acl+Vx_j.(P_1.P_2-Acl)).\rho A_j-(Va_{j-1}.Acl+Vx_{j-1}.$$
$$(P_1.P_2-Acl)).\rho A_{j-1}+(Vy_j.\rho A_j-Vy_{i-1}.\rho A_{i-1})\ P_1.dx = 0 \qquad (3.1)$$

$$dF_{ar_x}=(Va_j^2.Acl+Vx_j^2.(P_1.P_2-Acl)).\rho A_j-(Va_{j-1}^2.Acl+$$
$$+Vx_{j-1}^2(P_1.P_2-Acl)).\rho A_{j-1}+(Vx_j.Vy_j.\rho A_i-Vx_{i-1}.Vy_{i-1})P_1.dx$$

onde P_1 e P_2 são os passos transversais e longitudi- (3.2)
nais dos filamentos, e Acl área transversal que subentende o fluido arrastado.

$$dF_{ary} = (Vy_j^2 \cdot \rho A_j - Vy_{i-1}^2 \cdot \rho A_{i-1})P_1 \cdot dx + (Vy_j \cdot Vx_j \cdot \rho A_j - Vy_{j-1} \cdot Vx_{j-1} \cdot \rho A_{j-1})(P_1 \cdot P_2 - Acl) \quad (3.3)$$

$$(Va_j \cdot Acl + Vx_j \cdot (P_1 \cdot P_2 - Acl) + Vy_j \cdot P_1 \cdot dx) \cdot \rho A_j \cdot cpA_j \cdot T_{Aj} = QPOL + (Va_{j-1} \cdot Acl + (Vx_{j-1} \cdot (P_1 \cdot P_2 - Acl)) \cdot \rho A_{j-1} \cdot cpA_{j-1} \cdot T_{Aj-1} + Vy_{i-1} \cdot \rho A_{i-1} \cdot P_1 \cdot dx \cdot cpA_{i-1} \cdot TA_{i-1} \quad (3.4)$$

onde QPOL é o calor cedido pelo plímero (J/S).

Este sistema de equações pode ser resolvido por métodos parabólicos, para um dado número de carreiras do feixe e até a região de cristalização.

RESULTADOS

As figs. 4.1-6 apresentam resultados obtidos com este modelo completo para 20 carreiras de filamentos resfriados pela corrente de ar. As figs. 4.1 e 4.2 mostram perfis de temperatura e áreas das secções dos filamentos em função da distância da fieira. Observa-se uma redução substancial da secção do filamento no início do processo (primeiro terço), permanecendo, então, quase que constante até se atingir a temperatura de cristalização (67°C) ou de transição vítrea. Os filamentos das carreiras posteriores necessitam 50% ou mais distância para se solidificarem.

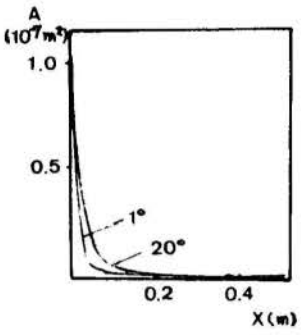

Fig.4.1-Área do filamento (A-Área do filamento(m^2)).

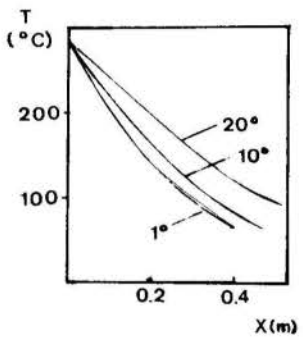

Fig.4.2-Temperatura do filamento. (T- temperatura (°C)

A fig.4.3 mostra que as forças atingidas na região de cristalização variam significativamente entre as carreiras: 1,64 x 10^{-3} N na primeira, 1,33 x 10^{-3} N na vigésima. Esta variação sugere que para este processo isto leve a obtenção de diferentes graus de orientação molecular entre os filamentos que formam o fio, comprometendo a qualidade do produto final. Esta observação indica que o processo de resfriamento pode ser melhorado.

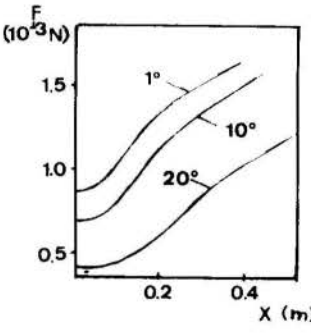

Fig.4.3-Força do filamento (F-força no filamento(N)).

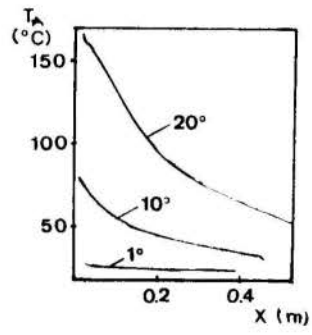

Fig.4.4-Temperatura do ar após o filamento. (T_A-temperatura do ar(°C)).

As figs. 4.5 e 4.6 mostram as componentes de velocidade do ar nas direções x e y. A fig.4.5 mostra que Vx (vertical) aumenta com a distância da fieira, da mesma forma que na fig.4.6 Vy(horizontal). Verifica-se que este fato é mais pronunciado nos filamentos mais afastados da câmara de insuflamento de ar. Verifica-se ainda, que Vy diminui à medida que o ar ultrapassa os filamentos e Vx aumenta nesta direção. No 20º filamento devido ao empuxo ($T_A \simeq 170°C$)ocorre reversões no fluxo(Fig.4.5) para x pequeno.

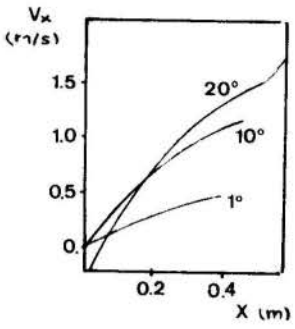

Fig.4.5-Velocidade do ar de resfriamento (Vx-Velocidade do ar na direção x(m/s)).

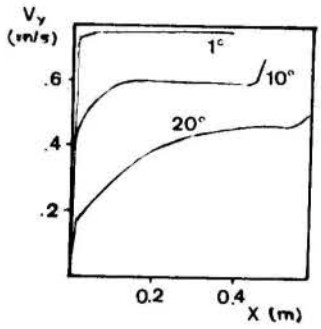

Fig.4.6-Velocidade do ar de resfriamento. (Vy-Velocidade do ar na direção y(m/s)).

RESULTADOS COM DEFLEXÃO DO FILAMENTO

Os filamentos sujeitos a ação da força de arraste do ar de resfriamento sofrem deflexão e consequentemente se curvam. Esta deflexão pode ser calculada a partir de um balanço de forças aplicado ao filamento. Um exemplo é mostrado na fig.5.1, que mostra a deflexão lateral do filamento função da distância da fieira. Neste caso não há indicação de filamentos se tocarem, mas se um filamento encostar no outro antes de sua solidificação poderá ocorrer "colagem" entre estes.

O estudo dos resultados do efeito da deflexão mostra que seu efeito sobre o resfriamento e transição vítrea é pequeno, e não precisa ser incluído nestas análises.

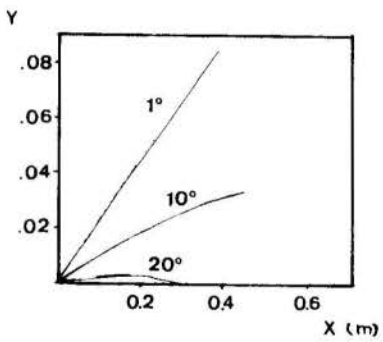

Fig.5.1-Deflexão dos filamentos. (y - deflexão (m)).

COMENTÁRIOS E CONCLUSÕES

Os resultados confirmam a necessidade de se melhorar o projeto de sistemas de resfriamento usados em processos industriais. A qualidade de fibra dependerá de como o ar de resfriamento é soprado sobre o fio, e do número de fileiras de filamentos.

O modelo proposto e empregado confirma que a força nos filamentos é variável e que ar é arrastado.

Este estudo foi realizado para condições típicas de fiação de fibras de poliester, ou seja:

T_0 = temperatura de extrusão = 285°C
T_2^1 = temperatura de transição vítrea = 67°C
T^A = temperatura do ar = 25°C
D^A = diâmetro de furo da fieira = $3,81 \times 10^{-4}$ m
G = vazão em massa do filamento = 10^{-3} kg/min.
V_A = velocidade do ar = 48 m/min
V_2^A = velocidade de enrolamento = 1500 m/min.

Nos testes numéricos para fins de comparações com dados de outras referências da literatura foram empregadas, as propriedades de fibras de poliéster fundido (PET) correlacionados por (Dutta e Nadkarni |1|):

massa específica-

$$\rho = 1375,0 - 0,75.T \ (kg/m^2) \qquad (6.1)$$

calor específico

$$c_p = 995,0+3,87.T \ (J/s.m^2.°C) \qquad (6.2)$$

viscosidade à taxa de cizalhamento zero-

$$\eta_o = \frac{\eta_e}{3} = 9,76 \times 10^{-3}.(0,611)^{5,2893}.e^{(6923,7/(T+273))} \qquad (6.3)$$

onde T é a temperatura do filamento em °C, variando de 60°C a 310°C.

No entanto, como seus resultados |1| são para modelo simplificado de força constante, não mostramos aqui comparações. Este modelo é somente válido para baixas velocidades de enrolamento.

A análise dos resultados de simulação do processo de extrusão permitiu concluir que os parâmetros que controlam a qualidade do filamento, em particular, sua birrefrigência óptica são: temperatura de extrusão, viscosidade, velocidade de enrolamento. A vazão de polímero, velocidade e temperatura do ar tem efeito menor, em particular para fieiras pequenas.

Por outro lado, no caso de fieiras com elevado número de filamentos (acima de 20), na direção do fluxo de ar, o modelo completo aqui apresentado tem sua utilização aconselhada.

Nos casos analisados o insuflamento de ar foi considerado uniforme e unidirecional, tendo em vista a análise da situação encontrada na indústria. A partir do modelo apresentado pode-se analisar outros sistemas de resfriamento de filamentos, ou seja, câmara de insuflamento com perfil de velocidade e/ou temperatura do ar de resfriamento variável com a distância da fieira, sopra fios anular, etc.

Outro fenômeno que pode ser estudado é o ar que arrastado acompanha o fio. Observou-se que sua velocidade acompanha a velocidade do fio tornando-se assintótica junto com este. Tanto a velocidade da corrente de ar de resfriamento como a do ar arrastado aumentam com a distância da fieira produzindo o que na prática é chamado de "bombeamento de ar".

REFERÊNCIAS BIBLIOGRÁFICAS

[1] DUTTA,A., NADKARNI,V.M., Identifying Critical Process Variables in PET Melt Spinning. Textil Research Journal, New York, (54): 35-42, 1984.

[2] KASE,S., MATSUO,T., Studies on Melt Spinning II. J.Appl. Polym. Sci., New York, (11): 251-287, 1967.

[3] GEORGE,H.H., Model Steady State Melt Spinning at Temperature Takeup Speeds. Polym. Eng.and Sci. Massachusetts, 22. (5): 292-299, 1982.

[4] YASUDA,H., ISHIHARA,H., Computer Simulation of Melt Spinning and its Application to Actual Process. Soc.Fiber Sci.Tech. Japan, Japan. 34.(1): 20-27, 1978.

[5] LÓRA,M.A., Modelo Matemático para Simulação do Resfriamento de Filamentos de Poliester Durante a Fiação. Dissertação de Mestrado apresentada à EPUSP. Junho, 1988, 130 págs.

SUMMARY

The spinning process of poliester yarns is analysed. Numerical simulation of flow and heat transfer predicts velocity and temperature profiles. The model assumes a nonisothermal cooling process by a cross air stream, uniaxial elongation due to spinning, and variable properties dependent on temperature. Effects of gravity, inertia and drag forces on the yarn are analysed. Heat, mass and momentum balances for infinitesimal cells include effects of heating and air flow direction. Forces balances on the yarn analyses its deflexion due to air flow. Numerical results are presented.

III ENCIT – Itapema, SC (Dezembro 1990)

CONJUGATE CONVECTION-CONDUCTION IN A ROTATING DISK

R.H. MARTINEZ*, C.A.C. ALTEMANI
Departamento de Energia - FEM - UNICAMP
Caixa Postal 6122 - CEP 13.081 - Campinas - SP
*Permanent Address: Universidade de Santiago del Estero - Argentina

SUMMARY

A numerical solution was obtained for a conjugate convective and conductive problem of a rotating disk heated at its edge and submerged in a large body of fluid. The results were obtained for a dimensionless temperature and for the Nusselt number distributions at the disk surface in terms of parameters of the problem.

INTRODUCTION

The geometry of a rotating disk has so many applications in engineering problems that it is constantly addressed in the technical literature of several fields, including the thermal and fluids engineering. The present work refers to a simple problem of conjugate heat transfer in a thin wall disk rotating in a quiescent fluid.

Consider, as indicated in Fig.1, a disk of radius r_o and thickness 2δ in a large body of quiescent fluid at a temperature T_o. When the disk rotates with ω constant, there is an induced movement of the fluid, described by von Karman in 1921 [1]. If the temperature of the disk is distinct from that of the fluid, there will be a heat transfer at their interface. Solutions for the heat transfer problem were obtained through a technique analogous to that employed for the flow problem. In [2,3] an isothermal disk was considered in a fluid at a distinct temperature. In [4] a similar solution was obtained when the disk temperature relative to the fluid surrounding it changed as an exponent of the radial position. In [5] an analysis was made for a disk heated only at a ring of its surface and adiabatic at the remainder of it. In this case the fluid temperature could present, near the heated disk, strong radial gradients. If the diffusive radial term of the energy equation could not be neglected, it became elliptic, preventing the boundary layer approximations employed in the previous works. A numerical solution to the elliptic form of the energy equation was then obtained for a relatively large domain of fluid above the disk surface. For comparison purposes, the same disk temperature distribution of [4] was input to the analysis of [5]. The comparison indicated [5] that the effects of radial diffusion in the fluid could be neglected when the disk temperature changed with the radial position with an exponent smaller than four.

In these previous works, the thermal boundary conditions were specified at the disk surface. In a real-life engineering problem however, this may not be known, for example when a heat flux is imposed at the outer border of the disk. In this case, the radial heat conduction within the disk material, together with the axial convective mechanism described previously, will determine the temperature distribution at the disk-fluid interface. The solution of this conjugate conduction-convection problem motivated the present work.

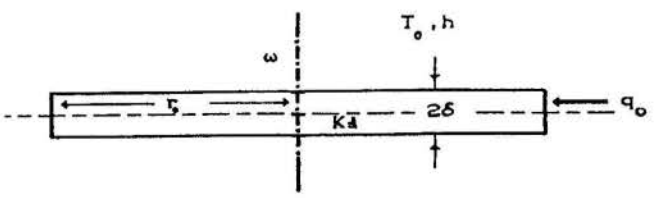

Fig.1 Diagram of the Heated Disk

ANALYSIS

The analysis was performed under steady state conditions, for laminar induced flow, considering constant properties. Effects of natural convection were neglected, so that it was assumed that $Gr/Re^2 \ll 1$, within the range of $Re < 10^5$.

Neglecting the axial conductive resistance across the disk, its temperature T_d is governed by the one-dimensional energy equation

$$d(r\delta k_d . dT_d/dr)/dr - r.h.(T_d - T_o) = 0 \quad (1)$$

In equation (1), k_d is the thermal conductivity of the disk material, $h(r)$ is the local convective coefficient and T_o is the fluid temperature far from the disk. The boundary conditions to (1) take into account the symmetry at the disk centerline and the radial influx of heat q_o at its border:

$$r = 0 \qquad dT_d/dr = 0 \quad (1a)$$

$$r = r_o \qquad dT_d/dr = q_o/k_d \quad (1b)$$

Employing now dimensionless varibles defined by $\eta = (r/r_o)$ and $\varphi = (T_d - T_o)/(q_o . r_o/k_d)$, the energy equation (1) becomes

$$d(\eta . d\varphi/d\eta) - \eta . (r_o^2/\delta k_d) . h(\eta) . \varphi = 0 \quad (3)$$

with boundary conditions

$$\eta = 0 \qquad d\varphi/d\eta = 0 \quad (3a)$$

$$\eta = 1 \qquad d\varphi/d\eta = 1 \quad (3b)$$

The product $h(\eta).\varphi(\eta)$ in equation (3), employing the definition of $\varphi(\eta)$, can be rearranged as

$$h(\eta).\varphi(\eta) = (k_d/q_o r_o).q(\eta) \quad (4)$$

In this equation, $q(\eta) = h(\eta).(T_d(\eta) - T_o)$ is the axial convective heat flux at a position η of the disk surface.

At the disk-fluid interface, the continuity of heat flux requires that

$$q(\eta) = -k_f . (\partial(T_f - T_o)/\partial z)_{\eta,o} \quad (5)$$

In (5), k_f is the thermal conductivity of the fluid surrounding the disk and $T_f(\eta,0)$ is the fluid temperature at the position η of the interface with the disk. This temperature is the same as $T_d(\eta)$ of the disk surface in order to preserve the continuity of temperature.

The fluid temperature distribution near the disk is governed by the boundary layer energy equation, expressed for laminar steady state regime with constant properties in the form

$$\rho c_p (u . \partial T_f/\partial r + w . \partial T_f/\partial z) = k_f \partial^2 T_f/\partial z^2 \quad (6)$$

In equation (6) (ρc_p) is the product of the density and the specific heat of the incompressible fluid and $\underline{u}$ and $\underline{w}$ are respectively the radial and the axial velocity components of the fluid flow.

When $(T_d(\eta) - T_o)$ can be expressed by an exponent of $\underline{r}$, ie, in the form $(a_\lambda . r^\lambda)$, equation (6) was transformed [4] into an ODE:

$$\theta''(\xi)/Pr = H(\xi).\theta'(\xi) + \lambda . F(\xi).\theta(\xi) \quad (7)$$

In equation (7), $\xi = z.(\omega/\nu)^{0.5}$ is the similarity variable of von Karman. $F(\xi)$ and $H(\xi)$ are respectively the radial and the axial dimensionless velocity components of the fluid flow. Pr is the Prandtl number of the fluid. $\theta(\xi)$ is a dimensionless temperature defined by $(T_f - T_o)/(T_d - T_o)$ and $\theta'(\xi)$ and $\theta''(\xi)$ are derivatives of θ with respect to ξ The boundary conditions to (7) consider the fluid temperature at the disk interface and far from it:

$$\theta(0) = 1 \qquad \text{and} \qquad \theta(\xi \to \infty) = 0 \quad (7a)$$

In terms of ξ and θ, the heat flux defined in equation (5) becomes

$$q(\eta) = -k_f (\omega/\nu)^{0.5} . (T_d(\eta)-T_o) . \theta'(0) \quad (8)$$

In equation (8), $\theta'(0)$ is a solution to equation (7), depending on the parameters λ and Pr.

Adopting $(\nu/\omega)^{0.5}$ as a characteristic length, then for each value of λ there is an uniform value of the Nusselt number at the disk surface, given by

$$Nu_\lambda = - \theta'_\lambda(0) \quad (9)$$

where Nu_λ depends on the Prandtl number of the fluid.

Suppose now that the dimensionless temperature at the disk surface can be expressed by the series

$$\varphi(\eta) = \Sigma_\lambda (b_\lambda . \eta^\lambda) \quad (10)$$

Since equation (6) is linear, then a linear superposition of solutions to equation (7), corresponding to each term of (10), satisfies this wall temperature distribution. As reviewed in the Introduction, the results [4] of the boundary layer energy equation (7) agree with those of an analysis [5] based in the elliptic form of the energy equation when $\lambda<4$. In order to ensure physical realism with the boundary layer results, the series (10) will be restricted to λ between 0 and 3. Thus, the convective heat flux corresponding to equation (10) can be expressed by

$$q(\eta) = k_f (q_o r_o / k_d) (w/\nu)^{0.5} \Sigma_\lambda Nu_\lambda b_\lambda \eta^\lambda \quad (11)$$

where the sum is within the indicated range. From equations (10) and (11), the Nusselt number distribution at the disk surface is given by

$$Nu(\eta) = \Sigma_\lambda (Nu_\lambda . b_\lambda . \eta^\lambda) / \Sigma_\lambda (b^\lambda . \eta^\lambda) \quad (12)$$

Note from this equation that at the center of the disk (η=0) $Nu(0)=Nu_o$, independently of the coefficients b_λ

Substituting equation (11) into equations (4) and (3), the energy equation becomes

$$d(\eta . \beta . d\varphi/d\eta) = \eta . Re^{0.5} . \Sigma_\lambda (Nu_\lambda . b_\lambda . \eta^\lambda) \quad (13)$$

where $\beta = (k_d . \delta / k_f . r_o)$, and $Re = w . r_o^2 / \nu$.

Equation (13) is subjected to the same boundary conditions (3a) and (3b). The parameter β characterizes a relative thermal conductance of the disk wall. Larger values of this parameter are expected to be related to a more uniform wall temperature in the solution to equation (13).

SOLUTION

The solution procedure was based on an iterative scheme described by the following steps:

1. From the physical parameters of the disk and fluid, the values of Pr, Re and of Nu_λ (λ from 0 to 3) were obtained.
2. A dimensionless temperature profile was assumed, through the coefficients b_λ of the polynomial equation (10).
3. The assumed polynomial temperature profile was used as an input to the RHS of equation (13). A numerical integration of the LHS of this equation gave rise to a new distribution $\varphi(\eta_j)$ at the grid points distributed on the disk surface.
4. The numerical distribution was compared to the assumed polynomial distribution calculated at each grid point. If there were not enough agreement at all grid points, the process continued to step 5.
5. A least squares regression was employed to adjust a new third order polynomial to the numerical solution just obtained, and then step 3 was repeated.

The numerical integration performed in step 3 employed the method of control volumes [7] and it is described in details in [6]. The number of grid points on the disk surface was varied in an initial study of the

problem. It was found that above 40 grid points the results nearly coincided, so that this number was adopted in the results presented. The convergence was reched when the difference between the assumed and the numerically obtained values of $\varphi(\eta_j)$ in step 4 was smaller than 10^{-7} for all grid points. Usually about 5 iterations were necessary to attain convergence.

RESULTS

The results will be presented in terms of the dimensionless temperature $\varphi(\eta)$ and of the local Nusselt number.

Figures (2) and (3) show the distribution of $\varphi(\eta)$ for two extreme values of β, considering Pr = 0.72, characteristic of air. It is evident that for smaller values of β the disk temperature becomes less uniform, attaining a maximum value at the outer border. It is noted also that the temperatures become smaller as the Reynolds number increases, due to larger velocities and convective heat transfer coefficients at the disk suface. When both effects are present, ie, for large Re and small β, the solution method employed in the present work may not be adequate. This is because the third order polynomial fitting will not be adequate to represent the disk surface temperature distribution.

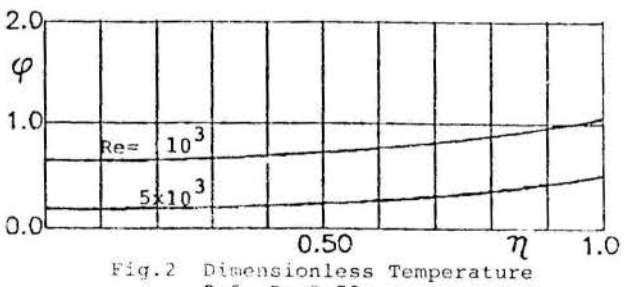

Fig.2 Dimensionless Temperature
β=5, Pr=0.72

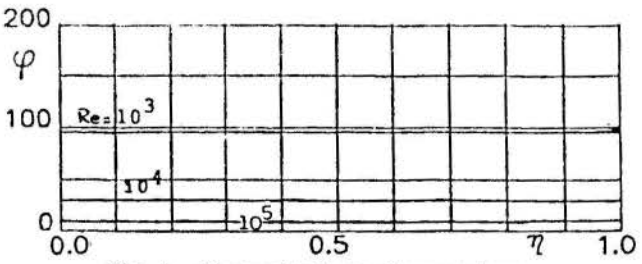

Fig.3 Dimensionless Temperature
β=500, Pr=0.72

Figures 4 and 5 present Nusselt number distributions associated to the previous figures. At the center of the disk, all distributions tend to the same value Nu_o (dependent on Pr) associated to equation (12). Larger values of β indicate a trend to an isothermal disk and therefore to an uniform distribution of Nusselt. The decrease of the disk temperature with Re is determinant to the corresponding increase of $Nu(\eta)$. For each value of Re, the distribution of Nu increases with η because, according to equation (12), $Nu_{\lambda+1} > Nu_\lambda$.

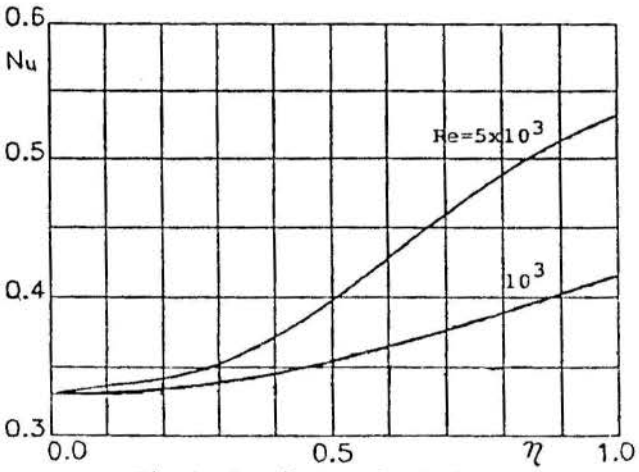

Fig.4 Local Nusselt Number
β=5, Pr=0.72

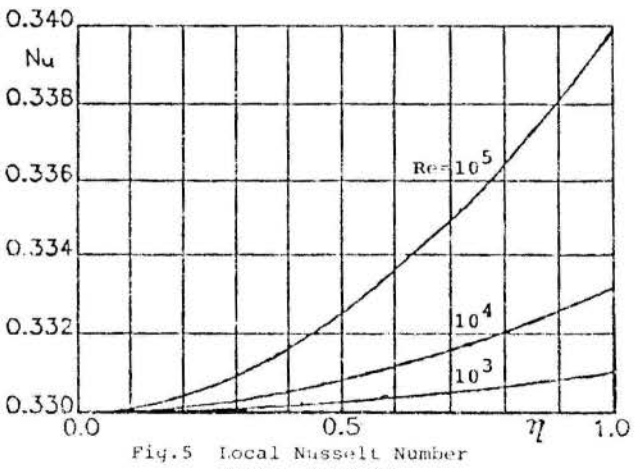

Fig.5 Local Nusselt Number
β=500, Pr=0.72

In order to have some perspective of the effect of the conjugate problem, the following comparison was made. The obtained value of Nu_o at the center (η=0) of the disk (for each Pr) was assumed to prevail all over the disk surface. Under these conditions, the disk temperature presents a distribution

analogous to that in a fin with uniform heat transfer coefficient to the surroundig fluid. When h is uniform, equation (3) has an analytical solution expressed in terms of Bessel functions. The temperature distribution thus obtained was compared with that of the conjugate problem. Figure 6 presents one comparison for the case of Pr=0.72, Re=5000 and β=5. In this case the analytical temperature distribution presented values almost 40% above that of the conjugate problem. For larger values of β, this difference will be smaller because the solution of the conjugate problem will present more uniform temperature and Nusselt number distributions on the disk surface.

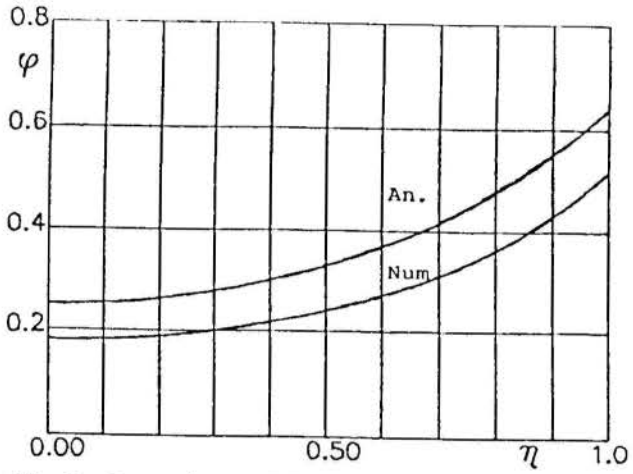

Fig.6 Comparison of Temperature Distributions
β=5, Pr=0.72, Re=5000

REFERENCES

[1] Schlichting, H., Boundary Layer Theory, McGraw Hill, New York, 6th Edition, 1968.

[2] Millsaps, K and Pohlhausen, K., "Heat Transfer by Laminar Flow from a Rotating Plate", J. Aeronautical Sciences, vol.19, pp.120-126,1952.

[3] Sparrow, E.M. and Gregg, J.L.,"Heat Transfer from a Rotating Disk to Fluids of any Prandtl Number", ASME J. Heat Transfer, vol.81, pp.249-251, AUG 1959.

[4] Hartnett, J.P.,"Heat Transfer from a Nonisothermal Disk Rotating in Still Air", ASME J. Applied Mechanics, vol. , pp.95-96, FEB 1959.

[5] Oehlbeck, D.L. and Erian, F.F.,"Heat Transfer from Axisymmetric Sources at the Surface of a Rotating Disk", Int. J. Heat and Mass Transfer, vol.13, pp.601-610, 1979.

[6] Martinez, R.H.," Condução e Convecção Termica Acopladas num Disco em Rotação, MsC Thesis (in portuguese), nr.14/90, FEM - UNICAMP, 1990.

[7] Patankar, S.V.,"Numerical Heat Transfer and Fluid Flow, Hemisphere, New York, 1980.

III ENCIT – Itapema, SC (Dezembro 1990)

PERFORMANCE OF INTERNALLY FINNED TUBES FOR THE HEATING OF RADIATING GAS FLOWS

Juan C. Morales, Departamento de Mecánica, Universidad Simón Bolivar, Caracas 1080-A, Venezuela
Antonio Campo, School of Mechanical Engineering, Purdue University, West Lafayette, IN 47907, USA
Carlos Schuler, Dept. of Mechanical Engineering, University of California, Berkeley, Ca 94720, USA

ABSTRACT

An analysis of the simultaneous effect of forced convection and radiation in the thermal entrance region of internally finned tubes is presented. The radiative contribution of the gas is modeled by the P-1 method, which provides an additional partial differential equation of elliptic type. Invoking the gray gas model, the governing equations of conservation are solved numerically using a finite-volume procedure. Heat transfer augmentation due to the longitudinal array of fins and participating radiation is represented by the mean bulk temperature distribution.

INTRODUCTION

Mori el al. [1] have suggested that heat transfer by combined convective and radiative transfer in participating gas flows is very important in the analysis of high temperature heat exchangers. In these applications, unless radiation is very weak or very strong, the conservation equations of mass, momentum energy and radiative transport must be solved simultaneously in order to determine local temperatures and local heat transfer rates in the participating gas medium.

In light of the foregoing, the primary objective of this paper is to explore the enhancing effects of thermal radiation on laminar forced convection of high temperature gas flows through internally longitudinal finned tubes. An exhaustive literature review on the subject of combined mechanisms reflects that this particular problem has not been investigated so far. For concreteness, the present analysis focuses a situation wherein the temperature develops in a longitudinal finned tube, wherein the velocity is taken as fully developed. The computed 2-D velocity profile, of course, depends on the specific number of longitudinal fins deployed in the tube cross-section. Hence, the distorted velocity profile is taken as an input for the 3-D equation of energy conservation. Turning the attention to the radiation analysis, the participating medium is assumed as a gray gas, capable of emitting and absorbing radiant energy with negligible scattering. Furthermore, the tube walls are considered black, whereas the fins are relatively thick and are equally distributed in the cross-section of the tube.

The applicable radiative transport equation (RTE), based on the P-1 method, is coupled with a finite-volume code which is used to solve the set of conservation equations numerically. Computed results are presented for the axial variation of the mean bulk temperature as a function of the controlling parameters describing the combined heat exchange process. These numerical results will be useful to the thermal designer for predicting the level of heat transfer intensification.

BASIC EQUATIONS

Consideration is given to the cross-section of the internally finned tube pictured in Fig. 1a. By virtue of the symmetries, it is only necessary to analyze the flow and heat transfer in the computational domain of Fig. 1b. For the situation of fully developed velocity u(r,θ), the dimensionless variables and parameters are

$$U=\frac{u}{r_0^2(-dp/dz)/\mu},\quad \eta=\frac{r}{r_0},\quad Re=\frac{2\bar{u}r_0}{\nu}$$

$$t=\frac{T}{T_{ref}},\quad Z=\frac{z}{r_0 RePr},\quad \tau=\hat{\beta}r_0 \qquad (1)$$

$$G^*=\frac{G}{4\sigma T_{ref}^4},\quad N=\frac{\sigma r_0 T_{ref}^3}{k}$$

Accordingly, the conservation equations may be expressed as follows:

MOMENTUM

$$\frac{1}{\eta}\frac{\partial}{\partial\eta}\left(\eta\frac{\partial U}{\partial\eta}\right)+\frac{1}{\eta^2}\frac{\partial^2 U}{\partial\theta^2}+1=0 \qquad (2)$$

ENERGY

$$\frac{1}{2}\frac{U}{\bar{U}}\frac{\partial t}{\partial Z}=\frac{1}{\eta}\frac{\partial}{\partial\eta}\left(\eta\frac{\partial t}{\partial\eta}\right)+\frac{1}{\eta^2}\frac{\partial^2 t}{\partial\theta^2}+4N\tau(G^*-t^4) \qquad (3)$$

RADIATIVE TRANSFER

$$\frac{1}{\eta}\frac{\partial}{\partial\eta}\left(\eta\frac{\partial G^*}{\partial\eta}\right)+\frac{1}{\eta^2}\frac{\partial^2 G^*}{\partial\theta^2}=3\tau^2(G^*-t^4) \qquad (4)$$

where U, t and G* designate the velocity, temperature and irradiation of the participating gas in dimensionless form. Moreover, the tube wall and the array of straight fins were supposed to be of high thermal conductivity, so that both would

assume a uniform temperature over the cross-section of the tube.

$$U = 1, \quad t = t_e \tag{5}$$

at the entrance

$$U = 0, \quad t = 1, \quad \frac{\partial G^*}{\partial \eta} = -\frac{3}{2}\tau(G^* - t^4) \tag{6}$$

at the solid walls

$$\frac{\partial U}{\partial \theta} = \frac{\partial t}{\partial \theta} = 0, \quad \frac{\partial G^*}{\partial \eta} = 0 \tag{7}$$

on the symmetry lines

where $\partial/\partial\eta$ denotes the normal derivative.

TREATMENT OF THE RADIATIVE TRANSFER EQUATION

The rigorous formulation of the 3-D energy equation describing laminar forced convection of a gas that emits and absorbs radiation involves a nonlinear integro-partial differential equation [2]. In this regard, in order to carry out the computations it is usually necessary to implement an iterative approach in which the integral terms and the differential terms of the energy equation are solved consecutively. In fact, it is also well known that the numerical solution of this intricate equation is quite involved and requires large amounts of computing time and storage. Alternatively, in order to bypass this elaborate procedure the approximate differential method, the P-1 method will be employed here. It is documented by Ozisik [2]. In essence, this method seeks to replace the highly complex energy equation and the radiative transfer equation (RTE) in three dimensions by a system of coupled partial differential equations that depend on both temperature and irradiation, for instance eqs.(3) and (4). Correspondingly, the numerical solution of this coupled system seems to be easier to obtain than the original nonlinear integro-partial differential equation.

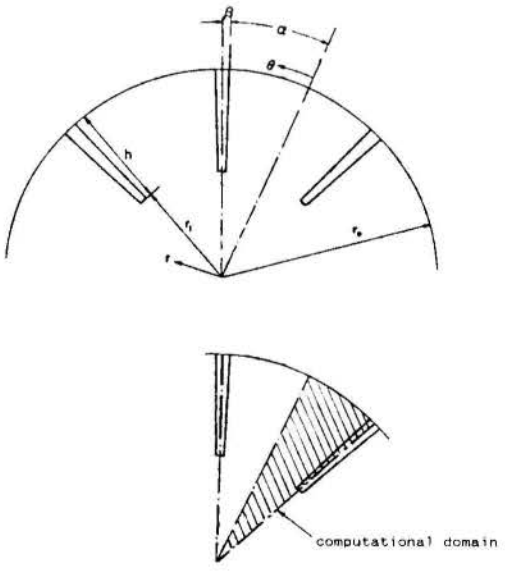

Fig. 1 Geometry of the problem

PARAMETERS OF INTEREST

Pressure drop: The pressure drop due to internal finning, may be conveniently presented through the value of fRe used in [3]:

$$fRe = \frac{2\pi/A_f}{\overline{U}} \tag{8}$$

where A_f defines the dimensionless flow area.

Heat Transfer: The heat transfer calculations will rely on the computation of the mean bulk temperature distribution:

$$t_b = \frac{\int_A U t dA}{\int_A U dA} \tag{9}$$

where the integration was performed over the flow cross-section A_f.

In light of the foregoing, the total heat transfer Q_T in a tube of length L carrying a high temperature gas flow may be easily obtained:

$$Q_T = \dot{m} C_p (T_{bL} - T_e) \tag{10}$$

Likewise, upon introduction of an ideal heat transfer Q_∞ between z = 0 (the entrance) and $z = \infty$

$$Q_\infty = \dot{m} C_p (T_\infty - T_e) \tag{11}$$

the bulk temperature ratio T_b/T_{ref} may be associated with a heat transfer efficiency Ω

$$\Omega = \frac{Q_t}{Q_\infty} \tag{12}$$

NUMERICAL ANALYSIS

The system of conservation equations were solved numerically by the standard finite-volume procedure described by Patankar [4].

Turning the attention to the radiative contribution of the participating gas at elevated temperature, the two dimensional radiative transfer equation (RTE) modeled by the P-1 method, supplies an elliptic equation of diffusion-convection type. Thus, the discretization introduced to obtain a finite-difference form of the RTE employs the same finite volumes utilized for the conservation equations of momentum and energy.

The procedure for solving the corresponding set of algebraic equations is based on the line-by-line method delineated in [4]. In addition, the computations were performed with uniform spacings on a 22x22 grid in the η-θ coordinate system.

As a verification of the computational procedure, numerical values of the friction factor represented by the suitable parameter fRe were compared with the analytical predictions reported by Soliman and Feingold [3]. Additional results were determined for high temperature gas flows through finless

tubes accounting for participating radiation. As may be observed in Fig. 2, the mean bulk temperature distribution agrees well with the classical solution of Pearce and Emery [5] for a wide range of radiation parameters considered.

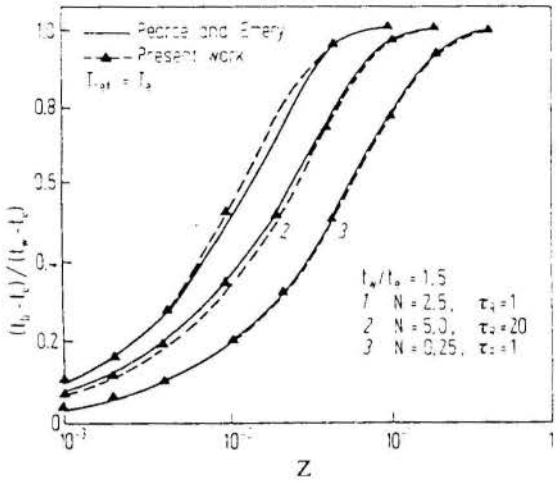

Fig. 2 Mean bulk temperature distribution for plain tubes

RESULTS AND DISCUSSION

Although the Nusselt number is traditionally the dimensionless parameter employed in presenting results for internal forced convection problems, there is a good justification not to adopt this approach here. In fact, for engineering purposes the most important information is the heat transfer enhancement in a certain tube length due to the addition of fins with respect to a finless tube. Correspondingly; this may be readily accomplished, via an overall energy balance, by combining the mean bulk temperature distribution and eq.(10).

An examination of the conservation equations reveals the presence of six prescribable parameters. However, in the presentation of results some of them will remain fixed; for instance the fin angle $2\beta = 6°$, the dimensionless fin height H = 0.5, the number of fins NF = 0, 3 and 5, and the entrance-to wall-temperature ratio $t_e = 0.5$.

Figs. 3 and 4 have been prepared to illustrate the influence of the radiative mechanism in a gas flow through the finned pipe. This influence will be represented by various combinations of the optical thickness τ and the radiation-conduction parameter N. First, considering $\tau = 1$ and N = 1, it is seen in Fig. 3 that the bulk temperatures increase slowly with Z^+. This is an expected behavior due to the fact that thermal radiation is rather weak.

Conversely, when thermal radiation is stronger $\tau = 5$ and N = 5, the aforementioned trends are modified as evidenced in Fig. 4. Accordingly, the mean bulk temperature for each group of fins rise more rapidly than before and the region of thermal saturation for each NF occurs at a shorter value of Z^+.

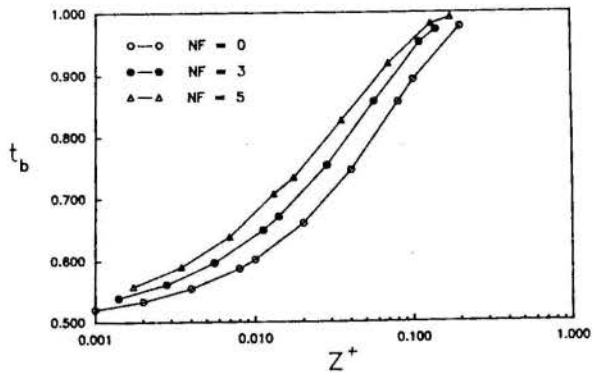

Fig. 3 Mean bulk temperature distribution for finned tubes $\tau = 1$ and N = 1

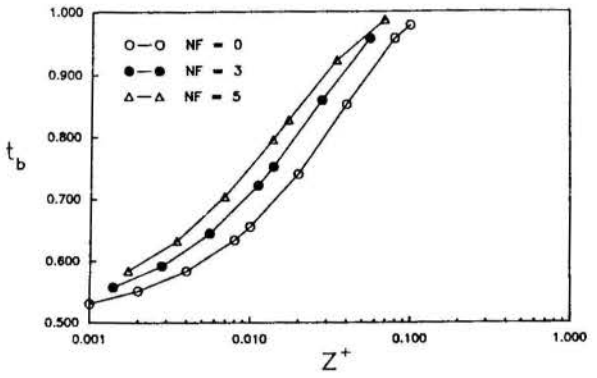

Fig. 4 Mean bulk temperature distribution for finned tubes $\tau = 5$ and N = 5

As a concluding remark it may be said that the exclusion of radiation may lead to large errors in the thermal analysis of participating gases flowing at elevated temperatures through longitudinal finned tubes.

REFERENCES

[1] Mori, Y., Sheindlin, A.E. and Afgan, N.H.,"High Temperature Heat Exchangers," Hemisphere, New York, N.Y., 1986.

[2] Ozisik, N.,"Radiative Transfer," Wiley, New York, N.Y., 1973.

[3] Soliman, H.M. and Feingold,"Analysis of Fully Developed Laminar Flow in Longitudinal Finned Tubes," Chem. Engng. J., Vol. 14, pp. 119-128, 1977.

[4] Patankar, S.V., "Numerical Heat Transfer and Fluid Flow," Hemisphere, New York, N.Y., 1980.

[5] Pearce, B. and Emery A.,"Heat Transfer by Thermal Radiation and Laminar Forced Convection to an Absorbing Fluid in the Entry Region of a Pipe," J. Heat Transfer Vol. 92, pp. 221-230, 1970.

NOMENCLATURE

c_p	specific heat at constant pressure (J/kg-K)
f	friction factor
G	total irradiation (W/m^2)
G^*	dimensionless total irradiation, eq.(1)
H	dimensionless fin height, h/r_o
h	fin height (m)
k	thermal conductivity (W/m-K)
m	mass flow rate (kg/s)
N	radiation-conduction parameter, eq.(1)
NF	number of fins
p	pressure (N/m_2)
Q_T	total heat transfer (W)
Q_∞	ideal heat transfer (W)
Re	Reynolds number for finned tube, eq.(1)
Re_s	Reynolds number for smooth tube
r	radial coordinate (m)
r_o	pipe radius (m)
T	absolute temperature (K)
T_{ref}	reference temperature (K), $T_{ref} = T_w$
T_b	mean bulk temperature (K)
T_e	entrance temperature (K)
T_w	wall temperature (K)
t	dimensionless temperature, eq.(1)
U	dimensionless velocity, eq.(1)
U	dimensionless mean velocity
u	mean velocity (m/s)
Z	dimensionless axial coordinate, eq.(1)
Z^+	dimensionless axial coordinate, ZRe/Re_s
z	axial coordinate (m)

Greek Letters

2β	angle subtended by one fin
$\hat{\beta}$	extinction coefficient (m^{-1})
σ	Stefan-Boltzmann constant (W/m^2-K^4)
τ	optical thickness, eq.(1)
Ω	heat transfer efficiency, eq.(12)
η	dimensionless radial coordinate, eq.(1)
θ	angular coordinate
ν	kinematic viscosity (m^2/s)

III ENCIT – Itapema, SC (Dezembro 1990)

SOLUTION FOR UNSTEADY HEAT TRANSFER IN THE THERMAL ENTRANCE REGION OF A CIRCULAR DUCT WITH PERIODIC VARIATION OF INLET TEMPERATURE

WILSON F.N. SANTOS and JERÔNIMO DOS SANTOS TRAVELHO
Instituto de Pesquisas Espaciais
Laboratório Associado de Combustão e Propulsão
Caixa Postal 01, Cachoeira Paulista, SP, 12630

ABSTRACT

This work presents an alternative solution of the conjugated laminar forced convection heat transfer in the thermal entrance region of a circular duct with periodically varying inlet temperature, and time and space dependent wall temperature. The solution is obtained by using Laplace transform. Amplitude of oscillations and phase lags, with respect to the inlet condition, are obtained for wall temperature, wall heat flux and fluid bulk temperature.

INTRODUCTION

The objective of this work is to obtain an analytical solution, in closed form, for the transient conjugated heat transfer in a circular tube. The study of unsteady state conjugated forced convection heat transfer in ducts, subjected to periodic time variation of the inlet condition, provides important information for the control of heat exchangers. In this kind of study, the main interest consists in determining the wall temperature, wall heat flux and the fluid bulk temperature. These quantities are usually obtained from the temperature fields of the flowing fluid and of the solid materials which surround the flow. These fields must be found simultaneously, because of the coupling between them. However, the solution of conjugated problems in unsteady conditions encounters severe mathematical difficulties, and normally an approximate solution using the standard simple quasi-steady approach is assumed.

It appears that Sparrow and Farias [1], were the first investigators to analytically study a problem of this type. These authors studied the transient conjugated problem for slug flow between parallel plates, and obtained a series solution. The solution presented by them, leads to a complex eigenvalue problem which depends on the wall and fluid physical properties and on the oscillation frequency of the temperature. A trial and error procedure was employed by Sparrow and Farias for the numerical evaluation of the real and imaginary parts of the eigenvalues. Cotta et al.[2], advanced the analysis of Sparrow and Farias by considering transient forced convection in both parallel plates channel and circular duct, and adopted the sign-count method to obtain the complex eigenvalues.

The difficulty associated with the analytical solution of this problem has been related with the solution of the resulting complex eigenvalue problem. Therefore, Travelho and Santos [3] presented an alternative way of solving this problem by considering transient forced convection in parallel plates channel with the same physical conditions presented by Sparrow and Farias and Cotta et al., without the need of determining the complex eigenvalues. These eigenvalues were avoided by applying the Laplace transform to the equation and to the boundary conditions of the problem. The inverse transform was obtained numerically. In [4], Travelho and Santos further advanced the analysis of Ref. [3] by analytically obtaining the inverse Laplace transform.

This work considers a physical situation similar to that analyzed in [3] for the case of circular duct. Like in [3], Laplace transform is applied in the variables and boundary conditions of the problem, eliminating the complex eigenvalue problem.

ANALYSIS

In the physical situation, a fluid, in laminar flow developed hydrodynamically, with the inlet temperature varying periodically in time, is moving within a circular duct of radius a and thickness ℓ. The wall and fluid transport properties are assumed to be constant and the axial conduction and viscous dissipation are neglected. The wall temperature variation is not specified in advance, but is dinamically determined by the balance between the heat transfer rate and the energy stored for the conditions stated. The energy equation, under such conditions, is given by

$$\frac{\partial T(r,z,t)}{\partial t} + u\,\frac{\partial T(r,z,t)}{\partial z} = \alpha\,\frac{1}{r}\,\frac{\partial}{\partial r}\left[r\,\frac{\partial T(r,z,t)}{\partial r}\right] \qquad (1a)$$

in $0 < r < a$, $z > 0$, $t > 0$
where α is the thermal diffusivity of fluid. The inlet and boundary conditions are

$$T(r,o,t) = T_o + \Delta T_o\, e^{i\omega t} \qquad 0 < r < a,\ t > 0 \qquad (1b)$$

$$\left.\frac{\partial T(r,z,t)}{\partial r}\right|_{r=0} = 0 \qquad z > 0,\ t > 0 \qquad (1c)$$

$$-k\left.\frac{\partial T(r,z,t)}{\partial r}\right|_{r=a} = \rho_w c_w \ell\,\frac{\partial T(a,z,t)}{\partial t} \qquad z > 0, t > 0 \qquad (1d)$$

where T_o is the cycle mean temperature, ΔT_o is the

amplitude of inlet oscillations, ω is the frequency of oscillations, k is the thermal conductivy of fluid, ρ_ω is the wall density and c_ω is the wall specific heat.

In the present work, it is not necessary to state the initial condition (t=0), since one only seeks a periodic solution to problem (1).

The utilization of the slug flow model (u = U = constant) and the introduction of the following dimensionless groups

$$R = \frac{r}{a} \; ; \; Z = \frac{\alpha z}{Ua^2} \; ; \; \tau = \frac{\alpha t}{a^2} \; ; \; \Omega = \frac{\omega a^2}{\alpha} \; ; \; a^* = \frac{\rho c_p a}{\rho_\omega c_\omega \ell}$$

$$b^* = \frac{\Omega}{a^*} \; ; \quad \theta(R,Z,\tau) = \frac{T(r,z,t)-T_0}{\Delta T_0}$$

in equations (1a-1d) leads to:

$$\frac{\partial \theta}{\partial \tau}(R,Z,\tau) + \frac{\partial \theta}{\partial Z}(R,Z,\tau) = \frac{1}{R} \frac{\partial}{\partial R} \left[R \frac{\partial \theta}{\partial R}(R,Z,\tau) \right] \quad (2a)$$

in $0 < R < 1$, $Z > 0$, $\tau > 0$

$$\theta(R,0,\tau) = e^{i\Omega\tau} \qquad 0 < R < 1, \; \tau > 0 \quad (2b)$$

$$\left. \frac{\partial \theta(R,Z,\tau)}{\partial R} \right|_{R=0} = 0 \qquad Z > 0, \; \tau > 0 \quad (2c)$$

$$a^* \left. \frac{\partial \theta(R,Z,\tau)}{\partial R} \right|_{R=1} + \frac{\partial \theta(1,Z,\tau)}{\partial \tau} = 0 \quad Z>0, \tau>0 \quad (2d)$$

The dimensionless parameters a* and b* which appear in the dimensionless group, characterize the effects of wall capacitance to heat transfer.

In order to obtain a periodic solution for the problem (2), a periodic temperature solution, was assumed. This solution has the form,

$$\theta(R,Z,\tau) = \psi(R,Z) \, e^{i\Omega(\tau-Z)} \quad (3)$$

Equations (2a-2d) together with equation (3), give

$$\frac{\partial \psi(R,Z)}{\partial Z} = \frac{1}{R} \frac{\partial}{\partial R} \left[R \frac{\partial \psi(R,Z)}{\partial R} \right] \quad (4a)$$

in $0 < R < 1$, $Z > 0$

$$\psi(R,0) = 1 \quad (4b)$$

$$\left. \frac{\partial \psi(R,Z)}{\partial R} \right|_{R=0} = 0 \quad (4c)$$

$$\left. \frac{\partial \psi(R,Z)}{\partial R} \right|_{R=1} + ib^* \psi(1,Z) = 0 \quad (4d)$$

METHOD OF SOLUTION

A formal solution to problem (4) is obtained through the use of the classical integral transform technique [2], which results in the complex eigenvalue problem. To eliminate the difficulties to obtain the complex eigenvalues, the present work solves the problem (4) by using the Laplace transform to the variable Z, then the equation (4a-4d) become

$$s\tilde{\psi}(R,s) - 1 = \frac{1}{R} \frac{\partial}{\partial R} \left[R \frac{\partial \tilde{\psi}(R,s)}{\partial R} \right] \quad (5a)$$

$$\left. \frac{\partial \tilde{\psi}(R,s)}{\partial R} \right|_{R=0} = 0 \quad (5b)$$

$$\left. \frac{\partial \tilde{\psi}(R,s)}{\partial R} \right|_{R=1} + ib^* \tilde{\psi}(1,s) = 0 \quad (5c)$$

where $\tilde{\psi}(R,s)$ is defined as

$$\tilde{\psi}(R,s) = \lim_{Z \to \infty} \psi(R,Z) = \int_0^\infty \psi(R,Z) \, e^{-sZ} \, dZ \quad (6)$$

and s is the Laplace transform parameter.

The solution to problem (5) is given by

$$\tilde{\psi}(R,s) = \frac{1}{s} - \frac{ib^*}{s} \left[\frac{I_0(\sqrt{s}\,R)}{\sqrt{s}\, I_1(\sqrt{s}) + ib^* I_0(\sqrt{s})} \right] \quad (7)$$

where I_0 and I_1 are the modified Bessel function of the second kind.

As mentioned before, the main objective of this work is to determine the quantities of interest such as wall temperature, wall heat flux and fluid bulk temperature in the thermal entrance region. Therefore, this situation occurs for small values of Z, corresponding to large values of s in the transformed plane.

Rearranging the equation (7) and setting R=1, one obtains:

$$\tilde{\psi}(1,s) = \frac{1}{\sqrt{s}\left[\sqrt{s} + ib^* \frac{I_0(\sqrt{s})}{I_1(\sqrt{s})}\right]} \quad (8)$$

After introducing the large argument expansions of the Bessel functions (two terms) of equation (8) as available in [5], and to expand the resulting expression in terms of the conventional method of partial fractions, the inverse transform is obtained [6] as

$$\psi(1,Z) = \frac{1}{y_1 - y_2} \left[y_1 e^{y_1^2 Z} \operatorname{erfc}(-y_1\sqrt{Z}) - y_2 e^{y_2^2 Z} \operatorname{erfc}(-y_2\sqrt{Z}) \right] \quad (9)$$

where y_1 and y_2 are obtained as follows

$$y_{1,2} = -\frac{ib^*}{2} \pm \left[\frac{ib^*}{2} \left(\frac{ib^*}{2} - 1 \right) \right]^{1/2} \quad (10)$$

The function W(x), tabulated in Ref. [5], is often used instead of the error function when the latter has a complex argument. This function is defined as follows

$$W(z) = e^{-x^2} \operatorname{erfc}(-ix) \quad (11)$$

By using this function the equation (10), one obtains

$$\psi(1,Z) = \frac{1}{y_1 - y_2} \left[y_1 W(-iy_1\sqrt{Z}) - y_2 W(-y_2\sqrt{Z}) \right] \quad (12)$$

The dimensionless wall temperature $\theta_w(Z,\tau)$ is given by

$$\theta_w(Z,\tau) \equiv \theta(1,Z,\tau) = \psi(1,Z)\, e^{i\Omega(\tau-Z)} \qquad (13)$$

where the periodic part, equation (12), is defined here as

$$\psi_w(Z) \equiv \psi(1,Z) = \frac{1}{y_1-y_2}\left[y_1 W(-iy_1\sqrt{Z}) - y_2 W(-iy_2\sqrt{Z})\right] \qquad (14)$$

The wall heat flux $\theta_h(Z,\tau)$ is obtained as

$$\theta_h(Z,\tau) = -\left.\frac{\partial\theta(R,Z,\tau)}{\partial R}\right|_{R=1} = -\left.\frac{\partial\psi(R,Z)}{\partial R}\right|_{R=1} e^{i\Omega(\tau-Z)} \qquad (15)$$

the periodic part of the wall heat flux is obtained by using equation (4d) together with equation (12). Thus, one has

$$\psi_h(Z) \equiv -\left.\frac{\partial\psi(R,Z)}{\partial R}\right|_{R=1} = ib^*\psi(1,Z) \qquad (16)$$

The dimensionless fluid bulk temperature $\theta_b(Z,\tau)$ is determined from its definition as being

$$\theta_b(Z,\psi) = 2\int_0^1 R\theta(R,Z,\tau)\, dR = \left[2\int_0^1 R\psi(R,Z)\, dR\right] e^{i\Omega(\tau-Z)} \qquad (17)$$

where the periodic part of the fluid bulk temperature is defined as

$$\psi_b(Z) \equiv 2\int_0^1 R\psi(R,Z)\, dR \qquad (18)$$

The Laplace transform with respect to Z, gives

$$\tilde{\psi}_b(s) = 2\int_0^1 R\tilde{\psi}(R,s)\, dR \qquad (19)$$

by inserting $\tilde{\psi}(R,s)$ from equation (7) into equation (19), the transformed fluid bulk temperature is obtained after a direct integration as

$$\tilde{\psi}_b(s) = \frac{1}{s} - \frac{2ib^*}{s^{3/2}}\left[\frac{I_1(\sqrt{s})}{\sqrt{s}\, I_1(\sqrt{s}) + ib^* I_0(\sqrt{s})}\right] \qquad (20)$$

By using a similar procedure used to obtain the inverse transformation of the wall temperature, one obtains the inverse transformed of equation (20). Thus, the periodic part of dimensionless fluid bulk temperature becomes

$$\psi_b(Z) = -3 - \frac{2ib^*}{y_1-y_2}\left[\frac{1}{y_1} W(-iy_1\sqrt{Z}) - \frac{1}{y_2} W(-iy_2\sqrt{Z})\right] \qquad (21)$$

From a practical point of view and for applications it would be very useful to put the quantities of interest mentioned before, in terms of amplitudes, A(Z) and phase lags, $\Phi(Z)$. This way, the amplitudes $A_w(Z)$, $A_h(Z)$ and $A_b(Z)$ and phase lags $\Phi_w(Z)$, $\Phi_h(Z)$ and $\Phi_b(Z)$ are obtained as follows

$$A(Z) = |\psi(Z)| = \{[Re(\psi)]^2 + [Im(\psi)]^2\}^{1/2} \qquad (22)$$

$$\Phi(Z) = tg^{-1}\left[\frac{Im(\psi)}{Re(\psi)}\right] - \Omega Z \qquad (23)$$

where $Re(\psi)$ amd $Im(\psi)$ are the real and imaginary parts of the ψ_w, ψ_h and ψ_b given by equations (14), (16) and (21).

RESULTS AND CONCLUSIONS

The results obtained through the use of the equations (14), (16) and (21) are shown in Figures 1 (a) to 3(b). Comparison is made between the present solution and the solution obtained by Cotta et al.[2]. 25 eigenvalues were used as listed in Reference [2], for each value of b*. The major discrepances ocurred for the phase lag of the wall temperature. The phase lags are the ones more prone to generate errors because in the thermal entrance they are very small quantities, and a small error in the complex temperature would produce noticeable changes in their values. However, the agreement is very good in the whole interval of interest. One should notice that the eigenvalues solution will give better results for large values of Z, because the error introduced by taking a finite number of eigenvalues decreases in this case. On the other hand, the solution presented here will give better solution for small values of Z. This happens because in the transformed plane the expansion of Bessel functions was made in order to obtain good precision in the asymptotic region.

Therefore, the disagreement between the solutions for the large values of Z occurs bacause the present solution start to loose precision. However, the disagreement which happens for small values of Z is due to the relative small number of eigenvalues used in the eigenvalue solution. This small number is the responsible for the slight overshooting which occurs for the amplitude of the wall temperature for small values of Z. The reader should also notice that the present solution is very easy to be used because only the parameters y_1 and y_2 need to be calculated, and this calculation is straightforward.

ACKNOWLEDGMENTS

This work was supported by FAPESP (Fundação de Amparo à Pesquisa do Estado de São Paulo) under the contract no. 90/0076-3 to whom the authors are gratefull.

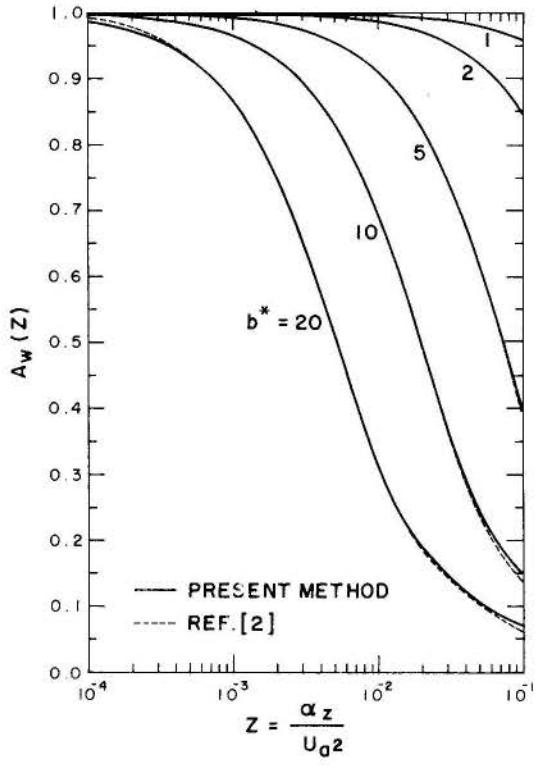

Fig. 1(a) - Comparison between wall temperature amplitudes as a function of Z, alculated by using the presen method and by using series solution.

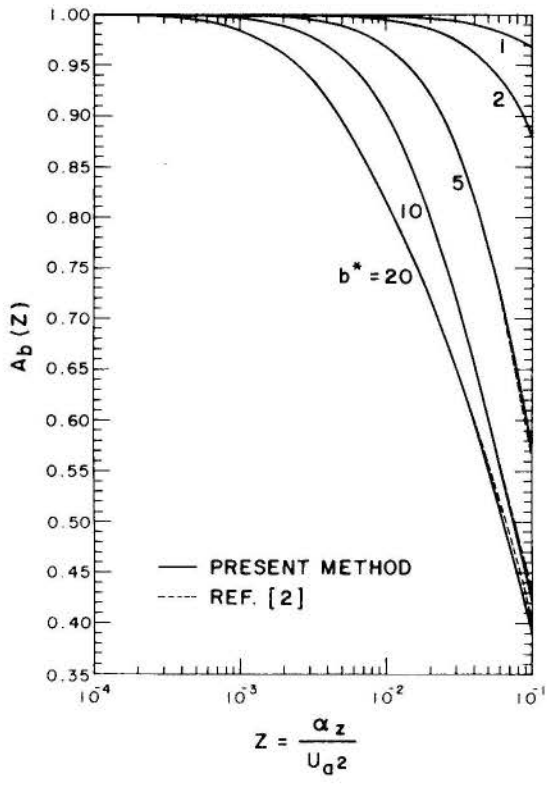

Fig. 2(a) - Comparison between bulk temperature amplitudes as a function of Z, calculated by using the present method and by using series solution.

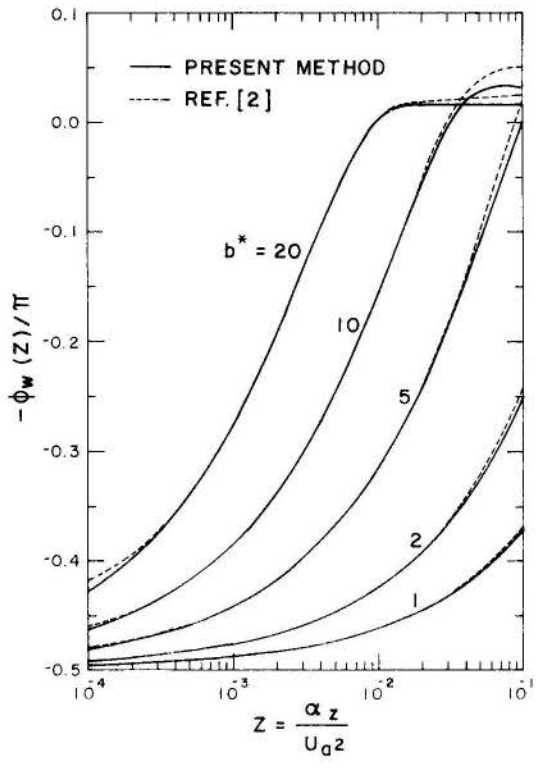

Fig. 1(b) - Comparison between wall temperature phase lags by using the two methods.

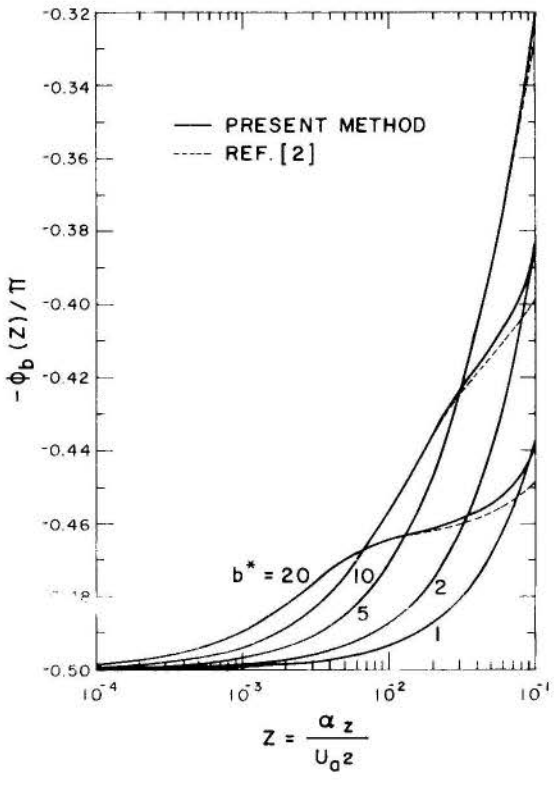

Fig. 2(b) - Comparison between bulk temperature phase lags by using the two methods.

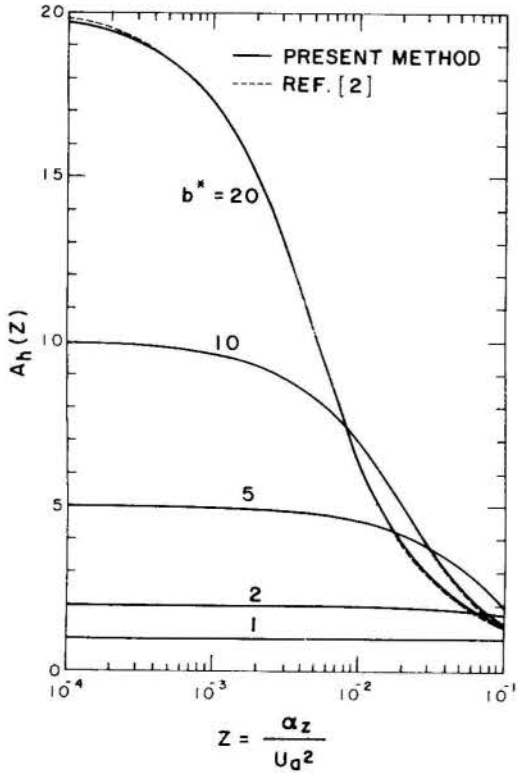

Fig. 3(a) - Comparison between wall heat flux amplitudes, as a function of Z, calculated by using the present method and by using series solution.

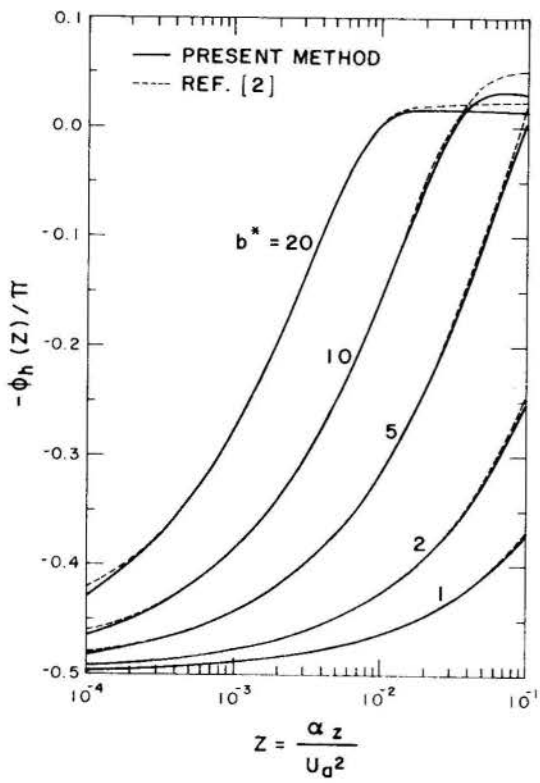

Fig. 3(b) - Comparison between wall heat flux phase lags by using the two methods.

REFERENCES

[1] Sparrow, E. M. and Farias, F.N., "Unsteady Heat Transfer in Ducts with Time-varying Inlet Temperature and Participating Walls", Int. Journal of Heat and Mass Transfer 11, 837-853, 1968.

[2] Cotta, R.M., Mikhailov, M.D. and Özisik, M.N., "Transient Conjugated Forced Convection in Ducts with Periodically varying Inlet Temperature", Int. Journal of Heat and Mass Transfer 30, 2073-2082, 1987.

[3] Travelho, J.S. and Santos, W.F.N., "Transferência de calor transiente no interior de dutos com temperatura variando periodicamente na entrada", II ENCIT - Encontro de Ciências Térmicas, Vol. 1, 315-317, Águas de Lindóia, SP, 1988.

[4] Travelho, J.S. and Santos, W.F.N., "Solution for Transient Conjugated Forced Convection in the Thermal Entrance Region of a Duct with Periodically Varying Inlet Temperature", Journal of Heat Transfer (submitted).

[5] Abramowitz, M. and Stegun, I.A., "Handbook of Mathematical Functions with Formulas, Graphs and Mathematical Tables", National Bureau of Standards Appl. Math. Ser. 55, 1964.

[6] Roberts, G.E. and Kaufman, H. "Tables of Laplace Transforms", W.B. Sounders and Co., Philadelphia, PA, 1966.

III ENCIT – Itapema, SC (Dezembro 1990)

DESENVOLVIMENTO HIDRODINÂMICO E PERDA DE CARGA EM CONFIGURAÇÕES CIRCULARES LISAS E ALETADAS

Philemon Melo Cunha
Francisco Eduardo Mourão Saboya
Departamento de Engenharia Mecânica
Pontifícia Universidade Católica do Rio de Janeiro

RESUMO

Foram determinados em levantamento experimental os coeficientes de perda de carga para o escoamento turbulento em tubos de seção circular com aletas - na forma de pinos - colocados internamente. Foram colocadas várias tomadas de pressão ao longo dos tubos para avaliar os comprimentos de desenvolvimento, que são mostrados graficamente.

INTRODUÇÃO

No estudo dos trocadores de calor compactos ou aletados torna-se necessário um bom conhecimento do impacto de se colocar aletas para aumento da troca de calor. Sabe-se que com a colocação de aletas ou pinos aumenta-se também a área de troca de calor e por vezes provoca uma melhor mistura do fluido de escoamento.

Perigoso se torna porém, concluir que por haver uma maior troca de calor também haveria uma melhor performance do trocador. Sabe-se que a colocação de qualquer elemento perturbador no escoamento, aumenta também a potência necessária para provocá-lo. Daí a necessidade de um conhecimento da perda de carga em cada seção a ser adotada, e quanto maior for o número e arranjos disponíveis dessas seções, mais dados se terá para a otimização de determinada configuração que se queira.

As seções estudadas neste trabalho são circulares com aletas (pinos) variando seu comprimento (altura), conseguindo-se daí, a informação do desenvolvimento do escoamento, assim como as correlações com número de Reynolds e comparação com tubo liso.

Carnavos [1] estudou seções circulares com aletas retangulares e helicoidais colocadas na parte externa e interna de tubos. Nieckele [2] fez experimentos, e obteve correlações para a colocação de pinos também na parte externa de tubos. Braga [3] estudou a colocação de aletas retangulares e segmentadas defasadas longitudinalmente, também na parte externa de tubos. Braga [4] obteve correlações para seções triangulares com uma parede adiabática e pinos nos lados internos do triângulo, variando o ângulo dos lados pinados de 60º, 90º e 120º. Todos os trabalhos citados apontam para trocadores que passam, de preferência, o fluido com menor coeficiente de troca de calor na parte externa, com exceção do primeiro para aletas retangulares e do último para pinos. Justifica-se daí, o estudo de seções circulares com aletamento interno em forma de pinos, objeto deste trabalho.

PRESENTE TRABALHO

Optou-se pelas seções circulares com pinos, colocados internamente pela necessidade de mais esta configuração à disposição de projetistas de trocadores de calor compactos [5].

A seção escolhida foi a de tubos circulares com 6 (seis) pinos colocados radialmente de diâmetro d em disposição defasada longitudinalmente para dois comprimentos de pinos: H= 3d e H= 2d conforme a Figura 1.

A perda de carga ΔP_t foi expressa como a soma da perda de carga no tubo liso ΔP_d com a perda de carga em consequência à presença dos pinos ΔP_p.

$$\Delta P_t = \Delta P_d + \Delta P_p \tag{1}$$

$$f_d = \Delta P_d/((\ell\ \rho\ V^2)/(2D)) \tag{2}$$

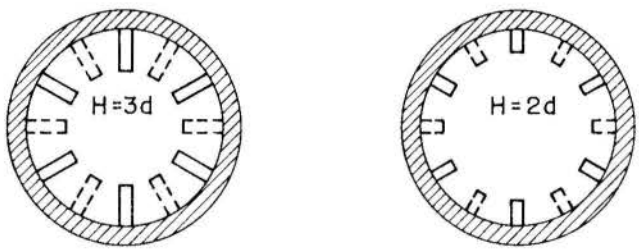

Fig. 1 – Seções estudadas

$$K_p = \Delta P_p/((M_\ell \rho V^2)/2) \tag{3}$$

Por substituição de (2) e (3) em (1) tem-se

$$\Delta P_t = (f_d(\ell/D) + M_\ell K_p)\rho V^2/2 \tag{4}$$

onde

$$V = \dot{m}/\rho A \tag{5}$$

f_d Coeficiente adimensional de perdas no tubo liso

ℓ Comprimento do tubo

M_ℓ Número de fileiras longitudinais dos pinos

K_p Coeficiente adimensional de perda de carga localizada por fileira de pinos

ρ Densidade do fluido

$\dot{m}$ Fluxo de massa do fluido

V Velocidade média do fluido na seção A

A Área transversal do tubo liso.

Por outro lado pode-se definir coeficiente de perda de carga total f_t como:

$$f_t = \Delta P_t/((\ell/D)\rho V^2/2) \tag{6}$$

onde se tem de (4) e (6)

$$f_t = f_d + M_\ell K_p(D/\ell) \tag{7}$$

O objetivo então, será determinar:

f_d = f(Re) para calibração do sistema

f_{t2} = f(Re) H = 2d

f_{t3} = f(Re) H = 3d

K_{p2} e K_{p3}

METODOLOGIA EXPERIMENTAL

O fluido de trabalho foi o ar de uma sala, mantido sob controle de temperatura, pressão e umidade relativa. Para a coleta de dados, construiu-se uma bancada de testes. A mesma era composta de um Bocal, para a medida de Vazão, acoplada a um manômetro diferencial onde se lia uma altura h. A seguir havia um tubo de latão (de bom acabamento interno) que após o desenvolvimento hidrodinâmico, tinha pinos internos e, disposição defasada longitudinalmente, e terminava com um comprimento de seção lisa para propiciar o redesenvolvimento. A seguir vinha uma válvula (tipo "borboleta") que possibilitava o controle da vazão e consequentemente de Re (Reynolds). O escoamento entrava então em um exaustor, que bombeava o ar para fora da sala. Ver o esquema na Figura 2.

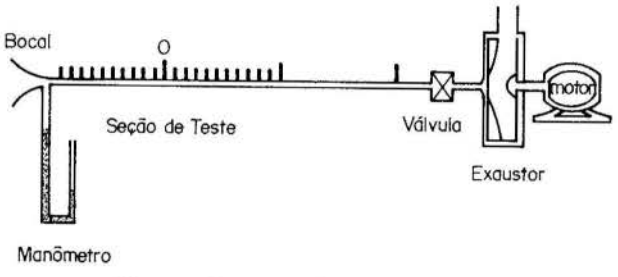

Fig. 2 – Esquema do sistema montado

O Bocal (medidor de vazão) foi construido em resina e comparado com uma placa de Orifício calibrada, assim como verificados os resultados para a perda de carga em tubos - de conhecimento na literatura afim - obtendo-se boa confiabilidade nas leituras de vazão, e velocidade média. A escolha do Bocal se deu pela não necessidade de comprimento de desenvolvimento antes do mesmo, já que se tratava de "Bocal de entrada".

O tubo que continha a seção de testes (2m de comprimento e diâmetro de 28,5 mm) foi usinado nas extremidades para o acoplamento, e a furação para a montagem dos pinos foi realizada em uma freza equipada com cabeçote divisor para a perfeita distribuição dos pinos, e colocação por interferência. Em seguida, os pinos foram soldados e usinados externamente para melhor vedação e objetivos futuros.

A válvula "borboleta" era de concepção simples, mas garantia um controle de vazão dentro da faixa de Reynolds que se desejava.

O ventilador (exaustor, para trabalhar na sucção) era centrífugo e mantinha boa estabilidade para garantir um regime permanente. As tomadas de pressão (para perda de carga) foram distribuidas longitudinalmente ao tubo, (tanto no liso quanto nos pinados) tendo como referência um ponto 0 colocados no início da seção de testes; daí os valores negativos e positivos que se observa no gráfico de desenvolvimento. O sistema para estas medidas de pressão foi o BARATRON (equipamento com sinal elétrico) cuja sonda permitia uma resolução de 10^{-3} mmHg, necessária para o caso de ar nestas configurações, medindo perda de carga.

Os instrumentos para medir a temperatura e umidade relativa para o cálculo das propriedades eram simples, com resolução de 0,5 ºC e 1% respectivamente.

DESENVOLVIMENTO DO ESCOAMENTO

Procurou-se determinar o comprimento de desenvolvimento do escoamento (no tubo liso isto serviu como calibração do sistema, visto que já existem resultados na literatura), que pode ser observado nos próximos gráficos. Observa-se que o desenvolvimento na região pinada é muito rápido, ou seja, pequeno comprimento de desenvolvimento (em torno de 3 diâmetros).

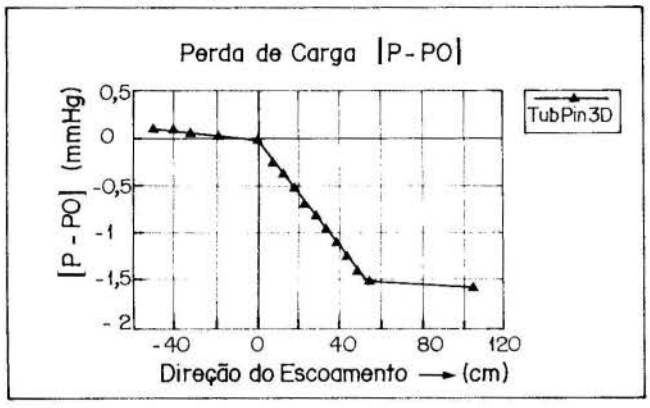

Fig. 3 – Distribuição de Pressão [H = 3d] Re = 10^4

Este gráfico representa a diferença de pressão entre o ponto a ser medido e a pressão no ponto 0 (início da seção pinada), para altura de pinos H igual a 3 vezes o seu diâmetro d.

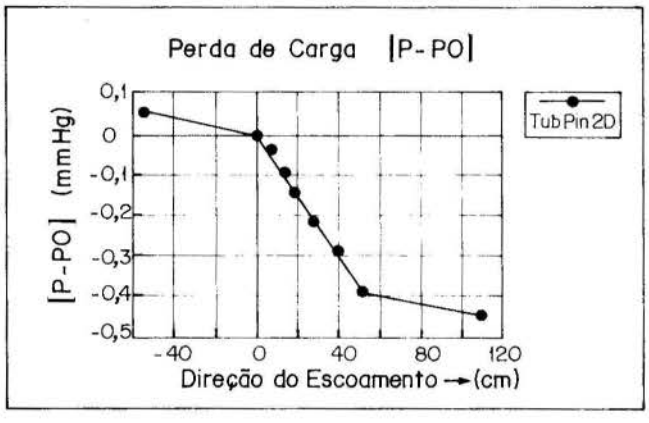

Fig 4 – Distribuição de Pressão [H = 2d] Re = 7 x 10^3

Este gráfico representa a diferença de pressão entre o ponto a ser medido e a pressão no ponto 0 (início da seção pinada), para altura de pinos H igual a 2 vezes o diâmetro d.

COEFICIENTES DE PERDA DE CARGA [f, K_p]

Os coeficientes de perda de carga f_d f_t e K_p foram determinados pelas equações (2), (6) e (7) quando substituidos os dados colhidos durante as experiências. Foram realizadas em torno de 300 "corridas" para cada seção, para garantir a repetibilidade, e uma boa faixa de Reynolds mostrada a seguir.

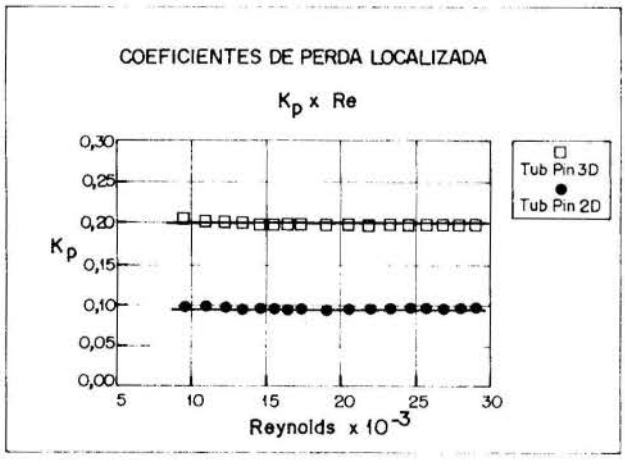

Fig. 5 – Variação do coeficiente de perda localizada K_p com Reynolds

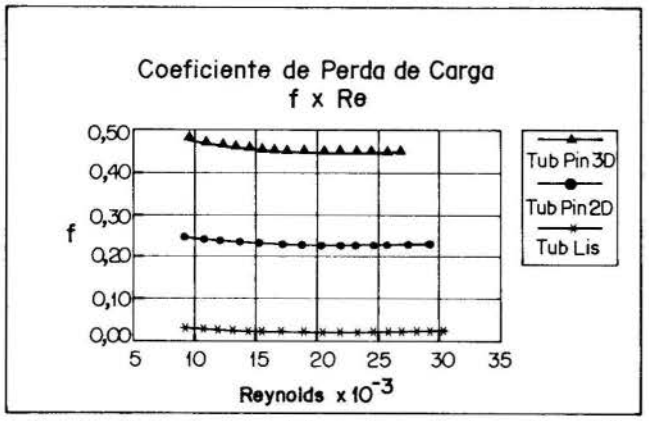

Fig. 6 – Variação do coeficiente de perda f com Reynolds

Procurou-se correlacionar o fator de fricção f e o coeficiente de perda localizada K_p com o número de Reynolds do escoamento. Nos gráficos elaborados foram feitos ajustes de curvas para a correlação dos dois adimensionais. Os resultados e correlações estão no próximo item.

RESULTADOS E CONCLUSÕES

As correlações para o fator de perda de carga como função de Reynolds para tubulações circulares aletadas internamente (252 pinos por tubo) foram determinadas para dois comprimentos de pinos diferentes [H= 2d e H = 3d].

O gráfico para K_p mostra uma pequena variação do coeficiente de perda de carga com Reynolds devido à presença dos pinos. As correlações obtidas pelo ajuste de curvas são:

H= 2d	$f_{t2} = 0{,}36\ \mathrm{Re}^{-0{,}044}$	$K_{p2} = 0{,}095$
H= 3d	$f_{t3} = 0{,}78\ \mathrm{Re}^{-0{,}056}$	$K_{p3} = 0{,}20$

Estas correlações foram determinadas através de programas de computador na sua forma global e localizada.

Verifica-se que a variação de f e K_p com Reynolds é bastante pequena, justificando-se considerá-los como constantes para cada comprimento de pino, em escoamento turbulento.

Também se observa que, com o aumento de 50% no comprimento dos pinos a perda de carga dobra, o que parece desaconselhar a configuração de H= 3d.

AGRADECIMENTOS

Os autores agradecem o apoio financeiro do CNPq durante esta fase da pesquisa.

REFERÊNCIAS BIBLIOGRÁFICAS

[1] Carnavos, T. C., "Cooling Air in turbulent Flow with Internally finned Tubes", Heat Transfer Engineering, Vol. 1, nº 2, 1979, pp. 41-46.

[2] Nieckele, A.O., "Determinação dos Coeficientes de Transporte em um Trocador Bi-Turbular Pinado", Tese de Mestrado, Departamento de Engenharia Mecânica PUC/RJ, 1981.

[3] Braga, C. V.M. and Saboya, F.E.M., "Turbulent Heat Transfer and Pressure Drop in Smooth and Finned Annular Ducts", Proceedings of the Eighth International Heat Transfer Conference and Exibition, San Francisco CA August 1986, 2831-2836.

[4] Braga, S.L., "Coeficientes de Transporte em Dutos Triangulares Lisos e Pinados". Tese de Doutorado, Departamento de Engenharia Mecânica, PUC/RJ, 1985.

[5] Cunha, P.M., "Características Termohidráulicas de Escoamentos Turbulentos em Configurações Circulares Lisas e Pinadas", Tese de Doutorado, Departamento de Engenharia Mecânica, PUC/RJ, 1987.

ABSTRACT

Pressure drop data have been obtained experimentally for the turbulent flow in circular tubes internally finned with pin fins. Pressure taps have been installed axially along the tubes to evaluate the lengths for flow development, which are presented graphically.

III ENCIT – Itapema, SC (Dezembro 1990)

Passive Heat Transfer Enhancement by Surfaces with Spanwise Riblets

Cristina H. Amon
Carnegie Mellon University
Department of Mechanical Engineering
Pittsburgh, PA, 15213, U.S.A.

Numerical investigations of the flow pattern and forced convective heat transfer in channels containing V-grooved riblets on one wall, are presented. The riblet surface profile is designed to excite Tollmien-Schlichting instabilities in the channel flow. As a result, traveling waves are observed at moderately low Reynolds numbers inducing oscillatory separated flows which enhance mixing, and hence, augment convective heat transport. Direct numerical simulations by a spectral element-Fourier method are performed in the laminar and transitional flow regimes, at Reynolds numbers encountered in compact heat exchanger applications. This geometry is found to offer a significant improvement in heat transfer/pumping power performance relative to a flat channel and it is comparable to other augmentation schemes.

INTRODUCTION

The need for lightweight, space saving, and economical heat exchangers has driven the development of compact surfaces which has received a great deal of attention in the research community.

Compact heat transfer surfaces are found in many important technological applications such as in heat exchanger devices encountered in automobiles, air conditioning, electronic cooling, waste and heat recovery, cryogenics, spacecraft, and aircraft. Recently, their application has been extended to ocean-, solar-, and geo-thermal energy conversion systems due to the interest for energy conservation and alternative energy resources [1].

The effort to understand the convection mechanisms and to predict heat transfer coefficients and pressure drops in compact heat exchangers has generated different investigation approaches. As pointed out by Joshi and Webb [2], these approaches include data acquisition for actual cores or scaled-up models, empirical correlations, flow visualizations, mass transfer data for scaled-up models, and numerical solutions. Basically, three broad approaches can be adopted, namely acquisition and correlation of empirical date, qualitative observations of the convection process, and numerical solutions with analytical modeling. In this work, numerical simulations are performed using the spectral element-Fourier method (SEFM) [3] which combines the advantages of both globally unstructured and locally structured spatial discretizations, where the global decomposition in macro-elements allows geometric flexibility and the local structure permits an efficient high-order approximation by spectral techniques with rapid convergence and high accuracy. The spectral element-Fourier method is a domain-decomposition technique in which the interface continuity constraints are imposed only via a variational formulation as in the p-type finite element method. A three-step splitting scheme is used for the semi-discrete temporal discretization, reducing the governing equations to hyperbolic and elliptic partial differential equations. For the Navier-Stokes equations, the nonlinear convective term is treated explicitly with collocation operators, while the pressure and viscous contributions are handled implicitly with variational projection operators.

Traditionally, the increase in heat transfer in compact heat exchangers has been achieved by adding either extended surfaces to increase the surface-area-to-volume ratios or louvers to interrupt thermal boundary layers. Of the many enhanced plate-fin or tube-fin geometries, the offset strip fins are the most common configurations.

Recently, attention has been focused on innovative heat transfer enhancement techniques which are based on flow destabilization mechanisms that promote large-scale convecting mixing, and therefore increase heat transport. These mechanisms require a separated flow region and flow unsteadiness obtained by active flow modulation [4,5] or passive supercritical flow destabilization [6,7,8].

In the present work, we study numerically the heat transfer enhancement in compact heat exchanger geometries which is induced by passive flow destabilization. This is achieved by designing the heat exchanger surface to excite normally damped Tollmien-Schlichting modes in order to enhance convective mixing and induce self-sustained oscillatory flows. The geometry, shown in Figure 1, consists of parallel channels with one surface containing spanwise aligned riblets of triangular shape. Two different channel heights or wall-to-wall spacing are employed (geometries G1 and G2) to study the effect of the relative dimensions on the flow pattern and heat transfer characteristics.

Experimental work on this wall shape was performed by Greiner et al. [9]. This paper compares numerical and experimental results for geometry G1 and extends previous experimental results including a detailed study of the flow patterns and a parametric study to determine the frequency of the self-sustained oscillatory flow as well as the traveling wave structures.

PROBLEM DESCRIPTION AND NUMERICAL TECHNIQUE

The physical problem: We consider internal flow in the two-dimensional channel shown in Figure 1. The channel consists of a flat wall and a corrugated wall containing spanwise aligned riblets. The flow configuration is

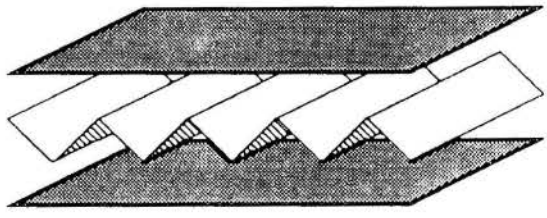

Figure 1. Schematic of the compact heat exchanger geometry.

Nomenclature

d	riblet depth (Figure 1)
h	half-channel height
h_i	Lagrangian interpolants
k	thermal conductivity
K	element number
l	riblet length (Figure 1)
n	periodicity index
Nu	Nusselt number, $q''h/k\overline{\Delta T}$
P	pressure
Pr	Prandtl number, ν/α
q"	heat flux
Re	Reynolds number, (3/2) Vh/ν
r,s	local elemental coordinates
t	time
T	temperature
T	period of self-sustained oscillatory velocity
$\overline{\Delta T}$	time- and space-averaged temperature difference
u,v	velocity components in the x- and y-directions
$\vec{v}$	vector velocity $(u\,\hat{x} + v\,\hat{y})$
V	channel-averaged velocity
α	streamwise wavenumber, or thermal diffusivity
β_q	Adams-Bashforth coefficients
∂D	boundary of the computational domain
ν	kinematic viscosity
Π	pressure head
σ	growth or decay rate
$\vec{\omega}$	vorticity

Subscripts

B	bottom wall
c	critical
TS	Tollmien-Schlichting
T	top wall

Superscripts

n	time step

geometrically described by the riblet transverse spacing or geometric periodicity length l, channel height 2h, and riblet depth d (Figure 2). The corrugated wall is maintained isothermal while the flat wall is exposed to a uniform heat flux.

The computational problem: The geometry shown in Figure 1 consists of a large number of transverse riblets in the x-direction. We are interesting in studying the flow pattern and heat transfer characteristics in the region where the flow becomes periodically fully developed. Because of the periodicity in the flow conditions in the x-direction and the homogeneity in the z-direction, the computational domain is restricted to the region between the dotted lines shown in Figure 2.

Governing equations:

We consider here Newtonian, incompressible two-dimensional flows with constant properties, which are governed by the Navier-Stokes and energy equations written in the following form,

$$\frac{\partial \vec{v}}{\partial t} = \vec{v} \times \vec{\omega} - \vec{\nabla}\,\Pi + (1/\mathrm{Re})\,\nabla^2 \vec{v} \qquad (1)$$

$$\frac{\partial T}{\partial t} = -\,\vec{\nabla}\cdot(\vec{v}\,T) + (1/\mathrm{Re.Pr})\,\nabla^2 T \qquad (2)$$

where $\vec{v}\,(\vec{x},t) = u\,\hat{x} + v\,\hat{y}$ is the velocity; $\vec{x}$ and t are space and time, respectively; ω is the vorticity $\vec{\omega} = \vec{\nabla} \times \vec{v}$; Π is the pressure head $\Pi = p + |v|^2/2$ with p the pressure; T is the temperature; Re is the Reynolds number and Pr is the Prandlt number. In addition, to satisfy equation 1, the velocity field has to be divergence free (i.e., $\vec{\nabla}\cdot\vec{v} = 0$) in order to satisfy the incompressibility condition.

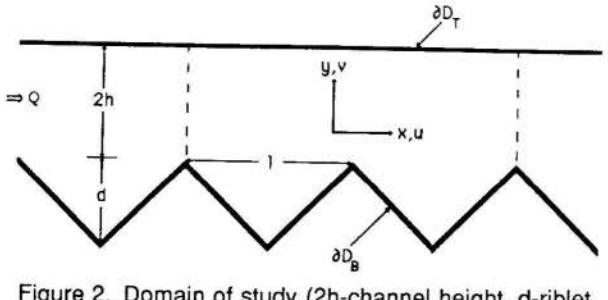

Figure 2. Domain of study (2h-channel height, d-riblet depth, l-riblet transverse spacing).

The velocity boundary conditions are Dirichlet on rigid walls, Neumann on outflow, and periodicity on homogeneous or fully developed directions. The thermal boundary conditions are uniform heat flux on the top flat wall and constant temperature on the bottom wall.

For the geometry shown in Figure 2, parameters and variables are non-dimensionalized by scaling the velocities by (3/2)V where V is the cross-channel time-average velocity, the lengths by half-channel height h, and the temperature by q"h/k where q" is the uniform flux imposed at the wall and k is the thermal conductivity of the fluid.

To solve numerically the above system of equations, we first proceed with the temporal discretization of the equations. Different approaches can be followed which would lead to a different reduced system of equations; several of the most frequently schemes are discussed in [10]. An attractive time-discretization scheme, due to its ease of implementation in complex geometries, is the multi-fractional step method, followed first by Orszag and Kells [jfm]. This fractional step leads conveniently to a decoupled system of Helmholtz operators for the pressure and viscous contributions. We can therefore write the three main substeps as follows:

$$\frac{\hat{\vec{v}}^{n+1} - \vec{v}^{n}}{\Delta t} = \sum_{q=0}^{2} \beta_q \left(\vec{v}^{n-q} \times \vec{\omega}^{n-q}\right) \qquad (3)$$

$$\frac{\hat{\vec{v}}^{n+1} - \hat{\vec{v}}^{n+1}}{\Delta t} = -\,\vec{\nabla}\,\Pi \qquad (4a) \qquad\qquad \vec{\nabla}\cdot\hat{\vec{v}}^{n+1} = 0 \qquad (4b)$$

$$\Downarrow$$

$$\nabla^2 \Pi = \frac{\vec{\nabla}\cdot\hat{\vec{v}}^{n+1}}{\Delta t} \qquad (4c)$$

$$\frac{\vec{v}^{n+1} - \hat{\vec{v}}^{n+1}}{\Delta t} = \frac{1}{\mathrm{Re}}\,\nabla^2 \vec{v}^{n+1} \qquad (5)$$

Equation (3) represents explicit treatment of the convective term, where β_q is the third-order Adams-Bashforth coefficients $\beta_0 = 23/12$, $\beta_1 = -16/12$ and $\beta_2 = 5/12$. We choose Adams-Bashforth third-order method due to its low dispersion errors and the relatively large portion of the imaginary axis included within the absolute stability region of the scheme. Equation (4a) accounts for the pressure contribution. It is converted to an elliptic equation (4c) when

the incompressibility condition is ensured by equation (4b). Both, the pressure and viscous terms (4c and 5) are handled implicitly by Euler Backward and Crank-Nicolson schemes, respectively. These steps are unconditionally stables and result in an efficient inversion of the global matrix. The time-step size is therefore dictated by equation (3) and time-accuracy considerations.

The spatial discretization proceeds using collocation for the nonlinear convective term (3) and variational spectral element formulation for the pressure (4c) and viscous (5) terms. The spectral element method is a high-order weighted-residual technique [11,12] that combines the flexibility of the finite element schemes with the good resolution and convergency properties of spectral methods. In the isoparametric spectral element method, the two-dimensional computational domain is first partitioned into four-sided, non-overlapping subdomains or elements. A typical subdomain decomposition is shown in Figure 3A. Each subdomain is then isoparametrically mapped from the physical (x,y) space to the local (r,s) coordinate system (Figure 3B). Note that complex geometries can be easily handled by combining mapping techniques with element domain decomposition.

Within each element, the unknowns (i.e., velocity, pressure, and temperature) and the data (i.e., geometry) are represented as a tensor-product of high-order Lagrangian interpolants through Gauss-Lobatto Chebyshev collocation points, defined as

$$\left(\vec{x},\vec{v},\Pi\right)_n^k\ (r,s) \;=\; \sum_{i=0}^{N}\sum_{j=0}^{N}\left(\vec{x},\vec{v},\Pi\right)_{ij}^k h_i(r)\,h_j(s)$$

where $h_i(r)$ and $h_j(s)$ are Nth-order interpolants that satisfy $h_i(\zeta_j)=\delta_{ij}$ at the local (r,s) coordinates. A typical spectral element mesh with interpolants of seventh order (N=7), is shown in Figure 4. In order to guarantee rapid convergence of the resulting expansions, the local and physical collocation points are chosen to be the Gauss-Lobatto Chebyshev points, defined as $x_j^i = \cos \pi j/N^i$.

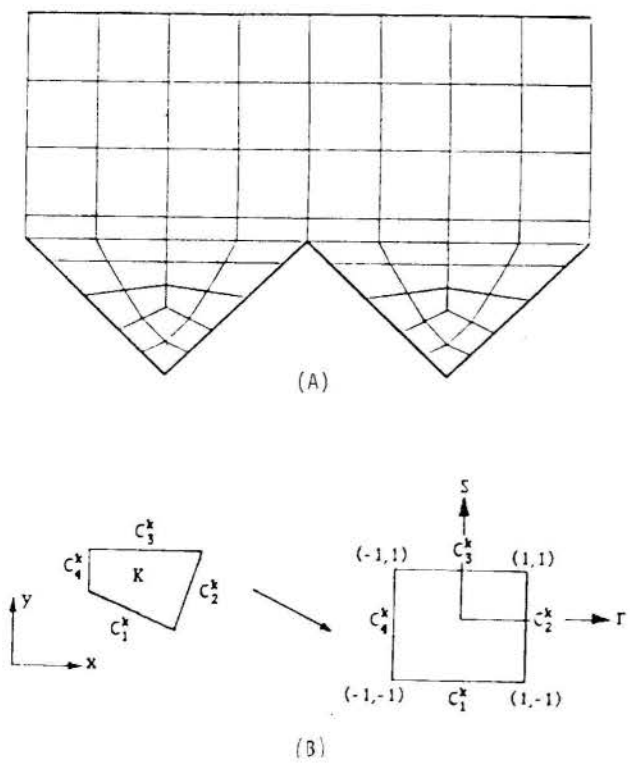

Figure 3. (A) Subdomain decomposition of the physical computational domain (x,y). (B) Isoparametric mapping of a typical element K.

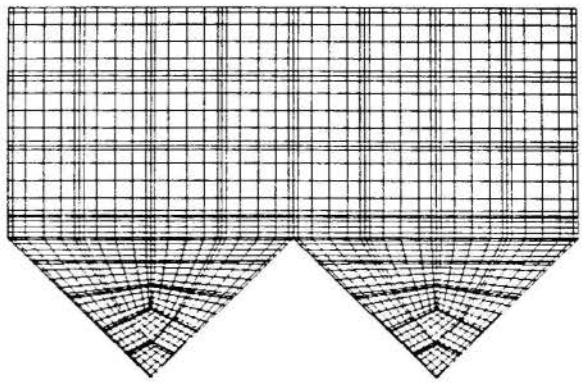

Figure 4. Computational domain and spectral element mesh.

RESULTS AND DISCUSSION

In this section, numerical results are presented describing the flow field and heat transfer in channels with V-grooved riblets for two different geometries. The geometry G1 corresponds to non-dimensional riblet length l/h=2.4 and riblet depth d/h=1.2, and G2 corresponds to l/h=4.8 and d/h=2.4. The computational domain and a typical spectral element mesh for G1 are shown in Figure 4. The flow visualizations obtained by numerical simulations are compared with the experimental results [9] for the G1 geometry.

The steady-state subcritical flow field for G1 is shown in Figure 5 where the flow is from left to right. Figure 5A shows the numerical results for the velocity field which is obtained by integrating the unsteady governing equations starting from arbitrary initial conditions, until convergency to a stable steady state is achieved. Figure 5B shows the streaklines for the experimental flow visualization captured by injecting colored dye at the leading edge of the

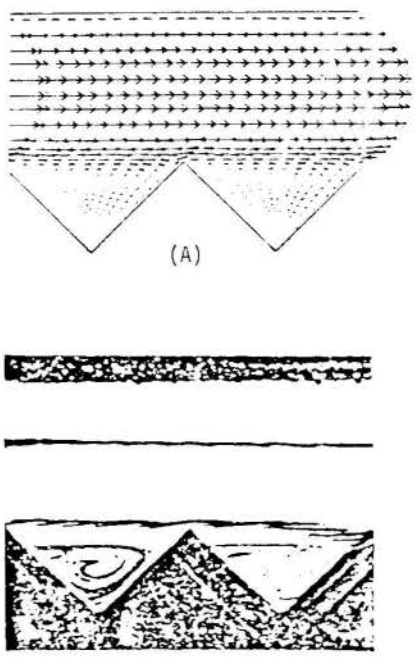

Figure 5. Steady-state flow visualizations for G1.
(A) Velocity vectors numerically computed.
(B) Streaklines experimentally obtained.

thirty-eighth riblet. Both, the experimental and numerical results indicate the existence of a separated flow region with a large-scale, slowly recirculating vortex and almost no communication between the riblet and channel flows. This is clearly seen from the channel velocity profile in Figure 5A which is very close to a parabolic plane-Poiseuille-flow profile. It is also corroborated by the experimental flow visualization (Figure 5B) where the channel streaklines do not mix with the recirculating riblet flow.

Above a critical Reynolds number Re_c this flow becomes exponentially unstable to small disturbances until nonlinear effects stabilize the velocity at some fixed amplitude. A time-asymptotic result for the convergence of the streamwise velocity to its steady-periodic state for G1 is shown in Figure 6. It is seen that the least stable mode is oscillatory with a linear growth rate and period of σ=0.0232 and $\mathbf{T}_1$=9.84, respectively. Notice that for a plane channel wave corresponding to the same wavenumber and Reynolds number, the decay rate and period are σ_{TS}=-0.01436 and $\mathbf{T}_{TS}$=9.768, verifying the flow destabilizing effect of the riblets. The frequency of the growing mode and ensuing oscillatory velocity is very close to the Tollmien-Schlichting [13] frequency corresponding to the same spatial structure (i.e. wavelength)of *one* wave per *two* riblets. The selection of one wave per two riblets as the most unstable flow configuration is clearly depicted in the instantaneous velocity vectors plotted in Figure 7A, and it is corroborated by the experimental flow visualization shown in Figure 7B.

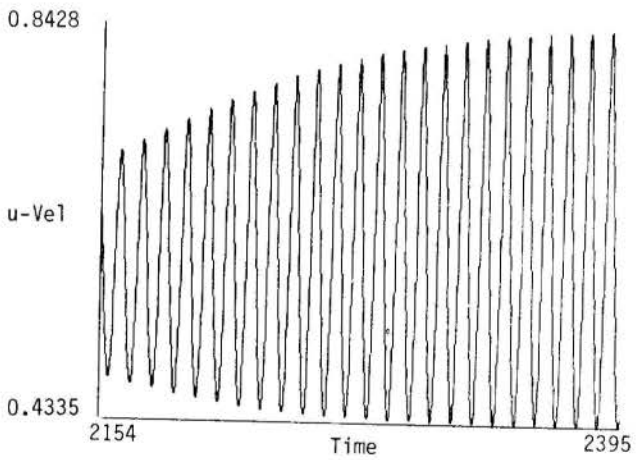

Figure 6. Streamwise velocity as a function of time, converging to its steady periodic regime. The period of oscillation is $\mathbf{T}_1$ = 9.84.

The evolution of the flow structure during one period of the self-sustained oscillation is shown in Figure 7A by instantaneous velocity vectors in a sequence of three time frames within one flow cycle. The flow is supercritical and the traveling waves indicate that the flow has undergone a bifurcation from a steady, time-independent state of Figure 5 to a time-periodic self-sustained oscillatory flow. Free shear layers span the riblet openings and separate the mainstream from recirculating flow regions in the riblet cavities. Periodic interruptions of the shear layers cause their instabilities to project energy onto the normally damped Tollmien-Schlichting modes in order to sustain them. The waviness of the channel flow induces the ejection of the vortices from the riblet cavities when the low pressure region associated with the crest of the wave passes over it. Subsequently, mainstream fluid fills the riblet cavity and a new vortex grows and protrudes into the mainstream, thus, enhancing mainstream and riblet flow mixing. As the Reynolds number is increased further, similar flow patterns are obtained with larger amplitude waves and stronger mixing. For higher Reynolds numbers the flow becomes three-dimensional, leading to early transition to turbulence [14].

An important aspect in our numerical simulation is the selection of the computational domain and the imposition of periodic fully-developed flow boundary conditions over a region comprising 'n' geometrically periodic riblets of length 'l' (Figure 2). For example, in the G1 geometry analyzed above, the system chooses the least stable solution that corresponds to one wave per two riblets (n=2) which is the physically realizable solution also corroborated by experimental flow visualizations (Figure 7B). However, numerical simulations in computational

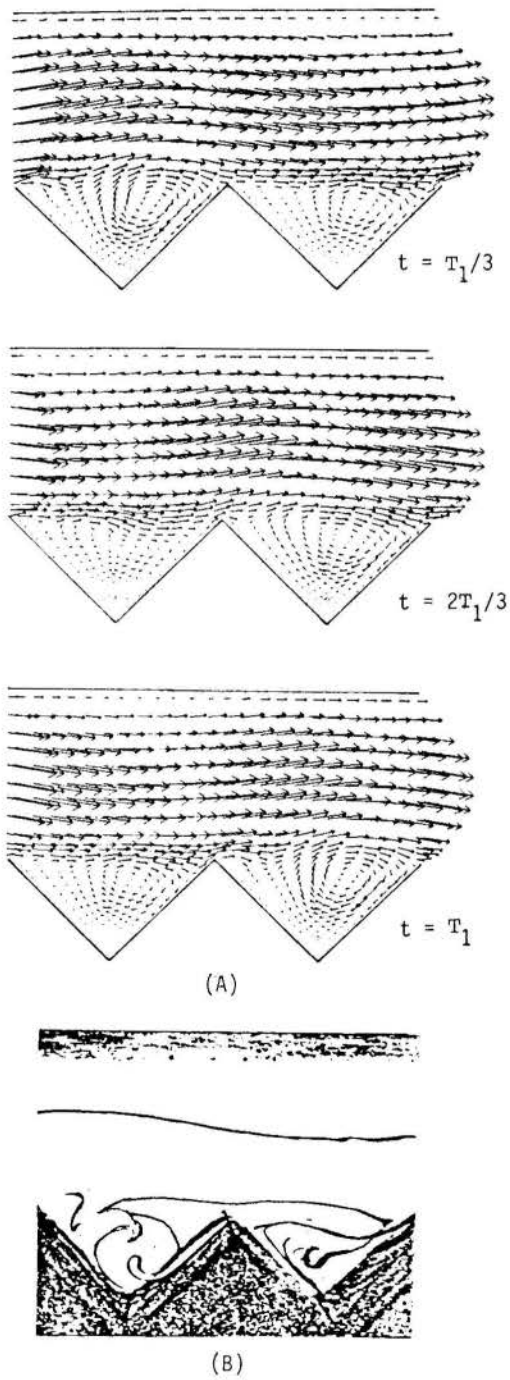

Figure 7. Visualization of the self-sustained oscillatory flow for G1 depicting a one-wave solution per two riblets. (A) Instantaneous velocity vectors at 3 times during one cycle $\mathbf{T}_1$. (B) Experimental streaklines.

domains which impose flow periodicity over one or three riblets (n=1,3) for G1, yield more stable flows (i.e., higher critical Reynolds number) than the ones physically attainable. This indicates the importance of selecting the valid computational domain. Therefore, to establish the required computational domain in the absence of experimental information, we either simulate the flow in multi-periodic domains or solve the linearized Orr-Sommerfeld equations [13] to determine the least stable channel mode usually referred to as Tollmien-Schlichting waves. For a given Reynolds number and wave number ($\alpha=2\pi h/nl$), we obtain a discrete spectrum of complex eigenvalues yielding nontrivial solutions, where the real part is the phase speed and the imaginary part is the growth rate of the corresponding eigenfunctions. The least channel stable mode, triggered by the riblets, corresponds to the eigenfunction associated with the maximum growth rate.

In the second geometry, G2, the channel height has been reduced by a factor of two, relative to G1, so that the riblets are larger compared to the channel dimension. The instantaneous supercritical flow fields at Re=800 are presented in Figure 8 at three times during one period ($\mathbf{T}_2$=2.79) of self-sustained oscillation. The propagation of the wave at the Tollmien-Schlichting wave speed can be followed up in time through the flow cycle. These figures clearly indicate a one-wave solution per geometric periodicity length l and the same flow pattern in each riblet, with all the riblet vortices ejected simultaneously to the mainstream. Therefore, for these flow conditions, it suffices to utilize a computational domain comprising only one riblet. Note that the traveling wave number α for this geometry G2 is the same as in G1, which is not surprising since Orr-Sommerfeld solution depends weakly on Re.

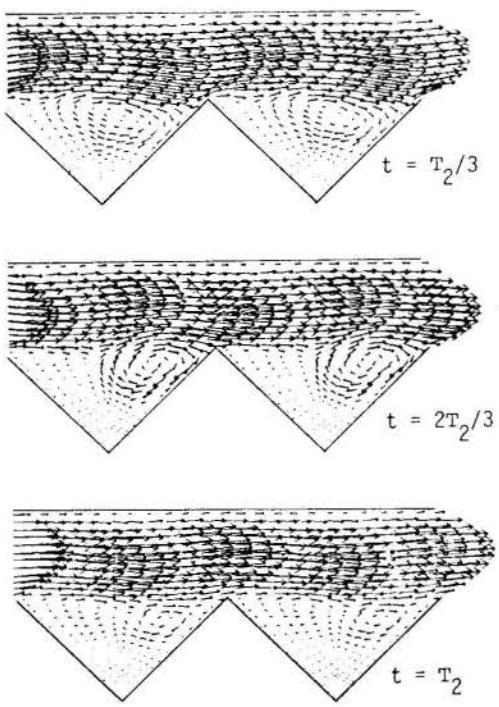

Figure 8. Instantaneous velocity vectors during one cycle $\mathbf{T}_2$ of the self-sustained oscillatory flow for G2. A two-wave solution is obtained in the n=2 domain.

The instantaneous isotherms corresponding to the flow field of Figure 8 at t=2$\mathbf{T}_2$/3 are presented in Figure 9. The relatively uniform temperature in the riblet regions indicates the effect of the convective mixing between the riblet and channel flows due to the self-sustained oscillations. Also, note the creation of thin thermal boundary layers on the channel top wall induced by the thermal traveling wave. These results suggest that at moderate Reynolds numbers, the riblet surfaces should provide a better performance than flat-walled passages. This is, indeed, the case. The channel with riblets offers significantly higher heat transfer for a given pumping power, by a factor of approximately 3.5, compared to a flat channel in the laminar-transitional regime.

The performance of these surfaces is comparable with other augmentation schemes based on flow destabilization mechanisms which induce self-sustained oscillatory flows either by placement of cylindrical promoters [6,8] or by interruption of surfaces [7]. However, the geometric configuration presented in this paper is simpler to manufacture since it does not require the addition of cylinders or the construction of interrupted surfaces.

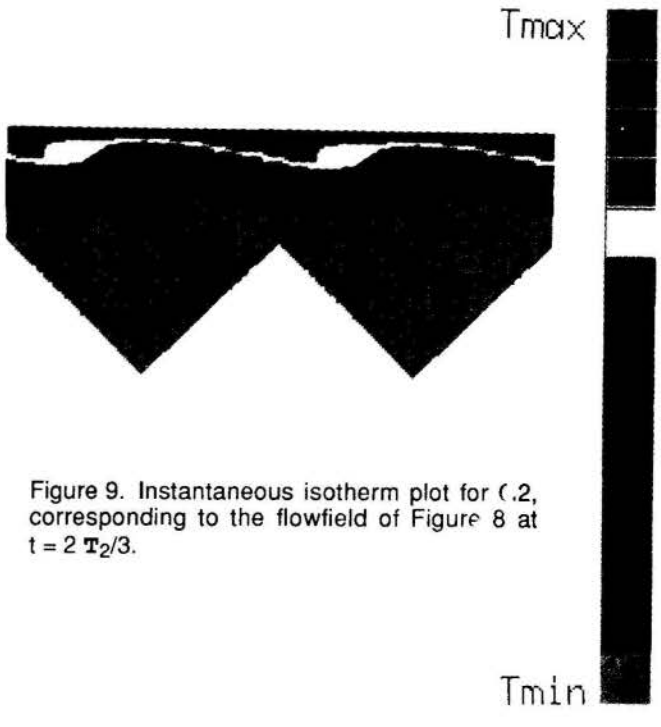

Figure 9. Instantaneous isotherm plot for Re=800, corresponding to the flowfield of Figure 8 at t = 2 $\mathbf{T}_2$/3.

CONCLUSION

The passive flow destabilization, induced by the spatially periodic disturbances introduced by the riblets, sustains the oscillatory flow, the Tollmien-Schlichting traveling waves and the vortex ejections which are the flow mechanisms responsible for enhancing the overall mixing, and hence, improving the heat transfer performance.

ACKNOWLEDGEMENT

The author gratefully acknowledges the financial support of the National Science Foundation under Grant CBT 89-08808 and the computing time provided by Cray Research, Inc. and Pittsburgh Supercomputing Center.

REFERENCES

[1] Mori, Y. and Nakayama, W., "Recent Advances in Compact Heat Exchangers in Japan," Compact Heat Exchangers History, Technological Advancement and Mechanical Design Problems, ASME, New York, HTD-10, pp. 5-16, 1980.

[2] Joshi, H.M. and Webb, R.L., "Heat transfer and friction in the offset strip-fin heat exchanger," Int. J. Heat Mass Transf., 30, pp. 69-84, 1987.

[3] Amon, C.H., "Spectral Element-Fourier Approximation for the Navier-Stokes Equations: Some Aspects of Parallel Implementation," Parallel and Vector Computation in Heat Transfer, ASME, HTD-133, pp. 11-18, 1990.

[4] Ghaddar, N.K., Magen, M., Mikic, B.B. and Patera, A.T., "Numerical Investigation of Incompressible Flow in Grooved-Channels; Part 2," J. Fluid Mech., Vol. 168, pp. 541-552, 1986.

[5] Amon, C.H., Mikic, B.B. and Korin, E., "Effect of Oscillatory Flow on Heat Removal from Circular Fins," Cooling Technology for Electronic Equipment, Hemisphere, Washington DC, pp. 125-138, 1988.

[6] Karniadakis, G.E., Mikic, B.B. and Patera, A.T., "Minimum-Dissipation Transport Enhancement by Flow Destabilization: Reynolds Analogy Revisited," J. Fluid Mech., Vol. 192., pp. 365-378, 1988.

[7] Amon, C.H. and Mikic, B.B., "Numerical Prediction of Convective Heat Transfer in Self-Sustained Oscillatory Flows," J. Thermophys. Heat Transf., Vol. 4, pp. 239-246, 1990.

[8] Ratts, E., Amon, C.H., Mikic, B.B. and Patera, A.T., "Cooling Enhancement of Forced Convection Air Cooled Chip Array through Flow Modulation Induced by Vortex-Shedding Cylinders in Cross-Flow," Cooling Technology for Electronic Equipment, Hemisphere, Washington DC, pp. 183-194, 1988.

[9] Greiner, M., Chen, R.-F. and Wirtz, R.A., "Heat Transfer Augmentation through Wall-Shape Induced Flow Destabilization," ASME Heat Transf. Conf., HTD-107, pp. 337-342, 1989.

[10] Orszag S.A., Israeli M. and Deville M.O., "Boundary Conditions for Incompressible Flows," J. Scien. Comp., Vol. 1, pp. 75-111, 1986.

[11] Patera, A.T., "A Spectral Element Method for Fluid Dynamics: Laminar Flow in a Channel Expansion," J. Comp. Phys., Vol. 54, pp. 468-477, 1984.

[12] Amon, C.H. and Mikic, B.B. "Spectral Element Simulations of Unsteady Forced Convective Heat Transfer," Numerical Heat Transfer, to appear, 1990.

[13] Drazin, P.G. and Reid, W.H., "Hydrodynamic Stability," Cambridge University Press, Cambridge, 1981.

[14] Amon, C.H. and Patera, A.T., "Numerical Calculation of Stable Three-Dimensional Tertiary States in Grooved-Channel Flow," Phys. Fluids A, Vol. 1(12), pp. 2005-2010, 1989.

Numerical Investigation of three Dimensional Flows and Heat Transfer in Fin-Tube Exchanger

A.Bastani, N.K. Mitra, M.Fiebig
Institut fuer Thermo-und Fluiddynamik Ruhr-Universität BochumPostfach 102148,4630 Bochum,FRG

SUMMARY

The computation of the flow field and heat transfer between two plate fins of a compact cross flow heat exchanger with staggered tubes has been carried out in Renolds number range of 40 to 2000. Thee Nusselt nummber plots on the fin show deterioration of heat transfer by 50%, or more in the stagnation zone of the rear tube due the wake of the preceding tube. The Nusselt number distribution on the tube near the jun-cture of the tube and the fin deviates substantially from the two dimensinal prediction.

Nomenclature

- a = thermal diffusivity
- B = breadth of the channel
- D = tube diameter
- H = channel height(fin spacing)
- L = channel length
- L1 = axial distance of the first tube from the channel entrance
- p = pressure nondimensionalized with ρu^2_{av}
- S1 = Tube spacing
- T = nondimensional tempratur, 0 at inlet, 1 on the wall
- t = time nondimensionalized with H/u_{av}
- u = nondimensioal axial velocity
- u_{av} = average axial velocity
- v = nondimensional spanweise velocity
- w = nondimensional normal velocity
- X_i = x ,y , z cartesian coordinates (nondimensionalized with H)
- Pr = Prandtl number
- Re = Reynolds number = $\frac{u_{av} H}{\nu}$
- Nu = Nusselt number based on the difference between the wall and the inlet temperatures
- ν = dynamic viscosity

INTRODUCTION

Compact cross flow fin- tube heat exchangers, where a bank of tubes share a number of common plate fins, find applications in many industrial plants and apparatus. Typically a liquid flows throughthe tubes and a gas (often air) flows through the channel formed by the neighboring fin plates, see fig. 1.

The gas flow between two neighboring fins can be modeled as a nonisothermal flow in a rectangular channel with a built-in array of cylindrical obstacles.

Depending on the design criterion and applicaton, the tubes in the array can be arranged in different ways. The selecton of the optimum design of a heat exchanger for a given applicaton will therefore need a large data base of the heat exchanger performance depending on geometrical and flow parameters. Such data base can be obtained from a large number of experimental measurements. The experiments, however, are expensive and time-consuming. Moreover, they give only global information. The alternative to the experiments is the development of a computer code that can numerically simulate the velocity and temperature fields in a rectangular channel with a built-in array of tubes. A parametric study of heat exchanger performance with the help of the computer code will be less expensive and faster than with the experiments. Furthermore, a computer simulation will give detailed velocity and temperature fields. This will enable the designer to pinpoint the location of areas (and possibly the causes) of heat transfer degradation so that he can take remedial measures against them.

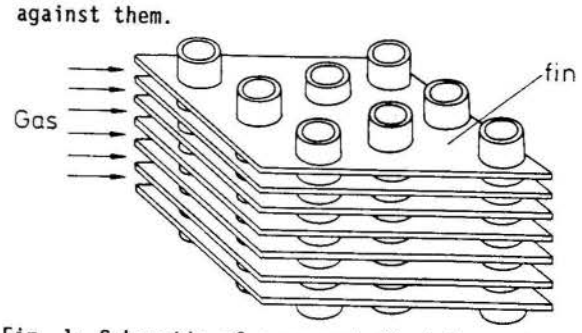

Fig. 1: Schematic of a compact fin-tube heat exchanger

The purpose of the present work is the development of a computer code and numerical investigations of three dimensional flow and temperature fields in a rectangular channel with a built-in bank of cylindrical obstacles in staggered arrangment.

Two dimensional simulations of flow past a tube bundle have been reported by Le Feuvre (1973), Launder and Massey (1978), Chen (1984), Fujii et al. (1984) and wung and Chen (1989). The simulation of the tube bank in all the above works has been achieved by selecting as the computional domain a rectangle with two (at most three) tubes. The implicit assumption here is that the (two dimensioal) tube bank can be divided n such rectangular elements and the flow field of one element will be repeated (spatially periodic) in all the elements. The computational results give the Nusselt number (Nu) distributions on the tubes. The values of Nu depend on the flow Reynolds number Re and the tube spacing. Staggered arrangement of tubes give larger Nu and flow loss (pressure drop) than in-line arrangments. Because of the two dimensional modeling, these computations can not show the heat transfer to the fin and hence not useful for the fin-tube heat exchangers. Numerical simulations of three dimensional flows past a cylinder bank in a channel have not yet been reported. Mitra et al. (1986) reported prelimi-nary studies of the flow field and heat transfer in a rectangular channel with only one built-in cylinder. The results of one cylinder can not be extrapolated to a bank of cylinders since the effect of the interference of the tubes can not be deduced. The present work will concentrate its attention on this inter-ference and its effects on the flow field. Periodic boundary conditons at the inlet and exit are not used.

MATHEMATICAL FORMULATION

Computational Domain

The cross flow heat exchanger is modeled by a rectangular channel of lenght L and breadth B wit four tubes of diameter D in three staggered rows. see fig 2. The top and the bottom walls of the channel are the fins and the channel height (fin spacing) is H. The symmetry condition can be assumed at the midplane (z = H/2) as well as on the side walls. This model heat exchanger configuration represents the computational domain.

The geometrical parameters L1, S1 and B have been selscted from lierature and are typical in many applications. Their influence on heat transfer will be studied in future work. The large channel length in the wake of the last tube is selected in order to contain any passible back flow in the wake in the computational domain.

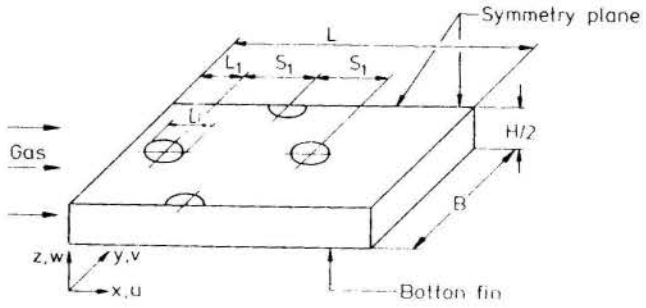

Fig. 2: Computational domain. For the present case: L/D = 12, L1/D = 2, S1/D = 2, H/D = 1, B/D = 3. Computation is performed in z-direction form z=0 to H/2

Flow model

Because of the geometrical copmplexity, folw field in the channel may contain separation bubbles, recirculating zones and vortex street in the wake of the tubes. Hence the flow should be described by complete nonsteady Navier-Stokes equations. The flow is assumed to be laminar since the characteristic Reynolds number, based on the channel height H or the tube diameter D, is often small (around 1000) in many practical applications. Furthermore, in order to reduce the computational effort, the flow medium is assumed to be incompressible with constant properties.

Governing equations

The governing equations can be written in cartesian coordinates for the flow in the channel and in cylindrical polar coordinates for the flow in the neighborhood of a tube. Alternatively, the flow can be described with bodyfitted coordinates.The computational scheme for the last alternative will require large computer memory. In the present work, the flow is described in overlapping cartesian and cylindrical polar coordinates (Launder and Massey, 1978). The basic equations only in cartesian coordinates in nondimensional form are given below

$$\frac{\partial u_i}{\partial x_i} = 0 \qquad (1)$$

$$\frac{\partial u_i}{\partial t} + \frac{\partial (u_i u_j)}{\partial x_i} + \frac{\partial p}{\partial x_i} = \frac{\nabla^2 u_i}{Re_H} \qquad (2)$$

$$\frac{\partial T}{\partial t} + \frac{\partial (u_i T)}{\partial x_i} = \frac{\nabla^2 T}{Re_H \, Pr} \qquad (3)$$

All length coordinates have been nondimensionalized with the channel height H. The velocity components u_i have been nondimensionalized with u_{av}, the average velocity at the inlet, the pressure with ρu^2_{av} and the temperature with the wall and the inlet temperature. The Reynolds number Re_H is $u_{av}\, H/\nu$ and Prandtl number Pr is ν/a. The other symbols have usual meanings. The dissipation terms in the energy equation have been neglected.

The boundary conditions are given below:

x = 0: u = parabolic in x-z plane, v = w = 0, T = 0

x = L/H: $\frac{\partial}{\partial x}$ (u, v, w, T) = 0

z = 0 : No-slip condition, T = 1

z= 1/2

y = $\pm \frac{B}{2H}$

} Symmetry condition

On the tube surface: u_i = 0, T = 1

COMPUTATIONAL SCHEME

The basic equations have been solved by SOLA algorithm, a modified version of the marker and cell (MAC) technique (Hirt et al.; 1975). To this purpose the computational domain is first discretized into grids in form of rectangular parallelopipeds. The cylinder is simulated by Cartesian grids. When a converged solution in these grids is obtained, a second step of computations with polar grids in the neighborhood of the tube followed.

The SOLA uses staggered grids i.e. the dependent variables are not defined at the same point. The pressure and the temperature are defined in the center of a cell, the velocity components on the midpoint of the cell faces on which they are normal. The computation proceeds in two steps. In the first step the momentum equation are solved explicitly from known velocity and pressure fields in order to obtain these field values ar the time $(t + \delta t)$. In the second step a pressure-velocity updating is performed in a way that corresponds to the solution of Poissen equation for pressure. This updating is continued until the continuity equation is locally satisfied on each cell. Then the solution for the next time step is performed. The procedure is continued until a steady or periodic solution is obtained. Since the momentum equations are uncoupled from the energy equation, the latter can be solved whenever required. The details of the computational scheme along with a flow chart is given by Hirt et al. (1975).

RESULTS AND DISCUSSION

Computational results have been obtained for Reynolds numbers Re_H of 40, 100, 200, 400, 800, 2000 in a heat exchanger with D/H = 1, L1/H = 2, S1/H = 2, B/H = 3 and L/H = 12, see fig. 2. The nondimensional length, breadth and height of the computational domain are 12 * 3 * 0.5. The number of grids that has been used for coputation in this domain is 96 * 36 * 8.

Figure 3 shows vector plots of the cartesian velocity components on the midplane (z = 1/2) of the channel for Re = 200, 800 and 2000. all the computations give steady flows. Hence any asymmetry in the velocity vectors in the wake of the tube is absent. A boundary layer separation, indicated by the vanishing radial gradient of the azimuthal velocity on the tube surface appears only close to the channel wall (z = 0.0625) on the first tube with the Re = 40. With Re = 200, the radial gradient of azimuthal velocity varishes on first tube surface an the angular locations of 130°, 138° and 141° at heights from the bottom fin of 0.0625, 0.25 and 0.5 respectively.

With the Re = 800 and 2000, the corresponding angles are 117° , 137° and 120°, 143°, at z = 0.0625 and 0.25 respectively. At midplane (z = 0.5), the flow remains attached to the tube. The symmetry conditions on the two side boundaries and the blockage due to the second row of tubes cause an increase in velocity in the wake of the first tube and hinder separation. In the wake of the tube of the third row, boundary layer separation appears at all Reynolds number and at all heights. The separation angles increase with the distance from the bottom fin,and are equal to 108°, 124° and 156° for Re = 800 and 108°, 126° and 160° for Re = 2000 at hights 0.0625, 0.25 and 0.5 respectively.

Figures 4a and 4b compare the Nusselt number distributions at the midplane of the tube in the first and last row. The Nusselt number Nu is definded with the difference of the inlet and the wall temperatuer, hence Nu is equal to the nondimensional temperature gradient on the tube. As expected, Nu is larger on the stagnation point of the first tube and is equal to 4.5, 14.5 and 18.5 for Re = 40, 200, and 400

respectively. Experiments in unbounded medium give Nu = 6 and 14 for Re = 40 and 200 (Zukauskas, 1987). Two dimensional computational results for Re = 200 presented in Zukauskas, 1987, agree quite well with the corresponding Nu distribution in fig. 4a. On the third tube, the Nu distributions are even quantitatively different from that on the first tube for Re $\geq$ 40. The wake of the first tube reduces the velocity of the fluid particles coming to stagnation point of the third tube and thereby reduces the Nu at the stagnation point. The blockage due to the second column of the tubes increases the azimuthal velocity at the angular location of approximately 50° in the neighborhood of third tube. Here Nu reaches the peak values.

Figures 5a and 5b compare Nu on the first and third tubes at a height of z = 0.0625. Qualitatively, the Nu distributions in figs 4a and 5a are similar. The quantitative reduction (nearly 80% at Re = 40)is due to the smaller velocities close to the fin. At low Re the heat transfer characteristic worsens more for the third tube than for the first. The sharp drop to a minimum in Nu at heigh Re in figs. 4 and 5 corresponds to the boundray layer separation.

The Nu contoures on the plate for Re = 800 and 2000 are shown on figs. 6a. One notices large Nu (isolines 7-8) due to the formation of the horse shoe vortex in front of the first tube. The second row of the tubes reduces the area with low Nu in the wake of the first tube. The heat transfer deterioration in the wake of the first cylinder covers a much larger area (isoline 1) for Re = 800 than for Re = 2000. Because of the reduction of the velocity, Nu in the stagnation point of the third tube is smaller than the corresponding Nu for the first tube. However, the bockage due to the second row of tubes enhances Nu near the third tube at angular locations between 20° to 90° for Re = 2000.

Fig. 7 compares the distributions of the spanwise average Nusselt numbers Nu(x) on the fin for Reynolds numbers of 40, 200, 800, 2000. Nu here is defined with the difference of the bulk temperature and the wall temperature. Hence far downsteam (x = 12) Nu tends to be constant. Up to x = 1, Nu goes down as typical of a thermally developing flow, then it reaches a peak in front of the first tube because of the horse shoe vortex. A second smaller peak appears due to the blockage. Nu falls down in the space between the first and the second rows of tubes. This distribution of Nu is qualitatively repeated farther downsteam. The peak values of Nu in the stagnation points of consecutive rows diminish. The peak value of Nu in front of the first tube is 26. The corresponding value in front of the third tube is only 18.

CONCLUSION

The present work shows that the Nusselt numbers on the tubes near the juncture of fin in a fin-tube compact heat exchanger can be much smaller (by 80% at Re = 40) than the Nusselt number predicted by the two dimesoinal flows. The Nusselt numbers on the fin can widely vary depending on the Reynolds number. At Re = 2000, the local Nusselt number on the fin at the stagnation zone of the tube can become nine times larger than that in the wake. Present investigations show where the modification of the fin surface or the positioning of turbulators should be useful.

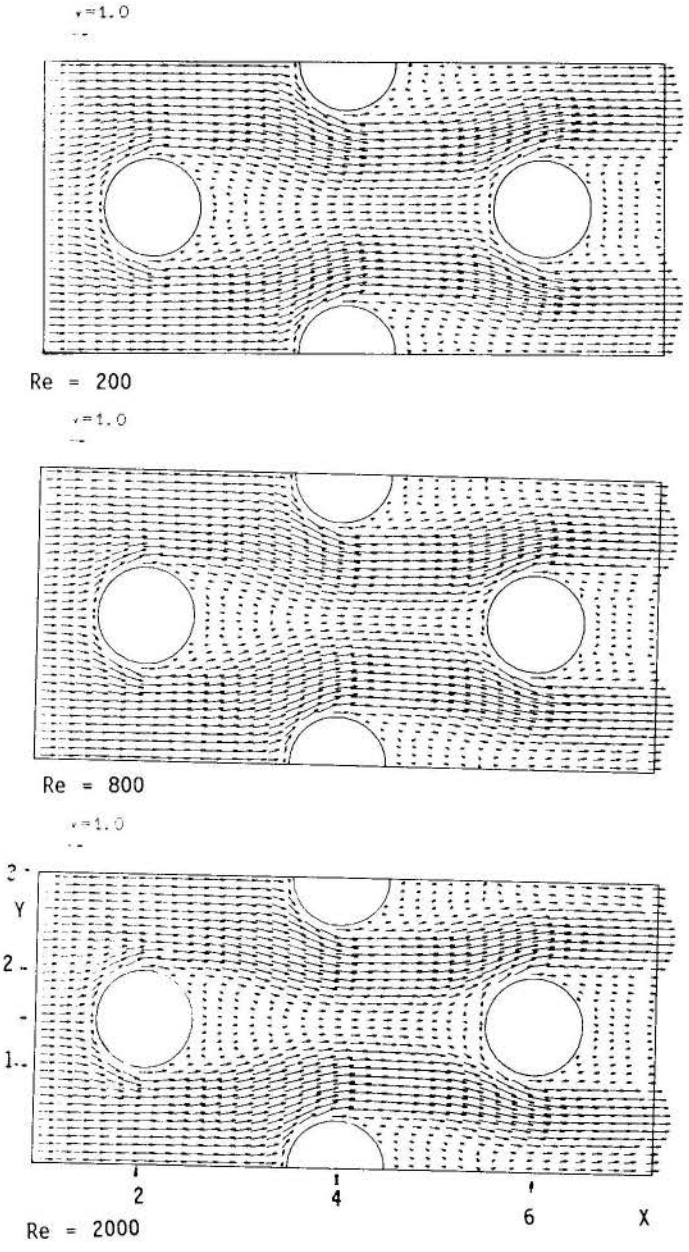

Fig.3 Velocity vectors at the midplane (z = 1/2) for Re = 200, 800, and 2000.The flow field in the wake is steady. No vortex street is observed.

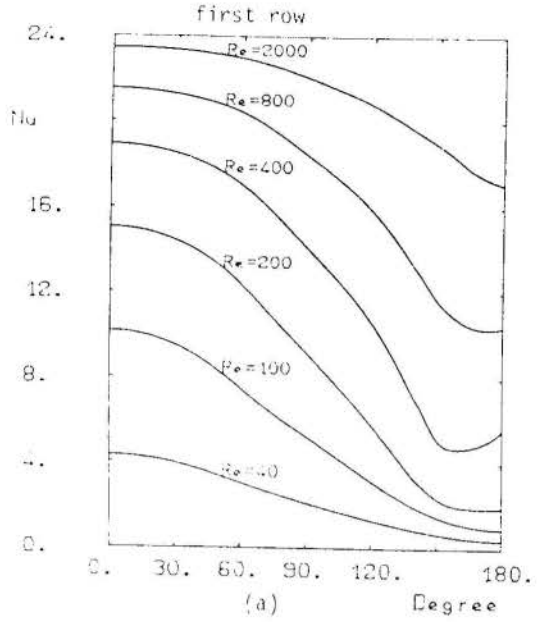

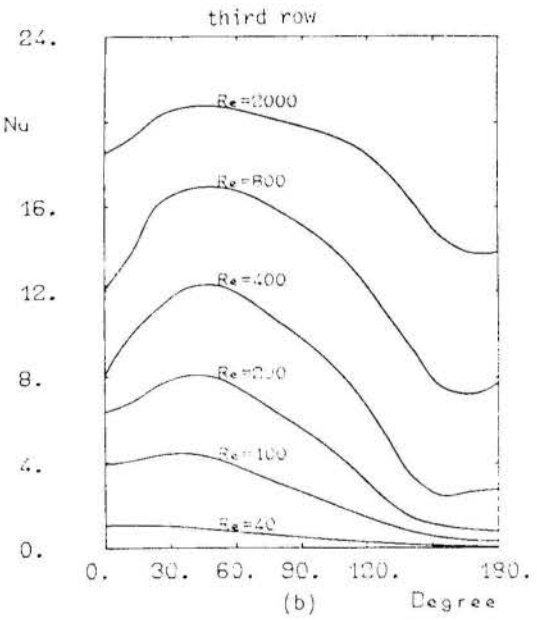

Fig.4 Nusselt number distributions on the (a) first and the(b) third tubes at z = 1/2 for different Re.

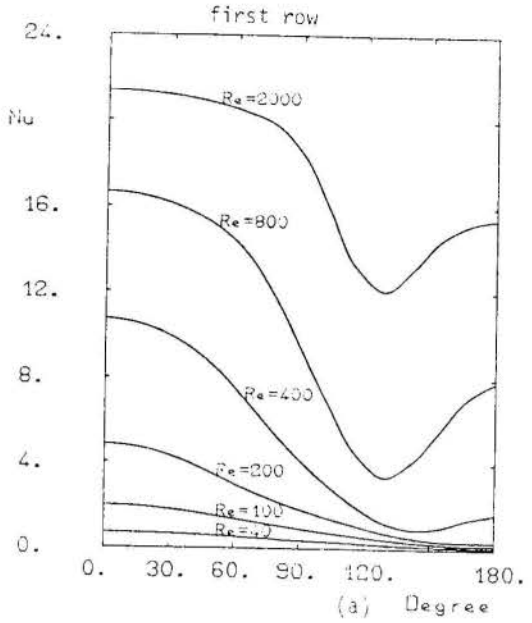

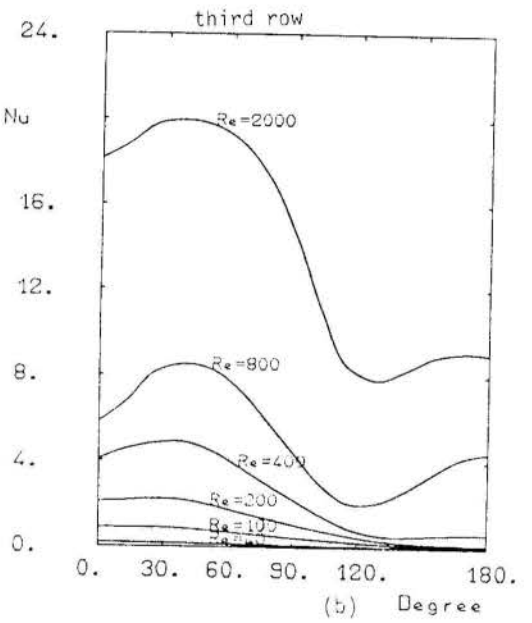

Fig.5 Nusselt number distributions on the (a) first and the(b) third tubes at z = 0.0625 for different Re.

Contuour	1	2	3	4	5	6
Nu	4.	5.6	6.5	9.5	14.0	24.

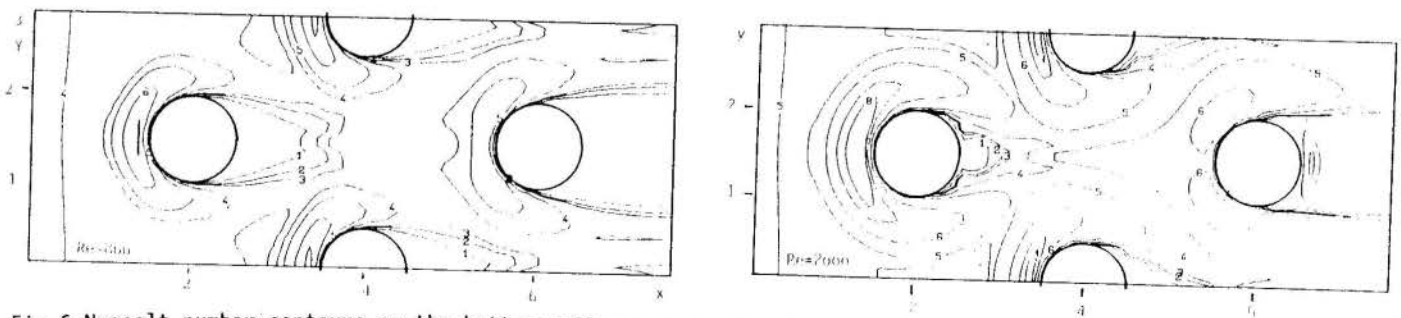

Fig.6 Nusselt number contours on the bottom wall (fin) for (a) Re = 800 and (b) Re = 2000.

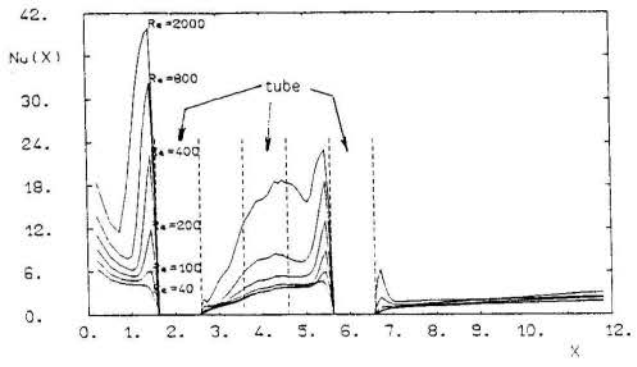

Fig.7 Spanwise average Nusselt number on the fin for different Re. Nu here is defined with the difference of the bulk temperature and the wall temperature.

REFERENCES

* Chen, C.j. and Chen, H.C., 1984 "Development of Finite Analytic Numerical Methods for unsteady Two Dimensional Navier-Stokes Equations". *journal of Computational Physis, vol.53,pp. 209-226*
* Fujii, M., Fujii, T. and Nagata, T., 1984, "A Numerical Analysis of Laminar Flow and Heat Transfer of Air in an In-Line Tube Bank", *Numerical Heat Tr nsfer, vol. 7,pp. 89-110*
* Hirt, C.W., Nichols, B.D. and Romero,N.C.,1975, "SOLA A Numerical Solution Algorithm for Transiet Fluid Flows", *Los Alamos Scientific Laboratory Rep. LA-5652.*
* Le Feuvre, R.F., 1973,"Laminar and turbulent Forced Convection Processes through In-Line Tube Banks,"HTS/74/5, *mechanical Eng. Dept., Imperial College, London.*
* Mitra, N.K., Kiehm P. and Fiebig, M., 1986, "Numerical Investigation of Heat Transfer in Flows in Two- and Three-Dimensional Channels with Built-in Cylinder", AIAA-86-1329, AIAA/ASME *4th Thermo-physics and heat Transfer Conference, Boston, Mass.*
* Wung, T.S. and Chen, C.J., 1989, "Finite Analytic Solution of Convective heat Transfer for Tube Arrays in Cross Flow, Part I -Flow Field analysis Part II - Heat Transfer Analysis", ASME *journal of Heat Transfer, vol. 111, pp 633-648*
* Zukauskas, A., 1987, "Heat Transfer from Tubes in Cross Flow",*Advances in Heat Transfer, Chapter 2; Hartnett, J.P. et al., ed., Academic Press, New York, vol. 18, pp. 87-157.*

III ENCIT – Itapema, SC (Dezembro 1990)

HEAT TRANSFER AND FLOW CHARACTERISTICS OF TWO-DIMENSIONAL JETS IMPINGING ON HEATED PROTRUSIONS WITH CROSSFLOW OF THE SPENT AIR

G.L. Whidden, J. Stevens, and B.W. Webb
Heat Transfer Laboratory
Department of Mechanical Engineering
Brigham Young University
Provo, UT 84602

SUMMARY

The flow structure and local heat transfer characteristics of two-dimensional slot jets impinging on heated protrusions has been investigated. The spent air was constrained to exit at one end of the channel, forming a crossflow. The effects of three parameters on the heat transfer were examined for an array of five protruding heat sources. They include the jet slot width, distance between the jet exit and the protrusion, and the average jet Reynolds number. Laser-Doppler velocimeter measurements were made to detail the mean and turbulent flow structure in the channel.

NOMENCLATURE

b	protrusion height, Fig. 1
h	heat transfer coefficient
H	height of the channel, b+z
k	thermal conductivity (W/mK)
L	streamwise length of, and spacing between each protrusion,
Nu	local Nusselt number, $Nu = q_{conv}L/k(T_s - T_j)$
$\overline{Nu}$	average Nusselt number for a protrusion, $q_{conv}L/(\overline{T_s} - T_j)$
Q_{tot}	total volume flow rate through all jets
q_{conv}	protrusion convective heat flux
q_{Ohm}	protrusion heat flux due to Ohmic dissipation
Re	average jet Reynolds number, $\rho \bar{V}_j w/\mu$
s	spanwise depth of the flow channel
T_j	fluid inlet temperature of the jets
T_s	surface temperature of the protrusion
u	local crossflow mean velocity
u'	local RMS of the streamwise turbulent fluctuation
U	local channel mean velocity
V_j	average jet velocity, $Q_{tot}/5sw$
w	width of slot jet, Fig. 1
x	streamwise distance in channel beginning at leading edge of protrusion 1, Fig. 1
y	coordinate direction normal to channel floor
z	distance from jet to protrusion, Fig. 1
μ	dynamic viscosity
ρ	density

INTRODUCTION

Impinging jets have long been recognized for their superior transport characteristics. Much of the gas jet impingement heat transfer research has been motivated by the need for enhanced cooling of gas turbine blades. Recently, impinging jets have found application in the electronics industry. Increasing miniaturization of electronic components and resultant rise in heat flux at the chip level has spawned research aimed at improved understanding of the fundamentals of heat transfer in discrete heating situations. Cooling methodologies are sought which feature decreasing pressure drop and increasing heat transfer coefficient. In applications where channel flow alone is inadequate, impinging jets provide a viable method of increasing the heat transfer coefficient. This study has as objective the characterization of heat transfer from a two-dimensional array of heated protrusions cooled by planar air jets with crossflow of the spent fluid. Such a configuration has been proposed for use in the electronics industry.

A significant body of literature dealing with jet impingement heat transfer exists, and recent reviews are available (Downs and James, 1987). Impinging jet heat transfer with crossflow of the spent fluid is not as well understood. This problem has been studied primarily with high velocity jets aimed at smooth surfaces under a variety of geometric jet configurations (Metzger *et al.*, 1979; Florschuetz *et al.*, 1980; Florschuetz *et al.*, 1981; Florschuetz *et al.*, 1984; Florschuetz and Su, 1987).

Only recently have studies treating heat transfer characteristics of air jets impinging on arrays of heated protrusions appeared in the literature. Hamadah (1989) examined heat transfer characteristics of arrays of circular air jets impinging on an array of blocks mounted on a flat surface. It was determined that impingement heat transfer coefficients are 60 - 80% higher than those of the channel flow for the same mass flow rate, but the heat transfer coefficients are identical for the same pumping power. Hollworth and Durbin (1989) investigated arrays of round air jets impinging on a uniform array of rectangular elements. The spent air formed a crossflow that was constrained to exit at one end of the channel. Heat transfer coefficients for various protrusions in the array were reported along with the system pressure drop. Heat transfer was found to be highest for protrusions at the end of the channel. Additionally, the highest pressure drop was found to occur across the orifices.

The review of literature presented in the foregoing paragraphs reveals very little research dealing with impingement heat transfer with crossflow, with virtually no study of two-dimensional jets. Additionally, investigations of the flow structure has gone unaddressed. This paper reports on a study designed to investigate the mechanisms of flow and heat transfer in such a system. In particular, the effects of jet Reynolds number, jet width, and spacing between the jet and heated protrusion are studied.

EXPERIMENTAL APPARATUS

A channel and heater assembly were designed and constructed to permit velocity and heat transfer measurements over a broad range of experimental parameters. As shown in Fig. 1, the apparatus consisted generally of a channel containing five heated protrusions, a jet plate, plenum, centrifugal blower, and instrumentation and metering equipment. The regenerative blower was operated in suction mode to draw air into the plenum, past the flow-straightening screens, through the five planar nozzles and into the channel. The spent air formed a crossflow which was constrained to exit at one end of the two-dimensional channel. Flow meters were placed between the channel and the blower to monitor the total mass flow in the system.

The plenum was constructed of plywood, forming a large cross-sectional-area duct. Ambient air was drawn into the plenum, through the screens, and subsequently through the jet plate. The purpose of the screens was to establish as nearly uniform flow as possible, and to isolate the channel flow from disturbances in the ambient conditions.

Jet plates were fabricated from 19.5 mm thick Plexiglass plate, and were attached to one end of the the plenum. The jet plate also acted as one wall of the channel. Five slots were milled into the Plexiglass on 25.4 mm centers spanning the full width of the channel, forming the jets. The jets were contoured with a smooth contraction as shown in Fig. 1 by milling the slot from an initial width of 2w at the inlet to the nozzle width w halfway through the thickness of the plate, at a 45° angle. The jets were positioned so that impingement occurred perpendicular to the surface at the exact center of each

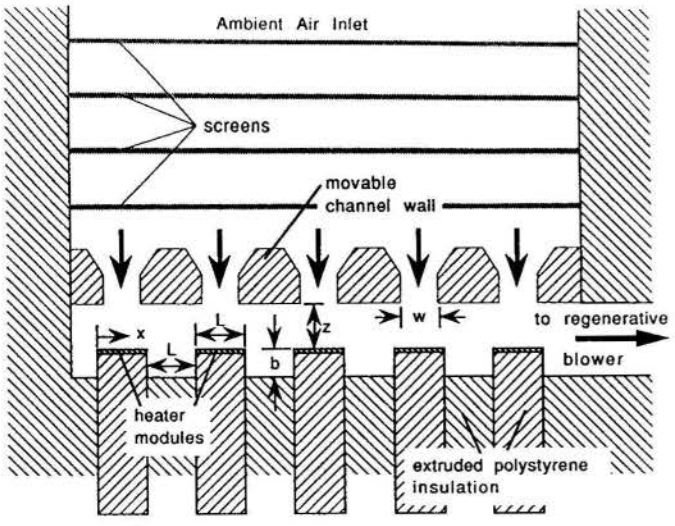

Fig. 1. Schematic of experimental apparatus.

protrusion. Two sets of jet plates were fabricated permitting the study of two jet widths, w = 6.35 and 12.7 mm.

The channel contained five protrusions which spanned the full channel width, s = 24.4 cm. Each protrusion consisted of a strip of stainless steel foil 0.0254 mm thick, epoxied to a section of phenolic fiberboard of the same length and width. The fiberboard and stainless steel strip were then epoxied to a similar section of Styrofoam which formed the bulk of the protrusion. Five identical such heater assemblies were inserted into slots in a section of 3.81 cm thick Styrofoam which formed the remainder of the thermally active wall. The heater protrusion into the channel was held fixed in this study at b = 6.35 mm. Additionally, the heated protrusion width and spacing were constant at L = 12.7 mm.

The metallic foil was heated by passing direct current from a DC power supply with voltage and current stable to 0.01%. Each of the five heater foils was sandwiched between large aluminum busbars running the length of the channel. The Ohmic dissipation in each of the five heaters was determined from the voltage-current product measured at the heated surface. The total current was displayed by the power supply to 0.01 A, while the voltage drop was measured with voltage taps attached to the foil heaters. The Ohmic dissipation was thus measured to an estimated accuracy of 2%, and was found to be the same in each of the five heaters to within 3%.

The local temperature was measured at five equally-spaced locations along each protrusion, as shown in Fig. 2(a). Copper-constantan thermocouples made of 0.0127 cm diameter wire were epoxied in holes drilled in the phenolic substrate with the beads against the underside of the metallic foil. One thermocouple was placed at the leading and trailing edges of the heater, one in the center, and the remaining two were placed between the center and each edge. All thermocouple arrays were in the spanwise center of the channel, as illustrated in Fig. 2(b). Thermocouple leads were passed through holes drilled into the Styrofoam. The ambient air temperature was measured with a single thermocouple in the plenum upstream of the flow straightening screens. Thermocouple voltages were read to 1 μV. Raw temperature data were recorded with an HP 3497A data acquisition system for later data reduction.

As explained previously, air was drawn through the plenum by a regenerative blower placed downstream of the channel. Rotameter type air flow meters with calibrated accuracy of 5% were placed just upstream of the blower, enabling the total air flow rate to be measured. Three flow meters of different measurement ranges were connected in a parallel flow circuit.

The walls at the spanwise extremities of the channel were fabricated of Plexiglass to permit optical access. A laser-Doppler velocimeter (LDV) system was used to obtain local mean velocities and RMS turbulent fluctuations of the component aligned parallel to the channel (crossflow velocity component). A TSI Model 1980B LDV system, coupled with a 5W Spectra-Physics Model 2016 Argon ion laser were used. The flow was seeded with a Fairchild six-jet atomizer with manufacturer-reported mean droplet size of just under 1 μm. Frequency shifting was used to enable detection of flow reversals.

The Reynolds number characterizing each flow experiment was based on the average jet velocity and jet width:

$$Re = \rho \bar{V}_j w/\mu \qquad (1)$$

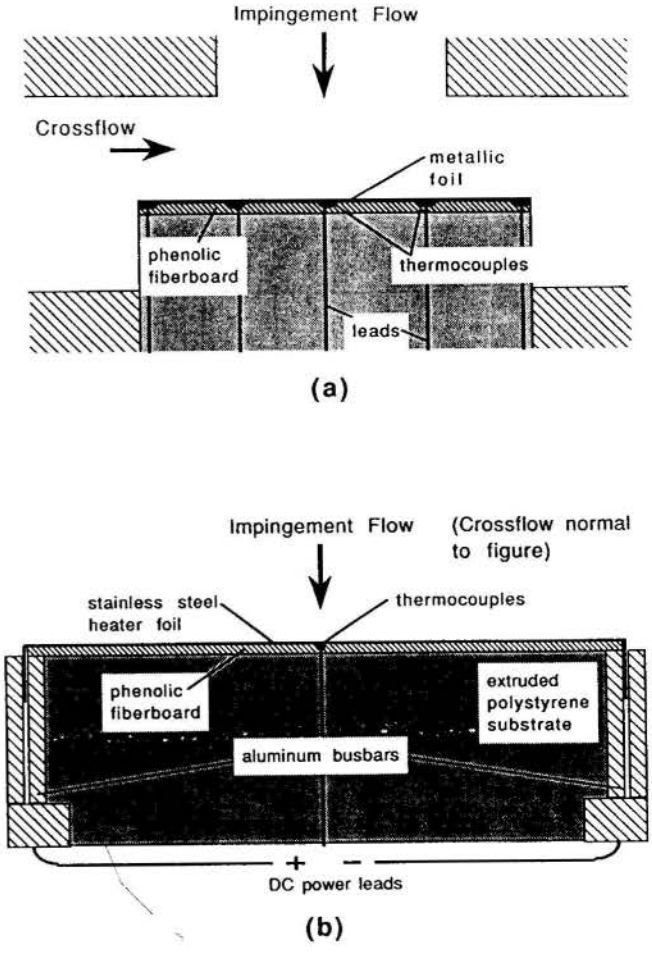

Fig. 2. Detail of the heater modules, a) cross-section at the horizontal midplane of the channel, b) spanwise cross-section of heater module.

The average jet velocity was determined from the total air flow rate measured at the flow meters, $\bar{V}_j = Q_{tot}/5sw$. Since it will be shown subsequently that the mass flow through each of the five jets was different, this Reynolds number thus represents the average Reynolds number for each of the five jets. The radiative heat flux dissipated from each protrusion was determined using a gray-surface enclosure analysis with the measured temperatures and surface emissivities taken from the literature (Incropera and DeWitt, 1990). The maximum radiation loss was less than 6% of the Ohmic heat flux in all experiments (Whidden, 1990). The local Nusselt number, defined as

$$Nu = q_{conv}L/k(T_s - T_j) \qquad (2)$$

was based on the protrusion length L as the characteristic length. The average Nusselt number was based appropriately on the average temperature difference for the isoflux heating surfaces, and was determined by integrating the local temperature data

$$\overline{Nu} = q_{conv}L/k(\overline{T_s - T_j}) \qquad (3)$$

In practice, the discrete temperature data were weighted by an appropriate heater surface area element in performing the surface temperature integration.

Not all energy generated Ohmically in the metallic foil was convected away from the top surface of the protrusions. Some of the energy was redistributed through the underlying substrate. In order to quantify the magnitude of the losses, a two-dimensional analysis of conduction in the heater module was performed. The differential equation governing conduction in the composite heater module was solved numerically. The analysis revealed that the maximum total energy loss through the sides of the heater protrusions was less than 10% of the total Ohmic dissipation in the heater foil for all experiments. However, the fraction of the Ohmic flux that enters the convective air locally along the exposed surface of the foil was predicted to fall rapidly in a small region near the edges, with values as low as 70% there. Details of the conjugate heat transfer analysis may be

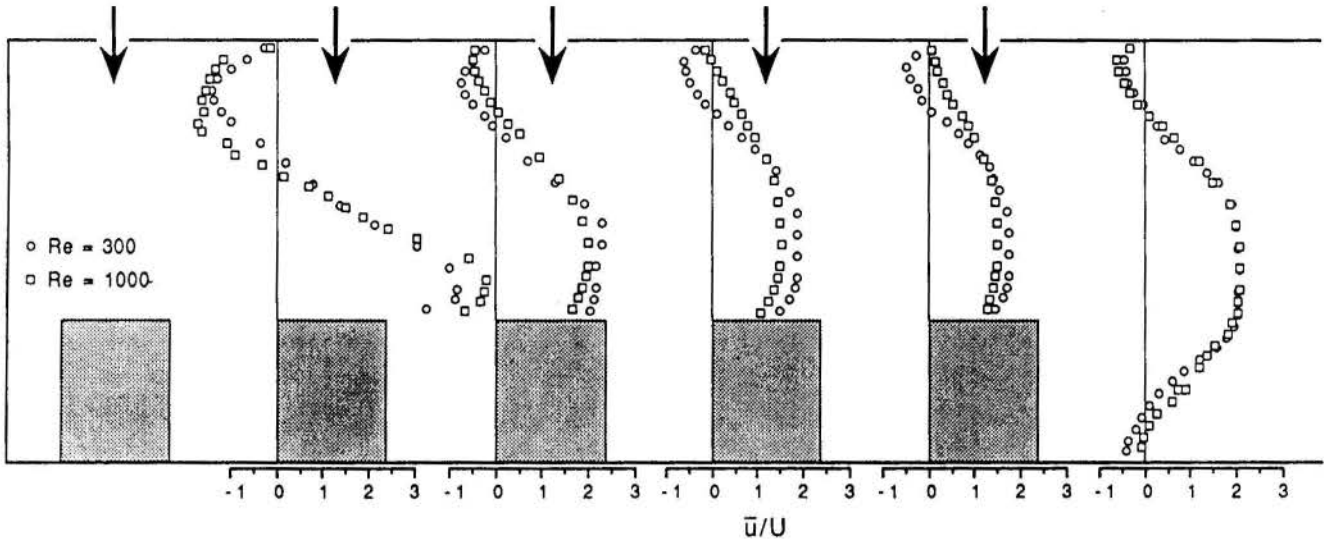

Fig. 3. Profiles of the normalized mean crossflow velocity at various channel locations for Re = 300 and 1000, z/w = 2.0, w = 6.35 mm.

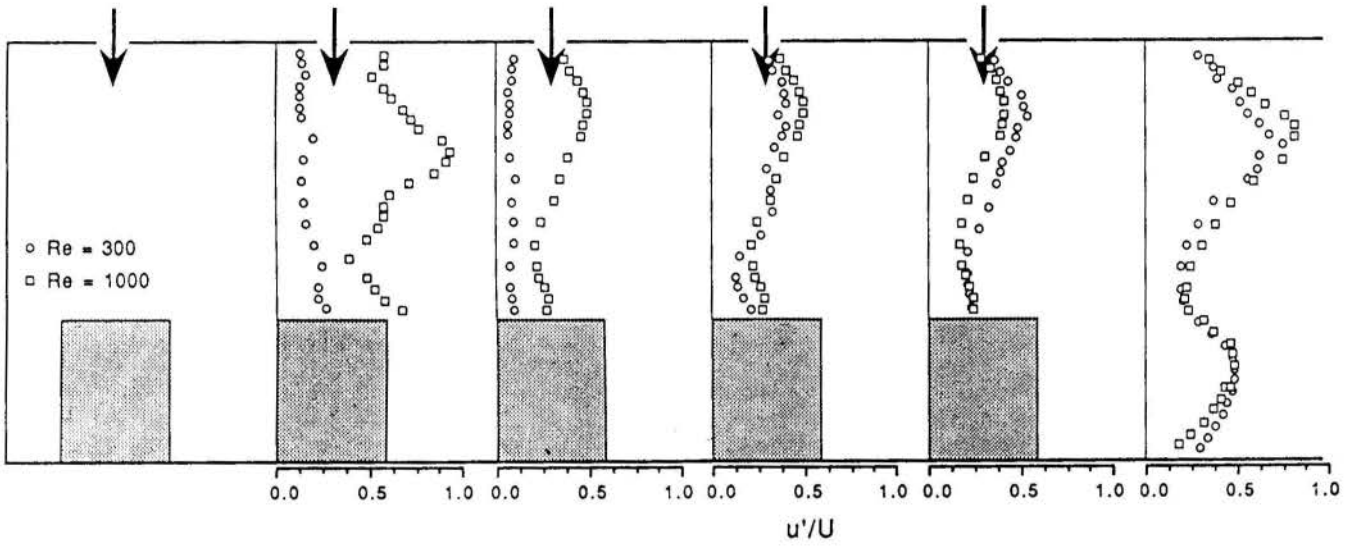

Fig. 4. Profiles of the normalized crossflow RMS velocity fluctuation at various channel locations for Re = 300 and 1000, z/w = 2.0, w = 6.35 mm.

found elsewhere (Whidden, 1990).

An analysis using the method of Kline and McClintock (1953) was performed to quantify the potential error in the experimental data. The uncertainty in Nusselt number was found to be dominated by the uncertainty in the convective heat flux, due to the conjugate effects in the substrate. Hence, the local heat transfer data should be viewed with some caution particularly near the edges due to the high uncertainty in q_{conv} there. However, the average Nusselt numbers are valid to within 12%. The uncertainty in Reynolds number was found to be 7%.

EXPERIMENTAL RESULTS

As stated previously, the parameters investigated in the heat transfer study were the jet Reynolds number, nozzle-to-heater spacing, and the nozzle width. The average jet Reynolds number was varied in the range $200 \leq Re \leq 1200$ and the jet-to-heater spacings studied were in the range $3.2 \leq z \leq 12.7$ mm. Both jet widths (w = 6.35 and 12.7 mm) were investigated for these parameters. In addition, the flow structure was characterized for a more restricted set of the geometric and flow parameters. Laser-Doppler velocimeter measurements were made for Re = 300 and 1000, z/w = 2.0, w = 6.35 mm, and for Re = 300, z/w = 0.5, w = 12.7 mm. The parameters for the convective heat transfer from the protrusions were characterized in non-dimensional form by the local and average Nusselt number and the channel Reynolds number. The streamwise length of the protrusion was chosen as the characteristic length in the local and average Nusselt number, while the jet width was used in defining the Reynolds number. The nozzle-to-protrusion spacing was normalized as z/w. Note then, that a change in z also changed the channel height, H. This will become significant in the composite correlation for the average Nusselt number to be presented. The experimental results will be presented first as a discussion of the flow structure drawn from the LDV measurements. The heat transfer from the protrusions will then be presented and discussed.

Flow Structure

Figure 3 illustrates profiles of the crossflow velocity component (parallel to the channel axis) normalized by the local channel average velocity, $\bar{u}/U$, for Re = 300 and 1000, z/w = 2.0 for the smaller nozzle width, w = 6.35 mm. The profiles were measured at the leading edge of the last four protrusions with a final profile located one repeating module (protrusion length plus protrusion spacing) downstream of heater five as seen on the superimposed channel schematic shown in the figure. The local mean velocity profiles, $\bar{u}(y)$, at each channel axial location were integrated to determine the local channel average velocity, U. All profiles were measured at the spanwise center of the channel. The velocity scale for each profile is shown with the zero-velocity reference located at the channel measurement location. Additionally, the respective heater locations and channel axial dimensions are drawn to scale. The airflow enters the channel through each of the five jets and impinges on the five protrusions. The spent air forms a channel crossflow that is constrained to exit to the right in the figure. The first (leftmost) protrusion experiences virtually no crossflow effects, while the fifth (rightmost) protrusion experiences crossflow comprised of the full cumulative mass flow through the first four jets. Figure 3 illustrates a hydrody-

namic development region near the first protrusion module for both Reynolds numbers studied. The crossflow velocities are observed to be as high as four times the local channel average velocity at the leading edge of the second heater. The crossflow that exists above heaters 2 through 5 is confined to a zone roughly half the effective channel area, z/2, as seen by the high velocities in the region just above each protrusion. The crossflow velocities are seen to be nearly twice the local channel average in this region for both Reynolds numbers.

Figure 3 reveals that there is very little change in the normalized velocity profiles, $\bar{u}/U$, between locations at the final three protrusions. It may be suggested that the profiles are nearly periodically fully-developed, with only one or two repeating modules of length required to achieve this fully-developed condition. Recirculation zones are found next to the nozzle plate immediately downstream of each jet at nearly all measurement locations. Velocities in these zones of reverse flow approach $\bar{u}/U \approx 1.5$ for both Reynolds numbers. The zones of recirculating flow are caused by the interaction of the jet flow and the crossflow in the channel. As the jet enters the channel it is deflected downstream. The deflection causes a general counter-clockwise rotation of the fluid downstream of each jet and adjacent to the jet plate, resulting in the recirculation zone there. The reverse flow is less pronounced for Re = 1000, and effectively vanishes between the third and fifth protrusion. This may be due to the increased strength of the crossflow in the channel at the higher Reynolds number, damping the fluid rotation. A recirculation zone in the region near the jet plate, away from the protrusion, may influence heat transfer at the protrusion only as it promotes the general level of turbulence in the flow. This will be illustrated in the RMS velocity data to follow.

The turbulence intensity corresponding to the mean velocity measurements of Fig. 3 are shown in Fig. 4. This turbulence intensity is defined as the ratio of the RMS fluctuation about the local mean velocity, to the local channel average at that channel axial location, u'/U. Again, the channel axis and relative protrusion dimensions are drawn to scale, with the normalized RMS velocity scale being shown below each u'/U profile. Figure 4 shows that the turbulence intensity for the Re = 300 data ranges from approximately 15% in the center of the channel to a maximum of 80% in the recirculation zone adjacent to the nozzle plate downstream of the last protrusion. The mean level of turbulence intensity is roughly 20%. By contrast, the level of turbulence for the Re = 1000 data ranges from 20% near the channel center to nearly 100% near the recirculation zones with a mean value of about 40%. The turbulence intensity profiles of Fig. 4 reveal more clearly a development length of two or three repeating modules before a nearly fully-developed condition is reached; there is very little change in the u'/U profiles between the fourth and fifth protrusions for a given Reynolds number. Additionally, the u'/U profiles are nearly the same at the fourth and fifth heaters for the Re = 300 and Re = 1000 data.

It is interesting to note that even for such low average jet Reynolds numbers, turbulent fluid motion is seen to prevail. A local channel Reynolds number based on the effective channel flow area, z, may be calculated as $Re_z = NRe(z/w)$, where N is the number of jets upstream of the location where Re_z is to be determined. Note that this definition still assumes equal distribution of the total flow rate between all five jets. As will be quantified later, the flow rate is in reality nonuniform, with most of the mass flow rate entering the channel through the downstream nozzles. For the Re = 300 data seen in Fig. 4, the local channel Reynolds number lies in the laminar channel flow range ($Re_z \leq 1000$) well past the second jet. It may be suggested that the interaction between jet flow and crossflow, coupled with the presence of the protruding heaters, causes early transition to turbulent flow as evidenced by the high turbulence intensity observed in Fig. 4. It is primarily the locations of the jet flow/crossflow interaction where the turbulence intensity is the highest. The strong turbulent motion is a more effective transport mechanism than its laminar flow counterpart. This will be demonstrated by a comparison of the experimental local Nusselt number data with laminar flow predictions in a section to follow. Regions of high turbulence also occur near the surfaces of the heated protrusions.

A pressure gradient exists inside the channel with the highest pressure located at the closed end, and the lowest pressure at the open end. The pressure inside the plenum is constant, resulting in a nonuniform distribution of airflow through the five nozzles. As a result, the fifth jet was seen to have the highest flow rate, and the first nozzle the lowest. This is consistent with previous impingement studies involving crossflow (Hamadah, 1989; Hollworth and Durbin, 1989). The local mean velocity profiles were integrated across the channel in order to determine the flow rate through each jet. This is expressed as a cumulative percentage of the total volumetric flow rate in Fig. 5. The figure illustrates the cumulative flow fraction immediately downstream of each jet. For example, it may be observed that for Re = 300, z/w = 2.0, the percentage of total flow entering the channel through jets one through five (determined from the difference in successive values of Q/Q_{tot}) was 7, 9, 14, 19, and 52%, respectively. If the flow rate were uniformly distributed between jets the Q/Q_{tot} profile would be a straight line between 0.2 at jet 1 and 1.0 at jet 5, as illustrated in the figure. Hence, the nonuniformity of the flow rate distribution among the jets may be gaged by the degree of nonlinearity of the Q/Q_{tot} profile. The nonuniform distribution of mass flow rate is more severe for the planar, relatively low velocity jets studied here than the higher velocity jets studied previously (Hamadah, 1989; Hollworth and Durbin, 1989). The data show that almost 80% of the total flow rate may enter the last nozzle (for the Re = 300, z/w = 0.5 configuration). The difference in nonuniformity of flow distribution among jets is seen to be only moderate for increasing Reynolds numbers at a given nozzle size, as seen by a comparison of the Re = 300 and 1000 data for z/w = 2.0, w = 6.35 mm. By contrast, the large jet widths with small nozzle-to-protrusion spacing result in significantly more nonuniformity than the smaller jet widths, seen by comparing the Re = 300 data. The higher constriction of the channel flow for decreasing z/w undoubtedly results in more severe maldistribution of the mass flow rate in the jets.

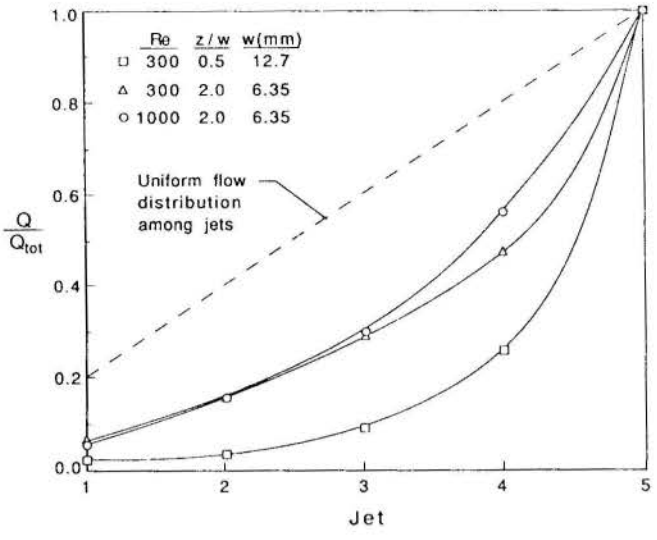

Fig. 5. Cumulative fraction of volume flow rate through the five planar jets for the flow and geometric configurations shown.

Heat Transfer

The experimentally-determined local Nusselt number along each of the five heater surfaces is shown in Fig. 6 for the Re = 300, z/w = 2.0, w = 6.35 configuration. The figure also illustrates the results of a laminar flow and heat transfer prediction for the same flow rate and geometric configuration. The coupled partial differential equations governing conservation of mass, momentum, and energy were solved with a finite difference technique using a 30 x 99 grid. The SIMPLER algorithm was employed to treat the coupling between momentum and continuity (Patankar, 1980). The experimentally-measured mass flow rate was imposed at each jet exit, thus accounting for the nonuniformity in total flow distribution among nozzles observed in Fig. 5. Two sets of predictions are shown, with and without conjugate effects included in the heater assemblies. The simulation including conjugate effects accounts for the composite, finite-conductivity nature of the metallic foil/phenolic board/Styrofoam heater assembly. Details of the simulation and solution methodology may be found elsewhere (Whidden, 1990). While it should be remembered that the experimental Nusselt number data at the edges of the heaters are subject to considerable uncertainty, definite trends are evident. The local heat transfer data indicate that the Nusselt number profile is cup-shaped with a minimum in the center of the heated surface. The shape of the local heat transfer coefficient profiles agree qualitatively with the laminar flow predictions. This unusual cup-shaped local heat transfer behavior is believed due to the complex interaction between impinging flow and crossflow. The initial decrease in Nu seen for the second and subsequent heaters is a result of the formation of a thermal boundary layer from the crossflow in the channel. The rise in Nu toward the trailing edge of the heaters arises due to the injection of the impinging jet, which has the effect of thinning the thermal boundary layer with the associated increase in heat transfer coefficient there.

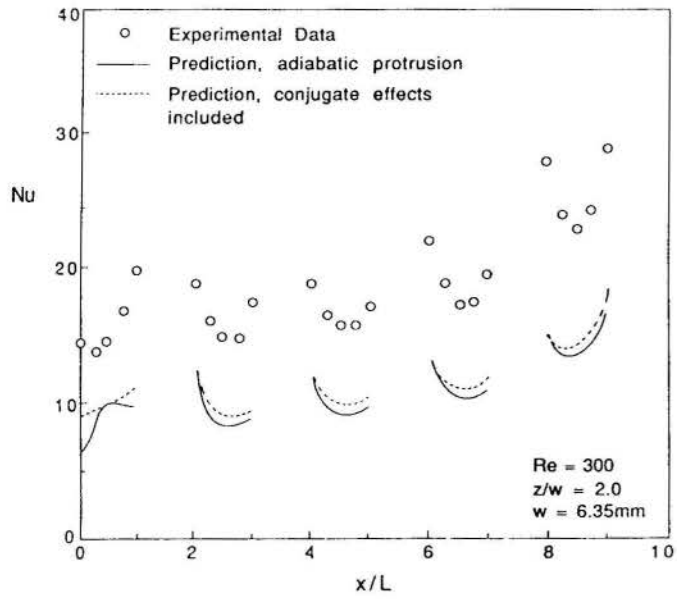

Fig. 6. Experimentally-determined and laminar flow predictions for the local Nusselt number along each of the five heater surfaces for Re = 300, z/w = 2.0, w = 6.35.

The cup-shaped local Nusselt number profile is radically different from that found for impinging planar jets without crossflow, where the maximum local heat transfer coefficient occurs at the stagnation point (Gardon and Akfirat, 1966). A maximum in the local heat transfer near the stagnation centerline of the jet is seen only for the first protrusion without conjugate effects. It may be seen that the laminar flow predictions are consistently 50 - 100% below the experimental data. As expected, the analysis including conjugate effects predicts local Nusselt numbers higher than the adiabatic substrate predictions. However, the difference in the adiabatic and conjugate substrate predictions is only slight, and is unable to explain the large discrepancy between prediction and experimental data. It can only be concluded that, despite the low Reynolds number characterizing the experimental data, the flow and transport are predominantly turbulent. This was corroborated by the local RMS velocity data of Fig. 4, where u'/U average values were roughly 20% for the Re = 300 data. Despite the obvious inadequacy of the laminar flow model, the predicted mean velocity profiles agreed quite well with the experimental LDV velocity data; the general recirculating flow and impinging flow/crossflow interaction was captured in the laminar flow analysis (Whidden, 1990).

The dependence of the average Nusselt number on nozzle-to-protrusion spacing, z/w, is illustrated in Fig. 7 for the first, third, and fifth heaters. The data are shown for both nozzle widths, w = 6.35 and 12.7 mm, and for two Reynolds numbers, Re = 400 and 1000. It may be observed that the large nozzle width shows a generally decreasing trend with z/w for both Re = 400 and 1000 at all heaters. On the other hand, the average Nusselt number for the small nozzle width increases with z/w for heater 1, tends to a local maximum for heater 3, and decreases with z/w for heater 5. This is observed for both Reynolds numbers shown. To explain the average Nusselt number behavior it must be remembered that there are two basic flow mechanisms contributing to the heat transfer from each of the protrusions. These two mechanisms are crossflow and impingement flow. The average Nusselt number behavior may then be explained in terms of these two mechanisms for the two nozzle widths studied. For a given Reynolds number the total flow rate is constant for both nozzle widths, but the average velocity through the small jets is double that in the larger jets. The larger jets thus yield less intense jet impingement flow and heat transfer. An increase in z/w causes an associated increase in the channel cross-sectional area, with a resultant decrease in the crossflow velocity. Hence, in the large jet configuration, where the impingement flow is relatively weak, the average Nusselt number is expected to drop for increasing z/w due to the reduced intensity of the primary transport mechanism, the channel crossflow heat transfer.

For the small jets, the jet impingement flow influences the heat transfer more significantly due to the higher jet velocities. When z/w is large, the crossflow velocity is at a minimum due to the large cross-sectional area of the channel. Hence, at large z/w the higher velocity and momentum of the small jets allows greater penetration through the weakened crossflow to the heated surface. Since jet impingement heat transfer is generally more effective than channel flow, the resulting higher values of average Nusselt number for large z/w are seen. Additionally, it is expected that the effects will be more pronounced for higher Re, which is the case in Fig. 7. By contrast, when z/w is small the channel cross-sectional area is considerably less, increasing the crossflow velocity. The jet impingement flow momentum is now smaller relative to the crossflow, and its effectiveness in penetrating the crossflow is reduced. It can then be argued that for small z/w the predominant heat transfer mechanism is channel flow, and hence the lower $\overline{Nu}$ values are observed. A local maximum near z/w = 1.0 for Re = 400 with the large jets, and near z/w = 2.0 for Re = 1000 with the small jets is observed on heater 3. The crossflow and jet interaction experience some trade-off, where at low z/w channel crossflow heat transfer is dominant, whereas at high z/w jet impingement transport dominates. It may be suggested that the point of maximum $\overline{Nu}$ is the value of z/w where both mechanisms act in unison.

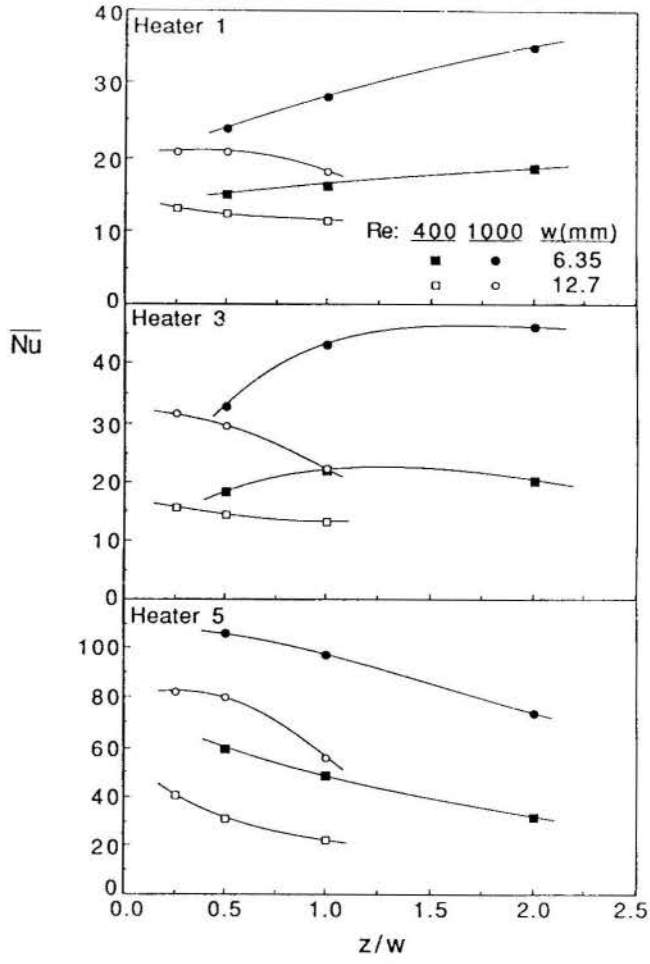

Fig. 7. Dependence of the average Nusselt number on nozzle-to-protrusion spacing for the first, third, and fifth heaters: Re = 400 and 1000, w = 6.35 and 12.7 mm.

The fifth protrusion did not exhibit the same behavior as its upstream neighbors. It was the only protrusion where the average Nusselt number dependence on nozzle-to-protrusion spacing was identical; $\overline{Nu}$ is seen to decrease with z/w in Fig. 7 for both nozzle widths at both Reynolds numbers. The last protrusion causes a large recirculation zone and high levels of turbulence as the channel Reynolds number, Re_z, becomes large due to the cumulative effect of the spent air from the upstream nozzles. The flow here is very turbulent and the crossflow velocities are high. All of these effects increase as z/w decreases, tending to dominate any jet impingement effects that may exist. Hence, the fifth protrusion is influenced predominantly by channel crossflow effects for both nozzle widths.

Correlation of Average Nusselt Number

All of the experimental average Nusselt number data were correlated using a multiple linear regression to quantify the importance of the parameters discussed in this study. The correlation used is of the form

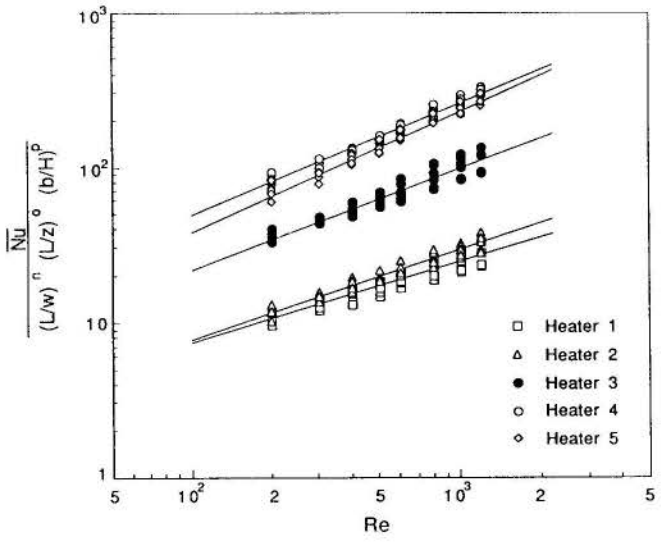

Fig. 8. Composite correlation of all experimental data for the five heaters.

$$\overline{Nu}_i = A_i\, Re^{m_i}\, (L/w)^{n_i}\, (L/z)^{o_i}\, (b/H)^{p_i} \qquad (4)$$

where $\overline{Nu}_i$ is the average Nusselt for heater i, and the flow and geometric parameters are as defined in the Nomenclature. Table 1 lists the coefficient and exponents, A_i, m_i, n_i, o_i, and p_i determined from the least-squares regression for each of the heaters, along with the average and maximum error for each data set. The correlation is illustrated in Fig. 8 for all of the experimental data. The correlation is valid in the range $200 \le Re \le 1200$, $0.25 \le z/w \le 1.0$ for the 12.7 mm nozzle width, and $0.5 \le z/w \le 2.0$ for the 6.35 mm nozzle width. The correlation shows some interesting trends. The average Nusselt number is seen to depend roughly on $Re^{0.6}$. However, the cumulative effect of crossflow is evident by the increasing exponent on Re, m_i; If the flow through each jet is increased by a given amount, the crossflow at the end of the channel is increased by roughly 4 - 5 times that amount. The result is that the successive downstream heaters approach a Reynolds number relationship more nearly that of conventional channel flow, for which the Nusselt number dependence is given by the Dittus-Boelter relation for fully-developed turbulent channel flow, $Nu \propto Re^{0.8}$. A correlation in terms of the dimensionless nozzle-to-protrusion spacing, z/w, was not possible. This is evidenced by the variation in exponents of L/w and L/z. If a correlation in terms of z/w was possible, these two parameters would exhibit the same relationship, and n_i and o_i would be identical since z/w can be built from the ratio (L/w)/(L/z). Note also that the ratio of protrusion height to channel height, b/H, was necessary in developing the correlation.

CONCLUSIONS

The flow structure and heat transfer characteristics of a two-dimensional array of heated protrusions cooled by planar jet impingement with crossflow of the spent air have been investigated experimentally. The parameters varied experimentally included average jet Reynolds number, nozzle-to-protrusion spacing, and nozzle width. Laser-Doppler velocimetry was used to map mean flow and turbulent fluctuations of the crossflow velocity component. The LDV results show the presence of recirculation zones and highly turbulent flow even for low jet Reynolds numbers. High turbulence intensity was observed in regions of significant interaction of the jet impingement flow with the channel crossflow. Significant nonuniformity in the distribution of mass flow delivered to each jet was observed, and was found to be dependent on the jet width and nozzle-to-protrusion spacing.

Two mechanisms were observed which affected the heat transfer. The first was jet impingement, and the second was crossflow of the spent air. The average Nusselt number experienced some trade-off where at low z/w with large jets the heat transfer was dominated by the crossflow, whereas at high z/w with small jets the heat transfer was dominated by jet impingement. A maximum in average Nusselt number with z/w was observed when the jet impingement flow and crossflow acted with near-equal intensity. A correlation for the average Nusselt number for each heater was developed in terms of the average jet Reynolds number and the geometric parameters of the problem.

Table 1. Coefficient, exponents, and average and maximum error for the average Nusselt number correlation, Eqn. (4)

Heater	A_i	m_i	n_i	o_i	p_i	Avg. Err. (%)	Max. Err. (%)
1	0.668	0.520	0.458	-0.125	0.132	7.7	19.3
2	0.540	0.578	0.428	-0.081	0.202	6.6	15.7
3	1.092	0.652	0.494	-0.580	1.188	9.1	21.2
4	1.767	0.723	0.554	-0.848	1.878	6.3	16.0
5	1.036	0.783	0.486	-0.316	1.372	7.2	21.6

ACKNOWLEDGEMENTS

This work was supported in part by the U.S. National Science Foundation under grant CBT-8552493.

REFERENCES

Downs, S.J. and James, E.H., 1987, "Jet Impingement Heat Transfer - A Literature Survey," ASME Paper No. 87-HT-35, ASME, New York.

Florschuetz, L.W., Berry, R.A. and Metzger, D.E., 1980, "Periodic Streamwise Variations of Heat transfer Coefficients for Inline and Staggered Arrays of Circular Jets with Crossflow of Spent Air," *ASME Journal of Heat Transfer*, Vol. 102, pp. 132-137.

Florschuetz, L.W., Metzger, D.E. and Su, C.C., 1984, "Heat Transfer Characteristics for Jet Array Impingement With Initial Crossflow," *ASME Journal of Heat Transfer*, Vol. 106, pp. 34-41.

Florschuetz, L.W. and Su, C.C., 1987, "Effects of Crossflow Temperature on Heat Transfer Within an Array of Heated Jets," *ASME Journal of Heat Transfer*, Vol. 109, pp. 74-82.

Florschuetz, L.W., Truman, C.R. and Metzger, D.E., 1981, "Streamwise Flow and Heat Transfer Distributions for Jet Array Impingement with Crossflow," *ASME Journal of Heat Transfer*, Vol. 103, pp. 337-342.

Gardon, R. and Akfirat, J.C., 1966, "Heat Transfer Characteristics of Two-Dimensional Air Jets," *ASME Transactions Series C*, Vol. 88, pp. 101-108.

Hamadah, T.T., 1989, "Impingement Cooling of of a Simulated Electronics Package With a Square Array of Round air Jets," *Heat Transfer in Electronics - 1989*, ASME, New York, pp. 107-112.

Hollworth, B.R. and Durbin, M., 1989, "Impingement Cooling of Electronics," *Heat Transfer in Electronics - 1989*, ASME, New York, pp. 89-96.

Incropera, F.P. and DeWitt, D.P., 1990, *Introduction to Heat Transfer*, 2nd Edition, John Wiley and Sons, New York.

Kline, S.J. and McClintock, F.A., 1953, "Describing Uncertainties in Single-Sample Experiments," *Mechanical Engineering*, pp. 3-12.

Metzger, D.E., Florschuetz, L.W., Takeuchi, D.I., Behee, R.D. and Berry, R.A., 1979, "Heat Transfer Characteristics for Inline and Staggered Arrays of Circular Jets with Crossflow of Spent Air," *ASME Journal of Heat Transfer*, Vol. 101, pp. 526-531.

Patankar, S.V., 1980, *Numerical Heat Transfer and Fluid Flow*, Hemisphere, Washington, D.C.

Whidden, G.L., 1990, "Local Heat Transfer Characteristics of Two-Dimensional Jets Impinging on Heated Protrusions with Crossflow of Spent Air," M.S. Thesis, Dept. of Mechanical Engineering, Brigham Young University, Provo, Utah.

III ENCIT – Itapema, SC (Dezembro 1990)

FULL POTENTIAL FLOW SIMULATION ABOUT WING CONFIGURATIONS

BENTO S. DE MATTOS
EMBRAER
DTE / TEE / EAD
12225 – São José dos Campos – SP

JOÃO LUIZ F. AZEVEDO
Centro Técnico Aeroespacial
Instituto de Atividades Espaciais
12225 – São José dos Campos – SP

SUMMARY

The development of a three-dimensional transonic flow solver based on the full potential formulation is described. The Holst and Ballhaus artificial density scheme is used for the spatial discretization of the governing equation. Convergence to steady state is achieved through iteration in pseudo-time using the AF2 implicit approximate factorization algorithm. The implementation of circulation boundary conditions, which are essential in order to obtain accurate lifting solutions, is described in detail. The code was applied to wing-like configurations, and the results are in good agreement with the available data.

INTRODUCTION

The development of modern computational tools that can aid in the aerodynamic design of current vehicles is a constant concern in many aerospace-related organizations nowadays. This is quite justifiable considering the potential savings that can be realized if the typically wind tunnel oriented aerospace vehicle design is directed more towards computation. It has been shown in many instances that the cost of computation has been constantly reduced over the years, and the trend has not shown any signs of change. Moreover, the added flexibility provided by the computer allows for a faster development stage of new configurations, and this translates directly in a shorter time-to-market of new designs. Therefore, the aerospace industry, and research institutions, are being forced into developing their computational codes for aerodynamic analyses in order to remain competitive.

In this context, the present work describes the development of a three dimensional flow solver based on the full potential formulation for the analysis of transonic flow about wing-like configurations. The mathematical formulation considers the isentropic flow hypothesis together with the mass and momentum conservation equations. This allows the derivation of the full potential equation and an expression for the density. Holst and Thomas[1] three dimensional adaptation of the AF2 approximate factorization algorithm is used for the solution of the steady full potential equation in conservative form. The stability of the calculation process in supersonic flow regions is achieved through the use of Holst and Ballhaus[2] artificial density scheme.

An algebraic mesh generator[3] was developed in order to provide the aerodynamic solver with body conforming O-H type meshes in the chordwise and spanwise planes, respectively. The grid generator allows for the control of wake and external boundary position, the smoothness of interior point distribution, and grid stretching. Results are presented for wings mounted between two walls, and for wings mounted against a wall with the other end free. Unswept wings mounted between two infinite walls in a potential flow essentially represent 2-D flow conditions. The latter cases are the counterpart, in this simplified numerical simulation, of a wing mounted in a fuselage.

THEORETICAL FORMULATION

The full potential equation can be written in conservative form for 3-D cartesian coordinates as

$$(\rho\phi_x)_x + (\rho\phi_y)_y + (\rho\phi_z)_z = 0 \tag{1}$$

where ϕ is the complete velocity potential, and the subscripts indicate partial derivatives with respect to each coordinate direction. If velocities are made dimensionless with respect to the critical speed of sound a_*, and density is nondimensionalized by the stagnation density ρ_t, one can obtain an expression for the density as

$$\rho = \left[1 - \frac{\gamma-1}{\gamma+1}\left(\phi_x^2 + \phi_y^2 + \phi_z^2\right)\right]^{1/(\gamma-1)} \tag{2}$$

Here, we have used the continuity equation in steady form, and the momentum conservation equations together with the potential flow hypothesis.

It is usually convenient to rewrite the above equations in general curvilinear coordinates that conform to the body of interest. Besides making the code implementation much more general, this makes the mesh spacing uniform in computational space and facilitates the implementation of boundary conditions. The transformation is typically known only numerically, and it is of the form

$$\begin{aligned} \xi &= \xi(x,y,z) \\ \eta &= \eta(x,y,z) \\ \zeta &= \zeta(x,y,z) \end{aligned} \tag{3}$$

The full potential equation can be rewritten in the new coordinate system, still in conservation-law form, as

$$\left(\frac{\rho U}{J}\right)_\xi + \left(\frac{\rho V}{J}\right)_\eta + \left(\frac{\rho W}{J}\right)_\zeta = 0 \tag{4}$$

The expression for density becomes

$$\rho = \left[1 - \frac{\gamma-1}{\gamma+1}\left(U\phi_\xi + V\phi_\eta + W\phi_\zeta\right)\right]^{1/(\gamma-1)} \tag{5}$$

The contravariant velocity components are given by

$$\begin{aligned} U &= A_1\phi_\xi + A_4\phi_\eta + A_5\phi_\zeta \\ V &= A_4\phi_\xi + A_2\phi_\eta + A_6\phi_\zeta \\ W &= A_5\phi_\xi + A_6\phi_\eta + A_3\phi_\zeta \end{aligned} \tag{6}$$

The various metric terms are defined as

$$\begin{aligned} A_1 &= \xi_x^2 + \xi_y^2 + \xi_z^2 \\ A_2 &= \eta_x^2 + \eta_y^2 + \eta_z^2 \\ A_3 &= \zeta_x^2 + \zeta_y^2 + \zeta_z^2 \\ A_4 &= \xi_x\eta_x + \xi_y\eta_y + \xi_z\eta_z \\ A_5 &= \xi_x\zeta_x + \xi_y\zeta_y + \xi_z\zeta_z \\ A_6 &= \eta_x\zeta_x + \eta_y\zeta_y + \eta_z\zeta_z \end{aligned} \tag{7}$$

and the Jacobian of the transformation is given by

$$\begin{aligned} J = (&x_\xi y_\eta z_\zeta + x_\zeta y_\xi z_\eta + x_\eta y_\zeta z_\xi \\ &- x_\zeta y_\eta z_\xi - x_\eta y_\xi z_\zeta - x_\xi y_\zeta z_\eta)^{-1} \end{aligned} \tag{8}$$

A schematic description of the transformation from physical to computational domain is shown in Fig. 1.

FINITE DIFFERENCE EQUATIONS

For transonic flow, Eq. 4 is of mixed elliptic-hyperbolic type. In physical terms, this means that the field has both subsonic and super-

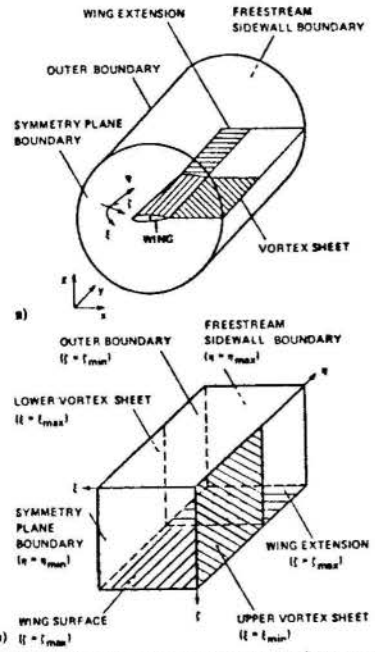

Figure 1: Physical space to computational space mapping.

sonic regions. An appropriate spatial differencing algorithm, which is capable of capturing this mixed character of the governing equation, is the Holst and Ballhaus artificial density scheme[2,4,5]. This difference scheme applied to the 3-D full potential equation in conservation-law form for general curvilinear coordinates yields[1]

$$\overline{\delta}_\xi \left(\frac{\tilde{\rho}U}{J}\right)_{i+\frac{1}{2},j,k} + \overline{\delta}_\eta \left(\frac{\bar{\rho}V}{J}\right)_{i,j+\frac{1}{2},k} + \overline{\delta}_\zeta \left(\frac{\hat{\rho}W}{J}\right)_{i,j,k+\frac{1}{2}} = 0 \qquad (9)$$

where the $\overline{\delta}_\xi(\ )$, $\overline{\delta}_\eta(\ )$ and $\overline{\delta}_\zeta(\ )$ are standard 1st order backward difference operators in the ξ, η and ζ-directions, respectively.

We observe that the scheme is essentially a centrally differenced algorithm, in which stability in supersonic regions of flow is achieved by an upwind bias of the density coefficients $\tilde{\rho}$, $\bar{\rho}$ and $\hat{\rho}$. These density coefficients are defined by

$$\begin{aligned}
\tilde{\rho}_{i+\frac{1}{2},j,k} &= [(1-\nu)\rho]_{i+\frac{1}{2},j,k} + \nu_{i+\frac{1}{2},j,k}\rho_{i+r+\frac{1}{2},j,k} \\
\bar{\rho}_{i,j+\frac{1}{2},k} &= [(1-\nu)\rho]_{i,j+\frac{1}{2},k} + \nu_{i,j+\frac{1}{2},k}\rho_{i,j+s+\frac{1}{2},k} \\
\hat{\rho}_{i,j,k+\frac{1}{2}} &= [(1-\nu)\rho]_{i,j,k+\frac{1}{2}} + \nu_{i,j,k+\frac{1}{2}}\rho_{i,j,k+t+\frac{1}{2}}
\end{aligned} \qquad (10)$$

Here, the ν coefficient, and the r, s and t indices are responsible for providing the upwind influence. The indices are defined such that

$$\begin{aligned}
r &= \begin{cases} +1 & \text{, for } U_{i+\frac{1}{2},j,k} < 0 \\ -1 & \text{, for } U_{i+\frac{1}{2},j,k} > 0 \end{cases} \\
s &= \begin{cases} +1 & \text{, for } V_{i,j+\frac{1}{2},k} < 0 \\ -1 & \text{, for } V_{i,j+\frac{1}{2},k} > 0 \end{cases} \\
t &= \begin{cases} +1 & \text{, for } W_{i,j,k+\frac{1}{2}} < 0 \\ -1 & \text{, for } W_{i,j,k+\frac{1}{2}} > 0 \end{cases}
\end{aligned} \qquad (11)$$

and the switching function $\nu_{i+\frac{1}{2},j,k}$ is given by

$$\nu_{i+\frac{1}{2},j,k} = \begin{cases} \max\left[\left(M^2_{i,j,k}-1\right)C, 0\right] & \text{, for } U_{i+\frac{1}{2},j,k} > 0 \\ \max\left[\left(M^2_{i+1,j,k}-1\right)C, 0\right] & \text{, for } U_{i+\frac{1}{2},j,k} < 0 \end{cases} \qquad (12)$$

Similar expressions are used for $\nu_{i,j+\frac{1}{2},k}$ and $\nu_{i,j,k+\frac{1}{2}}$. The local Mach number, M, can be obtained from

$$M^2 = \frac{2M^2_\star}{(\gamma+1)-(\gamma-1)M^2_\star} \qquad (13)$$

where $M^2_\star = U\phi_\xi + V\phi_\eta + W\phi_\zeta$. The C constant is user specified, and the suggested range is $1.0 \le C \le 2.0$.

The density here is always calculated at the mesh half points where it is needed. This is more expensive than computing the density at the mesh point themselves and then obtaining the density at half points by averaging. However, our computations showed that it does produce much better shock resolution and it is, therefore, adopted in the present work. We emphasize that this procedure will require the computation, and storage, of three sets of density coefficients per mesh point throughout the entire mesh. For instance, at $\left(i+\frac{1}{2},j,k\right)$ points, the U velocity component is given by

$$\begin{aligned}
U_{i+\frac{1}{2},j,k} &= A_{1_{i+\frac{1}{2},j,k}}\phi_{\xi_{i+\frac{1}{2},j,k}} + A_{4_{i+\frac{1}{2},j,k}}\phi_{\eta_{i+\frac{1}{2},j,k}} \\
&\quad + A_{5_{i+\frac{1}{2},j,k}}\phi_{\zeta_{i+\frac{1}{2},j,k}}
\end{aligned} \qquad (14)$$

and similar expressions can be written for the other contravariant velocity components V and W. Here,

$$\begin{aligned}
\phi_{\xi_{i+\frac{1}{2},j,k}} &= \phi_{i+1,j,k} - \phi_{i,j,k} \\
\phi_{\eta_{i+\frac{1}{2},j,k}} &= \frac{(\phi_{i+1,j+1,k} - \phi_{i+1,j-1,k} + \phi_{i,j+1,k} - \phi_{i,j-1,k})}{4} \\
\phi_{\zeta_{i+\frac{1}{2},j,k}} &= \frac{(\phi_{i+1,j,k+1} - \phi_{i+1,j,k-1} + \phi_{i,j,k+1} - \phi_{i,j,k-1})}{4}
\end{aligned} \qquad (15)$$

With the above quantities, the density $\rho_{i+\frac{1}{2},j,k}$ can be calculated by Eq. 5. A similar procedure is used for the $\left(i,j+\frac{1}{2},k\right)$ and $\left(i,j,k+\frac{1}{2}\right)$ points in the present implementation.

Similarly, the metric terms are also computed at the half points by 2nd order finite difference formulas, instead of using averages. Again, this is more expensive and requires the evaluation of three sets of metric terms per mesh point. As above, this additional work is more than justified by the increased accuracy that can be achieved, especially for meshes with high levels of stretching which are typical of many aerodynamic computations.

THE AF2 ALGORITHM

Relaxation schemes for the conservative, steady full potential equation can be written in general delta form[6] as

$$NC^n_{i,j,k} + \omega\, L\phi^n_{i,j,k} = 0 \qquad (16)$$

Here, n is the iteration index, ω is a relaxation parameter, and $L\phi^n_{i,j,k}$ is the residue, i. e. , it is a measure of how well we are satisfying the governing equation. Hence,

$$L\phi^n_{i,j,k} = \overline{\delta}_\xi \left(\frac{\tilde{\rho}U}{J}\right)^n_{i+\frac{1}{2},j,k} + \overline{\delta}_\eta \left(\frac{\bar{\rho}V}{J}\right)^n_{i,j+\frac{1}{2},k} + \overline{\delta}_\zeta \left(\frac{\hat{\rho}W}{J}\right)^n_{i,j,k+\frac{1}{2}} \qquad (17)$$

$C^n_{i,j,k}$ is the n-th iteration correction

$$C^n_{i,j,k} \equiv \phi^{n+1}_{i,j,k} - \phi^n_{i,j,k} \qquad (18)$$

and the N operator is chosen to approximate L as closely as possible. Obviously, the solution of such an implicit three dimensional operator would be quite expensive. Hence, the method goes on to approximately factor this $N \equiv L$ operator in order to obtain an efficient solution algorithm. The standard ADI-type algorithm would factor this 3-D operator into a sequence of three completely decoupled 1-D operators. The AF2 algorithm still factors the left-hand side into three operators. However, one of the directions is split in two of the operators, which automatically adds time-like dissipation in this particular direction and also simplifies the inversion work by avoiding one tridiagonal solution[6].

The AF2 algorithm for the 3-D case can be expressed in the following sequence of steps.

- Step 1 :

$$\left(\alpha - \frac{1}{A_k}\vec{\delta}_\eta A_j \overline{\delta}_\eta\right) g^n_{i,j} = \alpha\,\omega\, L\phi^n_{i,j,k} + \alpha\, A_{k+1}\, f^n_{i,j,k+1} \qquad (19)$$

- Step 2 :

$$\left(A_k \mp \beta_\xi \vec{\overline{\delta}}_\xi - \frac{1}{\alpha}\vec{\delta}_\xi A_i \overline{\delta}_\xi\right) f^n_{i,j,k} = g^n_{i,j} \qquad (20)$$

- Step 3 :

$$\left(\alpha + \overline{\delta}_\zeta\right) C^n_{i,j,k} = f^n_{i,j,k} \qquad (21)$$

As before, the $\overline{\delta}_\xi$, $\overline{\delta}_\eta$ and $\overline{\delta}_\zeta$ are standard 1st order backward difference operators, and the $\vec{\delta}_\xi$ and $\vec{\delta}_\eta$ are 1st order forward difference operator. The ζ-direction derivatives are the ones split among the various steps. The $\vec{\overline{\delta}}_\xi$ denotes a backward or forward operator, whatever gives an upwind influence, and the sign of the corresponding term should be chosen such that the magnitude of the main diagonal element is

increased. The $\beta_\xi \vec{\delta}_\xi$ term is adding temporal damping to the centrally differenced ξ-direction. In the present implementation, the β_ξ coefficient was varied between 0.10 and 0.40 for supersonic flow regions. This coefficient was set to zero in subsonic regions. The A_i, A_j and A_k coefficients are defined by

$$\begin{aligned} A_i &= \left(\frac{\hat{\rho} A_1}{J}\right)^n_{i-\frac{1}{2},j,k} \\ A_j &= \left(\frac{\hat{\rho} A_2}{J}\right)^n_{i,j-\frac{1}{2},k} \\ A_k &= \left(\frac{\hat{\rho} A_3}{J}\right)^n_{i,j,k-\frac{1}{2}} \end{aligned} \tag{22}$$

The α parameter can be interpreted as the inverse of a time step in the pseudo-time march represented by the iterative process. For efficiency reasons, it is actually important to cycle over an α-sequence, instead of using a constant value for this parameter. A discussion of α-sequences is presented by Holst[6], Ballhaus et al.[7] and Sankar and Malone[8], among others. A detailed comparison of the use of α-sequences versus constant α is given in Ref. [9] for a simple test problem. The following sequence was adopted in the present work.

$$\alpha_\ell = \alpha_{high} \left(\frac{\alpha_{low}}{\alpha_{high}}\right)^{\ell/(nb-1)} \tag{23}$$

where nb is the number of elements in the sequence, and $\ell = 0, 1, \ldots, (nb-1)$. The values of the various parameters typically used for most of the computations performed here were $nb = 5$, $\alpha_{low} = 0.82$ and $\alpha_{high} = 23$. The α_{low} and α_{high} values were adjusted in a trial-and-error basis for faster convergence of the initial computations, and it was observed that they yielded efficient convergence for all cases considered.

Steps 1 and 2 are solved concurrently for each k-plane, starting at $k = NK$, which means the wing surface in the present case, and marching backwards in k. Step 1 requires the solution of a standard tridiagonal operator in the η-direction. A periodic tridiagonal solution in the ξ-direction is performed in step 2, since O-type meshes are used in chordwise planes. After the intermediate variable $f^n_{i,j,k}$ is found for the entire mesh, step 3 can be performed by sweeping forward in the ζ-direction.

BOUNDARY CONDITIONS

The condition of flow tangency at solid surfaces is obtained by setting the normal velocity component to zero at the wing surface. In computational space, this can be interpreted as having the contravariant velocity component $W = 0$. The implementation of this condition in the residue computation yields

$$\left(\frac{\hat{\rho} W}{J}\right)_{i,j,NK+\frac{1}{2}} = -\left(\frac{\hat{\rho} W}{J}\right)_{i,j,NK-\frac{1}{2}} \tag{24}$$

Moreover, the condition of zero W contravariant velocity component allows us to write (see Eq. 6)

$$(\phi_\zeta)_{k=NK} = -\frac{A_5}{A_3}\phi_\xi - \frac{A_6}{A_3}\phi_\eta \tag{25}$$

This expression avoids the use of a non-centered difference operator in the ζ-direction at $k = NK$. In a similar fashion, the tangency condition at the symmetry plane is obtained by setting $V = 0$. The procedure is exactly similar to the one described above and, again, the definition of the contravariant velocity components can be invoked to avoid the computation of non-centered η-differences at the boundary. Periodic boundary conditions are used in the ξ-direction.

An extremely important aspect of potential flow computations is the implementation of circulation boundary conditions. Potential flows require the enforcement of some form of Kutta condition in order to obtain lifting solutions. A considerable amount of effort in the present work was spent in finding out efficient ways of implementing the Kutta condition. The authors were able to identify at least three different ways for computing the circulation. All of them yielded, however, comparable results. Here, due to space limitations, we will restrict ourselves in describing the form of Kutta condition implementation used for the majority of the 3-D computations.

The approach implemented here follows the work of Jameson[10] and Holst[6] in which the potential is broken as the summation of two parts as

$$\phi = \overline{\phi} - \Gamma\xi \tag{26}$$

Here, $\overline{\phi}$ will take care of all the nonlinear contributions to the velocity potential. The second term represents a vortex of strength $2\pi\Gamma$, and it will be used to enforce the Kutta condition. The interesting point in this approach is that the potential $\overline{\phi}$ is a continuous function throughout the whole field, and the jump in the velocity potential across the wake is taken care by the second term. Moreover, derivatives of ϕ are identical to derivatives of $\overline{\phi}$, except for the ξ-derivatives. These are given by

$$\phi_\xi = \overline{\phi}_\xi - \Gamma \tag{27}$$

The Kutta condition is enforced by setting ϕ_ξ to zero at the trailing edge. This is equivalent to state that the flow is not allowed to "make the turn" around the trailing edge. Hence, the circulation can be calculated from

$$\Gamma = \overline{\phi}_{\xi_{1,j,NK}} = \frac{\overline{\phi}_{2,j,NK} - \overline{\phi}_{NI-1,j,NK}}{2} \tag{28}$$

We remark that both $i = 1$ and $i = NI$ correspond to points along the wake. In other words, there are two computational points for each position in physical space along the wake. Moreover, the potential that is actually stored in the computer is $\overline{\phi}$. The complete velocity potential can always be recovered using Eq. 26, if it is needed.

The velocity potential jump across the wake must be explicitly enforced. This is done here by solving for ϕ from $i = 2$ to $i = NI$. The potential values at $i = 1$ are obtained from

$$\phi^n_{1,j,k} = \phi^n_{NI,j,k} + \Gamma^n_j \tag{29}$$

A circulation boundary condition must also be enforced in the far-field. The rational here is that the circulation computed by a line integration along the far-field boundary must be exactly equal to that obtained by integration along the airfoil surface. Hence, the freestream values attributed to the potential in the far-field are modified to take into account the existence of a vortex of strength $2\pi\Gamma$ located at the airfoil quarter chord point.

The implicit implementation of boundary conditions is also very important in order to develop a robust and efficient algorithm. Of particular concern is, again, the correct treatment of the circulation in the implicit operators. Hence, in the tridiagonal solution in step 2, one must take into account the periodicity in the ξ-direction as well as the jump in the potential along the wake. The system of equations to be solved in step 2 can be schematically represented by[11]

$$a_i f_{i-1,j,k} + b_i f_{i,j,k} + c_i f_{i+1,j,k} = d_i \tag{30}$$

where $i = 2, \ldots, NI$. Observing that $C^n_{1,j,k} - C^n_{NI,j,k} = \Delta\Gamma^n_j$, one can obtain from step 3 that

$$f^n_{1,j,k} = \left(\alpha + \overline{\delta}_\zeta\right) C^n_{1,j,k} = \left(\alpha + \overline{\delta}_\zeta\right)\left(C^n_{NI,j,k} + \Delta\Gamma^n_j\right) \tag{31}$$

Hence,

$$f^n_{1,j,k} = f^n_{NI,j,k} + \alpha\,\Delta\Gamma^n_j \tag{32}$$

If we, then, take $i = 2$ in Eq. 30 and use the result above, we can write for the first equation in the tridiagonal system in the ξ-direction that

$$b_2 f^n_{2,j,k} + c_2 f^n_{3,j,k} + a_2 f^n_{NI,j,k} = d_2 - a_2\,\alpha\,\Delta\Gamma^n_j \tag{33}$$

With a similar development, we can obtain for the trailing edge point in the lower surface of the wake, i. e. , for $i = NI$, that

$$a_{NI} f^n_{NI-1,j,k} + b_{NI} f^n_{NI,j,k} + c_{NI} f^n_{2,j,k} = d_{NI} + c_{NI}\,\alpha\,\Delta\Gamma^n_j \tag{34}$$

It is clear, however, that at this point in the computation we cannot simply compute $\Delta\Gamma^n_j = \Gamma^{n+1}_j - \Gamma^n_j$, because Γ^{n+1}_j is not known yet. This quantity can be computed only after the update of the solution $\overline{\phi}^{n+1}$ for the mesh interior points. The procedure adopted here consists, then, in computing $\Delta\Gamma^n_j$ using an estimated value of Γ^{n+1}_j. This estimated value is used only for this computation, and never for the explicit update of the circulation boundary conditions previously described. Hence, we have that

$$\Delta\Gamma^n_j = \left(\Gamma^{n+1}_j\right)_{estimated} - \Gamma^n_j \tag{35}$$

where

$$\left(\Gamma^{n+1}_j\right)_{estimated} = 2\,\Gamma^n_j - \Gamma^{n-1}_j \tag{36}$$

It was observed that the convergence rate for the correct circulation value was still not satisfactory with the above procedure. Therefore, following suggestions in the literature[5], we decided to underrelax

the circulation computation. The procedure finally implemented here consisted in calling $\tilde{\Gamma}_j^n$ the value of Γ computed by Eq. 28. This value is underrelaxed such that

$$\overline{\Gamma}_j^n = R_g \tilde{\Gamma}_j^n + (1 - R_g)\, \Gamma_j^{n-1} \tag{37}$$

and we, then, compute

$$\Gamma_j^n = \frac{1}{2}\left[\overline{\Gamma}_j^n + \left(\Gamma_j^n\right)_{estimated}\right] \tag{38}$$

The estimated values of Γ at the new time level $n+1$, required for the implicit computations, are obtained from Eq. 36, and $\Delta\Gamma_j^n$ can then be calculated from Eq. 35. The underrelaxation parameter R_g is specified by the user. For the present computations, the value $R_g = 0.50$ was used for all cases.

For the initialization of step 1 with $k = NK$, see Eq. 19, the value of $f_{i,j,NK+1}^n$ is required. This value cannot be usually calculated, since it is the value of a property "inside" the wing. The procedure adopted here was to assume $f_{i,j,NK+1}^n = 0$, and we remark that this is consistent with the steady-state solution. Further discussion of the implicit numerical boundary conditions can be found in de Mattos[12].

RESULTS

The meshes used in the computations to be presented here were all generated algebraically. The interested reader is referred to the work of de Mattos[12] for the details of the grid generation algorithm used. It suffices now to say that O-H meshes were used in the chordwise and spanwise planes, respectively, and that care was exercised in order to ensure orthogonality at the wing surface. A detailed view of the grid close to the airfoil for the case of the CBA-123 root section is shown in Fig. 2. It is clear from the figure that the present mesh generator does not provide an extremely good resolution in the wake region. This is a consequence of imposing orthogonality at the wing surface with an O-type mesh. In sectors of high curvature of the airfoil surface, the resultant grid is rather coarse away from the airfoil. Nevertheless, we did not observe any inaccuracy in the solutions that could be attributed to this lack of resolution in the wake region.

The initial computations performed here considered a rectangular wing mounted between two infinite walls. As discussed before, this actually represents 2-D flow, and it was used mainly with the purpose of validating the code developed. Many subcritical cases for this configuration are also presented by de Mattos[12]. Here, we will describe only the most interesting results. The pressure coefficient distribution for a wing of aspect ratio 10, with a NACA 0012 airfoil, is shown in Fig. 3 for the case of $M_\infty = 0.40$ and $\alpha = 4°$. The computational mesh used in this calculation has $89 \times 11 \times 22$ grid points in the ξ, η and ζ-directions, respectively. The present computational results are compared with those obtained with the TRANSEP program[13]. It is clear that the results are in good agreement. We observe, however, that the suction peak at the airfoil leading edge, especially for this high angle of attack case, is very sensitive to the grid stretching used.

Another subcritical case run for the rectangular wing between two infinite walls considers a 16% thick, cambered airfoil. Actually, this is the airfoil used at the wing root section of the CBA-123. The pressure coefficient distribution for this case is shown in Fig. 4. The computational results are compared with those obtained with the TRANSEP code and with experimental results measured at the CTA/PAR-L wind tunnel. The two computational results agree well among themselves, except close to the trailing edge. The agreement with the experimental data is not as good. Nevertheless, the comparison seems to fav the computations obtained with the present code.

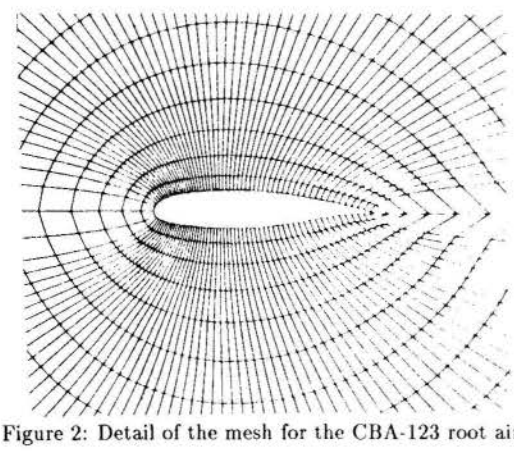

Figure 2: Detail of the mesh for the CBA-123 root airfoil.

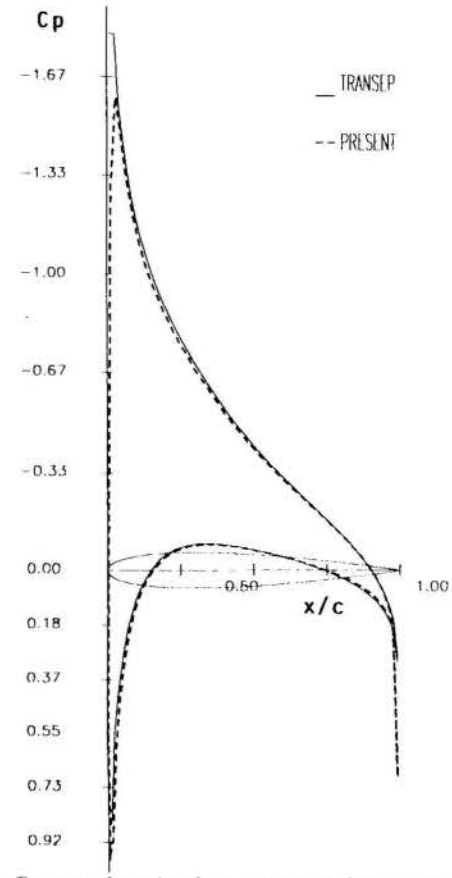

Figure 3: Rectangular wing between two infinite walls ($M_\infty = 0.4$ and $\alpha = 4°$).

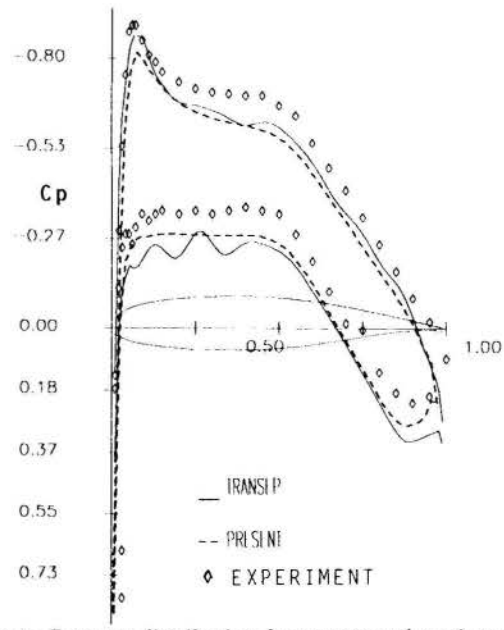

Figure 4: Pressure distribution for a rectangular wing with a 16 thick, cambered airfoil ($M_\infty = 0.20$ and $\alpha = 0°$).

Supercritical results for the unswept wing between two walls a presented for the case of a constant NACA 0012 airfoil section alo the span. Fig. 5 shows the pressure coefficient distribution for freestream Mach number $M_\infty = 0.85$ and $\alpha = 0°$. The present comp tations are compared with TRANSEP results and with Euler calcul tions presented by Pulliam[14]. The conservative full potential resu obtained with the present formulation present a shock which lies fu ther downstream, and that is stronger, than the shock obtained wi the Euler formulation. The nonconservative TRANSEP results giv shock upstream of the correct position. Both behaviors are typical full potential computations without boundary layer correction. Ma

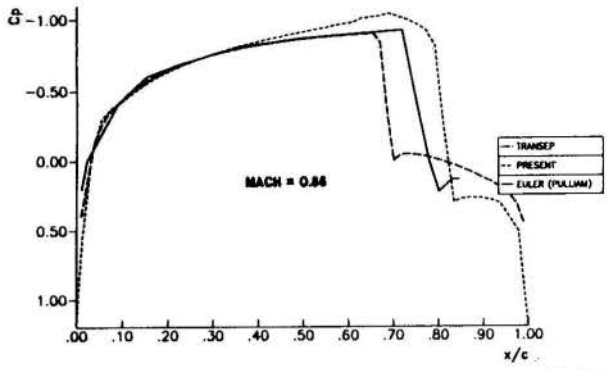

Figure 5: Supercritical results for unswept wing between walls ($M_\infty = 0.85$ and $\alpha = 0°$).

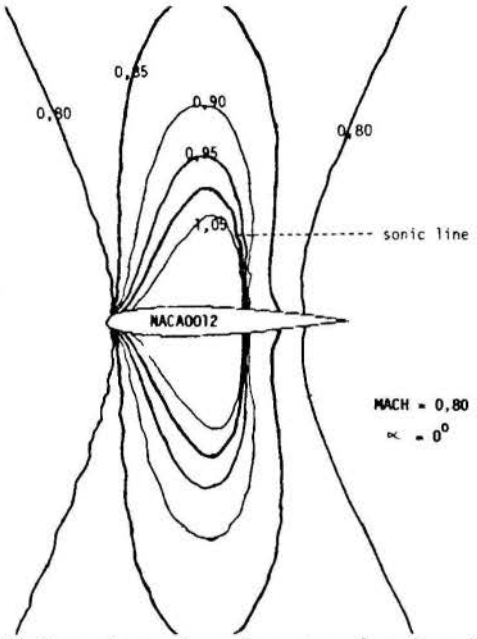

Figure 6: Mach number contours for rectangular wing with NACA 0012 airfoil ($M_\infty = 0.80$ and $\alpha = 0°$).

number contours in a chordwise plane for this wing at $M_\infty = 0.80$ and $\alpha = 0°$ are shown in Fig. 6. The pressure coefficient distribution for the same freestream Mach number and $\alpha = 1.25°$ is shown in Fig. 7. This latter result is compared with those obtained with TRANSEP. The agreement is good, except for the position of the lower surface shock. Again we remember that a non-conservative formulation has a tendency of causing a shock further upstream. It is intriguing, however, that the upper surface pressure distribution did not present the same behavior. Both $M_\infty = 0.80$ cases were also presented by Pulliam[14], and the qualitative comparison of our computations indicates good agreement with his results.

Pressure coefficient distributions along several spanwise sections for a 30° swept wing mounted between two infinite walls are shown in Fig. 8. The wing aspect ratio is 1.9 and the wing sections use a NACA 0015 airfoil. The flow is supercritical with a freestream Mach number $M_\infty = 0.86$ and zero degrees angle of attack. Pressure contours on the wing surface for this case are shown in Fig. 9. Although we do not have any independent result with which to compare this computation, it is interesting to observe that it does somewhat reproduce the expected qualitative behavior. However, it is also important to point out that the "inboard" shock, thinking in terms of a sweptback wing, is a bit too far aft, and the shock is rather smeared over a few grid points especially towards the "outboard" sections.

Finally, we considered the flow over an untapered, 30° sweptback wing with an aspect ratio of 10. The NACA 0012 airfoil is used for all spanwise sections. The wing is mounted at an infinite wall at the root and the tip is free. A freestream Mach number $M_\infty = 0.86$ and zero angle of attack were considered. Pressure coefficient distributions over various wing sections are shown in Fig. 10. The pressure coefficient distribution at the root section obtained with the present code is compared with that obtained with Jameson's FLO22 code[15] in Fig. 11. The comparison for the tip section is shown in Fig. 12. The agreement is still reasonably good, although certainly not perfect. At this

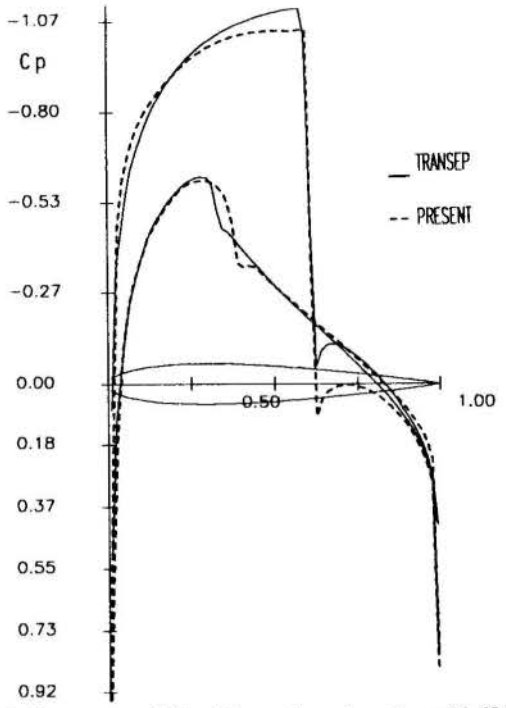

Figure 7: Pressure coefficient for rectangular wing with NACA 0012 airfoil ($M_\infty = 0.80$ and $\alpha = 1.25°$).

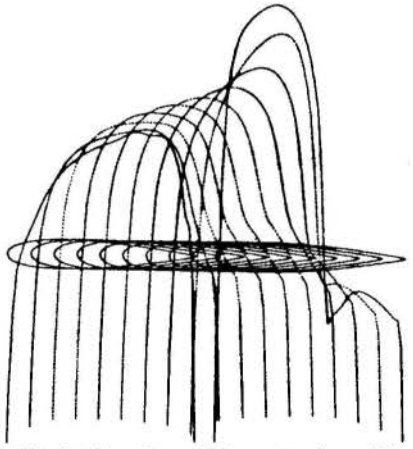

Figure 8: Cp distributions for a 30° swept wing with a NACA 0015 airfoil ($M_\infty = 0.86$ and $\alpha = 0°$).

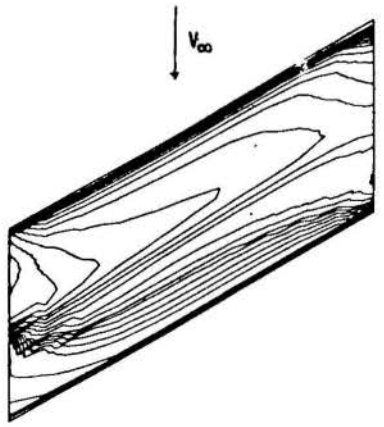

Figure 9: Pressure coefficient contours on the wing upper surface ($M_\infty = 0.86$ and $\alpha = 0°$).

point, however, it is difficult to assess the accuracy of the FLO22 computations themselves. Hence, it is also difficult to make any definite statement about the accuracy of the present computations. The ideal situation would involve the comparison of these computations with experimental data. Nevertheless, it is clear that the present calculations are capturing the correct trend of the results.

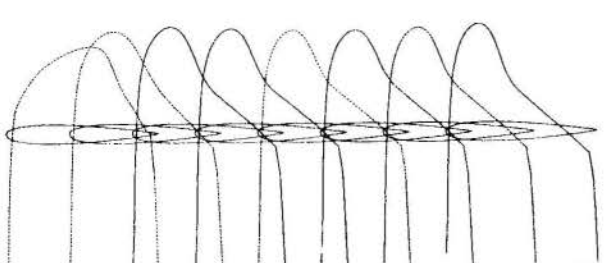

Figure 10: Pressure coefficient distributions on a 30° sweptback, aspect ratio 10 wing ($M_\infty = 0.86$ and $\alpha = 0°$).

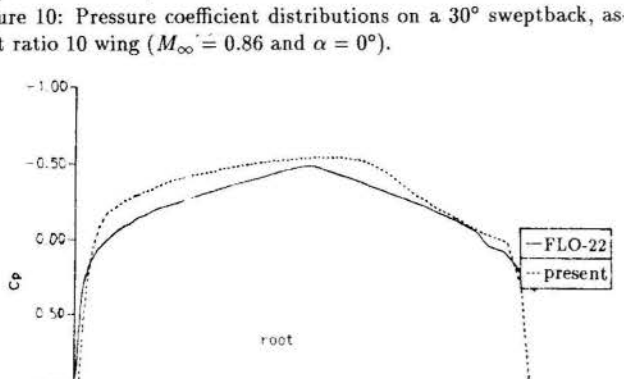

Figure 11: Comparison of pressure coefficient distribution for the root section ($M_\infty = 0.86$ and $\alpha = 0°$).

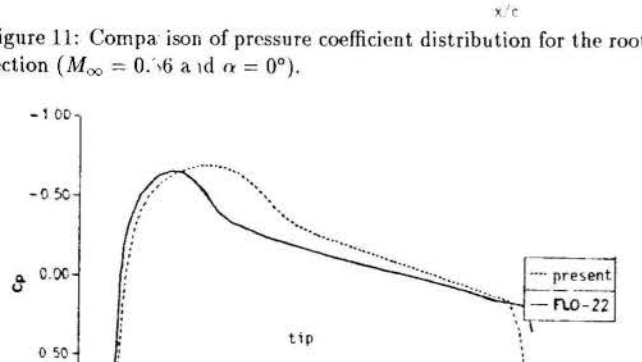

Figure 12: Comparison of pressure coefficient distribution for the tip section ($M_\infty = 0.86$ and $\alpha = 0°$).

CONCLUSIONS

The development of a three-dimensional, conservative, full potential solver was discussed, and results for wing-like configurations were presented. The implementation of circulation boundary conditions was one of the major hurdles for the accurate computation of lifting solutions, and the experience obtained was described in as much detail as the space permitted. The results presented provide some validation of the code, at least for wing alone configurations.

The algorithm implemented is extremely efficient and convergence to plotting accuracy is usually achieved with the order of 20 to 30 iterations, even for lifting cases. A typical run would require about 8 CPU minutes in an IBM 3090 with only one CPU and without vectorization. This is about one-third of the cost usually required by a lifting solution with the nonconservative 3-D code FLO22. We observe further that the code could be still optimized by computing all metric terms at the start of the calculation and storing them. This was not done here because we were afraid of penalizing too much the storage required by the code. This turned out to be not true, at least for the facility we have at hand, but the optimization was never implemented.

As a continuation of the present effort, the authors feel that the next logical step would be the consideration of more realistic wing-fuselage combinations. The grid generation requirements in such cases would certainly be much more stringent, and whether the present implementation of the algorithm will behave as well for such interference flowfields is still an open question. Moreover, the present code showed small inaccuracies in the wing extension region in the computation of lifting cases. At the moment, these inaccuracies are being attributed to the singularities that occur in the metric terms computation in this region. This, however, must also be fully understood before we could claim that a production code is available.

REFERENCES

[1] Holst, T.L., and Thomas, S.D. "Numerical Solution of Transonic Wing Flowfields," *AIAA Journal*, Vol. 21, No. 6, June 1983, pp. 863-870.

[2] Holst, T.L., and Ballhaus, W.F., "Fast Conservative Schemes for the Full Potential Equation Applied to Transonic Flows," *AIAA Journal*, Vol. 17, No. 2, Feb. 1979, pp. 145-152.

[3] Fletcher, C.A.J., *Computational Techniques for Fluid Dynamics 2 — Specific Techniques for Different Flow Categories*, Springer-Verlag, New York, 1988.

[4] Holst, T.L., and Albert, J., "An Implicit Algorithm for the Conservative, Transonic Full-Potential Equation with Effective Rotated Differencing," NASA TM-78570, 1979.

[5] Holst, T.L., "Implicit Algorithm for the Conservative Transonic Full-Potential Equation Using an Arbitrary Mesh," *AIAA Journal*, Vol. 17, No. 10, Oct. 1979, pp. 1038-1045.

[6] Holst, T.L., "Approximate-Factorization Schemes for Solving the Transonic Full-Potential Equation," in *Advances in Computational Transonics*, W.G. Habashi, editor, Pineridge Press, Swansea, U.K., 1985, pp. 59-82.

[7] Ballhaus, W.F., Jr. , Jameson, A., and Albert, J., "Implicit Approximate Factorization Schemes for the Efficient Solution of Steady Transonic Flow Problems," *AIAA Journal*, Vol. 16, No. 6, June 1978, pp. 573-579.

[8] Sankar, N.L., and Malone, J.B., "Solution Techniques for the Steady and Unsteady Transonic Full Potential Equations," in *Advances in Computational Transonics*, W.G. Habashi, editor, Pineridge Press, Swansea, U.K., 1985, pp. 257-287.

[9] Morgenstern, A., Jr. , and Azevedo, J.L.F., "Influence of Convergence Parameters and Mesh Refinement on Full-Potential Solutions of Airfoil Flows," *Proceedings of the 10th Brazilian Congress of Mechanical Engineering*, Vol. I, Rio de Janeiro, RJ, Dec. 5-8, 1989, pp. 149-152.

[10] Jameson, A., "Transonic Potential Flow Calculations Using Conservative Form," *Proceedings of the AIAA 2nd Computational Fluid Dynamics Conference*, 1975, pp. 148-155.

[11] Baker, T.J., and Forsey, C.R., "A Fast Algorithm for the Calculation of Transonic Flow over Wing/Body Combinations," *AIAA Journal*, Vol. 21, No. 1, Jan. 1983, pp. 60-67.

[12] de Mattos, B.S., "Calculation of Three-Dimensional Transonic Potential Flow Using an Implicit Approximate Factorization Algorithm," Master's Dissertation, Instituto Tecnológico de Aeronáutica, São José dos Campos, SP, Brasil, Mar. 1990 (in Portuguese, original title is "Cálculo do Escoamento Potencial Transônico Através de um Algoritmo Implícito de Fatorização Aproximada").

[13] Carlson, L.A., "TRANSEP : A Program for High Lift Separated Flow About Airfoils," NASA CR 3376, Dec. 1980.

[14] Pulliam, T.H., "Implicit Finite-Difference Methods for the Euler Equations," in *Advances in Computational Transonics*, W.G. Habashi, editor, Pineridge Press, Swansea, U.K., 1985, pp. 503-542.

[15] Jameson, A., Caughey, D.A., Newman, P.A., and Davis, R.M., "A Brief Description of the Jameson-Caughey NYU Transonic Swept Wing Computer Program — FLO22," NASA TMX-73996, 1976.

III ENCIT – Itapema, SC (Dezembro 1990)

TWO DIMENSIONAL FULL POTENTIAL SOLUTIONS OF LIFTING AIRFOIL FLOWS

A. MORGENSTERN JR., J. L. F. AZEVEDO and B. S. DE MATTOS
Centro Técnico Aeroespacial — EMBRAER
Instituto de Atividades Espaciais — DTE / TEE / EAD
12225 — São José dos Campos — SP

SUMMARY

The application of two-dimensional transonic flow solvers based on the conservative full potential formulation is described. The Holst and Ballhaus artificial density scheme is used for the spatial discretization of the governing equation. Convergence to steady state is achieved through iteration in pseudo-time using the AF2 implicit approximate factorization algorithm. Results for lifting cases are presented, and compared to the available data. The effects of angle of attack, freestream Mach number, and overall grid smoothness and orthogonality on the accuracy of the computations are investigated.

INTRODUCTION

Airfoil fows are of fundamental importance in many aerodynamic applications. Therefore, the interest in developing computational tools that are able to simulate such type of flows is rather obvious. Moreover, since the problem is treated in a two dimensional fashion, computational requirements are much less stringent. This accounts for much more freedom in trying out different concepts when developing a flow solver code. Despite the less severe computational requirements, these fows can actually be quite complex. The combination of fast turnaround time and complex physics makes airfoil flows ideal candidates for algorithm development test cases.

The present work is aimed at studying transonic potential flows over two dimensional airfoils. The formulation used is based on the full potential equation written in steady, conservation-law form for a 2-D, body-conforming, curvilinear coordinate system. The iteration scheme adopted here is the AF2 algorithm, or approximate factorization scheme 2. The spatial discretization employs the Holst and Ballhaus[1] artificial density scheme, which provides the appropriate upwind influence in regions of supersonic flow. Boundary conditions are implemented implicitly which improves the robustness of the overall algorithm. Lifting solutions are obtained by adding a compressible vortex correction to the freestream far-field boundary, and by imposing the potential jump across the wake.

Two different automatic mesh generators were implemented. The first was an elliptic[2] grid generator which computes the mesh point positions as a solution of Laplace's equation. Dirichlet-type boundary conditions are used in this case in the normal direction by specifying the position of the grid points over the airfoil surface and on the outer boundary. The other grid generator uses an algebraic method[3] that allows for the control of wake and external boundary positions, as well as orthogonality at computational domain boundaries. Results for lifting cases are presented, and compared to computations performed with available commercial codes.

GOVERNING EQUATION

The full potential equation can be written in conservative form for a 2-D, body-conforming, curvilinear coordinate system as

$$\left(\frac{\rho U}{J}\right)_\xi + \left(\frac{\rho V}{J}\right)_\eta = 0 \tag{1}$$

If velocities are made dimensionless with respect to the critical speed of sound a_*, and density is nondimensionalized by the stagnation density ρ_t, the expression for the density in the curvilinear coordinate system can be written as

$$\rho = [1 - \frac{\gamma - 1}{\gamma + 1}(U\phi_\xi + V\phi_\eta)]^{1/(\gamma-1)} \tag{2}$$

Here, ϕ is the complete velocity potential, and the subscripts indicate partial derivatives with respect to each coordinate direction. The U and V are the contravariant velocity components which are given by

$$U = A_1\phi_\xi + A_2\phi_\eta, \qquad V = A_2\phi_\xi + A_3\phi_\eta \tag{3}$$

The metric coefficients are defined as

$$A_1 = \xi_x^2 + \xi_y^2, \quad A_2 = \xi_x\eta_x + \xi_y\eta_y, \quad A_3 = \eta_x^2 + \eta_y^2 \tag{4}$$

The coordinate transformation is typically known only numerically, and it is of the form

$$\xi = \xi(x, y) \qquad \eta = \eta(x, y) \tag{5}$$

This mapping from physical space to computational space is illustrated schematically in Fig. 1. The Jacobian of the transformation can be computed from

$$J = (x_\xi y_\eta - x_\eta y_\xi)^{-1} \tag{6}$$

and the various metric terms are given by

$$\begin{aligned} \xi_x &= J y_\eta & \xi_y &= -J x_\eta \\ \eta_x &= -J y_\xi & \eta_y &= J x_\xi \end{aligned} \tag{7}$$

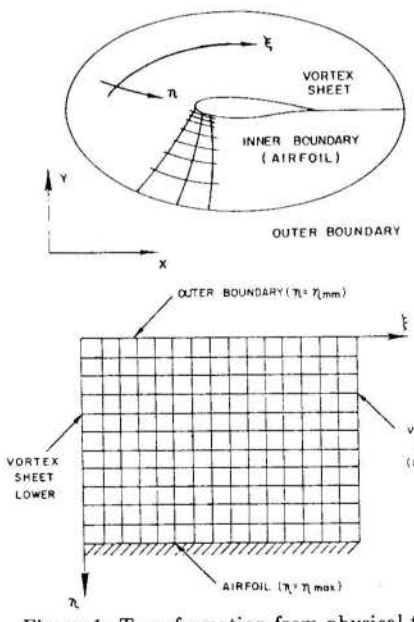

a) Physical domain

b) Computational domain

Figure 1: Transformation from physical to computational domain.

GRID GENERATION

The construction of suitable computational grids is an essential part of these finite difference calculations. In the present work, O-type meshes were generated about arbitrary 2-D airfoils using two different grid generation schemes, an algebraic generator and an elliptic solver. These schemes produced meshes that differ significantly in their interior point distribution, despite having the same point distri-

bution on the airfoil surface and on the external boundary. As we will also show, this can have some effect on the final result of the aerodynamic calculations, regardless of mesh refinement. Both grid generation schemes allow for the control of external boundary and surface mesh distribution. However, the algebraic grid generator[3,4] permits control of wake position, smoothness of interior point distribution and grid stretching. Moreover, it generates a mesh that has the property of orthogonality at the airfoil surface and outer boundary. The elliptic grid generator[2] computes the mesh point distribution as a solution of Laplace's equation, and places no requirement on orthogonality at the airfoil surface.

Elliptic Grid Generation. The elliptic grid generator employed in this work is an adaptation of the scheme presented by Thompson et al.[2]. It establishes a regular and smooth mesh distribution around arbitrary bodies through numerically generated solutions of Laplace's equation.

The equations are transformed to a computational domain where ξ and η are the independent variables and x and y are the dependent variables. The transformed equations are given by

$$\begin{aligned} Ax_{\xi\xi} - 2Bx_{\xi\eta} + Cx_{\eta\eta} &= 0 \\ Ay_{\xi\xi} - 2By_{\xi\eta} + Cy_{\eta\eta} &= 0 \end{aligned} \tag{8}$$

where

$$A = x_\eta^2 + y_\eta^2, \quad B = x_\xi x_\eta + y_\xi y_\eta, \quad C = x_\xi^2 + y_\xi^2 \tag{9}$$

The numerical solution is achieved by establishing a finite difference aproximation to Eq. 8. All derivatives are replaced by standard second-order accurate finite differences. Thus, a residual operator is given by

$$L(\ )_{i,j} = [A_{i,j}\delta_{\xi\xi} - 2B_{i,j}\delta_{\xi\eta} + C_{i,j}\delta_{\eta\eta}](\ )_{i,j} \tag{10}$$

where the indices (i,j) indicate the mesh point position, and

$$\begin{aligned} \delta_{\xi\xi}(\ )_{i,j} &= (\ )_{i+1,j} - 2(\ )_{i,j} + (\ )_{i-1,j} \\ \delta_{\xi\eta}(\ )_{i,j} &= \frac{1}{4}[(\ )_{i+1,j+1} - (\ )_{i+1,j-1} + \\ &\quad (\ )_{i-1,j+1} - (\ )_{i-1,j-1}] \\ \delta_{\eta\eta}(\ )_{i,j} &= (\ )_{i,j+1} - 2(\ )_{i,j} + (\ )_{i,j-1} \end{aligned} \tag{11}$$

The mesh is assumed periodic in the ξ-direction. Hence, given boundary values on the airfoil surface and on the outer boundary, and an initial solution for $x_{i,j}$ and $y_{i,j}$, the final interior values are computed by relaxation. The relaxation scheme employed is the alternate direction implicit (ADI) algorithm presented by Holst[5]. This is an approximate factorization type scheme, and it can be expressed as

$$N\Delta(\ )_{i,j}^n + \omega L(\ )_{i,j}^n = 0 \tag{12}$$

In this case, the N operator is such that

$$\alpha N(\ )_{i,j}^n = -\left(\alpha - A_{i,j}^n\delta_{\xi\xi}\right)\left(\alpha - C_{i,j}^n\delta_{\eta\eta}\right)(\ )_{i,j}^n \tag{13}$$

Here, α and ω are relaxation parameters and n is the iteration index. Moreover, one should observe that we are solving for the correction in the dependent variable, i. e. , $\Delta(\ )_{i,j}^n = (\ )_{i,j}^{n+1} - (\ )_{i,j}^n$. An algorithm in this form is said to be in *delta form*. This has several advantages for the solution of steady-state finite difference problems. The solution for each iteration can be obtained in a two-step sequence as follows.

- Step 1 :

$$\begin{aligned} \left(\alpha - A_{i,j}^n\delta_{\xi\xi}\right) f_{i,j}^n &= \alpha\omega L x_{i,j}^n \\ \left(\alpha - A_{i,j}^n\delta_{\xi\xi}\right) g_{i,j}^n &= \alpha\omega L y_{i,j}^n \end{aligned} \tag{14}$$

- Step 2 :

$$\begin{aligned} \left(\alpha - C_{i,j}^n\delta_{\eta\eta}\right)\Delta x_{i,j}^n &= f_{i,j}^n \\ \left(\alpha - C_{i,j}^n\delta_{\eta\eta}\right)\Delta y_{i,j}^n &= g_{i,j}^n \end{aligned} \tag{15}$$

As mentioned above, we have that

$$\Delta x_{i,j}^n = x_{i,j}^{n+1} - x_{i,j}^n, \quad \Delta y_{i,j}^n = y_{i,j}^{n+1} - y_{i,j}^n \tag{16}$$

and $f_{i,j}^n$ and $g_{i,j}^n$ are intermediate results. In step 1, the f and g arrays are obtained by solving two periodic tridiagonal matrix equations for each η = constant line. The values of x and y, for the $n+1$ iteration level, are then obtained in the second step from the f and g arrays by solving two standard tridiagonal matrix equations for each ξ = constant line.

Algebraic Grid Generation. The algebraic grid generation scheme used in the present work was discussed by Fletcher[3]. The actual implementation of the scheme, however, follows the work of de Mattos[4]. The scheme generates a computational mesh that is orthogonal to the airfoil surface as well as to the outer boundary. The outer boundary used in the present work is defined as a circumference of radius 5.5 times the airfoil chord.

The concept involved in the present algebraic grid generator is one of defining intermediate surfaces between the airfoil and the outer boundary. For this reason, the method is sometimes called the multi-surface algorithm. These surfaces will allow for greater control of the interior mesh point distribution and not necessarily they will coincide with any final grid location. In particular, if two interior surfaces are used, which is the case here, one can obtain a mesh which is orthogonal to both boundaries. The process of constructing these interior surfaces starts by linearly interpolating them between the two bounding surfaces. This yields two surfaces which are in the correct physical location, but that do not have the correct relation between the corresponding ξ-points. This dependence is, then, modified such that lines going through corresponding points in the airfoil surface and the adjacent interior surface are orthogonal to the airfoil surface. Similarly, lines going through corresponding points in the outer surface and its adjacent interior surface must be orthogonal to the first.

Given the coordinates of all four surfaces, the computation of the interior point distribution by the multisurface algorithm in this case can be implemented as

$$x_{i,j} = \sum_{\ell=1}^{4} S_\ell \bar{X}_{\ell,i} \qquad y_{i,j} = \sum_{\ell=1}^{4} S_\ell \bar{Y}_{\ell,i} \tag{17}$$

Here i and j are the coordinate position indices in the ξ- and η-directions, respectively. The index ℓ indicates one of the four basic curves previously described. In the present nomenclature, $\ell = 1$ is the airfoil surface, and $\ell = 4$ is the outer boundary. $\bar{X}_{\ell,i}$ and $\bar{Y}_{\ell,i}$ are the coordinates of i-points along each of the ℓ-curves. Finally, the blending functions S_ℓ are defined by

$$\begin{aligned} S_1 &= \left(1 - s^2\right)(1 - a_1 s) \\ S_2 &= s(1-s)^2(a_1 + 2) \\ S_3 &= s^2(1-s)(a_2 + 2) \\ S_4 &= s^2[1 - a_2(1-s)] \end{aligned} \tag{18}$$

where

$$a_1 = \frac{2}{(3a_w - 1)}, \quad a_2 = \frac{2}{(2 - 3a_w)}, \quad a_w = 0.64 \tag{19}$$

In the above equations s is a normalized parameter in the η-direction. It is set equal to zero on the airfoil surface and equal to one at the outer boundary. The choice of the sequence of values for the parameter s will essentially determine the grid stretching in the normal direction.

FINITE DIFFERENCE FORMULATION

The spatial differencing scheme used in the present study is the Holst and Ballhaus[1,6] artificial density scheme. By this scheme, artificial viscosity is intrinsically added in supersonic regions through an upwind bias of the density coefficients. The difference scheme applied to the 2-D full potential equation in conservation-law form for general curvilinear coordinates yields[5,7]

$$\bar{\delta}_\xi\left(\frac{\tilde{\rho}U}{J}\right)_{i+\frac{1}{2},j} + \bar{\delta}_\eta\left(\frac{\tilde{\rho}V}{J}\right)_{i,j+\frac{1}{2}} = 0 \tag{20}$$

where $\bar{\delta}_\xi$ and $\bar{\delta}_\eta$ are standard 1st-order accurate backward difference operators in the ξ and η directions, respectively. Stability in supersonic regions of flow is achieved by an upwind bias of the density coefficients. In the present implementation, it proved not to be necessary to perform any upwinding of the density coefficient in the η-direction. Hence, we used $\tilde{\rho}_{i,j+\frac{1}{2}} = \rho_{i,j+\frac{1}{2}}$ in the computations performed here. The $\tilde{\rho}_{i+\frac{1}{2},j}$ density coefficient is defined by

$$\tilde{\rho}_{i+\frac{1}{2},j} = (1 - \nu_{i+k,j})\rho_{i+\frac{1}{2},j} + \nu_{i+k,j}\,\rho_{i+2k-\frac{1}{2},j} \tag{21}$$

The ν coefficient and the k index are responsible for providing the upwind influence, where

$$k = \begin{cases} 0 & \text{when } U_{i+\frac{1}{2},j} > 0 \\ 1 & \text{when } U_{i+\frac{1}{2},j} < 0 \end{cases} \tag{22}$$

and the switching function $\nu_{i+k,j}$ is given by

$$\nu_{i+k,j} = \max[0, (M^2_{i+k,j} - 1)C] \tag{23}$$

Here, C is a user specified constant, and the suggested range is $1.0 \leq C \leq 2.0$.

The contravariant velocity components in Eq. 20 are given by

$$\begin{aligned} U_{i+\frac{1}{2},j} &= A_{1_{i+\frac{1}{2},j}} \phi_{\xi_{i+\frac{1}{2},j}} + A_{2_{i+\frac{1}{2},j}} \phi_{\eta_{i+\frac{1}{2},j}} \\ V_{i,j+\frac{1}{2}} &= A_{2_{i,j+\frac{1}{2}}} \phi_{\xi_{i,j+\frac{1}{2}}} + A_{3_{i+\frac{1}{2},j}} \phi_{\eta_{i,j+\frac{1}{2}}} \end{aligned} \tag{24}$$

The metric coefficients A_1, A_2 and A_3, and the Jacobian J are calculated at the mesh half-points. This is more expensive than computing them at the mesh integer points and then obtaining their values at half-points by averaging. However, our computations showed that the present procedure produces much better shock resolution and it was therefore, adopted in this work. The potential derivatives in Eq. 24 are given by

$$\begin{aligned} \phi_{\xi_{i+\frac{1}{2},j}} &= \phi_{i+1,j} - \phi_{i,j} \\ \phi_{\eta_{i+\frac{1}{2},j}} &= \frac{(\phi_{i+1,j+1} - \phi_{i+1,j-1} + \phi_{i,j+1} - \phi_{i,j-1})}{4} \\ \phi_{\xi_{i,j+\frac{1}{2}}} &= \frac{(\phi_{i+1,j+1} - \phi_{i-1,j+1} + \phi_{i+1,j} - \phi_{i-1,j})}{4} \\ \phi_{\eta_{i,j+\frac{1}{2}}} &= \phi_{i,j+1} - \phi_{i,j} \end{aligned} \tag{25}$$

With the above quantities, the densities $\rho_{i+\frac{1}{2},j}$ and $\rho_{i,j+\frac{1}{2}}$ can be calculated by Eq. 2.

ITERATION SCHEME

Relaxation schemes for the conservative, steady full potential equation can be written in general delta form[7] as

$$NC^n_{i,j} + \omega L\phi^n_{i,j} = 0 \tag{26}$$

where n is the iteration index, and ω is a relaxation parameter. $L\phi^n_{i,j}$ is the nth iteration residue, and it is defined by Eq. 20. $C^n_{i,j}$ is the nth iteration correction given by

$$C^n_{i,j} = \phi^{n+1}_{i,j} - \phi^n_{i,j} \tag{27}$$

The N operator is chosen to approximate L as closely as possible. For the AF2 implicit approximate factorization scheme, the ξ- or η-difference approximation is split between two steps to generate time-dependent dissipation important to the stability of the pseudo-time march convergence process.

The N operator employed in this case splits the η-operator and, hence, generates a $\phi_{\eta t}$-type term providing temporal damping in the η-direction. In order to provide time-dependent dissipation in the ξ-direction, a $\phi_{\xi t}$-type term is added explicitly to the ξ-operator. This term is of the form

$$\mp\alpha\beta\vec{\bar{\delta}}_\xi$$

The parameter β is a user specified constant which can be adjusted as needed. The $\vec{\bar{\delta}}_\xi$ notation indicates that the ξ-difference operator is always upwind. For a typical airfoil flowfield and with our convention of positive ξ-direction, this operator will be a forward difference in the lower surface and a backward difference in the upper surface. The sign is chosen so as to increase the magnitude of the matrix main diagonal coefficient. The N operator can be expressed by

$$\begin{aligned} \alpha N C^n_{i,j} &= -\left[\alpha - \bar{\delta}_\eta \left(\frac{\bar{\rho} A_3}{J}\right)_{i,j-\frac{1}{2}}\right] \\ &\quad \left[\alpha\bar{\delta}_\eta - \bar{\delta}_\xi \left(\frac{\bar{\rho} A_1}{J}\right)_{i+\frac{1}{2},j} \vec{\delta}_\xi \mp \alpha\beta\vec{\bar{\delta}}_\xi\right] C^n_{i,j} \end{aligned} \tag{28}$$

Here, α is a convergence acceleration parameter, and the $\vec{\delta}_\xi$ and $\vec{\delta}_\eta$ are standard 1st-order forward difference operators. The proper choice of the α and ω parameters affect significantly the convergence rate of the solution. A detailed discussion on suitable choices for these parameters is presented by Ballhaus et al.[8], Holst[7], and Morgenstern and Azevedo[9], among others.

The AF2 algorithm can be implemented in a two step format as follows.

- Step 1 :
$$\left[\alpha - \vec{\delta}_\eta \left(\frac{\bar{\rho} A_3}{J}\right)_{i,j-\frac{1}{2}}\right] f^n_{i,j} = \alpha\omega L\phi^n_{i,j} \tag{29}$$

- Step 2 :
$$\left[\alpha\bar{\delta}_\eta - \bar{\delta}_\xi \left(\frac{\bar{\rho} A_1}{J}\right)_{i+\frac{1}{2},j} \vec{\delta}_\xi \mp \alpha\beta\vec{\bar{\delta}}_\xi\right] C^n_{i,j} = f^n_{i,j} \tag{30}$$

The solution of the simple bidiagonal matrix of step 1 for each ξ = constant line yields the intermediate result $f^n_{i,j}$. The correction array $C^n_{i,j}$ is then obtained by the solution of the tridiagonal matrix equation of step 2 for each η = constant line.

BOUNDARY CONDITIONS

The condition of flow tangency on the airfoil surface requires that the η-component of the contravariant velocity should vanish at the surface. The implementation of this condition in the residual computation requires that

$$\left(\frac{\rho V}{J}\right)_{i,NJ-\frac{1}{2}} = -\left(\frac{\rho V}{J}\right)_{i,NJ+\frac{1}{2}} \tag{31}$$

where NJ is the j index at the airfoil surface. In a similar fashion, to impose the tangency condition in equations in which ϕ_η is required at the airfoil surface, the $V = 0$ condition is used to obtain

$$(\phi_\eta)_{i,NJ} = -\left(\frac{A_2}{A_3}\phi_\xi\right)_{i,NJ} \tag{32}$$

Periodic boundary conditions are used in the ξ-direction since O-type meshes are employed.

At the outer boundary, for lifting cases, the velocity potential is modified to take into account the circulation. This circulation boundary condition is applied by adding the usual vortex solution to the initial far-field velocity potential. Hence, the potential at the outer boundary can be written as

$$\phi = \phi_{initial} + \phi_{vortex} \tag{33}$$

where $\phi_{initial} = \phi_\infty$ and

$$\phi_{vortex} = -\frac{\Gamma}{2\pi} tan^{-1}\left(\frac{\beta y}{x}\right) \tag{34}$$

Here, Γ is the circulation strength, $\beta = \sqrt{1 - M^2}$, and x and y are the coordinates of the outer boundary mesh point in a coordinate system which has the vortex core at its origin. In the present work, the vortex core position was assumed to be at the airfoil quarter chord point. The circulation is computed by enforcing the Kutta condition at the airfoil trailing edge. This is acomplished by setting ϕ_ξ to zero at the airfoil trailing edge. Hence, the circulation can be calculated by

$$\tilde{\Gamma}^n = \phi^n_{NI-1,NJ} - \phi^n_{2,NJ} \tag{35}$$

where $i = 1$ represents points along the wake lower surface, and $i = NI$ denotes points on the wake upper surface.

In order to obtain an acceptable convergence rate, the value of circulation $\tilde{\Gamma}^n$ obtained from the expression above must be either underrelaxed or overrelaxed. The procedure adopted here computes

$$\overline{\Gamma}^n = R_g\tilde{\Gamma}^n + (1 - R_g)\Gamma^{n-1} \tag{36}$$

where R_g is a relaxation parameter specified by the user. A suitable value used in the present work is $R_g = 0.5$. Finally, the value of circulation which is actually accepted as the circulation at time level n is

$$\Gamma^n = \frac{1}{2}\left(\overline{\Gamma}^n + \Gamma^n_{estimated}\right) \tag{37}$$

Here, $\Gamma^n_{estimated}$ is the value of circulation at iteration level n estimated at the end of the $(n-1)$-th iteration cycle. This value is required for the implicit implementation of boundary conditions, as we will see shortly. The need for this averaging between the under- or overrelaxed value of circulation at the present time level and the value estimated at the end of the previous time level is discussed by Holst and Thomas[10]. At the end of the n-th iteration, we must compute the estimated value $\Gamma^{n+1}_{estimated}$, which is done here using

$$\Gamma^{n+1}_{estimated} = 2\Gamma^n - \Gamma^{n-1} \tag{38}$$

Further discussion of the circulation computation procedure is presented by de Mattos and Azevedo[11]. We observe, however, that the form of computing $\tilde{\Gamma}^n$ in the present work is different from that adopted in Ref. [11].

The velocity potential jump across the wake must be explicitly enforced, and this is done here by making

$$\phi^n_{NI,j} = \phi^n_{1,j} + \Gamma^n \tag{39}$$

along the entire vortex sheet. Moreover, in the tridiagonal solution in step 2, one must take into account the periodicity in the ξ-direction as well as the jump in the potential along the wake. In differencing the correction across the wake, the jump condition becomes

$$\Gamma^{n+1} - \Gamma^n = C^n_{NI,j} - C^n_{1,j} \tag{40}$$

Since Γ^{n+1} is unknown at this point in the computation, its value must be estimated as described above. Hence, for the implicit solution we obtain the relation

$$C^n_{NI,j} = C^n_{1,j} + \left(\Gamma^{n+1}_{estimated} - \Gamma^n\right) \tag{41}$$

In step 1, the value of $f_{i,NJ+1}$ is required as a special boundary condition inherent to the AF2 algorithm. The procedure adopted here was to assume $f_\eta = 0$ at the airfoil surface, which is also the implicit boundary condition used by Holst[5]. We remark, however, that imposing f itself equal to zero at the airfoil surface[11] also produces good results.

COMPUTATIONAL RESULTS

As previously discussed, two different mesh generator concepts were implemented in the present work. In order to be able to compare the results obtained with the different meshes, all cases considered a grid with 99 x 24 points in the ξ- and η-directions, respectively. Moreover, all grids use an O-type mesh topology, and the external boundary is a circumference of radius 5.5 times the airfoil chord. The distribution of mesh points along the airfoil surface and on the outer boundary is also the same for all cases. A partial view of the mesh generated by the elliptic solver for a NACA 0012 airfoil is shown in Fig. 2. We observe that the mesh point distribution is very smooth, but it is clear that η grid lines are not orthogonal to the airfoil surface. An example of a grid generated by the algebraic process is shown in Fig. 3 for a NACA 64A410 airfoil. In this case, the orthogonality at the airfoil surface is evident. However, it also becomes clear that the mesh refinement in the regions upstream of the leading edge and along the wake is not very good. This is a direct consequence of forcing the η grid lines to leave the airfoil in the normal direction in regions of high surface curvature. A more direct comparison of the meshes generated by both algorithms is shown in Fig. 4. In this case, the geometry of a NACA 0012 section was used and all grid parameters are the same, as previously discussed. The regularity of the elliptic generated mesh, as well as the orthogonality at the surface for the algebraic mesh, are quite evident from this figure. Nevertheless, the differences between the two resultant meshes are remarkable.

The pressure coefficient distribution on the airfoil for a NACA 0012 section at freestream Mach number $M_\infty = 0.63$ and $\alpha = 2°$ is shown in Fig. 5. The computations performed with the present algorithm, and using both meshes, are compared with the results obtained with the non-conservative, commercial TRANSEP code[12]. We observe that the results obtained with the mesh generated by the elliptic solver seem to have a better agreement with the TRANSEP resuls, except for the suction peak on the airfoil leading edge. Nevertheless, both results are very good in this case, which is not surprising for such a simple subcritical flow case. Results for a supercritical case for the same airfoil are shown in Fig. 6. The flow conditions in this case are $M_\infty = 0.75$ and $\alpha = 2°$. The present computational results are again compared with those obtained with the TRANSEP code. The difference in the shock position for the calculations with the present algorithm is quite large. The shock obtained for the solution with the algebraic grid is located farther downstream than the one obtained with the elliptic grid. The former is at about 58% chord while the latter is at 53% chord. Both shocks have approximately the same strength. We remark that the TRANSEP shock is located upstream of both the previous results at about 45% of the chord, which is the expected behavior. Non-conservative codes allow for the creation of

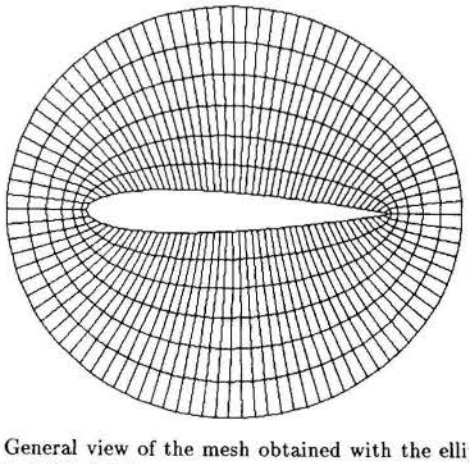

Figure 2: General view of the mesh obtained with the elliptic solver for a NACA 0012 airfoil.

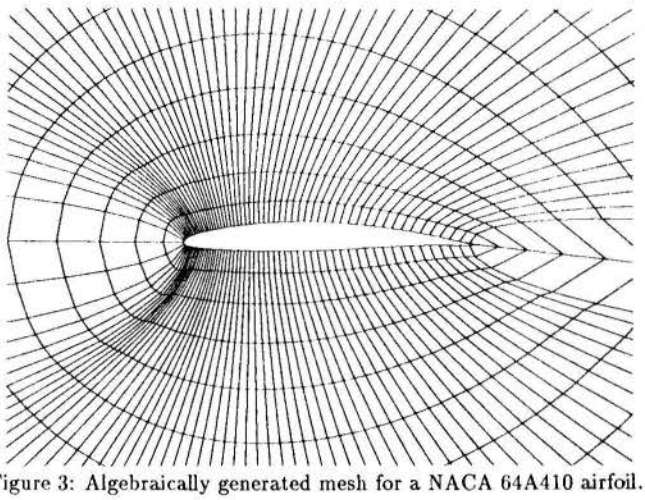

Figure 3: Algebraically generated mesh for a NACA 64A410 airfoil.

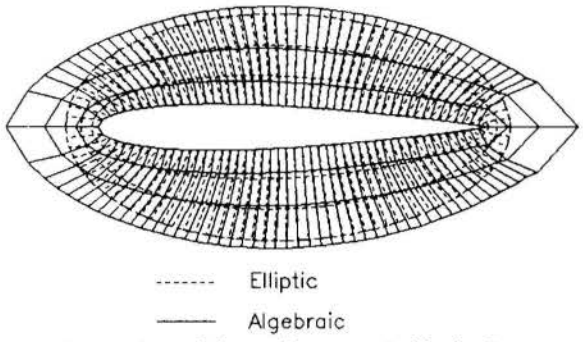

Figure 4: Comparison of the meshes generated by both processes for a NACA 0012 airfoil.

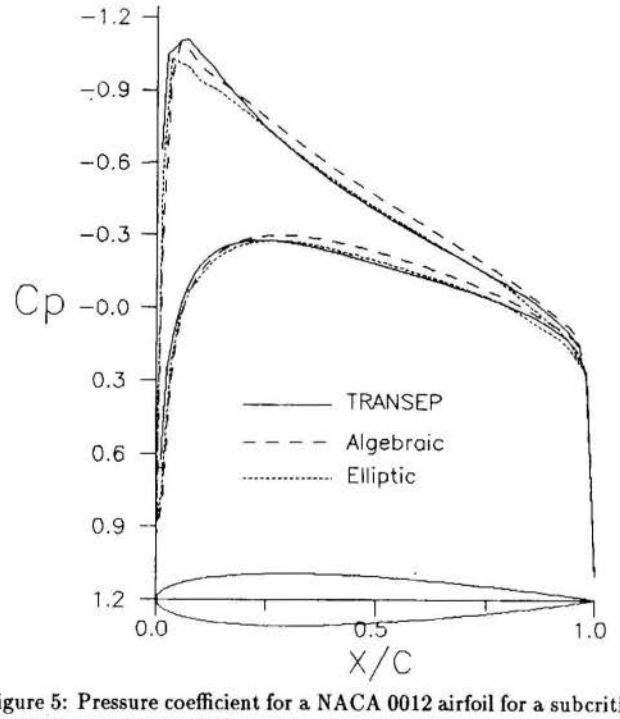

Figure 5: Pressure coefficient for a NACA 0012 airfoil for a subcritical case ($M_\infty = 0.63$, $\alpha = 2°$).

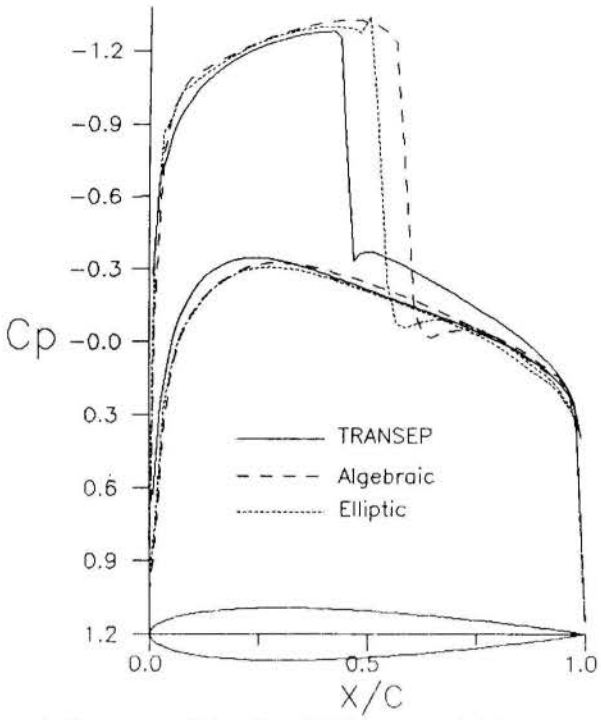

Figure 6: Pressure coefficient for a NACA 0012 airfoil for a supercritical case ($M_\infty = 0.75$, $\alpha = 2°$).

mass across the shock which manifests itself as if simulating a boundary layer. The result of this numerical process is a weaker shock located further upstream, which actually turns out to be closer to what happens in practice. Although further validation would be necessary, the authors believe at this point that the correct full potential solution in this case is the one obtained for the algebraic grid. Despite the fact that the elliptic grid seems to be smoother, the fact that η lines are not orthogonal to the airfoil surface may cause inaccuracies in the implementation of the flow tangency condition. We must emphasize, however, that $V = 0$ is the correct way of enforcing the zero normal velocity boundary condition, regardless whether the grid is orthogonal to the surface or not. Moreover, we also observe that the elliptic grid solution presents a pre-shock oscillation which may be an indication of too little artificial dissipation.

Pressure coefficients for a NACA 64A410 at $M_\infty = 0.7$ and $\alpha = 0°$ are shown in Fig. 7. As before, computations with the present method using both algebraic and elliptic grids are compared with results obtained with the TRANSEP code. In general, the results are in good agreement. The shock obtained with the non-conservative formulation is weaker than that produced by the conservative computations, as should be expected. Pressure contours for the same airfoil at $M_\infty = 0.72$ and $\alpha = 0°$ are shown in Fig. 8. This solution was obtained using the grid generated algebraically. The concentration of contours on the airfoil upper surface clearly indicates the shock location in this case. The pressure coefficient distribution for an EA153809 airfoil at $M_\infty = 0.5$ and $\alpha = 0°$ is shown in Fig. 9. The computations with the present algorithm used the algebraic grid, and the present results are compared with those obtained with the TRANSEP and BIDIM[13] codes. The latter is a subsonic, 2-D, panel code with boundary layer correction. Except for the suction peak on the lower surface of the airfoil leading edge, the results do agree reasonably. The results in the trailing edge region for both TRANSEP and BIDIM are not very good, and the present computations show a much better behavior.

The last cases considered in the present work involve a BM170410 airfoil, and all the results computed with the present formulation used the algebraic grid. The pressure coefficient distribution for a $M_\infty = 0.7$ and $\alpha = 0°$ case is shown in Fig. 10. This is a slightly supercritical case in which $C_p^* = 0.78$. We observe that the present method did capture a very weak shock terminating the supersonic flow region. This effect is not captured by the TRANSEP computation. Moreover, the solution at the airfoil trailing edge with the present method is also slightly better than the TRANSEP result. Along most of the airfoil surface, however, the results are in good agreement. The lift

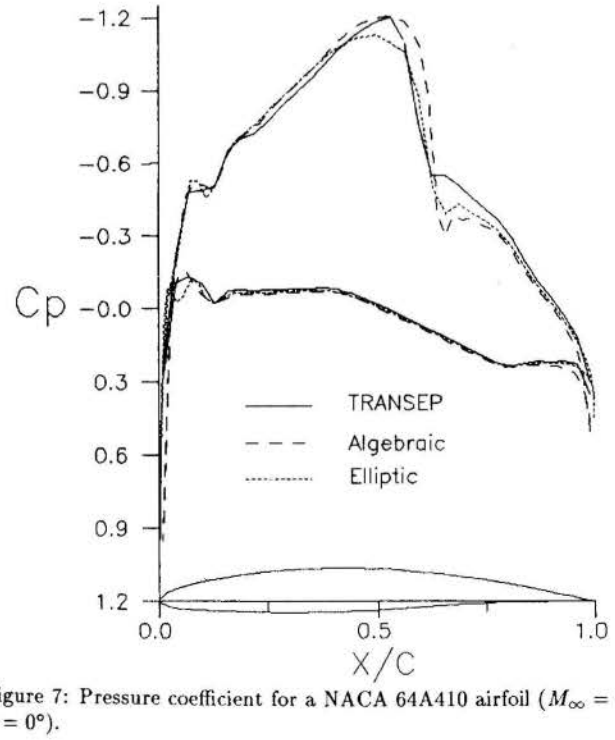

Figure 7: Pressure coefficient for a NACA 64A410 airfoil ($M_\infty = 0.7$, $\alpha = 0°$).

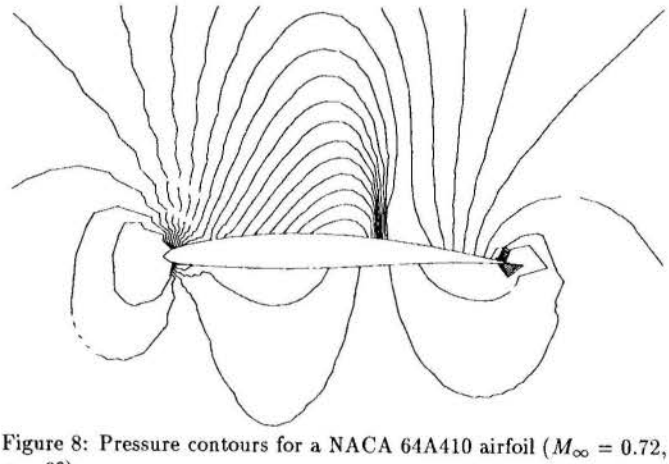

Figure 8: Pressure contours for a NACA 64A410 airfoil ($M_\infty = 0.72$, $\alpha = 0°$).

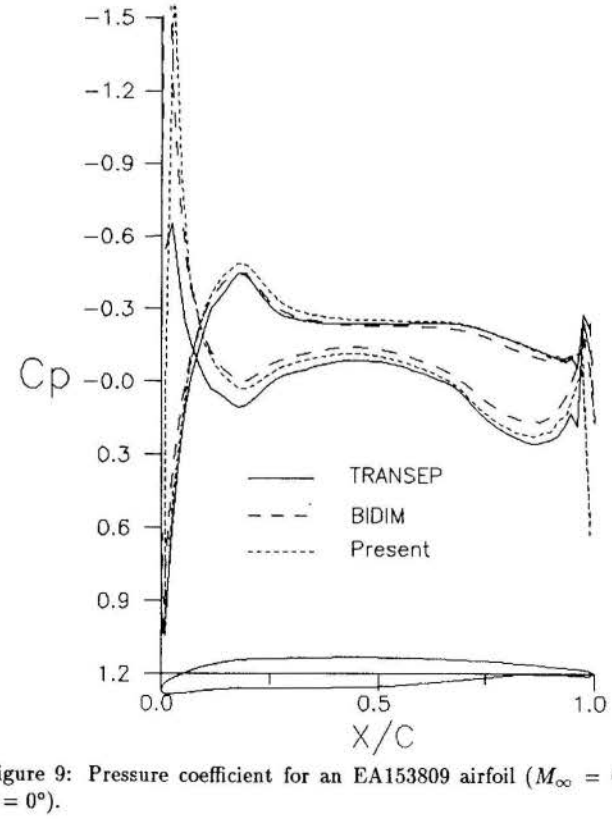

Figure 9: Pressure coefficient for an EA153809 airfoil ($M_\infty = 0.5$, $\alpha = 0°$).

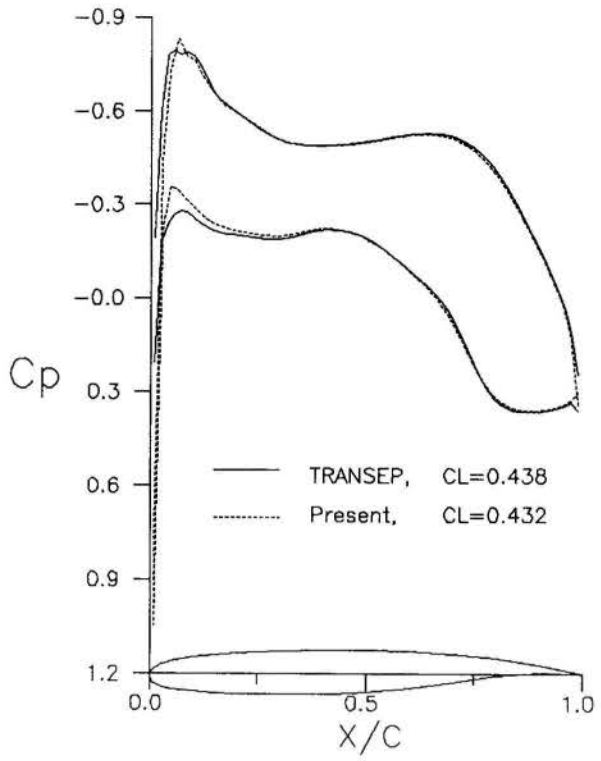

Figure 10: Pressure coefficient for a BM170410 airfoil for a slightly supercritical case ($M_\infty = 0.7$, $\alpha = 0°$).

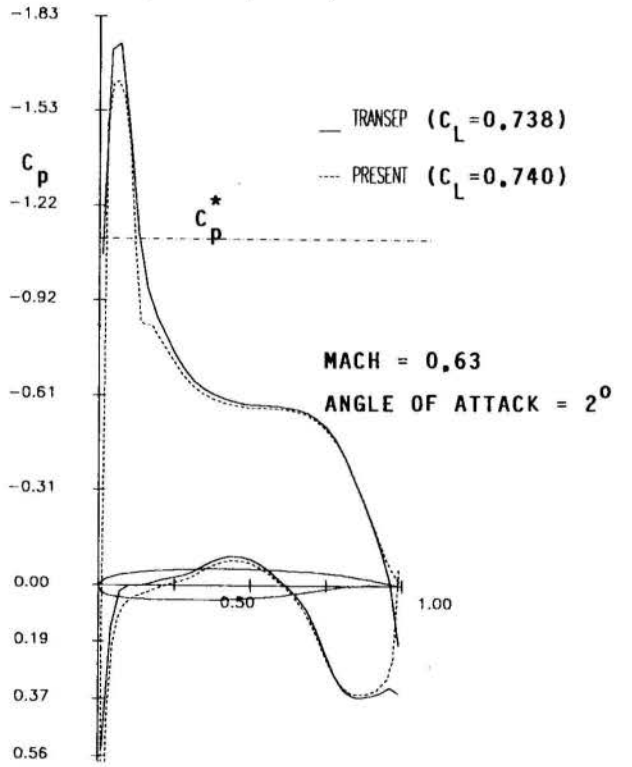

Figure 11: Pressure coefficient for a BM170410 airfoil for a supercritical case ($M_\infty = 0.63$, $\alpha = 2°$).

coefficient in the case of the solution with the present formulation is $c_\ell = 0.432$. This value should be compared with $c_\ell = 0.438$ obtained by the TRANSEP solution. It is clear that the agreement is very good. Results for a truly supercritical case are shown in Fig. 11. Here, a flight condition of $M_\infty = 0.63$ and $\alpha = 2°$ is considered. Again, there is a good correspondence between the present results and those obtained with the TRANSEP code. The present formulation seems to produce a sharper shock, although the shock location is somewhat the same for both results. The present formulation, however, seems to underpredict the leading edge suction peak as compared to the TRANSEP result. Once more, the comparison of the lift coefficients obtained from both codes is extremely good.

CONCLUDING REMARKS

The development of a finite difference algorithm for the solution of the conservative, transonic full potential equation in two dimensions was described. Several lifting airfoil flow cases were studied, and these provided for some validation of the computational procedure developed. The quality of the results obtained with the present code is, at least, comparable with that which can be obtained with available commercial codes. In some instances, we were able to show that the present algorithm does provide better accuracy in the results.

The present work has also shown the importance of the grid generation algorithm in the accurate computation of aerodynamic flowfields. Two different grid generation schemes were implemented, and the relative merits of both were discussed. Despite producing a smoother mesh throughout the flowfield, the elliptic solver grid generator cannot ensure orthogonality at the airfoil surface. This can be a serious handicap for the computation of strong shocks over thicker airfoils.

REFERENCES

[1] Holst, T.L., and Ballhaus, W.F., "Fast Conservative Schemes for the Full Potential Equation Applied to Transonic Flows," *AIAA Journal*, Vol. 17, No. 2, Feb. 1979, pp. 145-152.

[2] Thompson, J.F., Thames, F.C., and Mastin, C.M., "Automatic Numerical Generation of Body-Fitted Curvilinear Coordinate System for Field Containing Any Number of Arbitrary Two-Dimensional Bodies," *Journal of Computational Physics*, Vol. 15, 1974, pp. 299-319

[3] Fletcher, C.A.J., *Computational Techniques for Fluid Dynamics 2 — Specific Techniques for Different Flow Categories*, Springer-Verlag, New York, 1988.

[4] de Mattos, B.S., "Calculation of Three-Dimensional Transonic Potential Flow Using an Implicit Approximate Factorization Algorithm," Master's Dissertation, Instituto Tecnológico de Aeronáutica, São José dos Campos, SP, Brasil, Mar. 1990 (in Portuguese, original title is "Cálculo do Escoamento Potencial Transônico Através de um Algoritmo Implícito de Fatorização Aproximada").

[5] Holst, T.L., "Implicit Algorithm for the Conservative Transonic Full-Potential Equation Using an Arbitrary Mesh," *AIAA Journal*, Vol. 17, No. 10, Oct. 1979, pp. 1038-1045.

[6] Holst, T.L., and Albert, J., "An Implicit Algorithm for the Conservative, Transonic Full-Potential Equation with Effective Rotated Differencing," NASA TM-78570, 1979.

[7] Holst, T.L., "Approximate-Factorization Schemes for Solving the Transonic Full-Potential Equation," in *Advances in Computational Transonics*, W.G. Habashi, editor, Pineridge Press, Swansea, U.K., 1985, pp. 59-82.

[8] Ballhaus, W.F., Jr. , Jameson, A., and Albert, J., "Implicit Approximate Factorization Schemes for the Efficient Solution of Steady Transonic Flow Problems," *AIAA Journal*, Vol. 16, No. 6, June 1978, pp. 573-579.

[9] Morgenstern, A., Jr. , and Azevedo, J.L.F., "Influence of Convergence Parameters and Mesh Refinement on Full-Potential Solutions of Airfoil Flows," *Proceedings of the 10th Brazilian Congress of Mechanical Engineering*, Vol. I, Rio de Janeiro, RJ, Dec. 5-8, 1989, pp. 149-152.

[10] Holst, T.L., and Thomas, S.D. "Numerical Solution of Transonic Wing Flowfields," *AIAA Journal*, Vol. 21, No. 6, June 1983, pp. 863-870.

[11] de Mattos, B.S. and Azevedo, J.L.F., "Full Potential Flow Simulation About Wing Configurations," Paper submitted to the 3rd Brazilian Thermal Science Meeting, Itapema, SC, Dec. 1990.

[12] Carlson, L.A., "TRANSEP : A Program for High Lift Separated Flow About Airfoils," NASA CR 3376, Dec. 1980.

[13] Stevens, W.A., Goradia, S.H., and Braden, J.A., "Mathematical Model for Two-Dimensional Multi-Component Airfoils in Viscous Flow," NASA CR-1443, July 1971.

III ENCIT – Itapema, SC (Dezembro 1990)

FLOW FIELD SIMULATION ON SYMMETRICAL AEROFOIL AT DIFFERENT ANGLES OF ATTACK

VILLAR ALE, J. A., FERREIRA, V.C.S and SADHU, D.P.
Federal University of Rio Grande do Sul - UFRGS
Department of Mechanical Engineering - PROMEC
Sarmento Leite, 425 - PAlegre - RS- CEP 90050

SUMMARY

In this work the results of a numerical simulation for a two dimensional flow around a symmetrical aerofoil with different angles of attack is presented. At the present stage the flow is considered inviscid and incompressible. The numerical model is based on the through flow theory used to solve a three dimensional flow in a turbomachine cascade.

INTRODUCTION

In wind turbine theory the forces acting on an elemental blade section are determined based on aerodynamic characteristics of a single aerofoil. The total force is given by integrating the whole length of the blade. For a multiblade wind turbine (horizontal axis turbine - HAWT) this theory may give erroneous results. Cascade calculations are more appropriate because the influence of two adjacent blades is always taken into account. On the other hand in vertical axis turbine (VAWT) an isolated aerofoil theory is suitable but as the angle of attack varies constantly at each revolution the lift and drag coefficients get modified due to the frequency of changing the blade position.

Taking all this into account a numerical method based on cascade analysis is now being studied to simulate the pressure distribution along the blade surfaces for various angles of attack and at different situations. The aim is to develop a more general program for wind turbine design.

The computer program originally written by Goulas [1] is based on the through-flow theory presented by Wu [2] modified by Marsh [3], Bosman and Marsh [4] and adapted by Ferreira [5] for an axial water turbine. The new version of this program now presented, can simulate a symmetric, non-symmetric as well as any curved camber line aerofoil, isolated or in a cascade situation running at different angles of attack.

The present paper NACA 0012 aerofoil is simulated. Isolated aerofoil can be represented in the program by increasing the spacing (pitch-to-chord ratio) between two consecutive blades of a cascade. After reaching large value for the pitch the free stream flow would be undisturbed along a path in the middle of the blade passage.

GENERAL FORMULATION

The through-flow theory proposed by Wu [2] simulates a three dimensional problem by solving a series of two dimensional ones. This is achieved by an appropriate combination of two different kind of stream functions: S1, representing a Blade-to-blade stream surface and the S2 a Hub-to-Shroud stream surface. For an isolated static aerofoil the stream surface S1 is used.

The mathematical formulation for this surface (S1) is presented in refs. [2], [3], [4] and is modified with special derivatives and geometrical condition to define the flow along the stream surface. In cylindrical coordinates the stream funcion is given by:

$$\frac{1}{r^2}\frac{\partial^2\psi}{\partial\theta^2} + \frac{\partial^2\psi}{\partial z^2} = f(z,\theta) \qquad (1)$$

where

$$f(z,\theta) = W_z\frac{1}{r}\frac{\partial}{\partial\theta}(B\rho) - W_u\frac{\partial}{\partial z}(B\rho) + (\rho B)\frac{2dI}{d\psi} -$$

$$- \frac{TB\rho}{W^2}\left[\frac{1}{r}\frac{\partial S}{\partial\theta}(W_z - W_r\mathrm{Tan}\lambda) - \frac{\partial S}{\partial z}(W_u - W_r\mathrm{Tan}\mu)\right] +$$

$$B\rho\left[\frac{1}{r}\frac{\partial W_r}{\partial\theta}\mathrm{Tan}\lambda - \frac{\partial W_r}{\partial z}\mathrm{Tan}\mu\right] - B\rho\left[\frac{W_u}{r} + 2\omega\right]\mathrm{Tan}\lambda$$

In this equation, W_z, W_r, W_u are the components of the relative velocity **W**, λ and μ angles defining the local geometry of the stream surface; B is the thickness of stream surface, ω the angular velocity , ρ is fluid density, T is temperature, S is entropy and I is the rothalpy.

For the flow through a stationary blade row, $\omega = 0$, and the relative velocity vetor **W** becomes **V** (V_z, V_r and V_u).

This stream function is a second order differential equation for both variables involved (z-θ). Therefore four boundary conditions all over the flow domain are necessary. The first boundary condition states that there is no mass flow across the pressure and suction side of the blade. That is the solid boundaries are impermeable and the velocity vector will be tangential at each point. The condition is:

$$\psi_{wall} = \text{const} \qquad (2)$$

A second condition states that the flow velocity **W** at inlet is specified. The distribution of stream function is obtained by:

$$\psi_{inlet} = -r \int B\rho W_z \, d\theta + C_1(z) + C_2 \qquad (3)$$

where C_1 and C_2 are determinated knowing the stream function at the first point: $\psi(\theta_o, z_o) = \psi_o$.

The third condition assumes that at the exit, the stream function is calculated, according to the following expression:

$$\psi_{exit} = \int B\rho W_z \, d\theta + \psi_E \qquad (4)$$

where ψ_E is the value of the stream function at certain point E (see Fig. 1). The value of ψ_E defines the flow angle at the exit. ψ_E may be known from experimental data. If not, an iterative process must be used involving the trailing edge condition. The trailing edge condition assumes that there is no loading on the trailing edge.

Finally the periodicity condition is assumed, that is points situated one pitch apart should have same the properties.

NUMERICAL SOLUTION

The classic step towards a numerical solution of partial differential equations (PDE) is to replace the derivatives by algebraic expressions. By solving the equivalent system of liner equations the unknown variables were determined at each point of the grid.

The numerical solution scheme adopted is a finite difference approximation by using a Taylor series expansion.

The partial derivatives at point o are expressed in terms of n surrounding points, as:

$$\frac{\partial f}{\partial x_i} = \sum_{k=1}^{n} \alpha_{ik} f_k - f_o \sum_{k=1}^{n} \alpha_{ik} \qquad (5)$$

$$\frac{\partial^2 f}{\partial x_i^2} + \frac{\partial^2 f}{\partial x_j^2} = \sum_{k=1}^{n} \alpha_{ijk} f_k - f_o \sum_{k=1}^{n} \alpha_{ijk} \qquad (6)$$

where the indices i and j ($i \neq j$) stand for the independent variables and f for any unknown variable (ψ, W, etc...). The coefficients α_{ik} and α_{ijk} (weighting coefficients) are calculated by expanding the variable f_i in a Taylor series.

For high accuracy the number of surrounding points n should be as great as possible. The computational time imposes a limit because cost increases with the increment of n. The compromise between a desired accuracy and the time consumption are achieved for n = 9. The accuracy in this case is of the fourth order [1].

The original cylindrical coordinate system is changed to the cartesian one by the transformation $r\Delta\theta = \Delta x$, $\Delta z = \Delta z$,
The grid for the numerical scheme is then a plane formed by i rows in x-direction and j columns in z-direction. Fig. 1 show the grid used for different angles of attack.

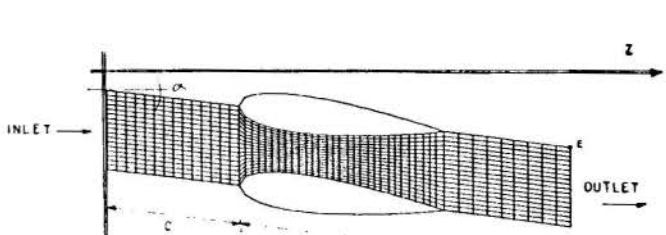

Fig. 1 Grid for different angles of attack

SOLUTION OF THE EQUATIONS

The stream function is then represented by:

$$\frac{\partial^2 \psi}{\partial x^2} + \frac{\partial^2 \psi}{\partial z^2} = f(x,z) \qquad (7)$$

After substitution, for the numerical scheme presented , a linear system of equation is obtained, as:

$$[A]\,[\psi] = [F] \qquad (8)$$

The matrix of the coefficients [A] has a banded form. The solution of the system is achieved using a pivotal Gaussian elimination which transforms the banded matrix to an upper triangular. By back substitution the values of $[\psi]$ are determined.

To start the process an initial value for the distribution of the stream function $[\psi]^{i=o}$ is assumed. Normally the initial value is obtained from the boundary conditions. The following steps are taken:

(a) A given velocity profile at the inlet is assumed.

(b) The ψ at the inlet is obtained by integrating the axial component of the inlet velocity (Eq. 3) . The value of the stream function at stagnation point in the leading edge is given and the stream function in the upper boundary is obtained . The stream function in the lower boundary is determined by the periodicity condition.

(c) The initial distribution of $[\psi]^{i=o}$, all over the domain is obtained from the boundary conditions given in item (b).

(d) The right hand side of Eq. 8 is then calculated based on the value of $[\psi]^{i=o}$.

(e) The left hand side of Eq. 8 is solved. New value for the stream function $[\psi]^{i=1}$ is calculated based on the item (d).

(f) The new value of $[\psi]^{i=1}$ is compared with the initial one. The convergence criterion is :

$$\frac{|[\psi]^{i} - [\psi]^{i-1}|}{|[\psi]^{i-1}|} < \gamma \qquad (9)$$

where the superscript "i" is the order of iteration.

(g) Not satisfied with the convergence criterion a new iteration is started with a new value for ψ. The next value $[\psi]^{i+1}$ is calculated according Eq. 10:

$$[\psi]^{i+1} = a[\psi]^{i-1} + (1-a)[\psi]^{i} \qquad (10)$$

where "a" is the relaxation fator here used as 0.5.

(h) Back to item (d) the process is repeated until the convergence criterion is satisfied.

(i) When the solution is considered converged the Kutta condition [1] is verified at the trailing edge. If the difference in static pressure at both sides, the upper (P_s) and lower (P_p) sides of the trailing edge exceeds a certain specified tolerance, δ (= .01, in this case) :

$$P_s - P_p > \delta \qquad (11)$$

a new value of the stream function at a stagnation point is selected and the whole process starts again from item (d).

(j) Finally the solution for the stream function $[\psi]$ defines the streamline pattern. By differentiating the stream function with respect to x and z it is possible to calculate V_z and V_x at each grid point.

RESULTS

A NACA 0012 profile at 0^o ,4^o ,8^o and 12^o angle of attack is simulated. The results are compared with the experimental ones of Michos et al. [6].

Fig. 2 shows a comparison of the pressure coefficient for both sides (pressure and suction) at zero angle of attack. The following figures (Fig. 3, 4 and 5) show results for the pressure coeficients at other angles of attack 4^o, 8^o and 12^o.

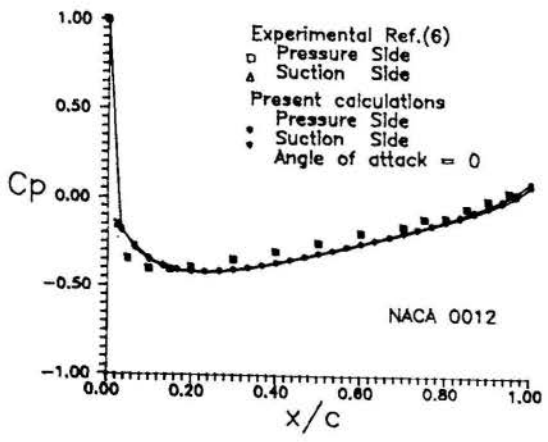

Fig. 2 Pressure Distribution $\alpha = 0^o$

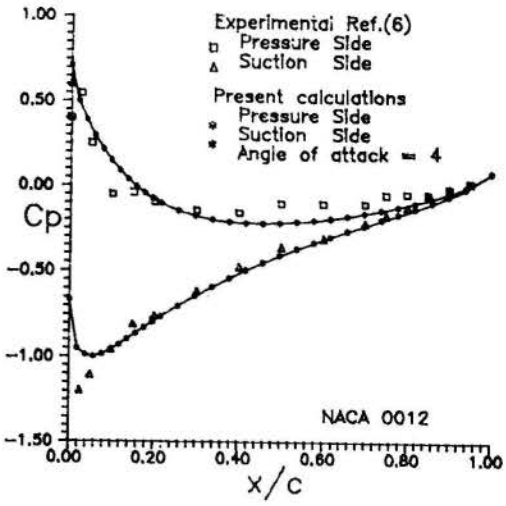

Fig. 3 Pressure Distribution $\alpha = 4^o$

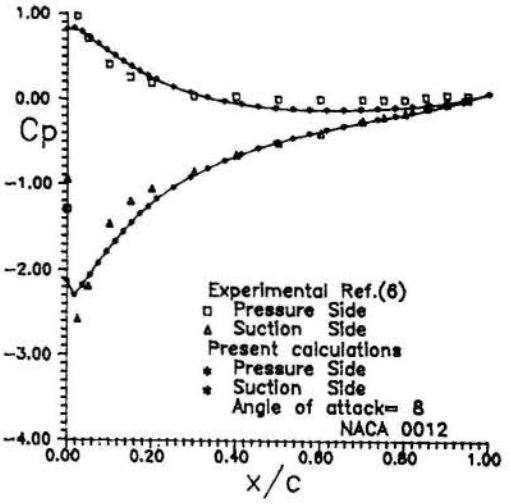

Fig. 4 Pressure Distribution $\alpha = 8^o$

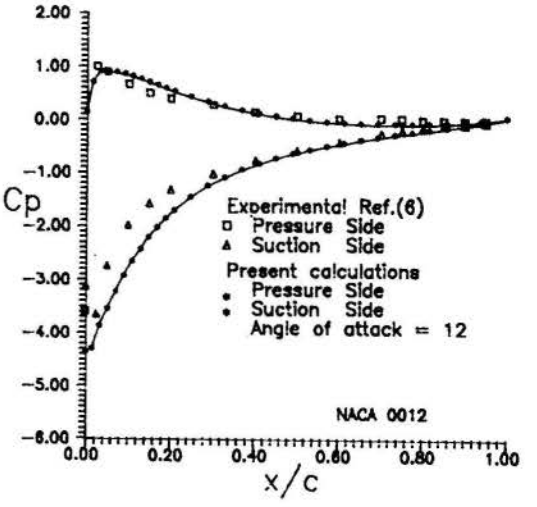

Fig. 5 Pressure Distribution $\alpha = 12^o$

CONCLUSIONS

The distribution of pressure on blade surfaces obtained by this model approximates the experimental results. The discrepancy exists more near the leading edge where exact value of the stream function is difficult to find due to finite grid mesh size.

In the region of the leading edge special consideration should be given due to the developement of a very high velocity gradient. There, the mesh size limits the calculation accuracy. Near this region the initial stream function value dictates the iteration rate for the calcultation. In this work the initial value is considered to be proportional to the angle of attack.

Uniform mesh sizes are adopted in this work. However non uniform and more dense mesh near the boundaries are being developed.

A PC-AT, with 1.2 Mb memory on board is utilised for these simulations. Its use limits the number of points up to 990. For better results finer and larger mesh numbers would be necessary and this will need a mainframe computer.

The model is still restricted to angles of attack below stall. The model's non-viscous analysis does not take into account the boundary layer development and consequent flow separation .

The data from this work may be useful for steady state operation of HAWT where angle of attack remain constant at each blade element. However, in VAWT, where the angle of attack is subjected to variation at the same blade element on each revolution and in HAWT operated on 'Yaw', the present data may not yet be suitable.

FERENCES

Goulas A. -"A computer program for the prediction of the flow field inside a compressor"- 84/AG/74 Internal Report DFEI, Cranfield Institute of technology May - 1984.

[2] Wu. H. C. -"A general theory of three dimensional flow in subsonic and supersonic turbomachines of axial, radial and mixed flow types". NACA - TN 2604, 1952.

[3] Marsh, H. -"A digital computer program for through-flow fluid mechanics in an arbitrary turbomachine, using a matrix method." ARC - RAM No 3509 , july - 1966

[4] Bosman ,C., Marsh H.,-"An improved method for calcultati n g the flow in turbomachines, including a consistent loss model" J. Mech. Eng. Science - Vol 16, No 1, pp 12-35 1974. May - 1984 .

[5] Ferreira, V. C. S. -"Flow Patterns Inside a turbine type flowmeter"; PhD Thesis. Departament of fluid Engineering and Instrumentation. Cranfield Intitute of Techonology April - 1988.

[6] Michos A., Bergeles G. and Athanassiadis N. -"Aerodynamics characteristics of NACA 0012 aerofoil in relation to wind generators." Wind Engineering - Vol, No4, pp. 247 - 1983.

[7] Abbout H., Von Doenhoff A. E., -"Theory of wing sections," New york, Dover Publications, Inc, 1959.

[8] Tzabiras, G., Dimas A. and Loukakis, T., -"A Numerical Method for the calculation of incompressible, steady, separated flows around aerofoils." International Journal for numerical methods in fluids, Vol. 6, pp 789-809, - 1986.

[9] Boletis ,E., et Al. -"A complete inverse calculation procedure for the optimization of horizontal-axis wind turbine Aerofoils." Proceedings European Community Wind Energy Conference , Denmark , 8-10 pp 208-221 ,June - 1988 .

III ENCIT – Itapema, SC (Dezembro 1990)

AERODINÂMICA SUBSÔNICA COMPRESSÍVEL - MOVIMENTO OSCILATÓRIO: FORMULAÇÃO PELO POTENCIAL DE VELOCIDADE

MARCOS VINÍCIUS BORTOLUS
Departamento de Engenharia Mecânica - UFMG
Av. Antônio Carlos, 6627 - 31.270 - B.Horizonte - MG
PAULO AFONSO O. SOVIERO
Instituto Tecnológico de Aeronautica-ITA-S.J.dos Campos/SP

SUMÁRIO

A partir de uma formulação pelo potencial de velocidade do escoamento potencial linearizado e com a hipótese de movimento oscilatório, chega-se à equação de Helmholtz. Utilizando-se o método das singularidades, a solução para essa equação é estruturada a partir de uma solução elementar do operador de Helmholtz e da análise de algumas de suas propriedades sobre uma superfície de descontinuidade. A estruturação desenvolvida permite a aplicação em configuração complexas. Elementos da teoria de distribuições são ainda utilizadas neste método.

INTRODUÇÃO

A determinação da distribuição de pressão em corpos aerodinâmicos em movimento oscilatório é um importante problema nas teorias de estabilidade e aeroelasticidade. Devido às dificuldades na realização de medições, os métodos numéricos(caso mais comum) ou teóricos representam, mais ainda, soluções de grande interesse para o problema.

No caso do escoamento subsônico compressível, diversos métodos têm sido desenvolvidos a partir de Küssner [1] e podem ser divididos em duas categorias: 1) Método de funções modais e 2) Método de elementos discretos. Watkins et alii [2] desenvolveram o primeiro para aplicações práticas e Rowe et alii [3] utilizaram esse método para determinação de carregamentos provocados por superfícies de controle em movimento. Um exemplo de método de elementos discretos utilizado com freqüência é o desenvolvido por Albano e Rodden [3], que é uma extensão do método de *"vortex lattice"* (vide, por exemplo, referência [5]), empregado no cálculo de asas em escoamento permanente. Os métodos de Ueda e Dowell [6] e o de Haviland e Yoo [7] são, também, exemplos interessantes do método de elementos discretos.

A maior parte dos métodos encontrados se aplicam somente ao caso de asas, como o de Albano e Rodden[4], o de Küssner[1] e o de Ueda e Dowell[6]. Outros, como o de Morino e Kuo[8] e o de Giesing et alii[9], são utilizados para cálculo de configurações complexas. O primeiro utiliza uma formulação pelo potencial de velocidade e o último uma formulação pelo potencial de aceleração.

No presente trabalho o método das singularidades é aplicado ao caso subsônico compressível, a partir de uma formulação pelo potencial de velocidade. Com o método das singularidades o problema é estruturado de forma a permitir aplicações em configurações complexas e tem a vantagem de trabalhar, na sua essência, com elementos familiares ao aerodinamicista. Além disso, a formulação pelo potencial de velocidade feita a exemplo de Morino e Kuo[8] e de Haviland e Yoo[7] leva a núcleos de equações integrais mais simples que no caso da formulação pelo potencial de aceleração, casos de Küssner[1], Albano e Rodden[4] e outros.

O potencial de velocidade, no caso de aerodinâmica subsônica compressível linearizada não-permanente, satisfaz à equação da Onda. Utilizando a hipótese de movimento harmônico e introduzindo as transformações generalizadas de Prandtl-Glauert chega-se ao operador de Helmholtz. A aplicação do método das singularidades consiste em encontrar uma solução elementar desse operador, analisar suas propriedades para determinar singularidades pertinentes, e gerar a solução a partir da superposição dessas singularidades.

MODELO MATEMÁTICO DO ESCOAMENTO

O potencial de velocidade, quando a velocidade do escoamento não-perturbado V_∞ está na direção x, satisfaz à equação(vide, por exemplo, referência[10])

$$\nabla^2\zeta - \frac{1}{a^2_\infty}\left[\frac{\partial}{\partial t} + V_\infty \frac{\partial}{\partial x}\right]^2 \zeta = 0 \qquad (1)$$

sendo que ζ é a diferença entre o potencial de velocidade do escoamento e o potencial de velocidade do escoamento não-perturbado e a_∞ a velocidade do som do escoamento não-perturbado.

Supondo que o escoamento uniforme seja perturbado por um corpo vibrando harmonicamente, o potencial ζ pode ser escrito na forma

$$\zeta\,(x,y,z,t) = e^{iwt}\,\hat{\phi}\,(x,y,z) \qquad (2)$$

e a equação (1) se transforma em

$$\beta^2\frac{\partial^2\hat{\phi}}{\partial x^2} + \frac{\partial^2\hat{\phi}}{\partial y^2} + \frac{\partial^2\hat{\phi}}{Mz^2} - \frac{2i\omega V_\infty}{a^2_\infty\partial x} + \frac{\omega^2}{a^2_\infty}\hat{\phi} = 0 \qquad (3)$$

onde $\beta^2 = 1 - M^2$ e M é o número de Mach do escoamento não-perturbado.

Fazendo $\phi = e^{(-iw\,V_\infty x/a^2_\infty\,\beta^2)}\,\hat{\phi}$ e utilizando as transformações de Prandtl-Glauert

$$X = \frac{x}{L}\;;\; Y = \frac{\beta}{L}\,y;\; Z = \frac{\beta}{L}\,z \qquad (4)$$

onde L é um comprimento característico, a equação(3) se reduz à equação de Helmholtz.

$$\nabla^2\,\phi + K^2\,\phi = 0 \qquad (5)$$

onde $K = \dfrac{\omega\,L}{a_\infty\beta^2}$

A dedução da equação(5) para o caso bidimensional pode ser encontrada em[10].

Observando-se a equação(5), nota-se que essa se transforma na equação de Laplace, quando K tende a zero, ou seja, o problema a ser resolvido é o do cado oscilatório incompressível. Semelhante análise pode ser en-

contrada em [11]. Considere-se, agora, a freqüência reduzida K_r, definida pela expressão abaixo

$$K_r = \frac{\omega L}{V_\infty} \tag{6}$$

A figura 1 mostra a variação da relação (K/K_r) com o número de Mach. Observa-se que essa relação decresce com o decréscimo de M. Para que se tenha valores suficientemente pequenos de K no caso de números de Mach maiores (alto subsônico), é necessário que a freqüência reduzida seja suficientemente pequena. Por outro lado, nota-se que para M < 0,62 (vide fig. 1) a relação (K/K_r) é menor que um. Assim, para valores não muito pequenos de K_r, K pode ser suficientemente pequeno dependendo do número de Mach. Os valores de K_r de interesse prático são, em geral, menores que um.

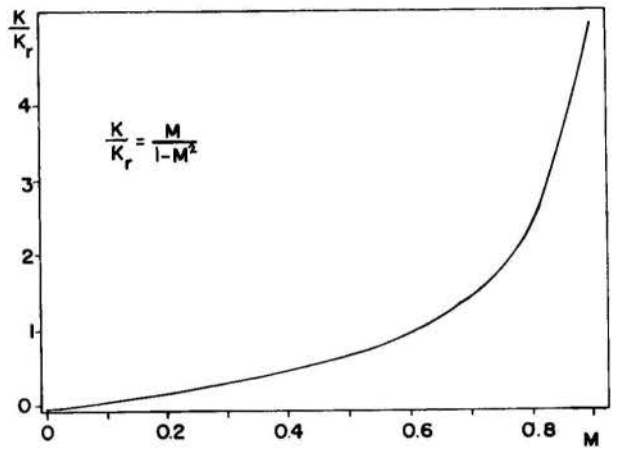

Fig. 1 Relação K/K_r em função do número de Mach.

APLICAÇÃO DO MÉTODO DAS SINGULARIDADES

O potencial ϕ definido anteriormente satisfaz à equação de Helmholtz.

$$\mathfrak{L}(\phi) = \nabla^2 \phi + K\phi = 0 \tag{5}$$

onde $\mathfrak{L}$ é o operador de Helmholtz. De acordo com Bousquet [12], conhecendo-se uma solução elementar do operador de Helmholtz, ou seja, uma função E que satisfaça a seguinte equação

$$\mathfrak{L}(E) = \delta \tag{7}$$

onde δ é o delta de Dirac, pode-se determinar ϕ a partir da seguinte equação

$$\phi = T_\Sigma * E \tag{8}$$

onde o sinal * representa o produto de convolução e T_Σ uma distribuição a suporte limitado (vide referência |13|) tal que $T_\Sigma = \mathfrak{L}(\phi)$. O suporte de T_Σ é exterior ao domínio físico de modo que $\mathfrak{L}(\phi) = 0$ no domínio físico.

A distribuição T_Σ é escolhida de maneira que ϕ satisfaça às condições de contorno. Em geral, existe uma grande variedade de distribuições compondo T_Σ. A análise de descontinuidades admissíveis do potencial regido pela equação de Helmholtz, sobre uma superfície, fornece subsídios à escolha das distribuições que vão compor T_Σ.

Solução Elementar. Demonstra-se a seguir que a função

$$E = \frac{e^{iKr}}{4\pi r} \tag{9}$$

onde $r = (x^2 + y^2 + z^2)^{1/2}$, é uma solução elementar do operador de Helmholtz $\mathfrak{L}$.

A distribuição T_G associada a uma função G é dada por

$$< G, f > = \int_{R^3} G\, f\, dv \tag{10}$$

onde f é uma função do espaço D de funções indefinidamente deriváveis a suporte limitado.

Sendo a função E localmente somável, pode-se definir a distribuição T_E. Assim, se E é uma solução elementar de $\mathfrak{L}$ e como $< \delta, f > = f(o)$, tem-se que

$$< \mathfrak{L}(T_E),\ f > = f(o) \tag{11}$$

Uma distribuição é um funcional linear. Portanto,

$$T_{\mathfrak{L}(E)} = T_{\nabla^2 E} + T_{K^2 E} \tag{12}$$

A função E apresenta uma singularidade na origem e a integração será feita para $r > \varepsilon$. Em seguida, calcula-se o limite quando ε tende a zero. A Distribuição T_{K^2E} é então dada por

$$< K_E^2,\ f > = \lim_{\varepsilon \to o} \int_{r>\varepsilon} K^2 \frac{e^{iKr}}{4\pi r} f\, dv \tag{13}$$

pela definição da derivada de uma distribuição, $T_{\nabla^2 E}$ se torna

$$< \nabla^2 E,\ f > = < E,\ \nabla^2 f > = \lim_{\varepsilon \to o} \int_{r>\varepsilon} \frac{e^{iKt}}{4\pi r} \nabla^2 f\, dv \tag{14}$$

Aplicando a segunda identidade de Green às funções E e f, tem-se que

$$\int_{r>\varepsilon} (E\, \nabla^2 f - f\, \nabla^2 E)\, dv = \int_{r=\varepsilon} (f \frac{\partial E}{\partial r} - E \frac{\partial f}{\partial r})\, ds \tag{15}$$

mas

$$\nabla^2 E = - K^2 \frac{e^{iKr}}{4\pi r},\ \forall\ r > \varepsilon \tag{16}$$

assim, a equação (15) se torna

$$\int_V \nabla^2 \frac{e^{iKr}}{4\pi r} dv = -\int_V K^2 \frac{e^{iKr}}{4\pi r} f\, dv - \frac{1}{4\pi} \int_S f(iK \frac{e^{iKr}}{r} - \frac{e^{iKr}}{r^2})\, ds + \frac{1}{4\pi} \int_S \frac{\partial f}{\partial r} \frac{e^{iKr}}{r}\, ds \tag{17}$$

Como S é a superfície definida por $r = \varepsilon$,

$$\int_V \nabla^2 f \frac{e^{iKr}}{4\pi r} dv = -\int_V K^2 \frac{e^{iKr}}{4\pi r} f\, dv - \frac{iKe^{iK\varepsilon}}{4\pi} \int_{r=\varepsilon} f\, ds + \frac{e^{iK\varepsilon}}{4\pi\varepsilon^2} \int_{r=\varepsilon} f\, ds + \frac{e^{iK\varepsilon}}{4\pi\varepsilon} \int_{r=\varepsilon} \frac{\partial f}{\partial r}\, ds \tag{18}$$

Calculando o limite, quando ε tende a zero, a equação (18) se reduz a

$$\int_V \nabla^2 f \frac{e^{iKr}}{4\pi r} dv = -\lim_{\varepsilon \to o} \int_V K^2 \frac{e^{iKr}}{r} f \, dv + f(o) \quad (19)$$

Somando as equações (13) e (19) chega-se à equação (11), como pretendido, ou seja, mostra-se que E, de fato, é uma solução elementar de f.

Estudo de Algumas Propriedades do Operador de Helmholtz Através de uma Superfície de Descontinuidade. Supõe-se que a solução ϕ seja uma função duas vezes diferenciável, exceto sobre uma superfície S onde ela sofre uma descontinuidade. De acordo com a teoria das distribuições (vide referência [13]), a distribuição $\partial^2\phi/\partial x^2 i$ é dada por

$$\frac{\partial^2 \phi}{\partial x^2_i} = \left\{ \frac{\partial^2 \phi}{\partial x^2_i} \right\} + \frac{\partial}{\partial x_i} \left[\tau_o \cos \theta_i \delta_s \right] + \tau_i \cos\theta_i \delta_s \quad (20)$$

onde τ_o e τ_i são os saltos de ϕ e $\frac{\partial \phi}{\partial x_i}$, respectivamente, quando à superfície S é atravessada no sentido da normal $\vec{n}$ à superfície; θ_i é o ângulo entre a normal e o eixo 0_{xi}; e $\{\partial^2\phi/\partial x_i^2\}$ é a distribuição baseada na função $\partial^2\phi/\partial x_i^2$.

Somando-se as derivadas da distribuição ϕ nas três direções, tem-se

$$\sum_{i=1}^{3} \frac{\partial^2 \phi}{\partial x_i^2} = \sum_{i=1}^{3} \left\{ \frac{\partial^2 \phi}{\partial x^2_i} \right\} + \sum_{i=1}^{3} \frac{\partial}{\partial x_i} \left[\tau_o \cos \theta_i \delta_s + \left[\tau_i \cos \theta_i \delta_s \right] \right] \quad (21)$$

Adicionando-se $K^2 \phi$ aos dois membros, a equação (21) se torna

$$\mathcal{L}(\phi) = \{\mathcal{L}(\phi)\} + \sum_{i=1}^{3} \left\{ \frac{\partial}{\partial x_i} \left[\tau_o \cos \theta_i \delta_s \right] + \left[\tau_i \cos\theta_i \delta_s \right] \right\} \quad (22)$$

Mas como $\{\mathcal{L}(\phi)\} = 0$, então

$$\mathcal{L}(\phi) = \sum_{i=1}^{3} \frac{\partial}{\partial x_i} \left\{ \left[\tau_o \cos \theta_i \delta_s \right] + \tau_i \cos\theta_i \delta_s \right\} \quad (23)$$

sendo $\tau_i = \cos\theta_i$, a equação (23) se reduz a

$$\mathcal{L}(\phi) = \left[\tau_o \right] \frac{\partial \delta_s}{\partial n} + \left[\frac{\partial \phi}{\partial n} \right] \delta_s \quad (24)$$

onde $[\tau_o]$ e $\left[\frac{\partial \phi}{\partial n}\right]$ representam as descontinuidades de ϕ e $\partial\phi/\partial n$, respectivamente, sobre a superfície S.

Portanto, o operador de Helmholtz admite as mesmas características de descontinuidade que o operador de Laplace, ou seja, descontinuidade do potencial associada à distribuição δ_s e descontinuidade de derivada normal do potencial associada à distribuição $\frac{\partial \delta_s}{\partial n}$. A análise do operador de Laplace é feita em [12].

A distribuição δ_s pode ser interpretada como uma distribuição de fontes de massa sobre uma superfície e $\partial\delta_s/\partial n$, conseqüentemente, como uma distribuição superficial de dipolos normais.

DISTRIBUIÇÕES DE FONTES E DIPOLOS NORMAIS

Os procedimentos de cálculos do potencial e da velocidade, devido a distribuições superficiais de fontes e dipolos normais, são mostrados a seguir. Para isso, define-se como velocidade no espaço transformado $\vec{V}_T$ o gradiente do potencial ϕ.

Inicialmente, para efeito de exemplificação, mostra-se o caso da fonte puntual.

Fonte Puntual. O potencial num ponto M(x,y,z) qualquer devido a uma fonte de intensidade situada num ponto P(x', y', z') é dado por

$$\phi = \frac{m'}{4\pi R} e^{iKR} \quad (25)$$

onde $R = \left[(x-y')^2 + (y-y')^2 + (z-z')^2 \right]^{1/2}$. A velocidade é dada por

$$\vec{V}_T = \text{grad } \phi = \frac{m}{4\pi} \left(\frac{K i e^{iKR}}{R^2} - \frac{e^{iKR}}{R^3} \right) \vec{PM} \quad (26)$$

A figura 2 mostra a variação da parte real de ϕ em função de R devido a uma fonte situada na origem e de intensidade $m = 4\pi$, para alguns valores de K.

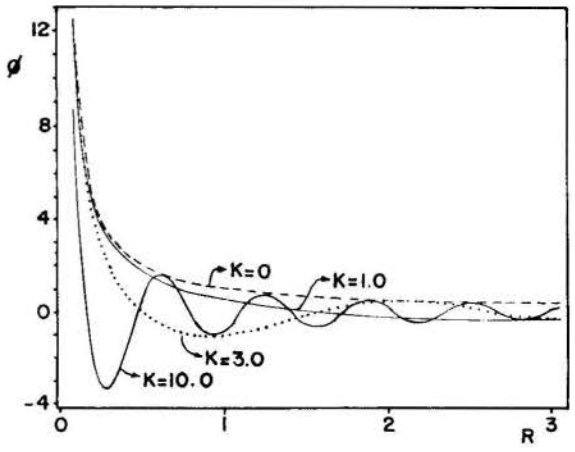

Fig. 2 Potencial devido a uma fonte puntual.

DISTRIBUIÇÃO SUPERFICIAL DE FONTES

A partir da equação (7), tem-se que o potencial num ponto M(x,y,z) devido a uma distribuição de fontes numa superfície S qualquer é dado por

$$\phi = \tau \delta_s * E = \frac{1}{4\pi} \int_{PES} \tau(P) \frac{e^{iKR}}{R} ds \quad (27)$$

onde τ é a densidade superficial e $R = \left[(x-y')^2+(y-y')^2+(z-z')^2\right]^{1/2}$, sendo que (x',y',z') são as coordenadas de um ponto P pertencente à superfície S.

A integral acima não é definida se o ponto M estiver sobre a superfície S. Assim, (vide ref. [12]) o potencial num ponto H da superfície é definido da seguinte maneira:

Seja M um ponto vizinho de H e situado sobre a normal à superfície S, que passa por H. A normal é orientada no sentido de H para M. Define-se o potencial em H como sendo o limite do potencial em M, quando M tende para H. Seja β_ε a parte da superfície S interior a um círculo de raio ε e β_ε' a parte de S exterior a esse círculo. Sendo assim,

$$\phi(M) = \frac{1}{4\pi} \int_{PE\ \beta_\varepsilon} \tau(P) \frac{e^{iKR}}{R} ds + \frac{1}{4\pi} \int_{PE\ \beta_\varepsilon'} \tau(P) \frac{e^{iKR}}{R} ds \quad (28)$$

O potencial em M não depende de ε. Então, pode-se escrever que

$$\phi(H) = \lim_{\varepsilon \to o} \phi(H) = \lim_{\varepsilon \to o} \left[\lim_{M \to H} \phi(M) \right] \quad (29)$$

após alguns desenvolvimentos chega-se a

$$\phi(H) = \frac{1}{4\pi} \int \tau(P) \frac{e^{iKR}}{R} ds \qquad (30)$$

onde o símbolo $\int$ significa Integral no valor principal de Cauchy. A Figura 3 mostra a variação da parte real do potencial, devido à distribuição superficial de fontes ($\tau = 4\pi$) num quadrado de lado unitário. O cálculo é feito num ponto H situado sobre o eixo normal ao centro do quadrado. A integração foi feita numericamente.

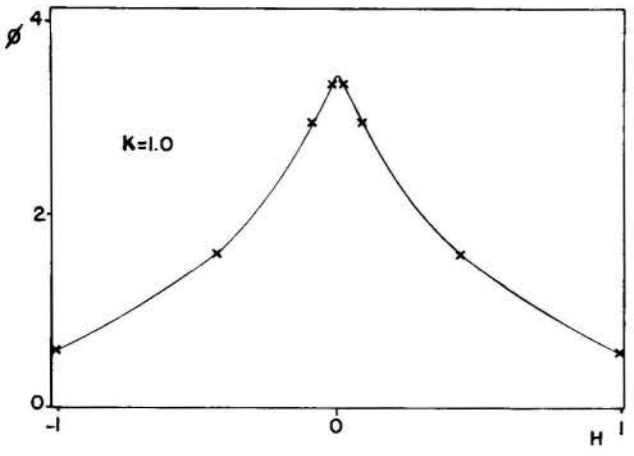

Fig. 3 Potencial devido a uma distribuição superficial de fontes.

No caso da velocidade obtém-se que

$$\vec{V}_T(M) = \frac{1}{4\pi} \int_{PES} \tau(P) \left(k_i \frac{e^{iKR}}{R^2} - \frac{e^{iKR}}{R^3} \right) \vec{PM}\, ds \qquad (31)$$

para um ponto M fora da superfície. Para um ponto H da superfície

$$\vec{V}_T(H) = -\frac{\tau(H)}{2} \vec{n} + \frac{1}{4\pi} \int \tau(P) \left(Kie^{iKR} \frac{}{R^2} - \frac{e^{iKR}}{R^3} \right) \vec{PH}\, ds \qquad (32)$$

onde $\vec{n}$ é a normal à superfície em H, no sentido de H para M.

No caso de uma superfície plana, a componente normal de velocidade é dada por

$$\vec{V}_{Tn} = -\frac{\tau(H)}{2} \vec{n} \qquad (33)$$

Nesse caso a velocidade normal recebe uma descontinuidade de $[-\tau(H)]$, sobre a superfície S em H. A descontinuidade aparece na parte real de $\vec{V}_T$, pois a parte imaginária de $e^{iKR}/4\pi R$ não é, na verdade, uma singularidade. Na figura 4 é mostrada a variação da componente normal da velocidade devido a uma distribuição superficial de fontes ($\tau = 2$) num disco de raio unitário. A velocidade é calculada num ponto sobre o eixo normal ao centro do disco. Nesse caso, a solução é obtida analiticamente.

DISTRIBUIÇÃO SUPERFICIAL DE DIPOLOS NORMAIS

Repetindo-se o mesmo procedimento que foi feito no caso anterior, encontra-se que o potencial para um ponto M fora da superfície é dado por

$$\phi(M) = \nu \frac{\delta_s}{n} * E = \frac{1}{4\pi} \int_S \nu \frac{\partial}{\partial n} \left(\frac{e^{iKR}}{R} \right) ds \qquad (34)$$

onde ν é a densidade superficial de dipolos normais. Para um ponto da superfície o cálculo é formalmente idêntico ao feito no caso da velocidade devido à distribuição superficial de fontes. Assim,

$$\phi(H) = -\frac{1}{2} \nu(H) + \int \nu(P)\, \vec{n}.\mathrm{grad}\left(\frac{e^{iKR}}{R} \right) ds \qquad (35)$$

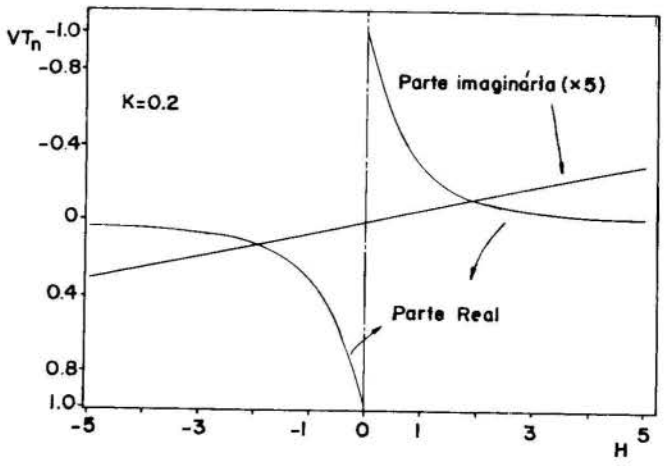

Fig. 4 Componente normal de velocidade devido a uma distribuição superficial de fontes.

Percebe-se, portanto, uma descontinuidade no potencial de $[-\nu(H)]$, sobre a superfície S. No caso da figura 4, substituindo V_{Tn} por ϕ, tem-se o potencial devido a uma distribuição de dipolos normais ($\nu(H) = 2$) para a mesma situação.

Para a velocidade, obtém-se que, sendo M um ponto fora da superfície

$$\vec{V}_T(M) = \frac{1}{4\pi} \int_{PES} \underset{M}{\mathrm{grad}} \left[\nu_n . \mathrm{grad}\left(\frac{e^{iKR}}{R} \right) \right] ds \qquad (36)$$

onde $\underset{M}{\mathrm{grad}}$ é o gradiente em relação as coordenadas (x,y,z) do ponto M.

No caso de um ponto H sobre a superfície

$$\vec{V}(H) = -\frac{1}{2} \underset{x,y}{\mathrm{grad}}\, \nu + \vec{n} \lim_{\varepsilon \to o} \left[\frac{1}{4\pi} \int \nu \left(ki \frac{e^{iKR}}{R^2} - \frac{e^{iKR}}{R^3} \right) ds + \frac{\cos K\varepsilon}{2\varepsilon} \nu \right] \qquad (37)$$

onde $\underset{x,y}{\mathrm{grad}}\, \nu$ é o gradiente de ν no plano x,y calculado em H.

Se a superfície S é plana, a expressão $(\underset{x,y}{\mathrm{grad}}\, \nu)$ representa o saldo de velocidade tangencial, sobre a superfície em H.

Na figura 5, tem-se a velocidade normal (parte real) induzida por uma distribuição superficial de dipolos normais num disco de raio unitário. Nesse caso, também, a velocidade é calculada num ponto situado no eixo normal ao disco.

CONCLUSÕES

No caso da aerodinâmica subsônica compressível oscilatória, o potencial satisfaz à equação de Helmholtz. Para valores suficientemente pequenos de K, essa equação se reduz à equação de Laplace. Na obtenção da solução da equação de Helmholtz pelo Método das Singularidades utiliza-se singularidades do tipo fonte e/ou dipolo normal, como no caso da equação de Laplace. A escolha das singularidades depende das condições de contorno do problema em questão. De modo geral, escolhe-se aquela ou aquelas singularidades que possuem maior ação sobre as condições de contorno (vide referência [12]). Como visto, a distribuição superficial de fontes provoca descontinuidade na velocidade normal e a de dipolos normais descontinuidades no potencial e na velocidade

tangencial. No caso de asas, p.ex., utiliza-se a distribuição de fontes no problema da espessura e a distribuição de dipolos normais na determinação da sustentação. O método das singularidades permite aplicações em configurações complexas. No momento, o cálculo de asas em movimento oscilatório está sendo desenvolvido.

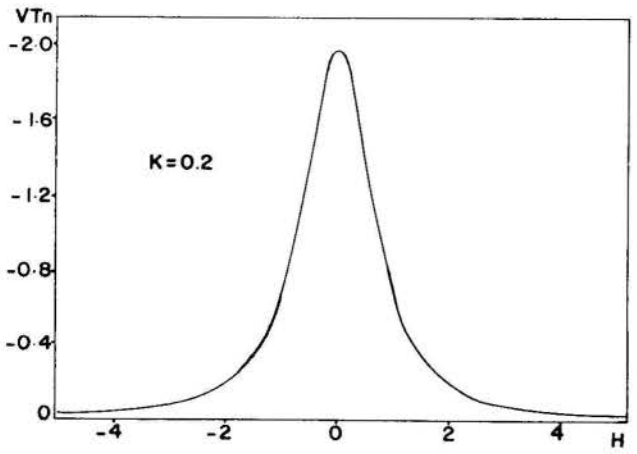

Fig. 5 Velocidade normal devido a uma distribuição superficial de dipolos normais.

REFERÊNCIAS

[1] Küssner, H.G., "General Airfoil Theory", NASA TM 979, 1941.

[2] Watkins, C.E., Woolston, D.S. and Cunninghan, H.J., "A systematic Kernel Function Procedure for Determining Aerodynamic Forces on Oscillating or Steady Finite wings at subsonic speeds", NASA TR R-48, 1959.

[3] Rowe, W.S., Redman, M.C., Ehlers, F.E. and Sebastian, J.D., "Prediction of unsteady Aeronaynamics Loadings Caused by Leading Edge and Trailing Edge Control Surface Motion in Subsonic Compressible Flow-Analysis and Results", NASA CR2543, 1975.

[4] Albano, E. and Rodden, W.P., "A Doublet- Lattice Method for Calculating Lift Distributions on Oscilating Surfaces in Subsonic Flows", AIAA Journal, Vol. 7, pp. 626-633, 1969.

[5] Schlichting, H. and Truckenbrodt, E., "Aerodynamics of the Airplane" Editora McGraw-Hill International, New York, 1979.

[6] Ueda, T. and Dowell, E.H., "A New Solution Method for Lifting Surfaces in Subsonic Flow","AIAA Journal, Vol. 20, pp. 348-355, 1982.

[7] Haviland, J.K. and Yoo, Y.S., "Downwash-Velocity Potential Method for Oscillating Surfaces", AIAA Journal, Vol. 11, pp. 607-612, 1973.

[8] Morino, L. and Kuo, C.C., "Subsonic Potential Aerodynamics for Complex Configurations: A General Theory", AIAA Journal, Vol. 12, pp.191-197, 1974.

[9] Giesing, J.P., Kalman, T.P. and Rodden, W.P., "Subsonic Steady and Oscillatory Aerodynamics for Multiple Interfering Wings and Bodies", Journal of Aircraft, Vol. 9, pp. 693-702, 1972.

[10] Bisplinghoff, R.L., Ashley, H. and Halfman, R.L., "Aeroelasticity", Editora Addison-Wesley Publishing Company, New York, 1957.

[11] Krasnov, N.F., "Aerodynamics", Vol. 1, Editora Mir Publishers, Moscou, 1985.

[12] Bousquet, J., "Méthode des Singularités", Cours ENSAE, 1982.

[13] Schwartz, L., "Méthodes Mathématiques pour les Science Physiques", Editora Hermann, Paris, 1965.

ABSTRACT

Helmholtz's equation is obtained from a formulation of the linearized potential flow and the potential velocity, considering the oscillatory movement hypothesis. The Singularities Method is used to obtain the solution for this equation. This solution originates from the analysis of some properties of Helmholtz's operator on a discontinous surface and one of its elementary solutions. The developed formulation enables its application in complex configurations. Concepts of the theory of distributions are also employed in this method.

III ENCIT – Itapema, SC (Dezembro 1990)

UM MÉTODO NUMÉRICO PARA RESOLVER O ESCOAMENTO SOBRE CORPOS ROMBUDOS PLANOS

Roberto da Mota Girardi
Paulo Afonso de Oliveira Soviero
Instituto Tecnológico de Aeronáutica-ITA
12225-São José dos Campos-SP

RESUMO

O escoamento médio sobre um corpo rombudo plano pode ser abordado através da chamada teoria da linha de corrente livre. Nesta teoria, admite-se que na região exterior à esteira e ao corpo o escoamento é potencial. A fronteira da esteira média é modelada através das linhas de corrente livre e no interior desta esteira o escoamento é desconsiderado. Neste trabalho, a teoria acima é resolvida numericamente através do método dos paineis. Após uma discussão do esquema numérico, obtem-se as soluções dos escoamentos descolados sobre uma placa plana normal e sobre um cilindro no regime subcrítico. Verifica-se excelente acordo entre os resultados numérico, analítico e experimental.

INTRODUÇÃO

Devido ao continuo desprendimento de vórtices, o escoamento sobre um corpo rombudo varia com o tempo, de uma forma quase periódica, para altos números de Reynolds. Considerando-se uma média temporal, verifica-se que o escoamento médio próximo a base do obstáculo é constituido por uma "região de água morta" (onde a velocidade é muito baixa) limitada pelas camadas de cisalhamento livre que se originam nos pontos de separação. Esta configuração foi observada por Fage & Johansen [5], que estudaram vários corpos rombudos e verificaram que a pressão média ao longo da base dos mesmos é praticamente constante.

No modelo da linha de corrente livre [11], as camadas de cisalhamento livre, do escoamento médio descrito acima, são representadas por superfícies de descontinuidade, chamadas de linhas de corrente livre, nas quais a pressão é especificada. Fora da esteira admite-se escoamento potencial, enquanto dentro da mesma tem-se uma região de água morta.

O modelo descrito acima foi estabelecido pela primeira vez por Kirchhoff [11], para o escoamento médio sobre a placa plana normal ao escoamento não perturbado, cuja velocidade é V_∞. Neste modelo foi admitido que a pressão na base e nas linhas de corrente livre é igual à do escoamento não perturbado (p_∞). Com esta abordagem foi obtido um coeficiente de arrasto igual a 0,88, que é aproximadamente a metade do valor determinado experimentalmente. Resultados análogos foram determinados por Rayleigh [11] para o escoamento sobre a placa plana inclinada.

O estudo experimental do escoamento sobre a placa plana inclinada foi realizado por Fage & Johansen [5], onde foi verificado que a pressão média na base é sempre menor que p_∞. Este resultado indicou que as discrepâncias observadas nos coeficientes de arrasto, calculados por Kirchhoff e Rayleigh [11], são uma conseqüência da pressão na base ser feita igual a p_∞.

Em 1954, Roshko [13] modificou o modelo da linha de corrente livre, permitindo que a pressão na base (p_b) fosse fixada de forma arbitrária (P_b é normalmente obtido da experiência). Para resolver este problema analiticamente, Roshko [13] utilizou o chamado plano do hodógrafo recortado ("notched hodograph"), que é compatível com uma configuração na qual as linhas de corrente livre são divididas em duas partes: (i) Na primeira, caracterizada pelas curvas AB e A'B' (vide figura-1a), tem-se pressão constante igual a p_b e (ii) na segunda parte, a pressão varia de p_b até p_∞ ao longo das semi-retas paralelas a direção de V_∞ , cujas origens são os pontos B e B'.

A solução de Roshko [13] depende de um único parâmetro, que é o coeficiente de pressão na base (Cp_b). Fixando-se um valor para (Cp_b), obtem-se a distribuição de pressão na parte frontal do obstáculo e a forma e posição das linhas de corrente livre. Este modelo produziu resultados analíticos que concordam muito bem com a experiência para os escoamentos sobre a placa plana normal e sobre uma cunha.

Em 1955, aparentemente de forma independente, Woods [14] formulou uma teoria análoga a de Roshko [13], na qual os efeitos de compressibilidade são levados em consideração. Sua solução para o cilindro concorda muito bem com a experiência.

Wu [15] e Abernathy [1] generalizaram o modelo acima para o caso da placa plana em incidência, verificando ótima correlação entre teoria e experiência.

Parkinson & Jandali [12] propuseram uma outra solução para o modelo da linha de corrente livre. Nesta, a esteira média é ocupada pelo jato gerado por duas fontes, colocadas na superfície de um cilindro (em sua base) e as linhas de corrente livre constituem a fronteira entre este jato e o escoamento externo. Os resultados obtidos com esta abordagem concordam muito bem com a experiência para vários corpos rombudos, como a placa plana normal, cunha e cilindro circular nos regimes subcrítico, supercrítico e transcrítico.

Hayashi & Endô [7] generalizaram o esquema de Parkinson & Jandali [12] para o caso de um perfil arbitrário, obtendo resultados muito bons para a distribuição de pressão.

Bristow & Grose [4] e Johnson [10] propuseram esquemas de cálculo, baseados no método dos paineis, para obter a solução da teoria da linha de corrente livre, para o caso particular do escoamento descolado sobre um perfil com alto ângulo de incidência.

Com base no método acima, Henderson [8] estudou o escoamento descolado sobre perfis com multiplos elementos, obtendo resultados razoáveis para os coeficientes de sustentação, arrasto e momento.

No presente trabalho, apresenta-se um método numérico, baseado no método dos paineis [11], para obter uma solução geral do modelo da linha de corrente livre. Com isto é possível analisar qualquer corpo rombudo bidimensional e ainda, estudar diferentes condições de contorno sobre as linhas de corrente livre.

DESCRIÇÃO DO MÉTODO NUMÉRICO

O escoamento incompressível e potencial, externo ao obstáculo e sua esteira média, é descrito pela equação de Laplace, com condições de contorno mistas, isto é, em parte da fronteira tem-se velocidade normal nula e no restante a velocidade tangente é especificada, como mostrado na figura- 1a.

Para resolver este problema é conveniente utilizar o método dos paineis [9], devido a sua simplicidade e flexibilidade, permitindo o estudo de geometrias complexas, assim como a fácil alteração da distribuição de pressão ao longo dos trechos AB e A'B'.

No método dos paineis, é necessária apenas uma discretização da fronteira do escoamento, que no caso particular esquematizado na figura- 1a, é constituida pela parte frontal do obstáculo e pelas linhas de corrente livre .

No caso bidimensional, o elemento básico da discretização é um segmento de curva (painel), no qual é feita uma repartição de singularidades [3]. Utilizando-se uma discretização com N_T elementos e satisfazendo- se as condições de contorno impostas na

fronteira, obtem-se um sistema de equações lineares, do tipo

$$[A][X] = [B] \qquad (1)$$

onde [A] é a matriz dos coeficientes de influência, que depende apenas da geometria da fronteira, [B] é o vetor dos termos independentes e [X] é o vetor das incógnitas, que são as intensidades das repartições de singularidade de cada painel. Com a solução do sistema (1), tem-se os campos de velocidade e pressão do escoamento estudado.

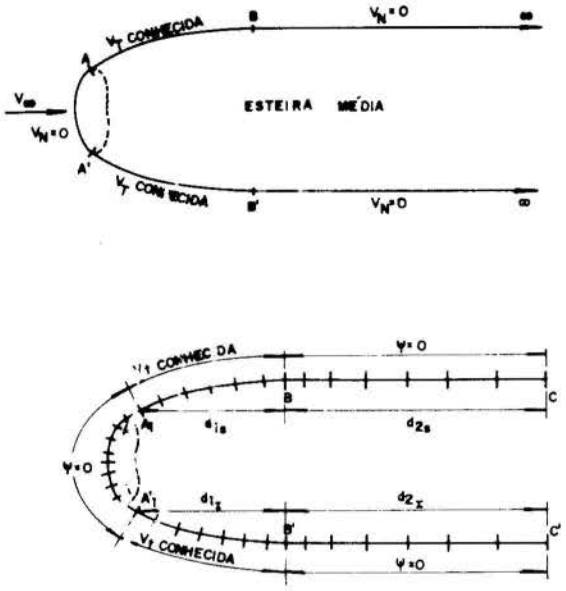

Figura-1 : Condições de contorno sobre o obstáculo e suas linhas de corrente livre

Para o problema não linear analisado neste trabalho, surgem algumas dificuldades para a aplicação do método acima. Inicialmente, observa-se na figura-1a, que uma parte da fronteira a ser discretizada é constituida pelas linhas de corrente livre, que são infinitas. Um segundo problema aparece devido ao fato das condições de contorno serem mistas. Como será visto adiante, isto implica em uma difícil escolha do tipo de singularidade a ser repartida no painel. Por fim, deve ser salientado que a forma e posição da fronteira da esteira média , compativeis com as condições de contorno impostas, não são conhecidas "a priori". Sua determinação é feita através de um processo iterativo, onde uma forma, inicialmente dada, é modificada até que ocorra compatibilidade com as condições de contorno.

Análise da Singularidade O elemento principal do método numérico usado neste trabalho é um segmento de reta ou curva, onde é feita uma repartição de singularidades, que pode ser dos tipos fonte, dipólo e vórtice [9] . Teoricamente, qualquer uma destas singularidades pode ser usada, desde que as condições de contorno sobre o obstáculo sejam satisfeitas . Entretanto, do ponto de vista numérico, a escolha do tipo de singularidade tem grande importância para se evitar problemas de imprecisão e instabilidade numérica [9] .

Segundo Bousquet [3], a escolha do tipo de singularidade depende das condições de contorno do problema analisado . A configuração utilizada neste trabalho, assim como suas condições de contorno são mostradas na figura- 1a. Trata-se de um problema de Poincaré da equação de Laplace [9], onde a velocidade normal (V_n) é especificada em uma parte da fronteira, enquanto a velocidade tangente (V_t) é dada no restante da mesma .

Levando em conta a regra da eficácia [3], a escolha natural da singularidade recai sobre o painel tipo fonte, na região da fronteira onde V_n é dada, e no painel tipo vórtice, onde V_t é especificada. Neste caso a matriz dos coeficientes de influência possue os elementos da diagonal principal dominantes em relação aos demais, fato que garante o bom condicionamento da mesma.

A solução deste esquema numérico fornece resultados muito imprecisos nas vizinhanças dos pontos A,B,C,A', B' e C' , que são causados pela utilização de paineis de tipos diferentes . Neste caso, na interface de cada trecho da fronteira, observam-se grandes variações de intensidade de cada tipo de singularidade.

Problemas semelhantes aos relatados acima ocorrem na solução numérica do escoamento incompressivel e potencial sobre um perfil fino com grande carregamento, onde a imprecisão dos cálculos é associada ao aparecimento de gradientes elevados da intensidade de fonte [10].

Outras combinações de singularidades como fonte e dipólo tangente, vórtice e dipolo normal acarretam o mesmo tipo de problema discutido acima.

A partir das experiências relatadas acima, procurou-se montar um esquema numérico que utilizasse apenas um tipo de singularidade em toda a fronteira .

Uma das possibilidades é a utilização do painel com intensidade de fonte constante . Neste caso , alguns elementos da matriz dos coeficientes de influência são zeros , entretanto a matriz não é singular . Este esquema fornece resultados muito interessantes nos paineis localizados na primeira parte das linhas de corrente livre, onde a velocidade tangente é especificada . Este tipo de condição de contorno é responsável por uma distribuição de fontes alternada, isto é, uma fonte seguida de um sumidouro e assim sucessivamente, que causam instabilidade numérica no processo iterativo, necessário para a obtenção da forma final da fronteira da esteira média.

Os resultados precedentes indicam que a singularidade adequada para a solução deste problema é o painel com repartição constante de dipolo tangente, pois o campo de velocidades, induzido pelo mesmo, é idêntico ao produzido por uma fonte e um sumidouro , localizados nas extremidades do painel [6] . Outro detalhe importante é o fato da velocidade normal ser nula no centro do painel (ponto de controle) e a função corrente (ψ) sofrer um salto, quando o mesmo é atravessado de um lado para outro .

Nos trechos onde a velocidade normal é nula, tem-se função corrente constante . Teoricamente estas condições de contorno são equivalentes, entretanto, recorrendo-se a regra da eficácia [3] ,verifica-se que, do ponto de vista numérico, a função corrente é mais adequada para um painel com as caracteristicas acima .

Tendo em vista as considerações feitas anteriormente, implementou-se um esquema numérico que utiliza um único tipo de singularidade , o painel com repartição constante de dipolo tangente, e condições de contorno mistas, com velocidade tangente especificada na primeira parte das linhas de corrente livre e função corrente constante no restante da fronteira, como mostrado na figura-1b. As equações necessárias para a confecção do presente método numérico são apresentadas no apêndice - A.

Determinação da Forma das Linhas de Corrente Livre A fronteira do escoamento potencial e incompressível, constituida pela parte frontal do obstáculo e linhas de corrente livre, é discretizada em N_T paineis retos (vide figura-1b). Os segmentos de reta AA_1 e $A'A'_1$, chamados, neste trabalho, de paineis de controle, são tangentes ao obstáculo nos pontos de separação A e A'. Embora pertençam às linhas de corrente livre, são tratados como parte do obstáculo. A condição de contorno imposta nestes paineis é $\psi = 0$ e a posição dos mesmos permanece inalterada durante o processo iterativo . Como será mostrado a seguir, estes paineis tem grande importância na determinação das distâncias d_{1_I} e d_{1_S}, que são desconhecidas "a priori".

A solução numérica do modelo descrito acima é alcançada quando se encontra a forma e posição das linhas de corrente livre , compativeis com as condições de contorno especificadas . Para tanto , utiliza-se o processo iterativo, descrito abaixo.

Inicialmente são dadas , de maneira arbitrária, uma forma e posição para as linhas de corrente livre. Satisfazendo-se as condições de contorno no centro de cada um dos N_T paineis (pontos de controle), obtem-se um sistema com N_T equações lineares, cuja solução fornece as N_T intensidades de dipolo tangente. Com isto é possivel se calcular a velocidade e a pressão em qualquer ponto do escoamento.

Em geral, a fronteira dada inicialmente não é uma linha de corrente do escoamento calculado. Neste caso, tem-se velocidade normal (V_n) diferente de zero sobre os segmentos A_1B e A'_1B' . Movimentando-se os paineis que pertencem a estes segmentos, de modo a alinha-los à direção do escoamento local, obtem-se uma nova fronteira da esteira média.

Considerando-se a nova geometria, resolve-se o sistema (1) e obtem-se o campo de velocidades do escoamento em estudo. No caso das velocidades normais, sobre os segmentos A_1B e A'_1B', não terem valores suficientemente baixos, o processo iterativo continua. Caso contrario, a convergencia foi alcançada e a fronteira da esteira média é uma linha de corrente do escoamento.

RESULTADOS DO PRESENTE MÉTODO

O método numérico desenvolvido neste trabalho é usado para obter os parâmetros dos escoamentos médios sobre a placa plana normal e sobre o cilindro circular. Estas geometrias possuem solução analítica, propiciando uma comparação dos resultados numéricos com os analíticos.

Placa Plana Normal O escoamento descolado médio sobre a placa plana normal à direção do escoamento não perturbado (V_∞) é analisado numéricamente com duplo objetivo: (i) mostrar a forma de operação do método numérico exposto na seção anterior, com particular atenção na determinação das distâncias d_{1_S} e d_{1_I} e (ii) validar o esquema numérico, comparando seus resultados com os analíticos obtidos por Roshko [13].

Inicialmente é especificado um valor para o coeficiente médio de pressão na base . Em seguida, são dadas , de maneira arbitrária, a forma e posição das linhas de corrente livre, que normalmente são segmentos de reta paralelos a direção de V_∞ , como mostrado na figura-2a . A primeira parte deste segmento , com comprimento $d_1 = d_{1_I} = d_{1_S}$, se deforma durante o processo iterativo, como pode ser visto na figura-2 . A segunda parte, com comprimento $d_2 = d_{2_I} = d_{2_S}$, não tem sua forma modificada e se mantem paralela a direção de V_∞ .

No presente método numérico, d_1 e d_2 devem ser especificados no inicio do cálculo. O comprimento d_2 é feito bem maior que a distância característica do obstáculo (d) , de modo a garantir que o truncamento das linhas de corrente livre não tenham influência no escoamento próximo ao corpo . O valor de d_1 , inicialmente dado de forma arbitrária, é posteriormente corrigido através de um segundo processo iterativo .

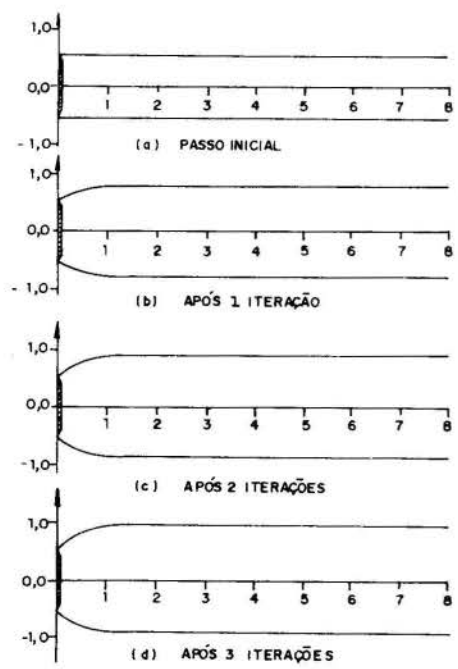

Figura-2: Forma e posição das linhas de corrente livre, $d_1/d = 1,5$; $d_2/d = 30$; $Cp_b = -1,372$.

A discretização da parte frontal do obstáculo e da fronteira da esteira média é feita de modo que não existam diferenças acentuadas no tamanho de paineis vizinhos .

Na figura-2 , são mostrados todos os passos do esquema iterativo, necessário para a determinação da forma e posição das linhas de corrente livre . Obtida a convergência, que neste caso é alcançada após quatro iterações, calcula-se a velocidade e pressão nos paineis de controle, que desempenham papel fundamental no presente esquema de cálculo.

Como definido anteriormente, os paineis de controle pertencem à fronteira da esteira média e são adjacentes aos pontos de separação . Uma vez que o campo de pressões do escoamento é contínuo, conclue-se que as pressões na base do obstáculo e nos paineis de controle devem ser aproximadamente iguais.

No caso particular relativo a figura-2 , o coeficiente de pressão na base foi fixado, no inicio do cálculo, com o valor de $Cp_b = -1,372$, entretanto nos paineis de controle tem-se $Cp_c = 0,98$. Esta discrepância é uma conseqüência da arbitrariedade do valor de d_1 , fixado no inicio do cálculo. Na solução analítica do mesmo problema [13], tem-se um comprimento d_1 para cada coeficiente de pressão na base, mostrando que existe uma relação de compatibilidade entre estes parâmetros.

A determinação do valor de d_1 , compatível com Cp_b fixado no inicio do cálculo, é feita através de um segundo processo iterativo, cujos resultados estão apresentados na figura-3 . Variando-se o valor de d_1 tem-se diferentes valores para o coeficiente de pressão nos paineis de controle (Cp_c). A convergencia deste segundo processo iterativo é alcançada quando $Cp_c = Cp_b$.

Terminada a execução dos dois processos iterativos, tem-se o campo de pressões do escoamento assim como a configuração da esteira média. Observa-se na figura-4 que os resultados numérico, analítico e experimental, para a distribuição de pressão na parte frontal da placa plana, são praticamente coincidentes, garantindo um cálculo preciso para o coeficiente médio de arrasto.

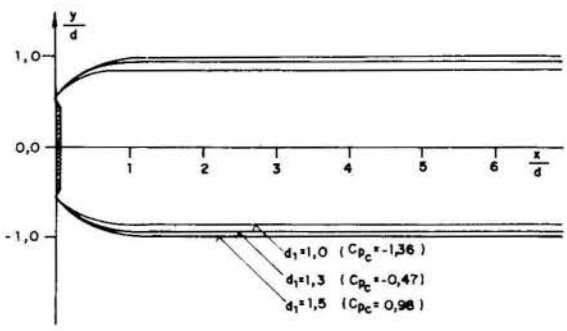

Figura-3: Forma e posição da fronteira da esteira média em função do comprimento d_1 .

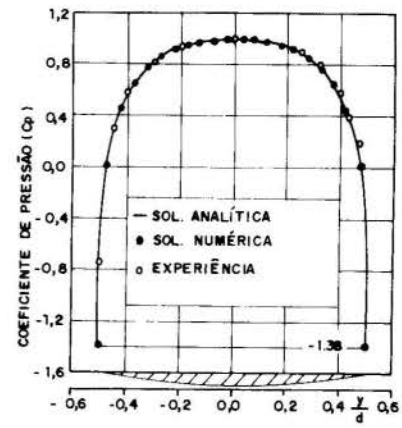

Figura -4: Distribuição de pressão na parte frontal da placa plana , para $Cp_b = -1,372$

Cilindro Circular no Regime Subcrítico No obstáculo analisado anteriormente, os pontos de separação da camada limite são fixados pela geometria dos mesmos. No caso do cilindro circular o ponto de separação varia com o número de Reynolds [2]. No regime subcrítico, o escoamento na camada limite é laminar e o descolamento da mesma ocorre a aproximadamente 82°, do ponto de estagnação a montante.

O problema da determinação dos pontos de separação foi abordado por Henderson [8] e Hayashi & Endô [7], para o escoamento sobre perfis em alto ângulo de incidência. Nestes trabalhos foi utilizado um processo iterativo, onde um cálculo do escoamento potencial sobre o corpo e sua esteira média era alternado com um cálculo de camada limite.

No presente trabalho, os pontos de separação são considerados conhecidos e normalmente obtidos da experiência. (através da distribuição média de pressão ou da tensão de cisalhamento na superfície do corpo [2]).

Após os dois processos iterativos descritos na seção precedente, obtem-se a forma e posição das linhas de corrente livre e também a distribuição de pressão na parte frontal do cilindo circular

A solução analítica de Roshko [13] é obtida admitindo- se que a linha de corrente livre possui a mesma curvatura que o cilindro circular no ponto de separação. Esta hipótese acarreta uma distribuição de pressão sem gradiente adverso (figura-5), o que, entretanto, é essencial para que haja descolamento em obstáculos como este.

Como observado por Parkinson & Jandali [12], a curvatura da fronteira da esteira média, no ponto de separação, deve ser côncava, quando vista de fora da esteira. Este detalhe importante resulta naturalmente da presente solução numérica, como mostrado na figura-6, fornecendo uma distribuição de pressão que concorda muito bem com a experiência (vide figura- 5).

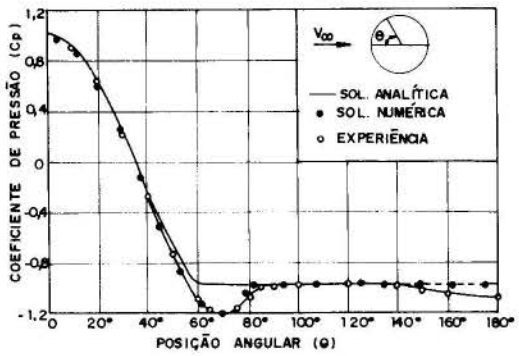

Figura-5: Distribuição média de pressão no cilindro. Re = 14.500 ; θ_s = 82° ; Cp_b = -0,96.

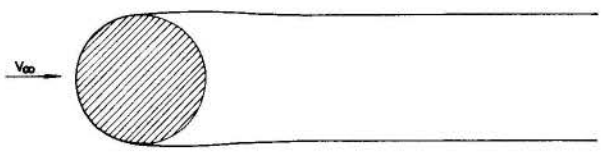

Figura-6: Forma e posição das linhas de corrente livre para o cilindro θ_s = 82°; Cp_b = -0,96

CONCLUSÃO

Com o modelo da linha de corrente livre [11], pode-se obter excelentes resultados para a distribuição de pressão na parte frontal de um corpo rombudo, desde que a pressão na base do mesmo seja conhecida.

As soluções analíticas obtidas anteriormente se restringem a geometrias particulares e as soluções numéricas de Bristow & Grose [4] e Johnson [10] são específicas para perfis en alto ângulo de incidência.

No presente trabalho apresentou-se um método numérico geral para a solução do modelo da linha de corrente livre, isto é, pode- se analisar formas complexas de corpos bidimensionais e ainda, variar as condições de contorno aplicadas à fronteira da esteira média.

Para o escoamento sobre o cilindro circular no regime subcrítico e para a placa plana normal ao escoamento não perturbado, o presente método forneceu resultados que concordam muito bem com as soluções analíticas e também com a experiência.

Neste trabalho as condições de contorno sobre as linhas de corrente livre não foram variadas. Na referência [6] foi mostrado que a variação destas condições de contorno é muito importante para se modelar o comprimento da região de formação da esteira de corpos rombudos.

REFERÊNCIAS BIBLIOGRÁFICAS

[1] ABERNATHY, F.H. Flow over on inclined plate. J.Basic Eng. (Trans. of ASME), vol. 84 , pp. 380-388, 1962.

[2] ACHENBACH, E. Distribution of local pressure and skin friction around a circular cylinder in cross-flow up to Re = 5 x 10^6. J. Fluid Mech, vol. 34, pp. 625-639, 1968.

[3] BOUSQUET, J. Methode des Singularites. Ecole Nationale Superieure de L' Aeronautique et de L'Espace, Toulouse, France, 1982.

[4] BRISTOW, D.R. & Grose, G.G. Modification of the Douglas Neumann program to improve efficiency of predicting component interference and high lift characteristics. Washington, DC, NASA, 1978. (NASA CR-3020).

[5] FAGE, A. & JOHANSEN, F.C. On the flow of air behind an inclined flat plate of infinite span. Proc. Roy. Soc. London A, vol. 116, pp. 170-197, 1927.

[6] GIRARDI, R. M. Modelo Aerodinâmico do Escoamento Plano sobre Corpos Rombudos. Tese de Doutorado, Instituto Tecnológico de Aeronáutica, S J Campos, SP, 1989.

[7] HAYASHI, M. & ENDÔ, E. A method for calculating the flow around arbitrary airfoil sections with separation. Japan Soc. Aero. Space Sci. vol. 20, pp. 113-124, 1977.

[8] HENDERSON, M. L. Two-dimensional separated wake modeling and its use to predict maximum section lift coeficient. AIAA 16th Aeroespace Sciences Meeting, Huntsville, Alabama, 1978 (AIAA paper 78-156).

[9] HUNT, B. The panel method for subsonic aerodynamic flows. VKI Lectures Series on Compt. Fluid Dyn., 1978.

[10] JOHNSON, F.T. A general panel method for the analysis and design of arbitrary configurations in incompressible flows. Washington, DC, NASA, 1980. (NASA CR-3079).

[11] MILNE-THOMSON, L.M. Theoretical Hydrodynamics. 5 ed., London, Great Britain, MACMILLAN, 1974.

[12] PARKINSON, G. V. & JANDALI, T. A wake source model for bluff body potencial flow. J. Fluid Mech., vol. 40, pp. 577-594, 1970.

[13] ROSHKO, A. A new hodograph for free-streamline theory. Washington, DC, NACA, 1954. (NACA TN-3168).

[14] WOODS, L.C. Two-dimensional flow of a compressible fluid past given curved obstacles with infinite wakes. Proc. Roy. Soc. London A, vol 227, pp. 367-386, 1955.

[15] WU, J.C. Theory for aerodynamic force and moment in viscous flows. AIAA J., vol. 19, pp. 432-441, 1981.

APÊNDICE - A

Neste apêndice, são apresentadas as equações que descrevem o potencial complexo e a velocidade complexa conjugada para um painel com distribuição constante de dipolo tangente.

Seja um painel reto genérico j, definido por suas extremidades Z_{j+1} e Z_j . Sobre este painel é feita uma repartição de dipolo tangente com densidade constante $\nu_j = \frac{d\mu}{ds}$. O potencial complexo F(Z) e a velocidade complexa conjugada $V^*(Z)$ em um ponto Z são dados respectivamente por [6]

$$F(Z) = \frac{\nu_j}{2\pi} \log \left[\frac{Z - Z_{j+1}}{Z - Z_j} \right] \qquad (2)$$

$$V^*(Z) = \frac{\nu_j}{2\pi} \left[\frac{1}{Z - Z_{j+1}} - \frac{1}{Z - Z_j} \right] \qquad (3)$$

A equação (3) é válida para um ponto Z qualquer, mas a equação (2) só pode ser usada para um ponto Z que não pertence ao painel. Os potenciais complexos em pontos vizinhos ao ponto de controle (ponto médio do painel j) são dados por [6]

$$F(Z^+_{c_j}) = i \frac{\nu_j}{2} \qquad (4)$$

$$F(Z^-_{c_j}) = - i \frac{\nu_j}{2} \qquad (5)$$

onde $Z^+_{c_j}$ é um ponto vizinho ao ponto de controle a esquerda do painel (lado do painel onde o versor normal é positivo) e $Z^-_{c_j}$ é um ponto vizinho a direita.

Uma vez que $F(Z) = \phi + i\psi$, observa-se que o potencial de velocidade (ϕ) é contínuo, mas a função corrente (ψ) sofre um salto, quando o painel é atravessado, tal que

$$[\ \psi\ ] = \psi\ (Z^+_{c_j}) - \psi\ (Z^-_{c_j}) = \nu_j \qquad (6)$$

ABSTRACT

The mean flow over a plane bluff body can be analysed by the so called free streamline theory. In this theory, it is assumed potential flow in the region outside the body and its wake. The flow inside this region is disregarded and the boundary of the mean wake is modeled by the free streamline. In this work, the above theory is solved numerically by the panel method. After an analysis of the numerical procedure, the solutions of the separated flows over a normal flat plate and a circular cylinder in the subcritical regime are obtained. Excelent agreement between numerical, analytical and experimental results are observed in both cases.

III ENCIT – Itapema, SC (Dezembro 1990)

SINGULAR INTEGRALS IN THEORETICAL AERODYNAMICS THEIR ORIGIN AND COMPUTATION

Maurício Pazini Brandão
Instituto Tecnológico de Aeronáutica
São José dos Campos, SP, 12225, Brazil

SUMMARY

Singular integrals appear in theoretical aerodynamics whenever one attempts to integrate a governing equation of the Laplacian or wave type. Depending on the nature of the sources or the geometry of the boundary conditions, stronger singularities are revealed. Here we prove the usefulness of the concept of finite-part of singular integrals in their computation. Integrals with multiple singularities within the integration domain are also discussed. Finally, postulates for the finite-part of singular integrals in multi-dimensional domain are introduced.

INTRODUCTION

Modern computational analyses of fluid flows are based on the solution of the Euler or Navier-Stokes' equations by means of finite-difference, finite-volume or finite-element techniques. The largest segment of the aerodynamic community is devoted to these techniques by employing powerful computational resources. However, there is still room for traditional tools of aerodynamic analysis, as well as for emerging methods, provided they show some usefulness for special applications.

There is no doubt that homogeneous or inhomogeneous forms of the Laplacian and wave equations play important roles in aerodynamics. Problems of incompressible flow require the solution of a Laplacian equation for variables of interest, like the velocity potential for example. Problems of steady compressible flow can be modeled by a Poisson equation after a suitable transformation of variables. Yet problems of unsteady compressible flow demand the solution of a wave equation, the same happening for problems of linear acoustics.

The special importance of these two equations for aerodynamics can also be extended to other branches of theoretical physics. Electrodynamics, magnetism, elasticity, and fracture mechanics are just examples of areas of research where these equations appear, usually associated to a context involving some potential theory.

A modern branch of non-linear acoustics, namely, the *Acoustic Analogy* of Lighthill [1], makes also use of the wave equation and Laplace's equation. But this time there is no potential assumption presupposed. Instead, there is just a clever rearrangement of first conservation principles. The equation of Lighthill is a concise statement of the Navier-Stokes' equation in a wave-like form. It is valid for free flows without boundaries. Its sequel, the equation developed by Ffowcs Williams and Hawkings [2], includes the effect of moving boundaries. These two forced wave equations yield Poisson equations in their incompressible limits. Therefore, this line of research also leads to forms of the traditional equations of aerodynamics.

Logic recommends that these differential equations be solved by following integration paths. The transformation of the governing equations via Green's functions into integral equations is currently considered as a form of the Boundary Element Method if boundary sources are involved. This is the case with the present research, which includes boundary and volume sources.

It happens that the basic integral solution of the equation of Laplace is singular when source and observer coincide. The same can be concluded with respect to the wave equation. Therefore, the singularity of the integral solution is established from the very beginning of the solution process.

Stronger singularities are introduced when derivatives of singular integrals are required. Furthermore, integrable singularities may be revealed simultaneously in other places of the integration domain by the geometry of the boundary. This combination of singularities forces the analyst to handle complicate integration algorithms.

Here we discuss the efficiency of some of these integration techniques. The computation of the derivative of a first-order singular integral is performed by following three differents paths and the most efficient one is indicated. The discussion is completed with some considerations about multi-singular integrals and singular integrals in unbounded domains.

This study is geared towards a solution of the Ffowcs Williams and Hawkings equation. However, since for compressible flows the equation is of the wave type and for incompressible problems it is of the Laplacian type, the present considerations may apply to other contexts as well. Therefore, the contributions here are of theoretical and computational nature and are not restricted to the particular field of aerodynamics.

SINGULAR INTEGRALS - ORIGIN

The equation of Ffowcs Williams and Hawkings [2] describes the pressure perturbations p created in a quiescent fluid of undisturbed density ρ_o due to the motion of a body of surface described by the equation $f = 0$. For compressible flows, the equation reads as follows:

$$\bar{\Box}^2 \left[c^2(\rho - \rho_o)\right] = \frac{\bar{\partial}}{\partial t}\left[\rho_o u_i \frac{\partial f}{\partial x_i}\,\delta(f)\right] - \frac{\bar{\partial}}{\partial x_i}\left[\mathcal{P}_{ij}\frac{\partial f}{\partial x_j}\,\delta(f)\right] + \frac{\bar{\partial}^2 \mathcal{T}_{ij}}{\partial x_i \partial x_j} \qquad (1)$$

Here, $\bar{\Box}^2$ is the generalized wave operator applied to $c^2(\rho - \rho_o)$, which equals the perturbation pressure p to first order. The forcing terms of this wave equation are of two types: the monopole and dipole are boundary contributors, indicated by the Dirac delta function of the body surface; and the quadrupole is a volume effect, valid for the unbounded domain of fluid outside the surface.

For incompressible flows, equation (1) reduces to

$$\bar{\nabla}^2 p = -\frac{\bar{\partial}}{\partial t}\left[\rho_o u_i \frac{\partial f}{\partial x_i}\,\delta(f)\right] + \frac{\bar{\partial}}{\partial x_i}\left[\mathcal{P}_{ij}\frac{\partial f}{\partial x_j}\,\delta(f)\right] - \frac{\bar{\partial}^2 \mathcal{T}_{ij}}{\partial x_i \partial x_j} \quad (2)$$

This time $\bar{\nabla}^2$ is the generalized Laplacian operator applied directly to the perturbation pressure p. $\mathcal{P}_{ij}$ is the compressive stress tensor and $\mathcal{T}_{ij}$ is another stress tensor which has been named after Lighthill [1]. For more information on this, the reader may consult Farassat [3] or Brandão [4].

Equations (1) and (2) are our prototypes for the discussion that follows concerning flow problems in compressible and incompressible mediums. As prototypes, they are very convincing, for they are general representatives of inhomogeneous wave and Laplacian equations. Furthermore, they are *exact* representations of the conservation laws of mass and momentum and incorporate boundary conditions as source terms.

Integration is the best solution path for these equations because integration is the mathematical operation for inverting differentiations and the boundary terms (monopole and dipole) acquire workable meaning only after being integrated.

The impulsively excited three-dimensional equations

$$\frac{1}{c^2}\frac{\partial^2 \mathcal{C}}{\partial t^2} - \frac{\partial^2 \mathcal{C}}{\partial x_i \partial x_i} = \delta\left(\vec{x}(t) - \vec{y}(\tau)\right)\,\delta(t-\tau)$$

$$\frac{\partial^2 \mathcal{I}}{\partial x_i \partial x_i} = \delta\left(\vec{x}(t) - \vec{y}(t)\right)$$

have solutions given respectively by

$$\mathcal{C}(\vec{x},\vec{y},t,\tau) = \frac{\delta(g)}{4\pi r} \quad (3)$$

$$\mathcal{I}(\vec{x},\vec{y},t) = -\frac{1}{4\pi r} \quad (4)$$

In solution (3)

$$g = \tau - t + \frac{r}{c} = 0$$

is a sphere of signals emitted at the source point $\vec{y}$ at retarded time τ and

$$r = |\vec{x}(t) - \vec{y}(\tau)|$$

is the distance traveled by the information from the source towards the observer $\vec{x}$ at actual time t. In the incompressible solution (4), τ becomes equal to t and r becomes equal to the instantaneous distance between a source and the observer.

Equations (3) and (4) are the basic solutions for the wave and Laplacian equations. For solid background on this, the reader may look into Morse and Feshbach [5]. Due to the fact that equations (1) and (2) are *linear* for the variables of interest, the principle of superposition is formally applicable. Thus, full integral transformations of these equations are allowed. The compressible equation (1) then leads to

$$4\pi c^2(\rho - \rho_o) = \frac{\bar{\partial}}{\partial t}\int_{-\infty}^{t}\int_{\mathcal{V}} \frac{\rho_o u_i}{r}\frac{\partial f}{\partial x_i}\,\delta(f)\,\delta(g)\,d\mathcal{V}\,d\tau$$

$$-\frac{\bar{\partial}}{\partial x_i}\int_{-\infty}^{t}\int_{\mathcal{V}} \frac{\mathcal{P}_{ij}}{r}\frac{\partial f}{\partial x_j}\,\delta(f)\,\delta(g)\,d\mathcal{V}\,d\tau$$

$$+\frac{\bar{\partial}^2}{\partial x_i \partial x_j}\int_{-\infty}^{t}\int_{\mathcal{V}} \frac{\mathcal{T}_{ij}}{r}\,\delta(g)\,d\mathcal{V}\,d\tau \quad (5)$$

Similarly, the incompressible equation (2) yields

$$4\pi p = \frac{\bar{\partial}}{\partial t}\int_{\mathcal{V}} \frac{\rho_o u_i}{r}\frac{\partial f}{\partial x_i}\,\delta(f)\,d\mathcal{V}$$

$$-\frac{\bar{\partial}}{\partial x_i}\int_{\mathcal{V}} \frac{\mathcal{P}_{ij}}{r}\frac{\partial f}{\partial x_j}\,\delta(f)\,d\mathcal{V} + \frac{\bar{\partial}^2}{\partial x_i \partial x_j}\int_{\mathcal{V}} \frac{\mathcal{T}_{ij}}{r}\,d\mathcal{V} \quad (6)$$

Here, $d\mathcal{V}$ stands for an element of volume of the unbounded domain of fluid outside the surface $f = 0$. From these results we observe that

- if a solution is possible, it can be used for the near field and boundary (aerodynamics) or the far field (aeroacoustics);
- the right hand side leads to surface integrals on the boundary $f = 0$ and to volume integrals in the outside domain;
- the integrals involved are singular because r goes to zero within the integration region; and
- single and double derivatives of singular integrals are required to yield the pressure perturbation.

Researchers argue on how integrals like those appearing in equations (5) and (6) should be evaluated. Some defend the idea that derivatives should be performed only after the computation of the associated integrals. Others believe that derivatives should be performed first and integrals later. We shall clarify this issue in this paper with the objective of obtaining better computational efficiency.

The geometry of the boundary may introduce further singularities. The derivative of the shape of airfoils with rounded leading edges usually brings in terms weakly singular there. For example, if the leading edge is placed at $x = a$, the equation describing the airfoil section has a term proportional to $(x-a)^{\frac{1}{2}}$. A first derivative of this function with respect to x produces a term proportional to $(x-a)^{-\frac{1}{2}}$. Bodies with rounded leading and trailing edges have geometrical singularities at both edges. Although these are integrable singularities, they help in complicating the practical computation of the associated integrals. This fact is discussed later in this paper.

Finally, there is another aspect of singular integrals appearing in aerodynamics which is not explored here, but is quoted for the sake of completeness. It refers to vortical flows in incompressible fluids. It is well-known that the velocity field induced by a vortex filament may be described in this case by the Biot-Savart law, which is singular in the immediate vicinity of the vortex. This theory introduces singularities near the edges of a thin wing, for example, at an angle of incidence with the oncoming flow. This aspect is linked to the classical downwash integral, which reads as follows in two-dimensional domain:

$$w(x_o, 0) = \lim_{y \to 0}\frac{1}{2\pi}\int_a^b \frac{\mathcal{F}(x)(x_o - x)}{(x_o - x)^2 + y^2}\,dx$$

Here, w is the induced velocity on the plane of the wing due to a vorticity distribution of intensity $\mathcal{F}(x)$. This integral clearly leads to a Cauchy Principal Value problem. However, we should note that no new mechanism is introduced in this analysis beyond those already discussed, since Biot-Savart's law comes from the formal solution of a Poisson equation.

In summary, singular integrals appear in theoretical aerodynamics from two mechanisms. The first is the own solution procedure for the governing equations, which is basically singular. The second is the geometry of the body surface. Couplings between these two processes are also possible if one is interested in investigating fluid properties near the edges of an airfoil.

SINGULAR INTEGRALS - COMPUTATION

Due to computational difficulties, the treatment of singularities is usually avoided. It is our interest to discuss how singular integrals should be computed for better efficiency. By better efficiency we imply better accuracy with the least computational effort.

The solution of the Ffowcs Williams and Hawkings equation requires surface and volume integrals for three-dimensional problems, and line and surface integrals for two-dimensional problems. For the sake of simplicity, most of the discussion here is limited to integrals with one integration variable. However, the principles examined with the aid of these integrals are general and very clarifying. Some extensions to two and three-dimensional domains of integration are presented later.

According to Carslaw [6], an integral of the type

$$\Im = \int_a^b \frac{\mathcal{F}(x)}{(x_o - x)^\alpha}\, dx \qquad (7a)$$

with $a \le x_o \le b$ has meaning in the sense of Riemann only if $\alpha < 1$. In this case, ordinary integration schemes may be used, as long as the weak singularity is approached adequately. For an algorithm that works well, see Stoer and Bulirsch [7]. When $\alpha = 1$, the integral has a sense established as the Principal Value of Cauchy, i.e.

$$\Im = \lim_{\epsilon \to 0} \left\{ \int_a^{x_o - \epsilon} \frac{\mathcal{F}(x)}{(x_o - x)}\, dx + \int_{x_o + \epsilon}^b \frac{\mathcal{F}(x)}{(x_o - x)}\, dx \right\} \qquad (7b)$$

Finally, when $\alpha > 1$ the integral diverges in the Riemann sense, but acquires a special meaning introduced by Hadamard [8] as

$$\Im = \lim_{\epsilon \to 0} \left\{ \int_a^{x_o - \epsilon} \frac{\mathcal{F}(x)\, dx}{(x_o - x)^\alpha} + \int_{x_o + \epsilon}^b \frac{\mathcal{F}(x)\, dx}{(x_o - x)^\alpha} + \mathcal{H}(\varepsilon) \right\} \qquad (7c)$$

Here, $\mathcal{H}(\varepsilon)$ is the function of ε which cancels out *exactly* the explosive parts of the diverging integrals. This function can be obtained from the analysis of the integral in the neighborhood of the singularity, i.e. in the domain $x_o - \varepsilon \le x \le x_o + \varepsilon$ in the case above. Anyway, the outcome of the limiting process (7c) is finite and unique. To this meaning of the integral Hadamard gave the name *finite-part*.

There are physical reasons for interpreting singular integrals which appear in aerodynamics in their finite-part. These reasons are based on the fact that fluid properties have finite and continuous descriptions in most ordinary circumstances. Hence, every link in a mathematical description of these physical processes should have a well-defined, finite, and continuous representation. The concept of finite-part was established without ambiguities and yield the expected behavior for the fluid properties in a flow. Therefore, it should be adopted as a standard procedure in analyses like the ones discussed in this paper.

In the fifties there was considerable amount of research in aerodynamics by making use of this idea. To quote an example, Lomax, Heaslet, and Fuller [9] studied the fundamental equations for subsonic and supersonic wing theory by considering source, doublet and vortex distributions in potential flows. The concept of finite-part is used throughout this work to interpreted the arising singularities. The reader may look at this reference and at the papers cited therein for further information.

Mangler [10] has given several formulas for the numerical computation of the finite-part of singular integrals which appear routinely in aerodynamics. These formulas are based on the definition (7c). However, the computation in this form is not efficient because

- it requires the evaluation of two integrals whose integrands *explode* near the integration limits;
- it also requires the not so easy analytical determination of the regularizing function $\mathcal{H}(\varepsilon)$; and finally
- it demands the evaluation of a numerical limit as ε goes to zero.

To improve the efficiency of computations of this kind, the author has proposed [11] first the cancelation of the singularities inside the integrand, and second the evaluation of the remaining finite-part integrals by means of analytical, exact formulas. We shall see here how this proposition works in practice.

To illustrate the discussion, let us consider the following problem which is basic for the computation of the contribution of monopole and dipole sources in two-dimensional flows:

$$\Im = \frac{d}{dx_o} \int_a^b \frac{\mathcal{F}(x)}{x_o - x}\, dx \qquad (8)$$

where $a \le x_o \le b$. Since the integral has sense in the meaning defined by Cauchy, a first answer may be written formally as

$$\Im = \lim_{\epsilon \to 0} \left\{ \lim_{h \to 0} \frac{1}{h} \left[\int_a^{x_o + h - \epsilon} \frac{\mathcal{F}(x)\, dx}{x_o + h - x} + \int_{x_o + h + \epsilon}^b \frac{\mathcal{F}(x)\, dx}{x_o + h - x} - \int_a^{x_o - \epsilon} \frac{\mathcal{F}(x)\, dx}{x_o - x} - \int_{x_o + \epsilon}^b \frac{\mathcal{F}(x)\, dx}{x_o - x} \right] + 2\, \frac{\mathcal{F}(x_o)}{\varepsilon} \right\} \qquad (8a)$$

This answer evaluates first the integral and later the derivative. The integral is computed by following the traditional (Mangler's) way. Note that the process involves a double numerical limit (in ε and h) and that integrands are singular near the limits of integration. The last term in the answer gives the function $\mathcal{H}(\varepsilon)$ for the case under consideration.

To overcome some of the numerical difficulties posed by the answer (8a), let us first *regularize* the integrand at x_o. This widely used "trick" for the evaluation of first-order singular integrals seems to have been proposed first by Carleman [12]. Although some researchers still call this technique a "trick", it forms the basis for a modern interpretation of the finite-part of singular integrals [11]. The second possible answer, therefore, is given by

$$\Im = \lim_{h \to 0} \frac{1}{h} \left[\int_a^b \frac{\mathcal{F}(x) - \mathcal{F}(x_o + h)}{x_o + h - x}\, dx - \int_a^b \frac{\mathcal{F}(x) - \mathcal{F}(x_o)}{x_o - x}\, dx + \mathcal{F}(x_o + h) \log \frac{x_o + h - a}{b - x_o - h} - \mathcal{F}(x_o) \log \frac{x_o - a}{b - x_o} \right] \qquad (8b)$$

This time the numerical limit is simple (in h only). Besides, the integrands are well-behaved at the singularity (provided the first derivative of $\mathcal{F}(x)$ exists and is finite near x_o). Thus, no special problems are posed for the computation of the integrals. In conclusion, the answer (8b) is more efficient than (8a). However, it still evaluates first the integral and later the derivative.

Let us now first perform the derivative. The result is a second-order singular integral which should be interpreted according to the concept of finite-part, i.e.

$$\Im = -\, \mathcal{FP} \int_a^b \frac{\mathcal{F}(x)}{(x_o - x)^2}\, dx$$

By following the rules expressed in reference [11], the third answer reads

$$\Im = -\int_a^b \frac{\mathcal{F}(x) - \mathcal{F}(x_o) + (x_o - x)\mathcal{F}'(x_o)}{(x_o - x)^2}\, dx + \mathcal{F}'(x_o) \log \frac{x_o - a}{b - x_o} + \frac{\mathcal{F}(x_o)(b - a)}{(x_o - a)(b - x_o)} \qquad (8c)$$

Note that this answer involves no numerical limits and that the integrand is continuous at x_o, provided the second derivative of $\mathcal{F}(x)$ exists and is finite there. Except for the regularized integral, which can be evaluated very accurately, the remaining terms are given in closed form. Therefore, there should be no doubts about the advantages of the answer (8c) in terms of accuracy and programming over the two previous ones.

Although the discussion above is centered on second-order singular integrals, there is no limitation in the order of the singularity. In other words, there is no limit on how many times we can carry out differentiations of a first-order singular integral, as long as the result is interpreted in its finite-part.

The technique of regularization used in the interpretation of strongly singular integrals is also useful in the computation of weakly singular integrals. For example, the simple problem

$$\Im = \int_a^b \frac{\mathcal{F}(x)}{\sqrt{x-a}}\, dx$$

may be easily solved by integration by parts, provided the function $\mathcal{F}(x)$ is sufficiently well-behaved. However, this requires the analytical or numerical evaluation of the first derivative of $\mathcal{F}(x)$. Instead, it is more efficient to use the formula below

$$\Im = \int_a^b \frac{\mathcal{F}(x) - \mathcal{F}(a)}{\sqrt{x-a}}\, dx + 2\sqrt{b-a}\,\mathcal{F}(a)$$

This time no derivative of $\mathcal{F}(x)$ is necessary and the integral can be computed with high accuracy by using ordinary integration schemes.

The integral above does not require the use of the concept of finite-part and does not appear directly in aerodynamic problems. However, it helps us in developing efficient integration routines for the computation of integrals which do appear in aerodynamics. For example, in the analysis of airfoils with rounded leading edge and chord placed in the domain $-1 \le x \le 1$ we need to evaluate the integral

$$\Im = \mathcal{FP} \int_{-1}^{1} \frac{\mathcal{F}(x)\, dx}{\sqrt{x+1}\,(x_o - x)} \tag{9}$$

One answer for this problem may be obtained with regularization of the root at x_o only and by making use of Gauss-Jacobi integration rules [13] to handle the weak singularity at the leading edge. This answer is given by

$$\Im = \int_{-1}^{1} \frac{\mathcal{F}(x) - \mathcal{F}(x_o)}{\sqrt{x+1}\,(x_o - x)}\, dx + \frac{\mathcal{F}(x_o)}{\sqrt{x_o+1}} \log \frac{\sqrt{2}+\sqrt{x_o+1}}{\sqrt{2}-\sqrt{x_o+1}} \tag{9a}$$

An alternative answer may be developed with *simultaneous regularization* of the root at the observer and at the leading edge. In this case we may use symmetric Gauss-Legendre integration rules [13] because the integrand poses no special problems. This answer reads

$$\Im = \int_{-1}^{1} \left[\mathcal{F}(x) - \mathcal{F}(-1)\frac{x_o - x}{x_o + 1} - \mathcal{F}(x_o)\frac{x+1}{x_o+1}\right] \frac{dx}{\sqrt{x+1}\,(x_o - x)}$$
$$+ \frac{\mathcal{F}(x_o)}{x_o+1}\left[-2\sqrt{2} + \sqrt{x_o+1}\,\log\frac{\sqrt{2}+\sqrt{x_o+1}}{\sqrt{2}-\sqrt{x_o+1}}\right]$$
$$+ \mathcal{F}(-1)\frac{2\sqrt{2}}{x_o+1} \tag{9b}$$

The answers (9a) and (9b) are equivalent. However, for accuracy better than 10^{-6} formula (9a) require quadrature rules of order 96 or greater, whereas formula (9b) attains the same performance with order 32. Therefore, although the answer (9b) with Gauss-Legendre quadrature looks more extensive, it is about three times more efficient than the answer (9a) with quadrature of the Gauss-Jacobian type.

The above results seem to suggest that for optimized computation of integrals we should regularize not only strong singularities, but also weak singularities of the polynomial type which may appear in the integration domain. This uniqueness of procedure yields additional savings in code development and programming techniques.

Singularities of fractional order are also common in aerodynamics. If in problem (9) the observer is placed at the leading edge of the airfoil, there results a singularity of order 3/2

$$\Im = -\,\mathcal{FP} \int_{-1}^{1} \frac{\mathcal{F}(x)}{(x+1)^{\frac{3}{2}}}\, dx \tag{10}$$

This problem may be regarded as the coalescence between a first-order solution singularity at the observer and a half-order geometrical singularity at the leading edge. It is obvious that this merging process should be interpreted under the concept of finite-part. Mangler [10] has presented a discussion and formulas applicable to this case. These formulas follow the idea expressed in the definition (7c), i.e.

$$\Im = -\lim_{\varepsilon \to 0}\left[\int_{-1+\varepsilon}^{1} \frac{\mathcal{F}(x)}{(x+1)^{\frac{3}{2}}}\, dx + \mathcal{H}(\varepsilon)\right] \tag{10a}$$

In contrast, we propose the following answer:

$$\Im = -\int_{-1}^{1} \left[\mathcal{F}(x) - \mathcal{F}(-1) - (x+1)\mathcal{F}'(-1)\right] \frac{dx}{(x+1)^{\frac{3}{2}}}$$
$$- 2\sqrt{2}\,\mathcal{F}'(-1) \tag{10b}$$

This result presents a regular integrand in the whole interval and avoids the determination of the function $\mathcal{H}(\varepsilon)$, as well as the numerical limit of formula (10a).

PRACTICAL EXAMPLES

Consider the following function:

$$\mathcal{F}(x) = 0.12\left(2.0994\sqrt{1+x} - 1.2170625 - 1.575625\,x\right.$$
$$\left. - 0.1935\,x^2 + 0.101625\,x^3 - 0.0634375\,x^4\right) \tag{11}$$

This function is continuous, with continuous derivatives in the semi-open interval $-1 < x \le 1$ and represents the upper surface of a NACA 0012 airfoil [14]. Our purpose here is to use this function to test the three possible answers to the problem (8) discussed in the previous section. These answers, for an observer placed at the quarter chord ($x_o = -0.5$), are given by

- Derivative of the Cauchy Principal Value

$$\Im_1 = \lim_{\varepsilon \to 0}\left\{\lim_{h \to 0}\frac{1}{h}\left[\int_{-1}^{-0.5+h-\varepsilon} \frac{\mathcal{F}(x)\, dx}{-0.5+h-x}\right.\right.$$
$$+ \int_{-0.5+h+\varepsilon}^{1} \frac{\mathcal{F}(x)\, dx}{-0.5+h-x} + \int_{-1}^{-0.5-\varepsilon} \frac{\mathcal{F}(x)\, dx}{0.5+x}$$
$$\left.\left. + \int_{-0.5+\varepsilon}^{1} \frac{\mathcal{F}(x)\, dx}{0.5+x}\right] + 2\,\frac{\mathcal{F}(-0.5)}{\varepsilon}\right\} \tag{11a}$$

- Derivative of the regularized first order singular integral

$$\Im_2 = \lim_{h \to 0}\frac{1}{h}\left[\int_{-1}^{1} \frac{\mathcal{F}(x) - \mathcal{F}(-0.5+h)}{-0.5+h-x}\, dx\right.$$
$$+ \int_{-1}^{1} \frac{\mathcal{F}(x) - \mathcal{F}(-0.5)}{0.5+x}\, dx$$
$$\left. + \mathcal{F}(-0.5+h)\log\frac{0.5+h}{1.5-h} + \mathcal{F}(-0.5)\log 3\right] \tag{11b}$$

- Finite-part of the second order singular integral

$$\Im_3 = -\int_{-1}^{1} \frac{\mathcal{F}(x) - \mathcal{F}(-0.5) - (0.5+x)\mathcal{F}'(-0.5)}{(0.5+x)^2}\, dx$$
$$- \mathcal{F}'(-0.5)\log 3 + \frac{8}{3}\,\mathcal{F}(-0.5) \tag{11c}$$

Figure 1 shows the convergence of the limit in answer (11a) towards the direct result given by (11c) (0.5303572 to seven decimal places). The double limit presents a slight overshoot of the correct result and takes a lot of computing time as ε goes to zero. Figure 2 depicts similar behavior for the answer (11b). However, there is no overshoot in this case.

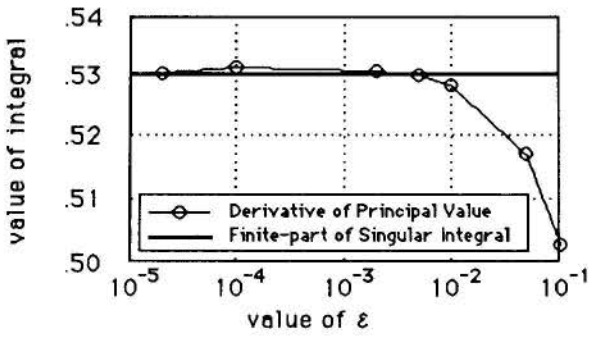

Figure 1: The convergence of answer (11a) for $h = 10^{-8}$.

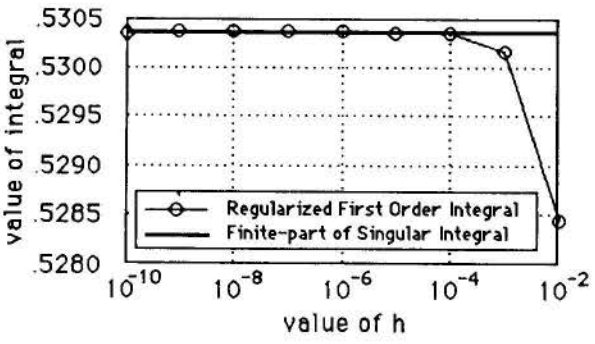

Figure 2: The single limit for answer (11b) of the test integral.

The three answers yield the same number as result for the derivative of a first-order singular integral. Besides, there are increasing computational savings and improvements in accuracy by going from answers a to c. Therefore, we should admit that the concept of finite-part is not only correct, but also provides a more efficient manner of computing singular integrals.

SOME EXTENSIONS AND DISCUSSION

The Ffowcs Williams and Hawkings equation has source terms on the boundary of a moving body (monopole and dipole), and in the flow outside the body (quadrupole). Here we discuss in general terms how these source contributions can be integrated and introduce ideas about the finite-part of singular integrals in multi-dimensional domains.

For two-dimensional problems, we may use a combination of Cartesian and cylindrical coordinate systems to handle the boundary and volume sources respectively. Both systems have a z coordinate which runs from $-\infty$ to $+\infty$. It is interesting to integrate along this direction first. Then, boundary terms become line integrals and volume terms turn into surface integrals. For problems of unsteady compressible flow, it is useful to consider a hypothetical fluid which is compressible on the plane (x, y) or (r, θ), but incompressible in the z direction, otherwise this first integration becomes terribly difficult. Furthermore, it should be noted that integrands inversely proportional to r give no contribution to two-dimensional problems [4].

Once the z integration has been performed, line integrals can be computed by using Cartesian coordinates because most airfoil shapes are described analytically in that way. The integration rules necessary for this job have been given in reference [11].

However, quadrupole sources pose new problems because their domain of integration is infinite. The natural system of coordinates for this case is a polar system with origin on the observer. The major problem resides in the computation of integrals of the following type:

$$\Im = \int_{\mathcal{S}} \frac{\mathcal{F}(r,\theta)}{r^2}\, d\mathcal{S}$$

where $\mathcal{F}(r,\theta)$ vanishes if r goes to infinity. Since the element of surface $d\mathcal{S}$ may be written as $r dr d\theta$, there results an integral inversely proportional to r on an unbounded plane. To this author's knowledge, there is no discussion of the concept of finite-part for this case in the literature. So, by similarity of procedure, we introduce the following interpretation of the integral:

$$\mathcal{FP} \int_{\mathcal{S}} \frac{\mathcal{F}(r,\theta)}{r^2}\, d\mathcal{S} = \int_{\mathcal{S}} \frac{\mathcal{F}(r,\theta) - \mathcal{F}(0,\theta)}{r^2}\, d\mathcal{S}$$

This interpretation indicates that near the observer the integrand behaves like the omni-directional derivative of the function $\mathcal{F}(r,\theta)$ with respect to r. A consequence of this postulate is that if $\mathcal{F}(r,\theta)$ would be a constant, say $\mathcal{A}$, then

$$\mathcal{FP} \int_{\mathcal{S}} \frac{\mathcal{A}}{r^2}\, d\mathcal{S} = 0$$

For three-dimensional problems boundary terms yield surface integrals and volume terms produce volume integrals. The natural systems of coordinates to be used now are body-conformed systems for the boundary sources and the spherical system with origin coinciding with the observer for the quadrupole. The novelty in both cases is that now integrals inversely proportional to r should not be discarded because for the monopole and dipole the surface domain is finite, e.g. a finite wing; and for the quadrupole, although the integration domain is infinite, pressure and velocity perturbations vanish at infinity.

The surface integrals present no special problems for their computation. However, quadrupole sources require the evaluation of the following integral:

$$\Im = \int_{\mathcal{V}} \frac{\mathcal{F}(r,\theta,\phi)}{r^3}\, d\mathcal{V}$$

Since the element of volume $d\mathcal{V}$ may be written as $r^2 \sin\theta dr d\theta d\phi$, we obtain an integral inversely proportional to r in an unbounded volume. To this author's knowledge, this is also new in the literature. Therefore, we introduce the following interpretation of the integral:

$$\mathcal{FP} \int_{\mathcal{V}} \frac{\mathcal{F}(r,\theta,\phi)}{r^3}\, d\mathcal{V} = \int_{\mathcal{V}} \frac{\mathcal{F}(r,\theta,\phi) - \mathcal{F}(0,\theta,\phi)}{r^3}\, d\mathcal{V}$$

Likewise, in the neighborhood of the observer the integrand behaves as the omni-directional derivative of $\mathcal{F}(r,\theta,\phi)$ with respect to r. A consequence of this second postulate is that if $\mathcal{F}(r,\theta,\phi)$ would be a constant, say $\mathcal{B}$, then

$$\mathcal{FP} \int_{\mathcal{V}} \frac{\mathcal{B}}{r^3}\, d\mathcal{V} = 0$$

When performing actual computations, the integration domain for the quadrupole will be finite, i.e. we will consider only the region of fluid where substantial activity occurs in terms of pressure and velocity perturbations. In addition, the surface and volume domains will be discretized in some way. Surfaces may become a collection of curved panels and volumes may be represented by a group of body-conformed cells. Here it is important to call the attention for the fact that discretization should happen only *after* regularization. Otherwise, with the refinement of the computational grid, strongly singular panels or cells will appear to spoil the efficiency we are trying to reach with this discussion.

Therefore, the above postulates may open the road to an emerging computational method for problems of fluid flow. There are reasons to believe that this method may be more efficient than existing ones, but considerable amount of research is still necessary to support this statement.

CONCLUSIONS

Singular integrals in theoretical aerodynamics originate from two sources. First, they result from the application of a basic integral solution by superposition to an equation of the Laplacian or wave type. Derivatives of this solution help in yielding even stronger singularities. Second, they stem naturally from the geometrical singularity introduced by boundaries with rounded edges. Since these entities, equations and bodies, are certainly object of studies in aerodynamic applications, aerodynamicists should be prepared to deal with this problem in their work.

Singular integrals should be interpreted under the concept of *finite-part*. The present interpretation of the idea is clearly superior than other concepts regarding singular integrals for the following reasons:

- it provides a finite interpretation for improper integrals with internal singularities of any order greater than one;
- it reproduces with clear improvements the Cauchy Principal Value of first-order singular integrals;
- it yields more efficient integration schemes for weak singularities (with order less than one); and
- it avoids the creation of "holes" around singularities and subsequent limits to reduce their size to zero.

Some researchers consider the idea of finite-part of singular integrals as an *ad-hoc* concept, deprived of substantial basis and confirmation. Here we hope to have proved, first, that the concept is correct and well-established. Second, that the idea yields the most efficient algorithms for the computation of singular integrals. With these contributions we try to unveil the suspicion with which the concept has been considered before.

This discussion may help in the understanding of integral equations of the singular type and improve their solution procedure. Efficient integration techniques have been presented for the computation of strong singular integrals in one-dimensional domain and postulates have been introduced for the interpretation of first order singularities in unbounded multi-dimensional domains. With these results, a mixed boundary-volume element method [15] may become feasible with the application of the Ffowcs Williams and Hawkings equation to problems of aerodynamics and aeroacoustics.

REFERENCES

[1] Lighthill, M.J. - "On Sound Generated Aerodynamically I. General Theory", Proc. Royal Society of London, A211, pp. 564-587, 1952.

[2] Ffowcs Williams, J.E. and Hawkings, D.L. - "Sound Generation by Turbulence and Surfaces in Arbitrary Motion", Phil. Trans. Royal Society of London, A264, pp. 321-342, 1969.

[3] Farassat, F. - "Advanced Theoretical Treatment of Propeller Noise", von Kármán Institute for Fluid Dynamics, Belgium, Lecture Series 81-82/10, 1982.

[4] Brandão, M.P. - "Towards the Unification of Acoustics and Fluid Mechanics", Applied Mechanics Reviews, Vol. 42, N. 11, Part 2, pp. S20-S31, 1989.

[5] Morse, P.M. and Feshbach, H. - Methods of Theoretical Physics, McGraw-Hill, pp. 834-857 and 1252-1256, 1953.

[6] Carslaw, H.S. - Introduction to the Theory of Fourier's Series and Integrals, Dover, pp. 125-133, 1950.

[7] Stoer, J. and Bulirsch, R. - Introduction to Numerical Analysis, Springer-Verlag, pp. 152-154, 1980.

[8] Hadamard, J.S. - Lectures on Cauchy's Problem in Linear Partial Differential Equations, Dover, New York, pp. 117-158, 1952.

[9] Lomax, H., Heaslet, M.A., and Fuller, F.B. - "Integrals and Integral Equations in Linearized Wing Theory", NACA Report 1054, 1951.

[10] Mangler, K.W. - "Improper Integrals in Theoretical Aerodynamics", Aeronautical Research Council, Tech. Rept. CP 94 (14,394), 1951.

[11] Brandão, M.P. - "Improper Integrals in Theoretical Aerodynamics - The Problem Revisited", AIAA Journal, Vol. 25, N. 9, pp. 1258-1260, 1987.

[12] Carleman, T. - "Sur la résolution de certaines équations intégrales", Arkiv för Matematik, Astronomi och Fysik, (in French), Vol. 16, N. 26, 1922.

[13] Stroud, A.H. and Secrest, D. - Gaussian Quadrature Formulas, Prentice-Hall, 1966.

[14] Abbott, I.H. and von Doenhoff, A.E. - Theory of Wing Sections, Dover, pp. 113-114, 1959.

[15] Brandão, M.P. - "A Mixed Volume-Boundary Element Approach for Incompressible Flows", to be presented at the Second Pan-American Congress of Applied Mechanics, Valparaiso, Chile, 1991.

III ENCIT – Itapema, SC (Dezembro 1990)

AERODYNAMIC EXPERIMENTAL INVESTIGATION OF THE BRAZILIAN SATELLITE LAUNCH VEHICLE (V L S)

PAULO MORAES JR. - ADRIANO AUGUSTO NETO
INSTITUTO DE ATIVIDADES ESPACIAIS
CENTRO TÉCNICO AEROESPACIAL
12225 SÃO JOSÉ DOS CAMPOS - SP/BRAZIL

SUMMARY

Force and pressure measurements have been carried out on 1:40 and 1:15 smooth models of the VLS Launch Vehicle in low and high speed wind tunnels. The test programme included simultaneous measurements on the complete vehicle as well on one booster at Mach numbers from 0.5 to 4.0 to establish the basic aerodynamic coefficients. Schlieren photographs were taken for detailled analysis of the flow pattern in the region between booster and central body. Also the lift -off conditions were simulated. The test results and comparisons of theoretical drag and pressure predictions with experimental data are shown.

INTRODUCTION

The first Brazilian Satellite Launch Vehicle, shortly VLS, is of the cluster type with four strap-on boosters around the central core, as shown in Fig.1 .

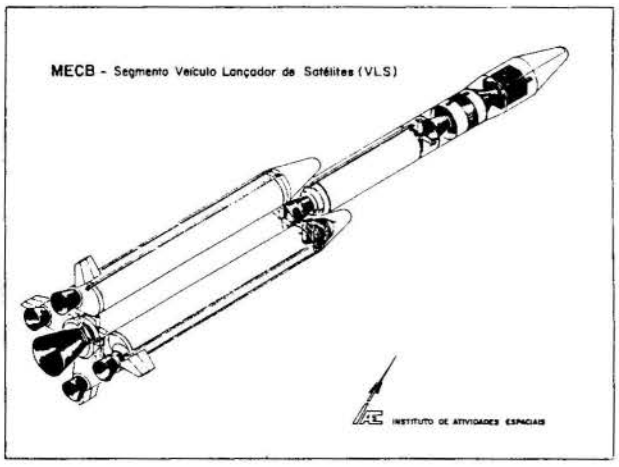

Fig 1 : V L S - Configuration

The hammer-head type fairing and the parallel staged boosters, building the first stage, represent a very complex configuration for theoretical or numerical prediction of its aerodynamic characteristics. None of the existing semi-empirical calculation procedures can be sucessfully used for such a configuration and, the application of numerical codes make necessary a strong modelling of the geometry, three-dimensional Navier-Stokes formulation and of course high performance computers. So several wind tunnel tests have to be done in order to get accurate and detailed information on the VLS global and local aerodynamic characteristics.

With this purpose a general wind tunnel test programme was established which covers a wide range of configurations and test parameters, as for instance Mach number, angle of incidence and Reynolds number, simulating in this way the expected flight trajectory of the vehicle.

The main aspect of such tests lies in the determination of the global aerodynamic characteristics, forces and moments, in the simulation of the lift-off conditions, and finally in the estimation of load distributions by means of pressure measurements over the central body and booster surface for all speed regimes. Because of the lack of high speed wind tunnels in Brazil the most part of these tests has been made outside the country.

One important approach of the experimental investigation concerns the simulation of the flight conditions during the booster separation. After burn out of the first stage motors, aprox. 65 s of flight (Mach = 4.0, altitude = 32 km), the four boosters will separate simultaneously from the central core. This is a very delicate operation since the separation of the boosters could introduce aerodynamic interference problems, so that a detailed analysis of the event will be required in order to prevent and avoid collision of the bodies and, consequent mission failure.

For this reason, and because of the difficulty in obtaining analytical and numerical results for the aerodynamic coefficients, specific wind tunnel tests were performed.

The present paper briefly describes the test models and facilities used and, shows and discusses the most significant results. Also comparisons of the experimental data with theoretical/numer cal results are presented.

WINDTUNNEL TEST PROGRAMME, CONFIGURATIONS & PARAMETERS

The general wind tunnel testing programme comprised three different series:

1. **Acquisition of global characteristics:**
   - measurement of force and moments in a trisonic wind tunnel ;
2. **Simulation of the lift-off conditions:**
   - force measurements in a large scale subsonic wind tunnel and,
3. **Acquisition of local characteristics:**
   - measurement of local pressures in high speed wind tunnels .

A fourth test series is also planned and will be performed later to confirm the global aerodynamic characteristics of the flight configuration.

Global Aerodynamic Characteristics:

A first test series was performed in a trisonic, 0.5 < MACH < 4.5, blow - down type wind tunnel with a test section size of 60 x 60 cm^2, and comprised force and moment measurements with a six component internal strain-gauge balance. The test results, in the form of aerodynamic coefficients, were then used for performance evaluation, to simulate the dynamics of the

bodies, and so to characterize and well define the first stage separation. These derivatives are also required for estimation of vehicle loads and analysis of the vehicle control system.

The test configurations used in the wind tunnel are shown schematically in Fig. 2 .

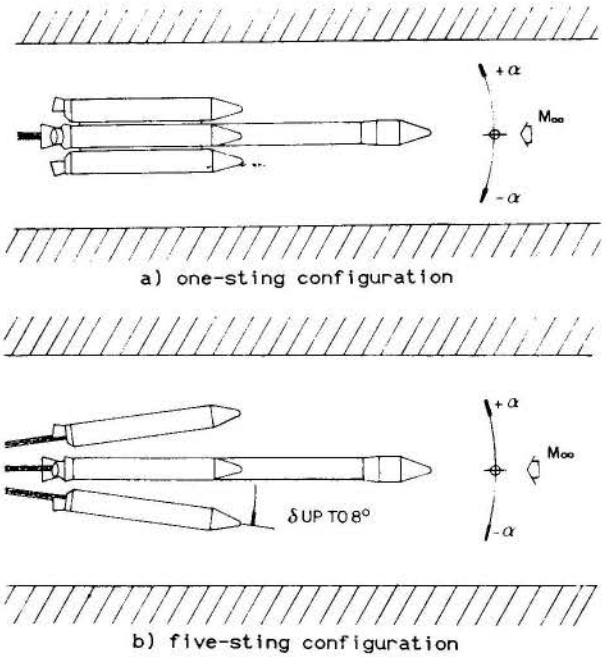

Fig. 2: Wind Tunnel Testing Configurations

The test models were scaled 1:40 and presented smooth surfaces. By these tests no attempt has been made to represent stringers and aerials. Although the booster/core clearance has been varied, its effect is relatively small and will not be discussed here.

In the first testing configuration, Fig. 2a, the boosters were attached to the central body and only one balance, mounted inside the core vehicle, was used to measure the characteristics of the complete configuration. Later, in order to simulate the separation of the boosters, a five-sting configuration has been used, Fig 2b, in which two six-component balances were placed one inside the central body and another inside one of the boosters. The data were then measured and recorded simultaneously.

The following parameters have been measured as a function of free-stream Mach number, $0.5 < \text{Mach} < 4.0$, and angle of incidence, $0^\circ < \alpha < 6^\circ$:

- normal, axial and side force coefficients ;
- pitching, rolling and yawing moment coefficients ;
- centre of pressure position.

A sketch of the axes system defining force and moment orientation is given in Fig. 3.

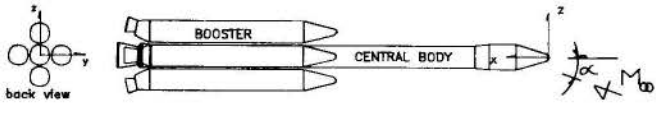

Fig.3: Wind Tunnel Testing Axes System

Simulation of the Lift-Off Conditions:

The aim of these tests lies in the simulation of the conditions established during prelaunch and launching of the vehicle which is exposed to surface steady winds and gusts and to the turbulent wake due to the complex environment: umbilical mast, gantry and other nearby structures. The structural response of the vehicle to wind excitation and turbulence produces unsteady loads which must be considered in its design.

While for conventional configurations the steady drag loads can be calculated using drag coefficients for two-dimensional cylinders or cone-cylinders combinations, for cluster configurations, such as the VLS, with external conduits and protuberances, influenced by the presence of adjacent tower and jet deflector structures, the steady loads have to be estimated from wind tunnel tests.

The tests were performed in a subsonic wind tunnel, $V < 45$ m/s, with a 2 x 3 sq. meters test section. The tests included forces and moment measurements with a three-component external balance for the configurations shown in Fig. 4. The test model, in 1:15 scale, was configurated with simplified protuberances.

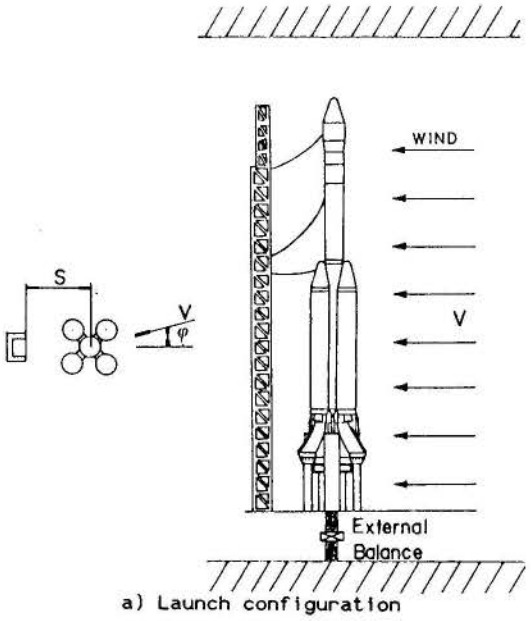

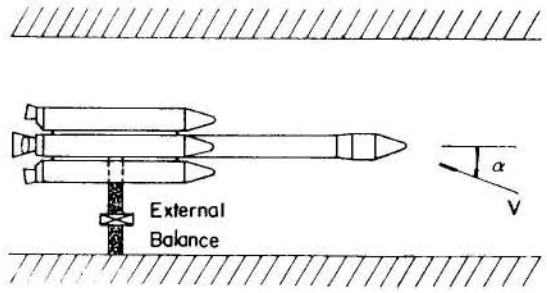

Fig.4: Simulation of the Lift-Off Conditions

The following parameters were simulated:

- wind velocity $V = 30.6, 36.2, 43.1$ m/s ;
- wind direction $\phi = 0^0, 45^0, 90^0, 135^0, 180^0$;
- angle of incidence $\alpha = 0^0, 60^0, 90^0$;

by measuring: drag, normal force, pitch/yaw moment and center of pressure.

Local Aerodynamic Characteristics:

In a third testing series, pressure measurements were performed for configurations similar to that of the first testing series (Fig.2), in continuous ($0.5 < \text{MACH} < 2.5$, 1.75×1.77 m^2) and blow-down ($2.5 < \text{MACH} < 3.75$, 0.78×0.76 m^2) wind tunnels. The test model, 1:15 scaled, was configurated with 320 pressure taps distributed axially and radially over the central body and boosters surfaces. The test parameters included

Mach numbers from 0.5 up to 3.75, Reynolds number from 9 up to 30 million per meter and angle of incidence up to 6 degrees. Also here the booster separation were simulated in order to verify its influence on the aerodynamics of the central body. The Reynolds number has been varied for the same Mach number to investigate its influence on the flow behaviour around the fairing.

The results of these tests are very useful to get more detailed information about the flowfield in the region between the bodies. Moreover, pressure measurements will be extremely useful for the validation of numerical codes being developed by CTA/IAE in cooperation with the SINMEC Group at the Universidade Federal de Santa Catarina [1] .

In order to allow a good analysis of the test results, Schlieren photographs were taken for the tests with transonic and supersonic speeds, which show the shock wave pattern around the model at various incidence and Mach numbers, as well as some flow details.

RESULTS

Vehicle Aerodynamics:

The six-component measurement delivers three forces (axial, normal and lateral) and three moments (pitch, yaw and roll).

In the Figs. 5 and 6, global aerodynamic characteristics: slope of the normal force coefficient $C_{n\alpha}$, center of pressure location Xcp/L (L: Vehicle total length) and axial force coefficient Cx, are presented for the complete model (first stage) and for the configuration without boosters (second stage).

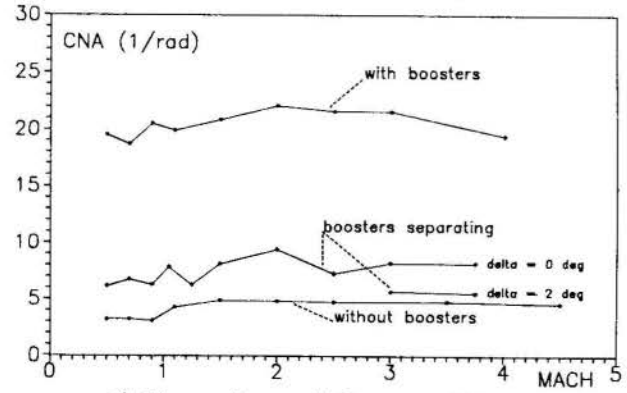

a) Slope of normal force coefficient

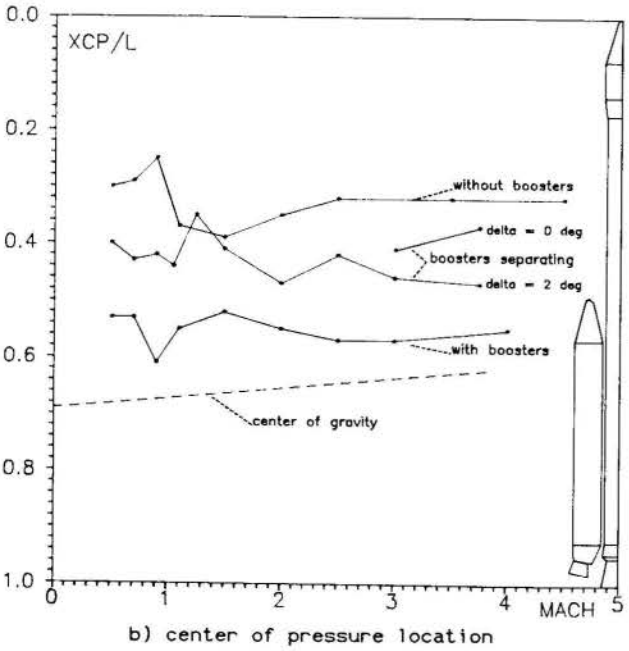

b) center of pressure location

Fig. 5: VLS - Static Longitudinal Characteristics

Both configurations are aerodynamically unstable, Fig. 5b. In order to reduce the static margin and so to alleviate the attitude control system of the first stage (by secondary injection), stabilizing fins will be placed on the boosters aftbody. For the second stage fins are not adequate since the separation of the boosters already occurs in very high altitude, by high Mach number and low dynamic pressure.

The axial force coefficient presented in Fig. 6 agrees well with previous calculations. Nevertheless it is expected that the inclusions of stringers, aerials and some others protuberances will increase the drag coefficient by aproximatelly 25% .

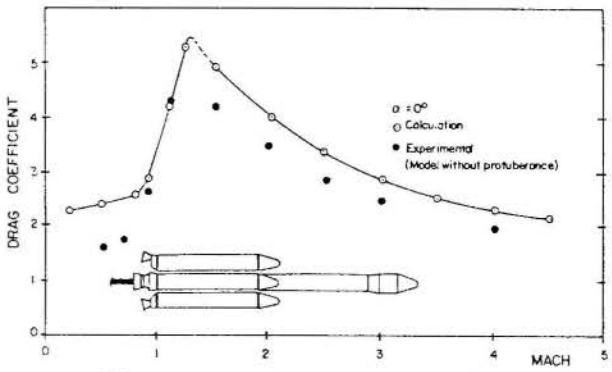

Fig. 6: VLS - Drag vs Mach Number

Booster Separation Aerodynamics:

A very critical event during ascent flight of the VLS is the separation of its first stage.

For analysis of this problem the most important parameter is the lateral (side) force coefficient Cy, acting on the boosters. The resultant side force on the booster is originated from the interference flowfield between this and the central body, Fig. 7 .

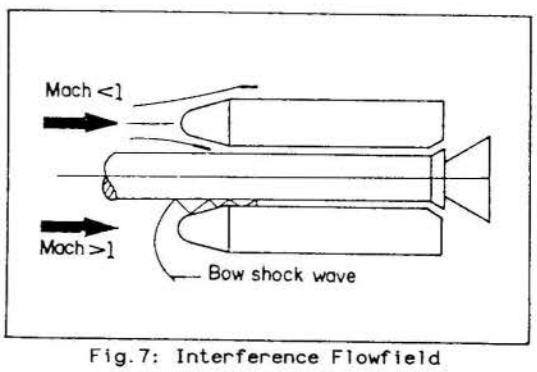

Fig.7: Interference Flowfield

For free stream Mach numbers less then the unity, subsonic flight, the flow in the influence region of booster-central body will mostly accelerate so that the pressure decreases considerably. The integration of these pressures around the booster surface will give a resultant side force directed towards the central body, Fig. 8 . For supersonic Mach numbers an opposite effect occurs. Because of the bow shock wave in front of the booster nose, the flow will decelerate due to the compression through the reflected shock waves from the adjacent surfaces. The integration of the pressure distribution over the booster shows, in this case, a resultant side force from the booster outwards.

For the above mentioned reasons, the booster mechanical attachment system will be compressed during subsonic flight and later, tensioned in the supersonic flight regime.

Unfortunately force measurements furnish as result at all, a resultant force and of course its acting location. An analysis of Fig. 9 shows moreover that the side force, determined here from local pressures, is distributed along the booster surface by different orientation. It means for the supersonic case, Fig. 9a, that while the aft part of the body has a small resultant towards the core, the forebody will

try to leave it. For subsonic speeds, Fig. 9b, the local force distribution indicates an opposite effect.

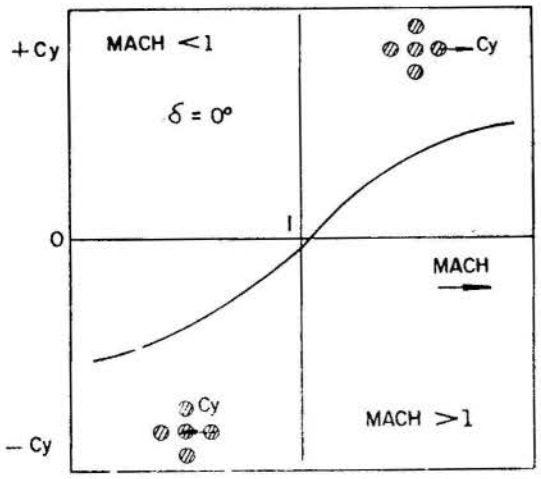

Fig. 8: Booster Side Force vs Mach Number

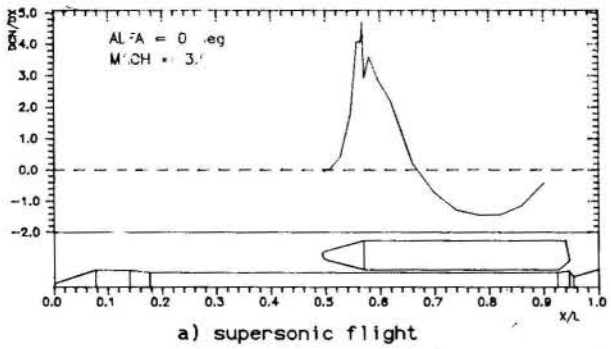

a) supersonic flight

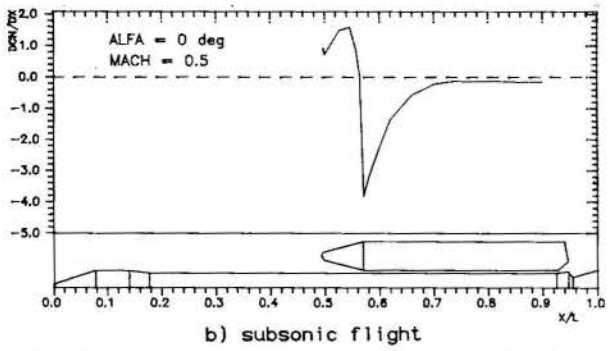

b) subsonic flight

Fig. 9: Local Force Distribution on the Booster

During the separation manoeuvre the boosters describe a linear, by use of springs or pneumatic actuators and, an angular motion, due to the aerodynamic moment. If it is assumed that the relative velocity between booster and central body is almost zero, the aerodynamic behaviour of each body will be of course influenced by the proximity of the other one. Pressure distributions over the surface of the central body show clearly the influence of the booster proximity, Fig. 10 .

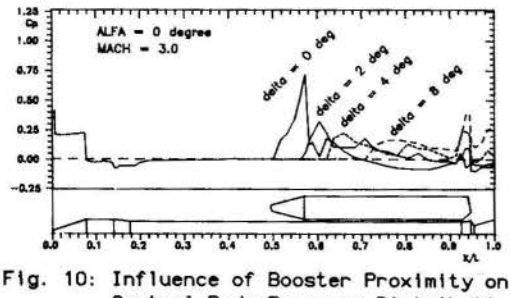

Fig. 10: Influence of Booster Proximity on Central Body Pressure Distribution

Experiment vs Computation:

The pressure measurements are also very useful for validation of numerical codes.

Fig. 11 presents a comparison between numerical and experimental results for the pressure coefficient Cp over the VLS fairing for two Mach numbers. The numerical results are originated from Euler calculations and considered zero angle of incidence [2]. The agreement between computation and experiment is quite good and shows the ability of the numerical procedure in predicting the flowfield over non-conventional configurations.

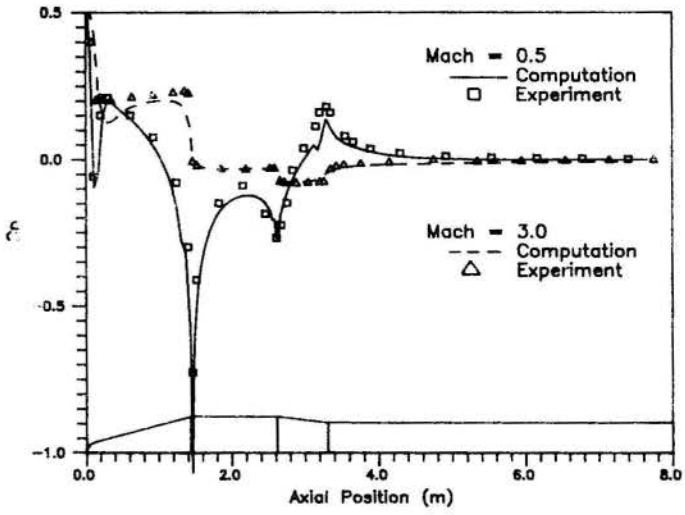

Fig. 11: VLS - Pressure Distribuiton Calculation vs Experiment

Fig. 12 shows pressure distributions for Mach = 3.0 with variation of the Reynolds number. These results are now being analysed and will allow the prediction of local flow separations as well the validation of numerical codes with Navier-Stokes formulation, also under development by CTA/IAE

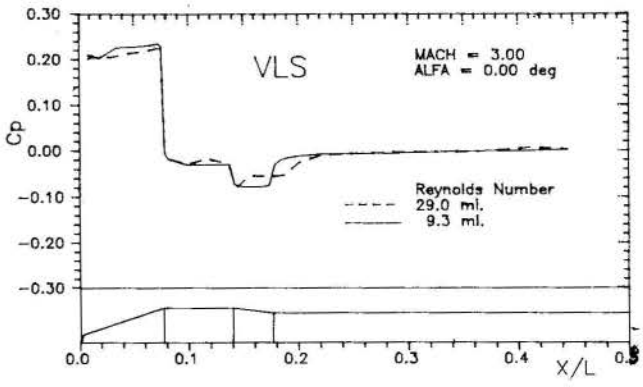

Fig. 12: VLS - Pressure Distribution Influence of Reynolds number

Lift-Off Aerodynamics:

The test results are summarized in Figures 13 and 14.

In Fig. 13 the steady drag coefficient of the vehicle is shown as function of the wind orientation for various wind velocities. While the wind velocity and the presence of the umbilical tower practically do not affect the resulting force coefficient for wind orientations up to 135°, the influence is considerably when the umbilical tower is placed in the wind mean direction (ϕ = 180°).

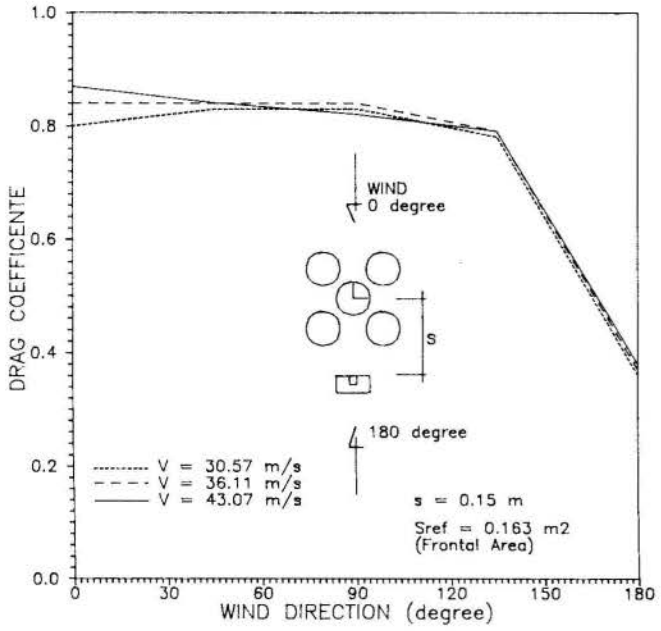

Fig. 13: VLS - Launching Aerodynamics

The first flight phase immediatelly after launch is characterized by low velocity and high angle of attack. Fig. 14 shows the corresponding drag and normal force coefficients.

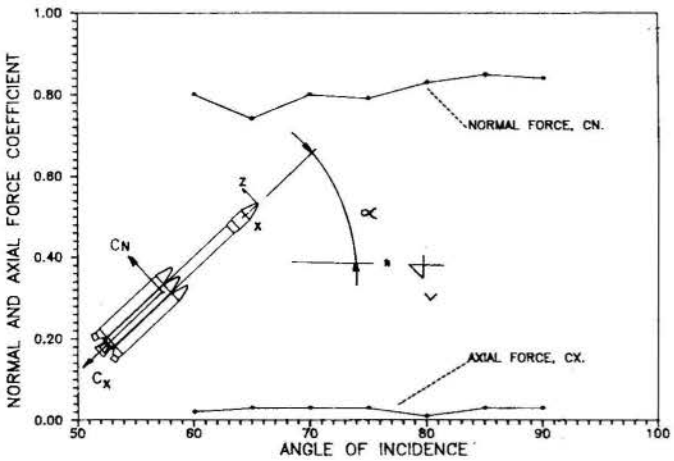

Fig. 14: VLS - Flight at Low Velocity and High Angle of Attack

CONCLUSIONS

Several wind tunnel tests have been performed in high speed facilities for the VLS, because of the difficulty in estimating its aerodynamic characteristics by theoretical or numerical calculations. The test results show that the first stage configuration is aerodynamically unstable, so that stabilizing surfaces will be necessary to alleviate the attitude control system. Despite the complexity of the configuration, theoretical drag predictions are in good accordance with experimental data. Also numerical predictions of the pressure distribution over the fairing agrees well with experimental results. The Mach number has a marked influence on the booster side force orientation and the booster proximity affects considerably the aerodynamcis of the central body. The lift-off conditions are influenced specially by the environment around the vehicle and the surface wind orientation.

REFERENCES

[1] Azevedo, J. L. F., Moraes Jr., P., "Retrospectiva do Desenvolvimento de Códigos Computacionais para Aplicações Aerodinâmicas no IAE," Paper submitted to the 1st Brazilian Symposium of Aerospace Technology, 27-31 Aug. 1990, São José dos Campos/SP, Brazil

[2] Moraes Jr., P., Zdravistch, F., Azevedo, J. L. F., "Aerodynamics of the Brazilian Satellite Launch Vehicle (VLS) during First Stage Separation," AIAA 8th Applied Aerodynamics Conference, 20-22 Aug. 1990, Portland/Oregon, USA

III ENCIT – Itapema, SC (Dezembro 1990)

ESTUDO DO ESCOAMENTO NA SEÇÃO DE TESTES DE UM TÚNEL TRANSÔNICO COM PAREDES POROSAS, CONSIDERANDO A PRESENÇA DE UM MODELO

ROBERTO DA MOTA GIRARDI
PEDRO PAGLIONE
Instituto Tecnológico de Aeronáutica - ITA
12225 - São José dos Campos, S.P.

SUMÁRIO

O escoamento no interior da seção de teste de um túnel de vento transônico é analizado, de maneira simplificada, através da teoria unidimensional do escoamento compressível. Considera-se fluxo de fluido através das paredes laterais, a inclinação das mesmas e também a presença de modelos no interior da seção de testes. Da solução numérica da teoria acima, são obtidas as distribuições, ao longo do comprimento da seção de teste, do número de Mach, da pressão estática e da velocidade do fluido que atravessa as paredes laterais. Verifica-se então, a variação dos parâmetros acima quando se alteram a razão de bloqueio do modelo, a inclinação das paredes laterais e a vazão em massa que é retirada do escoamento no interior do túnel de vento.

INTRODUÇÃO

A partir da década de 40, houve necessidade de ensaios aerodinâmicos de aeronaves com velocidade próxima à do som. Nos túneis de vento da época, cujas paredes eram sólidas, os ensaios de aviões em número de Mach (M) próximo de 1, só eram realizados para modelos muito pequenos. Além disto, ensaios com M = 1,0 não podiam ser executados devido ao fenômeno do entupimento ("shocking") [1].

Para resolver o problema mencionado acima, as paredes laterais da seção de testes, de um túnel de vento, são perfuradas ou eslotadas e o ar é succionado parcialmente para fora desta seção. Esta retirada de fluido permite a utilização de modelos maiores, evita o fenômeno de entupimento para M = 1,0 e também, elimina ou, pelo menos, minimiza a reflexão de ondas de choque e de expansão, que são geradas em modelos ensaiados nos regimes transônico e supersônico [2].

Esta sucção de fluido provoca variações indesejáveis nos parâmetros do escoamento que podem ser minimizados através da inclinação das paredes laterais [3]. A combinação acima tem como vantagem adicional a diminuição da espessura da camada limite, que acarreta melhor desempenho das paredes perfuradas no cancelamento de ondas de choque e de expansão [2].

No presente trabalho é feita uma estudo paramétrico da inclinação das paredes laterais, da vazão retirada e da razão de bloqueio de modelos colocados no interior de um túnel de vento trasônico. O objetivo desta análise é fornecer dados para o dimensionamento da seção de teste e para a calibração do escoamento no interior da mesma.

A análise precedente será realizada com base na teoria unidimensional do escoamento compressível [1], que foi escolhida por sua simplicidade. Por outro lado, pode-se esperar resultados bastante razoáveis porque a vazão retirada do escoamento principal é muito pequena (da ordem de 2%) e porque a inclinação das paredes laterais é da ordem de minutos.

Dentro da teoria unidimensional, a presença de um modelo no interior da seção de teste é considerada através da variação da área transversal do mesmo. Não é possível um estudo de modelos em incidência e ondas de choque obliquas não podem ser consideradas. Por outro lado, a presença de um modelo acarreta variações localizadas nos parâmetros do escoamento, que provocam uma resposta das paredes perfuradas, a qual será analisada no presente trabalho.

Para finalizar, deve-se notar que as poucas informações encontradas na literatura aberta resolviam as equações linearizadas do escoamento unidimensional. Neste trabalho, além de se considerar as equações completas do escoamento unidimensional, verifica-se as alterações acarretadas devido a inclusão de um modelo no interior do escoamento.

MODELO MATEMÁTICO

Para estudar o escoamento unidimensional no interior de uma seção de ensaio, recorre-se ao volume de controle diferencial mostrado na figura 1.

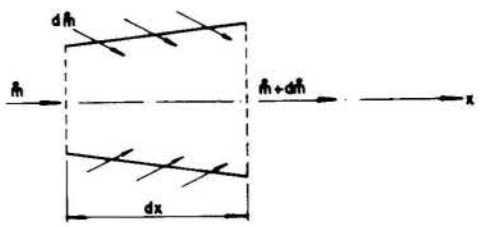

Fig. 1 Esquema de um elemento diferencial da seção de testes

Devido à variação de área transversal (dA) e da vazão em massa (dm) que entra pelas paredes laterais, cuja área é A_L, ocorre variação da pressão estática (p), da densidade (ρ), da velocidade (V) e da entralpia (h).

As propriedades acima estão vinculadas pelas equações de conservação da massa, da quantidade de movimento e da energia, assim como pelas equações constitutivas que descrevem um gás perfeito.

Para o escoamento considerado neste trabalho, as equações acima são dadas por, [1] :

$$\frac{dM^2}{M^2} = -\frac{2\left(1+\frac{\gamma-1}{2}M^2\right)}{1-M^2}\frac{dA}{A} + \left[\frac{2(1+\gamma M^2)(1+\frac{\gamma-1}{2}M^2)}{1-M^2} - \right.$$

$$\left. - \frac{1+\gamma M^2}{1-M^2}\left(\frac{\gamma-1}{2}M^2\right) - \frac{\gamma M^2\left(1+\frac{\gamma-1}{2}M^2\right)}{1-M^2}\frac{2V_I\cos\theta_I}{V}\right]\frac{d\dot{m}}{\dot{m}} +$$

$$+ \frac{\gamma M^2\left(1+\frac{\gamma-1}{2}M^2\right)}{1-M^2}\left(4f\frac{dx}{D_h} + \frac{dD}{\frac{1}{2}\gamma p M^2 A}\right) \qquad (1)$$

$$\frac{dP}{P} = \frac{\gamma M^2}{1-M^2}\frac{dA}{A} + \left[\frac{\gamma M^2}{1-M^2}\frac{\gamma-1}{2}M^2 + \right.$$

$$\left. + \frac{\gamma M^2\,[1+(\gamma-1)M^2]}{2(1-M^2)}\cdot\frac{2\,V_I\cos\theta_I}{V} - \frac{2\gamma M^2\left[1+\frac{\gamma-1}{2}M^2\right]}{1-M^2}\right]\frac{d\dot{m}}{\dot{m}} -$$

$$- \frac{\gamma M^2[1+(\gamma-1)M^2]}{2(1-M^2)}\left(4f\frac{dx}{D_h} + \frac{dD}{\frac{1}{2}\rho\, p\, M^2 A}\right) \qquad (2)$$

Como pode ser observado, o sistema constituido pelas equações (1) e (2) pode fornecer as variações de Mach (M) e da pressão estática (p) ao longo do comprimento dx. Para tanto é necessário conhecer a variação da área transversal (dA) e o fluxo da massa injetada na seção de testes ($d\dot{m}$). As equações (1) e (2) são gerais e consideram o atrito nas paredes laterais da seção de testes (f), o arrasto do modelo (D), a velocidade (V_I) e o ângulo (θ_I) do escoamento que entra na seção de testes através dos furos ou eslotes das paredes laterais. Outros parâmetros encontrados nas equações (1) e (2) são a razão entre calores específicos (γ) e o diâmetro hidraúlico da seção de testes (D_h).

A variação da área da seção transversal (dA) ocorrre devido a inclinação das paredes laterais superior e inferior e também devido a presença de um modelo no interior da seção de testes.

A vazão em massa ($d\dot{m}$) que atavessa as paredes laterais (perfuradas ou eslotadas) é descrita pela relação empírica, [2],

$$\frac{d\dot{m}}{dA_L} = -\frac{2(p-p_c)}{V_\infty\, k} \qquad (3)$$

onde p_c é a pressão estática no plenum, V_∞ é uma velocidade característica do escoamento e k é um coeficiente de perda de carga. É importante se observar que o parâmetro k é obtido empiricamente e depende do número de Mach do escoamento e das características das paredes laterais (porosidade, espessura e inclinação dos furos).

Levando-se em consideração que os parâmetros dA, dA_L, k, f e D são conhecidos ao longo do comprimento da seção de testes, verifica-se que as equações (1), (2) e (3) formam um sistema de equações diferenciais ordinárias não-lineares, cujas incógnitas são o número de Mach, a pressão estática e a vazão em massa que atravessa as paredes laterais.

SOLUÇÃO NUMÉRICA

O sistema constituído pelas equações (1), (2) e (3) é resolvido numericamente. O objetivo desta solução é obter as distribuições de pressão estática (p), de número de Mach (M) e da vazão em massa ($d\dot{m}$) ao longo da seção de testes, cujo comprimento é L.

Para controlar a vazão em massa que atravessa as paredes laterais, é necessário se especificar um valor para a pressão no plenum (p_c).

Com um valor fixado de p_c e especificando-se as condições iniciais, o sistema de equações (1), (2) e (3) é resolvido usando-se o método de Runge-Kutta Fehlberg 7/8 ordem [4], onde uma integração é efetuada de x = 0 até x = L.

Com isto, é possível se calcular a vazão em massa total ($\dot{m}_T$), definida pela equção (4), que atravessa as paredes laterais e é retirada pelo sistema de exaustão do plenum.

$$\dot{m}_T = \int_0^L d\dot{m}(x) \qquad (4)$$

No presente trabalho, deseja-se obter a distribuição dos parâmetros do escoamento ao longo da seção de testes, para um valor especificado da razão entre $\dot{m}_T$ e $\dot{m}$. Este vínculo é satisfeito através de um processo iterativo, onde a pressão no plenum p_c é variada até que o valor especificado para a razão $\dot{m}_T/\dot{m}$ seja alcançado.

Embora o esquema iterativo proposto seja simples, sua convergência é difícil de ser alcançada. Isto ocorre porque o parâmetro $\dot{m}_T$ sofre grandes variações quando se faz uma pequena alteração na pressão no plenum (p_c).

RESULTADOS

Neste trabalho, analisa-se o escoamento na seção de testes de um túnel de vento com transpiração nas paredes laterais, considerando-se a presença de um modelo.

O modelo utilizado é o AGARD-B, [5], que é mostrado na figura 2 e cujo contorno da ogiva é descrito pela equação (5).

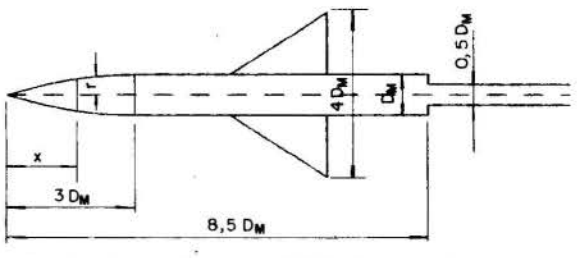

Fig. 2 Modelo de calibração AGARD-B com diâmetro D_M.

$$r = \frac{x}{3}\left[1 - \frac{1}{9}\left(\frac{x}{D_M}\right)^2 + \frac{1}{54}\left(\frac{x}{D_M}\right)^3\right] \qquad (5)$$

A razão de bloqueio é definida como a razão entre a área frontal do modelo e a área transversal da seção de testes do túnel de vento.

Uma análise paramétrica do escoamento no interior da seção de testes é feita, tomando-se como exemplo o túnel de vento transônico piloto do Centro Técnico Aeroespacial (CTA), cuja a seção de testes tem as seguintes dimensões: altura de 0,25 m, largura de 0,30 m e comprimento de 1,00 m. Neste exemplo, o coeficiente de arrasto do modelo estudado é C_d = 0,02, o coeficiente de atrito nas paredes laterais (f) é nulo e a pressão estática no início da seção de testes sempre igual a $0{,}6625 \times 10^5$ Pa.

Variação da Razão de Bloqueio do Modelo. Nas figuras 3, 4 e 5 são apresentadas as distribuições de número de Mach (M), pressão estática (p) e velocidade adimensional nos furos das paredes laterais (V_I/V_∞) ao longo do comprimento da seção de testes, respectivamente

Estes resultados foram obtidos para M = 0,80 no início da seção de testes e vazão em massa total retirada através das paredes laterais ($\dot{m}_T$) igual a 2% da vazão em massa do escoamento principal. As paredes superior e inferior desta seção são inclinadas de 20,0 minutos cada uma e formam um duto ligeiramente convergente. O valor desta inclinação é tal que a distribuição de velocidade nos furos, sem a presença de

modelo, é aproximadamente uniforme. Este resultado pode ser observado na figura 5, para o caso onde a razão de bloqueio é nula.

Ainda para seção de testes vazia (bloqueio nulo) verifica-se nas figuras 3 e 4, que o número de Mach varia linearmente e que a pressão estática é aproximadamente constante ao longo do comprimento desta seção.

A colocação de um modelo no interior da seção de testes provoca alterações no escoamento a montante do mesmo. Isto ocorre porque o escoamento é subsônico e portanto, perturbações a jusante se propagam para montante.

Na região a montante do modelo observa-se uma diminuição no número de Mach (figura 3), um aumento da pressão estática (figura 4) e portanto um aumento da vazão em massa retirada nesta região (figura 5). Estes resultados são uma conseqüência da transpiração de massa através das paredes laterais.

Na região da ogiva do modelo ocorre uma aceleração do escoamento devido à presença do mesmo no interior do túnel de vento. Isto acarreta a diminuição da pressão estática e da vazão em massa retirada.

Na região a jusante da ogiva (corpo do modelo), não ocorre mais variação de área devido a presença do modelo, porém, o escoamento continua acelerando devido a uma retirada de massa insuficiente. Como conseqüência, observa-se uma diminuição da pressão estática até um valor igual ao da pressão estabelecida no plenum. Neste ponto, a vazão que atravessa a parede perfurada é nula e a partir dele observa-se massa entrando na seção de testes.

Esta injeção de massa no escoamento produz um efeito de bocal convergente, resultando no aumento acentuado do número de Mach.

Na interface entre a base do modelo e o suporte do mesmo, verifica-se uma variação brusca dos parâmetros do escoamento, causada pelo aumento brusco da área ocupada pelo fluido. É interessante notar que, após a base do modelo, o escoamento se comporta como se o bloqueio fosse nulo.

O escoamento analisado acima mantém seu comportamento quando a razão de bloqueio é alterada. Observa-se apenas maiores variações dos parâmetros do escoamento devido ao incremento do gradiente da área da seção transversal, quando o diâmetro do modelo é aumentado.

Deve-se notar que o esquema do modelo, apresentado nas figuras 3, 4 e 5, corresponde a uma razão de bloqueio de 1,0%. O outro modelo é mais curto como pode ser visto pelos resultados mostrados nas figuras citadas acima.

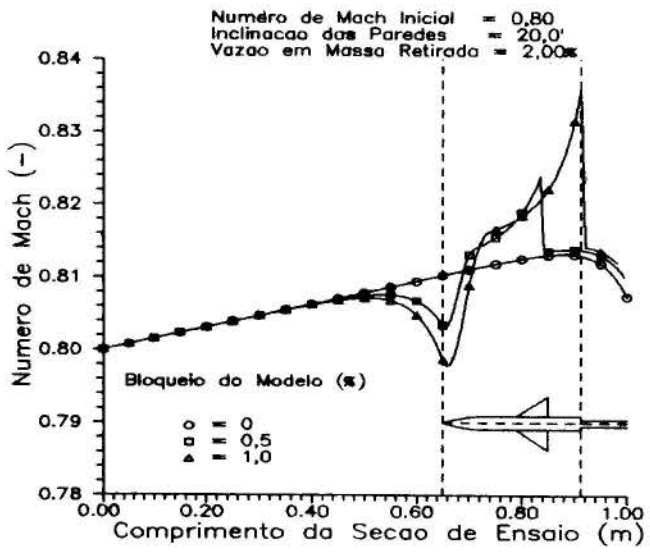

Fig. 3 Variação da distribuição do número de Mach com relação à razão de bloqueio do modelo. (regime subsônico)

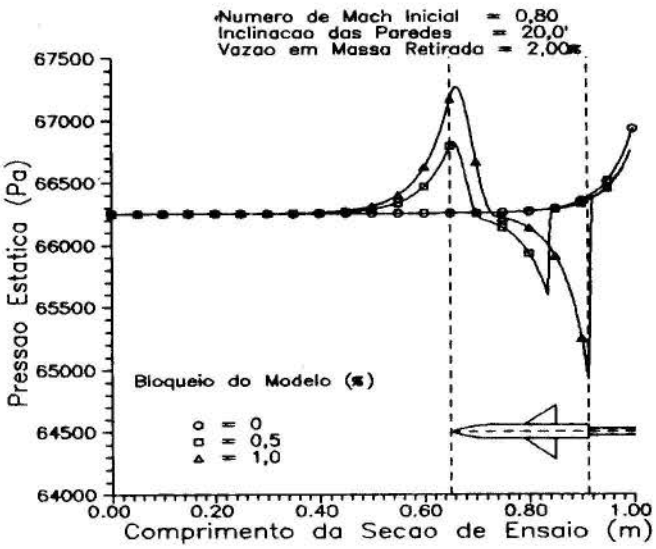

Fig. 4 Variação da distribuição de pressão com relação à razão de bloqueio do modelo. (reg. subsônico)

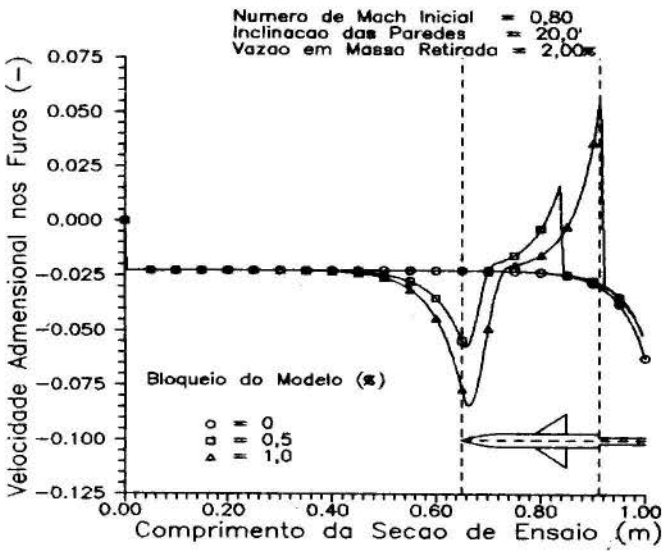

Fig. 5 Variação da distribuição da velocidade adimensional com relação à razão de bloqueio do modelo. (regime subsônico)

Em um túnel de vento pode-se obter escoamento supersônico de duas maneiras: (i) fazendo-se uma expansão em um bocal convergente-divergente ou (ii) através de uma expansão produzida por uma retirada de massa do escoamento no interior da seção de testes. A segunda alternativa funciona bem para número de Mach até 1,20 aproximadamente, [2].

Neste trabalho, adota-se a segunda alternativa, considerando-se que no início da seção de testes o número de Mach é igual a um. Admite-se, também, que o escoamento é livre de ondas de choques. A variação de área, devido a presença do modelo, é equivalente a uma contração suave das paredes laterais da seção de testes.

Nas figuras 6, 7 e 8 estão apresentadas as variações dos parâmetros do escoamento, para o caso onde a vazão em massa retirada através das paredes laterais é 2% e o ângulo de inclinação das paredes superior e inferior é de 21,5 minutos.

Como no caso subsônico, para este ângulo a distribuição de velocidade adimensional é constante ao longo da seção de testes (vide figura 8), quando não se considera a presença de modelo (bloqueio nulo).

Ainda para o caso de bloqueio nulo, verifica-se que a pressão estática é constante ao longo da seção de testes (figura 7) e que o número de Mach aumenta

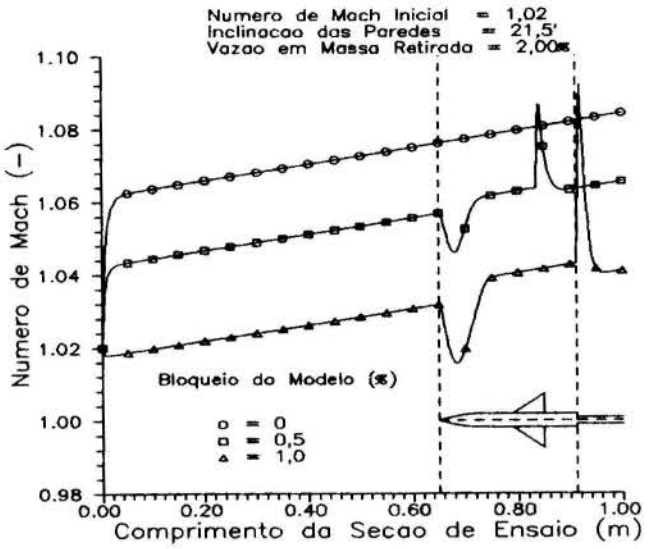

Fig. 6 Variação da distribuição do número de Mach com relação à razão de bloqueio do modelo. (regime supersônico)

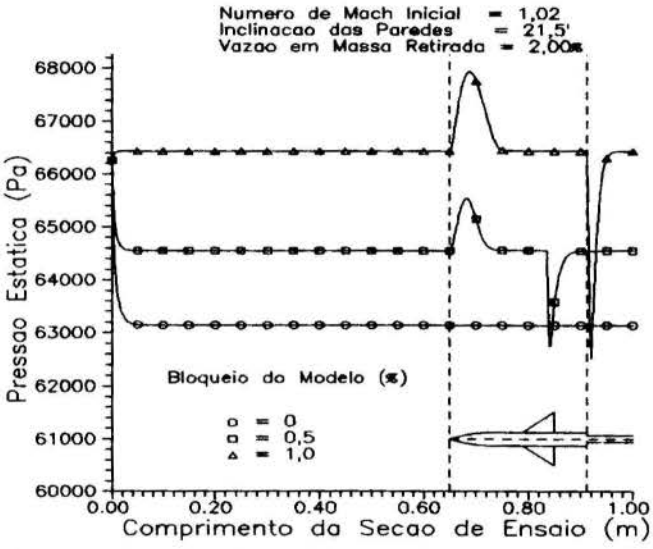

Fig. 7 Variação da distribuição de pressão com relação à razão de bloqueio do modelo. (regime supersônico)

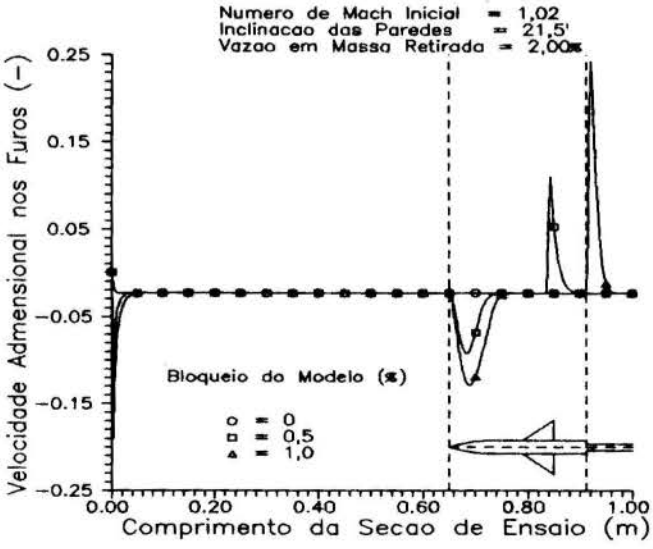

Fig. 8 Variação da distribuição da velocidade adimensional com relação à razão de bloqueio do modelo. (regime supersônico)

linearmente (figura 6). Pode-se observar que o número de Mach no início desta seção é igual a 1,02. Experiências numéricas mostraram que este é o mínimo valor possível para o número de Mach, pois abaixo deste valor, ocorrem problemas numéricos porque M=1,0 é um ponto singular das equações (1) e (2).

Como pode ser visto na figura 6, o aumento da razão de bloqueio do modelo provoca uma diminuição do número de Mach do ensaio e um aumento da pressão estática (figura 7). Isto ocorre porque a vazão em massa retirada através das paredes laterais é fixa e a presença do modelo provoca uma modificação na distribuição de velocidade adimensional ao longo do comprimento da seção de testes (figura 8).

Para a seção de ensaio analisada neste trabalho e para a configuração especificada acima, modelos com razão de bloqueio um pouco maior que 1,0 provocariam o fenômeno do entupimento.

Nas figuras 6, 7 e 8 pode-se observar que não existe perturbação do escoamento a montante do modelo. Isto ocorre porque o escoamento na seção de testes é supersônico.

Na região da ogiva do modelo, ocorre uma diminuição da área da seção transversal que acarreta uma redução do número de Mach do escoamento (figura 6). Devido a isto, tem-se um aumento da pressão estática (figura 7) e da vazão em massa retirada (figura 8).

Na região seguinte, não há variação da área transversal devido à presença do modelo. No entanto, o aumento da vazão em massa retirada, provoca uma expansão do escoamento e um aumento do número de Mach (figura 6). Esta variação dos parâmetros do escoamento termina quando a pressão estática volta a ter um valor igual ao da pressão a montante do modelo (figura 7).

Na interface entre o modelo e seu suporte, observa-se uma expansão do escoamento devido a um aumento brusco da área da seção trasnsversal. Nesta região, ocorre um fluxo de massa para o interior da seção de testes (figura 8). Isto causa um efeito equivalentee a uma contração da área da seção transversal, que ocasiona uma diminuição do número de Mach (figura 6).

Variação da Inclinação das Paredes. Para verificar o efeito da inclinação das paredes superior e inferior sobre os parâmetros do escoamento, fixou-se o número de Mach inicial, o bloqueio do modelo e a vazão em massa retirada.

Para inclinação nula, verifica-se uma intensa variação do número de Mach (figura 9) e da velocidade adimensional nos furos (figura 10) no final da seção de testes. É nesta região que, praticamente, toda a vazão em massa retirada atravessa as paredes laterais. A camada limite no início desta seção praticamente não é succionada, sendo isto indesejável quando se considera o problema do cancelamento de ondas de choque e de expansão nas paredes do túnel de vento.

Como pode ser verificado na figura 10, a distribuição de velocidade, ao longo do comprimento do túnel de vento, vai se uniformizando a medida que as paredes inferior e superior da seção de testes são inclinadas, tansformando esta seção em um bocal ligeiramente convergente. (O ângulo de inclinação é da ordem de minutos de grau).

Este ângulo de inclinação das paredes tem um limite superior, que depende do valor da vazão em massa retirada do escoamento principal. No caso particular da figura 9, para ângulos um pouco maiores que 20 minutos, ocorre uma aceleração do escoamento ao longo da secão de testes que tende para número de Mach igual a um.

No caso do escoamento supersônico, toda a vazão em massa retirada do escoamento principal atravessa as paredes laterais, na região inicial da seção de testes, quando a inclinação das paredes é nula [2]. Aumentando-se esta inclinação (convergência das paredes), observa-se que a vazão em massa é retirada de maneira mais uniforme, [2].

Na figura 11, pode-se observar que o número de Mach, a montante do modelo, diminue conforme se aumenta a inclinação das paredes. Esta inclinação possui um

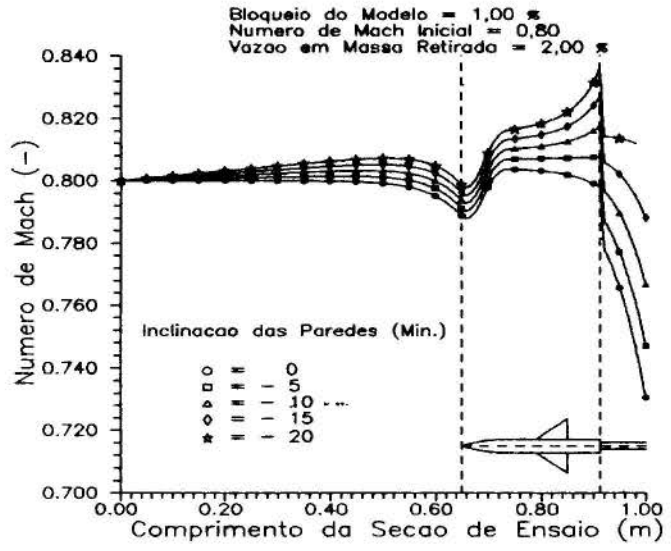

Fig. 9 Variação da distribuição do número de Mach com relação à inclinação das paredes. (regime subsônico)

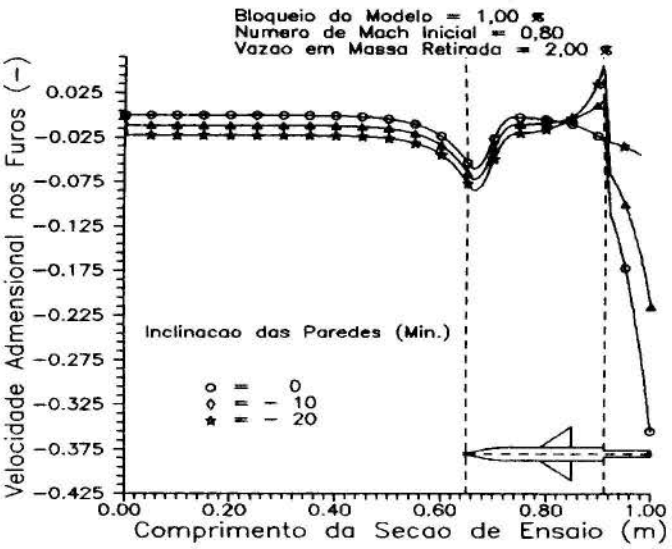

Fig. 10 Variação da distribuição da velocidade adimensional com relação à inclinação das paredes. (regime subsônico)

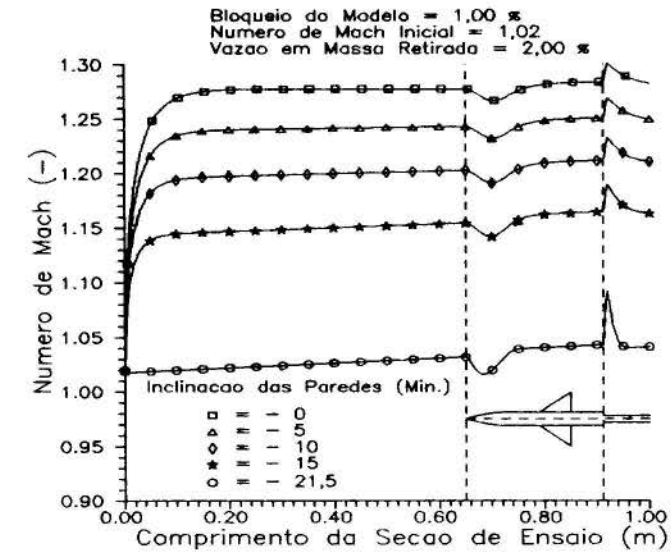

Fig. 11 Variação da distribuição do número de Mach com relação à inclinação das paredes. (regime supersônico)

limite superior, que é alcançado quando ocorre o fenômeno do entupimento.

Com relação ao modelo, verifica-se um aumento da perturbação causada pelo mesmo conforme a inclinação das paredes é aumentada (figura 11).

Variação da Vazão Retirada. Mantendo-se todos os demais parâmetros fixos, foi feita uma variação do valor da vazão em massa retirada pelas paredes laterais. Para o caso do escoamento supersônico, verifica-se que um incremento na vazão retirada acarreta um aumento do número de Mach a montante do modelo (figura 12). Isto já era esperado, pois quanto maior for a vazão retirada, tanto maior será a expansão do escoamento no interior da seção de testes.

Os resultados apresentados na figura 12 foram obtidos para uma inclinação de 20 minutos das paredes superior e inferior. Neste caso, a velocidade nos furos das paredes tem um valor praticamente constante ao longo do comprimento da seção de testes. Esta é uma característica desejável quando se quer minimizar o problema da reflexão de ondas de choque e de expansão [2].

Por fim, verificou-se que a variação da vazão retirada não altera de forma significativa os parâmetros do escoamento no regime subsônico.

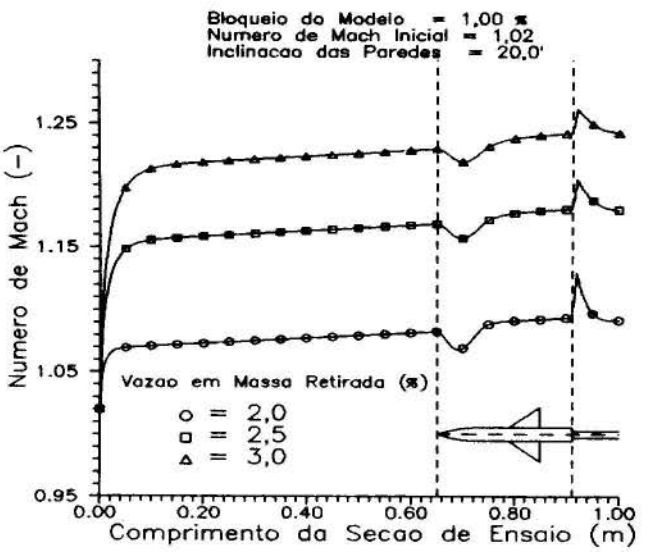

Fig. 12 Variação da distribuição do número de Mach com relação à vazão em massa retirada. (regime supersônico)

CONCLUSÃO

Neste trabalho foi realizada uma análise paramétrica das propriedades do escoamento no interior da seção de testes de um túnel transônico com paredes porosas, considerando-se a presença de um modelo.

É importante ressaltar aqui, que a solução numérica das equações descritivas do modelo do escoamento é difícil de ser alcançada pois, variações extremamente pequenas da pressão no plenum acarretam alterações consideráveis na vazão em massa retirada.

Sem o modelo, obtem-se uma distribuição uniforme da vazão em massa retirada ao longo da seção de testes, através da inclinação das paredes laterais. Neste caso, a distribuição do número de Mach é linear, enquanto que a pressão estática permanece praticamente constante.

A inclusão de um modelo no interior da seção de testes provoca uma alteração na distribuição da vazão retirada, sendo esta a causa da mudança dos demais parâmetros do escoamento. No caso do regime supersônico, as paredes perfuradas atuam no sentido de minimizar as pertubações causadas pela presença do modelo.

Com relação à variação da razão de bloqueio do modelo, observa-se que apenas a intensidade das propriedades do escoamento é alterada. Além disto, no regime supersônico, verifica-se uma variação do número de Mach a montante do modelo, que é inversamente proporcional à razão de bloqueio.

Aumentando-se a inclinação das paredes laterais, a distribuição da vazão retirada tende a se uniformizar. Esta inclinação é limitada pela ocorrência do fenômeno do entupimento. Deve-se notar ainda que, no regime supersônico, esta inclinação das paredes modifica o número de Mach a montante do modelo.

Quanto à variação do valor total da vazão em massa retirada pelo sistema de exaustão do plenum, não se observam variações significativas das propriedaes do escoamento no regime subsônico. Por outro lado, no regime supersônico, um aumento desta vazão retirada acarreta um acréscimo no número de Mach a montante do modelo, sendo que isto é utilizado para controlar o número de Mach desejado para um ensaio.

Por fim, deve-se enfatizar que na teoria unidimensional, usada neste trabalho, os parâmetros do escoamento nas paredes da seção de testes possuem valores maiores que os reais.

REFERÊNCIAS BIBLIOGRÁFICAS

[1] Shapiro, A.H. "The Dynamics and Thermodynamics of Compressible Fluid Flow", John Wiley & Sons, USA, 1953.

[2] Goethert, B.H. "Transonic Wind Tunnel Testing", Pergamon Press, 1961.

[3] Escosteguy, J.P.C. & Ortega, M.A. "Simplified Analysis of the flow in a Transonic Wind Tunnel Test Section with Ventilated Walls", II Encontro Nacional de Ciências Térmicas, Águas de Lindóia, 1988.

[4] Kraft, D.,"FORTRAN-Programme zur numerischen Lösung optimaler Steuerungsprobleme", DFVLR-Mitt. 80 - 03, Oberpfaffenhofen, 1980.

[5] Lorenz-Meyer, W., "Kanlkorrekturen für den transsonischen Windkanal der Aerodynamischen Versuchsanstalt Göttingen bei Messungen an dreidimensionalen Modellen", Z.Flugwiss., Vol. 10, No. 11, pp. 454-461, 1971.

[6] Baldwin, B.S.; Turner, J.B. & Knechtel, E.D. "Wall Interference in Wind Tunnels with Slotted and Porous Boundaries at Subsonic Speed", NACA TN-3176, USA, 1954.

[7] Spiegel, J.M.; Tunnell, P.J. & Wilson, W.S. "Measurements of the Effects of Wall Outflow and Porosity on Wave Attenution in a Transonic Wind Tunnel with Perforated Walls", NACA TN-4360, USA, 1958.

SMMARY

A simplified one-dimensional analysis of the flow in the test section of a transonic wind tunnel is performed. The flow through the walls (mass extraction), the inclination of both upper and lower walls and the presence of models are considered. The flow model is described by a system of three non-linear ordinary differential equations and the solution is numerical. The distributions of Mach number, static pressure and velocity of fluid crossing the walls are obtained along the test section length. The variation of these parameters with respect to model blockage ratio, walls inclination and mass extraction is studied.

III ENCIT – Itapema, SC (Dezembro 1990)

AVALIAÇÃO FUNCIONAL DO SISTEMA DE EVACUAÇÃO FORÇADA DA SEÇÃO DE TESTES DE TÚNEIS TRANSÔNICOS

JOÃO BATISTA PESSOA FALCÃO FILHO, Engº.Mec.Aer.
CTA - IPD - GTTS
12225 - São José dos Campos - SP

RESUMO

É apresentada justificativa para a utilização do Sistema de Extração Forçada em túneis transônicos, relacionando os principais parâmetros para a definição deste sistema, sendo dada especial atenção ao parâmetro umidade presente no escoamento sob aspectos técnicos e de custos e analisadas as principais implicações em túneis pressurizados, onde a presença de vazamentos pelas paredes estruturais do túnel, causados pela diferença de pressão, requer um sistema de secagem do ar. Para isto foi desenvolvida rotina numérica em diferenças finitas para cálculo da evolução da umidade na seção de testes durante um ensaio.

INTRODUÇÃO

A existência da evacuação da seção de testes está estreitamente relacionada com as grandes dificuldades encontradas na obtenção do regime transônico durante o desenvolvimento dos túneis de alta velocidade.

As primeiras dificuldades encontradas foram em alto subsônico, onde, na tentativa de estabelecimento do regime transônico, ocorriam reflexões de ondas nas paredes do túnel, que incidiam sobre o modelo. Além disso, mesmo sendo numa faixa estreita, o fenômeno do "entupimento" da seção de testes causava um pulo entre o alto subsônico e o baixo supersônico, não se podendo atingir a faixa transônica propriamente dita ($0,75<Mach<1,20$). Mesmo sendo possível contornar esses problemas com um projeto de um túnel de seção aberta, o aumento da potência requerida torna a solução inviável, recaindo a solução de paredes semi-abertas (com presença de fendas ou de perfurações) com evacuação da seção de testes, que apresenta uma redução da potência total não só na faixa transônica, mas em todo o regime de velocidade, como solução indiscutível do estado da arte.

Este trabalho apresenta os principais fatores na justificativa de utilização e definição deste sistema, dando atenção especial ao critério de umidade em túneis pressurizados, através de desenvolvimento de rotina numérica para cálculo da umidade no túnel durante o ensaio.

Aspectos tecnológicos e de custos estarão sempre presentes nas análises aqui apresentadas.

DEFINIÇÃO DO SISTEMA DE EXTRAÇÃO

Adicionalmente uma variação contínua do número de Mach na faixa transônica pode ser obtida usando-se uma garganta sônica e controlando-se a extração do ar pelas paredes semi-abertas. Esse controle pode ser feito por meio do controle da pressão na câmara que circunda a seção de testes (câmara "Plenum") através da posição de flape ou extensão das fendas para readmissão do fluxo ao circuito do túnel na entrada do difusor. Muitos túneis usam esta solução.

Entretanto, é bem conhecido hoje o processo tecnológico da evacuação forçada que permite, adicionalmente a esta solução: 1) grande economia de potência, 2) atingir Mach > 1,2 com garganta sônica, 3) incorporar controle de umidade no túnel e 4) simplificar o processo de pressurização do túnel.

A figura 1 mostra o esquema físico da utilização dupla da evacuação forçada e da sucção com readmissão pelo flape.

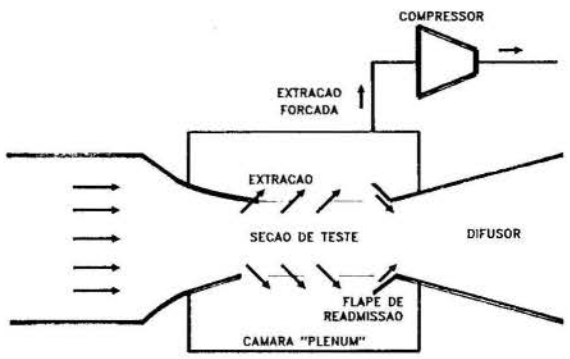

figura 1: esquema da evacuação

A figura 2 apresenta dados de experiências realizadas no túnel piloto do AEDC de 1 pé² (0,0929m²) de área da seção de testes com paredes perfuradas com 22.5 % de área aberta e 1/4 pol (0,00635m) de diâmetro de perfurações para diferentes combinações de extração forçada e posicionamento do flape para readmissão do escoamento na entrada do difusor (referência[1]).

Mesmo sendo para Mach=1,0 na seção de testes, as curvas de potência apresentam a mesma tendência para qualquer velocidade, onde vemos que o ganho de potência é muito mais sensível utilizando-se a extração forçada, restando à extração com readmissão pelo flape um recurso para melhor distribuição do Mach ao longo da seção de testes (referência [1]).

Assim, na prática, o valor inicial para determinar a porcentagem de extração forçada é o valor mínimo necessário para se evitar o entupimento com flapes de readmissão fechados (extração forçada pura).

Pelo gráfico da figura 2, extração de 2,4% do fluxo principal.

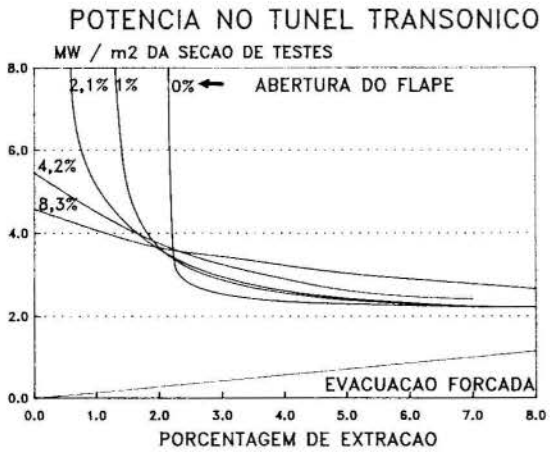

figura 2: túnel piloto do AEDC, Mach = 1,0

Outros parâmetros atuam no sentido de diminuir a porcentagem de extração necessária, flexibilizando, assim, a utilização do sistema de evacuação. São eles: 1) abertura do flape de readmissão, 2) extensão do comprimento das fendas, 3) divergência das paredes, 4) porcentagem de área aberta das paredes, 5) tamanho e inclinação das perfurações e 6) garganta supersônica.

A partir disso, concluimos que um valor menor de extração forçada pode ser utilizado, se o projeto do túnel incorpora essas caracteristicas. No nosso caso do túnel transônico do projeto TTS, pelas caracteristicas presentes (ver tabela 1), foi escolhido o valor de 2% do fluxo principal de extração forçada a Mach 1,0 (referência [2]).

tabela 1: caracteristicas do túnel transônico

Pressurização..... 50000 Pa a 300000 Pa
Mach S.Testes..... 0,2 a 1,3
Seção de Testes.... 2,4 x 2,0 x 6,5 m·m·m
Extração forçada de 2% e readmissão por flapes
Convergência/Divergência das paredes 0,5 graus
S.T. Semi-Aberta (5%), 12 fendas longitudinais
inserções de alumínio para variação de 0 a 11%

UMIDADE NO TUNEL

Em túneis pressurizados, a umidade no escoamento torna-se ainda mais critica, sendo sua definição e controle essenciais para uma boa qualidade no escoamento e, portanto, na confiabilidade da aquisição de dados, conforme analisado a seguir.

A umidade absoluta no túnel deve se manter abaixo de um valor que não venha a provocar condensação de vapor d'água no modelo. Para isto é necessário que a temperatura estática na seção de testes seja maior que a temperatura do ponto de orvalho, e atribuindo empiricamente um valor de 5K como margem de segurança, temos $T = T_{orv} + 5$.

A partir da definição da umidade especifica e com a consideração de que a pressão de vapor P_v (obtida a partir das tabelas usuais) é bem menor que a pressão estática na seção de testes, ou seja, a umidade especifica no túnel $w_t << 1$, obtemos uma expressão para o cálculo da umidade especifica requerida no túnel para que não haja condensação

$$w_t = 0,622\ P_v\ (1+0,2M^2)^{3,5} \qquad (1)$$

M (Mach na seção de testes), 1,4 (razão entre os calores especificos a pressão constante e a volume constante), 0,622 (razão entre os pesos moleculares do vapor d'água e do ar seco).

Assim, obtemos a figura 3 que apresenta as curvas da umidade especifica para cada valor de pressurização do túnel.

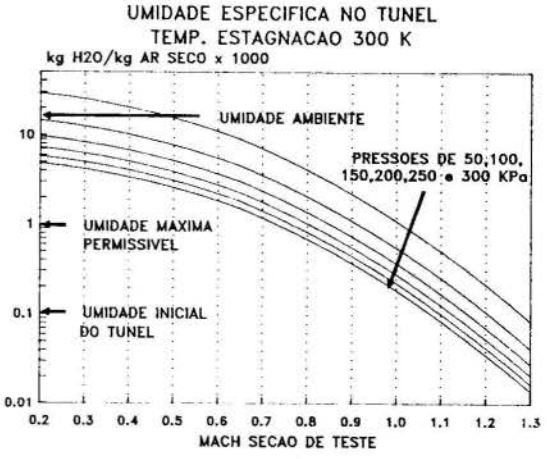

figura 3: curvas do túnel do projeto TTS

Na condição mais critica, pressão de estagnação de P_o = 300000 Pa e Mach na seção de testes M = 1,3 quando aplicado o critério de 5K acima do ponto de orvalho, uma umidade no túnel de w_t = 0,000015 kg H_2O / kg ar seco seria necessária, que é impraticável pelos recursos tecnológicos e de custo.

Considerando que: 1) na busca de um projeto economicamente viável, constatamos que a frequência tipica de solicitação de ensaios a Mach > 0,9 é de cerca de 15 % do tempo total de utilização, analisados vários túneis no mundo (referência [5]); 2) os custos envolvidos e a complexidade de um secador que atenda efetivamente aos requisitos de umidade para Mach > 0,9 são excessivos; 3) em regimes de alta velocidade é possivel conviver com certo grau de saturação no escoamento, sem afetar significativamente a confiabilidade dos dados obtidos no ensaio, pelo fato do escoamento só concluir o processo de condensação após a região na qual será colocado o modelo, e mesmo em caso do processo de condensação ocorrer na região do modelo, a quantidade de água condensada ser muito pequena para que venha a mascarar os dados lidos (referência [3]). Chegamos, assim, num valor prático baseado na experiência de operação em outros túneis de w_t =0,001 kg H_2O / kg ar seco, que chamamos de umidade limite (referência [2] e figura 4).

O critério de custo levou também a operar o túnel num processo não continuo, fazendo-se uma secagem do ar no túnel antes da realização do ensaio durante um tempo conveniente com o túnel despressurizado (vazamento nulo pelas paredes do túnel) até que a umidade no túnel atinja o valor de w_t =0,0001 kg H_2O/kg ar seco, depois iniciando-se o processo de pressurização do túnel e depois o ensaio. O valor de w_t foi determinado após a análise dos resultados da figura 6.

Através dos vazamentos externos pelas paredes do túnel este valor atingirá o valor limite de w_t = 0,001 kg H_2O / kg ar seco num tempo suficiente para a realização do ensaio.

A figura 4 compara o critério de umidade empregado no projeto do túnel transônico TTS com outros túneis (referência [4]).

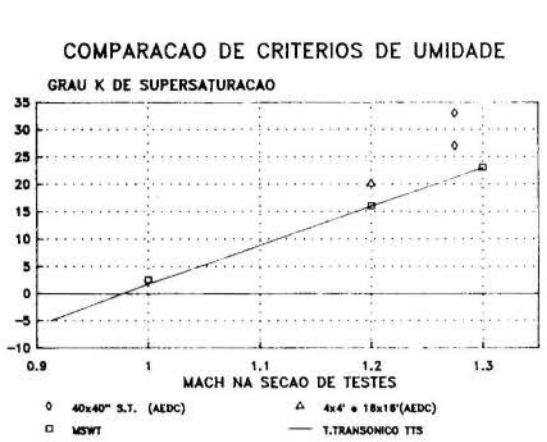

figura 4: umidade em outros túneis

MODELO MATEMÁTICO

Para a determinação da evolução da umidade no túnel foi desenvolvido modelamento matemático considerando extração forçada de 2% do fluxo de massa máximo pela seção de testes através de compressores centrífugos, conforme esquema mostrado na figura 5. O fluxo extraído pelos compressores é readmitido no túnel após passar por secadores, na tentativa de manter a umidade absoluta no túnel em limites apropriados por um tempo suficiente para a coleta de dados do ensaio. Os vazamentos inevitáveis pela paredes do túnel, devido à diferença de pressão, causam a entrada de ar úmido do ambiente para dentro do túnel em caso de ensaio com o túnel subpressurizado e, no caso oposto, o túnel sobrepressurizado perde ar seco para o ambiente, tendo que ser readmitida a mesma quantidade para manter a pressão no túnel constante. Em ambos os casos foi considerado que, apenas parte do ar passa pelos compressores, por uma limitação econômica, tornando o sistema mais flexível (fácil ajuste de secagem). A consideração básica é de que seja secado 50% do ar pelos compressores, ou seja, $(1-\Theta)=0,5$. A figura 5 ilustra o balanço de massa no túnel nos dois casos (sobrepressurizado e subpressurizado).

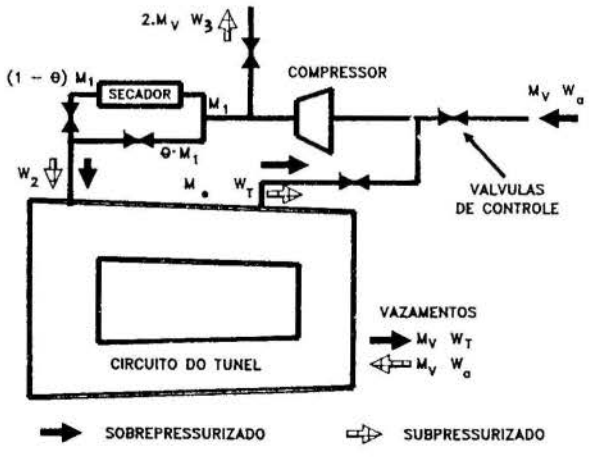

figura 5: esquema do sistema a ser modelado

W_2 , W_3 variáveis auxiliares
W_a =umid.espec.atmosférica(kgH_2O/kg ar seco)
W_s =umid.espec.sai do secador(kgH_2O/kg ar seco)
m_e =fluxo de massa de extração forçada (kg/s)
m_v =fluxo de massa de vazamento (kg/s)
$(1-\Theta)$=razão de ar efetivamente secado

A partir das relações gerais da mistura de gases e vapor d'água,

$$W_{mistura} = \frac{W_{gas1} m_{gas1} + W_{gas2} m_{gas2}}{m_{gas1} + m_{gas2}} , \quad (2)$$

e aplicando o princípio da conservação de massa ao modelo descrito na figura 5, cuja equação geral na forma diferencial é

$$d \cdot W_T = \frac{m_{H2O\ entra} - m_{H2O\ sai}}{M_{ar}} \cdot dt , \quad (3)$$

obtemos como equação de evolução da umidade no túnel, em diferenças finitas, nos dois casos:

Sobrepressurizado:

$$W_{t(N+1)} = W_{t(N)} + \frac{\Delta t (m_v + m_e)}{M_a [1+W_{t(N)}]} \frac{A_1 m_e + A_2 m_v}{A_3 m_e + A_4 m_v} \quad (4)$$

Subpressurizado:

$$W_{t(N+1)} = W_{t(N)} + \frac{\Delta t\ m_e}{M_a [1+W_{t(N)}]} \frac{A_1 m_e - A_5 m_v}{A_3 m_e - A_6 m_v} \quad (5)$$

onde,
$A_1 = (1 - \Theta)(W_s - W_{t(N)})$
$A_2 = \Theta W_a + (1 - \Theta) W_s - W_{t(N)}$
$A_3 = 1 + (1 - \Theta) W_s + \Theta W_{t(N)}$
$A_4 = 1 + (1 - \Theta) W_s + \Theta W_a$
$A_5 = (1 - \Theta) W_s - W_a - \Theta W_{t(N)}$
$A_6 = -(1 - \Theta) W_s - W_a + \Theta W_{t(N)}$
M_{ar} = massa total de ar no túnel

m_e é calculado a partir da razão de extração de 2% do fluxo principal (pela seção de testes), obtido pela equação da continuidade na seção de testes:

$$m_e = 0,02 \frac{A_{st} P_o M}{(1 + 0,2 M^2)^3} \frac{1,1832}{(R T_o)^{0,5}} , \quad (6)$$

onde A_{st}, P_o, M e T_o, respectivamente, são a área, a pressão de estagnação, o Mach e a temperatura de estagnação na seção de testes e R a constante do ar.

Como o tamanho e a forma dos furos são totalmente não previsíveis numa fase de projeto, o fluxo de vazamento externo através das paredes do túnel, m_v, foi obtido aproximando-se o escoamento pela área de vazamento, Av, em isentrópico e com bocal convergente. Assim, temos a seguinte relação que nos dá o fluxo em função da relação entre as pressões nos dois lados da parede, obtida a partir da equação de "St. Venant e Wantzel" (referência [6]):

$$m_v = \frac{P_1 \cdot A_v}{(1,4 T_o R)^{0,5}} [9,8 K^{1,429} (1-K^{0,286})^{0,5}] \quad \ldots (7)$$

onde K é a razão de pressões totais dos dois lados da parede do túnel ($K=P_2/P_1$), P_1 a pressão maior, T_o a temperatura de estagnação no túnel. A equação é válida para $K > 0,5283$. Abaixo desse valor o fluxo permanece constante pelo estabelecimento da velocidade sônica nos furos de vazamento.

A tabela 2 apresenta os parâmetros principais requeridos para a determinação das curvas de evolução da umidade no túnel:

tabela 2 : Principais Parâmetros do Sistema

Volume do túnel	6300	m^3
Area da Seção de Teste	4,8	m^2
Porcentagem de ar pelo secador	50	%
Porcentagem de extração forçada	2	%
Pressão Ambiente	101300	Pa
Temperatura de Estagnação da S.T.	300	K
Area de Vazamento	$3,23x10^{-3}$	m^2
Umidade sai do secador:	$2x10^{-5}$	kgH_2O/kg ar seco
Umidade ambiente	$1,8x10^{-2}$	kgH_2O/kg ar seco
Umidade inic.no túnel	$1x10^{-4}$	kgH_2O/kg ar seco

RESULTADOS

A figura 6, obtida a partir do modelamento descrito, mostra a evolução da umidade para Mach=1,0 na seção de testes. O aspecto do gráfico é o mesmo para outros valores de Mach. Observamos que a condição critica é quando temos o túnel sub-pressurizado. Assim as figuras 3 e 6 resumem os principais fatores para a solução, sendo a sobrepressão, critica para a definição do critério de umidade (determinação de w_1) e a subpressão, critica quanto à duração do ensaio.

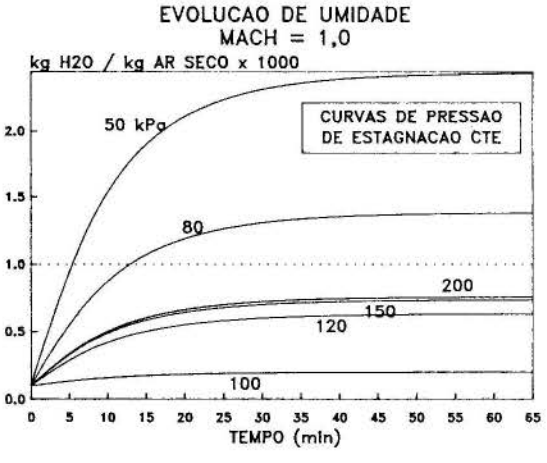

figura 6: umidade variando com P estagnação

Mesmo apresentando-se a curva de pressão de estagnação de 50000 Pa mais critica, o valor utilizado para a extração forçada foi de 2% do fluxo principal, que representou neste caso 10 kg/s enquanto que a capacidade do sistema de evacuação é de 2% do fluxo principal máximo, ou seja, cerca de 60 kg/s, e a capacidade de secagem 50% deste valor. Assim, pode-se empregar o recurso de se fazer uma extração maior que 2% e/ou fazer passar um fluxo efetivo maior pelo secador $(1-\theta) > 50\%$. A figura 7 mostra como a evolução da umidade no túnel é afetada pelo parâmetro $(1-\theta)$. A pressão de estagnação é constante e igual a 50000 Pa. Vemos que utilizando 100% pelo secador o acréscimo do tempo de ensaio é de 5 para 7,5 minutos.

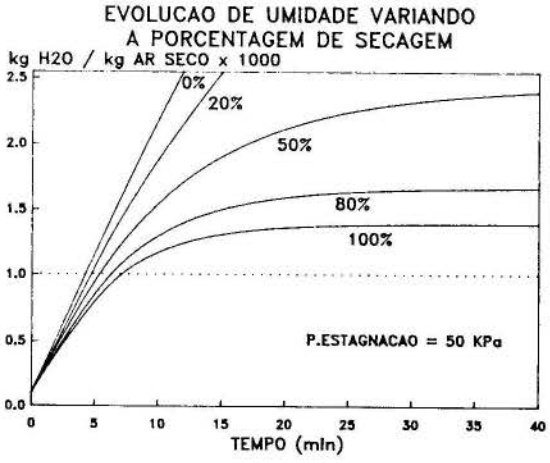

figura 7: umidade variando fluxo pelo secador

O sistema concebido apresenta grande flexibilidade operacional, permitindo contornar vários problemas que possam surgir, por exemplo, a área de vazamento ser maior, ou a necessidade de testes especificos pelo emprego de soluções que incorporem variação dos parâmetros:

. umidade inicial no túnel ($w_{t\,i}$)
. porcentagem do fluxo pelo trocador $(1-\theta)$
. fluxo de extração forçada ,

para se atingir a umidade limite no túnel (w_1) num tempo de ensaio conveniente em condições de pressão de estagnação e Mach na seção de testes.

REFERÊNCIAS

[1] GOETHERT, Bernhard H. - "Transonic Wind Tunnel Testing", Pergamon Press, 1961.

[2] RELATÓRIO DE MISSÃO AO EXTERIOR - "Projeto Conceptual do Túnel Transônico",GTTS-GER-G016, CTA, setembro de 1989.

[3] BURGESS, W.C. & SHEASHORE, F.L., "Criterious for Condensation-Free Flow in Supersonic Tunnels", NACA TN-2518, USA, 1951.

[4] PROJETO MSWT - Comunicação Pessoal com Engo.Chris D.Hayes da SVERDRUP Tech.Inc.,1988.

[5] "Demanda Energética do Túnel Transônico" - relatório interno GTTS, GER-T009/88, 1988.

[6] CHAPMAN,A.J;WALKER,W.F. - "Introductory Gas Dynamics", Holt,Rinehart and Winston, Inc. 1971.

ABSTRACT

It is presented a justification for the Forced Mass Extraction System used in Transonic Wind Tunnels, showing the System main parameters. Special attention is given to the humidity in the tunnel, considering technical and cost aspects. Yet it is analized the main impacts in pressurized tunnels, where normal leakage through the tunnel structural walls caused by pressure differential requires a Dryer System. Then it is developed numerical routine based in finite differences for determining the Test Section humidity variation during the test.

III ENCIT – Itapema, SC (Dezembro 1990)

UNSTEADY AERODYNAMIC LOADS OF VERTICAL AXIS WIND TURBINE

D. Sadhu
Mechanical Engineering Department
Federal University of RGS, P. Alegre, RS, Brazil

SUMMARY

The periodic change of angle of attack of the blade elements on each revolution of vertical axis wind turbine leads to the development of dynamic stall. The unsteady aerodynamic blade forces are evaluated by analytical time delay indicial method and compared with experimental data. The complex flow field around the rotor swept area is defined through momentum theory and the results are incorporated in analytical model.

INTRODUCTION

In vertical axis wind turbine (VAWT) the blade elements experience a periodic change of angle of attack (α) in each revolution. At low tip speed ratio (λ), α exceeds static stall angle (α_{ss}) and the blade works in dynamic stall condition which overdrives the aerodynamic lift (C_l) when $\dot{\alpha}$ is positive and underdrives it when $\dot{\alpha}$ is negative. The abrupt change in lift forces increase unsteady blade loads that can be damaging to wind turbine structure and the dive trains. During starting, stopping and opeartion at occasional sudden gust, the rotor also experience the abrupt load variation. On the other hand as the compartively high aerodynamic forces available due to the dynamic stall behaviour, it is possible to operate the VAWT at λ as low as 1.5 and produce power at high wind when the aerogenerator is connected with mains grid running at constant speed. Thus, the use of stall regulation has led to controlled power output in all wind speeds without reefing (1). The ability to predict dynamic stall is therefore of crucial importance for determining the blade forces of VAWT leading to its design optimization.

Experimental data of pressure distributions on VAWT blades at field tests and that of oscillating aerofoils in wind tunnel simulated to VAWT blade operration along with an anlytical model for the unsteady aerodynamic blade loading are presented.

DYNAMIC STALL MODELS

The static airfoil characteristics for diferent angle of attack are related with the lift coefficient (C_l) and the drag coefficient (C_d) and is well defined for most of the airfoils. But when the same airfoil suffers a dynamic change in angle of attack ($\dot{\alpha}$) the corresponding values of C_l and C_d get modified.

Well elaborated studies (2) on this subject explains that when α of a dynamic airfoil exceeds α_{ss} it experiences over its lifting surfaces the shedding and passage of vortex like disturbances and consequently its characteristics get modified as shown in fig. 1. The parameters that influence the modifications are reduced frequency, airfoil shape, amplitude of oscillation, Mach number, Reynolds number, type of motion, three dimensional and turbulence level effect.

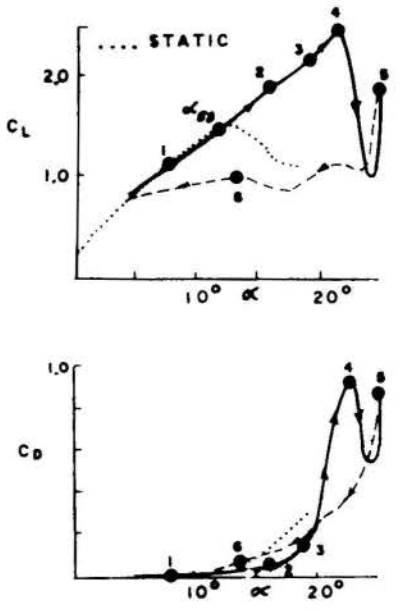

Fig. 1. Dynamic Stall Effect on VR-7 Airfoil at $\alpha = 15^{\circ} + \sin \omega t$ (2).

There exist several emperical and analytical models for predicting dynamic stall development on scillating airfoils such as.

(a) Boeing-Vertol gamma function method (3,4)
(b) UTRC α,A,B, method (5,6)
(c) MIT method (7)
(d) Lockheed method (8,9)
(e) Time delay method (10,11)

Other emperical model that can be noted (12) is based on the study of vortex shedding from the airfoil during dynamic stall and

another model (13) involes the trailing edge and leading edge vortex shedding. and a semiemperical model (14) is used to describe the dynamic stall of helicopter rotor in forward flight.

In some of the analysis (15,16) of VAWT aerodynamic foreces the dynamic stall characteristics had been approximated using the Boeing Vertol model. In these analyses a modified angle of attack α_m is used to find the values of C_l and C_d, and is related as :

$$\alpha = \alpha_{eff} - \Gamma . A \left[\dot{\alpha}_{eff} C/2W \right]^{1/2} S \quad (1)$$

where,

$A = 0.75 + 0.25\ S$, and
$\Gamma = 1.40 - 6.0.(0.06 - t/C)$, and α_{eff} is effective angle of attack of the wind inflow. C is the airfoil chord, W is the relative wind speed, t is maximum thickness of the airfoil and S is the sign + or - of $\dot{\alpha}$.
C_l and C_d are determined as :

$$C_l = [\alpha_{eff} / (\alpha_m - \alpha_{eff})] C_{l(\alpha)_m} \quad (2)$$

and,

$$C_d = C_{d(\alpha)_m} \quad (3)$$

The important parameter associated with unsteady flows about airfoils, the reduced frequency k is in fact an angle derived from referring rate of change of angle to the time base t. Hence, in VAWT this dynamic stall parameter is given as

$$k = \dot{\alpha} C / W = \{[(\lambda/\omega)\cos\theta - \lambda\sin\theta + \lambda^2]/(W/\omega R)^3 C/R \quad (4)$$

It may be noted that the equation [4]holds good only when the wind flow plane is parallel to the vertical axis plane of the turbine . Any flow curvature or wind flow deviation would modify the α and in consquence the $\dot{\alpha}$. In reality with heavy rotor loading the fluid flow around the swept area tends to be curved due to the reactions of the blade aerodynamic forces . Hence, it is necessary to define the exact value of α at each azimuth position of the blade element to apply this

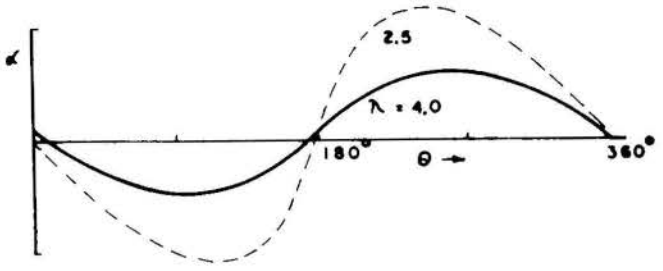

Fig. 2. Variation of α along Azimuth of VAWT

model. In addition the oscillatory motion is not a simple sine wave particularly when the λ is small as shown in fig.2.

MOMENTUM MODEL OF VAWT

The flow field around the swept area of the VAWT rotor is defined using a quasisteady analytical approach based on the momentum principle and blade element theory for each streamtube passing through the roror. The aerodynamic forces as they act on the blade elements are shown in fig. 3. The blade component forces along the chord (F_t) and along its normal (F_n) exert forces along the

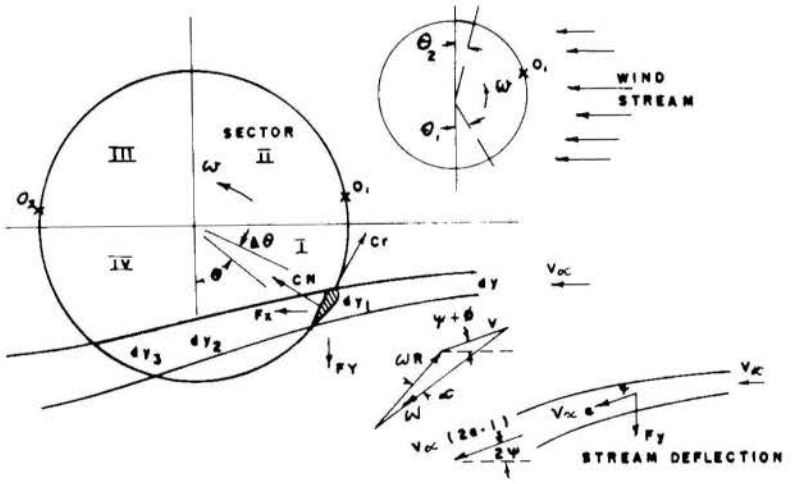

Fig. 3. Schematic Diagram of Velocity and Forces in a Streamtube of a VAWT Rotor.

X and Y axes. In all the four sectors of the swept area I to IV the component forces along X remain in the same direction and are used to find the axial interference factor (a). Whereas the component forces along Y in sector I and II are opposing and similarly they are in sector III and IV. In most of the aerodynamic analysis of VAWT their effect on the stream tubes were ignored understanding that they cancel each other or the effect was considered negligible. In the actuator cylinder model (17) it is found to have substantial effect on the streamtubes. In the present analysis the forces along Y are incorporated to find each streamtube deflection ψ.

The theoretical analysis proceeds with step by step improvements of the calculations transporting new constrains as they are found. In the first step the analysis initiates with the C_l and C_d values

corresponding to static airfoil data and the stream flow parallel to each other. (a) in the upwind sector is determined from the equation [5].

$$a = K.K_o / \left[K.K_o + \int_{\theta - \Delta\theta/2}^{\theta + \Delta\theta/2} f(\theta)\, d\theta \right] \qquad (5)$$

where, $K = 8\pi R/BC$, $K_o = \mathrm{Sin}(\theta+\Delta\theta/2) - \mathrm{Sin}(\theta-\Delta\theta/2)$

$$f(\theta) = (W/V)^2 . (C_n . \mathrm{Cos}\theta + C_t . \mathrm{Sin}\theta)$$

B=Number of blades, V=Local wind speed ($V = a.V_\alpha$ in the upwind sector)

θ = Azimuth angle, $\Delta\theta$ = azimuth angular variation in step,

C_n = Normal force coefficient

C_t = Tangential force coefficient

In the downwind the axial interference factor (a') follows the same equation [5] with the modification of local velocity which is $V = a'.(2.a-1).V_\alpha$.

Once the (a) and (a') of each streamtubes converged, the blade forces F_t and F_n are found at corresponding azimuth θ with the converged value of W by the following relation.

$$F_t = 1/2\rho W^2 . C . C_t \text{ and } F_n = 1/2\ \rho\ W^2 . C . C_n$$

Once the blade forces are found the streamtube deflection caused by these forces and its curvature due to flow expansion are found by the following procedures.

Streamtube Deflection (ψ)

The compenent force along Y is calculated at each azimuth position as :

$$F_y = [F_t \mathrm{Sin}\theta + F_n \mathrm{Cos}\theta] . B\Delta\theta/2\pi \qquad (6)$$

This force tends to deflect the flow perpendicular to the mainstream wind direction. The azimuth position where this force is near zero the streamtube becomes parallel to the original flow and this point is called null point 'O_1' in the upstream and 'O_2' in the downstream shown in fig.3.

Once these points are found the value of ψ for each streamtube on either side is found from the following equation.

$$\text{Upstream - } \mathrm{Tan}\,\psi = F_y/(2mV(1-2a) \qquad (7)$$

$$\text{Downstream- } \mathrm{Tan}\psi' = F_y/(2m'V(1-2a)(1-2a') \qquad (8)$$

where, m is the mass flow in the upstream and m' is the mass flow in the downstream. It is assumed that ψ would develop twice the value at the rotor when they are far down stream wake, following the momentum theory.

Stream Tube Expansion (ϕ)

The flow expansion near the rotor takes place on both sides of the null point. The theory derived by Durand (18) is utilised to find ϕ of each streamtube. In VAWT as the flow retards near the swept area due to energy extraction each stream tube tends to take the form shown in fig.4. Thus, The axial interferenc factor varies along the X axis,

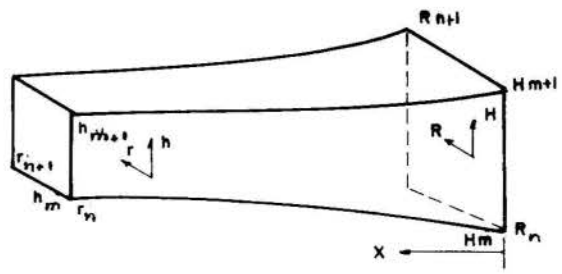

Fig.4. Streamtube Expansion near Rotor Surface

which is related to the (a) at the rotor surface by the following equation.

$$a_x = a \int_{R_n}^{R_{n+1}} \int_{H_m}^{H_{m+1}} \frac{X.dR.dH}{[X^2+(R-r)^2+(H-h)^2]^{3/2}} \qquad (9)$$

The equation [9] is solved numerically for discrete values of X. From the continuity equation the sectional area of each streamtube along X is found by the following equation.

$$a_x (r_{n+1} - r_n)(h_{m+1} - h_m) = a (R_{n+1} - R_n)(H_{m+1} - H_m) \qquad (10)$$

At fixed height of the turbine the expansion angle is calculated along the radius only. From the equation [10] the variation of the streamrube dimensions along X are found and the expansion angle ϕ at the rotor surface is found from the slope of the curve where X=0.

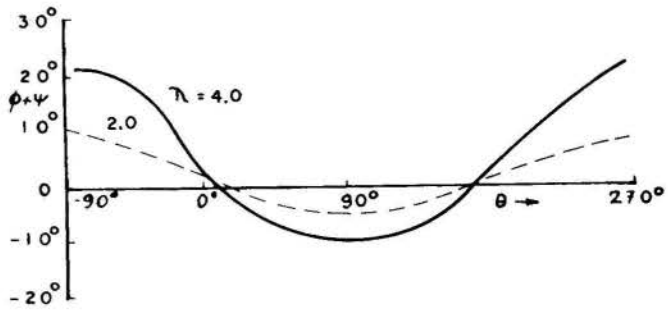

Fig. 5. Streamtube Curvature at Rotor Surface

Streamtube Curvature ($\psi+\phi$)

In subsequent step of the calculation each streamtube is assigned with curvature equal to the summation of its ψ and ϕ. The local velocity of the wind at the rotor surface thus could be defined by its direction and magnitude. The velocity diagram is modified accordingly in this step of calculation and the results get modified slightly but only a few cycles are required for the convergence. The variation of streamtube curvature at the rotor surface along the azimuth positions in the upwind and downwind side derived after the unsteady blade forces incorporated in the analysis is shown in fig.5.

Once the streamtubes around the rotor surface are defined the angle of attack for

the discrete azimuth position of the blade elements are found as:

$$\text{Tan}^{-1}\alpha = -\frac{\text{Sin}(\theta-\psi-\phi)}{\lambda + \text{Cos}(\theta-\psi-\phi)} \qquad (11)$$

The streamtubes curving provide the blades in the upwind to cover less circumferential area $(180^{o}- \theta_1 - \theta_2)$ with downwind side as the blade find zero angle of incidence at θ_1 and $180^{o}- \theta_2$ azimuth positions. The flow also becomes skewed by $\theta_1 - \theta_2$ towards sector I. The variation of θ_1 and θ_2 with λ is compared with experimental data (19) in fig. 6. Maximum curvature θ_1 becomes asymptotic towards λ - 5.0 in the theoretical analysis.

THEORETICAL AERODYNAMIC FORCES

In the final stage of the analysis the unsteady aerodynamic forces of the blade elements are estimated and incorporated in equation (1). The time delay indicial method (110,20) is selected for this estimation. In this method the static flow characteristics of an aerofoil are used in combination with emperically determined time constants that produce appropriate lags in the formation of circulation and the creation and growth of seperation. The dynamic stall event is assumed to be dependent on a dimensionless constant $\tau = W\Delta t/C$, where τ is identified with the parameter $s = 2Wt/C$ which is fundamental to expressions for the indicial aerodynamic response in the attached flow regime. At time t_o when α_{ss} is reached the momentum stall begins at time $t_1 = t_o + \tau_1 C/W$ and $C_{l\,max}$ occurs at $t_2 = t_o + \tau_2 C/W$. For $t < t_1$, $t < t_2$ C_l continue this trend. The aerodynamic center of pressure moves reerward and also increases the momentum coefficient (C_m) during the time interval. After the lift stall at $t = t_2$, C_l decreases by an emperical exponential law with respect to time. Values τ_1=2.6 and τ_2=6.0 are assumed here for time constant inaccordance with Sirkosky (13). Also is considered a simple drag relationship, $C_d = C_l . \text{Tan}\alpha$, that obtains once the leading edge suction is lost at τ_1.

Following the time history of α at each azimuth or corresponding t and Δt, C_n and C_t are estimated.

EXPERIMENTAL WORK

In this study four experimental works are consulted. Two of them are in wind tunnel test and two are on wind turbines in atmospheric wind measuring the pressure distributions on the blade surfaces.

The Glasgow University performed tests on NACA 0012, 0015, 0015,0018,0021,0025 and 0030 sections oscillating with simulated $\dot{\alpha}$ of VAWT. 30 pressure transducers were fixed inside the airfoils to measure the pressure distributions

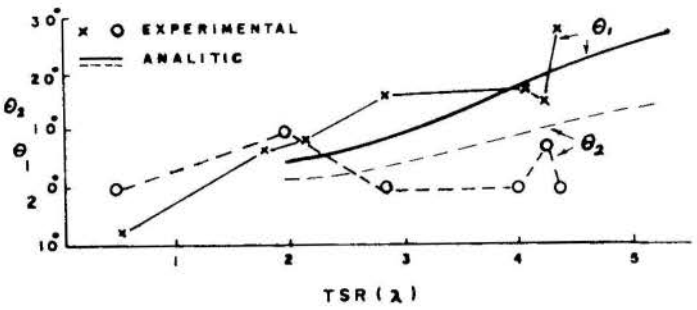

Fig. 6. Maximum streamtube inclination in the upwind of VAWT rotor surface

along the chord on both surfaces. The blade chord was 0.55m and span 1.61m provided upto 2 million Reynolds number (21).

At the University College of London NACA 0015 and 0020 sections were tested in wind tunnel. There the airfoil remains rigidly fixed to a rotating disc to create a VAWT analog effect on the airfoil. 50 transducers were fixed inside each airfoil, though only 46 were effectively used to record the pressures. The blade chord was 0.60m and span 0.60m privided upto 1 million Reynolds number (22).

The 25m VAWT at Camarthan Bay, S.Wales has two 18m long straight hinged blades with 1.25m chord of NACA 0015 section prives with mean Reynolds number of the blades upto 2.4 million and with a maximum above 4 million. 17 pressure transducers were fixed inside the blades along the chord and located 1.38m above the centre hinge.

In the RAL 6m two straight fixed bladed tirbine, tests were carried out on NACA 0015 section in one blade and NACA 0020 section in other blade. Both had 0.30m chord and 3.0m span and provided Reynolds number upto 0.7 million. There were 32 pressure transducers inside each blade to provide pressure distributions on both surfaces on each revolution, which means in every 1.4^{o} interval azimuth position data were collected. On each set up data for 80 revolutions were recorded. The wind speed was recorded at 3 diameter distance in the predominent wind direction and 5 point anemometer probe fixed at the leading edge of the blade register real wind velocity it encountered. Load cells on the blade hinge at the cross arms measured the net tangential forces on the blades. All the data were normalised with the stagnant pressure of the leading edge. Unfortunately the data are still in the stage of processing and could not be compared with other results

COMPARISON OF THEORY AND EXPERIMENTAL DATA

In wind tunnel test the flow remain parallel and could not be idealy simulated with the real VAWT operation. The data of the Glasgow windtunnel test for test for λ=2.5 is compared with the 25m VAWT for λ=2.0 in fig.7 and 8. In the upwind pass the correlation is good, while exist difference in the downwind pass, which may be attributed to the difficulties in estimating the α in field test where the flow becomes very disturbed by the upwind wake compared to the very symetrical α scedule of the wind tunnel test.

The UCL tests were mainly for high reduced frequency though λ could be as low as 2.0. Hence, they are not suitable for

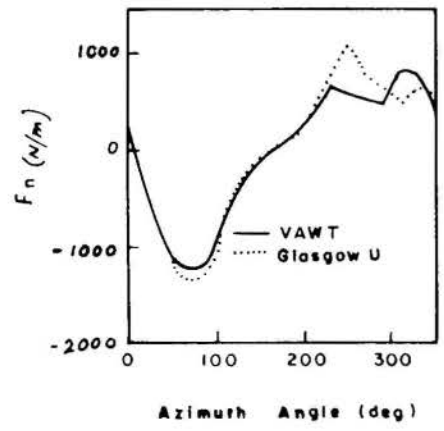

Fig. 7. Variation of Normal Blade Force along the Azimuth Angle

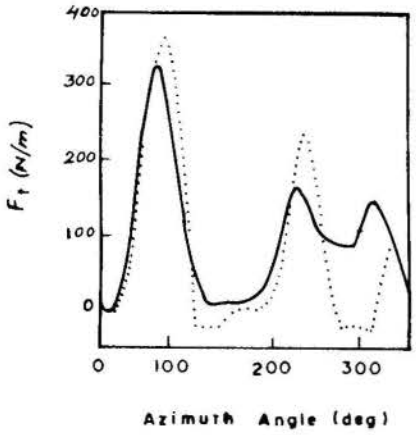

Fig. 8. Variation of Tangential Blade Force along the Azimuth Angle

comparison with 25m VAWT. Howver they are compared with theory as shown in Fig. 9 &10 for λ=2.0 at reduced frequency 0.25. Comparison with theory for normal force is encouraging, while exist discrepancies in tangential force. This may be due to wind tunnel corrections needed, but the excessive heaving force in this test may deform the flow around the test area which is not considered in theory of VAWT.

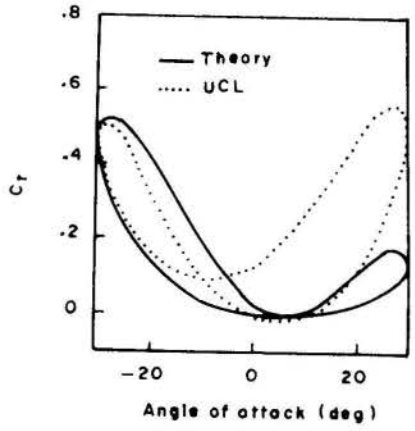

Fig. 9. Variation of Tangential Force Coefficient with Angle of Attack

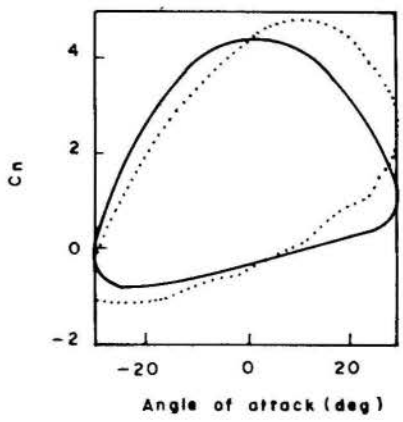

Fig. 10. Variation of Normal Force Coefficient with Angle of Attack

The variation of normal and tangential forces are shown in fig.11 to 14 comparing theory with the 25m VAWT. At λ=2 in VAWT, α attends value upto 29° in upwind whereas in downwind it attends 23°. It demonstrates that a complete collapse of leading edge suction, however in the downwind the reattachment of the flow takes place sooner. At corresponding high λ=4.1, α remains within 15° . In most of the λ the theory and experimental aerodynamic loading is in good agreement.

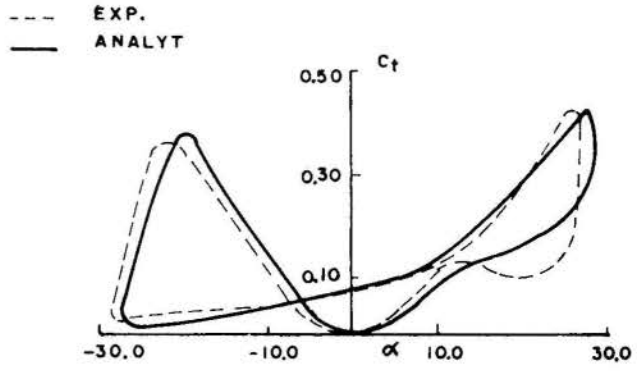

Fig. 11. Tangential Force Coefficient at λ=2.0

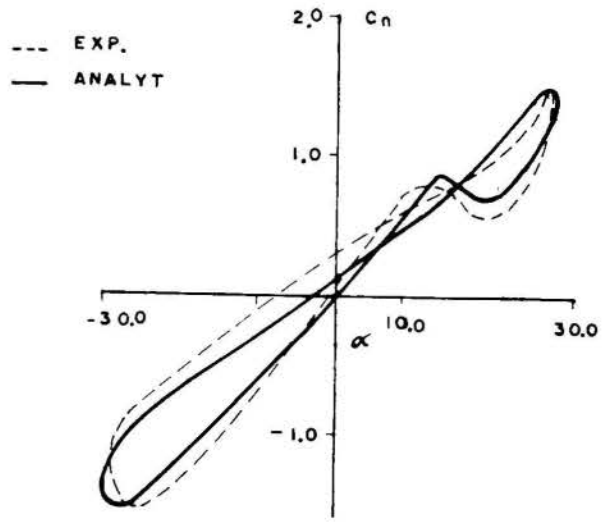

Fig. 12. Normal Force Coefficient at λ=2.0.

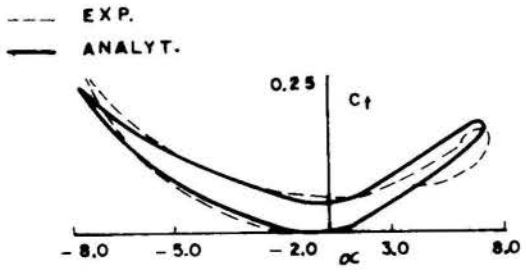

Fig. 13. Tangential Force Coefficient at λ=4.1

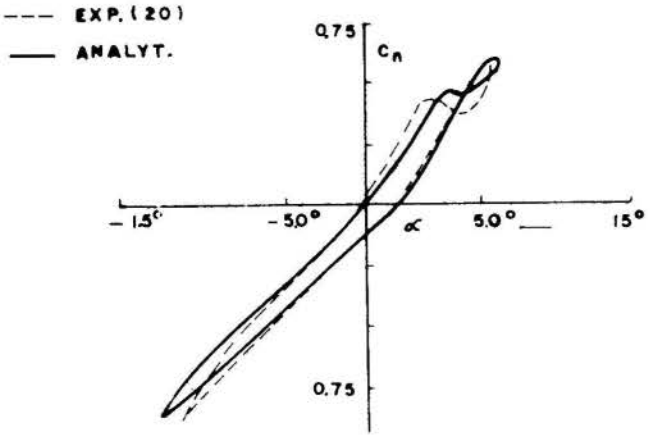

Fig. 14. Normal Force Coefficient at λ=4.1.

CONCLUSIONS

Better understanging of the aerodynamic forces applied to VAWt is necessary for it optimum design. The experimental data collected so far helps to provide data on various blade sections. It is expected that the recent data recorded on the RAL 6m VAWT would provide further insight of the blade forces and the flow field

ACKNOWLEDGEMENTS

This work was supported by CNPq grant no. 205578-88.5/RS and was realised at the Rutherford Appleton Laboratory, U.K. The author is grateful to Prof. N.H.Lipman at RAL for the invitation to work on this project there and all the helps given during his stay there.

REFENCES

(1) S.J.R. Powels,"Analysis of Results from the U.K. Vertical Axis Wind Turbine Test Programme",Proc. ECWEC, Herning, Denmark, 6-10, June, 1988, pp.55-59.

(2) McCroskey, W.J.,"The Phenomenon of Dynamic Stall", NASA Technical Memorendum 81264,TR (1981).

(3) Haris, F. D. et. al., "Rotor High - Speed Performance, Theory Vs Test", AHS, 15(3), (1970).

(4) Gormont,R.E, "A Mathematical Model of Unsteady Aerodynamics and Radial Flow for Application to Helicopter Rotors", U.S. MROL, TR-72-67, (1973).

(5) Carta,F.O.et.al."Investigation of airfoil Dynamic Stall and its Influence on Helicopter Control Loads:", US Army, AMROL TR-72-51, (1972).

(6) Bielawa,R.L,"Synthasized Unsteady Airfoill Data with Applications to Stall-Flutter Calculations",AHS Report No.936 (1976).

(7) Johnson,W, "The Effect of Dynamic Stall on the Response and Airloading of Helicopter Rotor Blades",AHS, 14(2), 68-79, (1969).

(8) Ericsson,L.E. and Reading, J.P, "Dynamic Stall Analysis in the Light of Recent Numerical and Experimental Results", J. Aircraft,13(4),248-55,(1976).

(9) Ericsson,L.E. and Reading,J.P, "Dynamic Stall at High Frequency and Large Amplitude",J.Aircraft,17(3),136-142,(1980)

(10)Beddoes,T.S,"A Qualititive Discussion of Dynamic Stall Prediction Methods for Unsteady Seperated Flows", Paper No.3&15, AGARD R-670,(1980)

(11)Carlson,R.G.et.al,"Dynamic Stall Modelling and Correlation with Experimental Data on Airfoils and Rotors', Paper No.2, NASA, SP-352, (1974).

(12)Gangeani,S.T, "Prediction of Dynamic Stall and Unsteady Airloads for Rotor Blades", Presented at the 37th Anual Forum of AHS, N.Orleans ,LA, May 1981.

(13)Beddoes,T.S, "Representation of Airfoil Behaviour", Vertica, Vol.7,No.2,pp.183-197 1983.

(14)Tran,C.Tand Falchero,D,"Application of the ONERA Dynamic Stall Model to a Helicopter Blade in Forward Flight", Vertica, Vol.6, pp. 219-239,(1982).

(15)Read,S and Sharp,D.J,"An Extended Multiple Streamtube Theory for Vertical Axis Wind Turbines", 2nd.BWEA Workshop,65-72,(1980).

(16)Paraschivolu,I,"Predicted and Experimental Aerodynamic Forces on the Darrieus Rotor", J.of Energy, 7(6),610-615, (1983).

(17)Madsen,H.A,"On the Ideal and Real Energy Conversion in a Straight Bladed Vertical Axis Wind Turbine", Aalborg University Centre -9220, (1983).

(18)Durand, W. F, ed. "Aerodynamic Theory", Vol. IV, California Institute of Technology Publications, (1943).

(19)Harris,A, "Report on 25m VAWT at Camarthan Bay, VAWT,McAlpine Ltd.,U.K. (1989).

(20)Leishman,J.G. and Beddoes, T. S, "A Generalised Model for Airfoil Unsteady Aerodynamic Behaviour and Dynamic Stall Using the Indicial Method", 42nd. Annual Forum of the AHS, Washington,D.C.,(1986).

(21)R.K.Angell et.al,"Collected Data for Tests on a NACA 0018 Aerofoil", University of Glasgow, Dept. of Aeronautics & Fluid Mechanics, G.U. Aero Report 8815, (1988).

(22)Clayton, B. R. and Filby, P, "VAWT Blade Aerodynamics Simulation with Reference to NACA 0015 Profile",Proceedings of EWEC'89, Glasgow, pp.106-111.

III ENCIT – Itapema, SC (Dezembro 1990)

NUMERICAL SIMULATION OF HIGH SPEED FLOWS OVER COMPLEX SATELLITE LAUNCHERS

FRANZ ZDRAVISTCH
Centro Técnico Aeroespacial
Instituto Tecnológico de Aeronáutica
12225 — São José dos Campos — SP

JOÃO LUIZ F. AZEVEDO
Centro Técnico Aeroespacial
Instituto de Atividades Espaciais
12225 — São José dos Campos — SP

SUMMARY

The flowfield over an axisymmetric vehicle configuration is simulated using the Euler and the thin layer Navier-Stokes equations. These sets of equations are implemented in a finite difference context using the Beam and Warming implicit approximate factorization algorithm. Turbulence closure is obtained with the two-layer Baldwin and Lomax algebraic eddy viscosity model. Computational results are compared with experimental data and the agreement is good. An interesting new approach for handling the implicit artificial dissipation terms is suggested. Considerations about extension and further validation of the present work are also discussed.

INTRODUCTION

The progress recently achieved in the field of Computational Fluid Dynamics, together with the massive increase in performance of present computers has allowed the simulation of flowfields of practical interest. The lack of adequate computational resources has hindered part of the development of CFD codes at both ITA and IAE. Nevertheless, the work has proceeded considering mostly two-dimensional and axisymmetric cases. The need for reliable computational tools is ever more evident considering the increasing complexity of aerospace vehicles and the always increasing costs of wind tunnel tests.

The work at IAE considering more complex formulations, such as those based on the Euler or the Navier-Stokes equations, started almost half a decade ago. It was primarily concerned with explicit schemes and there was great emphasis on the supersonic regime. The latter would allow the use of the parabolized Navier-Stokes equations for many geometries of interest, and the corresponding increase in computational efficiency. The former would account for the easiness of programming and the lack of powerful enough computers that could efficiently deal with implicit methods. More recently, it became evident that it was necessary to develop more powerful computational tools that could handle more complex flow regimes and/or geometries.

The present work describes, then, part of this effort in developing two dimensional, axisymmetric solvers based on the Euler and Navier-Stokes formulations. We chose to work with the Beam and Warming algorithm[1,2]. The actual implementation, however, is closer to that presented by Pulliam and Steger[3,4], and Deiwert[5]. The two-layer algebraic Baldwin and Lomax[6] turbulence model was used. The applications presented here consider external vehicle aerodynamics and the results include both inviscid and turbulent thin-layer Navier-Stokes cases. The computations show good agreement with the experimental data.

GOVERNING EQUATIONS

The two dimensional azimuthal-invariant form of the thin-layer Navier-Stokes equations was used here. Derivation of these equations can be found in Nietubicz, Pulliam and Steger [7], and applications in Deiwert[5] and Sahu[8]. The thin layer azimuthal invariant (or generalized axisymmetric) Navier-Stokes equations can be written in conservation-law form for a body-conforming curvilinear coordinate system as

$$\frac{\partial \bar{Q}}{\partial \tau} + \frac{\partial \bar{E}}{\partial \xi} + \frac{\partial \bar{F}}{\partial \eta} + \bar{H} = Re^{-1}\frac{\partial \bar{S}}{\partial \eta} \tag{1}$$

where $\xi = \xi(x,y,t)$ is the body oriented coordinate in the streamwise direction, $\eta = \eta(x,y,t)$ is the coordinate normal to the body surface, and $\tau = t$ is the time. The vector of conserved quatities is

$$\bar{Q} = J^{-1}\begin{Bmatrix} \rho \\ \rho u \\ \rho v \\ e \end{Bmatrix} \tag{2}$$

The inviscid flux vectors are given by

$$\bar{E} = J^{-1}\begin{Bmatrix} \rho U \\ \rho u U + p\xi_x \\ \rho v U + p\xi_y \\ (e+p)U - p\xi_t \end{Bmatrix} \tag{3}$$

$$\bar{F} = J^{-1}\begin{Bmatrix} \rho V \\ \rho u V + p\eta_x \\ \rho v V + p\eta_y \\ (e+p)V - p\eta_t \end{Bmatrix} \tag{4}$$

and the source term is given by

$$\bar{H} = J^{-1}\begin{Bmatrix} 0 \\ 0 \\ -p/R \\ 0 \end{Bmatrix} \tag{5}$$

where $R = R(\xi,\eta,\tau)$ is the radius in the natural inertial cylindrical coordinates. The viscous flux vector $\bar{S}$ can be written as

$$\bar{S} = J^{-1}\begin{Bmatrix} 0 \\ \mu m_1 \frac{\partial u}{\partial \eta} + \frac{\mu}{3}\eta_x m_2 \\ \mu m_1 \frac{\partial v}{\partial \eta} + \frac{\mu}{3}\eta_y m_2 \\ \mu m_1 m_3 + \frac{\mu}{3} m_2 (\eta_x u + \eta_y v) \end{Bmatrix} \tag{6}$$

where $m_1 = \eta_x^2 + \eta_y^2$, $m_2 = \eta_x u_\eta + \eta_y v_\eta$, and $m_3 = \frac{1}{2}\left(u^2+v^2\right)_\eta + \frac{\gamma}{Pr}\left(e_i\right)_\eta$.

The usual nomenclature is being used here, such that ρ is the density, u and v are cartesian velocity components, e is the total energy per unit of volume, Re is the Reynolds number, and Pr is the Prandtl number. Moreover, it is assumed in the above that a suitable nondimensionalization of the governing

equations was performed. In the present case, these variables were made dimensionless with respect to freestream quantities, exactly as done by Pulliam and Steger[3] and Pulliam[9].

The pressure, p, is obtained from the equation of state for perfect gases

$$p = (\gamma - 1)\,\rho e_i \tag{7}$$

where e_i is the specific internal energy. The total energy per unit of volume is defined as

$$e = \rho\left[e_i + \frac{1}{2}\left(u^2 + v^2\right)\right] \tag{8}$$

The contravariant velocity components can be written as

$$\begin{aligned} U &= \xi_t + \xi_x u + \xi_y v \\ V &= \eta_t + \eta_x u + \eta_y v \end{aligned} \tag{9}$$

The Jacobian of the transformation, J, can be calculated considering that

$$J^{-1} = R(x_\xi y_\eta - x_\eta y_\xi) \tag{10}$$

and the various metric terms can be expressed as

$$\begin{array}{ll} \xi_x = JRy_\eta & \eta_x = -JRy_\xi \\ \xi_y = -JRx_\eta & \eta_y = JRx_\xi \\ \xi_t = -x_\tau\xi_x - y_\tau\xi_y & \eta_t = -x_\tau\eta_x - y_\tau\eta_y \end{array} \tag{11}$$

We observe that the Euler equations can be recovered simply by neglecting the right-hand side of Eq. 1.

TURBULENCE MODELING

The turbulence model adopted in the present work is that due to Baldwin and Lomax[6]. For wall-bounded shear layers, a two-layer formulation is used such that

$$\mu_t = \begin{cases} (\mu_t)_{\text{inner}} & ,\eta \le \eta_{\text{crossover}} \\ (\mu_t)_{\text{outer}} & ,\eta > \eta_{\text{crossover}} \end{cases} \tag{12}$$

where η is the normal distance from the wall, and $\eta_{\text{crossover}}$ is the smallest value of η at which values from the inner and outer formulas are equal.

The formulation used in the inner region is

$$(\mu_t)_{\text{inner}} = \rho\ell^2|\omega| \tag{13}$$

Here, ρ is the density, and the length scale ℓ is given by

$$\ell = \kappa\eta\left[1 - \exp\left(-\frac{\eta^+}{A^+}\right)\right] \tag{14}$$

where $\eta^+ = \eta\sqrt{\rho_w\tau_w}/\mu_w$, $\kappa = 0.4$ and $A^+ = 26$. The velocity scale is given by $\ell|\omega|$, where $|\omega|$ is the magnitude of the local vorticity vector. For an axisymmetric formulation, and a non-spinning body, this can be written in general curvilinear coordinates as

$$|\omega| = \left|\left(\frac{\partial\xi}{\partial x}\frac{\partial v}{\partial\xi} + \frac{\partial\eta}{\partial x}\frac{\partial v}{\partial\eta}\right) - \left(\frac{\partial\xi}{\partial y}\frac{\partial u}{\partial\xi} + \frac{\partial\eta}{\partial y}\frac{\partial u}{\partial\eta}\right)\right| \tag{15}$$

The formulation for the outer region is given by

$$(\mu_t)_{\text{outer}} = K\,C_{cp}\,F_{\text{wake}}\,F_{Kleb}(\eta) \tag{16}$$

where F_{wake} is defined as

$$F_{\text{wake}} = \text{the smaller of}\left(\begin{array}{c} \eta_{\max} F_{\max} \\ C_{wk}\,\eta_{\max} U^2_{\text{dif}}/F_{\max} \end{array}\right) \tag{17}$$

Here, $F_{\max}$ is the maximum value of the function

$$F(\eta) = \eta|\omega|\left[1 - \exp\left(-\frac{\eta^+}{A^+}\right)\right] \tag{18}$$

and $\eta_{\max}$ is the value of η at which this maximum occurs. U_{dif} is the difference between the maximum and minimum total velocities in the profile along the η-coordinate line. Hence,

$$U^2_{\text{dif}} = \left(u^2 + v^2\right)_{\max} - \left(u^2 + v^2\right)_{\min} \tag{19}$$

For boundary layers, this minimum velocity is obviously defined as zero. Finally, the Klebanoff intermittency factor is given by

$$F_{Kleb}(\eta) = \left[1 + 5.5\left(\frac{C_{Kleb}\,\eta}{\eta_{\max}}\right)^6\right]^{-1} \tag{20}$$

The various parameters that appear in the formulation have the following values: $C_{cp} = 1.6$, $K = 0.0168$, $C_{wk} = 0.25$ and $C_{Kleb} = 0.3$.

BOUNDARY CONDITIONS

At the body wall, the condition of flow tangency for the Euler formulation is enforced by imposing that the V contravariant velocity component is equal to zero. Hence, the cartesian velocity components at the wall can be obtained from

$$\left\{\begin{array}{c} u \\ v \end{array}\right\} = J^{-1}\left[\begin{array}{cc} \eta_y & -\xi_y \\ -\eta_x & \xi_x \end{array}\right]\left\{\begin{array}{c} U \\ 0 \end{array}\right\} \tag{21}$$

For the Navier-Stokes formulation, the no-slip condition is imposed at the wall. This can be accomplished by also setting the other contravariant velocity, U, to zero. Moreover, zero normal pressure gradient is imposed at the wall for both formulations, and the wall is assumed to be adiabatic for the viscous computations.

In the Euler case, one cannot say much about the temperature boundary condition at the wall. This is because the formulation does not allow for the development of a thermal boundary layer. Nevertheless, the assumption of zero normal temperature gradient at the wall is completely consistent with an inviscid formulation and, hence, this is the condition used at the wall. Actually, the numerical implementation of this boundary condition turns out to be exactly equal to that of an adiabatic wall, which is the condition being used in the viscous case, as mentioned above.

Freestream conditions are imposed at the upstream and lateral far-field boundaries. Symmetry boundary conditions are used at the upstream centerline, and all quantities are obtained by extrapolation of interior data at the downstream boundary. Zero-th order extrapolation is used in this latter case, in order to simplify the code implementation. It must be pointed out that, for a subsonic outflow case, this procedure is not completely consistent with a characteristic-type analysis[10] at the downstream boundary. Nevertheless, it did not seem to cause any trouble for the subsonic freestream cases studied in the present work. This is probably due to the fact that the geometries considered here have a very long cylindrical afterbody section. Hence, the pressure does invariably return to its freestream value before reaching the downstream boundary.

NUMERICAL IMPLEMENTATION

The governing equations were discretized in a finite difference context according to the Beam and Warming[1,2] implicit approximate factorization scheme. The implicit Euler method is used for the time march, and central differences are used to approximate the spatial derivatives. The resulting scheme is

second order accurate in space, but only first order accurate in time. The algorithm can be written in operator form as

$$L_\xi L_\eta \Delta\bar{Q}^n = R_\xi + R_\eta - \Delta t\, \bar{H}^n \qquad (22)$$

Here,

$$\begin{aligned} L_\xi &= I + \Delta t\, \delta_\xi \hat{A}^n - Di_\xi \\ L_\eta &= I + \Delta t\, \delta_\eta \hat{B}^n - \Delta t\, Re^{-1} \bar{\delta}_\eta J^{-1} \hat{M}^n J - Di_\eta \\ R_\xi &= -\Delta t\, \delta_\xi \bar{E}^n + De_\xi \bar{Q}^n \\ R_\eta &= -\Delta t\, \delta_\eta \bar{F}^n + \Delta t\, Re^{-1} \bar{\delta}_\eta \bar{S}^n + De_\eta \bar{Q}^n \end{aligned} \qquad (23)$$

In the above formulation, $\hat{A}$, $\hat{B}$ and $\hat{M}$ are the flux Jacobian matrices. The reader is referred to Pulliam and Steger[4] for the form of these matrices in the two dimensional case. The δ_ξ and δ_η are three-point central difference operators. The Δ_ξ, Δ_η and ∇_ξ, ∇_η are standard forward and backward difference operators, respectively. The n-th iteration correction is $\Delta\bar{Q}^n = \bar{Q}^{n+1} - \bar{Q}^n$. Moreover, standard central difference midpoint operators are used to discretize the viscous derivatives. This allows for an uniform treatment of the viscous terms on both right and left-hand sides, while maintaining the tridiagonal structure of the left-hand side matrices.

Since the spatial derivatives are being approximated by central difference operators, artificial dissipation terms must be explicitly added to the algorithm. These terms are represented by the De and Di operators in the expressions above. A simple constant coefficient numerical dissipation model was primarily adopted in the present work. In this case, the artificial dissipation operators are given by

$$\begin{aligned} De_\xi &= -\varepsilon_E \Delta t\, J^{-1} (\nabla_\xi \Delta_\xi)^2 J \\ De_\eta &= -\varepsilon_E \Delta t\, J^{-1} (\nabla_\eta \Delta_\eta)^2 J \\ Di_\xi &= \varepsilon_I \Delta t\, J^{-1} \nabla_\xi \Delta_\xi J \\ Di_\eta &= \varepsilon_I \Delta t\, J^{-1} \nabla_\eta \Delta_\eta J \end{aligned} \qquad (24)$$

Here, fourth difference operators are being used in the right-hand side, and second difference ones are being added to the left-hand side. This, again, has the objective of maintaining the tridiagonal nature of the implicit operators.

Some tests were also carried out using Pulliam's nonlinear artificial dissipation model[11]. In the present implementation, however, only the right-hand side, or explicit, operators De_ξ and De_η were replaced by the nonlinear ones. For the cases treated here, the nonlinear model did not yield remarkable improvements over the simpler constant coefficient model. On the other hand, it did cause a considerable increase in the computational time per iteration. Hence, we did stay with the constant coefficient model for the majority of the simulations performed here. For more information in the nonlinear artificial dissipation model, the reader is referred to Pulliam[11], Pulliam and Steger[4], and Chaussee and Pulliam[12].

The source term was treated explicitly in the present implementation. As a general rule, all boundary conditions were also implemented explicitly. Implicit boundary conditions were only used for the Navier-Stokes case at the body wall. Zero normal pressure gradient, adiabatic wall and no-slip conditions at the body surface were enforced using

$$\begin{aligned} \delta\rho_{i,1} &= \delta\rho_{i,2} \\ \delta u_{i,1} &= 0 \\ \delta v_{i,1} &= 0 \\ \delta p_{i,1} &= \delta p_{i,2} \end{aligned} \qquad (25)$$

which yields

$$\Delta\bar{Q}_{i,1} = J_{i,1}^{-1} M_{i,1} \begin{bmatrix} 1 & 0 & 0 & 0 \\ 0 & 0 & 0 & 0 \\ 0 & 0 & 0 & 0 \\ 0 & 0 & 0 & 1 \end{bmatrix} M_{i,2}^{-1} J_{i,2}\, \Delta\bar{Q}_{i,2} \qquad (26)$$

Here, $j = 1$ represents the point at the body wall and $j = 2$ the next point in the normal direction. Moreover, $M = \partial Q/\partial V$ is the transformation matrix that relates variations in the unconservative variables, $V = (\rho, u, v, p)^T$, with those in the conservative ones. Finally, it is important to mention that the code was implemented in standard Fortran, and the results to be presented here were all obtained in IBM PC-like microcomputers with Definicon DSI-020 coprocessor boards.

GRID GENERATION

The mesh point distribution over the geometrical space in which the flow is to be computed is always a critical aspect for a successful calculation. It must be balanced enough to cover the entire flowfield avoiding regions with excessive lackness of points. On the other hand, points must be clustered in regions in which phenomena such as boundary layers, expansions and shock waves occur, without exceeding our available computational capabilities.

In this case the grid was generated algebraically, using exponential stretching to cluster points near the body wall and expansion corners. In the forebody region, point coordinates are calculated by intersecting 3rd degree polynomials ($y = a_1 x^3 + b_1 x^2 + c_1 x + d_1$) in the longitudinal direction with fraction exponent polynomials ($y = a_2 x^{f_1} + b_2 x^{f_2} + c_2 x + d_2$) in the normal direction. The values of polynomial coefficients and exponents are calculated to fit appropriate point distribution, normality at the body wall and external boundary, and mesh orthogonality. The freestream boundary is located at 20 body base diameters normal to the body wall. A typical grid has 85 × 50 points in the longitudinal and normal directions, respectively. A complete mesh can be seen in Fig. 1 and a detailed view of the forebody region is shown in Fig. 2.

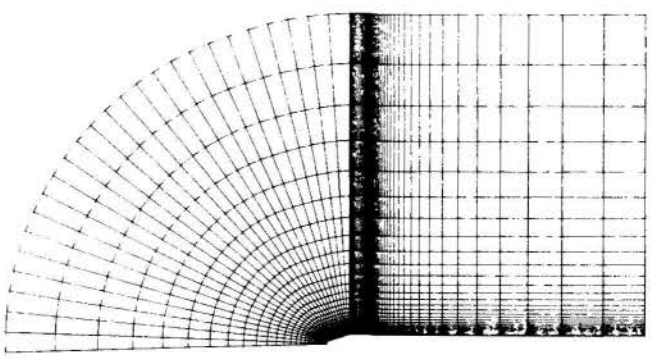

Figure 1: Complete configuration.

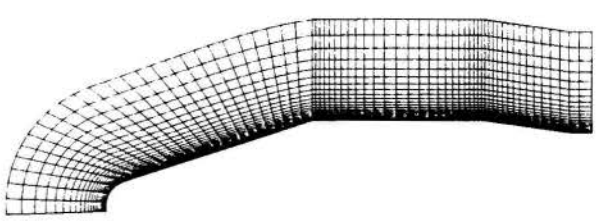

Figure 2: Forebody detail.

LAUNCH VEHICLE RESULTS

Results for a typical axisymmetric launch vehicle configuration were obtained for subsonic, transonic and supersonic freestream conditions. The particular configuration used here is that of the Brazilian satellite launcher (VLS) during 2nd stage flight. The details of the experimental investigation which yielded the wind tunnel results used for comparison with the present computations are reported by Moraes and Neto[13]. The pressure coefficient distribution over the body for a freestream Mach number of 0.5 is shown in Fig. 3, and compared with experimental data. The Reynolds number for this computation is 25.4×10^6, based on the cylindrical afterbody diameter. We observe a reasonably good agreement between computation and experiment, especially considering that the grid is still rather coarse for such a complex configuration. For the results obtained with the inviscid formulation, an over-expansion is observed in the computed pressures at the forebody cone-cylinder junction. In the viscous turbulent case, this effect is not present and results are improved.

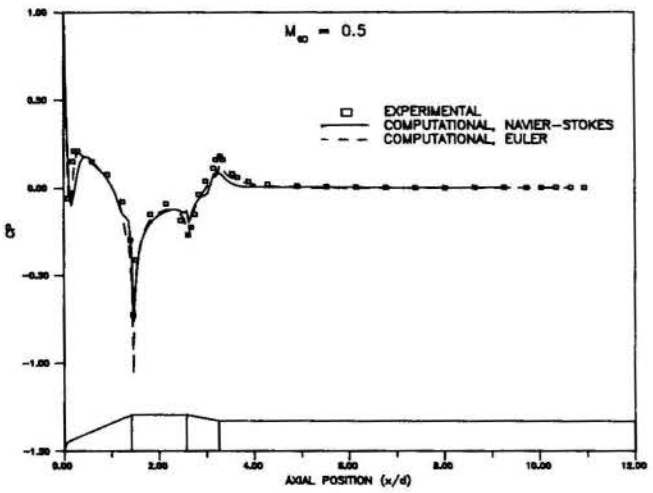

Figure 3: Subsonic freestream case ($M_\infty = 0.5$).

The pressure coefficient distribution on the body for a transonic freestream Mach number $M_\infty = 0.9$, and $Re = 25 \times 10^6$ based on the afterbody diameter, is shown in Fig. 4. Only Euler results are presented in this case. Although agreement between experimental and computed data is not as good as for the subsonic case, results are still satisfactory. At transonic speeds the shock wave interacting with the body wall would require a localized mesh refinement, which is not achieved with the present grid.

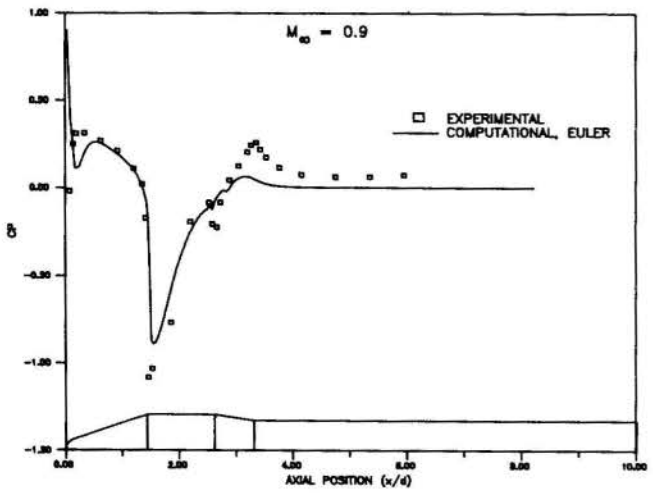

Figure 4: Transonic inviscid solution ($M_\infty = 0.9$).

The results for a freestream Mach number $M_\infty = 3.0$, and $Re = 28.7 \times 10^6$ based on the afterbody diameter, are shown in Fig. 5. The agreement between computation and experiment is quite good. The pressure distribution along the upstream centerline is shown in Fig. 6. The pressure rise across the detached bow shock has the correct magnitude, but the shock is a little smeared over a few grid points. This is to be expected with the Beam and Warming algorithm using a 4th-order constant coefficient artificial dissipation model. Velocity vector plots are also shown in Figs. 7 for this supersonic flow case at the forebody cone-cylinder intersection and at the boattail region. These viscous computational results reproduce the physical behavior that should be expected in this case.

We also found out in the course of the present investigation an interesting inexpensive way of achieving good spatial gradient resolution at the same time that maintaining a robust time march process. We observed that the amount of artificial dissipation required to stabilize the numerical computations was causing some small deterioration in the quality of the solutions. The procedure adopted to overcome the problem consisted in using the standard constant coefficient artificial dissipation model previously described with ε_E chosen to be of order one, as typically recommended in the literature. On the other hand, ε_I is

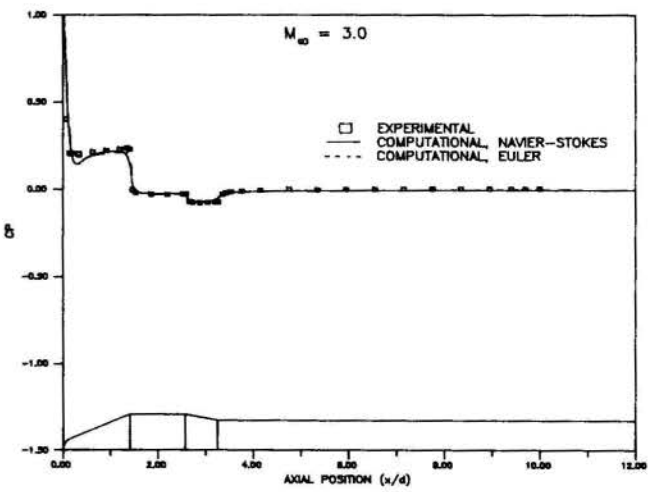

Figure 5: Supersonic case ($M_\infty = 3.0$).

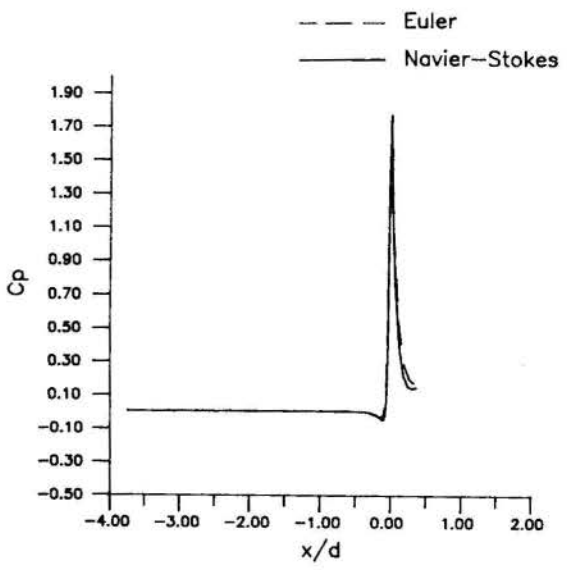

Figure 6: Pressure distribution along upstream centerline for the supersonic case.

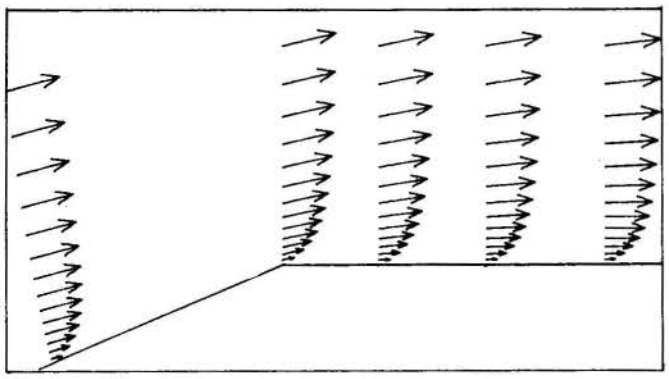

(*a*) Forebody cone-cylinder intersection.

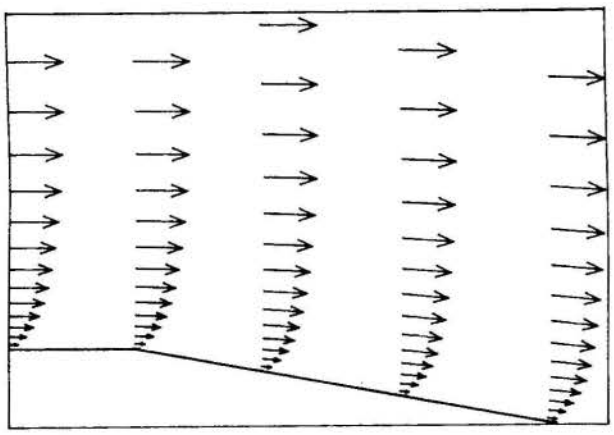

(*b*) Boattail region.

Figure 7: Velocity vectors for the viscous supersonic case.

chosen to be much greater than the usual relation $\varepsilon_I = 2\varepsilon_E$, also typically found in the literature. Hence, by keeping low levels of numerical dissipation in the right-hand side, better spatial resolution is achieved without compromising the numerical stability of the scheme. A comparison between the results obtained with this new way of setting ε_I and the standard one is shown in Fig. 8 for the subsonic computations previously reported. The improvement in spatial resolution is quite evident from this figure. Of course, this is good only for steady state computations, and we also observed that it has a somewhat detrimental effect on the convergence rate.

CONCLUDING REMARKS

Euler and thin layer Navier-Stokes computations for axisymmetric launch vehicle flows were presented. The results show good agreement with the available experimental data, and the discrepancies observed have been discussed. It is clear that some work is still needed in order to improve the quality of the computations. Adaptive meshing would certainly improve the results obtained for the transonic case.

In the longer run, we would be very much interested in extending the current capability in order to be able to treat three dimensional problems. At the moment, however, the computational hardware available to us does not allow the consideration of any practical 3-D configuration. The computational time for the axisymmetric vehicle cases presented here is of the order of 3.5 minutes in the DSI-020 board per iteration. Considering that it typically takes of the order of some 3500 iterations to obtain convergence, one can easily realize that we are dealing with a problem as complex as we probably will be able to handle

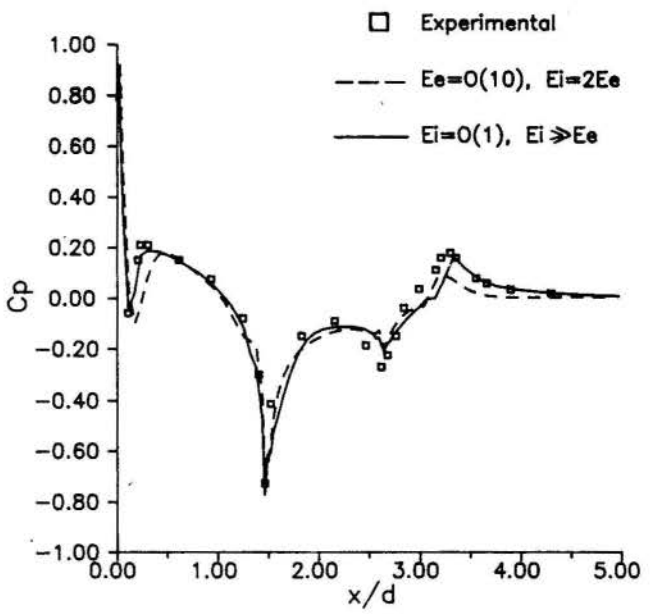

Figure 8: Effect of modified artificial dissipation implementation on the pressure distribution for subsonic case.

with the present hardware.

Furthermore, as the complexity of the flowfields increase, there is more need for easy-to-use graphics post-processing software. These tools are presently being developed by the group at IAE and associated co-workers. They will be required in order to accomplish a more thorough understanding of the details of the various flowfields being computed.

ACKNOWLEDGEMENTS

The authors wish to express their gratitude to CAPES which is providing support for the first author's graduate work at Instituto Tecnológico de Aeronáutica.

REFERENCES

[1] Beam, R.M., and Warming, R.F., "An Implicit Finite-Difference Algorithm for Hyperbolic Systems in Conservation-Law Form," *Journal of Computational Physics*, Vol. 22, Sept. 1976, pp. 87-110.

[2] Beam, R.M., and Warming, R.F., "An Implicit Factored Scheme for the Compressible Navier-Stokes Equations," *AIAA Journal*, Vol. 16, No. 4, April 1978, pp. 393-402.

[3] Pulliam, T.H., and Steger, J.L., "Implicit Finite-Difference Simulations of Three-Dimensional Compressible Flow," *AIAA Journal*, Vol. 18, No. 2, Feb. 1980, pp. 159-167.

[4] Pulliam, T.H., and Steger, J.L., "Recent Improvements in Efficiency, Accuracy and Convergence for Implicit Approximate Factorization Algorithms," AIAA Paper 85-0360, AIAA 23rd Aerospace Sciences Meeting, Reno, Nevada, Jan. 1985.

[5] Deiwert, G.S., "Supersonic Axisymmetric Flow over Boattails Containing a Centered Propulsive Jet," *AIAA Journal*, Vol. 22, No. 10, Oct. 1984, pp. 1358-1365.

[6] Baldwin, B.S., and Lomax, H., "Thin Layer Approximation and Algebraic Model for Separated Turbulent Flows," AIAA Paper No. 78-257, Jan. 1978.

[7] Nietubicz, C.J., Pulliam, T.H., and Steger, J.L., "Numerical Solution of the Azimuthal-Invariant Thin-Layer Navier-Stokes Equations," AIAA Paper 79-0010, 17th Aerospace Sciences Meeting, New Orleans, LA, Jan. 1979.

[8] Sahu, J., "Computations of Supersonic Flow over a Missile Afterbody Containing an Exhaust Jet," *Journal of Spacecraft and Rockets*, Vol. 24, No. 5, Sept.-Oct. 1987, pp. 403-410.

[9] Pulliam, T.H., "Euler and Thin Layer Navier-Stokes Codes: ARC2D, ARC3D," Notes for *Computational Fluid Dynamics User's Workshop*, The University of Tennessee Space Institute, Tullahoma, Tenn. , March 12-16, 1984.

[10] Azevedo, J.L.F., "Euler Solutions of Transonic Nozzle Flows," Paper submitted to the 3rd Brazilian Thermal Sciences Meeting, Itapema, SC, Dec. 1990.

[11] Pulliam, T.H., "Artificial Dissipation Models for the Euler Equations," *AIAA Journal*, Vol. 24, No. 12, Dec. 1986, pp. 1931-1940.

[12] Chaussee, D.S. and Pulliam, T.H., "Two-Dimensional Inlet Simulation Using a Diagonal Implicit Algorithm," *AIAA Journal*, Vol. 19, No. 2, Feb. 1981, pp. 153-159.

[13] Moraes, P., Jr. , and Neto, A.A., "Aerodynamic Experimental Investigation of the Brazilian Satellite Launch Vehicle (VLS)," Paper submitted to the 3rd Brazilian Thermal Science Meeting, Itapema, SC, Dec. 1990.

III ENCIT – Itapema, SC (Dezembro 1990)

INVISCID FLOWS THROUGH NORMAL AND OBLIQUE SHOCK WAVES IN EQUILIBRIUM AIR CONSIDERING HIGH TEMPERATURE EFFECTS

JORGE KOREEDA
IEA - ITA - CTA
12225 - S. J. Campos - SP, Brazil

JOSÉ NIVALDO HINCKEL
DEM/VET - INPE
12201 - S. J. Campos - SP, Brazil

SUMMARY

This article analyses high temperature effects in inviscid flows through normal and oblique shock waves in equilibrium air. The thermodynamic properties are calculated from scratch using TERMO, a computational code developed by the authors, which is based on statistical mechanics methods. Results from 1 up to 10 km/s freestream velocities are presented and discussed from a molecular point of view, and comparisons are made with the thermally and calorically perfect gas model.

INTRODUCTION

In hypersonic flows, we have to deal with high temperatures and enthalpies. These are favorable conditions for the appearance of the so-called high temperature effects. They are the dissociation and the ionization phenomena, vibrational and electronic excitation of the molecules of the gas etc. (See *Anderson*, 1989, Ref. [1].)

The high temperature effects are very important in the reentry, and currently a new application has entered in the scene: the design of hypersonic transportation vehicles.

Many works were developed in the 50's and 60's, modeling these effects in equilibrium air. These results have then been used in the analysis of high energetic flows through shock waves and nozzles. Nevertheless, none of them determines the flow parameters using the thermodynamic properties calculated from scratch (using the concepts of statistical mechanics – see *Koreeda*, 1990, Ref. [2]). In fact, tables and interpolated functions are used instead.

In the following we will see results and discussions for inviscid flows through normal and oblique shock waves, where the high temperature effects in equilibrium air are calculated from scratch by the use of the computational code presented in Ref. [2]. This code calculates the equilibrium air properties through statistical mechanics and uses recent spectroscopic data of the atoms and molecules (see *Koreeda & Hinckel*, 1989, Ref. [3] and Ref. [2]).

SHOCK EQUATIONS

Fundamental equations. The equations for mass, momentum, energy, the equation of state and the shock inclination angle are:

$$\Delta\overline{u} = 1 - \frac{\rho_1}{\rho_2} \tag{1}$$

$$\frac{p_2}{p_1} = 1 + \frac{\rho_1 u_1^2}{p_1}\Delta\overline{u} \tag{2}$$

$$\frac{h_2}{h_1} = 1 + \frac{u_1^2\Delta\overline{u}}{2h_1}(2 - \Delta\overline{u}) \tag{3}$$

$$\rho_2 \longleftarrow \text{TERMO}\,(p_2, T_2) \tag{4}$$

$$\beta = \arctan\left[\frac{1}{\tan\theta}\left(\frac{1}{2}\left(\frac{\rho_2}{\rho_1} - 1\right) \pm \sqrt{\frac{1}{4}\left(\frac{\rho_2}{\rho_1} - 1\right)^2 - \tan\theta\frac{\rho_2}{\rho_1}}\right)\right] \tag{5}$$

The subscripts "1" and "2" are assigned respectively to the conditions ahead and behind the shock. The velocity normal to the shock is represented by u. The relative variation of the normal velocities $\Delta\overline{u}$ is defined as $(u_1 - u_2)/u_1$. β is the acute angle between the shock and the original direction of the flow before it, and θ is the flow deflection angle also relative to its original direction.

The Eqs. (1) to (5) are general and can be applied to a mixture of chemically reacting gases in equilibrium [1]. The high temperature effects in air are included by the use of the procedure TERMO, presented in Ref. [2]. It is important to note that the properties are not those of a thermally and calorically perfect gas (TCPG) but they are calculated as function of the (pressure, temperature) pair.

Computational algorithm. The equations for mass, momentum and energy can be reduced by using the equation of state to a system of two nonlinear algebraic equations to determine the (p, T) pair downstream the shock, given the upstream conditions and the geometry of the problem (the flow deflection angle θ is assumed known):

[1] In the presence of strong external electromagnetic fields or when the Debye length (page 342, Ref. [4]) has the same magnitude of the mean free path of the particles, these equations no longer hold.

$$f_1(X_1, X_2) = 1 + \frac{\rho_1 u_1^2}{p_1}\Delta\overline{u}(X_1, X_2) - \exp(X_1) = 0 \quad (6)$$

$$f_2(X_1, X_2) = 1 + \frac{u_1^2}{2h_1}\Delta\overline{u}(X_1, X_2)\,[2 - \Delta\overline{u}(X_1, X_2)] - \frac{h_2(X_1, X_2)}{h_1} = 0 \quad (7)$$

where $X_1 = \ln(p_2/p_1)$ and $X_2 = \ln(T_2/T_1)$.

In the case of the oblique shock, Eq. (5) must be used as an auxiliary equation to Eqs. (6) and (7), since u_1 and u_2 depend on the inclination angle β.

The system composed by Eqs. (6) and (7) was solved using the Newton–Raphson's method. The computational code was written and compiled in Borland's Turbo Pascal 5.0 and implemented in an 10 Mhz PC-XT clone with math-coprocessor. The calculation of each (p_2, T_2) pair took from 30 to 90 seconds. (The procedure TERMO takes approximately 2 seconds to calculate the thermodynamic properties for a given (p, T) pair).

In the case of the normal shock, the flow parameters were calculated for freestream velocities from 1 to 10 km/s with an interval of 0.2 km/s. In the case of the oblique shock, after the determination of the maximum flow deflection angle θ_{max} the post-shock conditions were calculated for $\theta = 0$ to $\theta = \theta_{max}$ with intervals of 2 degrees.

AIR COMPOSITION

At room temperature, it is assumed the air composition of the standard atmosphere up to 86 km of altitude: 78.084% of nitrogen, 20.948% of oxygen and 0.968% of argon (see Ref. [2]). This region is specially important because it is there that occurs most of the reentry deceleration, and also includes the shuttle and rocket ascent paths and the flight corridors of the air-breathing hypersonic vehicles.

At high temperatures, the code TERMO considers the following species: N_2, O_2, NO, N, O, Ar, N_2^+, O_2^+, NO^+, N^+, O^+, Ar^+ and free electrons.

NORMAL SHOCK

The flow temperature variation across the normal shock is shown in Fig. 1. As a consequence of a higher velocity there is an increase in the temperature after the shock. This makes possible the processes of dissociation and ionization. The behavior of the molar mass, which depends directly on the chemical composition, is shown in Fig. 2.

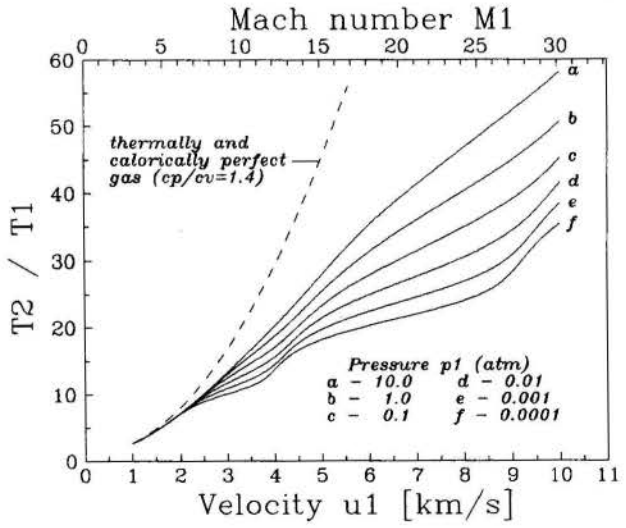

Figure 1: Temperature across the normal shock. ($T_1 = 273$ K)

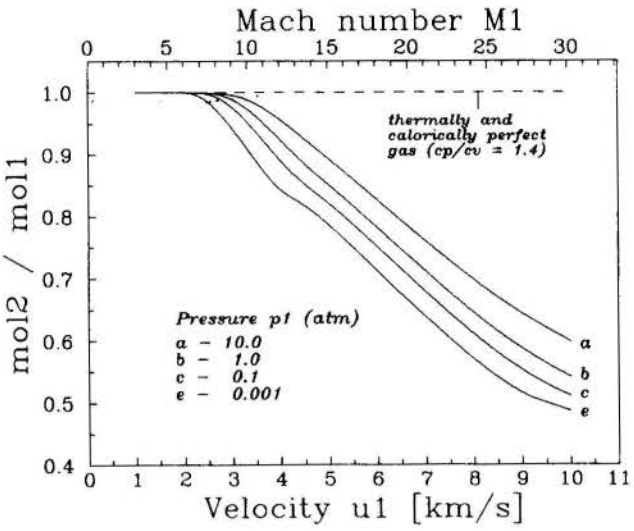

Figure 2: Molar mass across the normal shock. ($T_1 = 273$ K)

The kinetic energy of the incoming flow is first converted into thermal translational energy behind the shock. However a considerable amount is absorbed by the chemical reactions and the internal modes of energy of the atoms and molecules, therefore making the temperature lower than the case of a mixture of chemically inert gases.

The variations in the slopes of the curves in Figs. 1 and 2, notably at lower pressures before the shock, are related with the dissociation of oxygen, the dissociation of nitrogen and the ionizations (mainly of atomic nitrogen), respectively with increasing velocity.

Low values of pressure favor the processes of dissociation and ionization (see Ref. [2] or [3]). Hence at lower pressures, before and after the shock, the reactions are more active resulting in lower values of T_2/T_1 and mol_2/mol_1.

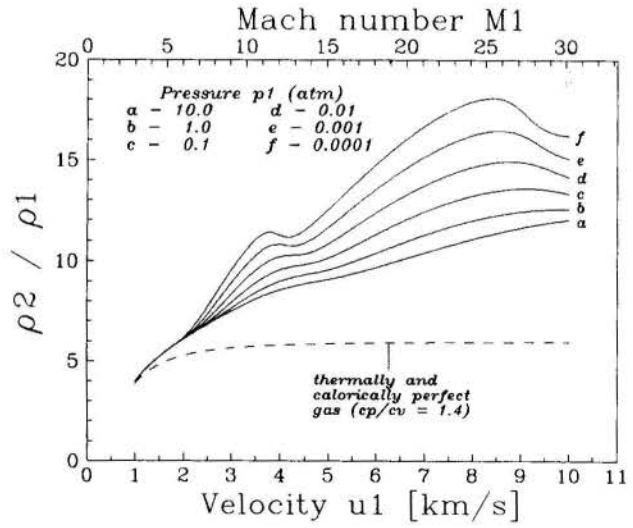

Figure 3: Density across the normal shock. ($T_1 = 273$ K)

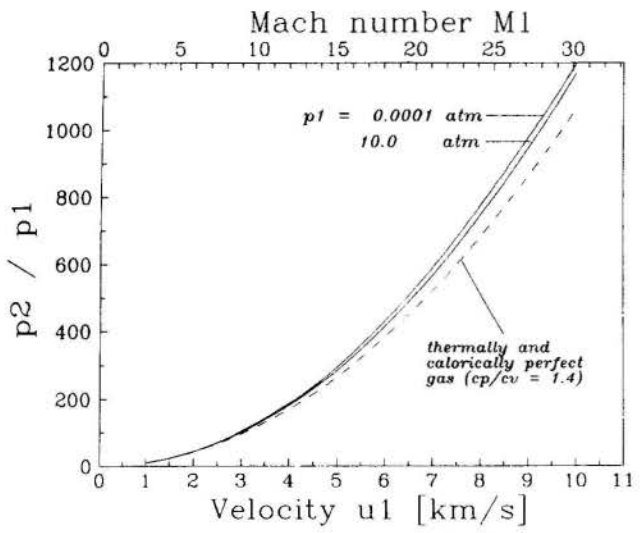

Figure 4: Pressure across the normal shock. ($T_1 = 273$ K)

With the increasing number of species due to the dissociation and ionization processes, the ratio of densities after and before the shock (Fig. 3) is higher than the value predicted by the TCPG model. Among the curves shown in Fig. 3, the one associated with $p_1 = 0.0001$ atm is the most affected by the high temperature effects. Let us examine this curve closely.

At $M_1 = 6$, dissociation rates of oxygen becomes important, causing a greater slope of the ρ_2/ρ_1's curve. However, competing with the growing temperature after the shock, there is also a growing pressure. The pressure ratio after and before the shock is not very much different from that predicted by the TCPG model (see Fig. 4), but the growing pressure has the effect of making difficult the dissociation (and ionization) processes. Then, the oxygen dissociation continues, but not as fast as if the pressure was constant. In particular, at M_1 between 11 and 13, the growing pressure is effectively more important than the growing temperature on the oxygen dissociation. As a consequence, there is a "hump" in the ρ_2/ρ_1's curve. At higher Mach numbers, the temperature becomes again more important than the pressure and ρ_2/ρ_1 grows. At $M_1 = 25$ the pressure starts again to be more important than the temperature, but now the nitrogen dissociation is affected.

If we consider a sphere of radius r in an hypersonic flow, the distance δ of the detached shock to the sphere is proportional to the inverse of the densities ratio ρ_2/ρ_1. Therefore, accordingly to the results shown in Fig. 3, the shock is closer to the sphere, or in general to a blunt-body, when high temperature effects are taken into account. For example, for the upstream conditions $T_1 = 273$ K, $p_1 = 0.001$ atm and $M_1 = 26$ ($u_1 = 8.7$ km/s), we have $\rho_2/\rho_1 = 16.3$ and then $\delta/r = 0.0613$. On the other hand the TCPG model predicts $\rho_2/\rho_1 = 6$, in the limit of high velocities for $\gamma = 1.4$, and we have $\delta/r = 0.167$, which is equal to 2.7 times the value calculated for high temperature effects.

The entropy behavior is shown in Fig. 5. As we have seen, low pressures favor chemical reactions, so the curve associated with $p_1 = 0.0001$ atm departs more from the TCPG curve than the one associated with $p_1 = 10$ atm departs from its respective TCPG curve.

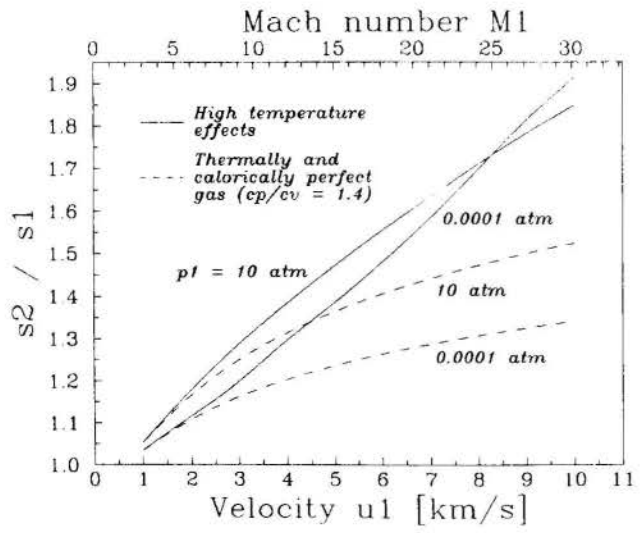

Figure 5: Entropy across the normal shock. ($T_1 = 273$ K)

OBLIQUE SHOCK

In the TCPG model there is a well-known relation among the Mach number before the shock, the shock angle β and the deflection angle θ, generating an unique M–β–θ diagram for a given gas. But at high velocities, as a consequence of the high temperature effects, we no longer have a unique diagram. Instead, we have a U–β–θ diagram (U stands for the velocity before the shock) for each (p_1, T_1) pair, or alternatively, for a given altitude in the atmosphere. An U–β–θ diagram is shown in Fig. 6.

Some important characteristics of an hypersonic flow can be seen in the U–β–θ diagrams. The limit for the maximum deflection angle is much higher when we consider high temperature effects. And for the same deflection angle the associated week shock has a smaller shock angle in comparison with the TCPG model. Hence, if we consider an attached week shock in a wedge, then the shock is closer to the body than we would expect using a TCPG model.

The flow temperature variation across an oblique shock is shown in Fig. 7. It is also shown a comparison with a simulation presented in Ref. [5].

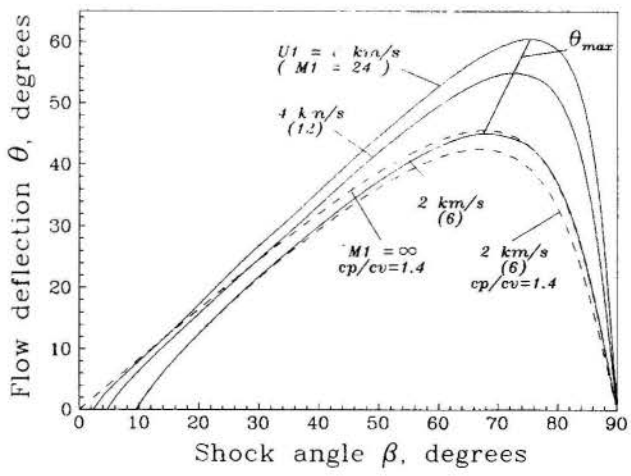

Figure 6: U–β–θ diagram for equilibrium air. The dashed lines represents a thermally and calorically perfect gas ($\gamma = 1.4$). ($p_1 = 0.01$ atm and $T_1 = 273$ K)

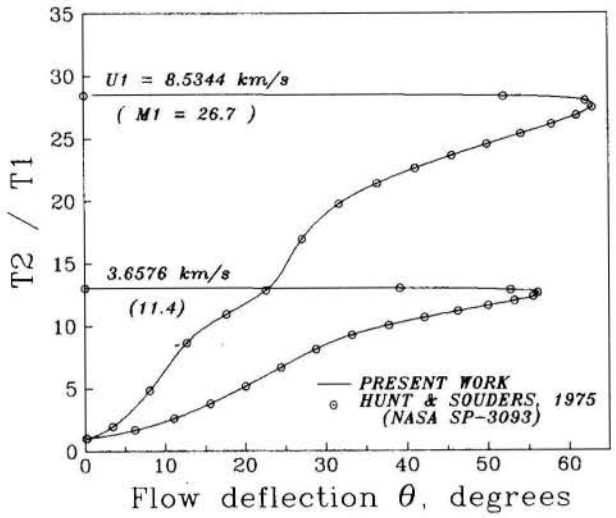

Figure 7: Temperature across an oblique shock. Conditions upstream the shock, at 60.96 km of altitude: $p_1 = 9.796\ N/m^2$, $T_1 = 253.888\ K$, $\rho_1 = 2.716 \times 10^{-4}\ kg/m^3$.

FINAL REMARKS

For a better understanding of the results presented in this article, it is important to know the physical phenomena that occur at high velocities. Many important characteristics for equilibrium air are presented in Ref. [2] and [3].

One of these phenomena is that, due to the high temperature effects, the specific heats are much higher than the prediction of a TCPG model. So, in the reentry, the temperature is in fact much lower than we would expect using a TCPG model. The energy that in a TCPG is due to the thermal translational energy only, in a mixture of chemically reacting gases it is distributed among the contribution of the chemical reactions and the excitation of the internal modes of energy of the molecules (rotation, vibration, electronic) and consequently the thermal translational energy, and therefore the temperature, is lower. If this was not true, tremendously high temperatures could occur.

A possible application of the results presented here is the analysis of flows in shock tubes operating on hypersonic velocities, which are the most powerful apparatus for studying high temperature effects. With the growing interest in hypersonic applications, such as the reentry and the design of hypersonic transportation vehicles, the hypersonic shock tube becomes an indispensable experimental instrument, but a theoretical modeling is also important to understand the phenomena and because of the inherent difficulties in dealing with high temperatures conditions.

REFERENCES

[1] ANDERSON, John D. Jr. *Hypersonic and high temperature gas dynamics.* McGraw-Hill, 1989. 690p.

[2] KOREEDA, Jorge. *Thermodynamic properties of air in equilibrium at high enthalpies and their utilization in flows through normal and oblique shock waves and quasi-one-dimensional nozzles* (in Portuguese). Master's Thesis, Instituto Tecnológico de Aeronáutica, SJ Campos - SP, Brazil, 1990.

[3] KOREEDA, Jorge & HINCKEL, J. N. "Calculation of thermodynamic properties of air at high enthalpies." *Proceedings of the 10th Brazilian Congress of Mechanical Engineering,* Vol. I, pp. 121-124, Rio de Janeiro, RJ, Brazil, 1989.

[4] JACKSON, John D. *Classical Electrodynamics.* New York, John Wiley, 1962. 641p.

[5] HUNT, James L. & SOUDERS, Sue W. "Normal- and oblique-shock flow parameters in equilibrium air including attached-shock solutions for surfaces at angles of attack, sweep, and dihedral." *NASA SP-3093,* 1975.

III ENCIT – Itapema, SC (Dezembro 1990)

EULER SOLUTIONS OF TRANSONIC NOZZLE FLOWS

JOÃO LUIZ F. AZEVEDO
Centro Técnico Aeroespacial
Instituto de Atividades Espaciais
12225 – São José dos Campos – SP

SUMMARY

The flowfield on two dimensional nozzles is simulated using the Euler equations. This set of equations is implemented in a finite difference context using the Beam and Warming implicit approximate factorization scheme. The implicit Euler method is used for the time march, and spatial derivatives are centrally differenced. Special attention is dedicated to the implementation of numerical boundary conditions through the use of one dimensional characteristic relations. Agreement between computational and experimental results is quite good. Existing discrepancies are discussed, and suggestions for continuation of the present work are presented.

INTRODUCTION

Nozzle flows play an important role in many aerospace applications. Of particular interest to us at IAE are rocket engine nozzles. It is clear, however, that before one can venture into solving such flowfields with all their actual complexities, it is necessary to develop the required computational tools. Moreover, for their somewhat simple geometry, nozzles provide a good test case for the development of flow simulation codes. The present work is concerned with investigating the flowfield in a two dimensional, transonic, convergent-divergent nozzle. The emphasis is placed, however, in terms of code development and validation, and proper boundary condition implementation, since the flow itself is quite simple for the case considered here.

The flowfield is simulated using the 2-D Euler equations. It is clear that viscous effects can be important in many nozzle flow applications. Here, however, an inviscid formulation is used as an evolutionary step towards the development of the complete capability of simulating such flowfields. The present work uses the Beam and Warming implicit approximate factorization algorithm[1,2], and it follows much of the implementation presented by Pulliam and Steger[3,4], Pulliam[5,6], and Deiwert[7]. The implicit Euler method is used for the time-march, and standard 2nd-order central differences are used to approximate the spatial derivatives. Standard 4th-order artificial dissipation terms are added to the explicit operators, and 2nd order ones are used in the left-hand side operators. Boundary condition implementation was based on the concept of the one-dimensional characteristic relations of the inviscid gasdynamic equations. The meshes used in the present investigation were generated by algebraic methods, and exponential grid stretching was employed where appropriate.

The study consisted basically in applying the methodology developed to the same nozzle problem using different grids, both in terms of mesh refinement and conditions at the entrance. The objective was to assess the accuracy of the present solutions as compared with other computational results and experimental data. The grid refinement study was also performed aiming at achieving grid independent solutions. The governing equations are presented next, followed by a discussion of the boundary condition implementation using characteristic relations. The numerical implementation is, then, presented and the computational results obtained in this investigation are discussed.

GOVERNING EQUATIONS

The Euler equations can be written in conservation-law form for a body-conforming, 2-D, curvilinear coordinate system as

$$\frac{\partial \bar{Q}}{\partial \tau} + \frac{\partial \bar{E}}{\partial \xi} + \frac{\partial \bar{F}}{\partial \eta} = 0 \tag{1}$$

The vector of conserved quatities is

$$\bar{Q} = J^{-1} \begin{Bmatrix} \rho \\ \rho u \\ \rho v \\ e \end{Bmatrix} \tag{2}$$

The inviscid flux vectors are given by

$$\bar{E} = J^{-1} \begin{Bmatrix} \rho U \\ \rho u U + p\xi_x \\ \rho v U + p\xi_y \\ (e+p)\,U - p\xi_t \end{Bmatrix} \tag{3}$$

$$\bar{F} = J^{-1} \begin{Bmatrix} \rho V \\ \rho u V + p\eta_x \\ \rho v V + p\eta_y \\ (e+p)\,V - p\eta_t \end{Bmatrix} \tag{4}$$

The usual nomenclature is being used here, such that ρ is the density, u and v are cartesian velocity components, and e is the total energy per unit of volume. Moreover, it is assumed in the above that a suitable nondimensionalization of the governing equations was performed. For instance, for the internal flow cases considered here, the density is referred to the reservoir stagnation density (ρ_t), velocity components are normalized by the reservoir critical speed of sound (a_*), and the total energy per unit of volume is referred to $\rho_t a_*^2$.

The pressure, p, is obtained from the equation of state for perfect gases

$$p = (\gamma - 1)\,\rho e_i \tag{5}$$

where e_i is the specific internal energy. The total energy per unit of volume is defined as

$$e = \rho \left[e_i + \frac{1}{2}\left(u^2 + v^2\right) \right] \tag{6}$$

The contravariant velocity components can be written as

$$\begin{aligned} U &= \xi_t + \xi_x u + \xi_y v \\ V &= \eta_t + \eta_x u + \eta_y v \end{aligned} \tag{7}$$

The Jacobian of the transformation is given by

$$J = (x_\xi y_\eta - x_\eta y_\xi)^{-1} \tag{8}$$

and the various metric terms can be expressed as

$$\begin{array}{ll} \xi_x = Jy_\eta & \eta_x = -Jy_\xi \\ \xi_y = -Jx_\eta & \eta_y = Jx_\xi \\ \xi_t = -x_\tau\xi_x - y_\tau\xi_y & \eta_t = -x_\tau\eta_x - y_\tau\eta_y \end{array} \tag{9}$$

BOUNDARY CONDITIONS

The subject of enforcing numerical boundary conditions has received special attention in the present work. It has been shown in the literature [8] that improper "extrapolation rules" can even lead to numerical instability of the overall scheme. Here, the implementation of numerical boundary conditions was based on the one-dimensional characteristic relations of the inviscid gas-dynamic equations. The basic concept is that the Euler equations can be diagonalized by a similarity transformation [9]. With this diagonalization, one-dimensional characteristic relations can be derived which represent the propagation of flow information along the characteristic lines (see, for example, MacCormack[10] and Roe[11]).

From the local slope of the characteristics, it is possible to determine how many conditions should be specified at a given boundary and how many should be extrapolated from interior information. This is important to guarantee the well-posedness of the initial boundary value problem[8]. For those conditions that must be extrapolated, the suggestion[10] is again to use the characteristic relations instead of some arbitrary extrapolation rule. The former carries some physics of the phenomena into the extrapolation process and, therefore, should provide for a more robust way of enforcing the numerical boundary conditions. The particular characteristic relation that should be used in each case is the one associated with the characteristic speed that is carrying information from the interior to the boundary.

The one-dimensional characteristic relations could be derived for a general curvilinear coordinate system. However, they are usually found in the literature for a cartesian system. It must be emphasized that, at the boundaries we might be interest in using these relations, the curvilinear and cartesian coordinates are essentially aligned. Moreover, the use here of the relations in cartesian coordinates has the objective of simplifying their numerical implementation. The formulation used here can be found in MacCormack[10], and the one-dimensional characteristic relations associated with "operation" in the x-direction for a two-dimensional flow can be written as

$$\begin{aligned} \frac{\partial\rho}{\partial t} - \frac{1}{a^2}\frac{\partial p}{\partial t} &= -u\left(\frac{\partial\rho}{\partial x} - \frac{1}{a^2}\frac{\partial p}{\partial x}\right) \\ \frac{\partial v}{\partial t} &= -u\frac{\partial v}{\partial x} \\ \frac{\partial p}{\partial t} + \rho a\frac{\partial u}{\partial t} &= -(u+a)\left(\frac{\partial p}{\partial x} + \rho a\frac{\partial u}{\partial x}\right) \\ \frac{\partial p}{\partial t} - \rho a\frac{\partial u}{\partial t} &= -(u-a)\left(\frac{\partial p}{\partial x} - \rho a\frac{\partial u}{\partial x}\right) \end{aligned} \tag{10}$$

Here, a is the speed of sound, and it is interesting to observe that u, u, $u+a$ and $u-a$ are the eigenvalues of the inviscid flux Jacobian matrix associated with the cartesian flux vector E. Similar expressions could be derived for "operation" in the y-direction, but those will not be necessary in our case.

NUMERICAL IMPLEMENTATION

The governing equations were discretized in a finite difference context according to the Beam and Warming[1,2] implicit approximate factorization scheme. The implicit Euler method is used for the time march, and central differences are used to approximate the spatial derivatives. The resulting scheme is second order accurate in space, but only first order accurate in time. The algorithm can be written in operator form as

$$L_\xi L_\eta \Delta\bar{Q}^n = R_\xi + R_\eta \tag{11}$$

Here,

$$\begin{aligned} L_\xi &= I + \Delta t\,\delta_\xi\hat{A}^n - \varepsilon_I\Delta t\,J^{-1}\nabla_\xi\Delta_\xi J \\ L_\eta &= I + \Delta t\,\delta_\eta\hat{B}^n - \varepsilon_I\Delta t\,J^{-1}\nabla_\eta\Delta_\eta J \\ R_\xi &= -\Delta t\,\delta_\xi\bar{E}^n - \varepsilon_E\Delta t\,J^{-1}\left(\nabla_\xi\Delta_\xi\right)^2 J\bar{Q}^n \\ R_\eta &= -\Delta t\,\delta_\eta\bar{F}^n - \varepsilon_E\Delta t\,J^{-1}\left(\nabla_\eta\Delta_\eta\right)^2 J\bar{Q}^n \end{aligned} \tag{12}$$

In the above formulation, $\hat{A}$ and $\hat{B}$ are the inviscid flux Jacobian matrices. The reader is referred to Pulliam and Steger[4] and Pulliam[5,6] for the form of these matrices in the two dimensional case. The δ_ξ and δ_η are three-point central difference operators. The Δ_ξ, Δ_η and ∇_ξ, ∇_η are standard forward and backward difference operators, respectively. The n-th iteration correction is $\Delta\bar{Q}^n = \bar{Q}^{n+1} - \bar{Q}^n$.

Higher order artificial dissipation terms are also added, as one can see from the expressions above, in order to control nonlinear instabilities. A simple constant coefficient numerical dissipation model was adopted here. Fourth difference operators are used in the right-hand side. Second difference operators are added to the left-hand side. Ideally, one would like to use in the left-hand side the same artificial dissipation operators that are added to the right-hand side of the equations[4]. However, the use of fourth difference operators in the left-hand side would spoil the tridiagonal nature of these operators. It is, therefore, avoided on the grounds of computational efficiency. Moreover, for more complex flowfields such as those with shock waves or other discontinuities, the use of more robust nonlinear artificial dissipation models is strongly recommended (see, for instance, Pulliam and Steger[4] and Pulliam[5,12]).

The code was implemented in standard Fortran, and it is currently running in microcomputer environments. To be more exact, all the results that will be presented here were obtained in IBM PC-like microcomputers with Definicon DSI-020 coprocessor boards. It is clear that the run time for any practical configuration in this type of equipment will be rather large, and this has been a severe limitation on the size of the grids we have been able to use even for a simple geometry as the present one.

RESULTS

The numerical solutions to be presented here consider a two dimensional, transonic convergent-divergent nozzle. The throat is located half way between the entrance of the convergent section and exit planes. The total lenght of the nozzle is 0.38 ft (0.116 m), and the throat half-height is 0.045 ft (0.014 m). The wall dimensionless radius of curvature at the throat is 2, referred to the throat half-height, the convergent angle is 22.33°, and the divergent angle is 1.21°. More details on the nozzle geometric definition can be found in MacCormack[13]. The stagnation conditions at the entrance station are T_t = 531.2 °R (294.8 K) and P_t = 2117.0 lb/ft^2 (1.0136 × 10^5 N/m^2), but since all flow variables are nondimensionalized these particular values do not come into play for an inviscid computation.

An initial grid used in this investigation can be seen in Fig. 1, and this is what we will be referring here as the coarse grid. It has 21 points in the streamwise direction and 12 points in the other direction. Due to the symmetry of the flow, only the

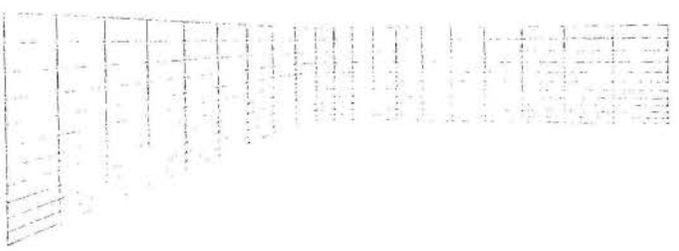

Figure 1: Coarse nozzle grid (21 × 12 points).

lower half of the computation domain was used. Nevertheless, the grid has one point "above" the centerline in order to make it easier to enforce the symmetry boundary condition. The grid was generated with algebraic methods, and exponential stretching was used in order to cluster grid points at the nozzle wall and at the throat. All the computations that will be presented are Euler results, which explains that there was no need for a better clustering of grid points at the wall.

Zero normal pressure gradient is assumed at the wall, and the flow is considered tangent to the wall. Symmetry boundary conditions are used at the nozzle centerline, as discussed above. Total temperature and total pressure, as well as the flow entrance angle, are given and assumed constant at the entrance station. For all simulations performed here, the flow entrance angle was assumed to be zero. The stagnation conditions are used as initial conditions throughout the nozzle. At the exit station, while the flow remains subsonic, the exit pressure is fixed at one-third of the initial total pressure. After the flow becomes supersonic at the exit, all quantities are extrapolated from interior values.

We observe that at any boundary we need to know four flow quantities in a two dimensional case. At the entrance station, since the flow is always subsonic, the characteristics-type analysis previously presented states that three conditions must be specified and one should be extrapolated from interior information. Since the $(u - a)$ characteristic speed is the one that is carrying information from the interior to the boundary in this case, the fourth equation in the set of Eqs. 10 is used to obtain the u velocity component at the entrance. Note that, since total pressure and the flow angle are fixed at the entrance, the static pressure can be written simply as a function of the u velocity component. While the flow remains subsonic at the exit station, static pressure is considered known and the first three equations in set 10 are used to extrapolate the other three quantities. After the exit flow becomes supersonic, the characteristics-based analysis tells that no property can be specified there, since the state at the exit must be completely determined by interior information. Hence, all four relations in Eqs. 10 are used in order to determine the flow properties at the exit station.

The evolution of the pressure distribution along the nozzle wall as the iterations progress can be seen in Fig. 2. A constant dimensionless time step of 0.01 was used in all computations. We observe from Fig. 2 that the solution has converged to plotting accuracy after 5500 iterations. Nevertheless, it took all the 7500 iterations for which the computation has been run to drop the maximum residue in the field about 5 to 6 orders of magnitude, as we can see in Fig. 3. The present computational results are compared with experimental results by Mason et al.[14] in Fig. 2 and are compared with MacCormack's results[13] and the same experimental results in Fig. 4.

A grid refinement study was performed by doubling the grid

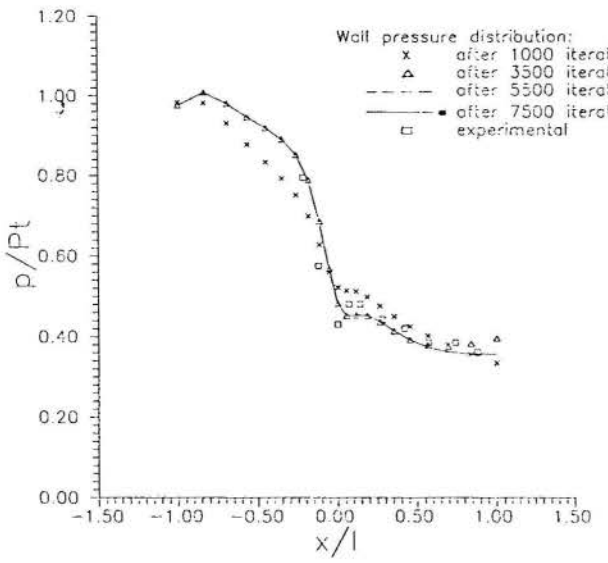

Figure 2: Evolution of the nozzle wall pressure distribution.

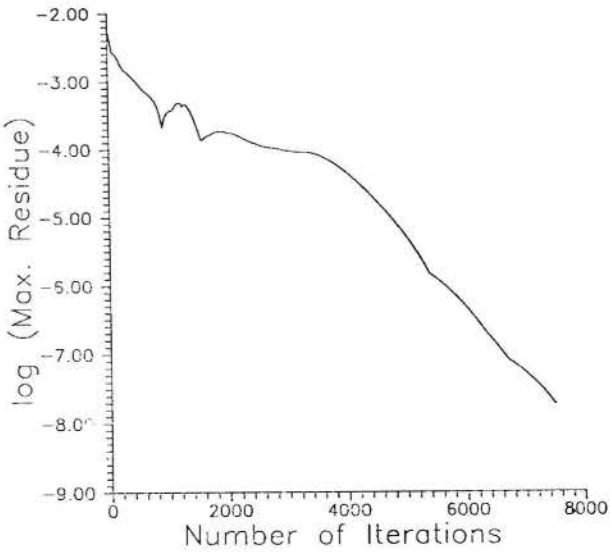

Figure 3: Convergence history for the coarse grid computation.

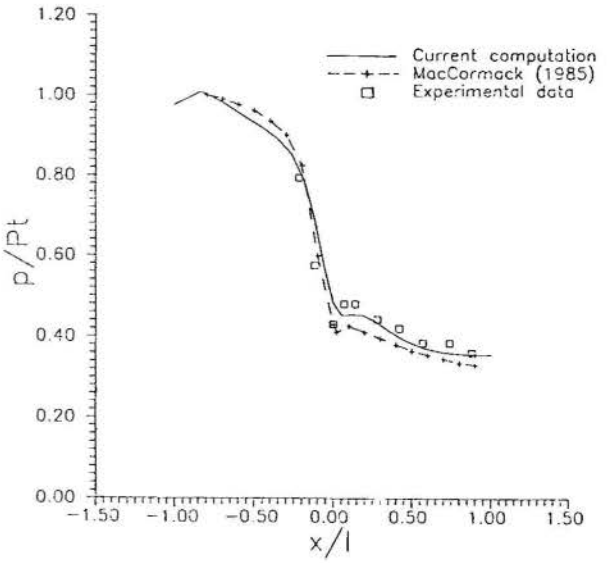

Figure 4: Comparison of coarse grid results with other computational and experimental results.

size in both coordinate directions. This new refined grid is shown in Fig. 5. The wall pressure distributions for both fine (41×22) and coarse (21×12) grids are compared in Fig. 6 with MacCormack's[13] and experimental[14] results. We observe that we do need the finer grid in order to capture the correct slope of pressure distribution in the rapid expansion region right before the throat. Moreover, the wall pressure behavior through the throat is correctly captured by the fine grid computation, but it is missed by both the coarse grid results and MacCormack's. We further observe that the agreement with the experimental data for the region downstream of the throat seems to favor the present computations. A possible explanation for this behavior can be also found in Ref. [13] and it is associated with the order of accuracy of the methods. The present computations, although

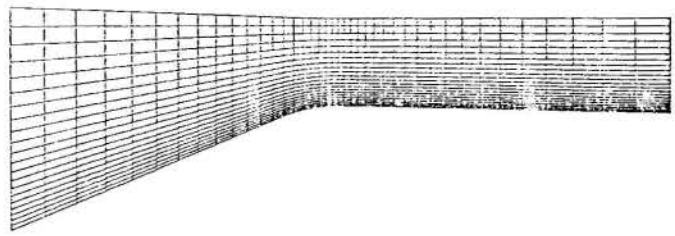

Figure 5: Refined nozzle grid (41×22 points).

using only an Euler formulation, are second order accurate in space. MacCormack's results are based on the Navier-Stokes equations, but are only first order accurate in space. Finally, Fig. 7 shows the wall pressure distribution evolution, as iterations progress, for this refined grid case. We notice that the solution has converged to plotting accuracy at about 5000 iterations.

We observe, however, that the behavior of the wall pressures near the entrance are not very smooth in the present computations. This is associated with the fact that it is rather artificial to start the computation already at the convergent wall while assuming a zero inflow angle, as done here. The correct approach would have been to add a constant area duct upstream of the current entrance station in order to impose the correct entrance boundary conditions. This observation is corroborated by noticing that the centerline pressure distribution is much smoother, as we can see from Fig 8, and by recent nozzle flow computations by Silva[15].

In order to prove our point, and to make sure that these wall pressure oscillations near the entrance were not due to our proposed numerical boundary condition scheme, one more test case was considered. Here, as mentioned above, a constant area duct was added upstream of the previous entrance station. The refined grid was used and 8 more equally spaced grid points were added upstream of the convergent section. The x-grid spacing was chosen equal to the x-spacing of the next two grid

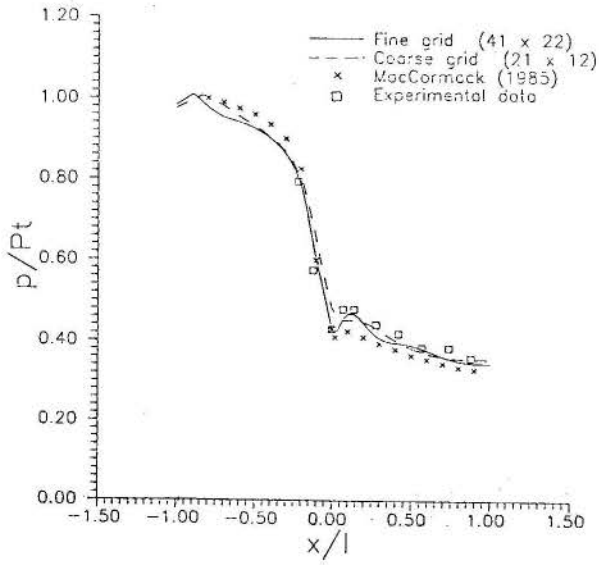

Figure 6: Grid refinement effect on the wall pressure distribution.

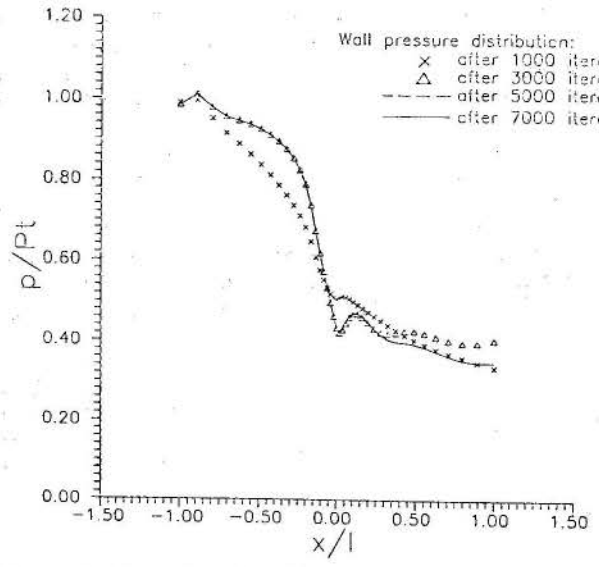

Figure 7: Evolution of wall pressure distribution for fine grid case.

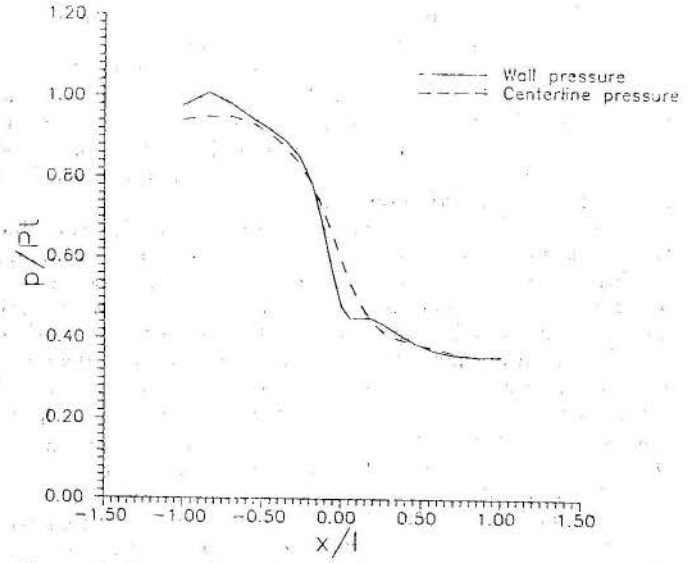

Figure 8: Comparison of centerline and wall pressure distributions for the coarse grid computation.

points in the previous grid. This new grid is shown in Fig. 9, and the present computational results are compared with the experiment[14] in Fig. 10. This figure also shows the pressure distribution at different levels along the iteration process. It was observed that the addition of the straight entrance section seemed to slow down the convergence process, at least in terms of the drop in the original residue. This is shown in Fig. 11, in which the convergence history for the refined grid without the straight entrance is compared with that for the current case. One can observe that, for the same level of residue drop, more than twice as many iterations were required for the case with the straight entrance.

The behavior of the pressure distribution at the centerline is presented in Fig. 12, and a summary of all wall pressure results obtained in the present investigation, with comparison with other data, is shown in Fig. 13. Finally, Fig. 14 presents pressure and Mach number contours in the nozzle for the refined grid

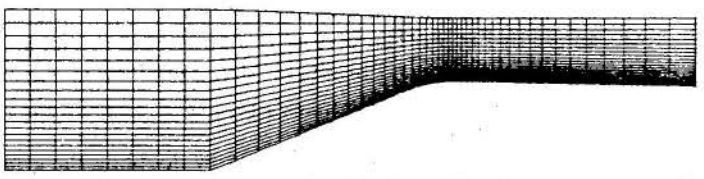

Figure 9: Refined grid with added straight duct upstream of convergent section (49 × 22 grid points).

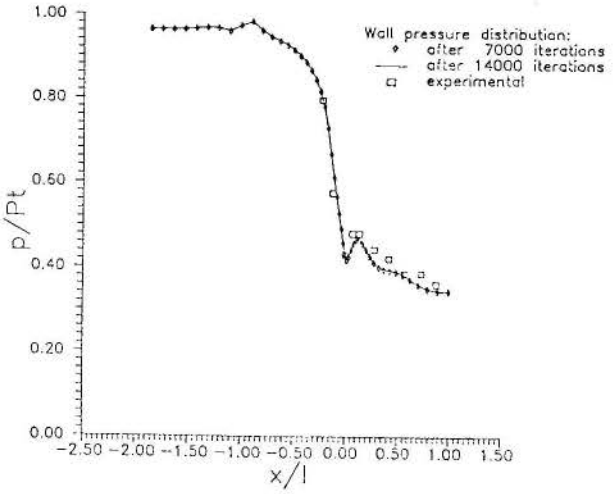

Figure 10: Comparison of wall pressure distribution for refined grid with straight entrance section.

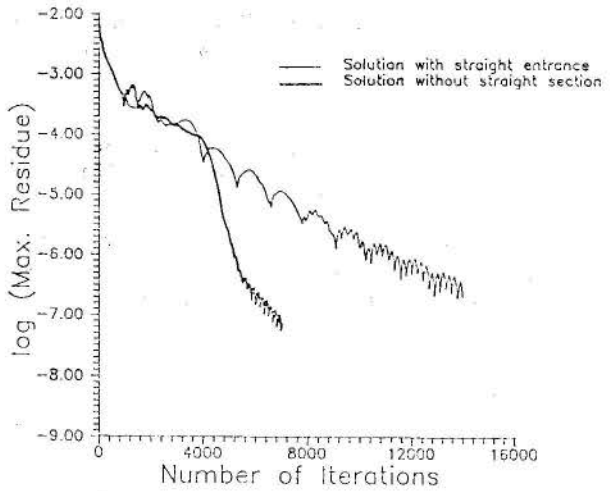

Figure 11: Comparison of convergence history for fine grid with and without straight entrance section.

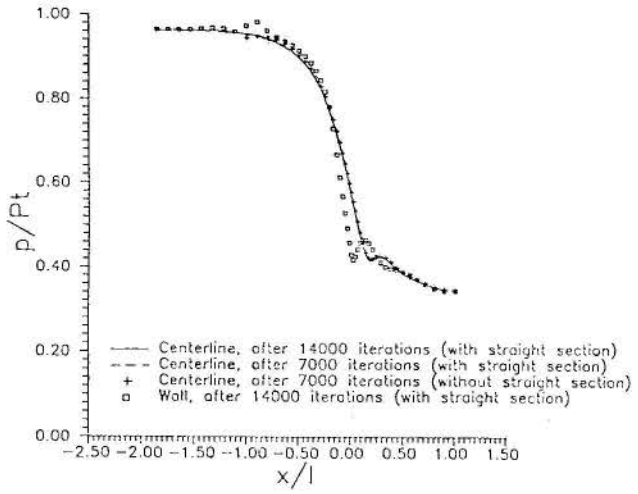

Figure 12: Comparison of the pressure distribution at the nozzle centerline.

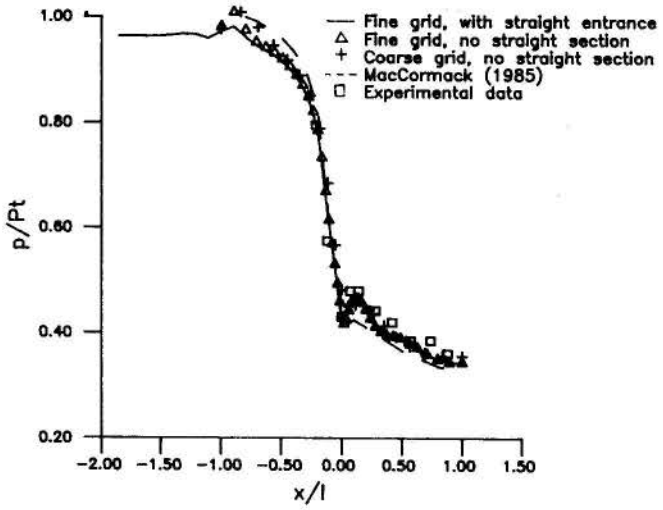

Figure 13: Summary of results obtobtained for the wall pressure distribution.

with added straight entrance section. These results show that the use of characteristic relations is a very robust way of enforcing entrance and exit numerical boundary conditions. The pressure distributions at the entrance, for the case with the added straight section, do not present any oscillations, as one can see from Figs. 10, 12 and 13. Moreover, it is quite clear from these figures that the pressure oscillation at the wall at the beginning

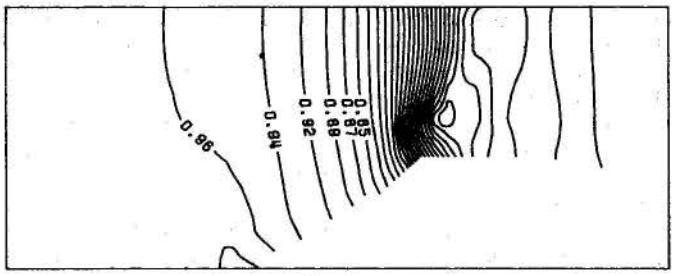

(*a*) Pressure contours.

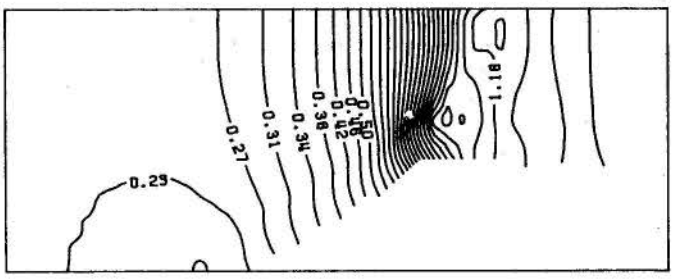

(*b*) Mach number contours.

Figure 14: Flowfield visualization for transonic convergent-divergent nozzle.

of the convergent section, which is still present in these latter results, is a local effect. In other words, the sudden curvature in the wall causes a local pressure rise which is what the present results are capturing. As one moves away from the wall, this effect obviously fades away and this is, again, being correctly represented in the present computations.

We would like to close this discussion of the present results by emphasizing that, so far, no attempt was made to improve the computational efficiency of the method. All cases were run using the same constant dimensionless time step of 0.01, and the same level of artificial dissipation was added for all computations. This allows for a more uniform comparison of results presented here. Moreover, another reason for requiring so many iterations before we accepted convergence in these computations is because we insisted in at least 5 to 6 orders of magnitude drop in the residue. It is clear from the figures shown that convergence to plotting accuracy was achieved much before that. For the sake of computational cost statistics, it may be interesting to observe that the coarse grid computations use approximately 2.1 CPU seconds per iteration in the Definicon DSI-020 board. The fine grid calculations, without straight entrance section, use about 9.0 CPU seconds per iteration in the same equipment, and the computations with the fine grid and straight entrance section take about 10.3 CPU seconds per iteration. For the 14000 iterations ran in this last case, this means a total cost of about 40 CPU hours.

CONCLUDING REMARKS

Numerical flow simulations on a two-dimensional convergent-divergent transonic nozzle were presented using an Euler formulation. The emphasis of the present work has been in terms of code development and validation, and no attempt was made to achieve faster convergence rates. Of special interest was the development of a robust way of implementing numerical boundary conditions through the use of the one dimensional characteristic relations for the inviscid gasdynamic equations.

The results obtained do provide a validation of the code developed, as well as of the procedure for entrance and exit boundary condition implementation. They also suggest many interesting areas for the continuation of the current effort. For instance, the discrepancies observed between the present results and MacCormack's in the initial portion of the convergent section may be

due to a poor treatment of the pressure boundary condition at the wall in the present case. This difference could be worsened if more realistic rocket engine nozzles were considered, and it should be investigated. More realistic rocket engine nozzle flows themselves are an interesting extension of the present work. By "more realistic" we mean nozzles with steeper convergent and divergent sections, with smaller throat radius of curvature, and with higher stagnation temperatures and pressures. It is still an open question whether the present implementation of the method would behave as well under such more stringent conditions. Moreover, the convergence history results indicate some oscillation of the residue as we approach convergence on both fine grid studies. This should also be further investigated.

Finally, as a conclusion, it is interesting to observe that the Beam and Warming algorithm is extremely simple to implement since it is based on central differences and, obviously, structured grids. Hence, it may never achieve the computational efficiency of other more complex, usually upwind, schemes. However, on the point of view of the user, this loss in terms of efficiency must always be weighted against the easiness of programming and the overall time it takes, starting from scratch, to come up with a working code that can provide the answers the project needs.

REFERENCES

[1] Beam, R.M., and Warming, R.F., "An Implicit Finite-Difference Algorithm for Hyperbolic Systems in Conservation-Law Form," *Journal of Computational Physics*, Vol. 22, Sept. 1976, pp. 87-110.

[2] Beam, R.M., and Warming, R.F., "An Implicit Factored Scheme for the Compressible Navier-Stokes Equations," *AIAA Journal*, Vol. 16, No. 4, April 1978, pp. 393-402.

[3] Pulliam, T.H., and Steger, J.L., "Implicit Finite-Difference Simulations of Three-Dimensional Compressible Flow," *AIAA Journal*, Vol. 18, No. 2, Feb. 1980, pp. 159-167.

[4] Pulliam, T.H., and Steger, J.L., "Recent Improvements in Efficiency, Accuracy and Convergence for Implicit Approximate Factorization Algorithms," AIAA Paper 85-0360, AIAA 23rd Aerospace Sciences Meeting, Reno, Nevada, Jan. 1985.

[5] Pulliam, T.H., "Euler and Thin Layer Navier-Stokes Codes: ARC2D, ARC3D," Notes for *Computational Fluid Dynamics User's Workshop*, The University of Tennessee Space Institute, Tullahoma, Tenn. , March 12-16, 1984.

[6] Pulliam, T.H., "Implicit Finite-Difference Methods for the Euler Equations," in *Advances in Computational Transonics*, W.G. Habashi, editor, Pineridge Press, Swansea, U.K., 1985, pp. 503-542.

[7] Deiwert, G.S., "Supersonic Axisymmetric Flow over Boattails Containing a Centered Propulsive Jet," *AIAA Journal*, Vol. 22, No. 10, Oct. 1984, pp. 1358-1365.

[8] Warming, R.F., "Topics in Computational Fluid Dynamics," Notes for course AA215A, Dept. of Aeronautics and Astronautics, Stanford University, Stanford, CA, Jan.-Mar. 1984.

[9] Warming, R.F., Beam, R.M., and Hyett, B.J., "Diagonalization and Simultaneous Symmetrization of the Gas-Dynamic Matrices," *Math Comp.* , Vol. 29, No. 132, Oct. 1975, pp. 1037-1045.

[10] MacCormack, R.W., "An Introduction and Review of the Basics of Computational Fluid Dynamics," AIAA Professional Study Series on Computational Fluid Dynamics, Snowmass, Colorado, June 1984.

[11] Roe, P.L., "Characteristic-Based Schemes for the Euler Equations," *Annual Review of Fluid Mechanics*, Vol. 18, 1986, pp. 337-365.

[12] Pulliam, T.H., "Artificial Dissipation Models for the Euler Equations," *AIAA Journal*, Vol. 24, No. 12, Dec. 1986, pp. 1931-1940.

[13] MacCormack, R.W., "Current Status of Numerical Solutions of the Navier-Stokes Equations," AIAA Paper 85-0032, AIAA 23rd Aerospace Sciences Meeting, Reno, Nevada, January 14-17, 1985.

[14] Mason, M.L., Putnam, L.E., and Re, R.J., "The Effect of Throat Contouring on Two-Dimensional Converging-Diverging Nozzles at Sonic Conditions," NASA Technical Paper 1704, 1980.

[15] Silva, L.F.F., "Evaluation of the Transonic Region in Convergent-Divergent Nozzles," Master's Dissertation, Instituto Tecnológico de Aeronáutica, São José dos Campos, Brasil, Oct. 1989 (in Portuguese, original title is "Avaliação da Região Transônica em Bocais Convergente-Divergente").

III ENCIT – Itapema, SC (Dezembro 1990)

AVALIAÇÃO DA REGIÃO TRANSÔNICA EM BOCAIS CONVERGENTE-DIVERGENTE

LUIS FERNANDO FIGUEIRA DA SILVA
GORDIANO DE FARIA ALVIM FILHO
PEDRO PAGLIONE
Instituto Tecnológico de Aeronaútica (CTA ITA IEA)
1225 - São José dos Campos, SP - Brasil

SUMÁRIO

Este trabalho avalia a extensão da região transônica que ocorre no escoamento adiabático de um fluído não viscoso no interior de bocais convergente-divergente do tipo encontrado em motores a jato e túneis de vento. Utilizou-se um método numérico de diferenças finitas para resolver as equações do escoamento sem viscosidade (equações de Euler). Os resultados obtidos foram comparados com trabalhos experimentais e teoricos. Estes resultados possibilitaram avaliar a extensão da região transônica nos bocais convergente-divergente.

INTRODUÇAO

Este trabalho, extraido de [1], surgiu da necessidade de um melhor conhecimento da região transônica de bocais convergente-divergente, com a finalidade de encontrar uma linha inicial de Mach constante a jusante da garganta geométrica, a qual servirá de partida para o método das caracteristicas. Este método possibilitará a obtenção da geometria ótima da parte divergente do bocal. Compreende-se como condição ótima aquela que fornece o empuxo máximo de um motor a jato.

A alternativa escolhida para a determinação desta linha foi resolver o sistema de equações que descreve o escoamento através do bocal pelo método de MacCormack [2].

FORMULAÇAO DO PROBLEMA

Admitindo-se que as forças de volume podem ser negligenciadas, bem como a influência da viscosidade, para um escoamento com simetria axial, sem turbulência e adiabático, as equações de Euler são escritas em coordenads generalizadas [3] sob a forma da lei de conservação como :

$$\frac{\partial \vec{Q}}{\partial \tau} + \frac{\partial \vec{E}}{\partial \xi} + \frac{\partial \vec{F}}{\partial \eta} + \vec{H} = 0 \qquad (1)$$

onde :

$$\tau = t \quad \xi = \xi(x,y) \quad \eta = \eta(x,y)$$

$$\vec{Q}=J^{-1}\begin{bmatrix}\rho\\ \rho u\\ \rho v\\ e\end{bmatrix},\ \vec{E}=J^{-1}\begin{bmatrix}\rho U\\ \rho uU + \xi_x p\\ \rho vU + \xi_y p\\ (e+p)U\end{bmatrix},\ \vec{F}=J^{-1}\begin{bmatrix}\rho V\\ \rho uV + \eta_x p\\ \rho vV + \eta_y p\\ (e+p)V\end{bmatrix},$$

$$\vec{H}=J^{-1}\begin{bmatrix}0\\ 0\\ p/\eta\\ 0\end{bmatrix}$$

$$U = \xi_x u + \xi_y v \qquad V = \eta_x u + \eta_y v$$

$$\xi_x = J\eta y_\eta \qquad \xi_y = -J\eta x_\eta \qquad \eta_x = -J\eta y_\xi \qquad \eta_y = J\eta x_\xi$$

$$J^{-1} = \eta(x_\xi y_\eta - x_\eta y_\xi)$$

Para transformar o domínio físico (x,y) no domínio computacional (ξ,η), utiliza-se [2] :

$$\xi = B + \frac{1}{\tau}\,\mathrm{senh}^{-1}\left[\left(\frac{x}{x_t} - 1\right)\mathrm{senh}(\sigma B)\right] \qquad (2)$$

$$\eta = y/S(x)$$

onde :

$$B = \frac{1}{2\tau}\ln\left[\frac{1 + (e^{\sigma} - 1)(x_t/x_e)}{1 + (e^{-\sigma} - 1)(x_t/x_e)}\right]$$

S(x) - função que dá forma do contorno do bocal
x_e - comprimento do bocal
x_t - comprimento até a garganta
σ - fator de elongamento da malha ($0<\sigma<\infty$)

Solução do Sistema de Equações

Conforme mencionado acima, o sistema de diferenças finita utilizado foi o proposto por MacCormack (tipo "predictor-corrector"[2])

Aplicando-se este método à equação (1), obtém-se :

Predictor :

$$Q^{n+1}_{i,j_p} = Q^{n}_{i,j} - \frac{\Delta t}{\Delta \xi}(E^{n}_{i+1,j} - E^{n}_{i,j}) - \frac{\Delta t}{\Delta \eta}(F^{n}_{i,j+1} - F^{n}_{i,j}) - \Delta t\, H_{i,j} \qquad (3)$$

Corrector :

$$Q^{n+1}_{i,j_c} = \frac{1}{2}\left[Q^{n+1}_{i,j_p} + Q^{n}_{i,j} - \frac{\Delta t}{\Delta \xi}\left(E^{n+1}_{i,j_p} - E^{n+1}_{i-1,j_p}\right) - \frac{\Delta t}{\Delta \eta}\left(F^{n+1}_{i,j_p} - F^{n+1}_{i,j-1_p}\right) - \Delta t\, H_{i,j}\right] \qquad (4)$$

Parte-se de uma condição inicial, faz-se sucessivas aplicações das equações (2) e (4) para os pontos do domínio computacional e considerando-se as condições de contorno, chega-se à convergência do processo, desde que respeitado o limite de estabilidade abaixo, [2].

$$4\frac{\Delta t^3}{\Delta x^4}(|u| + |v| + 2a)^4 \cong 1 \qquad (5)$$

onde a é a velocidade do som.

Para garantir a estabilidade do método , foi adicionada uma dissipação artificial [5] às equações:

$$D_\xi Q^n_{i,j} = \frac{\Delta t}{\Delta \xi^2}\varepsilon(Q^n_{i+1,j} - 2Q^n_{i,j} + Q^n_{i-1,j}) \qquad (6)$$

$$D_\eta Q^n_{i,j} = \frac{\Delta t}{\Delta \eta^2}\varepsilon(Q^n_{i,j+1} - 2Q^n_{i,j} + Q^n_{i,j-1}) \qquad (7)$$

O parâmetro ε é de ordem 1 para as direções ξ e η, resultado este obtido de cálculos numéricos.

Condições de Contorno

As soluções do sistema acima deverão respeitar as seguintes condições :

a) Eixo de Simetria

$$U_{i,M} = U_{i,M-1} \qquad (8)$$

$$V_{i,M} = - V_{i,M-1} \qquad (9)$$

b) Contorno do Bocal

$$-\frac{\partial p}{\partial \eta} = \begin{cases} 0, \text{ parede plana} \\ \rho_{i,M-1}\dfrac{u^2_{i,M-1} + v^2_{i,M-1}}{R}, \text{ parede curva} \end{cases} \qquad (10)$$

A componente contravariante V é igual a zero (pelo paralelismo do escoamento) e a outra U é igual nos pontos (i,M) e (i,M-1)

c) Entrada e Saida do Bocal

Embora as deduções abaixo sejam apresentadas para um sistema de coordenadas cartesianas, a extensão para coordenadas generalizadas é feita pela substituição das componentes das velocidades cartesianas pelas contravariantes e das coordenadas cartesianas pelas generalizadas. Considera-se conhecidas três grandezas independentes : p_0 e T_0 (pressão e temperatura de estagnação), ϑ (ângulo entre o vetor velocidade e o eixo de simetria). As equações características do escoamento unidimensional na direção x são dados, [6] e [7], por :

$$\frac{\partial \rho}{\partial t} - \frac{1}{a^2}\frac{\partial p}{\partial t} = - u\left(\frac{\partial \rho}{\partial x} - \frac{1}{a^2}\frac{\partial p}{\partial x}\right) \qquad (11)$$

$$\frac{\partial v}{\partial t} = -u\frac{\partial v}{\partial x} \qquad (12)$$

$$\frac{\partial p}{\partial t} - \rho a\frac{\partial u}{\partial t} = - (u - a)\left[\frac{\partial p}{\partial x} - \rho a\frac{\partial u}{\partial x}\right] \qquad (13)$$

$$\frac{\partial p}{\partial t} + \rho a\frac{\partial u}{\partial t} = - (u + a)\left[\frac{\partial p}{\partial x} + \rho a\frac{\partial u}{\partial x}\right] \qquad (14)$$

c1) Entrada do Bocal

Neste caso, a velocidade é obtida através da equação (13) em conjunto com as seguintes equações :

$$v = u \tan \vartheta \qquad (15)$$

$$p = p_0(A)^{\frac{\gamma}{\gamma-1}} \; ; \; T = T_0 A \qquad (16)$$

$$\text{onde : } A = 1 - \frac{\gamma-1}{\gamma+1}(1 + \tan^2\vartheta)\left(\frac{u}{a^*}\right)^2 \qquad (17)$$

$$\frac{\partial p}{\partial t} = \frac{\partial u}{\partial t}\frac{\partial p}{\partial u} = \frac{\partial p}{\partial u}\frac{\delta u^n_{i,j}}{\Delta t} \qquad (18)$$

Transformando a equação (13) em diferenças finitas e utilizando-se as relações acima, encontra-se :

$$\delta u^n_{i,j} = \frac{R_3}{\left(\dfrac{dp}{du}\right)^n_{2,j} - (\rho a)^n_{2,j}} \qquad (19)$$

onde

$$R_3 = - \left(\frac{\lambda_3}{1 - \lambda_3}\right)_{2,j}\left[p^n_{2,j} - p^n_{1,j} - (\rho a)^n_{2,j}(u^n_{2,j} - u^n_{1,j})\right]$$

$$\lambda_3 = -(u - a)\frac{\Delta t}{\Delta x} \; , \qquad \Delta x = x_{i+1,j} - x_{i,j}$$

c2) Saida do Bocal

De maneira análoga ao item anterior, transformando as equações (11) a (14) em diferenças finitas, em conjunto com as equações (15) a (18), obtém-se, para condições de saida supersônicas, as seguintes relações a serem utilizadas (como extrapolações) :

$$\delta p^n_{N,j} = \frac{R_3 + R_4}{2} \qquad (20)$$

$$\delta \rho^n_{N,j} = R_1 + \delta p^n_{N,j} / a^2_{N-1,j} \qquad (21)$$

$$\delta v^n_{N,j} = R_2 \qquad (22)$$

$$\delta u^n_{N,j} = \frac{R_4 - R_3}{2}\frac{1}{(\rho a)^n_{N-1,j}} \qquad (23)$$

onde

$$R_1 = - \left(\frac{\lambda_1}{1 + \lambda_1}\right)_{N-1,j}\left[\rho^n_{N,j} - \rho^n_{N-1,j} - \frac{1}{a^2_{N-1,j}}\Delta p^n_{N,j}\right.$$

$$R_2 = - \left(\frac{\lambda_1}{1 + \lambda_1}\right)_{N-1,j}\left(v^n_{N,j} - v^n_{N-1,j}\right)$$

$$R_3 = - \left(\frac{\lambda_3}{1 - \lambda_3}\right)_{N-1,j}\left[\Delta p^n_{N,j} - (\rho a)^n_{N,j}\,\Delta u^n_{N,j}\right]$$

$$R_4 = - \left(\frac{\lambda_4}{1 - \lambda_4}\right)_{N-1,j}\left[\Delta p^n_{N,j} - (\rho a)^n_{N-1,j}\,\Delta u^n_{N,j}\right]$$

$$\lambda_1 = - u\frac{\Delta t}{\Delta x} \; ; \; \lambda_4 = -(u+a)\frac{\Delta t}{\Delta x} \; ;$$

$$\Delta \alpha^n_{N,j} = \alpha^n_{N,j} - \alpha^n_{N-1,j} \; ; \; \alpha = p, \; u$$

Para a atualização no tempo (instante 'n + 1') dos valores das fronteiras, usa- se :

$$p^{n+1}_{i,j} = p^n_{i,j} + \delta p^n_{i,j} \qquad (24a)$$

$$\rho^{n+1}_{i,j} = \rho^n_{i,j} + \delta \rho^n_{i,j} \qquad (24b)$$

$$v^{n+1}_{i,j} = v^{n}_{i,j} + \delta v^{n}_{i,j} \qquad (24c)$$

$$u^{n+1}_{i,j} = u^{n}_{i,j} + \delta u^{n}_{i,j} \qquad (24d)$$

d) Condição Inicial

Como condição de partida para o cálculo, supõe-se o fluido em repouso com pressão igual à de estagnação no domínio, à exceção da seção de saida, cuja pressão é arbitrada como uma fração da pressão de estagnação.

RESULTADOS E SUA ANÁLISE

Inicialmente, avalia-se a capacidade do presente método em reproduzir resultados experimentais para geometrias de bocais convergente-divergente com simetria axial. Os valores experimentais ao longo da parede do bocal obtidos na literatura [8], são apresentados sob forma de gráficos de pressão estática, adimensionalizada pelo valor da pressão reservatório. As geometrias analisadas são representadas esquematicamente nas Fig.1 (casos 1, 2, 3 e 5) e Fig.4 (caso 4), enquanto que os valores característicos dos ensaios encontram-se na Tab.1.

Para a simulação numérica, utilizou-se uma malha de 20 x 10 (nas direções ξ e η respectivamente), concentrada na região da garganta (σ = 5,0). Esta escolha foi motivada por considerações de precisão (maior quanto mais refinada for a malha) e velocidade de processamento (menor quanto mais refinada for a malha). Os coeficientes de dissipação artificial (ϵ) foram iguais a 1,4 nas direções ξ e η. Estes foram ajustados com base em tentativas numéricas e permaneceram constantes para todos os casos.

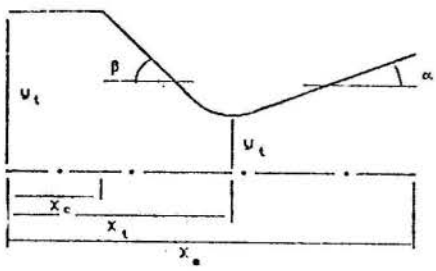

Fig. 1. Representação esquemática do bocal convergente-divergente cônico

Tab. 1. Dimensões dos bocais e características do escoamento (relativo à Fig. 1.)

		caso 1	caso 2	caso 3	caso 4	caso 5
	P_0 (MPa)	1,723	1,034	1,723	20,00	1,723
	T_0 (K)	833,3	289,0	833,3	3036,0	833,3
	γ	1,4	1,4	1,4	1,23	1,4
	R_g (J/Kg.K)	287,0	287,0	287,0	866,7	287,0
	y_t (cm)	9,02	7,75	8,00	12,7	1,0
Adimensional	X_t	6,2	6,5	5,7	2,83	2,0
Adimensional	R_t	2,0	2,0	0,625	1,5	Diversos
Adimensional	X_e	2,2	2,6	2,5	0,79	0,5
Adimensional	X_s	8,9	9,0	11,6	5,67	3,0
Adimensional	α (°)	15,0	15,0	15,0	—	15,0
Adimensional	β (°)	30,0	30,0	45,0	—	30,0

Os resultados correspondentes aos casos 2 e 3 são mostrados nas Fig.2 e Fig.3 respectivamente.

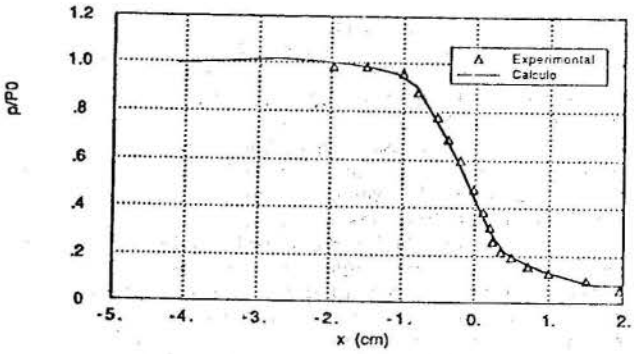

Fig. 2. Perfil de pressão na parede Caso 2

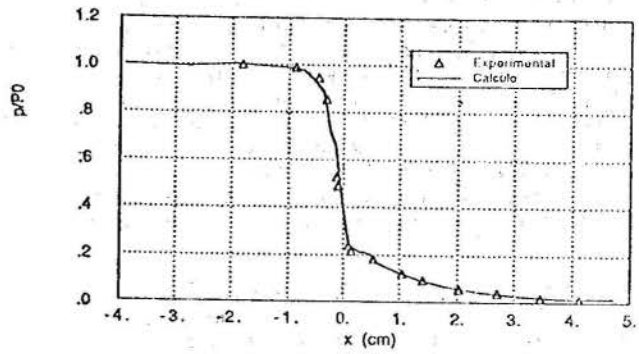

Fig. 3. Perfil de pressão na parede Caso 3

Observa-se a excelente correlação entre os resultados teóricos e experimentais, inclusive para o bocal de menor raio de curvatura o qual apresenta uma queda brusca de pressão na região da garganta (caso 3).

A Fig.4 representa um projeto de bocal que produz o empuxo máximo e cujo contorno foi determinado pelo método das características [9]. As dimensões deste bocal foram obtidas considerando o número de Mach na seção de saida igual a 2,5 e as condições de reservatório indicadas na Tab.1 (caso 4)

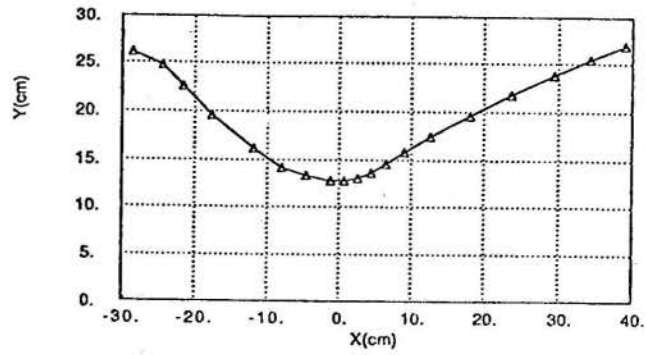

Fig. 4. Contorno do bocal de máximo empuxo Caso 4

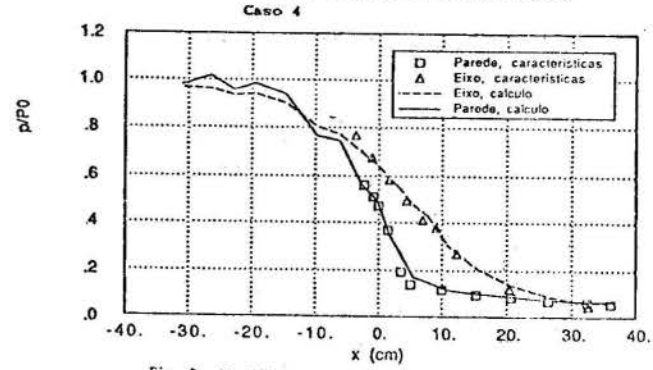

Fig. 5. Perfil de pressão na parede e no eixo Caso 4

Na Fig.5 é mostrada a comparação da razão entre pressões estática e de reservatório ao longo da parede e do eixo de simetria do bocal. Nota-se que os valores calculados pelo método das características ao longo do divergente do bocal e aqueles calculados pelo presente método apresentam uma concordância muito satisfatória. Deve-se notar aqui, que o método das características possui um tempo de execução consideravelmente menor que o método utilizado neste trabalho.

Após a validação do método pela comparação dos seus resultados com aqueles experimentais obtidos na referência [8], e com valores teóricos provenientes do método das características segundo a referência [9], foram feitos uma série de cálculos para se poder avaliar a região transônica em bocais convergente-divergente.

Nesta avaliação, foram traçadas linhas de número de Mach constante ao longo dos bocais, os quais apresentam raios de curvatura adimensionais iguais a 2,5, 2,0, 1,5, 1,25, 1,0 e 0,625, conforme mostram as figuras abaixo. Estes valores, asim como os números de Mach 0,8, 1,0 e 1,2, foram selecionados visando a comparação das linhas de Mach constante com aquelas determinadas através da utilização das séries de Sauer [10], Kliegel-Levine [11] e Hall [12].

Todas as figuras aqui mostradas correspondem à geometria de bocais e condições de reservatório segundo o caso 5 da Tab.1.

Das figuras 6 a 13, vê-se que as linhas de Mach constante obtidas pelas séries de Sauer e de Hall aproximam- se daquelas calculadas pelo presente método, apenas para os raios de curvatura superiores a 2,0 e 1,5 respectivamente. A série de Kliegel-Levine mantém-se em boa concordância com relação ao método aqui utilizado, mesmo para raios de curvatura bem pequenos (R = 0,625)

Em virtude da série de Kliegel-Levine abranger uma maior faixa de raios de curvatura, ela foi utilizada na investigação da região transônica no bocal. Esta investigação consistiu em estabelecer comparações entre os resultados deste trabalho e aqueles obtidos através desta série, para as linhas de número de Mach constante iguais a 0,6, 0,8, 1,0, 1,2 e 1,4, e os raios de curvatura acima mencionados. Algumas desta comparações estão mostradas nas figuras 14 a 17.

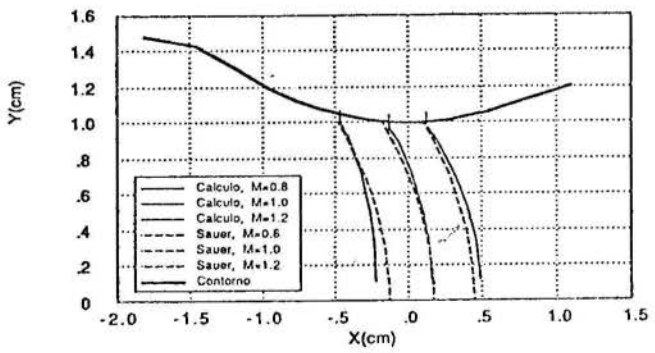

Fig. 6. Linhas de número de Mach Constante, R=2,5 Calculado x Sauer (Caso 5)

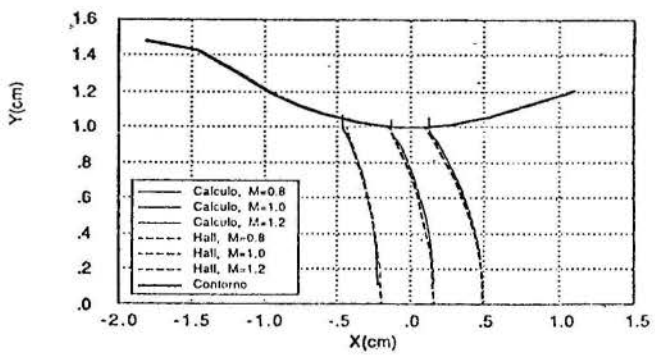

Fig. 7. Linhas de número de Mach Constante, R=2,5 Calculado x Hall (Caso 5)

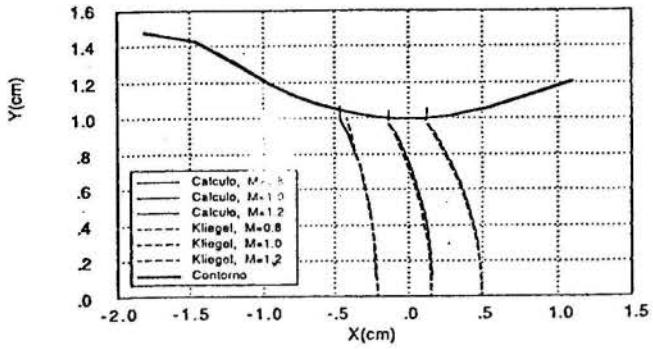

Fig. 8. Linhas de número de Mach constante, R=2,5 Calculado x Kliegel & Levine (Caso 5)

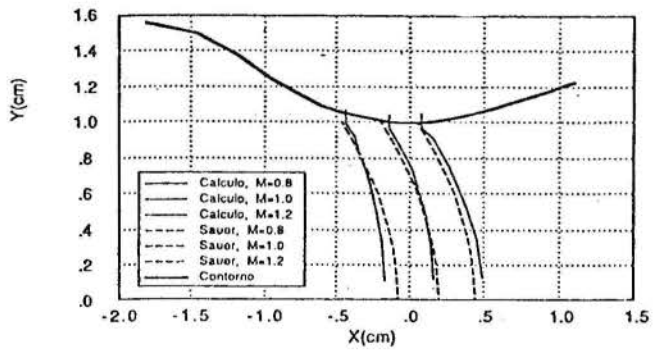

Fig. 9. Linhas de número de Mach Constante, R=2,0 Calculado x Sauer (Caso 5)

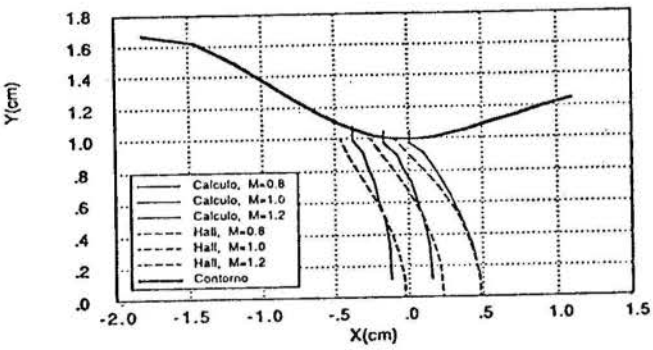

Fig. 10. Linhas de número de Mach Constante, R=1,25 Calculado x Hall (Caso 5)

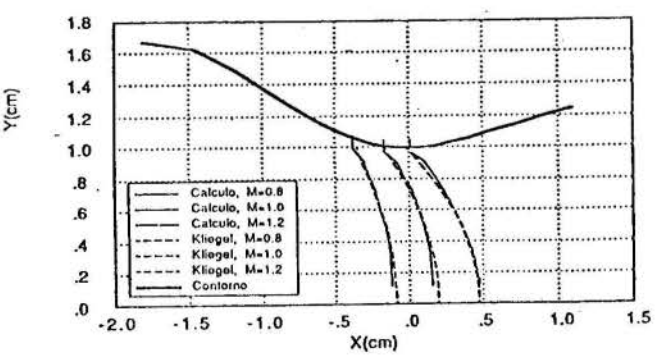

Fig. 11. Linhas de número de Mach Constante, R=1,25 Calculado x Kliegel & Levine (Caso 5)

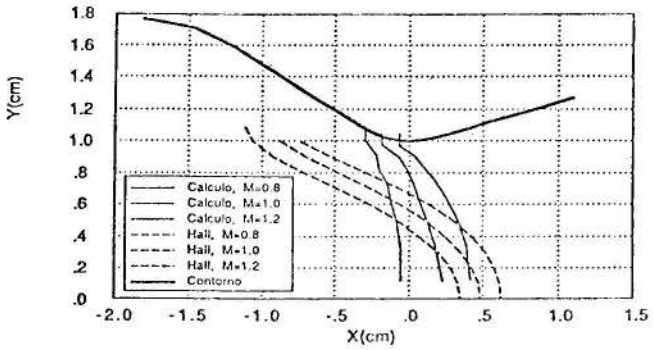

Fig. 12. Linhas de número de Mach Constante, R=0,625 Calculado x Hall (Caso 5)

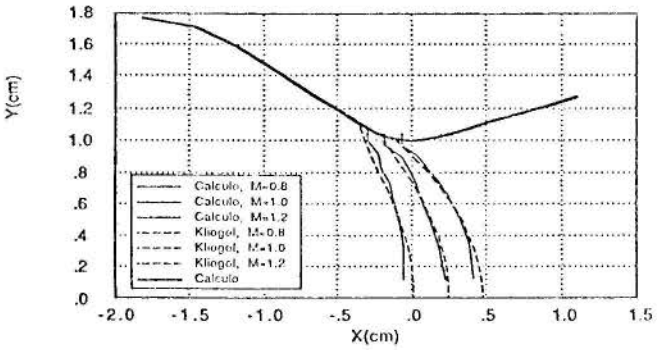

Fig. 13. Linhas de número de Mach Constante, R=0,625 Calculado x Kliegel & Levine (Caso 5)

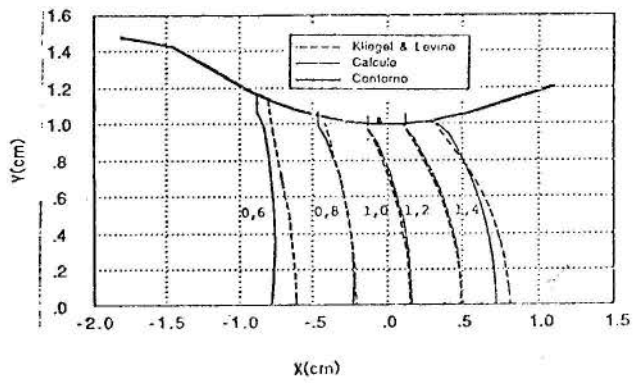

Fig. 14. Linhas de número de Mach Constante, R=2,5 (Caso 5)

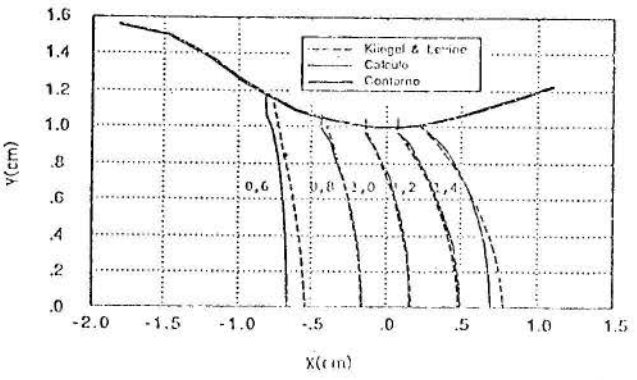

Fig. 15. Linhas de número de Mach Constante, R=2,0 (Caso 5)

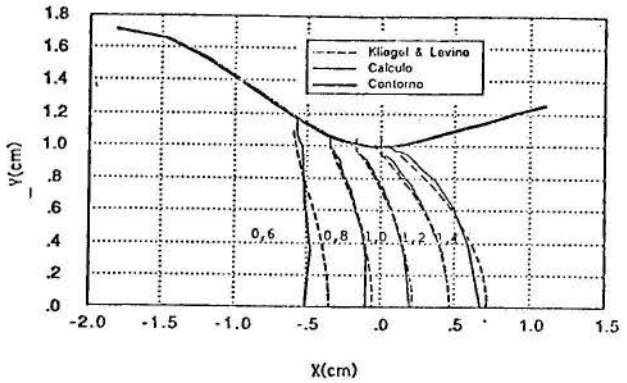

Fig. 16. Linhas de número de Mach Constante, R= 1,0 (Caso 5)

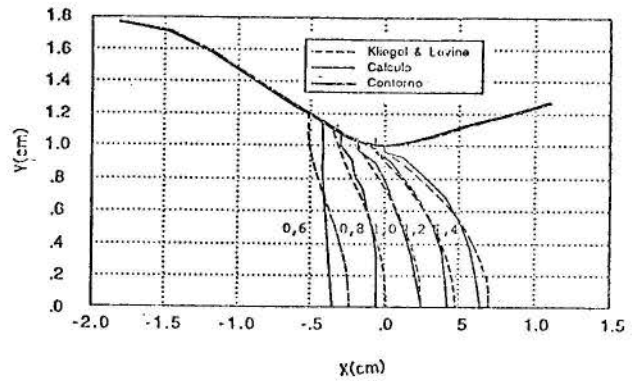

Fig. 17. Linhas de número de Mach Constante, R=0,625 (Caso 5)

Observa-se que para todos os valores de raio de curvatura, existe correspondência entre o presente método e a série de Kliegel-Levine numa faixa de número de Mach entre 0,8 e 1,2. Para números de Mach fora desta faixa, a discrepância entre estes dois métodos aumenta sensivelmente, como pode ser vista nas figuras acima, para as linhas de Mach 0,6 e 1,4. Desta forma, sob o ponto de vista de soluções idênticas entre o presente método e aquele que utiliza a série de Kliegel-Levine, pode-se delimitar a região transônica como a faixa entre os números de Mach 0,8 e 1,2.

CONCLUSÕES

Em virtude da validação do método por comparação com valores experimentais da pressão estática ao longo da parede do bocal em todos os regimes de escoamento, [8], e com aqueles valores teóricos obtidos pelo método das características na região supersônica, considerou-se que o presente método é adequado para descrever a região transônica no interior de bocais convergente-divergente. Isto permitiu encontrar a faixa de raios de curvatura onde as séries de Sauer, Hall e Kliegel-Levine podem ser utilizadas para a determinação deste regime.

A importância do resultado acima prende-se ao fato de que os cálculos, utilizando-se estes tipos de séries de potência, são extremamente simples e rápidos em comparação com aqueles obtidos pelo presente método.

REFERÊNCIA

[1] Silva, L. F. F., Avaliação da Região Transônica em Bocais Convergente-Divergente, Tese de Mestre em Ciências, ITA, São José dos Campos, 1989.

[2] MacCormack, R. W. "The Effect of Viscosity in Hypervelocity Impact Cratering", AIAA Paper 69-354, Cincinatti, Ohio, 1969

[3] Deiwert, G. S., "Supersonic Axisymmetric Flow over Boattails Containing a Centered Propulsive Jet", AIAA Journal, Vol.22, No.10, pp 1358-1359, Oct. 1984.

[4] Anderson, D. a.; Tannehill, J. C. and Pletcher, R. H., Computational Fluid Mechanics and Heat Transfer, MacGraw Hill, Washington, 1984.

[5] Pulliam, T. H. , "Artificial Dissipation Models for the Euler Equations", AIAA Journal, Vol.24, No.12, pp 131-1940, Dec. 1986.

[6] Cambier, L. et alii, "A Multi Domain Approach for the Computational of Viscous Transonic Flows by unsteady Type Methods", Recent Advances in Numerical Methods in Fluids, Vol.3, Swansea, Pineridge Press, 1984 (ONERA TP 1985-66)

[7] Brochet, J. "Calcul Numérique d'Écoulements Internes Tridimensionnels Transoniques", La Rech. Aérosp., No 1980-5, pp 301-315, Sept.-Oct. 1980.

[8] Back, L. H. et alii, "Comparison of Mesured and Predicted Flow through Conical Supersonic Nozzles, with Emphasis on the Transonic Region", AIAA Journal, Vol.3, No.9, pp 1606-1614, Sept. 1965

[9] Paglione, P.; Girardi, R. M., "Análise Teórica e Experimental para Bocais de Tração Máxima", Anais do II Encontro Nacional de Ciencias Térmicas (ENCIT 88), Águas de Lindóia, pp 45-48, 1988

[10] Sauer, R., "general Characteristics of the Flow through Nozzles and near Critical Speeds", NACA TM-1147, NACA, 1947.

[11] Kliegel, J. R. ; Levine, J. N., "Transonic Flow in Small Throat Radius of Curvature Nozzles", AIAA Journal, Vol.7, No.7, pp 1375-1378, Jul.1969.

[12] Hall, I. M., "Transonic Flow in Two Dimensional and Axially Symmetric Nozzles", Quart. J. of Mech. and Appl. Math., Vol.XV, No.4, pp 487-508, 1980.

SUMMARY

This work evaluates the extent of the transonic region that occurs in the adiabatic flow of non-viscous fluid through converging-diverging nozzles as those found at jet engine and wind tunnels. A finite difference numerical method was used to solve the inviscid flow equation (Euler Equations). The results obtained were compared with experimental and theoretical work. This results allow the evaluation of the extent of the transonic region in converging-diverging nozzles.

III ENCIT – Itapema, SC (Dezembro 1990)

DETERMINAÇÃO DO FLUXO DE CALOR EM ESCOAMENTO SUPERSÔNICO UTILIZANDO A TEORIA DE AQUECIMENTO CINÉTICO DE VAN DRIEST

PAULO GILBERTO DE PAULA TORO
CENTRO TÉCNICO AEROESPACIAL - INSTITUTO DE ATIVIDADES ESPACIAIS
12.225 - SÃO JOSÉ DOS CAMPOS - SP

RESUMO

O conhecimento preciso do fluxo de calor (aquecimento cinético) é muito importante para projeto estrutural e para especificações das proteções térmicas de veículos supersônicos e hipersônicos. Aquecimento cinético é o aquecimento da superfície de um corpo como resultado de ar escoando à alta velocidade sobre a mesma. Há numerosas investigações a cerca de aquecimento cinético. Resultados deste estudo indicam que a teoria de Van Driest prediz com precisão o fluxo de calor. Avalia-se o aquecimento cinético para a ogiva principal do VLS, onde cargas úteis estarão alojadas e protegidas termicamente.

INTRODUÇÃO

Projetos preliminares e estudos de otimização de veículos espaciais requerem técnicas que determinem a taxa de fluxo de calor de maneira rápida e precisa, de forma que não comprometam o desempenho do veículo quanto à sua função estrutural e possibilite especificar proteções térmicas que visem proteger, de elevadas temperaturas, os equipamentos eletrônicos e as cargas úteis, alojadas no interior do mesmo.

A superfície externa de tais veículos recebe energia térmica proveniente tanto da radiação quanto da convecção de calor, elevando sua temperatura.

Na plataforma de lançamento, os gases de exaustão à altas temperaturas, oriundas da queima do combustível, aquecem por radiação e convecção de calor, tanto a plataforma quanto a superfície externa do veículo. Durante o vôo ascendente, parte da energia cinética, contida no escoamento do ar, é convertida em energia térmica que será absorvida, por condução de calor , pela estrutura do veículo. Durante o vôo propulsado, a superfície externa do veículo fica exposta à radiação térmica emitida pela pluma, formada pelos produtos de combustão dos propulsores.

Faz parte do projeto do Veículo Lançador de Satélites (VLS), desenvolvido pelo IAE/CTA, um estudo de análise térmica desses fenômenos de aquecimento em regiões críticas, tais como ogiva e base do veículo.

Um modelo conservativo que permite avaliar o aquecimento durante a partida do veículo, na plataforma de lançamento, é apresentado na ref. [1]. A teoria, bem como o modelo desenvolvido para o cálculo do fluxo de calor emitido pela pluma, durante o vôo propulsado, é apresentado pela ref. [2].

Este trabalho trata do aquecimento, proveniente do escoamento do ar, sobre a superfície externa da ogiva principal do VLS, dentro da qual estará alojado o Satélite. A ogiva representa um dos segmentos mais delicados, visto as exigências impostas quanto às condições ambientais térmicas externas e internas desta. São considerados como parâmetros limitantes, para a análise térmica da ogiva principal, a constante solar, para o alijamento da coifa, e a temperatura de 60 °C para o ambiente onde estará alojado o Satélite.

Em trajetória ascendente de vôo, o VLS desenvolverá diversos regimes de velocidades em um meio considerado contínuo.

Cálculos preliminares de fluxo térmico, considerando que toda a energia cinética é convertida em energia térmica, indicam que o alijamento da coifa deve ocorrer a cerca de 140 s do lançamento do veículo.

Em altitudes baixas, o campo de escoamento do ar atmosférico pode ser considerado contínuo e de equilíbrio químico, não ocorrendo os fenômenos de dissociação e ionização do ar.

A Figura 1 ilustra os regimes de velocidades do VLS, durante o vôo ascendente, e o tipo de formulação a ser utilizada para a determinação do escoamento ao redor do veículo, considerando os cálculos preliminares sobre a abertura da ogiva. A literatura relata que entre Mach 3 e 4 ocorrem as maiores taxas de fluxo de calor e conforme Figura 1 cerca de 74% do tempo de vôo ascendente, o VLS estará em velocidade supersônica (Mach entre 1,2 e 5) e hipersônica (Mach ≥ 5), portanto esta análise mostra a importância de se quantificar o aquecimento cinético. A Figura 1 também mostra que 81% do tempo, o VLS estará voando no meio considerado contínuo.

Através de pesquisa bibliográfica constatou-se que inúmeras investigações teóricas e experimentais sobre cálculo de aquecimento cinético foram feitas. Spalding & Chi [3] e Hopkins & Inouye [4] analisaram diversas teorias existentes de aquecimento cinético, comparando os resultados calculados com dados experimentais e ambos concluiram que a teoria de Van Driest [5] é a que melhor quantifica o fluxo de calor em escoamento supersônico.

AQUECIMENTO CINÉTICO

O aquecimento cinético ocorre quando um fluido escoa em alta velocidade sobre a superfície de um corpo. O aquecimento cinético, conforme é mostrado na Figura 2, é o resultado de dois processos, que transformam energia cinética de movimento em energia térmica. Esses processos são:

* atrito

Devido aos efeitos viscosos, o fluido (ar) ao interagir com a superfície do veículo é desacelerado gerando calor. Considerando-se as altas velocidades desenvolvidas por tais veículos, deve-se analisar cuidadosamente a energia térmica resultante do atrito viscoso.

* compressão

O escoamento supersônico resulta na formação de uma onda de choque, a qual é destacada da superfície

do corpo. Ao atravessar a onda de choque o fluido sofre uma forte compressão gerando, portanto, calor.

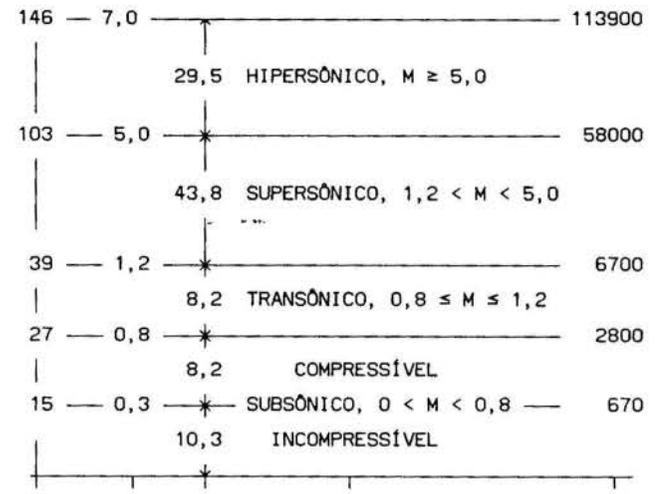

REGIME DE VELOCIDADE DURANTE O VÔO

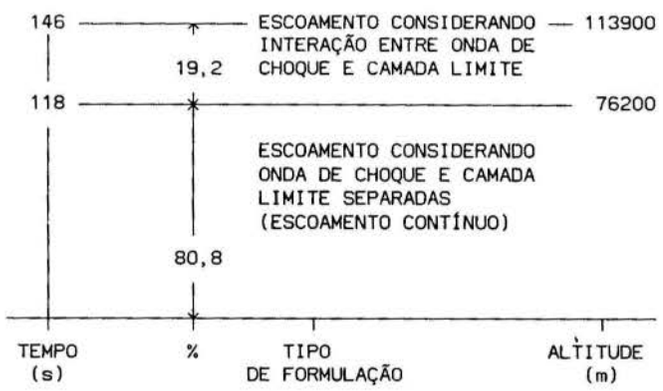

CLASSIFICAÇÃO DO ESCOAMENTO DURANTE A TRAJETÓRIA

Figura 1. Regimes de vôo do VLS e tipo de escoamento.

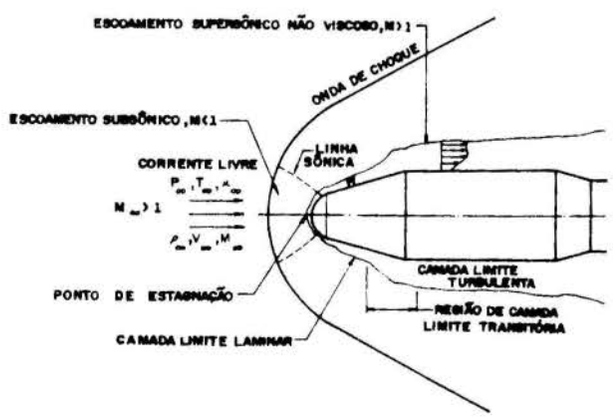

Figura 2. Escoamento supersônico sobre um corpo rombudo.

Nem toda a energia cinética convertida em energia térmica é transferida para a superfície do veículo. Parte desta energia é consumida pelos fenômenos da dissociação, ionização e da recombinação, fenômenos estes ocorridos em escoamento alto supersônico e hipersônico. Outra parte da energia é transferida para o escoamento não perturbado, pelo fato deste estar a uma temperatura mais baixa.

As condições de escoamento sobre corpos rombudos são caracterizados pela baixa velocidade, devido à brusca desaceleração do escoamento através da onda de choque. Na maioria dos casos práticos, a camada limite na região de estagnação é laminar e a transferência de calor é definada pelo processo de camada limite laminar. O regime é considerado laminar para número de Reynolds menor que $5,0 \times 10^5$; acima desde valor o regime é turbulento.

O atrito entre as camadas de fluido geram calor sendo transferido para a superfície externa da ogiva principal do VLS, provocando um aquecimento sobre esta. Portanto haverá uma transferência de calor, primeiramente por convecção, do ar para a superfície do veículo, e em seguida por condução, através de sua estrutura.

Nos instantes iniciais, esta transferência de calor dar-se-á da estrutura do veículo para a atmosfera, isto porque, a temperatura ambiente diminui com a altitude. Porém devido ao atrito viscoso, a temperatura do escoamento externo à camada limite tornar-se-á superior à temperatura da superfície do veículo, mudando então a direção do fluxo de calor, do escoamento do ar para a parede do veículo.

Para números de Mach maiores de 0,3 o regime de vôo passa de incompressível para compressível, causando um aumento significativo na temperatura do escoamento externo à camada limite, portanto aumentando o fluxo térmico e consequentemente aumentando a temperatura da parede do veículo.

Para números de Mach maior que a unidade ocorre as maiores taxas de fluxo de calor para a superfície do veículo, isto porque, quando este atinge velocidade supersônica aparece uma onda de choque comprimindo o ar sobre a superfície do veículo, aumentando drasticamente a temperatura do escoamento entre a onda de choque e a superfície do veículo e consequentemente a temperatura de parede.

Em qualquer dessas fases de vôo, a energia térmica do escoamento será transferida ao longo do tempo através da parede do veículo, aumentando a temperatura da mesma e consequentemente a temperatura do ambiente interno do veículo, ambiente este que aloja equipamentos eletrônicos com temperaturas máximas de operação especificadas. A rapidez do aumento da temperatura da parede e a do ambiente interno é função do tipo de material e da espessura da parede.

Existem , portanto, dois problemas distintos, a convecção de calor (aquecimento cinético) entre a camada limite e a superfície externa do veículo, e a condução de calor dentro da estrutura do veículo.

O objetivo deste trabalho, é determinar o fluxo de calor, ou seja, coeficiente de convecção e a temperatura de referência (recuperação) para o escoamento supersônico. Este passo é feito utilizando a teoria de aquecimento cinético de Van Driest [5]. A condução de calor é tratada separadamente, pois depende não só dos materiais a serem utilizados mas também das espessuras dos materiais envolvidos.

Van Driest [5] recomenda que os coeficientes de convecção para os escoamentos laminar e turbulento em torno de um cone sejam respectivamente $\sqrt{3}$ e $\sqrt{2}$ dos coeficientes de convecção da placa plana, considerando-se o mesmo número de Mach, o mesmo número de Reynolds e a mesma razão de temperaturas entre a temperatura da parede e a temperatura externa à camada limite. O coeficiente de convecção para escoamento laminar e turbulento sobre um cilindro longitutinal, são considerados idênticos aos da placa plana nas mesmas condições citadas anteriormente.

EQUACIONAMENTO DO AQUECIMENTO CINETICO

O fluxo de calor por convecção, em escoamento supersônico, pode ser determinado utilizando a lei de resfriamento modificada de Newton :

$$\dot{q} = h\,(Tr - Tw) \qquad (1)$$

sendo q o fluxo de calor em (W/m^2). O coeficiente de convecção, h em (W/m^2K), pode ser calculado por :

$$h = \rho_\infty\, V_\infty\, cp\, C_{H\infty} \qquad (2)$$

onde, ρ, V, cp e C_H são respectivamente a massa especifica, velocidade do escoamento, calor específico a pressão constante e o número de Stanton. O índice ∞, indica a condição de escoamento não perturbado pela onda de choque.

Van Driest [5] cálcula o número de Stanton através de:

$$C_{H\infty} = \frac{c_1}{Pr^{c_3}\left[Re_{D\infty}\, x/D\right]^{1-c_2}} \left[\frac{\beta D}{V_\infty}\,\frac{\rho_\delta}{\rho_\infty}\right]^{c_2} \left[\frac{\mu_\delta}{\mu_\infty}\right]^{1-c_2} \qquad (3)$$

onde: $\beta D/V_\infty$ é o gradiente de velocidade na camada limite, assumindo para o escoamento supersônico, $M_\infty \geq 1$, no ponto de estagnação:

$$\frac{\beta D}{V_\infty} = \left\{ 8\,\frac{(\gamma-1)M_\infty^{\,2}+2}{(\gamma-1)\,M_\infty^{\,2}} \left[1+\frac{\gamma-1}{2}\,\frac{(\gamma-1)M_\infty^2+2}{2\gamma M_\infty^2-(\gamma-1)}\right]^{\left(-\frac{1}{\gamma-1}\right)} \right\}^{1/2} \qquad (4)$$

e fora do ponto de estagnação tem-se:

$$\frac{\beta D}{V_\infty} = \frac{V_\delta}{V_\infty} \qquad (5)$$

onde M é o número de Mach. Os números de Reynolds Re_D e o Prandtl Pr são calculados considerando as propriedades dos escoamento não perturbado. O comprimento caracteristico é o diametro D da ogiva. c_p é o calor especifico e γ a razão entre os calores especificos. A viscosidade dinâmica μ é calculada através da lei de Sutherland. O índice δ indica as condições fora da camada limite e a variável x é a coordenada natural, medida do ponto de estagnação até o ponto desejado, acompanhando a curvatura da superfície. Para ser consistente com a equação (3), a coordenada x no ponto de estagnação deve ser igual a D. As constantes c_1, c_2 e c_3 são apresentadas na Tabela I.

Tabela I. Valores das constantes c_1, c_2 e c_3.

	TIPO DE ESCOAMENTO				
	LAMINAR		TURBULENTO		
GEOMETRIA	c_1	c_2	c_1	c_2	c_3
PONTO DE ESTAGNAÇÃO	0,763	0,5	-	-	0,6
ESFERA	0,763	0,5	0,042	0,8	0,6
CONE	$\sqrt{3}\times 0{,}332$	0,5	$\sqrt{2}\times 0{,}030$	0,8	2/3
CILINDRO	0,332	0,5	0,030	0,8	2/3

A temperatura de recuperação, Tr em Kelvin, é calculada por:

$$Tr = T_\delta \left[1 + r\,\frac{\gamma-1}{2}\,M_\delta^2\right] \qquad (6)$$

sendo r o fator de recuperação dado por:

$$r = Pr^{1/2}, \quad \text{escoamento laminar}$$

$$r = Pr^{1/3}, \quad \text{escoamento turbulento} \qquad (7)$$

O aquecimento cinético, conforme equação (1), é função:

- da trajetória (velocidade e propriedades termofísicas do escoamento não perturbado pela onda de choque);
- do escoamento aerodinâmico (propriedades termofísicas do escoamento externo à camada limite);
- da temperatura da parede (propriedades termofísicas do material);
- da geometria do veículo (rombudo, cone) e
- do tipo de escoamento do fluido (laminar ou turbulento).

As propriedades do escoamento não perturbado pela onda de choque são obtidas da atmosfera padrão [6]. As propriedades do escoamento aerodinâmico (campo de velocidade e de pressão) são obtidas da ref. [7]. A temperatura e a massa específica sobre o corpo são calculadas respectivamente pela relação de isoentropia e pela lei do gás perfeito.

RESULTADOS E COMENTÁRIOS

As Figuras 5, 6 e 7 apresentam o aquecimento cinético considerando:

- conceito de parede fria, especificando-se as temperaturas de parede de 30 °C, 130 °C e 230 °C;
- geometria da ogiva principal do VLS, Figura 3;
- trajetória de vôo ascendente até 150 s, Figura 4;

* escoamento aerodinâmico para os números de Mach 1.5, 2.0, 3.0 e 4.0, ref. [7].

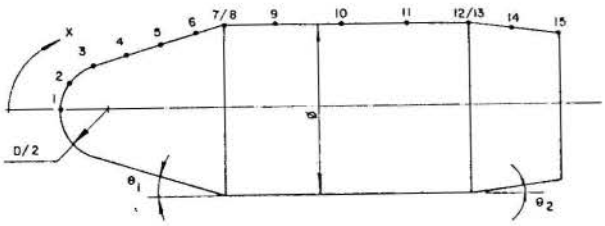

Figura 3. Geometria da ogiva principal do VLS.

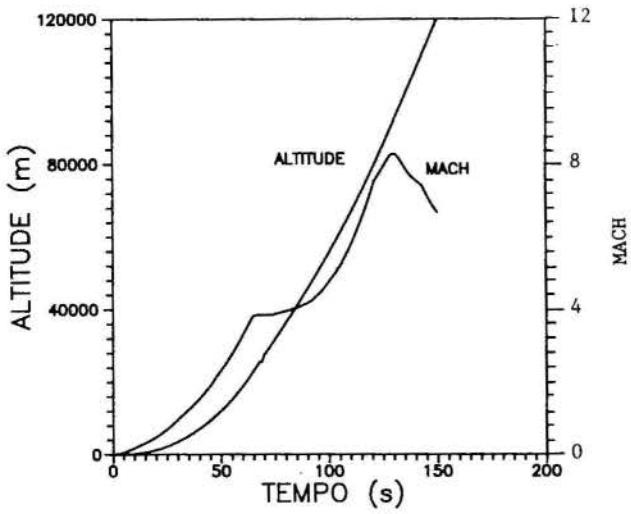

Figura 4. Trajetoria do VLS.

Observa-se da Fig. 5, para números de Mach de 1.5, 2.0 e 3.0, que o fluxo de calor no ponto de estagnação (escoamento laminar, Tab. I) é inferior ao calculado para os pontos situados em sua vizinhança imediata (escoamento turbulento). Para Mach 4 , o escoamento sobre a ogiva é laminar, tendo-se então no ponto de estagnação o máximo fluxo de calor.

A Fig. 7 mostra que o fluxo de calor, para Mach 1.5 e 2.0, é negativo. Isto indica que o fluxo de calor está direcionado da estrutura do veículo para o escoamento, Tw > Tr. Sabendo-se que isto não ocorre, para velocidades supersônicas, conclui-se que a temperatura de parede, para estes números de Mach, deverá ser inferior a 230 •C. Analogamente, da Fig. 6 tem-se a informação, da curva de Mach 2, que a temperatura dos pontos 1 (estagnação) e 2 deverão ser superiores a 130 •C, porém para o restante dos pontos, deverão ser inferiores a esta temperatura. Da Fig. 5, observa-se que para qualquer número de Mach e para qualquer ponto sobre a ogiva, a temperatura será sempre superior a 30 •C.

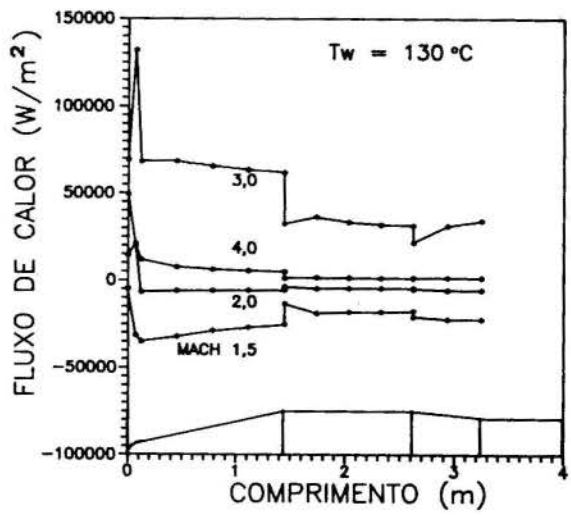

Figura 6. Fluxo de calor sobre a ogiva do VLS.

Em qualquer fase de vôo, a energia térmica, do escoamento, será transferida, ao longo do tempo, através da parede do veículo aumentando a temperatura da mesma e consequentemente a temperatura do ambiente interno do veículo. Da análise realizada sobre os níveis de temperatura da parede da ogiva, nota-se a importância de considerar o tipo de material e a espessura da parede, a ser utilizada na construção de tal ogiva.

Uma vez que a geometria da ogiva principal do VLS possui simetria axial, o escoamento aerodinâmico e consequentemente o fluxo térmico também são simétricos axialmente. Além disso o problema é transiente por natureza, já que o veículo estará com velocidade e altitude diferentes a cada instante, Fig. 4. Devido a

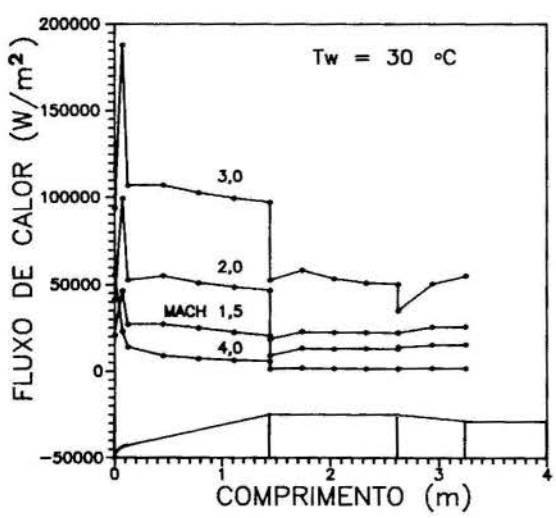

Figura 5. Fluxo de calor sobre a ogiva do VLS.

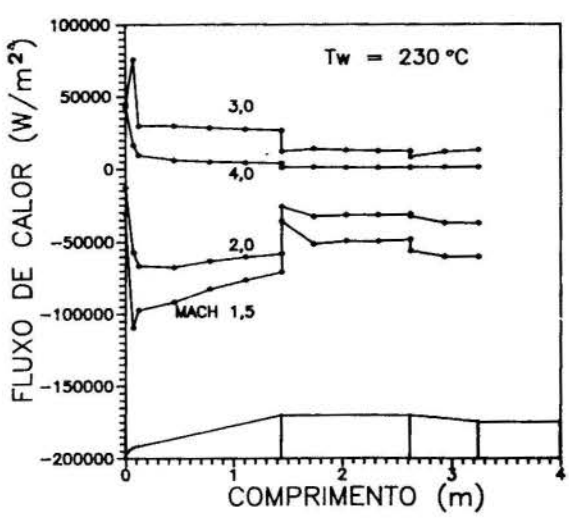

Figura 7. Fluxo de calor sobre a ogiva do VLS.

complexidade do problema no que se refere ao regime de vôo (subsônico, transônico, supersônico, hipersônico) e a geometria do veículo (esférica, cilíndrica, cônica), torna-se árduo a determinação do escoamento aerodinâmico, do fluxo térmico e por conseguinte a determinação da temperatura da parede.

ACOPLAMENTO CONVECÇÃO CONDUÇÃO

O ponto de estagnação, além de fazer parte da região de maior fluxo térmico durante o vôo, permite um modelamento simples e preciso quanto a determinação do escoamento aerodinâmico e do fluxo térmico. Portanto, para este ponto determinou-se, através do acoplamento da convecção com a condução de calor, os níveis de temperatura da parede, ao longo do tempo de vôo ascendente, considerando uma espessura de 12 mm de fibra de vidro com resina fenólica.

A temperatura da parede é obtida através da análise de transferência de calor por condução em coordenadas esféricas, considerando que a transferência é unidimensional (geometria simétrica axialmente) e transiente. Portanto a temperatura é da forma: $T = T(r,t)$, logo:

$$\frac{1}{r^2}\frac{\partial}{\partial r}\left[r^2 k \frac{\partial T}{\partial r}\right] = \rho\, cp \frac{\partial T}{\partial t} \qquad (8)$$

onde: r é a coordenada radial, k , ρ, cp são respectivamente a condutividade térmica , a massa específica e calor específico do material da parede.

Para a solução desta equação diferencial são necessárias a condição inicial e as condições de contornos. A condição inicial é dada por:

$$T(r,0) = Ti \qquad (9)$$

onde: Ti é a temperatura do ar no instante do lançamento. As condições de contornos são dadas por:

$$-k \frac{\partial T}{\partial r}(ri,t) = 0 \qquad (10)$$

$$k\frac{\partial T}{\partial r}(re,t) = h\left[Tr - T(re,t)\right] + \alpha G - \varepsilon \sigma \left[T(re,t)\right]^4 \qquad (11)$$

onde: h é o coeficiente de convecção (2), Tr a temperatura de recuperação (6). α, ε são respectivamente a absortividade e emissividade do material. σ a constante de Stefan-Boltzmann e G a radiação solar incidente.

É utilizada a técnica numérica de volumes de controle para a solução deste problema. A técnica é apresentada por Patankar [8], e consiste em integrar a equação diferencial em cada um dos volumes de controles existente na discretização do problema.

O coeficiente de convecção (2) ou o número de Stanton (3) são funções tanto das propriedades externas à camada limite, quanto das propriedades do escoamento não perturbado pela onda de choque. As propriedades do escoamento não perturbado são obtidas da atmosfera padrão, ref. [6], e as propriedades do escoamento externo à camada limite são obtidas utilizando a teoria de choque frontal, para o cálculo das propriedades após o choque [9], e escoamento isoentrópico, desde o choque até a superfície externa do veículo.

A Figura 8 apresenta, para o ponto de estagnação, o fluxo de calor , ao longo do tempo.

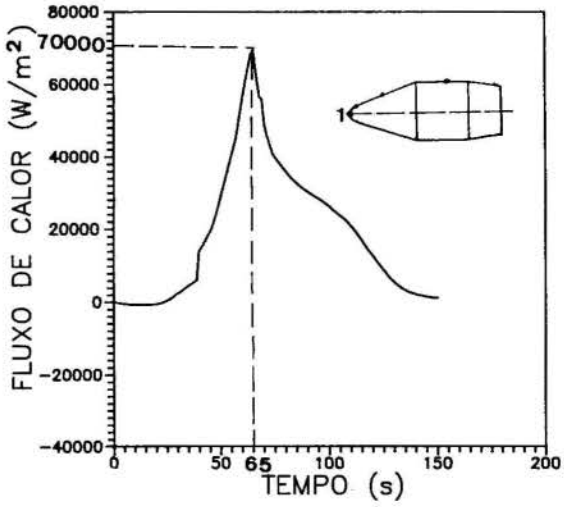

Figura 8. Fluxo de calor.

Da Fig. 8, podem ser obtidas duas informações . Primeiro, o fluxo térmico máximo ocorre, como esperado, em torno de **65** s, ou seja, entre Mach 3 e 4. Segundo, a coifa pode ser alijada em torno de 145 s de vôo, pois neste instante tem-se, praticamente, o fluxo térmico de 1,2 kW/m² sobre o ponto de estagnação da ogiva principal do VLS. Após o alijamento da coifa, o Satélite estará exposto a radiação solar incidente.

Finalmente, a Fig. 9 apresenta a temperaturas das superfícies externa e interna, para o ponto de estagnação.

A temperatura da superfície interna é um parâmetro importante para a especificação da temperatura do ambiente interno da ogiva. O Satélite estará alojado, durante o vôo, dentro da coifa, até a abertura da mesma, que deverá ser alijada em torno de 145 s, conforme Fig. 9. Verifica-se que após 145 s de vôo, a temperatura da superfície interna é inferior a 60 °C.

A temperatura da superfície externa permite especificar a espessura e/ou material da parede, proporcionando temperatura interna adequada. A temperatura da superfície externa máxima é de **370** °C, em torno de **65** s de vôo, coincidentemente ao fluxo térmico máximo.

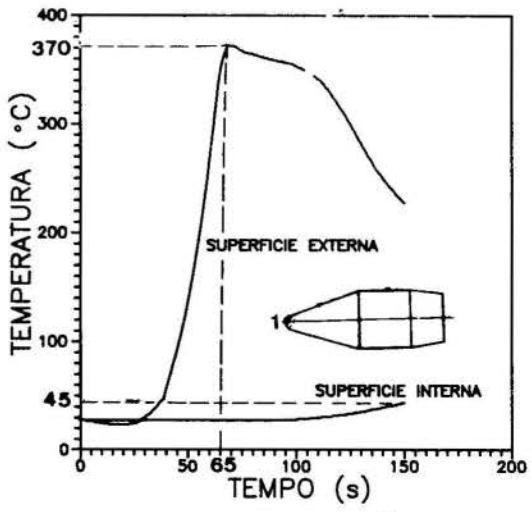

Figura 9. Temperaturas das superfícies externa e interna.

As referências [10] e [11] apresentam em detalhes as formulações, respectivamente, do aquecimento cinético, sobre a ogiva principal do VLS, e da condução de calor, para a determinação dos níveis de temperatura da parede.

CONCLUSÕES

A teoria de aquecimento cinético de Van Driest é utilizada para o cálculo do fluxo de calor sobre a ogiva principal do VLS, durante a fase de vôo ascendente até 150 s, considerando parede fria, com temperaturas de parede de 30 °C, 130 °C e 230 °C. Esta formulação, parede fria, não permite o conhecimento dos níveis reais de fluxo térmico e das temperaturas das superfícies externa e interna, pois não leva em conta a espessura e o tipo de material a ser utilizada na confecção de tal ogiva. O acoplamento do aquecimento cinético com a condução de calor proporciona não só o conhecimento dos níveis de temperatura da parede, como também possibilita especificar proteções térmicas que visem proteger, de elevadas temperaturas, os equipamentos eletrônicos e as cargas úteis, alojadas no interior dos veículos espaciais.

Foi considerado a condução de calor, para o ponto de estagnação, com 12 mm de espessura de fibra de vidro com resina fenólica. Os resultados obtidos, indicam que o fluxo térmico máximo ocorre entre Mach 3 e 4, como esperado, e que após 145 s de vôo ascendente, o fluxo térmico, no ponto de estagnação, é inferior à constante solar podendo a coifa ser alijada. No final de 145 s a temperatura do ambiente interno, onde está alojado o Satélite, é inferior a 60 °C, de forma a não comprometer o desempenho tanto do Satélite quanto dos equipamentos eletrônicos colocados no seu interior.

REFERÊNCIAS BIBLIOGRÁFICAS

[1]. Carvalho, T. M. B., Análise térmica da estrutura de foguetes a propelente sólido durante a partida, Trabalho de graduação, UFRJ, Rio de janeiro, 1989.

[2]. Pessoa Filho, J. B. e Cotta, R. M., Analytical Models for radiative heat transfer from solid propellant rocket exhaust plumes, 10th Brazilian Congress of Mechanical Engineering, vol. 1, pp. 313-316, Brazil, 1989.

[3]. Spalding, D.B. e Chi, S.W., The Drag of a Compressible Turbulent Boundary Layer on a Smooth Flat with and without Heat Transfer, Journal of Fluid Mechanics, pp 117-143, Jan. 1964.

[4]. Hopkins, E.J. e Inouye, M., An Evaluation of Theories for Predicting Turbulent Skin Friction and Heat Transfer on Flat Plates at Supersonic and Hypersonic Mach Numbers, AIAA Journal, vol 9, n° 6, pp 993-1003, Jun. 1971.

[5]. Van Driest, E.R., The Problem of Aerodynamic Heating, Aeronautical Engineering Review, vol. 15, n° 10, pp 26-41, Oct. 1956.

[6]. U.S.STANDARD ATMOSPHERE, 1962

[7]. Morgenstern JR., A. ; Nascimento, D. P. e Lobão, D. C., Distribuição de Pressão na Parte Alta do VLS, CTA/IAE-ETP, Abr 88.

[8]. Patankar, Suhas V., Numerical Heat Transfer and Fluid Flow, McGraw - Hill Book Co., 1980.

[9]. Ames Reserch Staff., Equations, Tables, and Charts for Compressible Flow, NACA 1135, 1953.

[10]. Toro, P. G. P., Determinação do aquecimento cinético sobre a ogiva do VLS, CTA/IAE-ETP, Jun 1988.

[11]. Toro, P. G. P., Aquecimento cinético e temperaturas na ogiva principal do VLS, CTA/IAE-ETP, Set 1989.

ABSTRACT

Accurate knowledge of heat flux, due to aerodynamic heating, is very important for the structural design and specification of thermal protections for supersonic and hypersonic vehicles. Aerodynamic heating is originated from high velocity flows over a solid surface. Several investigations have already been made about this problem. Results from these investigations indicate that Van Driest's theory predicts accurately the heat flux. The present paper evaluates the aerodynamic heating for the VLS fairing, where the payload is located and which must be thermally protected.

III ENCIT – Itapema, SC (Dezembro 1990)

INTEGRAL METHOD APPLIED TO THE CALCULATION OF SEPARATION POINT AND BASE PRESSURE OF INCLINED WEDGES AT SUPERSONIC SPEEDS

DALTON VINICIUS KOZAK
PROJEPRO Projetos de Processamento Ltda.
Rua Tocantins 37, Cristo Rei
80050 - Curitiba-PR - Brasil

SUMMARY

A method is presented based on the formulation proposed by Klineberg and Kubota for prediction of the exhaust plume/boundary layer interactions at supersonic speeds. In this work the original equations are adapted to calculate the flow over inclined wedges. The pressure distribution over the body is obtained, as well as the separation point and wedge base pressure. Computational results are presented showing some features of this type of flow.

NOMENCLATURE

α	$=(U/U_e)_{\psi=0}$ for reversed flow $=(U/U_e)_{Y=0}$ for foward flow; also sonic velocity
b	geometric parameter (fig.2)
C	$(\mu/\mu_\infty)/(T/T_\infty)$
C_1	$\frac{1+m_j}{1+m_\infty}\left(\frac{p_j}{p_\infty}\right)\frac{\gamma-1}{\gamma}$
f	$\left[2+\frac{\gamma+1}{\gamma-1}\frac{m_e}{1+m_e}\right]\mathcal{X}+\frac{3\gamma-1}{\gamma-1}+\frac{M_e^2-1}{m_e(1+m_e)}Z$
F	$\mathcal{X}+\frac{1+m_e}{m_e}$
$\mathcal{X}$	Θ_i/δ_i^*
J	Θ_i^*/δ_i^*
K	$\delta_{i2}^*/\delta_{i1}^*$
m	$\frac{\gamma-1}{2}M^2$
$\mathring{m}$	$\int_0^\delta \rho u dy$, boundary-layer mass flow
M	Mach number
R	$(2\delta_i^*/U_e^2)\int_0^\infty\left(\frac{\partial U}{\partial Y}\right)^2 dY$, laminar dissipation integral
$Re_{\delta_i^*}$	$\frac{a_\infty}{\nu_\infty}M_\infty\delta_{i1}^*$, Reynolds number
s	streamwise coordinate
T	static temperature
u,v	physical velocity components
u^*	$(u/u_e)_{Y=0}$, dividing streamline velocity ratio
U	transformed velocity
U_o	$(U/U_e)_{Y=0}$, centerline velocity ratio
U_o'	$\partial U_o/\partial\alpha$
y^*	distance from centerline to dividing streamline
Y	transformed normal coordinate
Z	$(1/\delta_i^*)\int_0^{\delta_i}\frac{U}{U_e}dY$, velocity integral
α	u_1/u_2, velocity ratio
β_1	$\frac{a_1\rho_1}{a_\infty\rho_\infty}$
β_2	$C\frac{a_1p_1M_\infty}{a_\infty p_\infty M_1}$
γ	ratio of specific heats
δ	viscous-layer thickness
δ_i	transformed thickness
δ_i^*	$\int_0^\infty\left(1-\frac{U}{U_e}\right)dY$, transformed displacement thickness
θ	$\tan^{-1}v_e/u_e$, local streamline inclination
Θ_i	$\int_0^\infty\frac{U}{U_e}\left(1-\frac{U}{U_e}\right)dY$, transformed momentum thickness
λ	$\frac{\rho_o v_o}{\rho_1 u_1}$, mass-flow parameter
ξ	parameter defined in eq.7
φ	zero-shear line inclination
ν	kinematic viscosity
μ	viscosity coefficient

Subscripts

e	local external, inviscid
i	transformed, incompressible
j	jet, exhaust
o	trailing-edge boundary layer
1	upper flow

2	lower flow
∞	freestream
ψ=0	dividing streamline

INTRODUCTION

A method is presented in this work which concerns a typical problem involving the strong interaction between an under-expanded rocket exhaust plume and the boundary layer flow along the surface of a vehicle at supersonic speeds. As can be seen in Fig. 1, when a supersonic jet expands at the nozzle exit, it produces a rise in pressure that is partially comunicated upstream through the viscous layer. For a sufficiently large ratio of the jet exit pressure (pj) to the undisturbed pressure (p∞), separation occurs somewhere forward the base. The region of separated flow can be quite extensive, particularly for laminar flows, and the stability and control of the vehicle may be seriously affected. This type of flow is a typical strong-interaction problem where the location of the separation point depends on the initial jet deflection, which in turn depends on the extent of the region of separated flow. Because of this complexity, a way to simplify the flow analysis is the utilization of an integral or moment method, as done previously by many authors in strong-interaction problems [1][2].

The viscous layer at the edge of the plume is divided into two parts and the boundary-layer equations are integrated across each part and transformed into an equivalent incompressible form. Similarity solutions are used to relate the profile quantities to a single parameter, which allows the flowfield to be completely described in terms of six quantities. A system of nonlinear ordinary differential equations with the appropriate boundary conditions determines their distribution.

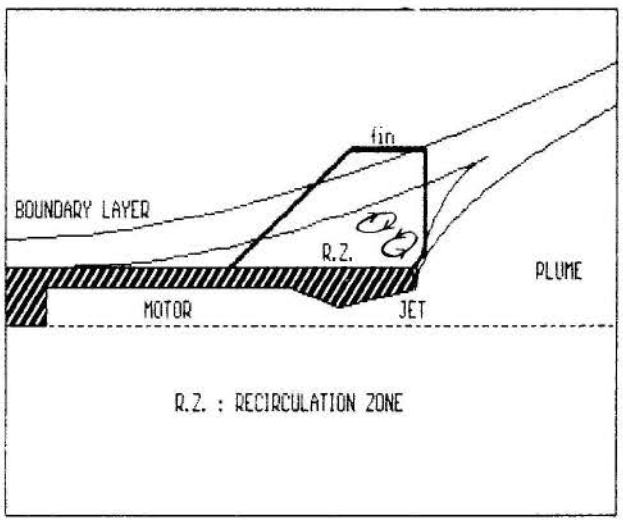

Fig.1: Rocket exhaust plume/boundary layer interaction

To obtain the complete solution for the exhaust plume/boundary layer interactions, the plume must be joined to the separated flow region on the body, and to accomplish this matching, certain joining relations must be specified. As originally shown by Crocco and Lees [3], an integral formulation leads to the conclusion that near-wake flow is subcritical and must pass smoothly through a critical point downstream the reversed flow region. The same type of behavior is exhibited by the plume edge mixing region, which is similar to an asymmetric wake, and the uniqueness of initial conditions for any problem is assured by the requeriment for the correct trajectory to pass through the critical point. An iterative procedure is then required to join the two branches of the solution: one coming from the body in downstream direction, and the other obtained integrating away from the critical point in either upstream and downstream directions.

In order to develop the formulation for this type of problem, a simpler two-dimensional model was chosen. The supersonic flow over a wedge at angle of attack represents a similar problem, where the leeward flow simulates the external body flow, while the windward flow expansion at trailing edge simulates the exhaust jet. The wake behind the wedge is similar to the plume edge mixing layer.

LAMINAR FLOW THEORY

The Wedge flow. To calculate the flow over the wedge it is assumed that the boundary layer interaction upstream of the trailing edge is equivalent to the free interaction that occurs upstream of a compression corner or forward facing step. The analysis for the leeward separating boundary layer flow is therefore identical with the one described in [2]. Assuming a location for the begining of the interaction, a departure integral is obtained leaving the equilibrium solution for undisturbed flat plate flow toward separation. Integration of the equations proceeds smoothly through the separation point to the specified location of the trailing edge, where initial conditions for the wake flow computation are determined.

The Mixing Flow Region (Wake). The set of equations used in the solution of the wake flow are essentially the same as those derived by Klineberg and Kubota [4]. However, small diferences were detected in some equations coefficients, and the equations here obtained are:

Equations for upper flow:

$$\mathcal{H}_1\frac{d\delta^*_{i1}}{ds} + \delta^*_{i1}\frac{d\mathcal{H}_1}{ds} + (2\mathcal{H}_1+1)\delta^*_{i1}\frac{d\ln M_1}{ds} - \beta_{i1}\lambda\left(1-\frac{U_o}{U_1}\right) = 0 \quad (1)$$

$$J_1\frac{d\delta^*_{i1}}{ds} + \delta^*_{i1}\frac{dJ_1}{ds} + 3J_1\delta^*_{i1}\frac{d\ln M_1}{ds} - \beta_{i1}\lambda\left[1-\left(\frac{U_o}{U_1}\right)^2\right] = \frac{\beta_2 R_1}{Re\,\delta^*_{i1}} \quad (2)$$

$$F_1\frac{d\delta_{i1}^*}{ds} + \delta_{i1}^*\frac{d\mathcal{H}_1}{ds} + f_1\delta_{i1}^*\frac{d\ln M_1}{ds} + \frac{\beta_1}{m_1}(\lambda-\varphi) = \frac{\beta_1}{m_1}\theta_1 \quad (3)$$

Equations for lower flow:

$$\mathcal{H}_2\frac{d\delta_{i1}^*}{ds} + \delta_{i1}^*\frac{d\mathcal{H}_2}{ds} + (2\mathcal{H}_2+1)\alpha^2\delta_{i1}^*\frac{d\ln M_1}{ds} + \mathcal{H}_2\delta_{i1}^*\frac{d\ln K}{ds} + \beta_1\frac{\lambda\alpha\xi}{K}(1-\frac{U_o}{U_2}) = 0 \quad (4)$$

$$J_2\frac{d\delta_{i1}^*}{ds} + \delta_{i1}^*\frac{dJ_2}{ds} + 3J_2\alpha^2\delta_{i1}^*\frac{d\ln M_1}{ds} + J_2\delta_{i1}^*\frac{d\ln K}{ds} + \beta\frac{\lambda\alpha\xi}{K}[1-(\frac{U_o}{U_2})^2] = \frac{\beta_2\alpha R_2}{Re_{\delta_{i1}^*}}(\frac{\xi}{K})^2 \quad (5)$$

$$F_2\frac{d\delta_{i1}^*}{ds} + \delta_{i1}^*\frac{d\mathcal{H}_2}{ds} + f_2\alpha^2\delta_{i1}^*\frac{d\ln M_1}{ds} + F_2\delta_{i1}^*\frac{d\ln K}{ds} - \alpha\xi\frac{\beta_1}{K}(\frac{\lambda}{m_2}+\frac{\alpha\varphi}{m_1}) = -\alpha^2\xi\frac{\beta_1\theta_2}{m_1K} \quad (6)$$

There is an additional parameter ξ that is not present in the previous formulation. Nevertheless, the final computation is little affected, since the value of this parameter is always close to the unity ($\xi \simeq 1$). This parameter is simply given by

$$\xi = 1/\sqrt{C_1} \quad (7)$$

To solve the system of differential equations obtained from eqs 1-6 , it is necessary to express the derivatives of the profiles quantities in terms of derivatives of the dependent variables. In this work one of the derivatives was found to be different from former derivations. We obtain

$$\frac{d\mathcal{H}_2}{ds} = \mathcal{H}_{2\alpha}\frac{d\alpha_1}{ds} + \mathcal{H}_{2m}\frac{d\ln M_1}{ds} \quad (8)$$

where

$$\mathcal{H}_{2\alpha} \equiv (\frac{\partial\mathcal{H}_2}{\partial\alpha_1}) = \alpha\mathcal{H}'(\alpha_2) \times [U_{o_1}'(\alpha_1)/U_{o_2}'(\alpha_2)] \quad (9)$$

and

$$\mathcal{H}_{2m} \equiv (\frac{\partial\mathcal{H}_2}{d\ln M_1}) = \frac{\alpha}{(1+m_1)} \times \mathcal{H}'(\alpha_2)\,[U_{o_1}(\alpha_1)/U_{o_2}'(\alpha_2)] \quad (10)$$

A difference exists between relation (10) and the equivalent in [4]. Despite this, no significant discrepancies were observed in the final computational results.

Joining Relations. As said before, an assumption is made that the boundary-layer interaction upstream of the trailing edge is equivalent to the free interaction upstream of a compression corner or a forward facing step. With this procedure, the flow parameters can be calculated at the trailing edge, and the initial conditions for the wake can be determined.

There are four initial values to be fixed: M_1, δ_{i1}^*, α_1 and K. Therefore, four joining conditions are necessary to determine then uniquely. Three joining conditions require continuity of the edge Mach number M_1, of the velocity ratio of the upper flow dividing streamline u^*, and the boundary layer mass flow $\mathring{m}$, which is proportional to $M_1\delta_1^*Z_1$. The last condition

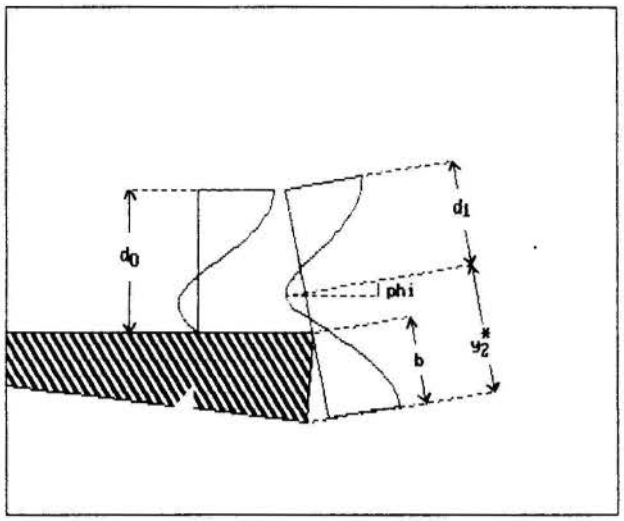

Fig. 2: Geometric joining relation [4]

is a geometric relation, and at this point a small modification is introduced to consider the base influence, which was not considered in [4] (Fig. 2). The fourth joining relation is:

$$(\delta_1+y_2^*-b)\cos\varphi = \delta_o \quad (11)$$

SYSTEM SOLUTION

The solution of the system of equations obtained for the flow over the wedge and

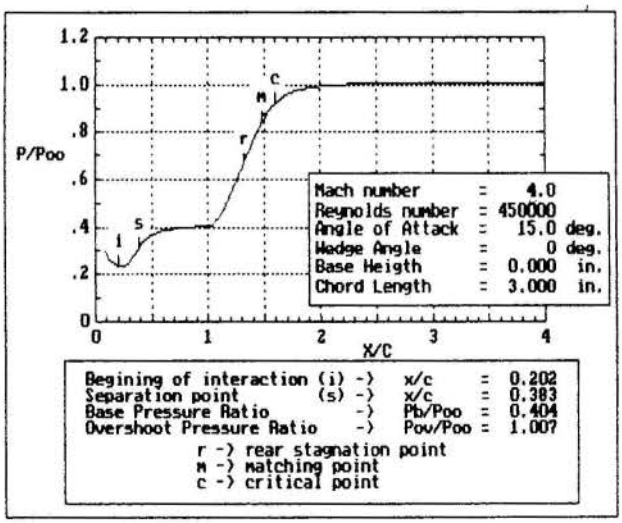

Fig. 3: FLOW OVER A FLAT PLATE
Pressure Distribution along the Streamline Direction s

wake flow follows the same procedure used for the calculation of the flow over a flat plate at angle of attack [4]. For checking the computer program developed for this work, results for these cases were successfuly reproduced (Fig. 3 and 4). Unfortunately, no experimental data were available for the wedge flows calculated here. The only experimental result obtained covers a situation were the assumptions made are no longer valid. However, these data provide some information about the qualitative behavior of wedge flows.

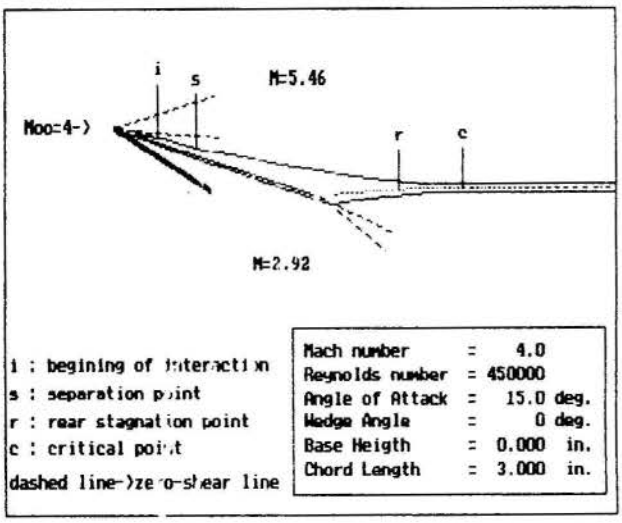

Fig. 4: FLOW OVER A FLAT PLATE
Boundary and Mixing Layers
Visualisation

The calculation program used was developed on a PC-XT computer using the Borland's Turbo Pascal Compiler Version 5.5.

RESULTS

Fig. 5 shows the pressure distribution over an inclined wedge and its wake. The pressure plateau observed after flow separation at the leeward side is consistent

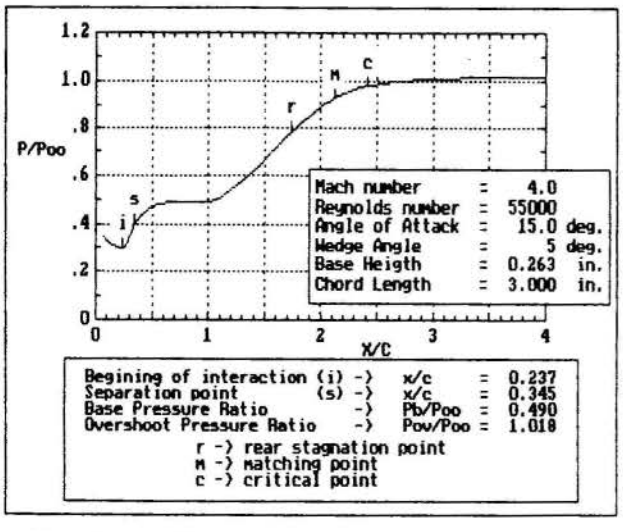

Fig. 5: FLOW OVER INCLINED WEDGE
Pressure Distribution along the
Streamline Direction s

with previous experimental results, where the plateau pressure was measured to be virtually the same as the base pressure [5]. A small pressure overshoot is initially observed in the wake at certain distance downstream of the base, which is followed by a gradual decay to the freestream conditions. The present model does not predict this wake pressure decay since the second family of characteristics is not considered in the calculation of the edge inviscid flow.

Experimental data for thick wedges [5], obtained for Reynolds numbers ranging from 14000 to 55000 and laminar flow, show that the pressure overshoot increases with the angle of attack. It was also observed that

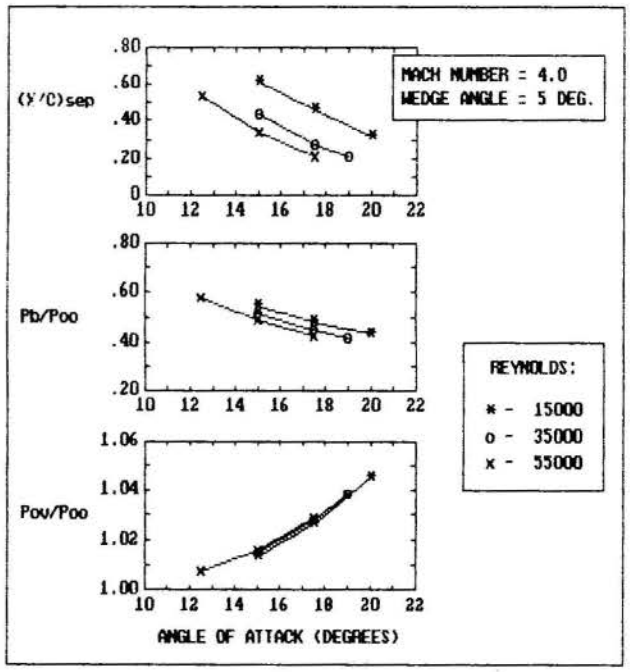

Fig. 6: FLOW OVER INCLINED WEDGE
Separation Point, Base Pressure
and Pressure Overshoot Variations

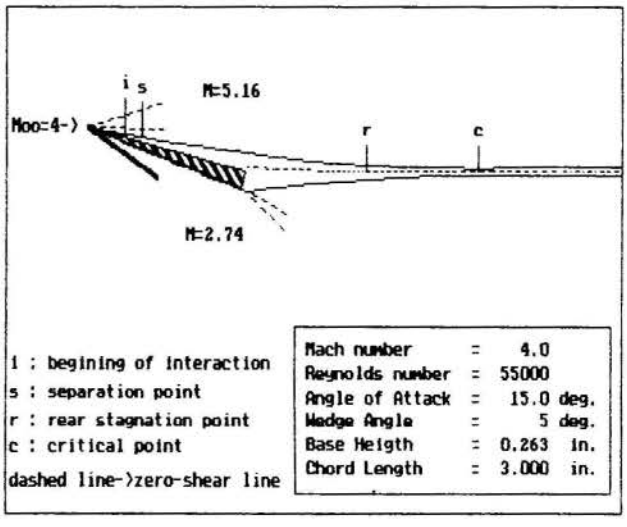

Fig. 7: FLOW OVER INCLINED WEDGE
Boundary and Mixing Layers
Visualisation

the lower the Reynolds number, the higher

the pressure overshoot. The Reynolds number effect is much smaller than that of the angle of attack. This type of behavior is partially shown in Fig.6, where the flow over a 5 degree wedge was calculated. The Reynolds number influence has an inverse behavior in this case, but other computational results not presented here for higher wedge angles and Mach numbers confirm the tendency shown in [5]. The pressure overshoot can be explained by the difference between the compression strength of the flow in the leeward and windward sides, which causes an upwash directly behind the trailing edge. The separation point and base pressure ratio variations are also shown is this figure.

Finally, in Fig.7 is presented an approximated visualisation of the flow over an inclined wedge. The separation point and wake stagnation section are shown. The edges of the boundary and mixing layers are also outlined.

CONCLUSIONS

The integral method applied to the calculation of separation point and base flow over wedges showed reasonable qualitative results, although no specific experimental data were available for comparison. The merit of this formulation is the relative simplicity in the analysis of this type of inviscid-viscous strong-interaction flow. The equations can be adapted to calculate the axisymmetric case, and turbulent flow can also be included with some modifications in the formulation.

The model must include the method of characteristics to calculate the inviscid flow field if it is intended to calculate an axisymmetric flow. For the two-dimensional case, the simple Prandtl-Meyer relation is sufficient to determine the inviscid edge velocities.

REFERENCES

[1] Lees, L. and Reeves, B.L., "Supersonic Separated and Reattaching Laminar Flows: I. General Theory and Application to Adiabatic Boundary-Layer/Shock Wave Interaction", AIAA Journal, Vol.2, N.11, November 1964, pp.1907-1920.

[2] Klineberg, J.M. and Lees, L., "Theory of Laminar Viscous-Inviscid Interactions in Supersonic Flow", AIAA Journal, Vol.7, N.12, December 1969, pp. 2211-2221.

[3] Crocco, L. and Lees, L., "A Mixing Theory for the Interaction Between Dissipative Flows and Nearly Isentropic Streams", Journal of the Aeronautical Sciences, Vol.19, N.10, October 1952, pp. 649-675.

[4] Klineberg, J.M., Kubota, T. and Lees, L., "Theory of Exhaust-Plume/Boundary Layer Interactions at Supersonic Speeds", AIAA Paper N.70-320, AIAA 8th Aeroespace Sciences Meeting, New York, January 1970.

[5] Wu, J.J. and Behrens, W., "An Experimental Study of Hypersonic Wakes behind Wedges at Angle of Attack", AIAA Journal, Vol.10, N.12, December 1972, pp.1582-1589.

III ENCIT – Itapema, SC (Dezembro 1990)

MODELAGEM DA EQUAÇÃO DE TRANSPORTE EM ESCOAMENTOS TURBULENTOS PARA A VARIÂNCIA DA FLUTUAÇÃO DE TEMPERATURA

GILMAR MOMPEAN MUNHOZ DA CRUZ
Departamento de Energia - FEM/UNICAMP
13081 - Campinas, SP.

RESUMO

O presente artigo tem como objetivo a modelagem da equação relativa a variância da flutuação de temperatura em escoamentos turbulentos, dentro da hipótese de grandes valores do número de Reynolds e Peclet. Apresenta-se uma análise da sensibilidade do fator R utilizado para obter a taxa de dissipação da flutuação de temperatura. O modelo é testado sobre dois tipos de configuração: escoamento atrás de grelha e jato axi-simétrico de ar aquecido.

INTRODUÇÃO

A predição do campo de temperatura e de suas características flutuantes é importante para numerosas instalações industriais e em particular para os reatores nucleares. As zonas de mistura entre escoamentos de temperatura muito diferentes dão lugar a fortes gradientes de temperatura e de flutuações, se o escoamento é turbulento. É o caso na saída de um reator nuclear ou em algumas regiões, onde o escoamento apresenta temperaturas diferentes do meio em questão. Tais flutuações de temperatura solicitam as estruturas e podem criar uma fadiga térmica dos materiais. Logo, é importante conhecer tais flutuações térmicas na origem desse fenômeno.

A fim de determinar as flutuações de temperatura, construiu-se um modelo baseado na equação diferencial exata de transporte para essas flutuações. Para a modelagem dessa equação, a hipótese de grandes valores do número de Reynolds e Peclet é utilizada: os efeitos moleculares são desprezados em relação aos efeitos de inércia. Dois termos devem ser modelados: termo de difusão devido à convecção turbulenta e o termo de dissipação. Nesse modelo a relação (R) entre os tempos de decaimento das turbulências mecânica e térmica é empregado para obter a taxa de dissipação da flutuação de temperatura.

O modelo é validado inicialmente sobre uma configuração que corresponde a um escoamento atrás de uma grelha. Os resultados do cálculo são comparados com as medidas de [5] e [9]. Apresenta-se também uma análise da sensibilidade do fator R sobre as flutuações de temperatura, para o caso de um jato axi-simétrico turbulento de ar aquecido. Os resultados são comparados com as medidas fornecidas em [10].

EQUAÇÕES DE TRANSPORTE DAS GRANDEZAS MÉDIAS

Hipóteses. O fluido é considerado incompressível e newtoniano. As propriedades físicas viscosidade, condutividade térmica e calor específico são consideradas constantes. Quanto à densidade prevê-se sua dependência da temperatura a partir do desenvolvimento de primeira ordem:

$$\rho(T) = \rho(T^O) + \frac{\partial \rho}{\partial T}(T-T^O) \qquad (1)$$

As variações da densidade são levadas em conta só mente no termo de forças de volume da equação de quantidade de movimento. O conjunto dessas hipóteses constitui a aproximação de Boussinesq.

Para o tratamento do escoamento turbulento utiliza-se a decomposição de Reynolds, que iguala as variáveis aleatórias à soma de um valor médio e um valor flutuante em torno dessa média:

$$\phi = \overline{\phi} + \phi' \qquad (2)$$

Essa decomposição é aplicada para as variáveis velocidade, pressão e temperatura nas equações locais instantâneas. Obtêm-se assim as seguintes equações de conservação para as grandezas médias.

Conservação da massa:

$$\frac{\partial \overline{U}_i}{\partial x_i} = 0 \qquad (3)$$

Conservação da quantidade de movimento:

$$\frac{\partial \overline{U}_i}{\partial t} + \frac{\partial}{\partial x_j}(\overline{U_j U_i}) = -\frac{\partial \overline{P}^*}{\partial x_i} + \frac{\partial}{\partial x_j}\left(\nu \frac{\partial \overline{U}_i}{\partial x_j} - \overline{u_i u_j}\right) + -g_i \beta \overline{T} \qquad (4)$$

onde: $\overline{P}^* = \frac{\overline{P}}{\rho^O} - \vec{g}\,\vec{OM}\,(\beta \overline{T^O} + 1)$ e M é o ponto corrente do domínio estudado.

Conservação de Energia:

$$\frac{\partial \overline{T}}{\partial t} + \frac{\partial}{\partial x_i}(\overline{U_i T}) = \frac{\partial}{\partial x_i}\left(\alpha \frac{\partial \overline{T}}{\partial x_i} - \overline{u_i \theta}\right) \qquad (5)$$

Esse sistema de equações apresenta duas novas incógnitas, que são os momentos de segunda ordem, o tensor de Reynolds ($\overline{u_i u_j}$) e o fluxo de calor turbulento ($\overline{u_i \theta}$).

MODELO DE TURBULÊNCIA

Hidrodinâmica. Para a determinação do tensor de Reynolds, utiliza-se a hipótese da viscosidade

turbulenta (ν_t).

$$-\overline{u_i u_j} = \nu_t D - \frac{2}{3} k \delta_{ij} \qquad (6)$$

onde D é o tensor de deformação. A viscosidade turbulenta é determinada a partir do modelo k-ε:

$$\nu_t = C_\mu \frac{k^2}{\varepsilon}, \text{ onde } C_\mu = 0.09 \qquad (7)$$

As equações para k (energia cinética de turbulência e ε (taxa de disspação da energia cinética de turbulência) podem ser encontradas em [1].

Térmica. O fluxo de calor turbulento é determinado utilizando-se a hipótese de uma difusividade térmica turbulenta (α_t):

$$\overline{u_i \theta} = -\alpha_t \frac{\partial \overline{T}}{\partial x_i}, \text{ onde } \alpha_t = \frac{\nu_t}{Pr_t} \qquad (8)$$

A difusividade térmica turbulenta fica determinada com a escolha de um número de Prandtl turbulento constante. Geralmente Pr_t=0.9 é empregado.

Equação da flutuação de temperatura:

A equação para a variância da flutuação de temperatura é obtida a partir da equação da energia, com a decomposição de Reynolds, pela diferença entre as formas instantânea e média:

$$\frac{\overline{D\theta^2}}{Dt} = \frac{\partial}{\partial x_j}\left(\alpha \frac{\partial \overline{\theta^2}}{\partial x_j} - \overline{u_j \theta^2}\right) - 2\overline{u_j \theta} \frac{\partial \overline{T}}{\partial x_j} - 2\alpha \frac{\overline{\partial \theta}}{\partial x_j}\frac{\overline{\partial \theta}}{\partial x_j} \qquad (9)$$

-1- -2- -3- $-P_\theta-$ $-\varepsilon_\theta-$

Significado físico dos termos:

-1- Termo transiente e convectivo do campo de velocidade média
-2- Difusão molecular
-3- Difusão devida à convecção turbulenta
$-P_\theta-$ Produção pelo gradiente de temperatura média
$-\varepsilon_\theta-$ Dissipação das flutuações de temperatura

Como a hipótese de grandes valores de números de Reynolds é utilizado, o termo de difusão molecular pode ser desprezado [2]. O termo de difusão devida a convecção turbulenta é modelado a partir da lei do tipo primeiro gradiente:

$$-\overline{u_j \theta^2} = C_\theta \frac{k^2}{\varepsilon} \frac{\partial \theta^2}{\partial x_j} \qquad (10)$$

Os valores de C_θ empregados são:

AUTORES	C_θ
Spalding [3]	0.13
Lemos [4]	0.10

Com as hipóteses acima, a equação para a variância da flutuação de temperatura se reduz a:

$$\frac{\overline{D\theta^2}}{Dt} = \frac{\partial}{\partial x_j}\left(C_\theta \frac{k^2}{\varepsilon} \frac{\overline{\partial^2}}{\partial x_j}\right) - 2\overline{u_j \theta} \frac{\partial \overline{T}}{\partial x_j} - \varepsilon_\theta \qquad (11)$$

O termo de dissipação é geralmente modelado a partir da relação entre o tempo de decaimento da turbulência térmica e o tempo de decaimento da turbulência hidrodinâmica. Por definição essa relação se exprime por:

$$R = \frac{\tau_\theta}{\tau} = \frac{\overline{\theta^2}}{2\varepsilon_\theta} \frac{\varepsilon}{k} \qquad (12)$$

Vários autores trabalham na determinação do fator R a partir de experiências de grelha. Em [5] encontra-se uma revisão das medidas existentes para uma turbulência de grelha aquecida, e alguns valores medidos pelos próprios autores. Eles mostram que os valores de R podem variar de 0.4 a 1.6 para os casos estudados.

Nos trabalhos de modelagem da equação da flutuação de temperatura, a fim de determinar a taxa de dissipação, encontra-se os seguintes valores utilizados para R:

. Ljuboja & Rodi [6] utilizam R=0.8 para calcular um jato turbulento sobre uma parede.
. Pimont [7] trabalha com R=0.5 para o cálculo de um escoamento de sódio líquido dentro de um tubo aquecido com fluxo de calor constante.

TRATAMENTO NUMÉRICO

O método dos volumes finitos é empregado na discretização espacial. As equações de conservação são integradas sobre um volume de controle, depois o teorema de Gauss é utilizado para a transformação das integrais de volume em integrais de superfície. Todas as grandezas escalares são tratadas no centro dos volumes, as grandezas vetoriais são localizadas no centro das faces do volume, essa escolha constitui a abordagem da malha entrelaçada. As equações são discretizadas no tempo na forma semi-implícita. Esse método é derivado do método SOLA desenvolvido por HIRT, NICHOLS e ROMERO [8].

RESULTADOS E COMENTÁRIOS

O modelo desenvolvido é utilizado para três configurações:

a) escoamento de ar isotérmico atrás de uma grelha;
b) escoamento de ar atrás de uma grelha com gradiente de temperatura;
c) jato axi-simétrico turbulento de ar.

A primeira configuração, utiliza uma grelha com passo B=2,54 cm colocada no interior de um túnel de vento vertical. A secção de teste tem um comprimento de 16,7B e uma área de 16Bx16B. A velocidade média do ar é de 6,5 m/s. O número de Reynolds baseado no passo da grelha é 10.000. A porosidade da grelha é 0,66, constituída de barras quadradas de 0,476 x 0,476 cm. Entre as várias medidas apresentadas em [5], dois casos são utilizados para comparação com o modelo. O primeiro caso com uma média do ar de 300 K e o segundo com uma temperatura de 308 K.

Essa configuração permitiu validar o modelo para uma situação isotérmica (temperatura média constante). Os resultados dos cálculos são comparados com as medidas de flutuação de temperatura na figura 1. A ausência de gradiente de temperatura, permite validar o modelo para o caso onde somente os termos de transporte e dissipação são considerados na equação (11) da variância de flutuação de temperatura. Os valores do fator R utilizados no modelo são fornecidos pelas medidas experimentais.

Para a segunda configuração (b), Sirivat & Warhaft [9] utilizaram a mesma geometria da experiência anterior. Para efeito de comparação entre o cálculo e as medidas, foi selecionado o ensaio com velocidade do ar de 3,4 m/s (número de Reynolds de 5200) e gradiente de temperatura de 8,1° C/m.

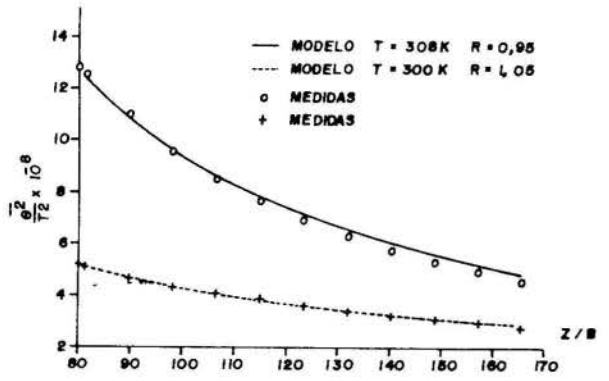

Fig. 1. Comparação entre cálculo e medidas da evolução da variância de flutuação de temperatura. Grelha isotérmica.

A figura 2 mostra os resultados obtidos com a equação (11), utilizando o fator R=0,8 e o número de Prandtl turbulento Prt=0,35, obtidos experimentalmente para essa configuração [9]. Nessa experiência todos os termos da equação (11) da flutuação de temperatura, convecção, difusão, dissipação e produção devido ao gradiente de temperatura são importantes.

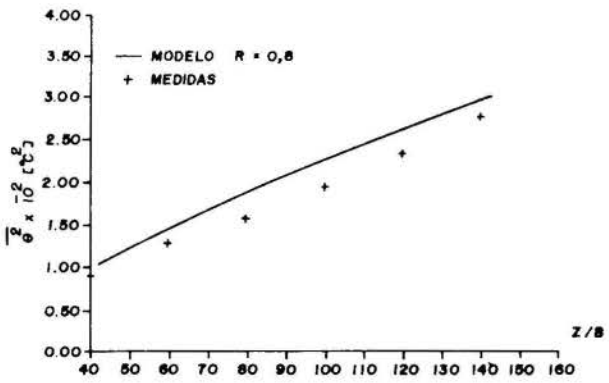

Fig. 2 Comparação entre cálculo e medidas da flutuação de temperatura. Grelha com gradiente térmico.

A figura 3 ilustra a terceira configuração estudada, jato axi-simétrico turbulento de ar. Essa configuração é constituída por um jato anular de diâmetro interno

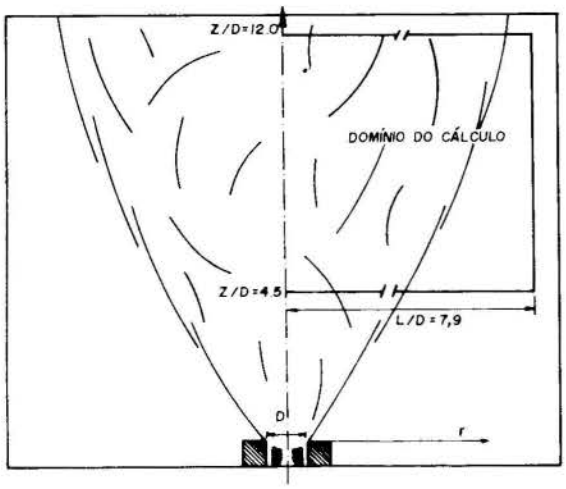

Fig. 3 Jato axi-simétrico turbulento de ar. Domínio de cálculo.

d=18,3mm e diâmetro externo D=25,3mm. O jato sai do conduto anular com uma vazão de 15 m^3/h (número de Reynolds=8.200). O conduto é ligeiramente aquecido através de resistências elétricas, a fim de aquecer o jato. A diferença máxima de temperatura entre o jato e o ambiente é de 22K. esta experiência, relatada em [10], fornece medidas de perfil de velocidade, temperatura e flutuações de temperatura em várias secções transversais.

O domínio de cálculo é situado entre uma distância de Z/D=4,5 e Z/D=12. A largura do domínio é de L/D=7,9. Esse domínio está mostrado na figura 3.

Os resultados mostrados nas figuras 4 e 5 são referentes às comparações entre cálculo e medidas dos perfis de flutuação de temperatura, em duas secções Z/D=8 e Z/D=11 respectivamente. Nessas figuras mostra-se a influência do fator R sobre o nível de flutuação de temperatura. Nota-se que a medida que os valores de R aumentam, mais os valores calculados se distanciam dos valores medidos para a flutuação de temperatura. Os valores de $\overline{\theta^2}$ aumentam quando R aumenta, pois R é inversamente proporcional à taxa de dissipação da flutuação de temperatura. Para essa configuração não existem valores de R medidos para comparação com os valores utilizados no cálculo. Os resultados do modelo utilizado mostram que o valor de R=0,3 fornece um acordo satisfatório com as medidas de flutuação de temperatura.

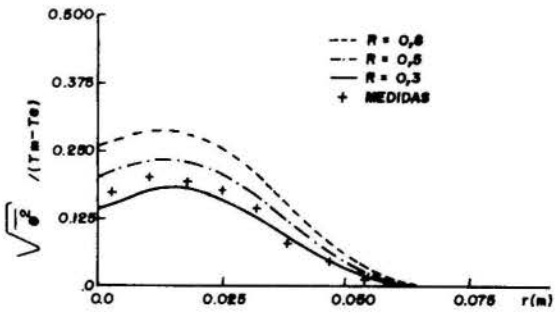

Fig. 4 Comparação entre cálculo e medidas para o perfil de flutuação de temperatura e influência do fator R.
Jato axi-simétrico turbulento de ar (Z/D=8).

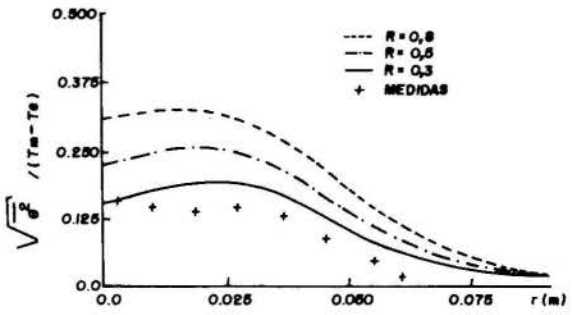

Fig. 5 Comparação entre cálculo e medidas para o perfil de flutuação de temperatura e influência do fator R.
Jato axi-simétrico turbulento de ar (Z/D=11).

Os valores das condições limites empregadas, as malhas utilizadas, bem como uma comparação com outros perfis para velocidade, temperaturas e diversas grandezas turbulentas são fornecidos em detalhes em [11].

CONCLUSÕES

Os resultados apresentados permitem tirar as

conclusões seguintes:

O bom acordo entre os cálculos e as medidas, para a flutuação de temperatura, obtidos com esse modelo depende essencialmente dos valores utilizados para o fator R.

No caso de jato de ar turbulento, o valor de R obtido numericamente (0,3) não foi ainda verificado experimentalmente.

Nas duas configurações de grelha estudadas, os valores de R utilizados são fornecidos pelas experiências. O emprego desses valores no modelo fornecem um bom resultado, validando assim o modelo para aplicações em turbulência de grelha isotérmica e com gradiente de temperatura.

REFERÊNCIAS

[1] Rodi, W., "Turbulence models and their application in hydraulics - A state of the art review", SFB 80/T/127, Universidade de Karlsruhe, Germain, 1978.

[2] Tennekes, H. and Lumeley, J.L., A first course in turbulence", MIT - Press Cambridge, 1977.

[3] Spalding, D.B., Concentration fluctuation in a round turbulent free jet", Chem. Eng. Science, Vol. 26, pp. 95-107, 1971.

[4] Lemos, M.J.S. and Sesonske, A., "Turbulence in combined convection in mercury pipe flow", I.J.H. and Mass Transfer, Vol. 28, pp. 1067-1088, 1985.

[5] Warhaft, Z. and Lumeley, J.L., "An experimental study of decay of temperature fluctuations in grid generated turbulence", J.Fluid Mech., Vol. 88, pp. 659-684, 1978.

[6] Ljuboja, M. and Rodi, W., "Prediction of horizontal and vertical turbulent buoyant wall jets", J. of Heat Transfer, Vol. 103, pp. 343-349, 1981.

[7] Pimont, V., "Étude et modélisation d'écoulements turbulemts de métaux liquides", Thése de Dr. Ingénieur, École Centrale des Arts et Manufactures, Paris, 1983.

[8] Hirt, C.W., Nichols, B.D. and Romero, N.C., "SOLA - Numerical Solution Algorithm for Transient Fluid Flow", Los Alamos Scientific Laboratory, Report LA-5852, 1975.

[9] Sirivat, A. and Warhaft, Z., "The effect of a passive cross-stream temperature gradient on the evolution of temperature variance and heat flux in grid turbulence", J. Fluid Mech., Vol. 128, pp. 323-346, 1982.

[10] Bahraouri, E.M. et Fulachier, L., "Quelques résultas sur un jet turbulent axisymetrique fortement chauffé", Journées d'Etudes, Institut de Mecanique Statistique de la Turbulence, 1985.

[11] Cruz, G.M.M., "Modélisation des écoulements turbulents avec transferts thermiques en convection mixte", Thèse de Doctorat, Ecole Centrale de Lyon, 1989.

ABSTRACT

A model for the variance temperature fluctuation equation is presented for turbulent flows with Reynolds and Peclet numbers ranging from 5000 to 10000.

The dissipation rate of temperature fluctuation is obtained by using the ratio of time scales of turbulent temperature and velocity fields (factor R).

The model is tested against experimental data from turbulent flow below a grid. A sensibility analysis of the factor R is performed for fairly hot axisymmetrical air jets.

III ENCIT – Itapema, SC (Dezembro 1990)

BUSCA DE UMA FORMULAÇÃO UNIFICADA PARA O PROBLEMA DE TRANSFERÊNCIA DE GRANDEZAS FÍSICAS EM ESCOAMENTOS TURBULENTOS

HARRY EDMAR SCHULZ
Departamento de Hidráulica e Saneamento da Escola de Engenharia de São Carlos, Universidade de São Paulo
Av. Dr. Carlos Botelho, 1465, CEP. 13560 - S. Carlos - SP, BR

RESUMO

Equações são desenvolvidas com base em modelos físicos (ou conceituais) que consideram o movimento de um turbilhão no meio líquido. Obteve-se uma formulação para a transferência de grandezas físicas em escoamentos turbulentos que reproduz resultados observados experimentalmente. As equações são apresentadas na forma de um conjunto de duas equações diferenciais, sendo que o desenvolvimento das mesmas segue os padrões usualmente encontrados em abordagens termodinâmicas de processos físicos.

INTRODUÇÃO

A quantificação da transferência de grandezas físicas em escoamentos turbulentos, como massa, calor, ou quantidade de movimento (grandezas comumente estudadas em fenômenos de transporte) segue, usualmente, procedimentos de análise dimensional nos quais algumas grandezas convenientemente definidas (coeficientes de transferência, escala de velocidade, escalas geométricas) são agrupadas em números adimensionais que são posteriormente relacionados entre si. Esta forma de análise produz excelentes resultados, os quais são utilizados nas mais diferentes aplicações.

Surgem, contudo, diferentes análises para diferentes experimentos (por exemplo, formas distintas de gerar turbulência podem ser utilizadas) e percebe-se que a mera correlação entre adimensionais não produz necessariamente um aprofundamento do conhecimento físico dos processos de troca em meios turbulentos. Não se possui, ainda, um único equacionamento básico que possa ser aplicado às diferentes condições experimentais e que forneça informações acerca da transferência de massa, calor e quantidade de movimento em meios turbulentos.

O presente artigo apresenta uma primeira proposta de formulação que visa reunir as informações mencionadas acima. A análise, apresentada em detalhes, conduz a um conjunto de equações que resume algumas observações sobre troca de grandezas físicas encontradas na literatura. A transferência de massa é inicialmente abordada (dissolução de sólido), sendo posteriormente associada à transferência de calor. Utiliza-se um modelo conceitual de escoamento em tubo (ligado à troca de quantidade de movimento) que leva a relações que envolvem os três mecanismos de troca. A análise segue aquelas de Schulz (1985, 1989, 1990a, 1990b) nas quais a dissipação de energia foi considerado o parâmetro fluidodinâmico fundamental.

DESENVOLVIMENTOS ANALÍTICOS

Considerações Gerais. As expressões que quantificavam a transferência de grandezas físicas em escoamentos turbulentos utilizam, usualmente, uma forma do número de Reynolds convenientemente definida e dois ou mais adimensionais associados à grandeza física propriamente dita. Observa-se que situações geométricas semelhantes conduzem também a expressões adimensionais semelhantes, o que sugere o uso de analogias entre processos de troca para determinar um parâmetro desconhecido ou cuja medida seja difícil. Analogias como as de Reynolds, von Karman e de Prandtl-Taylor podem ser encontradas na literatura (ver Arpaci & Larsen (1984), por exemplo) sendo seu uso bastante generalizado.

O fato de as expressões mencionadas estarem vinculadas a geometrias consideradas estabelecidas "a priori" (placa plana, esfera, tubo) limita a sua aplicação e levanta a questão da possibilidade de haver um equacionamento mais geral, no qual as condições geométricas não são relevantes para a análise dos fenômenos de transferência. Uma análise neste sentido é apresentada a seguir, na qual sugere-se que as informações acerca da geometria sejam inseridas apenas após o desenvolvimento das equações.

Análise da Dissolução de um Sólido Solúvel. Parte-se de um caso de transporte de massa no qual não são definidos nem a direção preferencial do escoamento turbulento nem a forma geométrica do volume que contém o fluido escoando. Considera-se o processo de dissolução unidimensional de um sólido, sugerido por Schulz & Giorgetti (1987). Neste caso tem-se:

$$dh/dt = -v \qquad (1)$$

$$M/Mo = 1 - vt/ho \qquad (2)$$

h e M são a espessura e a massa instantâneas do sólido, sendo ho e Mo as espessura e massa iniciais, v é o parâmetro que descreve a dissolução do sólido, denominado de velocidade de desgaste (v é uma forma de exprimir a velocidade da reação de dissolução), t é a variável tempo. A figura 1 mostra o processo de dissolução considerado.

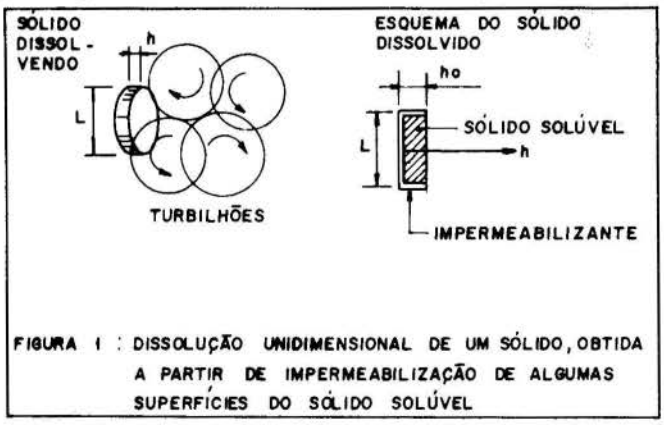

FIGURA 1 : DISSOLUÇÃO UNIDIMENSIONAL DE UM SÓLIDO, OBTIDA A PARTIR DE IMPERMEABILIZAÇÃO DE ALGUMAS SUPERFÍCIES DO SÓLIDO SOLÚVEL

Não havendo limites geométricos estabelecidos, não é possível definir escalas de velocidades a partir desses limites. Trabalhou-se, então, com os elementos de fluido que apresentam movimentos relativos entre si e que atuam no processo de dissolução. Considerou-se um turbilhão de volume $\forall$ e estabeleceu-se uma primeira relação entre este volume e grandezas mensuráveis externamente a todo o sistema. Estudos anteriores na área de absorção de gases por líquidos (Schulz (1985,1989,1990a)) que se basearam nos desenvolvimentos de Corrsin (1964) para misturadores isotrópicos, mostraram que a potência consumida por unidade de volume pode ser considerada um parâmetro fundamental na quantificação da taxa de absorção do gás. Este parâmetro foi utilizado juntamente com o volume do turbilhão na forma:

$$\dot{U} = \dot{u} \cdot \forall \qquad (3)$$

$$d\dot{U} = \dot{u} d\forall + \forall\, d\dot{u} \qquad (4)$$

$\dot{U}$ é a potência total dissipada no turbilhão.

O problema fundamental é relacionar o parâmetro que quantifica a dissolução do sólido v, com as grandezas $\dot{u}$ e $\forall$. Sugeriu-se que é possível estabelecer uma função do tipo

$$\phi' = \phi'(v, \dot{u}, \forall) \qquad (5)$$

que relaciona de forma conveniente as variáveis em questão. A função ϕ' não possui, evidentemente, sentido físico estabelecido. Como introdução ao equacionamento seguido, arbitrou-se a forma

$$d\phi' = (\alpha v^{\beta})\, \dot{u}\, d\forall + (\gamma\, v^{\delta})\, \forall\, d\dot{u} \qquad (6)$$

As razões que levaram a este arbítrio foram:

- A expressão 6 é suficientemente próxima de outra com significado físico claro (equação 4).
- A expressão 6 permite, através de variações nas constantes α, β, γ e δ, arbitrar diferentes pesos para cada parcela e diferentes influências da velocidade de desgaste nessas parcelas.

Evidentemente outras formas para ϕ' podem ser sugeridas.

Simplificações algébricas conduzem rapidamente a:

$$d\phi = (\tau\, v^{\beta})\, \dot{u}\, d\forall + v^{\delta}\, \forall\, d\dot{u} \qquad (7)$$

Onde $d\phi = d\phi'/\gamma$ e $\tau = \alpha/\gamma$

Davies (1972) relata resultados de diferentes fontes e apresenta um desenvolvimento adimensional no qual se admite que a escala de turbilhões importante para a descrição do fenômeno deve ser da ordem de grandeza do sólido em dissolução. Posteriormente, a partir dos resultados experimentais, verifica que a dissolução independe da dimensão do sólido. Esta observação é aqui introduzida considerando uma relação bi-unívoca entre $\dot{u}$ e v.

$$v = v(\dot{u}) \qquad e \qquad \dot{u} = \dot{u}(v)$$

$$d\dot{u} = (d\dot{u}/dv)\, dv \qquad (8)$$

Unindo 7 e 8 tem-se

$$d\phi = (\tau\, v^{\beta})\, \dot{u}\, d\forall + v^{\delta}\, \forall\, (d\dot{u}/dv)\, dv \qquad (9)$$

A variável ϕ, sem significado físico estabelecido, representa um problema na análise objetiva do fenômeno. Para transpor esta dificuldade efetuou-se a análise da derivada segunda da expressão 9, obtendo:

$$[\partial\phi/\partial\forall]_{v} = \tau v^{\beta}\dot{u}, \qquad [\partial\phi/\partial v]_{\forall} = v^{\delta}\forall(d\dot{u}/dv)$$

$$[\partial^2\phi/\partial v\partial\forall] = \dot{u}\tau\beta v^{\beta-1} + \tau v^{\beta}(\partial\dot{u}/\partial v)$$

$$[\partial^2\phi/\partial\forall\partial v] = v^{\delta}\,(\partial\dot{u}/\partial v)$$

As variáveis colocadas em índice são mantidas constantes na operação indicada entre colchete. Igualando as duas derivadas segundas e lembrando que $\dot{u} = \dot{u}(v)$, tem-se, após algumas manipulações:

$$d\dot{u}/\dot{u} = \{[\tau\beta v^{\beta-1}]/[v^{\delta} - \tau v^{\beta}]\}dv \qquad (10)$$

A expressão 10 não produz uma relação utilizável entre $\dot{u}$ e v, uma vez que três constantes, remanescentes da expressão inicial arbitrada, são desconhecidas. Procurou-se, então, diminuir o número de graus de liberdade através de considerações físicas acerca do escoamento de um turbilhão no meio líquido. Admitiu-se, neste estágio do desenvolvimento, que a ordem de grandeza do turbilhão seja tal que contenha a maior parte do espectro de energia correspondente às escalas de dissipação. Desta forma, ao haver um deslocamento deste turbilhão no meio líquido, há também uma dissipação de energia em seu interior, a qual foi equacionada, de forma aproximada, a partir de uma analogia com escoamento em tubos. Ao longo do tempo em que um turbilhão se desloca sem perder a sua individualidade, pode-se estabelecer um perfil de velocidade que evolui em seu interior a partir das fronteiras do mesmo. Essas fronteiras são entendidas como superfícies de velocidade nula que separam movimentos em direções opostas. Portanto durante um certo intervalo de tempo é possível entender o movimento turbilhonar como o movimento no interior de um "tubo" cuja área varia. Frisa-se que este é um modelo físico aproximado. O esquema da Figura 2 elucida a analogia.

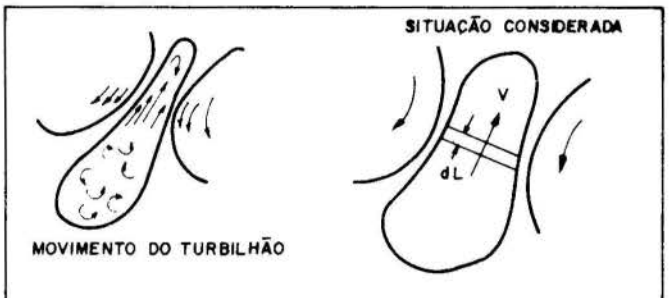

FIGURA 2 : HIPÓTESE DO ESCOAMENTO EM TUBO DO TURBILHÃO, COM PAREDES DO "TUBO" CORRESPONDENDO ÀS SUPERFÍCIES DE VELOCIDADE NULA

Utilizando a fórmula de Darcy-Weisbach para escoamentos em tubos, tem-se:

$$dhp = fV^2\, dL/2gD \qquad d\dot{U} = \rho g\, Q\, dhp$$

hp é a perda de carga (m), f é o fator de atrito, L e o comprimento do tubo (m) e D é o seu diâmetro (m), V e a velocidade na seção (m/s) Q é a vazão escoando (m^3/s) ρ é a massa especifica do líquido (kg/m^3), g é a aceleração da gravidade (m/s^2) e $\dot{U}$ é a potência dissipada (W).

Para o turbilhão pode-se fazer:

$$\dot{U} = \int d\dot{U} = \int(\rho g V^3\, fA\, dL)/(2gD) = (\rho f/2)\int_{\forall}(V^3/D)d\forall \qquad (11)$$

$d\forall = AdL$, onde A e a área da seção considerada.

Nesta primeira análise considerou-se a agitação

turbulenta suficientemente intensa para que f seja constante. O diâmetro D do turbilhão não é conhecido, mas relacionou-se este diâmetro com o volume $\mathcal{V}$ na forma:

$$D \alpha \mathcal{V}^{1/3} \quad \text{ou seja} \quad D = w\ \mathcal{V}^{1/3} \qquad (12)$$

A união de 11 e 12 produz:

$$\dot{U} = (X/\mathcal{V}^{1/3}) \int_{\mathcal{V}} V^3\ d\mathcal{V} \qquad (13)$$

w e X são constantes (X envolve a massa específica do líquido. Desta forma, a rigor, X é constante em se mantando constante a temperatura).

Obtém-se $\dot{u}$ dividindo 13 pelo volume $\mathcal{V}$. Extraindo o logaritmo da expressão resultante, diferenciando-a, e multiplicando-a por $\dot{U} = \dot{u}.\mathcal{V}$ tem-se:

$$\dot{U}\ d\{\ell n\ [\int_{\mathcal{V}} V^3\ d\mathcal{V}]\} = (4/3)\ \dot{u}\ d\mathcal{V} + \mathcal{V}\ d\dot{u} \qquad (14a)$$

Ou

$$d\psi = \dot{U}\ d\{\ell n[\int_{\mathcal{V}} V^3\ d\mathcal{V}]\} \qquad (14b)$$

$$d\psi = (4/3)\ \dot{u}\ d\mathcal{V} + \mathcal{V}\ d\dot{u} \qquad (14c)$$

As expressões 14 estão relacionadas com a dissipação de energia que ocorre em um turbilhão e são "semelhantes" à equação 9. Para que esta última "englobe" a informação gerada com as equações 14, sem perder os pesos relativos das parcelas que aparecem na expressão 14c, é preciso que os expoentes da velocidade de desgaste v sejam os mesmos ($\beta=\delta$) e que $\tau = 4/3$. Assim:

$$d\phi = (4/3)\ v^{\beta}\ \dot{u}\ d\mathcal{V} + v^{\beta}\ \mathcal{V}\ d\dot{u} \qquad (15)$$

Evidentemente $d\phi = v^{\beta}\ d\psi$. Na expressão 14b a função $d\phi$ é definida por

$$d\phi = v^{\beta}\ \dot{U}\ d\{\ell n\ [\int_{\mathcal{V}} V^3\ d\mathcal{V}]\} \qquad (16)$$

Verifica-se que todas as grandezas envolvidas na definição 16 têm sentido físico claro. A análise feita, portanto, permitiu relacionar a função ϕ com parâmetros conhecidos e diminuiu sensivelmente os graus de liberdade existentes na equação original.

Com os graus de liberdade iniciais até o momento já avaliados é possível simplificar a expressão 10 e integrá-la. Tem-se, então:

$$\dot{u} = a.v^{-4\beta} \quad \text{e} \quad v = b.\dot{u}^{-1/(4\beta)} \qquad (17 \text{ e } 18)$$

a e b são constantes de integração. β é o único parâmetro inicialmente arbitrado que permanece sem avaliação numérica. Conclui-se, contudo, que a velocidade de desgaste (velocidade de reação) pode ser expressa como uma potência da taxa de dissipação de energia, independente do valor de β.

Unificação das Informações Acerca de Transferência

As expressões 1 e 2 foram desenvolvidas considerando a evolução da fase sólida no processo de dissolução. Se a fase líquida for considerada, pode-se utilizar a expressão usual de transferência, na forma:

$$\dot{M} = Km.Ac.(C_s - C) \qquad (19)$$

$\dot{M}$ é a descarga de massa que entra no meio líquido, Ac é a área de contato entre sólido e líquido, C é a concentração de sólido dissolvido no meio líquido, sendo C_s a sua concentração de saturação. Km é o coeficiente de transferência de massa.

A expressão 2, quando rearranjada para exprimir a descarga de massa produz:

$$\dot{M} = v.Ac.\rho m \qquad (20)$$

ρm é a massa específica do sólido.

Em processos de dissolução nos quais o volume de água é grande em relação à massa a ser dissolvida, pode-se admitir C constante e igual a zero. Desta forma, de 19 e 20 obtém-se:

$$v/Km = C_s/\rho m \qquad (21)$$

Como nem C_s e nem ρm dependem da agitação no meio (dependem apenas da temperatura de trabalho), pode-se dizer que, mantida a temperatura constante, v é sempre proporcional a Km, Proporcionalidades similares podem ser obtidas entre os coeficientes de transferência de massa (Km) e de calor (Kc) em geometrias semelhantes. Por exemplo, para escoamentos em camadas limites laminares, tem-se:

$$Nu = 0{,}664\ Re_L^{1/2}\ Pr^{1/3} \quad \text{e} \quad Sh = 0{,}664\ Re_L^{1/2}\ Sc^{1/3} \qquad (22)$$

Nu, Pr, Sh, Sc e Re_L são, respectivamente, os números de Nusselt, Prandtl, Sherwood, Schmidt e Reynolds, este último associado à dimensão L do escoamento. A primeira equação está relacionada com o transporte de calor enquanto a segunda está relacionada com o transporte de massa. Percebe-se, dada a semelhança das expressões, que Km α Kc para transferências ocorrendo em um mesmo meio, sob as mesmas condições de agitação e mantendo a temperatura constante. ($Km = Sh.Dm/L$ e $Kc = Nu.K/L$, onde Dm é a difusividade molecular do soluto no solvente e K é a condutividade térmica do meio). Como conclusão, Km α Kc α v.

Schulz (1990a) analisou a dissolução para as situações de turbilhões maiores e turbilhões menores que a dimensão L do sólido imerso no meio líquido. Na presente análise está-se considerando apenas o caso de turbilhões menores que a dimensão L.

A situação de escoamento junto ao sólido foi analisada considerando a escala dos turbilhões (D) envolvidos no processo e a sua velocidade característica. Uma medida desta velocidade é a intensidade turbulenta u'. A Figura 3 apresenta um esquema do escoamento não preferencial existente e a situação de estudo.

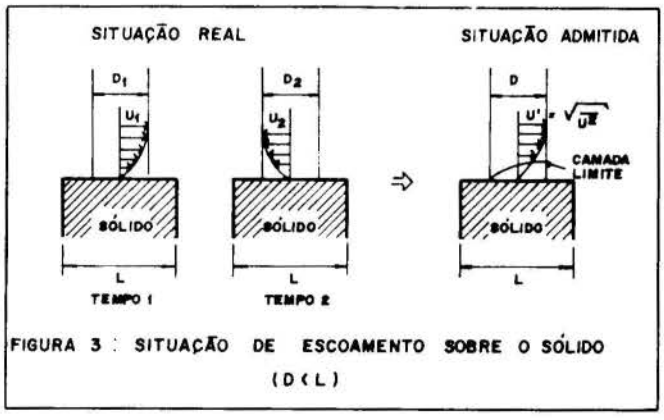

FIGURA 3 : SITUAÇÃO DE ESCOAMENTO SOBRE O SÓLIDO (D < L)

Admitindo que a camada limite que se forma durante a evolução de um turbilhão sobre o sólido seja de natureza viscosa (muito embora o escoamento como um todo seja turbulento) e utilizando o equacionamento para camadas limites laminares ao longo de cada evolução (equações 22), a quantificação de Km pode ser feita:

$$Km = 0{,}664 \cdot (u' \cdot D/\nu)^{1/2}\ Sc^{1/3}\ Dm/D \qquad (23)$$

Hinze (1959) apresenta conclusões, baseadas em análises dimensionais, relacionando as escalas de velocidade e de comprimento dos turbilhões em faixas distintas do espectro de turbulência com a taxa de dissipação de energia no meio. Essas relações são fornecidas na Figura 4 para uma situação de agitação na qual se estabeleceu uma região de equilíbrio universal.

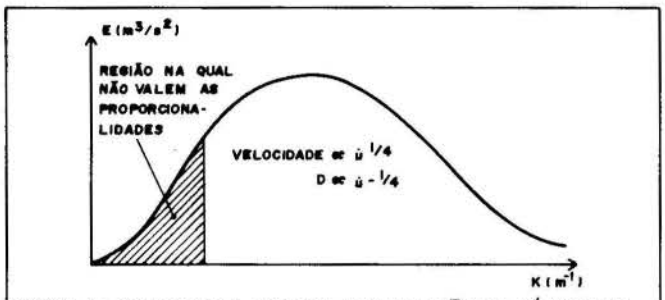

FIGURA 4 : ESPECTRO DE ENERGIA (EM RELAÇÃO AO NÚMERO DE DE ONDAS K) MOSTRANDO AS PROPORCIONALIDADES EXISTENTES PARA VELOCIDADE E ESCALA DOS TURBILHÕES

Verifica-se que a maior parte do espectro apresenta as proporcionalidades:

$$D \alpha \dot{u}^{-1/4} \quad e \quad u' \alpha \dot{u}^{1/4} \qquad (24)$$

Estas proporcionalidades produzem uma dependência para Km em relação a $\dot{u}$ na forma (equação 23):

$$Km \alpha \dot{u}^{1/4} \qquad (25)$$

Uma vez que se concluiu que $Km \alpha Kc \alpha \nu$, tem-se

$$Kc \alpha \dot{u}^{1/4} \quad e \quad \nu \alpha \dot{u}^{1/4} \qquad (26)$$

A informação 26, quando lançada na equação 18, conduz ao resultado $\beta = -1$, o que implica que as equações 15 e 16 adquirem a forma:

$$d\phi = (4/3\nu)\ \dot{u}\ d\forall + (\dot{u}/\nu)\ \forall\ d\dot{u} \qquad (27)$$

$$d\phi = (\dot{U}/\nu)\ d\{\ell n\ [\int_{\forall} V^3\ d\forall]\} \qquad (28)$$

As equações 27 e 28 podem ser desenvolvidas facilmente para a situação isoø (isto é, $d\phi = 0$). Utilizando a equação 17 com $\beta = -1$ na equação 27 obtém-se:

$$d\phi = (4a\nu^3/3)\ d\forall + (4\forall\ \nu^2 a)\ d\nu$$

Para $d\phi = 0$ resulta:

$$d\forall/\forall = -3\ d\nu/\nu$$

Ou seja, integrando a expressão acima:

$$\forall \nu^3 = \text{Constante.} \qquad (29)$$

A equação 28 conduz imediatamente a

$$\int_{\forall} V^3\ d\forall = \text{Constante} \qquad (30)$$

De 29 e 30 tem-se:

$$\nu^3 \alpha (1/\forall) \cdot \int_{\forall} V^3\ d\forall \qquad (31)$$

Isto é, a velocidade de desgaste está relacionada com a velocidade média do turbilhão. É de esperar, portanto, que a intensidade turbulenta e a velocidade de desgaste apresentem comportamentos semelhantes, produzindo $\nu \alpha u'$. Considerando esta proporcionalidade e lembrando que $\forall \alpha D^3$ obtém-se, a partir da equação 29:

$$u'^3\ D^3 = \text{Constante}, \quad \text{ou} \quad u'D = \text{Constante}; \quad \text{ou}$$

$$Re_D = \text{Constante}.$$

Isto é, situações isoø correspondem a situações nas quais o número de Reynolds associado ao turbilhão não varia. Esta conclusão levou em conta que a viscosidade cinemática do fluido mantém-se constante para temperaturas mantidas também constantes. Evidentemente obtém-se desta situação que

$$D \alpha \dot{u}^{-1/4} \quad \text{ou} \quad \forall \alpha \dot{u}^{-3/4} \qquad (33)$$

Discussões Acerca dos Desenvolvimentos. As análises feitas mostraram que as seguintes grandezas associadas a escoamentos turbulentos apresentam relações de proporcionalidade entre si:

$$Km \alpha Kc \alpha \nu \alpha u' \qquad (34)$$

Uma equação que envolva uma dessas variáveis pode também ser expressa a partir de qualquer uma das remanescentes. Desta forma pode-se fazer:

$$d\phi = (4\dot{u}/3x)\ d\forall + (\forall/x)\ d\dot{u} \qquad (35a)$$

$$d\phi = (\dot{U}/x)\ d\{\ell n\ [\int_{\forall} V^3\ d\forall]\} \qquad (35b)$$

x é qualquer das variáveis apresentadas nas relações 34. Segundo as equações 35, todas apresentam comportamento semelhante e da forma $x \alpha \dot{u}^{1/4}$. Para obter as equações 35 foram utilizados resultados das mais diversas formas de abordar o problema da turbulência, desde expressões semi-empíricas, como as equações de Darcy-Weisbach e de transferência de calor e massa em camadas-limite, até resultados relacionados com as escalas de velocidade e comprimento dos diferentes tamanhos de turbilhões que compõe o espectro da turbulência. As expressões 35 resumem essas informações e permitem resgatá-las a partir de operações relativamente simples. Como um exemplo, caso se deseje obter a expressão de perda de carga em um escoamento, a seqüência inversa dos passos que conduziram às expressões 15, com $\beta = -1$, permitem chegar a

$$hp = \text{Constante} \cdot V^2 \cdot L/D$$

Verifica-se que esta expressão vale para fatores de atrito constantes, uma decorrência das simplificações feitas quando do desenvolvimento das expressões 35.

A forma de abordar o problema de dissolução não considerou a geometria do escoamento. Sendo válida a conclusão de que $\beta = -1$, a expressão 18 contém apenas um parâmetro que pode envolver esta geometria, ou seja, a constante de integração b. Como conclusão, alterações geométricas devem poder ser levadas em conta a partir de uma função multiplicadora conveniente. Também não foram considerados efeitos da temperatura. Schulz (1990a) mostrou, a partir do fato de que a velocidade de desgaste é uma medida da velocidade de reação de dissolução, que o efeito da temperatura pode ser descrito através da função de Arrhenius. Evidentemente a influência da temperatura em parâmetros como Kc e u' devem ser melhor estudados. O fato de haver uma semelhança de comportamento para com a agitação turbulenta do meio não implica em semelhança para com variações de temperatura.

Comprovações Experimentais de Diferentes Fontes.

A Figura 5, adaptada de Davies (1972), mostra que dados de diferentes experimentos de transferência de calor e massa podem ser expressos como função da potência dissipada elevada ao expoente 1/4. Os desenvolvimentos descritos por Davies se baseiam em análises dimensionais e os dados estudados são lançados em gráfico na forma adimensional.

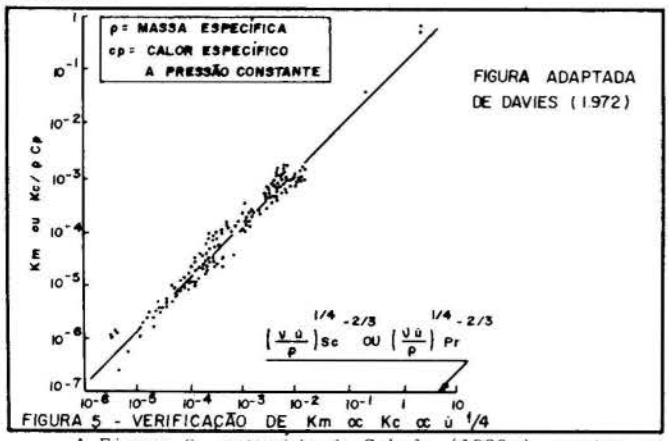

FIGURA 5 - VERIFICAÇÃO DE Km ∝ Kc ∝ $\dot{u}^{1/4}$

A Figura 6, extraída de Schulz (1990a), mostra resultados de dissolução de ácido oxálico em água obtidos em um tanque no qual a agitação era produzida pela rotação de uma hélice. Verifica-se que o comportamento $v \propto \dot{u}^{1/4}$ surge como uma tendência a ser seguida para as maiores agitações. A Figura 7, também extraída de Schulz (1990a), mostra resultados de dissolução de ácido oxálico em água para experimentos realizados em um canal de recirculação de água de 20,0 m de comprimento. Verifica-se, novamente, o comportamento seguindo o expoente 1/4 da potência dissipada. Neste canal a rugosidade do fundo foi variada para observar a influência de alterações geométricas nas expressões em questão. Verificou-se que o seu efeito pode ser incluído na análise a partir de uma função multiplicadora que o expresse convenientemente, o que coincide com as sugestões anteriormente feitas. No presente caso utilizou-se uma potência do diâmetro da rugosidade artificial introduzida.

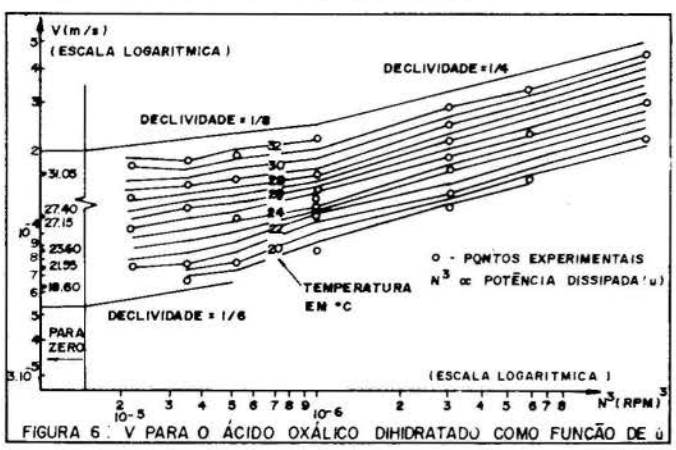

FIGURA 6 - V PARA O ÁCIDO OXÁLICO DIHIDRATADO COMO FUNÇÃO DE $\dot{u}$

CONCLUSÕES

Obteve-se um conjunto de duas equações diferenciais que reproduz comportamentos de coeficientes de transferência de massa e calor observados experimentalmente (equações 35). A análise feita permitiu mostrar que também a evolução das escalas de velocidade e comprimento dos turbilhões em relação à potência dissipada no meio é obtida através dessas equações (as previsões coincidem com aquelas obtidas por razões dimensionais para diferentes regiões do espectro de turbulência). Como o modelo físico de escoamento dos turbilhões utilizou a expressão de Darcy-Weisbach para quantificar a potência dissipada, também a avaliação da perda de carga em um escoamento está embutida nas expressões finais. É interessante notar que a formulação fornece, portanto, informações concernentes a detalhes intrínsecos da turbulência (as escalas mencionadas) e informações "macroscópicas" relacionadas com as conseqüências de haver uma agitação turbulenta no meio (os coeficientes de transferência e a perda de carga).

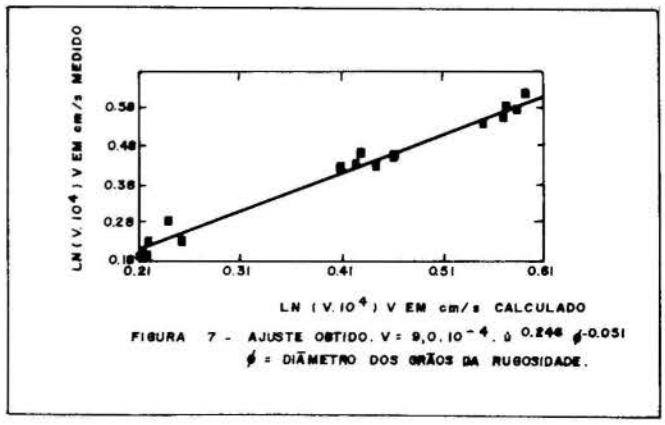

FIGURA 7 - AJUSTE OBTIDO. V = 9,0.10⁻⁴. $\dot{u}^{0.246}$ $\phi^{-0.051}$
ϕ = DIÂMETRO DOS GRÃOS DA RUGOSIDADE.

AGRADECIMENTOS

Ao Centro de Recursos Hídricos e Ecologia Aplicada, (CRHEA-SHS-EESC-USP) pelo espaço físico cedido à parte experimental do trabalho.

Ao CNPq, pelo financiamento da pesquisa.

REFERÊNCIAS BIBLIOGRÁFICAS

[1] Arpaci, V.S. and Larsen, P.S., "Convection Heat Transfer". Prentice-Hall, Inc. New Jersey. 1984.

[2] Davies, J.T., "Turbulence Phenomena". Academic Press. New York. 1972.

[3] Hinze, J.O., "Turbulence". McGraw Hill. New York.1959.

[4] Schulz, H.E., "Investigação do Mecanismo de Reoxigenação da Água em Escoamento e sua Correlação com o Nível de Turbulência junto à Superfície". Dissertação de Mestrado, Escola de Engenharia de São Carlos, Universidade de São Paulo, São Carlos, SP, Brasil, 1985.

[ ] Schulz, H.E., "Modelos Matemáticos para Reoxigenação em Canais de Pequeno Porte com Base na Teoria Estatística da Turbulência". Anais do 4º Simpósio Luso-Brasileiro de Hidráulica e Recursos Hídricos, vol.2, pp. 618-631, Lisboa, Portugal, 1989.

[6] Schulz, H.E., "Investigação do Mecanismo de Reoxigenação da Água em Escoamento e sua Correlação com o Nível de turbulência junto à Superfície". Tese de Doutorado, Escola de Engenharia de São Carlos, Universidade de São Paulo, São Carlos, SP, Brasil,1990a.

[7] Schulz, H.E., "Desenvolvimentos Comparativos para a Quantificação dos Coeficientes de Troca de Massa em Interfaces Sólido-Líquido e Líquido-Gás". Artigo Proposto para apresentação no III Encontro Nacional de Ciências Térmicas, Itapema, SC, Brasil, 1990b.

[8] Schulz, H.E and Giorgetti, M.F., "Medida Indireta do Coeficiente de Reoxigenação de águas Naturais - Modelos Matemáticos para a Velocidade de Desgaste de Sondas Solúveis". Anais do I Simpósio Brasileiro de Transferência de Calor e Matéria, pp. 179-187, Campinas, SP, Brasil, 1987.

[9] Corrsin, S., "The Isotropic Turbulent Mixer: Part II Arbitrary Schmidt Number". A.I.Ch.E. Journal, U.S.A.,

10(6):870-877, november, 1964.

ABSTRACT

Studies based on conceptual models considering the movement of an eddy in a liquid medium led to a formulation for the transfer of physical properties in turbulent flow. This formulation is presented in the form of a set of two differential equations. The approach follows the usual procedures found in the thermodynamics treatments of physical processes. The theoretical results reproduce well the experimental behavior.

III ENCIT – Itapema, SC (Dezembro 1990)

WALL PRESSURE FLUCTUATIONS IN ROD BUNDLES

Sergio Viçosa Möller *)

Programa de Pós-Graduação em Engenharia Mecânica da UFRGS
Rua Sarmento Leite, 425 - 90050 Porto Alegre RS - Brazil

SUMMARY

Microphones and hot wires were applied for the measurement of wall pressure fluctuations and velocity fluctuations in rod bundles with several aspect ratios. By means of auto and cross spectral density functions their interdependence was investigated. Results show that the pressure fluctuations in rod bundles are mainly associated with the phenomenon of quasi-periodic flow pulsations between subchannels.

INTRODUCTION

Pressure fluctuations of the turbulent flow on a channel wall have considerable practical interest, since they influence the boundary layer, produce noise and can induce vibrations on the channel. The fluctuating pressure field in a turbulent flow is a summation of contributions from the turbulent velocity fluctuations. In incompressible flows, the pressure fluctuations are related to the velocity fluctuations through Poisson's equation, obtained from the divergence of the momentum equation [1]

$$\nabla^2 p = - \frac{\partial^2}{\partial x_i \partial x_j} (u_i u_j) \qquad (1)$$

At a given point of the flow field and its boundaries, the pressure fluctuations are produced by momentum fluctuations at many other points of its surrondings. The amplitude of the pressure fluctuations is influenced by velocity fluctuations whithin a distance comparable with the wavelenght of the respective component of the turbulent velocity.

In rod bundles the turbulent flow is governed by the presence of large-scale coherent structures, producing quasi periodic flow pulsations across the gaps [2,3], resulting strongly anisotropic turbulence intensities, which distribution differs considerably from their distribution in pipe flow [4]. This phenomenon of "flow pulsations" between two neighbouring subchannels has a characteristic frequency, which depends on the bundle geometry (P/D, W/D) and the flow velocity, generating a dynamic pressure field on the rods and on the channel wall with the same characteristic frequency of the flow pulsations.

The determination of the pressure field by means of Eq. (1) seems to be very difficult, or even impossible, as the most of the turbulence problems are, due to the stochatic nature of the turbulent flow. Therefore, experimental studies on the pressure and velocity fluctuations in turbulent flows are necessary to obtain additional informations to help the comprehension of these phenomena. Some of the most important experimental works in flat plate, channel and rod bundle flow are listed below.

Measurements of wall pressure fluctuations in a boundary-layer wind tunnel were performed by Bull [5], by means of piezoelectric pressure transducers and using hot wire anemometry for the measurements of velocity fluctuations. His results show that there are two "families" of pressure sources which differently influence the pressure field. The first one is associated with the turbulent motion in the constant stress layer; the other one comprises components which wavelenght is greater than about twice the boundary-layer thickness.

Langeheinecken [6] measured the interdependence betweeen wall-pressure and velocity fluctuations in a pipe flow. His measurements showed that the occurence of high amplitude peaks in the wall pressure are closely connected to the velocity field. The behaviour of the pressure fluctuations were found to be associated with horse shoe turbulence structures on the walls.

In annular channels with three different hydraulical diameters and water as the working fluid, Mulcahy et al. [7] found that the dominant source of excitation pressures were different for the largest and the smallest diameters. In the narrowest channel they were due to developing boundary-layer turbulence created by the transition from a pipe to an anular region, while inthe channel with the largest hydraulical diameter they were more closely associated with fully developed

*) Formerly at the
CNEN - Instituto de Engenharia Nuclear
Rio de Janeiro, Brazil

boundary-layer turbulence.

Wall pressure fluctuations of the turbulent flow of water in a 7-rod bundle were measured by Lin et al. [8]. The test section had a hydraulical diameter D_e = 8.6 mm, but no information about P/D-ratio was given. The measurements were performed on the central rod and on one of the outer rods. On the inner rod they found an homogeneous pressure field which was independent of the circumferencial position, this not being the case for the outer rods of the test section. There, the pressure field was found to be a function of the hydraulical diameter and of the geometry of the channel

The purpose of this paper is to present results of measurements of velocity and wall pressure fluctuations in rod bundles, their mutual relationship and their characteristics as a function of the flow and of the geometry of the bundle.

APPARATUS AND EXPERIMENTAL TECHNIQUE

The experimental set up consists of a 7 m long rectangular channel with four aluminium tubes which simulated the rods. The geometry of the bundle could be changed by displacing one of the short walls or by using tubes with different diameters. The measurements were performed at about 20 mm before the outlet. Air was the working fluid. A schematic of the cross section of the channel is shown in Fig. 1 together with the locations of the measurements described. A list of the geometries investigated is given in Table 1 together with rod and hydraulical diameter, where "a" stands for asymmetrical arrangement of the rods. The experiments were controlled by a PDP 11/23 computer [9], which positioned the probes, performed measurements and kept the Reynolds number constant during an experiment by adjusting the speed of the blower. Velocity and wall shear stresses were measured by means of Pitot and Preston tubes. Turbulent fluctuating velocities were measured by DISA constant temperature anemometers. The probes had one wire perpendicular to the main flow and a 45° slant wire. Brüel & Kjaer capacitive microphones, with 4.5 mm diameter, flush mounted with the wall, were applied for the measurements of wall pressure fluctuations.

Table 1. Main dimensions of the cross section.

W/D	P/D	D_e (mm)	D (mm)	
1.045	1.149	47.29	139.0	
1.071	1.007	44.67	157.5	
1.071	1.017	45.92	157.5	
1.071	1.036	48.11	157.5	
1.072	1.072	52.65	157.5	
1.071	1.100	55.57	157.5	
1.071	1.148	60.85	157.5	
1.147	1.037	59.22	139.0	
1.147	1.147	71.58	139.0	
1.183	1.224	76.10	139.0	
1.072	1.036	42.56	139.0	a
1.223	1.036	76.10	139.0	a

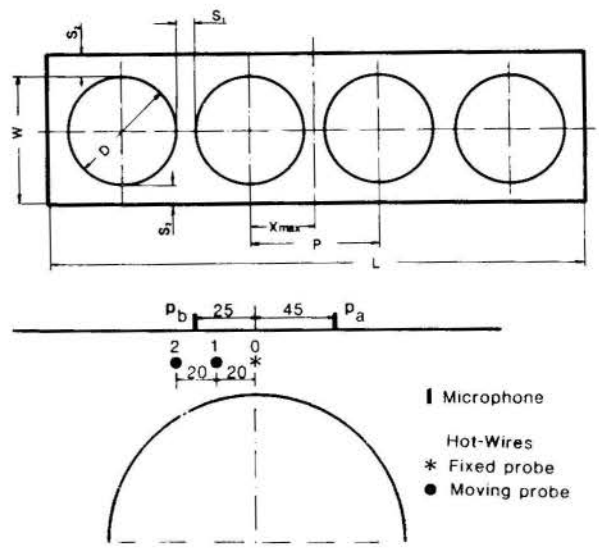

Fig. 1: Schematic of the cross section.

During an experiment the output signals of the hot wires and of the microphones were recorded simultaneously with an analog "FM" tape recorder for spectra and correlation measurements. Afterwards they were digitized and stored on a digital tape for the evaluation of the results on a large IBM computer. The FTFPS subroutine of the IMSL Library [10] was used for the calculation of the spectral functions.

EXPERIMENTAL RESULTS

Velocity Measurements. Figure 2-a and b show the logaritmic velocity profile measured at the channel wall and at the rod wall, respectively, of one subchannel of the rod bundle with P/D=W/D=1.07. The experimental values are compared to Nikuradse's law of the wall for the pipe flow [11].

Auto Spectral Densities. The spectra of two components of the fluctuating velocity in the gap between rod and channel wall are shown in Fig. 3. the spectrum of the axial component is similar to those observed in pipes [12], however, the azimuthal component shows a very pronounced peak at 62.5 Hz. At a location 20 mm from the gap, a peak appears also in the spectrum of the axial component at the same frequency of the azimuthal component. This peak frequency corresponds to the dominant frequency of the flow pulsation for this geometry and Reynolds number.

The spectra of the pressure fluctuations on both sides of the gap between rod and channel wall are shown in Fig. 4. The spectra exhibit not only the characteristic peaks of the flow near the gaps , but also several narrow peaks which disappear in the spectrum of $p_a - p_b$ since they have the same phase and intensity and are supposed to be produced by resonances of the test section. In the spectrum of the pressure difference, the peak corresponding to the flow pulsation is magnified, and lies at the same frequency as

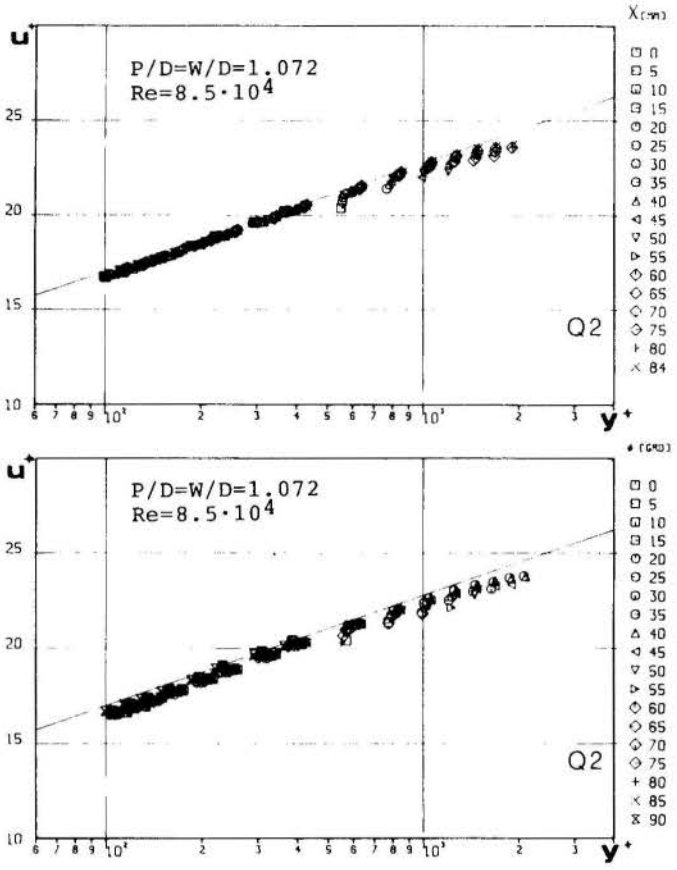

Fig. 2: Logaritmic velocity profile at the channel wall (a) and at the rod wall (b).

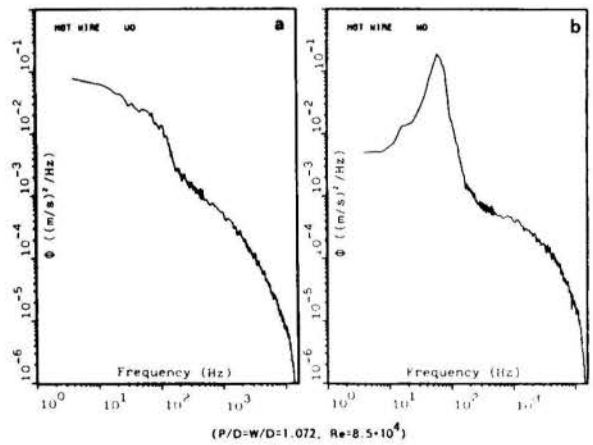

Fig. 3: Spectra of the axial (a) and the azimuthal (b) components of the fluctuating velocity at the center of the gap between rod and channel wall.

in the spectra of the fluctuating velocities. auto spectral densities of the wall pressure fluctuations at the subchannel center line have also peaks which are smaller than near the gaps, with the same dominant frequency.

The peak-frequency in spectra depends on the gap spacing and the flow velocity. It can be expressed in form of a Strouhal number, defined with the friction velocity, u*, and the rod diameter as a function of the gap width [2,3] as

$$Str^{-1} = (f\ D/u^*)^{-1} = 0.808\ S/D + 0.056\ . \qquad (2)$$

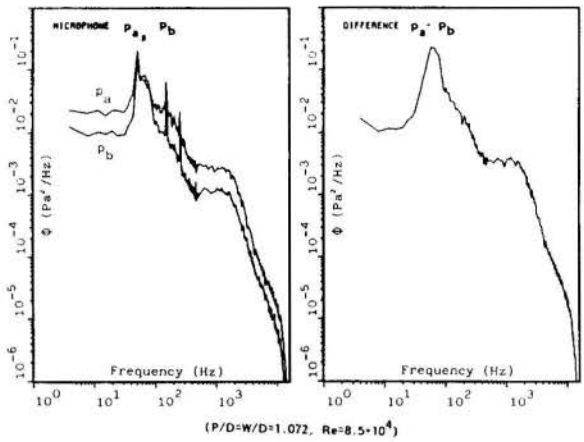

Fig. 4: Spectra of the wall pressure fluctuation at locations near the gap between rod and channel wall and of the pressure difference.

Cross Spectral Densities. Figure 5 shows the cross spectral density function Φ of the azimuthal fluctuating velocity in the gap between the rods and at location 1 (See Fig.1) and their coherence function C. The former is represented by its modulus and phase angle. The cross spectrum has a peak at 62.5 Hz, similarly to the power spactra of these functions. The phase angles from 10 to about 200 Hz are almost constant, slightly below 360^{o}, actually below 0^{o}, showing that this component propagate from the center of the subchannel toward the gap. After 200 Hz the phase angle has a random distribution, demonstrating that the eddies are small and that the turbulent motion tends to isotropy. Within this frequency range, the coherence function rises until a maximum of 0.96 (96 % coherence) and decays to almost zero at 200 Hz, where the random distribution of the phase angle begins. The behaviour of the coherence function demonstrate that although the flow pulsations have a central peak-frequency, they influence a wide range of frequencies, for the flow conditions shown, from 10 to 200 Hz, that means, a wide range of eddy sizes.

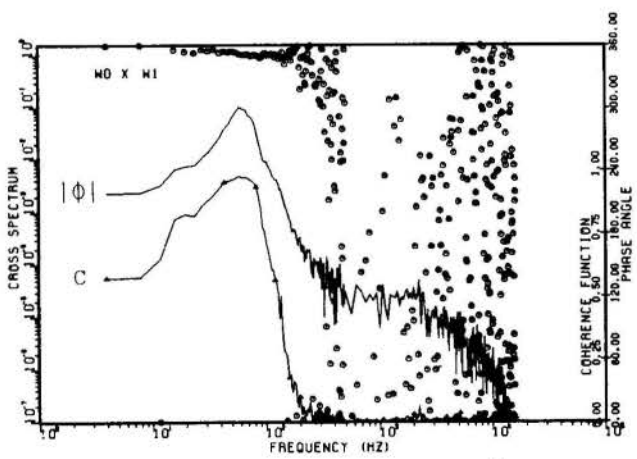

P/D=W/D=1.072; Re=8.5·10⁴

Fig. 5: Cross spectral density Φ and coherence function C of the azimuthal fluctuating velocities at locations 0 and 1.

The same functions are shown in Fig. 6 for the pressure fluctuations at locations on both sides of the gap. The cross spectral density has a region between 30 and 100 Hz forming a flat peak, which central frequency cannot be identified, due to the resonance peaks, which appear also in this plot. The phase angle is slightly below 180°. This is due to the fact that the microphones are not symmetrically placed with respect to the gap. apart of the resonance peaks, which have very high coherence, the coherence functions define two frequency ranges: the first one, up to 30 Hz, corresponds to the plane waves (sound, fan effects, etc.); the second one, from 30 to 100 Hz, corresponding to the flow pulsations. In this range, in spite of the relative large distance between the microphones, the coherence function has values of almost 0.5 (50 % coherence).

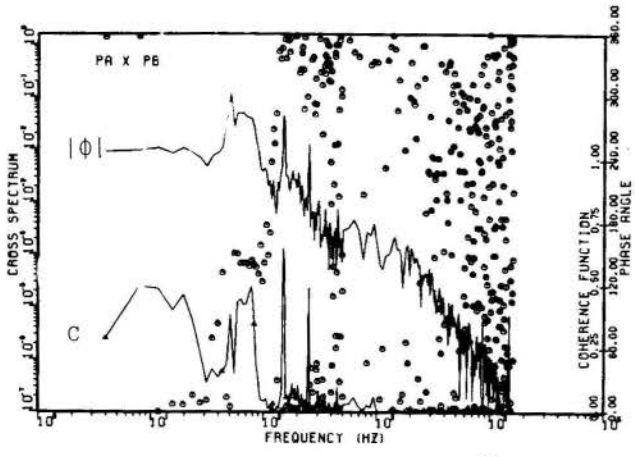

P/D=W/D=1.072; Re=8.5·10⁴

Fig. 6: Cross spectral density Φ and coherence function C of the wall pressure fluctuations at location a and b.

The cross spectrum and coherence function of the pressure fluctuation p_b and the azimuthal component w_0 is shown in Fig. 7. Both functions have peaks at 62.5 Hz. The coherence function has non zero values from 20° to 150° with peak values at 62.5 Hz of about 0.88 (88 % coherence). The discontinuity at 50 Hz is due to the presence of the narrow resonance peak in the spectrum of the pressure fluctuation which do not correlate with the fluctuating velocities.

CONCLUSIONS

Results of the spectra of the turbulent fluctuating velocities and pressure fluctuations show that the flow pulsations generate a dynamic pressure field near the gaps, with the same characteristic peak-frequency of the pulsations. The effects of this phenomenon propagate throughout the subchannel and influence the pressure field in the form given by Eq. (1), but the regions near the gaps, where the flow pulsations occur, are the ones which are the most affected by the flow pulsations. Coherence

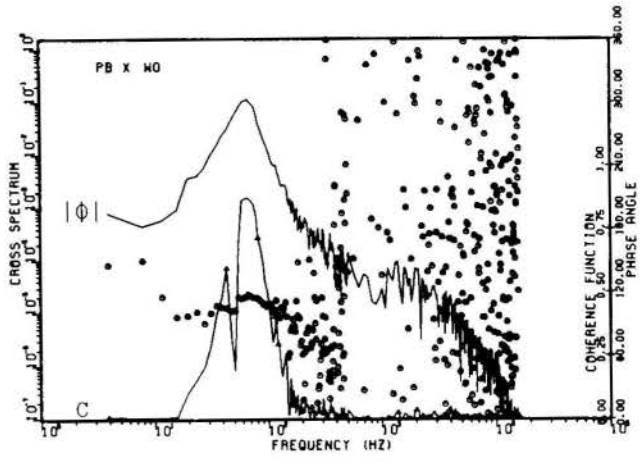

P/D=W/D=1.072; Re=8.5·10⁴

Fig. 7: Cross spectral density Φ and coherence function C of the azimuthal fluctuating velociy at location 0 and the pressure fluctuation at location b.

functions of the pressure and velocity fluctuations near the gaps have very high values. By means of these functions the frequency range affected by the flow pulsation is determined to be about one decade centered at the peak frequency for this geometry and flow velocity.

The measurements of pressure fluctuations were performed only at the channel wall, nevertheless, the dynamic pressure field on the rod walls must have the same behaviour near the gaps as on the channel wall.

The influence of tipical turbulence structures, like the horse shoe structures, observed in pipe flow by Langeheinecken was not observed, since they happen in a range of dimensionless distance to the wall up to $y^+ \tilde{=} 125$, in the law of the wall, and the measurements closest to the walls where performed at about $y^+ \tilde{=} 100$. It is also not expected that the 4.5 mm diameter microphones used in this work would be able to resolve the influence of eddies smaller than this size (about 1.5 mm), which is slightly larger than the resolution for transverse components of the fluctuating velocities measured with the double-wire probes [13].

The comparison of the spectra of the wall pressure fluctuation at locations near the gaps and at the subchannel center line confirms the results of Lin et al. that on the rods near the wall the pressure field is a function of the position. This should be expected also on the inner rod, but no information was given in Ref. [8] about the P/D-ratio, so that its influence could not be estimated.

The analysis of the spectral functions show that the pressure fluctuations in rod bundles are strongly associated with the flow pulsations, so that, they can be the the most important driving force of flow induced vibrations in rod bundles [14].

Results presented in this paper are related only to one geometry rod bundle (P/D = W/D = 1.072) and one Reynolds number (Re = $8.5 \cdot 10^4$), but they are similar in all geometries investigated. The characteristic frequency of the flow pulsations and the pressure fluctuations is the same. This frequency is a function of the flow velocity and the gap width, as demonstrated in Refs. [2,3], and is given by Equation (2) in Strouhal number form as a function of the dimensionless gap width S/D.

ACKNOWLEDGEMENTS

This research work was performed at the Institut für Neutronenphysik und Reaktortechnik of the Kernforschungszentrum Karlsruhe, F. R. Germany. The Author is greatfully indebted to Prof. K. Rehme, for his guidance, trust and encouragement during the execution of this work.

Author wants to thank the DAAD - Deutscher Akademischer Austauschdienst, F. R. Germany, for granting him a fellowship. Thanks are also due to the CNEN - Comissão Nacional de Energia Nuclear, Brazil, for the additional financial support.

REFERENCES

[1] Willmarth, W. W., Pressure fluctuations beneath turbulent bondary layers, Ann. Rev. of Fluid Mech., 7 (1975) 13-88.

[2] Möller, S. V., Experimentelle Untersuchung der Vorgänge in engen Spalten zwischen den Unterkanälen von Stabbündeln bei turbulenter Strömung, Dissertation, Universität Karlsruhe (TH), Karlsruhe, 1988; also, KfK 4501, Kernforschungszentrum Karlsruhe, 1989.

[3] Möller, S. V., On phenomena of turbulent flow through rod bundles, Proc. 4th International Topical Meeting on Nuclear Reactor Thermal- Hydraulics, Eds. U. Müller, K. Rehme and K. Rust, pp. 1287-1293, Karlsruhe, F. R. G., October 10-13, 1989; also: Exp. Thermal and Fluid Science, Vol.4, nº 1, to appear in 1990.

[4] Rehme, K., The structure of turbulent flow through rod bundles, Proc. 3rd International Topical Meeting on Nuclear Reactor Thermal-Hydraulics, Vol.2, Paper 16.A, newport, October, 1985; also: Nucl. Engrg. Des., 99 (1987) 141-154.

[5] Bull, M. K., Wall-pressure fluctuations associated with subsonic turbulent boundary flow, J. Fluid Mech., 28 (1967) 141-154.

[6] Langeheinecken, T., Zusammenhänge zwischen Wanddruck- und Geschwindigkeitsschwankungen in turbulenter Rohrströmung (Experimentelle Untersuchung), Mitteilung aus dem Max-Plank Institut für Strömungsforschung und der Aerodynamischen Versuchsanstalt, Nr. 70.

[7] Mulkahy, T. M., Wambsganss, M.W., Lin, W. H., Yeh, T. T. and Lawrence, W. P., Measurements of wall-pressure fluctuations on a cylinder in annular water flow with upstream disturbances, Part I: no flow spoilers, GEAP-24310, DOE/N/4175-15, ANL-CT-81-11, General Electric Co. (1981).

[8] Lin, W. H., Wambsganss, M. W., and Jendredzejczyk, J. A., Wall pressure fluctuations within a seven rod array, GEAP-24375, DOE/ET/34209-20, General Electric Co.(1981).

[9] Rehme, K., Rechnergesteuert Versuchsanlage zur Messung von Geschwindigkeits- und Turbulenzverteilung mit Hitzdrähten, KfK 3744, Kernforschungszentrum Karlsruhe, 1984.

[10] IMSL Library, IMSL lib 0008, Vol. 2 Chap. F, The IMSL Inc., Houston, USA, 1980.

[11] Nikuradse, J., Gesetzmässigkeiten der turbulenten Strömung in glatten Rohren, VDI-Forschungsheft 356, 1932.

[12] Lawn, C. J., The determination of the rate of dissipation in turbulent pipe flow, J. Fluid Mech., 48 (1971) 477-505.

[13] Möller, S. V., Limitações no uso de anemômetros de fio quente duplos para medições de turbulência, Proc. 10th Brazilian Congress of Mechanical Engineering, Vol. I, pp. 217-220, Rio de Janeiro, Brazil, 1989.

[14] Paidoussis, M. P., Flow - induced vibrations of heat exchangers and reactor components: Critical unresolved problems, in Practical Experiences with Flow-Induced Vibrations, Symposium in Karlsruhe, Sep. 3-6, 1979, Editors E. D. Naudascher and D. Rockwell, Springer, Berlin, 1980.

III ENCIT – Itapema, SC (Dezembro 1990)

MODELO DE MISTURA TURBULENTA TRANSVERSAL EM ESCOAMENTO AXIAL EM FEIXES DE VARETAS

PEDRO CARAJILESCOV
Departamento de Engenharia Mecânica
Pontifícia Universidade Católica do Rio de Janeiro

RESUMO

O presente trabalho consiste no desenvolvimento de um modelo para a obtenção da difusividade transversal turbulenta a ser utilizada no cálculo do efeito da mistura térmica turbulenta (mixing) em escoamentos axiais em feixes de varetas. Os resultados obtidos foram comparados com correlações existentes e utilizadas em programas de análise termohidráulica de combustíveis nucleares, podendo ser considerados satisfatórios.

INTRODUÇÃO

Geralmente, elementos combustíveis de reatores nucleares consistem de feixes de varetas dispostas em arranjos triangulares ou quadrados, com o refrigerante escoando axialmente através desta rede de subcanais interconectados. Um dos principais limites de projeto é aquele em que o fluxo de calor crítico não deva ser excedido em qualquer ponto do núcleo. Em caso contrário, a temperatura da vareta subiria rapidamente, resultando em oxidação ou fusão do revestimento do combustível e consequente liberação de material radioativo para o refrigerante.

O método usual de se calcular o fluxo crítico de calor consiste em se obter as condições locais do refrigerante, em cada subcanal, e aplica-las em alguma correlação adequada de fluxo crítico de calor. Normalmente, este procedimento é realizado através de programas computacionais do tipo COBRA [1] ou THINC [2], que resolvem as equações da continuidade, quantidade de movimento e energia para todos os subcanais, de forma acoplada. Uma descrição adequada do mecanismo de mistura turbulenta (mixing) entre os subcanais é essencial para que resultados confiáveis sejam obtidos.

Figura 1 apresenta dois subcanais interligados em um arranjo quadrado. A troca líquida de entalpia devido à mistura turbulenta, que ocorre na fronteira dos dois subcanais, é representada por um hipotético fluxo de massa transversal por unidade de comprimento, m^*_{ij}, produzindo:

$$m^*_{ij}(h_i - h_j) = \rho b \epsilon \left(\frac{dh}{dz}\right)_{ij} \tag{1}$$

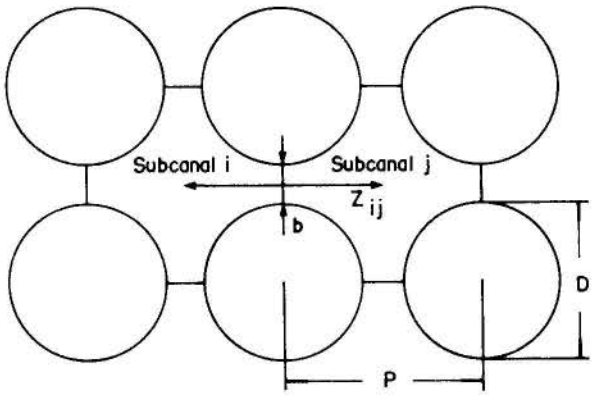

Fig. 1 – Subcanais interligados em um arranjo quadrado.

Aproximando o gradiente de entalpia médio por:

$$\left(\frac{dh}{dz}\right)_{ij} \approx \frac{h_i - h_j}{Z_{ij}} \tag{2}$$

obtemos:

$$m^*_{ij} = \frac{\rho b \epsilon}{Z_{ij}} \tag{3}$$

Inúmeros trabalhos foram realizados objetivando à obtenção da difusividade turbulenta transversal. Uma clássica revisão dos trabalhos é fornecida por Rogers e Todreas [3]. Observa-se que a maioria dos trabalhos executados até aquela época e outros mais recentes representam correlações de dados experimentais, utilizando a relação de Reichardt [4], válida para o núcleo de escoamentos turbulentos em tubos:

$$\frac{\epsilon}{\nu} \sim Re\sqrt{\frac{f}{2}} \tag{4}$$

Desta forma, até o momento, existe controvérsia sobre a influência do tipo de arranjo e dos parâmetros geométricos na mistura turbulenta.

O presente trabalho consiste no desenvolvimento de um modelo teórico para a difusividade turbulenta transversal, onde a influência dos parâmetros geométricos e operacionais é claramente estabelecida.

MODELO PROPOSTO

A vazão em massa instantânea, por unidade de comprimento, que atravessa o espaço entre duas varetas, do subcanal i para o canal j, pode ser escrita na forma:

$$m' = \int_b \rho w' \, dy \tag{5}$$

onde w' representa a velocidade transversal instantânea do fluido. Considerando-se que a velocidade transversal média é nula, w' representa a flutuação turbulenta da velocidade.

Assumindo densidade constante, a média temporal de m' será obtida integrando-se m' sobre um tempo T, longo comparado com o tempo de difusão turbulenta, isto é:

$$\overline{m'} = \frac{1}{T}\int_0^T m' \, dt = \frac{1}{T}\int_0^T dt \left[\rho \int_b w' \, dy\right] = 0 \tag{6}$$

Definindo-se:

$$w_{ij} = \begin{cases} w', & se \quad w' \geq 0 \\ 0, & se \quad w' < 0 \end{cases} \qquad e \qquad w_{ji} = \begin{cases} w', & se \quad w' < 0 \\ 0, & se \quad w' \geq 0 \end{cases}$$

segue:

$$m' = \rho \int_b dy \left[\frac{1}{T} \int_0^T w' dt \right] = \underbrace{\rho \int_b dy \left[\frac{1}{T} \int_0^T w_{ij} dt \right]}_{\overline{m'_{ij}}} +$$

$$\underbrace{\rho \int_b \left[\frac{1}{T} \int_0^T w_{ji} dt \right]}_{\overline{m'_{ji}}} = 0 \qquad (7)$$

Desta expressão, observa-se que o primeiro termo da direita representa a vazão em massa de fluido, por unidade de comprimento, que atravessa do subcanal i para o subcanal j, enquanto o segundo termo representa o que vai do subcanal j para o subcanal i.

Obviamente,

$$| \overline{m'_{ij}} | = | \overline{m'_{ji}} | = m_{ij} \qquad (8)$$

Assim:,

$$m_{ij} = \frac{1}{2} \left[| \overline{m'_{ij}} | + | \overline{m'_{ji}} | \right] = \frac{\rho}{2} \int_b dy \left[\frac{1}{T} \int_0^T | w' | dt \right] \qquad (9)$$

Ainda:

$$m_{ij} = \rho \int_{b/2} dy \, | \overline{w'} | \qquad (10)$$

onde

$$| \overline{w'} | = \frac{1}{T} \int_0^T | w' | dt \qquad (11)$$

Considerando a distribuição de w' como sendo aproximadamente normal, observa-se que:

$$| \overline{w'} | = \sqrt{\frac{2}{\pi}} \sqrt{\overline{w'^2}} \qquad (12)$$

Desta forma, de (10) e (12), vem:

$$m_{ij} = \sqrt{\frac{2}{\pi}} \rho \int_{b/2} \sqrt{\overline{w'^2}} \, dy \qquad (13)$$

A intensidade de turbulência $\sqrt{\overline{w'^2}}$, obtida experimentalmente para diversos tipos de geometria, incluindo feixes de varetas, foi correlacionada por Bobkov e outros [5] na forma:

$$\sqrt{\overline{w'^2}} = u \left(1 - \frac{u_b}{u_{max}} \right) C e^{-B(y/(b/2))} \qquad (14)$$

onde u, u_b e u_{max} são as velocidades axiais local, média e máxima, ao longo da normal à parede. B e C são constantes empíricas, iguais a 1,17 e 0,60, respectivamente.

Observando-se que o perfil de velocidade axial, ao longo de uma linha normal à parede, pode ser aproximado pelo perfil logaritmico, na região do núcleo turbulento, vem:

$$u = \frac{u_\tau}{k} \ell n(E^* \eta) \qquad (15)$$

onde:

$$\eta = \frac{y}{(b/2)}$$

$$E^* = \frac{E u_\tau b}{2\nu}$$

Substituindo (14) e (15) na equação (13) e efetuando-se a integração, obtém-se:

$$m_{ij} = \frac{C}{\sqrt{2\pi k}} (\rho b u_\tau) \left(1 - \frac{u_b}{u_{max}} \right) I \qquad (16)$$

onde:

$$I = \int_0^1 \ell n(E^* \eta) e^{-B\eta} d\eta \qquad (17)$$

Pode-se demonstrar que:

$$\left(1 - \frac{u_b}{u_{max}} \right) I \approx \left(\frac{1 - e^{-B}}{B} \right) \ell n 4 \qquad (18)$$

de onde vem:

$$m_{ij} = \frac{C \, \ell n \, 4}{\sqrt{2\pi k}} \left(\frac{1 - e^{-B}}{B} \right) (\rho b u_\tau) \qquad (19)$$

A vazão m_{ij} transporta entalpia do subcanal i para o subcanal j e vice-versa, provocando a mistura turbulenta. Esta vazão, no entanto, não transporta massa com a entalpia média dos subcanais i e j, mas massa com a entalpia das proximidades da fronteira entre os subcanais. Assim, pode-se escrever o transporte de entalpia na forma:

$$m^*_{ij} (\bar{h}_i - \bar{h}_j) = m_{ij} (h_{i,m} - h_{j,m}) \qquad (20)$$

Os subscritos m indicam propriedades nas proximidades da fronteira entre os subcanais i e j.

Fazendo:

$$\frac{\bar{h}_i - \bar{h}_j}{Z_{ij}} \simeq \frac{h_{i,m} - h_{j,m}}{2\ell} \qquad (21)$$

onde ℓ representa o comprimento de mistura turbulenta de Prandtl, na região do gap, e fazendo

$$\ell \simeq k \left(\frac{b}{2} \right) \qquad (22)$$

vem:

$$m^*_{ij} = \frac{k b}{Z_{ij}} m_{ij} \qquad (23)$$

Combinando as equações (3) e (23),

$$\frac{\epsilon}{\nu} = \frac{k}{\rho \nu} m_{ij} \qquad (24)$$

Substituindo, nesta expressão, o valor de m_{ij}, dado pela equação (19), vem:

$$\frac{\epsilon}{\nu} = \phi \frac{b \, u_\tau}{\nu} \qquad (25)$$

com

$$\phi = \frac{C \, \ell n \, 4}{\sqrt{2\pi}} \left(\frac{1 - e^{-B}}{B} \right) = 0{,}196 \qquad (26)$$

Esta equação pode ser reescrita na forma:

$$\frac{\epsilon}{\nu} = \psi Re \sqrt{\frac{f}{2}} \qquad (27)$$

Nesta expressão:

$Re = (D_h \bar{u}_b / \nu)$ = número de Reynolds do escoamento;

$\sqrt{\frac{f}{2}} = (\bar{u}_\tau / \bar{u}_b)$ com f = fator de atrito;

$$\psi = \phi \sqrt{\frac{\tau}{\bar{\tau}}} \left(\frac{b}{D_h} \right) \qquad (28)$$

com τ = tensão de cisalhamento na parade.

A barra, sobre as variáveis, indica valor médio sobre o subcanal e D_h é o diâmetro hidráulico de um subcanal.

Comparando-se a equação (28) com a equação (4), observa-se que o parâmetro ψ representa a constante de proporcionalidade da relação de Reichardt, fornecendo a influência da geometria e das condições operacionais.

RESULTADOS

A aplicação da equação (27) exige o conhecimento da relação $\tau/\bar{\tau}$, calculada na região entre as varetas. No presente caso, foi utilizada a relação de Ibragimov [6]:

$$\frac{\tau}{\bar{\tau}} = \tilde{G}\left[1 - exp\left(-\frac{7,7}{\gamma^{0,8}}\frac{\hat{y}}{\hat{y}_{av}}\right)\right] \qquad (29)$$

onde:

$$\gamma = \frac{A_c}{\hat{y}_{av}^2}$$

com A_c = área de uma região típica do subcanal, representada na Figura 2.

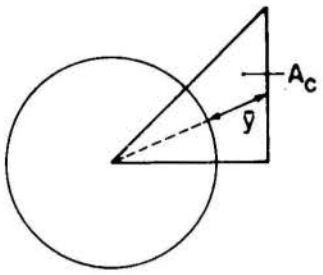

Fig 2 – Região típica de um subcanal

A constante G representa um parâmetro de normalização da relação (29).

Diversos autores, entre os quais pode se mencionar Moyer [7], sugerem um valor constante para ψ igual a 0,05, o qual tem sido amplamente utilizado. Figura 3 apresenta os valores de ψ em função de b/D, para arranjos quadrado e triangular das varetas, obtidos através do modelo proposto.

Observa-se que, para o mesmo b/D, a difusividade turbulenta transversal é maior para arranjos triangulares do que para arranjos quadrados, devido à maior contribuição do mixing, na região do gap destes arranjos, para a variação da entalpia média dos subcanais.

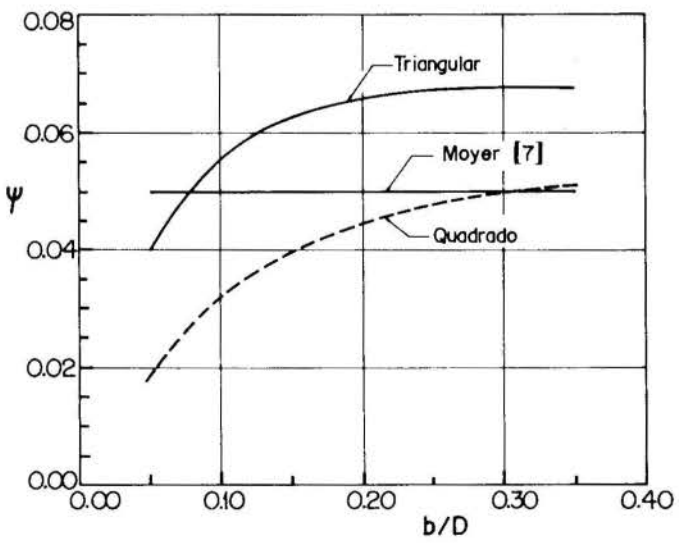

Fig. 3 – Comparação entre a correlação de Moyer e o presente modelo

Ainda, para baixos valores de b/D, a difusividade obtida tende a decrescer devido à redução da intensidade de turbulência na região do gap.

Estes fatos são claramente observados pelo presente modelo. Obviamente, o modelo proposto deverá ser amplamente validado através de comparações com dados experimentais.

Por simplicidade de utilização, sugerem-se as seguintes expressões para ψ:

Arranjo quadrado:

$$\psi = 0,09\left(\frac{b}{D}\right)^{0,5} \qquad (30)$$

Arranjo triangular:

$$\psi = 0,09\left(\frac{b}{D}\right)^{0,25} \qquad (31)$$

Estas expressões foram obtidas através de ajustes dos resultados apresentados na Figura 3.

REFERÊNCIAS

[1] Rowe, D. S., "COBRA-IIIC: A digital computer program for steady state and transient thermal hydraulic analysis of rod bundle nuclear fuel elements", BNWL-1695 (1973).

[2] Chelemer, H. et al., "THINC-IV - An improved program for thermal-hidraulic analysis of rod bundle cores", WCAP-7956, (1973).

[3] Rogers. J. T. and Todreas, N. E., "Collant interchannel mixing in reactor fuel rod bundles single-phase coolants", ASME Winter Annual Meeting, (1968).

[4] Reichardt, M., "Complete representation of turbulent velocity distribution in smooth pipe", Zeit. Ang. Math. Meth. 31, (1951).

[5] Bobkov, V. P. et al., "Correlation of experimental data of the pulsation velocity intensity for turbulent fluid flow in channels of different form", Fluid Dynamics, Vol. 3, Nº 3, (1968), pp. 111-113.

[6] Ibragimov, M. Kh. et al., "Calculation of the tangential stresses at the wall of a channel and the velocity distribution in a turbulent flow of liquid", Sov. Atomic Energy, Vol. 21, nº 2, (1966), pp. 731-739.

[7] Moyer, C. B., "Coolant mixing in multi-rod fuel bundles", Riso Report Nº 125, (1966).

ABSTRACT

The present work consists in the development of a model for the transversal eddy diffusivity to account for the effect of turbulent thermal mixing in axial flows in rod bundles. The results were compared to existing correlations that are currently being used in reactor thermalhydraulic analysis and considered satisfactory.

III ENCIT – Itapema, SC (Dezembro 1990)

TURBULENT CONVECTIVE HEAT AND MASS TRANSFER IN THE DEVELOPING REGION OF ELLIPTICAL DUCTS

H. T. M. Vinagre and P. R. Souza Mendes
Department of Mechanical Engineering
Pontifícia Universidade Católica – RJ
Rio de Janeiro, RJ 22453 – BRAZIL

ABSTRACT

Mass transfer experiments were performed to determine local heat and mass transfer coefficients for the turbulent flow in a duct with elliptical cross section. The naphthalene sublimation technique was employed to obtain the experimental results. Both entrance-region and fully-developed results were obtained. The Reynolds number was varied in the overall range of 7000–60,000, whereas values of 0.12, 0.25 and 0.5 for the aspect ratio were investigated. The fully developed transport coefficients obtained were compared with the ones available in the open literature for parallel plates and circular tubes, and it was found that the coefficients are quite insensitive to aspect ratio variations.

INTRODUCTION

Ducts with elliptic cross section have a definite niche in the heat exchanger industry. This is chiefly due to the low form drag observed in the external transverse flow past either one or a bundle of these ducts.

Consequently, a great number of investigations about the various flow and heat transfer situations involving this geometry are reported in the open literature. Both internal and external flows have been studied, and a broad view of the information available on the subject can be obtained in [1].

Heat transfer in the fully developed region of laminar flows in elliptical ducts has been studied analitically by a number of authors, e.g., Dunwoody [2], Bathy [3] and Ebadian et al. [4]. Experimental results for the same problem are reported by Oliver and Rao [5].

Entrance region results for this problem are also available. The hydrodynamic problem has been studied via an integral method by Bathy [6], via finite differences by Garg and Velusamy [7], and experimentally by Abdel-Wahed et al. [8]. The related heat transfer problem has been studied theoretically by Dunwoody [2] and by Schenk and Han [9].

Results for turbulent flows in elliptical ducts are more infrequent. All investigations reported were focused on the fully developed region of the flow. Velocity distributions and friction factors have been obtained experimentally by Cain and Duffy [10]. Friction factors for another range of the cross-section aspect ratio have been determined by Barrow and Roberts [11], and a useful correlation is available in [1].

Nusselt numbers for the turbulent fully developed flow in elliptical ducts are presented by Barrow and Roberts [11] for water ($Pr = 6.5$), and by Cain et al. [12] for air ($Pr = 0.7$) and water ($Pr = 6.5$). The Nusselt number results of both papers agree within 5% with the Gnielinski correlation for circular tubes [1].

The experimental investigation reported in the present paper was focused on the entrance region of the turbulent flow in elliptical ducts. The main objective of the study was the determination of the axial distribution of the Nusselt number for the inlet condition of simultaneous hydrodinamic and thermal development. The thermal boundary condition investigated was uniform wall temperature. The Reynolds number Re was varied in the range 7000–60,000, and three different aspect ratios have been investigated, namely, 0.12, 0.25 and 0.5. The results obtained pertain to a Prandtl number equal to $Pr = 2.5$.

EXPERIMENTAL APPARATUS AND PROCEDURE

The heat transfer coefficients have been determined experimentally with the aid of the naphthalene sublimation technique. In reality, only mass transfer data were measured in the laboratory, and then the corresponding heat transfer coefficients were calculated with basis in the analogy between the heat- and mass-transfer mechanisms. A detailed description of this technique is available in [13].

The test section. The test section is described with the aid of Fig. 1, where the assembly employed is illustrated. Further details can be found in [14]. Modules were assembled together to form an elliptical duct. A module was basically a brass ring (48.0 mm ID, 63.0 mm OD, 20 mm long) with its inner surface coated with solid naphthalene.

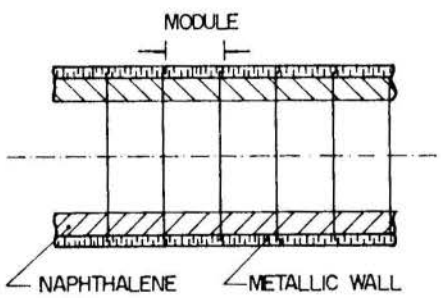

Fig. 1 – An elliptical duct assembly.

The naphthalene was cast inside the ring to form the inner surface, as illustrated in Fig. 2. The test section consisted of 25 modules assembled in sequence. A piece of elastic hose involved tightly the whole outer surface of the assembly during the runs, to eliminate air leaks between adjacent modules.

The naphthalene coating procedure is now described. The first step was to remove from all modules, by melting and evaporation, the coating remaining from the preceding data run. Then, a mold was assembled as suggested in Fig. 2. The components of the mold included the ring, end caps which mated with the recesses at the respective ends of the ring, and an elliptical shaft. The shaft served as the centerbody of the mold, and its surface had been polished to a mirrorlike finish. The shaft was positioned in the mold such that the major axis direction was at a 25 degree angle with the radial direction toward

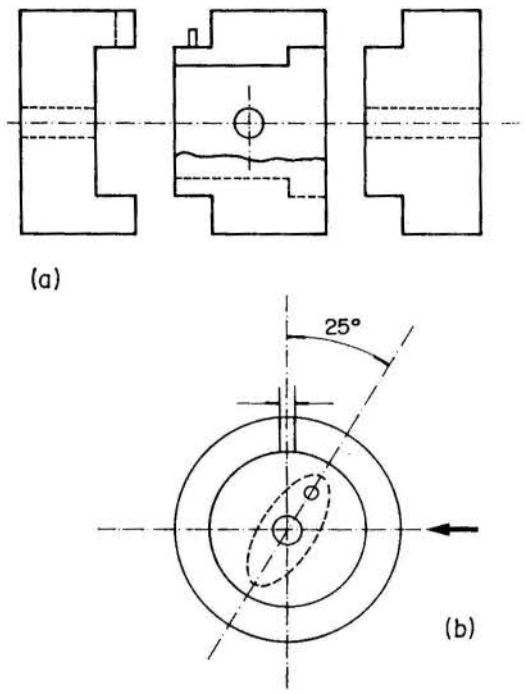

Fig. 2 – The casting set, with ring, caps and shaft.

the pouring hole in the ring (Fig. 2). This angle provided the highest surface quality.

The cavity between the ring and the shaft was filled with molten naphthalene. Once the naphthalene had solidified, the shaft and end caps were removed, and an excellent finish of the resulting naphthalene surface was obtained. Finally, the pouring hole in the ring was sealed with tape to prevent undesirable sublimation. A thermocouple was cast into the naphthalene layer of one of the modules, flush with its inner surface.

Three different types of test section were employed in the experiments, each one characterized by a different aspect ratio of the elliptic cross section. For each of these test sections, a different elliptic shaft was carefully machined with a mill, as described in [14].

Air loop. Air was drawn from the laboratory into the test section, whose inlet was centered in a large baffle plate. Downstream of the test section, which was oriented horizontally, a transition piece conveyed the flow to a length of flexible tubing. This tubing was connected at its downstream end to the flow metering section. Then followed a plenum chamber, and, further downstream, two valves. One of the valves was used to select the flow rate, whereas the second was a cut-off valve. A small length of pipe bridged across the laboratory wall to connect the flow circuit to blowers. These blowers were installed in a contiguous room, where the air was finally exhausted. Therefore, the air loop was open, and was operated in the suction mode.

Instrumentation. The mass of the modules was measured immediately before and after each data run, to allow the determination of the transport coefficients at each module. An analytical balance with a resolving power of 0.1 mg and a capacity of 200 g was employed in the mass measurements. Typical changes in mass during a data run were in the range of 0.1 g.

The air flow rate in the test section was determined with an orifice-type flowmeter, fabricated in accordance with the *ASME* standards and calibrated to ensure its accuracy.

Temperature measurements were made with the aid of two different instruments. The temperature of the naphthalene surface was measured with a copper-constantan thermocouple. A calibration using a platinum-resistance thermometer indicated a maximum deviation of 0.08°C. The temperature of the airflow aproaching the duct inlet was determined with an *ASTM 63C* mercury thermometer, whose smallest division was 0.1°C. Thermocouple *emf*'s were read during the course of a data run from a voltmeter having a 1 μV resolution.

Procedure. Inasmuch as several aspects of the experimental procedure have already been mentioned, only a few additional details need to be discussed. The naphthalene-coated modules were left in the air-conditioned laboratory room overnight in order to attain thermal equilibrium with the room air. To avoid sublimation and to guarantee an ambient air free from naphthalene vapor in the laboratory, the modules were wrapped in aluminum foil at all times during the equilibration period.

Just before the beginning of a data run, the modules were individually weighed and then assembled to form the test section. The blower had been warmed up in advance to provide a steady flow from the moment of activation. After the period of duration of the run, the test section was disassembled and the modules reweighed. During all of these operations, the modules were manipulated using pincers.

To obtain a correction for possible extraneous sublimation which might have ocurred between the two weighings, a so-called after-run was performed. During the after-run, the whole procedure of the actual data run was repeated, except for the fact that the blower was never activated. The mass measurements following the after-run provided the sought-for correction, which was of the order of 4%.

Data reduction. The modules are numbered from 1 to 25, the first one ($i = 1$) being located at the section inlet, and i increasing in the flow direction.

The net amount of mass sublimed during a data run from the $i^{\underline{\text{th}}}$ module, M_i, was employed to determine its per-module average mass transfer coefficient K_i, which is defined as

$$K_i \equiv \frac{\dot{M}_i}{A_s \Delta\rho_{n,i}} \tag{1}$$

$\dot{M}_i$ is the mass transfer rate at the $i^{\underline{\text{th}}}$ module, A_s is its surface area of mass transfer, $\Delta\rho_{n,i}$ is the naphthalene-vapor density difference which drives mass transfer, to be discussed shortly.

The mass transfer rate $\dot{M}_i$ is determined by taking the ratio between the (corrected) amount of mass sublimed from module i and the time duration τ of the data run, i.e., $\dot{M}_i = M_i/\tau$.

The difference in naphthalene vapor densities that appears in eq. (1) is the log-mean density difference corresponding to the $i^{\underline{\text{th}}}$ module, defined as

$$\Delta\rho_{n,i} \equiv \frac{(\rho_{nw} - \rho_{nb,i-1}) - (\rho_{nw} - \rho_{nb,i})}{\ln\left[(\rho_{nw} - \rho_{nb,i-1}) \,/\, (\rho_{nw} - \rho_{nb,i})\right]} \tag{2}$$

The quantity ρ_{nw} is the density of naphthalene vapor at the duct wall, and is evaluated with the aid of the perfect-gas law. Therefore, $\rho_{nw} = M_n p_{nw}/\mathcal{R}T_w$, where M_n is the molecular weight of naphthalene vapor, equal to 128.17 [15], and $\mathcal{R}$ is the universal perfect gas constant. The duct wall temperature T_w is measured with the thermocouple embedded in the naphthalene layer. The vapor pressure of naphthalene vapor p_{nw} is evaluated at the wall temperature according to Sogin's [13] expression

$$\ln p_{nw} = 31.23252 - \frac{8587.36}{T_w} \tag{3}$$

The other quantities that appear in eq. (2) are $\rho_{nb,i-1}$ and $\rho_{nb,i}$. They represent respectively the bulk vapor density at the inlet

and exit of the $i^{\underline{th}}$ module. Clearly,

$$\rho_{nb,i} = \rho_{nb,i-1} + \frac{\dot{M}_i}{\dot{m}/\rho} \tag{4}$$

where $\dot{m}$ is the air mass flow rate and ρ is the air density, evaluated at the inlet conditions. Assuming that the air at the test section inlet is free from naphthalene vapor, i.e., $\rho_{nb,0} = 0$, then

$$\rho_{nb,i} = \sum_{j=1}^{i} \frac{\dot{M}_j}{\dot{m}/\rho} \tag{5}$$

The Reynolds number is defined as

$$Re \equiv \frac{4\dot{m}}{\mu P} \tag{6},$$

where μ is the air viscosity, evaluated at the inlet conditions. P is the perimeter of the elliptic cross section, which is a function of its aspect ratio $\alpha^* \equiv b/a$, a and b being respectively the major and minor axis lengths of the cross section (please see insertion of Fig. 3). This dependence on the aspect ratio is such that it appears the complete elliptic integral of second kind of $(1-\alpha^{*2})$. The following expression avoids the evaluation of the elliptic integral and gives a very good approximation for P:

$$P = \pi b \left(1 + \frac{1}{\alpha^*}\right) \frac{64 - 3\lambda^4}{64 - 16\lambda^2}, \tag{7}$$

where $\lambda \equiv (1-\alpha^*)/(1+\alpha^*)$.

The Sherwood number corresponding to the $i^{\underline{th}}$ module is given by

$$Sh_i = \frac{\rho D_h Sc K_i}{\mu}, \tag{8}$$

where $D_h = 4\pi ab/P$ is the hydraulic diameter and Sc is the Schmidt number, equal to 2.5 for naphthalene diffusion in air.

Uncertainty analysis. The measurement uncertainties have been estimated according to [16]. The Reynolds number uncertainty obtained was 2.7%. The Sherwood number displayed an uncertainty of 8.9%, mainly due to a temperature depression observed, which was caused by the absorption of latent heat of sublimation.

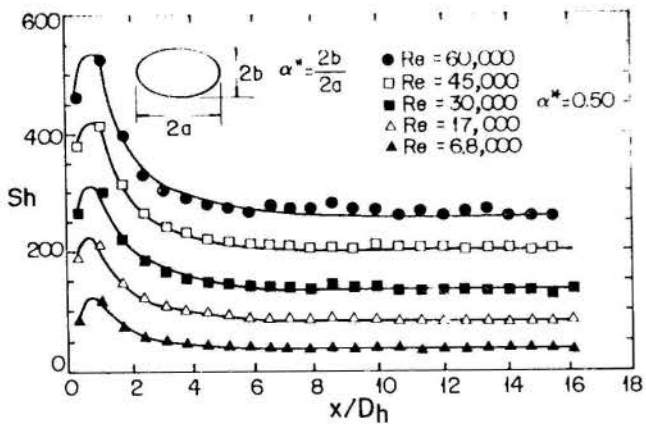

Fig. 3 – Axial distribution of Sh. $\alpha^* = 0.5$.

RESULTS AND DISCUSSION

The experimental results presented in this section have been obtained from mass transfer experiments. Therefore, they appear in the form of dimensionless mass transfer coefficients,

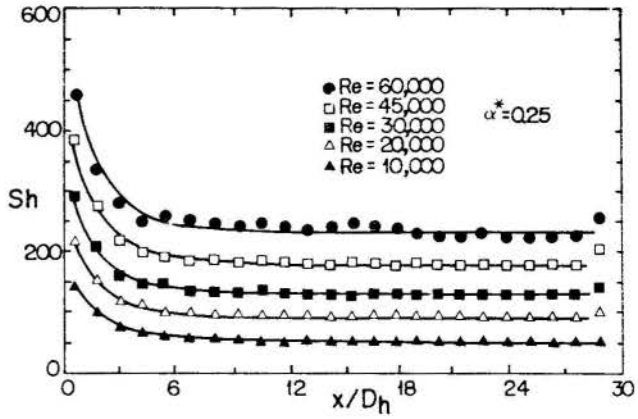

Fig. 4 – Axial distribution of Sh. $\alpha^* = 0.25$.

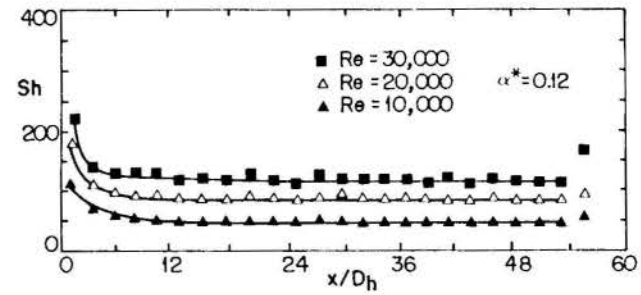

Fig. 5 – Axial distribution of Sh. $\alpha^* = 0.12$.

i.e., Sherwood numbers. Since the mass transfer involved was of naphthalene vapor diffusing in air, the data pertain to a Schmidt

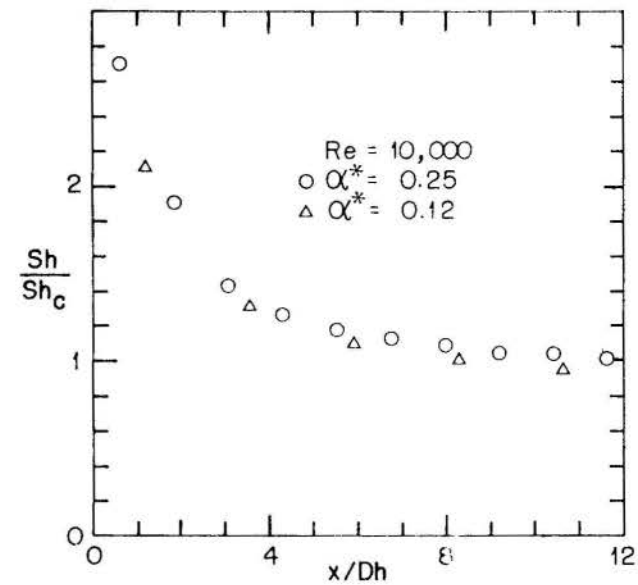

Fig. 6 – Axial distributions of Sh/Sh_c. $Re = 10{,}000$.

number Sc of 2.5. However, as mentioned earlier, the analogy between heat and mass transfer implies that all Sherwood numbers obtained for $Sc = 2.5$ are also Nusselt numbers for Prandtl number $Pr = 2.5$ (and for a boundary condition of uniform wall temperature).

Entrance region results. Figs. 3–5 illustrate the axial distribution of the cross-section average Sherwood number for different values of the Reynolds number. The axial coordinate x is equal to zero at the duct inlet, and increases in the flow di-

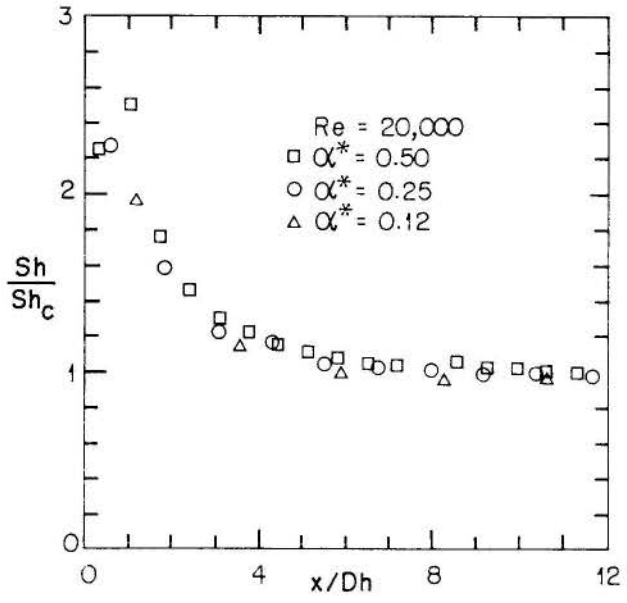

Fig. 7 – Axial distributions of Sh/Sh_c. Re = 20,000.

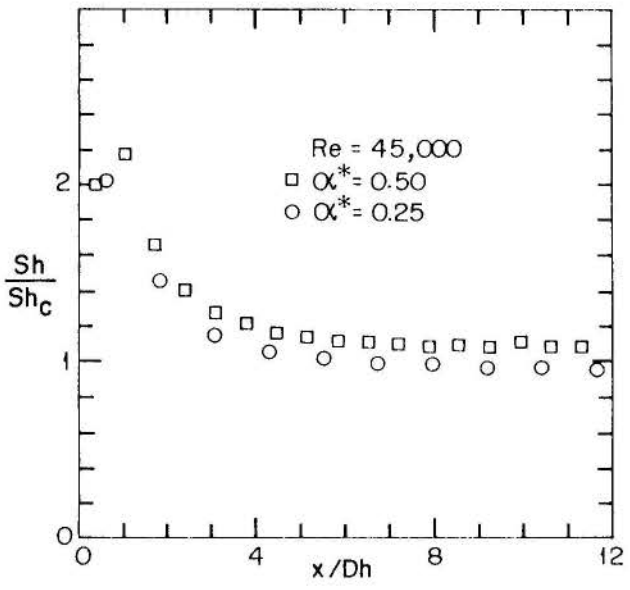

Fig. 9 – Axial distributions of Sh/Sh_c. Re = 45,000.

rection. The data points in these figures correspond to the Sh_i values calculated with eq. (8), which were plotted at the x/D_h locations of the respective module midpoints.

For α^* = 0.5 (Fig. 3), the Sherwood number increases with the axial coordinate near the duct inlet, reaches a maximum, and then decreases monotonically to its fully developed value. This trend is repeated for the five Reynolds numbers investigated, and is due to the well known vena contracta effect.

For α^* = 0.25 and 0.12 (Figs. 4 and 5 respectively), no maximum is observed. The Sherwood number decreases monotonically from the duct inlet to the fully developed region, for all Re studied. The main shortcoming of the experimental strategy adopted in the present research was that the module length could not be shorter than about 20 mm, due to pratical limitations. Close to the duct inlet, where the Sherwood number varies very fast with the axial coordinate, the resolution obtained with this technique was poor, especially for the lower values of the aspect ratio (or hydraulic diameter). Therefore, vena contracta effects might have passed unnoticed for α^* = 0.25 and 0.12.

It can also be seen from Figs. 3–5 that the length of the entrance region is about 6 to 8 hydraulic diameters, being a very weak function of the Reynolds number and also of the aspect ratio. It is worth noting, however, that the axially-averaged Sherwood number (not shown), averaged from $x = 0$ to $x = x$, may need 70 or more hydraulic diameters to attain a value which is nearly the same as the fully developed local Sh.

A direct comparison among the results for the three different aspect ratios is also illustrative. Figs. 6–10 show axial distributions of the ratio Sh/Sh_c between the local Sherwood number for the elliptical duct Sh and the fully developed Sherwood number for the circular tube Sh_c. The values of Sh_c were obtained from the Gnielinski correlation [1].

It can be seen from these figures that, for low Reynolds numbers (Figs. 6–8), the aspect ratio α^* affects very little the local Sherwood number in the entrance region of the flow. For higher Reynolds numbers (Figs. 9 and 10), a mild dependence on α^* is observed, the Sh for α^* = 0.5 displaying values slightly higher than the ones for α^* = 0.25.

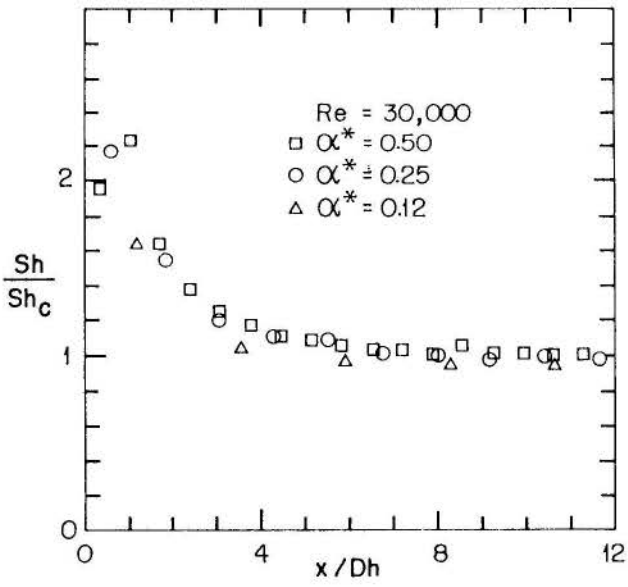

Fig. 8 – Axial distributions of Sh/Sh_c. Re = 30,000.

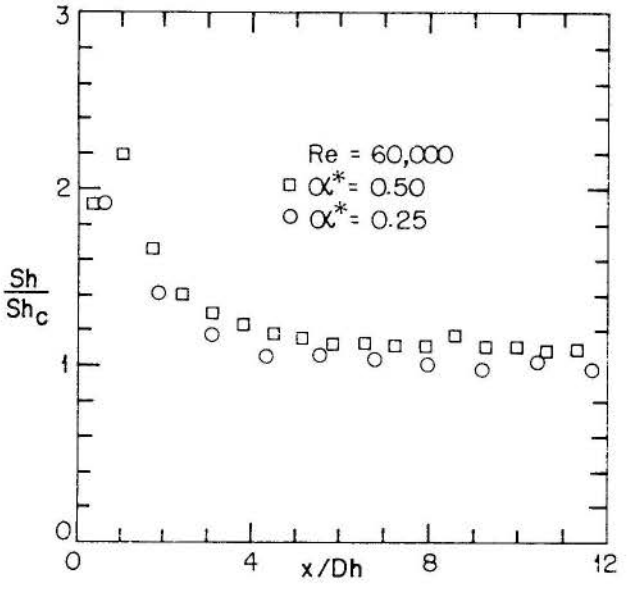

Fig. 10 – Axial distributions of Sh/Sh_c. Re = 60,000.

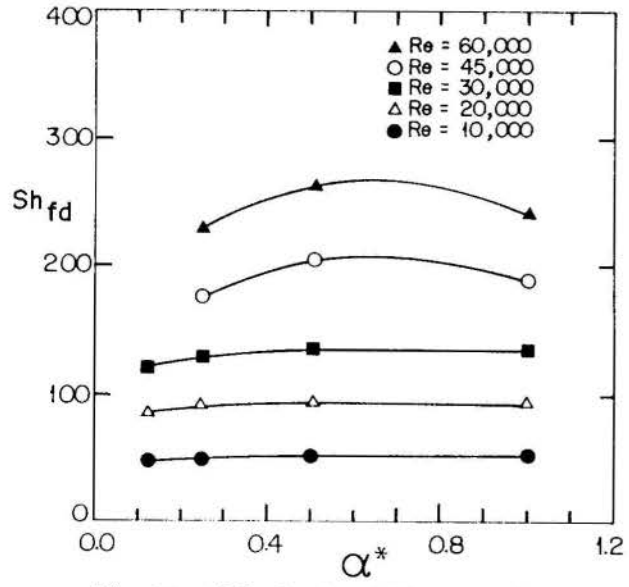

Fig. 11 – Fully developed Sh versus α^*.

Fully developed region results. Fig. 11 illustrates the dependence of the fully developed value of the Sherwood number, Sh_{fd}, on the aspect ratio α^*. In this figure, some of the points shown were read from a *log-log* plot of $Sh_{fd} \times Re$ for each of the aspect ratios α^* (graph shown in Fig. 12), in order to allow the construction of the curves for fixed Re's.

For Re = 10,000, 20,000 and 30,000, there is essentially no dependence of Sh_{fd} on the cross section aspect ratio, except for small aspect ratios (α^* = 0.12 and 0.25). For α = 0.12, the fully developed Sherwood number is about 10% lower than for

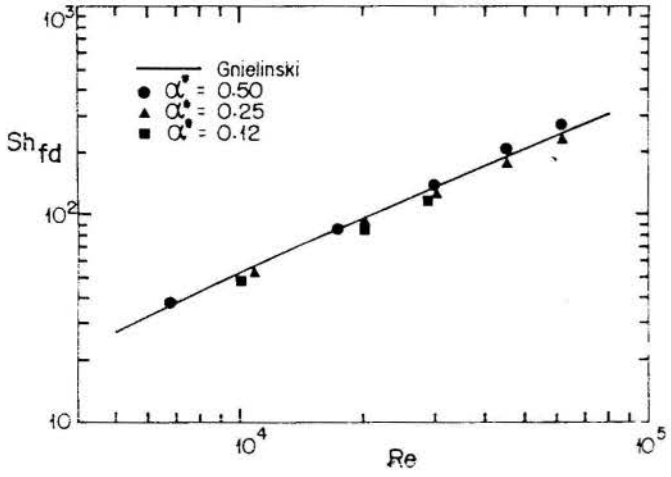

Fig. 12 – Fully developed Sh versus Re.

α^* = 1 (circular tube), whereas for α^* = 0.25, it is about 5.5% lower.

For Re = 45,000 and 60,000, however, the trend changes qualitatively, and a maximum occurs at α^* slightly beyond 0.5. For both values of Re, the Sh_{fd} value is about 9% higher than the one for the circular tube (α^* = 1).

This comparison with circular tube results is better illustrated in Fig. 12, where the Sh_{fd} values for the three aspect ratios investigated are plotted as a function of the Reynolds number, together with the prediction of the Gnielinski [1] correlation for the circular tube. Firstly it is observed that the fully developed results for the flow in elliptical ducts is close to the ones for the circular tube, although not as close as the results of [11] and [12] for other Prandtl numbers.

It is also seen that, for α^* = 0.12 and 0.25, the slopes of the curves are about the same as the one for the circular tube. The Sh_{fd} values for both aspect ratios are lower than Sh_c, the ones for α^* = 0.12 being lowest. For α^* = 0.5, however, the slope of the curve is clearly steeper than the Gnielinski curve, and the Sh_{fd} values for this aspect ratio become higher than Sh_c for $Re > \simeq$ 30,000.

FINAL REMARKS

Experiments have been performed to measure transport coefficients for the turbulent flow in elliptical ducts. Both entrance region and fully developed results were obtained.

It was observed that the ratio betwen the entrance region Sherwood number and the fully developed Sherwood number for the circular duct (Sh/Sh_c) is not very sensitive to the cross section aspect ratio, especially for lower Reynolds numbers.

The fully developed Sherwood number Sh_{fd} obtained (for Pr = 2.5) is smallest for low aspect ratios α^*, and, for low Reynolds numbers, tends to the fully developed Sherwood number for the circular tube (Sh_c) as the aspect ratio increases. For higher values of Re, however, a maximum value of Sh_{fd} is observed at α^* slightly above 0.5.

For Re = 10,000, 20,000 and 30,000, the Gnielinski correlation for circular tubes overpredicts Sh_{fd} in 11% for α^* = 0.12, in 7.5% for α = 0.25, and underpredicts Sh_{fd} in 3% for α = 0.5. For Re = 45,000 and 60,000, it overpredicts Sh_{fd} in 6% for α = 0.25 and underpredicts Sh_{fd} in 9% for α = 0.5.

The results available in the literature for other Prandtl numbers [11], [12] are much better correlated (within 5%) by the Gnielinski correlation [1].

REFERENCES

[1] S. Kakaç, R. K. Shah and W. Aung, 1987, *Handbook of Single-Phase Convective Heat Transfer*, J. Wiley & Sons, New York.

[2] N. T. Dunwoody, 1962, "Thermal results for forced heat convection through elliptical ducts," *J. Applied Mechanics* **29**, pp. 165–170.

[3] M. S. Bathi, 1984, "Heat transfer in the fully developed region of elliptical ducts with uniform wall heat flux," *J. Heat Transfer* **106**, pp. 895–898.

[4] M. A. Ebadian, H. C. Topakoglu and O. A. Arnas, 1986, "On the convective heat transfer in a tube of elliptic cross section maintained under constant wall temperature," *J. Heat Transfer* **108**, pp. 33–39.

[5] D. R. Oliver and S. S. Rao, 1979, "Heat transfer to Newtonian liquids in laminar flow in straight horizontal elliptical tubes," *Trans IChemE* **57**, pp. 104–112.

[6] M. A. Bathy, 1983, "Laminar flow in the entrance region of elliptical ducts," *J. Fluids Engineering* **105**, pp. 290–296.

[7] V. K. Garg and K. Velusamy, 1987, "Finite difference analysis of flow development in elliptical ducts," *ASME Winter Annual Meeting*, Boston, Ma., paper no. 87-WA/FE-9.

[8] R. M. Abdel-Wahed, A. E. Attia and M. A. Hifni, 1984, "Experiments on laminar flow and heat transfer in an elliptical duct," *Int. J. Heat Mass Transfer* **27**, pp. 2397–2413.

[9] J. Schenk and B. S. Han, 1966, "Heat transfer from laminar flow in ducts with elliptic cross section," *Appl. Sci. Res.* **17**, pp. 96–114.

[10] D. Cain and J. Duffy, 1971, "An experimental investigation of turbulent flow in elliptical ducts," *Int. J. Mech. Sci.* **13**, pp. 451–459.

[11] H. Barrow and A. Roberts, 1970, "Flow and heat transfer in elliptic ducts," *Heat Transfer 1970*, Versailles, paper no. FC 4.1.

[12] D. Cain, A. Roberts and H. Barrow, 1973, "An experimental investigation of turbulent flow and heat transfer in elliptical ducts," *Wärme- und Stoffübertragung*, **2**, pp. 101–107.

[13] P. R. Souza Mendes, 1988, "The Naphthalene Sublimation Technique," *Proc. First World Conference on Experimental Heat Transfer, Fluid Mechanics and Thermodynamics*, Elsevier, pp. 446–460.

[14] H. T. M. Vinagre, 1987, "Experimental determination of the heat transfer coefficient in ducts of elliptic cross section," M.S. Thesis, Pontifícia Universidade Católica - RJ, Rio de Janeiro, Brazil (in Portuguese).

[15] H. H. Sogin, 1958, "Sublimation from disks to air streams flowing normal to their surfaces," *ASME Transactions* **80**, pp. 61–71.

[16] R. J. Moffat, 1988, "Describing the uncertainties in experimental results," *Experimental Thermal and Fluid Science* **1**, pp. 3–17.

III ENCIT – Itapema, SC (Dezembro 1990)

NUMERICAL CALCULATION OF HEAT TRANSFER IN A TURBULENT SEPARATED-REATTACHING SHEAR FLOW

by

J.C.F. Pereira and J.M.P. Rocha

Instituto Superior Técnico
Department of Mechanical Engineering
Av. Rovisco Pais
1096 Lisboa Codex
Portugal

SUMMARY

The paper reports calculations of heat transfer in a separated-reattaching turbulent shear flow. The plane, two-dimensional, backward-facing step flow is studied with emphasis on the turbulent thermal field. An algebraic second-moment closure is employed for the modelling of turbulent fluxes. A transport equation for the dissipation rate of temperature fluctuations variance is also incorporated. The reported results show that the model provides an acceptable description of the general behaviour of the flow.

INTRODUCTION

Current interest in the computation of convective heat transfer in separated-reattaching turbulent shear flows is strongly motivated by the great number of practical engineering devices in which combined phenomena of separation-reattachment and heat transfer occur. In these conditions, the thermal field is known to be greatly influenced by the mechanical characteristics of the flow, promoting an augmentation in the heat transfer rates within the recirculation zone compared with an attached flow. A number of studies [1, 2, 3] have attempt to compute heat transfer rates in separated shear layers, with special emphasis in the reattachment zone. Almost all of these computations have incorporated a first-moment turbulence closure (the k-ε eddy viscosity/diffusivity model, EVM), and log-laws for the numerical modelling of the near-wall flow. The partial sucess in the computations seems to be motivated by the limitations of the models employed in the representation of the near wall flow. Considerably less attention has been given to the calculation of turbulence characteristics as velocity-temperature correlations and the scalar-variance and to the examination of the performance of existing turbulence models in the simulation of scalar-dispersion in recirculating flows.

The objective of the present study is to test an algebraic second-moment closure (ASM) in a separated-reattaching flow with heat transfer. The model incorporates simplified algebraic transport equations for the turbulent fluxes. An important feature is that additionally to the transport equations for the turbulence parameters k, ε and temperature fluctuations variance $\langle\theta^2\rangle$, the model also comprises a transport equation for the dissipation rate of $\langle\theta^2\rangle$. This paper attempts to provide an examination of the performance of the model compared with the results of the k-ε eddy-viscosity/diffusivity closure and with experimental measurements. The already known difficulties in the wall flow treatment are not attempt to be solved. Moreover, the difficulties experienced in previous studies to reduce numerical errors in the computation of recirculating flows [4] are avoided by the use of a low-order convection-discretization scheme, considering that the aim of the study is to compare two closure levels and the numerical errors which arise are of the same magnitude for both. The next section of the paper presents the mathematical model adopted; next, results are reported and discussed. Conclusions are drawn at the end of the paper.

MATHEMATICAL MODEL

The Reynolds-averaged form of the governing equations for a turbulent, steady, high Reynolds number flow of an incompressible fluid read, in cartesian tensor notation,

$$\frac{\partial U_i}{\partial x_i} = 0 \quad , \tag{1}$$

$$\frac{\partial}{\partial x_j}\left(U_j U_i\right) = -\frac{1}{\rho}\frac{\partial P}{\partial x_i} - \frac{\partial}{\partial x_j}\left(\langle u_i u_j\rangle\right) , \tag{2}$$

$$\frac{\partial}{\partial x_j}\left(U_j \Theta\right) = -\frac{\partial}{\partial x_j}\left(\langle u_i \theta\rangle\right) . \tag{3}$$

U_i and u_i represent the x_i-component of mean and fluctuating velocity, respectively; P is the pressure and ρ the fluid density; Θ represents the mean-temperature excess above ambient, $T - T_{ref}$, where T_{ref} is the freestream temperature; θ is the temperature fluctuation. < > stands for the temporal average of the quantity.

An Algebraic Second-Moment closure is employed to calculate the turbulent fluxes $\langle u_i u_j\rangle$ and $\langle u_i\theta\rangle$. The transport equations for these quantities can be written symbollicaly as

$$C_{ij} - D_{ij} = \mathcal{P}_{ij} + \mathcal{R}_{ij} - \varepsilon_{ij} \tag{4}$$

$$C_{i\theta} - D_{i\theta} = \mathcal{P}_{i\theta} + \mathcal{R}_{i\theta} - \varepsilon_{i\theta} \tag{5}$$

where

$$\mathcal{P}_{ij} = -\left(\langle u_i u_k\rangle \frac{\partial U_j}{\partial x_k} + \langle u_j u_k\rangle \frac{\partial U_i}{\partial x_k}\right),$$

$$\mathcal{P}_{i\theta} = -\left(\langle u_j \theta\rangle \frac{\partial U_i}{\partial x_j} + \langle u_i u_j\rangle \frac{\partial \Theta}{\partial x_j}\right),$$

$\mathcal{P}_{i\theta,1}$ $\mathcal{P}_{i\theta,2}$

where C_{ij} and $C_{i\theta}$ represent convection terms and D_{ij} and $D_{i\theta}$ the diffusive terms. In the equations (4, 5) apart from the production terms $\mathcal{P}_{ij}$, $\mathcal{P}_{i\theta}$ which require no modelling, all the remaining terms in the RHS representing redistribution and dissipation rates of $\langle u_i u_j\rangle$ and $\langle u_i\theta\rangle$ must be approximated. The models of [5, 6, 7, 8] are adopted to represent the pressure-redistribution processes as

$$\mathbf{R}_{ij} = -C_1 \frac{\varepsilon}{k}\left(\langle u_i u_j\rangle - \frac{2}{3} k \delta_{ij}\right) - C_2\left(\mathcal{P}_{ij} - \frac{2}{3}\mathcal{P}\delta_{ij}\right),$$

$\mathbf{R}_{ij,1}$ $\mathbf{R}_{ij,2}$ (6)

$$\mathbf{R}_{i\theta} = -C_{\theta 1}\frac{\varepsilon}{k}\langle u_i \theta\rangle - C_{\theta 2}\mathcal{P}_{i\theta,2},$$

$\mathbf{R}_{i\theta,1}$ $\mathbf{R}_{i\theta,2}$ (7)

where

$$\mathcal{P} = -\langle u_i u_j\rangle \frac{\partial U_i}{\partial x_j}$$

The model proposed in [9, 10] is adopted to account for pressure wall-reflection effects in the Reynolds stress tensor components yielding a term which is additive to (6) as

$$\mathbf{R}^{w}_{ij} = C_1^{w}\frac{\varepsilon}{k}\left(\langle u_k u_m\rangle n_k n_m \delta_{ij} - \frac{3}{2}\langle u_k u_i\rangle n_k n_j - \frac{3}{2}\langle u_k u_j\rangle n_k n_i\right) f\left(\ell/n_i r_i\right)$$

$\mathbf{R}^{w}_{ij,1}$

$$+ C_2^{w}\left(\mathbf{R}_{km,2} n_k n_m \delta_{ij} - \frac{3}{2}\mathbf{R}_{ik,2} n_k n_j - \frac{3}{2}\mathbf{R}_{jk,2} n_k n_i\right) f\left(\ell/n_i r_i\right)$$

$\mathbf{R}^{w}_{ij,2}$ (8)

and in the same way for model (7),

$$\mathbf{R}^{w}_{i\theta} = -C_{\theta 1}^{w}\frac{\varepsilon}{k}\langle u_k \theta\rangle n_i n_k f\left(\ell/n_i r_i\right)$$

$\mathbf{R}^{w}_{i\theta,1}$

$$+ C_{\theta 2}^{w} C_{\theta 2}\mathcal{P}_{k\theta} n_i n_k f\left(\ell/n_i r_i\right)$$

$\mathbf{R}^{w}_{i\theta,2}$ (9)

where ℓ is the characteristic turbulent local length scale and r_i the coordinates of position vector. The magnitude of these corrections is controlled by the function f, which reads

$$f = \frac{k^{3/2}/\varepsilon}{C_w n_i r_i}, \quad (10)$$

where the constant C_w is fixed so that f takes on a value of unity in local equilibrium near wall turbulence, $C_w = 2.5$. It was assumed likewise [11] that the reflection effects of the two walls can be superimposed.

The dissipation rates are modelled assuming local isotropy at the small-scale motions as

$$\varepsilon_{ij} = \frac{2}{3}\varepsilon\delta_{ij}, \qquad \varepsilon_{i\theta} = 0 \quad (11)$$

The convection-diffusion terms in equations (4, 5) are approximated in the framework of an ASM closure [12, 13] by

$$C_{ij} - D_{ij} = \frac{\langle u_i u_j\rangle}{k}(P - \varepsilon), \quad (12)$$

$$C_{i\theta} - D_{i\theta} = \frac{\langle u_i \theta\rangle}{2k}(P - \varepsilon). \quad (13)$$

To obtain the turbulence scales, transport equations for ε and $\langle\theta^2\rangle$ are solved,

$$\frac{\partial U_j \varepsilon}{\partial x_j} = C_{\varepsilon 1}\frac{\varepsilon}{k}\mathcal{P} - C_{\varepsilon 2}\frac{\varepsilon^2}{k} + \frac{\partial}{\partial x_j}\left(C_\varepsilon \frac{k}{\varepsilon}\langle u_j u_k\rangle \frac{\partial \varepsilon}{\partial x_k}\right), \quad (14)$$

$$\frac{\partial U_j \langle\theta^2\rangle}{\partial x_j} = 2\mathcal{P}_\theta - 2\varepsilon_\theta + \frac{\partial}{\partial x_j}\left(C_\theta \frac{k}{\varepsilon}\langle u_j u_k\rangle \frac{\partial \langle\theta^2\rangle}{\partial x_k}\right), \quad (15)$$

where

$$\mathcal{P}_\theta = -\langle u_i \theta\rangle \frac{\partial \Theta}{\partial x_i}.$$

The closure of turbulent thermal field is completed providing the model to calculate the dissipation rate of temperature fluctuations variance. The majority of the previous studies have adopted the similarity hypothesis between mechanical and thermal fields. From the definition of the time-scale ratio R,

$$2\varepsilon_\theta = \frac{1}{R}\frac{\varepsilon}{k}\langle\theta^2\rangle, \quad (16)$$

ε_θ can be computed prescribing a value to R, usually equal to 0.5. A more general route adopts a transport equation for the quantity. Extending the modelled equation proposed by Newman *et al.* [14] to non-homogeneous flows it can be written as

$$\frac{\partial U_j \varepsilon_\theta}{\partial x_j} = C_{P1}\frac{\varepsilon_\theta}{\langle\theta^2\rangle}\mathcal{P}_\theta + C_{P2}\frac{\varepsilon_\theta}{k}\mathcal{P} - C_{D1}\frac{\varepsilon_\theta^2}{\langle\theta^2\rangle}$$

$$- C_{D2}\frac{\varepsilon}{k}\varepsilon_\theta + \frac{\partial}{\partial x_j}\left(C_{\varepsilon\theta}\frac{k}{\varepsilon}\langle u_j u_k\rangle\frac{\partial \varepsilon_\theta}{\partial x_k}\right). \qquad (17)$$

Computations were also performed with the k-ε eddy-viscosity turbulence model [15] incorporating the generalized gradient hypothesis [16] to represent the turbulent diffusivity tensor. The constants which appear in the models above are presented in Table 1 and 2 and are the same as proposed in previous studies.

Table 1 - Value of Turbulence Model Constants.

C_1	C_2	C_1^w	C_2^w	$C_{\theta 1}$	$C_{\theta 2}$	$C_{\theta 1}^w$	$C_{\theta 2}^w$	C_ε	$C_{\varepsilon 1}$	$C_{\varepsilon 2}$	C_θ
1.8	0.55	0.5	0.3	2.8	0.55	0.75	0	0.15	1.44	1.92	0.25

Table 2 - Value of ε_θ-equation Constants

$C_{\varepsilon\theta}$	C_{P1}	C_{P2}	C_{D1}	C_{D2}
0.15	1.7	0.71	0.88	2.0

NUMERICAL MODEL

The numerical model is based on a finite-volume discretization of the governing equations, employing a staggered grid for the mean-velocity components relatively to scalar properties. In addition to this usual practice, the incorporation of an algebraic second-moment closure model in the numerical code has required additional stability-promoting numerical measures. The practices suggested in [11] were adopted, which can be summarized in the following: i) A staggered grid arrangement for the second-moments; ii) The insurance of positiveness of normal stresses by special matrix solution arrangement; iii) Treatment of source/sink terms in momentum equations via a "pseudo-viscosity" device. These and other measures have secured that the convergence of the iterative solution process would not be damaged by temporary computation of physically meaningless values of the variables.

Despite the inclusion of the above referred numerical devices to insure a stable iterative solution process, the algebraic form of Reynolds stresses and heat fluxes equations leads to serious difficulties in the convergence and accuracy of solution process. These difficulties, also experienced by Huang and Leschziner [11] in isothermal flows calculations, could be overcame by the use of strong underrelaxation factors.

The hybrid central upwind differencing scheme is used to approximate the convective terms in all differential transport equations. The SIMPLE Algorithm [17] was chosen for the pressure-velocity coupling correction and the Strong Implicit Procedure [18] is employed for the solution of the set of the algebraic equations.

The computations to be presented relate to the flow studied experimentally by Vogel and Eaton [19]. The solution domain was chosen so that the measured inlet conditions could be specified, at - 3.8 step heights. The length of the test section was extended up to 18 step heights, see Figure 1. The boundary conditions at the walls for velocity components, k and ε are specified using wall functions [15]. At the lowest wall a constant flux condition is imposed for temperature; zero wall flux is prescribed for $\langle\theta^2\rangle$ and ε_θ. At the first computational node located at $y^+ = 30$ the Reynolds stresses and turbulent heat fluxes are computed with EVM formulae, yielding non-zero boundary conditions for the quantities.

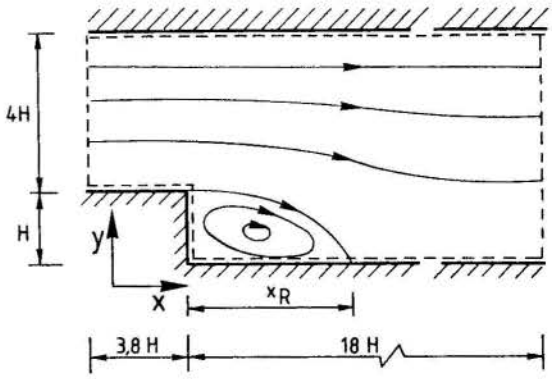

Figure 1. — Flow Configuration Considered: Plane Single-Sided Backward Step.

The computations were performed using a 50 x 32 control volumes grid. Grid-dependence tests were made indicating that the differences between the results in this grid and a 100 x 64 control volumes grid are not significant. The sums of the absolute residuals of mean field variables were used for monitoring convergence. The iterative process was terminated after the normalized residuals fell below 1%. The computations were performed in a VAX - 6000/440 computer.

RESULTS AND DISCUSSION

The computed streamwise mean velocity profiles upstream and downstream of the reattachment point are presented in Figure 2 (a, b). Upstream of reattachment, the growth of the upper shear layer, due to entrainment of non-vortical fluid, and the intensity of the backflow in the recirculation zone are correctly simulated considering that the effect of the discrepancy in reattachement length is compensated by plotting the computations versus the non-dimensional coordinate $x^* = (x - x_R)/x_R$ as in [19]. The developing boundary layer (Figure 2b) is somewhat less accuratly computed with some discrepancy in the near wall region, $y/H < 0.75$, as also observed in the calculations presented by McGuirk *et al.* [4], obtained with a differential Reynolds stress closure. No significant differences arise from the comparison between ASM and EVM results. Both models underpredict the reattachment length by about 20-25% with ASM leading to a longer value. It is a well known feature of both first and second-moment closures which does not depend on the grid refinement nor on the wall treatment adopted.

Figure 3 (a, b) shows the profiles of mean-

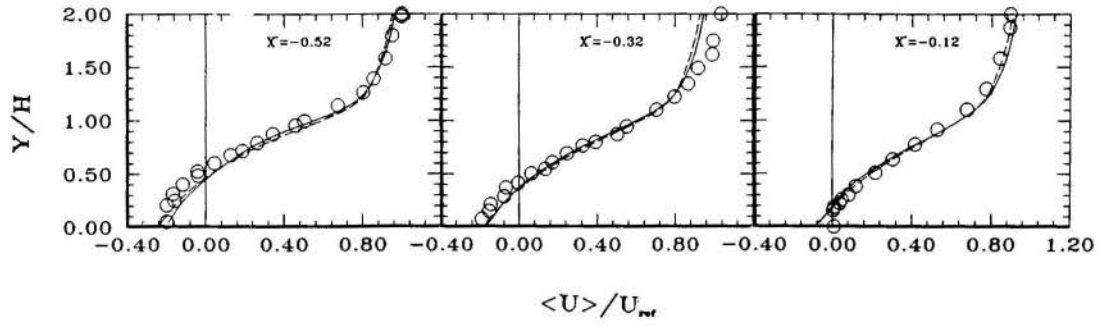

(a)

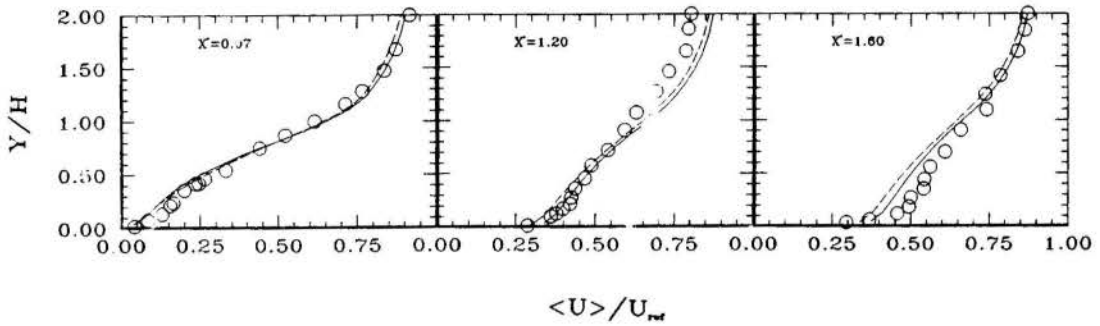

(b)

Figure 2. — Axial Velocity Profiles; (a) Upstream of Reattachment; (b) Downstream of Reattachment. Experiments: Symbols, [19]; Computations: —— ASM, ----- EVM.

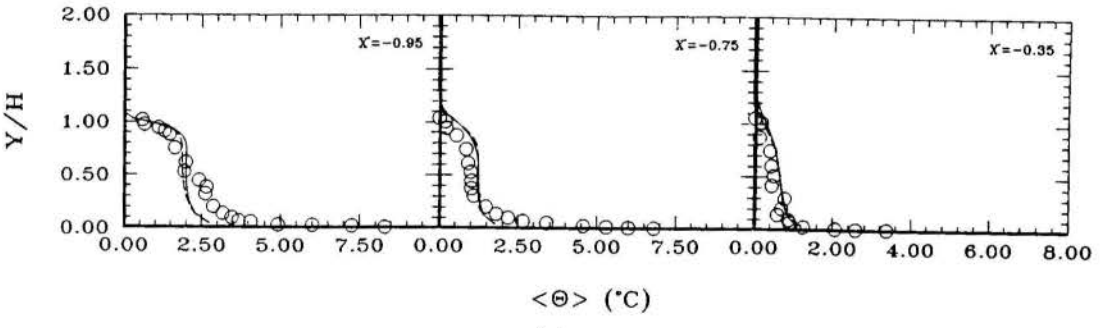

(a)

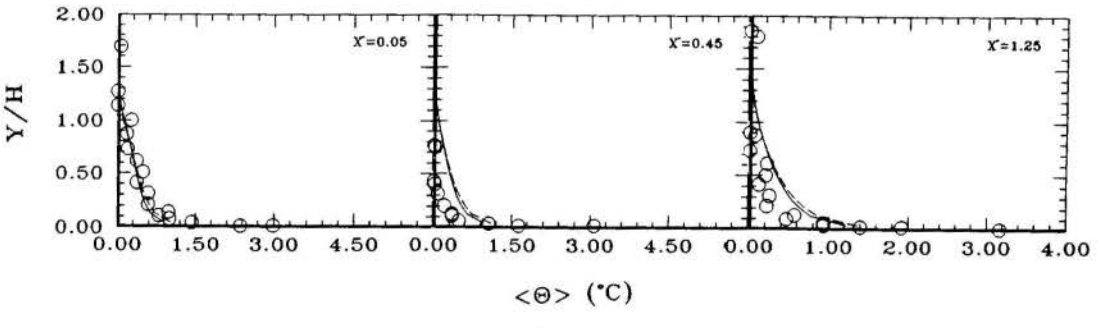

(b)

Figure 3. — Mean Temperature Excess; (a) Upstream of Reattachment; (b) Downstream of Reattachment. Experiments: Symbols, [19]; Computations: —— ASM, ----- EVM.

temperature excess. The profiles are in dimensional coordinates due to the absence of a constant reference value for the temperature. Measurements show that the steepest gradients occur with exception to the streamwise locations close to the step face, in the region close to the wall, which is conduction dominated. The first computational node is located at $y^+ = 30$, which represents a distance from the wall considerably greater than the conduction-dominated layer thickness. Considering the grid and boundary conditions adopted for the wall (prescribed heat flux), these steep gradients are not captured in the computation, and consequently, nor their effects on turbulence quantities, as discussed later on in the paper. At $x^* = -0.95$, the computations reflect the effect of high vertical velocities transporting warmer air across the recirculation region yielding a steep gradient near $y/H \cong 1$. This indicates that the warmer, low speed recirculating air is not so rapidly transported across the bordering shear layer, as inferred also in [19]. Further downstream, Figure 3 (a, b), convective mixing processes produce a temperature drop perdominantly in the vicinity of the wall and the temperature gradient across the shear layer rapidly vanishes. The computations reflect quite well this mechanism again with no significant advantage from any model, despite the inability of the models to capture temperature development at the near vicinity of the wall.

With regard to turbulence field quantities, Figure 4 displays the computation of streamwise Reynolds stress component $\langle u^2 \rangle$. ASM correctly computes the peak value and its location. The maximum value is approximatly 17% normalized by the freestream mean velocity. In contrast, EVM underpredicts the experimental values. Figure 5 shows the crosswise Reynolds stress component $\langle v^2 \rangle$. The anisotropy induced in the Reynolds stress tensor due to the presence of the wall is correctly simulated by ASM which predicts $(\langle u^2 \rangle / \langle v^2 \rangle)^{1/2} \cong 1.4$. EVM yields equal magnitudes for $\langle u^2 \rangle$ and $\langle v^2 \rangle$, leading to an overprediction of the $\langle v^2 \rangle$ experimental values. The energy transfer mechanism among energy components due to the pressure wall-reflection effects on crosswise velocity fluctuations is not captured by this model. This tendency was also observed in former computations [4].

A number of studies [20-23] have reported numerical calculations using a transport equation for the dissipation rate of the scalar-variance. These studies performed on simple flow geometries without separated regions, established part of the four model constants which appear in equation (17), while only a few studies (see e.g. [24]) have incorporated the transport equation in complex flows calculations. While consensus exists regarding the values of the constants C_{P1}, C_{D1}, C_{D2} (compare [20-23]) the constant C_{P2} which affects the term representing production of ε_θ due to mechanical mean-turbulence fields interactions, has not yet a definite value. Jones and Musonge [21] and Nagano and Kim [22] used rather different values for C_{P2}, 1.44 and 0.7, respectively. In the present study, computations were performed with several values of C_{P2} ranging from 0.6 to 1.44. It was decided to retain $C_{P2} = 0.71$ in accord with [22], which provided the best general agreement. Figure 6 shows a comparison between computed and measure temperature variance profiles. In the ASM model, the transport equation and a prescribed constant time-scale ratio $R = 0.5$ were incorporated in the calculation of ε_θ. At $x^* = -0.3$ both models predict a nearly constant level of temperature variance across the recirculation zone and the decrease in magnitude across the shear layer, in close agreement with experiments. At separation, the primary transport mechanism in crosswise direction in the bordering shear layer is the turbulent transport, as the streamlines are nearly parallel to the surface and the magnitude of the production of $\langle \theta^2 \rangle$ is dictated by the intensity of cross-correlation $\langle v\theta \rangle$ (see Figure 7). As a consequence of the failure of the model to capture the steep temperature gradients the production of $\langle \theta^2 \rangle$ is strongly underpredicted, yielding a lower local level. In contrast, at the wall the low level of $\langle v\theta \rangle$ indicates that the transport mechanism is other than turbulence. In the vicinity of the wall, mean-field gradients control the heat transfer rates and the inaccurate description of the temperature profile by the model yields a strong underprediction of temperature fluctuation. In addition, the level of $\langle \theta^2 \rangle$ in the adjacents layers near the wall is also too low affecting the transport across the recirculation zone.

In the developing boundary layer the experimental profiles exhibit a monotonic decrease from the wall to the freestream. Nevertheless, even in the outer zone, $y/H > 0.5$, the levels of $\langle \theta^2 \rangle$ are finite, which indicates that the significant contribution to production of $\langle \theta^2 \rangle$ comes from turbulent transport of heat, since temperature gradients are small in this region. The computations reflect this variation in shape of the experimental profile. At this streamwise location, the inaccuracy of the model description of the near wall temperature evolution is also reflected in the discrepancy observed between computation and experimental values.

It is important to note that the constant time scale ratio model for calculating ε_θ also produces a fairly good description of $\langle \theta^2 \rangle$ development, possibly indicating that the departure from a similarity state between turbulent mechanical and thermal fields is small. Presumably this flow is not a stringent test to the model.

The cross component of the turbulent heat flux vector is shown in Figure 7. Both models overpredict the peak level at y/H - 0.7.

The change in dominance between the bordering shear layer and the wall region is observed in streamwise location $x^* = -0.3$. Both models capture this change. Unfortunatly, the measurements are not detailed enough at the wall to provide a evaluation of the accuracy of the predictions. For streamwise distances greater than $x^* = -0.3$ the influence of the wall is dominant and $\langle v\theta \rangle$ profile peaks at the wall, dropping to zero at the free shear layer. ASM captures quite well this development, while EVM responses slower to this change. Further downstream in the recirculation region the peak diminuishes in intensity and the level inside the bubble increases. This evolution is captured by ASM. The profiles produced by EVM are strongly influenced by the wall and the inner zone is significantly overpredicted.

CONCLUSIONS

Numerical computations of convective heat dispersion in a backward-facing step turbulent flow were presented. The closure of the mean-field equations was made incorporating an algebraic second-moment model for heat fluxes and four

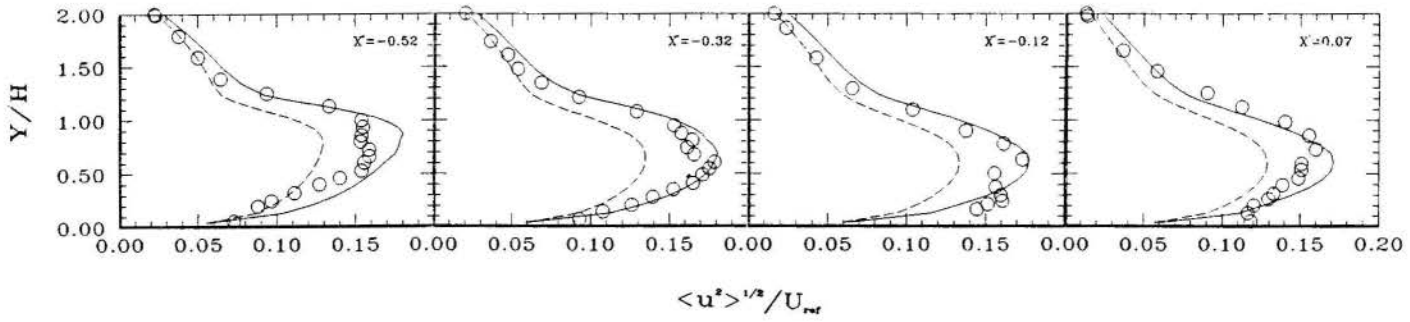

Figure 4. — Streamwise Normal Component of Reynolds Stress Tensor; Experiments: Symbols, [19]; Computations: —— ASM, ----- EVM.

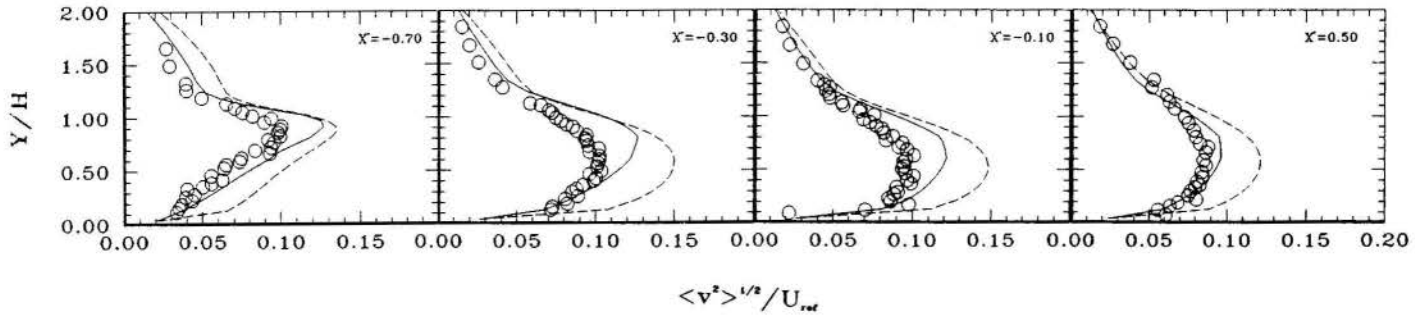

Figure 5. — Crosswise Normal Component of Reynolds Stress Tensor; Experiments: Symbols, [19]; Computations: —— ASM, ----- EVM.

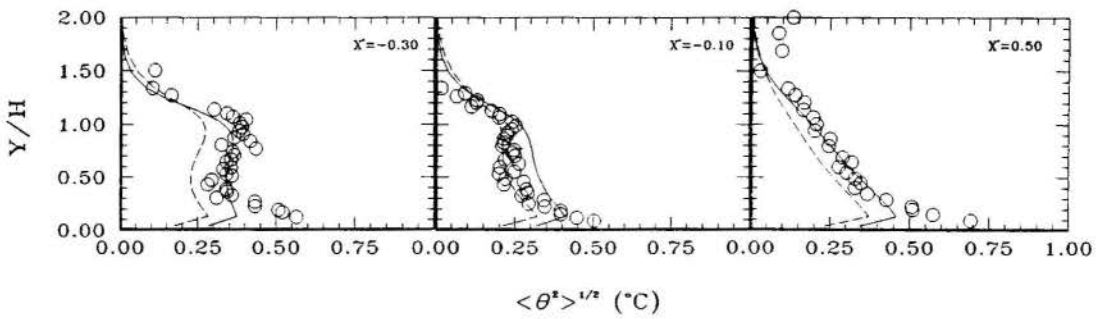

Figure 6. — Temperature Fluctuations Variance; Experiments: Symbols, [19]; Computations: —— ASM, with ε_θ-equation, ----- ASM, without ε_θ-equation.

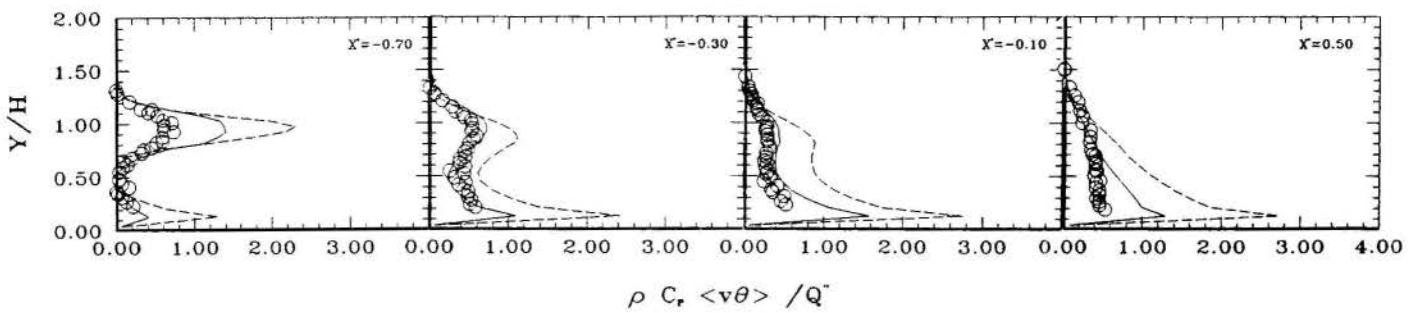

Figure 7. — Crosswise Turbulent Heat Flux; Experiments: Symbols, [19]; Computations: —— ASM, ----- EVM.

transport equations for turbulence basic parameters. Comparisons of the results with experimental data including also k-ε model computations, showed an acceptable agreement between both mean and turbulent fields provided by ASM, which can be considered within experimental errors for the majority of the comparisons. In contrast some results computed with EVM model showed significantly greater discrepancies. Although not pursued in the present study an important issue in numerical research still continues to be the improvement of near wall treatment.

ACKNOWLEDGEMENTS

The authors are grateful to Ms. C. Calta for the helpful review of the manuscript. The text was typed by Sofia Arruda.

REFERENCES

[1] Chieng, C.C. and Launder B.E. *Num. Heat Transfer*, Vol. 3, pp. 189-207, 1980.

[2] Gooray, A.M., Watkins, C.B. and Aung, W. *J. Heat Transfer*, pp. 70-76, 1985.

[3] Proud'homme, M. and Elghobashi, S. *Num. Heat Transfer*, Vol. 10, pp. 349-368, 1986.

[4] McGuirk, J.J., Papadimitriou, C. and Taylor A.M.K.P. *5th Symp. Turbulent Shear Flows*, 1985.

[5] Rotta, J.C. *Zeitschr für Physik*, Vol. 4, pp. 547-572, 1951.

[6] Naot, D., Shavit, A. and Wofshtein, M. *Israel Journal of Technology*, Vol. 88, pp. 259, 1970.

[7] Monin, A.S. *Izv. Atmo. and Oceanic Phys.*, Vol. 1, pp. 45-54, 1965.

[8] Launder, B.E. *J. Fluid Mech.*, Vol. 67, pp. 569-581, 1975.

[9] Shir, C.C. J. Atmos. Sci. 30, pp. 1327-1339, 1973.

[10] Gibson M.M. and Launder, B.E. *J. Fluid Mech.*, Vol. 86, Part 3, pp. 494-511, 1978.

[11] Huang, P.G. and Leschziner, M.A. *5th Symp. Turbulent Shear Flows*, 1985.

[12] Rodi, W. *ZAMM*, Vol. 56, pp. 219-221, 1976.

[13] Gibson M.M. and Launder, B.E. *J. Heat Transfer.*, Vol. 98, pp. 81-87, 1976.

[14] Newman, G.R., Launder, B.E. and Lumley, J.L. *J. Fluid Mech.*, Vol. 11, pp. 217-232, 1981.

[15] Launder, B.E. and Spalding, D.B. *Comp. Meth. Appl. Mech. Eng.*, Vol. 3, pp. 269-289, 1974.

[16] Daly, B.J. and Harlow, J.F. *Phys. Fluids*, Vol. 13, pp. 2634-2649, 1970.

[17] Spalding, D.B. *Int. J. of Num. Meth. in Eng.*, Vol. 4, pp. 551-555, 1972.

[18] Stone, H.L. SIAM *J. Numer. Anal.*, Vol. 5, No. 3, pp. 530-558, 1968.

[19] Vogel, J.C. and Eaton, J.K. *5th Symp. Turbulent Shear Flows*, 1985.

[20] Elghobashi, S. and Launder, B.E. *Phys. Fluids*, Vol. 16, (9), pp. 2415-2419, 1983.

[21] Jones, W.P. and Musonge, P. *4th Symp. Turbulent Shear Flows*, 1983.

[22] Nagano, Y. and Kim, C. *J. Heat Transfer*, pp. 583-589, 1988.

[23] Gibson, M.M., Jones, W.P. and Kanellopoulos, V.E. *6th Symp. Turbulent Shear Flows*, 1987.

[24] Durão, D.F.G., Pereira, J.C.F. and Rocha, J.M.P. *7th Symp. on Turbulent Shear Flows*, Stanford, M-11, 1989.

III ENCIT – Itapema, SC (Dezembro 1990)

COMPUTATION OF THREE DIMENSIONAL TURBULENT FLOWS IN A RECTANGULAR CHANNEL WITH A BUILT-IN VORTEX GENERATOR

J. X. Zhu, N. K. Mitra, M. Fiebig

Institut für Thermo- und Fluiddynamik
Ruhr-Universität Bochum
4630 Bochum, FRG

SUMMARY

The influence of a longitudinal vortex generator, a delta winglet pair which can be produced by two different methods, on heat transfer and flow loss in turbulent channel flows is investigated. No obvious difference in the total heat transfer enhancement and flow losses increment connected with the two production methods of delta winglets can be confirmed. For the two investigated cases, the mean heat transfer enhancement over the entire channel reaches about 19% and the additional flow losses amounts to 310% compared to the channel flow without vortex generator.

INTRODUCTION

Turbulent flows and heat transfer in a parallel wall channel occur frequently in many heating and cooling devices. A typical example is a plate fin heat exchanger. Fig. 1 shows a configuration of a finned tube heat exchanger, which consists of flat channels built by parallel walls. Generally a liquid flows through the tubes and a gas flows through the channels formed by parallel plate fins. In the channel boundary layers grow along the two opposite channel walls. The growth of the boundary layer increases the thermal resistance between the fluid and the channel walls.

In order to enhance heat transfer at the fin plates, longitudinal vortices (LV) can be introduced into the channel flow[1,2,3,4]. LV promote mixing of the fluid between the near wall and the core region of the channel. This disturbs the growth of boundary layers on the fin plates and thus enables high rates of heat transfer at the plates. LV can be produced by placing vortex generating devices in form of wings or winglets at the channel wall.

The vortex generators (VG), for example a pair of delta winglets, can be produced by means of two methods. For the first method, small triangular pieces of the fin can be punched out of the plate and bent in such a way that they, while remaining attached to the plate at their base, will stick out like a half wing (winglet) in the flow between two plates with a angle of attack to the streamwise direction. In the following text this manufacture method will be refered as "with stamping". In stead of stamping the VG can also be mounted on the plate, which will be refered as "without stamping". The VG can in principle be of triangular (delta) or rectangular shape. In this study only delta half wings (winglets) are considered. Fig. 2 illustrates a VG in the form of a delta winglet pair (DWP) produced by the two methods.

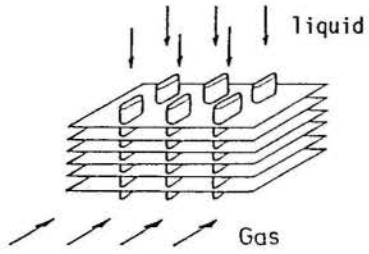

Fig. 1. Schematic of a compact gas-liquid heat exchanger with extended surfaces finned tube.

The purpose of the present work is to predict the effects of a DWP produced by the two methods on the heat transfer augmentation and flow loss increment in turbulent channel flows.

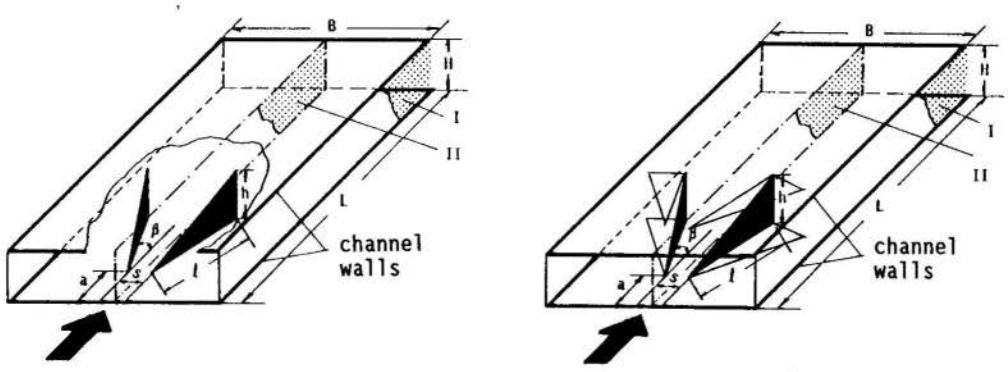

(a) without stamping (b) with stamping

Fig. 2. Computational domain: A parallel wall channel with a delta winglet (a) mounted on or (b) punched out of the channel bottom wall. In a fin-plate exchanger the element may be repeated in span and vertical directions.

MATHEMATICAL FORMULATION

Computational domain. Details of the geometry chosen for the present analysis are shown in Fig. 2, where (a) and (b) illustrate parallel wall channels with a DWP mounted on or punched out of the channel bottom wall respectively. The thickness of the VG is ignored. All dimensions in Fig. 2 (a) and (b) are the same. The dimensions of the computational domain and the VG relative to the channel height H are taken as:

$$B = 6\,H, \quad L = 10\,H, \quad l = 2\,H, \quad h = H$$
$$a = 0.5\,H, \quad s = 0.5\,H, \quad \beta = 25^{\circ}$$

The height of the delta winglets is equal to the channel height, so that this VG can act also as fin-spacers in the heat exchanger.

Because of the symmetry about the planes I and II, the computations are performed only for the region within these two planes in z - direction.

Governing equations. The Reynolds averaged Navier Stokes and energy equations in conjunction with the eddy viscosity concept are used to describe the incompressible flows in the computational domain. These equations are written in a Cartesian tensor form as

Continuity:

$$\frac{\partial U_i}{\partial x_i} = 0 \tag{1}$$

Momentum:

$$\rho \frac{DU_i}{Dt} = -\frac{\partial p}{\partial x_j} + \frac{\partial}{\partial x_j}\left[(\mu + \mu_t)\left(\frac{\partial U_i}{\partial x_j} + \frac{\partial U_j}{\partial x_i}\right) - \frac{2}{3}\rho\, k\delta_{ij}\right] \tag{2}$$

Energy:

$$\rho \frac{DT}{Dt} = \frac{\partial}{\partial x_j}\left[(\Gamma + \Gamma_t)\frac{\partial T}{\partial x_j}\right] \tag{3}$$

where the turbulent viscosity μ_t and the turbulent dynamic thermal diffusivity Γ_t are given by

$$\mu_t = c_\mu \rho k^2/\epsilon \tag{4}$$

$$\Gamma_t = \frac{\mu_t}{Pr_t} \tag{5}$$

The turbulence kinetic energy k and its dissipation rate ϵ are computed from the standard k-ϵ model of Launder and Spalding[5]:

$$\rho \frac{Dk}{Dt} = \frac{\partial}{\partial x_j}\left(\frac{\mu_t}{\sigma_k}\frac{\partial k}{\partial x_j}\right) + G - \rho\epsilon \tag{6}$$

$$\rho \frac{D\epsilon}{Dt} = \frac{\partial}{\partial x_j}\left(\frac{\mu_t}{\sigma_\epsilon}\frac{\partial \epsilon}{\partial x_j}\right) + c_1 \frac{\epsilon}{k} G - c_2 \rho \frac{\epsilon^2}{k} \tag{7}$$

G denotes the production rate of k which is given by:

$$G = \mu_t \left(\frac{\partial U_i}{\partial x_j} + \frac{\partial U_j}{\partial x_i}\right)\frac{\partial U_i}{\partial x_j} \tag{8}$$

The standard constants are employed:

$$c_\mu = 0.09, \quad c_1 = 1.44, \quad c_2 = 1.92$$
$$\sigma_k = 1.0, \quad \sigma_\epsilon = 1.3, \quad Pr_t = 0.9$$

Boundary conditions.

Entrance

Hydrodynamically developed flow and a uniform temperature T_o are assumed at the inlet of the channel in the present study. The inlet velocity, k and ϵ profiles are obtained from a calculation of 2D turbulent duct flow.

Exit

At the outlet the streamwise gradients of all variables are set to zero:

$$\frac{\partial f}{\partial x} = 0, \qquad f = (U, V, W, k, \epsilon, T) \tag{9}$$

Symmetry

At the symmetry planes (I and II) the normal velocity component and the normal derivatives of all other variables are set to zero:

$$W = 0; \qquad \frac{\partial f}{\partial z} = 0, \qquad f = (U, V, k, \epsilon, T) \tag{10}$$

Walls

Wall functions given by Launder and Spalding[5] are employed to prescribe the boundary conditions along the channel walls. The wall functions are applied in terms of diffusive wall fluxes. For the wall-tangential moment these are the wall shear stresses:

$$\tau_w = \frac{\rho U_p c_\mu^{1/4} k_p^{1/2} \kappa}{\ln(Ey^+)} \tag{11}$$

with the non-dimensional wall distance y^+ defined as:

$$y^+ = \frac{\rho y_p c_\mu^{1/4} k_p^{1/2}}{\mu} \tag{12}$$

and $\kappa \simeq 0.42$, $E = 9.0$.

The subscript p refers to the grid point adjacent to the wall. The production rate of k and the averaged dissipation rates over the near-wall cell for the k-equation as well as the value of ϵ at the point p are computed respectively from

$$G_p = \tau_w \frac{U_p}{y_p} \tag{13}$$

$$\bar{\epsilon} = \frac{1}{y_p}\int_0^{y_p} \epsilon\, dy = \frac{c_\mu^{3/4} k_p^{3/2}}{\kappa\, y_p} \ln(Ey^+) \tag{14}$$

$$\epsilon_p = c_\mu^{3/4} \frac{k_p^{3/2}}{\kappa y_p} \tag{15}$$

For the temperature boundary condition, the heat flux to the wall is derived from the thermal wall function[5]

$$q_w = \frac{(T_w - T_p)\rho c_p c_\mu^{1/4} k_p^{1/2}}{Pr_t\left[\frac{1}{\kappa}\ln(Ey^+) + P\right]} \tag{16}$$

where the empirical P function is specified as:

$$P = \frac{\pi/4}{\sin(\pi/4)}\left(\frac{A}{\kappa}\right)^{1/2}\left(\frac{Pr}{Pr_t} - 1\right)\left(\frac{Pr_t}{Pr}\right)^{1/4} \tag{17}$$

and the wall temperature T_w is a constant in the present work, $T_w = 2T_o$.

Periodicity

The stamping regions at the channel top and bottom walls are treated with periodic boundary conditions which are defined as follows:

$$f_T = f_B, \quad \left.\frac{\partial f}{\partial y}\right|_T = \left.\frac{\partial f}{\partial y}\right|_B, \quad f = (u,v,w,k,\epsilon,T) \qquad (18)$$

$_T$ - top wall, $_B$ - bottom wall

NUMERICAL PROCEDURE

A numerical procedure, based on the SOLA algorithm[6], was modified by the authors' group for the investigation of the velocity and temperature fields in 3D laminar channel flows with longitudinal vortex generators[3]. In the present work, this procedure has been extended to solve turbulent problems.

The SOLA algorithm solves the time dependent Navier-Stokes equations directly for the primitive variables. The modification used here retains the solution route of the SOLA algorithm; an explicit time step for the momentum equations is followed by an implicit, iterative pressure and velocity upgrading.

In order to validate the modified computer program, the code has been used to simulate a well documented 3D turbulent flow experiment of Pauley ad Eaton[4]. The comparison between the numerical simulation and experiment shows a reasonable agreement[7].

RESULTS AND DISCUSSION

The governing equations are solved numerically for a Reynolds number Re_H = 50000 and a Prandtl number Pr = 0.7 to predict the flow and temperature fields in the two ducts shown in Fig. 2. For the sake of comparison, a hydrodynamically developed thermally developing turbulent channel flow (without VG) is calculated with the same flow and boundary conditions as described above. Henceforth this flow is referred to as the base flow.

Effects of the two manufacture methods of DWP on the flow fields, heat transfer enhancement and flow losses increase are compared in Figs. 3 - 7. In Figs. 3 - 5 the results without stamping are presented in (a) and the results with stamping are presented in (b) respectively.

Fig. 3 shows the development of the cross flow and the divergence of the vortices along the streamwise direction in the two channels. At cross section x/H = 1.3 of (b) the inflow and outflow through the stamping holes of the top and bottom walls are evident. The cross section x/H = 9.3 reveals that the divergence of the vortices generated by the DWP without stamping is larger than with stamping.

Similar distributions of the turbulent kinetic energy are found in Fig. 4 for the two cases. The dotted lines in Fig. 4 at the cross sections x/H = 4.3 and x/H = 9.3 indicate the position of the k-isoline 2 of the base flow. In the undisturbed region of the cross section x/H = 1.3, a typical distribution of the turbulence energy in a 2D channel flow, where the turbulence energy increases with proximity to the wall, is observed. Higher turbulence kinetic energy is produced around VG by the interaction between the main flow and VG. At the downstream locations (x/H = 4.3 and x/H = 9.3) the flows with VG contain larger k-values in almost all areas of the sections than the base flow. This could be an important contribution to the heat transfer enhancement in the channel, since it means a significant increase of the turbulent thermal diffusivity in the flows. In the core region of the vortices at cross section x/H = 4.3 the level of the turbulence energy is one order of magnitude higher than that for the base flow. The influnce of the inflow through the stamping hole at the top wall on k-distribution can be seen at cross section x/H = 1.3 and is still recognizable at

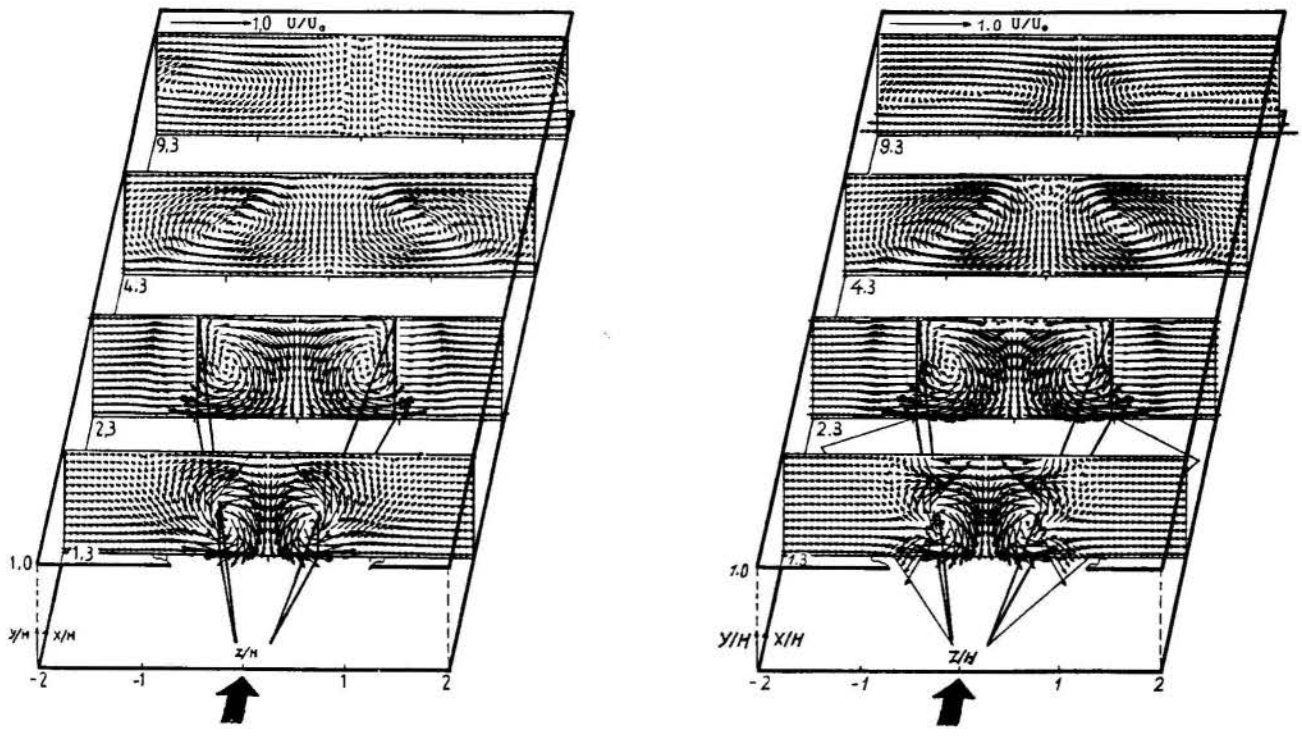

(a) without stamping

(b) with stamping

Fig. 3. Cross sectional velocity vectors at axial locations x/H = 1.3, 2.3, 4.3 9.3, showing the formation and extent of the longitudinal vortices.

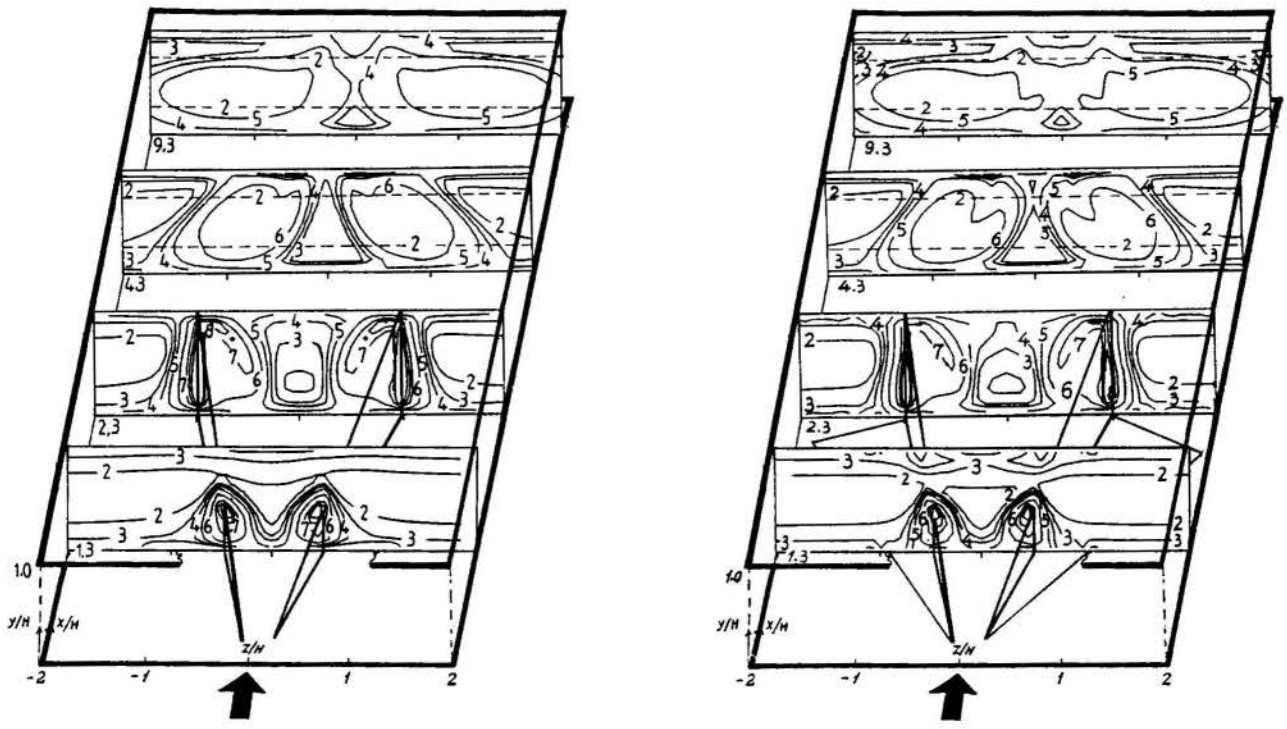

(a) without stamping (b) with stamping

Fig. 4. Contours of the turbulent kinetic energy at cross sections x/H = 1.3, 4.3 and 9.3

the downstream location of x/H = 4.3.

Fig. 5 displays contours of Nusselt number for the top and the bottom wall of the two channels shown in Fig. 2. The dotted lines in Fig. 5 stand for Nusselt number distribution on the channel walls in the base flow. Nusselt number is evaluated by

$$Nu = \frac{Re\ Pr\ q_w}{c_p\ \rho\ U_o\ (T_w - T_B)} \tag{19}$$

Eq. (19) is derived from

$$Nu = \alpha\ D_h / \lambda \tag{20}$$

with the aid of $q_w = \alpha(T_w - T_B)$ and the definitions of Re and Pr.

A piece of VG is plotted in Fig. 5(a) to show its position on the bottom wall. In the vicinity of the base of VG a low Nusselt number region exists at the pressure side, where the minimum value of Nu (line 2) is about 60% of that of the base flow (line 5). At suction side the Nu number increases rapidly in normal direction away from the VG (from line 2 to line 7). In the area between the vortices, the downwash effect of the secondary flow(ref. Fig. 3) leads to a great heat transfer augmentation; here the maximum Nusselt number (line 9) is nearly 50 % higher than the Nu value of the base flow (line 5). In the wake of the VG a low-Nu-region stretches downstream.

As shown in Fig. 2 the rear edges of the DWP touch just the top wall. Around the front of those edges the Nusselt number reaches its maximum value for the top wall (line 9). Upstream of the contact point the values of Nu are everywhere greater than those of the base flow. In the wake region of the contact point, boundary layer is thickened by the upwash flow (ref. Fig. 3), which gives rise to the low Nu values in this region.

On the bottom wall of the case with stamping(Fig. 5 (b)), the Nu-distribution at suction side of the VG and downstream of it is very similar to that of the case without stamping in the same region, what may be resulting from the same flow situation of the both cases in this area. Near the short perpendicular side of the punched hole and downstream of it, due to developing flow effects the heat transfer rates are quite high. On the top wall, owing to the influnce of inflow through the punched hole, Nu-distribution is rather different as in case (a).

Fig. 6 shows the ratios of spanwise averaged Nusselt number Nu_x on the top and bottom wall respectively to the Nusselt number of the base flow Nu_{ox} along the streamwise direction, which indicates the streamwise heat transfer enhancement produced by the DWP in the two cases.

The spanwise averaged Nusselt number Nu_x is defined as

$$Nu_x = \frac{1}{B} \int_{-B/2}^{B/2} Nu\ dz \Big|_x \tag{21}$$

In Fig. 6 the broken curves present results of the case with stamping. For the both cases, the spanwise averaged heat transfer enhancement reaches a maximum value in a small distance behind the VG on the bottom wall but in a large distance behind the VG on the top wall.

The DWP produces 20% mean heat transfer enhancement over the entire heat transfer surface on the top wall and 17.7% enhancement on the bottom wall in the case without stamping; and produces 18.7% heat transfer enhancement on the top wall and 18.3% enhancement on the bottom wall in the case with stamping. The mean value of top and bottom walls is 18.5% for the case with stamping and is 18.8% for the case without stamping.

The flow losses are evaluated by using the kinetic energy equation in [8], which is simplified for the present problem as follows:

$$\Phi_{12} = \frac{1}{2}(\alpha_1 - \alpha_2)\ U_o^2 + \frac{p_1 - p_2}{\rho} \tag{22}$$

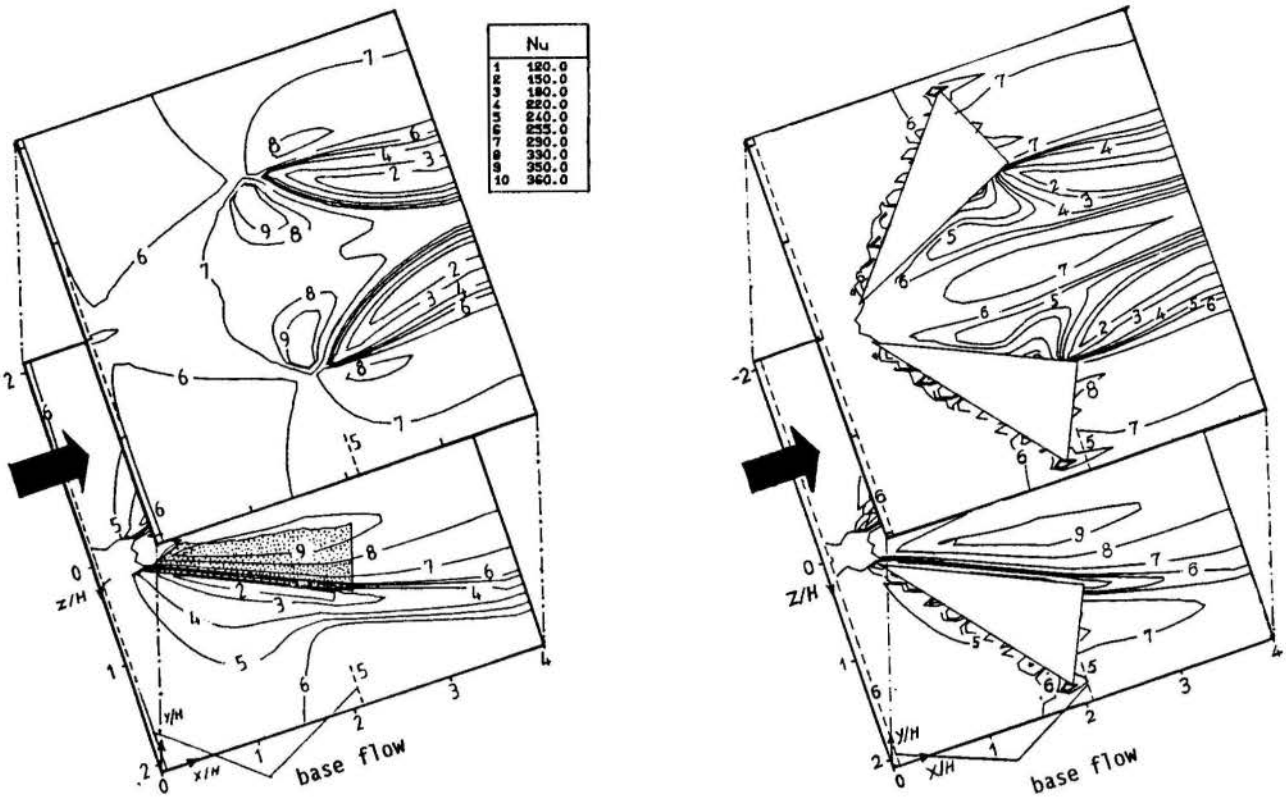

(a) without stamping

(b) with stamping

Fig. 5. Local heat transfer coefficients: Contours of Nusselt number on the top bottom walls from leading edge to the downstream location x/H = 4

where

$$\Phi_{12} = \frac{P_D}{\dot{M}} \tag{23}$$

is the specific dissipation. The variables α and P_D in eqs. (22) and (23) are kinetic energy correction factor and disspation respectively, which are described in detail by Gersten[8]. The dissipation P_D indicates the loss of mechanical energy due to friction and turbulent mixing. For the convenience of analysis, a dimensionless number, called dissipation number[9], is derived from eq. (22):

$$C_\varphi = \frac{\Phi_{12}}{U_o^2}\frac{H}{\Delta x}$$

$$= \frac{1}{2}(\alpha_1 - \alpha_2)\frac{H}{\Delta x} + \frac{1}{2}C_p\frac{H}{\Delta x} \tag{24}$$

where the index 1 means inlet, index 2 means an arbitary axial location at the downstream and Δx indicates the distance between the locations 1 and 2.

Fig. 7 shows relative increase of the dissipation numbers between the two investigated cases and base flow $(C_\varphi - C_{\varphi o})/C_{\varphi o}$. $C_{\varphi o}$ is the C_φ value of the base flow. The broken curve presents here again the result of the case with stamping. The relative increase of the flow losses induced by the DWP over the entire channel are equal for the two investigated cases and amounts 310%.

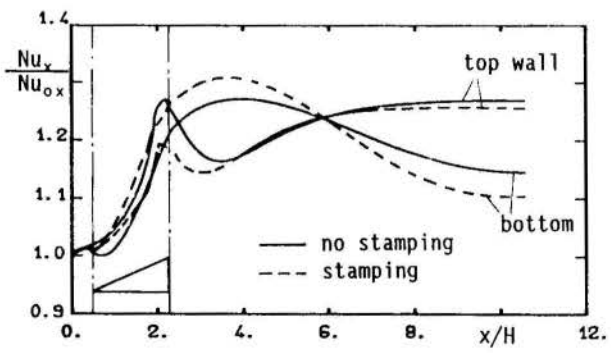

Fig. 6. Ratios of the spanwise averaged Nusselt number between the flows with and without VG, showing the local heat transfer augmentation on top and bottom walls by VG along streamwise direction.

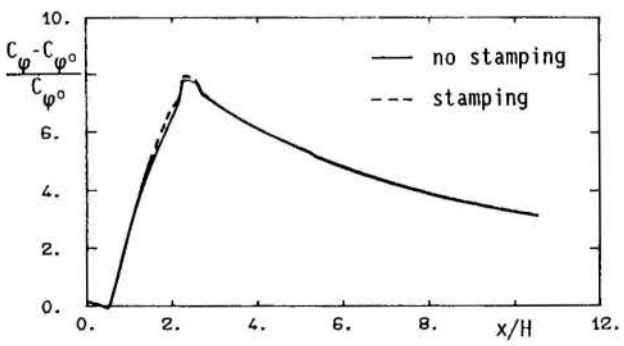

Fig. 7. Relative increase of the dissipation number over the region from entrance to axial location x between the flows with and without VG, showing the additional flow losses caused by VG along streamwise direction.

CONCLUSION

The built-in delta winglet pair with or without stamping in a turbulent channel flow has different influnce on the local flow field and local heat transfer rate. But the total effects of the DWP with or without stamping on heat transfer and flow loss are almost the same. The mean heat transfer enhancement over the entire channel, induced by the DWP in the present cases, is about 19% for a wall area which is 30 times the area of the delta winglets. The additional flow losses of the present cases amounts to 310%.

ACKNOWLEDGEMENT

The first author gratefully acknowledge the scholarship provided by the Konrad-Adenauer-Stiftung.

REFERENCES

[1] Edwards, F.J. and Alker, C.J.R., "The Improvement of Forced Convection Surface Heat Transfer Using Surface Protrusions in the Form of (A) Cubes and (B) Vortex Generators", Proc. 5th Int. Heat Transfer Conference, Vol.2, Tokyo, 1974

[2] Fiebig, M., Kallweit, P. and Mitra, N.K., "Wing Type Vortex Generators for Heat Transfer Enhancement", Proc. 8th Int. Heat Transfer Conference, Vol.6, San Francisco, 1986

[3] Fiebig, M., Brockmeier, U., Mitra, N.K., Güntermann, Th., "Structure of Velocity and Temperature Fields in Laminar Channel Flows with Longitudinal Vortex Generators", Numerical Heat Transfer, Part A, Vol.15, pp. 281-302, 1989

[4] Pauley, W.R. and Eaton, J.K., "The Effect of Embedded Longitudinal Vortex Pairs on Turbulent Boundary Layer Heat Transfer", Proc. Second Int. Symposium on Transport Phenomena in Turbulent Flow, pp. 487-500, Tokyo, 1987

[5] Launder, B.E. and Spalding, D.B., "The Numerical Computation of Turbulent Flows", Comput. Methods Appl. Mech. Eng., Vol.3, pp. 269-289, 1974

[6] Hirt, C.W., Nichols, B.D. and Romero, N.C., "SOLA - A Numerical Solution Algorithm for Transient Fluid Flows", Los Alamos Scientific Laboratory Rept. LA-5652, Los Alamos, New Mexico, 1975

[7] Zhu, J.X., Fiebig, M. and Mitra, N.K., "Numerical Simulation of a 3-D Turbulent Flow Field with Longitudinal Vortices", submitted to the ASME Winter Annual Meeting, Dallas, November 1990

[8] Gersten, K., Fluid Mechanics and Heat Transfer; Introduction and Fundamentals, Heat Exchangers Design Handbook, Hemisphere Publishing Corporation, Vol. 2, chapter 2.2.1-4, 1983

[9] Brockmeier, U., "Numerisches Verfahren zur Berechnung Dreidimensionaler Strömungs- und Temperaturfelder in Kanälen mit Längswirbelerzeugern und Untersuchung von Wärmeübergang und Strömungsverlust", (in Germen), Ph.D. Thesis, Ruhr-Universität Bochum, FRG, 1987

III ENCIT – Itapema, SC (Dezembro 1990)

ARRASTO EM CAMADAS LIMITE COMPRESSÍVEIS COM ADIÇÃO DE MASSA – UMA ABORDAGEM ASSINTÓTICA

CLÁUDIO. C. PELLEGRINI
Laboratório de Mecânica dos Fluidos/Aerodinâmica
Programa de Eng. Mecânica (COPPE/UFRJ)
C. P. 68503 – Rio de Janeiro, Brasil – 21945

Neste trabalho, o método das expansões assintóticas combinadas juntamente com a técnica das variáveis intermediárias é utilisado para obter uma fórmula para o cálculo do arrasto em escoamentos turbulentos, compressíveis, com injeção normal de fluido através de uma parede adiabática. Novas expressões são propostas para descrever a dependência das constantes k, A e Π que aparecem na solução com o número de Mach e com a taxa de injeção. Os resultados teóricos são comparados com dados experimentais mostrando boa concordância para médias e baixas taxas de injeção. Além disso, a análise fornece uma expressão para o perfil de velocidades, que concorda melhor com os dados do que as de trabalhos anteriores.

1 - INTRODUÇÃO

Os problemas de camada limite compressível turbulenta com injeção de fluido vem sendo estudados sistemáticamente desde os anos 50, quando pela primeira vez se pensou na utilização deste método como uma maneira eficaz de se proteger superfícies aerodinâmicas dos efeitos das altas temperaturas. Desde então, motivado por esta entre outras aplicações de grande importância, a determinação dos coeficientes de arrasto e de troca térmica em escoamentos deste tipo tem se apresentado como um formidável problema de engenharia. Muitas teorias tem sido propostas, mas a solução definitiva de certas questões ainda está por vir, em parte por conta de problemas na modelagem da própria turbulência, em parte por falta de concordância entre os dados experimentais dos diversos autores.

Dentre todos os resultados obtidos nestes últimos trinta anos, a maioria é devida a Squire e seus alunos na Universidade de Cambridge [1–5]. Nestes trabalhos; contudo, o coeficiente de arrasto (Cf) é calculado através da equação integral do momento linear, dado o perfil de velocidade, método que como aponta a ref. [6] tende a ser impreciso. A própria ref. [6] propõe como método alternativo para o cálculo de Cf que a transformação de Van Driest seja aplicada à equação do arrasto dedusida na ref. [7] para o caso compressível. Contudo, a despeito das previsões teóricas de Cf apresentarem boa concordância com os dados experimentais de Squire [2], a teoria é matematicamente pouco rigorosa e não fornece boas predições para o perfil de velocidades.

O objetivo do presente trabalho é obter uma expressão para o cálculo de Cf em escoamentos compressíveis com injeção que seja matemáticamente rigorosa, o que no conhecimento do autor ainda não foi feito. Para isso, utiliza-se o método das expansões assintóticas combinadas de maneira ligeiramente distinta da forma clássica, empregando-se a técnica das variáveis intermediárias [8,9] na escolha das funções que fazem o esticamento das coordenadas. A concordância entre as previsões teóricas para Cf e os dados experimentais da ref. [2] é boa, e a expressão para o perfil de velocidades proposta concorda melhor com os experimentos das refs. [2] e [5] do que a proposta pela ref. [6]. Além disso, o método utilizado tem a vantagem de poder ser usado na dedução de equações para o coeficiente de troca térmica e para o perfil de temperatura compressíveis com injeção, expressões que até o momento são inéditas.

2 - DETERMINAÇÃO DAS FUNÇÕES DE ESTICAMENTO

Consideremos, de início, um escoamento turbulento, compressível e bidimensional, de um fluido Newtoniano. O sistema básico de equações que rege um escoamento deste tipo pode ser encontrado no trabalho de Van Driest [10]. Consideremos ainda que o fluido em estudo escoe sobre uma superfície plana, adiabática e porosa, através da qual se esteja injetando fluido de mesma espécie química, na direção normal ao escoamento, com velocidade constante V_w, e que a temperatura mantenha-se constante na direção do escoamento, fora da camada limite.

Colocado o problema, analisemos as equações que o governam em primeira ordem de aproximação, utilisando o método das variáveis intermediárias. Esta análise, além de fornecer importantes informações sobre a física do problema, mostra quais os esticamentos de coordenadas apropriados à posterior solução assintótica das equações. Considerando a ordem de grandeza máxima de todas as variáveis envolvidas, propomos a adimensionalização das equações através das seguintes expressões:

$$\psi_{ad} = (\psi - \psi_w)/(\psi_\infty - \psi_w) \tag{2.1}$$

$$U'_{ad} = U'/u_\tau \tag{2.2}$$

$$V'_{ad} = V'/u_\tau \tag{2.3}$$

$$\rho'_{ad} = \rho'/\rho_\infty(u_\tau/U_\infty) \tag{2.4}$$

$$P'_{ad} = P'/\rho_\infty u_\tau^2 \tag{2.5}$$

$$\mu_{ad} = \mu'/\mu_\infty \tag{2.6}$$

$$X_{ad} = X/X \tag{2.7}$$

$$Y_{ad} = Y/(\delta\eta) \tag{2.8}$$

Nesta lista, bem como em tudo que se segue, todas as variáveis têm o significado clássico. A variável ψ pode assumir os valores U, V, P, ρ, (ρU), e (ρV); os índices ad, ∞ e w representam respectivamente variável adimensional, valores no escoamento externo à camada limite e na parede; η é a função de esticamento das coordenadas; u_τ é a velocidade de fricção, definida por $u_\tau = \sqrt{\tau_w/\rho_w}$, com τ_w sendo o atrito na parede.

O motivo pelo qual o valor u_τ foi utilizado na adimensionalização da flutuação turbulenta U' é que, como indica Afsal

[11], a ordem de grandeza de U' varia entre 0 e este valor. Medidas posteriores de Kistler e Chen [12] e de Morkovin [13] mostraram que $ord(U'/U_\infty) = ord(V'/U_\infty) = ord(\rho'/\rho_\infty) = ord(\sqrt{P'/\rho_\infty U_\infty^2})$, (onde *ord* significa ordem de grandeza) de modo que todas as variáveis turbulentas adimensionais têm ordem entre 0 e 1.

Aplicando às equações de Van Driest o método das variáveis intermediárias de forma clássica, obtemos o seguinte conjunto de aproximações de primeira ordem para a equação do momento linear na direção X:

$ord(1) \geq ord(\eta) > ord(\epsilon^2/\gamma)$:

$$(\rho U)U_x + (\gamma\eta)^{-1}(\rho V)U_y = -\frac{\Delta P}{\rho_\infty U_\infty^2}P_x \qquad (2.9)$$

$ord(\eta) = ord(\epsilon^2/\gamma)$:

$$(\rho U)U_x + (\gamma\eta)^{-1}(\rho V)U_y = -\frac{\Delta P}{\rho_\infty U_\infty^2}P_x - \left[\left(\frac{\rho\Delta\rho}{\rho_\infty} + \frac{\rho_w}{\rho_\infty}\right)\overline{U'V'}\right]_y \qquad (2.10)$$

$ord(\epsilon^2/\gamma) > ord(\eta) > ord(Re_\infty\gamma\epsilon)^{-1}$:

$$\left(\frac{\rho_w}{\rho_\infty}\right)\left(\overline{U'V'}\right)_y = 0 \qquad (2.11)$$

$ord(\eta) = ord(Re_\infty\gamma\epsilon)^{-1}$:

$$\left(\frac{\rho_w}{\rho_\infty}\right)\left(\overline{U'V'}\right)_y = (\mu U_y)_y \qquad (2.12)$$

$ord(\eta) < ord(Re_\infty\gamma\epsilon)^{-1}$:

$$(\mu U_y)_y = 0 \qquad (2.13)$$

onde $\epsilon = u_\tau/U_\infty$, $\gamma = \delta/X$ e $Re_\infty = \rho_\infty U_\infty X/\mu_\infty$.

Os conjuntos de equações correspondentes às equações da continuidade e do momento linear na direção Y fornecem respectivamente $ord(U) = ord(V/\delta\eta)$, para todo η, e $P_y = 0$, para $ord(1) \geq ord(\eta) \geq ord(\epsilon^2/\gamma)$, $P_y = \left(\overline{V'V'}\right)_y$, para $ord(\eta) < ord(\epsilon^2/\gamma)$. Na dedução das aproximações acima, uma consideração extra foi feita: baseado na condição de contorno da parede, isto é, $U = V = \rho = 0$, assumimos que nas camadas mais próximas à esta, U, V e ρ são de ordem inferior a unitária. Os resultados já existentes para o caso sem injeção mostram que esta hipótese é razoável

De acordo com as definições de Lagerstron e Casten [9] sobre domínio de validade das equações aproximadas, vemos que é suficiente resolver as equações (2.10) e (2.12) para descrever toda a camada limite, pois elas são "suficientemente ricas" para conter todas as outras. Assim sendo, o escoamento fica dividido em duas regiões, a mais próxima à parede, que chamaremos *região da parede*, e a mais distante, que chamaremos *região da esteira*. Os valores de η que levam a estas duas regiões são os esticamentos de coordenadas apropriados para a análise assintótica, ou seja:

$$\eta_e = \epsilon^2/\gamma \qquad (2.14)$$

$$\eta_p = (Re_\infty\epsilon\gamma)^{-1} \qquad (2.15)$$

η_p para a região da parede e η_e para a regiào da esteira.

3 - ANÁLISE ASSINTÓTICA DAS EQUACÕES

Na análise assintótica das equações do escoamento, as duas regiões em que este se divide, definidas pelos esticamentos (2.14) e (2.15), serão estudadas separadamente. Uma diferente adimensionalização será utilizada em cada caso, fazendo com que todas as variáveis não-dimensionais tenham ordem de grandeza unitária em ambas as regiões. De fato, se assim não fosse, suas ordens teriam que ser consideradas durante a posterior coleta dos termos de mesma ordem nas equações esticadas.

Assim, as duas sub-seções seguintes começam com uma adimensionalização de variáveis diferente da proposta na seção anterior, e utilisando as funções de esticamento de coordenadas encontradas nesta, obtém, através do método das expansões assintóticas, soluções para as duas regiões do escoamento.

3.1 - Região da Parede. Para adimensionalizar as equações que governam o problema nesta região, vamos considerar a hipótese apoiada nos resultados existentes para o caso incompressível, que $ord(U) = ord(U') = ord(u_\tau)$. Além disso, vamos considerar que hipótese semelhante seja válida para as outras variáveis médias do escoamento, isto é, que $ord(\psi - \psi_w) = ord(\psi')$, para $\psi = V$, ρ, P, (ρU) e (ρV). Deste modo, considerando a ordem de grandeza das flutuações turbulentas de acordo com as refs. [14] e [15], a expressão (2.1) fica substituída pela expressão geral $\psi_{ad} = (\psi - \psi_w)/\psi_\tau$, onde ψ_τ é o termo da ordem da flutuação de ψ. Além disso, na expressão (2.6) vamos substituir o valor de referência μ_∞ por μ_w, e na (2.8) faremos $\eta = 1$, pois não existe esticamento ainda. Todas as outras expressões de adimensionalização são iguais às apresentadas na seção anterior.

Adimensionalizando então as equações do escoamento na forma proposta, e procedendo o esticamento de coordenadas de acordo com (2.9) e (2.15), observa-se que a correção ao termo de atrito devido à injeção na equação do momento linear tem ordem V_w/u_τ. Assim, para que as equações aproximadas de segunda ordem dêem conta deste efeito, nossas expansões serão feitas no parâmetro $\tilde{\epsilon}/\epsilon$ $(= V_w/u_\tau)$, pequeno por hipótese. A expressão geral dessas expansões, válida para todas as variáveis, é então:

$$\psi = \psi_{11} + (\tilde{\epsilon}/\epsilon)\psi_{21} + \epsilon\psi_{12} + \tilde{\epsilon}\psi_{22} + (\tilde{\epsilon}/\epsilon)^2\psi_{31} + \epsilon^2\psi_{13} + (\tilde{\epsilon}/\epsilon)^3\psi_{41} + \epsilon^3\psi_{14} + \cdots \qquad (3.1)$$

A expansão (3.1) foi feita também em torno do parâmetro pequeno ϵ, de modo a que as equações aproximadas de segunda ordem possam dar conta de efeitos desta ordem, se necessário. Substituindo a expressão (3.1) nas equações não dimensionais esticadas, e coletando termos de mesma ordem de grandeza, temos para as duas primeiras ordens de aproximação da equação do momento linear em X:

$$1^a\ ordem: \quad \left(\mu^+ U^+_{11_{y^+}}\right)_{y^+} - \left(\overline{U'V'}\right)^+_{11_{y^+}} = 0 \qquad (3.2)$$

$$2^a\ ordem: \quad U^+_{11_{y^+}} = \left(\mu^+ U^+_{21_{y^+}}\right)_{y^+} - \left(\overline{U'V'}\right)^+_{21_{y^+}} \qquad (3.3)$$

onde $y^+ = yu_\tau/\nu_w$ é a coordenada esticada, $U^+ = U(y^+)$ e $\mu^+ = \mu(y^+)$. Estas equações, de acordo com a teoria das variáveis intermediárias, valem até a parede.

Bejan [14] apresentou solução para a equação (3.2), mas verificou que a concordância com dados experimentais, no caso incompressível, não é boa. Para contornar tal problema, ele propôs que se resolvesse a equação (3.2) desprezando-se o termo laminar, de modo a adicionar mais um grau de liberdade à solução, melhorando consideravelmente a concordância.

Para repetir o procedimento de Bejan, no escopo da teoria que estamos usando, resolvemos as equações (3.2) e (3.3) numa região mais próxima ao escoamento externo, aonde, como mostra a equação (2.11), não aparece o termo laminar. Nesta região, contudo, não se dispõe de condições de contorno adequadas, de modo que algumas constantes a determinar aparecerão no resultado. Assumindo válida a teoria do comprimento de mistura de Prandtl como modelo de turbulência, a solução das equações (3.2) e (3.3) na região fica:

$$U_{11}^{+} = \left(\frac{1}{k}\ln y^{+} + A\right) \tag{3.4}$$

$$U_{21}^{+} = \frac{1}{4}\left(\frac{1}{k} ln y^{+} + A\right)^{2} \tag{3.5}$$

onde k e A são as constantes a determinar. Substituindo estas duas equações na expansão (3.1), desfazendo o esticamento, e redimensionalizando, temos finalmente:

$$U = \left(\frac{1}{k}\ln y\frac{u_\tau}{\nu_w} + A\right) + \frac{V_w}{4}\left(\frac{1}{k}\ln y\frac{u_\tau}{\nu_w} + A\right)^{2} \tag{3.6}$$

3.2 - Região da Esteira. Nesta região, todas as variáveis médias tem a ordem de grandeza de seus respectivos valores no escoamento externo. Com as relações de ordem de grandeza dadas nas refs. [14] e [15], a adimensionalização de variáveis nesta região fica, então, dada pelas expressões (2.1)–(2.8) fazendo $\eta = 1$. Assim, se fizermos o esticamento de coordenadas nas equações não-dimensionais, utilizando a expressão (2.14), em seguida substituirmos nas expressões resultantes expansões assintóticas semelhantes à expressão (3.1), e coletarmos termos de primeira ordem, a equação do momento linear em X resultante será formalmente idêntica à equação (2.10).

Como no caso da região da parede, esta equação não será resolvida na forma em que aparece, também por causa das dificuldades matemáticas envolvidas, neste caso devido ao termo contendo flutuações turbulentas. Outrossim, ela será resolvida numa região mais próxima ao escoamento externo aonde, como mostra a equação (2.10), o termo turbulento pode ser desprezado. Nesta região valem ainda as condições de contorno do escoamento externo, de modo que a solução de primeira ordem, já colocada na forma não-esticada, dimensional, é:

$$U = U_\infty \tag{3.7}$$

Para a segunda ordem de aproximação, não é possível encontrar solução analítica simples para a equação obtida nem na região mais próxima ao escoamento externo. O problema é contornado propondo uma extensão à solução dada por Coles [15], que é válida para o caso incompressível sem injeção. Baseado na observação de um grande número de experimentos, Coles propôs a seguinte expressão para o perfil de velocidades:

$$U = u_\tau\left(\frac{1}{k}\ln y\frac{u_\tau}{\nu_w} + A + \frac{\Pi}{k}w(\frac{y}{\delta})\right) \tag{3.8}$$

onde Π é uma constante a determinar, e $w(y/\delta)$ é uma função de caráter universal. A expressão (3.8), de acordo com Coles, vale desde a limite inferior da região da parede até a extremidade da camada limite. Se reescrevermos esta expressão na forma

$$U = U_\infty + u_\tau\left[\frac{1}{k}\ln\frac{y}{\delta} + \frac{\Pi}{k}\left(w(\frac{y}{\delta}) - 2\right)\right] \tag{3.9}$$

veremos que a correção de segunda ordem à expressão (3.7) é uma função de (y/δ). Uma extensão à idéia de Coles para o caso compressível pode ser tentada de várias formas. A ref. [6] apresenta uma possível. Neste trabalho propomos a que nos parece mais simples, observando as expressões (3.6) e (3.8), ou seja:

$$\begin{aligned} U = &\left[\frac{1}{k}\ln y\frac{u_\tau}{\nu_w} + A + \frac{\Pi}{k}w(\frac{y}{\delta})\right] \\ &+ \frac{V_w}{4}\left[\frac{1}{k}\ln y\frac{u_\tau}{\nu_w} + A + \frac{\Pi}{k}w(\frac{y}{\delta})\right]^{2} \end{aligned} \tag{3.10}$$

Essa expressão, como a de Coles, se reduz à solução da região da parede quando $y \to 0$, pois $w \to 0$, sendo válida portanto para ambas as camadas. Deste modo, não há necessidade de passar-se pelo processo de combinação das soluções. De fato, se tivéssemos obtido a aproximação de segunda ordem para o perfil de velocidades, resolvendo a equação aproximada correspondente, ao invés de recorrer à solução de Coles extendida, não haveria combinação possível, pois a análise por variáveis intermediárias da seção 2 deixa claro que as equações resolvidas são intermediárias, e não principais, como seria preciso para que houvesse combinação. Além disso, a mesma análise deixa claro, através da equação (2.13), que a expressão (3.10) não vale até a parede, região aonde predomina o termo laminar (por isso mesmo chamada sub-camada laminar).

3.3 - Equação do Arrasto. Para obter uma expressão para o cálculo do arrasto a partir do perfil de velocidades, basta conhecer algum par de valores (y, U) pertencente à função (3.10). Tomando o ponto (δ, U_∞) temos:

$$U_\infty = \left(\frac{1}{k}\ln\delta\frac{u_\tau}{\nu_w} + A + 2\frac{\Pi}{k}\right) + \frac{V_w}{4}\left(\frac{1}{k}\ln\delta\frac{u_\tau}{\nu_w} + A + 2\frac{\Pi}{k}\right)^{2} \tag{3.11}$$

No caso que estamos estudando, as expresões (3.10) e (3.11), juntamente com uma expressão para o cálculo de δ (como o balanço integral do momento linear em X, por exemplo), permitem que se calcule o arrasto associado ao escoamento. Este é o resultado central deste trabalho.

4 - DETERMINAÇÃO DAS CONSTANTES

Como dissemos em seções anteriores, a dependência de k, A e Π com alguns parâmetros do escoamento precisa ser levantada experimentalmente. Seguindo o método clássico, utilizado por exemplo na ref. [7], os dados experimentais das refs. [16] e [2] foram representados em gráfico na forma $\Phi \times \ln(yu_\tau/\nu_w)$, como sugere a equação (3.6), onde $\Phi = (2u_\tau/V_w)(\sqrt{1 + UV_w/u_\tau^2} - 1)$, se $V_w \neq 0$, e $\Phi = U/u_\tau$ se $V_w = 0$. A fig.1 ilustra o fato com os dados para Mach = 2.5 da ref. [2].

A análise realizada mostra que k e Π variam com o número de Mach, e que A varia, além disso, com a taxa de injeção. Tais resultados são conhecidos na literatura, e já foram publicados anteriormente por Mabey, ref. [17], e por Squire, ref. [1], entre outros. A variação de A com V_w pode ser observada na fig. 1, onde $f = \rho_w V_w/\rho_\infty U_\infty$ é a taxa de injeção. Os valores experimentais obtidos pela análise para k, e A no caso sem injeção, aparecem representados em gráfico nas figs. 2 e 3. No caso de Π, observou-se que sua variação com Mach pode ser bem de-

scrita se tomarmos $P = 2\Pi/k = 1.75$, valor menor do que o encontrado geralmente na literatura. Nos gráficos das figs. 2 e 3 aparecem, além dos valores experimentais, uma representação dos polinômios que melhor se ajustam a estes. Uma vez estabelecida a dependência de A com o número de Mach, a teoria de Simpson, ref. [18] foi usada para descrever sua dependência simultâneamente com V_w e com Mach. Os polinômios ajustados, o valor proposto para P, e a curva de Simpson para a A são mostrados abaixo:

$$k = 0.398 + 0.017\mathrm{M} - 0.028\mathrm{M}^2 + 0.013\mathrm{M}^3 - 0.001\mathrm{M}^4 \quad (4.1)$$

$$P = 2\Pi/k = 1.75 \quad (4.2)$$

$$A_O = 3.959 + 0.622\mathrm{M} - 0.742\mathrm{M}^2 + 0.353\mathrm{M}^3 - 0.042\mathrm{M}^4 \quad (4.3)$$

$$A = \frac{2u_\tau}{V_w}\left(\sqrt{\frac{U_a^+ V_w}{u_\tau} + 1} - 1\right) - \frac{1}{k}\ln U_a^+ \quad (4.4)$$

onde U_a^+ é obtido resolvendo-se $U_a^+ = (1/k)\ln U_a^+ + A_O$, sendo A_O o valor de A para o caso sem injeção, dado na expressão (4.3), e M é o número de Mach.

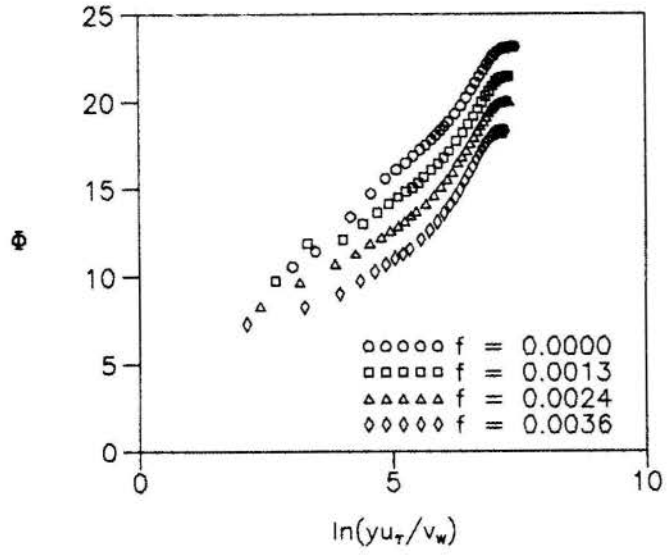

Fig. 1 – Variação de A com a taxa de injeção, para Mach = 2.5

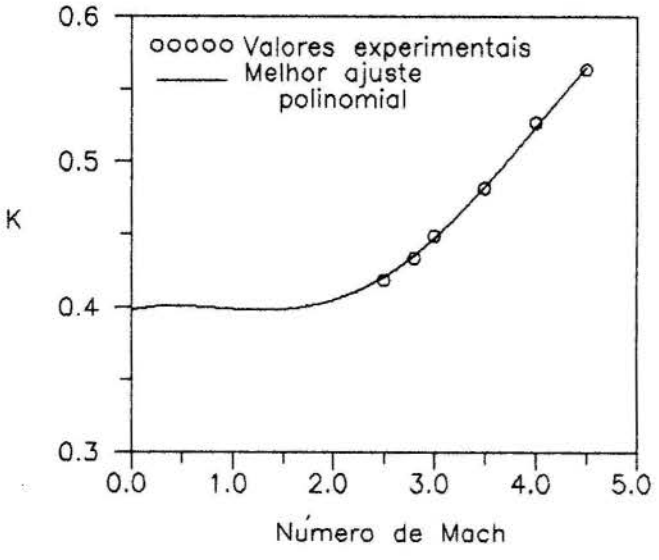

Fig. 2 – Variação de K com o número de Mach

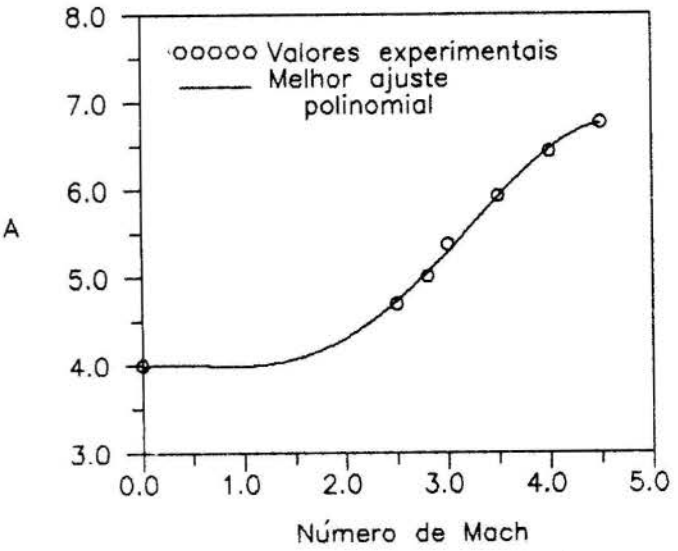

Fig. 3 – Variação de A com o número de Mach para o caso sem injeção

Predições de Cf através das expressões (3.11) e (4.1)–(4.4) podem ser vistas na fig. 4. A concordância com os dados experimentais da ref. [2] é bastante boa nas taxas de injeção média e baixa. Predições do perfil de velocidades aparecem nas figs.5, 6 e 7, mostrando melhor concordância com os dados da mesma referência que a teoria da ref. [6].

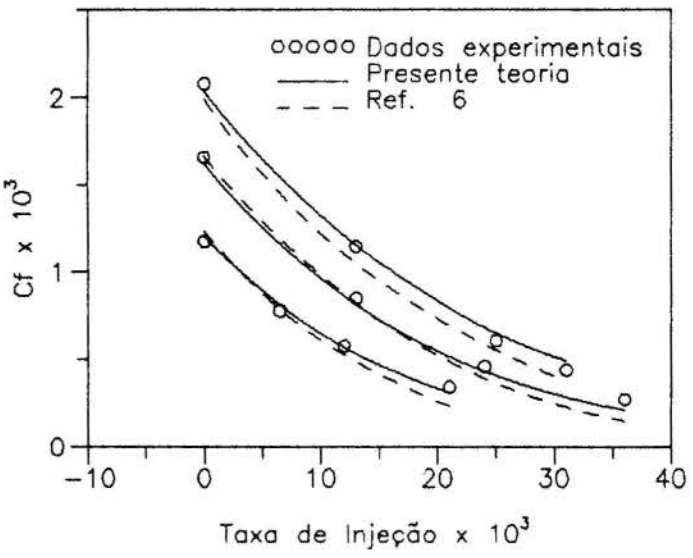

Fig. 4 – Coeficiente de arrasto

5 - CONCLUSÃO

O método das variáveis intermediárias, juntamente com a teoria das expansões assintóticas combinadas, foi usado para propor uma solução ao escoamento turbulento, compressível, com injeção de massa, de uma forma matematicamente rigorosa. O resultado central deste estudo são as expressões do arrasto (3.11) e do perfil de velocidades (3.10), cuja análise conduz a resultados bastante interessantes.

Em primeiro lugar, chama a atenção o fato de que as expressões propostas são idênticas às do caso incompressível, sendo o efeito da compressibilidade levado em conta apenas pelas constantes k, A e P. Comparação entre teoria e expe-

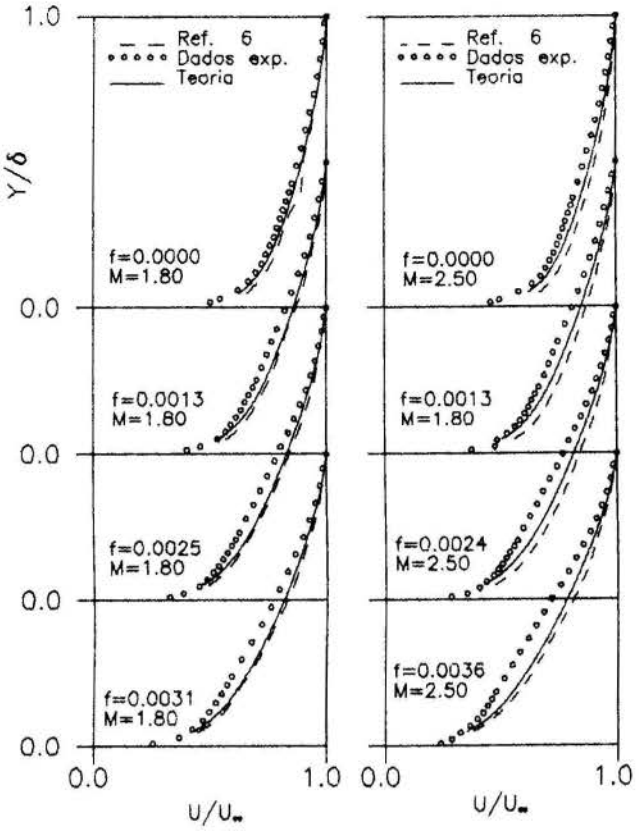

Fig. 5 – Perfis de velocidade, para Mach = 1.8

Fig. 6 – Perfis de velocidade, para Mach = 2.5

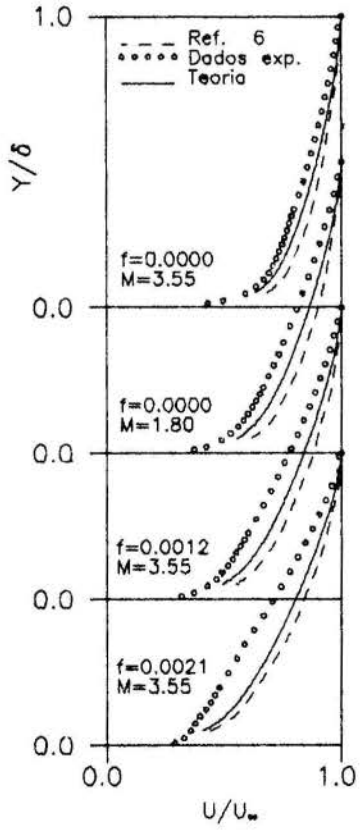

Fig. 7 – Perfis de velocidade, para Mach = 3.6

rimento mostrada na seção 4 através dos dados das refs. [16], [2] e [6], mostra que tal hipótese é de fato razoável, uma vez que os perfis de velocidade para o caso sem injeção concordam de maneira excelente com a teoria. A análise deixa claro ainda que o formato do perfil de velocidades, na região mais afastada da parede, afasta-se do previsto pela expressão (3.10) à medida que a injeção aumenta, sendo contudo a concordância com dados experimentais melhor do que a encontrada em trabalhos anteriores.

Por outro lado, as constantes k, A e Π, obtidas como o foram, dependem fortemente dos valores medidos de Cf. Para o caso sem injeção, os dados utilizados (ref. [16]) são considerados por vários autores, até o momento, como o caso teste, de modo que as expressões propostas para k, A_O e P são, de fato, confiáveis. A única consideração a respeito, é que P, exibe valores menores dos que os geralmente encontrados na literatura, o que sugere que os experimentos não foram realizados com um número de Reynolds em que P se encontre totalmente desenvolvido. No caso com injeção contudo, o próprio autor das experiências (ref. [2]) propõe correções aos seus valores, que são os únicos disponíveis, e que, como aponta a ref. [7], são tão menos confiáveis quanto mais alta é a injeção. Por este motivo, a expressão para A fica bem menos confiável do que as três anteriores, e fica explicado porque, de maneira geral, a concordância na Fig. 4 piora à medida que a injeção aumenta.

Pelo que foi dito, fica claro que as expressões que descrevem a dependência das três constantes devem ser consideradas com bastante cuidado. Não é aconselhável extrapolá-las, pois sua validade foi testada apenas nos limites estabelecidos pelos dados experimentais.

A solução desenvolvida no presente trabalho pode ser utilizada para propor expressões para o cálculo do coeficiente de troca térmica e do perfil de temperatura. Esse procedimento está sendo levado a cabo pelo autor no momento, e seus resultados serão publicados em breve.

Agradecimentos: O autor gostaria de expressar seu agradecimento aos Srs. M. A. F. Medeiros e A. P. Silva Freire pelos conselhos e sugestões recebidas durante o curso desta pesquisa. O trabalho teve apoio financeiro do Conselho Nacional de Desenvolvimento Científico e Tecnológico (CNPQ), e da Federação de Amparo à Pesquisa do Estado do Rio de Janeiro (FAPERJ).

6 - REFERÊNCIAS

[1] L. C. SQUIRE,'A law of the wall for compressible turbulent boundary layers with air injection', *J. Fluid Mech.*, vol. **37**, pp. 449–456 (1969).

[2] L. C. SQUIRE,'Further experimental investigations of compressible turbulent boundary layers with air injection', *A-RC R&M*, No. **3627**, (1970).

[3] L. C. SQUIRE,'Eddy viscosity distributions in compressible turbulent boundary layers with air injection', *Aero Q.*, vol. **XXIII**, pp. 169–182 (1971).

[4] L. C. SQUIRE and V. K. VERMA,'The calculation of compressible turbulent boundary layers with fluid injection', *ARC CP*, No. **1265**, (1973).

[5] L. O. F. JEROMIN,'An experimental investigations of compressible turbulent boundary layers with air injection', *A-RC R&M*, No. **3526**, (1968).

[6] A. P. SILVA-FREIRE,'An extension of the transpired skin-friction equation to the compressible turbulent boundary layers', *Int. J. Heat Mass Transfer*, vol. **31**, pp. 2395–2398 (1988).

[7] A. P. SILVA-FREIRE,'An asymptotic solution for transpired incompressible turbulent boundary layers', *Int. J. Heat Mass Transfer*, vol. **31**, pp. 1011–1021 (1988).

[8] S. KAPLUN, 'Fluid mechanics and singular perturbations', *Academic Press, San Diego*, (1967)

[9] P. A. LAGERSTROM and R. G. CASTEN,'Basic concepts underlying singular perturbation techniques', *SIAM*, vol. **14**, pp. 63–120 (1972).

[10] E. R. VAN DRIEST,'Turbulent boundary layers in compressible fluids', *North American Aviation, Inc.*, vol. **18**, pp. 145–160 (1951).

[11] N.AFZAL,'A higher order theory for compressible turbulent boundary layers at moderately large Reynolds number', *J. Fluid Mech.*, vol. **57**, pp. 1–27 (1973).

[12] A. L. KISTLER and W. S. CHEN,'A fluctuating pressure field in a supersonic turbulent boundary layer', *J. Fluid Mech.*, vol. **16**, pp. 41–64 (1963).

[13] M. V. MORKOVIN,'Effects of compressibility on turbulent flows', *Méchanic de la turbulence*, pp. 367–380 (1962).

[14] A. BEJAN, 'Convection heat transfer', *John Wiley and Sons*, (1984)

[15] D. COLES,'The law of the wake in the turbulent boundary layer', *J. Fluid Mech.*, vol. **1**, pp. 191–226 (1956).

[16] H. H. FERNHOLZ and P. J. FINLEY,'A critical compilation of compressible turbulent boundary layer data', *Advisory Group for Aeroespace Research & Development (AGARD)–North Atlantic Treaty Organization*, No. **223**, (1977).

[17] D. G. MABEY, 'Some boundary layer measurements on a flat plate at Mach numbers from 2.5 to 4.5', *AGARD* Conf. proc. 93', paper No. 2, (1971)

[18] R. L. SIMPSON,'Characteristics of turbulent boundary layers at low Reynolds numbers with and without transpiration', *J. Fluid Mech.*, vol. **42**, pp. 769–802 (1970).

ABSTRACT

The matched assymptotic expansions method togheter with the intermediate variable techniques is used in this work to obtain an expression for the calculation of the skin-friction coeficient in turbulent compressible flows with normal injection through an adiabatic, porous wall. New expressions are proposed to describle the dependence of the constants k, A and Π appearing on the skin-friction equation on the Mach number and injection rate. Theoretical results are compared with experimental data and show good agreement for medium and low injection rates. The analyses also provides an expression for the velocity profile that agrees better with the data considered than the ones found in the literature.

III ENCIT – Itapema, SC (Dezembro 1990)

ANALYSIS OF THERMAL TURBULENT BOUNDARY LAYERS OVER ROUGH SURFACES

ATILA P. SILVA FREIRE AND MIGUEL H. HIRATA
Laboratório de Mecânica dos Fluidos/Aerodinâmica,
Programa de Engenharia Mecânica(COPPE/UFRJ),
C.P. 68503, 21945 Rio de Janeiro, Brasil.

The present work uses the logarithmic distribution approach to study thermal turbulent boundary layers over rough surfaces. It is shown that the similarity parameter used to describe the dynamic boundary layer, the displacement in origin, can also be used to describe the thermal boundary layer. The analysis provides expressions for both the inner and the outer parts of the boundary layer. The theoretical results are successfully tested against four different sets of data.

1. INTRODUCTION

The flow of a fluid over surfaces which are not aerodynamically smooth occurs in many situations of technological interest. As a result, many works have been published which deal with this subject. Basically, two approaches are used by researchers: 1) the logarithmic distribution approach[1,2,3,4,5,6] and 2) the discret element approach [7,8,9]. The former approach assumes the existence of a logarithmic distribution of mean velocity profile in a region near the wall, so that the problem is reduced to the determination of appropriate length scales and of universal parameters. The discrete element approach on the other hand concentrates on analysing the blockage effect of each individual roughness element on the flow. The total force of the roughness elements on the flow can then be accounted for by including a form drag term in the momentum equation.

The aim of the present work is to extend the logarithmic distribution approach to the case with heat tranfer. In particular, we want to address the question of the choice of the similarity parameters. In this connection we show that a single length scale can be used to represent both the "k" and the "d" types of roughness, this scale being the same as for the velocity distribution.

In section two we briefly review previous analyses developed for the dynamics of the flow, introducing the law of the wall and the law of the wake expressions in terms of the displacement in origin[4]. In section three some theoretical results are invoked [13,14,15] so that universal laws can be proposed for the thermal boundary layer for comparison with the rough surface velocity profiles. Comparison of results with experimental data is also made in section three.

2. TWO TYPES OF ROUGHNESS

Two types of roughness are normally classified in literature depending on the roughness elements geometry (Figs. 1 and 2).

If the elements are sufficiently set apart ($\lambda > 4w$) so that large eddies are formed and shed into the flow behind and above the elements (Fig.1), we have a "k" type roughness. In this case a fully turbulent layer of length scale proportional to the height of the elements, k, occurs which must match with the flow described by the velocity defect expression. The law of the wall can then be written as [1,2,3]

$$\frac{U}{u_\tau} = \frac{1}{K} \ln \frac{y + \epsilon}{\epsilon} + A - D \quad , \qquad (1)$$

where K and A are universal constants with typical values 0.41 and 5.0, ϵ is the displacement in origin* and D is a parameter which depends on the type of roughness. The notation is classical. Thus u_τ denotes the friction velocity ($=\sqrt{\tau_w/\rho}$).

On a surface where on the other hand the elements are closely spaced ($\lambda < 2w$), a recirculating

*the displacement in origin is the distance below the crest of the elements where the origin of the profiles must be located so that similarity laws apply.

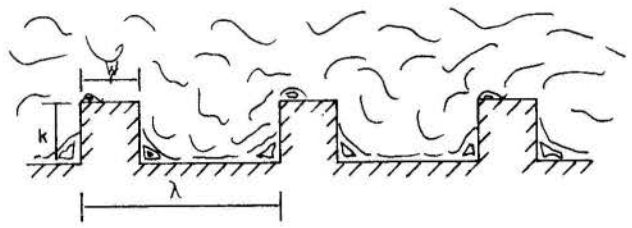

Fig. 1. "k" type roughness.

flow develops in the cavities (Fig. 2). Thus in this situation the flow in the grooves is separated from the main flow through a thin shear layer which develops on the top of the cavities. For this configuration little eddy shedding into the outer flow occurs. Rough walls with such features are called "d" type rough walls.

Despite significant differences from the physics of "k" type walls, the flow over "d" type rough walls can also be described by expression (1) if only parameter D is adequately corrected[4]. This expression can be extended to the defect region if Coles' wake function is considered so that we have [1,4]

$$\frac{u}{u_\tau} = \frac{1}{K}\ln\frac{y+\epsilon}{\epsilon} + A - D + \frac{\pi}{K}W\left[\frac{y}{\delta}\right], \qquad (2)$$

where $\pi(=0.55)$ is a universal constant and W is a universal function.

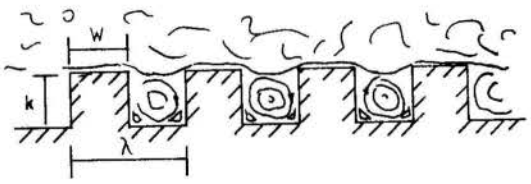

Fig. 2. "d" type roughness.

Since equations (1) and (2) are now well established, present research has concentrated on the development of means of evaluating the error in origin ϵ and parameters D. The introduction of these two new parameters, however, makes the classical approaches for the determination of u_τ inaccurate. In fact, experimental techniques which make use of Preston or Staton tubes cannot be used since they require the previous knowledge of D. Momentum-integral methods cannot be used either if pressure gradients are present. Hence, we are left with the graphical method introduced by Clauser[10] for finding the friction velocity, u_τ. This method is very imprecise for rough wall flows since many combinations of parameters (u_τ,ϵ,D) will give nearly straight lines which can be interpreted as the correct velocity distribution[2]. Clauser graphical procedure has then been reduced to a mere way of determining parameters ϵ and D, as long as u_τ can be found through any other method. Even so, determination of ϵ is difficult and requires an elaborated graphical procedure.

3. THE TRANSFER OF HEAT

Rough surfaces have widely been used in engineering applications as a means of enhancing transfer of heat at walls. It is thus only reasonable to expect that many works presented in literature should deal with this type of application. Unfortunately, this is not the case and we may safely say that our present understanding of the physics of the process of transfer of heat is well behind our present understanding of the physics of the process of transfer of momentum. In fact, contributions to the heat transfer problem basically resume to what is typically presented in Refs.[8,9,11,12]. Thus much remains to be done.

In the present analysis we are interested in studying the two surface geometries depicted in Figs. 1,2. Specifically, we want to extend equations (1) and (2) to the case where transfer of heat takes place. This will be done theoretically in accordance with some recently derived results(Refs. 13,14,15).

In a recent analysis[13], we have shown that application of the intermediate variable technique[16] to the problem of a two-dimensional, incompressible, turbulent boundary layer, reveals that both the dynamic and thermal boundary layers have a classical two-deck structure whose characteristic length scales in regions close to the wall are respectively ν/u_τ and $P_r\nu/u_\tau$ (P_r the Prandtl number). More importantly, we have shown that the fully turbulent region for both boundary layers is ordered by the same scale, ϵ^2(=non-dimensional friction velocity). This result clearly suggests that if the roughness elements are such that they penetrate well into the turbulent region so that configurations similar to those shown in Figs.(1,2) are obtained, then the length scale for the temperature profile for flows over rough surfaces should also be ϵ, the displacement in origin given by equation (1). This result follows from the fact that in the fully turbulent region heat and momentum are transfered by similar processes[13].

To find the characteristic temperature we refer

to [14,15]. In those references, it is shown that a straightforward choice for the characteristic temperature is the friction temperature ($t_\tau = q_w/\rho c_p u_\tau$), so that we can write

$$\frac{t - t_w}{t_\tau} = \frac{1}{K_T} \ln \frac{y + \epsilon}{\epsilon} + B - E \,, \qquad (3)$$

where K_T and B are universal constants and E is a function of the roughness.

The above equation can be extended to the outer part of the boundary layer if we consider Coles' equation [14,15] and write

$$\frac{t - t_w}{t_\tau} = \frac{1}{K_T} \ln \frac{y + \epsilon}{\epsilon} + B - E + \frac{\pi_T}{K_T} W\left[\frac{y}{\delta_T}\right] \,, \qquad (4)$$

where π_T = universal constant.

Equation (4) evaluated at point $(y,t) = (\delta_T, t_\infty)$ can now be used to find t_τ if the constants and the displacement in origin ϵ are known. Parameters u_τ and t_τ are then used to find directly the friction coefficient, C_f $(= 2(u_\tau/u_\infty)^2)$, and the Stanton number, S_t $(= u_\tau t_\tau/((t_\infty - t_w)u_\infty))$. However, as pointed out in [15], this procedure has some inconveniences. Since S_t has u_τ and t_τ in its definition, uncertainties in the evaluation of these two quantities have an additive effect, yielding large inaccuracies in the prediction of S_t.

To avoid this difficulty, we propose the following alternative approach[15]. Replace t_τ in Eq.(4) by $(t_\infty - t_w)\sqrt{S_t}$ to obtain

$$\frac{t - t_w}{(t_\infty - t_w)\sqrt{S_t}} = \frac{1}{K'_T} \ln \frac{y + \epsilon}{\epsilon} + B' + E' + \frac{\pi'_T}{K'_T} W\left[\frac{y}{\delta_T}\right] \,. \qquad (5)$$

Now S_t can be evaluated directly from Eq.(5) if we make $y = \delta_T$, $t = t_\infty$, and the involved constants are determined.

The problem of a turbulent boundary layer flowing over a rough surface with addition of heat has then been reduced to the determination of parameter E' since the other constants are given in [15] and ϵ is given by the dynamics of the flow.

To verify our assumptions we consider the experimental data of Refs.[7,11,17,18]. The flow conditions in these Refs. do not exactly reproduce those desired here, in particular, in what concerns the roughness geometry. They yield, however, independent sets of data obtained in different experimental facilities which cover a wide range of conditions. Hence, despite the discrepancies between some of our assumptions and the experimental flow conditions, we have decided to compare our predictions with the data of Refs.[7,11,17,18].

Since values of δ, δ_T and ϵ are not given in those Refs., comparison will be made through terms $\ln(y+\epsilon)/\epsilon$ in Eqs. (2) and (5). If these two terms are about equal, and we make the hypothesis that δ and δ_T have the same order of magnitude[13], then we may conclude ϵ is the same for both the dynamic and the thermal boundary layers.

The results are presented in Table 1. To find these results we have considered constants D, K', B', π' and E' to assume the values 0.35, 0.43, 5.1, 0.47 and 2.5 respectively.

Table 1.

Author	C_f	S_t	$\ln((y+\epsilon)/\epsilon)$	
			Eq. 2	Eq. 5
Gowen, Smith				
R-1	0.0185	0.0069	0.97	0.97
R-2	0.0165	0.0068	1.22	1.01
R-3	0.0255	0.0090	0.34	0.37
Healzer (X = 1 m)	0.005	0.0025	4.91	4.39
Ligrani (δ_2 = 1 cm)	0.0019	0.002	6.11	5.4
Taylor (X = 1 m)	0.005	0.0023	4.90	4.76

As can be seen, the agreement is good even for the data of Ligrani whose value of S_t is above the expected trend.

These preliminary results, although not conclusive, indicate that our assumptions are fundamented yielding reasonable results if adequate values of E' are chosen. Current research is now being undertaken so that more appropriate values of E' can be found.

4. CONCLUSION

The present work has used asymptotic results ([13,16]) and previous analyses developed for flow over rough surfaces (Refs. 1,2,3,4,5,6), and for thermal boundary layers (Refs. 14,15), to suggest that Eq.5 can be used to

describe the behaviour of thermal boundary layers over rough surfaces. This equation has the advantage of dispensing a evaluation of the error in origin for the thermal problem, thus greatly simplifying the analysis of the problem.

5. REFERENCES

1. Perry, A. E. and Joubert, P. N.;"Rough-wall boundary layers in adverse pressure gradients", Journal of Fluid Mechnics, 17, 193-211, 1963.
2. Perry, A. E., Schofield, W. H. and Joubert, P. N.;"Rough wall turbulent boundary layers", Journal of Fluid Mechanics, 37, 383-413, 1969.
3. Antonia, R. A. and Luxton, R. E.;"The response of a turbulent boundary layer to a step change in surface roughness. Part 1: Smooth to rough.", Journal of Fluid Mechanics, 48, 721-761, 1971.
4. Schofield, W. H.;"Measurements in adverse-pressure-gradient turbulent boundary layers with a step change in surface roughness", Journal of Fluid Mechanics, 70, 573- 593, 1975.
5. Wood, D. H. and Antonia, R. A.;"Measurements in a turbulent boundary layer over a d-type surface roughness", Journal of Applied Mechanics, 591-596, 1975.
6. Antonia, R. A. and Wood D. H.,"Calculation of a turbulent boundary layer downstream of a small step change in surface roughness", Aeronautical Quarterly, 26, 202-210, 1975.
7. Taylor, R. P., Coleman H. W. and Hodge, B. K.;"Prediction of heat transfer in turbulent flow over rough surfaces", Journal of Heat Transfer, 111, 568-572, 1989.
8. Finson, M. L.;"A model for rough-wall turbulent heating and skin-friction", AIAA Paper No 82-0199, 1982.
9. Christoph, G. H. and Pletcher, R. H.,"Prediction of rough wall skin-friction and heat transfer", AIAA J, 21, 509-515, 1983.
10. Clauser, F. H.,"The turbulent boundary layer", Appl. Mech., 4, 1-51, 1956
11. Ligrani, P.M.;"The thermal and hydrodynamic behaviour of thick rough-wall turbulent bounday layers", Report No HMT-29, Stanford University, 1979.
12. Pimenta, M. M.;"The turbulent boundary layer: an experimental study of the transport of momentum and heat with the effect of roughness", Report HMT-21, Stanford University, 1975.
13. Silva Freire, A. P. and Hirata, M. H.;"On the matching conditions for turbulent boundary layer problems with heat transfer", II Encontro Nacional de Ciencias Termicas, 241-244, 1988.
14. Medeiros, M. F., and Silva Freire A. P.;"The thermal turbulent boundary layer in an incompressible flow", X Congresso Brasileiro de Engenharia Mecanica, 65-69, 1989.
15. Medeiros, M. F., Pellegrini, C. C. and Silva Freire, A. P.;"The turbulent boundary layer with addition of mass and heat", International Symposium on Engineering Turbulence Modelling and Measurements, Dubrovinik, 1990.
16. Silva Freire, A. P. and Hirata, M. H.;"Approximate solutions to singular perturbation problems: the intermediate variable technique", J. Math. Analysis and Applications, 145, 241-253, 1990.
17. Gowen, R. A. and Smith, J. W.;"Turbulent heat transfer from smooth and rough surfaces", Int. J. Heat Mass Transfer, 11, 1657-1673, 1968.
18. Healzer, J. M., Moffat, R. J. and Kays, W. M.;"The turbulent boundary layer on a rough porous plate: experimental heat transfer with uniform blowing", HMT Report No 18, Stanford University, 1974.

III ENCIT – Itapema, SC (Dezembro 1990)

SPATIAL DEVELOPMENT OF FREE SHEAR LAYER INSTABILITY BY A DISCRETE VORTEX METHOD

Jian Su and Atila P. Silva Freire
Laboratório Mecânica dos Fluidos/Aerodinâmica
Progama de Engenharia Mecânica–COPPE/UFRJ
Caixa Postal 68503, 21945 Rio de Janeiro, Brazil

ABSTRACT

The object of the present work is to study the early stages of evolution of a spatially-developing shear layer using a discrete vortex method. The vortex sheet is subject to three types of disturbances located at its origin: periodical, pulse-type and random disturbances. The calculation is performed until nonlinear effects become important and the vortex sheet starts to roll up.

1. INTRODUCTION

A shear layer is a common phenomenon in fluid mechanics which is manisfested primarily in two forms: wall boundary layer and free shear layer. These two types of layers are associated with a variety of applications of interest, so that they have been extensively studied in the literature.

Free shear layers, in particular, have received great attention recently in connection with the study of coherent structures in turbulent flows[1,2]. These layers are the simplest case of shear flow that can be produced, and hence have become a base test flow to experiment theories developed to describe flow at high Reynolds number.

The advanced theories have dealt with both laminar and turbulent shear layers, using analytical methods, numerical solution of the full Navier-Stokes equation, vortex methods and stability analysis. In fact, great emphasis has been placed on the development and on the formalism of vortex dynamics methods due to their flexibility[3–7]. Vortex dynamics methods can be divided into two classes: discrete methods and spectral methods. Discrete methods are easier to implement than spectral methods, but are subject to strong numerical instability, which lead to chaotic motion after a finite time if care is not taken. They have , however, been extensively used in literature to study the early phase of evolution of disturbances in shear layers[8–13].

In the classical theory of hydrodynamic instability, periodic disturbances are imposed on the linearized Navier-Stokes equation[14,15]. The problem of stability is then reduced to an eigenvalue problem whose solution yields the degree of amplification or damping as a function of the undisturbed mean flow and of the wavelength of the disturbance. Most of the studies conducted on stability using vortex methods have also imposed periodic disturbances on the flow[8,10,11,12]. Furthermore, these studies have simulated temporally-developing shear layers and the analogy between this type of growing layers and "real" measured spatially-developing ones is imperfect[5,9,16].

The study of temporal stability has been preferred by researchers for two reasons: 1) the Orr-Sommerfeld equation is better handled for high Re when the wavenumber is real, 2) temporal modes result naturally from the Fourier transform in space and the Laplace transform in time of an initial value problem for the linearized equation and boundary conditions. Spatial modes, however, do not satisfy the boundary conditions for unbounded flows at any instant and hence seem to render the problem mathematically ill-posed. Gaster[17-19] rectified that showing that the forced oscillation of a boundary layer due to a source of fixed frequency at a fixed point on the wall, turned on at an initial instant, led to an initial value problem whose unboundness of the disturbance as $x \to \infty$ arises only after $t \to \infty$ for fixed x.

The present work simulates for the first time the early stages of evolution of a spatially-developing shear layer using a discrete vortex method. This new approach allows for three different types of boundary conditions to be imposed at the origin of the shear layer to simulate the external forcing: periodical disturbances, pulse-type disturbances, and random disturbances. The evolution is followed until nonlinear effects come into play and the vortex layer starts to roll up. The convective nature of the free shear layer instability for a velocity ratio of 1.0 is clearly observed. Results are presented for different initial forcing amplitudes.

2. THE DISCRETE VORTEX METHOD

A brief description of the discrete vortex method is given below. For a complete account of the method the reader is referred to refs.[20,21].

For a two-dimensional, incompressible flow of a inviscid fluid, the equations of motion can be written as

$$\frac{D\omega}{Dt} = 0, \tag{1.a}$$

$$\nabla^2 \Psi = -\omega. \tag{1.b}$$

where D/Dt indicates a total derivative, ∇^2 is the Laplace operator, and ω and Ψ denote respectively vorticity and the stream function. Thus, the stream function can be found from a simple integration over the vorticity distribution, that is

$$\Psi(z_0) = -\int \omega(z) G(z, z_0) dz, \tag{2}$$

where $G(z, z_0)$ is the green function, defined as

$$G(z, z_0) = \frac{1}{2\pi} \ln |z - z_0|. \tag{3}$$

The nonlinear problem defined by Eqs(1.a-b) is of difficult treatment with only a few simple analytical solutions being available. To study more general configurations we use the fact that in real flows vorticity is normally concentrated in small regions. Then, if the initial distribution of vorticity can be de-

fined, Eqs(1a-1b) can be integrated numerically as an initial value problem. The evolution of the vorticity field with time can then be used to find the evolution of the velocity field through Eq.(2).

In a standard procedure, the shear layer is represented by many discrete vortex markers. Since Helmholtz theorem guarantees that the point vortices will not lose their identity, the evolution of the shear layer can be traced through the Lagrangian evolution of the point markers.

The method can be summarized as follows.

At time $t = 0$, the initial vortex distribution is specified at N nodal points

$$\Gamma_1(z_1^0),\ \Gamma_2(z_2^0),\ \ldots,\ \Gamma_i(z_i^0),\ \ldots,\ \Gamma_N(z_N^0).$$

The induced velocity calculated from the distribution of the point markers is obtained from

$$\Psi = \sum_{i=1}^{N} \Psi_i = -\sum_{i=1}^{N} \frac{\Gamma_i}{2\pi} \ln|z - z_i|. \tag{4}$$

The motion of the point vortices is given by

$$u_i = \frac{dx_i}{dt} = -\sum_{\substack{j=1 \\ j\neq i}}^{N} \frac{\partial \Psi}{\partial y}. \tag{5.a}$$

$$v_i = \frac{dy_i}{dt} = \sum_{\substack{j=1 \\ j\neq i}}^{N} \frac{\partial \Psi}{\partial x}. \tag{5.b}$$

so that the new position of the vortices is found from

$$z_i^{n+1} = z_i^n + (u_i, v_i)\Delta t. \tag{6}$$

The induced velocities are updated and the calculation proceeds in time.

3. INSTABILITY OF THE FREE SHEAR LAYER

Since comprehensive reviews about free shear layers are available in literature, e.g. see [2], we mention here just the basic facts about them.

Free shear layers are formed at the interface between two parallel streams moving at different velocities. Experiments[22-24] have shown that they are linearly unstable, degenerating into regions of concentrated vorticity when subject to disturbances. The formation of these vortical structures, that is, their early generation from the Kelvin-Helmholtz shear instability and their association (vortex pairing) process, have given rise to the concept of coherent structures.

To study the instability of free shear layers, using vortex dynamics, one of the crucial points is the choice of the method used to distribute the vorticity. This can be done basically in three ways: 1) to consider the shear layer in the asymptotic limit as $Re \to \infty$ as a vortex sheet, 2) use many vortex markers, and 3) to bound the vorticity and distribute it over finite regions of the flow.

Here we use the vortex sheet approach. Hence, our flow field is represented by two streams with different velocities separated by a semi-infinite plate and by a semi-infinite vortex sheet (Fig.1).

The origin of the coordinate system is located as shown in Fig. 1.

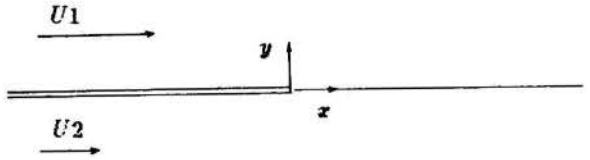

Fig.1. Flow configuration.

To implement the numerical calculations we discretize part of the vortex sheet located in interval $(0, L)$ into N point vortices. The remaining part of the sheet retains its original continuous form.

Each point vortex is located at the mid-point of the section it represents and has the total circulation of this section. Then, if the intensity of the sheet is

$$\gamma = U_1 - U_2, \tag{7}$$

and the circulation of the point vortices is

$$\Gamma = \gamma \Delta s, \tag{8}$$

the motion of each point vortex is descibed by

$$u_i = \frac{dx_i}{dt} = \int_{-\infty}^{0} \frac{\gamma}{2\pi} \frac{y_i}{(x_i - x)^2 + y_i^2} dx + \sum_{\substack{j=1 \\ j\neq i}}^{N} \frac{\Gamma_j}{2\pi} \frac{(y_i - y_j)}{(x_i - x_j)^2 + (y_i - y_j)^2} + \int_{L}^{+\infty} \frac{\gamma}{2\pi} \frac{y_i}{(x_i - x)^2 + y_i^2} dx, \tag{9.a}$$

$$v_i = \frac{dy_i}{dt} = \int_{-\infty}^{0} \frac{\gamma}{2\pi} \frac{-(x_i - x)}{(x_i - x)^2 + y_i^2} dx + \sum_{\substack{j=1 \\ j\neq i}}^{N} \frac{\Gamma_j}{2\pi} \frac{-(x_i - x_j)}{(x_i - x_j)^2 + (y_i - y_j)^2} + \int_{L}^{+\infty} \frac{\gamma}{2\pi} \frac{-(x_i - x)}{(x_i - x)^2 + y_i^2} dx. \tag{9.b}$$

To study the spatial evolution of shear layers, we introduce three different types of disturbance at the origin.

The first type of disturbance is a periodic disturbance with fixed frequency at the origin of the mixing layer. This can be physically realized by an oscillation of the splitter plate, or by a loud-speaker, or by a vibrating ribbon. At each time step a new point vortex is generated and shed into the flow at position

$$x = U\Delta t, \tag{10.a}$$

$$y = A\sin\omega t, \tag{10.b}$$

where $U = (U_2 + U_1)/2$, A is the amplitude of the disturbance and ω its frequency.

The above parameters can be rewritten in the following non-dimensional form

$$t^* = t/T = t\omega/2\pi,\ x^* = x/ut,\ y^* = y/uT, \tag{11}$$

so that equations (10.a-b) become

$$x^* = \Delta t^*, \tag{12.a}$$

$$y^* = A^*\sin(2\pi t^*). \tag{12.b}$$

To perform our calculations we represent a part of the vortex sheet by 80 point vortices distributed in the interval (0,4). After each time step new vortices are added to our computational scheme so that fine details of the roll-up process can be captured.

4. RESULTS AND DISCUSSION

Results for three different amplitude values, nominally 0.001, 0.01, and 0.05 are shown in Figs.2,3,4. Here, it is of interest to note that according to Eqs.(12.a-b), an increase in the forcing frequency, ω , will simply shorten the physical time in which the roll-up occurs. For the smaller amplitude, the initial amplification is clearly seen. The larger amplitude induces the shear layer roll-up after a short time.

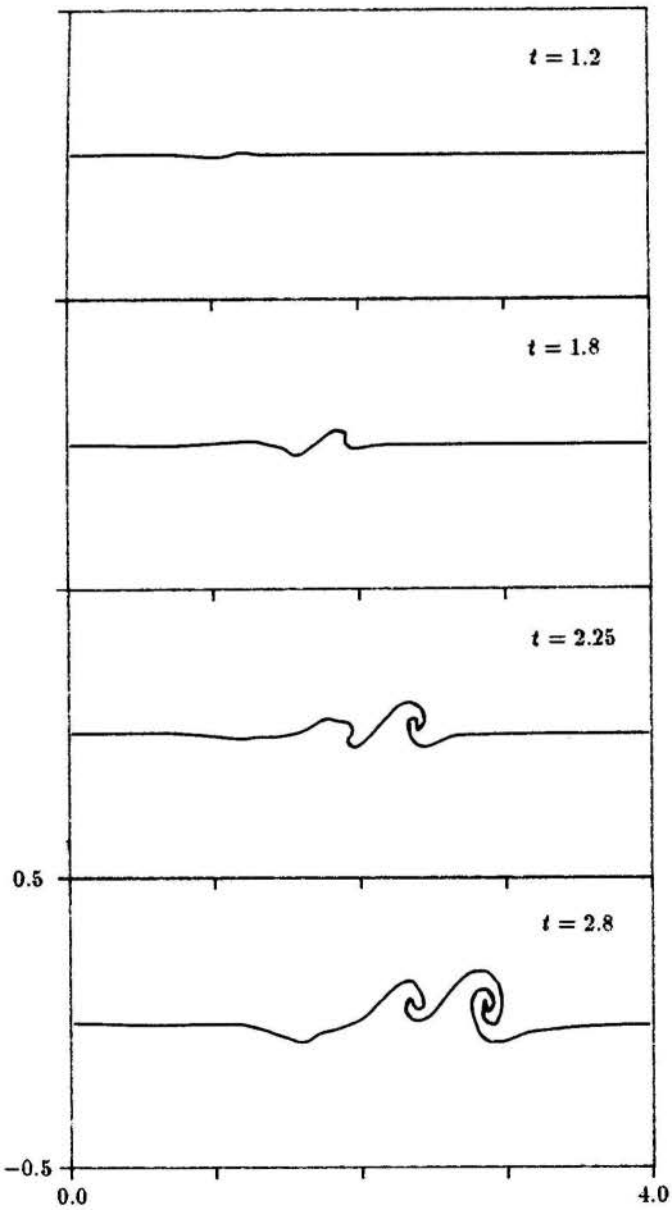

Fig.2. Spatial development of a free shear layer subjected to a sinusoidal disturbance with amplitude 0.001.

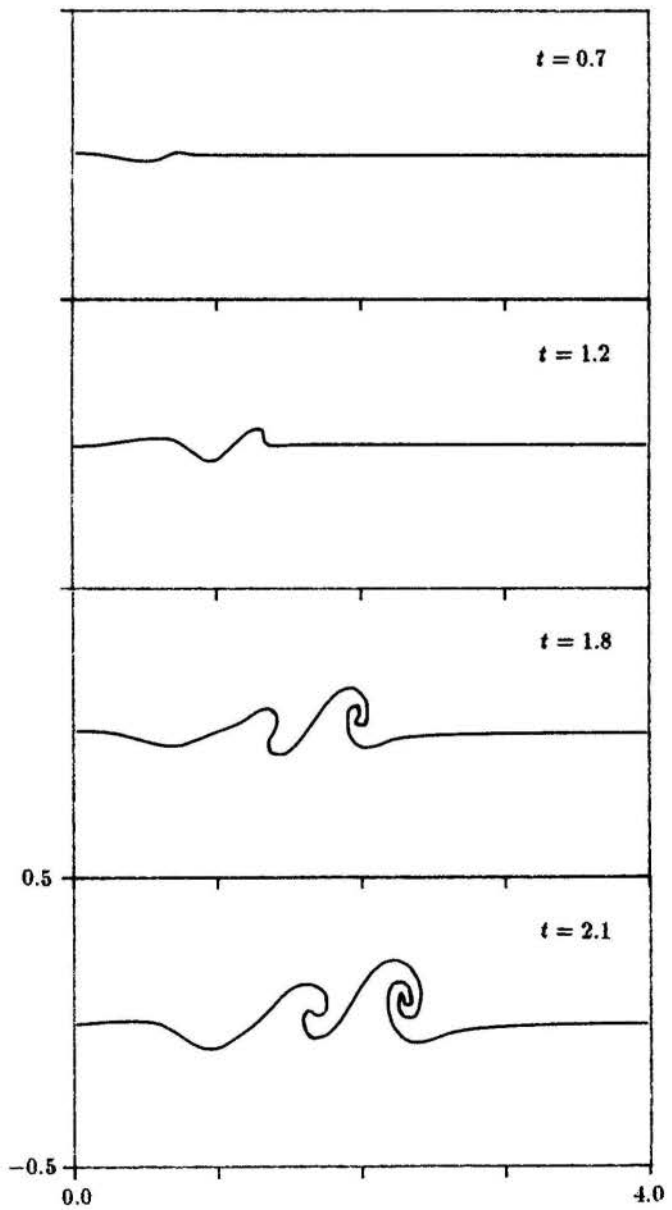

Fig.3. Spatial development of a free shear layer subjected to a sinusoidal disturbance with amplitude 0.01.

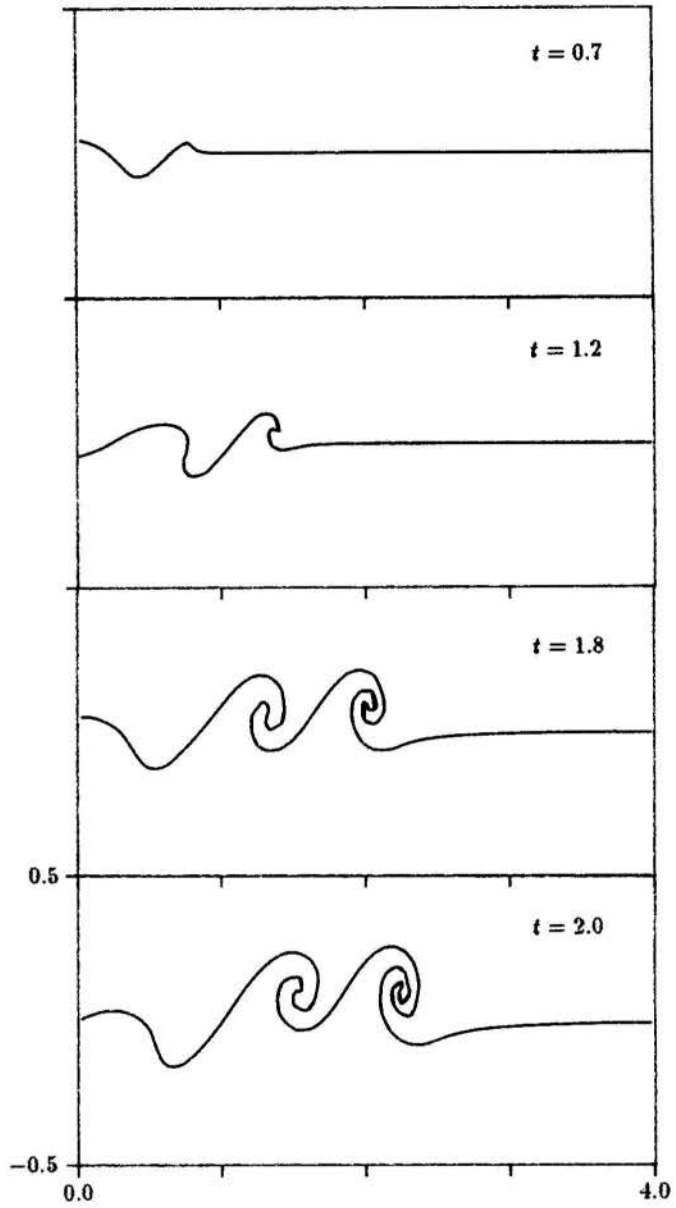

Fig.4. Spatial development of a free shear layer subjected to a sinusoidal disturbance with amplitude 0.05.

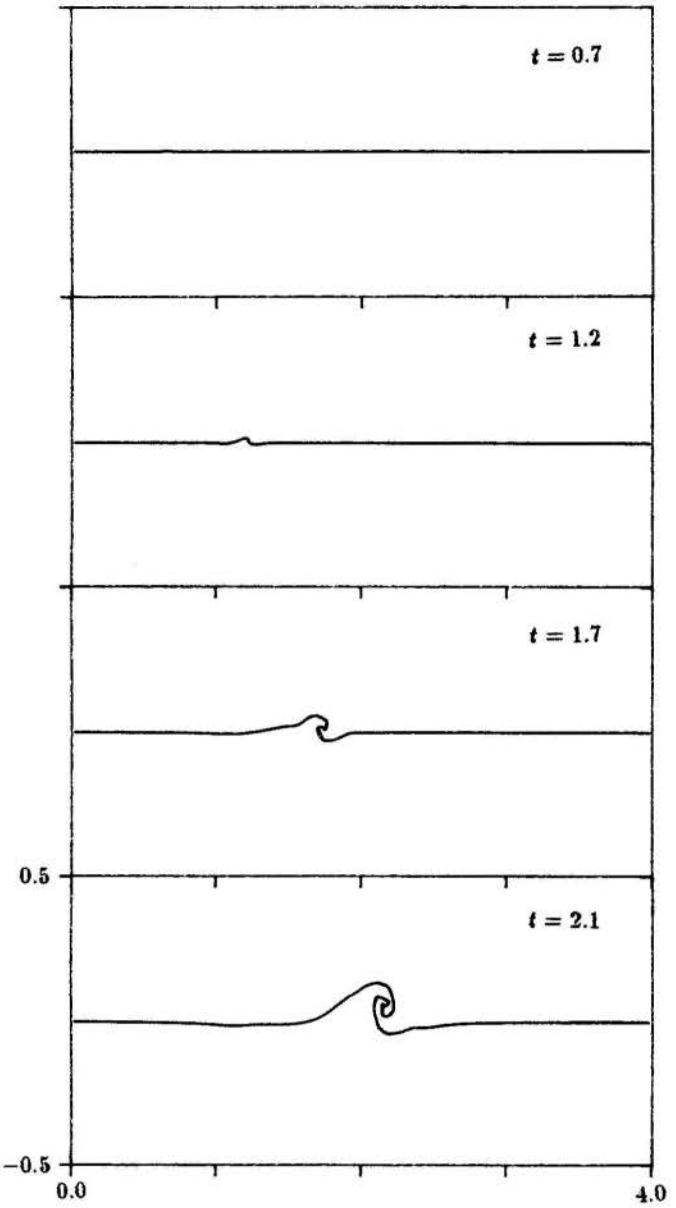

Fig.5. Spatial development of a free shear layer subjected to a pulse-type disturbance with amplitude 0.01.

The second type of disturbance to be imposed on the flow is the pulse-type perturbation. The disturbance is imposed on the flow just for a short time interval, being henceforth ceased. For this case one value of amplitude(=0.01) is considered. The vortex sheet is observed (Fig. 5) to form a single region of concentrated vorticity after a short time. Thus roll-up will occur with any type of perturbation.

To simulate a more " real" type of disturbance we have subject the flow to random disturbances at the tip of the splitter plate. For this case, the amplitude of the disturbances is bounded to a specified value (=0.01). Again, all the disturbances are amplified and nonlinear roll-up occurs(Fig.6).

Figs.(2-6) clearly show that in the late stages of evolution full nonlinear effects are captured. Despite the three different types of disturbances subject to the original flow, we observe that the perturbed free shear layer evolves in a similar way. It is of interest to note that, in Fig. 6, the second "wave" of larger amplitude overtakes the first "wave" of smaller amplitude. This result, which was obtained here for the first time from a numerical analysis, cannot be presently explained by the authors.

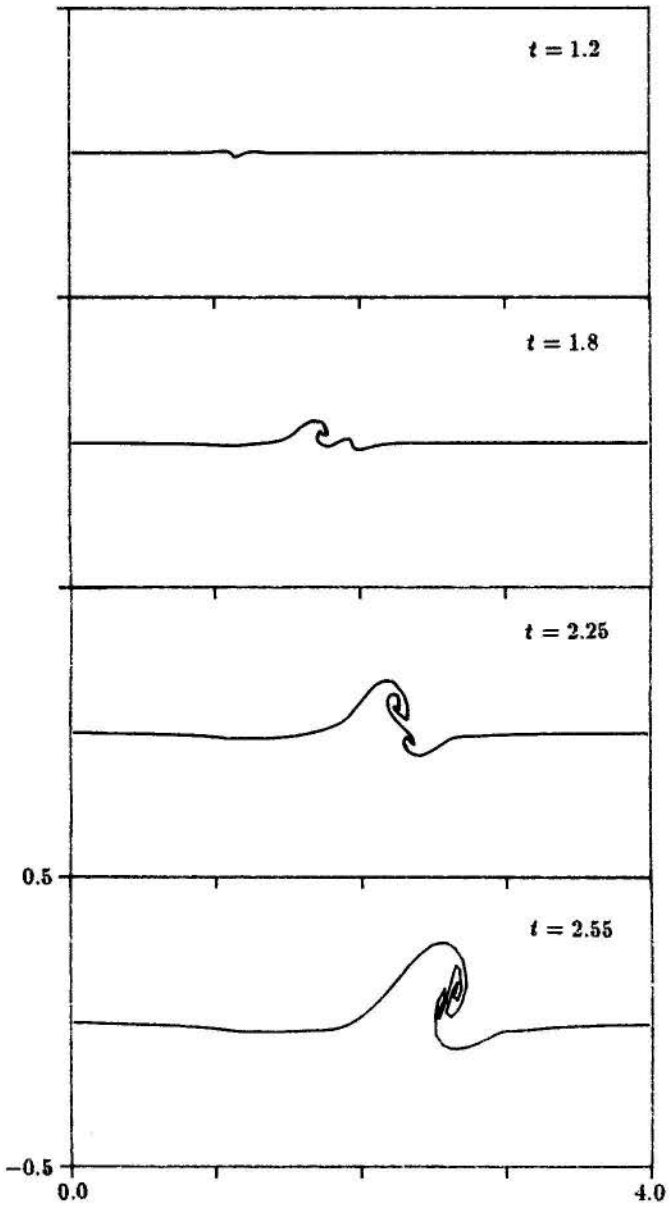

Fig.6. Spatial development of a free shear layer subjected to a random disturbance with maximum amplitude 0.01.

5. CONCLUSION

A procedure has been presented which simulated the spatial evolution of the free shear layer subject to disturbances of various types. The results show good qualitative agreement with the experimental work of other authors, thus succeding in predicting some nonlinear effects. The formation of concentrated regions of vorticity is, in particular, shown in some detail.

ACKNOWLEDGEMENT One of the authors, J.S., is grateful to CAPES for the financial help received during the preparation of this work.

REFERENCES

[1] Brown, G.L. and Roshko, A., "On density effects and large structure in turbulent mixing layers," *Journal of Fluid Mechanics*, Vol. 64, pp. 775–816,1974.

[2] Ho,C.M. and Huerre, P., "Perturbed free shear layer," *Annual Review of Fluid Mechanics*, Vol. 16, pp.365–424,1984.

[3] Chorin ,A.J., "Numerical study of slightly viscous flow," *Journal of Fluid Mechanics*,Vol.57,pp.785–796,1973.

[4] Saffman, P.G. and Baker, G.R., "Vortex Interactions," *Annual Review of Fluid Mechanics*, Vol. 11,pp.95–122, 1979.

[5] Aref,H, "Integrable, chaotic and turbulent vortex motion in two-dimensional flows," *Annual Review of Fluid Mechanics*, Vol. 15, pp.345–389,1983.

[6] Leonard, A., "Computing three-dimensional incompressible flows with vortex elements," *Annual Review of Fluid Mechanics*, Vol. 17, pp.523–559,1985.

[7] Sarpkaya,T. "Computational methods with vortices — the 1988 Freeman scholar lecture," *ASME Journal of Fluid Engineering*,Vol.111,pp.5–52, 1988.

[8] Acton,E., "The modelling of large eddies in a two dimensional shear layer," *Journal of Fluid Mechanics*,Vol.76, pp.561–592, 1976.

[9] Aref,H and Siggia,E.C., "Vortex dynamics of the two-dimensional turbulent shear layer," *Journal of Fluid Mechanics*,Vol.100, pp.705–737,1980.

[10] Pozrikidis,C. and Higdon,J.J.L., "Nonlinear Kelvin-Helmholtz instability of a finite vortex layer," *Journal of Fluid Mechanics*,Vol.157,pp.225–263,1985.

[11] Higdon,J.J.L. and Pozrikidis,C., "The self-induced motion of vortex sheets," *Journal of Fluid Mechanics*,Vol. 150, pp.203–231,1985.

[12] Ashurst, W.T. and Meiburg,E., "Three-dimensional shear layer via vortex dynamics," *Journal of Fluid Mechanics*, Vol.189,pp.87–116,1988.

[13] Krasny, R. "A study of singularity formation in a vortex sheet by the point vortex approximation," *Journal of Fluid Mechanics*,Vol.167, pp.65–93,1986.

[14] Drazin, P.G. and Reid, W.H., *Hydrodynamic Stability*, Cambridge University Press,1981.

[15] Maslowe,S.A. "Shear layer instability," in Swinney,H.L. and Gollub, J.P.(eds), *Hydrodynamic Instabilities and the Transition to Turbulence*, Topics in Applied Physics, Vol.45,Springer,1981.

[16] Corcos,G.M. and Sherman,F.S., "The mixing layer: deterministic models of a turbulent flow. Part 1. introduction and the two-dimensional flow," *Journal of Fluid Mechanics*, Vol.139,pp.29–65,1984.

[17] Gaster,M., "A note on the relation between temporally-increasing and spatially-increasing disturbances in hydrodynamic stability," *Journal of Fluid Mechanics*,Vol. 22,pp.222–224,1962.

[18] Gaster,M., "Growth of disturbances in both space and time," *Physics and Fluids*,Vol.11,pp.723–727,1968.

[19] Gaster,M., "The development of three-dimensional wave packets in a boundary layer," *Journal of Fluid Mechanics*, Vol.32,pp.173–184,1963.

[20] Anderson, C. and Greengard, C.(Eds.), "Vortex Methods," *Lecture Notes in Math.*, No. 1360, Springer, 1987.

[21] Marchioro, C. and Pulvirenti, M., "Vortex Methods in two-dimensional fluid mechanics," *Lecture Notes in Phys.*, No. 206, Springer, New York, 1984.

[22] Miskad, R.W. "Experiments on the nonlinear stages of free shear layer transition ," *Journal of Fluid Mechanics*,Vol.56, pp.695–719,1972.

[23] Winant ,C.D. and Browand, F.K., "Vortex pairing: the mechanism of turbulent mixing layer growth at moderate Reynolds number," *Journal of Fluid Mechanics*,Vol. 63, pp.237–255,1974.

[24] Ho, C.M. and Huang, L.S., "Subharmonics and vortex merging in mixing layers," *Journal of Fluid Mechanics*,Vol.119, pp.443–473,1982.

III ENCIT – Itapema, SC (Dezembro 1990)

A CAMADA LIMITE TÉRMICA TURBULENTA COM TRANSPIRAÇÃO

MARCELLO A. FARACO MEDEIROS
Laboratório de Mecânica dos Fluidos/Aerodinâmica
Programa de Eng. Mecânica (COPPE/UFRJ)
21945 – Rio de Janeiro, Brasil – C. P. 68503

O presente trabalho analisa teoricamente a transferência de calor na camada limite turbulenta com transpiração. A análise revela a existência de duas leis — uma para a região interna e outra para a externa da camada limite — que recaem nas conhecidas Lei da Parede e Lei da Esteira *aplicadas a problemas térmicos quando a taxa de transpiração tende a zero. A partir destas leis são propostas uma expressão para o perfil de temperatura e uma equação para o número de Stanton. A comparação com dados experimentais mostra excelente concordância.*

I. INTRODUÇÃO

Os escoamentos turbulentos permanecem ainda como um desafio à engenharia. A habilidade na predição dos parâmetros de tais escoamentos é, de fato, limitada. No entanto, desde a metade deste século, o conhecimento dos princípios básicos da turbulência, na camada limite, tem permitido a abordagem de problemas específicos com soluções analíticas simples. Permanece ainda a esperança de que problemas mais complexos possam ser contemplados por tal simplicidade, e os resultados ora apresentados podem alimentar esta esperança.

Este trabalho possui como objetivo central a análise da transferência de calor na camada limite turbulenta sobre uma placa porosa sujeita a injeção ou sucção de fluido, concentrando-se na busca de expressões para o perfil de temperatura e em equações para o cálculo do calor trocado entre o fluido e a superfície. A motivação específica para este estudo repousa no fato de que a transpiração — como são referidas indistintamente a injeção ou sucção de fluido através da superfície — constitui-se numa forma eficaz de controle de certos parâmetros do escoamento [1,2], destacando-se os coeficientes de atrito e de troca térmica. Com efeito, a injeção de fluido é considerada para aplicação em escoamentos a altíssimas temperaturas — por exemplo, os que ocorrem em turbinas a gás e veículos espaciais — com a finalidade de promover o isolamento das superfícies, ou ainda o resfriamento ativo das mesmas.

Historicamente, os avanços em camada limite turbulenta têm sido fortemente apoiados em dados experimentais. Destes avanços, os estudos em camada limite com transpiração aparecem como uma exceção, visto que os trabalhos teóricos remontam aos anos 50 e 60 [3,4,5] enquanto a maior gama de dados experimentais foi obtida no final da década de 60 e ao longo dos anos 70 [1,6,7,8]. Isto se deve em parte ao sucesso da abordagem de Spalding [4] — como atesta [2] — que desenvolveu uma expressão que determina o coeficiente de atrito ($= Cf$) e o número de Stanton ($= St$) para o caso com transpiração a partir de seus respectivos valores em escoamentos sem transpiração (Cf_0, St_0). Todavia, devido aos pequenos valores de Cf e St nos casos com injeção de fluido, e consequentemente as grandes incertezas em suas medidas, para este autor parece temerário validar uma teoria apenas pela verificação dos valores preditos para estes dois parâmetros. Uma teoria que forneça outros aspectos para comparação com dados experimentais — como os perfis de velocidade e temperatura — possui, inegavelmente, uma confiabilidade muito maior, além é claro, de permitir a predição de outros parâmetros do escoamento.

O fato de que os trabalhos teóricos em transpiração concentram-se num período anterior aos experimentos de Stanford era no início deste projeto um indício de que progressos relevantes poderiam ser feitos nesta área. Alguns destes progressos são aqui apresentados.

II. A CAMADA LIMITE TÉRMICA TURBULENTA

As bases do estudo em camada limite turbulenta são as famosas leis fundamentais — *Lei da Parede* e *Lei da Esteira*. A primeira, com validade nas proximidades da parede, pode ser deduzida da equação

$$\frac{\partial T}{\partial y} = 0 \tag{2.1a}$$

$$T(0) = T_w = u_\tau^2 \rho = U_\infty^2 \rho \frac{Cf}{2} \tag{2.1b}$$

na qual empregamos uma nomenclatura clássica e, em especial, as definições de u_τ e Cf são decorrentes da Eq.(2.1b). Da Eq.(2.1a) vem que T é constante e igual a T_w ao longo da região interna [9]. Nesta região as velocidades são baixas devido à condição de não deslizamento e os gradientes na direção normal à parede são altos. Este fato sugere que, na equação de Navier-Stokes, desprezemos os termos de inércia face aos termos viscosos sendo portanto a Eq.(2.1a) obtida a partir de uma hipótese.

Na Eq.(2.1a), T representa tensões tanto turbulentas quanto laminares. Na vizinhança imediata da parede, as tensões laminares são preponderantes, logo substituindo

$$T = \mu \frac{\partial U}{\partial y} \tag{2.2}$$

na Eq.(2.1a) e aplicando a condição de não deslizamento na parede obtemos que

$$u^+ \stackrel{def}{=} \frac{U}{u_\tau} = y^+ \stackrel{def}{=} \frac{y u_\tau}{\nu} \tag{2.3}$$

Ainda na região interna, um pouco mais distante da parede

o escoamento é dominado pelas tensões turbulentas. Adotamos então o modelo de comprimento de mistura :

$$\frac{\tau}{\rho} = k_m^2 y^2 \left(\frac{\partial U}{\partial y}\right)^2 \qquad (2.4)$$

Aplicando Eq.(2.4) na Eq.(2.1) obtemos

$$u^+ = \frac{1}{k_m} \ln y^+ + A \qquad (2.5)$$

A e k_m são parâmetros obtidos experimentalmente, aos quais, respectivamente, 5,5 e 0,41 são valores comumente atribuidos. As expressões (2.3) e (2.5) podem ser sumariamente escritas como

$$u^+ = f_m(y^+) \qquad (2.6)$$

que é a *Lei da Parede* em sua forma geral, sendo a Eq.(2.5) a forma como é normalmente citada.

A *Lei da Esteira* por sua vez é escrita como

$$\frac{U - U_\infty}{u_\tau} = g_m\left(\frac{y}{\delta_m}\right) \quad , \qquad (2.7)$$

onde δ_m é a espessura da camada limite cinética. De forma diversa da *Lei da Parede*, a *Lei da Esteira* é obtida a partir de comprovação experimental, e descreve o perfil de velocidade na região externa da camada limite. Por região externa da camada limite queremos nos referir a uma região ainda pertencente à camada limite e por isso usamos a preposição de. Não se trata pois do escoamento livre que é uma região externa à camada limite.

As leis fundamentais — Eq.(2.6) e Eq.(2.7) — possuem suas correspondentes aplicadas ao perfil de temperatura. Na ausência de gradientes de pressão e de altas velocidades, se focalizarmos a região interna da camada limite térmica turbulenta podemos, de forma semelhante ao que fizemos para obter a Eq.(2.1a), desprezar os termos convectivos da equação da energia e obter

$$\frac{\partial \dot{Q}''}{\partial y} = 0 \quad , \qquad (2.8a)$$

$$\dot{Q}''(0) = \dot{Q}''_w = \rho c_p u_\tau t_\tau = \rho c_p U_\infty (T_\infty - T_w) St \quad , \qquad (2.8b)$$

onde t_τ e St tem suas definições decorrentes da Eq.(2.8b). Na Eq.(2.8a), $\dot{Q}''$ reune os efeitos de condução e condução turbulenta, logo, o calor é constante e igual a $\dot{Q}''_w$ ao longo da região interna [9]. Na região de dominância da condução o perfil de temperatura pode ser obtido pela substituição de

$$\dot{Q}'' = -k\frac{\partial T}{\partial y} \quad , \quad T(0) = T_w \qquad (2.9)$$

na Eq.(2.8), fornecendo

$$t^+ \stackrel{def}{=} \frac{T - T_w}{t_\tau} = y^+ Pr \qquad (2.10)$$

O modelo de comprimento de mistura clássico aplicado a problemas térmicos é :

$$\frac{\dot{Q}''}{\rho c_p} = k_m k_t y^2 \frac{\partial T}{\partial y}\frac{\partial U}{\partial y} \qquad (2.11)$$

Substituindo a Eq.(2.11) na Eq.(2.8) e empregando juntamente a Eq.(2.5) resulta

$$t^+ = \frac{1}{k_t} \ln y^+ Pr + B \qquad (2.12)$$

Os experimentos atribuem a k_t pouca ou nenhuma dependência com Pr, no entanto B sofre, de Pr, grande influência [10,11]. Para ar, os valores medidos de k_t variam de 0,4 à 0,45, enquanto B situa-se em torno de 5.0 [12]. No presente trabalho são adotados $k_t = 0,45$ e $B = 4,9$, Fig.1.

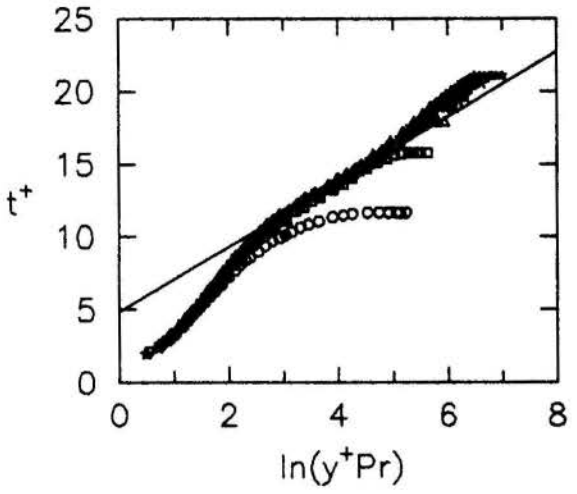

Fig.1 – Lei da Parede
(Re_δ entre 170 e 3180)

As Eq.(2.10) e (2.12) resumem-se a:

$$t^+ = f_t(y^+, Pr) \qquad (2.13)$$

Que o perfil de temperatura é função do número de Pr faz parte do senso comum.

Para a região externa da camada limite comprova-se experimentalmente que :

$$\frac{T - T_\infty}{t_\tau} = g_t\left(\frac{y}{\delta_t}\right) \quad , \qquad (2.14)$$

onde δ_t é a espessura da camada limite térmica, Fig.2. A literatura em geral considera que o perfil de temperatura na região externa independe de Pr. As Eq.(2.13) e (2.14) são respectivamente as *Lei da Parede* e *Lei da Esteira* aplicadas a problemas térmicos [10,13,14].

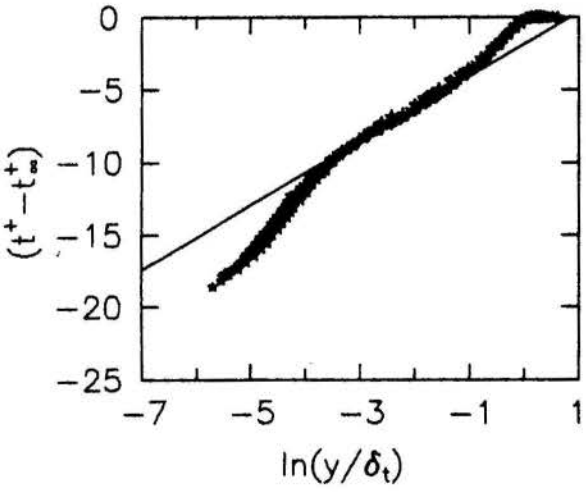

Fig.2 – Lei da Esteira
(Re_δ entre 1870 e 3180)

Retornando agora ao problema dinâmico, as Eq.(2.6) e (2.7) podem ser resumidas na expressão

$$u^+ = f_m(y^+) + h_m\left(\frac{y}{\delta_m}\right) \quad , \qquad (2.15)$$

onde h_m tende a anular-se para valores pequenos de y recaindo

na Eq.(2.6) nesta região. Pela propriedade logarítmica de f_m, a Eq.(2.7) também é decorrência imediata. Desprezando a subcamada laminar, Coles [15] propôs a seguinte expressão :

$$u^+ = \frac{1}{k_m}\ln y^+ + A + \frac{\Pi_m(x)}{k_m} w\left(\frac{y}{\delta_m}\right) \quad , \qquad (2.16)$$

onde w é a função de Coles, dada por pontos, e Π_m, um fator de escala, sendo então a Eq.(2.16) uma equação universal para o perfil de velocidade. Ora, das Eq.(2.13) e (2.14) podemos deduzir uma equação similar à Eq.(2.15) para a temperatura e verificar a validade da expressão

$$t^+ = \frac{1}{k_t}\ln y^+ Pr + B + \frac{\Pi_t(x)}{k_t} w\left(\frac{y}{\delta_t}\right) \quad . \qquad (2.17)$$

No item IV, Fig.7, a Eq.(2.17) é comparada com os dados experimentais mostrando excelente concordância. Muitas expressões universais têm sido propostas para o perfil de temperatura [11]. A Eq.(2.17) destaca-se entre estas por sua simplicidade, no entanto, somente recentemente foi apresentada [13,14].

As Eq.(2.16) e (2.17) possuem uma segunda aplicação imediata. Empregando-as para a extremidade da camada limite, obtemos expressões para u_τ e t_τ — e indiretamente para Cf e St —, a saber :

$$\frac{U_\infty}{u_\tau} = \frac{1}{k_m}\ln\frac{\delta_m u_\tau}{\nu} + A + 2\frac{\Pi_m(x)}{k_m} \quad , \qquad (2.18)$$

$$\frac{T_\infty - T_w}{t_\tau} = \frac{1}{k_t}\ln\frac{\delta_t u_\tau}{\nu} Pr + B + 2\frac{\Pi_t(x)}{k_t} \quad , \qquad (2.19)$$

Estas expressões combinadas com os perfis de velocidade e temperatura e com as equações de conservação na forma intergral fornecem valores de Cf e St.

III. O EFEITO DA TRANSPIRAÇÃO

Do ponto de vista das equações de conservação, a transpiração significa uma alteração na condição de contorno :

$$V(0) = V_w \neq 0 \quad , \qquad (3.1)$$

onde V é a componente da velocidade perpendicular à superfície. Torna-se ilícito então desconsiderar os termos de inércia e convecção na direção y presentes nas equações que regem os fenômenos de transferência, no entanto, desconsideraremos a variação de V ao longo da camada limite. A Eq.(2.1) torna-se então

$$\frac{\partial T}{\partial y} = \rho V_w \frac{\partial U}{\partial y} \quad . \qquad (3.2)$$

Integrando e aplicando a condição de contorno (2.1b) temos

$$\frac{\tau}{\rho} = V_w U + u_\tau^2 \qquad (3.3)$$

e usando o modelo de comprimento de mistura, Eq.(2.4), resulta

$$\frac{2}{v_w^+}\left[\sqrt{1 + u^+ v_w^+} - \sqrt{1 + u_a^+ v_w^+}\right] = \frac{1}{k_m}\ln\frac{y^+}{y_a^+} \quad . \qquad (3.4)$$

onde $v_w^+ = \frac{V_w}{u_\tau}$. O par (u_a^+, y_a^+) representa uma condição de contorno genérica, e experimentalmente verifica-se que k_m não varia com a transpiração. Observa-se ainda que a região completamente turbulenta do escoamento com transpiração inicia-se para valores de u^+ em torno de 11 [16]. Adotando então $u_a^+ = 11$, Simpson determinou experimentalmente que y_a^+ vale também 11, independentemente de v_w^+. Outras expressões para y_a^+ são encontradas na literatura, mas, como ficará claro, para o perfil de temperatura de escoamentos de ar, não é necessária grande acurácia neste ponto.

A Eq.(3.4) mostra então que existe uma transformação F_m tal que

$$F_m(V_w, U, u_\tau) = f_m(y^+) \quad , \qquad (3.5)$$

ou seja, faz coincidir os perfis com transpiração sobre o perfil do escoamento sobre placa impermeável, na região interna da camada limite. Para a região externa, Stevenson[17] demonstrou que

$$F_m(V_w, U, u_\tau) - F_m(V_w, U_\infty, u_\tau) = g_m\left(\frac{y}{\delta_m}\right) \quad . \qquad (3.6)$$

Como no item II, podemos sumarizar as *Lei da Parede* e *Lei da Esteira* aplicadas a escoamentos com transpiração na equação

$$\frac{2}{v_w^+}\left[\sqrt{1 + u^+ v_w^+} - \sqrt{1 + u_a^+ v_w^+}\right] = \frac{1}{k_m}\ln\frac{y^+}{y_a^+} + \frac{\Pi_m}{k_m} w\left(\frac{y}{\delta_m}\right) \qquad (3.7)$$

a qual recai na Eq.(2.16) no limite de V_w tendendo a zero.

Tendo desenvolvido no item II para camada limite térmica uma teoria similar à aplicada ao problema dinâmico, podemos antever que equações equivalentes à Eq.(3.7) resultarão para o perfil e temperatura. Com efeito, se $V_w \neq 0$, a Eq.(2.8a) deve ser substituída por:

$$\frac{\partial \dot{Q}''}{\partial y} = \rho c_p V_w \frac{\partial T}{\partial y} \qquad (3.8)$$

que integrando e aplicando $\dot{Q}''(0) = \dot{Q}''_w$ resulta

$$\frac{\dot{Q}''}{\rho c_p} = V_w(T - T_w) + u_\tau t_\tau \quad . \qquad (3.9)$$

Pelo modelo de comprimento de mistura — Eq.(2.11) —, da Eq.(3.9) obtemos

$$k_m k_t y^2 \frac{\partial T}{\partial y}\frac{\partial U}{\partial y} = V_w(T - T_w) + u_\tau t_\tau \quad . \qquad (3.10)$$

A Eq.(3.4) fornece uma expressão para U que é substituída na Eq.(3.10) a qual pela integração resulta em

$$\Phi_t^+ \stackrel{\text{def}}{=} \frac{k_m}{k_t}\frac{2}{v_w^+}\left\{\left(\frac{v_w^+ t^+ + 1}{v_w^+ t_b^+ + 1}\right)^{\frac{k_t}{2k_m}}\left[\frac{v_w}{2}\left(\frac{1}{k_m}\ln\frac{y_a^+}{y_b^+ Pr}\right) + \sqrt{1 + v_w^+ u_a^+}\right] - \sqrt{1 + v_w^+ u_a^+}\right\} = \frac{1}{k_t}\ln\frac{y^+ Pr}{y_b^+ Pr} \qquad (3.11)$$

Da análise dos perfis de temperatura constata-se que em escoamentos com transpiração, o valor de t^+ para o qual a região completamente turbulenta tem origem é aproximadamente constante e igual ao caso sem transpiração. Este valor pode ser obtido pela interseção das equações para a região laminar e turbulenta, Eq.(2.10) e Eq.(2.12). O valor de t^+ que satisfaz ambas as equações é $t^+ = 10,0$ o qual assumiremos como t_b^+. Sendo t_b^+, por hipótese, pertencente tanto à região turbulenta quanto à região laminar, podemos obter uma equação para $y_b^+ Pr$ via uma expressão para o perfil desta última [18]. Assim, substituindo Eq.(2.9) na Eq.(3.9) segue

$$\frac{k}{\rho c_p}\frac{\partial T}{\partial y} = V_w(T - T_w) + u_\tau t_\tau \qquad (3.12)$$

Integrando Eq.(3.12) e utilizando a condição de contorno na parede, $T(0) = T_w$, resulta

$$t^+ = v_w^+(e^{v_w^+ y^+ Pr} - 1) \quad . \tag{3.13}$$

assim

$$y_b^+ Pr = \frac{\ln(v_w^+ t_b^+) + 1}{v_w^+} \quad . \tag{3.14}$$

A Fig.3 mostra a validade das Eq.(3.11) e Eq.(3.14). Note-se que o termo

$$\ln \frac{y_a^+}{y_b^+ Pr}$$

é muito pequeno para escoamento de ar. Devido a isto, a discussão sobre a melhor expressão para y_a^+ torna-se irrelevante. Conclui-se então que existe uma função F_t tal que

$$F_t(u_\tau, t_\tau, V_w, (T - T_w)) = f_t(y^+, Pr) \quad . \tag{3.15}$$

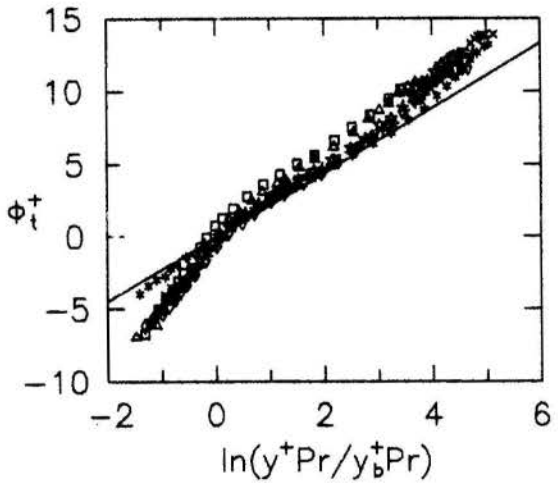

Fig.3 – Lei da Parede para escoamentos com transpiração (v_w entre −0.002 e 0.005)

A *Lei da Esteira* segue então analogamente como mostra a Fig.4.

A equação

$$\frac{k_m}{k_t}\frac{2}{v_w^+}\left\{\left(\frac{v_w^+ t^+ + 1}{v_w^+ t_b^+ + 1}\right)^{\frac{k_t}{k_m}}\left[\frac{v_w}{2}\left(\frac{1}{k_m}\ln\frac{y_a^+}{y_b^+ Pr}\right) + \sqrt{1 + v_w^+ u_a^+}\right] - \sqrt{1 + v_w^+ u_a^+}\right\} = \frac{1}{k_t}\ln\frac{y^+ Pr}{y_b^+ Pr} + \frac{\Pi_t}{k_t} w\left(\frac{y}{\delta_t}\right) \quad . \tag{3.17}$$

decorre da *Lei da Parede* — Eq.(3.15) — e da *Lei da Esteira* — Eq.(3.16) — como no item II, e uma equação para t_τ resulta da aplicação da Eq.(3.17) ao par (δ_t, T_∞) :

$$\frac{T_\infty - T_w}{t_\tau} = -\frac{1}{v_w^+} + \left[\frac{\frac{2}{v_w^+}\left(\frac{1}{k_m}\ln\frac{y^+ Pr}{y_b^+ Pr} + 2\frac{\Pi_t}{k_m}\right) + \sqrt{1 + v_w^+ u_a^+}}{\frac{2}{v_w}\left(\frac{1}{k_m}\ln\frac{y_a^+}{y_b^+ Pr}\right) + \sqrt{1 + v_w^+ u_a^+}}\right]^{\frac{2k_m}{k_t}} \frac{1 + v_w^+ t_b^+}{v_w^+} \quad . \tag{3.18}$$

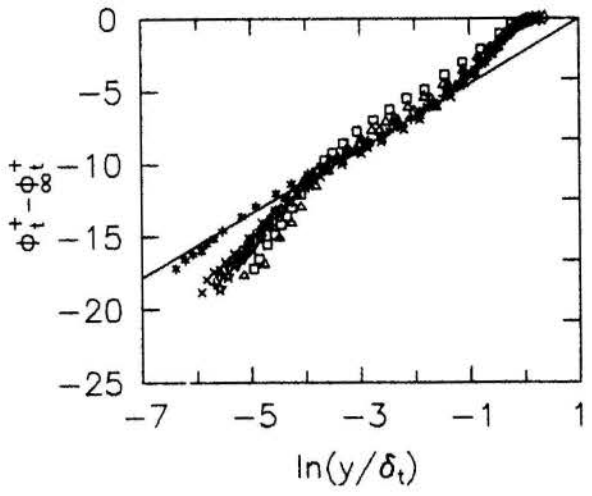

Fig.4 – Lei da Esteira para escoamentos com transpiração (v_w entre −0.002 e 0.005)

IV. ANÁLISE DOS RESULTADOS

Tendo sido este trabalho fortemente baseado em dados experimentais, uma questão central que se coloca diz respeito à qualidade de tais dados. Os valores de k_t e B foram obtidos a partir dos dados de Blackwell [8] para escoamento sem transpiração, os quais concordam muito bem com as já bem estabelecidas expressões para o perfil de velocidade. Os dados de Whitten [6] e Simpson [7], empregados na análise dos perfis com transpiração, apresentam um espalhamento muito maior, mesmo nos casos sem injeção ou sucção, e por esta razão foram preteridos frente a ref.[8] para determinação dos parâmetros básicos. Os valores de Cf medidos são questionados [1], atribuindo-se erros na faixa de até 10%. Este é inclusive o motivo pelo qual Simpson apresenta $k_m = 0,44$ como o valor que melhor descreve seus experimentos, enquanto que para os dados de Blackwell, $k_m = 0,41$.

Quanto aos valores de St, as diferenças existem mas não são significativas diante do espalhamento dos dados de Whitten, de forma que o valor de k_t obtido através dos dados de Blackwell representa bem seus perfis. A mesma análise se aplica aos valores de A e B.

A partir dos valores de k_t e B, obtemos uma expressão para y_b^+ que é analisada a seguir. Pelas Eq.(3.11) e Eq.(3.14) podemos dizer que para $y^+ Pr = 50$

$$\Phi_t^+(50) = \frac{1}{k_t}\ln\frac{50 v_w^+}{\ln(v_w^+ t_b^+) + 1} \quad , \tag{4.1}$$

A Fig.5 compara os valores experimentais de $\Phi_t^+(50)$ com a Eq.(4.1). Apesar do espalhamento experimental, podemos notar que esta não descreve bem o escoamento com sucção. Os valores de Re_Δ (Reynolds entalpia) muito baixos talves sejam a causa desta discordância visto que nesta faixa as expressões de temperatura é provável tenham de ser corrigidas tal qual as de velocidade [16]. No entanto, a escassez de dados experimentais não permite uma análise fidedigna destas correções. Nos casos com injeção existe uma concordância qualitativa. As discordâncias se justificam em parte pelas diferenças entre os trabalhos de Blackwell [8] e Whitten [6]. Tendo em conta a Fig.5, a análise da Fig.7 revela que os erros da Eq.(4.1) comprometem seriamente apenas as previsões dos casos com sucção ($v_w^+ < 0$), concordando melhor para escoamentos com injeção ($v_w^+ > 0$) que são os de maior interesse prático.

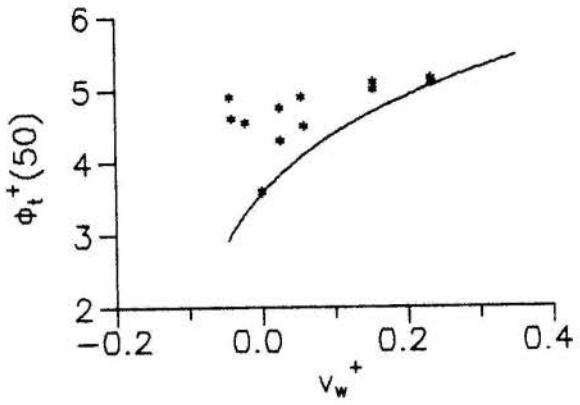

Fig.5 – Análise da Eq.(4.1)

O segundo ponto fundamental na análise de parâmetros diz respeito aos valores de Π_t. Inúmeros trabalhos dão conta da variação de Π_m com Re_θ, bem como do seu valor assintótico, 0.55. Para Π_t era de se esperar um comportamento qualitativamente semelhante com relação a Re_Δ. Os valores de Re_Δ dos casos sem injeção disponíveis são muito baixos. A injeção tem como um de seus efeitos, o aumento do valor de Re_Δ, que permitiu através da abordagem aqui apresentada, avaliar o comportamento de Π_t em camada limite bem desenvolvida. A Fig.6 apresenta os valores de Π_t coletados dos dados de Blackwell e Whitten. Verifica-se de fato uma variação para valores baixos de Re_Δ e a seguir um comportamento assintótico. A curva sugere a variação e o valor da assíntota, no entanto, a quantidade dos dados experimentais não é suficiente para apontar um valor definitivo para este comportamento assintótico.

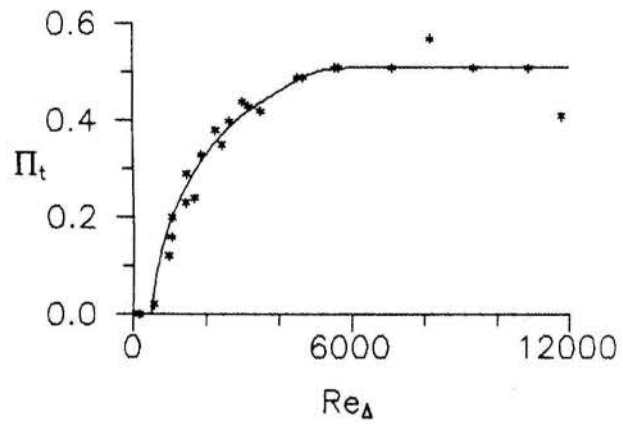

Fig.6 – Variação de Π_t com Re_Δ

Finalmente, a Fig.7 representa uma comparação entre a Eq.(3.17) e os dados experimentais de Whitten. Os valores de Π_t empregados foram obtidos das curvas da Fig.6. Observamos que a Eq.(3.17) descreve bem o perfil de temperatura mesmo para altas taxas de injeção. As previsões de St feitas pela Eq.(3.18) são comparadas com dados experimentais na Tab.1 mostrando excelente concordância para os casos de injeção.

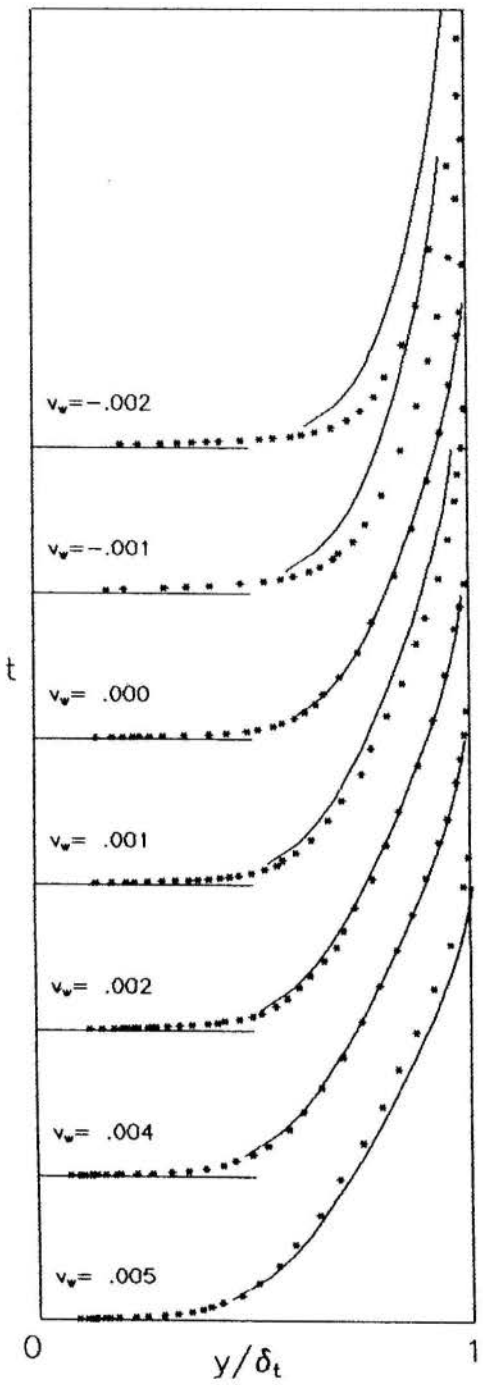

Fig.7 – Comparação da Eq.(3.17) com os dados experimentais de [6]

Tabela 1

v_w	Re_Δ	$St_{exp.}$ [6]	$St_{teo.}$ Eq.(3.18)
$-2.5\ 10^{-3}$	$9.6\ 10^2$	$3.46\ 10^{-3}$	$3.73\ 10^{-3}$
-2.2	$1.4\ 10^3$	3.14	3.30
-1.1	$1.7\ 10^3$	2.63	2.79
0.0	$3.5\ 10^3$	1.95	1.96
0.0	$4.7\ 10^3$	1.82	1.83
0.9	$5.7\ 10^3$	1.43	1.47
1.0	$4.5\ 10^3$	1.52	1.57
1.8	$7.1\ 10^3$	1.12	1.17
1.9	$5.5\ 10^3$	1.23	1.24
3.7	$1.1\ 10^4$	0.66	0.66
3.9	$8.2\ 10^3$	0.69	0.72
4.8	$1.2\ 10^4$	0.50	0.48
5.0	$9.4\ 10^3$	0.53	0.52

V.CONCLUSÃO

Este trabalho aborda o problema da camada limite turbulenta com transpiração de modo a permitir uma análise detalhada da transferência de calor. A *Lei da Parede* proposta é de fato eficaz para transformar perfis de casos com transpiração de forma que se possa tratá-los na região interna através da metodologia desenvolvida para placas impermeáveis, como revela o paralelismo, na região completamente turbulenta, entre as curvas apresentadas na Fig.3. O pequeno espalhamento dos valores de Π_t coletados atestam por sua vez a validade da *Lei da Esteira* confirmando assim a *Lei da Parede* que lhe deu origem.

Fica claro ainda que o ponto frágil desta análise não é outro senão a determinação de y_1^+. Fig.5. A expressão proposta possui a vantagem de não depender de novos parâmetros experimentais dependentes da taxa de transpiração, mas neste ponto poder-se-ia considerar mais adequada a utilização de uma correlação experimental para y_1^+. Isto não é feito aqui posto que não se trata apenas de descrever o fenômeno, mas sim de compreendê-lo, e neste ponto a Eq.(3.14) cumpre um papel importante. Uma análise cuidadosa das Fig.5 e 7 permite perceber que as discordâncias são em geral decorrentes de erros na obtenção de y_1^+, visto que a curva proposta e a descrita pelos dados experimentais são paralelas na região externa da camada limite. Exceção é feita para a taxa mais alta de injeção: neste caso o que se verifica é que o perfil transformado afasta-se do formato logarítmico.

Pelo presente método a boa descrição dos perfis é determinante e suficiente para que se obtenha precisão nos valoresde St preditos. Digna de nota é a acurácia apresentada nos casos de injeção alta quando os valores de St são muito pequenos. Enfim concluímos que a abordagem ora apresentada em geral prevê valores de St em boa concordância com os dados experimentais e, o que pode ser mais significativo, quando não o faz revela a discordância em sua origem permitindo fácil correção.

Agradecimentos: o autor agradece a A. P. Silva-Freire e C. C. Pellegrini pelas frutuosas discussões que contribuiram sobremaneira para a realização deste trabalho. O auxílio financeiro durante a execução deste projeto foi prestado pela CAPES.

VI. REFERÊNCIAS

[1] MOFFAT, R. J. and KAYS, W. M., "The Turbulent Boundary Layer on a Porous Plate: Experimental Heat Transfer with Uniform Blowing and Suction", *Int. J. Heat Mass Transfer*, vol. 11, pp. 1547-1566 (1968).

[2] KAYS, W. M. and MOFFAT, R. J., "The Behavior of Transpired Turbulent Boundary Layers", *Stanford University Report* No. HMT-20 (1975).

[3] RUBESIN, M. W., "An Analytical Estimation of the Effect of Transpiration Cooling on the Heat Transfer and Skin Friction Characteristics of a Compressible Turbulent Boundary Layer", *NACA TN 3341* (1954).

[4] SPALDING, D. B., "A Standard Formulation of the Steady Convective Mass Transfer Problems", *Int. J. Heat Mass Transfer*, vol. 1, pp. 192-207 (1960).

[5] TORII, K., NISHIWAKI, N. and HIRATA, M., "Heat Transfer and Skin Friction in Turbulent Boundary Layer with Mass Injection", *Proceedings of Third International Heat Transfer Conference*, vol. 3, pp. 34-48, Chicago (1966).

[6] WHITTEN, D. G., KAYS, W. M., MOFFAT, R. J., "The Turbulent Boundary Layer on a Porous Plate: Experimental Heat Transfer With Variable Suction, Blowing and Surface Temperature", *Stanford University Report* No. HMT-3 (1967).

[7] SIMPSON, R. L., "The Turbulent Boundary Layer on a Porous Plate: An Experimental Study of the Fluid Dynamics with Injection and Suction", *Ph.D thesis*,Stanford (1968).

[8] BLACKWELL, B. F., KAYS, W. M. ,MOFFAT, R. J., "The Turbulent Boundary Layer on a Porous Plate: an Experimental Study of the Heat Transfer Behavior with Adverse Pressure Gradients", *Stanford University Report* No. HMT-16 (1972).

[9] KESTIN, J. and KICHARDSON, P. D., "Heat Transfer Across Turbulent, Incompressible Boundary Layers", *Int. J. Heat Mass Transfer*, vol. 6, pp. 147-189 (1963).

[10] KADER, B. A. and YAGLOM, A. M., "Heat and Mass Transfer Laws for Fully Turbulent Wall Flows", *Int. J. Heat Mass Transfer*, vol. 15, pp. 2329-2351 (1972).

[11] KADER, B. A., "Temperature and Concentration Profiles in Fully Turbulent Boundary Layers", *Int. J. Heat Mass Transfer*, vol. 24, pp. 1541-1544 (1981).

[12] PLECTHER, R. H., "Progress in Turbulent Forced Convection", *ASME Journal of Heat Transfer*, vol. 110, pp. 1129-1144 (1988).

[13] MEDEIROS, M. A. F. and SILVA-FREIRE, A. P, "The Thermal Turbulent Boundary Layer in an Incompressible Flow", *Anais do X Congresso Brasileiro de Engenharia Mecânica*, vol. 2, pp. 65-68, Rio de Janeiro (1989).

[14] MEDEIROS, M. A.F., PELLEGRINI, C. C. and SILVA-FREIRE, A.P., "The Turbulent Boundary Layer with Addition of Mass and Heat", *International Symposium on Engineering Turbulence Modelling and Measurements*,Dubrovnik (1990).

[15] COLES, D., "The Law of The Wake in the Turbulent Boundary Layer", *J. Fluid Mech.*, vol. 1, pp. 191-226 (1956).

[16] SIMPSON, R. L., "Characteristics of Turbulent Boundary Layer at Low Reynolds Number with and without Transpiration", *J. Fluid Mech.*, vol. 42, pp. 769-802 (1970).

[17] STEVENSON, T. N., "A Modified Velocity Defect Law for Turbulent Boundary Layers with Injection", *Cranfield College of Aero. Rep.* No.170 (1963).

[18] BLACK, T. J. and SARNECKI, A. J., "The Turbulent Boundary Layer with Suction or Injection", *A. R. C. R. & M. 3389* (1965).

ABSTRACT

This work presents a theoretical analysis of the heat transfer in transpired turbulent thermal boundary layers. The analysis reveals the existence of two laws — one for the inner region and other for the outer — which reduce to the well-knowm *Thermal Law of the Wall* and *Thermal Law of the Wake* when the transpired velocity is zero. From this laws we propose an expression for the temperature profile and an equation for the Stanton Number. The comparison with the experimental data shows excelent agreement.

III ENCIT – Itapema, SC (Dezembro 1990)

SOLUÇÃO ANALÍTICA DO PROBLEMA DE ABLAÇÃO COM FLUXO DE CALOR TRANSIENTE

DINIZ, A.J. & APARECIDO, J.B.
Depto. de Engenharia Mecânica - FEIS/UNESP
Av. Brasil 56 - Fone (0187) 62-3466
15378 - Ilha Solteira - SP

RESUMO

O processo de ablação como mecanismo de proteção térmica tem sido muito utilizado em numerosas aplicações na engenharia.

O problema se caracteriza não linear e envolve o movimento do contorno.

A transferência de calor é estudada utilizando a Técnica de Transformada Integral Generalizada, buscando como resultados a profundidade e taxa de ablação.

INTRODUÇÃO

Condução de calor através de sólidos seguido de uma superfície ablativa é de grande interesse em muitas aplicações da engenharia, [1]. Este tipo de problema é essencialmente caso especial de ampla classe do problema de mudança de fase revista por [2]. Estudos teóricos e experimentais foram realizados utilizando hipóteses de ablação permanente e transiente com solução aproximada ou puramente numérica. Problemas envolvendo meios infinitos são frequentemente analizados e em corpos finitos são totalmente limitados, [3, 4].

Um procedimento que vem sendo aplicado em busca de solução exata é a técnica de transformada integral generalizada (TTIG), a qual tem sido aplicada em problemas complexos que não possam ser resolvidos pelas técnicas de separações de variáveis, variáveis complexas, etc. Uma análise ampla no que se refere à técnica da transformada integral (TTI) para solução de certa classe de problema de difusão foi apresentada por [5].

O presente trabalho baseou-se na ref. [3]. O motivo dessa escolha é devido a introdução de várias soluções onde a taxa e a profundidade de ablação são criticamente comparadas. As soluções abrangem o Método Integral do Balanço de Calor, o Método Integral do Momento - θ (Teta) e o Método Diferenças Finitas. Então este trabalho vem extender a solução [6], uma vez que a posição e a velocidade da fronteira em movimento são desconhecidas, e ainda dar continuidade ao trabalho [7]. Além da taxa e a profundidade ablativa apresenta-se também o perfil de temperatura dependendo do tempo.

ANÁLISE

Considere-se a condução de calor em uma placa de espessura finita com propriedades físicas constantes e inicialmente a uma temperatura T_o, com uma face isolada e a outra sujeita a um fluxo de calor transiente. Após o período de aquecimento pré-ablativo, inicia-se a fase ablativa, onde o material fundido é desprendido da superfície do corpo. As equações que governam o problema são as seguintes:

- Período pré-ablativo:

$$\frac{\partial\theta(\chi,\tau)}{\partial\tau} = \frac{\partial^2\theta(\chi,\tau)}{\partial\chi^2} \quad , \quad \begin{matrix} 0 < \tau < \tau_m \\ 0 < \chi < 1 \end{matrix} \tag{1}$$

com condição inicial e de contorno

$$\theta(\chi,0) = 0 \qquad 0 \le \chi \le 1 \tag{2}$$

$$-\frac{\partial\theta(\chi,\tau)}{\partial\chi}\bigg|_{\chi=0} = Q(\tau) \; ; \; \frac{\partial\theta(\chi,\tau)}{\partial\chi}\bigg|_{\chi=1} = 0 \quad , \tag{3}$$

$$0 < \tau < \tau_m$$

- Período Ablativo

$$\frac{\partial\theta(\chi,\tau)}{\partial\tau} = \frac{\partial^2\theta(\chi,\tau)}{\partial\chi^2} \quad , \tag{4}$$

$$S(\tau) < \chi < 1 \quad , \quad \tau > \tau_m$$

condição inicial e de contorno

$$\theta(\chi,\tau_m) = \theta_m(\chi) \quad , \; 0 \le \chi \le 1 \tag{5}$$

$$\frac{\partial\theta(\chi,\tau)}{\partial\chi}\bigg|_{\chi=1} = 0 \; , \; \theta(\chi,\tau) = 1\bigg|_{\chi=S(\tau)} \tag{6}$$

condição de acoplamento

$$-\frac{\partial\theta}{\partial\chi}(\chi,\tau) + \upsilon\frac{dS}{d\tau}(\tau) = Q(\tau) \quad \chi = S(\tau) \tag{7}$$

onde $\theta_m(\chi)$ é a distribuição de temperatura na placa quando inicia a ablação, com $\tau = \tau_m$, obtido no perío

do pré-ablativo. O parâmetro υ do balanço de energia da face ablativa, é o inverso do número de Stefan e $S(\tau)$ é a posição dependente do tempo dentro da fronteira móvel ablativa.

O problema pré-ablativo, dado pela equação (1) é resolvido aplicando TTIG. Para isto um problema auxiliar é adotado:

$$\mu^2 \psi(\chi) = L\,\psi(\chi) \quad , \quad L = -\frac{\partial^2}{\partial \chi^2} \tag{8}$$

com as seguintes condições de contorno

$$\left.\frac{\partial \psi(\chi)}{\partial \chi}\right|_{\chi=0} = 0 \quad ; \quad \left.\frac{\partial \psi(\chi)}{\partial \chi}\right|_{\chi=0} = 0 \tag{9}$$

obtendo assim a seguinte par de transformada integral

$$\tilde{\theta}_i(\tau) = \int_0^1 \psi_i(\chi)\ \theta(\chi,\tau)\, d\chi \qquad \text{Trans.} \tag{10}$$

$$\theta(\chi,\tau) = \sum_{i=0}^{\infty} \frac{\psi_i(\chi)}{\int_0^1 \psi_i^2(\chi) d\chi}\, \tilde{\theta}_i(\tau) \qquad \text{Inversa} \tag{11}$$

Substituindo a equação (10) na equação (4), obtemos a seguinte equação diferencial de 1ª ordem:

$$\frac{d\tilde{\theta}_i(\tau)}{d\tau} + \mu_i^2\, \tilde{\theta}_i(\tau) = Q(\tau) \tag{12}$$

com a condição inicial

$$\tilde{\theta}_i(0)\Big|_{\text{inicial}} = 0$$

A solução da equação (12) nos leva a distribuição de temperatura da fase pré-ablativa.

$$\theta(\chi,\tau) = \theta_{av}(\tau) + 2\sum_{i=1}^{\infty} \psi_i(\chi)\cdot$$

$$\int_0^{\tau} Q(\tau)\, \exp\left[-\mu_i^2(\tau-\tau')\right] d\tau' \qquad \tau < \tau_m \tag{13}$$

onde $\psi_i(\chi) = \cos \lambda_i \chi$ e $\lambda_i = i\pi$ são, respectivamente a auto função e auto valores. O potencial médio

$$\theta_{av}(\tau) = \int_0^{\tau} Q(\tau)\, d\tau \tag{14}$$

Assim, a distribuição de temperatura inicial para o período ablativo é

$$\theta_m(\chi) = \theta_{av}(\tau_m) + 2\sum_{i=1}^{\infty} \cos(i\pi\chi)$$

$$\int_0^{\tau_m} Q(\tau')\, \exp\left[-\mu_i^2(\tau_m - \tau')\right] d\tau' \tag{15}$$

A solução do problema ablativo, por onde envolve a posição do contorno em movimento, $S(\tau)$ é determinado juntamente com a distribuição de temperatura. Solução analítica para problemas de mudança de fase através da (TTIG) já tem sido apresentado por [4]. Baseado em [6] a completa solução da equação (4) é considerada. Para facilidade analítica uma mudança de variável é feita nas equações (4-7).

$$\theta^*(\chi,\tau) = \theta(\chi,1) - 1 \qquad S(\tau) < \chi < 1\,, \quad \tau < \tau_m \tag{16}$$

Também, envolvendo a coordenada espacial $\eta = 1 - \chi$ e denotando a posição de fronteira com $\eta_b(\tau) = 1 - S(\tau)$, as equações serão reescritas como:

$$\frac{\partial \theta^*(\eta,\tau)}{\partial \tau} = \frac{\partial^2 \theta^*(\eta,\tau)}{\partial \eta^2} \qquad 0 < \eta < \eta_b(\tau)\,, \quad \tau < \tau_m \tag{17}$$

$$\theta^*(\eta,\tau)\Big|_{\eta=\eta_b(\tau)} = 0 \ ; \ \left.\frac{\partial \theta^*(\eta,\tau)}{\partial \eta}\right|_{\eta=0} = 0 \tag{18}$$

$$\theta^*(\eta,\tau_m) = \theta(1-\eta,\tau_m) - 1 \qquad \tau > \tau_m \tag{19}$$

$$\frac{\partial \theta^*(\eta,\tau)}{\partial \eta} - \left.\frac{d\eta_b(\tau)}{d\tau}\right|_{\eta=\eta_b(\tau)} = Q(\tau) \qquad \tau > \tau_m \tag{20}$$

Para aplicação da técnica adotamos o seguinte problema auxiliar dependendo do tempo

$$\frac{\partial^2 \phi(\eta)}{\partial \eta^2} + \lambda^2 \phi(\eta) = 0 \qquad 0 < \eta < \eta_b(\tau) \tag{21}$$

$$\left.\frac{\partial \phi(\eta)}{\partial \eta}\right|_{\eta=0} = 0 \quad \text{e} \quad \phi(\eta)\Big|_{\eta=\eta_b(\tau)} = 0 \tag{22}$$

Resolvendo esse problema encontramos:

$$\lambda_i(\tau) = \frac{(2_i - 1)\pi}{2\eta_b(\tau)} \quad \text{e} \quad \phi_i(\eta) = \cos\left[\lambda_i(\tau)\eta\right] \tag{23}$$

O par de transformada integral é

$$\tilde{\theta}_i^* = \int_0^{\eta_b(\tau)} K_i(\eta,\tau)\, \theta^*(\eta,\tau)\, d\eta \qquad \text{transf.} \tag{24}$$

$$\theta^*(\eta,\tau) = \sum_{i=1}^{\infty} K_i(\eta,\tau)\ \tilde{\theta}_i^*(\tau) \quad \text{inversa} \tag{25}$$

onde a auto função normalizada é

$$K_i(\eta,\tau) = \frac{\phi_i(\eta,\tau)}{\left[\int_0^{\eta_b(\tau)} \cos^2[\lambda_i(\tau)\eta]\, d\eta\right]^{1/2}} \tag{26}$$

Aplicando o operador $\int_o^{\eta_b(\tau)} K_i(\eta,\tau)\, d\eta$ na equação (17) e nas condições de contorno, equação (18), temos

$$\int_o^{\eta_b(\tau)} K_i(\eta,\tau)\, \frac{\partial \theta^*(\eta,\tau)}{\partial \tau}\, d\eta +$$

$$+ \lambda_i^2(\tau)\, \tilde{\theta}_i^*(\tau) = 0 \qquad (27)$$

O termo não transformado da eq. (27), aplicando a inversa eq. (25), e substituindo dentro da integral, temos

$$\frac{d\tilde{\theta}_i^*(\tau)}{d\tau} + \lambda_i^2(\tau)\, \tilde{\theta}_i^*(\tau) +$$

$$\sum_{j=1}^{\infty} A_{ij}^*(\tau)\, \tilde{\theta}_j^* = 0 \qquad \tau > \tau_m \qquad (28)$$

A condição inicial eq. (19) operando com $\int_o^1 K_i(\eta,\tau)d\eta$ e com a condição de transformação, temos:

$$\tilde{\theta}_i^*(\tau) = \bar{g}_i^* = \int_o^1 K_i(\eta,\tau_m)\, \left[\theta_m(\eta-1)\right] \qquad (29)$$

Os valores de A_{ij}^* e $\bar{g}_i^*$ resolvidos são:

$$A_{ij}(\tau) = \frac{1}{2}\, \frac{(2_j-1)(2_i-1)(-1)^{i+j}}{\left[(i^2-i) - (j^2-j)\right]}$$

$$A_{ij}^*(\tau) = \frac{1}{\eta_b(\tau)}\, \frac{d\eta_b(\tau)}{d\tau}\, A_{ij}(\tau) \qquad (30)$$

$$A_{ii}^*(\tau) = 0 \qquad (31)$$

$$\bar{g}_i^* \Big|_{\tau=\tau_m} = \frac{2\sqrt{2}}{(2_i-1)\pi}(-1)^{i+1} \left[\theta_{av}(\tau)\right] \Big|_{\tau=\tau_m} +$$

$$\frac{4\sqrt{2}}{\pi}\, (2_i-1)(-1)^{i+1} \sum_{k=1}^{\infty} \frac{\tilde{\theta}_k(\tau_m)}{\left[(2_i-1)^2-4k^2\right]} \qquad (32)$$

onde

$$\tilde{\theta}_k(\tau_m) = \int_o^{\tau} Q(\tau)\, \exp\left[-(K\pi)^2(\tau_m-\tau')\right] d\tau'$$

A equação de acoplamento é escrita na forma de transformada, como segue; $\eta = \eta_b(\tau)$.

$$\frac{d\eta_b(\tau)}{d\tau} = \frac{\sqrt{2}}{2\nu\eta_b^{3/2}(\tau)}$$

$$\sum_{j=1}^{\infty} (2_j-1)\, \tilde{\theta}_j^*(\tau)(-1)^j - \frac{Q(\tau)}{\nu} \qquad (33)$$

com $\eta_b(\tau_m) = 1$ (34)

As equações (28) e (33) formam um sistema de equações diferenciais ordinárias de ordem infinita acopladas. Para efeitos computacionais as equações são truncadas para uma ordem N bastante grande e o potencial transformada é resolvido e aplicado na inversa eq. (25) para obter assim o perfil de temperatura, a qual mostra a profundidade e a taxa de ablação.

RESULTADO E DISCUSSÃO

As equações diferenciais definidas nas eqs. (32) e (33) com as condições iniciais eqs. (29) e (34) foram resolvidas numericamente usando a subrotina DGEAR, [8]. Os resultados numéricos foram a velocidade de ablação $v(\tau)$ e a profundidade $S(\tau)$, para fluxo de calor iguais a $Q = 2;\ 10\,\tau^2$ da referência [3]. As figuras (1) e (2) apresentam cada uma delas a comparação da espessura e velocidade para os seguintes métodos: (A) - Esquema de Diferença Finita; (B) - Método Integral do Balanço de Calor; (C) - Método Integral do Momento - θ e (D) - Técnica da Transformada Integral Generalizada, presente trabalho. O M.B.I.C. apresenta um sensível desvio, quanto à velocidade $v(\tau)$, da solução exata T.T.I.G., enquanto que o M.D.F. é aparentemente exato e suficiente para muitas propostas práticas, exceto para pequenos tempos no início de ablação. O M.I.M. - θ é uma aproximação que consideravelmente melhora o M.B.I.. As tabelas (1) e (2) mostram alguns resultados dos valores adimensionais da posição e da velocidade para os fluxos de calor indicados.

O valor de τ_m, quando a ablação inicia, também é apresentado e concorda com [3]. A figura (3) mostra o perfil de temperatura dentro da placa ablativa para o caso do fluxo de calor $Q(\tau) = 2{,}0$ e também para o período pré-ablativo, mostrando-se aceitável para a posição móvel da fronteira.

Tabela 1. Valores da espessura e velocidade de ablação para $Q(\tau) = 2$ e $\nu = 1$

$Q(\tau) = 2$	$\tau_m = 0.197$	$\nu = 1$
$\tau - \tau_m$	$S(\tau)$	$V(\tau)$
.0183	.004	0.33
.0549	.020	0.50
.1098	.052	0.65
.1463	.077	0.72
.2012	.120	0.83
.2561	.168	0.93
.3110	.222	1.03
.3476	.261	1.11
.4024	.325	1.22
.4573	.395	1.34
.5122	.472	1.48
.5488	.528	1.57
.6037	.619	1.73
.6585	.718	1.88
.7134	.824	1.98
.7500	.897	1.99

Tabela 2. Valores da profundidade e velocidade de ablação para $Q(\tau) = 10\tau^2$

$Q(\tau) = 10\tau^2$	$\tau_m = 0.487$	$\nu = 1$
$\tau - \tau_m$	$S(\tau)$	$V(\tau)$
0.0085	0.003	0.49
0.0512	0.040	1.15
0.1024	0.113	1.72
0.1537	0.216	2.27
0.2049	0.347	2.86
0.2561	0.511	3.57
0.3073	0.719	4.67
0.3500	0.963	6.99

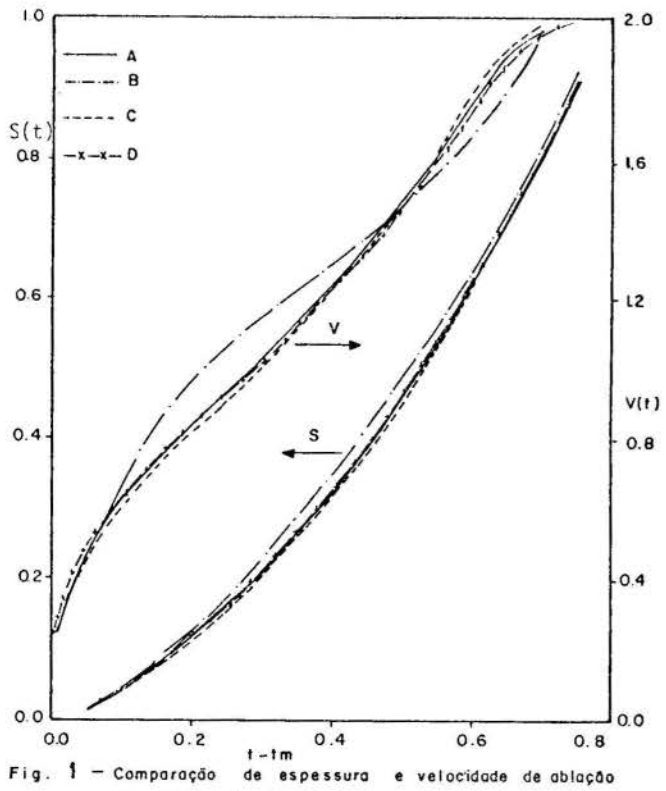

Fig. 1 – Comparação de espessura e velocidade de ablação dos varios métodos para Q(t) = 2

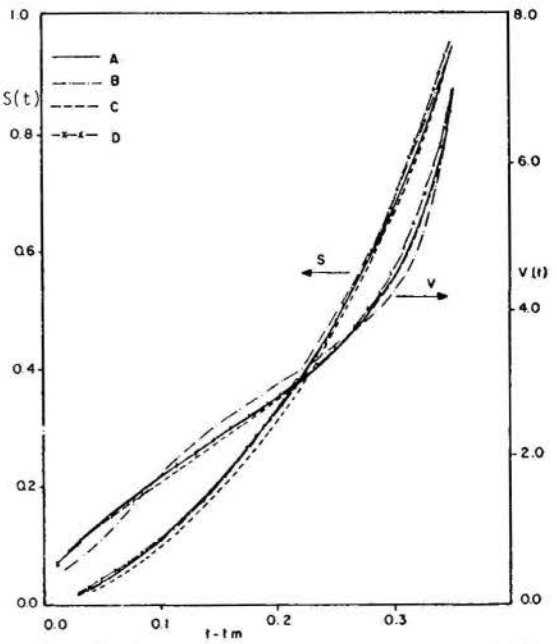

Fig. 2 – Comparação da espessura e velocidade de ablação de vários metodos para $Q(t) = 10t^2$

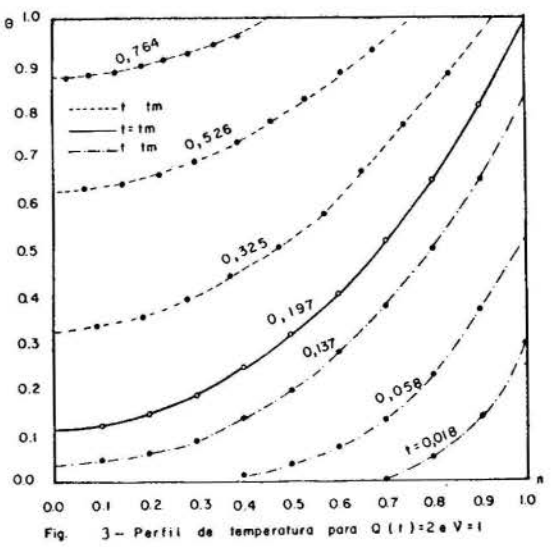

Fig. 3 – Perfil de temperatura para $Q(t) = 2$ e $V = 1$

ABSTRACT

Heat transfer followed by ablation in a slab sujected to a time-dependent boundary heat flux is analytically estudied, through application of the generalized integral transform technique. Results for the ablation depth and speed are reported for different boundary heat flux behaviors.

REFERÊNCIAS

[1] Sutton, G.W., "The initial Development of Ablation Heat Protection, An Historical Perspective", J. Spacecroft & Rochets v. 10, pp. 3-11, 1982.

[2] Özisik, M.N., "Heat Conduction", John Wiley, New York, 1980.

[3] Chung, B.T.F. and J.S. Hsiao. "Heat Transfer with Ablation in a Finite Slab Subjected to time-variant Heat Fluxes", AIAA Journal, v. 23 nº 1, pp. 145-150, 1985.

[4] Özisik, M.N. and S.I. Güceri, "A Variable Engevalue Approach to the Solution of Pahse-change Problems", Cam. J. Chem. Eng., v. 55, pp. 145-148, 1977.

[5] Mikhoilow, M.D. and Özisik, M.N., "Unified Analysis and Solutions of Heat and Mass Diffusion, John Wiley & Sons, New York, 1984.

[6] Cotta, R.M., "Diffusion in Media with Prescribed Moring Boundories". Application to Metals Oxidation at High Temperatures". II Latin American Congress of Heat the Mass Transfer, v. 1, pp. 502-512, São Paulo-Brasil, may 1986.

[7] Diniz, A.J.; Aparecido, J.B.; Cotta, R.M., "Heat Conduction with Ablation in a Finite Slab". Heat and Technology, Bologna. (to appear)

[8] ISML Libary Edition 7, GNB Building, 7500 BALLAsre LVd., Huston, TEXAS, 77036, 1979.

III ENCIT – Itapema, SC (Dezembro 1990)

CONVERGENCE ENHANCEMENT OF EIGENFUNCTION EXPANSIONS FOR NONHOMOGENEOUS ELLIPTIC DIFFUSION PROBLEMS

A.J.K. Leiroz and R.M. Cotta
Programa de Engenharia Mecânica - COPPE/UFRJ
Universidade Federal do Rio de Janeiro
Cidade Universitária - Cx.Postal 68503
Rio de Janeiro - RJ - 21945 - Brasil

ABSTRACT

An alternative procedure is proposed to accelerate the convergence of series solutions, for elliptic diffusion problems, obtained through the integral transform technique. The approach developed is critically compared to the direct use of the inversion formula for nonhomogeneous problems, in a two-dimensional application, in order to illustrate the improved convergence behavior.

INTRODUCTION

The exact solution of heat and mass diffusion problems has been recently reviewed [1] and presented in a systematic and unified form, based on application of the integral transform technique [1,2] to various different classes of problems. Although formal analytical solutions are readily obtainable as explicit inversion formula, the convergence of such eigenfuction expansions can be particularly affected by nonhomogeneous source terms, specially at the boundary conditions, and make such an approach not so efficient for computational purposes. However, a few procedures were developed within the last two decades [2-5] to overcome this difficulty by employing partial integration of the resulting inversion formula [2], separation of quasi-steady contribution [3], or splitting-up of the original problem into simpler ones [4,5], providing convergence acceleration with respect to the original inversion formula. The splitting-up procedure [1,4-5] is particularly elaborate and offers the best computational performance possible for this type of approach. Nevertheless, the additional analytical involvement is quite considerable, as required by the solution of the various separated problems, which might become prohibitive in multidimensional situations, even from a computational point of view. Besides, the source functions are required to have specific functional forms, such as q-order polynomials and exponentials, which to some extent limits the application of such analysis.

Quite recently [6], an alternative approach was proposed and utilized in the solution of transient one-dimensional diffusion problems, aimed at offering a more efficient computational tool for the development of automatic parabolic diffusion solvers [7]. This procedure is based simply in the integration, over the region, of the original partial differential equation, yielding improved series solutions in terms of a correction to the inversion formula. Motivated by an undergoing effort in the development of automatic solvers for multidimensional elliptic problems through the generalized integral transform technique [8,9], the present note brings the extension of the ideas in [6] to steady-state diffusion problems. An application is then more closely considered dealing with two-dimensional heat conduction in a plate with uniform surface dissipation, and numerical results presented to illustrate the degree of convergence enhancement attained.

ANALYSIS

A sufficiently general two-dimensional elliptic diffusion problem is here considered, where t stands for the independent space variable that shall not be elliminated through the integral transformation process. The problem formulation is then written as [1,8].

$$[w(x)L_t + L]T(x,t) = P(x,t) \quad , \text{ in } x_0 < x < x_1 \; , \quad t_0 < t < t_1 \qquad (1.a)$$

with boundary conditions

$$B_{x,k}T(x,t) = \phi_k(t) \quad , \text{ at } x=x_k \; , \; k=0,1 \qquad (1.b,c)$$

$$B_{t,k}T(x,t) = f_k(x) \quad , \text{ at } t=t_k \; , \; k=0,1 \qquad (1.d,e)$$

where the related operators are defined by

$$L_t \equiv -a(t)\frac{\partial}{\partial t}\left[b(t)\frac{\partial}{\partial t}\right] \qquad (1.f)$$

$$L \equiv -\frac{\partial}{\partial x}\left[k(x)\frac{\partial}{\partial x}\right] + d(x) \qquad (1.g)$$

$$B_{x,k} \equiv \left[\alpha_k - (-1)^k \beta_k \frac{\partial}{\partial x}\right] \qquad (1.h)$$

$$B_{t,k} \equiv \left[\delta_k - (-1)^k \gamma_k \frac{\partial}{\partial t}\right] \qquad (1.i)$$

The exact formal solution of problem (1) above is readily obtained through the integral transform technique [1], in terms of the associated auxiliary eigenvalue problem:

$$\frac{d}{dx}\left[k(x)\frac{d\psi_i(x)}{dx}\right] + [\mu_i^2 w(x) - d(x)]\psi_i(x) = 0 \; , \quad x_0 < x < x_1 \qquad (2.a)$$

with boundary conditions

$$B_{x,k}\psi_i(x) = 0 \quad , \quad \text{at } x = x_k \quad , \quad k=0,1 \qquad (2.b,c)$$

which provides the following integral transform pair

$$\bar{T}_i(t) = \int_{x_0}^{x_1} w(x)\frac{\psi_i(x)}{N_i^{1/2}} T(x,t)dx \; , \text{ transform} \qquad (3.a)$$

$$T(x,t) = \sum_{i=1}^{\infty} \frac{1}{N_i^{1/2}} \psi_i(x)\overline{T}_i(t) \quad , \text{ inversion} \quad (3.b)$$

where the normalization integral is defined as

$$N_i = \int_{x_0}^{x_1} w(x)\, \psi_i^2(x)dx \quad (3.c)$$

Eq. (3.b) provides the explicit inversion formula for the original potential, $T(x,t)$, in terms of the transformed quantities, $\overline{T}_i(t)$, which are obtained from solving the decoupled system of boundary value problems below:

$$L_t\overline{T}_i(t) + \mu_i^2\overline{T}_i(t) = \overline{g}_i(t) \quad , \quad t_0 < t < t_1 \, , \quad i=1,2,\ldots \quad (4.a)$$

$$B_{t,k}\overline{T}_i(t) = \overline{f}_{k,i} \quad , \quad \text{at } t=t_k \, , \; k=0,1 \quad (4.b,c)$$

where,

$$\overline{g}_i(t) = \frac{1}{N_i^{1/2}} \left[\sum_{k=0}^{1} \phi_k(t)\Omega_i(x_k) + \int_{x_0}^{x_1} P(x,t)\psi_i(x)dx \right] \quad (4.d)$$

$$\Omega_i(x_k) = \frac{\psi_i(x_k) + (-1)^k k(x_k) \dfrac{d\psi_i(x_k)}{dx}}{\alpha_k + \beta_k} \quad (4.e)$$

$$\overline{f}_{k,i} = \frac{1}{N_i^{1/2}} \int_{x_0}^{x_1} w(x)\psi_i(x)f_k(x)dx \quad , \; k=0,1 \quad (4.f,g)$$

The inversion formula (3.b) can be directly used for computational purposes whenever the source functions, at both equation and boundaries, $P(x,t)$ and $\phi_k(t)$, are not present. However, for a non-vanishing nonhomogeneous transformed source term, $\overline{g}_i(t)$, the series defined by eq. (3.b) might converge quite too slowly for practical purposes, specially for nonhomogeneous boundary conditions. Even worse, the flux defined through the derivative of $T(x,t)$ with respect to x, might cease to converge at all. The present approach is an attempt to overcome this difficulty, providing an alternative series which is uniformly convergent within the region and at the boundaries. It would be quite interesting to obtain such convergence improvement without recurring to additional solutions of separated problems, and making use only of the transformed potentials already obtained. For this purpose, the steps in [6] are now followed and integral balances over any portion of the domain are employed, together with direct use of the boundary equations thenselves, as shown below. First, eq. (1.a) is operated on with $\int_{x_0}^{x} dx$, to yield, after substitution of the inversion formula (3.b):

$$\sum_{i=1}^{\infty} \left[\overline{f}_i^*(x)L_t\overline{T}_i(t) + \overline{h}_i(x)\overline{T}_i(t) \right] - g(t) = k(x) \left.\frac{\partial T}{\partial x}\right|_x - k(x_0) \left.\frac{\partial T}{\partial x}\right|_{x_0} \quad (5.a)$$

where,

$$\overline{f}_i^*(x) = \frac{1}{N_i^{1/2}} \int_{x_0}^{x} w(x)\psi_i(x)dx \quad (5.b)$$

$$\overline{h}_i(x) = \frac{1}{N_i^{1/2}} \int_{x_0}^{x} d(x)\psi_i(x)dx \quad (5.c)$$

$$g(x,t) = \int_{x_0}^{x} P(x,t)dx \quad (5.d)$$

or, by recalling eq. (4.a) above for $L_t\overline{T}_i(t)$, the resulting expression for the flux at any position x, in terms of the flux at $x=x_0$, becomes

$$k(x) \left.\frac{\partial T}{\partial x}\right|_x = k(x_0) \left.\frac{\partial T}{\partial x}\right|_{x_0} + \sum_{i=1}^{\infty} \left\{ \overline{f}_i^*(x)\overline{g}_i(t) + \left[\overline{h}_i(x) - \overline{f}_i^*(x)\mu_i^2 \right] \overline{T}_i(t) \right\} - g(x,t) \quad (5.e)$$

Similarly, an expression relating the flux at position x to the boundary flux at $x=x_1$, could be obtained by operating on eq. (1.a) with $\int_x^{x_1} dx$, and is here omitted for the sake of conciseness. On the other hand, the potential at any position within the medium is determined from integration of eq. (5.e) from x to x_1, providing:

$$T(x,t) = T(x_1, t) - \hat{k}(x)k(x_0) \left.\frac{\partial T}{\partial x}\right|_x + \sum_{i=1}^{\infty} \left\{ \hat{\overline{f}}_i^*(x)\overline{g}_i(t) + \left[\hat{\overline{h}}_i(x) - \hat{\overline{f}}_i^*(x)\mu_i^2 \right] \overline{T}_i(t) \right\} + \hat{g}(x,t) \quad (6.a)$$

where,

$$\hat{k}(x) = \int_x^{x_1} \frac{1}{k(x)} dx \quad (6.b)$$

$$\hat{\overline{f}}_i^*(x) = \int_x^{x_1} \frac{\overline{f}_i^*(x)}{k(x)} dx \quad (6.c)$$

$$\hat{\overline{h}}_i(x) = \int_x^{x_1} \frac{\overline{h}_i(x)}{k(x)} dx \quad (6.d)$$

$$\hat{g}(x,t) = \int_x^{x_1} \frac{g(x,t)}{k(x)} dx \quad (6.e)$$

or, alternatively, by integrating from x to x_0 the expression that would relate the flux at position x to the boundary flux at x_1.

Therefore, such expressions provide alternative formulas for both the potential and its flux anywhere within the medium, provided the quantities at the boundaries are accurately known. The two boundary conditions, eqs. (1.b,c), together with eq. (5.e) evaluated at $x=x_1$, and eq. (6.a) evaluated at $x=x_0$, provide four simultaneous algebraic equations, with t as a parameter, for the four unknowns in the most general situation of nonhomogeneous third kind boundary

conditions, $k(x_0)\left.\frac{\partial T}{\partial x}\right|_{x_0}$, $k(x_1)\left.\frac{\partial T}{\partial x}\right|_{x_1}$, $T(x_0,t)$, and $T(x_1,t)$, which are solved to yield:

$$k(x_0)\left.\frac{\partial T}{\partial x}\right|_{x_0} = \frac{1}{\frac{\beta_0}{\alpha_0}+\frac{\beta_1}{\alpha_1}+\hat{k}(x_0)}\left[B(t) - \frac{\beta_1}{\alpha_1}A(t) + \frac{\phi_1(t)}{\alpha_1} - \frac{\phi_0(t)}{\alpha_0}\right] \tag{7.a}$$

$$k(x_1)\left.\frac{\partial T}{\partial x}\right|_{x_1} = k(x_0)\left.\frac{\partial T}{\partial x}\right|_{x_0} + A(t) \tag{7.b}$$

$$T(x_0,t) = \frac{\phi_0(t)}{\alpha_0} + \frac{\beta_0/\alpha_0}{\frac{\beta_0}{\alpha_0}+\frac{\beta_1}{\alpha_1}+\hat{k}(x_0)}\left[B(t) - \frac{\beta_1}{\alpha_1}A(t) + \frac{\phi_1(t)}{\alpha_1} - \frac{\phi_0(t)}{\alpha_0}\right] \tag{7.c}$$

$$T(x_1,t) = \frac{\phi_1(t)}{\alpha_1} - \frac{\beta_1/\alpha_1}{\frac{\beta_0}{\alpha_0}+\frac{\beta_1}{\alpha_1}+\hat{k}(x_0)}\left[B(t) - \frac{\beta_1}{\alpha_1}A(t) + \frac{\phi_1(t)}{\alpha_1} - \frac{\phi_0(t)}{\alpha_0}\right] - \frac{\beta_1 A(t)}{\alpha_1} \tag{7.d}$$

where,

$$A(t) = \sum_{i=1}^{\infty}\left\{\left[\bar{f}_i^*(x_1)\bar{g}_i(t) + \left[\bar{h}_i(x_1) - \bar{f}_i^*(x_1)\mu_i^2\right]\bar{T}_i(t)\right\} - g(x_1,t) \tag{7.e}$$

$$B(t) = -\sum_{i=1}^{\infty}\left\{\left[\hat{\bar{f}}_i^*(x_0)\bar{g}_i(t) + \left[\hat{\bar{h}}_i(x_0) - \hat{\bar{f}}_i(x_0)\mu_i^2\right]\bar{T}_i(t)\right\} + \hat{g}(x_0,t) \tag{7.f}$$

Simpler expressions are obtainable as special cases of the relations above, in the case of first/second kind boundary conditions, when either the potential or the flux is already prescribed at the boundary.

APPLICATION

A two-dimensional elliptic problem related to heat conduction in a square plate subjected to an uniform linear surface dissipation is now more closely considered. The problem formulation is given by:

$$\frac{\partial^2 T}{\partial t^2} + \frac{\partial^2 T}{\partial x^2} - BiT(x,t) = 0 \quad , \quad 0<x<1 \ , \ 0<t<1 \tag{8.a}$$

with boundary conditions

$$\frac{\partial T(0,t)}{\partial x} = 0 \quad ; \quad T(1,t) = e^{1-t} \quad , \quad 0 \leq t \leq 1 \tag{8.b,c}$$

$$\frac{\partial T(x,0)}{\partial t} = 0 \quad ; \quad T(x,1) = 1 \quad , \quad 0 < x < 1 \tag{8.d,e}$$

and correspondence to the general system (1) establishes

$$\begin{aligned} &a(t) = b(t) = 1 \ ; \ k(x) = w(x) = 1 \ ; \\ &d(x) = Bi \ ; \ x_0 = t_0 = 0 \ ; \\ &x_1 = t_1 = 1 \ ; \ P(x,t) = 0 \ ; \\ &\phi_0(t) = f_0(x) = 0 \ ; \ \phi_1(t) = e^{1-t} \ ; \\ &f_1(x) = 1 \ ; \ \alpha_0 = \delta_0 = 0 \ ; \\ &\beta_0 = \gamma_0 = 1 \ ; \ \alpha_1 = \delta_1 = 1 \ ; \\ &\beta_1 = \gamma_1 = 0 \end{aligned} \tag{9}$$

After solving the associated eigenvalue problem, the final expressions for the potential and flux, in terms of the transformed potentials are readily obtained from eqs. (6.a) and (5.e), respectively, since both the flux at x_0 and the potential at x_1, are known a priori.

Table 1. Convergence of present alternative solution (eq. 6.a) compared with the inverse formula (eq. 3.b) (Bi = 10)

N	x=0 t=0		x=0 t=0.5		x=0 t=0.9		x=0.5 t=0		x=0.5 t=0.5		x=0.5 t=0.9		x=0.9 t=0		x=0.9 t=0.5		x=0.9 t=0.9	
	ALT.	INV.	ALT.	INV.	ALT.	INV.	ALT.	INV.	ALT.	INV.	ALT.	INV.	ALT.	INV.	ALT.	INV.	ALT.	INV.
3	.1669	.4482	.2911	.4617	.7435	.8578	.4658	.5212	.4779	.5115	.7865	.8090	1.940	.7768	1.283	.5769	.9959	.5228
6	.2260	.0828	.3074	.2206	.7513	.6930	.4700	.6701	.4816	.6030	.7875	.8689	1.806	1.774	1.249	1.229	.9787	.9655
9	.2110	.3069	.3047	.3629	.7496	.7886	.4852	.4778	.4845	.4801	.7892	.7862	1.776	2.237	1.243	1.522	.9755	1.163
12	.2177	.1457	.3056	.2620	.7502	.7209	.4877	.3862	.4848	.4232	.7894	.7481	1.778	2.173	1.244	1.483	.9757	1.136
15	.2138	.2716	.3052	.3402	.7499	.7734	.4843	.4870	.4844	.4860	.7891	.7902	1.788	1.852	1.245	1.284	.9763	1.003
18	.2164	.1683	.3055	.2763	.7501	.7306	.4831	.5509	.4843	.5254	.7891	.8166	1.794	1.585	1.245	1.118	.9767	.8918
21	.2147	.2559	.3053	.3303	.7500	.7667	.4845	.4831	.4844	.4836	.7891	.7886	1.795	1.543	1.245	1.092	.9768	.8743
24	.2159	.1799	.3054	.2835	.7501	.7354	.4852	.4343	.4844	.4536	.7892	.7685	1.792	1.697	1.245	1.187	.9766	.9378
28	.2158	.1849	.3054	.2867	.7501	.7375	.4850	.4413	.4844	.4579	.7891	.7714	1.789	1.933	1.245	1.332	.9765	1.035

$$\frac{\partial T}{\partial x}(x,t) = \sum_{i=1}^{\infty} \left\{ \frac{1}{N_i} \frac{1}{\lambda_i} e^{(1-t)} (\cos \lambda_i + \right.$$

$$+ \lambda_i \operatorname{sen} \lambda_i) \operatorname{sen} \lambda_i x -$$

$$\left. - \frac{\lambda_i}{N_i^{1/2}} \operatorname{sen} \lambda_i x \overline{T}_i(t) \right\} \qquad (10)$$

$$T(x,t) = e^{(1-t)} + \sum_{i=1}^{\infty} \left\{ \frac{1}{\lambda_i} (\cos \lambda_i - \right.$$

$$- \cos \lambda_i x) \left[\frac{1}{N_i} \frac{1}{i} e^{(1-t)} (\cos \lambda_i + \right.$$

$$\left. \left. + \lambda_i \operatorname{sen} \lambda_i) + \overline{T}_i(t) \frac{\lambda_i}{N_i^{1/2}} \right] \right\} \qquad (11)$$

RESULTS AND DISCUSSION

Problem (8) was solved exactly by following the steps in the integral transform technique, and reaching an explicit expression for the potential T(x,t) as defined by the inverse formula, eq. (3.b). In addition, the alternative solution represented by eq. (6.a) was computationally implemented to allow for a critical analysis of convergence behavior for both expressions. These two series were evaluated for different truncation orders N, i.e., by retaining different number of terms in the infinite sums. Table 1 shows numerical results for N=3,6,9,12,15,18,21,24, and 28, from both eqs.(6.a) and (3.b). Clearly, the alternative series here proposed considerably enhances the convergence of the analytical solution, which wasn't yet attained, for different positions throughout the medium, by the formally exact inverse formula. The poor convergence of eq. (3.b) in regions close to the nonhomogeneous boundary is represented by the columns for x=0.9, where the improvement is particularly noticeable. Representative points at the midplane (x=0.5) and at the leftmost boundary (x=0) are also considered, with similar behavior.

In fact, the inverse formula exhibits an oscillatory behavior, as evident from figure 1 for the isotherms at the plate surface, fluctuating over the fully converged solution. The alternative solution damps such oscillations, correcting the inverse formula after every each additional term in the infinite sum.

The present approach is particularly suitable for implementation in automatic solvers, since only a few numerical integrations are eventually required to accomplish this task, as opposed to a considerable analytical and computational involvement when employing splitting up procedures.

NOMENCLATURE

- $a(t)$, $b(t)$ - coefficients in L_t operator
- $d(x)$ - coefficient in dissipation term of L operator
- $f_k(x)$ - t-boundary source functions (k=1,2)
- $k(x)$ - coefficient in diffusion term of L operator
- N - number of terms in truncated series
- N_i - norm of eigenvalue problem (2)
- $P(x,t)$ - equation source function
- t - space coordinate
- t_k - t-boundary coordinates (k=1,2)

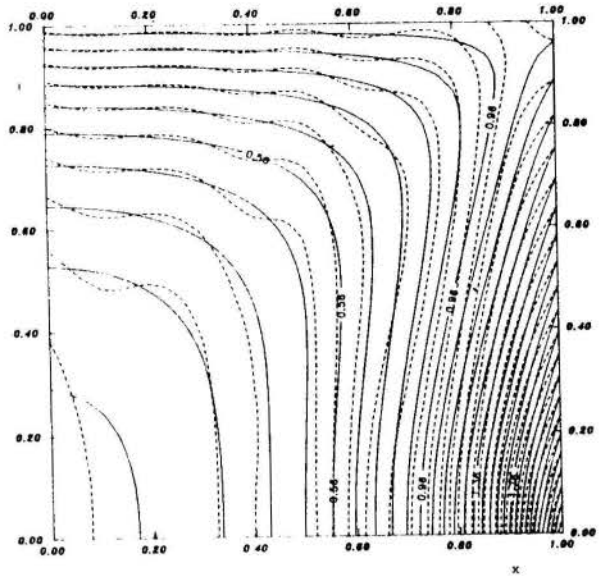

Alternative sol. - - - Inverse Formulae

Fig. 1 Isotherms at the plate surface from both alternative solution (eq. 6a) and inverse formula (eq. 3b), for Bi = 10 (28 terms; tol. = 10^{-6})

- $T(x,t)$ - potential (temperature, concentration, velocity, etc.)
- $\overline{T}_i(t)$ - integral transformed potential
- $w(x)$ - equation coefficient
- x - space coordinate
- x_k - x-boundary coordinates (k=1,2)

Greek symbols

- α_k - x-boundary coefficients (k=1,2)
- β_k - x-boundary coefficients (k=1,2)
- γ_k - t-boundary coefficients (k=1,2)
- δ_k - t-boundary coefficients (k=1,2)
- $\phi_k(t)$ - x-boundary source functions
- $\psi_i(x)$ - eigenfunctions of problem (2)
- μ_i - eigenvalues of problem (2)

REFERENCES

[1] Mikhailov, M.D. and M.N. Özisik, "Unified Analysis and Solutions of Heat and Mass Diffusion", John Wiley, New York, 1984.

[2] Özisik, M.N., "Heat Conduction", John Wiley, New York, 1980.

[3] Ölçer, N.Y., "Theory of Unsteady Heat Conduction in Multicomponent Finite Regions", Ingenieur-Archiv, V. 36, pp. 285-293, 1968.

[4] Mikhailov, M.D., "Splitting Up of Heat-Conduction Problem", Lett. Heat & Mass Transfer, V. 4, pp. 163-166, 1977.

[5] Mikhailov, M.D. and M.N. Özisik, "A Method of Accelerating the Convergence of Series Solutions", J. of the Franklin Inst., V. 322, nº 3, pp. 127-135, 1986.

[6] Scofano Neto, F., R.M. Cotta, and M.D. Mikhailov, "Alternative Approach to the Integral Transform

Solution of Nonhomogeneous Diffusion Problems", Int. Conf. of Advanced Computational Methods in Heat Transfer, "Heat Transfer 90", Southampton, UK, July 1990.

[7] Parouh, V.A. and M.D. Mikhailov, "One-Dimensional Heat and Mass Diffusion Modelling Software", Appl. Math. Modelling, V. 13, pp. 568-573, 1989.

[8] Cotta, R.M., A.J.K. Leiroz, and J.B. Aparecido, "Steady-State Diffusion Problems with Variable Equation Coefficients", Int. J. Heat & Technology, in press.

[9] Cotta, R.M., "Hybrid Numerical-Analytical Approach to Diffusion-Convection Problems", Proc. of the XV National Summer School (Invited Lecture), Institute of Applied Mathematics & Computer Science, Bulgaria, August 1989.

III ENCIT – Itapema, SC (Dezembro 1990)

SIMULAÇÃO DE TEMPERATURA NÃO ESTACIONÁRIA EM UM TROCADOR DE CALOR ATRAVÉS DE DERIVADA FRACIONÁRIA

RUBEM MÁRIO FIGUEIRÓ VARGAS
MARCO TÚLLIO DE VILHENA
JULIO R. CLAEYSSEN
Departamento de Engenharia Nuclear da UFRGS

SUMÁRIO

Sob condições de regime transiente, de um escoamento laminar bastante lento no tubo interno de um trocador de calor tipo tubo-carcaça, mediante uma mudança brusca de temperatura no ambiente externo do tubo, avalia-se a temperatura no lado interno da parede do tubo com o uso de teoria do cálculo fracionário. No modelo empregado leva-se em consideração a influência de capacidade térmica da parede do tubo.

INTRODUÇÃO

Nos projetos de trocadores de calor, geralmente, deseja-se conhecer a temperatura no lado interno da parede do tubo no interior da carcaça, a partir de uma mudança na temperatura do ambiente externo ao tubo. Assim que ocorre a mudança de temperatura, estabelece-se o regime transiente e é dentro do limite de validade deste regime que será modelado o processo de transferência de calor neste trabalho. Além disso, será levado em conta a influência da parede do tubo no cálculo do fluxo de calor que atravessa a parede.

Krishan [1] analisa o caso de um tubo no regime transiente sujeito a variação de temperatura ou de fluxo de calor na superfície externa. Empregando transformada de Laplace encontra uma solução para a temperatura no lado interno do tubo. Chen et. al. [2] empregando diferenças finitas soluciona um problema semelhante ao de Krishan. Sucec [3] considerando uma mudança na temperatura externa calcula a temperatura da parede interna do tubo, desprezando a influência da parede, por transformada de Laplace, apresentando também um critério que indica quando a capacidade térmica da parede do tubo pode ser negligenciada garantindo resultados precisos.

ANÁLISE

Seja um fluido incompressível escoando no interior de um tubo de raio interno R, numa determinada temperatura T_i, em regime laminar hidrodinamicamente desenvolvido. Quando, subitamente, a temperatura interna ao tubo muda para T_L, retirando, desta forma, o sistema do estado estacionário. Com esta mudança de temperatura surge um fluxo de calor através da parede do tubo de espessura b. Neste regime transiente, o tempo está dentro do domínio onde $t < \frac{x}{U_{máx}}$ [4,5], sendo x uma posição ao longo do eixo do cilindro e $U_{máx}$, a velocidade máxima do fluido. Considerando o caso em que o escoamento seja muito lento ("creeping flow"), ou seja, o número de Reynolds é pequeno ($R_e \to 0$) [2] e fazendo-se o balanço de energia no fluido e na parede do tubo, usando a continuidade da temperatura no lado interno da parede, podemos escrever o problema de transferência de calor da seguinte forma adimensionalizada [7]:

$$\frac{\partial^2 \Phi}{\partial z^2} + \frac{1}{z}\frac{\partial \Phi}{\partial z} = \frac{\partial \Phi}{\partial F} \qquad (1.a)$$

$$\frac{\partial \Phi}{\partial z} = 0 \ , \ z = 0 \ , \ F>0 \qquad (1.b)$$

$$\frac{\partial \Phi}{\partial z} = S(1-\Phi) - \left(1+\frac{b}{2R}\right)\frac{1}{\hat{a}}\frac{\partial \Phi}{\partial F} \ , \ z=1, F>0 \qquad (1.c)$$

$$\Phi = 0 \quad F = 0 \qquad (1.d)$$

onde $\Phi = \frac{T(x,r,t) - T_i}{T_L - T_i}$ = temperatura adimensional.

$F = \frac{\alpha t}{R^2}$ = número de Fourier

k = condutividade térmica do fluido

α = difusividade térmica do fluido

R = raio interno do tubo

$z = \frac{r}{R}$ = raio adimensional

b = espessura da parede do tubo

$\hat{a} = \frac{\rho C_p R}{\rho_w C_{pw} b}$ = razão entre as capacidades térmicas de armazenamento de energia do fluido e do material da parede.

U = coeficiente global de transferência de calor.

ρ, ρ_w = densidade do fluido e da parede, respectivamente.

C_p, C_{pw} = calor específico à pressão constante do fluido e da parede respectivamente.

$S = \frac{UR}{k}$ = coeficiente global de transferência de calor adimensional.

O perfil de velocidade no interior do tubo é dado por:

$$u(z) = U_{máx}\,(1 - z^2) \qquad (2)$$

Aplicando transformada de Laplace na equação (1.a) temos a seguinte solução:

$$\Phi(z,s) = AI_o(\sqrt{s}\, z) + B\, K_o(\sqrt{s}\, z) \qquad (3)$$

Sendo I_o e K_o as funções modificadas de Bessel e s o parâmetro de transformada de Laplace.

Como a função K_o não é limitada em z = 0, a constante B deve ser nula. Desta forma, a solução fica restrita a seguinte forma:

$$\bar{\Phi}(z,s) = A\, I_o(\sqrt{s}\, z) \qquad (4)$$

Derivando com relação a z a Equação (4) obtemos

$$\frac{\partial \bar{\Phi}(z,s)}{\partial z} = \sqrt{s}\, A\, I_1(\sqrt{s}\, z) \qquad (5)$$

Então a Equação (5) pode ser escrita como

$$\frac{\partial \bar{\Phi}(z,s)}{\partial z} = \sqrt{s}\, \frac{I_1(\sqrt{s}\, z)}{I_o(\sqrt{s}\, z)}\, \bar{\Phi}(z,s) \qquad (6)$$

Como é de interesse calcular a temperatura na parede interna do tubo do trocador de calor (z = 1) particularizamos a Equação (6) para este valor de z.

Agora, iremos usar alguns resultados da teoria do cálculo fracionário e conectá-los com a Equação (6).

A transformada de Laplace de derivada da ordem 1/2 de uma função $\Phi(F)$ é dada pela seguinte equação [8].

$$L\{\frac{\partial^{1/2}\Phi}{\partial F^{1/2}}\} = \sqrt{s}\, L\{\Phi\} - \frac{\partial^{-1/2}}{\partial F^{-1/2}}\, \Phi(0) \qquad (7)$$

A semi-integral de uma constante [8] tem a seguinte representação:

$$\frac{d^{-1/2}}{dF^{-1/2}}\, C = 2C\sqrt{\frac{x}{\pi}} \qquad (8)$$

No nosso problema a condição inicial é nula, e conseqüentemente a sua semi-integral, utilizando a Equação (8), é nula também. Com isto a Equação (7) reduz-se a seguinte forma:

$$L\{\frac{\partial^{1/2}\Phi}{\partial F^{1/2}}\} = \sqrt{s}\, \bar{\Phi} \qquad (9)$$

Agora, comparando a Equação (6) com a Equação (9) verificamos que se a razão $I_1(\sqrt{s})/I_o(\sqrt{s})$ for igual à unidade, obtemos:

$$L\{\frac{\partial^{1/2}\Phi(1,F)}{\partial F^{1/2}}\} = \frac{\partial\, \bar{\Phi}(1,s)}{\partial z} = L\,\{\frac{\partial\, \Phi(1,F)}{\partial z}\} \qquad (10)$$

ou

$$\frac{\partial \Phi(1,F)}{\partial z} = \frac{\partial^{1/2}\, \Phi(1,F)}{\partial F^{1/2}} \qquad (11)$$

Como desejamos conhecer a temperatura na parede interna do tubo, usamos a condição de contorno 1.c válida para z=1.

$$\frac{\partial^{1/2}\Phi(1,F)}{\partial F^{1/2}} = S[1-\Phi(1,F)] - \frac{(1+b/2R)}{\hat{a}}\, \frac{\partial \Phi(1,F)}{\partial F} \qquad (12)$$

A Equação (12) é uma equação semi-diferencial. Uma maneira de solucioná-la é aplicando transformada de Laplace em ambos os lados da equação, resultando a seguinte expressão para $\bar{\Phi}(1,s)$.

$$\bar{\Phi}(1,s) = \frac{S}{s\left[\sqrt{s} + \Omega s + S\right]} \qquad (13)$$

onde $$\Omega = \frac{(1+b/2R)}{\hat{a}} \qquad (14)$$

A inversão da Equação (13) é feita utilizando uma fórmula [9:pp 173], resultando uma expressão integral para a temperatura adimensional $\Phi(1,F)$.

$$\Phi(1,F) = S \int_0^{F/\Omega} \operatorname{erfc}\left[\frac{a}{2\sqrt{F-\Omega a}}\right] e^{-Sa}\, da \qquad (15)$$

Sendo a uma variável de integração.

A Equação (15) é a expressão analítica para a temperatura adimensional Φ na parede do tubo (z=1) em função do tempo adimensional F.

No caso limite, onde a influência da parede é desprezada no processo de transferência de calor, o termo â, que representa a razão entre as capacidades térmicas do fluido e da parede tende ao infinito. Em [3] encontra-se um critério que determina quanto â deve ser grande para desprezar-se a influência da parede. A solução obtida para o caso geral, Equação (15), pode ser particularizada para este caso tomando-se o limite da Equação (15) com $\hat{a} \to \infty$.

De acordo com a Equação (14), $a \to \infty$ equivale $\Omega \to 0$.

Então:

$$\lim_{\Omega \to 0} S \int_0^{F/\Omega} \operatorname{erfc}\left[\frac{a}{2\sqrt{F-\Omega a}}\right] e^{-Sa}\, da = S \int_0^{\infty} \operatorname{erfc}\left(\frac{a}{2\sqrt{F}}\right) e^{-Sa}\, da \qquad (16)$$

Usando-se equações integrais da função erro complementar presentes em [10], o limite da Equação (16) tem o seguinte final.

$$\Phi(1,F) = 1 - e^{S^2 F}\, \operatorname{erfc}(S\sqrt{F}) \qquad (17)$$

Os resultados expressos pelas Equações (15) e (17) contêm uma restrição quanto ao intervalo de tempo adimensional F onde possam ser aplicados. Esta restrição surge devido termos aproximado $I_1(\sqrt{s})/I_o(\sqrt{s})$ pela unidade. Para que esta aproximação seja verdadeira é necessário que $\sqrt{s} > 8$, este resultado é obtido mediante análise do gráfico destas funções (Fig. 98, pp 373) da referência [10]. Desejamos ter esta restrição em termos do adimensional F, para isto devemos aplicar a inversão de Laplace nesta restrição.

$$s > 64$$

$$s^2 > 64s$$

$$L^{-1}(\frac{1}{s^2}) < L^{-1}(\frac{1}{64s})$$

$$F < \frac{1}{64} \approx 0{,}015 \qquad (18)$$

A restrição dada pela Equação (18) representa o intervalo de validade das Equações (15) e (17).

Os resultados obtidos, expressos nas Equações (15) e (17), são plotados para alguns valores do coeficiente global de transferência de calor adimensional S. Note que para utilizar a Equação (15) precisamos do valor Ω. Para avaliarmos Ω consideramos um caso onde a tubulação seja aço Schedule 40 ($b=7,1\times10^{-3}$ m, $R=7,6\times10^{-2}$ m, $\rho\simeq7800\ \frac{kg}{m^3}$ e $C_p=0,47 kj/kg^oC$) percorrido interiormente por água a $400^oF(204,4^oC$, $\rho=859,4\ \frac{kg}{m^3}$ e $C_p=4,46 kj/kg^oC$). Neste sistema $\hat{a}\simeq10$ e por conseguinte $\Omega\simeq0,1$. Utilizamos este valor para Ω na Equação (15).

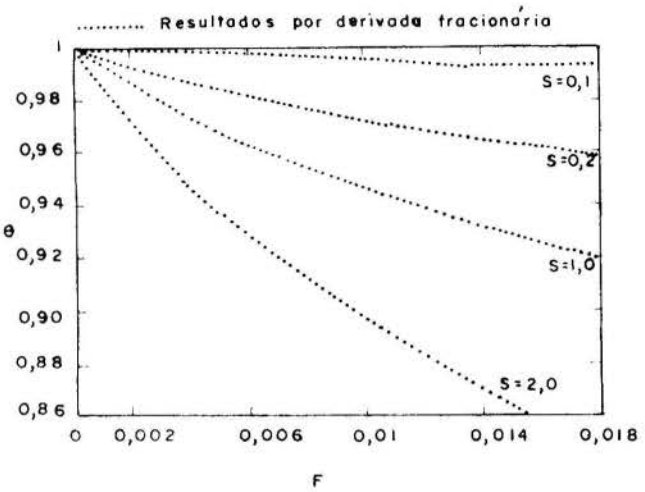

Fig. 1 - Temperatura adimensional ($\theta=1-\phi$) em função do tempo adimensional F levando em consideração a capacidade térmica da parede do tubo ($\Omega=0$)

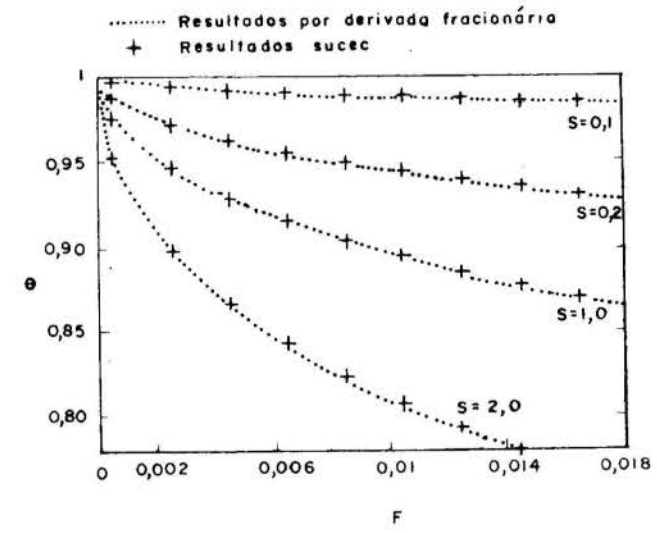

Fig. 2 - Temperatura adimensional ($\theta=1-\phi$) em função do tempo adimensional F sem considerar os efeitos da parede ($\Omega=0$) em comparação com os resultados de Sucec (1988).

CONCLUSÕES

Através do cálculo fracionário chega-se a uma solução analítica do problema de transferência de calor num tubo, onde não foi negligenciada a capacidade térmica da parede do tubo frente à capacidade térmica do fluido, em função do tempo adimensional F. Com o uso deste método não foi necessário a resolução completa do problema para o conhecimento de temperatura na parede interna do tubo. Contudo, a solução apresenta um intervalo limitado para a validade da solução encontrada.

A partir desta solução chega-se ao caso limite onde a parede é negligenciada. Sucec resolve o problema negligenciando a parede e consegue uma solução em série do adimensional F. No nosso trabalho, consegue-se uma solução em forma fechada que coincide com os resultados de Sucec. O que é importante ressaltar é que nem sempre pode-se negligenciar o efeito da parede na transferência de calor, isto se vê claramente no gráfico anterior, e nestes casos temos uma expressão analítica, a Equação (15) para previsões teóricas de temperatura na parede interna do tubo.

REFERÊNCIAS BIBLIOGRÁFICAS

[1] Krishan, B., "On Conjugated Heat Transfer in Fully Developed Flow", Int.J. Heat and Mass Transfer, vol. 25, Nº 2, pp 288-289, 1982.

[2] Chen, S.C., Amand, N.K., Tree, D.R., "Analysis of Transient Laminar Convective Heat Transfer Inside a Circular Duct", ASME Journal of Applied Mechanics, vol. 105, pp 922-924, 1983.

[3] Sucec, J., "Analytical Solution for Unsteady Heat Transfer in a Pipe", ASME Journal of Applied Mechanics, vol. 110, pp 850-856,1988.

[4] Rohsenow, W.M., Hartnett, J.P., "Handbook of Heat Transfer", 1ª edição, New York, McGraw-Hill Company, 1973.

[5] Rosenhead, L., "Laminar Boundary Layer", 1ª edição, New York, Ed. Clarendon Press, 1966.

[6] Slattery, J.C., "Momentun, Energy, and Mass Transfer in Continua", 1ª edição, Tokyo, McGraw-Hill Kogakusha, Ltd., 1972.

[7] Vargas, R.M.F., "Estudo de Temperatura Não Estacionária num Tubo pelo Método do Cálculo Fracionário", Porto Alegre, UFRGS, Programa de Pós-Graduação em Engenharia Mecânica, Dissertação de Mestrado, 1990.

[8] Oldham, K.B., Spanier, J., "The Fractional Calculus", 1ª edição, New York, Academic Press, 1974.

[9] Roberts, C.E., Kaufman, H., "Table of Laplace Transform", 1ª edição, New York, W.B. Saunders Company, 1966.

[10] Abramowitz, M., Stegun, J., "Handbook Mathematical Functions", 1ª edição, New York, Dover Publications INC, 1965.

ABSTRACT

For a heat exchanger under transient condition and slow laminar flow, the pipe inner wall surface temperature was calculated by fractional calculus for a sudden external temperature charge. The thermal wall pipe capacity was taken into account in the model.

III ENCIT – Itapema, SC (Dezembro 1990)

CÁLCULO DE ESCOAMENTOS LAMINARES E TURBULENTOS EM GEOMETRIAS COMPLEXAS USANDO MALHAS NÃO DESFASADAS

MARCELO H. KOBAYASHI e JOSÉ CARLOS F. PEREIRA
Instituto Superior Técnico
Departamento de Engenharia Mecânica
Av. Rovisco Paes - 1096 Lisboa Codex - Portugal

SUMÁRIO

Previsões numéricas de escoamentos laminares e turbulentos são apresentadas usando coordenadas curvilíneas generalizadas e malhas não desfasadas. O método de interpolação e acoplamento Pressão-Velocidade que possibilita o uso de malhas não desfasadas sem oscilações do campo de pressão é revisto e novas alterações são propostas. As modificações introduzidas permitem obter soluções independentes do factor de relaxação assim como uma boa taxa de convergência assegurando conservação de massa em coordenadas fortemente não ortogonais.

INTRODUÇÃO

O método de diferenças finitas/volume finito conjuntamente com o uso de malhas não ortogonais tem sido usado por vários autores para a previsão de escoamento de fluidos em geometrias arbitrárias, [1]-[3]. O uso de malhas não desfasadas reduz fortemente a complexidade geométrica e algébrica dos cálculos, em especial em escoamentos tridimensionais [4]. As principais vantagens do uso de malhas não desfasadas são: i) permitir localizar todas as variáveis dependentes no centro geométrico de cada Volume de Controle e ii) usar componentes cartesianas do vector velocidade em vez das suas componentes covariantes ou contravariantes, [5]-[7].

O uso de malhas não desfasadas é recente e desde [8] vários problemas tem sido detectados, entre eles a influência do factor de relaxação nas soluções numéricas, [9] e [10]. Quando combinadas com a não ortogonalidade da malha podem induzir problemas de conservação de massa, [11], se não houver cuidados especiais no acoplamento Pressão-Velocidade.

O objectivo deste trabalho consiste em apresentar um algoritmo de cálculo cujos modelos numéricos permitem evitar os dois problemas acima mencionados. Várias soluções numéricas de problemas teste são apresentadas neste trabalho. Os casos teste consistem em problemas cuja solução analítica é conhecido e em escoamentos laminares e turbulentos onde existem medidas experimentais.

EQUAÇÕES FUNDAMENTAIS

As equações que regem o escoamento de um fluido e o transporte de um escalar ϕ podem ser escritas em notação vectorial da seguinte forma:

$$\frac{\partial \rho}{\partial t} + \nabla.(\rho \mathbf{v}) = 0 \tag{1}$$

$$\frac{\partial \rho \mathbf{v}}{\partial t} + (\mathbf{v}.\nabla)\mathbf{v} = \nabla.\mathbf{T} + \mathbf{S}_v \tag{2}$$

$$\frac{\partial \rho \phi}{\partial t} + \nabla.(\rho \mathbf{v}\phi - \mathbf{q}) = S_\phi \tag{3}$$

onde ρ é a densidade do fluido, $\mathbf{v}$ o vector velocidade, $\mathbf{S}_v$ e S_ϕ o vector fonte de momentum e fonte de ϕ, respectivamente, t é o tempo, $\mathbf{T}$ o tensor tensões, ϕ o escalar transportado (temperatura, energia cinéctica, etc.) e $\mathbf{q}$ o vector fluxo difusivo de ϕ. Para o escoamento de um fluido Newtoniano $\mathbf{T}$ relaciona-se com o campo de velocidade e pressão através da seguinte equação constitutiva:

$$\mathbf{T} = -\left(p + \frac{2}{3}\mu \nabla.\mathbf{v}\right)\mathbf{I} + 2\mu \mathbf{D} \tag{4}$$

onde p é a pressão estática, μ a viscosidade dinâmica do fluido, $\mathbf{I}$ o tensor unitário de segunda ordem e $\mathbf{D}$ a taxa de deformação do fluido igual à parte simétrica do tensor gradiente de velocidade, em símbolos:

$$\mathbf{D} = \frac{1}{2}\left[\nabla \mathbf{v} + (\nabla \mathbf{v})^T\right] \tag{5}$$

onde o superscripto T denota o transposto de um tensor. O vector fluxo difusivo $\mathbf{q}$ relaciona-se com o escalar ϕ através de uma equação do tipo Lei de Fick como a seguir:

$$\mathbf{q} = \Gamma \nabla \phi \tag{6}$$

onde Γ representa a difusividade de ϕ.

COORDENADAS CURVILINEAS NÃO-ORTOGONAIS

Adoptou-se o sistema cartesiano como base vectorial para as grandezas vectoriais e tensoriais. A forma compacta das equações fundamentais, eq's (1)-(3) para um escoamento estacionário de um fluido Newtoniano e incompressível, em coordenadas curvilíneas generalizadas x^i vêm expressas na forma das eq's (7)-(9) em termos das suas componentes cartesianas:

$$\frac{1}{\sqrt{g}}\frac{\partial}{\partial x_j}\left[\sqrt{g}\left(\rho u_k \alpha^{kj}\right)\right] = 0 \tag{7}$$

$$\frac{1}{\sqrt{g}}\frac{\partial}{\partial x_j}\left[\sqrt{g}\left(\rho u_k u_i - T_{ki}\right)\alpha^{kj}\right] = S_i \tag{8}$$

$$\frac{1}{\sqrt{g}}\frac{\partial}{\partial x_j}\left[\sqrt{g}\left(\rho u_k \phi - q_k\right)\alpha^{kj}\right] = S_\phi \tag{9}$$

onde u_i é a componente cartesiana do vector velocidade, g é o determinante do tensor da métrica, $g = J^2$, J é o jacobiano da transformação $y^i = y^i(x^j)$ e α^{kj} a matriz transformação $\mathbf{i}^k = \alpha^{kj}\,\mathbf{e}_j$, onde $\mathbf{i}^k$ é o vector unitário na direcção y^k e $\mathbf{e}_j$ o vector base natural na direcção x^j.

O tensor tensões e o vector fluxo nestas condições escrevem-se:

$$T_{ki} = -p\delta_{ki} + 2\mu D_{ki} = -p\delta_{ki} + \mu\left(\frac{\partial u_i}{\partial x^l}\alpha_k^{\ l} + \frac{\partial u_k}{\partial x^l}\alpha_i^{\ l}\right) \tag{10}$$

$$q_i = \Gamma \frac{\partial \phi}{\partial x^l}\alpha_i^{\ l} \tag{11}$$

onde δ_{ij} é o delta de Kronecker (igual a 1 se $i = j$ e 0 se $i \neq j$) e $\alpha_j^{\ i} = \delta_{ij}\alpha^{ll}$.

DISCRETIZAÇÃO DAS EQUAÇÕES FUNDAMENTAIS

No intuito de obter-se equações em Diferenças Finitas a partir da eq.(9) utilizou-se o método das Diferenças Finitas/Volume Finito aplicados a coordenadas curvilíneas

generalizadas usando malhas não-desfasadas, ou seja todas as variáveis estão localizadas no centro geométrico de cada V.C. (ver Fig.(1)).

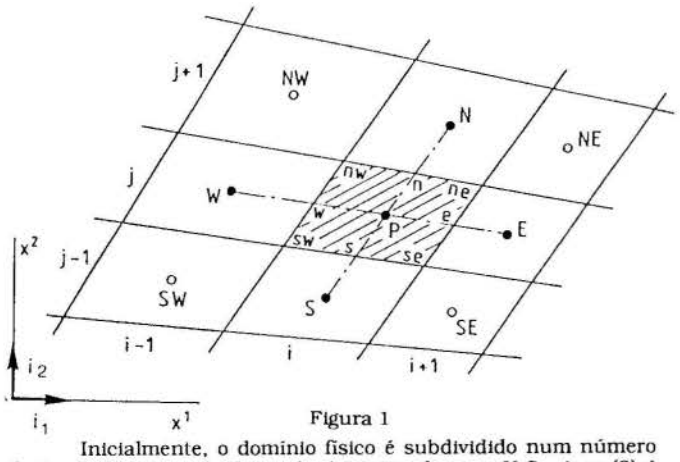

Figura 1

Inicialmente, o domínio físico é subdividido num número finito de Volumes de Controle denominados por V.C.. A eq.(9) é integrada sobre cada V.C., que para o caso bidimensional, aplicando o teorema de Gauss e tomando o valor médio do fluxo total sobre as faces conduz à seguinte equação integral:

$$J_1 \Big|_w^e + J_2 \Big|_s^n = \bar{S}_\phi \tag{12}$$

onde J_i representa o fluxo total do escalar ϕ que atravessa uma face do V.C. normal à coordenada x^i constante, e $\bar{S}_\phi$ representa o termo de fonte S_ϕ integrado e linearizado como:

$$\bar{S}_\phi = S_c + S_p \phi_p \tag{13}$$

O fluxo total J_i consiste de duas contribuições distintas: uma J_i^C devido à convecção e outra J_i^D devido à difusão. O termo difusivo é aproximado aplicando-se diferenças centrais às suas derivadas parciais o que resulta na seguinte expressão, por exemplo, para a face "este" do V.C.:

$$J_e^D = -\left(\frac{\Gamma}{\delta Vol}\right)_e D_{1e}^1 \left(\phi_E - \phi_P\right) - \left(\frac{\Gamma}{\delta Vol}\right)_e D_{2e}^1 \left(\phi_n - \phi_s\right)_e \tag{14}$$

onde δVol é o volume do V.C. e D_i^j é definido como:

$$\begin{aligned} D_1^1 &= \left(b_1^1\right)^2 + \left(b_2^1\right)^2 \\ D_2^1 &= D_1^2 = b_1^2 b_1^1 + b_2^2 b_2^1 \\ D_2^2 &= \left(b_1^2\right)^2 + \left(b_2^2\right)^2 \end{aligned} \tag{15}$$

e b_i^j é o correspondente em Diferenças Finitas ao cofactor β_i^j da transformação $y^i = y^i(xj)$.

O último termo da eq.(14) é resultante da não-ortogonalidade da malha, e é calculado por interpolação linear de $\delta\phi|_s^n$ avaliados em nós adjacentes. Neste trabalho optou-se pelo cálculo explícito do mesmo, isto é, a partir dos valores prévios de ϕ, por razões de simplicidade e, tendo em conta que tal procedimento não reduz a ordem do esquema, mas somente afecta a sua taxa de convergência.

Para a discretização do termo convectivo, também por simplicidade e robustez, utilizou-se o esquema Híbrido Central/"Upwind". Este método dá origem à seguinte equação, por exemplo, para a face 'este' do V.C.:

$$J_e^C = F_{1e} \phi_e \tag{16}$$

onde F_{1e} é definido como:

$$F_{1e} = \rho_e \left(u_1 b_1^1 + u_2 b_2^1\right)_e \tag{17}$$

e:

$$\phi_e = \left(\frac{u_{1e} + |u_{1e}|}{2|u_{1e}|}\right)\phi_P - \left(\frac{u_{1e} - |u_{1e}|}{2|u_{1e}|}\right)\phi_E \quad se\ |P_e| > 2 \tag{18}$$

$$\phi_e = \frac{\phi_P + \phi_E}{2} \qquad se\ |P_e| \le 2 \tag{19}$$

Aqui o número de Péclet é definido como se segue:

$$P_e = \frac{F_{1e}}{D_e} \tag{20}$$

e,

$$D_e = \frac{\Gamma_e}{(\delta Vol)_e} D_{1e}^1 \tag{21}$$

De forma similar pode-se calcular J_i para as outras faces do V.C..

A forma final das equações discretizadas a serem resolvidas é então obtida introduzindo-se equações do tipo eq.(14) e eq.(16) na eq.(12), tendo em conta as eq.(15), eq.(17)-(21), o que resulta na seguinte equação algébrica em ϕ:

$$a_p \phi_p = \sum a_{nb} \phi_{nb} + S \tag{22}$$

onde os coeficientes "a's" representam as contribuições convectivas e difusivas nas suas formas linearizadas dos pontos nodais, e S contém todos os termos que não são calculados a partir dos valores nodais de ϕ (eg. termos de fonte, valores conhecidos, o gradiente de pressão na equação de momentum, etc.)

ACOPLAMENTO PRESSÃO-VELOCIDADE

Para o cálculo do campo de pressões (o qual não possui uma equação diferencial explícita a ser discretizada) utilizou-se uma versão modificada do algoritmo SIMPLE, que será chamada SIMPLES a qual é ligeiramente diferente daquele proposto por [8]. Este último representou uma extensão para o seu uso em malhas não-desfasadas do "Semi Implicit Method for Pressure Linked Equations" proposto por [12] originalmente para malhas desfasadas. Neste trabalho, o algoritmo SIMPLES é introduzido de maneira a garantir soluções independentes do factor de relaxação utilizado nas equações de momentum e assegurar conservação de massa.

As equações linearizadas de momentum são reescritas em uma forma mais conveniente para manipulações futuras, como se segue:

$$u_{ip} = H_p(u_{in}) + \left(Q_i^1 \delta^1 p + Q_i^2 \delta^2 p\right)_p + S_i^p + (1 - \alpha)\, u_{ip}^n \tag{23}$$

onde o operador $H_p(u_{in})$ e Q_i^j são definidos como:

$$H_p(u_{in}) = \sum_n \frac{a_{in} u_{in}}{a_p^{ui}} \tag{24}$$

$$Q_i^j = -\frac{b_i^j}{a_p^{ui}} \tag{25}$$

onde a_p^{ui} representa o coeficiente de u_{ip}, S_i^p é o termo de fonte e $\delta^i p$ a diferença de pressão na direção x^i calculada por diferenças centrais 2 - δ.

O algoritmo SIMPLES é um método de solução do tipo Predictor/Corrector. O passo predictor consiste da solução da equação linearizada de momentum (eq.(23)) utilizando-se o campo de pressão da iteração anterior p^n (o superscrito denota o valor de um campo após a n-ésima iteração). O campo de velocidades resultante, indicado por u_i^*, é calculado como se segue:

$$u_{ip}^* = H_p(u_{in}^*) + \left(Q_i^1 \delta^1 p^n + Q_i^2 \delta^2 p^n\right)_p + S_i^p + (1 - \alpha)\, u_{ip}^n \tag{26}$$

Esse campo de velocidades não satisfaz, em geral, a restrição de continuidade, e portanto, é necessário corrigi-lo de maneira a que satisfaça simultaneamente as equações de momentum e continuidade.

Inicialmente a equação de continuidade é integrada, resultando na seguinte equação para o balanço de massa:

$$F_{1e} - F_{1w} + F_{2n} - F_{2s} = 0 \tag{27}$$

Quando se utilizam malhas desfasadas do tipo MAC [13], as células das velocidades estão deslocadas em relação aos outros escalares situando-se as velocidades nas faces dos V.C.'s destes últimos e, portanto F_i pode ser calculado directamente. Por outro lado, quando se utilizam malhas não desfasadas o fluxo F_i nas faces dos V.C.'s devem ser interpolados, e no caso de malhas não ortogonais e componentes cartesianas, as duas componentes (2-D)

de velocidade são requeridas nas faces dos V.C.'s (ver eq.(17)).

O cálculo destas componentes nas faces dos V.C.'s é crucial para o sucesso do método pois deve manter a ordem das aproximações, assegurar conservação de massa e evitar o desacoplamento pressão-velocidade. A forma correcta de derivar o passo corrector é obtida das equações de continuidade e momentum como indicado a seguir.

As componentes de velocidade u_{ic} nas faces dos V.C.'s são calculadas através da equação discretizada de momentum avaliada na face c(=e,w,n,s) do V.C., em símbolos:

$$u_{ic} = \overline{H_c(u_{ic})} + \left(Q_i^1 \delta^1 p\right)_c + \overline{S_i^C} + (1-\alpha)\, u_{ic}^n \qquad (28)$$

onde a barra sobreposta indica uma interpolação linear entre valores de nós adjacentes. Nessa equação, o gradiente de pressão é calculado por diferenças centrais 1- δ e o último termo é calculado directamente, isto é, sem interpolação linear dos valores anteriores, este método é denominado PWIMC, em contraste com aquele proposto por [8] no qual o último termo é interpolado linearmente, este último é denominado PWIMU.

Calculada desta maneira a ordem do método é mantida (interpolação linear de 2ª ordem), o acoplamento entre os campos de pressão e velocidade é assegurado (diferenças centrais 1- δ para o cálculo de $\delta^i p$) e finalmente o balanço de massa é garantido visto que nenhum termo é desprezado na equação de momentum.

O campo de velocidade é então calculado como se segue:

$$u_{ip}^{**} = H_p\left(u_{in}^{*}\right) + \left(Q_i^1 \delta^1 p^{*} + Q_i^2 \delta^2 p^{*}\right) + S_i^p + (1-\alpha)\, u_{ip}^n \qquad (29)$$

onde u_{ip}^{**} e p^{*} são os campos corrigidos de velocidade e pressão, respectivamente.

A subtração da eq.(26) da eq.(29) resulta na seguinte equação incremental para o campo de velocidades:

$$u_{ip}^{**} = u_{ip}^{*} + \left(Q_i^1 \delta^1 p' + Q_i^2 \delta^2 p'\right)_p \qquad (30)$$

de forma similar para as faces:

$$u_{ic}^{**} = u_{ic}^{*} + \left(Q_i^1 \delta^1 p' + Q_i^2 \delta^2 p'\right)_c \qquad (31)$$

onde o gradiente de pressão é calculado por diferenças centrais 2- δ na eq.(30) e 1- δ na eq.(31); p' (correção de pressão) é definido como:

$$p' = p^{*} - p^n \qquad (32)$$

A substituição da eq.(31) na equação de F_{ic} e deste na equação de continuidade dá origem à seguinte equação implícita em p':

$$a_P p' = \sum_{nb} a_{nb} p'_{nb} + S_m \qquad (33)$$

onde nb = W,E,N,S ;

$$S_m = F_{1e}^{*} - F_{1w}^{*} + F_{2n}^{*} - F_{2s}^{*}$$

e

$$F_{ic}^{*} = \rho_c\left(u_1^{*} b_1^i + u_2^{*} b_2^i\right)_c \qquad (34)$$

Após a solução deste sistema de equações obtem-se p' a partir do qual corrige-se os campos de velocidade e pressão através das eq.(30) aeq.(32). Escrita desta forma a equação de correcção de pressão envolve a valor de p' em nove pontos nodais vizinhos, e requer, portanto, algoritmos de solução para sistemas de equações cuja matriz de coeficientes é nona-diagonal e uma maior alocação de memória. Entretanto, quando a não-ortogonalidade das malhas não é muito severa, a contribuição devido as derivadas cruzadas na equação de correcção de pressão é pequena se comparada às derivadas na direcção do escoamento. Tendo isto em mente, aqueles termos relacionados às derivadas cruzadas na equação de correção de pressão são desprezados resultando num sistema de equações mais simples, penta-diagonal. Este procedimento não afecta a precisão do método e, em adição, melhora suas propriedades de convergência, facilita a implementação de condições de fronteira e por fim, permite o uso do mesmo algoritmo de solução de sistemas de equações tanto para a equação de correção de pressão como para as outras equações (eg. momentum e outros escalares).

Em resumo o algoritmo SIMPLES consiste dos seguintes passos:

1. Estima-se o campo de velocidades e pressões;
2. Calcula-se os coeficientes da equação de momentum e resolve-a obtendo-se o novo campo de velocidades;
3. Calcula-se os novos valores dos fluxos de massa F_{ic} utilizando-se equações do tipo, eq.(17) e eq.(28);
4. Calcula-se os coeficientes da equação de correção de pressão e resolve-a obtendo-se o campo de correção de pressão;
5. Corrige-se os campos de velocidade, pressão e fluxos com este campo de correção de pressão através das eq.(30) a eq.(32) (relaxada para acelerar a convergência);
6. Resolve-se as equações discretizadas de outros escalares, eg. k, ε e temperatura.
7. Repete-se este ciclo até alcançar o critério de convergência.

MODELO DE TURBULÊNCIA

Para o cálculo de escoamentos turbulentos utilizou-se o modelo k-ε de viscosidade turbilhonar. As tensões de Reynolds e os fluxos turbulentos são modelados usando a viscosidade e difusividade turbilhonar:

$$\overline{\rho u_m' u_i'} = \mu_t \left(\frac{\partial \bar{u}_i}{\partial x}^n \alpha_m + \frac{\partial \bar{u}_m}{\partial x}^n \alpha_i \right) - \frac{2}{3} k \delta_{mi} \qquad (35)$$

em que μ_t e Γ_ϕ^t são obtidos por:

$$\mu_t = C_\mu \rho \frac{k^2}{\varepsilon}^n \alpha_m \qquad (36)$$

$$\Gamma_\phi^t = \frac{\mu^t}{\mu_\phi} \qquad (37)$$

onde k e ε representam a energia cinética turbulenta e sua taxa de dissipação, C_μ é uma constante empírica.

A tabela 1 lista os valores de ϕ, Γ e S_ϕ para as equações de k e ε. Nesta tabela, G representa a taxa de produção de energia cinética turbulenta, definida como:

$$G = \mu_t \left(\frac{\partial \bar{u}_i}{\partial x}^n \alpha_j + \frac{\partial \bar{u}_j}{\partial x}^m \alpha_i \right) \left(\frac{\partial \bar{u}_i}{\partial x}^n \alpha_j \right) \qquad (38)$$

Tabela 1

ϕ	Γ	S_ϕ
k	$\frac{\mu_t}{\sigma_k}$	$G - \rho\varepsilon$
ε	$\frac{\mu_t}{\sigma_e}$	$C1 \frac{\varepsilon}{k} G - C^2 \rho \frac{\varepsilon^2}{k}$

Foram utilizados os valores *standard* das constantes empíricas (C_μ, C_1, C_2, σ_k e σ_ε) sugeridos por [14]. A Tabela 2 indica os valores das constantes.

Tabela 2

C_μ	C_1	C_2	σ_k	σ_ε
0.09	1.44	1.92	1.0	1.3

RESULTADOS

Cálculo de Escoamentos Laminares É fundamental para teste de algoritmos ou esquemas numéricos já que não existem erros inerentes à modelação da turbulência. Neste trabalho são apresentados cálculos de escoamentos laminares em geometria complexa no intuito de: i)estudar a influência do coeficiente de relaxação nas equações de momentum em malhas não desfasadas não ortogonais e ii)testar o algoritmo de cálculo, usando malhas curvilíneas não ortogonais, quanto a sua robustez, eficiência e precisão.

Dependência da Solução no Coeficiente de Relaxação. O primeiro teste corresponde ao problema proposto por [15], do cálculo de escoamento numa cavidade submetida a um campo de forças, para o qual foi derivada uma solução analítica (ver detalhes na referência citada). Foram efetuados diversos cálculos usando diferentes malhas e vários números de Reynolds. A Fig. 2 apresenta uma malha não-ortogonal de 16x10 V.C.'s, usada para testar a robustez do método. A Tabela 3 lista o erro máximo absoluto para as duas componentes de velocidade e pressão função do coeficiente de relaxação $\alpha = \alpha_{u1} = \alpha_{u2}$. Os resultados mostram que neste caso o esquema PWIMU é insensível ao uso de diferentes valores de α, sendo os erros máximos das soluções numéricas em relação à

solução analítica idênticas para os esquemas PWIMU e PWIMC. Este facto é atribuido à variação suave do gradiente de pressão.

Tabela 3

ERRO MÁXIMO ABSOLUTO			
$\alpha =$	U_1	U_2	P
0.1	2.32	4.13	2.53
0.5	3.51	4.52	2.63
0.6	3.79	4.81	2.65
0.7	4.02	5.06	2.67
0.8	4.20	5.27	2.69
0.9	4.35	5.46	2.71
1.0	4.47	5.62	2.73

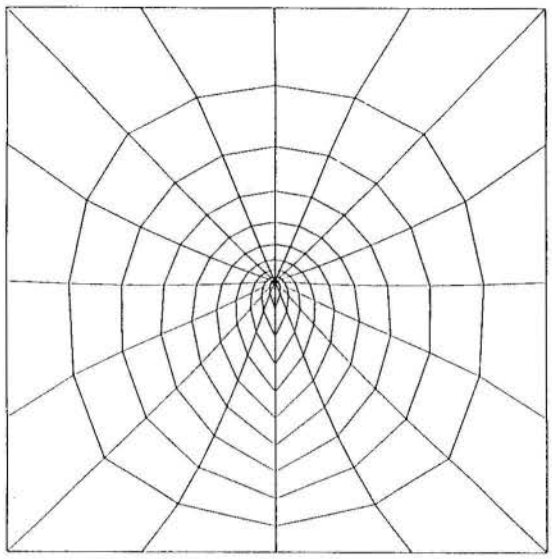

Figura 2

O segundo teste corresponde ao escoamento laminar através de uma contracção súbita em um tubo. Medidas experimentais de velocidade podem ser encontradas em [16]. Utilizou-se um número de Reynolds, baseado nas condições de entrada igual a 196 e um perfil parabólico de velocidades à entrada. A Fig. (3) mostra uma malha não-ortogonal típica, contendo 80x52 V.C.'s. A Tabela 4 lista os resultados obtidos para α = 0,1; 0,5; 0,8 e 1,0; (numa coordenada Y^1/D = 0,03952), função de um parâmetro de erro definido por $\eta = \frac{u_{1\alpha=1} - u_{1\alpha}}{u_{ref}} \times 100$. A última coluna lista os valores da componente axial obtida para α = 1, os quais são iguais aos resultados obtidos com o esquema PWIMC. O valor Y^1/D escolhido situa-se numa proximidade à jusante da contracção, em uma região de rápida variação do gradiente de pressão. Os resultados obtidos com PWIMU mostram uma forte dependência no coeficiente de relaxação, com o erro aumentando com a diminuição de α (η = 60% para α = 0,1). É evidente a partir dos resultados que o esquema PWIMC deve ser usado em detrimento ao esquema PWIMU.

O mesmo escoamento é utilizado para comparação entre resultados obtidos numa malha cilíndrica plana axissimétrica e outra curvilínea não-ortogonal. As Fig's (4a,c) apresentam as previsões numéricas e as medidas experimentais da componente axial de velocidade.

A comparação mostra que os resultados obtidos utilizando-se uma malha não-ortogonal, com o mesmo número de V.C.'s da malha ortogonal, estão em melhor concordância com as medidas experimentais. A este facto atribuiu-se o melhor alinhamento das linhas da malha com as linhas de corrente do escoamento, ver Fig's.(3-5). Nestas condições a falsa difusão induzida pelo esquema "Upwind" de 1ª ordem usado na discretização do termo convectivo é muito menor que no caso da malha cilíndrica axissimétrica.

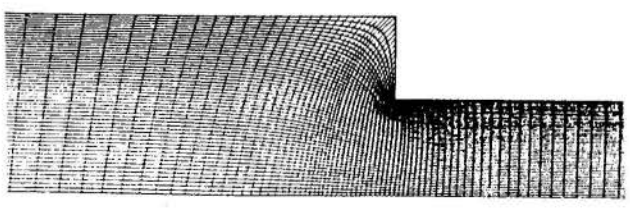

Figura 3 Malha

Tabela 4

Y^2	α = 0.1 η	α = 0.5 η	α = 0.8 η	α = 1 U_α = 1
0	-4.12	-1.45	-0.52	4.1090
1.805E-2	-4.10	-1.46	-0.52	4.1070
5.233E-2	-3.78	-1.35	-0.49	4.0940
8.293E-1	-4.07	-1.44	-0.51	4.0830
1.101E-1	-3.92	-1.45	-0.52	4.0750
1.342E-1	-3.85	-1.46	-0.50	4.0740
1-553E-1	-3.49	-1.42	-0.53	4.0850
1.739E-1	-2.20	-1.31	-0.51	4.1070
1.902E-1	-1.89	-1.05	-0.45	4.1360
2.043E-1	0.07	-0.50	-0.30	4.1490
2.166E-1	4.49	-0.09	-0.09	4.0930
2.273E-1	13.92	3.80	1.02	3.8760
2.366E-1	29.87	9.43	2.85	3.4120
2.447E-1	49.63	16.83	5.36	2.6970
2.520E-1	60.44	22.25	7.30	1.8290
2.584E-1	55.85	21.50	7.20	0.9540
2.642E-1	28.76	9.56	3.83	0.2375

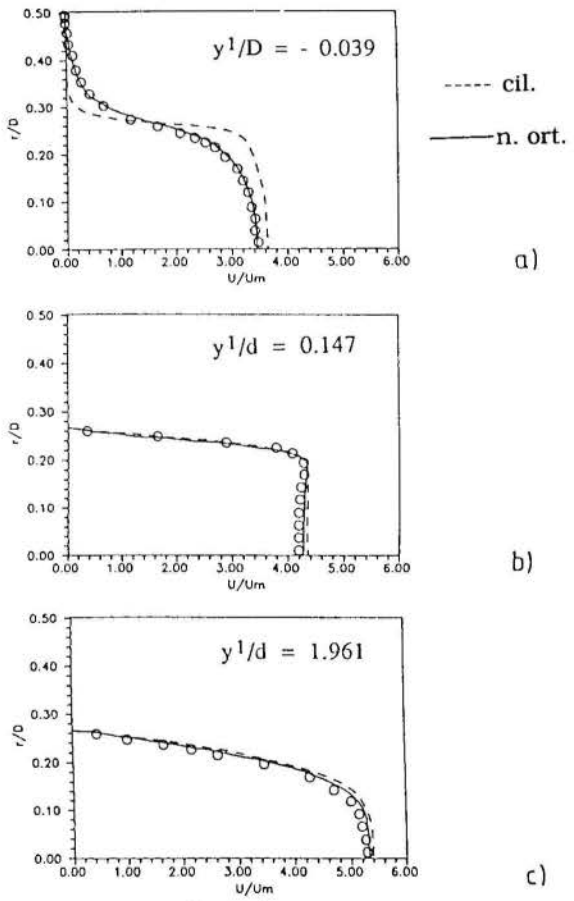

Figura 4

A taxa de convergência dos resíduos das equações de continuidade e momentum é apresentada na Fig.(6). Os resíduos das várias quantidades obtidas usando o algoritmo SIMPLES diminui sempre com o número de iterações até o critério de convergência, quando a soma dos valores normalizados e absolutos do resíduo em todos os pontos do domínio for menor ou igual a 10^{-3}. Nenhuma massa residual foi obsevada, como apontado por [11].

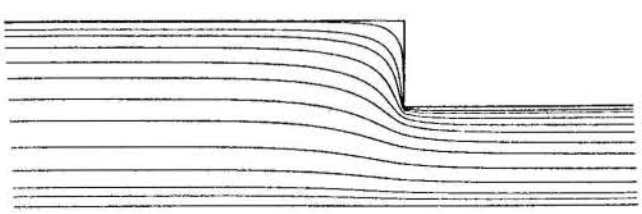

Figura 5 Linhas de Corrente

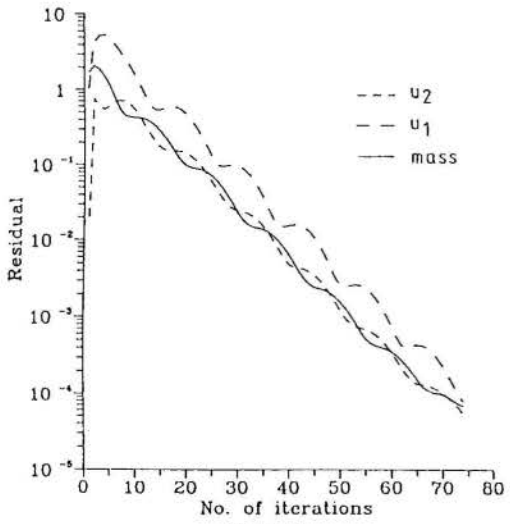

Figura 6

VÁLVULA PROSTÉTICA

O escoamento de sangue em torno de uma válvula prostética tipo esférica é considerado. O sangue é assumido Newtoniano e o escoamento axissimétrico. A geometria e as condições de fronteiras estão representadas na Fig. (7).

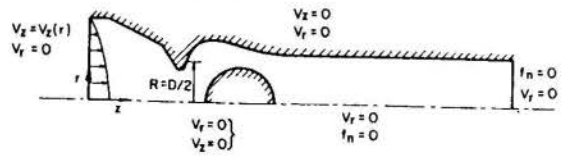

Figura 7

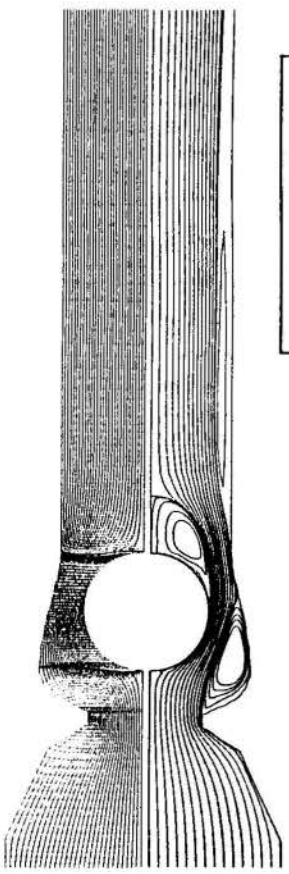

a	-467
b	-100
c	-10
d	0
e	10
f	100
g	400

Figura 8

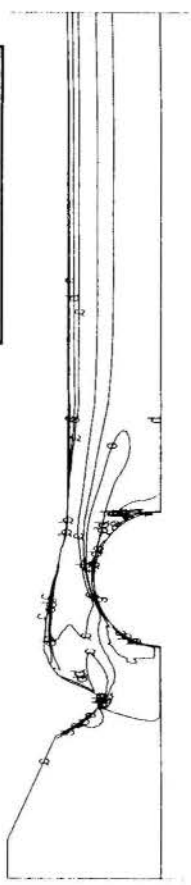

Figura 9

Figura 10

A entrada assumiu-se um escoamento totalmente desenvolvido (perfil parabólico), nas paredes e na esfera adoptou-se condições de não escorregamento, e gradiente nulo para as velocidades à saída. O número de Reynolds baseado no diametro, D (da artéria sem a presença da válvula) e na velocidade média é igual a 6000 (este valor é típico do escoamento em artérias).

A Fig.(8) apresenta as linhas de corrente previstas para uma malha contendo 160x30 V.C's., Fig. (9). Os resultados mostram três zonas de recirculação, uma separada no anel de costura, outra atrás da esfera e a terceira na parede da artéria oposta à valvula. Estas zonas de baixa velocidade favorecem a formação de trombus, que pode dar origem a trombose ou bloquear a válvula.

A Fig.(10) apresenta iso-linhas de tensão de corte. Duas zonas, de elevada tensão de corte são aparentes, uma na região inferior do anel de costura e outra sobre a esfera. O valor máximo de tensão de corte encontrado foi τ_{12}=483 din/cm^2 (4830 N/m^2), o qual pode causar danos às paredes da artéria e às particulas agarradas às mesmas ou à esfera, tendo em conta efeitos não-estacionários. Esses problemas, nomeadamente, a trombose e danos às paredes da artéria e hemácias têm sido observados em pacientes transplantados, [17].

CANAL DIVERGENTE

O último caso considerado é o escoamento de água em regime turbulento num canal divergente com as seguintes geometria, Fig. (11), e condições de fronteira: i)valores medidos de velocidade e fluctuação à entrada, condição de não escorregamento e Lei da Parede à superfície sólida, simetria na linha central e gradiente nulo à saída.

As Fig's.(12a,b) mostram perfis da velocidade axial a jusante $1D_1$e $10D_1$, do difusor, respectivamente. O segundo perfil $10D_1$ está em excelente concordância com os resultados experimentais. Por outro lado, a $1D_1$, o perfil previsto é mais "cheio" que aquele medido experimentalmente. Este resultado, tal como sugerido por [18], deriva de insuficiências do modelo k-ε de viscosidade turbilhonar. Não obstante, o perfil apresentado está em boa concordância com previções numéricas semelhantes obtidas por outros autores, [19].

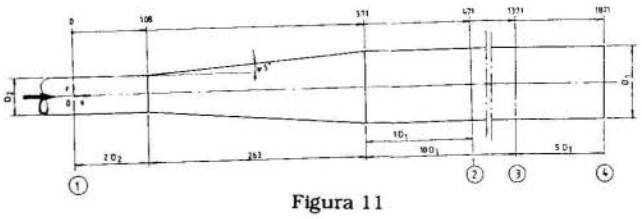

Figura 11

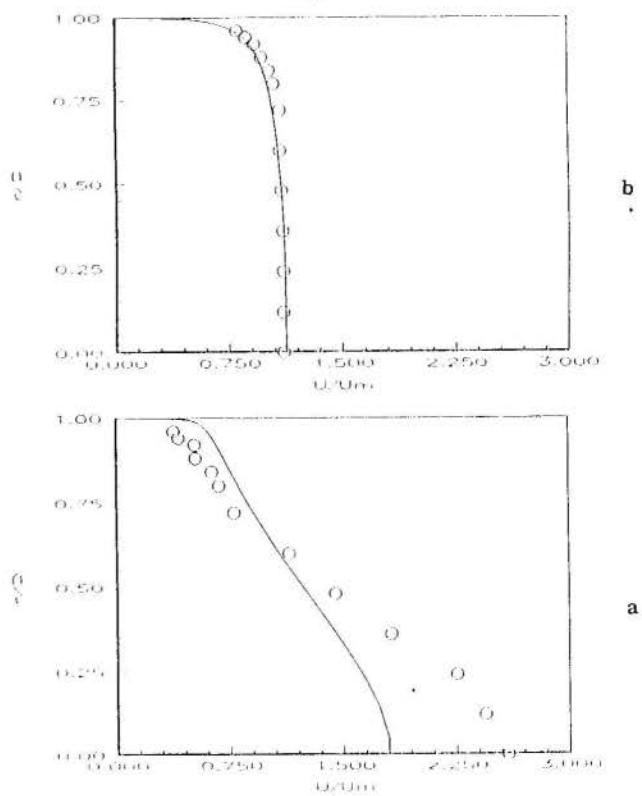

Figura 12

CONCLUSÕES

O algoritmo SIMPLES conjuntamente com dois métodos de acoplamento PWIMC e PWIMU foi aplicado a uma variedade de escoamentos. A comparação das soluções numéricas com soluções analíticas ou medidas experimentais permite inferir as seguintes conclusões:

1. O esquema SIMPLES assegura conservação de massa, boa taxa de convergência e suprime qualquer oscilação no campo de pressão.
2. O método PWIMC deve ser usado para evitar soluções que sejam dependentes do coeficiente de relaxação utilizado nas equações de momentum.
3. O algoritmo apresentado neste trabalho é recomendado para o cálculo do escoamento laminar ou turbulento, com ou sem transferência de calor em geomentrias complexas, sendo as suas principais características, simplicidade, boas propriedades de convergência e capacidade de evitar o desacoplamento pressão-velocidade.

REFERÊNCIAS

[1] Maliska, C.R. and Raithby, G.D., "A Method for Computing Three Dimentional Flows Using Non-Orthogonal Boundary-Fitted Co-Ordinates", International Journal for Numerical Methods in Fluids, Vol. 4, pp. 519-537, 1984.

[2] Demirdzic, I. Gosman, A.D., Issa, R.I. and Perić, M., "A Calculation Procedure for Turbulent Flow in Complex Geometries", Computers & Fluids, Vol. 15, nº 3, pp. 251-273, 1987.

[3] Karki, K.C and Patankar, S.V., "Solution of Some Two-Dimensional Incompressible Flow Problems Using a Curvilinear C oordinate System Based Calculation Procedure", Numerical Heat Transfer, Vol. 14, pp. 309-321, 1988.

[4] Coelho, P. and Pereira, J.C.F., "Calculation Procedure for 3D Laminar Flows in Complex Geometries Using a Non-Staggered Non-Orthogonal Grid System", Submited to Computers & Fluids.

[5] Perić, M., Kessler, R. and Scheuerer, G., "Comparison of Finite-Volume Numerical Methods with Staggered and Colocated Grids", Computers & Fluids, Vol. 16, pp. 389-403, 1988.

[6] Lapworth, B.L., "Examination of Pressure Oscilation Arising in the Computation of Cascade Flow Using a Boundary Fitted Co-Ordinate System", International Journal for Numerical Methods in Fluids, Vol. 8, pp. 387-404, 1988.

[7] Kobayashi, M.H. and Pereira, J.C.F., "Calculation of Incompressible Laminar Flows on Non-Staggered Non-Orthogonal Grids", Submited to Numerical Heat Transfer.

[8] Rhie, C.M. and Chow, W.L., "Numerical Study of the Turbulent Flow Past an Airfoil with Trailing Edge Separation", AIAA Journal, Vol. 21, pp. 1525-1532, 1983.

[9] Majumdar, M., "Role of Underrelaxation in Momentum Interpolation for Calculation of Flow with Non-Staggered Grids", Numerical Heat Transfer, Vol. 13, pp. 125-132, 1988.

[10] Kobayashi, M.H. and Pereira, J.C.F., "Numerical Comparison of Momentum Interpolation Methods and Pressure-Velocity Algorithms Using Non-Staggered Grids", To Be Published in Comunications in Applied Numerical Methods.

[11] Acharya, S. and Moukalled, F.H., "Improvements to Incompressible Flow Calculation on a Non-Staggered Curvilinear Grid", Numerical Heat Transfer, Part B, Vol. 15, pp. 131-152, 1989.

[12] Patankar, S.V. and Spalding, D.B., "A Calculation Procedure for Heat, Mass and Momentum Transfer in Three-Dimentional Parabolic Flows", International Journal of Heat and Mass Transfer, Vol. 15, pp. 1787-1806, 1972.

[13] Harlow, F.H. and Welch, J.E., "Numerical Calculation of Time-Dependent Viscous Incompressible Flow", Physics of Fluids, vol. 8, pp. 2182, 1965.

[14] Launder, B.E. and Spalding, D.B., "The Numerical Computation of Turbulent Flows", Computational Methods in Applied Mechanical Engineering, Vol. 3, pp. 269-289, 1974.

[15] Shih, T.M., Tan, C.H. and Hwang, B.C., "Effects of Grid Staggering on Numerical Schemes", International Journal for Numerical Methods in Fluids, Vol. 9, pp. 193-212, 1989.

[16] Durst, F. and Loy, T., "Investigations of Laminar Flow in a Pipe with Sudden Contraction of Cross Sectional Area", Computers & Fluids, Vol. 13, Nº 1, pp. 15-36 1986.

[17] Figliola, R.S. and Mueller, T.J., "On the Hemolytic and Thrombogenetic Potential of Occluder Prosthetic Heart Valves from *in vitro* Measurements", ASME Journal of Biomechanical Engineering, Vol. 103, pp. 83-90, 1981.

[18] Rodi, W. and Scheuerer, G., "Scrutinizing the k-ε Turbulence Model Under Adverse Pressure Gradient Conditions", ASME Journal of Fluids Engineering, Vol. 108, pp. 174-179, 1986.

[19] Durão, D.F.G. and Pereira, J.C.F., "Intercomparison of Flow Measurements and Computations: Computational Analysis", Final Report , IST, Lisbon-Portugal, 1989.

ABSTRACT

Numerical predictions of laminar and turbulent flows using general curvilinear coordinates and non-staggered grids are presented. The interpolation method and pressure velocity that allow the use of non-staggered grids is reviewed and some modifications are suggested. The proposed modifications yield solutions that are independent of the under relaxation factor used in the momentum equations, ensure mass conservation even in highly non-orthogonal grids, produced good convergence rates and prevent pressure-velocity decoupling.

III ENCIT – Itapema, SC (Dezembro 1990)

A BOUNDARY-FITTED NUMERICAL METHOD FOR THE SOLUTION OF THREE DIMENSIONAL ALL SPEED FLOWS USING CO-LOCATED VARIABLES

C. H. MARCHI, C. R. MALISKA & A. F. C. SILVA
Department of Mechanical Engineering
Federal University of Santa Catarina
P.O. Box 476 - 88049 - Florianópolis, SC, Brazil

SUMMARY

The solution of three dimensional compressible flow problems defined in arbitrary geometries requires the use of generalized coordinates in order to have flexibility in handling complex geometries. The use of segregated finite-volume methods requires special procedure to deal with the pressure-velocity coupling, involving, in general, staggered grids for promoting strenght to the coupling. Unfortunately the use of staggered grids introduces several difficulties in the computer code implementation. In this work a 3D numerical model is developed employing co-located variables for the solution of all speed flows.

INTRODUCTION

The majority of the existing numerical methods and computer codes for solving high speed compressible fluid flow problems belongs to the class of methods which employs the state equation for the pressure determination and the mass conservation equation for density calculation. It is well reported, however, that for low Mach number flows these methods are no longer suitable [1]. The other class of methods is the one where the density is determined from the state equation and pressure is found through an special equation derived using the mass conservation constraint. These methods are suitable for solving incompressible fluid flow problems or problems where the density is a function of temperature only. It is known that the development of the former class of methods occured among the aerospace numerical analysts while the latter class develop among the analysts involved with incompressible flow. It is illustrative to report some important differences between these two classes of methods. The former class of methods employ higher order finite-difference schemes using co-located variables, while the methods in the latter class employ the staggered grid arrangement, to cope with the pressure-velocity coupling, and derive the algebraic equations involving the conservation principles at control volume level, being called finite volume methods.

Very recently, extensions of the methodologies employed for incompressible flows have been applied with success in the solution of compressible fluid flow problems in cartesian [2,3] and general coordinate systems [4,5]. These methods form an equation for pressure, replacing, in the mass conservation equation, density by a linearized form of the state equation and velocity components by their respective momentum equations. The drawback of these methods is that they require the use of staggered variables in order to provide the adequate coupling between pressure and velocity/density. As a consequence of the staggered arrangement the computer code implementation becomes cumbersome, specially if variable grid spacing is used in three dimensions, because the different control volume locations and the corresponding metric storaging.

The alternative to this problem is to keep all variables stored at the same point, that is, all of them share the same elemental control volume. The use of co-located variables simplifies considerably the coefficients calculation and storaging, and geometrical data storaging. The difficulty associated with the use of co-located variables is the poor coupling it provides between pressure and velocity/density. This difficulty can be removed taking care in numerically approximating the pressure gradients.

Successful applications of finite volume methods for 2D problems using nonorthogonal grids with co-located variables can be seen in [6,7] for incompressible flows, in [8], among others, for cartesian grids and 2D incompressible flows, in [3] for 2D compressible flows in cartesian grids and in [4,5,9] for 2D compressible flows in general curvilinear coordinates.

The very good results obtained in [3,4,5,9] encouraged the authors the development of a numerical scheme using co-located variables for the solution of 3D flows. The method can solve compressible flow with presence of strong shocks as well as incompressible fluid flow problems, due to the special linearization performed for the mass flux in the mass conservation equation.

The development of such a method is the main purpose of the present paper. The model advances the state of the art in the solution of 3D all speed flows using co-located variables in the context of finite volume methods. Preliminary results, which demonstrates the aplicability of the method are also presented. It is belived that the development here in presented is in the direction of obtaining powerful, easy to implement and general numerical methods for the solution of all speed flows.

GOVERNING EQUATIONS

The Euler equations written for a general coordinate system (ξ, η, γ) for a generic scalar ϕ are

$$\frac{1}{J}\frac{\partial}{\partial t}(\rho\phi) + \frac{\partial}{\partial \xi}(\rho U\phi) + \frac{\partial}{\partial \eta}(\rho V\phi) + \frac{\partial}{\partial \gamma}(\rho W\phi) + \hat{p}^{\phi} = 0 \quad (1)$$

The ϕ variable represents the mass conservation equation, the three cartesian velocity components and the energy equation, being equal to 1, u, v, w and T, respectively. A state equation, as below, closes the system of equations which governs the three-dimensional flow of an inviscid fluid.

$$p = \rho RT \quad (2)$$

The Jacobian of the transformation and the contravariant velocity components appearing in Eq.(1)

are given by

$$J = [X_\xi Y_\eta Z_\gamma + X_\eta Y_\gamma Z_\xi + X_\gamma Y_\xi Z_\eta - X_\xi Y_\gamma Z_\eta - X_\eta Y_\xi Z_\gamma - X_\gamma Y_\eta Z_\xi]^{-1} \quad (3)$$

$$U = u.\bar{\xi}_X + v.\bar{\xi}_Y + w.\bar{\xi}_Z \quad (4)$$

$$V = u.\bar{\eta}_X + v.\bar{\eta}_Y + w.\bar{\eta}_Z \quad (5)$$

$$W = u.\bar{\gamma}_X + v.\bar{\gamma}_Y + w.\bar{\gamma}_Z \quad (6)$$

where

$$\bar{\xi}_X = Z_\gamma Y_\eta - Z_\eta Y_\gamma \qquad \bar{\eta}_X = Z_\xi Y_\gamma - Z_\gamma Y_\xi$$

$$\bar{\xi}_Y = Z_\eta X_\gamma - Z_\gamma X_\eta \qquad \bar{\eta}_Y = Z_\gamma X_\xi - Z_\xi X_\gamma$$

$$\bar{\xi}_Z = Y_\gamma X_\eta - Y_\eta X_\gamma \qquad \bar{\eta}_Z = Y_\xi X_\gamma - Y_\gamma X_\xi \quad (7)$$

$$\bar{\gamma}_X = Z_\eta Y_\xi - Z_\xi Y_\eta \qquad \bar{\gamma}_Z = Y_\eta X_\xi - Y_\xi X_\eta$$

$$\bar{\gamma}_Y = Z_\xi X_\eta - Z_\eta X_\xi$$

The source term, $\hat{p}^\phi$, in this case involving only the pressure field, for the three momentum conservation equations and for the energy equation are given below. For the mass conservation, of course, $\hat{p}^\phi$ is equal to zero.

$$\hat{p}^u = \left[\frac{\partial p}{\partial \xi}.\bar{\xi}_X + \frac{\partial p}{\partial \eta}.\bar{\eta}_X + \frac{\partial p}{\partial \gamma}.\bar{\gamma}_X\right] \quad (8)$$

$$\hat{p}^v = \left[\frac{\partial p}{\partial \xi}.\bar{\xi}_Y + \frac{\partial p}{\partial \eta}.\bar{\eta}_Y + \frac{\partial p}{\partial \gamma}.\bar{\gamma}_Y\right] \quad (9)$$

$$\hat{p}^w = \left[\frac{\partial p}{\partial \xi}.\bar{\xi}_Z + \frac{\partial p}{\partial \eta}.\bar{\eta}_Z + \frac{\partial p}{\partial \gamma}.\bar{\gamma}_Z\right] \quad (10)$$

$$\hat{p}^T = -\frac{1}{c_p J}\left[\frac{\partial p}{\partial t} + \nabla\cdot(p\vec{V}) - p\cdot\nabla\vec{V}\right] \quad (11)$$

DISCRETIZATION OF THE MOMENTUM AND ENERGY EQUATIONS

The algebraic equations are obtained employing the finite-volume method, that is, by integration of Eq.(1) over the elemental control volume shown in Fig.1 and integration in time. The resulting equation has the form

$$(M_P\phi_P - M_P^o\phi_P^o)/\Delta t + \dot{M}_e\phi_e - \dot{M}_w\phi_w + \dot{M}_n\phi_n - \dot{M}_s\phi_s + \dot{M}_d\phi_d - \dot{M}_f\phi_f + L[\hat{p}^\phi]_P\Delta\xi\Delta\eta\Delta\gamma = 0 \quad (12)$$

The subscripts e, w, n, s, d and f, appearing in the equations indicate the interface of the control volume of Fig. 1, while the subscripts E, W, N, S, D and F indicate the P neighbouring control volumes. For simplicity the dimensions of the elemental control volume in the transformed space, $\Delta\xi$, $\Delta\eta$ and $\Delta\gamma$ are taken equal to unity. In Eq.(12) M_P and M_P^o represent the mass inside the control volume in the time $t+\Delta t$ and t, respectively. $\dot{M}$ is the mass flux at the interface indicated by the subscript. $L[\hat{p}^\phi]$ represents the numerical approximation of the term $\hat{p}^\phi$. In this paper $\hat{p}^\phi$ is approximated by the Central Differencing Scheme (CDS) [10]. To illustrate $L[\hat{p}^u]$ is given by

$$L[\hat{p}^u]_P = \frac{(p_E - p_W)}{2\Delta\xi}(\bar{\xi}_X)_P + \frac{(p_N - p_S)}{2\Delta\eta}(\bar{\eta}_X)_P + \frac{(p_D - p_F)}{2\Delta\gamma}(\bar{\gamma}_X)_P \quad (13)$$

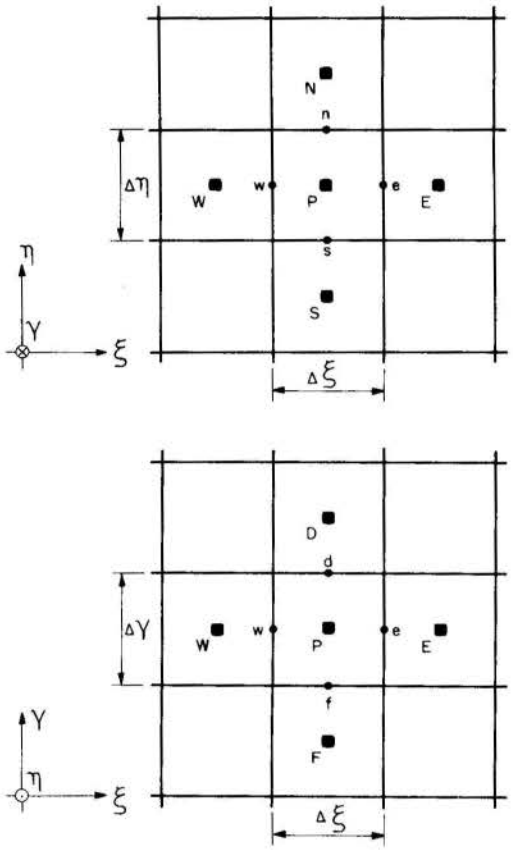

Fig. 1 Elemental control volume for P.

As the problem under consideration does not involve diffusive terms, evaluating the convective fluxes at the control volume interfaces through the Upstream Differencing Scheme (UDS) [10], the final discretized form of Eq.(1) is

$$a_P\phi_P = \sum(a_{nb}\phi_{NB})_P + M_P^o\phi_P^o/\Delta t - L[\hat{p}^\phi]_P\Delta\xi\Delta\eta\Delta\gamma \quad (14)$$

where

$$a_P = M_P^o/\Delta t + \sum a_{nb}$$

$$\sum a_{nb} = a_e + a_w + a_n + a_s + a_d + a_f$$

$$\sum(a_{nb}\phi_{NB})_P = a_e\phi_E + a_w\phi_W + a_n\phi_N + a_s\phi_S + a_d\phi_D + a_f\phi_F$$

$$a_e = -(1/2 - \bar{\alpha}_e)\dot{M}_e \qquad a_w = (1/2 + \bar{\alpha}_w)\dot{M}_w \tag{15}$$

$$a_n = -(1/2 - \bar{\alpha}_n)\dot{M}_n \qquad a_s = (1/2 + \bar{\alpha}_s)\dot{M}_s$$

$$a_d = -(1/2 - \bar{\alpha}_d)\dot{M}_d \qquad a_f = (1/2 + \bar{\alpha}_f)\dot{M}_f$$

Of course, for the Euler equations, the parameter $\bar{\alpha}$ assumes the value +1/2 and -1/2 dependending on the signal of the velocity at the interface under consideration. Since the implicit formulation is adopted, Eq.(14) originates a linear system for each dependent variable u, v, w and T. Recall that the coefficents of Eq.(14) are identical for u, v, w and T since the co-located arrangement of variables is employed.

DISCRETIZATION OF THE MASS CONSERVATION EQUATION

The method used in this work for finding pressure is an extension of the methodologies used in the solution of incompressible flows, that is, the mass conservation equation is transformed in an equation for pressure or pressure correction.

In the solution of compressible flows ρ and velocity are expressed in terms at pressure and substituted into the mass conservation equation forcing both density and velocity be active in this equation [2,10,11,12].

The discretized form of the mass conservation equation is obtained integrating this equation over space and time, giving

$$(M_P - M_P^o)/\Delta t + \dot{M}_e - \dot{M}_w + \dot{M}_n - \dot{M}_s + \dot{M}_d - \dot{M}_f = 0 \tag{16}$$

where $\dot{M}_e$, for example is expressed by

$$\dot{M}_e = (\rho_e^* U_e + \rho_e U_e^* - \rho_e^* U_e^*)\Delta\eta\Delta\gamma \tag{17}$$

It is seen by Eq.(17) that the velocity componentes which enters the mass conservation equation are the contravariant ones.

The key question now is to replace the mass fluxes as a function of pressure. Since in the mass flux calculation ρ and velocity are involved, both ρ and velocity need to be written as a function of pressure. Following the SIMPLEC [13] procedure to handle the pressure/velocity/density coupling the velocity and density are written as

$$\rho = \rho^* + \rho' \qquad \vec{V} = \vec{V}^* + \vec{V}' \tag{18}$$

where the corrections in $\rho^*$and $\vec{V}^*$ must be such that mass is conserved. The equation for $\vec{V}$ transforms in three scalar equations for the U, V and W contravariant velocity components. The star represents values from the previous iteration level, and the prime values need to be related to a pressure correction p' related to pressure by $p = p^* + p'$.

Density as a Function of p'. To obtain the relation between density and p' the state equation is linearized as

$$\rho = \rho^* + C^\rho . p' \tag{19}$$

where

$$C^\rho = 1/RT \tag{20}$$

for the special case of the fluid being a perfect gas.

Velocity Components as a Function of p'. The expressions for the contravariant velocity components as a function at p' are obtained from the momentum conservation equations. Consider that if a correct pressure field is introduced in the conservation equations it gives rise to correct u, v and w cartesian velocity components, and if a guessed pressure field p^* is introduced it gives rise to a estimated u^*, v^* and w^* velocities. Subtracting the equations one obtains, for exemple, for the u_e cartesian velocity component

$$u_e = u_e^* - \bar{d}_P^U . L[\hat{p}', u]_e \Delta\xi \tag{21}$$

The parameter $\bar{d}_P^U$ changes according to the pressure/velocity coupling method used. Using the above velocity components the expression for the contravariant component can be obtained as

$$U_e = U_e^* - \bar{d}_P^U . (p'_E - p'_P) . (\alpha_{11})_e \tag{22}$$

Similar equations can be written for the other five components which enters the mass conservation equation. In order to avoid a 19-point equation for p' the pressure gradients in the direction other than that of the velocity in consideration are neglected. For the SIMPLEC [13] method used here the expression for the $\bar{d}_P^U$ is

$$\bar{d}_P^U = (1/2) . (d_P + d_E)\Delta\eta\Delta\gamma \tag{23}$$

where

$$d_P = [a_P - \Sigma a_{nb}]^{-1} \tag{24}$$

Since the above equation is a velocity correction equation its form does not alter the converged results. Different equations influences only the convergence rate but not the final results.

Equation for p'. Introducing Eq.(19) and Eq.(22) for all densities and velocities which enter mass conservation in Eq.(16) with their mass flux terms linearized by Eq.(17), the resulting equation is an equation for p' in the form

$$A_P p'_P = \Sigma(A_{nb} p'_{NB}) + B \tag{25}$$

where

$$A_P = m_P^\rho C_P^\rho + m_e^{U-U} d_P^{U-U} (\alpha_{11})_e - m_w^{U-U} d_W^{U-U} (\alpha_{11})_w + m_n^{V-V} d_P^{V-V} (\alpha_{22})_n$$

$$- m_s^{V-V} d_S^{V-V} (\alpha_{22})_s + m_d^{W-W} d_P^{W-W} (a_{33})_d - m_f^{W-W} d_F^{W-W} (\alpha_{33})_f$$

$$B = \rho_P^0 \frac{\Delta\xi\Delta\eta\Delta\gamma}{J_P\Delta t} - m_P^\rho \rho_P^* - m_e^\rho \rho_E^* - m_w^\rho \rho_W^* - m_n^\rho \rho_N^* - m_s^\rho \rho_S^* - m_d^\rho \rho_D^* - m_f^\rho \rho_F^*$$

$$\sum(A_{nb}p'_{NB}) = A_e p'_E + A_w p'_W + A_n p'_N + A_s p'_S + A_d p'_D + A_f p'_F \tag{26}$$

$$A_e = - m_e^\rho C_E^\rho + m_e^{U-U} d_P^{U-U}(\alpha_{11})_e \qquad A_w = - m_w^\rho C_W^\rho - m_w^{U-U} d_W^{U-U}(\alpha_{11})_w$$

$$A_n = - m_n^\rho C_N^\rho + m_n^{V-V} d_P^{V-V}(\alpha_{22})_n \qquad A_s = - m_s^\rho C_S^\rho - m_s^{V-V} d_S^{V-V}(\alpha_{22})_s$$

$$A_d = - m_d^\rho C_D^\rho + m_d^{W-W} d_P^{W-W}(\alpha_{33})_d \qquad A_f = - m_f^\rho C_F^\rho - m_f^{W-W} d_F^{W-W}(\alpha_{33})_f$$

and

$$\alpha_{11} = (\bar{\xi}_X)^2 + (\bar{\xi}_Y)^2 + (\bar{\xi}_Z)^2$$

$$\alpha_{22} = (\bar{\eta}_X)^2 + (\bar{\eta}_Y)^2 + (\bar{\eta}_Z)^2$$

$$\alpha_{33} = (\bar{\gamma}_X)^2 + (\bar{\gamma}_Y)^2 + (\bar{\gamma}_Z)^2$$

$$m_P^\rho = \frac{\Delta\xi\Delta\eta\Delta\gamma}{J_P\Delta t} + (1/2 + \bar{\beta}_e)U_e^*\Delta\eta\Delta\gamma - (1/2 - \bar{\beta}_w)U_w^*\Delta\eta\Delta\gamma + (1/2 + \bar{\beta}_n)V_n^*\Delta\xi\Delta\gamma - (1/2 - \bar{\beta}_s)V_s^*\Delta\xi\Delta\gamma + (1/2 + \bar{\beta}_d)W_d^*\Delta\xi\Delta\eta - (1/2 - \bar{\beta}_f)W_f^*\Delta\xi\Delta\eta$$

$$m_e^\rho = (1/2 - \bar{\beta}_e)U_e^*\Delta\eta\Delta\gamma \qquad m_w^\rho = - (1/2 + \bar{\beta}_w)U_w^*\Delta\eta\Delta\gamma$$

$$m_n^\rho = (1/2 - \bar{\beta}_n)V_n^*\Delta\xi\Delta\gamma \qquad m_s^\rho = - (1/2 + \bar{\beta}_s)V_s^*\Delta\xi\Delta\gamma$$

$$m_d^\rho = (1/2 - \bar{\beta}_d)W_d^*\Delta\xi\Delta\eta \qquad m_f^\rho = - (1/2 + \bar{\beta}_f)W_f^*\Delta\xi\Delta\eta \tag{27}$$

$$m_e^U = [(1/2 + \bar{\beta}_e)\rho_P^* + (1/2 - \bar{\beta}_e)\rho_E^*]\Delta\eta\Delta\gamma$$

$$m_n^V = [(1/2 + \bar{\beta}_n)\rho_P^* + (1/2 - \bar{\beta}_n)\rho_N^*]\Delta\xi\Delta\gamma$$

$$m_d^W = [(1/2 + \bar{\beta}_d)\rho_P^* + (1/2 - \bar{\beta}_d)\rho_D^*]\Delta\xi\Delta\eta$$

$$m_w^U = - [(1/2 + \bar{\beta}_w)\rho_W^* + (1/2 - \bar{\beta}_w)\rho_P^*]\Delta\eta\Delta\gamma$$

$$m_s^V = - [(1/2 + \bar{\beta}_s)\rho_S^* + (1/2 - \bar{\beta}_s)\rho_P^*]\Delta\xi\Delta\gamma$$

$$m_f^W = - [(1/2 + \bar{\beta}_f)\rho_F^* + (1/2 - \bar{\beta}_f)\rho_P^*]\Delta\xi\Delta\eta$$

where the $\bar{\beta}$ coefficients are evaluated in the same way as the $\bar{\alpha}$ coefficients of Eq.(15).

THE STAR CONTRAVARIANT VELOCITIES AT THE INTERFACES

As is known the dependent variables in the momentum equations are the cartesian velocity components u, v and w. Since one is using co-located variables the u, v and w velocities are all stored at the center of the control volumes. In order to obtain an adequate coupling between pressure and velocity the correction equations which enters the mass conservation equation need to be written using velocities at the interfaces. However, there is no velocities stored at the interfaces. It is necessary, then to compute the star contravariant velocities at the interfaces as a function of the star cartesian velocities located in the center of the control volumes.

The PVF-A procedure to compute U^*, V^* and W^* at the interfaces is discribed in [3] for cartesian grids and in [4] for general curvilinear grids and is akin to Peric's [8] procedure for incompressible flows.

Taking as an example the calculation of U at the east face, one recognizes that u^*, v^* and w^* are needed at the east face. Writing Eq.(14) for the variable u for the control volume P for an estimated pressure field p^*, one gets

$$u_P^* = \frac{[\sum(a_{nb}u_{NB}^*)_P + M_P^0 u_P^0/\Delta t]}{(a_P)_P} - \frac{\Delta\xi\Delta\eta\Delta\gamma}{(a_P)_P}\cdot L[\hat{p}^{*u}]_P \tag{28}$$

and for the E control volume

$$u_E^* = \frac{[\sum(a_{nb}u_{NB}^*)_E + M_E^0 u_E^0/\Delta t]}{(a_P)_E} - \frac{\Delta\xi\Delta\eta\Delta\gamma}{(a_P)_E}\cdot L[\hat{p}^{*u}]_E \tag{29}$$

The velocity u^* at the east face using the PVF-A approach is obtained through the average of u_P^* and u_E^*, with exception of the pressure term, resulting in

$$u_e^* = \frac{[\sum(a_{nb}u_{NB}^*)_P + \sum(a_{nb}u_{NB}^*)_E + (M_P^0 u_P^0 + M_E^0 u_E^0)/\Delta t]}{[(a_P)_P + (a_P)_E]} - \frac{2\Delta\xi\Delta\eta\Delta\gamma}{[(a_P)_P + (a_P)_E]}\cdot L[\hat{p}^{*u}]_e \tag{30}$$

The $L[\hat{p}^{*u}]_e$ appearing in Eq.(30) is the numerical approximation of $\hat{p}^u$ as if the control volume were centered in "e". The expression for $L[\hat{p}^{*u}]_e$ is

$$L[\hat{p}^{*u}]_e = \frac{(p_E^* - p_P^*)}{\Delta\xi}(\bar{\xi}_X)_e + \frac{(p_N^* + p_{NE}^* - p_S^* - p_{SE}^*)}{4\Delta\eta}(\bar{\eta}_X)_e + \frac{(p_D^* + p_{DE}^* - p_F^* - p_{FE}^*)}{4\Delta\gamma}(\bar{\gamma}_X)_e \tag{31}$$

The cartesian velocity components v^* and w^* at the same interface are obtained in the same manner. Knowing u_e^*, v_e^* and w_e^* the U_e^* contravariant component can be calculated. The calculation of the remaining contravariant components follows the same procedure.

Velocity Corrections Using p'. The contravariant components are corrected using Eq.(22), for U, and using similar equations for V and W. These corrected velocities will be used for computing the coefficients for the next iteration level. The cartesian velocity components are corrected using the p' field by

$$u_P = u_P^* - d_P \cdot L[\hat{p}', u]_P \Delta\xi\Delta\eta\Delta\gamma$$

$$v_P = v_P^* - d_P \cdot L[\hat{p}', v]_P \Delta\xi\Delta\eta\Delta\gamma \qquad (32)$$

$$w_P = w_P^* - d_P \, L[\hat{p}', w]_P \Delta\xi\Delta\eta\Delta\gamma$$

Recall that the resulting expressions for $L[\hat{p}'\phi]$ are the same as for $L[\hat{p}^{\phi}]$ replacing p by p'.

SOLUTION PROCEDURE

The significant steps during the solution procedure now follow:

1. Domain discretization.
2. Estimative of u, v, w, T, p and ρ in t+Δt.
3. Computation of the coefficients and source term of the momentum equations. Solve for u^*, v^* and w^* using MSI [14] technique. Computation of the contravariant velocities at the interfaces of the control volumes.
4. Solve for p' using MSI. Compute $p = p^* + p'$.
5. Correction of u^*, v^* and w^*, using Eq. (32), of U^*, V^* and W^* using Eq.(22) and similar equations and correction of density using Eq.(19).
6. Solution of T using MSI. Computation of ρ using the state equation.
7. Iteration is necessary until convergence for the time step under consideration is reached.

PRELIMINARY RESULTS

The preliminary tests of the numerical method was realized solving four high speed flow problems. The first one aimed to test the invariant characteristic of a 2D plane flow along the axis of the cylinder, by solving the flow problem over a circular cylinder. In the direction of the cylinder axis three cell were used, with the total grid being 26x20x3. The results (not present here) show excellent agreement when compared with the 2D solution using 26x20 elemental volumes.

The second problem, with the objective of testing the symmetry characteristics of a 2D axisymmetric flow, was the flow over the nose tip of the Brazilian Launch Vehicle (VLS), with angle of attack (α) equal to zero and Mach number equal to 3.75. With α equal to zero the solution can be compared with the 2D axisymmetric solution. In this case the number of volumes in the axisymmetric direction can not be smaller as enough for applying boundary conditions, as in the 2D plane case, because the number of volumes defines the shape of the revolution body. Two grids with 30x24x10 and 30x24x20 were used. The results are shown in Fig. 2 where the triangles denote the experimental solution [15], curve 1 shows the 2D axisymmetric results (30x24) [5], curve 2 the 3D solution with 30x24x10 and curve 3 the solution with 30x24x20 volumes. It can be seen that the results with a more refined grid in the angular direction tends to the experimental results.

The third test was the solution of the VLS vehicle, again with α = 0 and Mach number 3.75 but extending the computational domain up to half of the third launching stage. Fig. 3 shows the results where the triangles are the experimental results [15] and the solid line the 3D numerical solution using 60x24x20 volumes distributed in 180°, which is equivalent of using 60x24x40 volumes.

The final test present here is the solution of the same flow as in the third test but with α = 5°, characterizing the flow as truly three-dimensional. The results of pressure coefficient (Cp) over the surface for θ = 90°, 160° and 230° are presented in Fig. 4, where the triangles represents the experimental results for α = 0. The numerical solutions were obtained using a convergence criterion in the pressure [4] of 10^{-5}, and 2×10^{-5}, for these second, third and last test, respectively. The fully 3D problem was not solved to a tighter convergence due solely to computer limitations.

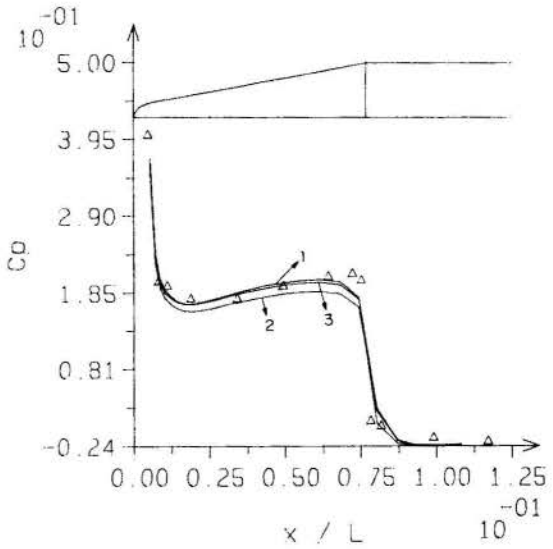

Fig. 2 Test of the symmetry characteristics.

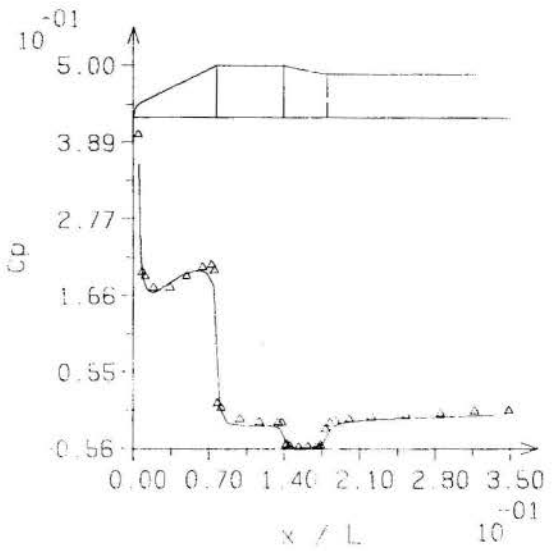

Fig. 3 Cp for Mach 3.75 and α = 0°.

CONCLUDING REMARKS

The development of a 3D numerical model for the solution of all speed flows using co-located variable was described. The model incorporates two importants features, namely, the possibility of solving flows ranging from low speed incompressible flows to compressible supersonic flows, and the use of co-located variables which introduces a tremendous simplicity in the code implementation when compared with the usual staggered grid. The model is also tailored to handle complex arbitrary geometries. The preliminary tests demonstrated that the method performs very well.

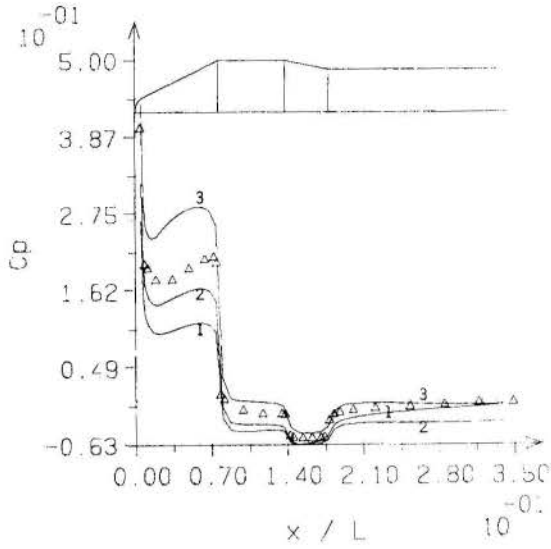

Fig. 4 Cp for Mach 3.75 and $\alpha = 5^{o}$.

ACKNOWLEDGMENTS

The partial financial support provided by Instituto de Atividades Espaciais IAE/CTA is gratefully acknowledged.

REFERENCES

[1] Anderson, D.A., Tannehill, J.C. and Pletcher, R.H., "Computational Fluid Mechanics and Heat Transfer," McGraw-Hill, Washington, 1984.

[2] Van Doormaal, J.P., "Numerical Methods for the Solution of Incompressible and Compressible Fluid Flows," Ph.D. Thesis, University of Waterloo, Ontario, Canada, 1985.

[3] Marchi, C.H., Maliska, C.R. and Bortoli, A.L., "The Use of Co-Located Variables in the Solution of Supersonic Flows," Proceedings of the 10th Brazilian Congress of Mechanical Engineering, Vol. 1, pp. 157-160, Rio de Janeiro, Brazil, 1989.

[4] Marchi, C.H. and Maliska, C.R., "The Use of Co-Located Variables in the Solution of Supersonic Flows," Submitted to Numerical Heat Transfer, 1990.

[5] Maliska, C.R., Silva, A.F.C. and Marchi, C.H. "Solução Numérica de Escoamentos Compressíveis Utilizando-se Variáveis Co-Localizadas em Coordenadas Generalizadas," Relatório ao IAE/CTA, parte 5, Florianópolis, SINMEC/EMC/UFSC, jun. 1990.

[6] Hsu, C., "A Curvilinear-Coordinate Method for Momentum, Heat and Mass Transfer in Domains of Irregular Geometry," Ph.D. Thesis, University of Minnesota, USA, 1981.

[7] Rhie, C.M., "A Numerical Study of the Flow Past an Isolated Airfoil with Separation," Ph.D. Thesis, University of Illinois, Urbana-Champaign, USA, 1981.

[8] Peric, M., Kessler, R. and Scheuerer, G., "Comparison of Finite-Volume Numerical Methods with Staggered and Colocated Grids," Submitted to Computers and Fluids, 1987.

[9] Bortoli, A.L., "The Use of Co-Located Variables in the Solution of Supersonic Flows," (in portuguese), M.Sc. Dissertation, Federal University of Santa Catarina, Florianópolis, SC, Brazil, 1990.

[10] Patankar, S.V., "Numerical Heat Transfer and Fluid Flow," McGraw-Hill, New York, 1980.

[11] Harlow, F.H. and Welch, J.E., "Numerical Calculation of Time-Dependent Viscous Incompressible Flow of Fluid with Free Surface", Physics of Fluids, Vol. 8, pp. 2182-2189, 1965.

[12] Silva, A.F.C. and Maliska, C.R., "Uma Formulação Segregada em Volumes Finitos para Escoamentos Compressíveis e/ou Incompressíveis em Coordenadas Generalizadas. Anais do II Encontro Nacional de Ciências Térmicas, p. 11-14, Aguás de Lindóia, Brasil, dez. 1988.

[13] Van Doormaal, J.P. and Raithby, G.D., "Enhancements of the simple method for predicting incompressible fluid flows. Numerical Heat Transfer, Vol. 7, pp. 147-163, 1984.

[14] Zedan, M. and Schneider, G.E., "3-D Modified Strongly Implicit Procedure for Finite Difference Heat Conduction Modelling," AIAA Journal, Vol. 21, n. 2, pp. 295-306, 1983.

[15] ONERA, "Essai du Lanceur Bresilien au 1/15 Soufflerie S2MA; Configuration VC - C (5 dards), Mach 1.500, 2.502, 3.747," France, decembre 1988.

III ENCIT – Itapema, SC (Dezembro 1990)

SEPARAÇÃO E BIFURCAÇÃO DE ESCOAMENTOS EM DIFUSORES RADIAIS

C.A. LANGER, A.T. PRATA E R.T.S. FERREIRA
Departamento de Engenharia Mecânica
Universidade Federal de Santa Catarina
Cx.Postal 476 - Florianópolis, SC - 88049

RESUMO

O presente artigo é uma investigação numérica de escoamentos radiais entre discos paralelos concêntricos. O espaçamento entre os discos foi mantido constante e o número de Reynolds do escoamento associado ao raio de entrada dos discos, Re, foi variado entre 10 e 1000. Para Re<62 o escoamento é paralelo. Em Re=62 surgem as primeiras regiões de recirculação, e em Re=113 o escoamento se bifurca em configurações simétrica e assimétricas observáveis através da existência de múltiplas soluções da equação de Navier-Stokes.

INTRODUÇÃO

O problema do escoamento radial entre discos paralelos é de grande interesse científico e tecnológico. Exemplos de aplicações incluem mancais axiais, impactores de aerosois, válvulas automáticas de compressores , etc. Inúmeros são os trabalhos que tratam dos diversos aspectos do escoamento em difusores radiais. Para revisão de alguns destes trabalhos, referência é feita aos artigos de Ferreira et al. [1] e Raal [2] para escoamentos laminares, e Deschamps et al. [3], Tabatabai e Pollard [4], e Ervin et al. [5] para escoamentos turbulentos.

A despeito do grande número de trabalhos que focalizam os escoamentos laminar e turbulento, muito poucos artigos investigaram a transição entre um regime e outro. No escoamento entre discos paralelos, o fluido ao escoar radialmente experimenta um acréscimo na área disponível de passagem. Na predominância de efeitos invíscidos a diminuição da velocidade associada ao aumento da área causa uma elevação da pressão na direção radial. Desta forma o fluido passa a escoar contra um gradiente adverso de pressão. Dependendo do gradiente de pressão adverso, o fluido pode se descolar das paredes do difusor dando origem a regiões de recirculação. Aparentemente a separação do escoamento é o primeiro passo para que o escoamento se torne instável e posteriormente turbulento. Existe ainda controvérsia na literatura em relação aos estágios pelos quais o escoamento, em um difusor radial, passa entre os regimes laminar e turbulento, conforme discutido a seguir.

Raal [2] investigou numericamente o escoamento laminar em difusores radiais e verificou a existência de regiões de recirculação. Tais regiões tendiam a crescer e moviam a montante à medida em que a vazão de fluido aumentava. Para sua análise, Raal assumiu escoamento em regime permanente e usou condição de simetria em relação ao plano médio que separa os dois discos.

Mochizuki e colaboradores [6,7] investigaram o escoamento em difusores radiais tanto numérico como experimentalmente. Diferentemente de Raal, tais autores afirmam que o fenômeno da separação do escoamento é de natureza não estacionária. Segundo estes autores, a separação do escoamento em difusores radiais, ocorre periodicamente e se alterna de ambas as paredes do difusor na mesma localização radial. Adicionalmente foi observado que o ponto de separação do escoamento move-se a montante com o aumento da vazão, e que a jusante do ponto de separação, as camadas viscosas se desenvolvem em esteiras de vórtices. Tais esteiras seriam similares àquelas observadas na ejeção periódica de vórtices que ocorre em escoamentos ao redor de cilindros.

Como complemento às observações contraditórias entre Raal [2] e Mochizuki e colaboradores [6,7], é pertinente citar o trabalho de Sobey e Drazin [8]. Este trabalho contém análise teórica, computação e experimentos em escoamentos em dutos simétricos na presença de uma expansão. À luz da teoria da bifurcação, com comprovação numérica e experimental, tais autores verificaram a existência de múltiplas configurações possíveis de serem encontradas em regime permanente. Neste trabalho é verificada a existência de parâmetros críticos a partir dos quais o escoamento bifurca em diferentes configurações estáveis. Em um primeiro estágio, tais configurações são possíveis de existir em regime permanente, mas com aumento do valor dos parâmetros que governam o escoamento, tais configurações tendem a se tornar instáveis e o escoamento passa a oscilar periodicamente.

O objetivo do presente trabalho é investigar numericamente o escoamento radial entre discos paralelos considerando a possibilidade de ocorrerem bifurcações, e desta forma, contribuir para elucidar os mecanismos associados à separação e estabilidade do escoamento em tais geometrias.

FORMULAÇÃO DO PROBLEMA

A geometria a ser investigada é apresentada na Fig. 1. Conforme observado na figura, os discos superior e inferior estão separados por um afastamento s. O escoamento se dá radialmente a partir de $r = r_1$, e procede até a saída do difusor em $r = r_2$. Mostrados na figura estão as coordenadas axial e radial, x e r, respectivamente. O escoamento é axisimétrico e as propriedades, incluindo a densidade, são assumidas constantes. Na ausência de forças de campo, o movimento é descrito pelas seguintes equações,

. Continuidade:

$$\nabla . \vec{u} = 0 \qquad (1)$$

. Conservação da quantidade de movimento linear:

$$\rho \partial \vec{u}/\partial t + \rho \vec{u} . \nabla \vec{u} = - \nabla p + \mu \nabla^2 \vec{u} \qquad (2)$$

onde $\vec{u}$ é o vetor velocidade cujas componentes axial e radial são u e v, respectivamente, p é a pressão, ρ é a densidade, μ é a viscosidade, e ∇ é o operador "nabla" em coordenadas cilíndricas.

Em termos adimensionais, as equações anteriores podem ser reescritas como,

$$\bar{\nabla} . \vec{U} = 0$$

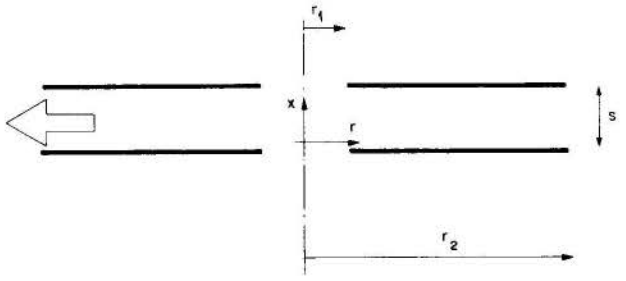

Fig. 1 - Geometria do difusor radial.

$$\partial\vec{U}/\partial\tau + \vec{U}.\bar{\nabla}\vec{U} = -\bar{\nabla}P + (1/Re)\bar{\nabla}^2\vec{U} \qquad (2)$$

onde as seguintes adimensionalizações foram adotadas,

$$\vec{U} = \vec{u}/\bar{v} \ , \quad P = p/(\rho\bar{v}^2) \ , \quad \tau = \bar{v}t/r_1$$

$$Re = \rho\bar{v}r_1/\mu \qquad (3)$$

e $\bar{v}$ é a velocidade radial média do fluido em $r = r_1$. O operador $\bar{\nabla}$ é o correspondente de ∇ adimensionalizado por r_1.

As condições de contorno para o problema serão agora apresentadas. A fim de simular escoamento irrotacional com um perfil de velocidade plano a montante do início do difusor, reproduzindo desta forma uma cascata infinita de discos paralelos, as condições para a entrada do difusor foram prescritas em $r_o<r_1$. Desta forma, fez-se para $R_o = r_o/r_1$, $V(X) = 1/R_o$, e $\partial U/\partial R = 0$, onde U e V são, respectivamente, as componentes axial e radial da velocidade adimensionalizadas por $\bar{v}$; X e R são, respectivamente, as coordenadas axial e radial adimensionalizadas por r_1.

Tal condição de contorno é idêntica àquela utilizada por Raal [2], que argumenta ser esta condição fisicamente mais realística, uma vez que possibilita a difusão de quantidade de movimento a montante da entrada dos discos.

Computacionalmente R_o é escolhido de forma que nesta posição os efeitos elípticos associados à presença dos discos não sejam sentidos. No presente trabalho fez-se $R_o = 2/3$ a exemplo do valor adotado por Raal [2].

Para $X = 0$ e $X = S$ ($S = s/r_1$), fez-se $U = V = 0$ quando $R>R_1$ e $U = \partial V/\partial X = 0$ quando $R_o\leq R\leq R_1$. Note-se que não foi feito uso da condição de simetria do difusor em relação ao plano $X = S/2$. Neste sentido a presente formulação difere drasticamente da de Raal [2] que impõe tal simetria. O uso da simetria em relação ao plano $X = S/2$ força o escoamento a ser simétrico mascarando assim a possibilidade de se obter soluções assimétricas a exemplo do que foi verificado por Sobey e Drazin [8], em dutos simétricos na presença de expansão.

Na saída do difusor, $R = R_2$, utilizou-se a condição de escoamento localmente parabólico, ou seja, $U = \partial(RV)/\partial R = 0$. O valor de R_2 foi cuidadosamente escolhido de forma que na saída do difusor os efeitos viscosos predominassem em virtude das baixas velocidades associadas às grandes áreas transversais disponíveis para o escoamento. Para valores do número de Reynolds mais elevados, utilizou-se valores maiores para R_2. Em geral, R_2 variou entre 20 e 30.

Como condição inicial fez-se $\vec{u} = 0$ para baixos valores do número de Reynolds ($Re<10$). A medida que buscava-se soluções para valores de Re mais elevados, utilizava-se como condição inicial as soluções já convergidas para aqueles valores de Re mais baixos.

A formulação do problema está agora completada. Os dois parâmetros que governam o escoamento são Re e S. A seguir será apresentada a metodologia de solução das equações diferenciais que descrevem o problema.

PROCEDIMENTO E DETALHES COMPUTACIONAIS

As equações diferenciais do problema foram resolvidas numericamente pelo método dos volumes finitos conforme esquema adotado por Patankar [9]. Tal metodologia tem sido amplamente utilizada em problemas de transferência de calor e escoamento de fluidos. Em essência o domínio de solução é dividido em pequenos volumes de controle não sobrepostos e as equações do problema são integradas ao longo de cada um destes volumes fornecendo um conjunto de equações algébricas. Na solução das equações algébricas adotou-se o método linha-por-linha, que é uma combinação do algoritmo de Thomas com Gauss-Seidel [9]. Para acelerar a convergência do método fez-se uso do algoritmo de correção em bloco de Settari e Aziz [10]. A integração no tempo foi feita adotando-se um esquema totalmente implícito.

Particular atenção foi dedicada à escolha da malha computacional para discretização do domínio de solução. A escolha apropriada da malha é de fundamental importância na captura das regiões de recirculação presentes no escoamento. A opção que se mostrou mais adequada foi uma malha uniformemente espaçada em X e variando ao longo de R através de uma lei de potência com expoente igual a 1,5.

A escolha do número de pontos nodais em cada direção foi feita de acordo com critérios de insensibilidade em relação aos campos de velocidade e pressão, respeitando o compromisso que há entre precisão e custo computacional. Para valores do número de Reynolds menores do que 300, utilizou-se uma malha de 70 x 70 pontos nodais nas direções X e R, respectivamente. Para valores de Re maiores do que 300, adotou-se uma malha com 70 x 105 pontos nodais (direção X e R, respectivamente).

Para o avanço no tempo, empregou-se um intervalo de $\Delta\tau = 0{,}001$, idêntico àquele adotado por Mochizuki e Yang [7]. Em cada intervalo de tempo a solução numérica era convergida de forma que o maior erro na conservação da massa para cada um dos volumes de controle ficasse sempre menor do que 10^{-11}.

A fim de validar a solução numérica, esta foi comparada com a solução analítica para a situação onde os efeitos viscosos prevalecem sobre os efeitos inerciais ($Re = 1$) e a concordância entre ambas foi excelente.

Em geral o tempo computacional requerido para se obter uma solução em regime permanente era extremanente dependente do número de Reynolds investigado. Para valores de $Re = 1000$ este tempo chegou a 30 horas em um computador IBM-4381.

Maiores informações sobre a metodologia numérica e testes associados ao programa computacional podem ser encontrados em [11].

RESULTADOS E DISCUSSÕES

Para todos os casos a serem reportados o espaçamento entre os discos, S, foi mantido constante e igual a 2. O número de Reynolds do escoamento, Re, foi variado entre 10 e 1000. Para os valores de $Re\leq 300$, o raio externo do duto, R_2, foi mantido igual a 20, ao passo que para $Re>300$ fez-se $R_2 = 30$.

As soluções a serem apresentadas são todas estacionárias. A despeito da inclusão dos termos temporais nas equações que descrevem o problema, as soluções avançavam no tempo sempre em direção a um regime estacionário. Nenhuma oscilação do escoamento a exemplo daquelas mencionadas por Mochizuki e colaboradores [6,7] foi observada para a faixa de número de Reynolds investigada.

Os primeiros resultados a serem explorados são os mapas das linhas de corrente do escoamento para diversos números de Reynolds. Com este fim a Fig. 2 foi preparada. Nesta figura são apresentadas as linhas de corrente para $Re = 100$, 113, 200, 300, 600 e 1000. Tais figuras representam cortes transversais ao longo do diâmetro dos discos, e perpendiculares ao plano destes; apenas uma metade destes cortes é apresentada uma vez que o escoamento é axisimétrico. Em todas as figuras o escoamento se dá da esquerda para a direita.

Nas figuras associadas a $Re = 100$, 113, 200 e 300 , vê-se que a dimensão radial do domínio de solução é menor do que aquela associada às figuras de $Re = 600$ e 1000 conforme discutido anteriormente. A mesma escala foi adotada para as direções axial e radial, e tal escala foi mantida em todas as figuras.

Para baixos números de Reynolds, $Re<62$, as linhas de corrente do escoamento são paralelas entre si e às paredes do difusor. Em $Re = 62$ surgem as primeiras regiões de recirculação, e o escoamento tem uma configuração ti-

picamente representada pela figura associada a Re = 100. Verifica-se que o escoamento é simétrico em relação ao plano médio que separa os dois discos. O valor de Re = 62 como sendo aquele correspondente ao início do descolamento do fluido das paredes do difusor concorda com o valor de Re = 64 observado por Raal [2]. A pequena variação entre estes valores de Re associados ao início do descolamento do fluido das paredes deve estar relacionada com imprecisões devidas ao uso de diferentes malhas computacionais.

A simetria do escoamento conforme observado na figura de Re = 100 sugere que o domínio computacional possa ser reduzido. Tal fato foi utilizado por Raal [2], bem como seus antecessores. Ao assumir esta simetria, tais autores perderam a oportunidade de observar aspectos relevantes associados ao escoamento a serem discutidos nos parágrafos subseqüentes.

Para Re = 113, o escoamento bifurca em configurações simétrica e assimétricas. A configuração simétrica é semelhante àquela observada para Re = 100. Na configuração assimétrica para Re = 113 mostrada na Fig. 2, verifica-se a existência de duas regiões de recirculação. Tais regiões surgem do aumento e da diminuição das regiões de recirculação observadas na configuração simétrica.

A partir de Re = 113, o escoamento apresenta diferentes configurações, observáveis através da existência de múltiplas soluções da equação de Navier-Stokes. Verifica-se a ocorrência de uma configuração simétrica, que em geral é instável a pequenas perturbações, e de duas configurações assimétricas, de natureza estável. A configuração simétrica bem como uma das configurações assimétricas são mostradas na Fig. 2 para Re = 200, 300, 600 e 1000. As outras configurações assimétricas foram omitidas, uma vez que são a imagem daquelas apresentadas na Fig. 2, em relação a um espelho colocado em qualquer um dos dois discos que compõem as paredes do difusor.

A natureza instável das soluções simétricas é observada através da dificuldade em obtê-las. Em geral, a solução numérica tende a convergir para as soluções assimétricas, e tal afirmação é tanto mais verdadeira quanto maior for o número de Reynolds. Para se obter uma solução simétrica para valores elevados de Re, alguns cuidados tiveram que ser tomados. No processo de solução das equações algébricas, as varreduras do algoritmo de Thomas ao longo das direções axiais eram eliminadas, e fatores de subrelaxação eram utilizados. Convém notar que para valores de Re = 600 e 1000, os próprios erros de truncamento introduziam perturbações que tornavam as soluções assimétricas. Tal fato era observado ao se avançar a solução simétrica no tempo além dos critérios de convergência estabelecidos, mesmo após o regime estacionário ter sido alcançado.

Observa-se da Fig. 2, que à medida em que o número de Reynolds aumenta diferentes regiões de recirculação surgem no escoamento assimétrico. Note-se que para a configuração assimétrica o escoamento flamba, e tal flambagem além de se tornar mais acentuada, se propaga a jusante do escoamento com o aumento do número de Reynolds. Para o escoamento simétrico, independente do número de Reynolds, ocorrem sempre duas regiões de recirculação.

Na Fig. 3 são apresentadas as isobáricas correspondentes às linhas de corrente da Fig. 2. Nos mapas das isobáricas foram incluídas setas que apontam no sentido de pressões crescentes, bem como as localizações de pontos de máximos e mínimos absolutos e locais no campo de pressão.

Para as configurações simétricas observa-se que a região de pressão máxima no escoamento se move a jusante com o aumento do número de Reynolds. Em geral, para o escoamento simétrico, a pressão cresce radialmente a partir da entrada do difusor, atinge um máximo e passa a decrescer. O crescimento radial da pressão é devido à diminuição da velocidade associada ao aumento da área disponível para o escoamento. Para o escoamento simétrico observa-se que na entrada do difusor a pressão é mais elevada na região central do escoamento, em virtude da presença das regiões de recirculação. Adicionalmente, no interior das regiões de recirculação as pressões não variam na direção axial.

Nas configurações assimétricas os campos de pressão apresentam um comportamento bem mais irregular do que nas configurações simétricas. Comparando as curvas para os escoamentos assimétricos das Figs. 2 e 3 observa-se que os pontos de pressão máxima locais coincidem com os pontos de reatamento do escoamento após as regiões de recirculação. Nestes pontos de reatamento a corrente principal do escoamento se choca com as paredes do difusor causando um aumento de pressão.

A cada posição radial pode-se integrar a distribuição de pressão na direção axial obtendo-se desta forma pressões médias. A variação das pressões médias ao longo de R são mostradas nas Figs. 4a) e b). Em cada figura foi plotada a curva de pressão média tanto para o escoamento simétrico como assimétrico. Observa-se que enquanto no escoamento simétrico a pressão cresce, atinge um máximo e decresce, no escoamento assimétrico tal fato não se verifica. Conforme já verificado pelas isobáricas da Fig.3, no escoamento assimétrico ocorrem regiões de máximos e mínimos locais. Na entrada do difusor, a pressão média para todos os casos está em torno de -0,5.

Distribuições das tensões de cisalhamento nas paredes do difusor são mostradas nas Figs. 5a) a d). A Fig. 5 a) apresenta, para a configuração simétrica, a tensão de cisalhamento em função de R para cinco valores de Re investigados no presente trabalho. Nas Figs. 5b) a d) são mostradas para diferentes valores de Re as tensões de cisalhamento para as configurações simétricas e assimétricas conjuntamente. Nestas figuras observam-se os efeitos das regiões de recirculação onde as tensões de cisalhamento possuem valores negativos. Para valores de Re mais elevados verifica-se que a tensão de cisalhamento pode assumir valores negativos ao longo de uma grande extensão radial.

CONCLUSÃO

Neste trabalho investigou-se numericamente o escoamento radial entre discos paralelos concêntricos. Embora exista um grande número de trabalhos nesta área, poucos artigos focalizam o problema da separação do escoamento em tais configurações. Adicionalmente, os artigos sobre separação de escoamentos radiais são contraditórios e pouco conclusivos. Neste contexto a presente investigação mostra, pela primeira vez, que a separação em escoamentos radiais ocorre inicialmente em regime permanente para Re = 62, e que a partir de Re = 113 o escoamento se bifurca em configurações simétrica e assimétricas observáveis através da existência de múltiplas soluções da equação de Navier Stokes.

REFERÊNCIAS BIBLIOGRÁFICAS

[1] Ferreira, R.T.S., Deschamps, C.J., and Prata, A.T., "Pressure Distribution Along Valve Reeds of Hermetic Compressors", Exp. Thermal and Fluid Science, Vol.2, pp. 201-207, 1989.

[2] Raal, J.D., "Radial Source Flow Between Parallel Disks", J. Fluid Mechanics, Vol. 85, part 3, pp. 401-416, 1978.

[3] Deschamps, C.J., Prata, A.T., Ferreira, R.T.S., "Modelagem de um Escoamento Turbulento em Presença de Estagnação, Recirculação, Aceleração e Gradientes de Pressão Adversos", Anais do X Congresso Brasileiro de Engenharia Mecânica, Vol. I, pp. 57-60, Rio de Janeiro, 1989.

[4] Tabatabai, M., and Pollard, A., "Turbulence in Radial Flow Between Parallel Disks at Medium and Low Reynolds Numbers", J. Fluid Mechanics, Vol.185, pp. 483-502, 1987.

[5] Ervin, J.S., Suryanarayana, N.V., and Ng H.C., "Radial, Turbulent Flow of a Fluid Between Two Coaxial Disks", J. Fluids Eng., Vol. 111, pp. 378-383, 1989.

[6] Mochizuki, S., and Yao M., "Flow Separation and Heat Transfer in Radial Flows Between Two Parallel Disks", Trans. of Japan Society of Mechanical Engineers, Vol. 49, pp. 426-432, 1983.

Re = 100, SIMÉTRICO

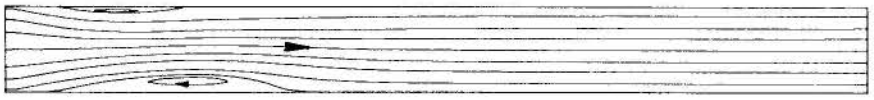

Re = 113, ASSIMÉTRICO

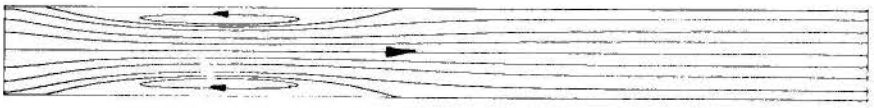

SIMÉTRICO

Re = 200

ASSIMÉTRICO

SIMÉTRICO

Re = 300

ASSIMÉTRICO

Re = 600, SIMÉTRICO

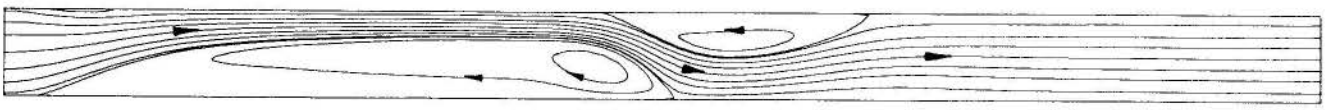

Re = 600, ASSIMÉTRICO

Re = 1000, SIMÉTRICO

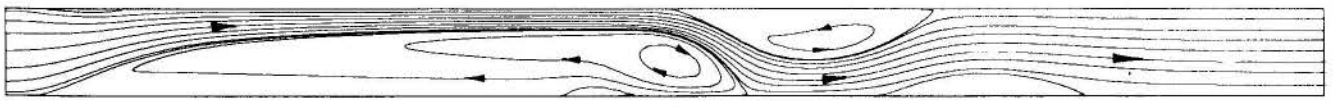

Re = 1000, ASSIMÉTRICO

Fig. 2 - Linhas de corrente características para diversos números de Reynolds.

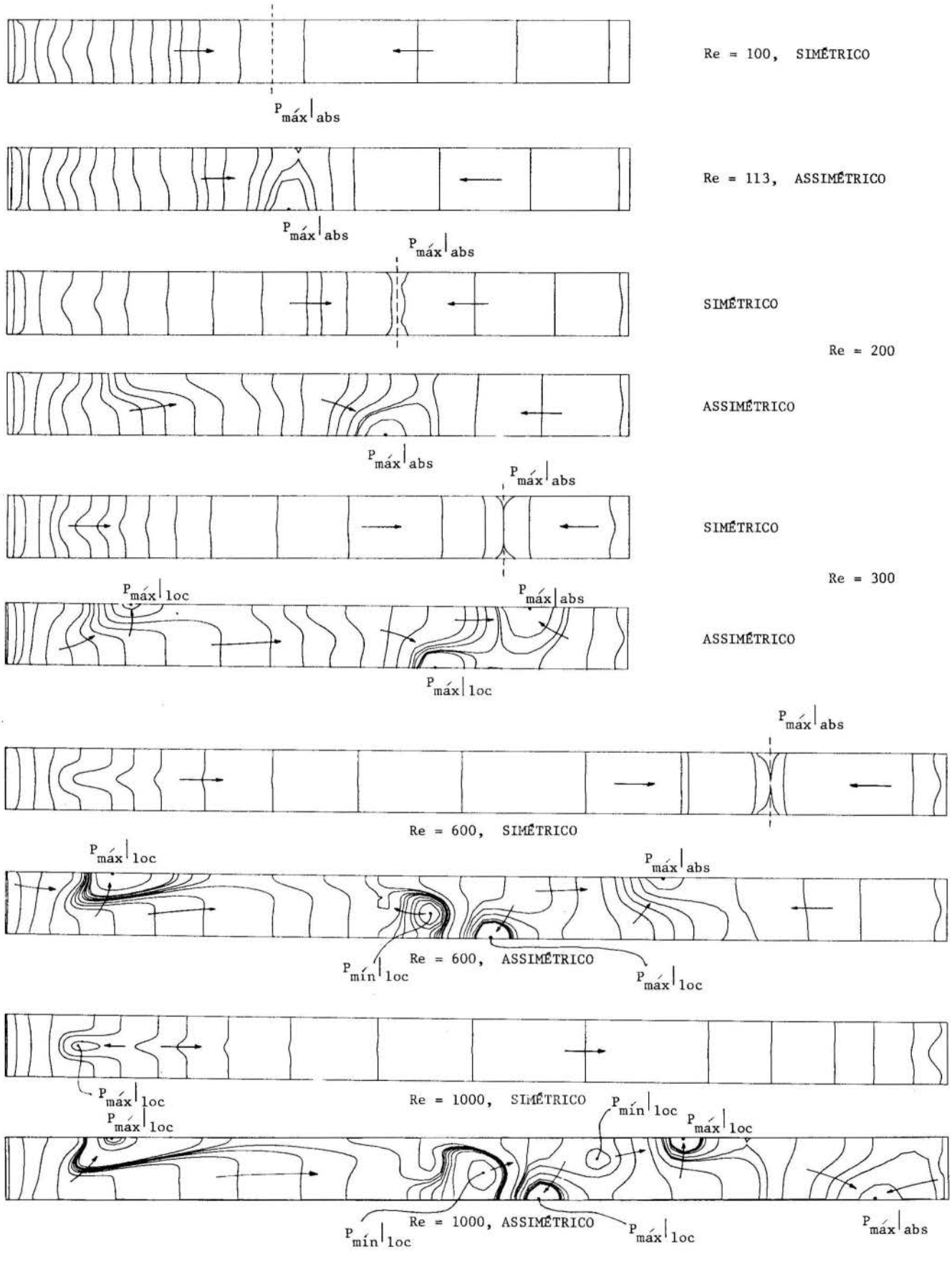

Fig. 3 - Isobáricas características para diversos números de Reynolds.

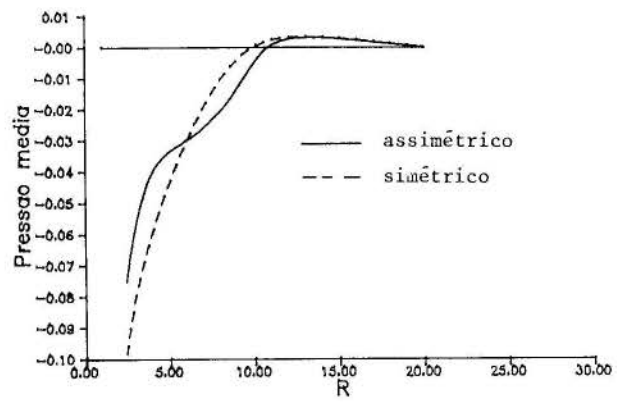

a) Re = 200

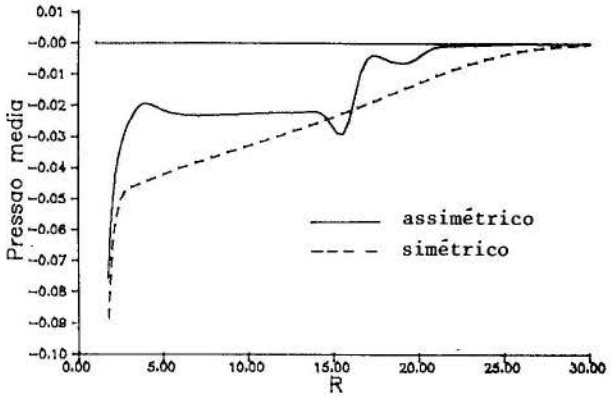

b) Re = 1000

Fig. 4 - Pressão média na secção transversal.

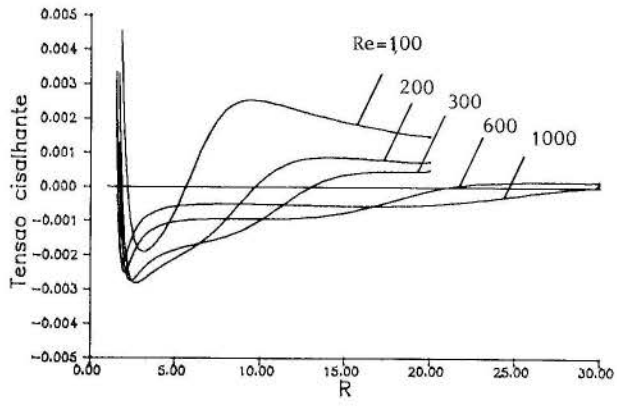

a) Escoamento simétrico

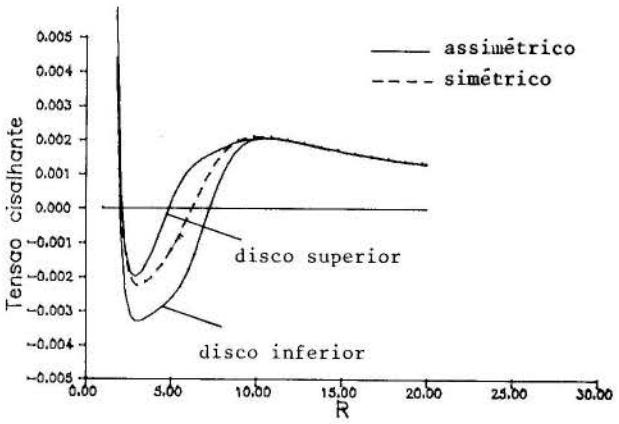

b) Re = 113

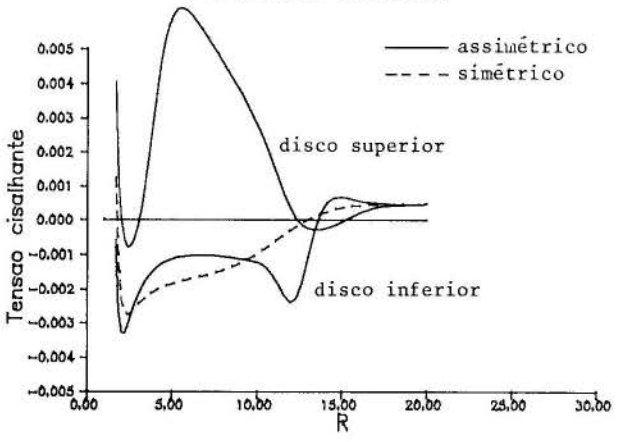

c) Re = 300

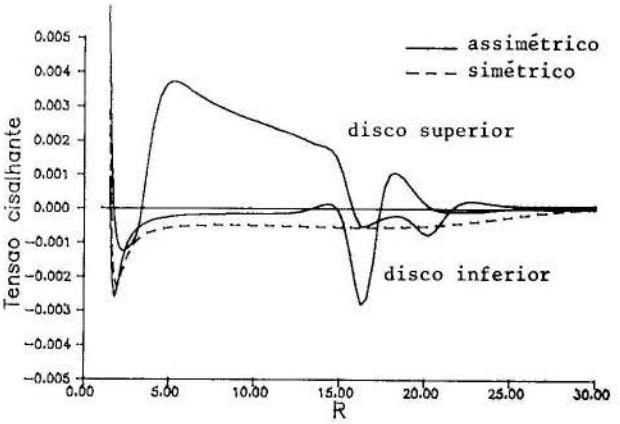

d) Re = 1000

Fig. 5 - Tensão cisalhante nas paredes do difusor.

[7] Mochizuki, S., and Yang, W.J., "Self-Sustained Radial Oscillating Flows Between Parallel Disks", J. Fluid Mechanics, Vol. 154, pp. 377-397, 1985.

[8] Sobey, I.J., and Drazin, P.G., "Bifurcations of Two-Dimensional Channel Flows", J. Fluid Mechanics, Vol. 171, pp. 263-287, 1986.

[9] Patankar, S.V., "Numerical Heat Transfer and Fluid Flow", Hemisphere Publishing Co., New York, 1980.

[10] Settari, A., and Aziz, K., "A Generalization of the Additive Correction Methods for the Iterative Solution of Matrix Equations", SIAM J. Numer. Analysis, Vol. 10, pp. 506-521, 1973.

[11] Langer, C.A., "Separação, Bifurcação e Transferência de Calor em Escoamentos Radiais", dissertação de mestrado em andamento, UFSC, Florianópolis, SC.

ABSTRACT

This work deals with a numerical investigation of radial flows between parallel concentric disks. The distance between the disks was kept constant and the flow Reynolds number varied from 10 to 1000. It was found that for Re<62 the flow is parallel. At Re=62 separation regions start to be observed, and for Re=113 the flow bifurcates in symmetric and asymmetric configurations. The bifurcation was detected through the existence of multiple solutions for the Navier-Stokes equation.

III ENCIT – Itapema, SC (Dezembro 1990)

ON THE INTRODUCTION OF ARTIFICIAL DISSIPATION IN NUMERICAL METHODS FOR FLUID FLOW PROBLEMS

Antonio Fábio Carvalho da Silva
Clovis Raimundo Maliska

Department of Mechanical Enginnering
P.O.Box, 476 - 88049 Florianópolis - SC - Brazil

SUMMARY

When finite volume methods are used in the solution of fluid flow problems it is normally employed some form of upwinding in order to avoid solution instabilities. In this paper the artificial dissipation introduced when upstream differencing is used is quantified in terms of the cell Peclet number, allowing a better understanding of the role of the numerical diffusion in the context of finite volume methods. It is shown that the upstream scheme is equivalent of using central differencing with the addition of a second order non linear artificial dissipation.

INTRODUCTION

Among the procedures for discretizing the governing partial differential equations of a fluid flow problem, two of them are largely employed by numerical analysts.

In the solution methods known as finite volume or control volume methods the equations in their divergent form are integrated over finite volumes conveniently layed out over the solution domain. As a result of the integration procedure the value of the dependent variable and its spatial derivative are required at the control volume interfaces. As the dependent variable is stored in the center of the control volume, interpolation functions are necessary to evaluate the interface values. The choice of the interpolation functions is of key importance in the solution methodology. Several are the existing possibilities, and each one gives rise to a different numerical solution for the same physical problem, since the interpolation function is intimately connected with the quality of the numerical method. Besides that, the stability of the method, normally of iterative nature, is strongly dependent of the interpolation function.

The simplest choice, the linear interpolation, is not always recommended due to several reasons. First of all, when the cell Reynolds number at the interface is greater than two, the coefficient which connects the dependent variable of the volume under consideration to the adjacent control volume results negative. If iterative methods of solution, like poiny-by-point, line-by-line, etc. are employed, the negative coefficients may cause divergence of the iterative procedure. In addition the central difference scheme (CDS), as is known the procedure where the interpolation is linear, is not dissipative, that is, it does not provide extra mechanisms for the dissipation of errors and perturbations that may occur during the solution, as can be demontrated through a linear stability analysis applied to algebraic operators. As a consequence the convergence rate of the CDS scheme is slow and the converged solutions may present undesirable wiggles. To avoid such a behaviour other differencing schemes are normally used. These schemes are designed in order to maintain the coefficients positive irrespect of the cell Reynolds number, thus allowing the solution to be obtained using the above cited iterative methods for the solution of the linear systems. Many of these schemes have the characteristics of recovering the CDS procedure when the cell Reynolds number is small and the UDS [1] when the cell Reynolds number is large. In the latter case the solution is said to be first order accurate. For intermediate values of the cell Reynolds number the methods use to evaluate the dependent variable at the control volume interface through the exact solution of the one-dimensional diffusion/convection problem. Due to this physical reasoning involving the evaluation of the flow properties at the interfaces these schemes are said to be more physically consistent than the CDS scheme.

In the solution of aerodynamic problems, specially the supersonic ones, the occurence of cell Reynolds number of order of 10000 is not uncommon. In these cases, even if sophisticated interpolation functions, using the cell Reynolds number as the main parameter, are used, the results will be equivalent of using the UDS scheme.

Turning the attention now to the finite difference method, it is seen that the discretization process is conceptually quite different. In these methods the derivatives of first and second order present in the partial differential equation are replaced by their numerical counterpart, normally in central form with the aim of minimizing the truncation errors of the approximation. To promote the stability of the solution, dissipative terms are added to the partial differential equations. Since these terms are chosen to be of fourth order the formal accuracy of the method remains of second order.

In the present work some techniques for introducing artificial dissipation are discussed. Solving the very well known lid-driven cavity problem, firstly it is demonstrated that the UDS scheme is analogous to the CDS scheme with a non-linear second order artificial dissipation. Following, the influences of the second and fourth order dissipative terms with constant coefficients are compared with the influences of the UDS scheme. Also, the results using the UDS scheme and using a fourth order scheme in the solution of a supersonic flow problem are compared. Finally, it is demontrated that the amount of artificial dissipation introduced by the UDS scheme is far more than necessary to guarantee the stability of the solution.

EQUIVALENCE BETWEEN UPWINDING AND ARTIFICIAL DISSIPATION

Recently [2] a segregated formulation in delta form was implemented. The important characteristic of this formulation is the fact that the unknows are temporal variations of the conserved properties. This approach is usually employed in the solution of compressible flows using finite-difference techniques with the linear systems originated from each conservation equation solved simultaneously. The

delta form has several advantages and no drawbacks when compared with conventional segregated formulations. Results pointing out these advantages are reported in [2] and [3].

For the sake of simplicity, consider the laminar, two dimensional, incompressible flow with constant properties. The discretized equations written for a generic scalar ϕ in delta form are [2]

$$a_P\Delta\phi_P - a_e\Delta\phi_E - a_w\Delta\phi_W - a_n\Delta\phi_N - a_s\Delta\phi_S = RHS \quad (1)$$

where

$$RHS = -\left[J_e - J_w + J_n - J_s\right] - L\,[P^{\phi}]^t \quad (2)$$

In Eq.(2) J denotes the convective and diffusive flux of ϕ at the interfaces of the elemental control volume. The RHS corresponds to the discretization of the steady state part of the partial differential equation. Writing ϕ and its derivative for the east face, for example, of a control volume by

$$\phi_e = (1/2+\alpha)\phi_P + (1/2-\alpha)\phi_E \quad ; \quad \left.\frac{\partial\phi}{\partial x}\right|_e = \beta\,\frac{\phi_E - \phi_P}{\Delta x} \quad (3)$$

the Eq.(2) can be put in the following form

$$RHS = -a_p^*\phi_P^t + a_e^*\phi_E^t + a_w^*\phi_W^t + a_n^*\phi_N^t + a_s^*\phi_S^t - L[P^{\phi}]^t\Delta V \quad (4)$$

Note that the term RHS depends only on known values and the coefficients a_p^*, a_e^*,... are not trully coefficients of a linear set of equations like the coefficients a_p, a_e, a_w,... present in the left hand side of Eq.(1). Note also that all the schemes based on one-dimensional interpolations are recovered with the use of Eq.(3). If the CDS scheme ($\alpha = 0$, $\beta = 1.0$) or UDS ($|\alpha| = 0.5$, $\beta = 1.0$) is employed, the a_e^* coefficient results, respectively

$$[a_e^*]_{CDS} = -\dot{M}_e/2 + D_e \quad (5)$$

or

$$[a_e^*]_{UDS} = (|\dot{M}_e| - \dot{M}_e)/2 + D_e \quad (6)$$

where

$$D_e = \Gamma^{\phi}\Delta y/\Delta x \quad ; \quad \dot{M}_e = \rho u_e \Delta y \quad (7)$$

Eq.(6), after some algebraic manipulations can be put in the form

$$[a_e^*]_{UDS} = -\dot{M}_e/2 + \Gamma^{\phi}\left[1 + |Pe|_e/2\right]\frac{\Delta y}{\Delta x} \quad (8)$$

where Pe is the Peclet number (Reynolds number in the case of momentum conservation) defined by

$$Pe|_e = \rho u_e \Delta x/\Gamma^{\phi} \quad (9)$$

If an effective diffusion coefficient is defined as

$$\Gamma^{\phi}_{eff} = \Gamma^{\phi}[1 + |Pe|_e/2] \quad (10)$$

Eq.(8) results

$$[a_e^*]_{UDS} = -\dot{M}_e/2 + D_{eff,e} \quad (11)$$

where

$$D_{eff} = \Gamma_{eff}\Delta y/\Delta x \quad (12)$$

Eq.(11) demonstrates that the coefficient obtained using the UDS approach is equivalent of using the CDS approach with an effective diffusion coefficient given by Eq.(10). Numerical experiments show that the solutions obtained with the UDS approach applied through Eq.(6) or Eq.(10) are identical. It is important to remember that in the solution of high speed flows the effective coefficient is much larger than the molecular coefficient.

As a conclusion, the UDS scheme is equivalent to the CDS scheme with a non-linear second-order dissipative term added to the discretized partial differential equations. Relations similar to Eq.(10) can be obtained for other schemes as exponential [1], WUDS [8], etc. Following, the consequences of the UDS scheme when applied to a specific problem are discussed. In fact the analysis is valid for all schemes represented by Eq.(3) but with a little more difficulty of identification.

Consequences of using the UDS Scheme. Solving the lid-driven cavity problem with Reynolds number equal to 1000, where the characteristic dimension is taken as the side of the square cavity and the characteristic velocity the velocity of the moving wall, using the CDS scheme with a 10X10 grid, the maximum nodal velocity, dimensionless with respect to the wall velocity, is 0.3732. Using the UDS scheme the same velocity reduces its value to 0.3098. Of course, the difference is not seen only in the maximum velocity. All fields of u, v and P show considerable differences. It is clear that with a very fine grid both results should be coincident, since the artificial diffusion introduced with the UDS diminishes with the cell size and both schemes reduce to the same.

The understanding that the UDS scheme is equivalent to the CDS with an artificial dissipation helps to explain why the maximum velocity is smaller when the UDS scheme is applied. The computation of the artificial dissipation coefficient, according to Eq.(10), at the interfaces of the control volumes will show that this coefficient is up to 15 times greater than the molecular coefficient. Using the UDS the artificial diffusion will only be zero at the walls of the cavity since they are impermeable, reducing the cell Reynolds number to zero. Therefore, the solution using UDS is physically equivalent of solving the problem of the lid-driven cavity with a fluid with different molecular viscosity, smaller at the wall. Since the movement of the interior fluid is induced by the stress occuring at the wall, it is clear why the maximum velocity is smaller using UDS.

Another very important point is to answer when to use the CDS or the UDS scheme. Obviously, the answer depends on the definition of criteria to be followed:

i) If the computer effort is taken into account the difference is considerable. 87 iterations for the UDS scheme against 212 for the CDS (keeping all other parameters constant). This behaviour is, as already discussed, due to the non-dissipative character of the CDS scheme.

ii) If the solution quality is the prime parameter, the solution obtained using CDS is superior, in the present test, as demonstrated by a grid refinement study.

In fact, the best way to answer this question would be to compare the solutions obtained with the same computer effort using both schemes. For the same computer effort the UDS scheme would allow the use of more refined grid. This test was not implemented because, among another reasons, the conclusion depends on the specific problem under analysis and so, can not be generalized.

ARTIFICIAL DISSIPATION WITH CONSTANT COEFFICIENTS

In the majority of the methods applied in the solutions of aerodynamic problems the discretization is done through finite-differences. To promote stability fourth-order dissipative terms with constant coefficients are introduced. Besides the fact that these terms are not expected to damage the solution it is illustrative to investigate the influences of second-order terms (like UDS) on the solution. To this end the lid-driven cavity problem is again considered.

A second-order dissipation can be introduced simply adding to the RHS term given by Eq.(4) a term $D_e^{(2)}$ of the type

$$D_e^{(2)} = \omega_e(\phi_N - 2\phi_P + \phi_S) + \omega_e(\phi_E - 2\phi_P + \phi_W) \quad (13)$$

where ω_e is the artificial dissipation coefficient and the subscript indicates that it actuates in the explicit part of the discretized governing equations. If the problem is solved with the RHS term evaluated using CDS and with $\omega_e = 0.003$ the solution is obtained in 80 iterations against 212 of the original CDS. The maximum nodal velocity, however, increased to 0.5601, is much larger than the ones reported above. It is easy to verify that the solution via CDS with $\omega_e = 0.003$ is identical to the solution via CDS with $\omega_e = 0.0$ and

$$Re_L = \frac{1}{0.001 + 0.003} = 250 \quad (14)$$

In fact, to add the dissipative terms given by Eq.(13) is equivalent of increasing the molecular viscosity of the fluid. Note that the dissipative coefficient introduced is three times the molecular coefficient, while in the solution via UDS (with dissipative terms of second-order but non-linear) this coefficient, in the problem analysed, varies from zero to 15 times the molecular coefficient. Futhermore, note that the same result obtained with $\omega_e = 0.003$ could be obtained simply placing $\alpha = 0$ and $\beta = 4$ in Eq.(3).

Fourth-order dissipation can be introduced if it is added to the RHS given by Eq.(4) terms like

$$D_e^{(4)} = \omega_e(\phi_{NN} - 4\phi_N + 6\phi_P - 4\phi_S + \phi_{SS}) +$$

$$+ \omega_e(\phi_{EE} - 4\phi_E + 6\phi_P - 4\phi_W + \phi_{WW}) \quad (15)$$

The number of iterations decreases with ω_e up to $\omega_e = 0.001$, when 145 iterations are needed, resulting in a maximum velocity of 0.51055. However, for ω_e larger than 0.001 the procedure diverges. The linear stability analysis applied to the methods of simultaneous solution show that the ω_e coefficient is upper bounded [4] and that this limit can be extended if second-order artificial dissipation is added to the left hand side of the equation, that is, to the implicit part of the equation.

An implicit second-order dissipation can be introduced if it is added to the left hand side a term of the type

$$D_i^{(2)} = -\omega_i \{[(\Delta\phi)_E - 2(\Delta\phi)_P + (\Delta\phi)_W] +$$

$$[(\Delta\phi)_N - 2(\Delta\phi)_P + (\Delta\phi)_S]\} \quad (16)$$

As a consequence the coefficients a_e, a_w, a_n e a_s will be augmented of ω_i while the a_p coefficient will be augmented of four times ω_i. As expected, for $\omega_i = 0.004$, the limit of ω_e, of 0.001 before, is extended to 0.0032. There is no, however, improvements in the convergence rate and the solution is poorer than the one obtained via CDS. The introduction of implicit dissipation with coefficient equal to 0.004, for example, is equivalent to adopt $\beta = 5$ in Eq.(3). Recall that the steady state solution does not depend on the coefficient evaluation when the formulation is in delta form.

A FINITE-VOLUME SCHEME FOR THE SIMULTANEOUS METHODS

In the methods where the discretization of the equations is done through central finite-differencing the convective term $-\partial(\rho uu)/\partial x$, for example, is approximated by

$$\frac{\partial}{\partial x}(\rho uu) \cong [(\rho uu)_E - (\rho uu)_W]/(2\Delta x) \quad (17)$$

where the E and W locations are shown in Fig. 1.

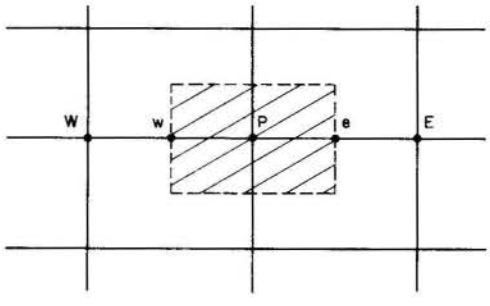

Fig. 1 A control volume for the B&W scheme.

In the other hand, one can imagine a control volume surrounding P and evaluate the same derivative through the following expression

$$\frac{\partial}{\partial x}(\rho uu) = [(\rho uu)_e - (\rho uu)_w]/\Delta x \quad (18)$$

Consider now the first part in the interior of the brackets. The term $(\rho uu)_e$ can be split in the product of a mass flux by a momentum flux, i.e,

$$(\rho uu)_e = (\rho u)_e (u)_e \quad (19)$$

Like in the segregated finite volume method, the mass flux can be estimated through the averaging process given by

$$(\rho u)_e = [(\rho u)_P + (\rho u)_E]/2 \quad (20)$$

The u velocity at east face can be evaluated by several schemes. In the next section results will be reported where the value of all the dependent variables at the interfaces were evaluated by the UDS scheme.

ANALYSIS OF THE INFLUENCES OF SEVERAL DISSIPATIVE TERMS IN THE SOLUTION OF A COMPRESSIBLE FLOW PROBLEM

The several schemes to intoduce artificial dissipation reported previously were implemented for the solution of the axisymmetric flow of air with free-stream Mach number equal to 1.5 against an hemisphere-cylinder shown in the insert of Fig. 2. The figure shows curves of C_p along the symmetry line obtained using simultaneous and segregated methods for several types of artificial dissipation. The solutions should predict the presence of a shock located approximately at $x/R = -0.6$ [7]. The curve (a) was obtained using the scheme proposed by Beam and Warming [4] with fourth-order dissipation with constant coefficients. The solution shows a smeared shock due

to the coarse grid employed. The non-physical prediction of negative C_p before the shock wave is characteristic of the fourth-order schemes. The (b) curve was obtained using the segregated method due to Maliska and Silva [6], implemented in nonorthogonal coordinates with the coefficients in all equations, included mass conservation, evaluated via CDS. The oscillation in the solution is not surprising since it is a characteristic of solutions free of extra dissipative terms in high Reynolds number flows. The shock, however, is well captured and located in only two cells. The curve (c) was obtained by the same scheme of curve (b) but with the CDS replaced by UDS. It is noted that there is no irrealistic values nor oscilations of C_p but the shock is strongly attenuated. If in the Beam and Warming scheme, the explicit part of the equations is evaluated using the UDS scheme, in the finite-volume approach proposed in the previous section of the present work, the C_p distribution (not shown in Fig. 2) is very similar to curve (c). This fact clearly demonstrates that the differences in the solutions must be credited to the way in which artificial dissipation is introduced. It should be also mentioned that in this case it is no longer needed to apply artificial dissipation to the simultaneous scheme through expressions like Eq.(15). Finally, it was tested a different scheme, were the number 2 appearing dividing the Peclet number in Eq.(10) is substituted by 20, giving rise to a dissipative scheme, non-linear, with ten times less dissipation than the UDS. The result is shown in curve (d). The shock is well captured, as in the case of the fourth-order scheme but without the negative values of C_p and maintaining the same convergence rate of the UDS scheme.

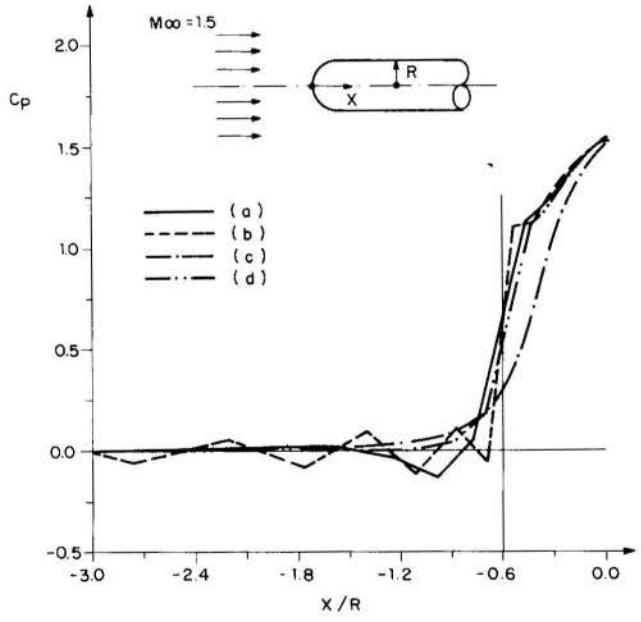

Fig. 2 The C_p curve obtained with a)the original Beam & Warming scheme and fourth order dissipation; b) the segregated FV scheme and CDS; c) the segregated FV scheme and UDS, and d) the segregated FV scheme and reduced artificial dissipation.

CONCLUDING REMARKS

The outcome of the present work reveals that:

a) The majority of the interpolation schemes employed in the finite-volume methods can be put in the form of a CDS scheme with the addition of non-linear second-order dissipation;

b) These schemes, which reduce to the UDS scheme for high cell Peclet numbers, introduce much more dissipative effects than necessary to promote stability and to eliminate spurious oscillations in the solution;

c) The differences observed in the solutions obtained via the segregated methods, as the one proposed in [6], and the simultaneous methods, as the one proposed in [4], are due to the way in which artificial dissipation is introduced;

d) The second-order dissipation with constant coefficients can be implemented in the finite-volume method by simply using values of β in Eq.(3) larger than unity; and

e) It is recommended that new schemes of introducing controlled artificial dissipation be devised in the context of the segregated methods. The study should be based on stability analysis, as is done in the context of simultaneous solution methods, and not on the maintenance of the positivity of the coefficients which, as demonstrated in [2], does not influence the stability of the iterative procedure.

ACKNOWLEDGMENTS

The partial financial support provided by Instituto de Atividades Espaciais/CTA is gratefully acknowledged.

REFERENCES

[1] Patankar, S., Numerical Heat Transfer and Fluid Flow, McGraw-Hill, New York, 1980.

[2] Silva, A.F.C. and Maliska, C.R., A Segregated Finite-Volume Method in Delta Form, Internal Report, Mechanical Engineering Dept., SINMEC - Computational Fluid Mechanics and Heat Transfer Group, SC, Brazil, 1990.

[3] Silva, A.F.C. and Maliska, C.R., An Approximate Factorization Scheme Applied to the Segregated Finite-Volume Methods, Proceedings of the III National Meeting of Thermal Sciences, Itapema, Brazil, 1990.

[4] Beam, R.M. and Warming, R.F., An Implicit Factored Scheme for the Compressible Navier-Stokes Equations, AIAA Journal, Vol.16, no.4, pp.393-402, 1978.

[5] Anderson, D.A.; Tannehill, J.C. and Pletcher, R.H., Computational Fluid Mechanics and Heat Transfer. McGraw-Hill, Washington, 1984.

[6] Maliska, C.R. and Silva, A.F.C., A Boundary-Fitted Finite Volume Method for the Solution of Compressible and/or Incompressible Fluid Flows using Both Velocity and Density Corrections, 7th International Conference on Finite Element Methods in Flow Problems, Huntsville, Alabama, USA, 1989.

[7] Azevedo, J.L.F., Transonic Aeroelastic Analysis of Launch Vehicle Configurations, Ph.D. Thesis, Stanford University, USA, 1988.

[8] Raithby, G.D., Prediction of Dispersion by Surface Discharge, Basin Investigation and Modelling Section, Canada Centre for Inland Waters, Burlington, Ontario, Canada, 1976.

III ENCIT – Itapema, SC (Dezembro 1990)

AN APPROXIMATE FACTORIZATION SCHEME APPLIED TO THE SEGREGATED FINITE-VOLUME METHODS

Antonio Fábio Carvalho da Silva
Clóvis Raimundo Maliska

Department of Mechanical Engineering
Federal University of Santa Catarina
P.O.Box, 476 - 88049 Florianópolis - SC - Brazil

SUMMARY

The approximate factorization (AF) scheme is largely employed in the methods in which the equation systems are solved simultaneously, like the well known Beam and Warming method. The advantage of the AF procedure is that two and three dimensional problems can be solved as a sequence of one dimensional problems.. The extension of the AF scheme, applied to the conventional segregated methods, realized in this work, demonstrates that the procedure works well for small time steps. For large time steps the procedure can be applied only to the momentum conservation equations.

INTRODUCTION

The numerical prediction of fluid flow and heat transfer phenomena normally leads to the solution of linear systems of algebraic equations. When the discretization is done using a structured grid the resulting matrix possesses a well defined structure. Using the finite volume approach, the matrices have, in problems defined in simply connected domains or without repetitive boundary conditions, a number of non zero diagonals equals to: i) five, in 2D problems employing a orthogonal discretization; ii) nine, in 2D problems with nonorthogonal discretization; iii) seven, in 3D problems with orthogonal discretization and iv) nine in 3D problems with a nonorthogonal discretization. These numbers increases if high order schemes are used to evaluate the convective and diffusive terms at the interfaces of the elemental control volume and decreases if some terms are explicitly evaluated, that is, they are added to the independent vector. In real problems when the discretization needs to be very fine the direct solutions of these equation systems is unfeasible.

In the methodologies which follow the procedure outlined in [1], the solution of the linear system of equations is generally done using iterative methods. These methods can be classified as implicit or semi-implicit, depending on the number of terms of the matrix which are removed from the matrix coefficients and introduced in the independent vector. In these methodologies, since the linear systems originated from each conservation principle are solved in a segregated manner, other iterative levels are needed for updating the coefficients and the source terms.

In the other hand, in the numerical schemes similar to the one proposed by Beam and Warming [2], where the equations are linearized using a Newton-Raphson procedure and are solved simultaneously, the only source of iteration is related to the solution of the linear system involved. It is wise to point out that, in these schemes, to each element in a matrix originated from a segregated approach corresponds to a 4X4 or 5X5 sub-matrix, depending wether the problem is 2D or 3D. This difficulty, however, is partially removed by the use of the approximate factorization process, where 2D and 3D problems are solved as a sequence of one dimensional ones. In this manner the matrices assume a block tridiagonal structure, to which efficient solvers can be applied [3] making the process, as a whole, non iterative.

The main goal of the present work is the development of an approximate factorization scheme applied to the solution of linear systems originated from methods which uses the segregated approach.

THE APPROXIMATE FACTORIZATION (AF) SCHEME APPLIED TO THE SIMULTANEOUS SOLUTION

In the solution of compressible flows the partial differential equations are linearized expanding the non linear terms about a known solution in time. The procedure is analogous to the Newton-Raphson method applied for the solution of non linear algebraic equations. Due to this linearization process the governing differential equations need to be solved simultaneously.

Consider, as an example, the 2D compressible flow of an inviscid fluid. The governing equations written in delta form [2][3], after the linearization process and time discretization assume the following form

$$\Delta U + \Delta t \left[\frac{\partial}{\partial x} (A\Delta U) + \frac{\partial}{\partial y} (B\Delta U) \right] = RHS \qquad (1)$$

where [A] and [B] are the jacobian matrices originated from the linearization process. ΔU is the time variation of the vector U, whose components are ρ, ρu, ρv and E_t, where E_t is the total energy by volume. After the spatial discretization of the derivatives, Eq.(1) gives rise to a block pentadiagonal linear system, where each block is a 4X4 matrix. The solution of this linear system is not trivial. Consider now the Eq.(1) written in the form of a differential operator applied to a unknown vector ΔU, resulting

$$\left[I + \Delta t \left[\frac{\partial A}{\partial x} + \frac{\partial B}{\partial y} \right] \right] \Delta U = RHS \qquad (2)$$

To avoid the solution of a block-pentadiagonal matrix, the differential operator is split in the product of two onedimensional operators, resulting in

$$\left[I + \Delta t \frac{\partial A}{\partial x} \right] \left[I + \Delta t \frac{\partial B}{\partial y} \right] \Delta U = RHS \qquad (3)$$

If one defines an auxiliary vector ΔU^* as

$$\Delta U^* = \left[I + \Delta t \frac{\partial B}{\partial y} \right] \Delta U \qquad (4)$$

and substitutes Eq.(4) in Eq.(3), ΔU^* can be found through the solution of a block tridiagonal matrix. Since ΔU^* is known, the ΔU vector can be found in the same manner using Eq.(4). In this way a 2D problem was solved through a solution of two 1D problems.

Obviously, the product of one-dimensional operators does not reproduce the original 2D operator, introducing an error in the ΔU vector. This error, however, is of order Δt^2, which is the same order of the errors introduced in the time discretization of the governing differential equations. Therefore, the approximate factorization process does not alter the order of the approximation errors of the whole solution, and the scheme can be considered as non-iterative. Recall that when the steady state is reached, the RHS of Eq.(2) vanishes and the only distribution of U which produces ΔU equal to zero is the distribution which satisfies the steady part of the discretized differential equations. Therefore, if the procedure converges, the solution obtained will be the correct solution for the steady state.

The approximate factorization scheme is widely used in the solution of compressible flows where the governing equations are solved simultaneously. The observed drawback of the process is the slow convergence when Δt increases, specially in 3D problems [4].

THE SOLUTION METHODS EMPLOYED IN THE CONVENTIONAL SEGREGATED FORMULATION

In the segregated formulation using finite-volume methods the differential equations are represented, for a 2D problem for example, as

$$\frac{\partial}{\partial t}(\rho\phi) + \frac{\partial}{\partial x}(\rho u\phi) + \frac{\partial}{\partial y}(\rho v\phi) = -P^{\phi} + \Gamma^{\phi}\left[\frac{\partial^2\phi}{\partial x^2} + \frac{\partial^2\phi}{\partial y^2}\right] \quad (5)$$

where ϕ plays the role of ρ, u, v, T, etc. The appearence of the diffusive terms, not included when the simultaneously formulation was described, and the exclusion of source terms are immaterial for the purpose of what follows. Eq.(5) discretized using finite volume method results in

$$a_p\phi_P - a_e^*\phi_E - a_w^*\phi_W - a_n^*\phi_N - a_s^*\phi_S = b \quad (6)$$

or, in matrix form, as

$$[A]\{\phi\} = \{b\} \quad (7)$$

As already pointed out, the direct solution of Eq.(7) is unfeasible. So, iterative procedures are employed, like the point-by-point Jacobi, Gauss-Seidel and SOR methods or the line-by-line methods, which requires the aplication of the TDMA [1] solver in lines and columns. Strongly implicit techniques are also used, like SIP [5], MSI [6] and the SIP version proposed in [7]. The point-by-point and line-by-line techniques, although easy in programing and efficient in coarse meshes are too time consuming in refined grids. Besides that, because of the explicit nature of the procedures, they require the positivity of the coefficients for achieving convergence [1][8]. This requirement is very strong since, for assuring the positivity of the coefficients, it is necessary to introduce some form of upwinding in the evaluation of the fluxes at the interfaces, with the consequent degradation of the solution due to numerical diffusion. One of the characteristics of the methodologies just mentioned is the capability of eliminating high frequency errors in the solution during the iterative procedure. The use of block correction schemes or multi-grid techniques speeds up the convergence process because they actuate in the damping of low frequency errors [9]. In the other hand, the strongly implicit procedures, based on the LU decomposition of the matrix of coefficients, although iterative, possess a high rate of convergence.

THE SEGREGATED FINITE-VOLUME METHOD IN DELTA FORM

If the exact solution of Eq.(7) is obtained, the errors in the distribution during the transient will be due solely to the spatial and temporal discretization. If the solution is iterative, another error is introduced depending on the truncation of the iterative cycles (convergence criterion). Even when the interest lies in the steady state solution if Eq.(7) is not solved subjected to a very strong convergence criterion, the resulting steady state solution will be wrong. It is well known the irrealistic solutions obtained when only few Jacobi iterations are performed.

Recently [8] the authors developed a segregated formulation in delta form. The main characteristic of this formulation is that the dependent variables are the time variations of the conserved properties. In delta form Eq.(6) assumes the following form

$$a_p\Delta\phi_P - a_e^*\Delta\phi_E - a_w^*\Delta\phi_W - a_n^*\Delta\phi_N - a_s^*\Delta\phi_S = RHS \quad (8)$$

where

$$\Delta\phi = \phi^{t+\Delta t} - \phi^{t} \quad (9)$$

Details of the development and a few tests can be found in [8]. By now it suffices to say that the term RHS is evaluated using known variables from the previous time level and it corresponds to the discretization of the steady state part of the governing differential equation, Eq.(5). Therefore, when the steady state is reached the RHS and, of course, $\Delta\phi$ vanish.

AN APPROXIMATE FACTORIZATION SCHEME APPLIED TO THE SEGREGATED FINITE VOLUME METHOD

The solution of Eq.(8) can be obtained by the same methods employed in the solution of Eq.(6). However, the delta form has the advantage that when the steady state is reached the RHS is zero, implying in a zero time variation for ϕ, even if approximate methods are used in the solution of Eq.(8). Therefore, the basic idea is, following what is done in the simultaneous solution methods, to develop a direct method for the solution of Eq.(8) whose errors introduced in the transient solutions be acceptable. To this end, consider Eq.(8) divided by a_p, resulting

$$\Delta\phi_P - a_e\Delta\phi_E - a_w\Delta\phi_W - a_n\Delta\phi_N - a_s\Delta\phi_S = RHS \quad (10)$$

For simplicity, consider the case in which the domain have been discretized by a 3X3 grid, without the use of fictitious points, shown in Fig.1.

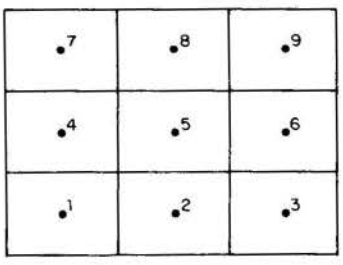

Fig. 1 A 3X3 grid.

The system of equations given by Eq.(10) can be represented by the following equation

$$[A]\{\Delta\phi\} = \{RHS\} \quad (11)$$

and the matrix [A] assumes the form

$$[A] = \begin{bmatrix} 1 & a_e & & a_n & & & & & \\ a_w & 1 & a_e & & a_n & & & & \\ & a_w & 1 & & & a_n & & & \\ a_s & & & 1 & a_e & & a_n & & \\ & a_s & & a_w & 1 & a_e & & a_n & \\ & & a_s & & a_w & 1 & & & a_n \\ & & & a_s & & & 1 & a_e & \\ & & & & a_s & & a_w & 1 & a_e \\ & & & & & a_s & & a_w & 1 \end{bmatrix} \quad (12)$$

An approximate factorization process to this problem can be established if one replaces the original problem, Eq.(11), by the problem

$$[A_x]\,[A_y]\,\{\Delta\phi\} = \{RHS\} \quad (13)$$

where

$$[A_x] = \begin{bmatrix} 1 & a_e & & & & & & & \\ a_w & 1 & a_e & & & & & & \\ & a_w & 1 & & & & & & \\ & & & 1 & a_e & & & & \\ & & & a_w & 1 & a_e & & & \\ & & & & a_w & 1 & & & \\ & & & & & & 1 & a_e & \\ & & & & & & a_w & 1 & a_e \\ & & & & & & & a_w & 1 \end{bmatrix} \quad (14)$$

and

$$[A_y] = \begin{bmatrix} 1 & & & a_n & & & & & \\ & 1 & & & a_n & & & & \\ & & 1 & & & a_n & & & \\ a_s & & & 1 & & & a_n & & \\ & a_s & & & 1 & & & a_n & \\ & & a_s & & & 1 & & & a_n \\ & & & a_s & & & 1 & & \\ & & & & a_s & & & 1 & \\ & & & & & a_s & & & 1 \end{bmatrix} \quad (15)$$

If one defines $\{\Delta\phi^*\}$ by

$$\{\Delta\phi^*\} = [A_y]\,\{\Delta\phi\} \quad (16)$$

Eq.(13) results

$$[A_x]\,\{\Delta\phi^*\} = \{RHS\} \quad (17)$$

Eq.(17) is a one-dimensional problem and can be easily solved through a TDMA-like procedure. In the sequence, Eq.(16) allows the calculation of $\{\Delta\phi\}$ in a similar fashion. Obviously, the approximate factorization procedure given by Eq.(13) does not reproduce the original problem given by Eq.(11). New terms, involving the product of two of the coefficients of the original system of equations, are present and are analogous to that which appears in Eq.(3) in excess to Eq.(2), related to the simultaneous scheme. Therefore, the problem actually solved by the aproximate factorization scheme is

$$\Delta\phi_P - a_e\Delta\phi_E - a_w\Delta\phi_W - a_n\Delta\phi_N - a_s\Delta\phi_S - a_ne\Delta\phi_{NE} - a_se\Delta\phi_{SE} - a_nw\Delta\phi_{NW} - a_sw\Delta\phi_{SW} = RHS \quad (18)$$

SOME NUMERICAL EXPERIMENTS

As a test, the well known problem of the lid-driven cavity was chosen. The solution was obtained for several values of the dimensionless time step defined as $\Delta t^* = \Delta t \cdot L/u_{wall}$, with Reynolds number equal to 1000. The cavity was discretized using a 10X10 grid uniformely spaced, and the SIMPLEC [10] method was used to deal with the pressure-velocity coupling. The solution was considered converged when

$$\frac{|\Delta\phi|}{u_{wall}} \leq 10^{-6} \quad (19)$$

for ϕ equal to u and v, in every cell of the domain. For the purpose of the test, a problem involving only a scalar field, like a conduction problem, could be solved. However, the chosen problem is far more complex, because it is a nonlinear problem with a strong coupling between the equations. Table 1 shows the number of iterations and the CPU effort in seconds to reach convergence, as a function of the dimensionless time step for three different situations, as i) the approximate factorization is not applied; ii) it is applied in the solution of the momentum equations, and iii) it is applied to all three linear systems, comprising momentum and mass conservation. When the approximate factorization process is not applied the equations are solved using the MSI [6] procedure. For the evaluation of ϕ at the interfaces of the control volumes the UDS scheme [1] was applied.

Table 1. Performance of the AF process with UDS.

Δt^*	MSI		AF in u,v		AF in u,v,P	
	IT	CPU	IT	CPU	IT	CPU
0.2	266	15.1	268	11.9	270	9.7
0.4	148	8.6	151	6.9	156	5.7
0.6	107	6.4	111	5.2	120	4.6
0.8	87	5.2	92	4.4	103	4.0
1.0	75	4.5	80	3.9	101	3.9
1.2	68	4.2	74	3.6	106	4.0
1.4	64	4.0	70	3.5	114	4.3
1.6	62	3.8	67	3.3	120	4.5
1.8	61	3.6	66	3.2	129	4.8
2.0	61	3.6	66	3.1	138	5.1

The results obtained demonstrate the savings in the computer effort when the approximate factorization is applied in the solution of the momentum equations, although the number of iterations is a little higher. The results of the third column, however, show that for Δt^* higher than 1.2 the application of the factorization process does not help in the convergence rate. Such results were expected since the errors introduced in the solution varies with Δt^2 and the errors are specially damaging when related to the mass conservation equation.

Table 2 shows the results of a more severe test where the UDS scheme is replaced by the CDS scheme. Because the CDS scheme is non dissipative the convergence rate is slower even solving the linear systems using MSI. The stars in the table indicate that the convergence was not reached in 1000 iterations. The results shown that for small values of Δt^* the approximate factorization is always of benefit. However, the global performance is more susceptible to the increase of the time step. Such a behaviour is easily explained. The coefficients a_e, a_w, a_n e a_s in Eq.(10) obey the following equation

$$a_e + a_w + a_n + a_s + M_p/(a_p^y \Delta t^* M_p) = 1 \quad (20)$$

where Δt is the time step and M_p is the mass inside the control volume. When the UDS scheme is applied the coefficients are all positives, and of course, all of them less than unity (and smaller as smaller the time step is). Therefore, the additional terms originated by the approximate factorization, resulting from product of two coefficients, are also small. By its turn, in the CDS scheme the coefficients can be negative with absolute value larger than unity. In this case the additional terms are harmful to the performance of the method for smaller Δt than are for the UDS scheme. It is important to point out that the use of point-by-point and line-by-line solvers would bring the procedure to divergence due to the presence of negative coefficients.

Table 2. Performance of the AF process with CDS.

Δt^*	MSI		AF in u,v		AF in u,v,P	
	IT	CPU	IT	CPU	IT	CPU
0.2	549	30.7	549	24.2	571	20.1
0.4	313	17.7	313	14.0	364	12.9
0.6	236	13.4	236	10.7	317	11.3
0.8	202	11.6	201	9.2	314	11.2
1.0	187	10.7	183	8.4	509	17.8
1.2	182	10.5	175	7.9	*	*
1.4	182	10.5	180	7.8	*	*
1.6	187	10.6	578	23.8	*	*
1.8	195	10.9	*	*	*	*
2.0	205	11.3	*	*	*	*

In order to have more informations about the behaviour of the AF procedure, few more tests were conducted using the lid-driven cavity problem, where the grid, the Reynolds number and the dimensionless time step were changed. The outcome of the tests are as follow. Keeping the same grid and the same Reynolds number but reducing the dimensionless time step, the performance of the AF procedure is superior of the MSI irrespective of using UDS or CDS, confirming the tendencies of Table 1 and 2. In these cases the number of iterations necessary for convergence is pratically the same for the three cases, requiring less CPU effort for the AF since the time per iteration of the AF scheme is smaller. This result was expected since smaller Δt^* imply in smaller coefficients a_e, a_w, a_n and a_s according to Eq.(20).

If the grid is refined the value of Δt^* for keeping the AF procedure advantageous reduces when compared with the Δt^* values for the 10X10 grid, regardless if the UDS or CDS is used. This result is surprisingly since the grid refinement increases the diffusive part of the coefficients, improving the stability characteristics. Probably, due to the fact that the grid refinement diminishes the quantity of mass M_p inside the control volumes, this would cause larger coefficients, according to Eq.(20). Despite this fact, for small values of Δt^*, the AF procedure performs better than the MSI method. The minimum CPU effort is, however, obtained with the MSI using larger time steps, and large enough to cause divergence of the AF procedure.

Finally, tests realized with a 20X20 grid indicated that the performance of the AF, when compared with the MSI, is independent of the Reynolds number. Using CDS the number of iterations for convergence increases with the Reynolds number, but this behaviour is also present in the MSI and in the AF for the two situations analyzed.

Partial Cancellation of the Additional Terms. The solution of the linear systems of equations through the AF procedure is an approximated process due to the presence of the additional terms shown in Eq.(18). The influence of these terms can be reduced if in the algebraic equation the partial cancellation of these terms is realized before the solution is carried out. Eq.(10) is then substituted by

$$\Delta\phi_p - a_e\Delta\phi_E - a_w\Delta\phi_W - a_n\Delta\phi_N - a_s\Delta\phi_S + \alpha\,(a_n a_e\Delta\phi_{NE} + a_s a_e\Delta\phi_{SE} + a_n a_w\Delta\phi_{NW} + a_s a_w\Delta\phi_{SW}) = RHS \qquad (21)$$

where α is a relaxation parameter. In order to mantain the pentadiagonal structure the ϕ values in NE, NW, SE and SW are expressed as a function of ϕ in P, E, W, N and S by expressions like

$$\phi_{NE} = \phi_N + \phi_E - \phi_P \qquad (22)$$

Similar procedure is also used in [6]. The use of this procedure to the test case with Reynolds number equal to 1000 and a 10X10 grid gives rise to good results when the AF was applied in the solution of the momentum equations. Even adopting the CDS scheme the solution was always obtained with almost the same number of iterations as when using MSI, but with 30% less computer effort for the whole range of Δt^* examined. Unfortunatelly the time step limitation continued to restrict the application of the AF to the solution of the mass conservation equation.

CLOSURE

The main goal of the present work was the development of a non-iterative scheme using the approximate factorization concept applied to pentadiagonal systems in the segregated framework. The tests carried out to illustrate the procedure demonstrated that it performs better than the MSI scheme when solving the momentum equations employing the UDS approximation. Still using the UDS approximation but now solving the mass conservation equation the performance deteriorates requiring smaller time steps in order to converge faster than the MSI. For the CDS approximation the time steps required are even more resctritive for the AF procedure to show better performance. However, the results obtained encourages further developments of the procedure in the context of the segregated methods of solution.

Finally, the analysis of the AF process proposed in the present work when compared with the AF in the context of simultaneous solution contributes for a better understanding of the latter and its known difficulty in handling transients with large time steps.

REFERENCES

[1] Patankar, S., Numerical Heat Transfer and Fluid Flow, McGraw-Hill, New York, 1980.

[2] Beam, R.M. and Warming, R.F., An Implicit Factored Scheme for the Compressible Navier-Stokes Equations, AIAA Journal, Vol.16, no.4, pp.393-402, 1978.

[3] Anderson, D.A.; Tannehill, J.C. and Pletcher, R.H. Computational Fluid Mechanics and Heat Transfer, McGraw-Hill, Washington, 1984.

[4] MacCormack, R.W., On the Development of Efficient Algorithms for Three Dimensional Fluid Flow, Journal of The Brazilian Society of Mechanical Sciences, vol.X, no.4, pp.323-346, 1988.

[5] Stone, H.L., Iterative Solution of Implicit Approximations of Multidimensional Partial Differential Equations, SIAM J. Numer. Anal., vol.5, pp.530-558, 1968.

[6] Schneider, G.E. and Zedan, M., A Modified Strongly Implicit Procedure for the Numerical Solution of Field Problems. Numerical Heat Transfer, vol. 4, pp.1-19, 1981.

[7] Peric, M., Efficient Semi-Implicit Solving Algorithm for Nine-Diagonal Coefficient Matrix, Numerical Heat Transfer, vol.11, pp.251-279, 1987.

[8] Silva, A.F.C. and Maliska, C.R., A Segregated Finite-Volume Method in Delta Form, Internal Report, Mechanical Engineering Dept., SINMEC - Computational Fluid Mechanics and Heat Transfer Group, SC, Brazil, 1990.

[9] Hutchinson, B.R and Raithby, G.D., A Multigrid Method Based on the Additive Correction Strategy, Numerical Heat Transfer, vol.9, pp.511-537 (1986).

[10] Van Doormaal, J.P. and Raithby, G.D., Enhancements of the SIMPLE Method for Predicting Incompressible Fluid Flows, Numerical Heat Transfer, Vol.7, pp.147-163, 1984.

III ENCIT – Itapema, SC (Dezembro 1990)

THE PIECE-WISE PARABOLIC FINITE ANALYTIC METHOD

Yuping Sun and Julio Militzer
Department of Mechanical Engineering
Technical University of Nova Scotia, P.O.Box 1000
Halifax, Nova Scotia, B3J 2X4 Canada

SUMMARY

In order to meet both the qualitative and quantative requirements of the convective diffusion process, a numerical scheme, called the Piece-Wise Parabolic Finite Analytic Method, is established using a piece-wise parabolic function as boundary condition. This scheme incorporates the local analytic solution of the convective diffusion equation into the numerical scheme. It is free from numerical diffusion and automatically incorporates the convective diffusion effects. The Piece-Wise Parabolic Finite Analytic Method (PPFAM) is used to discretize the stream function equation and vorticity equation. The numerical scheme thus obtained is used to simulate a laminar cavity flow and a laminar backward facing step flow. The numerical simulation shows that the PPFAM is the least affected by numerical diffusion among traditional numerical schemes and that it can provide a stable and accurate numerical solution for real flow problems.

INTRODUCTION

In Computational Fluid Dynamics (CFD) the traditional approach is to divide the calculation domain into a finite number of cells or calculation domains and assume that the dependent varibale has a unique value within the domain. The governing differential equations are replaced by algebraic equations using, for instance, Talyor series expansion to represent the different derivatives. This inherently introduces a truncation error. Among the several different schemes the Central Differencing Scheme (CDS) is second order, however, it is stable only for very small cell Reynolds numbers. In convection dominated flows the cell Reynolds numbers usually exceed those for which the CDS is still stable. To address this difficulty the so called Up-Wind Differencing Scheme, initially proposed by Courani et al [1], was developed. However, the stability is achieved at the cost of introducing large numerical diffusion and truncation error. Numerical diffusion is especially high when the grid is not aligned with the flow. Higher order approximations have been used to try to cure the problems arising from truncation. Leonard[2], for instance, developed a quadratic upwind interpolation formula. His formulation, however, may lead to negative coefficients, thus violating the maximam and minimum principle of the convective diffusion process. Patankar[3] proposed a power-law difference scheme as an alternative to the upwind scheme. This scheme was analyzed by Hoang et al [4]. They found that it suffers from approximately the same limitations as the upwind scheme, namely, it only produces good results when the flow is aligned with the grid. Raithby[5] developed the Skew-Up stream Differencing Scheme (SUDS), which accounts for the flow skewness with respect to the grid. This scheme is capable of producing significant reductions in numerical diffusion as described for example, by Militzer[6]. This, however, is accomplished at the expense of simplicity, since the influence of neighbouring nodes has to be also included in the expressions of the coefficients. A great achievement which gained popularity in recent years is the introduction of so called body fitted coordinate system. With this technique cells may be placed almost along the direction of flow, thus minimizing the numerical diffusion. Neverthless, numerical diffusion is still present, even when the cells are aligned with the flow.

In 1981 Chen[7,8] introduced the Finite Analytic Method (FAM). The calculation domain is divided into cells, but, unlike traditional finite difference methods, the value of the dependent variable is not assumed as a given function, for instance, a polynomial profile within the cell. It is rather given by the local analytic solution to the linearlized convective diffusion equation. This has the advantage of automatically simulating the convective diffusion effect and thus eliminating the numerical diffusion. In this method Chen uses a second order polynomial or a combined function of a linear and an exponential function for the boundary conditions. This, like Leonard's parabolic function, may have negative coefficients, resulting in divergence or oscillation for problems with high Reynolds number.

In the present contribution the boundary condition used in the FAM is replaced by a piece-wise parabolic function. This method is called here Piece-Wise Parabolic Finite Analytic Method (PPFAM). Among its advantages are continuous high order derivatives and accurate description of the convective diffusion process. Unlike the second degree polynomial or the combined linear and exponential function used in the FAM, the pice-wise parabolic function satisfies the maximum and minimum principle of the convective diffusion process. That is, it always produces stable and accurate results that never over-shoot or under-shoot the physical reality.

There is no standard procedure to test a novel numerical scheme. It is, nevertheless, generally accepted that recirculating flows are difficult to predict and that they can provide a means for comparison among different numerical schemes. In the present contribution the Piece-Wise Parabolic Finite Analytic Method (PPFAM) is used to solve two recirculating laminar flows, namely: a cavity flow and a asymmetric plane expansion flow(backward or rearward-facing step flow). Preference is given to laminar flows to avoid difficulties with turbulence modelling, which can significantly affect the results and lead to false conclusions about the numerical schemes themselves.

THE GOVERNING EQUATIONS

Let us consider the numerical simulation of a two dimensional, incompressible, laminar non-newtonian fluid flow with constant viscosity. The governing equations are the continuity equation and momentum or Navier-Stokes equations.

For two dimensional flows sometimes preference is given to using the governing equations with stream function and vorticity function as dependent variables which read

$$\frac{\partial^2\psi}{\partial x^2} + \frac{\partial^2\psi}{\partial y^2} = -\zeta \qquad (1)$$

$$u\frac{\partial\zeta}{\partial x} + v\frac{\partial\zeta}{\partial y} = \upsilon\left(\frac{\partial^2\zeta}{\partial x^2} + \frac{\partial^2\zeta}{\partial y^2}\right) \qquad (2)$$

$$u = \frac{\partial\psi}{\partial y}\ ,$$

$$v = -\frac{\partial\psi}{\partial x}\ ,$$

$$\zeta = \frac{\partial v}{\partial x} - \frac{\partial u}{\partial y}$$

where ψ is the stream function and ζ is the vorticity function, u and v are velocity components.

With properly specified boundary conditions we can solve the above governing equation numerically to obtain the flow field.

THE PIECE-WISE PARABOLIC FINITE ANALYTIC METHOD

The stream function and vorticity function equations can be written

in a general form as

$$L\zeta = \frac{\partial^2\zeta}{\partial x^2} + \frac{\partial^2\zeta}{\partial y^2} - 2A_x\frac{\partial\zeta}{\partial x} - 2A_y\frac{\partial\zeta}{\partial y} = -F \qquad (x,y) \in \Omega \qquad (3)$$

$$\zeta(x,y) = \zeta_\Gamma(x,y) \qquad (x,y) \in \partial\Omega \qquad (4)$$

where Ω is the finite domain, ζ is the dependent variable; x,y are independent variables; A_x and A_y are the convection speeds and F is the source term.

We first linearize equation (3) in the finite domain as:

$$L_c\zeta = \frac{\partial^2\zeta}{\partial x^2} + \frac{\partial^2\zeta}{\partial y^2} - 2A_{xp}\frac{\partial\zeta}{\partial x} - 2A_{yp}\frac{\partial\zeta}{\partial y} = -F_p \qquad (5)$$

By introducing the following transformation

$$\zeta_h = \zeta - \frac{F_p}{2}\frac{A_{xp}x + A_{yp}y}{A_{xp}^2 + A_{yp}^2} \qquad (6)$$

and substituting equation (6) into equation (5), a homogeneous equation is obtained:

$$L_c\zeta_h = \frac{\partial^2\zeta_h}{\partial x^2} + \frac{\partial^2\zeta_h}{\partial y^2} - 2A_{xp}\frac{\partial\zeta_h}{\partial x} - 2A_{yp}\frac{\partial\zeta_h}{\partial y} = 0 \qquad (7)$$

we approximate the real boundary condition by the following piece-wise parabolic function. For example, the boundary conditions on the north side read:

$$\zeta_{hn}(x) = \begin{cases} \zeta_{hnc} + \dfrac{\zeta_{hne} - \zeta_{hnc}}{h_x^{no}}x^{no} & x \in (0, h_x) \\ \zeta_{hnc} + \dfrac{\zeta_{hnw} - \zeta_{hnc}}{h_x^{no}}x^{no} & x \in (-h_x, 0) \end{cases} \qquad (8)$$

where no = 2, 4, 6, 8,....

The above piece-wise parabolic function is continuous and its derivatives are also continuous. And it satisfies the maximum and minimum principle. Then let

$$\zeta_y = \zeta_h e^{-A_x x - A_y y} \qquad (9)$$

which leads the equation for ζ_y to read

$$\frac{\partial^2\zeta_y}{\partial x^2} + \frac{\partial^2\zeta_y}{\partial y^2} - (A^2_{xp} + A^2_{yp})\zeta_y = 0 \qquad (x,y) \in \Omega \qquad (10)$$

$$\zeta_y(x,y) = \zeta_h(x,y)\, e^{-A_x x - A_y y} \qquad (x,y) \in \partial\Omega \qquad (11)$$

the boundary value problem described by equations (10) and (11) can be solved using the variable separation method. Evaluating the solution at point P then we have the following algebraic expression

$$\zeta_p = C_{ne}\zeta_{ne} + C_{nc}\zeta_{nc} + C_{nw}\zeta_{nw} + C_{wc}\zeta_{wc} + C_{ec}\zeta_{ec} + C_{se}\zeta_{se} + C_{sc}\zeta_{sc} + C_{sw}\zeta_{sw} + C_f F_p \qquad (12)$$

where C_{ne},...C_{ec} ,C_f are the piece-wise parabolic finite analytic coefficients. Their expressions can be found in Sun [9]. Furthermore, the PPFAM coefficients satisfy the following:

(i) $C_{ne} + ... + C_{ec} = 1$

(ii) $C_f > 0$, $0 < (C_{ne}, ..., C_{ec}) < 1$.

With the above properties we can prove that the PPFAM produces a convergent and accurate solution of the linear and non-linear convective diffusion problems(Sun [9]).

The piece-wise parabolic finite analytic scheme for the stream function, equation (1), can be written in the following form:

$$\psi_p = C_{ne}\psi_{ne} + C_{nc}\psi_{nc} + C_{nw}\psi_{nw} + C_{ec}\psi_{ec} + C_{wc}\psi_{wc} + C_{se}\psi_{se} + C_{sc}\psi_{sc} + C_{sw}\psi_{sw} + C_f\zeta_p \qquad (13)$$

The equation for vorticity function can be discretized similarly.

NUMERICAL SIMULATION OF THE CAVITY FLOW

As a first test of the piece-wise parabolic finite analytic method, the numerical simulation of the square cavity flow is performed. The cavity flow in the present study is induced by the top cover which moves at speed U_0. The physical constants describing the cavity flow are as follows: U_0 = 1.0 m/s, L = 1.0 m and $\upsilon = 0.1 \sim 5.0 \times 10^{-4}$ m^2/s.

We can solve simultaneously the coupled algebraic equations for stream function and equation for vorticity, to obtain the flow field using the Gauss-Siedel iteration method.

Figures 1 presents the results obtained for the cavity flow with Reynolds numbers equal 500. Table 1 gives the values of the maximum streamline calculated for each Reynolds number by different numerical schemes. With Reynolds number equal 10 all schemes give a solution, while with Reynolds number equal 500 the CDS diverges, and for Reynolds number equal 2000 only the up-wind numerical scheme and the PPFAM converge to a solution. It is worth noticing that consistently the PPFAM gives the largest value for the maximum streamline, which indicates that it is the least affected by numerical diffusion and thus the most accurate.

Table 1 $|\psi|_{max}$ for the Cavity Flow

	$\|\psi\|_{max}$				
	Re = 10	Re = 100	Re = 500	Re = 1000	Re = 2000
C.D. S.	0.0832	no solution	no solution	no solution	no solution
Upwind	0.0836	0.0920	0.0840	0.0650	0.0470
FAM	0.0839	0.0890	0.0851	no solution	no solution
PPFAM	0.0947	0.0997	0.10833	0.1023	0.1002

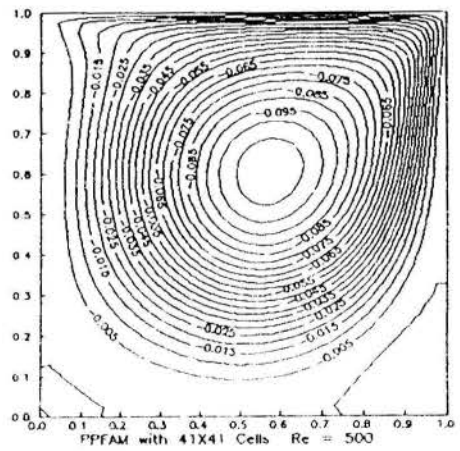

Fig. 1 Streamline contours for cavity flow with Re = 500

NUMERICAL SIMULATION OF THE BACKWARD FACING STEP FLOW

Another well known test problem for numerical schemes is the channel flow over a backward facing step. One of the challenge in the prediction of this flow is the determination of the position of reattachment point. Here the solution by the piece-wise parabolic finite analytic method is presented and the numerical results compared with those obtained from other numerical methods and with available experimental data[10], [11].

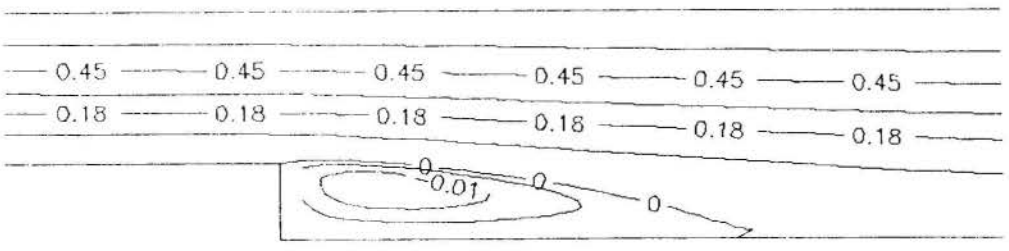

Fig. 2 Streamline countours for backward facing step channel flow with Re = 50

The following geometrical parameters define the flow domain: L = 21 m (the length of the channel); l = 3 m (the distance of the inflow to the corner of the step); H = 1.5 m (height of the channel after the step) and h = 1.0 m(height of the channel before the step).

The boundary conditions for u, v, ψ and ζ are specified as follows. At the entrance, the inlet flow is assumed fully developed. The wall boundary conditions is the standard adherence of the flow to the walls of the channel. At the outlet the boundary condition is the zero gradient in the direction of the flow.

The Gauss-Seidel iteration method is also used here to solve simultaneously the coupled discrete stream function and vorticity function equations. The upwind scheme, the finite analytic scheme and piece-wise parabolic finite analytic scheme are used respectively to perform the numerical simulation for the following cases:

1)	Re = 10	H =1.5 m	h = 1.0 m
2)	Re = 50	H =1.5 m	h =1.0 m

where $Re = \frac{(H-h)\,U_{max}}{\upsilon}$ and U_{max} is the maximum inlet velocity.

As shown in Fig. 2 and Table 2 the PPFAM produced the largest reattachment length. And furthermore, these results compare well with available experimental data[10], [11]. Table 2 lists the reattachment lengths obtained by the UDS, FAM, PPFAM and some experimental data. It shows that the PPFAM provides the best results for the backward facing step channel flow.

Table 2 Reattachment Distance and ψ_{min} for the Backward Facing Step Flo

	Re = 10		Re = 50	
	X_r	Ψ_{min}	X_r	Ψ_{min}
UDS	0.458	-0.00334	1.554	-0.01484
FAM	0.531	-0.00352	1.660	-0.01487
PPFAM	0.0.731	-0.00454	3.115	-0.01872
Uch2 [11]			1.42	
Exp.[10]			3.0	

CONCLUDING REMARKS

The following are the main conclusions about the piece-wise parabolic finite analytic method:

1) The coefficients are positive with sum equal to one.

2) The PPFAM is accurate and numerical diffusion free.

3) The PPFAM can provide a convergent solution for linear and non-linear problems.

4) The PPFAM is capable of producing stable and accurate simulations of recirculating laminar flows for a wide range of Reynolds numbers.

5). When compared with other more traditional numerical schemes(CDS, UDS and FAM) it produces better results both for the cavity and backward facing step flows.

6). For the backward facing step flow the reattachment distance predicted by the PPFAM compares well with available experimental data, and furthermore the predictions are better than those produced by CDS, UDS and FAM.

ACKNOWLEDGEMENTS

The first author would like to acknowledge the financial support from Technical University of Nova Scotia and Foulis Chair Foundation. The second author would like to acknowledge the financial support from the Natural Science and Engineering Council of Canada through its operating grant OGP0005451.

References

1. Courant, R., Isaacson, E., and Rees, M. "On the Solution of Non-Linear Hyperbolic Differential Equations by Finite Differences". Comm. Pure Appl. Math., Vol.5, pp.243.

2. Leonard, B.P., "A Stable and Accurate Convective Modelling Procedure Based on Quadratic Upstream interpolation". Compt. Meth. Appl. Mech. Engg. 19 (1979), pp. 59-98.

3. Patankar, S.V., "Numerical Heat Transfer and Fluid Flow". McGraw Hill, New York, 1980.

4. Huang, P.G., Launder, B.E. and Leschziner, M.A., "Discretization of Nonlinear Convective Process A Broad Range Comparison of Four Schemes". Comp. Meth. Appl. Mech. Engg. 48 (1985). pp. 1-24.

5. Raithby, G.D., "Skew Upwind Differencing Schemes for Problems Involving Fluid Flow". Compt. Meth. Appl. Mech. Engg. (1976). pp. 153-164.

6. Militzer, J. "The Dual Parallel Turbulent Jets: The Measurement and Prediction of the Mean Velocity Field". Ph.D. Thesis, U. of Waterloo, 1977.

7. Chen, C.J., Naseri-Nashet, H. and Ho, K.S., "Finite Analytic Numerical Solution of Heat transfer in two Dimensional Cavity Flow." Journal of Numerical Heat Transfer, Vol. 4. pp. 179-197 (1981)

8. Chen, C.J., and Chen, H.C., "Finite Analytic Numerical Method for Unsteady two Dimensional Navier-Stokes Equations." Journal of Computational Physics, Vol. 53, No.2, pp. 209-226 (1984)

9. Sun, Y., "The Piece-Wise Parabolic Finite Analytic Method and Its Application in Fluid Mechanics". M.A.Sc Thesis, Technical University of Nova Scotia, Halifax, Nova Scotia, Canada, May 1990.

10. Kuency, J.L. and Binder, G. "Viscous Flow over Backward facing Steps An Experimental Investigation". In: Analysis of Laminar Flow Over a Backward Facing Step, K. Morgan; J. Periaux; F. Thomasset (eds.), Braunschweig, Fed. Rep. Germany, Friedr. Vieweg & Sohn Verlagagesesellsch. mbH, 1984, pp. 32-47.

11. Bonnet, H., Leointe Y., Piquet, J. and Visonneau M. "The Backward-Facing Step Comparison of two Algorithms for Unsteady Navier-Stokes Equations". In: Analysis of Laminar Flow Over a Backward Facing Step, K. Morgan; J. Periaux; F. Thomasset (eds.), Braunschweig, Fed. Rep. Germany, Friedr. Vieweg & Sohn Verlagagesesellsch. mbH, 1984, pp. 63-79.

III ENCIT – Itapema, SC (Dezembro 1990)

COMPUTATION OF LAMINAR AXI-SYMMETRIC RECIRCULATING FLOWS USING PRIMITIVE VARIABLES AND A BLOCK-IMPLICIT SCHEME

Marcelo J.S. de Lemos

Departamento de Energia, ITA/CTA
São José dos Campos, São Paulo 12225

Abstract

This work presents numerical solutions for recirculating flows inside a short cylindrical tank. The situations analyzed comprise incompressible laminar flow in several cases of engineering interest. Recirculating motion is induced by either injecting fluid inside the tank or by moving one of its lid. The equations of motion and continuity of mass are solved in a coupled manner by means of a direct method in each computational cell. Iterations are performed alternating the most varying index in every sweep over the computational domain. Flow patterns and mass residual behavior are presented.

GENERAL REMARKS

The understanding and prediction of characteristics of complex flows have been the aim of many research endeavors for decades. The ability to correctly calculate main flow parameters has countless advantages in design and analysis of man-made crafts, environmental control and simulation, biomedical engineering and in many other areas.

For that matter, numerical solutions of coupled partial differential equations have become a common place strategy in solving a wide range of engineering problems. Solutions for equations governing fluid flow phenomena were first investigated in the academic media but are now being considered as a practical tool in research and industrial environments.

In spite of the ever greater use of Computational Fluid Dynamics (or CFD for short), the numerical solution of multi-dimensional flow equations is still a challenging task due to the intricate physical coupling among the variables involved. And yet, the rate of convergency of any algorithm is essentially dictated by the degree in which physical coupling is mimicked by the method in question. There is then much need for development of fast coupled algorithms for flow problems.

Acknowledging the growing importance of CFD studies, this work presents numerical solutions for recirculating flows inside a short cylinder. Results are shown for incompressible, constant property laminar flow. The numerical method herein solves, for each computational cell, all momentum and continuity equations in their so-called primitive variables ($\underline{u},\underline{w},P$). The implicit handling of the pressure-velocity interaction brings information from neighbor cells to the finite-volume immediately, thus increasing overall convergency rates. Moreover, the point-wise aspect of the error smoothing operator makes it attractive for use in more advanced computer architectures such as vector and parallel computers.

GOVERNING EQUATIONS AND NUMERICAL METHOD

Flow governing equations, in a compact notation embracing planar and axi-symmetric cases, can be readily written for two-dimensional laminar situations as:

$$\frac{\partial \rho w}{\partial z} + \frac{1}{r^n}\frac{\partial}{\partial r} r^n(\rho u) = 0 \qquad (1)$$

$$\frac{\partial(\rho uu)}{\partial z} + \frac{\partial}{r^n \partial r}(r^n \rho wu) = -\frac{\partial P}{\partial r} + \frac{\partial}{\partial z}\left[\mu \frac{\partial u}{\partial z}\right] + \frac{1}{r^n}\frac{\partial}{\partial r}\left[r^n \mu \frac{\partial u}{\partial r}\right] - n\frac{\mu u}{r^2} \qquad (2)$$

$$\frac{\partial}{\partial z}(\rho uw) + \frac{\partial}{r^n \partial r}(r^n \rho ww) = -\frac{\partial P}{\partial z} + \frac{\partial}{\partial z}\left[\mu \frac{\partial w}{\partial z}\right] + \frac{1}{r^n}\frac{\partial}{\partial r}\left[r^n \mu \frac{\partial w}{\partial r}\right] \qquad (3)$$

where u,w are the velocity components in the r,z directions, respectively, μ is the fluid molecular viscosity, ρ is the density, $\underline{n=1}$ for two-dimensional axi-symmetric cases and $\underline{n=0}$ for planar configurations.

Computational Grid. The set of equations for mass, and momentum (1)-(3) seen above is now discretized by means of the widely-used Control-Volume approach [1]. In this method, the computational domain is divided into finite non-overlapping regions containing each region a computational node. A typical computational grid is shown in Figure 1, displaying different control volumes for different variables. This "staggered" grid arrangement has well-established advantages in calculating fluid flow problems [2].

To every "main" control volume it is associated a grid point (i,j) and neighbor points at east (i+1,j), west (i-1,j), north (i,j+1) and at south (i,j-1), as shown in the Figure. For the r-momentum equation the faces of the volume at east and west are identified by the indexes (i+½,j) and (i-½,j), respectively. This same "staggering" is applied to the z-equation. The node (i,j) has coordinates (r_i, z_j) and the velocities $u_{i-\frac{1}{2},j}$, $w_{i,j-\frac{1}{2}}$ are positioned at the cell faces, or at $(r_{i-\frac{1}{2}}, z_j)$ and $(r_i, z_{j-\frac{1}{2}})$, respectively.

It is interesting to point out that in the finite-differencing below no assumption is made about the relative positioning grid point/cell face coordinates. So the use of "stretching" functions for concentrating or expanding points near walls and where a "smooth" stretching is necessary is readily applicable [3].

The differential equations are then integrated over each volume yielding a set of algebraic equations for each dependable variable. The discretization equations are thus obtained by doing:

$$\frac{1}{\text{Vol}} \int (\text{Differential Equation})\ d\text{Vol} \qquad (4)$$

Internodal variation for the dependent variables can be of different kind corresponding to different Finite-Difference Formulations. In the present work, for simplicity, the Upwind-Differencing-Scheme is used to model convective fluxes across volume faces. In addition, linear profiles are assumed in approximating diffusive fluxes whereas for source terms the values

prevail over the entire volume in question.

According to the "staggered" grid arrangement, the use of (4) involves integrations over different volumes for distinct variables. For circular geometries these volumes are promptly calculated as:

$$Vol_{i,j} = \frac{r^2_{i+\frac{1}{2}} - r^2_{i-\frac{1}{2}}}{2} (z_{j+\frac{1}{2}} - z_{j-\frac{1}{2}}) \quad \text{for eqn. (1)} \qquad (5)$$

$$Vol_{i-\frac{1}{2},j} = \frac{r^2_{i} - r^2_{i-1}}{2} (z_{j+\frac{1}{2}} - z_{j-\frac{1}{2}}) \quad \text{for eqn. (2)} \qquad (6)$$

and

$$Vol_{i,j-\frac{1}{2}} = \frac{r^2_{i+\frac{1}{2}} - r^2_{i-\frac{1}{2}}}{2} (z_{j} - z_{j-1}) \quad \text{for eqn. (3)} \qquad (7)$$

Discretized Equations. Integrating the continuity equation around point (i,j) following standard practices in numerical differentiation [4,5], one has:

$$a^c_i u_{i+\frac{1}{2},j} - b^c_i u_{i-\frac{1}{2},j} + c^c_j (w_{i,j+\frac{1}{2}} - w_{i,j-\frac{1}{2}}) = 0 \qquad (8)$$

where the geometric coefficients a^c_i, b^c_i and c^c_j make computations convenient and efficient and can be interpreted as (area of flow)/(volume of computational node).

For integrating the convection term in (2) around volume $Vol_{i-\frac{1}{2},j}$ one makes use here of the UPWIND formulation (see for example [2]). It is interesting to point out that when calculating convection fluxes the velocities are taken from the previous "iteration". Such linearization is later removed by the use of an iterative method. As mentioned above, the diffusion term uses the assumption of a linear profile for the component $u_{i-\frac{1}{2},j}$. In cylindrical geometries, the extra term appearing in the diffusion operator (last term in eqn. 2), can be conveniently treated as a "source", giving finally for the $u_{i-\frac{1}{2},j}$ equation:

$$a^u_{i-\frac{1}{2},j} u_{i-\frac{1}{2},j} = b^u_{i-\frac{1}{2},j} u_{i+\frac{1}{2},j} + c^u_{i-\frac{1}{2},j} u_{i-3/2,j} + d^u_{i-\frac{1}{2},j} u_{i-\frac{1}{2},j+1} + e^u_{i-\frac{1}{2},j} u_{i-\frac{1}{2},j-1} + f^u_{i-\frac{1}{2},j} + g^u_{i-\frac{1}{2}} [P_{i-1,j} - P_{i,j}] \qquad (9)$$

where the coefficients in (9) account for convection and diffusion mechanisms, as well as independent terms. The use of other finite-difference schemes for the convection and source terms would have been possible, giving finally distinct forms for the above coefficients [2].

For the axial velocity component, a similar discretizing strategy for all terms in (3) will give;

$$a^w_{i,j-\frac{1}{2}} w_{i,j-\frac{1}{2}} = b^w_{i,j-\frac{1}{2}} w_{i+1,j-\frac{1}{2}} + c^w_{i,j-\frac{1}{2}} w_{i-1,j-\frac{1}{2}} + d^w_{i,j-\frac{1}{2}} w_{i,j+\frac{1}{2}} + e^w_{i,j-\frac{1}{2}} w_{i,j-3/2} + f^w_{i,j-\frac{1}{2}} + g^w_{j-\frac{1}{2}} [P_{i,j-1} - P_{i,j}] \qquad (10)$$

For application in the numerical algorithm below, equations (9) and (10) can be conveniently recast into the form

$$u_{i-\frac{1}{2},j} = \hat{u}_{i-\frac{1}{2},j} + d^u_{i-\frac{1}{2},j} [P_{i-1,j} - P_{i,j}] \qquad (11)$$

where

$$\hat{u}_{i-\frac{1}{2},j} = \frac{\Sigma_{i-\frac{1}{2},j}}{a^u_{i-\frac{1}{2},j}}$$

$$\Sigma_{i-\frac{1}{2},j} = b^u_{i-\frac{1}{2},j} u_{i+\frac{1}{2},j} + c^u_{i-\frac{1}{2},j} u_{i-3/2,j} + d^u_{i-\frac{1}{2},j} u_{i-\frac{1}{2},j+1} + e^u_{i-\frac{1}{2},j} u_{i-\frac{1}{2},j-1} + f^u_{i-\frac{1}{2},j}$$

and

$$d^u_{i-\frac{1}{2},j} = \frac{g^u_{i-\frac{1}{2}}}{a^u_{i-\frac{1}{2},j}}$$

Similarly for w it follows:

$$w_{i,j-\frac{1}{2}} = \hat{w}_{i,j-\frac{1}{2}} + d^w_{i,j-\frac{1}{2}} [P_{i,j-1} - P_{i,j}] \qquad (12)$$

where

$$\hat{w}_{i,j-\frac{1}{2}} = \frac{\Omega_{i,j-\frac{1}{2}}}{a^w_{i,j-\frac{1}{2}}}$$

$$\Omega_{i,j-\frac{1}{2}} = b^w_{i,j-\frac{1}{2}} w_{i+1,j-\frac{1}{2}} + a^w_{i,j-\frac{1}{2}} w_{i-1,j-\frac{1}{2}} + a^w_{i,j-\frac{1}{2}} w_{i,j+\frac{1}{2}} + a^w_{i,j-\frac{1}{2}} w_{i,j-3/2} + f^w_{i,j-\frac{1}{2}}$$

and

$$d^w_{i,j-\frac{1}{2}} = \frac{g^w_{j-\frac{1}{2}}}{a^w_{i,j-\frac{1}{2}}}$$

NUMERICAL ALGORITHM

The Coupled Character of The Numerical Scheme. Only the cross-flow equations, namely r-, z-momentum and mass, are considered for coupled solution. Any other scalar variable ϕ, if considered, would be excluded from the implicit handling here studied, being this segregated treatment commonly used in several other methods, as in the SIMPLE family of algorithms [6,7]. In those techniques, the ϕ-equations are generally solved after iterations for the flow field have been performed, generally through the use of a pressure or pressure correction equation. In the present method, no such equations are made use of.

Accordingly, the treatment of the P-(u,w) coupling here presented uses a slight variation of the Symmetrical Coupled Gauss Siedel (SCGS) method of Vanka [8,9]. As shown below, in the SCGS method the continuity plus the r- and z-momentum equations are directly solved in each computational cell by inverting a matrix containing information on the corrections for velocities and pressure.

In the present case, it is suggested that the sweep throughout the domain takes alternating directions whenever the least varying index (the index changing the least in a FORTRAN language DO-LOOP) is of an even value. This "alternating" path has the purpose of "physically" connecting every cell with the one previously "visited" in the sequence throughout the field. For that, the method is herein recalled as Alternating SCGS procedure [10].

Essentially, that approach consists of finding the corrective values for u,w and P, such that the balance equations are correctly satisfied

Equations for the Residues. In order to set up a scheme to annihilate the residues of the flow equations, correction values are defined as differences between "exact" and "not-yet-converged" variables and can be written as:

$$u'_{i-\frac{1}{2},j} = u_{i-\frac{1}{2},j} - u^n_{i-\frac{1}{2},j} \qquad (13.a)$$

$$u'_{i+\frac{1}{2},j} = u_{i+\frac{1}{2},j} - u^n_{i+\frac{1}{2},j} \qquad (13.b)$$

$$w'_{i,j-\frac{1}{2}} = w_{i,j-\frac{1}{2}} - w^n_{i,j-\frac{1}{2}} \qquad (13.c)$$

$$w'_{i,j+\frac{1}{2}} = w_{i,j+\frac{1}{2}} - w^n_{i,j+\frac{1}{2}} \qquad (13.d)$$

$$P'_{i,j} = P_{i,j} - P^n_{i,j} \qquad (13.e)$$

where the subscripts identify locations in the cell, the superscript "'" distinguishes corrections and the symbol "n" corresponds to iteration "n".

Residuals for all four momentum equations and for

the continuity of mass are readily obtained by applying (13) into (8), (11) and (12). After rearranging, one has

$$R_{i-\frac{1}{2},j} = u^n_{i-\frac{1}{2},j} - \hat{u}_{i-\frac{1}{2},j} - d^u_{i-\frac{1}{2},j}\left[P_{i-1,j} - P^n_{i,j}\right] \quad (14.a)$$

$$R_{i+\frac{1}{2},j} = u^n_{i+\frac{1}{2},j} - \hat{u}_{i+\frac{1}{2},j} + d^u_{i+\frac{1}{2},j}\left[P_{i+1,j} - P^n_{i,j}\right] \quad (14.b)$$

$$R_{i,j-\frac{1}{2}} = w^n_{i,j-\frac{1}{2}} - \hat{w}_{i,j-\frac{1}{2}} - d^w_{i,j-\frac{1}{2}}\left[P_{i,j-1} - P^n_{i,j}\right] \quad (14.c)$$

$$R_{i,j+\frac{1}{2}} = w^n_{i,j+\frac{1}{2}} - \hat{w}_{i,j-\frac{1}{2}} + d^w_{i,j-\frac{1}{2}}\left[P_{i,j+1} - P^n_{i,j}\right] \quad (14.d)$$

$$R_{i,j} = a^c_i\, u^n_{i+\frac{1}{2},j} - b^c_i\, u^n_{i-\frac{1}{2},j} + c^c_j\,(w^n_{i,j+\frac{1}{2}} - w^n_{i,j-\frac{1}{2}}) \quad (14.e)$$

Note that, in (14), velocities and pressure outside the (i,j) volume are assumed as correct, since the decomposition (13) is not applied to the second and third terms on the right-hand-side of the residue formulas.

Solution Strategy. Inspecting (14), one can see that a system connecting the residuals and corrections can be written into matrix form as:

$$\begin{bmatrix} 1 & 0 & 0 & 0 & d^u_{i-\frac{1}{2},j} \\ 0 & 1 & 0 & 0 & -d^u_{i+\frac{1}{2},j} \\ 0 & 0 & 1 & 0 & d^w_{i,j-\frac{1}{2}} \\ 0 & 0 & 0 & 1 & -d^w_{i,j+\frac{1}{2}} \\ -b^c_i & a^c_i & -c^c_j & c^c_j & 0 \end{bmatrix} \begin{bmatrix} u'_{i-\frac{1}{2},j} \\ u'_{i+\frac{1}{2},j} \\ w'_{i,j-\frac{1}{2}} \\ w'_{i,j+\frac{1}{2}} \\ P'_{i,j} \end{bmatrix} = \begin{bmatrix} R_{i-\frac{1}{2},j} \\ R_{i+\frac{1}{2},j} \\ R_{i,j-\frac{1}{2}} \\ R_{i,j+\frac{1}{2}} \\ R_{i,j} \end{bmatrix} \quad (15)$$

The system (15) is then solved for each cell (i,j), giving the required corrections to annihilate the residuals for all five variables involved. The solution vector for the system above is easily obtained by directly inverting the matrix in (15). The required corrections for all variables involved are then obtained by doing,

$$P'_{i,j} = \frac{-b^c_i\, R_{i-\frac{1}{2},j} + a^c_i\, R_{i+\frac{1}{2},j} - c^c_j\,(R_{i,j-\frac{1}{2}} - R_{i,j+\frac{1}{2}}) - R_{i,j}}{-b^c_i\, d^u_{i-\frac{1}{2},j} - a^c_i\, d^u_{i+\frac{1}{2},j} - c^c_j\,(d^w_{i,j-\frac{1}{2}} + d^w_{i,j+\frac{1}{2}})} \quad (16)$$

Velocity corrections then follow as,

$$u'_{i-\frac{1}{2},j} = R_{i-\frac{1}{2},j} - d^u_{i-\frac{1}{2},j}\, P'_{i,j} \quad (17.b)$$

$$u'_{i+\frac{1}{2},j} = R_{i+\frac{1}{2},j} + d^u_{i+\frac{1}{2},j}\, P'_{i,j} \quad (17.c)$$

$$w'_{i,j-\frac{1}{2}} = R_{i,j-\frac{1}{2}} - d^w_{i,j-\frac{1}{2}}\, P'_{i,j} \quad (17.d)$$

$$w'_{i,j+\frac{1}{2}} = R_{i,j+\frac{1}{2}} + d^w_{i,j+\frac{1}{2}}\, P'_{i,j} \quad (17.e)$$

Convergency is monitored by checking the value of the norm of the mass residue at iteration "n" defined as:

$$Res^n = \frac{\left[\sum_{ij}(R^2_{i,j})\right]^{\frac{1}{2}}}{N \times M} \quad (18)$$

where N and M are the number of grid points in the radial and axial directions, respectively. Although it is recognized that (18) should include also some information on the momentum equation behavior, the use of (18) was found to be appropriate, at least for the cases run here.

RESULTS AND DISCUSSION

In this section results are presented for several flows of engineering interest. The geometry considered consists of a short cylindrical tank with and without inlet/outlet openings. The Reynolds number, defined as $\mu UR/\rho$, where R is the cylinder radius and U is a characteristic velocity (inlet or lid velocity), was taken as 1000. Mass conservation criterium was assumed satisfied for Res^n less than 1.0×10^{-4}. Test cases here presented are divided into two categories, namely flow-driven and lid-driven types. Flow-driven recirculating motions identify cases in which there is injection of fluid inside the cylinder. In lid-driven cases, cross-flow appears by shear due to the motion of one of the cylinder lids (see Appendix for boundary conditions).

All cases were run in a MOTOROLA based Personal Computer running at 20 MHz. A relaxation parameter α=0.85 was used in all computations. Also, all flow-driven cases were run with a grid of size 24x24. For lid-driven flows, the effect of the number of control-volumes was also investigated. The case are identified in Tables 1 and 2 below.

Figure 2 to 4 present vector plots for the flow field formed inside the tank for several combination of inlet and outlet openings (see Table 1). In those cases flow is pushed inward, perpendicularly to the tank entrance. In all plots, the center and size of the recirculating bubbles clearly appear. Figures 5 and 6 simulate fluid injection at 45° degrees with the normal to the surface. This is a typical situation occurring in internal combustion engines and chambers. Table 3 below gives running time for all five test cases (those are real CPU-time not accounting for system input/output overhead). It is worth noting the excellent time required for convergency, considering the modest speed of computation delivered by the used machine, the tightness of the convergency criteria and the damping action of the relatively low relaxation parameter.

Table 1 - Test Cases for Flow-driven Motion

Case	Type
a)	Center Injection with Tangential Ejection
b)	Center Injection with Lateral Ejection
c)	Tangential Injection with Lateral Ejection
d)	Middle Injection (at 45° deg.) with Middle Ejection
e)	Middle Injection (at 45° deg.) with Lateral Ejection

Table 2 - Test Cases for Lid-driven Motion

Case	Grid Size
f)	12 x 12
g)	18 x 18
h)	24 x 24
i)	48 x 48

Figure 7 shows the continuity equation residue calculate by (18). As far as computing time is concerned, the most difficult run was case d):Middle injection at an angle. Perhaps the extra computing effort required in case d) was due to the two large recirculation zones observed in the Figure 5 (at left and right of the incoming jet). One could speculate that, in this case, the smoothing operator would need a greater number of iterations to properly sweep out low-frequency errors. All other cases presented similar history in decreasing mass continuity residues.

Figure 8 shows the transverse fluid flow pattern for the case of radially expanding the top lid. In this test case, the recirculating bubble is driven by shear due to the outward radial motion of the cylinder upper cap. Several grid sizes were used in order to investigate the behavior of the present numerical scheme in systems of different sizes (Figure 8 shows results for a grid of 24x24). Computing times are shown in Table 4 with corresponding residue history plotted in Figure 9. The Table and Figure confirm, as expected, that for the lid-driven cases convergency rates are primarily dependent upon grid refinement. One should point out that, in obtaining the curves in Figure 9, no change was made in the relaxation factor. Finding an optimal

relaxation factor for the calculations in Table 4 could have decreased the running time required for finer grids.

Table 3 - Running Time for Flow-Driven Cases
Re=1000; α=0.85

Case	Running Time	Grid
a)	8 min 23 sec	24x24
e)	8 min 48 sec	24x24
b)	9 min 34 sec	24x24
c)	10 min 38 sec	24x24
d)	15 min 59 sec	24x24

Table 4 - Running Time for Lid-Driven Cases
Re=1000; α=0.85

Case	Running Time	Grid
f)	1 min 00 sec	12x12
g)	3 min 58 sec	18x18
h)	10 min 47 sec	24x24
i)	120 min 06 sec	48x48

It is also interesting to observe in Table 4 the sharp increase in CPU requirements for finer grids. Proper handling of a large number of grid nodes should include other numerical artifices for reducing computing time. Recent work has suggested the use of Multigrid-based techniques as a powerful tool for handling algebraic equation systems of a large size [11,12].

CONCLUDING REMARKS

This work showed numerical solutions for the governing equations describing the fluid motion inside a cylinder. Recirculating flow in the r,z plane was obtained by injecting mass and by expanding the top end cap of the cylindrical tank.

Governing equations were written in terms of the so-called primitive variables. Transport equations were integrated over a finite control-volume using the Upwind Finite-Differencing scheme for the convective fluxes. The discretized momentum equations are applied to each cell face and then, together with the mass-continuity equation, are solved simultaneously by means of a direct method in each computational cell. An Alternating Symmetrical Coupled Gauss-Siedel procedure was employed in which iterations are performed alternating the most varying index in every sweep over the computational domain.

Results were obtained for several configurations of practical engineering interest. Computations were performed on a Personal Computer for different grids in reasonable computing times. Flow patterns, mass residual behavior and computing time were reported.

ACKNOWLEDGEMENT

The author is grateful to CNPq - Conselho Nacional de Desenvolvimento Científico e Tecnológico, Brazil, for financial support during the preparation of this work.

REFERENCES

[1] Patankar, S.V., Spalding, D.B., A CALCULATION PROCEDURE FOR HEAT, MASS AND MOMENTUM TRANSFER IN THREE-DIMENSIONAL PARABOLIC FLOWS, Int. J. Heat Mass Transf., vol. 15, pp. 1787-1806 (1972)

[2] Patankar, S.V., NUMERICAL HEAT TRANSFER AND FLUID FLOW, Mc-Graw Hill, New York, (1980)

[3] deRivas, K.E., ON THE USE OF NON-UNIFORM GRIDS IN FINITE DIFFERENCE EQUATIONS, J. Comp. Phys., vol. 10, pp. 202-210 (1972)

[4] Anderson, D., Tannehill, J., Pletcher, R.H., COMPUTATIONAL FLUID MECHANICS AND HEAT TRANSFER, Hemisphere Publ., Washington D.C. (1984)

[5] Minkowycz, W.J., Sparrow, E.M. Eds., HANDBOOK OF NUMERICAL HEAT TRANSFER, John Wiley & Sons (1988)

[6] Patankar, S.V., A CALCULATION PROCEDURE FOR TWO-DIMENSIONAL ELLIPTIC SITUATIONS, Num. Heat Transf., vol. 4, pp. 409-425 (1981)

[7] Raithby, G.D., Schneider, G.E., UPSTREAM-WEIGHTED DIFFERENCING SCHEMES AND THEIR APPLICATION TO ELLIPTIC PROBLEMS INVOLVING FLUID FLOW, Computers & Fluids, vol. 2, pp. 191-206 (1974).

[8] Vanka, S.P., BLOCK-IMPLICIT CALCULATION OF STEADY TURBULENT RECIRCULATING FLOWS, Int. J. Heat Mass Transf., vol. 28, pp. 2093-2103 (1985)

[9] Vanka, S.P., BLOCK-IMPLICIT MULTIGRID SOLUTION OF NAVIER-STOKES EQUATIONS IN PRIMITIVE VARIABLES, J. Comp. Phys., vol. 65, pp. 138-158 (1986)

[10] deLemos, M.J.S., AN ALTERNATING SYMMETRICAL COUPLED GAUSS-SIEDEL PROCEDURE FOR TWO- AND THREE-DIMENSIONAL RECIRCULATING FLOWS, ASME Winter Meeting, Chicago, USA, Nov.28-Dec.2 (1988)

[11] Demuren, A.O., APPLICATION OF MULTI-GRID METHODS FOR SOLVING THE NAVIER-STOKES EQUATIONS, Proc. Ins. Mech. Eng., vol. 203, pp. 255-265 (1989).

[12] deLemos, M.J.S, A MULTIGRID COUPLED ALGORITHM FOR THE NUMERICAL SOLUTION OF RECIRCULATING FLOWS, in preparation, (1990).

Appendix. Boundary conditions of given-value type were employed in all cases. For lid-driven runs, cylinder lid motion was simulated by using a non null figure for the radial velocity located at the boundary.

Internal initial profiles were implemented as a bi-linear interpolation of boundary values. No investigation was performed in order to assess their influence on the final computing time.

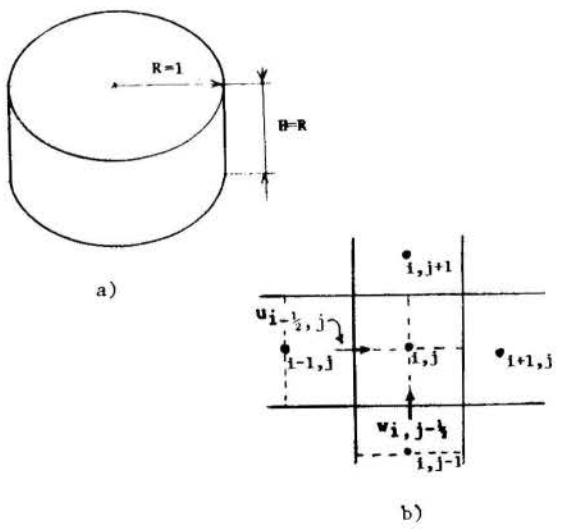

Figure 1 - a) Geometry Considered and
b) Control Volume notation

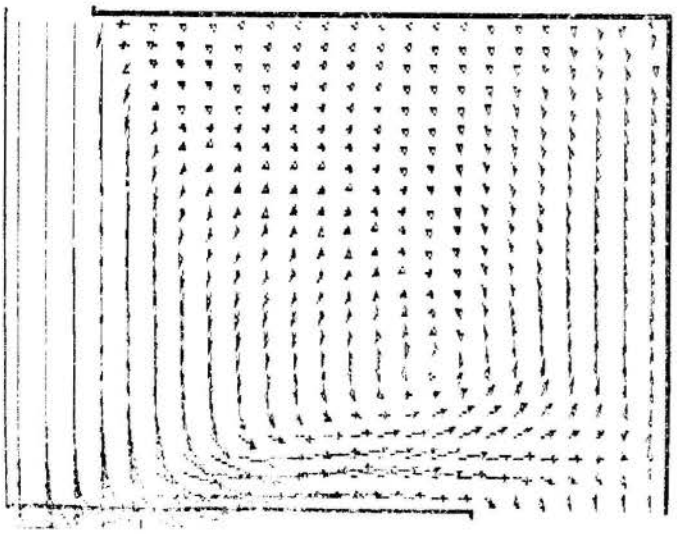

Figure 2 - Center Injection with Tangential Ejection

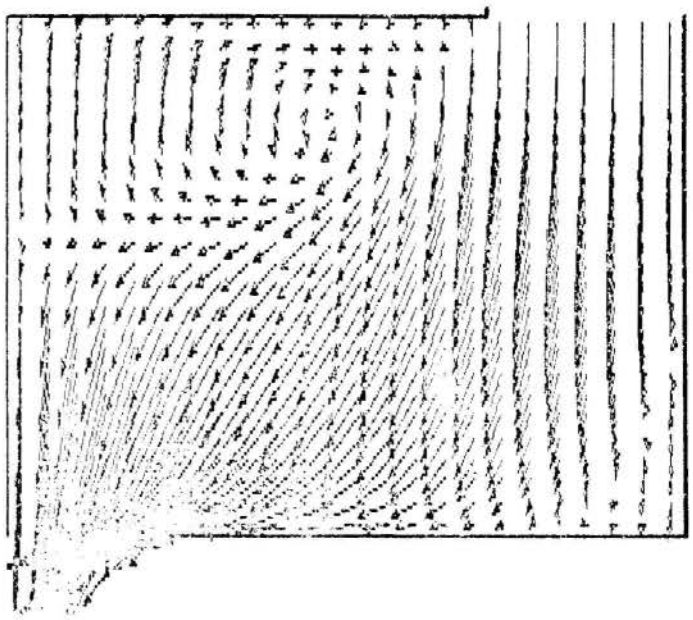

Figure 4 - Tangential Injection with Center Ejection

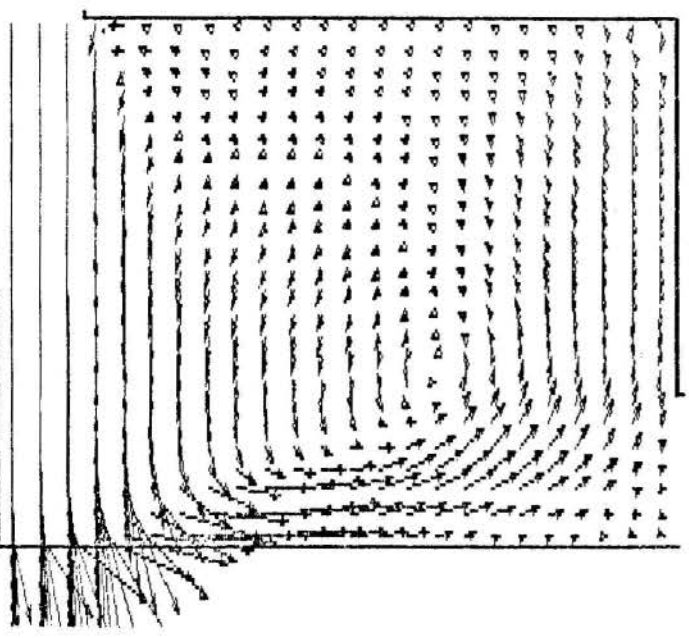

Figure 3 - Center Injection with Lateral Ejection

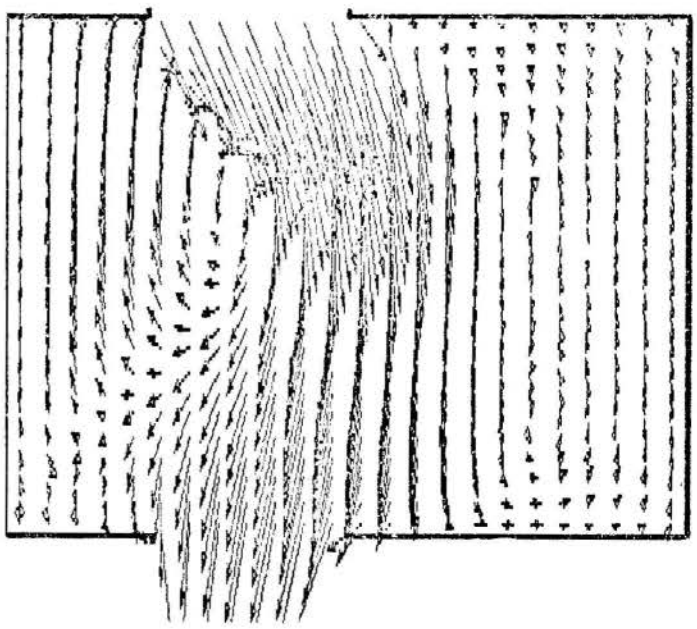

Figure 5 - Middle Injection at 45° degrees

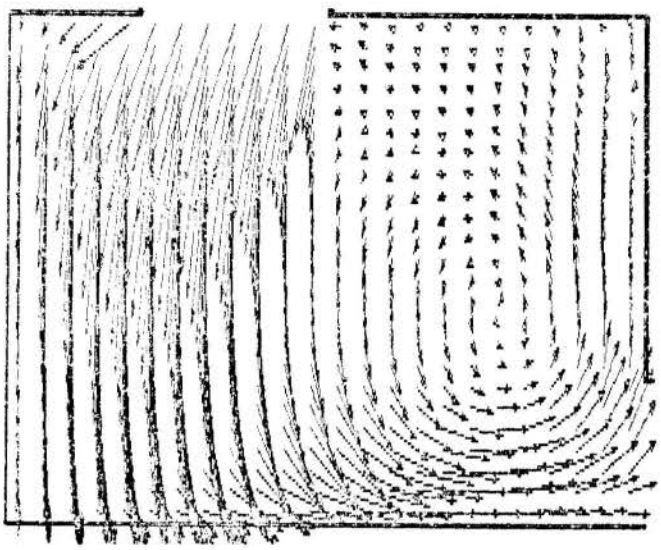

Figure 6 - Middle Injection with Lateral Ejection

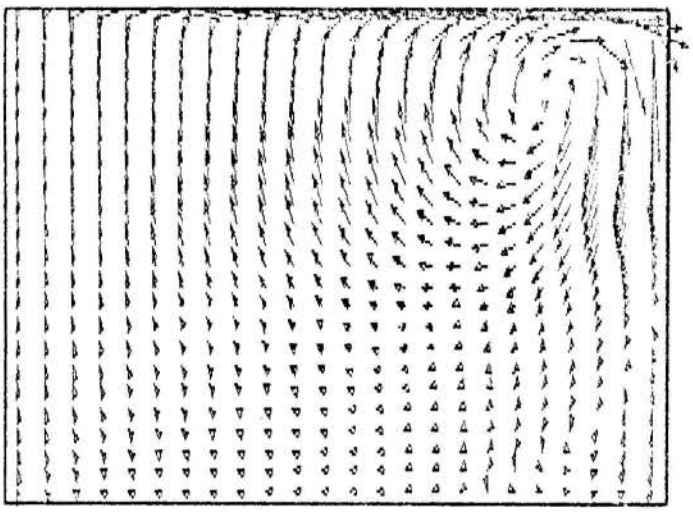

Figure 8 - Lid-Driven Flow Patterns

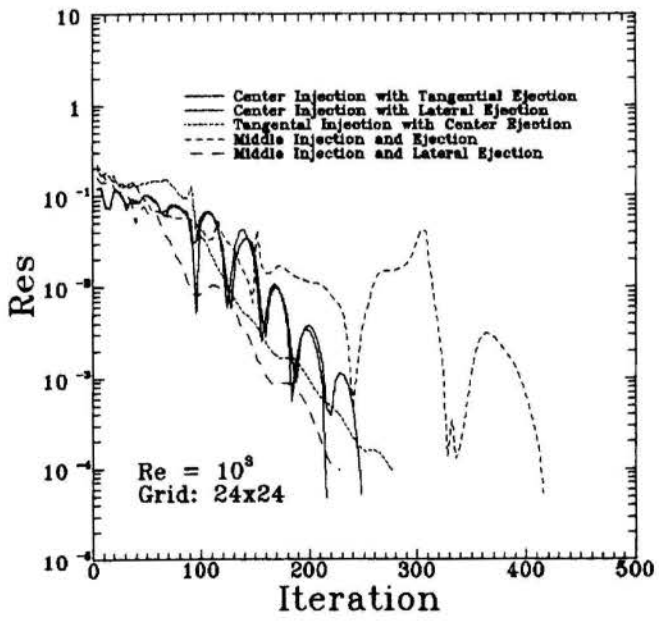

Figure 7 - Residuals for Flow-driven Cases

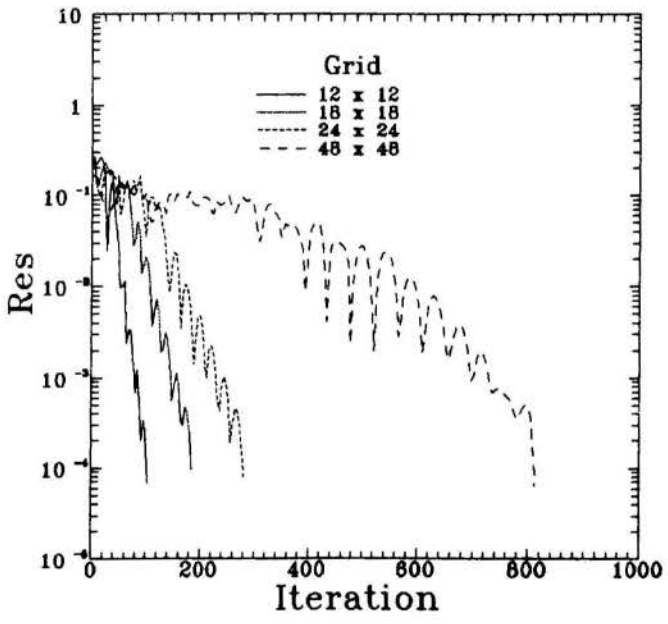

Figure 9 - Residuals for Lid-driven Cases

III ENCIT – Itapema, SC (Dezembro 1990)

DEVELOPMENT OF AN AXI-SYMMETRIC MIXING LAYER IN A DUCT OF CONSTANT CROSS SECTION

Edson Matsumoto
Marcelo J.S. de Lemos

Departamento de Energia, ITA/CTA
São José dos Campos, São Paulo 12225

Abstract

This work presents numerical predictions for the flow field formed by two coaxial streams confined in a circular tube. The widely-used marching-forward method of Patankar-Spalding was used for sweeping the computational domain. The standard k-ε model was applied for handling turbulence. Computations are first performed for laminar case in order to assess the reliability of the numerical code. Results are then presented for developing and fully-developed turbulent coaxial jets.

INTRODUCTORY REMARKS

Mixing layers confined in ducts of cross section of any shape represent an important class of flow in Aeronautical Engineering. The flow field formed by the exhaustion of gases in rocket boosters and by the mixing of streams with different velocities are just a few examples of this kind of flow in aircraft engineering.

Equally important, the use of numerical tools for design and analysis of complex geometries can provide such useful engineering information as turbulent transport rates and film coefficients. In addition, the adequate employment of numerical predictions, carefully combined with experimental work, can bring, in most cases, substantial savings to the overall process of analysis and optimization of a new design concept. Then, there seems to be much need for continuing research on reliable numerical tools.

Based on the foregoing, this work presents numerical results for the flow field formed by the development of two coaxial turbulent streams confined in a duct of constant cross section. The popular marching-forward method of Patankar [1,2] is employed together with the widely-used k-ε model of turbulence [3,4].

MATHEMATICAL MODEL AND NUMERICAL METHOD

Mean Flow. The equations of continuity of mass and x-momentum for a two-dimensional planar/axi-symmetric mixing layer can be readily written as,

$$\frac{\delta}{\delta x}(r^n \rho U) + \frac{\delta}{\delta r}(r^n \rho V) = 0 \qquad (1)$$

and

$$\rho U \frac{\delta U}{\delta x} + \rho V \frac{\delta U}{\delta y} = -\frac{\delta p}{\delta x} + \frac{1}{r^n}\frac{\delta}{\delta y}\left[r^n \mu_{ef} \frac{\delta U}{\delta y}\right] \qquad (2)$$

In (1)-(2) U and V are the velocity components in the axial and transverse direction, respectively, ρ the fluid density, p the static pressure and μ_{ef} the effective coefficient of exchange given as;

$$\mu_{ef} = \mu_t + \mu \qquad (3)$$

As usual, equations (1) and (2) are written in a compact notation embracing plans ($n=0$) and axi-symmetric ($n=1$) cases. Also, in (3) μ is the molecular viscosity and μ_t the turbulent viscosity given below.

Turbulence Model The statistical turbulence model k-ε has been extensively used in the literature for its characteristics of robustness and numerical stability. The classical work of Jones & Launder dated of 1972 [3] has been applied and extended to a wide variety of flow configurations for nearly twenty years now.

Basically, the model embodies the early idea of Prandtl/Kolmogorov that, in a turbulent flow, the apparent viscosity μ_t can be considered as proportional to the product of a characteristic velocity scale V´ and a characteristic length scale L´. In the k-ε model, the characteristic velocity scale is given by $V'=k^{1/2}$, being the characteristic length scale written as $L'=k^{3/2}/\epsilon$, implying for the turbulent viscosity

$$\mu_t = c_\mu \rho k^2 / \epsilon \qquad (4)$$

where c_μ is a constant.

Here it is further considered the case in [3] involving only flow regions of high local Reynolds numbers, or say, regions with Kolmogorov and macroscopic scales adequately separated [5]. With this, transport equations for k and ε can be written as

$$\rho U \frac{\delta k}{\delta x} + \rho V \frac{\delta k}{\delta y} = \frac{1}{r^n}\frac{\delta}{\delta y}\left[r^n \Gamma_k \frac{\delta k}{\delta y}\right] + S_k \qquad (5)$$

and

$$\rho U \frac{\delta \epsilon}{\delta x} + \rho V \frac{\delta \epsilon}{\delta y} = \frac{1}{r^n}\frac{\delta}{\delta y}\left[r^n \Gamma_\epsilon \frac{\delta \epsilon}{\delta y}\right] + S_\epsilon \qquad (6)$$

In (5)-(6) Γ_k and Γ_ϵ are given by

$$\Gamma_k = \mu + \frac{\mu_t}{\sigma_k} \qquad (7)$$

$$\Gamma_\epsilon = \mu + \frac{\mu_t}{\sigma_\epsilon} \qquad (8)$$

where the σ's are the turbulent Prandtl/Schmidt numbers for k and ε, respectively. The last terms in (5)-(6) are known as "source" terms and are given by;

$$S_k = \rho (P - \epsilon) \qquad (9)$$

$$S_\epsilon = \rho \frac{\epsilon}{k}(c_1 P - c_2 \epsilon) \qquad (10)$$

being $c_1=1,47$, $c_2=1,92$ and $c_\mu=0.09$. The production term in (9)-(10) reads

$$P = \frac{\mu_t}{\rho}\left[\frac{\delta U}{\delta y}\right]^2 \qquad (11)$$

Numerical Method. The numerical approach here adopted is the well-known parabolic solver technique of Patankar [1,2]. Details of this method can be found elsewhere and for that only general ideas are here presented. In addition, more elaborating aspects of the derivation below are presented in [6].

The method consists of first recasting (2), (5) and (6) onto a general transport equation of the form

$$\frac{\delta\Phi}{\delta x} + (a + bw)\frac{\delta\Phi}{\delta w} = \frac{\delta}{\delta w}\left[c \frac{\delta\Phi}{\delta w} \right] + d \qquad (12)$$

where

Φ = U, k or ϵ

$a = -(d\Psi_I/dx)/\Psi_{EI}$

$b = -(d\Psi_{EI}/dx)/\Psi_{EI}$

$c = r^{n2}\,\rho U\Gamma_\Phi/\Psi_{EI}^2$

$d = S_\Phi/(\rho U)$

and

$\Psi_{EI} = \Psi_E - \Psi_I$

Equation (12) is written in the so-called x-w coordinate system, being Ψ and w the dimensional and non-dimensional stream functions, respectively (see, for example [1]). Accordingly, subscripts I and E are relative to the "internal" an "external" boundary layer limits, respectively.

The second step is then to integrate (12) over the Control-Volume (or computational cell) shown in Figure 1. The conservation laws are then rewritten in their macroscopic counterpart form over the volume of the Figure, giving,

$$[\Psi_{EI,P}\,\Phi_P - \Psi_{EI,A}\,\Phi_{PA}](w_n - w_s) + \left[\dot{m}''\Phi - \Gamma_\Phi \frac{\delta\Phi}{\delta y}\right]_n r^n{}_n(x_P - x_A) - \left[\dot{m}''\Phi - \Gamma_\Phi \frac{\delta\Phi}{\delta y}\right]_s r^n{}_s(x_P - x_A) = (S_C + S_P\Phi_P)\left[r^n(y_n - y_s)\right]_P(x_P - x_A) \qquad (13)$$

In (13) the subscripts "P" and "A" are relative to downstream and upstream x-positions, respectively. Also, for numerical stability, source term linearization ($S_\Phi = S_C + S_P\Phi$) has been used [1]. After incorporating the linear formulation for the diffusion term, one finally gets,

$$a_P\Phi_P = a_N\Phi_N + a_S\Phi_S + a_{PA}\Phi_{PA} + b_P \qquad (14)$$

where

$$a_N = \frac{(\Gamma_\Phi\, r^n)_n\,(x_P - x_A)}{y_N - y_P}$$

$$a_S = \frac{(\Gamma_\Phi\, r^n)_s\,(x_P - x_A)}{y_P - y_S}$$

$$a_{PA} = \Psi_{EI}\,(w_n - w_s)$$

$$a_P = a_N + a_S + a_{PA} - S_P\left[r^n(y_n - y_s)\right]_P(x_P - x_A)$$

and

$$b_P = S_C\left[r^n(y_n - y_s)\right]_P(x_P - x_A)$$

The system (14) of algebraic equations can then be solved for each dependable variable Φ at each downstream position x_P.

Inlet and Boundary Conditions. Inlet flow for the central and annular jets are given a uniform distribution defining the velocity ratio U_s/U_i, where U_s and U_i are the inlet velocities for the annular and central regions, respectively. Following standard practices in the literature [7], the values of k at the inlet section correspond to a turbulence intensity of 0,1%, giving

$$k_{in} = 1.\times 10^{-3}\,U_m^2 \qquad (15)$$

where U_m is the overall mean velocity. Inlet profiles for ϵ follow such as [7];

$$\epsilon_{in} = (k_{in})^{3/2}/Ky' \qquad (16)$$

where K is the von Karman constant (K=0.4) and y' the distance to the wall.

For the centerline (y=0) the symmetry condition is implemented for all dependent variables (Φ=U, k and ϵ) as,

$$\left.\frac{\delta\Phi}{\delta y}\right|_{y=0} = 0 \qquad (17)$$

Wall proximity is handled by the usual **Wall Function** approach [7], giving for the wall shear stress

$$\tau_W = \frac{U_N\, c_\mu^{1/4}\, k_N^{1/2}}{\frac{1}{K}\ln\left[E\, y_N' \frac{\rho\,(c_\mu^{1/2} k_N)^{1/2}}{\mu} \right]} \qquad (18)$$

being $U^*=(\tau_W/\rho)^{1/2}$ and E a constant. Also, $U_N=U_N/U^*$ and $y_N=(\rho y_N' U^*)/\mu$. In (18) the subscript "N" identifies the grid point closest to the wall. In that region, the use of the **Wall Function** approach associated with the assumption of "local equilibrium" for turbulence ($P=\epsilon$) gives,

$$k_N = \tau_W/(\rho\, c_\mu^{1/2}) \qquad (19)$$

and for the dissipation rate ϵ_N at the same point,

$$\epsilon_N = (k_N)^{3/2}/(K\, y_N') \qquad (20)$$

The pressure gradient. Determination of the unknown pressure gradient is handled exactly as explained in [6]. That approach consists basically in finding the "zero" of a function f(dp/dx) defined as,

$$f\,(dp/dx) = [\,A_{calc} - A_{duct}\,]/\Psi_{EI} \qquad (21)$$

where the left hand side represents the discrepancy, at the downstream position, between the calculated and real duct areas. Solution of (21) can be achieved with an iterative Newton-Raphson method of the form

$$f^* + f'^*\,[\,(dp/dx) - (dp/dx)^*\,] = 0 \qquad (22)$$

where "starred" values are estimate quantities later improved in subsequent iterations. Typically, 3 to 4 iterations are necessary in solving (22) at each axial station.

RESULTS AND DISCUSSION

Laminar Flow. Although the present work was primarily concerned with fully turbulent regime, several

test calculations for laminar cases were also carried out in order to fully verify the correctness of the computer code. Also, to avoid difficulties in approximating velocity gradients in both layers (at the wall and in the mixing region), all results herein were obtained with an equally distributed (linear) grid along the duct radius and with N=50 control-volumes. A detailed discussion on solution dependence on the number and distribution of grid nodes is presented in [6]. Therefore, predictions reported in this paper already accounts for the optimal combination (N and grid layout) found out in that work.

Results for the axial velocity with U_e/U_1=2 and 0.5 are presented in Figures 2 and 3 for Re=500, being the x-coordinate non-dimensionalized in terms of r_o, the jet separation radius at x=0. The Figures clearly show the growth of the Boundary- and Thin-Shear-Layer along the developing regions. Also shown is a comparison with the fully developed analytical solution for axial positions sufficiently away from the duct entrance. Calculation of the parabolic profile seems to indicate the correctness of the computer programming.

Turbulent Flow. Before presenting results for turbulent flow, it is interesting to investigate the role of the position of the first grid point close to the wall. This preliminary study was found to be mandatory since detailed computation in the viscous-layer has been avoided. For validity of the Wall Function hypothesis, the non-dimensional wall coordinate y^+ defined above should lie in the range

$$20\text{-}30 < y^+ < 250\text{-}300 \qquad (23)$$

Therefore, for the same wall distance, y_N, the non-dimensional coordinate, y^+, will be a function of Re. In this work, several test calculations were carried out to investigate the use of different y^+ for the same Re. Table 1 below shows results for the friction factor f as a function of y^+, for Re = 388000. Results are compared with the well-known Blasius formula ($f_B = 0.079Re^{-.25}$, see for example Hansen [9]) and with the correlation of Techo et al [10] for smooth tubes:

$$4f_T = 0{,}86859 \ln\left[\frac{Re}{1.964 \ln Re - 3.8215}\right]^{-2} \qquad (24)$$

Table 1 - Influence of y^+ on friction factor f
Re=388000; f_B=0,012661; f_T=0,013793

y^+	f_{calc}	f_{calc}/f_B	f_{calc}/f_T
100	0,01397	1.10339	1,01283
175	0,01385	1,09391	1,00413
200	0,01383	1.09233	1,00268
225	0,01380	1,08996	1,00051
250	0,01378	1,08838	0,99927
275	0,01376	1,08680	0,99761
300	0,01374	1,08522	0,99616
325	0,01373	1,08443	0,99543
400	0,01367	1,07969	0,99108

Table 1 indicates an optimal value for y^+. The Table also shows that calculated f s, independently of y^+, are closer to the ones given by (24). In order to better evaluate the influence of y^+ on the solution, similar calculations were also performed for different Re. Calculations are presented in Table 2 together with relative errors to the Blasius and Techo et al [10] correlations, defined as,

$$e_B = \frac{f_{calc} - f_B}{f_B} \times 100 \qquad (25)$$

and

$$e_T = \frac{f_{calc} - f_T}{f_T} \times 100 \qquad (26)$$

Table 2 - Influence of Re on f

Re	y^+	f_{calc}	f_B	f_T	e_B%	e_T%
50000	38	0,02098	0,02113	0,02091	0,71	0,33
388000	250	0,01378	0,01266	0,01379	8,85	0,07
500000	320	0,01315	0,01188	0,01316	10,69	0,07

Table 2 shows that, for the range of Re considered, values of f are closer to (24) than to Blasius correlation. Considering the claim in Hansen [9] on the excellent precision of (24) for smooth tubes, in this work an empirical correlation for y^+ as a function of Re was obtained by curve-fitting the values in the Table. This equation reads,

$$y^+ = 6{,}2849\times10^{-4}\ Re + 6.1452 \qquad (27)$$

and was used for all turbulent flow predictions below.

With a discussion on y^+ assignment, results for turbulent flow can now be more clearly presented.

Calculations for turbulent flow with U_e/U_1=2 and 0.5 are shown in Figures 4 and 5. As expected, the Figures indicate a faster development with x/r_o than for the laminar case. The plots also show, as in their laminar counterpart, the growth of the two viscous-affected layers (close to the wall and in the mixing region). As mentioned before, all radial profiles were calculated with a linearly distributed grid and with 50 grid points.

Numerical predictions for the turbulent kinetic energy per unit mass, k, with U_e/U_1 = 2 and 0.5 are shown in Figures 6 and 7. It is very interesting to point out, for $x/r_o \approx 0$, the clear "*peak*" in the level of k associated with its high production rate in that region. As shown in equation 11, the production rate P is proportional to the square of the velocity gradient. Along the development region, turbulent kinetic energy is then transported to the pipe center by diffusion mechanism. Later, k is eventually dissipated down to a level compatible with the ones for fully developed flow [11]. It is important to emphasize, however, that the results here presented are all based on the use of the Wall Function and the Local Equilibrium hypotheses. In the literature, those ideas are usually pertinent to fully developed situations. Therefore, the conclusions here withdrawn are limited to the validity of those assumptions for the present flow configuration.

Results for the rate of turbulent kinetic energy dissipation, corresponding to the U e k cases above, are show in Figures 8 and 9. The Figures present a behavior for ϵ similar to the one for k in the region of high shear. The "*peak*" in ϵ profiles indicate that regions of high production rates of turbulent kinetic energy correspond also to regions of high dissipation rates. A quick inspection in equations (5) and (6) reveals that those two equations are "similar", except for the characteristic time rate ϵ/k (dimensions 1/time) and model constants. Therefore, this similar behavior, at least as far as trends in the profiles are concerned, seem to be explained if one considers the transport equations involved.

CONCLUDING REMARKS

This work presented a series of results relative to the numerical calculation of a confined flow. The configuration analyzed consisted of two coaxial turbulent jets inside a duct of constant cross section. Inlet profiles were assumed as uniformed in each stream.

Several testing calculations were reported for laminar flow with the aim of checking the correctness of the computer program developed. Also carried out was an

investigation on the location of the point closest to the wall when using the Wall Function approach.

Simulation for the mean and turbulent flow fields then followed for the cases of velocity ratio U_e/U_i greater and smaller than unity. Results for the mean velocity clearly shows the growth of the boundary layer close to the duct wall as well as the development of the Thin Shear Layer separating the two potential streams. Calculations for the turbulent field clearly shows, for the near entrance region, the effect of the high production term resulting from the steep velocity gradients in that location. Similar behavior was observed for the rate of dissipation of turbulent kinetic energy.

ACKNOWLEDGEMENT

The authors are thankful to CNPq for financial support during the preparation of this work.

REFERENCES

[1] Patankar, S.V., Spalding, B.E.., HEAT AND MASS TRANSFER IN BOUNDARY LAYERS, *2nd edition*, Intertext, London (1970).

[2] Patankar, S.V., Spalding, D.B., A CALCULATION PROCEDURE FOR HEAT, MASS AND MOMENTUM TRANSFER IN THREE-DIMENSIONAL PARABOLIC FLOWS, *Int. J. Heat & Mass Transf.*, vol. 15, pp. 1787-1806 (1972)

[3] Jones, W.P., Launder, B.E., THE PREDICTION OF LAMINARIZATION WITH A TWO-EQUATION MODEL OF TURBULENCE, *Int. J. Heat & Mass Transfer*, vol. 15, pp. 301-314 (1972).

[4] Launder, B.E., Spalding, D.B., THE NUMERICAL COMPUTATION OF TURBULENT FLOWS, *Comp. Meth. App. Mech. Eng.*, vol. 3, pp. 269-289 (1974)

[5] Hinze, J.O., Turbulence, *2nd. Edition*, McGraw-Hill (1975)

[6] Matsumoto, E., ESTUDO DE JATOS CONFINADOS, *MSc Thesis* (in portuguese), Dept. of Energy, ITA/CTA (1980)

[7] Launder, B.E., Spalding, D.B., LECTURES IN MATHEMATICAL MODELS OF TURBULENCE, *Academic Press*, New York (1972).

[8] Patankar, S.V., PARABOLIC SYSTEMS, *cap. 2 in HANDBOOK OF NUMERICAL HEAT TRANSFER*, Minkowycz et al eds., John Wiley & Sons, New York (1988)

[9] Hansen, A.G., FLUID MECHANICS, *John Wiley & Sons*, New York (1967)

[10] Techo, R., Tickner, R.R., James, E.E., AN ACCURATE EQUATION FOR THE COMPUTATION OF THE FRICTION FACTOR FOR SMOOTH PIPES FROM THE REYNOLDS NUMBER, *J. of Appl. Mechanics*, vol. 87, pp. 443 (1965).

[11] Laufer, J., THE STRUCTURE OF TURBULENCE IN FULLY DEVELOPED PIPE FLOW, NACA-TR-1174 (1954).

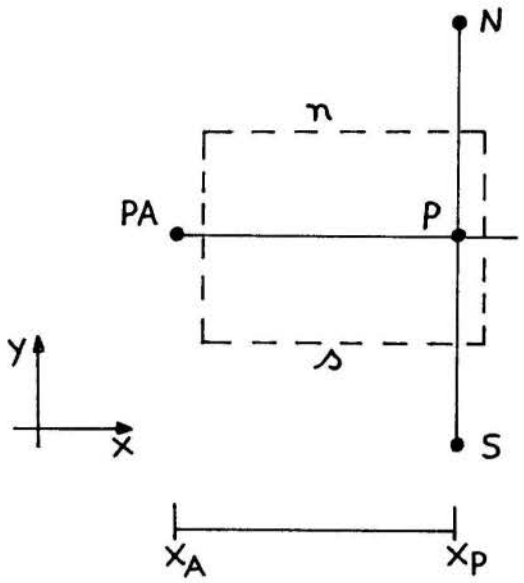

Figure 1 - Control Volume Notation

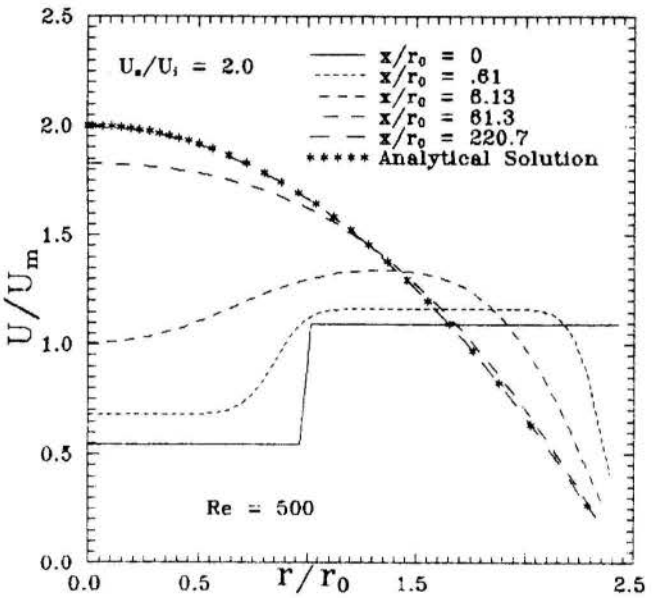

Figure 2 - Axial Velocity U/U_m, Re=500, U_e/U_i=2

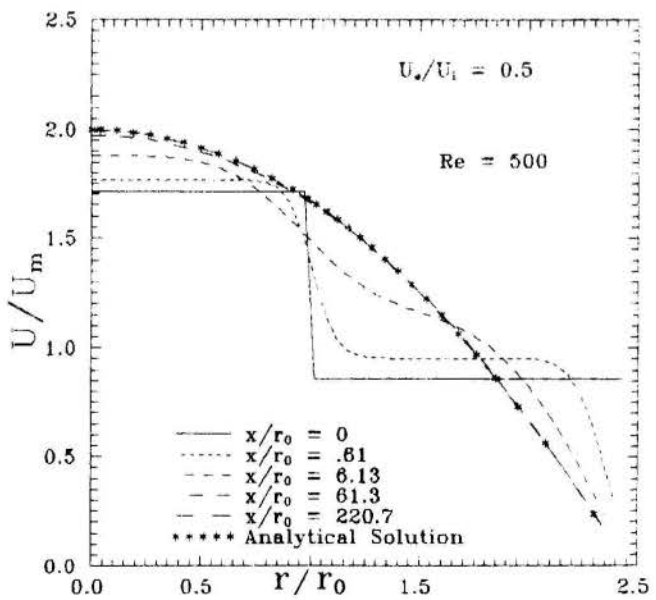

Figure 3 - Axial Velocity U/U_m, Re=500, U_e/U_i=0.5

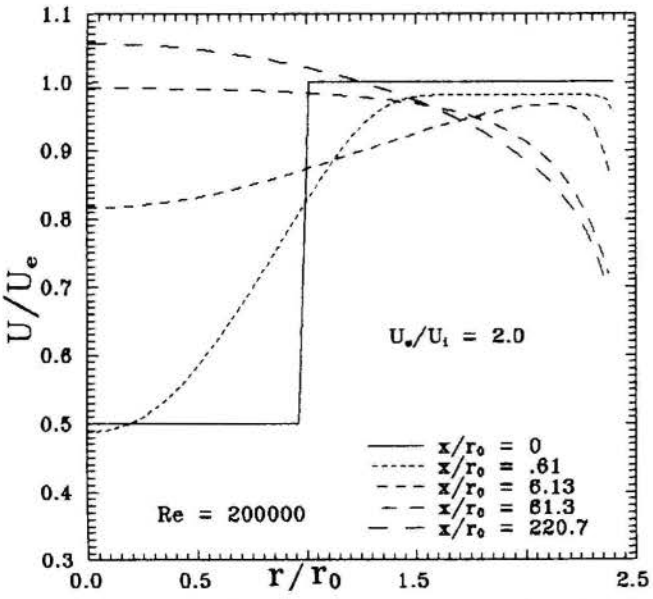

Figure 4 - Axial Velocity U/U_e, Re=200000, U_e/U_i=2

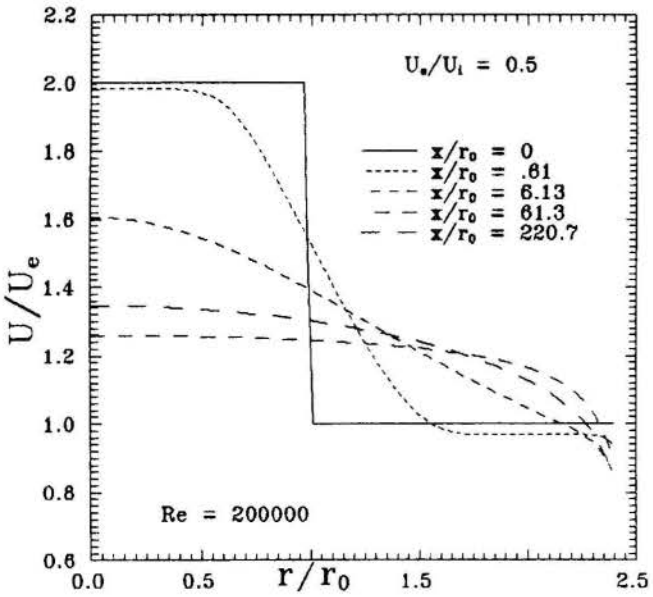

Figure 5 - Axial Velocity U/U_e, Re=200000, U_e/U_i=0.5

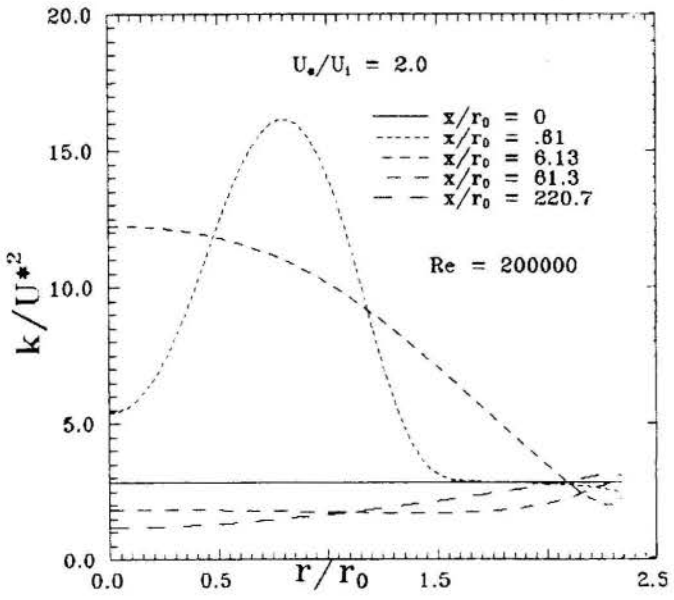

Figure 6 - Turbulent Kinetic Energy, k/U^{*2}, U_e/U_i=2

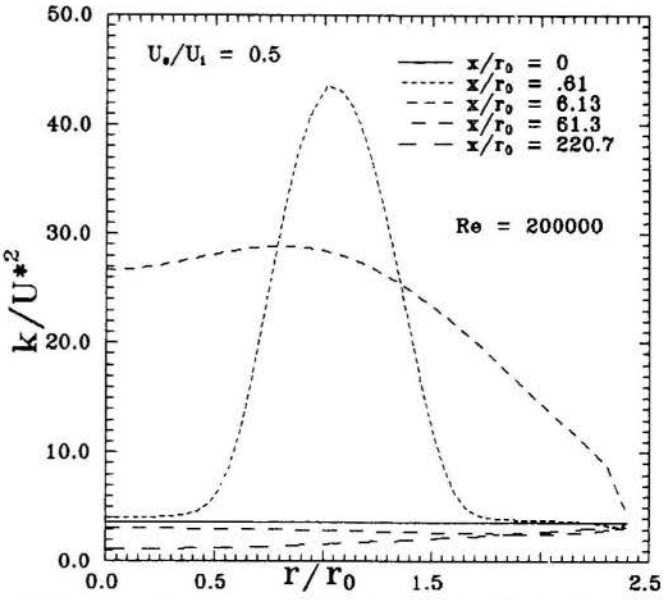

Figure 7 - Turbulent Kinetic Energy, k/U^{*2}, U_e/U_i=0.5

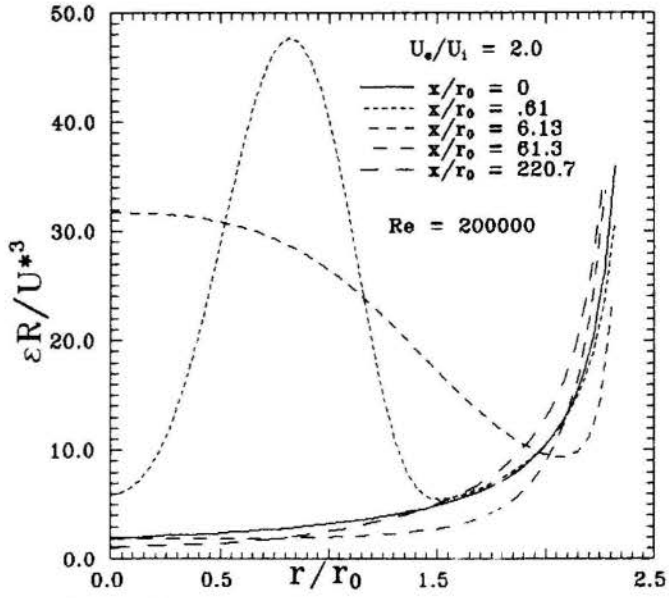

Figure 8 - Dissipation Rate, $\epsilon R/U^{*3}$, U_e/U_i=2

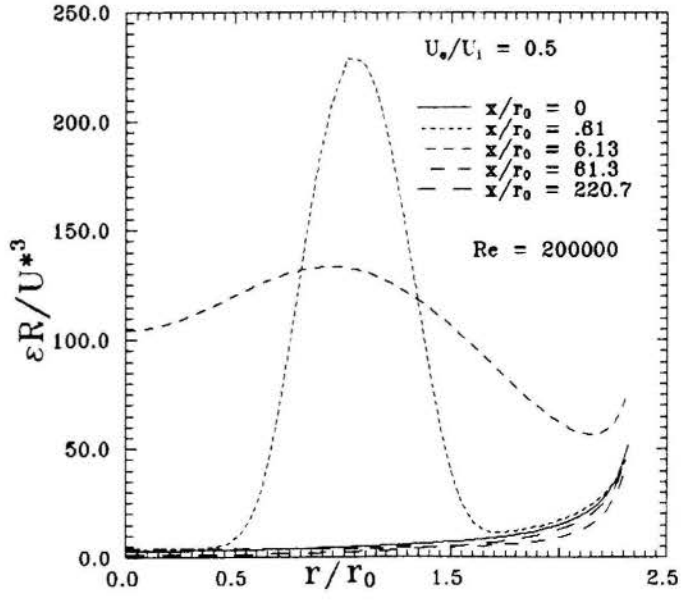

Figure 9 - Dissipation Rate, $\epsilon R/U^{*3}$, U_e/U_i=0.5

III ENCIT – Itapema, SC (Dezembro 1990)

DESEMPENHO DE DISCRETIZAÇÕES DE CINCO NÓS EM EQUAÇÕES DE TRANSPORTE EM FLUIDOS

JOSÉ RICARDO FIGUEIREDO
UNICAMP-FEM-DE
13081 - Campinas - SP. - Brasil

RESUMO

Faz-se um estudo comparativo das discretizações central, à montante, de Allen & Southwell e de Dennis & Hudson, para a equação bidimensional de transporte convectivo-difusivo, considerando o caso linearizado, homogêneo com coeficientes constantes. Soluções amostrais varrendo o espectro de Fourier da solução geral são usadas como casos testes. A generalidade do método permite discutir o conceito de difusão numérica que postula relação direta entre o erro numérico e o ângulo entre escoamento e grade numerica.

INTRODUÇÃO

Diversas questões relativas à solução numérica das equações de transporte convectivo-difusivo podem ser consideradas através do caso linear homogêneo bidimensional com coeficientes constantes em regime permanente:

$$u\frac{\partial\phi}{\partial x} + v\frac{\partial\phi}{\partial y} - \alpha\left(\frac{\partial^2\phi}{\partial x^2} + \frac{\partial^2\phi}{\partial y^2}\right) = 0 \qquad (1)$$

onde u e v são componentes de velocidade nas direções x e y respectivamente, ϕ representa uma propriedade intensiva tal como temperatura ou concentração, e α é a difusividade apropriada. A eq. (1) também pode ser vista como uma forma linearizada das equações de quantidade de movimento ou vorticidade para fluidos viscosos, considerando ϕ como um componente de velocidade ou vorticidade e α como a viscosidade cinemática.

A discretização de ambos os termos pelo diferenciamento central de segunda ordem leva a matrizes não diagonalmente dominantes quando um dos números Peclet celulares (ou reynolds celulares) for maior que 2 (em termos absolutos). Se o sistema de equações discretizadas for resolvido iterativamente a ausência de diagonalidade dominante pode causar instabilidade numérica, evitável em certos casos através de fatores de relaxação, ao custo de baixar velocidades de convergência. Os números de Peclet dividem os eixos em regiões onde a matriz se aproxima do caso singular, quando então temos métodos diretos de solução são instáveis ou inacurados.

Matrizes diagonalmente dominantes podem ser obtidas com diferenciamento central para os termos difusivos e o unilateral à montante para termos convectivos [1], introduzindo erros de primeira ordem, frequentemente prevalecendo difusão numérica por sua proporcionalidade à segunda derivada. Este erro pequeno em certos casos, particularmente se associado à camada limite sem gradientes de pressão adversos quando um dos eixos numéricos for paralelo à direção principal de escoamento. Mas o erro de primeira ordem tende a crescer em outras situações, em especial em regiões de recirculação.

O desempenho da discretização à montante em alguns casos-testes padrão (transporte convectivo de escalar com distribuição em degrau na direção cruzada, escoamento em rotação como sólido, e outros) têm levado muitos pesquisadores à conclusão de que, na ausência de termos fonte ou transientes, a difusão numérica da esquema à montante é essencialmente associada com o ângulo entre grade e escoamento, sendo desprezível para $\pm 45°$ e máxima para fluxos inclinados em $45°$ em relação à grade [2].

Tais limitações dos esquemas clássicos de diferenças finitas, que são compartilhadas pelos esquemas usuais em elementos finitos, explicam a necessidade de investigar procedimentos alternativos, aqui limitados a dois esquemas exponenciais de cinco nós, ambos de segunda ordem e diagonalmente dominantes.

O primeiro foi proposto por D.N. de G. Allen para resolver a equação de transporte da vorticidade, num artigo co-assinado por R.V. Southwell [3]. O assim chamado esquema de Allen & Southwell pode ser descrito com base numa curva exponencial para cada eixo coordenado, digamos, o eixo x, gerado como solução da equação

$$u\frac{d\phi}{dx} - \alpha\frac{d^2\phi}{dx^2} = k \qquad (2)$$

que pode ser vista como uma aproximação u i-dimensional da eq. (1) se as derivadas em y são assumidas localmente constantes. A solução, envolvendo o polinomial, é ajustada aos nós (i-1, j), (i, j) e (i+1, j).

O esquema foi posteriormente extendido a outras equações [4]. Muitas reinvenções e variações do esquema apareceram subsequentemente [5,6,7]. Apesar da convergência de segunda ordem, o esquema de Allen & Southwell foi criticado por apresentar difusão numérica [8].

O segundo esquema exponencial é o esquema de cinco pontos de Dennis & Hudson incorporado na eq. (13) de seu artigo [9]. É baseado em uma forma aproximada unidimensional coincidente com (2) no presente caso, embora em geral admita coeficientes variáveis. A variável ϕ é submetida a uma transformação exponencial que torna (2) uma equação do tipo Poisson. Esta é discretizada por diferenciamento central e então anti-transformada. Estes autores também apresentam um esquema mais acurado, de quarta ordem, obtido com um termo de correção a-posteriori, que não é aqui considerado por envolver nove nós, com maior complexidade computacional.

SOLUÇÕES EXATAS DA EQUAÇÃO DE TRANSPORTE

As coordenadas x e y na eq. (1) são transformadas rotacionalmente em s e n, respectivamente paralela e normal à corrente, como mostrado na fig. (1). As novas coordenadas são adimensionalizadas pelo comprimento do domínio quadrado, sem modificações notacionais. Finalmente, dividindo pelo coeficiente de difusividade, obtem-se:

$$Pe\frac{\partial\phi}{\partial s} - \frac{\partial^2\phi}{\partial s^2} - \frac{\partial^2\phi}{\partial n^2} = 0 \qquad (3.1)$$

onde Pe representa o número de Peclet global

$$Pe = \frac{L}{\alpha}\,(u^2 + v^2)^{1/2} \qquad (3.2)$$

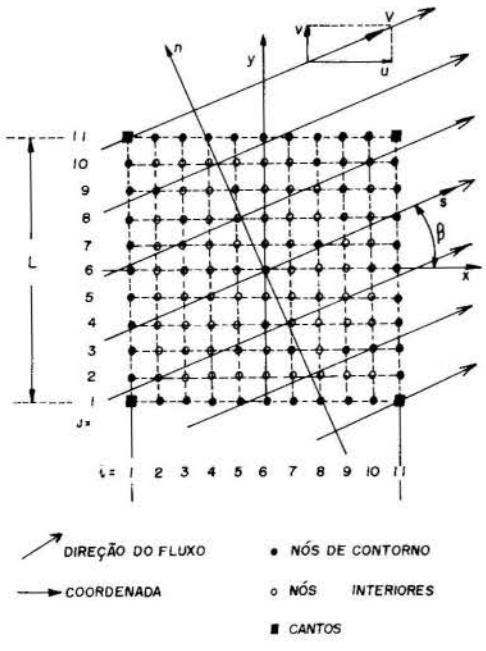

Fig. 1 Coordenadas analítica e numérica e grade 10x10.

Assumindo para (3.1) soluções na forma:

$$\phi(s,n) = S(s).N(n) \qquad (4.1)$$

obtem-se, de acordo com o método da separação de variáveis, as equações ordinárias simultâneas:

$$-\frac{d^2S}{ds^2} + Pe\,\frac{dS}{ds} \pm \lambda^2 S = 0 \qquad (4.2)$$

$$\frac{d^2N}{dn^2} \pm \lambda^2 N = 0 \qquad (4.3)$$

Se λ^2 é precedido pelo sinal positivo , as soluções tomam as formas:

$$\phi_A = \exp\{[Pe-(Pe^2+4\lambda^2)^{1/2}]s/2\}.\ \mathrm{sen}(\lambda n) \qquad (5.1)$$

$$\phi_B = \exp\{[Pe+(Pe^2+4\lambda^2)^{1/2}]s/2\}.\ \mathrm{sen}(\lambda n) \qquad (5.2)$$

junto com soluções em cos(λn), que diferem dos tipos A e B acima apenas por uma mudança de origem.

Quando λ^2 é precedido por sinal negativo, as formas reais das soluções dependem da razão λ/Pe. Se esta for menor que 0,5 haverá soluções de tipos:

$$\phi_C = \exp\{[Pe-(Pe^2-4\lambda^2)^{1/2}]s/2\}.\ \exp(\lambda n) \qquad (5.3)$$

$$\phi_D = \exp\{[Pe+(Pe^2-4\lambda^2)^{1/2}]s/2\}.\ \exp(\lambda n) \qquad (5.4)$$

Para λ/Pe>0.5 as soluções tomam as formas:

$$\phi_{CD} = \exp(\frac{Pe}{2}\,s).\sin[(\lambda^2-Pe^2/4)^{1/2}.s].\exp(\lambda n) \qquad (5.5)$$

$$\phi_{DC} = \exp(\frac{Pe}{2}\,s).\cos[(\lambda^2-Pe^2/4)^{1/2}.s].\exp(\lambda n) \qquad (5.6)$$

Para λ/Pe=0.5 todas as formas tendem para:

$$\phi_{C/D} = \exp(\frac{Pe}{2}\,s).\ \exp(\frac{Pe}{2}\,n) \qquad (5.7)$$

Em ambos os casos soluçoes simétricas em exp(-λn) também aparecem.

Para pequenas razões λ/Pe existem soluções nas formas A,B,C e D. Os tipos A e C são suaves na direção do escoamento, representando situações com difusão predominantemente cruzada, como por exemplo camadas limites hidrodinâmica e térmica [10], bem como as funções associadas aos casos-teste em que o conceito de difusão numérica é baseado. Opostamente, funções B e D com baixas razões λ/Pe apresentam grande difusão na direção do escoamento, que é particularmente alta na região próxima à fronteira de saída do domínio. As soluções elementares de todos os tipos com altas razões λ/Pe combinam difusão em ambas as direções.

PROBLEMA NUMÉRICO

Grades quadradas de refinamento variável são adotadas no domínio quadrado, como exemplificado na Fig(1) com uma grade de 10x10 espaçamentos.

Transformação rotacional permite obter as coordenadas s-n de cada ponto, de maneira que os valores exatos podem ser computados segundo uma das eqs.(5). Os valores exatos nos contornos são impostos como condição de Dirichlet para cada esquema. Os valores internos são armazenados para comparação posterior com as soluções numéricas.

Os esquemas de cinco nós resultam em equações de diferenças na forma:

$$A_{i-1,j}\cdot\phi_{i-1,j} + A_{i+1,j}\cdot\phi_{i+1,j} + A_{i,j-1}\cdot\phi_{i,j-1} +$$

$$+ A_{i,j+1}\cdot\phi_{i,j+1} + A_{i,j}\cdot\phi_{i,j} = 0 \qquad (6)$$

para cada nó interno (i,j).

Os coeficientes A são funções dos números de Peclet celulares:

$$\Delta Pe_x = \frac{u\Delta x}{\alpha} \qquad (7.1)$$

$$\Delta Pe_y = \frac{v\Delta y}{\alpha} \qquad (7.2)$$

que obedecem às relações gerais:

$$A_{i-1,j} = \pi(-\Delta Pe_x) \qquad (8.1)$$

$$A_{i+1,j} = \pi(\Delta Pe_x) \qquad (8.2)$$

$$A_{i,j-1} = \pi(-\Delta Pe_y) \qquad (8.3)$$

$$A_{i,j+1} = \pi(\Delta Pe_y) \qquad (8.4)$$

$$A_{i,j} = -(A_{i-1,j} + A_{i+i,j} + A_{i,j-1} + A_{i,j+1}) \qquad (8.5)$$

A função π(Pe) depende de cada discretização,como se segue:

Diferenciamento central:

$$\pi = 1 - \frac{\Delta Pe}{2} \qquad (9.1)$$

Esquema à montante:

$$\pi = \begin{cases} 1 & \text{se } \Delta Pe \geqslant 0 \\ 1-\Delta Pe & \text{se } \Delta Pe < 0 \end{cases} \qquad (9.2)$$

Esquema exponencial de Allen & Southwell:

$$\pi = \frac{\Delta Pe}{\exp(\Delta Pe) - 1} \qquad (9.3)$$

Esquema exponencial de Dennis & Hudson:

$$\pi = \exp(-\frac{\Delta Pe}{2}) \qquad (9.4)$$

As soluções numéricas foram obtidas por um procedimento iterativo coluna-a-coluna utilizando o algoritmo de Thomas para Matriz Tridiagonal. O processo iterativo era encerrado quando variações de ϕ entre iterações sucessivas fosse inferior a 10^{-9} vezes a diferença entre os valores máximo e mínimo da função exata. O diferenciamento central requereu um fator de relaxação para estabilidade; adotou-se o mínimo fator que torna a equação de diferenças diagonalmente dominante a cada passo. Os cálculos foram realizados em computadores PDP-10 e PDP-11 com precisão simples de 34 bits.

RESULTADOS

O fator de normalização do erro é definido pela diferença entre os valores máximo e mínimo da função exata discreta, excluindo os valores dos cantos. Tais valores não são envolvidos no problema numérico com esquemas de cinco nós; e sua exclusão do fator de normalização mostrou-se relevante para funções íngremes, levando a avaliações mais representativas dos erros [11].

A tabela 1 apresenta soluções numéricas obtidas pelos esquemas de segunda ordem, junto com a solução exata, para função tipo C com Pe=100, λ=2,22 e β=22,5 graus. A solução obtida com 10x10 espaçamentos é representada pelos valores ao longo das colunas i=2, i=6 e i=10 apenas.

No ponto (i,j)=(10,10) o diferenciamento central apresenta seu erro máximo, de 0,6% do fator de normalização; o erro do esquema de Allen & Southwell atinge 2,5%; e o de Dennis & Hudson 38%.

A tabela 2 considera a função D, mantendo Pe=100, λ=2,22 e β=22,5 graus. No mesmo ponto (10,10) o esquema de Allen & Southwell tem seu erro absoluto máximo de 0,6% do valor local (ou apenas 0,00007% do fator de normalização de $7{,}40\times10^{26}$). O erro do esquema de Dennis e Hudson atinge 6,6% do valor local. O diferenciamento central apresenta resultados oscilatórios inaceitáveis, com erro máximo em torno de meio fator de normalização.

Resultados para funções A e B, mantendo os parâmetros quantitativos, são muito similares a C e D respectivamente [11]. Claramente o diferenciamento central é o mais efetivo em casos de difusão cruzada com o escoamento e o esquema de Allen & Southwell é o melhor quando a difusão é paralela à convecção.

Os resultados acima são agora generalizados para outros ângulos e diferentes níveis de refinamento usando a curva logarítmica do erro versus espaçamento. Os erros são dados pela norma quadrática média, dividida pelo fator de normalização referido. O diferenciamento a montante é aqui incluído.

Tabela 1. Soluções Exata e de Segunda Ordem em Função C (Pe=100; λ=2,22; β=22,5°; 10x10 espaçamentos)

NÓ		SOLUÇÕES			
i	j	Exata	Diferença Central	Allen & Southwell	Dennis & Hudson
	11		3.89		
	10	3.16	3.16	3.18	3.38
	9	2.57	2.57	2.58	2.75
	8	2.09	2.09	2.10	2.24
	7	1.70	1.70	1.71	1.82
2	6	1.38	1.38	1.29	1.48
	5	1.12	1.12	1.13	1.20
	4	0.912	0.911	0.917	0.976
	3	0.741	0.741	0.745	0.793
	2	0.602	0.602	0.605	0.643
	1		0.490		
	11		2.82		
	10	2.29	2.28	2.36	3.22
	9	1.86	1.86	1.92	2.62
	8	1.51	1.51	1.56	2.13
	7	1.23	1.23	1.27	1.73
6	6	1.00	1.00	1.03	1.41
	5	0.813	0.811	0.837	1.14
	4	0.661	0.659	0.679	0.930
	3	0.537	0.536	0.550	0.752
	2	0.437	0.436	0.443	0.588
	1		0.355		
	11		2.04		
	10	1.66	1.64	1.75	3.06
	9	1.35	1.34	1.43	2.50
	8	1.10	1.09	1.16	2.03
	7	0.892	0.885	0.941	1.65
10	6	0.725	0.720	0.764	1.34
	5	0.589	0.586	0.619	1.09
	4	0.479	0.476	0.500	0.884
	3	0.389	0.388	0.402	0.706
	2	0.317	0.316	0.322	0.521
	1		0.257		

Tabela 2. Soluções Exata e de Segunda Ordem em Função D (Pe=100; λ=2,22; β=22,5°; 10x10 espaçamentos)

NÓ		SOLUÇÕES			
i	j	Exata	Diferença Central	Allen & Southwell	Dennis & Hudson
	11		7.20E-8		
	10	1.28E-9	-6.57E+23	1.16E-9	3.69E-10
	9	2.28E-22	9.65E+23	1.62E-11	1.35E-12
	8	4.04E-13	-5.50E+23	2.04E-13	4.10E-15
	7	7.19E-15	1.99E+23	2.35E-15	1.15E-17
2	6	1.28E-16	-5.39E+22	2.53E-17	3.94E-20
	5	2.27E-18	1.17E+22	2.57E-19	3.02E-22
	4	4.03E-20	-2.13E+21	2.50E-21	4.47E-24
	3	7.17E-22	3.33E+20	2.35E-23	8.65E-26
	2	1.27E-23	-5.02E+19	3.79E-25	5.45E-26
	1		2.26E-25		
	11		5.64E+8		
	10	1.00E+7	-2.01E+25	1.02E+7	7.52E+6
	9	1.78E+5	9.78E+24	1.83E+5	1.24E+5
	8	3.17E+3	-2.55E+24	3.27E+3	2.18E+3
	7	5.63E+1	4.81E+23	5.84E+1	3.87E+1
6	6	1.00E0	-7.78E+22	1.04E0	6.68E-1
	5	1.78E-2	1.29E+22	1.85E-2	1.22E-2
	4	3.16E-4	-2.47E+21	3.30E-4	2.17E-4
	3	5.61E-6	5.16E+20	5.86E-6	3.86E-6
	2	9.97E-8	-1.27E+20	1.04E-7	6.87E-8
	1		1.77E-9		
	11		4.42E+24		
	10	7.85E+22	-3.81E+26	7.90E+22	7.33E+22
	9	1.40E+21	2.85E+25	1.41E+21	1.30E+21
	8	2.48E+19	-1.83E+24	2.50E+19	2.30E+19
	7	4.41E+17	7.26E+22	4.45E+17	4.09E+17
10	6	7.83E+15	-9.98E+21	7.90E+15	7.27E+15
	5	1.39E+14	6.10E+21	1.40E+14	1.29E+14
	4	2.47E+12	-2.70E+21	2.50E+12	2.30E+12
	3	4.40E+10	8.90E+20	4.43E+10	4.08E+10
	2	7.81E+8	-3.17E+20	7.88E+8	7.25E+8
	1		1.39E+7		

$E \pm n = 10^{\pm n}$

A fig. (2) mostra o erro para a função tipo C.Em geral as posições relativas dos esquemas de segunda ordem é a mesma da tabela 1. O esquema à montante (M) é próximo ao de Allen & Southwell (AS) para grades grosseiras, mas o esquema de segunda ordem mostra sua superioridade com o refinamento. Os esquemas de Allen & Southwell e Dennis & Hudson (DH) coincidem a 45 graus. Na realidade as soluções, não apenas os erros, são coincidentes para qualquer função devido à proporcionalidade entre ambas as equações de diferenças quando os números de Peclet celulares nas duas direções são iguais.

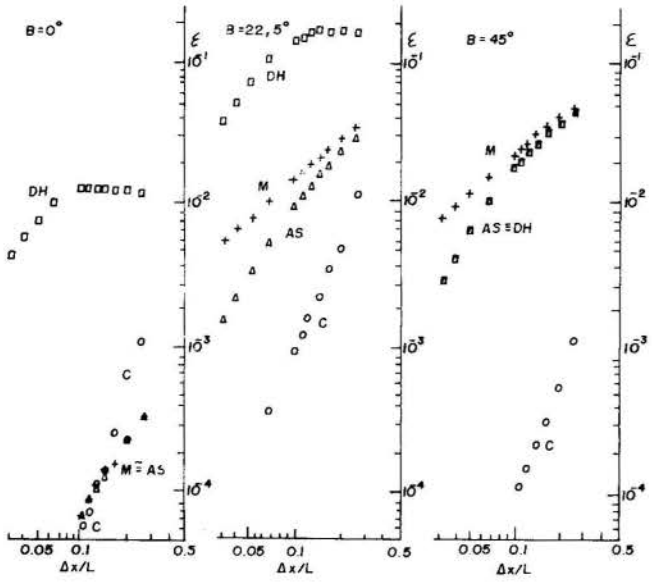

Fig. 2 Erro X Espaçamento para esquemas de cinco nós em função C, Pe=100, λ=2,22.

Confirmando o conceito angular de difusão numérica tanto o esquema à montante quanto o de Allen & Southwell aproximam o diferenciamento central (C) a zero graus, mas para os demais ângulos seus erros crescem muito mais significativamente.

A fig. (3) representa o erro na função D mantendo Pe e λ inalterados. O comportamento geral dos esquemas de segunda ordem repete aquele observado na tabela 2, exceto pela coincidência dos esquemas de Allen & Southwell e Dennis & Hudson a 45 graus. Para grades refinadas o esquema à montante mostra maior acuidade a 45 graus que o 0 graus, invertendo a tendência assumida pelo conceito angular de difusão numérica. Opostamente, o esquema de Allen & Southwell é de novo favorecido a 0 graus, onde tem erros desprezíveis.

Em ambos os casos C e D as curvas erro versus espaçamento do diferenciamento central se distancia de linhas retas de forma oscilatória para grades grosseiras, com altos números de Peclet celulares, o que foi atribuído a processo iterativo incompleto. À parte este fato, as curvas do diferenciamento central são mais próximas de linhas retas do que qualquer outro esquema. Mesmo a solução oscilatória apresentada na tabela 2 corresponde na fig. (3) a um ponto sobre a linha reta, cujo erro é dominado portanto pelo termo de segunda ordem.

Todos os outros esquemas, que são diagonalmente dominantes e cujas soluções e erros são limitadas, mostram curvas de erro versus espaçamento côncavas, indicando que o erro é em geral inferior ao valor assintótico extrapolado.

O comportamento de todos os esquemas em funções A e B com os mesmos Pe e λ é muito próximo ao seu desempenho nas funções C e D respectivamente, exceto para funções B a 45 graus onde todos os erros são cerca de

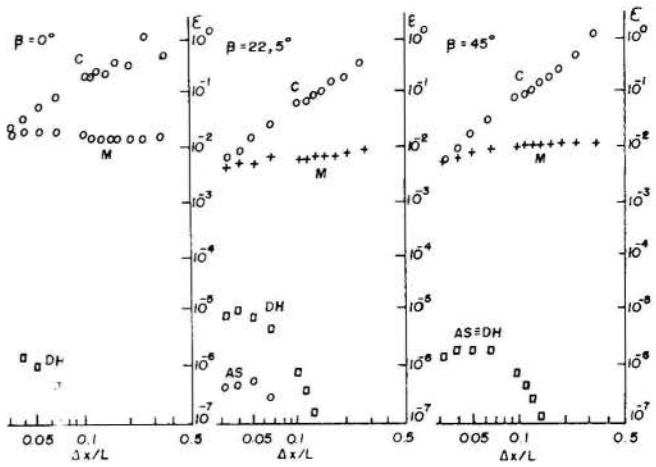

Fig. 3 Erro X Espaçamento para esquemas de cinco nós em função D, Pe=100, λ=2,22.

três ordens de magnitude inferiores a D devido à anti-simetria da função em torno do eixo s [11].

A fig. (4) apresenta o desempenho dos esquemas de segunda ordem nas funções A e B para Pe=10 e β=22,5 graus,com λ variável. Para o menor autovalor (λ=2) as posições relativas dos esquemas são análogas aos casos C e D previamente considerados, embora as curvas mostrem aspecto menos côncavo neste menor valor de Pe. Para λ=10 os erros de todas as discretizações são maiores e relativamente mais próximos entre si.

A evolução do desempenho dos esquemas com a frequência λ é mais complexa nos tipos C e D. O caso da função C/D é exemplificado na fig. (5) para Pe = 2λ = 4,44 com diferentes ângulos.

Os erros do esquema de Dennis & Hudson são desprezíveis. Claramente este esquema tem acuidade crescente com λ numa região das funções C e D até λ/Pe=0,5.

Os esquemas central e Allen & Southwell têm erros assintóticos coincidentes a 0 e a 22,5 graus, mas o esquema de Allen & Southwell tem valores nodalmente exatos

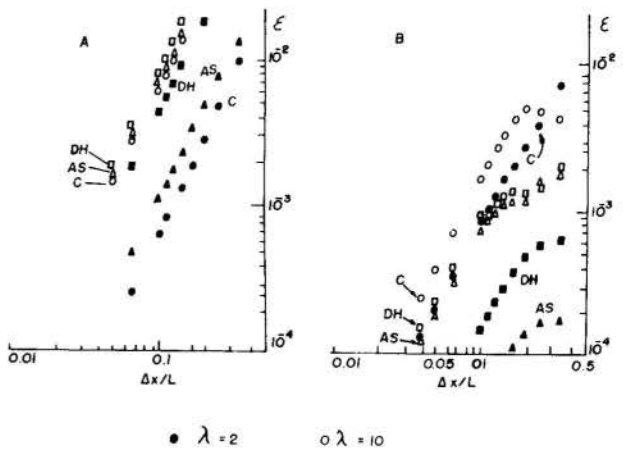

Fig. 4 Erro X Espaçamento para esquemas de segunda ordem em funções A e B; Pe=10.

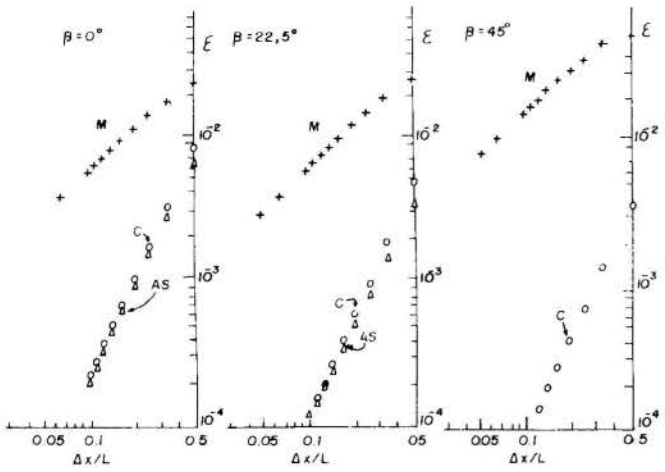

Fig. 5 Erro X Espaçamento para esquemas de cinco nós em função C/D, Pe=2λ=4,44.

a 45 graus, onde coincide com Dennis & Hudson. Aqui portando o esquema de Allen & Southwell desobedece a tendência afirmada pelo conceito de difusão numérica.

Valores mais altos de λ/Pe, implicando em funções CD e DC, são considerados na fig. (6) para o caso Pe=10, ß=22,5 graus e λ variável. O diferencimento central é favorecido para λ=6 em ambos os casos, apesar da otimalidade do esquema de Dennis & Hudson a λ=5 para este Pe. Para λ=10 os erros de todos os esquemas crescem e tendem a se aproximar entre si, analogamente aos casos A e B.

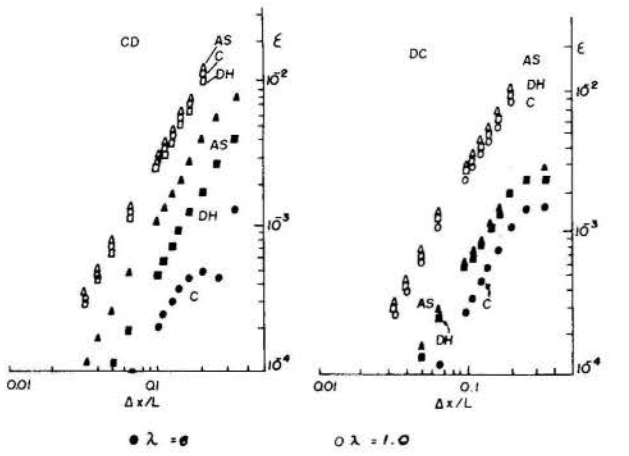

Fig. 6 Erro X Espaçamento para esquemas de segunda ordem em funções CD e DC; Pe=10.

CONCLUSÕES

Claramente o desempenho de todos os esquemas depende da solução particular da equação de transporte. O esquema de Allen & Southwell é favorecido em casos de difusão na direção do escoamento, associados a funções B e D com baixos λ/Pe. O diferenciamento central, à parte seus problemas de instabilidade, é favorecido em casos de difusão cruzada ao escoamento, dadas por funções A e C com baixos λ/Pe. O esquema de Dennis & Hudson é o melhor em torno do caso C/D com λ/Pe=0,5. Para λ/Pe em torno ou acima da unidade os erros de todos os esquemas são altos e próximos entre si, para quaisquer tipos de função.

Embora os esquemas de segunda ordem sejam necessariamente mais acurados que os de primeira para grades suficientemente refinados, os esquemas central e Dennis & Hudson mostraram-se, em alguns casos, muito piores que a à montante para grades moderamente refinadas. Neste sentido o esquema de Allen & Southwell é preferível como aquele que se provou quase sempre melhor que o esquema à montante, mesmo em grades grosseiras, num amplo conjunto de testes [11].

Mostrou-se que o conceito angular de difusão numérica é restrito a um subconjunto das possíveis soluções da equação de transporte, particularmente as funções A e C com baixos λ/Pe. Quando uma coordenada numérica é paralela ao fluxo, todos os erros associados aos termos convectivos, em particular os erros da discretização à montante, estão necessariamente na coordenada da direção do fluxo. Uma vez que as funções A e C com baixos λ/Pe apresentam baixas derivadas na direção do escoamento, os erros de convecção são desprezíveis. Se o fluxo é inclinado com respeito à grade há termos convectivos e altas derivadas em ambas as coordenadas numéricas, e o erro se torna considerável. Entretanto o desempenho do esquema à montante em outros tipos de função mostrou que aquela circunstância específica não pode ser tomada como base para uma teoria geral em análise numérica.

Embora baseada em experimentos com esquemas de cinco ponto, a conclusão acima é relevante para esquemas como o rotacional à montante [12,13] ou rotacional exponencial [14,15], que são esquemas de até nove pontos. Tais esquemas, inspirados pelo conceito angular de difusão numérica, evitam o efeito angular utilizando interpolação à montante ou exponencial apenas na coordenada orientada na direção do escoamento.

Os procedimentos rotacionais com o esquema à montante operam muito bem no caso das funções A e C com baixos λ/Pe, uma vez que reduzem o erro ao nível do erro do esquema à montante a zero graus. Mas o procedimento não aprimora a acuidade em funções B e D por exemplo onde o erro do esquema à montante a zero graus é maior que a 45 graus. Também o esquema rotacional exponencial não é sempre mais acurado que o exponencial, como mostrado na função C/D com λ/Pe=0,5. Outras excessões foram encontradas num conjunto mais amplo de testes [11].

REFERÊNCIAS

[1] P.J. Roache, Computational Fluid Dynamics (Hermosa Publishers, Albuquerque, New Mexico, 1972), p. 64.

[2] S.V. Patankar, Numerical Heat Transfer and Fluid Flow (Mc Graw-Hill, New York, 1980), p. 106.

[3] D.N. de G. Allen, and R.S. Southwell, Quart. J. Mech. and Applied Math. 8, 129 (1955).

[4] D.N. de G. Allen, Quart. J. Mech. and Applied Math. 15, 11 (1962).

[5] A.M. Il'in, Math. Notes, 6, 596 (1969).

[6] D.F. Roscoe, J. Inst. Maths. Applics. 16, 291 (1975).

[7] J.C. Chien, J. Comput. Phys. 20, 268 (1976).

[8] P.M. Gresho, and R.L. Lee, "Don't suppress the wiggles - They're Telling You Something", Finite Element Methods for Convection Dominated Flows, T.J.R. Hughes, ed. (ASME, New York, 1979), p. 37.

[9] S.C.R. Dennis, and J.D. Hudson, J. Inst. Maths. Applics. 26, 369 (1980).

[10] H. Schlichting, Boundary Layer Theory (Mc Graw-Hill, New York, 1979), p. 127.

[11] J.R. Figueiredo, tese de Doutorado, UNICAMP, 1988.

[12] G.D. Raithby, Comp. Meth. Applied Mech. Eng. 9, 153 (1976).

[13] J. Lillington, Int. J. Numer. Meth. Fluids 1, 3 (1981).

[14] T.J.R. Hughes, and A. Brooks, "A Multi-Dimensional Upwind Scheme with no Crosswind Diffusion", Finite Element Methods for Convection Dominated Flows, T.J.R. Hughes, ed. (ASME, New York, 1979).

[15] B.R. Baliga, and S.V. Patankar, Numerical Heat Transfer 6, 245 (1983).

ABSTRACT

A comparative study of central differencing, upwind, Allen & Southwell and Dennis & Hudson schemes is performed for the two-dimensional convective-diffusive transport equation, considering the linearized, homogeneous, constant-coeffients case. Sample solutions sweeping the Fourier spectrum of the general solutions are used as test-cases. Generality of the method allows the concept of numerical diffusion that postulates a direct relation between error and flow-to-grid angle to be discussed.

III ENCIT – Itapema, SC (Dezembro 1990)

FIXED-GRID SIMULATION OF PHASE CHANGE PROBLEMS: THE MUSHY-CELL APPROACH

M. Fabbri
Laboratório Associado de Sensores e Materiais - LAS
Instituto de Pesquisas Espaciais - INPE - Caixa Postal 515
12201 - São José dos Campos, SP - Brasil

SUMMARY

We describe a new technique for the simulation of quasi-equilibrium solidification processes. Results are obtained for pure heat conduction problems resembling one-dimensional freezing and bidimensional directional solidification in a rectangular cavity. We discuss some limitations of the method and sketch the possible applications for conductive/diffuse/convective phase-change situations.

1. INTRODUCTION

We investigate in this paper a new control-volume fixed- grid approach for the numerical simulation of transport phenomena involving liquid-solid(SL) phase changes. The motivation for developing a new scheme for this class of problems was the need of a reliable, simple and general framework where a host of complicated boundary conditions, material properties and coupled convection-diffusion transport could be incorporated. This situation arises typically in, e.g., bulk crystal growth from the melt. Specifically, we are interested in describing the bidimensional macrosegregation process that gives rise to the impurity distribution in as-grown $Pb_xSn_{1-x}Te$ crystals obtained by Bridgman and Vapor-Melt-Solid techniques. The compositional homogeneity in such pseudo-binary crystals is mainly dictated by the SL interface morphology during growth [1]. Interface tracking in bidimensional free-boundary problems is challenging, particularly when the heat transfer is coupled with mass diffusion and convection. This problem was first attacked by using time-dependent body-fitted coordinates [2,3], but this is a cumbersome approach requiring a lot of interpolation and coordinate mapping. Also, the error introduced by the quasi-stationary assumption in the moving-grid methods ammounts, for practical pourposes, to using from the start the more simple fixed-grid technique. If one is only interested in steady-state situations, a finite element approach with time-independent body-fitted coordinates generated self-consistently to fit the interface shape is also possible [4], but this technique requires a lot of computational resources, which prevents the method from having the flexibility to treat a broad class of situations. Also, we feel that a time-dependent simulation gives much insight into the mass-transport processes that takes place in a typical crystal growth experiment. Treating the transient regime by the finite-element self-consistent grid would be possible only with the help of a supercomputer.

Fixed grid techniques can be classified either as an enthalpy or as a regularization method. Regularization methods are based on some sort of smoothing of the enthalpy (H)-temperature (T) relationship, by assuming a finite "melting range" around the melting temperature T_M[5]. Some empiricism is necessary in order to assign meaningful values for the physical properties in the melting range; also, it is known that such smoothing procedure, although suitable for many complicated metallurgical processes [6], does not reproduce the richness of physical phenomena observed at the SL front, particularly the presence of mushy-regions [7]. The enthalpy method, which solves for the H-field from the previous values of the T-field, are effective only when the explicit time formulation is employed [8]; its implicit version gives rise to non-linear equations that can be solved with confidence only for small time-steps [9]. Implicit algorithms are known to be essential for obtaining stable solutions of the diffusion/convection equation in many practical situations that arise in crystal growth experiments [10].

Recent developed techniques are the permeability-continuum formulation (PCF) [11] and the phase-field model (PFM) [12]. PCF is obtained by assuming that mushy zones can be described as a sort of a permeable medium obeying a Darcy law, which is difficult to parametrize from first principles. The PFM employs an Helmoltz free-energy functional, from which a non-linear equation for a phase function is obtained that, in principle, is able of encompassing a whole class of influences, such as surface tension and supercooling; however, the phase function equation is usually very stiff, and become somewhat intractable when physical properties such as latent heat, specific heat and diffusivities are not constant. It appears that PFM has no hope to be applied with confidence for the case of binary alloys.

A somewhat distinct method based on the enthalpy formulation was developed by Voller and co-workers [13]. Basically, Voller's method isolates the latent heat contribution as a source term in the enthalpy conservation equation. The form of this source, being not explicit, requires the H-field to be solved in an autoconsistent, iterative manner for each time-step. In spite of this, Voller's technique is essentially stable and simple, due to the implicit control-volume discretization naturally evoked for its implementation. We therefore decided in favor of a fixed-grid approach that retains much of Voller's ideas, but instead of iterating over the H-field to get the right ammount for the heat sources, we thought it was simpler to treat the sensible part of the enthalpy as usual, and to use a "shooting" prescription for the time steps. This is done in such a way that a given part of the domain retains the same phase state during each time step

integration, and phase changes begin and terminate only at the end of a given time interval. In this way, integration of the transport equations can be done as usual, and boundary conditions are changed between time-steps, so as to simulate the actual phase state in each part of the domain. The control-volume formulation of Patankar and Spalding [14] is specially suited for this task, and permits a robust and flexible implementation of the algorithm. Since in our formulation no modifications are required neither in the transport equations nor in the essential method of solution, we think it is very flexible and can be applied without difficulty to a broad class of complicated phase-change problems. This technique, which we called the mushy-cell approach (MCA), is here first investigated to show its consistency and ability to reproduce actual physical situations that take place in continuous media.

We organize this paper in the following form. Section 2 describes the main ideas of MCA, and gives its control-volume version along with the basic assumptions concerning the physical properties of the cells undergoing phase changes. In Section 3 we give the algorithm adopted for its implementation. Section 4 displays some numerical results for one and two-dimensional domains, where it is shown that MCA reproduces well both quantitative and qualitative features of some basic solidification problems. Finally, in Section 5 we discuss briefly on the future applications we intend to make based on the MCA, and some of its limitations.

The present implementation of the MCA and the numerical results were made, to this moment, only for the case of a pure substance and conductive heat transfer. In this case, some analytical results are available for one-dimensional domains, and the qualitative features of two-dimensional directional solidification experiments are not so difficult to antecipate. Because of its very simple concept and flexible implementation, the extension of MCA to the more general diffusive/convective situations is expected to be easier than in Voller's original scheme, although it is not clear, by now, which one of the two approaches is better from the point of view of computational efficiency. Such studies are in progress at our laboratories and will be reported in near future.

2. THE MUSHY-CELL APPROACH (MCA)

Basic Ideas. The whole domain is divided into cells, whose shapes and sizes are maintained fixed during the calculations. FIG.1 displays a typicall cell configuration for a rectangular domain and a regular grid.

When phase change is taking place within a cell, the MCA associates the whole cell with the interface, a "mushy-cell" (m.c.). The physical properties of a m.c. are to be in accordance with the constitutive equations one chooses to model the actual thermodynamic relationship that the medium is expected to obey during a phase change. In the simplest case, namely for a pure substance in quasi-equilibrium conditions, the node temperature of an m.c. is to be held constant at T_M (= melting temperature) during the extraction of its latent heat content. A typical domain, at time t_0, will appear like FIG.1. When going from t_0 to $t_0+\Delta t$, the constraints imposed on the m.c.'s by the constitutive equations and thermodynamic relations will act as boundary conditions. Then the heat flux through each m.c. is computed and their latent heat is decreased (or increased) accordingly. Acceptable values for Δt are such as to guarantee that no qualitative changes occur during the time integration. At the end of the time step the cell's state is changed for those cells whose latent heat content, or either their temperature, are in accordance with the corresponding values for the new state, within a numerical error. Appropriate values for Δt when cells are near the beggining or the final of a phase change are quickly obtained by a simple iterative procedure (we use a linear "regula-falsi" prescription as a guess for Δt). Details of the algorithm are given in Section 3.

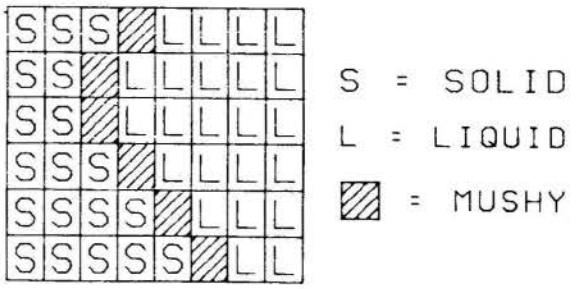

FIG.1 Schematic display of a typical computational domain in the MCA.

Control-volume discretization. Following the approach of Patankar [14], any dependent variable ϕ of interest (such as temperature, sensible enthalpy, concentration or velocity) obeys a conservation law of the form

$$\frac{\partial}{\partial t}(\rho\phi) + \mathrm{div}(\rho\vec{u}\phi) = \mathrm{div}(\Gamma \mathrm{grad}\phi) + S \qquad (1)$$

,where the units of ϕ are (physical units) per mass, ρ being the medium density. The second term in the LHS of (1) accounts for convection ($\vec{u}$ is the velocity field) and the first term in the RHS is the diffusion (Γ is the diffusion coefficient). The source contribution S represents all other effects that cannot be described as simple convective or diffusive (such as dissipative terms and internal sources).

Eq. 1 is a continuity equation in the reference frame which is stationary with the medium at rest. When the domain is subdivided into cells of fixed sizes and shapes, integration of (1) over a typicall cell will give a relationship between values of at neighboor nodes. Usually, a linear behaviour of ϕ is assumed within a cell and an implicit formulation is adopted for the time discretization. Also, the source term is linearized around the node value of ϕ. In the case of pure heat conduction with sources, for a bidimensional regular cartesian grid, each node gives rise to an algebraic equation of the form (FIG. 2 displays the basic nomenclature):

$$a_P T_P = a_W T_W + a_E T_E + a_S T_S + a_N T_N + b \qquad (2)$$

, where

$$a_W = k_w \Delta y/\Delta x \qquad a_E = k_e \Delta y/\Delta x$$

$$a_S = k_s \Delta x/\Delta y \qquad a_N = k_n \Delta x/\Delta y$$

$$b = S_C \Delta x \Delta y + a_P^0 T_P^0$$

$$a_P = a_E + a_W + a_S + a_N + a_P^0 - S_P \Delta x \Delta y$$

$$a_P^0 = \rho c_p \Delta x \Delta y / \Delta t$$

, and the source term was linearized accordingly to

$$S = S_C + S_P T_P \qquad (3)$$

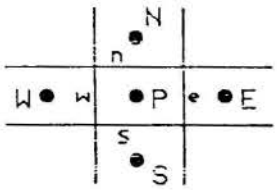

FIG.2 Nomenclature for the control-volume discretization.

k_i are the heat conductivities at each wall w,e,s and n, and c_p is the specific heat of the substance which fills P. It is known that the best choice for k_i which accounts for the actual heat fluxes between cells is given by the harmonic approximation [14]; for instance, the expression for k_w is

$$k_w = 2k_W k_P/(k_W + k_P) \qquad (4)$$

Eq. 2 is in implicit form, which means that the previous time value of the temperature field at node P is T_P^0, and all other node values that appear in (2) are current-time values.

Boundary conditions are easely incorporated in the control-volume discretized equation in the form of special sources. Since source terms are always written in the form of Eq. 3, it is very easy to impose particular conditions for the T-field (or else for the T-flux) at any specified node. For instance, if one wishes a constant temperature value for T_P, say T_M, it suffices to put $S_C = L*T_M$ and $S_P = -L$ in that node, where L is a very large number. Thus, time varying boundary conditions are easely handled by simply ascribing the actual values for S_C and S_P at each node for each time step.

Control-volume implementation of MCA. Basically, the heat equation is solved as usual for the sensible enthalpy terms, according to Eqs. 2, 3 and 4. To account for the latent heat contribution, a discrete field is defined such that H_i is zero for solid cells, L_F (=latent heat of fusion) for liquid and assumes any value between 0 and L_F in a m.c. The latent heat field H_i does not appear explicitly in the equations, but controls the ammount of time spent during phase change of each cell; in the present pure conductive problems the latent heat content of each m.c. is updated at the end of each time step according to the mean heat flux through the cells boundaries.

A more delicate issue address the problem of assigning specific values for the physical properties of a mushy cell. Specifically, given the values of ρ,c and k for the solid and liquid phases, we need a prescription to obtain these values for a m.c. Since at this time we are not concerned with convection terms, we simply assumed ρ constant throughout (density differences between solid and liquid were accounted for only to the extent of its influence on the net enthalpy content of each cell). Also, for pure substances, the melting temperature is constant (= T_M), and this eliminates the influence of the mushy-cell specific heat. For the heat conductivities, one must impose that the heat flux is continuous in time, so that no abrupt changes in k∇T is allowed to occur when a cell enters or leaves a process of phase change. The simplest prescription to deal with this, which is also correct in the limit of very small cells, is to assume a linear dependence of k with the cell's latent heat:

$$k_p = \frac{k^{liq} - k^{sol}}{L_F} H_p + k^{sol} \qquad (5)$$

Assigning definite physical properties for the m.c.'s is in fact one of the key points for the MCA, and we give more discussion about this in Section 5.

3. THE INTERFACE UPDATING ALGORITHM (IUA)

The control-volume MCA is implemented without difficulty, following the idea of updating internal boundary conditions and medium properties to keep track of the SL interface during time integration. The computational efficiency of the algorithm is of course strongly dependent on the judicious assignement of the auxiliary arrays used to store such information, and on the effectiveness of the time-shooting method adopted to guess the correct time steps during interface updating. Caution is also required to allow for any complicated phenomena which is likely to occur in bidimensional phase-change problems (such as the occurrence of remelting and non-connected boundaries).

The present version of our MCA implementation, which we called the interface updating algorithm (IUA), runs as follows (we assume T_M= 0 throughout):

1. Initialize fields h(sensible enthalpy) and H(latent heat).
2. Choose $(\Delta t)_0$, $(\Delta t)_{min}$, ε, T_{final}
3. t=0
4. $t = (\Delta t)_0$
5. $t = t + \Delta t$; if $t > T_{final}$, STOP
6. Integrate once, obtaining $h(t + \Delta t)$
7. Compute Q, the heat extracted from each m.c.
8. For each cell in the domain, verify the conditions:
   (a) If h > 0 then H is L_F
   (b) If h < 0 then H is 0
   (c) If h = 0 then
   $Q <= H - \varepsilon$ if Q >= 0
   $|Q| <= L_F - H - \varepsilon$ if Q < 0
9. If (a) and (b) and (c) in the whole domain, then
   - put H = H - Q in each m.c.
   - GO TO 5
10. Check if the changes were not "too large", that is,
   (A) If not(a), then $h < \varepsilon$ (this cell is ready to melt)
   (B) If not(b), then $h < -\varepsilon$ (this cell is ready to solidify)
   (C) If not(c), then
   $Q < H + \varepsilon$ if Q >= 0
   $|Q| < L_F - H + \varepsilon$ if Q <0

11. If (A)and(B)and(C) then
    - change boundaries accordingly
    - inform new interface position
    - update the values for the medium properties
    - put H = H - Q in each m.c.
    - GO TO 4
12. If not(A) or not(B) or not(C) then
    - put h = h(t), resetting the h-field
    - t = t - Δt
    - reduce Δt by a linear interpolation based on the temperature/flux values
    - if $\Delta t >= (\Delta t)_{min}$ then GO TO 5
      else STOP

Solution for the h-field in step 6 was done alternating line-column sweeps over the bidimensional domain, updating values by a simple Gauss-Sidel procedure.

4. NUMERICAL RESULTS

The ability of the MCA to reproduce the correct interface velocity of SL fronts in actual, continuous media was first checked by an unidimensional run simulating the solidification of a long slab of water. Analytical solutions are available for the Newman problem, where a semi-infinite slab of a pure substance, initially at a temperature $T_2 > T_M$, is subjected at its corner to a constant temperature $T_1 < T_M$. In FIG. 3 we compare the analytical solution [15] with the numerical results obtained with IUA. The physical constants were k^{ice}=0.0053, k^{water}=0.00144, c^{ice}=0.461, c^{water}=1.00, L_F=73.6 (c.g.s. units). Since the time spent by an m.c. during a phase change is roughly proportional to its latent heat content, we also checked the consistency of IUA results for different values of L_F (= 10.0, 73.6 and 200.0, displayed in FIG. 3). The semi-infinite domain was simulated by an initial run over the first 100 seconds of a 2 cm long slab, covered by a 500-point regular mesh.

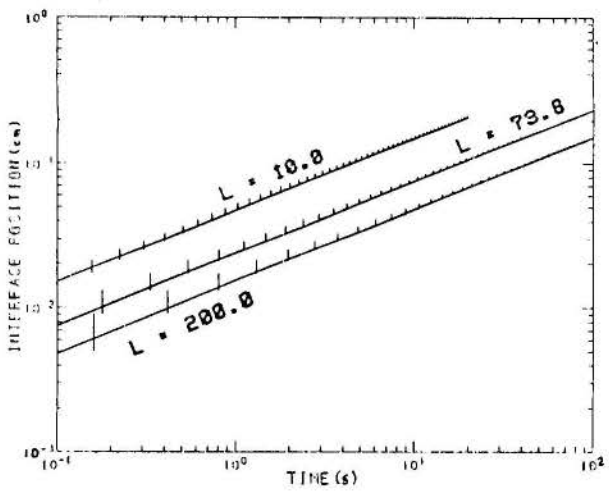

FIG.3 Results of IUA as compared to the analytical solutions. See text for discussion.

The bars in FIG. 3, which are of the same size of the discrete cells, give an idea of the error on the interface location introduced by the fixed-grid MCA. The runs were for T = +3°C and T = -5°C, and thus large temperature gradients are present near the SL interface during the initial stages of the solidification.

FIG. 3 clearly indicates that IUA does indeed yield very satisfactory results concerning the interface progression in time. Actually, we noted that the interface position was correctly predicted by IUA, on the average, even for rather coarse grids (a mesh with 100 points also gave results consistent with the analytical solution).

Bidimensional calculations were performed with IUA for simulating directional solidification experiments; this is a somewhat complicated situation, because the interface shape is strongly dependent on the different heat diffusivities of the solid, liquid and ampoule walls, as well as on the details of the furnace temperature profile.

FIG. 4 shows the interface progression during directional solidification of water inside a 2 cm diameter, 5 cm long, 1mm thick glass ampoule; the furnace profile was simulated by cold (-5°C) and hot(+8°C) plateaux with a linear gradient G = 32.5°C/cm in the "adiabatic" zone, moving at a speed of 15mm/h. This profile is imposed on the lateral walls of the ampoule; the left and right walls are kept at the same temperature of the corresponding corners. Initially, the whole ampoule and charge were termally stabilized with the furnace, whose profile is located such as to impose T = T_M at the left wall. Only half of the ampoule is shown, because of the simmetry with respect to the longitudinal axis. Thermal constants were those for water and ice, as mentioned before; for the ampoule, we took k^{glass} = 0.0028 and c^{glass} = 0.48 (c.g.s.). A coarse 50 x 10 regular grid was employed, which is enough for our purposes here.

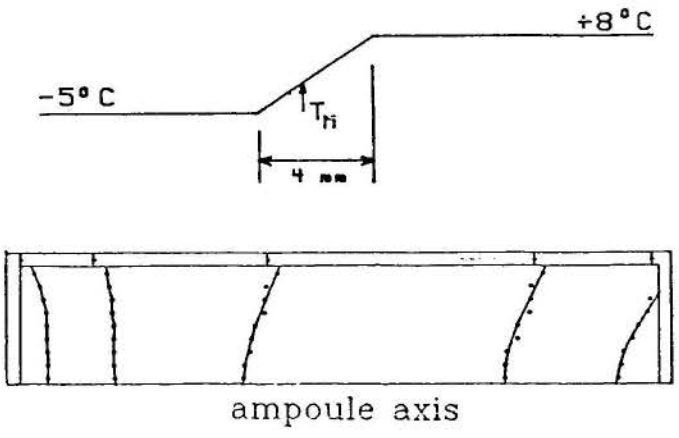

FIG.4 Water directional solidification inside a moving furnace. The small tips on the ampoule superior wall are the positions T_M of the furnace at the times when the interface profiles were taken.

We note in FIG. 4 that the interface changes its shape from concave toward the solid to concave toward the liquid during solidification; this effect is a consequence of the heat diffusivity in the solid being greater than in the liquid for the case of water. In the initial stages, heat is extracted from the SL interface mainly by axial conduction to the left ampoule wall; at later times, this process is much slower than the radial conduction to the lateral walls, and therefore the heat extraction is less effective for those points

near the ampoule axis. Of course this effect is strongly dependent on the furnace translation speed. For the values employed in FIG. 4, no steady-state was observed during the whole solidification process (the interface shape was always changing its curvature).

Very different qualitative behaviour is displayed in FIG. 5 for the case of a semiconductor material in which the heat diffusivity of the melt is greater than of the crystal (we used $k^{melt} = 0.36$, $k^{crystal} = 0.24$, $c^{melt} = c^{crystal} = 1.00$, $\rho^{melt} = \rho^{crystal} = 12.0$). The same interface shapes were obtained for furnace speeds ranging from 15 to 200 mm/h, with only a slight increase in curvature. In this case a steady state was reached very quickly and the interface shape does not change during most of the experiment. The ampoule was 1cm diameter, 0.25mm thick and a 100 x 20 mesh was used to cover the first 2.5 cm of its length.

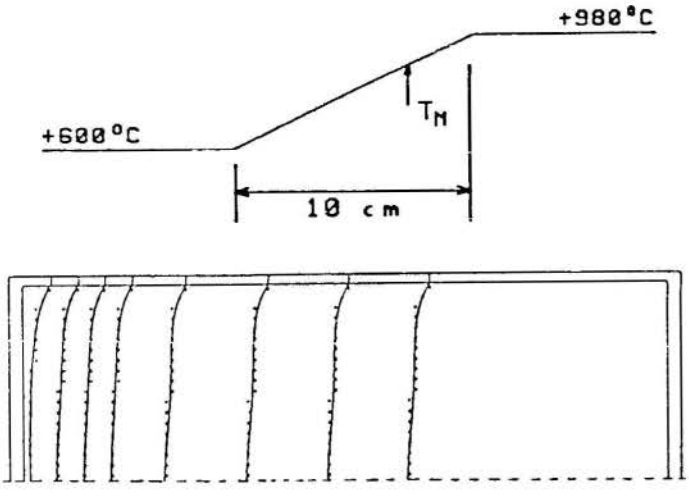

FIG.5 Same as FIG. 4 for a semiconductor-like material.

The small dots in FIGS. 4 and 5 are the center of the cells changing phase at the time when the interface profiles were taken; the continuous curves are obtained by some sort of best fit technique, interpolation or smoothing. We adopted a cubic spline smoother described by Reinsch [16].

We stress that the actual interface shape during solidification is also very much influenced by convection effects and radiation heat transfer [17], which can substantially modify the curvature and the simmetry of the profiles displayed in FIGS. 4 and 5.

All calculations were done in a simple PC-XT 10 Mhz personal computer, and typical bidimensional runs such that the one in FIG. 4 took nearly 8 hours of processing. Of course this timming can be reduced by one or two orders of magnitude if a more suitable machine is available.

5. DISCUSSION

The results shown in the preceeding section indicate that the MCA is able to reproduce the basic quantitative and qualitative features of the interface morphology in quasi-equilibrium solidification processes. IUA introduces a natural roughness in the interface location, but the same type of error, though sometimes hidden, also appears in any technique based on discretizations.

In convection/diffusion phase-change problems, non-slipping conditions are usually imposed at solid-liquid boundaries; hence, a technique must be devised to account properly for the matching of the velocity field in the vicinity of a mushy cell. Some suggestions to handle this situation were investigated by Voller et ali [18], and a couple of straightforward schemes were shown to work very satisfactory.

For the binary alloy solidification problem, it is very important to account correctly for the latent heat release at the melting range. In quasi-equilibrium conditions, use can be made of the phase diagram, and an equation of state relating internal energy, temperature and concentration can be obtained, which is valid for the liquid and solid, as well as for the mushy regions [19]. We feel that IUA is suited to handle this general situation, which will require the inclusion of the diffusion equation for the concentration field with a non-linear coupling with heat transfer (both conductive and convective). Since IUA proceeds along time integration over time intervals during which the SL interface is confined to a known region of the domain, it appears that convergence will be more easely reached than with the original Voller's scheme.

ACKNOWLEDGEMENTS

The Author is indebted to Prof. J. Szekely and Dr. J. Ilegbusi for useful discussions during his stay at the Dept. of Materials Science and Engineering of the Massachusetts Institute of Technology.

REFERENCES

[1] Brown, R.A., "Theory of Transport Processes in Single Crystal Growth from the Melt", AIChE Journal, Vol. 34(6), p.881-911, 1988.

[2] Sparrow, E.M.; Patankar, S.V.; Ramadhyani, S., "Analysis of Melting in the Presence of Natural Convection in the Melting Region", J.Heat Transfer, Vol. 99, p.520-526, 1977.

[3] Ramachandran, N.; Gupta, J.P.; Jaluria, Y., "Thermal and Fluid Flow Effects During Solidification in a Rectangular Enclosure", Int.J.Heat Mass Transfer, Vol. 25, p.187-193, 1982.

[4] Chang, C.J.; Brown, R.A., "Radial Segregation Induced by Natural Convection and Melt/Solid Interface Shape in Vertical Bridgman Growth", J.Cryst. Growth, Vol. 63, p.343-364, 1983.

[5] Szekely, J.; Themlis, N.J., "Rate Phenomena in Process Metallurgy", Chap. 10, Interscience, New York, 1970.

[6] Pehlke, R.D.; Marrone, R.E.; Wilkes, J.O., "Computer Simulation of Solidification", American Foundrymen's Society monograph, Des Plaines, Illinois, 1976.

[7] Basu, B.; Date, A.W., "Numerical Modelling of Melting and Solidification Problems - A Review", Sãdhanã, Vol. 13(3), p.169-213, 1988.

[8] Crank, J., "Free and Moving Boundary Problems", Oxford Univ. Press, New York, 1984.

[9] Desbiolles,J.-L. et ali., "Simulation of Solidification of Alloys by the Finite Element Method", Comp.Phys.Rep., Vol. 6, p.371-383, 1987.

[10] Derby, J.J.; Brown, R.A., "A Fully Implicit Method for Simulation of the One-dimensional Solidification of a Binary Alloy", Chem.Eng.Science, Vol. 41(1), p.37-46, 1986.

[11] Bennon, W.D.; Incropera, F.P., "A Continuum Model for Momentum, Heat and Species Transport in Binary Solid- Liquid Phase Change Systems I - Model Formulation", Int.J.Heat Mass Transfer, Vol. 30(10), p.2161-2170, 1987.

[12] Lin, J.T., "The Numerical Analysis of a Phase-field Model in Moving Boundary Problems", SIAM J.Numer.Anal., Vol. 25(5), p.1015-1031, 1988.

[13] Voller, V.R., "Implicit Finite- Difference Solutions of the Enthalpy Formulation of Stefan Problems", IMA J.Numer.Analysis, Vol. 5, p.201-214, 1985.

[14] Patankar, S.V., "Numerical Heat Transfer and Fluid Flow", Hemisphere, McGraw Hill, New York, 1980.

[15] Carslaw, H.S.; Jaeger, J.C., "Conduction of Heat in Solids", p.282- 286, Clarendon Press, Oxford, 1959.

[16] Reinsh, C.H., "Smoothing by Spline Functions", Num.Math., Vol. 10, p.177- 183, 1967.

[17] Rosenberger, F., "Fundamentals of Crystal Growth I", Chap. 6, Springer Verlag, Berlin, 1979.

[18] Voller, V.R.; Cross, M.; Markatos, N.C., "An Enthalpy Method for Convection/Diffusion Phase Change", Int.J.Numer.Meth.Eng., Vol. 24, p.271- 284, 1987.

[19] Wilson, D.G.; Alexiades, V.; Solomon, A.D., "The 1984 Model of Binary Alloy Solidification", in Free-Boundary Problems: Application and Theory Vol.III, p. 208-221, ed. by A. Bossavit, A.Damlamian and M. Fremond, Pitman Publishers, London, 1985.

III ENCIT – Itapema, SC (Dezembro 1990)

SOLUÇÃO NUMÉRICA DE PROBLEMAS DE CONDUÇÃO DE CALOR PELO MÉTODO DOS ELEMENTOS FINITOS USANDO ELEMENTOS QUADRILATERAIS DE TERCEIRA ORDEM

LUIZ FELIPE MENDES DE MOURA
UNICAMP – FEM/DETF
C.P. 6122
13081 – Campinas – SP

RESUMO

Neste trabalho é desenvolvido um método de elementos finitos para a solução de problemas bidimensionais de condução de calor em regime permanente. A utilização de elementos quadrilaterais de terceira ordem (12 nós por elemento) aumenta a precisão dos resultados mesmo para um número reduzido de elementos. Estes elementos (isoparamétricos) apresentam uma boa capacidade para se deformar, facilitando a adaptação dos elementos à geometria do corpo em estudo. O programa desenvolvido foi testado para o caso de dois problemas de condução de calor cujas soluções podem ser obtidas analiticamente. Um exemplo de aplicação foi incluído para demonstrar as capacidades do programa.

INTRODUÇÃO

Existem atualmente vários programas para o cálculo de problemas de condução de calor pelo método dos elementos finitos. Porém, a utilização de tais programas exige a discretização do domínio em um número relativamente grande de elementos, o que implica num longo trabalho de entrada de dados, além de exigir espaço de memória e tempo de cálculo incompatíveis com o emprego de microcomputadores de pequeno porte.

Neste trabalho, procurou-se desenvolver o método dos elementos finitos através da utilização de elementos quadrilaterais de terceira ordem (12 nós por elemento). Estes elementos, além de apresentarem um alto grau de precisão na representação da distribuição de temperaturas, podem ser adaptados à geometria do contorno através de deformações isoparamétricas. O emprego de tais elementos aumenta a dificuldade na determinação das matrizes elementares pois exige uma integração numérica, mas a redução do número de elementos necessários à uma dada precisão dos resultados conduz à diminuição do tempo total de cálculo. O espaço de memória é ainda reduzido pelo emprego do método de armazenagem da matriz global em um vetor, guardando apenas o perfil skyline da matriz.

FORMULAÇÃO DIFERENCIAL

Seja um domínio de volume v delimitado por uma superfície s. A equação de conservação do calor pode ser escrita da seguinte maneira:

$$L^T \; F - Q = 0 \qquad (1)$$

onde $F = \begin{vmatrix} fx \\ fy \\ fz \end{vmatrix}$ é o vetor dos fluxos de calor superficiais;

$L = [\frac{\partial}{\partial x} \; \frac{\partial}{\partial y} \; \frac{\partial}{\partial z}]^T$ é vetor dos operadores diferenciais;

e $Q =$ fluxo de calor volumétrico - (geração interna de calor).

A lei de Fourier para um meio isotrópico se exprime por:

$$F = - C.L^T \; T \qquad (2)$$

onde C é a condutividade térmica e
T é a temperatura.

Substituindo esta expressão na equação da conservação do calor, obtemos:

$$L^T \; (C \; L^T \; T) + Q = 0 \qquad (3)$$

A equação acima pode ser escrita na forma explícita:

$$\frac{\partial}{\partial x} \; (C \; \frac{\partial T}{\partial x}) + \frac{\partial}{\partial y} \; (C \; \frac{\partial T}{\partial y}) + \frac{\partial}{\partial z} \; (C \; \frac{\partial T}{\partial z}) + Q = 0 \qquad (4)$$

que é a forma habitual da equação da condução de calor.

No caso de um meio homogêneo onde a condutividade térmica é constante, a equação acima reduz-se a equação de Poisson:

$$C \; L^T \; L \; T + Q = 0 \qquad (5)$$

ou na forma explícita:

$$C \; \nabla^2 T + Q = 0 \qquad (6)$$

Esta equação está sujeita a dois tipos de condições de contorno:

- condições essenciais sobre uma parte S_1 da superfície S:

  $$T = \overline{T} \qquad (7)$$

  onde $\overline{T}$ são temperaturas especificadas.

- condições naturais sobre uma parte S_2 da superfície S:

  $$C \; n^T \; L^T T - \overline{q} - h(T - T_f) = 0 \qquad (8)$$

  ou na forma explícita:

  $$C \; \frac{\partial T}{\partial n} - \overline{q} - h(T - T_f) = 0 \qquad (9)$$

  onde n é o vetor dos cossenos diretores da normal à superfície externa;

  $\overline{q}$ é um fluxo de calor superficial especificado;

  h é o coeficiente de transferência de calor convectiva e

  T_f é a temperatura do fluido exterior ao domínio.

FORMULAÇÃO VARIACIONAL

A funcional associada a formulação diferencial(5)

desenvolvida acima pode ser escrita na forma seguinte [1]:

$$U = \frac{1}{2} \int_v C(LT)^T (LT)\, dv - \int_v QT\, dv - \int_{S_2} \bar{q}\, T\, dS$$

$$- \frac{1}{2} \int_{S_2} h\, T^2\, dS + \int_{S_2} h\, T_f T\, dS \qquad (10)$$

Aplicando o teorema de Euler podemos verificar que minimizar esta funcional U fornece a mesma distribuição de temperaturas sobre o domínio que a solução da equação diferencial do parágrafo precedente.

A formulação variacional integra as condições de contorno naturais, o que é normal pois estas condições representam uma conservação energética em termos de fluxo de calor. Por um outro lado, as condições de contorno essenciais (temperaturas especificadas) devem ser adicionadas à condição de otimização da funcional como se fossem "imposições" (no senso matemático do termo) e tratadas como tais, por exemplo, pelo método dos multiplicadores de Lagrange.

MÉTODO DOS ELEMENTOS FINITOS

O desenvolvimento do método dos elementos finitos foge aos objetivos deste trabalho. O leitor encontrará um tratamento completo e detalhado na obra de Zienkiewicz [2]. Vamos apenas introduzir alguns conceitos e notações necessárias ao desenvolvimento das equações(matriciais) dos elementos finitos.

Aproximação dentro do Elemento. As temperaturas dos diferentes nós de um elemento são representadas pelo vetor das temperaturas nodais:

$$T^n = [T_1 \ \ldots \ T_i \ \ldots \ T_n]^T \qquad (11)$$

Consideraremos uma aproximação do campo de temperaturas no interior do elemento fornecida por:

$$T^* = N\, T^n \quad , \quad N = [N_1 \ \ldots \ N_i \ \ldots \ N_n] \qquad (12)$$

ou então:

$$T^* = \sum_{i=1}^{n} N_i T_i \qquad (13)$$

onde as funções $N_i(x,y)$ são chamadas de funções de interpolação.

Neste trabalho foi escolhido um elemento quadrilateral de 12 nós (Figura 1). Devido ao seu alto grau de aproximação, este elemento apresenta a vantagem de possibilitar uma discretização com poucos elementos, evitando todas as dificuldades encontradas na determinação de malhas finas e conduzindo (para uma dada precisão) à sistemas de tamanho reduzido cujo tratamento seja compatível com utilização do microcomputador.

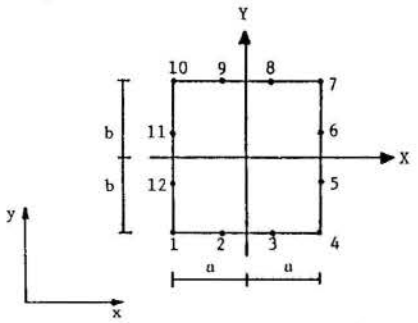

Fig. 1 Elemento retangular de 12 nós.

Funções de Aproximação. As funções de aproximação devem ser exprimidas em termos de um sistema de coordenadas de modo que as expressões obtidas sejam válidas para todos os elementos do domínio. No caso do elemento retangular de 12 nós e com os lados paralelos aos eixos das coordenadas globais x,y (Figura 1), define-se as coordenadas locais por:

$$X = \frac{x - x_c}{a} \qquad Y = \frac{y - y_c}{b} \qquad (14)$$

Assim, por exemplo, $X_4 = 1$ e $Y_4 = -1$.

As funções de interpolação do elemento utilizado são as seguintes:

$$N_1 = (1-X)(1-Y)(9X^2+9Y^2-10)/32$$
$$N_2 = 9(1-Y)(1-X^2)(1-3X)/32$$
$$N_3 = 9(1-Y)(1-X^2)(1+3x)/32$$
$$N_4 = (1+X)(1-Y)(9X^2+9Y^2-10)/32$$
$$N_5 = 9(1+X)(1-Y^2)(1-3Y)/32$$
$$N_6 = 9(1+X)(1-Y^2)(1+3Y)/32$$
$$N_7 = (1+X)(1+Y)(9X^2+9Y^2-10)/32$$
$$N_8 = 9(1+Y)(1-X^2)(1+3X)/32$$
$$N_9 = 9(1+Y)(1-X^2)(1-3X)/32$$
$$N_{10} = (1-X)(1+Y)(9X^2+9Y^2-10)/32$$
$$N_{11} = 9(1-X)(1-Y^2)(1+3Y)/32$$
$$N_{12} = 9(1-X)(1-Y^2)(1-3Y)/32$$

Pode-se constatar que as funções de interpolação definidas acima são polinômios incompletos de ordem 4. O emprego de funções de interpolação de ordem elevada impede o cálculo das matrizes elementares a partir de expressões explícitas. Este fato não chega a ser um problema mas implica em integrações numéricas cuja execução é relativamente lenta. Este é o preço a ser pago para chegar à uma eficiência aceitável usando meios de cálculo de baixa capacidade. Por um outro lado, estas funções permitem, como nós veremos a seguir, a eliminação quase completa do erro de aproximação do contorno do domínio.

Elementos Isoparamétricos. É claro que o elemento retangular apresentado no parágrafo precedente apresenta um defeito grave: a sua forma é pouco adaptada para cobrir um domínio de geometria complicada e ele induz à um grande erro de contorno a menos que seja utilizado em uma malha muito fina.

Vamos então usar um método de "deformação" de tais elementos. A deformação do elemento é obtida através de uma transformação geométrica de passagem do sistema local de coordenadas X,Y ao sistema global x,y do domínio (Figura 2). Esta transformação é do tipo:

$$x = \sum_{i=1}^{n} x_i N_i\,(X,Y) \qquad Y = \sum_{i=1}^{n} y_i N_i\,(X,Y) \qquad (15)$$

Como esta transformação utiliza as mesmas funções de interpolação (13) que as funções usadas na aproximação das temperaturas, ela é chamada de "transformação isoparamétrica".

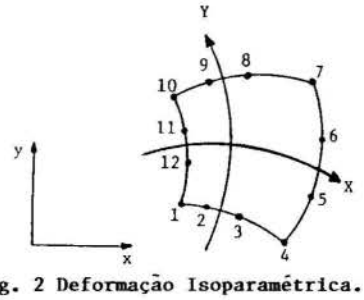

Fig. 2 Deformação Isoparamétrica.

Constata-se facilmente o interesse da transformação isoparamétrica que permite a discretização do domínio a partir de poucos elementos, aproveitando os lados curvilíneos para minimizar os erros de contorno. Veremos, em contra-partida, que a complexidade do tratamento dos elementos aumenta.

CÁLCULO DAS MATRIZES ELEMENTARES

Uma vez definido o elemento, devemos agora formular o seu comportamento térmico. Vamos aplicar o método de Ritz à expressão variacional (10) obtida acima. Exprimindo a funcional sobre o elemento em função das temperaturas aproximadas, obtemos:

$$U_e(T^*) = \frac{1}{2}\int_{v_e} C[LT^*]^T LT^* \, dv - \int_{v_e} QT^* \, dv$$

$$- \frac{1}{2}\int_{S_{2_e}} a T^{*2} \, ds + \int_{S_{2_e}} a T_f T^* \, ds - \int_{S_{2_e}} q T^* \, ds \quad (16)$$

onde v_e é o volume do elemento;

S_{2_e} é a parte do contorno submetida às condições de contorno naturais.

A função de aproximação definida acima é $T^* = N T^n$. Como a matriz T^n é independente de x,y, temos que $L(NT^n) = LNT^n$. Fazendo $B = LN$, a matriz B tem dimensão 2n se o elemento (bidimensional) suporta n nós.

Substituindo T* e B na funcional (16), temos:

$$U_e(T^n) = \frac{1}{2}\int_{v_e} T^{n,T} CB^T BT^n \, dv - \frac{1}{2}\int_{S_{2_e}} T^{n,T} a N^T N T^n \, ds$$

$$- \int_{v_e} T^{n,T} Q N^T \, dv - \int_{S_{2_e}} T^{n,T} q N^T \, ds + \int_{S_{2_e}} T^{n,T} a T_f N^T ds \quad (17)$$

Fazendo:

$$K_e = \int_{v_e} C B^T B \, dv + \int_{S_{2_e}} a N^T N \, ds \quad (18)$$

$$F_e = \int_{v_e} N^T Q \, dv + \int_{S_{2_s}} N^T (q - aT_f) \, ds$$

Obtemos:

$$U_e(T^n) = \frac{1}{2} T^{n,T} K_e T^n - T^n F_e \quad (19)$$

Segundo o método de Ritz, a melhor aproximação de T^n é aquela que, respeitando as condições de contorno essenciais, minimiza a funcional U_e. Esta condição se traduz por:

$$\frac{\partial U_e}{\partial T^n} = K_e T^n - F_e = 0 \quad (20)$$

O comportamento térmico do elemento é então representado pela relação:

$$K_e T^n = F_e \quad (21)$$

Integração Numérica. No desenvolvimento das matrizes elementares será necessário calcular as integrais sobre as fases e a superfície do elemento:

$$\int_{L_e} f_L(x,y) \, d\ell \quad \text{e} \quad \int_{S_e} f_S(x,y) \, ds \quad (22)$$

Como é impossível calcular analiticamente estas expressões, nós utilizaremos o método de integração numérica de Gauss que fornece uma boa aproximação destas integrais.

A matriz elementar contendo termos de sexta ordem, devemos tomar n = 4. A integração será feita então sobre 4 pontos de Gauss para as integrais de superfície e sobre 16 pontos de Gauss para as integrais de volume.

As coordenadas e os pesos para cada ponto são dados por:

i	X_i ou Y_i	w_i
1	-0,861136	0,3478548
2	-0,339981	0,6521452
3	+0,339981	0,6521452
4	+0,861136	0,3478548

CONSTITUIÇÃO DA MATRIZ GLOBAL

Consideremos agora o domínio na sua integralidade. Os nós são numerados de 1 a N (sistema global de numeração). Definiremos o vetor das temperaturas nodais como sendo:

$$T_N = [T_1 \; T_2 \ldots T_i \ldots T_N]^T \quad (23)$$

A matriz de condutividade global K e o vetor global dos fluxos nodais são constituídos a partir da contribuição das matrizes elementares e dos vetores dos fluxos de cada elemento. O sistema global de equações obtidos pode ser representado por:

$$K T_N = F \quad (24)$$

A matriz K apresenta características interessantes que tornam o método dos elementos finitos mais atraente. Ela é simétrica, definida positiva, singular e esparsa. Esta última propriedade é particularmente importante. Podemos dizer que dois nós são conectados se eles pertencem pelo menos à um mesmo elemento. Somente os nós concetados gerarão termos não nulos na matriz global, e cada nó só é conectado à uma pequena parte do conjunto global dos nós.

A matriz K é também determinada pela sua estrutura. A maneira de numerar a malha e de identificar as conexões nodais permite a localização dos termos não-nulos. Normalmente, tenta-se aproximar estes termos da diagonal da matriz. Desta forma é possível criar uma matriz banda, onde todos termos situados além de uma diagonal secundária são nulos.

Como a matriz K é simétrica, ela pode ser armazenada na forma de uma tabela de índice único, afim de economizar espaço de memória. Para cada coluna, partindo da diagonal para cima, existe um termo a partir do qual todos os outros são nulos por não-conexão. Pode-se então definir a altura skyline desta coluna e o perfil skyline da matriz. Evitar de armazenar zeros que se conhece a localização leva à uma economia de memória, o que conduz à métodos de armazenamento da matriz de eficiência crescente: meia matriz cheia, meia matriz banda e meia matriz skyline.

IMPLEMENTAÇÃO DAS CONDIÇÕES DE CONTORNO

As condições de contorno naturais foram integradas na formulação variacional e resultaram numa contribuição ao vetor do segundo membro, assim como o termo de geração interna de calor. A determinação dos elementos deste vetor será vista no capítulo seguinte.

Devemos então determinar as modificações necessárias à serem realizadas no sistema global para levar em consideração as condições de contorno essenciais (temperaturas especificadas). Existem vários métodos para implementar estas condições de contorno. O mais simples, em princípio, consiste em extrair do sistema global as equações correspondentes a uma temperatura especificada e reter somente o sub-sistema residual. Este método apresenta o inconveniente de necessitar longos cálculos de reestruturação da matriz global. Um outro método clássico consiste na utilização dos multiplicadores de Lagrange.

Supondo que existam condições de temperatura especificada em m nós, reagrupadas na forma matricial:

$$C T_N = [C_1 T_N \ldots C_i T_N \ldots C_m T_N] = 0 \quad (25)$$

com a condição do nó i: $T_i - \overline{T}_i = 0$.

Definiremos uma nova funcional de substituição:

$$U^{*'} = U^* + \lambda T_N = U^* + \Sigma \lambda_i C_i \quad (26)$$

onde λ_i são os multiplicadores de Lagrange.

Devemos agora minimizar $U^{*'}$ em relação às temperaturas nodais e aos multiplicadores de Lagrange. Obtemos então um novo sistema linear da forma:

$$K' T'_N - F' = 0 \quad \text{com} \quad T'_N = \begin{bmatrix} T_N \\ \lambda N \end{bmatrix} \quad (27)$$

O inconveniente deste método é o aumento da dimensão do sistema que passa de n a n+m. Por esta razão, optamos pela utilização de um método derivado do precedente, chamado de penalização.

Consideremos a funcional:

$$U^{*"} = U^{*} + \Sigma\ (\lambda_i C_i - \frac{1}{2}\lambda_i^2\ \varepsilon_i) \qquad (28)$$

com ε_i muito pequeno, de maneira que $U^{*"} \cong U^{*'}$.

A equação relativa é i-ésima condição de contorno é dada por:

$$\frac{\partial U^{*"}}{\partial \lambda_i} = C_i - \lambda_i \varepsilon_i = 0 \qquad (29)$$

ou seja $\lambda_i = C_i/\varepsilon_i$, e substituindo os valores de λ_i em (28) temos que:

$$U^{*"} = U^{*} + \frac{1}{2}\frac{C_i^2}{\varepsilon_i} \qquad (30)$$

A minimização da funcional em relação à i-ésima condição de contorno está, desta maneira, garantida. Devemos então resolver as n equações de minimização em relação às temperaturas: $\partial U^{*"}/\partial T_N = 0$, que conduzem à um sistema linear da forma $K"T_N = F"$ da mesma dimensão n que o sistema anterior.

O sistema é então modificado pelo acréscimo de $1/\varepsilon_i$ ao i-ésimo termo da diagonal de K, e de $\overline{T}_i/\varepsilon_i$ ao i-ésimo termo de F, ou seja:

$$K"_{i,i} = K_{i,i} + \frac{1}{\varepsilon_i} \quad \text{e} \quad F"_i = F_i + \frac{\overline{T}_i}{\varepsilon_i} \qquad (31)$$

Pode-se notar que a simetria da matriz é conservada.

O método de penalização comporta um certo risco associado à escolha de ε_i (risco de over flow ou falta de eficiência na penalização), e introduz uma aproximação adicional. Por um outro lado, este método apresenta as seguintes vantagens:

- só exige intervenções localizadas na matriz global, logo um baixo volume de cálculo;
- não aumenta a dimensão do sistema;
- contém a sua própria verificação, pois as temperaturas dos nós associados à uma condição de contorno são calculadas como as outras, o que permite constatar a qualidade com a qual a condição é respeitada.

Neste trabalho o valor de ε_i utilizado foi de $\varepsilon_i = 10^{-4}/K_{ii}$.

CONSTITUIÇÃO DO VETOR DOS FLUXOS

Trata-se aqui de determinar as contribuições das condições de contorno naturais (fluxo superficial especificado) e do termo de geração interna de calor, ao vetor do segundo membro do sistema global de equações.

A contribuição da geração interna de calor de cada elemento ao vetor dos fluxos é dada por $\int_{V_e} N^T Q\ dv$.

Esta quantidade é calculada pelo método de integração numérica de Gauss descrito anteriormente. Como os vetores elementares contém apenas termos de ordem 4, a integração pode ser feita sobre 9 pontos de Gauss. As coordenadas dos pontos de Gauss são X ou Y = $\pm$ 0,7745967 e, os produtos dos pesos $w_i w_j$ são:

- para os nós 1,3,7 e 9: 0,308642
- para os nós 2,4,6 e 8: 0,493827
- para o nó 5: 0,7901235

A contribuição do fluxo superficial de calor de cada segmento do contorno ao vetor dos fluxos é dada por $\int_{S_{2_e}} N^T q\ dS$.

Esta quantidade é calculada pelo método de integração numérica de Gauss. A integração é feita sobre 4 pontos de Gauss segundo o procedimento já desenvolvido anteriormente.

RESOLUÇÃO DO SISTEMA GLOBAL

Devemos calcular a solução do sistema linear:

$$K"\ T_N - F" = 0 \qquad (32)$$

Existem vários algorítimos para resolver sistemas lineares, mas a matriz K" sendo simétrica definida positiva, um dos métodos mais empregados é a fatorização de Choleski. Neste caso a matriz global pode ser decomposta sob a forma: $K" = S^T S$ onde S é uma matriz triangular superior que se calcula a partir das relações seguintes:

$$S_{11} = K"_{11};\ S_{1j} = \frac{K"_{1j}}{S_{11}};\ S_{ii} = \sqrt{K"_{ii} - \sum_{K=1}^{i-1} S_{Ki}^2};$$

$$S_{ij} = \frac{1}{S_{ii}}\left(K"_{ij} - \sum_{K=1}^{i-1} S_{Ki}S_{Kj}\right) \qquad (33)$$

onde j = i + 1, ... N.

Uma vez realizada a fatorização, deve-se calcular T_N, ou seja, resolver o sistema. Para tanto, faremos $G = S\ T_N$ e a partir do sistema decomposto $S^T S\ T_N - F" = 0$, obtemos $S^T G - F" = 0$ e $S^T N - G = 0$ que constituem dois sistemas triangulares de fácil resolução por substituição descendente e ascendente para obter G e T_N respectivamente.

RESULTADOS

O programa desenvolvido a partir do método de elementos finitos descrito acima foi testado para dois problemas de condução de calor cujas soluções podem ser obtidas analiticamente. Em seguida, o programa foi utilizado para resolver um problema mais complexo afim de demonstrar o seu potencial.

Whitley and Hromadka [3] sugerem um teste para verificar a precisão de soluções numéricas de problemas de condução de calor em regime permanente, com condições de contorno mistas. O problema consiste em determinar T(x,y) para:

$$\begin{array}{lll} \nabla^2 T = 0 & 0 < x < 1 \quad , \quad 0 < y < 1 & \\ T(0,y) = 0 & 0 < y < 1 & \\ T(1,y) = f(y) & 0 < y < 1 & (34) \\ \frac{\partial}{\partial y} T(x,0) = 0 & 0 < x < 1 & \\ T(x,1) = 0 & 0 < x < 1 & \end{array}$$

onde f(y) = min (exp(2y) - 1, exp(2(1-y)) - 1).

O domínio foi discretizado usando três malhas diferentes, com 4, 9 e 16 elementos. Os resultados obtidos são apresentados comparativamente na Tabela 1 para os pontos que apresentaram o maior erro em relação à solução analítica. Nas Figuras 3 e 4 são representados os dados da Tabela 1.

A Tabela 2 mostra os erros médios e máximos das soluções numéricas. Pode-se verificar que a discretização do domínio em apenas 9 (3x3) elementos já proporciona uma solução bastante precisa.

Em seguida, apresentaremos os resultados do teste do programa em relação à um problema de condução de calor bidimensional em regime permanente envolvendo geração interna de calor. O problema consiste em determinar T(x,y) para:

$$K\ \nabla^2 T + Q = 0$$

$$\frac{\partial}{\partial x} T(0,y) = 0 \qquad 0 < y < 1$$

$$\frac{\partial}{\partial y} T(x,0) = 0 \qquad 0 < x < 1$$

$$\frac{\partial}{\partial x} T(1,y) = -\frac{(T - T_\infty)}{K\ R_x} \qquad 0 < y < 1$$

$$\frac{\partial}{\partial y} T(x,1) = -\frac{(T - T_\infty)}{K\ R_y} \qquad 0 < x < 1$$

onde nas faces x = 1 e y = 1 ocorre transferência de calor para um meio à temperatura T_∞ através de uma resistência superficial (por unidade de área) R_x e R_y respectivamente.

Tabela 1. Resultados do problema de condições de contorno mistas.

	x = 0,7			x = 0,9	
y	ANAL.	4 ELEM.	9 ELEM.	ANAL.	16 ELEM.
0,1	0,392	0,426	0,392	0,352	0,345
0,2	0,437	0,510	0,448	0,511	0,520
0,3	0,493	0,610	0,516	0,716	0,743
0,4	0,535	-	0,547	0,922	0,980
0,5	0,539	0,536	0,486	1,023	1,031
0,6	0,490	-	0,539	0,902	0,915
0,7	0,397	0,418	0,437	0,672	0,671
0,8	0,275	-	0,296	0,431	0,437
0,9	0,140	-	-	0,208	0,212

Tabela 2. Comparação dos erros das soluções numéricas.

	4 ELEM.	9 ELEM.	16 ELEM.
$\bar{\varepsilon}$	9,6%	3,4%	2,2%
ε_{max}	23,7%	10,1%	6,6%

Os valores adotados para a geração interna de calor, a condutividade térmica, as resistências superficiais e a temperatura do meio exterior são:

$Q = 1000\ W/m^3$ $\quad K = 10\ W/m\ ^oC$
$R_x = 1\ m^2\ ^oC/W$ $\quad R_y = 0,1\ m^2\ ^oC/W$
$T_\infty = 0^oC$

A solução analítica deste problema, é descrita por Carslaw and Jaeger [4].

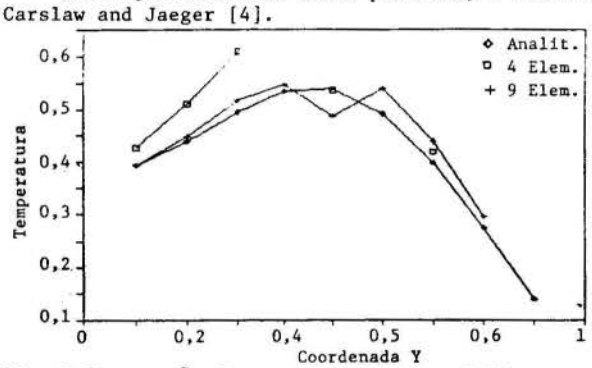

Fig. 3 Comparação dos resultados (x = 0,7).

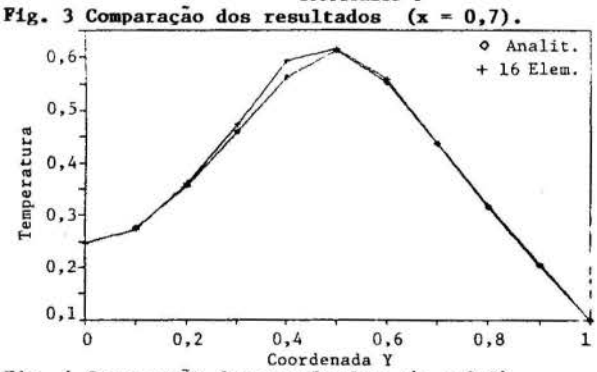

Fig. 4 Comparação dos resultados (x = 0,9).

Este problema foi resolvido numericamente discretizando-se o domínio em 4 (2x2) elementos. Os resultados obtidos representam um erro em relação à solução analítica sempre inferior à 0,2%. Na Tabela 3 são apresentados alguns valores da temperatura no contorno do domínio. A discretização do domínio em 9 (3x3) e 16 (4x4) elementos fornecem resultados cujo erro em relação à solução analítica é sempre inferior à 0,1%.

Os resultados obtidos neste problema são muito mais precisos que os resultados do primeiro problema, para um mesmo número de elementos. Isto ocorre porque, no primeiro caso, a distribuição de temperaturas (exponencial) na face x = 1 é aproximada pelas temperaturas especificadas nos nós do contorno, o que implica numa fonte de erro adicional quando o número de nós é pequeno. Já no segundo problema as condições de contorno (convecção) são distribuídas nas faces dos elementos.

O terceiro problema tratado neste trabalho representa um exemplo de aplicação do programa desenvolvido à um problema real. Um tubo de aço de seção interna circular e seção externa retangular é utilizado para geração de vapor por efeito Joule. A mistura água-vapor circula pelo interior do tubo. A superfície externa do tubo é isolada por uma camada de lã de vidro.

Tabela 3. Resultados do problema de geração interna de calor para a malha de 4 elementos.

	x = 0	x = 0,6	x = 1
	y=0 y=0,6 y=1	y=0 y=0,6 y=1	y=0 y=0,6 y=1
T (Anal.)	134,5 118,5 89,9	132,4 116,7 88,5	128,4 113,2 85,9
T (Num.)	134,5 118,5 89,9	132,4 116,7 88,5	128,4 113,2 85,8

Deseja-se saber qual a maior taxa de geração volumétrica de calor à ser aplicado no tubo sem que ocorra a fusão da parede do tubo ($T_{max} < 900^oC$). Trata-se então de aumentar gradualmente o valor da geração interna de calor aplicado ao tubo, verificando sempre o valor da maior temperatura obtida no domínio. Esta temperatura deve ocorrer na interface entre o tubo e o isolante.

Devido à simetria do problema, apenas 1/8 da seção transversal será discretizada. A Figura 5 mostra o domínio discretizado em 15 elementos (deformação isoparamétrica), assim como as condições de contorno. O valor do fluxo volumétrico de calor foi aumentado gradualmente à partir de $\dot{Q} = 10^6\ W/m^3$, onde a temperatura máxima obtida foi de aproximadamente 170°C, até $\dot{Q} = 10^7 W/m^3$, quando a temperatura atingiu valores próximos de 816°C.

A Figura 6 mostra a distribuição de temperaturas no domínio discretizado para o caso limite de $\dot{Q}=10^7 W/m^3$.

Este problema demonstra a capacidade do programa desenvolvido de representar geometrias complexas através da deformação dos elementos e de levar em conta uma variação da condutividade térmica e do fluxo volumétrico de calor de um elemento ao outro.

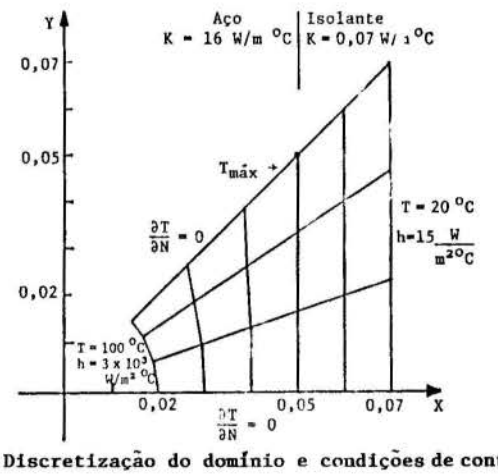

Fig. 5 Discretização do domínio e condições de contorno.

CONCLUSÕES

O método dos elementos finitos foi desenvolvido através da utilização de elementos quadrilaterais (isoparamétricos) de terceira ordem. A capacidade destes elementos de representar a distribuição de temperaturas com um alto grau de precisão aliada à capacidade de serem deformados para representar adequadamente o contorno do domínio, conduz à uma redução do número de elementos necessários à uma dada precisão dos resultados.

O programa desenvolvido foi testado em dois problemas de condução de calor para os quais a distribuição de temperaturas pode ser calculada analiticamente.

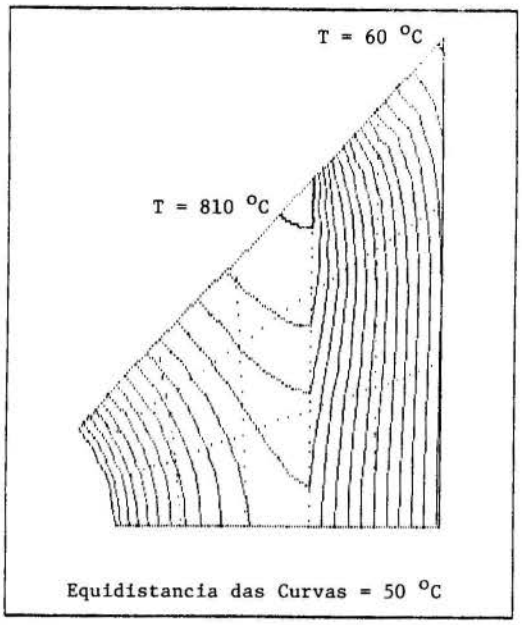

Fig. 6 Distribuição de temperaturas ($\dot{Q} = 10^7$ W/m^3).

Os resultados obtidos mostram que, mesmo usando poucos elementos, a precisão dos resultados é satisfatória.

O exemplo de aplicação do programa à um problema real mostrou que com apenas 15 elementos é possível representar a distribuição de temperatura em um domínio complexo tanto a nível da geometria quanto a nível de condutividade térmica e da geração volumétrica de calor.

REFERÊNCIAS

[1] C. Desai and J. Abel, "Introduction to the Finite Element Method", McGraw-Hill, New York (1971).

[2] O.C. Zienkiewicz, "Finite Elements in Engineering Science", McGraw-Hill, London (1971).

[3] R.J. Whitley and T.V. Hromadka II, "A test for Accuracy of Numerical Solutions of steady-state Heat Transfer Problems", Num.Heat Transfer, Vol. II, pp. 505-509 (1987).

[4] H.S. Carslaw and J.C. Jaeger, "Conduction of Heat in Solids", Oxford University Press, 2nd ed. (1959).

SUMMARY

In this paper, a finite element method is developed for the solution of two-dimensional steady-state heat conduction problems. A quadrilateral isoparametric element is used in conjunction with a third order interpolation function. This arrangement improves results accuracy (even for a few elements) and leads to a better representation of the boundaries by the element deformation.

The computer program developed was validated for two heat conduction problems with analytical solutions. A real problem is solved to demonstrate the numerical program capabilities. The results analysis shows that few elements are sufficient for acurate results.

III ENCIT – Itapema, SC (Dezembro 1990)

O SISTEMA SDP : ANÁLISE TÉRMICA TRANSIENTE

J. P. Gouvêa e F. Scofano Neto
Seção de Engenharia Mecânica e de Materiais, IME – RJ
M. S. Carvalho e M. V. A. Bianchi
Departamento de Engenharia Mecânica, PUC – RJ

SUMÁRIO

Este trabalho desenvolve um procedimento para a análise térmica linear transiente, empregando o método dos elementos finitos para a discretização espacial e métodos de integração direta para a discretização no domínio do tempo. Foram utilizadas as técnicas de organização de programas científicos previstas no sistema computacional SDP. A fim de avaliar a precisão do código, foram executados exemplos para comparação com soluções analíticas.

INTRODUÇÃO

No presente trabalho é apresentada a organização de programas para a resolução de problemas lineares de condução de calor, sob condições de contorno de temperatura prescrita, fluxo prescrito e mista (ou 3° tipo) com o auxílio do SDP – Sistema para Desenvolvimento de Programas Baseados no Método dos Elementos Finitos [1]. Este sistema estabelece regras de programação, organização de dados e documentação, dispondo de facilidades para manipulação de informações (banco de dados) e depuração de programas.

Foi utilizada uma formulação variacional, fazendo-se a aproximação espacial por elementos finitos [2] [4] e a integração temporal pelo método-θ de diferenças finitas [3].

A partir do ambiente computacional proporcionado pelo SDP, definem-se os diferentes módulos de programação.

De modo a validar o código, são apresentados alguns problemas, bem como uma avaliação crítica dos resultados obtidos quando comparados com soluções analíticas.

ORGANIZAÇÃO DOS PROGRAMAS

O trabalho foi desenvolvido baseado no sistema SDP, que se destina a auxiliar a elaboração de programas aplicativos técnico-científicos que utilizam o método dos elementos finitos. O SDP é uma proposta para o desenvolvimento de códigos, de modo a criar um ambiente computacional que dispõe de um sistema de gerenciamento de dados e facilidades para depuração e testes de rotinas. Possui ainda bibliotecas de procedimentos de cálculo com matrizes, solução de sistemas, cálculo de funções de interpolação, e outros.

A partir deste ambiente, este sistema estabelece níveis hierárquicos para programação (Fig. 1).

Aplicação. É um conjunto de programas, formando uma rede integrada, que permite a solução de um determinado problema. Como exemplos podem ser citados a análise estática e elasto-plástica de estruturas e as aplicações em mecânica dos fluidos e transferência de calor [1].

Processadores. São programas onde se iniciam os procedimentos de gerenciamento de memória, de rastreamento, organização dos bancos de dados, gerenciamento do acesso aos blocos funcionais. Os processadores executam tarefas inerentes a uma dada aplicação.

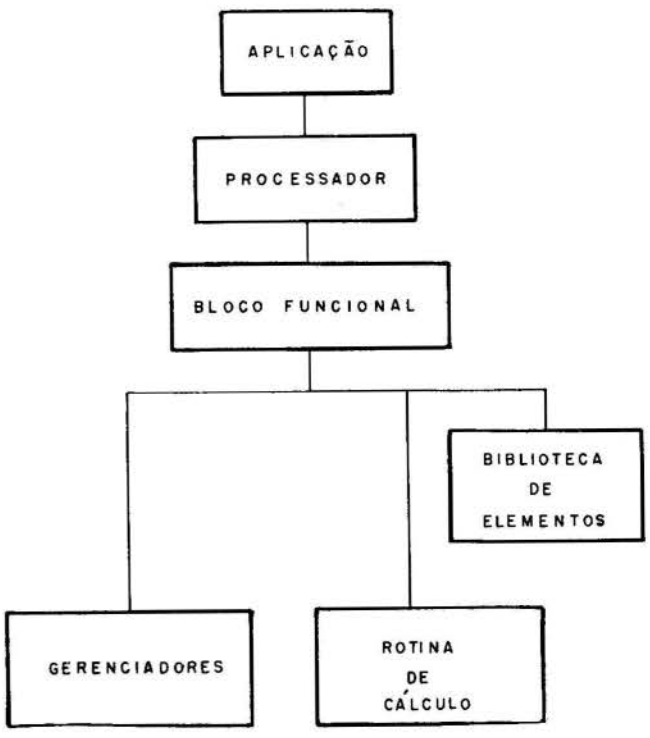

Fig. 1 – Organização dos Programas

Bloco Funcional. É encarregado de executar uma determinada tarefa e ativa uma série de procedimentos de cálculo e de gerenciamento. Um bloco funcional e suas sub-rotinas relacionadas formam um módulo de programação que somente transfere as informações necessárias e os resultados obtidos por um banco de dados. Com isto, esta estrutura torna-se altamente independente do resto do programa, dotando o código de uma grande flexibilidade.

Biblioteca de Elementos. É formada por rotinas que fornecem parâmetros ou ativam sub-rotinas de gerenciamento e de cálculo para um determinado elemento. Neste último caso pode ser considerada uma extensão de um bloco funcional.

Devido a esta estruturação, desenvolveu-se a aplicação de condução de calor em regime permanente utilizando-se os mesmos processadores e blocos funcionais da aplicação elasto-linear, mudando-se apenas a biblioteca de elementos. Com a elaboração de novos processadores obteve-se a análise para regime transiente.

O diagrama de blocos das duas aplicações desenvolvidas são mostrados nas Figuras 2 e 3.

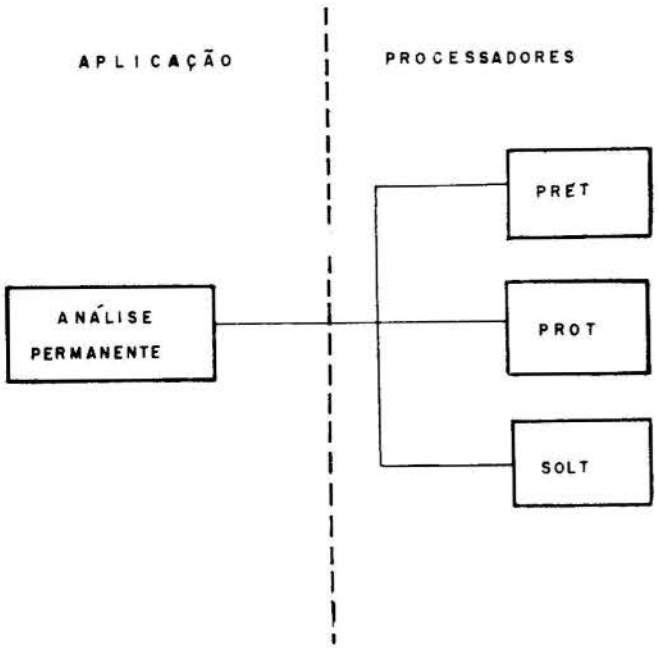

Fig. 2 – Diagrama de blocos para regime permanente

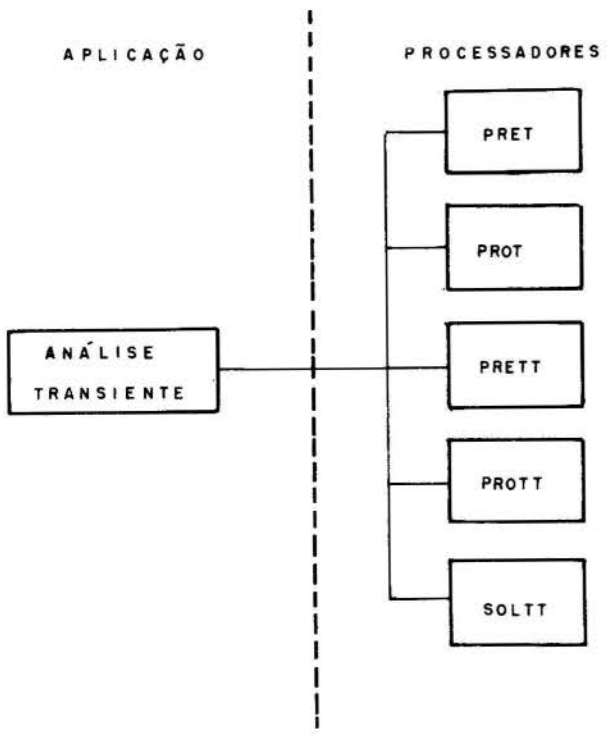

Fig. 3 – Diagrama de blocos para regime transiente

Os processadores são resumidamente descritos a seguir:

PRET. Cria no banco de dados as tabelas contendo os dados necessários ao problema a ser resolvido;

PROT. Cálculo das matrizes elementares de condutividade;

SOLT. Montagem das matrizes globais e solução do sistema de equações algébricas;

PRETT. Cria no banco de dados as tabelas contendo os dados necessários ao problema transiente;

PROTT. Cálculo das matrizes elementares de capacitância;

SOLTT. Montagem das matrizes globais e solução do sistema de equações algébricas.

FORMULAÇÃO DO PROBLEMA TÉRMICO

A equação da condução de calor tridimensional transiente em cordenadas cartesianas é dada por:

$$\rho c\frac{\partial T}{\partial t} = \frac{\partial}{\partial x}\left(k_{xx}\frac{\partial T}{\partial x}\right) + \frac{\partial}{\partial y}\left(k_{yy}\frac{\partial T}{\partial y}\right) + \\ + \frac{\partial}{\partial z}\left(k_{zz}\frac{\partial T}{\partial z}\right) + Q, \tag{1}$$

onde T é a temperatura, t é a coordenada tempo, Q é a taxa de geração de energia por unidade de tempo e volume, ρ é a massa específica, c é o calor específico e k_{xx}, k_{yy} e k_{zz} são as componentes do tensor condutividade térmica.

As condições de contorno são de 3 tipos:

$$T = T_p \quad \text{em } S_1\text{- Temperatura Prescrita} \tag{2}$$

$$-k\frac{\partial T}{\partial n} = q_n \quad \text{em } S_2 \text{ - fluxo prescrito} \tag{3}$$

$$-k\frac{\partial T}{\partial n} = h(T - T_\infty) \quad \text{em } S_3 \text{ - mista.} \tag{4}$$

Para a aplicação do método dos elementos finitos é necessário formular o problema através de um funcional I, o qual se pretende minimizar. As equações (1) a (4) podem ser representadas em uma forma variacional [2] como

$$I = \int_V \frac{1}{2}\left\{k_{xx}\left(\frac{\partial T}{\partial x}\right)^2 + k_{yy}\left(\frac{\partial T}{\partial y}\right)^2 + k_{zz}\left(\frac{\partial T}{\partial z}\right)^2 - \right. \\ \left. - 2\left(Q - \rho c\frac{\partial T}{\partial t}\right)T\right\} dV + \int_{S_2} qT dS + \\ + \int_{S_3}\frac{h}{2}(T^2 - 2TT_\infty + T_\infty^2)dS, \tag{5}$$

onde a distribuição de temperaturas T é tal que minimiza o funcional I.

Aproximando a distribuição de temperaturas por funções contínuas sobre os elementos escreve-se

$$T = [N]\{\phi\}, \tag{6}$$

sendo $[N]$ a matriz das funções coordenadas definidas de acordo com o tipo de elemento a ser utilizado (foi utilizado o elemento

isoparamétrico triangular) e $\{\phi\}$ o vetor que contém os valores das temperaturas dos pontos nodais (que são as incógnitas). Com este procedimento obtém-se um sistema de equações algébricas a ser resolvido.

A discretização espacial é feita utilizando uma família de elementos isoparamétricos triangulares de 3 a 6 nós. A idéia básica dos elementos isoparamétricos é utilizar a mesma função de interpolação para representar a geometria e o campo de variáveis. As funções de interpolação utilizadas são mostradas na Tabela 1 [5].

TABELA 1- FUNÇÕES DE INTERPOLAÇÃO

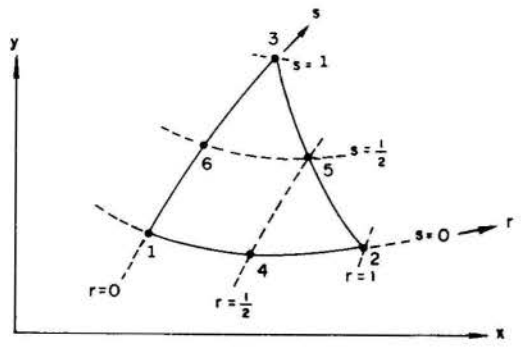

		i = 4	i = 5	i = 6
N_1 =	1-r-s	$-\frac{1}{2}N_4$	.....	$-\frac{1}{2}N_6$
N_2 =	r	$-\frac{1}{2}N_4$	$-\frac{1}{2}N_5$	
N_3 =	s	.....	$\frac{1}{2}N_5$	$-\frac{1}{2}N_6$
N_4 =	4r(1-r-s)			
N_5 =	4rs			
N_6 =	4s(1-r-s)			

No caso de regime permanente, o sistema de equações toma a forma:

$$[H]\{\phi\} = \{F\}, \tag{7}$$

onde $[H]$ é a matriz de condução global e $\{F\}$ é o vetor de carregamento térmico global. $[H]$ e $\{F\}$ são obtidos a partir de uma união das matrizes e vetores de carregamento elementares

$$[H] = \cup[h_e] \tag{8}$$

$$\{F\} = \cup\{f_e\}. \tag{9}$$

Os componentes h_{ij} e f_i são calculados por:

$$h_{ij} = \int_{V^e} \left[k^e_{xx}\frac{\partial N_i}{\partial x}\frac{\partial N_j}{\partial x} + k^e_{yy}\frac{\partial N_i}{\partial y}\frac{\partial N_j}{\partial y} + k^e_{zz}\frac{\partial N_i}{\partial z}\frac{\partial N_j}{\partial z}\right]dV^e + \int_{S^e_3} h^e N_i N_j dS^e \tag{10}$$

$$f_i = -\int_{V^e} Q^e N_i dV^e + \int_{S^e_2} q^e N_i dS^e - \int_{S^e_3} h^e T_\infty N_i dS^e, \tag{11}$$

onde o índice superior se refere ao elemento "e".

As três parcelas do vetor de carregamento térmico correspondem, respectivamente,à geração interna, ao fluxo prescrito e à parte não homogênea da convecção.

A solução deste sistema de equações é feita através de um método direto. A prescrição das temperaturas nodais é feita durante a resolução do sistema.

No caso de regime transiente, o sistema de equações obtido é:

$$[C]\{\dot{\phi}\} + [H]\{\phi\} = \{F\}, \tag{12}$$

onde $[C]$ é a matriz de capacitância térmica e $\{\dot{\phi}\}$ é o vetor que contém as derivadas temporais de ϕ.

De modo análogo ao regime permanente

$$[C] = \cup[C_e] \tag{13}$$

$$C_{ij} = \int_{V^e} \rho^e c^e N_i N_j dV^e. \tag{14}$$

Para resolver o sistema de equações diferenciais (12) será usado o método-θ de diferenças finitas [3]. A equação diferencial é resolvida em um tempo arbitrário entre t e $t+\Delta t$ definido por $t^* = t + \theta\Delta t$. Assim o sistema de equações é escrito em t^*:

$$\left(\frac{1}{\Delta t}[C] + \theta[H]\right)\{\phi\}_{t+\Delta t} = \left(\frac{1}{\Delta t}[C] - (1-\theta)[H]\right)\{\phi\}_t + (1-\theta)\{F\}_t + \theta\{F\}_{t+\Delta t}. \tag{15}$$

Determina-se então a distribuição de temperaturas no instante t+Δt a partir desta distribuição em t.

Ajustando o valor de θ entre 0 e 1, conforme o caso, obtém-se relações de recorrência diferentes para o cálculo da distribuição de temperaturas. Particularmente, fazendo θ=0, 0,5 e 1, obtém-se relações de recorrência bastante utilizadas que são, respectivamente, o método da diferença à frente (método explícito), método da diferença central (Crank-Nicolson) e o método da diferença à ré (método totalmente implícito).

ALGORITMO DA SOLUÇÃO TRANSIENTE

A fórmula de recorrência para a obtenção das temperaturas em cada instante é fornecida pela equação (15). Esta equação é da forma :

$$[A]\{\phi\}_{t+\Delta t} = \{B\}, \tag{16}$$

onde

$$[A] = \left(\frac{1}{\Delta t}[C] + \theta[H]\right) \tag{17}$$

e

$$\{B\} = \left(\frac{1}{\Delta t}[C] - (1-\theta)[H]\right)\{\phi\}_t + (1-\theta)\{F\}_t + \theta\{F\}_{t+\Delta t}. \tag{18}$$

A seqüência da solução transiente é:

- Cálculo de $[A]$ e sua respectiva triangularização;
- Cálculo de $\left(\frac{1}{\Delta t}[C] - (1-\theta)[H]\right)$, cujos valores são constantes durante a solução do problema.
- Para cada instante de tempo:
  - . Leitura do carregamento térmico em $t+\Delta t = \{F\}_{t+\Delta t}$
  - . Cálculo de $(1-\theta)\{F\}_t + \theta\{F\}_{t+\Delta t}$
  - . Cálculo de $\{B\}$
  - . Resolução do sistema (16).

RESULTADOS

Com o objetivo de verificar os resultados obtidos pelo programa, são resolvidos três exemplos que admitem solução analítica : dois em regime permanente e um em regime transiente.

Exemplo 1 – Regime Permanente. Obtenção da distribuição de temperaturas em uma coroa circular, de raio interno igual a 1 m e raio externo igual a 3 m, com as seguintes propriedades: $k_{xx} = 1{,}4\,W/m°C$, $k_{yy} = 1{,}4\,W/m°C$. A coroa é submetida às seguintes condições de contorno: Temperatura prescrita igual a 100°C no contorno interno e fluxo prescrito igual $10\,W/m^2$ no contorno externo.

Devido à simetria do problema, utilizou-se o domínio mostrado na figura 4, especificando fluxo igual a zero (isolamento) em $\alpha = 0°$ e $\alpha = 30°$.

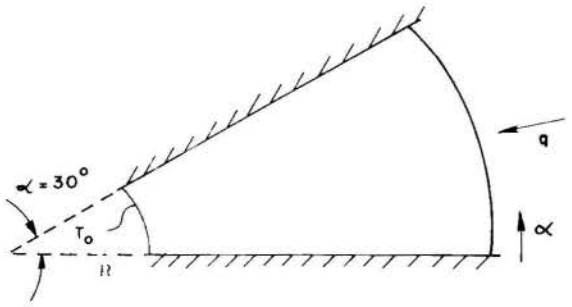

Fig. 4 – Domínio para a solução do Exemplo 1

O gráfico da figura 5 mostra a comparação entre a solução numérica e a solução analítica. O erro máximo obtido foi inferior a 0,5 %.

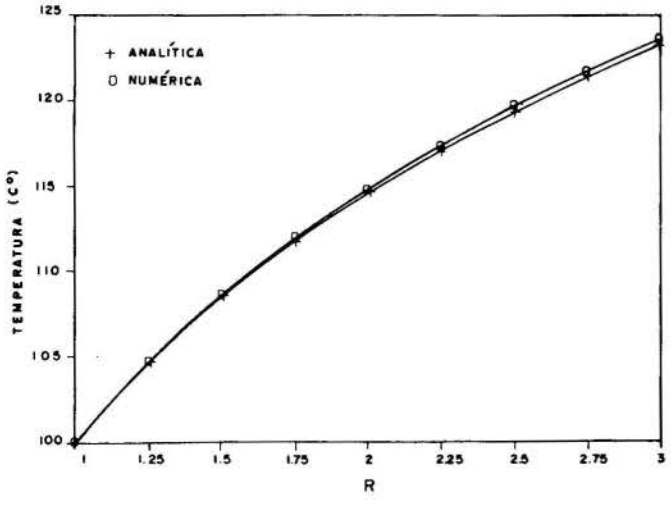

Fig. 5 – Comparação dos resultados do Exemplo 1

Exemplo 2 – Regime Permanente. Obtenção da distribuição de temperaturas em um domínio retangular com um furo circular excêntrico, com as seguintes propriedades: $k_{xx} = 20\,W/m°C$, $k_{yy} = 20\,W/m°C$ e $h = 200\,W/m^2°C$. O domínio do problema, bem como as condições de contorno são mostrados na figura 6.

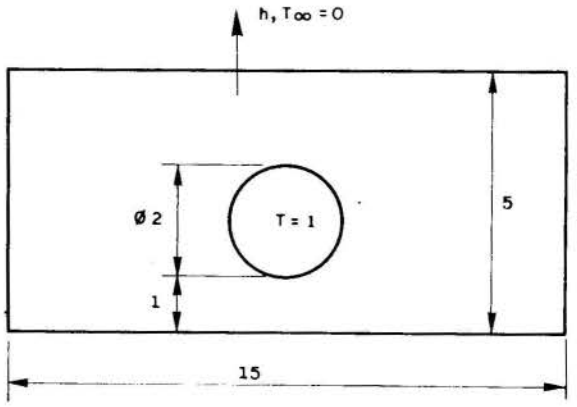

Fig. 6 – Domínio para a solução do Exemplo 2

Devido à simetria do problema, o domínio computacional utilizado corresponde à metade do domínio real.

O gráfico da figura 7 mostra a comparação do resultado numérico com o obtido analiticamente por Mey [6].

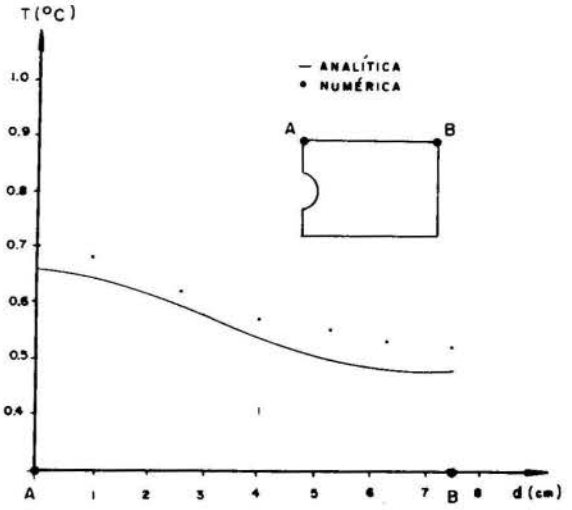

Fig. 7 – Comparação dos resultados do Exemplo 2

O erro máximo obtido foi da ordem de 3%. Caso fosse desejada uma solução mais precisa, dever-se-ia utilizar uma malha mais refinada. Os resultados mostrados foram obtidos com uma malha de 204 elementos (126 nós).

Exemplo 3 – Regime Transiente. Obtenção da distribuição de temperaturas em uma placa plana quadrada de lado igual a 3 m, com temperatura inicial igual a 30°C, com as seguintes propriedades: $k_{xx} = 204\,W/m°C$, $k_{yy} = 204\,W/m\,°C$, $\rho c = 2400\,J/m^3°C$. A condição de contorno em todas as arestas é do tipo temperatura prescrita e igual a 0 °C.

O domínio utilizado na solução do problema é mostrado na figura 8. Foram utilizados 121 nós, formando 200 elementos.

Utilizou-se um incremento de tempo (Δt) igual a 0,5. Foram obtidas as distribuições de temperatura a cada instante, e comparou-se a temperatura do centro da placa com o resultado obtido através da solução analítica, como é mostrado no gráfico da figura 9.

O erro máximo entre o resultado numérico e a solução analítica foi de 1 % , para o valor recomendado de $\theta = 1$ [3].

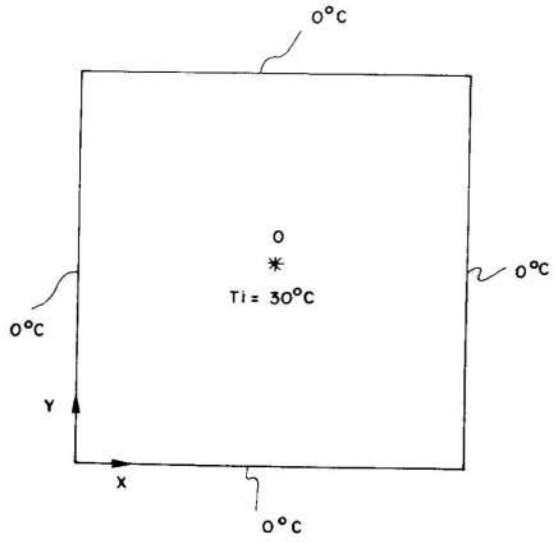

Fig. 8 – Domínio para a solução do Exemplo 3

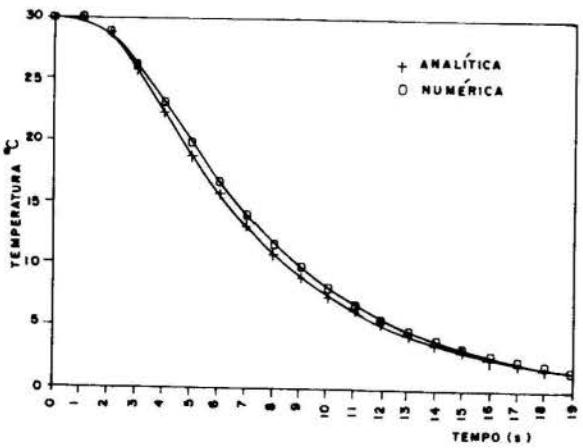

Fig. 9 – Comparação dos resultados do Exemplo 3

COMENTÁRIOS FINAIS

Utilizando-se a metodologia sugerida pelo SDP, foi implementada uma aplicação do método dos elementos finitos para a análise térmica de problemas lineares de condução de calor em regime permanente e transiente.

Verificou-se uma simplificação no trabalho de implementação de uma nova aplicação, uma vez que grande parte das rotinas utilizadas já estavam desenvolvidas.

Os resultados obtidos para os três problemas resolvidos apresentam boa concordância com suas soluções analíticas.

REFERÊNCIAS

[1] Gouvêa, J. P., "SDP: Sistema para Desenvolvimento de Programas Baseados no Método dos Elementos Finitos", *Tese de doutorado, Depto. Eng. Mec. PUC/RJ* (1986).

[2] Zienkiewicz, O. C. e Parenk, C. J., "Transient Field Problems: Two-dimensional and Three-dimensional Analysis by Isoparametric Finite Elements", *International Journal for Numerical Methods in Engineering*, v. 8, pp. 61–71 (1970).

[3] Burnett, D. S., *Finite Element Analysis*, Addison-Wesley Publishing Company (1987).

[4] Segerlind, L. J., *Applied Finite Element Analysis*, John Wiley & Sons Inc., New York (1976).

[5] Bathe, K. J., *Finite Element Procedures in Engineering Analysis*, Prentice Hall Inc., New Jersey (1982).

[6] Mey, G. D., "Temperature Distribuition in Floor Heating Systems", *International Journal of Heat and Mass Transfer*, v. 102, pp. 308–311 (1980).

AGRADECIMENTOS

À FAPERJ, pelo suporte financeiro para a realização deste trabalho.

ABSTRACT

The present work develops programs to solve unsteady heat conduction problems using the Finite Element Method for the space approximation and Finite Difference Method for the time approximation. The programs are structured according to the SDP system. The organization of programs and some results are shown.

III ENCIT — Itapema, SC (Dezembro 1990)

DETERMINAÇÃO DE FLUXOS DE CALOR EM CONDUÇÃO TRANSIENTE

CLODIO A. P. SARZETO - IME/RJ e COPPE/UFRJ
Praça Gen. Tibúrcio 80, Praia Vermelha, RJ
ABIMAEL F. DOURADO LOULA - LNCC/CNPq
Rua Lauro Muller, 455, 22290, RJ

RESUMO

Um esquema de pós-processamento, consistindo em adicionar os resíduos das equações constitutivas e de balanço, é proposto para melhorar a precisão de aproximações de elementos finitos para o fluxo de calor em problemas transientes de condução de calor. Análise numérica, estimativas de erro e resultados numéricos são apresentados confirmando a boa performance do método proposto.

INTRODUÇÃO

O tratamento de problemas dependentes do tempo pelo método dos elementos finitos usualmente objetiva a determinação de variáveis primais e suas derivadas espaciais. Nos modelos cinemáticos as variáveis primitivas são obtidas diretamente pela solução do sistema de equações algébricas resultantes da discretização espacial por elementos finitos e da aplicação de esquemas de diferenças finitas para a discretização no tempo, enquanto os campos derivados decorrem da interpolação inerente ao método. Em problemas de condução de calor que envolvem originariamente derivadas espaciais de segunda ordem do campo de temperaturas, as aproximações clásssicas de elementos finitos, baseadas no método de Galerkin com funções de interpolação de primeiro grau, aproximam a equação de equilíbrio de forma extremamente fraca e conduzem a aproximações imprecisas para o fluxo de calor.

As formulações tipo Petrov-Galerkin, inicialmente propostas para superar efeitos de trancamento ou "locking" em soluções numéricas de problemas da engenharia, como por exemplo, o problema da viga de Timoshenko [1], podem ser utilizadas para facilitar a construção e melhorar a precisão de aproximações de elementos finitos [2-3] ou ainda em pós-processamento de campos previamente determinados por qualquer método [4-5], com os mesmos objetivos.

Face aos bons resultados obtidos nas referências [4,5] em problemas estacionários propomos, neste trabalho, uma formulação de Petrov-Galerkin visando a obtenção de aproximações mais precisas para o fluxo de calor em problemas de condução transientes, através de um esquema de pós-processamento que utiliza o campo de temperaturas e sua derivada no tempo obtidos com o método de Galerkin.

PROBLEMA MODELO

Seja Ω um subconjunto aberto de R^2 com fronteira regular $\Gamma = \partial\Omega$. O problema modelo aqui considerado consiste em:

Para uma dada fonte de calor $f(\mathbf{x},t)$, $\mathbf{x} \in \Omega$, $t \in [0,T]$, determinar o fluxo de calor $\mathbf{p} : \Omega \times [0,T] \to R^2$ e o campo de temperaturas $u : \Omega \times [0,T] \to R$, satisfazendo, para todo tempo $t \in [0,T]$, a equação de balanço de fluxo

$$\rho c u_t + \mathrm{div}\mathbf{p} = f, \quad \text{em} \quad \Omega$$

a equação constitutiva (lei de Fourier)

$$\mathbf{p} = -K\nabla u \quad \text{em} \quad \Omega,$$

à condição de contorno

$$u(\mathbf{x}) = 0 \quad \text{em} \quad \Gamma$$

e à condição inicial

$$u(\mathbf{x},0) = v(\mathbf{x}) \quad \text{em} \quad \Omega,$$

onde ρ é a massa específica, c é o calor específico, K é um tensor simétrico e positivo definido representando a condutividade térmica do material, u_t denota a derivada de u em relação ao tempo, e os símbolos div e ∇ denotam os operadores divergência e gradiente, respectivamente.

Formulacao Variacional. Seja $L^2(\Omega)$ o espaço de Hilbert contendo funções escalares quadrado integráveis em Ω, com produto interno

$$(f,g) = \int_\Omega fg\, d\Omega \quad \forall f,g \in L^2(\Omega),$$

e norma induzida

$$\|f\| = (f,f)^{1/2}.$$

Consideremos ainda o espaço de Hilbert de ordem m,

$$H^m(\Omega) = \{f \in L^2(\Omega);\ \forall\alpha, |\alpha| \le m,\ \partial^\alpha f \in L^2(\Omega)\},$$

com o produto interno usual

$$(f,g)_m = \sum_{|\alpha|\le m} \int_\Omega \partial^\alpha f \partial^\alpha g\, d\Omega \quad \forall f,g \in H^m(\Omega),$$

norma

$$\|f\|_m = (f,f)_m^{1/2}$$

e seminorma

$$|f|_m = (\partial^m f, \partial^m f)^{1/2}.$$

Em particular consideremos o subespaço V de $H^1(\Omega)$ contendo funções que se anulam no contorno, isto é,

$$V = H_0^1(\Omega) = \{f \in H^1(\Omega),\ f = 0 \quad \text{em} \quad \Gamma\}.$$

A forma fraca do problema modelo proposto, em temperatura apenas como é usualmente apresentada em formulações cinemáticas, consiste em

Problema T: Para todo $t \in [0,T]$ achar $u \in V$, tal que

$$(u_t, w) + a(u, w) = (f, w) \quad \forall w \in V\,,$$

com

$$(u, w) = (v, w) \quad \forall w \in V, \quad t = 0$$

sendo

$$a(u, w) = (\nabla u, \nabla w)\,.$$

Onde admitimos $\rho c = 1$ e $K = I$, tensor identidade de segunda ordem, apenas para simplificar a apresentação.

Discretização Espacial. Por simplicidade admitimos ainda que Ω é um domínio poligonal discretizado por meio de uma malha uniforme com Ne elementos. Denotamos por h o diâmetro da malha, definido como $h = \max h_e$, onde h_e é o diâmeto do elemento e. Seja $S_h^k(\Omega) \subset H^1(\Omega)$ um espaço de elementos finitos de classe C^0 e grau k. Podemos então formular a seguinte aproximação de Galerkin para o **Problema T**, em $V_h^k = S_h^k \cap H_0^1(\Omega)$:

Problema $\mathbf{T_h}$: Para todo $t \in [0,T]$ achar $u_h \in V_h^k$ tal que

$$(u_{ht}, w_h) + a(u_h, w_h) = (f, w_h) \quad \forall w_h \in V_h^k\,,$$

com

$$(u_h, w_h) = (v, w_h) \quad \forall w_h \in V_h^k, \quad t = 0\,.$$

Para esta aproximação valem as seguintes estimativas de erro [6]:

Teorema 1: Se u e u_h são soluções dos **Problemas T** e $\mathbf{T_h}$, respectivamente, então, para $t \geq 0$, temos

$$\|u(t) - u_h(t)\| \leq \|v - v_h\| +$$

$$Ch^{k+1}\left(\|v\|_{k+1}\int_0^t \|u_t\|_{k+1}\,ds\right),$$

$$\|\nabla\left(u(t) - u_h(t)\right)\| \leq \|\nabla(v - v_h)\| +$$

$$Ch^k\left(\|v\|_{k+1} + \int_0^t \|u_t\|_{k+1}\,ds\right)$$

Discretização no Tempo. O **Problema $\mathbf{T_h}$** resultante da discretização de elementos finitos consiste em um sistema de equações ordinárias no tempo para cuja solução utilizamos o método implícto de Euler, no qual a derivada temporal no instante $t_n = n\Delta t$ é aproximada por

$$\partial_t u_h^n = \frac{u_h^n - u_h^{n-1}}{\Delta t},$$

em que $\Delta t = T/N$ é o intervalo de integração e u_h^n é o valor de $u_h(t)$ no instante $t_n = n\Delta t$. Deste modo o problema completamente discreto consiste em:

Problema T_h^Δ: Para $n = 1, 2, ..., N$ determinar $u_h^n \in V_h^k$ satisfazendo a

$$(u_h^n, w_h) + \Delta t(\nabla u_h^n, \nabla w_h) = (u_h^{n-1} + \Delta t f(t_n), w_h) \quad \forall w_h \in V_h^k$$

com condição inicial $u_h^0 = v_h$.

A análise numérica do **Problema $\mathbf{T_h^\Delta}$** conduz ao resultado seguinte, cuja demostração pode ser encontrada na referência [6].

Teorema 2: Sendo $u(t_n)$ e u_h^n soluções dos problemas **T** e $\mathbf{T_h^n}$, respectivamente, então, para $n \geq 0$, temos

$$\|u_h^n - u(t_n)\| \leq \|v_h - v\| +$$

$$C\left[h^2\left(\|v\|_{k+1} + \int_0^{t_n}\|u_t\|_{k+1}\,ds\right) + \Delta t\int_0^{t_n}\|u_{tt}\|\,ds\right].$$

Resultado semelhante pode ser demostrado para a derivada no tempo de $u(t)$, ou seja

Teorema 3: Sendo $u(t_n)$ e u_h^n soluções dos problemas **T** e $\mathbf{T_h^n}$, respectivamente, então, para $n \geq 0$, temos

$$\|\partial_t u_h^n - u_t(t_n)\| \leq \|\partial_t u_h(0) - u_t(0)\| +$$

$$C\left[h^2\left(\|u_t(0)\|_{k+1} + \int_0^{t_n}\|u_{tt}\|_{k+1}\,ds\right) + \Delta t\int_0^{t_n}\|u_{ttt}\|\,ds\right].$$

Para demonstração deste teorema ver [7] onde também é demostrado que o erro nas condições iniciais é atenuado com o tempo.

PÓS-PROCESSAMENTO DO FLUXO

Como se pode notar, pelo **Teorema 1**, a taxa de convergência em h para o gradiente de u é uma ordem a menos do que a taxa de convegência do próprio u. Portanto, com a formulação proposta a aproximação obtida para o fluxo será sempre menos precisa do que a aproximação obtida para a temperatura, uma vez que neste caso a aproximação do fluxo é dada por

$$p_h(t) = -\nabla u_h(t)\,.$$

Mais precisamente, com a formulação cinemática clássica apresentada anteriormente, temos as seguintes taxas de convergência do fluxo com relação a h:

$$\|\mathbf{p} - \mathbf{p_h}\| \leq C(u)h^k\,,$$

$$\|\mathrm{div}(\mathbf{p} - \mathbf{p_h})\| \leq C(u)h^{k-1}\,.$$

Visando a obtenção de aproximações mais precisas para o fluxo propomos um pós-processamento do mesmo, baseado em uma formulação do tipo Petrov-Galerkin[1,2], utilizando a equação constitutiva e a equação de balanço de fluxo. Para tanto introduzimos o espaço produto $U = L^2(\Omega)^2$ com norma

$$\|\mathbf{q}\| = (\mathbf{q}, \mathbf{q})^{1/2}\,,$$

e o subespaço

$$H(\mathrm{div}) = \{\mathbf{q} \in U\,,\ \mathrm{div}\mathbf{q} \in L^2(\Omega)\}$$

com norma

$$\|\mathbf{q}\|_{H(\mathrm{div})} = \{(\mathbf{q}, \mathbf{q}) + (\mathrm{div}\mathbf{q}, \mathrm{div}\mathbf{q})\}^{1/2}\,.$$

Seja $X_h^l \subset H(\mathrm{div})$ um espaço de elementos finitos de grau l, por exemplo o espaço de Raviart-Thomas[8]. Aqui, por simplicidade, e dado que a formulação proposta não está sujeita a restrições de compatibilidade, adotaremos $X_h^l = S_h^l \times S_h^l \subset H^1(\Omega) \times H^1(\Omega)$, que obviamente está contido em $H(\mathrm{div})$. O esquema de pós processamento consiste em conhecidos $u_h(t_n)$ e sua derivada no tempo $u_{ht}(t_n)$, de forma aproximada através da solução do problema completamente discreto apresentado anteriormente, calcular uma aproximação $\mathbf{p_h}(t_n) \in X_h^l$ para o fluxo no instante t_n satisfazendo a equação variacional

$$(\mathbf{p_h} - \nabla u_h, \mathbf{q_h}) + \delta(u_{ht} + \mathrm{div}\mathbf{p_h} + \nabla u_h - \mathbf{f}, \mathrm{div}\mathbf{q_h}) = 0\ \forall \mathbf{q_h} \in X_h^l\,,$$

que pode ser reapresentado na forma

Problema $\mathbf{PG_h}$: Achar $\mathbf{p_h} \in X_h^l$ tal que

$$a_\delta(\mathbf{p_h}, \mathbf{q_h}) = f_\delta(\mathbf{q_h} \quad \forall \mathbf{q_h} \in X_h^l,$$

em que $\delta > 0$ é uma função do diâmetro da malha h, e

$$a_\delta(\mathbf{p}_h, \mathbf{q}_h) = (\mathbf{p}_h, \mathbf{q}_h) + \delta(\mathrm{div}\mathbf{p}_h, \mathrm{div}\mathbf{q}_h)\,,$$

$$f_\delta(\mathbf{q}_h) = -(\nabla u_h, \mathbf{q}_h) + \delta(f - u_{ht}, \mathrm{div}\mathbf{q}_h)\,.$$

Estimativa de Erro. É interessante notar que, conhecidos u_h e u_{ht}, a equação variacional do pós-processamento corresponde a uma aproximação de elementos finitos conforme em uma única variável $\mathbf{p}_h$, à qual podemos aplicar técnicas usuais de análise numérica de problemas elípticos, uma vez que temos elipticidade e continuidade da forma bilinear $a_\delta(\cdot,\cdot)$ na norma

$$\|\mathbf{p}\|_\delta = \|\mathbf{p}\| + \sqrt{\delta}\|\mathrm{div}\mathbf{p}\|\,.$$

Deste modo demostramos facilmente a sequinte estimativa

$$\|\mathbf{p}-\mathbf{p}_h\|_\delta \le \|\mathbf{p}-\mathbf{q}_h\|_\delta + \frac{1}{\sqrt{\delta}}\|u_t - u_{ht}\| + \frac{1}{\sqrt{\delta}}\|u - u_h\| \forall \mathbf{q}_h \in X_h^l\,.$$

Diferentes escolhas de δ em função de h podem conduzir a diferentes taxas de convergência, consequentemente de precisão, para $\mathbf{p}_h$. Assim, por exemplo, tomando $l = k$ e escolhendo $\delta = h^2$ temos:

$$\|\mathbf{p} - \mathbf{p}_h\| \le C(u)h^k\,,$$

$$\|\mathrm{div}(\mathbf{p} - \mathbf{p}_h)\| \le C(u)h^k\,,$$

evidenciando que, neste caso, o ganho em relação ao método clássico de Galerkin é de uma ordem na taxa de convergência do divergente do fluxo. Por outro lado, adotando ainda $l = k$ e $\delta = h$ temos

$$\|\mathbf{p} - \mathbf{p}_h\| \le C(u)h^{k+1/2}\,,$$

$$\|\mathrm{div}(\mathbf{p} - \mathbf{p}_h)\| \le C(u)h^k\,,$$

o que significa um ganho adicional na taxa de convergência do fluxo. Ganho ainda maior é obtido adotando-se $l = k + 1$, ou seja interpolando-se o fluxo com polinômios um grau mais alto do que o adotado na interpolação da temperatura. Para maiores detalhes sobre a análise numérica, implementação e aplicações desta metodologia ver referência [7], onde a técnica de pós-processamento é também implementada elemento a elemento com o fluxo interpolado descontinuamente.

RESULTADOS NUMÉRICOS

Para confirmar as taxas de convergência em h, preditas na análise anteriormente apresentada, resolvemos numericamente um problema simples, consistindo na determinação dos campos de temperatura e fluxo em um domínio quadrado $\Omega = [0,1] \times [0,1]$, com condições de contorno e inicial homogêneas, submetido a uma fonte de calor

$$f = 10 \sin \pi x \sin \pi\,, y$$

cuja solução é

$$u(\mathbf{x}, t) = \frac{5}{\pi^2}(1 - e^{-2\pi^2 t}) \sin \pi x \cos \pi y\,.$$

Este problema foi então resolvido com malhas uniformes de 4, 16, 36 e 64 elementos bilineares ($k = l = 1$) e Δt suficientemente pequeno de modo a evitar que o erro da discretização temporal podesse poluir as taxas de convergência da discretização espacial ($\Delta t = 2.5 \times 10^{-4}$). De acordo com a análise devemos ter neste caso as seguites taxas de convergência:

a) Para a temperatura

$$\|u(t_n) - u_h(t_n)\| \le C(u)h^2\,,$$

$$\|\nabla u(t_n) - \nabla u_h(t_n)\| \le C(u)h\,,$$

b) Para o fluxo sem pós-processamento

$$\|\mathbf{p}(t_n) - \mathbf{p}_h(t_n)\| \le C(u)h\,,$$

$$\|\mathbf{p}(t_n) - \mathbf{p}_h(t_n)\|_{H(\mathrm{div})} \le C\,,$$

ou seja, neste caso não há convergência do fluxo na norma de $H(\mathrm{div})$.

c) Para o fluxo pós-processado com $\delta = h^2$

$$\|\mathbf{p}(t_n) - \mathbf{p}_h(t_n)\| \le C(u)h$$

$$\|\mathbf{p}(t_n) - \mathbf{p}_h(t_n)\|_{H(\mathrm{div})} \le C(u)h\,,$$

recuperando assim a convergência do fluxo em $H(\mathrm{div})$.

Os resultados da análise de convergência das aproximções de Galerkin para o campo de temperaturas e sua derivada no tempo, obtidas através da solução do **Problema** $\mathbf{T}_\mathbf{h}^\Delta$, estão mostrados na Fig. 1, onde se pode observar a confirmação das taxas de convergência previstas na análise (**Teoremas 2** e **3** com $k = 1$). A Fig. 2 confronta as taxas de convergência obtidas para o fluxo com a formulação de Galerkin, onde o mesmo é calculado como derivada do campo de temperaturas, e com a formulação de Petrov-Galerkin (pós-processamento), evidenciando um significativo ganho tanto em termos de taxa de convergência quanto de precisão com o pós-processamento, que neste caso apresenta inclusive taxas de convergência maiores do que as previstas na análise. A Fig. 3 apresenta taxas de convergência para o divergente do fluxo na norma do L^2, mostrando que neste caso o divergente do fluxo obtido com o método de Galerkin é não convergente. Isto significa que esta solução não aproxima a equação de equilíbrio no sentido da norma do L^2, o que não ocorre com a aproximação de Petrov-Galerkin cujo divergente converge com taxa da ordem de h, pelo menos, conforme previsto na análise e confirmado nesta experiência numérica.

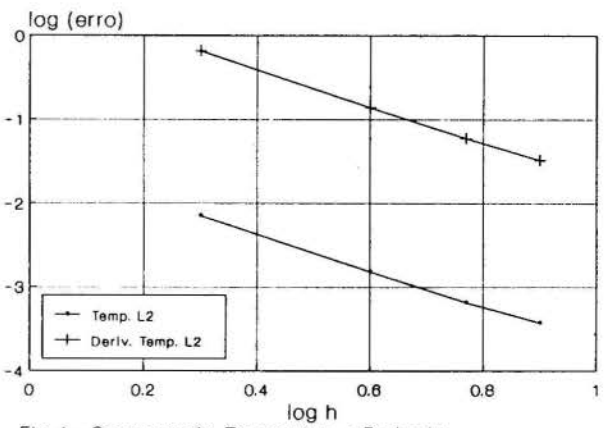

Fig. 1 - Convergencia. Temperatura e Derivada

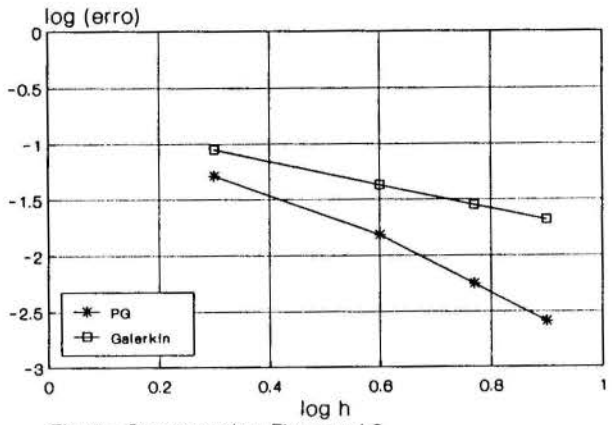

Fig. 2 - Convergencia - Fluxo em L2

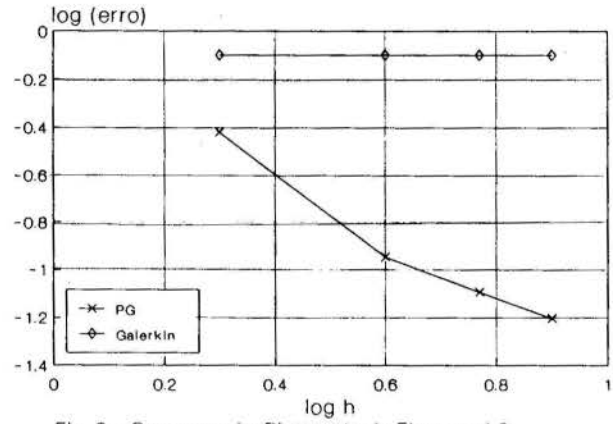

Fig. 3 - Convergencia. Divergente do Fluxo em L2

REFERÊNCIAS

[1] Loula, A.F.D., Hughes, T.J.R., Franca L.P. e Miranda, I. Mixed Petrov-Galerkin Method for the Timoshenko Beam, Comp. Meth. in Appl. Mech. and Engng. , 63, 133-154, 1987.

[2] Loula, A.F.D. e Toledo, E.M., Dual and Primal Mixed Petrov-Galerkin Finite Element Methods in Heat Transfer Problems, ENCIT 88, pp. 176-179, Aguas de Lindoia, SP, Brasil.

[3] Sarzeto, C.A.P. e Loula, AF.D., Uma formulação de Galerkin Modificada para Análise de Autovalores, X COBEM, vol A, pp. 145-148, Rio de Janeiro, Brasil.

[4] Toledo, E.M., Loula, A.F.D. e Guerreiro, J.N.C., Formulações Mistas de Petrov-Galerkin para Elasticidade Bidimensional, MECOM 89, Porto, Portugal, 1989.

[5] Toledo, E.M., Novos Métodos de Elementos Finitos Mistos com Pós-Processamento, Tese de Doutoramento, PEC/COPPE/UFRJ, 1990.

[6] Thomée, V., Galerkin F.E.M. for Parabolic Problems, Lecture Notes in Mathematic, 1054, Springer Verlag, 1984.

[7] Sarzeto, C.A.P., Análise Numérica de Formulações de Petrov-Galerkin em Problemas Transientes, Tese de Doutoramento, PEM/COPPE/UFRJ, 1990.

[8] Raviart, P.A. e Thomas, J.M., A Mixed Finite Element Method for Second Order Elliptic Problems, Mathematical Aspects of the Finite Element Method, Lecture Notes in Mathematics 606, Springer-Verlag, Berlin, 292-315, 1975.

ABSTRACT

A post-processing scheme, consisting in adding the residuals of both constitutive and balance equations, is proposed to improve the accuracy of finite element approximations of heat flux in transient heat conduction problems. Numerical analysis, error estimates and numerical results are presented confirming the good performance of the proposed method.

III ENCIT – Itapema, SC (Dezembro 1990)

APLICAÇÃO DE PROCEDIMENTO AUTO-ADAPTATIVO NA ANÁLISE DE PROBLEMAS TÉRMICOS NO REGIME PERMANENTE E TRANSIENTE

PAULO ROBERTO MACIEL LYRA
DEPARTAMENTO DE ENGENHARIA CIVIL/CT-UFPE/CNPq
C.P.7801,AG. C.UNIVERSITÁRIA CEP:50730

RESUMO

Este trabalho descreve um procedimento adaptativo do Método dos Elementos Finitos (MEF) onde o erro estimado (a-posteriori) é reduzido de forma eficiente por meio do refinamento automático de malhas (Versão-H). Os procedimentos apresentados permitem a análise de problemas governados pela equação de condução de calor no regime permanente e no regime transiente. Analisa-se, primeiramente, uma aplicação a problema de condução de calor no regime permanente e, em seguida são feitas considerações a cerca de análise no regime transiente.

INTRODUÇÃO

A precisão dos resultados obtidos por meio das análises numéricas é essencial para que se tenha um uso eficaz dos procedimentos numéricos no estudo de problemas práticos da Engenharia. Nos últimos anos grande foi o progresso alcançado no desenvolvimento de estimativas de erro a-posteriori (Flaherty, Paslaw, Shephard and Vasilakis [1]) as quais permitem uma estimativa do erro total em uma determinada norma, bem como, uma indicação da contribuição relativa de cada elemento finito nesse erro.

Essa análise de erros pode então ser combinada com um procedimento adaptativo de refinamento, no qual as aproximações são sucessivamente refinadas até alcançar um grau de precisão pré-determinado. Simultaneamente, é necessário que os procedimentos implementados sejam robustos e permitam uma análise numérica eficiente.

Para melhoria das soluções do MEF o mais comum é aumentar a ordem das funções de interpolação local e/ou aumentar o número de elementos nas regiões onde o modelo de elementos finitos leva a uma aproximação grosseira. A abordagem em que se melhora a solução através da divisão local dos elementos de acordo com a distribuição dos erros é conhecida como Versão-H do MEF.

A Versão-H tem recebido maior atenção no estudo de problemas elípticos. Neste trabalho apresentamos um possível procedimento para tratar problemas regidos por equações diferenciais parabólicas, tal como a equação de condução de calor no regime transiente.

No próximo tópico apresenta-se a estimativa e indicador de erros adotados. Em seguida, uma descrição suscinta da estratégia de refinamento de malhas (Versão-H) é feita dando-se especial atenção ao esquema para o caso de problemas que dependem do tempo. Os resultados numéricos são comparados com a solução analítica para o problema no regime permanente. Finalmente, são discutidas e feitas considerações pertinentes aos problemas transientes.

ESTIMATIVA DE ERROS A-POSTERIORI

Considerando a solução do problema de valor de contorno (PVC) abstrato abaixo:

Para $u,v \in H^1(\Omega)$, $\Omega \subset R^2$ encontre u tal que

$$b(u,v) = \ell(v) + \langle g,v\rangle_{\Gamma_N}, \quad \forall\, v \in H^1(\Omega) \tag{1}$$

onde $b(\cdot,\cdot)$ é simétrico positivo definido e bilinear contínuo. E $\langle g,v\rangle$ é correspondente a integral que resulta da condição de contorno tipo Cauchy. Pressupõe-se que a solução u é única e que a aproximação de elementos finitos u_h converge para u quando a dimensão da malha tende a zero $h \to 0$.

A aproximação de elementos finitos u_h de u é a solução de:

para $u_h, v_h \in V(\Omega)$ e $V \subset H^1(\Omega)$ encontre u_h tal que

$$b(u_h,v_h) = \ell(v_h)+\langle g,v_h\rangle_{\Gamma_N}, \quad \forall\, v_h \in V(\Omega) \tag{2}$$

Cada estimativa de erros irá tentar avaliar o erro exato $||u - u_h||$ através da norma definida por $b(\cdot,\cdot)$.

A estimativa de erros adotada foi desenvolvida por Zienkiewicz e Zhu [2] e baseia-se no cálculo da diferença entre o gradiente da solução aproximada de elementos finitos e o gradiente "suavizado". Esse último é obtido no pós-processamento através de projetores definidos de forma a termos valores dos gradientes com continuidade C^0 em todo o domínio do problema. Seja

$$u_h = \sum_i u_i\psi_i \quad e \quad G = grad(u_h) = (u_{hx},u_{hy}) \tag{3}$$

Define-se. então, o gradiente suavizado $\overline{G}=\sum_i \overline{G}_i\psi_i$ como:

$$\overline{G}_i = \frac{\int_\Omega \psi_i G d\Omega}{\int_\Omega \psi_i\psi_i d\Omega} \tag{4}$$

em seguida é feita a média nodal do gradiente da solução.

Usando-se os valores do gradiente G e do gradiente suavizado $\overline{G}$ a estimativa de erros pode ser avaliada, através da norma de energia, como:

$$||u-u_h||^2_\Omega = \sum_{e=1}^{Nel} \left[\int_{\Omega e} (\overline{G} - G)D^{-1}(\overline{G} - G)d\Omega\right] \tag{5}$$

onde D é o parâmetro referente às relações constitutivas do material.

As principais vantagens desta estimativa de erros são: facilidade de implementação e um pequeno tempo de computação. No trabalho de Lyra [3] mostra-se ainda que essa estimativa converge para o erro verdadeiro em uma variedade de problemas estudados.

Ao longo do trabalho sempre que nos referimos a erro estaremos utilizando a estimativa de erros dada na equação (5) exceto se for explicitado o contrário.

FORMULAÇÃO EM ELEMENTOS FINITOS

Equação de Condução de Calor. De acordo com a lei de Fourier da condução de calor num meio contínuo, o problema bidimensional de condução de calor no regime transiente pode ser descrito pela equação de campo, como segue:

$$\frac{\partial}{\partial x}\left(K_x \frac{\partial \phi}{\partial x}\right)+\frac{\partial}{\partial y}\left(K_y \frac{\partial \phi}{\partial y}\right)=Q(t)-\lambda\phi+C\frac{\partial \phi}{\partial t} \quad \forall (x,y) \in \Omega \qquad (6)$$

onde: ϕ = temperatura
Kx, Ky = condutividade térmica
$Q(t)$ = taxa de calor por unidade de volume
λ = coeficiente de radiação ou convecção
C = ρc = capacidade térmica, onde ρ é a densidade do material e c é coeficiente de calor específico

E as condições de contorno:

. Condições de contorno essenciais ou de Dirichlet - a temperatura é prescrita ($\overline{\phi}$)

$$\phi - \overline{\phi}(t) = 0 \quad \forall (x,y) \in \Gamma_D \qquad (7)$$

. Condições de contorno naturais ou de Cauchy
1. condição de fluxo ($\overline{q}$), ($\alpha = 0$)
2. condição de convecção ou irradiação ($\alpha (\phi - \phi_a)$), ($\overline{q} = 0$, $\alpha \neq 0$)

$$K_x \frac{\partial \phi}{\partial x} n_x + K_y \frac{\partial \phi}{\partial y} n_y + \overline{q}(t) + \alpha(\phi - \phi_a) = 0$$

$$\forall (x,y) \in \Gamma_C \qquad (8)$$

Nas quais n_x e n_y são os cossenos diretores entre a normal externa e os eixos x e y respectivamente; α é o coeficiente de radiação ou convecção, e ϕ_a é a temperatura ambiente ou a temperatura da fonte de radiação externa.

Para que o problema de valor inicial / contorno fique completo, a condição inicial de temperatura deve também ser especificada :

$$\phi = \phi^0 \quad \forall (x,y) \in \Omega \text{ para } t = 0 \qquad (9)$$

Discretizando o espaço por meio de elementos finitos e aplicando o método de Galerkin tem-se ao final um sistema de equações diferenciais ordinárias de primeira ordem.

$$C\frac{\partial \phi}{\partial t} + (K^k + K^c)\,\phi = F \qquad (10)$$

Discretizando o tempo por meio de diferenças finitas o problema pode ser expressado em um tempo $t+\Delta t$ como um sistema de equações algébricas linear conforme abaixo:

$$K^* \phi_{t+\Delta t} = F^*$$

$$\phi = \phi^0 \quad \text{para } t = 0 \qquad (11)$$

onde

$$K^* = \theta(K^k + K^c) + \frac{1}{\Delta t} C \qquad (12)$$

$$F^* = [K^* - (K^k + K^c)]\phi_t + [\theta F_{t+\Delta t} + (1 - \theta) F_t \qquad (13)$$

sendo: K^k a matriz de condutividade
K^c a matriz de convecção (ou radiação)
C a matriz de capacidade
F_i o vetor dos termos independentes
Δ_t o intervalo de tempo e θ um parâmetro de ponderação ($0 \leq \theta \leq 1$)

A equação (11) deve então ser resolvida a cada intervalo de tempo. O parâmetro θ pode variar de 0 (esquema explícito) a 1 (esquema totalmente implícito) e representa uma posição intermediária entre os pontos de integração no tempo.

Versão-H do MEF no Regime Permanente. Aplicando-se o método de Galerkin para MEF, com elementos isoparamétricos bilineares, o procedimento auto-adaptativo Versão-H para resolver equações diferenciais parciais elípticas pode ser sinteticamente descrito no algoritmo abaixo:

1. Introduzir dados do problema e tolerância do erro desejada;
2. Gerar o primeiro modelo;
3. Resolver sistema de equações algébricas;
4. Computar a estimativa de erros;
5. Aplicar critério de refinamento baseado no erro;
6. Se a malha tiver que ser refinada continue, senão pare.
7. Aplicar critérios de refinamento adicionais;
8. Gerar novo modelo e voltar ao passo 3;

OBSERVAÇÃO 1 - A solução do sistema de equações algébricas é efetuada utilizando o Método dos Gradientes Conjugadas com precondicionamento de Jacobi e implementado no esquema elemento - por - elemento. Com o intuito de acelerar a convergência do procedimento é utilizada a solução da última malha como dado inicial no esquema iterativo.

OBSERVAÇÃO 2 - O critério usado na escolha dos elementos a serem refinados baseia-se no conhecido "princípio da equidistribuição dos erros", no qual o procedimento adaptativo pode ser definido como um problema de otimização:

$$\text{Minimizar} \quad \underset{\{\text{através da adaptação}\}}{\text{Máximo}\ \lambda_i \quad i=1,2,\ldots Nel} \qquad (14)$$

onde λ_i é o indicador de erros do elemento i, e Nel é o número total de elementos do modelo, que é variável na Versão-H. Obtém-se assim ao final valores iguais para os indicadores de erro a menos de uma certa tolerância desejada.

OBSERVAÇÃO 3 - Existem inúmeras estratégias de refinamento baseadas no "Princípio da equidistribuição dos erros". A depender da escolha tem-se uma taxa de convergência, um grau de confiabilidade dos resultados e um custo correspondente (Lyra, Alves,Coutinho,Landau e Devloo[4]).

OBSERVAÇÃO 4 - Três são os critérios adicionais implementados, todos baseados em considerações topológicas. Os dois primeiros foram propostos por Bank [5] para tratar os vértices irregulares. O último pretende solucionar problemas relativos às singularidades na solução ([3]).

OBSERVAÇÃO 5 - Cada elemento finito é subdividido em quatro novos elementos. Para assegurar a conformidade dos elementos, e portanto a convergência do método, restrições são impostas a nível dos elementos (veja Devloo [6]).

Esquema Adaptativo para Problemas no Regime Transiente. Nos problemas parabólicos, onde a solução varia suavemente no tempo, a malha ótima do intervalo de tempo anterior pode ser usada como uma boa aproximação da malha desejada no intervalo de tempo seguinte. Dependendo da regularidade da solução, é viável utilizar a mesma malha para vários intervalos de tempo e então adaptá-la de acordo com a precisão desejada da solução.

O número de intervalos que se pode avançar no tempo antes de alterar a malha depende do problema em consideração, porém é importante ter em mente que se algum componente da solução tiver mudado e não foi avaliado em um intervalo intermediário, então esta perda não poderá ser recuperada nas soluções futuras, e ter-se-á um erro acumulado.

Em problemas de condução de calor têm-se características especiais, tais como: fontes de calor, obstáculos, cantos, fluxos de calor, etc. os quais são admitidos em posições estabelecidas. Nesses casos a capacidade de refinamento do modelo é necessária para tratar com as singularidades originadas nesses pontos especiais.

A capacidade de refinamento só se faz necessário em problemas regidos por equações diferenciais parciais hiperbólicas ou parabólicas com termos de advecção dominante, nos quais a solução se desloca sobre a malha durante um certo intervalo de tempo. Devloo [6] apresenta um esquema de refinamento/desrefinamento, para tratar problemas governados pelas equações de Navier-Stokes, onde o refinamento local segue a onda, e os elementos previamente refinados podem retornar a uma discretização mais grosseira. O tempo de computação diminui, uma vez que o número de graus de liberdade é reduzido, porém gasta-se um maior tempo no reordenamento da estrutura de dados. O balanço desses dois processos é que vai determinar a efetividade do uso ou não da capacidade de desrefinamento do programa.

Como fica claro da discussão anterior, os problemas parabólicos podem ser resolvidos utilizando-se as técnicas de estimativas de erros adotados em problemas elípticos. Essas estimativas irão gerir o processo de refinamento após o avanço de um número pré-determinado de intervalos de tempo.

Neste trabalho, propõe-se a estratégia apresentada resumidamente no algoritmo abaixo:

1. Gerar modelo;
2. Atualizar o vetor dos termos independentes $\{F^{t+\Delta t}\}$;
3. Avançar a solução no tempo (alguns intervalos);
4. Estimar o erro da nova solução;
5. Refinar os elementos de acordo com a estratégia de refinamento;
6. Se o número de elementos refinados no passo 5 for maior que zero

   . Então:

   (a) voltar o tempo em "$-\Delta t$".
   (b) guardar a solução em "$t - \Delta t$" como dados iniciais;
   (c) voltar para o passo 1;

   . Senão:

   (a) guardar a solução em "t" como dados iniciais;
   (b) se o intervalo de tempo da análise tiver acabado, pare.
   (c) voltar para o passo 2;

OBSERVAÇÃO 1 - Para o primeiro intervalo de tempo, esse algoritmo recai no algoritmo para problemas no regime permanente.

OBSERVAÇÃO 2 - Esta estratégia pode ser melhorada se for levado em conta o conhecimento "a priori" da intensidade da singularidade ou o comportamento assintótico da estimativa de erros no tempo.

OBSERVAÇÃO 3 - O esquema implícito ($\theta \geq 1/2$) é incondicionalmente estável e o intervalo de tempo Δt deve ser escolhido para satisfazer apenas a precisão e a eficiência da solução. Essa escolha é grandemente dependente da natureza das cargas, tipo e tamanho dos elementos, etc e muitas considerações práticas são encontradas na literatura (Damjanic e Owen [7]). O comportamento de muitos problemas térmicos é tal que as variações bruscas na temperatura se dissipam e é, portanto, interessante tentar usar um incremento de tempo não uniforme. Tem-se com isso um programa mais eficiente, uma vez que o número de intervalos de tempo e de iterações será reduzido. O esquema adotado é semelhante ao proposto por Pricketl e Lonnquist [8].

APLICAÇÕES TÍPICAS E DISCUSSÃO

Regime Permanente. Inicialmente apresentam-se alguns resultados numéricos para o problema modelo [8], no regime permanente (Ver Figura (1)).

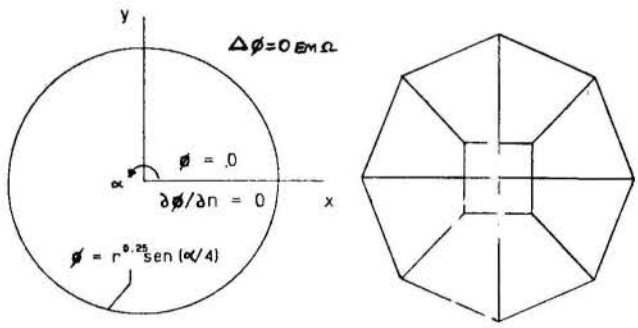

Fig. 1 Descrição do problema modelo (Regime Permanente)

Fig. 2 Malha inicial

Com respeito às condições de contorno, tem - se $\phi=0$, $\partial\phi/\partial x=0$ em $0 \leq x \leq r$, $y \geq 0$ e $\partial\phi/\partial x=0$ em $0 \leq x \leq r$, $y < 0$. Ao longo da circunferência, preescrevem-se condições de contorno de Dirichlet tais que $\phi=r^{1/4}sen(\alpha/4)$. Estas condições de contorno causam uma singularidade com termo dominante $r^{1/4}sen(\alpha/4)$ propagando-se a partir do centro do domínio. Este problema foi solucionado através do procedimento adaptativo do MEF Versão-H fazendo uso da estimativa a posteriori de erros descrita anteriormente. Adotou-se para a malha inicial aquela mostrada na Figura 2.

Especificou-se para a tolerância na equidistribuição dos erros (γ) o valor 0.20 e considerou-se um número máximo de refinamentos (NMAX) igual a 5. Para a aplicação do critério de singularidade, adotou-se $\overline{\theta} = 0.15$.

A solução do sistema de equações algébricas em cada etapa de refinamento é efetuada pelo Método dos Gradientes Conjugados com precondicionamento diagonal. A convergência é considerada atingida quando a norma euclideada dos resíduos for inferior a 10^{-3}. Dada as ca-

racterísticas geométricas do problema e das condições de contorno, a adaptação linear das mesmas fornece uma aproximação grosseira, tendo em vista a malha inicial dada na Figura 2. Desta forma, tanto a geometria quanto as condições de contorno foram adaptadas exatamente, permitindo a cada etapa de refinamento a reconstituição precisa do modelo.

Na Figura (3) apresenta-se a malha obtida ao final da análise, para o padrão de precisão pré-estabelecido. Deve-se salientar que os critérios adicionais de refinamento de caráter topológico foram pouco acionados. Tal característica é extremamente importante, já que, caso fosse necessário um número acentuado de refinamentos por estes critérios, a eficiência do procedimento auto-adaptativo Versão-H estaria comprometida.

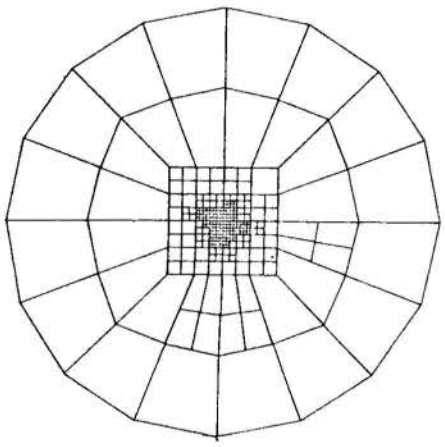

Fig. 3 Malha final

A história dos refinamentos pode ser avaliada nas Figuras (4 e 5) que apresentam respectivamente a evolução das temperaturas nodais e dos fluxos nodais suavizados em $y = 0$. Deve-se notar a boa aproximação obtido para a malha final com relação à solução exata do problema.

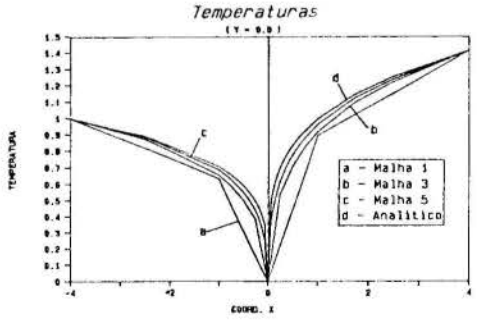

Fig. 4 Temperaturas nodais em $y = 0$

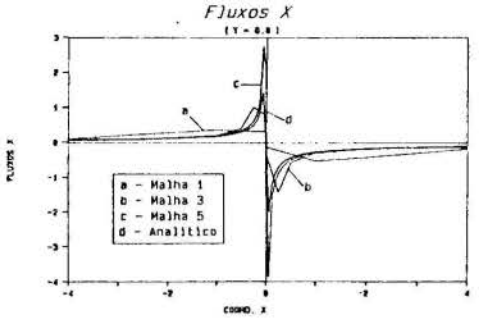

Fig. 5 Fluxos nodais suavizados em $y = 0$

Regime Transiente. A seguir faz-se uma discussão dos problemas transientes lineares, adotados pela NAFEMS [10]. No primeiro tem-se uma mudança entre dois diferentes estados permanentes após uma variação nas condições de contorno ou nos valores das fontes de calor.

As outras aplicações descritas dizem respeito a mudanças periódicas contínuas ou variações discretas não periódicas das condições de contorno ou das fontes de calor.

Aplicação 1 - Seja um domínio infinito com uma fonte pontual de calor no ponto A (Ver Figura 6), onde se tem:

Condições de contorno: $\phi = \phi_0$ para $r \to \infty$ e $t \geq 0$

Condição inicial : $\phi = \phi_0$ para $r \geq 0$ e $t = 0$

Fonte de Calor : $\lim_{r \to 0} \frac{\partial \phi}{\partial r} = \frac{Q}{2\pi K}$

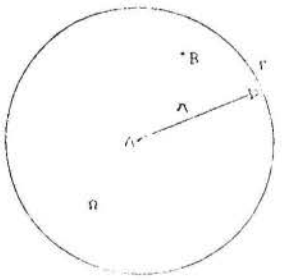

Fig. 6 Descrição da aplicação 1 (Regime transiente)

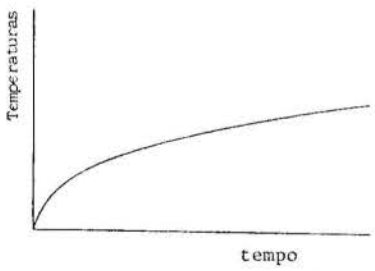

Fig. 7 Solução qualitativa da temperatura no ponto B qualquer no domínio Ω

O comportamento da temperatura, do ponto de vista qualitativo, para um ponto B qualquer, pode ser visto na Figura (7). É possível observar que para esta classe de problemas a necessidade de refinamento se dá no primeiro intervalo de tempo, e que uma vez alcançado um modelo discreto com erro dentro dos limites estabelecidos, nenhum refinamento será necessário nos intervalos seguintes. Deve-se ainda utilizar na integração no tempo um intervalo de tempo crescente sem riscos de perda de precisão da solução.

Aplicação 2 - Seja uma barra com temperatura constante e igual a zero em uma extremidade e uma variação senoidal na outra extremidade, onde:

Condições de contorno : $\phi = 0$ para $x = 0$

$\phi = 100 \operatorname{sen} \frac{2\pi t}{10}$ para $t \geq 0$,

Condição inicial : $\phi = 0 \ \forall x$ e $t = 0$

Neste tipo de problema o gradiente de temperatura varia muito no tempo. Utilizar um intervalo de tempo que ora aumente e ora diminua é uma tarefa difícil e a adoção de um incremento constante é provavelmente a melhor opção. O esquema de refinamentos pode ser ativado ao longo de toda a análise.

Aplicação 3 - Seja o problema onde as condições de contorno variam de valores discretos após alguns intervalos de tempo e depois permanecem constantes durante um período de tempo.

Este problema se comporta como uma repetição sucessiva da Aplicação 1. O incremento de tempo é crescente durante o intervalo no qual as condições de contorno são constantes e é então re-inicializado para o valor menor após a mudança nas condições de contorno. Mais uma vez os refinamentos de malha praticamente só ocorrem no início da integração no tempo.

CONCLUSÕES

A utilização dos procedimentos adaptativos representa uma diminuição do tempo dispendido na preparação dos dados e no lançamento do modelo e proporciona uma maior eficiência e confiabilidade dos resultados. Isso, principalmente, em se tratando de problemas com comportamento imprevisível ou onde o analista não tem nenhuma experiência prévia.

Apesar das análises qualitativas apresentadas para os problemas modelos descritos não serem conclusivas, elas permitem uma boa visão das características do procedimento de refinamento de malhas do MEF em problemas transientes de transferência de calor.

O programa com todas as características e sugestões descritas apresenta uma grande potencialidade para a análise de problemas práticos de engenharia, e este será o conteúdo do próximo trabalho que está sendo desenvolvido.

REFERÊNCIAS

[1] Flaherty, J.E., Paslow, P.J., Shephard, M.S. and Vasilakis, J.D., "Adaptive Methods for Partial Differential Equations", Proceedings of the Workshop on Adaptive Computational Methods for Partial Differential Equations, Rensselaer Polytechnic Institute, SIAM Issue, 1989.

[2] Zienkiewicz, O.C. and Zhu, J.Z., "A Simple Error Estimator and Adaptive Procedure for Practical Engineering Analysis", International Journal for Numerical Methods in Engineering, Vol. 24, pp 337-357, 1987.

[3] Lyra, P.R.M., "Uma Estratégia de Refinamento Auto-Adaptativo Versão-H do Método dos Elementos Finitos Aplicada a Problemas Bi-Dimensionais Regidos pela Equação de Campo", Tese de Mestrado, COPPE/UFRJ, Rio de Janeiro, 1988.

[4] Lyra, P.R.M., Alves, J.L.D., Coutinho, A.L.G.A., Landau, L., and Devloo, P.R.B., "Comparison of Local Mesh Refinement Strategies for the H-Version of Finite Element Method", X Congresso Ibero-Latino-Americano sobre Métodos Computacionais em Engenharia e II Encontro Nacional de Mecânica Computacional, Vol. 2, pp A/595-A/610, Porto, Portugal, 1989.

[5] Bank, R.E., "The Efficient Implementation of Local Mesh Algorithms", Adaptive Computational Methods for Partial Differential Equations, ed. by I. Babuska, J. Chandra and J.E. Flaherty, pp 74-84, SIAM, U.S.A., 1983.

[6] Devloo, P.B.R., "An H-P Adaptive Finite Element Method for Steady Compressible Flow", PhD Thessis The University of Texas at Austin, 1987.

[7] Damjanic, F. and Owen, D.R.J., "Practical Considerations for Thermal Transient Finite Element Analysis using Isoparametric Elements", Nuclear Engineering Design, Vol.69, pp 109-126, 1982.

[8] Prickett, T.A., and Lonnquist, C.G., "Selected Digital Computer Techniques for Goundwater Resources Evaluation", Illinois State Water Survey, Urbana, Bulletin 55, 1971.

[9] Bank, R., "A Posteriori Error Estimates, Adaptive Local Mesh Refinement and Multigrid Iteration, Multigrid Methods, Lecture Notes on Mathematics, nº 1026, Springer Verlag, pp. 8-22 (1985).

[10] Barlow, J., and Davies, G.A.O., "Selected F.E. Benchmarks in Structural and Thermal Analysis", FEBSTA, Rev. 2, National Agency for Finite Element Methods and Standards (NAFEMS), October 1987.

ABSTRACT

This work describes a procedure for the adaptive time dependent Finite Element Method using an automatic mesh refinement (H-Version) that efficiently reduces estimated errors(a posteriori) below pre-assigned limits.

Classical model problem for steady-state heat transfer are investidad, and the results are compared with the analytical solution. Then some typical time-dependent problems are qualitatively analysed.

III ENCIT — Itapema, SC (Dezembro 1990)

FORMULAÇÃO H AUTO-ADAPTATIVA DE ELEMENTOS DE CONTORNO PARA PROBLEMAS DE POTENCIAL

J. A. Costa Jr.
Departamento de Engenharia Mecânica
Pontifícia Universidade Católica do Rio de Janeiro

ABSTRACT

This paper presents the implementation of a self-adaptive mesh refinement to solve plane potential problems, using the Boundary Element Method. An error reduction method is utilized which observes variation in the local element and global solutions for two successive meshes. Based on these values, the method decides where further mesh refinement is needed. This adaptive technique is then utilized to analyze various potential problems. Numerical results for constant, linear and quadratic boundary elements are presented.

INTRODUÇÃO

Até recentemente as soluções dos problemas de engenharia usando os métodos numéricos consistia das seguintes etapas: baseado na experiência do analista e nas características do problema a ser analisado. Escolhia-se uma determinada malha de elementos e passava-se então à análise dos resultados. Caso o projetista não os considerasse satisfatório, repetia-se o procedimento utilizando-se de uma malha refinada. Este processo era bastante dispendioso em termos computacional e de esforço humano. A filosofia de projeto atual, conhecida como métodos adaptativos, leva o projetista a simplesmente escolher uma malha inicial para o problema; e empregar algum tipo de estimador de erro aposteriori como forma de mudar a estrutura de aproximação de uma maneira sistemática, visando uma melhora na qualidade da solução. As técnicas auto-adaptativas de se obter um aprimoramento da qualidade da solução são:

i - h, que refina a malha em zonas de maior erro;

ii - p, em que o gráu da função de interpolação e mudado localmente;

iii - r, o numero de nós e mantido constante e a malha é distorcida de forma a reposicionar os nós em áreas de maior erro;

iv - hp, como uma combinação das duas primeiras.

Estas técnicas auto-adaptativas foram bastantes estudadas para o Método dos Elementos Finitos (MEF) nos ultimos anos, baseados nos fundamentos matemáticos introduzidos por Babuska e outros [5-7] e implementados por Gago, Kelly e Zienkiewicz [30]. Uma recente revisão da literatura sobre os métodos auto adaptativos para o MEF é apresentado na referência [14] por Oden e Demkowicz. Também uma revisão sobre malhas adaptativas encontra-se no trabalho feito por Eiseman [11].

Apesar das técnicas auto adaptativas estarem num estágio bastante desenvolvido para o MEF, apenas recentemente o Método dos Elementos de Contorno (MEC) vem recebendo a atenção dos pesquisadores. Utilizando a técnica h de refinamento, Rencis e Mullen [21-22] desenvolveram formulações para problemas potenciais e de elasticidade, usando elementos constantes e estimadores de erro local e global. Posteriormente, Rencis e Jong [20], desenvolveram uma formulação baseada numa previsão de erro obtida dos conceitos desenvolvidos por Zienkiewicz [30], Hilton e Campbell [12], para o MEF.

No caso da técnica p, Alarcon e outros [2-4,23] desenvolveram uma formulação hierarquica utilizando funções de interpolação de Peano [16]. Também utilizando outras funções Alarcon e Cerrolaza [10] extenderam esta técnica para problemas potenciais tridimensionais e axissimétricos. Umetani [24] e Parreira [15] desenvolveram formulações p para elasticidade usando Galerkin. Apesar de a técnica p apresentar mais vantagens em relação o h para MEF, em se tratando do MEC esta técnica tem o incoveniente de alterar a estrutura convencional da formulação do método e das dificuldades de integração das integrais singulares.

No tocante a técnica r, Ingber e Mitra [13] e mais recentemente Carey e Kennon [9], publicaram trabalhos ilustrando a melhoria da solução dos problemas estudados devida a otimização do ponto nodal.

A técnica hp, foi recentemente proposta por Wendland [27-28] e por Rank [7-8]. Nestes trabalhos foi demostrado que a técnica p converge exponencialmente para contornos suaves e a técnica h apesar de não convergir exponencialmente como a p, apresenta melhores resultados para problemas singulares. Tendo em vista isto, Rank [9], desenvolveu uma formulação hp que de acordo com o elemento aplica a extensão h ou p, com um estimador de erros para ambos.

Este trabalho apresenta uma formulação h para problemas potenciais baseada nos conceitos proposto por Rencis e Mullen nas referências [21-22] . Elementos constantes , lineares e quadráticos, são utilizados na descretização do contorno e também algumas alterações do estimador de erro proposto por Rencis e Mullen [21], foram estudados. Vários exemplos são apresentados de forma demonstrar o aprimoramento da solução do problema com o uso de elementos lineares e quadráticos . Esta formulação tem como grande vantagem a possibilidade de ser implementada em qualquer programa de MEC, sem ter que alterar a estrutura basica dos programas clássicos de MEC.

PRELIMINARES E FORMULAÇÃO DO MEC.

Vários problemas de engenharia como condução de calor, campo elétrico, percolação etc, são governados pela seguinte equação de Laplace

$$\nabla^2 u = 0 \quad \text{em} \quad \Lambda \tag{1}$$

com as condições de contorno

$$\begin{aligned} u &= \bar{u} \quad \text{em} \quad \Gamma_u \\ \frac{\partial u}{\partial n} &= \bar{q} \quad \text{em} \quad \Gamma_q \end{aligned} \tag{2}$$

onde Λ é o domínio 2D do problema, n é normal ao contorno e $\bar{u}$ e $\bar{q}$ são valores conhecidos no contorno.

A formulação integral deste problema pode ser obtida fazendo-se uso da segunda identidade de Green [8], resultando

$$u(p) = \int_\Gamma (u^*(p,q)\frac{\partial u}{\partial n}(q) - u(q)\frac{\partial u^*}{\partial n}(p,q))d\Gamma \tag{3}$$

onde p é um ponto do interior do dominio Λ e u^* a solução fundamental da equação (1),

$$u^* = -\frac{1}{2\pi} lnr \tag{4}$$

r é a distância entre p e o ponto q do contorno.

A particularização da equação (3), para pontos no contorno, veja [8], resulta

$$cu(p) = \int_\Gamma u^*(p,q)\frac{\partial u}{\partial n}(q) - u(q)\frac{\partial u^*}{\partial n}(p,q)d\Gamma \tag{5}$$

onde

$c = \frac{1}{2}$ para um ponto em um contorno suave. No caso de vertice , c é o angulo correspondente dividido por 2π.

A equação integral (5) pode ser reduzida a um sistema algébrico de equação, discretizando o contorno. Ambas variáveis $(u, \frac{\partial u}{\partial n})$ são suportas variáveis numa certa forma entre os nós do elemento de contorno, isto é

$$\begin{aligned} u &= [N_1(\xi), N_2(\xi)\ldots] \begin{vmatrix} u_1 \\ u_2 \\ \vdots \end{vmatrix} \\ q &= \frac{\partial u}{\partial n} = [N_1(\xi), N_2(\xi)\ldots] \begin{vmatrix} q_1 \\ q_2 \\ \vdots \end{vmatrix} \\ d\Gamma &= J d\xi \end{aligned} \tag{6}$$

onde N_i são funções de interpolação, ξ coordenada natural do elemento, e J o Jacobiano

A forma discretizada da equação (6), resulta:

$$\begin{aligned} ci\ ui + \sum_{J=1}^{N} \int_{\Gamma_J} \frac{\partial u*}{\partial n} [N_1, N_2\ldots] \begin{bmatrix} u_1 \\ u_2 \\ \vdots \end{bmatrix} Jd\xi = \\ = \sum_{J=1}^{N} \int_{\Gamma_J} u^* [N_1, N_2, \ldots] \begin{bmatrix} q_1 \\ q_1 \\ \vdots \end{bmatrix} Jd\xi \end{aligned} \tag{7}$$

O indice i indica o nó do elemento de centro. A interpolação é extendida para numero N de elementos de contorno.

A equação anterior (7), pode ser expressa na forma matricial, comumente conhecida em MEC [8],

$$[H]\ [u] = [G]\ [q] \tag{8}$$

onde $[H][G]$ são matrizes calculadas e $[u]e[q]$ são os vetores definindo as variáveis no contorno.

A solução do problema é obtida forçando as condições de contorno no sistema de equações (8), e resolvendo o sistema linear de equações resultantes.

FORMULAÇÃO ADAPTATIVA

Atualmente, em métodos numéricos é de consideravel importância o controle do erro obtido pela aproximação numérica na solução dos problemas de engenharia. Para o Método dos Elementos Finitos, os conceitos do método Adaptativos foram introduzidos por Babuska e outros ref. [5-7]. O método adaptativo pode estimar o erro total em Elementos Finitos e ao mesmo tempo fornecer informações para redefinir os elementos de forma a se obter o erro a um nível especificado. Vários medidores de erro existem para problemas lineares e não lineares, produzindo um grande impacto entre os engenheiros, mostrando como a teoria matemática do MEF pode ser aplicada na solução de problemas de engenharia. Apesar dos métodos adaptativos estarem bem definidos para o MEF, o mesmo não aconteceu para MEC. A principal dificuldade que o MEC sofre é a falta de fundamentos matemáticos para o estabelecimento de estimadores de erro apropriados ao método. Apenas recentemente, o MEC vem recebendo contribuições nesta direção através dos trabalhos de Wendland [28] , Rank [8].

Este trabalho é basicamente uma extensão da técnica h adaptativa desenvolvida por Rencis e Mullen [21]. A seguir, serão descritos os conceitos básicos utilizadas para refinamento da malha de elementos de contornos proposto por Rencis [21] e extendido para elementos de ordem superior neste trabalho.

A técnica usada pela ref. [21] para o refinamento da malha começa com a definição de uma malha simples com poucos elementos necessários, apenas para definir a geometria e as condições de contorno. A seguir uma segunda malha uniforme com duas vezes o número de elementos da anterior é utilizada. Utilizando-se as soluções da primeira e da segunda malha, o número de divisões n requerido para se obter uma determinada precisão, pode ser calculado se as propriedades de convergência do MEC estiverem estabelecidas. Para isto, considere a seguinte estimativa de erro deduzida por Wendland [25-26]:

$$\int_\Gamma (u^{i-1} - u)^2 d\Gamma = k(h^{i-1})^2 + 0((h^{i-1})^3) \tag{9}$$

onde :

u^{i-1} = potencial ou deslocamentos no refinamento $(i-1)$

u = solução exata

h^{i-1} = tamanho do elemento no refinamento $(i-1)$

k = constante que depende de h

$0((h^{i-1})^3)$ = termo de mais alta ordem de erro no refinamento $(i-1)$

Para o refinamento i, tem-se:

$$\int_\Gamma (u^i - u)^2 d\Gamma = k(h^i)^2 + 0(h^i)^3) \tag{10}$$

Subtraindo-se a equação (10) de (9) e fazendo-se $u = u^i$ que é a solução mais proxima da exata até o momento , é possivel obter a seguinte expressão

$$\Delta u_i = \int_\Gamma (u^{i-1} - u^i)^2 d\Gamma = k(h^{i-1})^2 - k(h^i)^2 \tag{11}$$

Determinando o valor de k na expressão anterior, tem-se

$$k = \frac{\Delta u_i}{\left(1 - \frac{(h^i)^2}{(h^{i-1})^2}\right).(h^{i-1})^2} \tag{12}$$

Para obter-se o numero de divisões necessárias por elemento dentro de uma determinada tolerancia (ϵ), pode-se escrever baseado em (8):

$$\epsilon . \int_\Gamma u^2 d\Gamma = k(h^{i-1+n})^2 \tag{13}$$

sendo o termo da esquerda a tolerancia (ϵ) em função de k e do tamanho do elemento na $(i-1+n)$ iteração ideal.

Na iteração ideal, pode-se definir o tamanho do elemento como sendo:

$$h^{i-1+n} = \frac{h^{i-1}}{n} \tag{14}$$

onde, n = numero de divisões necessarias para a iteração ideal.

Igualando-se a expressão (13) em (12) e isolando-se o valor de n, é possivel obter a seguinte expressão

$$(n_j^{i+1})^2 = \frac{\Delta u_j^i}{\left(1 - \frac{(h_j^i)^2}{(h_j^{i-1})^2}\right).\epsilon.\int_\Gamma u^{i^2} d\Gamma} \tag{15}$$

sendo:

$$\Delta u_j^i = \int_\Gamma (u^{i-1} - u^i)^2 d\Gamma \tag{16}$$

onde n_j^{i+1} é o numero de divisões necessarias para o elemento j na iteração $i+1$.

As equações (16) e (13) quando a função u é constante fig. 1., reduzem-se as seguintes expressões:

$$\begin{aligned} \Delta u_j^i &= (u_j^{i-1} - u_j^i)^2 \ .h_j^i \\ \int_\Gamma u^2 d\Gamma &= \sum_{j=1}^{N_e} (u_j^i)^2 .h_j^i \end{aligned} \tag{17}$$

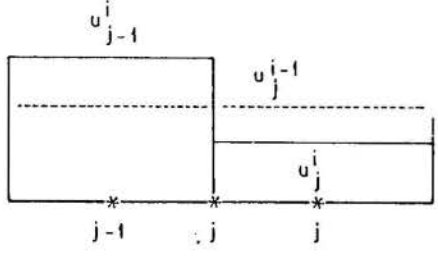

Figura 1 - Elemento constante após duas iterações sucessivas $i-1$ e i

As equações anteriores foram deduzidas por Rencis e Mullen na ref. [21]. No caso em que é suposta uma variação linear das variáveis do problema, para um elemento j com os nós j e $j+1$ pertencentes ao elemento, fig. (2), tem-se

$$\begin{aligned} \Delta u_j^i = \frac{h_j^i}{3}\left[(u_{j+1}^{i-1} - u_{j+1}^i) + (u_j^{i-1} - u_j^i)(u_{j+1}^{i-1} - u_{j+1}^i) + \right. \\ \left. (u_j^{i-1} + u_j^i)\right] \int_\Gamma u^2 d\Gamma = \sum_{j=1}^{N_e} \frac{h_j^i}{3}.\left[u_{j+1}^{i^2} + u_j^2.u_{j+1}^2 - u_j^2\right] \end{aligned} \tag{18}$$

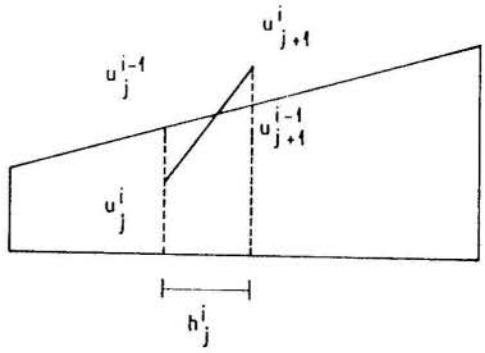

Figura 2 - Elemento Linear após duas iterações sucessivas.

Para a variação quadrática do potencial no interior do elemento j, com os nós $j1, j2 e j3$ pertencentes ao elemento, conforme fig. 3, obtem-se:

$$\begin{aligned} \Delta u_j^i = \frac{h_j^i}{15}\left[2(u_{j1}^{i-1} - u_{j1}^1) + 8(u_{j2}^{i-1} - u_{j2}^i) + 2(u_{j3}^{i-1} - u_{j3}^i) + \right. \\ + 2(u_{j1}^{i-1} - u_{j1}^i).(u_{j3}^{i-1} - u_{j3}^i) - (u_{j2}^{i-1} - u_{j2}^i) \\ \left. (u_{j3}^{i-1} - u_{j3}^i) + +2(u_{j1}^{i-1} - u_{j1}^i).(u_{j3}^{i-1} - u_{j3}^i)\right] \end{aligned}$$

$$\begin{aligned} \int_\Gamma u^2 d\Gamma = \sum_{j=1}^{N_e} \frac{h_j^i}{3}\left[2u_{j1}^{i^2} + 8u_{j2}^{i^2} + 2u_{j2}^{i^2} + 2u_{j1}^i.u_{j2}^i.u_{j3}^i + \right. \\ \left. + 2u_{j1}^i.u_{j2}^i\right] \end{aligned} \tag{19}$$

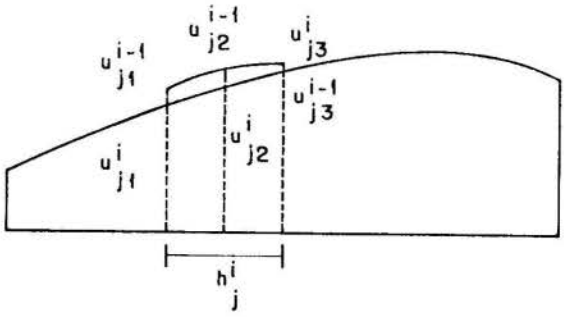

Figura 3 - Elemento Quadratico apoś duas interações sucessivas.

Há ainda a necessidade de se ter-se um parametro que meça o erro global cometido, pois a medida que se diminui desigualmente o tamanho dos elementos, gerando elementos muito menores que outros, pode-se introduzir êrros numéricos. O parametro de controle de erro global serve tanto para indicar que uma solução obtida já esta dentro da tolerância fixada, como também um controle de possíveis erros numéricos que fazem com que a solução não convirja. A expressão é a seguinte

$$\left(\int_\Gamma (u^i)^2 d\Gamma - \int_\Gamma (u^{i-1})^2 d\Gamma\right)^{1/2} \leq \epsilon \left(\int_\Gamma (u^i)^2 d\Gamma\right)^{1/2} \tag{20}$$

Sendo cada uma das integrais calculadas de acordo com as expressões e com as funções de interpolação correspondentes.

Se a relação anterior (20) for verdadeira, a solução obtida estará dentro da tolerancia global fixada.

Para analisar a evolução do erro global é necessario considerar as integrais das últimas três iterações sucessivas através da seguinte relação:

$$\left(\int_\Gamma (u^i - (u^{i-1})^2 d\Gamma\right)^{1/2} < \left(\int_\Gamma (u^{i-1})^2 - (u^{1-2})^2 d\Gamma\right)^{1/2} \tag{21}$$

Se a relação anterior for verdadeira, a solução estará convergindo; caso contrario estarão ocorrendo erros numéricos que farão com que a solução não convirja. O programa então deverá interromper a sua execução com a resposta mais correta sendo a iteração $i-1$, mesmo que ainda não se tenha chegado a aproximação desejada.

A técnica desenvolvida não preve a discretização dos elementos com u prescrito. Sendo assim, implementou-se uma rotina de discretização destes elementos, em que o usuario fornece o numero de divisões desejadas, via teclado. Esta rotina é bastante util, pois apesar da solução na maioria dos casos já ser satisfatória, pode-se ainda tentar melhorar-lá ou obter uma distribuição mais uniforme dos elementos, ou ainda, obter alguns valores intermediarios, sem ter que recorrer a uma interpolação manual da função.

RESULTADOS NUMÉRICOS

Exemplo 1 - Região quadrada com reentrâncias.

Neste exemplo, estuda-se uma região quadrada com reentrâncias, problema também resolvido por Rencis e Mullen e apresentado na ref. [15]. A geometria e as condições de contorno estão especificadas na fig. 14. Nos lados maiores AB, KL e LA, o potencial é prescrito. Nas reentrâncias, em cada face o fluxo assume um valor diferente, estando estes especificados na tabela ao lado da figura.

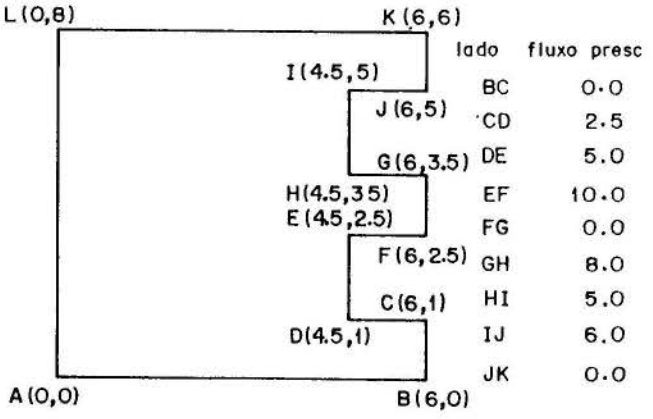

lado	fluxo presc
BC	0.0
CD	2.5
DE	5.0
EF	10.0
FG	0.0
GH	8.0
HI	5.0
IJ	6.0
JK	0.0

Figura 14 - Geometria e condições de contorno

Este problema foi resolvido para as funções de interpolação constante, linear e quadrática, utilizando-se a tecnica h-adaptativa proposta no trabalho. Os resultados encontram-se expressos nas tabelas 4 e 6, onde se indica o valor da integração do fluxo e do potencial no contorno. Indica-se também para efeito de comparação, a solução obtida com 80 elementos constantes e a melhor solução da ref. [24]. Como pode-se reparar há uma certa diferença entre os resultados, e isto se deve à grande complexidade do problema que não possui solução analítica exata.

Interação	Nn	$\int u d\Gamma$	$\int q d\Gamma$
1	12	274,15	107,14
2	24	255,61	108,91
3	41	249,04	108,87
4*	57	247,44	108,87
5**	80	249,41	109,51

Tabela 4 - Resultados Elementos Constantes:

Interação	Nn	$\int u d\Gamma$	$\int q d\Gamma$
1	12	219,4	62,87
2	48	241,70	102,86
3	55	241,60	103,09

Tabela 5 - Elemento Linear:

Interação	Nn	$\int u d\Gamma$	$\int q d\Gamma$
1	24	242,7	110,54
2	48	244,50	109,61
3*	54	245,35	109,61
4**	66	245,60	109,61

Tabela 6 - Resultados Elementos Quadrático:

* Iteração final sem discret. dos elementos com u prescrito

** Iteração final com discret. dos elementos com u prescrito.

*** Resposta com 80 elementos constantes : $\int u\, d\Gamma = 247,66$
$\int q\, d\Gamma = 109,51$

**** Melhor solução [21] : $\int u\, d\Gamma = 247,146$
$\int q\, d\Gamma = 108,88$

Nas figuras 5 e 7 mostram-se as discretizações iniciais e finais obtidas com a utilização das diferentes funções de interpolação. Note-se a concentração de elementos nas reentrâncias onde necessários um maior refinamento para se obter uma solução satisfatoria.

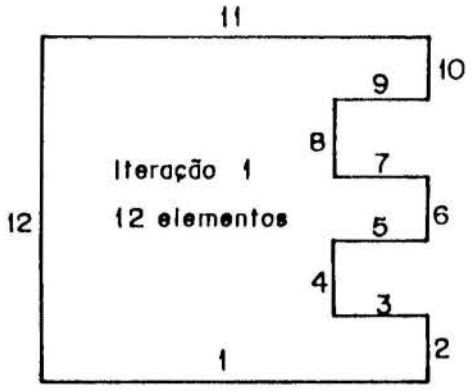

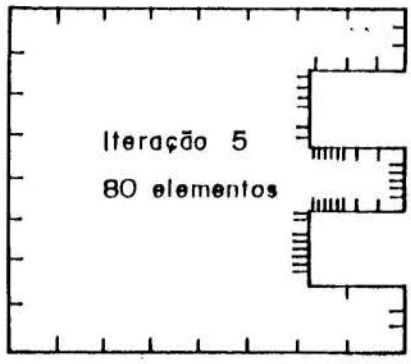

Figura 5 - Iteração Inicial e Final Elemento Constante

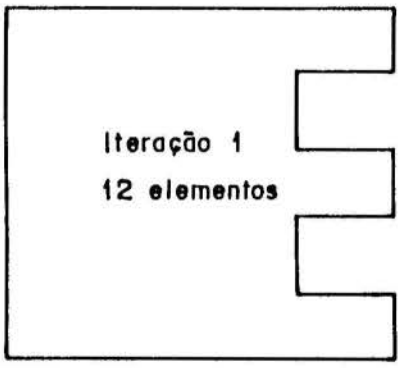

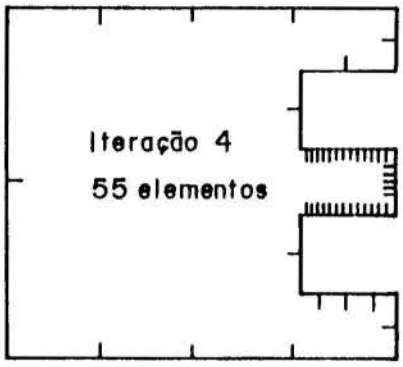

Figura 6 - Iteração Inicial e Final Elemento Linear

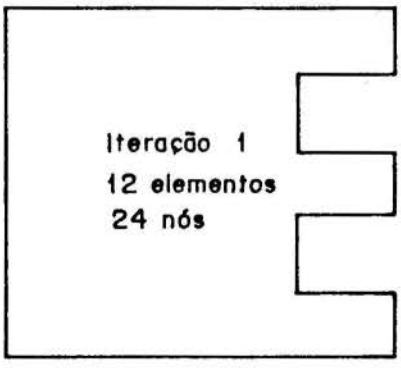

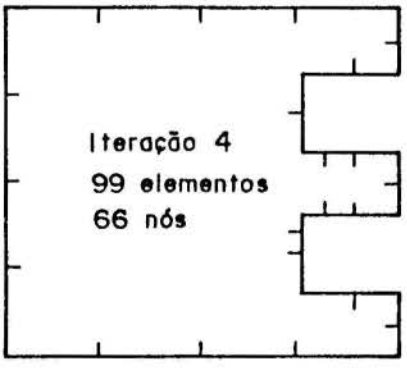

Figura 7 - Iteração Inicial e Final Elemento Quadrático

CONCLUSÕES

Foi apresentado um medidor h adaptativo para o Método dos Elementos de Contorno, aplicado à problemas da teoria do potencial.

Como vantagens da formulaçào h-adaptativa apresentada pode-se destacar a simplicidade de implementação em programas de MEC, não sendo necessário o desenvolvimento de programas específicos para este fim, podendo ser aplicado como um pré e pós-processador para qualquer programa de análise. Observou-se também que o medidor de erro adotado fornece bons resultados, mesmo na presença de zonas de singularidade, onde se exige uma maior discretização pela alta variação do potencial.

Apesar do estimador ser baseado na variação do potencial e de serem refinados somente os elementos em que o fluxo é prescrito, mostrou-se que a precisão obtida para os demais elementos é satisfatória. Para se melhorar a solução nessas regiões obtendo uma discretização mais uniforme , recorreu-se a uma subroutina em que o usuário entra com o numero de divisões para cada elemento. A utilização desta subroutina apresentou uma melhora dos resultados.

REFERENCIAS

[01] - Alarcón, E., Reverter, A. e Molina, J., Hierarchical Boundary Elements, Comp. and Struct., 20, 151-156, 1985.

[02] - Alarcón, E. e Reverter, A., P-Adaptive Boundary Elements, *Int. J. Num. Meth. Engng*, 23, 801-829, 1986.

[03] - Alarcón, E., Avia L. e Reverter A., On the Possibility of Adaptive Boundary Elements, *Proc. of the int. Conf. on Accuracy Estimates and Adaptative Refinements in Finite Element Comp.* (ARFEC), Lisboa, 1984.

[04] - Alarcón, E., Martin, A. e Paris, F., Boundary Elements in Potential and Elasticity Theory, *Comput. and Struct*, vol 10, pag. 351-362, 1979.

[05] - Babuska I. and Szabó, On the Rates of Convergence of the Finite Element Method, *Int. J. Num. Meth. Engng*, vol 18, 323-341, 1982.

[06] - Babuska I. and Dorr M.R., Error estimates for the Combined h and p Version of the Finite Element Method, *Numer. Math*, vol 25, 257-277, 1981.

[07] - Babuska, I., and Rheinboldt, W.C., A Posteriori Error Estimates for Finite Element Computations, *SIAM J. Numer. Anal.*, vol. 15, 736-754, 1978.

[08] - Brebbia, C.A., The B.E.M. for Engineers, *Pentechg Press*, London, Halstead Press, New York, 1978.

[09] - Carey, G.F. e Kennon, Adaptive Mesh Redistribution for a Boundary Method, *Int. J. Num. Meth. Engng.*, 24, 2315-2325, 1987.

[10] - Cerrolaza, M., Gong-Lera, M.S. e Alarcón, E., Elastostatics P-adaptive B.E. for micros, *Software for Engng. Workstation*, January, vol. 4, 1988.

[11] - Eiseman, P. , Adaptive Grid Generation, *Comput. Meths. Appl. Mech. Engng.* vol. 64, 321-376, 1987.

[12] - Hinton, E. and Campbell, J.S., Local and Global Smoothing of Discontinuous Finite Element Fuctions Using a Least Squares Method, *Int. J. Num. Engng*, vol 24, 1921-1939, 1974.

[13] - Ingber, M.S. e Mitra, A,K., Grid Optimization for B.E.M., *Int. J. Num. Meth.*, Engng., 23, 2121-2136, 1986.

[14] - Oden, J.T. and Demkowicz, Advances in Adaptive Improvements: A Survey of Adaptive Finite Element Methods in Computational Mechanics, in: *A.K. Noor and J.T. Oden*, eds., State of the Art Surveys in Comp. Mech. (ASME, New York, 1986).

15] - Parreira, P.G. Analise do erro no Método dos Elementos de Fronteira em Elasticidade, Tese de Mestrado, Univ. Técnica de Lisboa, 1987.

[16] - Peano, A.G., Hierarchies of Confoming Finite Elements for Plane Elasticity and Plane Bending, *Comput. and Maths. with Aplls.* 2, No. 3-4, 1979.

[17] - Rank, E., Adaptive B.E.M., Boundary Elements IX, *C.A. Brebbia Eds.* , pag. 259-278, 1984.

[18] - Rank, E., A Posteriori Error Estimates and Adaptive refinement for Some Boundary Integral Element Methods, *Proc. of the Int. Conf. on Accuracy Refinements in Finite Element Comp.* (ARFEC), Lisboa, 1984.

[19] - Rank, E., Adaptive h-, p- and h-p Versions for Boundary Intergral Elements Methods, *Int. Jour. for Num. Meth. in Engng*, vol. 28, 1335-1349, 1989.

[20] - Rencis, J.J. e Jong, K.Y., A Self-Adaptive H-Refinement Technique for the B.E.M., *Comp Methods in appl. Mech. and Eng.* , 1988.

[21] - Rencis, J.J. e Mullen, R.L., Self Adaptive Mesh Refinement for the Boundary Element Solutions of Laplace Equation, *Comp. Mech.*, vol 3, 309-319, 1988.

[22] - Rencis, J.J. e Mullen, R.L., Solution of Elasticity Problems by a Self Adaptive Mesh Refinement Technique for Boundary Element Computation, *Int. J. Num. Meth. Engng.*, 23, 1509-1527, 1986.

[23] - Reverter, A., Gonzales, A. e Alarcón, E., Indicators and Estimates in p-adaptive Boundary Elements, Boundary Elements VII, *C.A. Brebbia and G. Maier eds.*, Springer-Verlag, Berlin, 1985.

[24] - Umetani, S., *Reliability and Efficiency of the BEM in Elastostatics*, PhD. Thesis, Univ. of Southampton, 1986.

[25] - Wendland, W.L. Asymptotic Accuracy and Convergence, em Progress in B.E.M. (*C.A. Brebbia Ed.*) 289-313, Pentech Press, London, Plymouth, 1981.

[26] - Wendland, W.L., On Asymptotic Error Analysis and Underlyning Mathematical Principles for B.E.M., em *Boundary Element Technique in Computer Aided Engineering*, (C.A. Brebbia Ed.), Martines Nijhoff Plublishera, 417-436, 1984.

[27] - Wendland, W., Splines Versus Trigonometric Polynomials, *h-versus p-version in 2D Boundary Intergral Methods*, Preprint Nr. 925, TH Darmstedt, Fashbereich Mathematik, 1985.

[28] - Wendland, W.L. and Yu, D., Adaptive B.E.M. for Strongly Elliptic Integral Equations, Seminar Analysis and Anwendungen, Universitat Stuttgart, *Mathemattuber Institut A.*, Bericht Nr 4, 1988.

[29] - Zienkiewicz, O.C., Gago, J.P. and Kelly D.W., The Hierarchical Concept in Fnite Eement Aalysis, *Computers & Structures*, vol 16, 53-65,1983.

[30] - Zienkiewicz, O.C. and Zhu, J.Z., A Simple Error Estimator and Adaptive Procedure for Pratical Engineering Analysis, *Int. J. Num. Meth. Engng*, vol 24, 337-357, 1987.

III ENCIT – Itapema, SC (Dezembro 1990)

SIMULATION OF INCOMPRESSIBLE 2D AND 3D TURBULENT FLOWS BY FINITE ELEMENT METHOD

ANTONIO C. P. BRASIL JUNIOR
University of Brasilia - Dpto. of Mech. Engineering
G. BRUN, M. BUFFAT, Ph. CARRIERE & D. JEANDEL
Ecole Centrale de Lyon - Lab. Mécanique des fluides
69130 ECULLY - FRANCE

SUMMARY

A numerical method to solve the partial differential governing equations of the turbulent flows is presented. The standard k-ε model is used as the closure model of mean equations. The developed codes use a finite element approach to solve complex industrial 2D and 3D flows.

INTRODUCTION

The recent improvements in supercomputing presently allows scientists and engineers to performe numerical investigations in more and more realistic fluid dynamic problems. Some typical applications are aerodynamic and flows in the environmental and industrial processes. The main difficulties ccountered in this kind of situations are due to the strong dependence of the flow pattern on the turbulence characteristics and on the non trivial boundary conditions imposed by the complex geometries.

The aim of this work is the development of performant numerical techniques, based on a finite element method, to solve complex 2D and 3D turbulent flow problems. The basis of the method are given in the first two sections and results of some test cases are presented in the last section.

FORMULATION

The classical mean conservation equations for the incompressible newtonian flows, with the standard k-ε model are used. Introducing Ω a part of $\mathbb{R}^2$ or $\mathbb{R}^3$, the dimensionless form of the governing equations are:

$$\nabla . u = 0 \qquad (1)$$

$$u_t + \nabla . (u \otimes u) = -\nabla p + \nabla . (\Gamma_u . D) \qquad (2)$$

$$k_t + \nabla . (u . k) = \nabla . (\Gamma_k . \nabla k) + P - \varepsilon \qquad (3)$$

$$\varepsilon_t + \nabla . (u . \varepsilon) = \nabla . (\Gamma_\varepsilon . \nabla \varepsilon) + C_{\varepsilon 1} . P . \varepsilon / k - C_{\varepsilon 2} . \varepsilon^2 / k \qquad (4)$$

with

$$D = 0.5 . (\nabla u + \nabla^T u)$$

$$\Gamma_u = \left(\frac{1}{Re} + \frac{1}{Re_T} \right) , \quad \Gamma_k = \left(\frac{1}{Re} + \frac{1}{\sigma_k . Re_T} \right) ,$$

$$\Gamma_\varepsilon = \left(\frac{1}{Re} + \frac{1}{\sigma_\varepsilon . Re_T} \right) , \quad (1/Re_T) = C_\mu . k^2 / \varepsilon$$

$$P = (1/Re_T) . (D : D)$$

The standard values of constants are:

$$C_\mu = 0.09 , \quad C_{\varepsilon 1} = 1.44 , \quad C_{\varepsilon 2} = 1.92 ,$$

$$\sigma_k = 1.0 \quad \text{and} \quad \sigma_\varepsilon = 1.3 .$$

Typical inflow and outflow conditions are non-homogeneous Dirichlet or homegeneous Neuman boundary conditions for u, p, k and ε.

The computational domain vanishes just at a distance δ from the solid walls. For this surfaces a logarithmic wall function is imposed as boundary condition through the following process:

$$(u . t)_\delta = f(u_f) \qquad (5a)$$

$$(u . n)_\delta = 0 \qquad (5b)$$

$$(u . s)_\delta = 0 \qquad (5c)$$

$$k = u_f^2 / \sqrt{C_\mu} \qquad (6)$$

$$\varepsilon = u_f^2 / (k . \delta) \qquad (7)$$

where :

$$f(u_f) = Re.\delta.u_f \quad \text{if } Re.\delta.u_f < 11.6$$

or

$$f(u_f) = (u_f/C_1).\log(Re.\delta.u_f) + C_2$$

$$\text{if } Re.\delta.u_f > 11.6$$

and

$$u_f^z = \Gamma_u.\left.\frac{\partial(u.t)}{\partial n}\right|_\delta$$

The unit vectors n, t and s lead to a local framing deduced from the normal and tangential directions of the computed streamline at a point of the surface.

A set of initial conditions is given for the time integration of the equations.

NUMERICAL METHODS

Time integration

The parabolic system of differential equations (1)-(4) is discretised in time using a semi-implicit finite difference scheme of order $o(\Delta t)$. Denoting by the upperscripts n and n+1 tha values of dependent variables at time t and t+Δt respectvily, the discretised equations are :

$$\nabla.u^{n+1} = 0$$

$$\alpha.u^{n+1} + \nabla.(u^n \otimes u^{n+1}) = -\nabla p^{n+1} + \nabla.(\Gamma_u^n.\nabla u^{n+1}) + \nabla.(\Gamma_u^n.\nabla^T u^n) + \alpha.u^n$$

$$\alpha.k^{n+1} + \nabla.(u^{n+1}.k^{n+1}) = \nabla.(\Gamma_k^n.\nabla k^{n+1}) + p^{n+1} - \varepsilon^n.k^{n+1}/k^n + \alpha.k^n$$

$$\alpha.\varepsilon^{n+1} + \nabla.(u^{n+1}.\varepsilon^{n+1}) = \nabla.(\Gamma_\varepsilon^n.\nabla\varepsilon^{n+1}) + C_{\varepsilon 1}.p^{n+1}.\varepsilon^n/k^n - C_{\varepsilon 2}.\varepsilon^{n+1}.\varepsilon^n/k^n + \alpha.\varepsilon^n$$

where $\alpha = 1/\Delta t$

Except for the velocity and the pressure fields this scheme leads to a system of linear and uncoupled equations at each time step.

Finite elements discretisation

The time discretisation leads to a set of transport problems of the common form :

$$\begin{cases} find\ \phi \in H^1(\Omega)\ with \\ \alpha.\phi + \nabla.(u.\phi) - \nabla.(\Gamma.\phi) = S_\phi \end{cases}$$

The equivalent weak formulation is obtained using the weight residual method with ω weigth functions :

$$\begin{cases} find\ \phi \in H^1(\Omega)\ with\ \omega \in H_o^1(\Omega)\ , \\ \quad and \\ \alpha.\langle\phi,\omega\rangle + \langle u.\phi, \nabla\omega\rangle + \langle\Gamma.\nabla\phi, \nabla\omega\rangle = \langle S_\phi, \omega\rangle \\ where \\ \langle .,. \rangle = \int_\Omega (.,.).d\Omega \end{cases} \quad (8)$$

Then, the standard Galerkin method is applied, using the nodal basis functions N_i of the discret space $H^1_{\Omega,h}$:

$$\phi_h = \sum_{i=1}^{N} \phi_i.N_i \quad (9)$$

So the discrete solution of the problem is reduced to the solution of linear system of algebraic equations :

$$A.\Phi = b \quad (10)$$

where

$$A = A_D + A_C \quad (11a)$$

$$A_D^{ij} = \alpha.\langle N_i, N_j\rangle + \langle\Gamma.\nabla N_i, \nabla N_j\rangle \quad (11b)$$

$$A_C^{ij} = \langle u.N_i, \nabla N_j\rangle \quad (11c)$$

$$b_i = \langle S_{\phi,i}, N_i\rangle \quad (11d)$$

The nodal basis functions are classicaly obtained from the discretisation of Ω into a finite set of P1 triangular elements (tetraedrons in the 3D case). In order to satisfy the the Babûska-Brezzi stability conditions limiting the choice of discrete solution spaces for velocity and pressure, the P1/isoP2 element is used: The discrete pressure field is then piecewise linear and continuous on a standard coarse grid, and the discrete velocity field (or any scalar field) is also piecewise linear and continuous on a refined grid obtained from the coarse one by dividing each element into four (eigth in 3D) sub-elements (c.f BERCOVIER & PIRONNEAU[4]).

The approximation error given by the standard Galerkin method with the polynomial finite element interpolation is directly dependent on the local Reynolds (or Peclet) number (c.f. HUGHES[1]). Consequently, for the hight values of Reynolds number spurious oscillations appearing in the numerical results. A simple and efficient method to control the *"wiggles"* is to use an upwind like scheme in the streamline direction. In this work the *Anisotropic balancing dissipation* concept of KELLY *et al*[2] is used. Then, (11c) is changed for :

$$A_C^{ij} = \langle u.N_i, \nabla N_j\rangle + \mathbb{K}^{ij}.\langle\nabla N_i, \nabla N_j\rangle \quad (12)$$

where

$$\mathbb{K}^{ij} = \lambda . u_i . u_j . h . |u|^2 / 2 \qquad (13)$$

and $\lambda = \lambda(Pe_h)$

Solution of the velocity-pressure coupled problem

Applying the discretisation (10)-(13) for the continuity and momentum conservation equations, one can obtain the coupled system of linear equations :

$$\begin{bmatrix} A_u & 0 & 0 & B_x^T \\ 0 & A_v & 0 & B_y^T \\ 0 & 0 & A_w & B_z^T \\ B_x & B_y & B_z & 0 \end{bmatrix} \begin{bmatrix} u \\ v \\ w \\ p \end{bmatrix} \begin{bmatrix} f_u \\ f_v \\ f_w \\ 0 \end{bmatrix} \qquad (14)$$

Or in compact form :

$$\begin{cases} \mathbb{A} . u_h = -\mathbb{B}^T . p_h + f & (15a) \\ \mathbb{B} . u_h = 0 & (15b) \end{cases}$$

A well known method for the solution of (15) is the UZAWA algorithm (ARROW *et al*[10]) which propose the use of simple gradient algorithm for the dual problem :

$$[\mathbb{B} . \mathbb{A}^{-1} . \mathbb{B}^T] . p_h = [\mathbb{B} . \mathbb{A}^{-1}] . f \qquad (16)$$

The residual of (16) is the discrete divergence of the velocity field which is chosen as the search direction. So the algorithm to solve the pressure-velocity problem is given by :

```
Initialise p_h^0 ;
repeat
  begin
    solve  A . u_h^k = -B^T . p_h^k + f ;
(* calcul. of the search direction *)
    solve  C . d^k = B . u_h^k ;
(* search iteration                 *)
    p_h^(k+1) := p_h^k + ρ . d^k ;
    k := k + 1 ;
  end;
until ||B . u_h^k|| < eps  or k > kmax.
```

$\mathbb{C}$ denotes some preconditioning operator introduced to improve the convergence rate of the method. The CAHOUET & CHABARD[11] operator is used:

$$\mathbb{C}^{-1} = (1/Re) . \mathbb{M}^{-1} + (1/\Delta t) . \mathbb{D}^{-1} \qquad (17)$$

where $\mathbb{M}$ and $\mathbb{D}$ are matrices obtained on the coarse grid from:

$$\mathbb{M}^{ij} = \langle N_i, N_j \rangle \; ; \; \mathbb{D}^{ij} = \langle \nabla N_i, \nabla N_j \rangle$$

In practice, a variant of the preceding algorithm, using a conjugated gradient like method for unsymmetric and non-positive definite systems, is applied (c.f BUFFAT[3]).

Wall boundary conditions

Geometrical considerations

For 2D flows the normal and tangential vectors are easily defined on the side of a boundary element (Fig. 1a), so the unit vectors n and t may be calculated from the grid parameters. All the iterative calculations are performed on the sides of the elements and then extrapolated to the nodes using a vectorial addition between the two values calculated in the neighboring elements.

For 3D flows the problem is more complex since the direction of the tangetial vector is note knowed. The normal unity vector is calculated using the grid parameters. The tangential vectors are calculated using the values of the velocity field at the previous time step u^n. In fact we use the value of the geometrical projection of the velocity vector calculated at the inside node, on the tangential plane: This technique allows a change of the velocity direction on the boundary from its initial value.

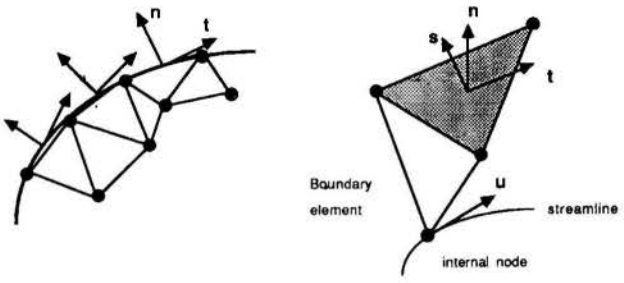

(a) (b)

Figure 1 : Velocity near wall conditions

iterative computation

The wall boundary conditions as defined in (5) provides extra non-linearity to the velocity-pressure problem and couples the velocity components. This particular problem is solved using an iterative method.

The velocity-pressure problem is solved at each time step using the velocity boundary conditions obtained from the previous time step. Then an iterative precesse is used including the

solution of the discretised momentum equation (15a), the calculations of the wall law (5) and of the tangential direction (for 3D flows). This algorithm is :

initialise $u^{*} := u^{n+1}$;

$t^{*} := t(u^{*})$;

$u_f^{2*} := \Gamma_u . (\partial u^{*} . t^{*} / \partial n)$;

repeat
begin

computation of b.c - eqs.(5)

solve $\mathbb{A} . u' = -\mathbb{B}^T . p + f$;

$t' := t(u')$;

$u_f^{2'} := \Gamma_u . (\partial u' . t' / \partial n)$;

$err := u_f^{2'} . t' - u_f^{2*} . t^{*}$;

$u_f^{2*} := u_f^{2'} + \omega . u_f^{2*}$;

end;

until $||err|| \leq eps$.

where ω is a relaxation parameter.

RESULTS AND DISCUSSION

The codes NATUR and NATUR3D are developed with all of numerical techniques presented in the preceding section. They also use advanced computational techniques for compact storage of the matrices and efficient methods to solve the linear systems.

The symmetric linear systems are solved via a conjugated gradient method precoditioning by an incomplete Cholesky factorisation. For the unsymmetric matrices the conjugate gradient square method with an ILU preconditioning is used (c.f. BUFFAT[3]).

The codes are optimised for the vector and parallel computations in a ALLIANT FX-80 supercomputer with four processors. The matrices and the right hand side terms assembly are paralellised using a graph coloring technic for the course grid elements. The solution of the triangular systems is parallelised by a level schedulling algorithm.

Two test cases are presented. All of these cases has 2D characteristics. They are used to check the validity of NATUR3D code. The 2D and 3D numerical and experimental results are compared.

Turbulent backward facing step

This test case is a classical workshop problem for laminar and turbulent flows, with well known characteristics of the recirculation flow. This problem was extensively analysed in two workshops on complex turbulent flows in 1980/81, and the results obtained in the present work are compared with the experimental results of KIM *et al*[7]

All the geometrical characteristics and the inflow boundary conditions were deduced from the experimental work. The Reynolds number is 44580.

For the 2D numerical simulation the computational domain is discretised with a 553 P1 nodes (2101 nodes for velocity) grid as shown in the Fig. 2. The 3D grid is obtained from the geometrical translation of the 2D one and include three 2D planes.

The streamline and the levels of k are presented in the Figs. 3 and 4. The velocity profile at the end of the recirculation zone (x/h=5.3) and the profile of k at x/h=10.3 are compared with the experimental datas in Figs. 5 and 6.

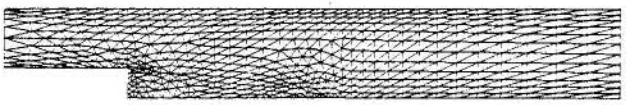

Fig. 2 : Coarse grid - 2D Backward facing step

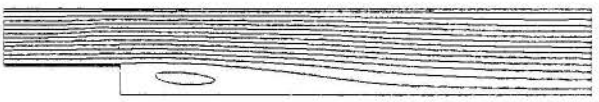

FIG. 3 : 2D results : Streamlines

FIG. 4 : 2D Results : k field

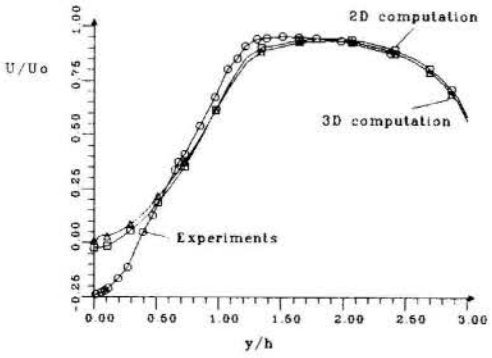

Fig. 5 : Velocity profile at x/h = 5.3

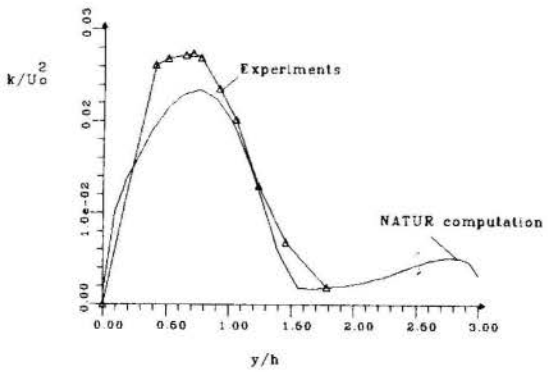

Fig. 6 : k profile at x/h = 10.3

The numerical and experimental results are in good agreement refering to the small differences also obtained in others numerical works (FONTOURA RODRIGUES[5]) which are commonly related with the use of the k-ε model in the recirculation zone.

As a conclusion, the reattachment length for different works are presented on the Table 1.

	Lc
2D computation	5.4
3D computation	5.2
FONTOURA (1990)	5.5 - 6.1
Experiments	6.0 - 8.0
MANSOUR *et al*(1983)	5.2

Table 1 : Lenght of the recirculation zone.

Annular turbulent jet

In this test case we study the turbulent flow in an annular turbulent jet for a value of the a Reynolds number equal to 8200. The experimental datas for this configuration are given by BAHRAOUI(1987).

The computational domain is located downstream of the potential core (x/D=4.5) and the inflow boundary conditions are deduced from the experimental profiles at this section. A reference pressure is specified on the outflow surface.

The two dimensional grid uses 221 P1 nodes. The 3D grid is obtained from the geometric rotation of the 2D grid and has 1547 P1 nodes (12376 velocity nodes).

The 3D results for the U component and for k are shown in Figs. 8 and 9. The 2D and 3D results are very close.

On Fig. 10 the velocity decrease along the axis is presented. On Fig. 11 and 12 the velocity and turbulent viscosity profiles are given for various axial positions.

A very good agreement between the numerical and the experimental results can be emphasized. A more complete presentation of the 2D calculations is given in BRUN (1988).

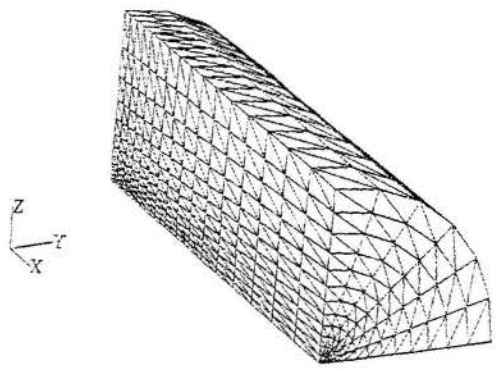

Fig. 7 : 3D coarse grid : Turbulent annular jet.

Fig. 8 : 3D results - U level

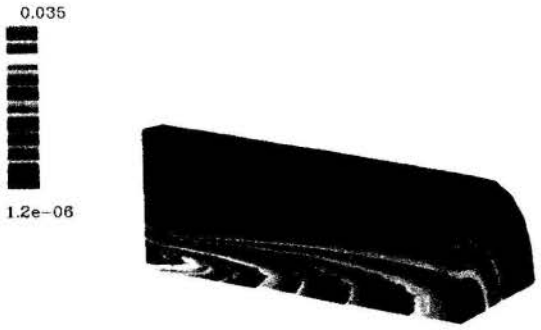

Fig. 9 : 3D results - k level

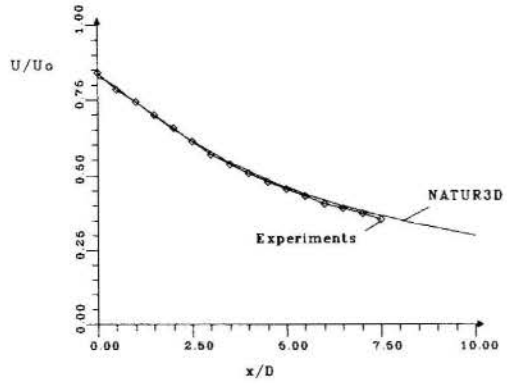

Fig. 10 : Velocity decreases through the X axis.

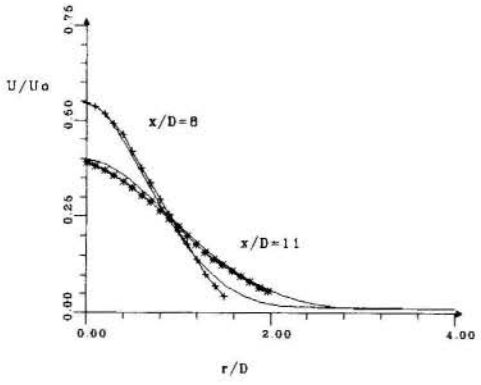

Fig. 11 : Velocity profiles

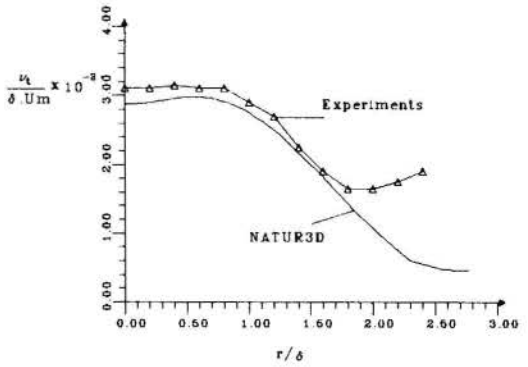

Fig. 12 : Turbulent viscosity profile at x/D = 11.0

ACKNOWLEDGMENTS

During the course of this work A. C. P. Brasil junior was partialy supported by the Brazilian governnement fellowship in CNPq/CEFI program, Proc. N° 920180/87.6.

REFERENCES

[1] T.G.R. Hughes, "Recent progress in the developement and understanding of SUPG methods with special reference to compressible Euler and Navier-Stokes equations", *Int. J. Num. meth. in fluids*, 7, 1261-1275, 1987.

[2] D.W. Kelly, S. Nakazawa, O.C. Zienkiewicz and J.C. Heinrich, "A note on anysotropic balancing dissipation in finite element method approximation to convection diffusion problems", *Int. J. Num. meth. eng.*, 15, 1705-1711, 1980.

[3] M. Buffat, to appear in *Int. J. Num. meth. in fluids*, 1990.

[4] M. Bercovier and O. Pironneau, "Error estimates for finite element method solution of the Stokes problem in the primitive variables", *Numer. math.*, 33, 1979.

[5] J.L.A. Fontoura Rodrigues Thèse Doctorat, Ecole centrale de Lyon, 1990.

[6] N.M. Mansour, J. Kim and P. Moin, "Computation of turbulent flows over a backward-facing step", Proc. of Turbulent shear flow simp., Karlsruhe, 1983.

[7] J. Kim, S.J. Kline and J.P. Johnston, "Investigation of reattaching turbulent shear layer: Flow over a backward facing step", *ASME J. FluidEng.*, 102, 1980.

[8] G. Brun, Thèse Doctorat, Ecole centrale de Lyon, 1988.

[9] E.M. Bahraoui, Thèse Doc. d'Etat, Univ. Marseille II, 1987.

[10] K.J. Arrow, L. Hurwicz and H. Uzawa, Studies in non-linear programing, Stanford Univ. press, 1958.

[11] J. Cahouet and J.P. Chabard, "Some fast 3D finite element solvers for the generalised Stokes problem", *Int. J. Num. meth. in fluids*, 8, 869-895, 1988.

III ENCIT – Itapema, SC (Dezembro 1990)

ON THE ESTIMATION OF THERMAL PROPERTIES OF NON-METALLIC MATERIALS

GILMAR GUIMARÃES
Departamento de Engenharia Mecânica
Universidade Federal de Uberlândia - Campus Santa Mônica
38400 - Uberlândia - MG - Brasil

ABSTRACT

This work presents an experimental technique for simultaneous determination of the thermal conductivity and diffusivity of non mettalic materials. The method uses parameter estimation techniques and is based on the flash method. A sample and easily constructed apparatus, a guarded hot plate, is used to generate the heat flux at the frontal face of the sample. The conductivity and diffusivity are determined by comparing the experimental temperatures and the temperatures estimated by the mathematical model. The difference in temperatures was less than 0.3 Celsius.

INTRODUCTION

The development of experimental technique for determining thermal parameter, e.g., thermal conductivity and diffusivity and contact resistance of non metallic materials have interested many researchers due their large application in engineering problems [1-6]. Standardized procedures using guarded hot plate in steady state are used to determine thermal conductivity [7]. However, there are no standardized techiniques to obtain thermal diffusivity, since transient techniques are also necessary. Thus, there are many ways to build mathematical models for the heat diffusion. In all cases, the experimental apparatus is constructed based on the pratical boundary conditions that can be obtained. Taylor [1], in a recent work presents the state-of-the-art of experimental techniques that have been developed for thermal diffusivity identification in solids materials. In this work, Taylor classified the methods based on temperature-time history in two main classes: periodic and non-periodic heat flow methods. The flash method which is a non-periodic heat flux is one of the most widely used. In this method the front surface of a sample is submitted to a very short burst of radiant energy. The source of radiant energy is usually a laser or a xenon flash lamp and irradiation time is of the order of one millisecond or less. The resulting temperature rise of the rear surface of the sample is measured, and thermal diffusivity values are computed from these temperature-versus-time data [1]. The development of an alternative method to investigate thermal physic properties, using a simple and easy feasible experimental apparatus was the great motivation of this work. The major difficulty, however, was to establish the mathematical model that should be able to compute the transiente heat flux input with time dependence by using the Joule effect instead of a heat pulse.

Is this sense, recently, Guimarães et al [9] have presented a mathematical model to measure thermal diffisivity with linear heat input at the front face of a sample keeping constant the rear face temperature. The interior transient temperature of the sample was measured by a automatic data acquisition system and the boundary conditions, i.e., the heat flux input and constant temperature was assured through a guarded hot plate. Thus, the thermal diffusivity could be obtained by comparing the mathematical model and the experimental temperature time histories.

The present work, uses the same experimental apparatus as in [9], however, the heat flux input at the front face of the sample is obtained by logarithmic adjust. This work uses the parameter estimation technique in [10] that permit simultaneous thermal conductivity and diffusivity determination. In this way, the error related to the conductivity values that appear in the mathematical model in [9] is minimized.

EXPERIMENTAL DESIGN AND APPARATUS

The experimental apparatus shown in figure 1 was used to obtain the boundary conditions.

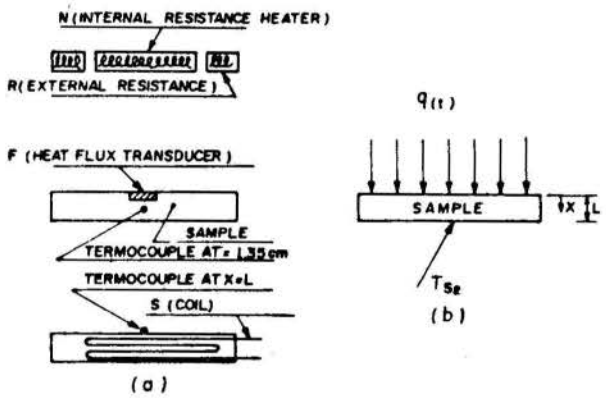

FIGURE 1. a) EXPLODED-VIEW OF EXPERIMENTAL APPARATUS

b) ESQUEMATICAL BOUNDARY CONDITIONS

The technique involves a unidirectional and uniform heat flux input at initial time, t = 0, at the superior face of the sample, subjected to a previous temperature distribution, F(x), keeping constant the inferior face at temperature, Ts_2. The thermal conductivity and diffusivity was then calculated from the mathematical model, the data acquired and the sample dimensions. The source of heat is obtained by using a internal resistance heater, N, based on the Joule effect. A external resistance, R , controls the lateral heat flux loss to surroundings. The heat flux applied is measured by a heat flux transducer, F, [9] and the internal temperature and the inferior surface temperature are monitored through thermocouples. The constant temperature Ts_2 in the inferior face is maintained by using a water coil, S.

MATHEMATICAL MODEL

Considering a plane sample subject to a initial temperature distribution, F(x). A pulse of heat is imposed at the superior surface while the other surface is maintained at temperature Ts_2. Under these conditions the appropriate boundary value problem is given by.

$$\frac{\partial^2 T}{\partial x^2} = \frac{1}{\alpha} \cdot \frac{\partial T}{\partial t} \qquad (1.a)$$

$$-K \left.\frac{\partial T}{\partial x}\right|_{x=0} = q(t) \qquad (1.b)$$

$$T(x,t) = Ts_2 \qquad \text{at } x = L, \quad t > 0 \qquad (1.c)$$

$$T(x,0) = F(x) = (Ts_2 - Ts_1) \cdot x / L + Ts_1 \qquad (1.d)$$

where

$$q(t) = a_0 \qquad \text{at } x = 0, \quad 0 < t < t_0$$

$$q(t) = a_1 + b_1 \cdot \mathrm{Ln}[t] \qquad \text{at } x = 0, \quad t > t_0$$

a_1 and b_1 are obtained by logarithmic adjust at the superior face of the sample as shown in figure 2.

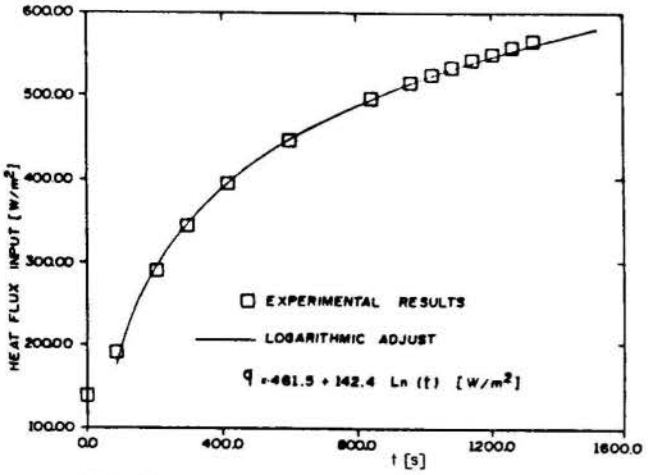

FIGURE 2 - LOGARITHMIC ADJUST FOR HEAT FLUX INPUT AT FRONT SURFACE

The partial time t_0 is used to avoid the discontinuity at $t = 0$ of logarithmic adjust. Ts_1 and Ts_2 are the superior and inferior temperatures of the sample, respectively and a_0 is the heat flux at time t_0 and K and α are the properties thermal conductivity and diffusivity. The solution to problem (1) is readily obtained using Green's function techniques and the resulting solution can be presented in the form

$$\begin{aligned} T(x,t) = {} & Ts_2 + (Ts_1 - Ts_2) / L \cdot (2/L) \sum_{n=1}^{\infty} e^{-\alpha \beta_n^2 \cdot t} \\ & \cdot (\cos \beta_n x) / \beta_n^2 + a_0 (L - x) \\ & - a_0 \cdot (2/L) \sum_{n=1}^{\infty} e^{-\alpha \cdot \beta_n^2 \cdot t_0} \cdot (\cos \beta_n x) / \beta_n^2 \\ & + (2/L) \sum_{n=1}^{\infty} e^{-\alpha \cdot \beta_n^2 \cdot t} (\cos \beta_n x) \\ & \cdot \{a_1 (e^{\alpha \cdot \beta_n \cdot t} - e^{\alpha \cdot \beta_n \cdot t_0}) / \beta_n^2 \\ & + b_1 [e^{\alpha \cdot \beta_n \cdot t} \cdot \mathrm{Ln}(t) - (e^{\alpha \cdot \beta_n \cdot t_0} \cdot \mathrm{Ln}(t_0) \\ & + \mathrm{Ln}(t/t_0) + \alpha \cdot \beta_n^2 \cdot (t - t_0) \\ & + (\alpha \cdot \beta_n^2 \cdot (t - t_0)^2) / 24)]\} \end{aligned} \qquad (2)$$

where β_n are the eigenvalue given by $\beta_n = 2\pi \cdot n / L$, being $n = 1,2,\ldots$

Having established the formal solution of the direct problem (1) we can estimate the parameter K and α from the temperature measurements taken at the interior point of the body ($x = 0.0138$ m).

In the method described by Beck and Arnold [10], the thermal diffusivity and conductivity are found by minimizing the sum of squares function

$$S = \sum_{i=1}^{n} [Y_i - T_i]^2 \qquad (3)$$

with respect to the parameter involved. In this case, K and α are the parameter estimated in order to obtain the best agreement between measured (Y_i) and estimated (T_i) temperatures from equation (2). The index i refers to time ($i = 1,2,\ldots,n$). One way of minimizing S, which is given by equation (3) is to set the first partial derivates with respect to the parameter equal to zero [10]. So that, we obtain a set of equation in K and α. The set of equations is solved simultaneously for the unknowns.

The partial derivates of S are

$$\frac{\partial S}{\partial K} = 2 \left(-\sum_{i=1}^{k} Y_i \cdot X_{1_i} + \sum_{i=1}^{k} T_i \cdot X_{1_i}\right) = 0 \qquad (4.a)$$

$$\frac{\partial S}{\partial \alpha} = 2 \left(-\sum_{i=1}^{k} Y_i \cdot X_{2_i} + \sum_{i=1}^{k} T_i \cdot X_{2_i}\right) = 0 \qquad (4.b)$$

where sensitivites coefficients X_1 and X, are respectively

$$\begin{aligned} X_1 = \frac{\partial T}{\partial K} = {} & (a / K^2) \cdot (2/L) \sum_{n=1}^{\infty} e^{-\alpha \cdot \beta_n^2 \cdot t_0} (\cos \beta_n x) / \beta_n^2 \\ & + (2/L) \sum_{n=1}^{\infty} e^{-\alpha \cdot \beta_n^2 \cdot t} (\cos \beta_n^2 x) / \beta_n^2 \\ & \{(-a_1/K^2) (e^{-\alpha \cdot \beta_n \cdot t} - e^{\alpha \cdot \beta_n \cdot t_0}) - (b_1/K^2) \\ & \cdot [e^{\alpha \cdot \beta_n \cdot t} \cdot \mathrm{Ln}(t) - (e^{\alpha \cdot \beta_n \cdot t_0} \cdot \mathrm{Ln}(t_0) + \mathrm{Ln}(t/t_0) \\ & + \alpha \cdot \beta_n^2 \cdot (t - t_0) + (\alpha \cdot \beta_n^2 \cdot (t - t_0)^2)/24)]\} \end{aligned} \qquad (5.a)$$

$$\begin{aligned} X_2 = \frac{\partial T}{\partial \alpha} = {} & (a_0/K) \cdot t_0 \cdot (2/L) \sum_{n=1}^{\infty} e^{-\alpha \cdot \beta_n^2 \cdot t_0} \cdot (\cos \beta_n x) \\ & - B_0 \cdot t \cdot (2/L) \sum_{n=1}^{\infty} e^{-\alpha \cdot \beta_n^2 \cdot t} \cdot (\cos \beta_n x) \\ & - t(2/L) \sum_{n=1}^{\infty} e^{-\alpha \cdot \beta_n \cdot t} (\cos \beta_n x) \{(a_1 / K) \\ & \cdot (e^{-\alpha \cdot \beta_n \cdot t} - e^{-\alpha \cdot \beta_n \cdot t}) + (b_1 / K) \\ & \cdot [e^{\alpha \cdot \beta_n \cdot t} \cdot \mathrm{Ln}(t) - (e^{\alpha \cdot \beta_n \cdot t} \ \mathrm{Ln}(t_0) + \mathrm{Ln}(t/t_0) \\ & + \alpha \cdot \beta_n^2 \cdot (t - t_0) + (\alpha \cdot \beta_n^2 \cdot (t - t_0)^2) / 24)]\} \\ & + (2/L) \sum_{n=1}^{\infty} e^{-\alpha \beta_n^2 \cdot t} \cdot (\cos \beta_n x) \{(a_1 / K) \\ & \cdot (e^{\alpha \cdot \beta_n \cdot t} \cdot e^{\alpha \cdot \beta_n \cdot t_0} \cdot t_0) + (b_1 / K) \\ & \cdot [e^{\alpha \cdot \beta_n \cdot t} \cdot t \cdot \mathrm{Ln}(t) - (e^{\alpha \cdot \beta_n \cdot t_0} \cdot t_0 \cdot \mathrm{Ln}(t_0) \\ & + (t - t_0) + \alpha \cdot \beta_n^2 (t - t_0)^2 / 12)]\} \end{aligned} \qquad (5.b)$$

where B_0 is a constant value, defined by $B_0 = (Ts_1 - Ts_2)/L$.

One of the simplest and most effective methods of minimizing the function S, is called the Gauss method [10]. Using the first two terms of a Taylor series in equation (4) we obtain.

$$K^{n+1} = K^n + \sum_{i=1}^{k} X_{1_i} \cdot (Y_i - T_i) / \Delta^n \qquad (6.a)$$

$$\alpha^{n+1} = K^n + \sum_{i=1}^{k} X_{2_i} \cdot (Y_i - T_i) / \Delta^n \text{ , where} \qquad (6.b)$$

$$\Delta^n = \sum_{i=1}^{k} X_{1_i}^2 \cdot X_{2_i}^2 - X_{1_i} \cdot X_{2_i} \qquad (6.c)$$

Then the parameters K and α can be estimated by a iterative procedure that continues until

$$\frac{K^{n+1} - K^n}{K^n} < \varepsilon \quad \text{and} \qquad (7.a)$$

$$\frac{\alpha^{n+1} - \alpha^n}{\alpha^n} < \varepsilon \qquad (7.b)$$

where ε is of the order 0.001.

The dimensionless sensitivities X_1^+ and X_2^+ have been plotted and investigated before the experimental realization in order to obtain a good accuracy in parameter estimation (figure 3). We observe that the optimal time is situated at dimensionless time interval $t^* = 0.6$ to 0.8. We noted that K and α for the other time have linear dependence and the parameter can not be estimated in this region.

UNCERTAINTIES ANALYSIS

Taylor [1] divide the errors of the experimental results in two types of errors: measurement error and non-measurement errors. Measurement errors are associated with uncertainties that exist in measured quantities contained in the equation used to compute the conductivity and diffusivity from experimental data. Non-measurement errors are associated with deviations of actual experimental from the boundary condition assumed in the model used to derive the equation for computing the parameters.

Measurement errors include errors related with determination of the effective thickness of the sample, the internal thermocouple position, the measurement of the time of heating. In addition, the time constant of the thermocouple and heat flux transducer should be considered too. In the non-measurement errors, the non-uniformity and heat loss are the main factors effect. However, these errors represent deviations from an ideal situation in which these effects, are assumed to be negligible [1]. Here, this effect can arise if compared with flash method. However, if the heat flux is monitored and the sample is a low conductivity material these deviations is minimized. The transducer calibration constant given presents an uncertainty of 2 W/m^2 approximately. Considering this deviations in equation (2) and a uncertainty of 2 mm in the tickness and thermocouple position we can obtain a deviation of less than 0.3 C in temperature estimated. Conservatively, we can admit an error associated with voltage signals acquisition an uncertainty of less than 0.1 C using an automatic data acquisition control system / HP-3054, [1].

RESULTS AND DISCUSSION

The thermal diffusivity and conductivity estimated for the plywood sample present a deviation compared with literature data [11] of less than 13% and 17,5%, respectively. However, we can note (figure 4) the power of the method. An excellent agreement between model and experimental data can be observed for time greater than 200 s. For lesser times, the logarithmic adjust and initial condition can effect the solution, due to the discontinuity at t = 0. The selection of the time interval, between 0.6 and 0.8 is of fundamental importance for optimization of the results. Previous knowledge of the behavior sensitivities permit us to choose the linear independence region of α and K. In this case, few iterations, n, are needed to estimate the properties (Table I). Table II presents the temperatures (Y_i) and times (t_i) used to estimate the parameter, the sum of square function (S_1). The sum of square function (S_t) was obtained during the entire experiment. We observed a divergence in estimation of K and α in the region of linear dependence (time less than 960 s - figure 3a). However, the best result for minimum s_t was obtained using all the experimental data. However, good results can also be obtained if only time belonging to the linear independence region is used like the times a-b-c shown in the Table III, (figure 3). The logarithmic adjust appears to be indeterminate at t = 0. This difficulty can be alliviated by choosing a small time t_0 and considering a heat flux constant until this time. The logarithmic adjust can be obtained with correlation factor of about 0.999 (figure 2). In this sense, the alternative form of heat flux imposed can be inserted in the model with excellent approximation. The temperature at the other face suffered a variation of 0.3 C during all the experiment (figure 4). This variation did not affect the results and can be neglected.

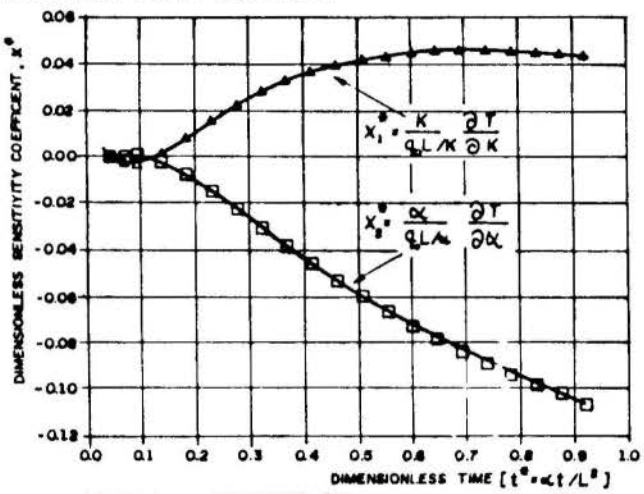

FIGURE 3a - SENSIVITIES FOR A SAMPLE SUBMITTED TO A TRANSIENT HEAT FLUX AT FRONT SURFACE. LOCATION X = 0.0138 m

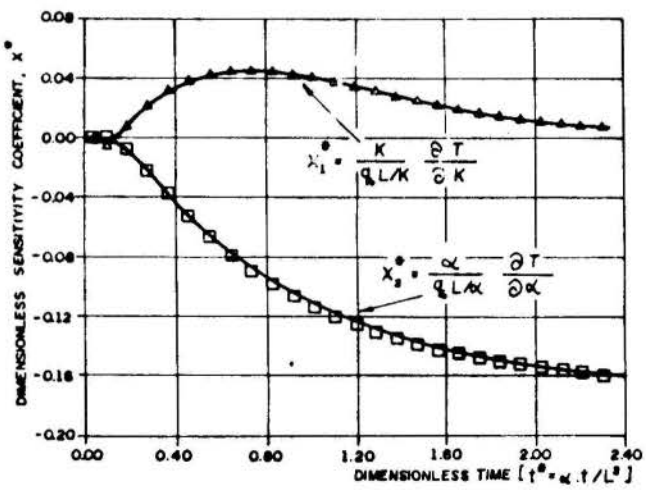

FIGURE 3b - SENSIVITIES FOR A SAMPLE SUBMITTED TO A TRANSIENT HEAT FLUX AT FRONT SURFACE. LOCATION X = 0.0138 m

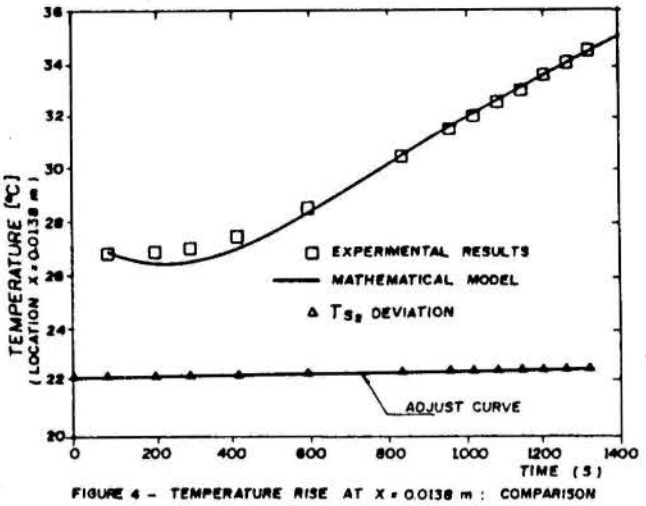

FIGURE 4 - TEMPERATURE RISE AT X = 0.0138 m : COMPARISON OF MATHEMATICAL MODEL WITH EXPERIMENTAL RESULTS SHOWN CONSTANT TEMPERATURE DEVIATION AT REAR SURFACE.

Table I. Interations, n, in the diffusivity and conductivity estimation with Y_1 obtained during the entire experiment (Table III).

n	K (W/mK)	α (m^2/S)	St (K)
0	0.01	2.0E-08	
1	0.1388	8.626E-08	
2	0.1551	1.446E-07	
3	0.1310	1.468E-07	
4	0.1405	1.561E-07	
5	0.1408	1.572E-07	
6	0.1410	1.574E-07	
7	0.1410	1.574E-07	7.126E-01

Table II. Diffusivity and conductivity estimation with Y_1 obtained for time indicated in table III.

Time	K(W/mK)	α (m^2/S)	S1 (K)	St (K)
a	0.141	1.575E-07	7.129E-01	7.126E-01
b	0.135	1.478E-07	3.272E-04	7.195E-01
c	0.135	1.473E-07	1.644E-03	7.228E-01
d	0.134	1.462E-07	5.968E-03	7.278E-01
e	0.133	1.440E-07	1.972E-03	7.370E-01
f	0.145	1.622E-07	1.856E-03	7.677E-01
g	0.126	1.354E-07	6.487E-05	7.952E-01
h	*	*	*	*
i	*	*	*	*
j	*	*	*	*

Table III. Times used for Y_1 aquisition, in seconds.

Time	Seconds
a	90-210-300-420-600-840-900-960-1020-1080-1140-1200-1260-1320
b	1080 - 1140 - 1200
c	1200 - 1200 - 1260
d	840 - 900 - 960 - 1100 - 1200 - 1260 - 1320
e	1080 - 1140 - 1200 - 1320
f	840 - 960 - 1020
g	960 - 1020 - 1080
h	90 - 210 - 300 - 420 - 600 - 840
i	210 - 300 - 420 - 600 - 840
j	300 - 420 - 600 - 840

CONCLUSION

Determination of thermal physical properties using parameter estimation techniques have shown to be efficient, particularly in thermal diffusivity estimation. The possibility of obtaining thermal conductivity simultaneously minimize the error related with its value inserted in the mathematical model and give a suitable technique for application in transient cases. The experimental apparatus used is a alternative that substitutes the use of costly equipament, like laser [1]. The Green's function permits the mathematical model to consider time dependent heat flux. A future work should investigate the temperature dependence in conductivity and diffusivity. In which case, a non-linear treatment in parameter estimation is necessary.

ACKNOWLEDGEMENTS

The author wishes to thank R.F. Miranda and L.C. Lima for encouraging this work and T.H. Ong for review of the manuscript.

REFERENCE

[1] Taylor, R.E., Heat Pulse Thermal Diffusivity Measurements, High-Temperatures - High Pressures, Vol 11, pp. 43 - 58, 1979.

[2] Touloukian, Y., Powell, R.W., Ho, C.Y., Nicolau, M. C., Thermal Diffusivity, Vol. 10, NY: IFI/PLENUM, 1973.

[3] Bittle, R.R. and Taylor, R.E., Step - Heating Techniques for Thermal Diffusivity Measurements of Large - Grained Heterogeneous Materials, Journal of the American Ceramic Society, Vol. 67, pp. 186 - 190 , March 1984.

[4] Kamiuto, K. and Iwamoto, M., Inversion Method for Determining Effective Thermal Conductivities of Porous Materials, Journal of Heat Transfer, Vol. 109, pp. 831-834, 1987.

[5] Beck, J.V., Combined Parameter and Function Estimation in Heat Transfer with Application to Contact Conductance, Journal of Heat Transfer, Vol. 110 , pp. 1046-1058, Nov. 1988.

[6] Rooke, S.P. and Taylor, R.E., transient Experimental Technique for the Determination of the Thermal Diffusivity of Fibrous Insulation, Journal of Heat Transfer, Vol 110, pp. 270-273, Feb. 1988.

[7] Guimarães, G., Cunha Neto, J.A.B., Philippi, P.C. e Nicolau, V.P., A sample Transducer for Measuring Heat Flux in Buildings, I Encontro Nacional de Ciências Térmicas, I ENCIT, pp. 155-158, Rio de Janeiro, Dez., 1988.

[8] Standard Test Method for Steady-State Thermal Transmission Properties by Means of the Guarded Hot Plate, ANSI/ASTM C, pp. 177-76, Vol 18, 1980.

[9] Guimarães, G., Santos, A.F.M. e Lima, L.C., Uso de um Fluxímetro Adaptado a um Dispositivo de Placa Quente Compensada para a Obtenção da Difusividade Térmica, X COBEM, RJ, Dez. 1989.

[10] Beck, J.V. and Arnold, K.J., Parameter Estimation in Engineering and Science, Wiley, N.Y., 1977.

[11] Incropera, F.P. and Dewit, D.P., Fundamentals of Heat Transfer, John Wiley & Sons, N.Y., 1981.

RESUMO

Este trabalho apresenta o desenvolvimento de uma técnica experimental para a determinação simultânea da condutividade e difusividade térmica. O método desenvolvido utiliza a técnica de estimativas de parâmetros e se baseia no método Flash. A modificação deste método consiste na substituição do pulso de calor na superfície da amostra, usualmente laser ou lâmpada Xenônio, ambos equipamentos de difícil acesso devido ao seu alto custo, por um aparato simples e de fácil execução, como uma placa quente compensada. O modelo matemático desenvolvido permite então a previsão da utilização do calor imposto na superfície frontal da amostra como uma função do tempo. A condutividade e a difusividade térmica são determinadas a partir da comparação entre temperaturas obtidas experimentalmente e estimadas através do modelo matemático, obtendo-se um desvio inferior a 0.3 C entre as curvas.

III ENCIT – Itapema, SC (Dezembro 1990)

ANÁLISE DA INFLUÊNCIA DA DIMENSÃO DOS TRANSDUTORES DE FLUXO DE CALOR EM UM DISPOSITIVO DE MEDIÇÃO DE PROPRIEDADES TÉRMICAS

Güths S., Philippi P.C., Nicolau V.P., Lamberts R.
Universidade Federal de Santa Catarina
Departamento de Engenharia Mecânica
Cx.P. 476, CEP 88049, Florianópolis - SC

O presente trabalho apresenta uma análise numérica de um método transiente para a medição das propriedades térmicas de materiais, especialmente materiais de construção civil. O método se baseia na utilização de um equipamento de placa quente protegida, em associação com transdutores de fluxo de calor, fornecendo simultaneamente a condutividade térmica e o calor específico de amostras homogêneas e planas. O dispositivo de medição é analisado teoricamente através de uma simulação numérica do sistema físico. Apresenta-se a influência das dimensões da área de medição dos transdutores de fluxo de calor.

INTRODUÇÃO

O conhecimento das propriedades térmicas dos materiais reveste-se de fundamental importância, quando é premente a racionalização do consumo de energia.

Desse modo, este trabalho analisa teoricamente um método de medição simultânea da condutividade térmica e calor específico de amostras planas e homogêneas. Esse método, baseado em Wattiau [1] e adaptado por Güths *et all.*[2], utiliza um dispositivo de placa quente protegida e dois transdutores de fluxo de calor. A ênfase desse trabalho em relação ao trabalho anterior [3] corresponde na determinação da influência da área de medição dos transdutores quando o dispositivo é submetido a condições adversas.

O método consiste em medir a energia total ($Q_{liq\ 1\text{-}2}$) que um corpo necessita trocar para passar de um estado de equilíbrio térmico (estado 1) para um estado estacionário com gradiente térmico (estado 2), e, a variação da temperatura média da amostra entre esses dois estados. Pela Lei da Conservação da Energia

$$Q_{liq\ 1\text{-}2} = \int_1^2 \rho c T dV \qquad (1)$$

onde ρ é a densidade, V é o volume, c é o calor específico e T a temperatura. Considerando a amostra homogênea tem-se:

$$c = \frac{Q_{liq\ 1\text{-}2}}{m\ (T_2 - T_1)} \qquad (2)$$

onde T_2 é a temperatura média da amostra no estado 2 e m a massa.

A condutividade térmica é determinada, utilizando a Lei de Fourier, no final da experimentação: — no estado de gradiente estacionário.

O EXPERIMENTO

Utiliza-se um dispositivo de placa quente protegida (com área de 300 x 300 mm^2) para gerar o estado de gradiente térmico estacionário através da amostra conforme mostra a Fig. 1.

Medem-se os fluxos de calor através de transdutores de fluxo de calor (TFC) e temperaturas através de termopares. A área de medição desses transdutores é objeto de análise desse trabalho. Como se trata de um método transiente, os fluxos de calor e

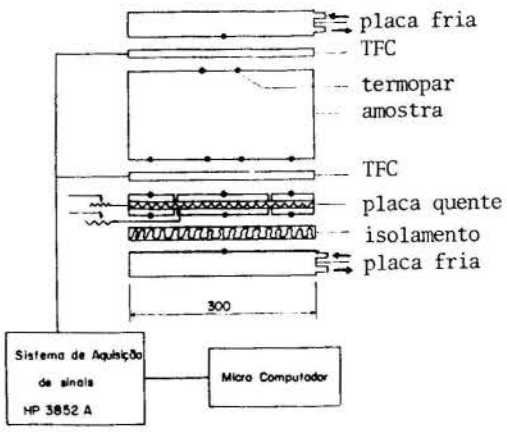

Fig. 1 Esquema do dispositivo experimental.

temperaturas devem ser registrados ao longo da experimentação.

Após o sistema entrar em equilíbrio térmico com a temperatura da placa fria (T_1), dissipa-se uma potência elétrica constante na placa quente até o sistema alcançar um estado de gradiente estacionário (estado 2).

Integrando-se a área compreendida entre os fluxos de calor registrados pelos transdutores superior e inferior (conforme mostrado na Fig.2), tem-se a energia liquida $Q_{liq\ 1\text{-}2}$ absorvida pelo sistema.

ANÁLISE NUMÉRICA

Simulou-se o sistema real de medição em um programa computacional resolvendo a equação da difusão de calor bidimensional e transiente, discretizando-a e integrando-a sobre um volume de controle retangular.

A solução do sistema linear é realizada através de uma adaptação do método de Gauss, conhecido como Algoritmo de Thomas, resolvido linha a linha em um transiente real, utilizando um sistema de 5 pontos com pontos fictícios nas fronteiras, e uma condição de simetria onde o fluxo de calor é nulo. A Fig.2 mostra a simulação do experimento real.

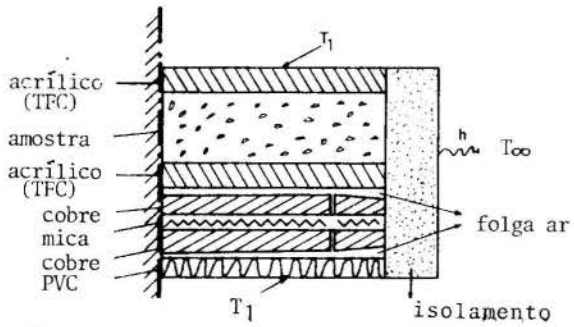

Fig. 2 Simulação do experimento real.

A Fig.3 mostra uma curva característica dos fluxos de calor medidos pelos transdutor superior (q_{sup}) e transdutor inferior (q_{inf}). Nessa figura mostra-se uma comparação entre valores experimentais (pontos discretos) e teóricos (linhas cheias) no ensaio de uma amostra de parafina industrial.

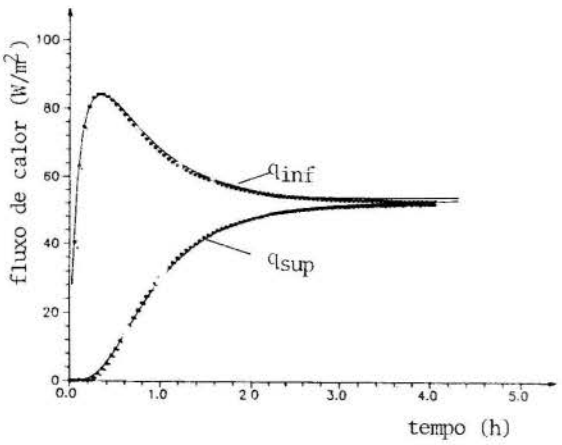

Fig. 3 Comparação entre fluxos de calor medidos experimentalmente (pontos discretos) e determinados na simulação numérica (linhas cheias).

Durante a experimentação, conforme descrito por Güths *et all.*[3], foram observados vários fenômenos que poderiam influenciar os resultados obtidos. Entre eles, i) fuga de calor para o meio ambiente através da superfície lateral da amostra, ii) desvios de planicidade da placa aquecedora central, e, iii) diferença de temperatura entre a placa aquecedora central e anel de proteção.

Nas figuras que seguem, apresenta-se o erro percentual na medição do calor específico (εc), em função da dimensão da área de medição do fluxo de calor medido a partir do centro da placa quente (L-TFC).

Salientando que a dimensão total da placa aquecedora central corresponde a 100 mm (medida a partir do centro) e o anel de proteção corresponde à região definida entre 100 e 150 mm.

A Fig.4 mostra o erro na medição do calor específico (εc) em amostras sujeitas a um coeficiente de convecção igual a 5 W/m^2.K, temperatura ambiente idêntica à da placa fria, e com diferentes condutividades térmicas (λ), mas mesmas capacidades térmicas.

Nota-se que o erro (εc) aumenta com a largura do transdutor (L-TFC). Quanto maior o transdutor, maior é a influência das perdas de calor laterais, aumentando o erro na medição do calor específico.

Nessa figura pode-se analisar a influência da condutividade térmica da amostra (λ). Nota-se que para transdutores com dimensões inferiores às da placa quente protegida, há um acréscimo do erro (εc) com a condutividade térmica. À medida que a dimensão do transdutor aproxima-se da dimensão total da placa quente, há uma inversão dessa tendência.

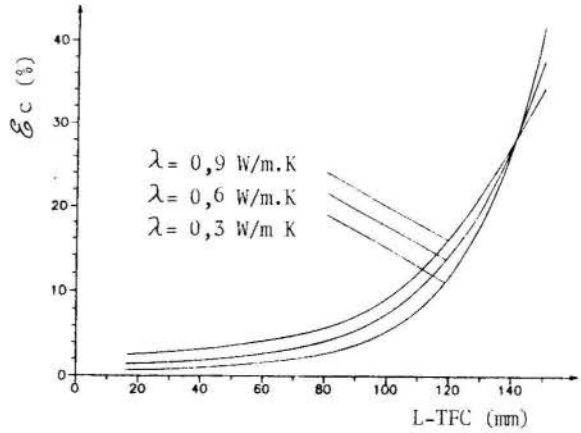

Fig. 4 Erro na medição do calor específico (εc) para amostras sem isolamento lateral, em função da dimensão dos transdutores (L-TFC).

Uma análise da Fig.5 auxilia na compreensão desse fenômeno. Nessa figura é mostrada uma comparação entre as isotermas de uma amostra com condutividade térmica igual a 0,6 W/m.K (linha cheia) com outra amostra com condutividade igual a 0,3 W/m.K (linha tracejada). As amostras estão sujeitas a um coeficiente de convecção igual a 5 W/m.K e temperatura ambiente idêntica à temperatura da placa fria (T_1).

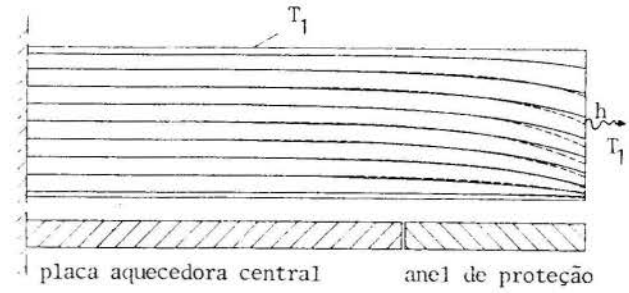

Fig. 5 Isotermas em amostras sujeitas a perda de calor lateral com condutividades térmicas igual a 0,6 W/m.K (linha cheia) e 0,3 W/m.K (linha tracejada).

Pode-se notar que na amostra mais isolante (linha tracejada) os desvios nas isotermas são mais acentuados, comparados com a amostra mais condutora. Mas isso ocorre apenas na região lateral.

Em uma região mais central, essas isotermas tornam-se mais estabilizadas. Isso significa que a perturbação causada pela fuga lateral não está afetando essa região; ou seja, os fluxos de calor no sentido horizontal — para a amostra mais isolante — são inferiores aos fluxos que ocorrem em uma amostra mais condutora. E como o erro na medição do calor específico (εc) está diretamente ligado às fugas de calor, amostras mais condutoras são suscetíveis a maiores erros de medição.

Então, para minimizar a influência das perdas de calor laterais, conforme já apresentado na Fig.4, deve-se utilizar transdutores com pequenas dimensões. Como limitação, os transdutores devem apresentar dimensões suficientemente grandes para compensar as não homogeneidades da amostra.

A Fig.6 mostra a relação existente entre o erro na medição do calor específico (εc), a largura dos transdutores (L-TFC) — medida a partir do centro do dispostivo — e a condutividade térmica (λ) de amostras com mesmas capacidades térmicas e dimensões, quando sujeitas a uma diferença de temperatura de 0,2 K entre a placa aquecedora central e o anel de proteção.

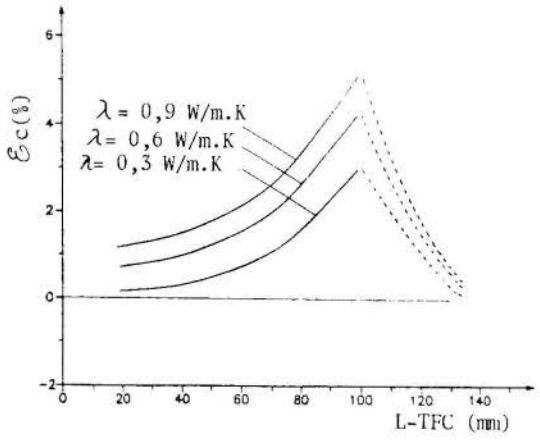

Fig. 6 Erro na medição do calor específico (εc) em função do tamanho dos transdutores (L-TFC) para amostras com diferentes condutividades térmicas (λ).

Inicialmente a Fig.6 mostra que o erro (εc) aumenta à medida que as dimensões dos transdutores se aproximam das dimensões da placa aquecedora central.

Apesar da análise de transdutores com dimensões superiores às da placa aquecedora central talvez não possuir uma aplicação prática, simularam-se transdutores com tais dimensões para tentar melhor compreender os fenômenos envolvidos.

Nota-se, então, que nessa região o erro diminui. De fato, como se simulou o dispositivo completamente isolado do meio ambiente, todo o fluxo de calor que deixa a superfície inferior da amostra, atinge a superfície superior da mesma. Dessa forma, utilizando transdutores com dimensões próximas à placa quente protegida (150 mm), todo o fluxo de calor é computado e o erro na medição do calor específico (εc) tende a zero.

Quanto à variação com a condutividade térmica da amostra, a explicação é idêntica à apresentada anteriormente.

Simularam-se ainda desvios de planicidade da placa quente protegida. Fez-se essa análise em função dos problemas encontrados nesse sentido durante medições experimentais. Na região central, a placa quente apresentou espessura superior (até 0,3 mm) em relação à espessura das regiões laterais.

Simulou-se esse fenômeno, conforme descrito por Güths *et all* [3], considerando a existência de uma camada de ar — com espessura variável — entre a placa quente e transdutor.

Na simulação do erro na medição do calor específico (εc) em função da dimensão dos transdutores, encontraram-se resultados semelhantes aos apresentados na figura anterior. Novamente, transdutores com maiores dimensões sofreram maiores influências do fenômenos de borda.

Quanto à medição da condutividade térmica, não se encontrou influência alguma da dimensão dos transdutores. De fato, como a condutividade térmica é calculada através da média dos fluxos de calor registrados pelos transdutores, os efeitos de borda ficam minimizados.

Conclusão

A simulação numérica do dispositivo mostrou ser uma importante ferramenta na análise qualitativa do método, na avaliação da influência dos diversos parâmetros envolvidos.

Através da análise apresentada, onde se constatou a grande influência da área de medição dos transdutores na geração de erros, aprimorou-se o dispositivo experimental, construindo transdutores com menores áreas de medição.

Referências

[1] Wattiau, F., "Contribuition a l'Etude Theorique Exp. Ech. Therm.", These de Docteur, Universidade de Lille, França, 1978.

[2] Güths, S., Philippi, P.C., Lamberts, R., Nicolau, V.P., "A Transient Method for Measuring Thermal Properties of Building Materials", Proceedings of Heat and Mass Transfer, Yugoslávia, 1989.

[3] Güths, S., Philippi, P.C., Lamberts, R., Nicolau, V.P., "Analise Numérica de um Método Transiete de Medição de Propriedades Térmicas", X Congresso Brasileiro de Engenharia Mecânica, Rio de Janeiro, 1989.

ABSTRACT

An analysis of a transient method for measuring heat capacity and thermal conductivity of flat samples of building materials is presented.

The influence of heat flux meters is analysed for extreme working operation.

III ENCIT – Itapema, SC (Dezembro 1990)

ON THE USE OF PHOTOTHERMAL DETECTION TECHNIQUES FOR THERMAL DIFFUSIVITY MEASUREMENTS

N.F. Leite and L.C.M. Miranda
Laboratório Associado de Sensores e Materiais
Instituto de Pesquisas Espaciais - Caixa Postal 515
12201 - São José dos Campos, SP, Brazil

SUMMARY

In this paper we report on the phototermal measurements of the thermal diffusivity of two-layer system and of polymer (PVDF) films subjected to different poling fields. The thermal diffusivity was measured using the so-called open photoacoustic cell (OPC) method in which the PA signal is investigated as a function of the modulation frequency, in a heat-transmission configuration.

INTRODUCTION

The photothermal techniques are becoming a valuable tool in the study of the physical properties of materials as well as in process monitoring, especially in the case of microelectronics industry [1,2]. These techniques are based upon the detection of thermal waves generated in a medium due to a periodic heat generation. The most common mechanism for producing thermal waves is the absorption of an intensity modulated light beam by a sample. Of the several mechanisms [2] available for detecting these waves, the gas-microphone photoacoustic (PA) detection is the most widely used so far. In this case, a sample is placed in a small, air-tight cell, at a given distance from a transparent window through which a light beam is incident upon the sample. As a result of the ligh-into-heat conversion, the sample is heated by the absorption of the modulated light beam. The heat flow from the sample to the surrounding air causes the pressure in the air chamber to fluctuate, which is sensed by a microphone mounted in one of the lateral cell walls.

Being a photothermal technique, the detected signal is strongly dependent upon the interplay of the sample optical absorption coefficient for the incident radiation, the light-into-heat conversion efficiency, as well as how the heat diffuses through the sample. The dependence of the PA signal on the absorption coefficient allow us to perform spectroscopic studies, whereas the fact that the signal is proportional to the light-into-heat conversion efficiency means that it is complementary to other photo-induced energy-conversion processes. This means that the PA detection can be used for obtaining information concerning the nonthermal deexcitation processes. Finaly, the fact that the PA signal depends on how the heat diffuses through the sample allows us to perform both thermal characterization of the sample (i.e., measurements of its thermal diffusivity and condutivity), and thermal imaging. This last point comes from the fact that the thermal wave generated by the absorption of an incident energetic pulse may be reflected and scattered as it encounters cracks, defects, and so on, thereby affecting the detected signal.

In this paper we report on the photothermal measurements of the thermal diffusivity of a two-layer system and of polymer (PVDF) films subjected to different poling fields. Apart from the interest in its intrinsic value, the importance of the thermal diffusivity as a physical quantity to be monitored is due to the fact that, like the optical absorption coefficient, it is unique for each material. This can be appreciated from the tabulated values given by Touloukian et. al [3], for a wide range of materials, such as, metals, minerals, foodstuffs, biological specimens and polymers. Furthermore, the thermal diffusivity is also known to be extremely dependent upon the effects of compositional and microstructural variables [4], as well as upon the processing conditions as in the cases of polymers [5,8], ceramics [4] and glasses [9].

TWO-LAYER SYSTEM

Consider the two-layer system shown schematically in Fig.1 consisting of a material 1 of thickness l_1 and of a material 2 with thickness l_2, having both the same cross-section. Let $l = l_1 + l_2$ denote the total sample thickness, α_i the thermal diffusivity, ρ_i the density, c_i the specific heat and k_i the thermal conductivity of material i (i=1,2). From the effective thermal resistance of this series two-layer system one finds the effective thermal conductivity, k , to be

$$k = \frac{l k_1 k_2}{l_1 k_2 + l_2 k_1}, \qquad (1)$$

the effective heat capacity is given by

$$v\rho c = v_1 \rho_1 c_1 + v_2 \rho_2 c_2, \qquad (2)$$

from eqs.(1) and (2), we can write the effective thermal diffusivity, $\alpha = k/\rho c$, of the two-layer system as

$$\alpha = \frac{1}{\frac{x^2}{\alpha_1} + \frac{(1-x)^2}{\alpha_2} + x(1-x)\left[\frac{\lambda}{\alpha_1} + \frac{1}{\lambda\alpha_2}\right]}, \qquad (3)$$

where $x = l_1/l$ measures the thickness fraction of material 1 in the composite sample and $\lambda = k_1/k_2$.

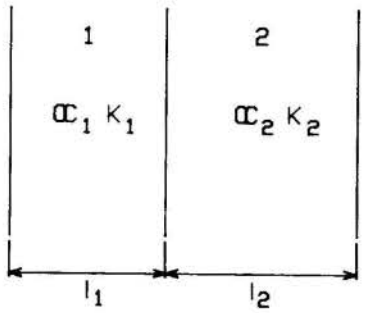

Fig. 1 Geometry for the two-layer system.

The two-layer system considered in this paper consisted of a 60 μm thick Al foil with one of its surfaces coated with white paint layer of variable thicknesses.

The thermal diffusivity was measured using the open-photoacustic cell configuration [10, 11] shown schematically in Fig. 2. It consists of mounting the sample directly onto a circular electret microphone. The typical design of an electret microphone [12, 13] consists of a metalized electret diaphgram (12 μm FEP with a 500-1000 Å thick deposited metal electrode) and a metal back plate separated from the diaphragm by an air gap (45 μm thick). The metal layer and the back plate are connected through a resistor R. The front sound inlet is a circular hole of 3mm diameter, and the front air chamber adjacent to the metalized face of the diaphragm is roughly 1mm thick. As a result of the periodic heating of the sample by the absorption of modulated light, the pressure in the front chamber oscillates at the chopping frequency, causing diaphragm deflections, which generates a voltage V across the resistor R. The pressure fluctuation in the PA cell is due to three main contributions [1, 14] (i) sample to gas thermal diffusion; this effect is sensitive to the sample surface temperature. (ii) sample thermal expansion. This effect depends on the average sample temperature, (iii) thermoelastic bending. This effect is due to the temperature gradient inside the sample along the thickness axis. It can be shown [11-15] that for samples such that its lateral dimension is much greater than its thickness, the thermoelastic bending is dominant over thermal expansion, so that the output voltage can be written as

$$V = V_0 \frac{jw\tau_E}{(1+jw\tau_E)} \frac{\beta I_0 e^{jwt}}{T_0\, l_g\, \sigma_g\, k_s \sigma_s} \times$$
$$\times \left\{ \frac{[1 - exp(-l_g\sigma_g)]}{\sinh(l_s a_s)} + \right.$$
$$\left. - \frac{3R^4\, \alpha_T\, T_0\, \alpha_s^{1/2}}{2R_c^2\, l_s^3 \sigma_s\, \alpha_g^{1/2}\, \sinh(l_s\sigma_s)} \times \right.$$
$$\left. \times \left[l_s \sigma_s \sinh(l_s\sigma_s) - \cosh(l_s\sigma_s) + 1 \right] \right\}, \qquad (4)$$

where $V_0 = l_0\, l_m\, \sigma_0/(l_b \varepsilon + l_m \varepsilon_g)$, $\tau_\varepsilon = R\,C$, $\sigma_i = (1+j)\, a_i$ with $a_i = (\pi f/\alpha_i)^{1/2}$ being the thermal diffusion coefficient of material i, R_c is the radius of the PA chamber in front of the microphone diaphragm (R_c = 3,5 mm), R is the radius of the microphone front hole (R=1,5mm), and α_T is the sample thermal expansion coefficient. The first term in Eq.(4) is due to the pressure fluctuation due to the air heating, whereas the second one is due to the sample's thermoelastic bending. The thermal diffusivity is obtained by fitting the experimental data to Eq. (4) leaving α_s as an adjustable parameter.

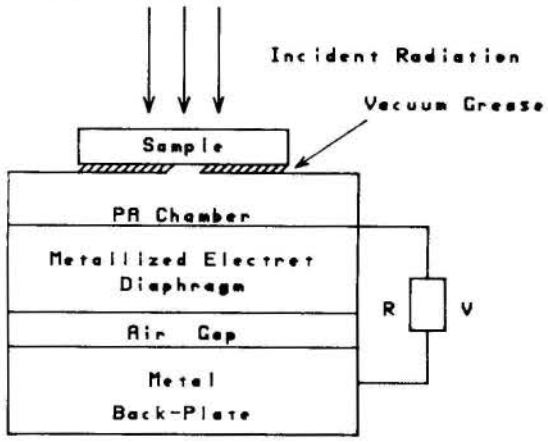

Fig. 2 Schematic Open-Photoacoustic cell geometry.

In Fig.3 we show the OPC data for α as a function of the thickness ratio parameter X, defined as the ratio of the Al thickness to the sample thickness, the solid line represents the result of the best fit of the thermal diffusivity data to Eq.(3), leaving

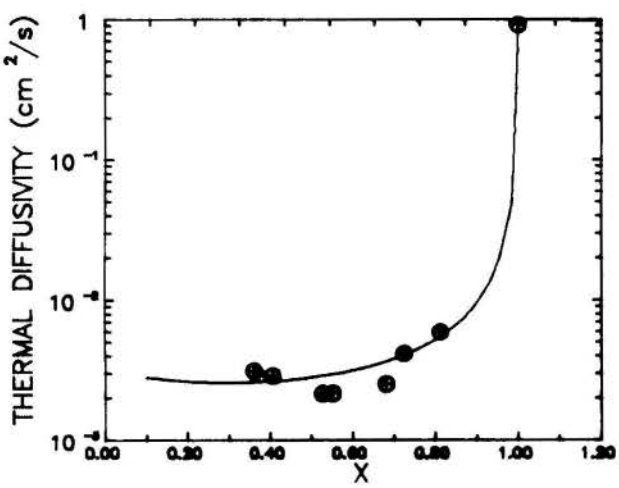

Fig. 3 Effective thermal diffusivity data for the Al-white paint samples, as a function of X.

α_1, α_2 and $\lambda = k_1/k_2$ as adjustable parameters. Here, the subscript 1 refers to the Al constituent. The data fitting procedure yielded the following values for the adjustable parameters: α_1 = 0.92 cm²/s, α_2 = 0.0030cm²/s and λ = 1000. The error in the data fitting was 0.2%/. In particular, we note that the obtained value for

α_1 agrees quite well with the literature value for Aluminum. Regarding the value of α_2 corresponding to the white paint, we could not find any reported data in the literature. However, what we can say is that the above value seems to be a reasonable one since it is of the order of magnitude of most polymers. From the adjusted value of λ, using the literature value of $k_1 = 2.37$W/cmK for Al, we have then estimated k_2 to be 2.37mW/cmK from which we got $\rho_2 c_2 = 0.79$J/cm K for the white paint specific heat. These values for the white paint thermal conductivity and specific heat are both of the same order of magnitude as those of vinyl acetate and similar polymers [16].

To make sure that the values of α_2 and k_2 obtained from our two-layer model was correct we have decided to measure the specific heat $\rho_2 c_2$. The values of $\rho_2 c_2$ can be measured from the OPC signal amplitude at low-frequencies where the sample is thermally thin. In this regime, the OPC signal is dominated by the gas thermal piston contribution, and it can be shown from Eq.(4) that, in this region, the OPC signal varies with the inverse of the specific heat, namely,

$$V \cong \frac{const}{(l\,\rho\,c)_s}, \tag{5}$$

Using Eq.(2) in Eq.(5), we can write the ratio of the microphone output signal for a given sample to that of the bare Al sample, at a fixed modulation frequency, as

$$V_{rel} = \frac{1}{1 + \frac{(1-x)}{x} r}, \tag{6}$$

where $r = \rho_2 c_2/\rho_1 c_1$ is the ratio specific heat to the Aluminum specific heat. In Fig. 4, we show the data we got for V_{rel} at 10Hz for our samples. To assure that the ratio was not affected by illumination effects, such as, illuminated area and power fluctuation, the OPC data shown in Fig. 4 was recorded using a 1.75mW stabilized He-Ne laser source. The solid line in Fig. 4 represents the best fit of the data to Eq.(6) leaving r as an adjustable parameter. The error in the fitting procedure was 2.5% and the value found for r was r = 0.40. From this value of r, using $\rho_1 c_1 = 2.57$J/cm K we got $\rho_2 c_2 = 1.03$J/cm K which is quite close to the one obtained above from the effective thermal diffusivity data.

In Fig. 5 we present the results for the thermal expansion coefficient we got from the OPC signal amplitude data fitting, as a function of the ratio parameter X. Figure 5 tells us that on increasing the paint layer thickness the thermal expansion coefficient

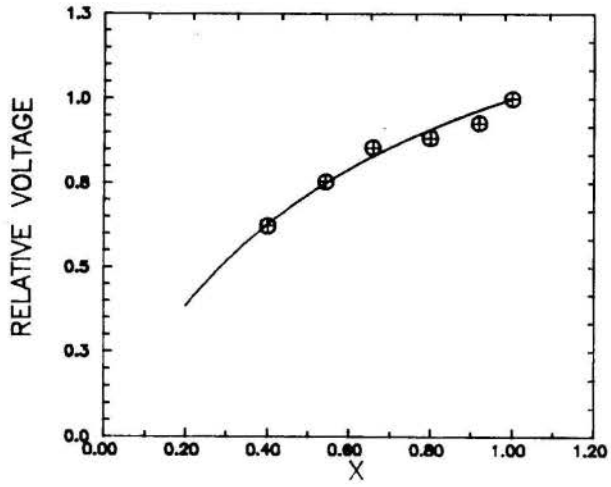

Fig. 4 Ratio of the OPC signal of the Al-white paint samples to the OPC signal of an uncoated 60 m thick Al sample, recorded at 10Hz modulation frequency using a He-Ne laser, as a function of X.

also increases. It eventually reaches a saturation when the paint layer is sufficiently thick. The solid line in Fig. 5 represents the best fit of the data to the theoretical expression for α_T as predicted by the effective sample model. This, in turn, is derived from the model developed above as follows. From Eq.(2) one has

$$\delta l\,\rho c = \delta l_1\,\rho_1 c_1 + \delta l_2\,\rho_2 c_2, \tag{7}$$

writing $\delta l = \alpha_T \Delta T\, l$ and $\delta l_i = \alpha_{Ti} \Delta T\, l_i$, and using Eqs.(1) and (3) one finds from Eq.(7)

$$\alpha_T = \alpha_{T1}\,\frac{x^2 + x(1-x)(\lambda+\xi) + \lambda\,\xi(1-x)^2}{x^2 + \gamma(1-x)^2 + x(1-x)(\lambda + \frac{\gamma}{\lambda})}, \tag{8}$$

where α_{Ti} is the thermal expansion coefficient of material i, λ is the ratio of the thermal conductivities of materials 1 and 2 as defined above, $\xi = (\alpha_{T2}/\alpha_{T1})(\rho_2 c_2/\rho_1 c_1)$ and $\gamma = \alpha_1/\alpha_2$. Equation (8) has in principle four adjustable parameters. However, from the thermal diffusivity data fitting two of them, λ and γ, were already determined, namely, $\lambda = 1000$ and $\gamma = 307$, at the same time that the thermal expansion coefficient for Aluminum is well known, $\alpha_{T1} = 0.000023\text{K}^{-1}$. We are thus left just with one adjustable parameter, namely, ξ. The result we got was $\xi = 6.46$, which gives us $\alpha_{T2} = 0.00048\text{K}^{-1}$ for the white paint thermal expansion coefficient. This value of α_{T2} is in reasonable agreement [17] with the ones of most rubber-like polymers, polyvinyl butyral and cellulose nitrate.

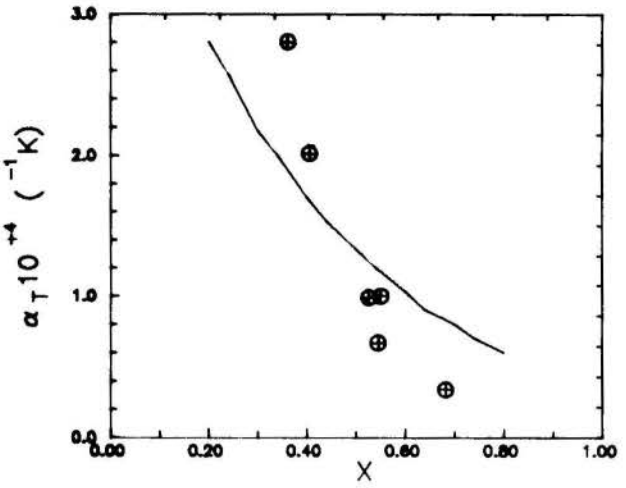

Fig. 5 Effective thermal expansion coefficient for the Al-white paint samples, as a function of X.

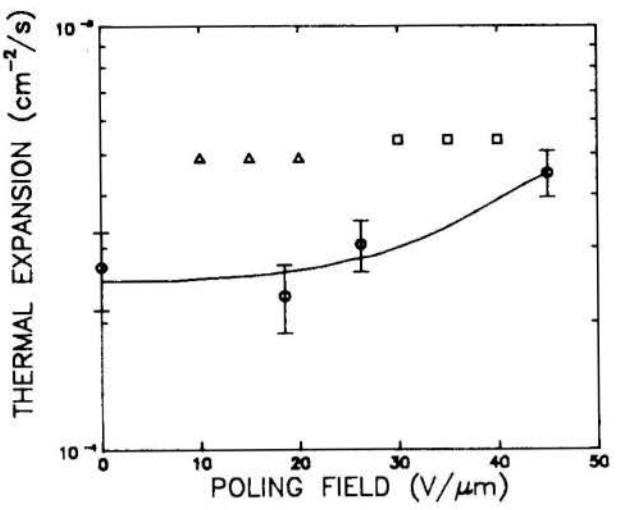

Fig. 6 Thermal diffusivity of the PVDF films as a function of the poling field. The square and triangles refer to the values of the Kynar and Solef piezo films, respectively.

POLING FIELD EFFECTS ON PVDF

The next example investigated is that of the effect of poling fields on the thermal diffusivity of PVDF films . Film casting from a DMFA solution was tried at different solution concentrations and drying temperatures. The prepared solutions and a clean glass substrate were warmed up to 60°C. The solution was then spread over this substrate and the temperature of 60°C was hold constant until complete evaporation of the solvent had occured. At a temperature of 60°C and a 5% (w/w) solution the viscosity is low enough and was found to be optimum for producing pinhole-free films. The final film thickness can be varied from 5 μm up to 30 μm depending on the solution concentration and drying temperature. At the above temperature and concentration the film thickness varied from 12 to 20 μm. The resulting films next underwent the Al electrode evaporation for the subsequent polarization process. The poling of the PVDF films was carried out in an oil bath heated to approximately 80°C and at dc electric fields up to 50V/μm for 1 h. The sample was subsequently cooled under the applied field. The final step was the painting black of the front electrode of the PVDF film.

As in several previous cases of polymer samples [5,8,11] the main contribution to the PA signal of our PVDF film samples came from the thermoelastic bending of the sample. In Fig.6 we summarize the results for the thermal diffusivity of our PVDF film as a function of the poling field obtained by fitting the experimental data to Eq.(4). Also shown in this figure are the values of α for two commercial polarized PVDF films. We note that at the highest poling field the value of α for our PVDF films is very close to those of the Kynar and Solef films. It was shown that thermal diffusivity exhibited a monotonically increasing behavior with the poling field. In particular, the dependence of the thermal diffusivity on the poling field is in qualitative agreement with what is intuitively expected. On increasing the poling field one increases the order in the system due to the enhancement of the ratio of oriented polar beta crystallites to the nonpolar alpha crystallites. Consequently, an enhancement of the heat conduction and thermal diffusivity would be expected.

CONCLUSION

In this paper we have discussed the photoacoustic measurements of the thermal properties of a sample. The measurements were carried out using the so-called OPC method and two different systems were studied. For the two-layer system we show that the thermal diffusivity as well as the thermal conductivity are completely determinated, based upon the effective sample model widely used in heat transfer problems, and for the PVDF film we show that the thermal diffusivity of these films are in good agreement with the commercially avaiable ones and exhibit a monotonically increasing behavior with the poling field.

We believe the accuracy together with its simplicity will render the proposed OPC method a reliable and simple technique for the complete photoacoustic characterization of the thermal properties of solid samples.

REFERENCES

[1] Rosencwaig, A., "Photoacoustics and Photoacoustic Spectroscopy" Ed. Wiley, N.Y., 1980.

[2] Vargas,H. and Miranda, L.C.M., Phys. Repts. vol.161, 43, 1988.

[3] Touloukian, Y.S., Powell, R.W., Ho, C.Y. and Nicolasu, M.C., "Thermal Diffusivity", Ed. IFI/Plenum, N.Y., 1973.

[4] Ziegler G. and Hasselman, D.P.H., J.Mater Sci. Vol.16, 495, 1981.

[5] Leite, N.F., Cella N., Vargas, H. and Miranda, L.C.M., J. Appl. Phys., Vol. 61, 3023, 1987.

[6] Torres-Filho, A., Perondi, L.F., and Miranda, L.C.M., J. Appl. Pol. Sci., Vol. 35, 103, 1988.

[7] Mertē, A., Korpiun, P., Lusher, E. and Tilgner, R., J. Physique Coll C6, Vol.44, 463, 1983.

[8] Torres-Filho, A., Leite, N.F., Miranda, L.C.M., Cella, N. and Vargas, H., J. Appl. Phys, Vol.66, 97, 1989.

[9] Bento, A.C., Vargas, H., Aguiar, M.M.F. and Miranda, L.C.M., Phys. Chem. Glasses Vol.28, 127, 1987.

[10] Silva, M.D., Bandeira, I.N. and Miranda, L.C.M.,J. Phys. E : Sci. Instrum., Vol.20, 1476, 1989.

[11] Perondi, L.F. and Miranda, L.C.M., J. Appl. Phys., Vol.62, 2955, 1987.

[12] Sessler, G.M., J. Acoust. Soc. Am., Vol.35, 1354, 1963.

[13] Sessler, G.M. and West, J.E.,"Electrets", Springer Series in Topics in Applied Physics Vol.33, Springer, Berlin, pp.347, 1980.

[14] McDonald, F.A., and Wetsel Jr., G.C., J. Appl. Phys., Vol.49, 2313, 1978.

[15] Rousset, G., Lepoutre, F. and Bertrand, L., J. Appl. Phys., Vol.54, 2383, 1983.

[16] Grzegorczyk, D. and Feineman, G., "Handbook of Plastics in Electronics", Reston, Publ. Co, Reston, VA, 1974.

[17] Roff, W.J., Scott, J.R. and Pacitti, J."Handbook of Common Polymers", CRC Press, Cleveland, Ohio, 1971.

III ENCIT – Itapema, SC (Dezembro 1990)

SEARCH ALGORITHMS FOR PARTICLE TRACKING VELOCIMETRY SYSTEMS

V. J. Bonna, M. C. F. Braga, C. M. P. Cunha and L. F. A. Azevedo
Departamento de Engenharia Mecânica
Pontifícia Universidade Católica Rio de Janeiro, RJ 22453 – BRASIL

ABSTRACT

The present paper describes two search algorithms developed to be used in a Particle Tracking Velocimetry System for instantaneous, full field velocity measurements. The algorithms were designed with the objective of identifying and characterizing particle streaks registered on time-exposure photographs of the flow investigated. Simulated binary digital images were used as input to test the performance of the algorithms. In the tests conducted, both algorithms were able to identify all elements of the test matrices and to properly assign them to a particular trace, after verifying their connectivity. The two algorithms attained the same accuracy level in the determination of the traces utilizing, however, different computer time and memory requirements.

INTRODUCTION

Flow visualization has always played a major role in the understanding of fluid flow phenomena and, as a consequence, in the development of the field of fluid mechanics. Since the early times, experiments employing a variety of visualization techniques have provided the necessary insight for the formulation and verification of several theories, ranging from creeping to supersonic flows. The book by Van Dyke [1] is an excellent example of such efforts, presenting an outstanding collection of visualization photographs of several classes of fluid flow phenomena.

The past decade has witnessed an important change in the way that flow visualization is utilized in fluid mechanics research. Due to the rapid development and avaiability of affordable computer hardware and digital image methods, flow visualization evolved from a qualitative to a quantitative tool, capable of providing instataneous, full field velocity measurements of transient flows. This capability of capturing *snap-shots* of isntataneous unsteady flows provides new information for the analysis of fluid flow phenomena, which is not attainable with any other tecnhique presently available. Full field measurements also allow the calculation of derivative or integral instantaneous quantities such as vorticity, rate-of-strain, circulation or fluxes. Instantaneous pressure fields can also be calculated by the substitution of the measured velocity field in the appropriate form of the momentum equation. Liquid crystal technology has also been used in conjuction with digital image techniques for the simultaneous determination of temperature and velocity fields (e. g., [2]).

Complete velocity fields are determined from displacement measurements taken from photographs of light scattered from small suspended particles moving along with the fluid. The particles are illuminated by a sheet of light which reveals two-dimensional velocity vectors. Currently, there are two classes of techniques in use for the determination of particle displacement fields. One of them, which is the object of the present paper, relies on the measurement of the length of streaks recorded by long-time-exposure photographs of illuminated particles. It is known as Particle Tracking Velocimetry (PTV). The other class utilizes optical transformations or direct autocorrelation of interrogation spots on double-exposure photographs of fine particles in highly seeded flows. This method, generally known as Particle Image Velocimetry (PIV), has demonstrated its potential in several applications, yielding accurate instataneous velocity fields with high spatial resolution [3]. These results, however, are still limited to flows with low turbulent Reynolds numbers.

A direct comparison of the two methods will undoubtedly favor PIV, specially with regard to the spatial resolution of the velocity data. However, PIV requires powerfull laser sources and expensive optical components to produce these data. PTV, on the other hand, can be implemented at a fraction of the cost, employing hardware normally available for standard flow visualization experiments, but still providing usefull information for fluid mechanics research. A brief description of the Particle Tracking Velocimetry technique will now be presented.

As already mentioned, PTV is a non-intrusive, relatively simple, and yet powerfull, technique for planar full field velocity measurements over extended flow areas. Its implementation involves seeding of the flow with small particles which are assumed to follow the fluid, and measuring their movement over a small period of time, by measuring the length of their traces left on time-exposure photographs. A narrow sheet of light is used to illuminate the particles present in a plane of the flow, thereby providing a two-dimensional *slice* of a possibly three-dimensional flow. The photographs of the particles are taken by a camera mounted at ninety degrees with the plane of study. Long exposure photographs will produce a field of traces that can be considered as projections of the instantaneous velocity vectors onto the plane of illumination.

The exposure time can be controlled by switching the illumination with the camera shutter kept open. As suggested by [4], the shape of the light pulse can be controlled and used to discard traces left by particles which happen to cross the illumination plane during the duration of the light pulse, in the case of three-dimensional flows. This can be achieved by using a pulse pattern in a dot-dash-dot format. The abscence of one of the safety dots on the traces captured by the photograph is an indication that the corresponding particle did not stay within the illuminating plane during the duration of the light pulse. These traces are discarded. Flow direction ambiguity can be resolved by utilizing an asymmetric (dot-dot-dash-dot) light pulse format.

A typical flow visualization experiment will produce a photograph containing a few thousand particle traces, which will require individual processing for trace validation (i. e., checking of the safety dots), and determination of the magnitude and direction of the velocity vectors. This task can be completed by manually processing a digitized image of the photograph, with the aid of a digitizing table and an adequate image editing software. Digital processing techniques can be utilized to enhance contrast and reduce background noise in the digitized image (e. g., [5]), prior to the measuring operation. After the lenght of each valid trace has been measured, interpolating algorithms are necessary to determine the velocity vectors at the desired locations in the flow domain. Even with the aid of a digitizing table, manual processing of the images may require hours of tedious work for a single flow visualization picture.

Automatic processing of the digitized images have been devised as an alternative for improving the performance of the measuring operation. Although some algorithms with this objective have been presented in the open literature (e.g., [6]), a detailed discussion of their implementation and performance is not available.

From the brief description of PTV just presented, it can be noted that several steps are involved in the determination of the instataneous velocity fields. These are: seeding of the flow, illumination, photographic registration, image digitization, image processing, measurement of the traces length, and velocity vectors interpolation. All these steps are equally important, and uncertainties associated with each one of them will contribute to the total uncertainty of the velocity measurement, as demonstrated in the paper by Agüí and Jiménez [4].

The authors are aware of the fact that all aspects of the technique should be addressed in an integrated manner, if a successfull measuring system is to be developed. Within this framework, a research program is being conducted at PUC/RJ with the objective of developing a complete full field velocity measuring system based on the Particle Tracking Velocimetry technique. The present paper, being part of this broader research program, is concerned with the automatic measuring of the particle traces. Its objective is to compare the performance of two algorithms developed to automatically identify and measure the traces present in flow visualization pictures. A detailed description of the algorithms will be presented shortly.

Computer generated binary images were utilized to test the algorithms developed. This strategy was adopted in order to furnish a controlled input to the two algorithms, thereby isolating the effects of others steps of the PTV technique on the performance tests. The tests conducted compared computer time, memory requirements, and accuracy of each algorithm.

TEST IMAGES

A digitized image can be represented in the computer memory by a two-dimensional array of elements to which an integer value is associated. Each element of this matrix would correspond to a picture element (pixel) on a monochromatic video display, where the integer value associated with each pixel represents its gray level.

A digitized image of a black and white flow visualization photograph displaying particle traces, will normally present pixels with a broad range of values of gray levels. Algorithms for identifying and measuring the traces length need an input image in binary form. This can be achieved by a thresholding procedure applied to the digitized form of the photograph, using an appropriate gray level value. In this procedure, pixels displaying a gray level value equal or above the threshold value are assigned the maximum gray level value, while those displaying gray level values below the threshold value are assigned the minimum gray level value. After this procedure is completed, the resulting digital image will be formed only by *white* and *black* pixels, i. e., minimum and maximum gray level values.

The binarization operation is an important part of PTV and should be used with extreme care since part of the particle traces on the digitized photographic image can be lost by not using an adequate thresholding gray level value. Additional information on binarization operations can be found elsewhere [7].

Since the main objective of the present work is to compare the performance of trace measuring algorithms, simulated binary images of particle traces were used for testing purposes. Those images were constructed by assigning to the elements of a matrix stored in the computer memory the values zero or one. The matrix elements with assigned values equal to one would correspond, in a real digitized image, to either an element of a particle trace or to background noise. On the other hand, matrix elements with an assigned value equal to zero would represent the image background.

The tests presented in the present paper were performed utilizing simulated binary images formed with sixty traces of different lengths (measured in pixels units), with inclinations with respect to the horizontal ranging from -90 to 90 degrees. They consisted, basically, of a comparison of the geometric characteristics of the traces present in the input test images with those determined by the measuring algorithms.

It should be mentioned that, at the present stage of development, the measuring algorithms are not capable of interpreting images displaying the safety dots mentioned in the Introduction. For this reason, the test images utilized did not display these trace patterns. Also, trace crossing was not allowed in the test images.

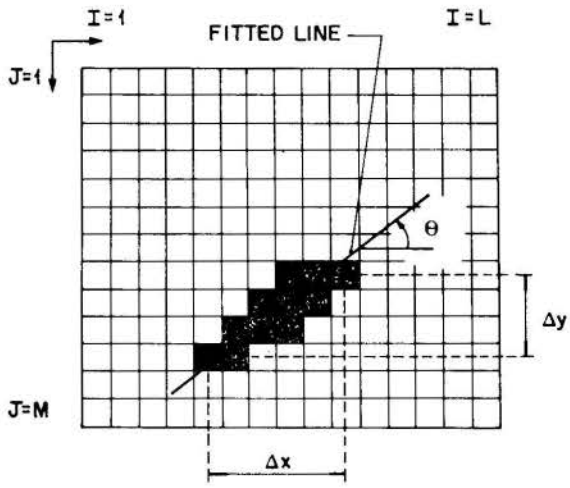

Fig. 1 – Schematic representation of the image matrix.

DESCRIPTION OF THE ALGORITHMS

The two measuring algorithms developed differ from each other with respect to the procedures utilized for searching the elements in the image matrix, and for assigning them to a particular trace. To facilitate future reference in the text, the algorithms are named as Global-Search and Family-Tree algorithms. They will now be described.

Global-Search Algorithm: This algorithm examines the binarized image matrix, element by element, looking for black elements (i. e., elements with values equal to 1). The black elements encountered are checked for connectivity and assigned to a particular trace. The name Global-Search stems from the fact that, in this algorithm, the image matrix is searched in a single sweep, as opposed to other methods where, once a black element is found, a local search in the neighborhood of the element is initiated to find other elements which belong to the same trace.

Figure 1 was constructed to facilitate the description of the algorithm. It presents a $L \times M$ image matrix with elements $E(I,J)$. The black squares in the figure represent elements with value equal to one, belonging to a trace. The following definitions will help the description of the algorithm:

- anterior neighbors of an element E(I,J) are the elements of the set:

$$\{E(I-1,J), E(I,J-1), E(I-1,J-1), E(I+1,J-1)\}$$

- an image element is marked by assigning an integer number (different from 0 or 1) to it.
- a trace is composed of elements with the same mark number.

The algorithm is formed by the following four routines:

Search Routine:

1- move to a new element in the image matrix, working from left to right, top to bottom (starting at element $E(1,1)$), until the last element, $E(L,M)$, is visited.

2- check if the element has a value equal to one (i. e., a black element). If not, return to step 1.

3- if there is no black anterior neighbor of the black element in question, mark the element with a new mark number and return to step 1.

4- if all black anterior neighbors have the same mark number, add this element to the trace to which the anterior neighbors belong, using the Add-Element Routine. Return to step 1.

5- if there are two black anterior neighbors with different mark numbers (note that there will be no more than two), add this element to either one of the traces using the Add-Element Routine, and join the two traces using the Join-Trace Routine. Return to step 1.

Add-Element Routine

1- assign to the black element in question the mark number of the black anterior neighbors.

2- store the x and y coordinates of the black element in question in an array that contains the coordinates of the other elements of the trace.

Join-Trace Routine

1- assign to all elements of the trace to be joined, the mark number of the elements of the trace to be kept.

2- store the x and y coordinates of the elements of the new trace obtained after the joining operation.

3- delete the joined trace.

Once all traces have been identified and stored, the displacement vectors are calculated by the following routine.

Vector Routine

1- determine the extreme x and y coordinates (i. e., x_{max}, x_{min}, y_{max}, y_{min}) of the elements of each trace found.

2- determine the angle of inclination with the horizontal, θ, of each trace by calculating the slope of the best straight line passing through the elements of the trace, utilizing a least-squares procedure.

3- determine the horizontal and vertical projections of each trace, Δx and Δy, by the following relations:

i f $|\theta| \geq 45°$, $\Delta y = y_{max} - y_{min}$ and $\Delta x = \Delta y / \tan\theta$

i f $|\theta| < 45°$, $\Delta x = x_{max} - x_{min}$ and $\Delta y = \Delta x . \tan\theta$

4- determine the magnitude of each trace by calculating:

$$L = (\Delta x^2 + \Delta y^2)^{1/2}$$

5- determine $\overline{x}$ and $\overline{y}$, the coordinates of the mid-point of the traces.

Family-Tree Algorithm: This algorithm, as the previous one, searches the binarized image matrix, element by element, looking for a black element. Once such element is found, a search procedure is initiated with the aim of finding all other black elements *descending* from this element, i. e., all other black elements which are neighbors of the *father* element in question. One of the *descendents* of the *father* elelemnt (i. e., one of the *son elements*) is choosen arbitrarily and a new search for *grandson* elements is implemented. One of the identified *grandson* elements is again choosen arbitrarily and the search for new descendents continues revealing the family tree, until an element with no descendents is found. At this point the procedure returns to the imediatly anterior ancestor, verifying if this element possess other *son* elements from which the family tree can progress. Once all the elements of the family are identified, the trace has been found and a least-squares procedure is employed to determine the displacement vector associated with that particular trace.

The detailed description of the algorithm is facilitated by reference to Figure 1, and to the following definitions:

- neighbors of an element $E(I,J)$ are the elements of the set:

$$\Big\{E(I+1,J), E(I-1,J), E(I+1,J+1), E(I+1,J-1),$$
$$E(I-1,J-1), E(I-1,J+1), E(I,J-1), E(I,J+1)\Big\}$$

- an image element is marked by assigning an integer number (different from 0 or 1) to it.

The algorithm is formed by the single routine now presented:

1- move to a new element in the image matrix, working from left to right, top to bottom (starting at element E(1,1)), until the last element, E(L,M), is visited.

2- verify if the element has a value equal to one (i. e., a black element). If not, return to step 1.

3- store the coordinates of the black element found in a temporary stack array (i. e., a last-in-first-out type array)

4- mark the element (say, with number 3).

5- the element belongs to a trace, so store its coordinates in an array.

6- verify among its eight neighbors if there is any unmarked black element. If not, go to step 9.

7- mark the neighbors found in step 6 with the same number,different from that used in step 4 (say, with number 2).

8- choose arbitrarily one of the neighbors marked in step 7, and return to step 3.

9- if the stack array is not empty, take the element at the top of the stack. Otherwise, return to step 1.

10- check among the eight neighbors of the element considered in step 9, those which display the mark number 2. If there is no such element, return to step 9.

11- choose arbitrarily one of the neighbors identified in step 10 and return to step 3.

After the procedure is completed all traces present in the image matrix are identified, and the coordinates of its elements stored. The Vector Routine described earlier is then used to calculate the displacement vectors.

RESULTS AND DISCUSSION

The performance of the two algorithms described were compared by running search tests on the simulated binary images discribed earlier. The tests encompassed comparisons of accuracy, computer time, and memory requirements.

Accuracy Tests

The results that will now be presented are a summary of the output obtained from the two algorithms, using the test matrices as input. Both algorithms were able to identify all black elements of the test matrices, and to properly assign them to the correct traces. In this regard, it can be said that, both algorithms presented perfect performances. Errors were only introduced when the least-squares procedure, utiltized for the determination of the geometric characteristics of the traces (i. e., trace length, angle of inclination and mid-point coordinates), was used.

Since the two algorithms employed the same least-squares procedure described in the Vector Routine, their results were identical, which justifies the presentation of a single set of output data, representing the performance of both of them.

Table 1 displays a comparison of selected input traces and the respective prediction of the algorithms. In this table, $\overline{x}$ and $\overline{y}$ represent the coordinates of the mid point of the traces, θ the angle of inclination with the horizontal (see Fig. 1), and L is length of the traces.

Table 1 – Comparison of input and predicted values.

TEST IMAGE				PREDICTED VALUES			
$\overline{x}$	$\overline{y}$	θ	L	$\overline{x}$	$\overline{y}$	θ	L
2.0	7.0	90.00	10.00	2.0	7.0	90.00	10.00
75.0	18.0	-75.96	8.25	75.0	18.0	-75.30	8.35
40.0	41.0	-56.31	7.21	40.0	41.0	-57.26	7.13
41.0	64.0	33.69	7.21	41.0	64.0	32.74	7.13
6.0	87.0	14.04	8.25	6.0	87.0	16.70	8.35
43.0	98.0	0.00	10.00	43.0	98.0	0.00	10.00

An overall inspection of the results presented in Table 1, reveals that the level of agreement obtained between the input test data and the values predicted by the algorithms is very good. Indeed, the coordinates of the mid point of the traces were exactly predicted by the algorithms, while small errors are verified in the predictions of trace length and angle of inclination. These errors attain maximum values for traces with inclinations close to 0 or 90 degrees.

Computer Time

A comparison of computer time may lead to erroneous conclusions since the algorithms have not yet been optimized. However, some general trends could be observed from the tests conducted.

For the test matrices utilized, having around sixty traces, the Global-Search algorithm was at least three times faster than the Family-Tree algorithm. However, the execution time was seen to be roughly proportional to the number of black elements for the Global-Search algorithm, while it increased at a significantly lower rate in the case of the Family-Tree algorithm. This

observation indicates that, for a higher number of traces, the Family-Tree algorithm seems to be a better choice, with regard to computer time. Further tests are presently beeing conducted to verify these trends.

The Global-Search algorithm identifies traces with negative inclinations faster than those with positive inclinations. This characteristic is inherent to the construction of the algortihm and it is due to the higher number of calls to the Join-Trace Routine, in the case of positively-sloped traces. The performance of the Family-Tree algorithm is not influenced by the trace inclination.

Memory Requirements

The same reasoning regarding the level of optimization of the algorithms mentioned with respect to the computer time tests, is applicable to the memory requirement tests.

Both algorithms require memory space to store the input image matrix. Besides that, the Global-Search algorithm requires additional arrays to store the identified traces. The size of this array is obtained multiplying the number of traces in the image, times the number of elements present in the longest trace. In a real flow visualization experiment, an estimate of the size of this array can be obtained by the previous knowledge of the particle concentration being used to seed the flow, and some estimate of the maximum velocity expected in the flow field.

The Family-Tree algorithm, on the other hand, needs a small amount of additional storage to implement the stack array mentioned in the description of the algorithm. The stack array is of the size of the longest trace in the image matrix, and it is a temporary array being re-used for all identified traces.

CONCLUDING REMARKS

The present paper described two search algorithms developed to be used in a Particle Tracking Velocimetry System. In the complete measuring system, the algorithms would be responsible for the automatic identification of black elements in a binarized input image matrix, and for assigning them to a particular trace, after checking their connectivity.

The tests conducted revealed that both algorithms were able to find all black elelemnts in the simulated image matrix, and correctly assign these elements to different traces. The geometric characteristics of the identified traces were calculated employing a least-squares procedure, which introduced small errors in the length and angle of inclination of the traces.

The two algorithms displayed different computer time and memory requirements. The Global-Search algorithm was significantly faster than the Family-Tree algorithm, for image matrices with a small number of traces. However, the extrapolation of the execution time for densily populated image matrices indicates that the Family-Tree algorithm will become faster.

As far as computer memory is concerned, the Family-Tree algorithm required less storage than the Global-Search algorithm. It should be mentioned that, the trends revealed by the tests conducted need further investigation, since neither one of the algorithms have been optimized with respect to computer time or memory requirements.

The algorithms were implemented in PASCAL, and were executed in a standard PC-XT running at 8 MHz. Typical execution times for identification of 60 traces in the test matrices were 4 and 12 seconds for the Global-Search and Family-Tree algorithms, respectively.

At this stage, it can be said that a binarized image is of fundamental importance for the proper performance of the search algorithms and, as a consequence, of the velocity measuring system as a whole. As the next step for future work, the research effort should be directed toward the development of efficient binarizing algorithms that preserves the original length of the traces and, at the same time, do not incorporate background noise to them.

The present work is the first part of a broader research program aimed at developing a complete Particle Tracking Velocimetry System for full field velocity measurements. Although successiull utilizations of PTV have already been reported in the literature, a complete system is not available as an *off-the-shelf* research tool. The possibility of capturing instantaneous complete velocity fields justifies the effort directed to the development of such a tool.

Acknowledgement

The first three authors gratefully acknowledge the support awarded by Fundação de Amparo à Pesquisa do Estado do Rio de Janeiro, FAPERJ.

REFERENCES

[1] Van Dyke, M.,"An Album of Fluid Motion," *The Parabolic Press*, California, 1982.

[2] Kimura, I., Takamori, T., Ozawa, M., Takenaka, N. and Manabe, Y., "Quantitative Thermal Flow Visualization Using Color Image Processing," in *Flow Visualization*, ASME FED–Vol. 85, Khalighi et al. ed., pp. 69–76, 1989.

[3] Adrian, R. J., "Applications of Particle Image Velocimetry," in *Flow Visualization*, ASME FED–Vol. 85, Khalighi et al. ed., pp. 23–28, 1989.

[4] Agüí , C. J. and Jiménez, J., "On the Performance of Particle Tracking," *Journal of Fluid Mechanics*, Vol. 185, pp. 447–468, 1987.

[5] Pratt, W. K., "Digital Image Processing," *John Wiley*, New York, 1978.

[6] Massons, J., Gavaldá, J., and Díaz, F., "Image Processing of Cylinder Wake Generation, " *Physics of Fluids A*, Vol. 1, No. 8, pp. 1414–1423, 1989.

[7] Castelman, K. R., "Digital Image Processing," *Prentice–Hall*, New Jersey, 1979.

III ENCIT – Itapema, SC (Dezembro 1990)

CALIBRAÇÃO DE MEDIDORES DEPRIMÓGENOS DE VAZÃO EM ESCOAMENTO AERIFORME COM DISPONIBILIDADE LIMITADA DE FLUIDO DE TRABALHO

DOUGLAS LAURIA
ESCOLA DE ENGENHARIA MAUÁ • ESCOLA POLITÉCNICA da USP
JOSÉ CARLOS LAURIA
ESCOLA DE ENGENHARIA MAUÁ
DEPARTAMENTOS DE ENGENHARIA MECÂNICA

RESUMO

Este trabalho discute a solução adotada para a calibração de ejetores em escoamentos compressíveis subsônicos quando o volume de ar disponível é reduzido, a partir de resultados obtidos no projeto de um sistema de medida para avaliação das características operacionais daqueles aparelhos. O ejetor foi tratado como um tubo de Venturi e calibrado a partir da comparação da razão entre sua leitura manométrica e a da placa de orifício correspondente.

INTRODUÇÃO

O trabalho apresenta uma solução para a calibração de um sistema de medida de vazão em escoamento compressível subsônico, quando se dispõe de um volume limitado para armazenamento de ar. O sistema de medição em questão foi projetado para avaliar o desempenho de aspiradores industriais de ar comprimido como parte de um programa de nacionalização de equipamentos. O objetivo principal foi o levantamento de curvas de calibração dos ejetores empregados nos aparelhos, originando este trabalho, no qual analisam-se e discutem-se os resultados experimentais mais significativos.

O ejetor foi tratado como um tubo de Venturi. Por meio de associações entre as vazões determinadas desta maneira e por placas de orifício, calculadas segundo normas [1], [2], e ainda [3], verificou-se experimentalmente um comportamento linear definido entre a razão das duas colunas manométricas na faixa inicial de vazão . Para vazões maiores o comportamento corresponde nitidamente ao de um escoamento transitório consequente à redução da massa de fluido armazenada.

A partir dos resultados experimentais obtidos com dois ejetores e duas placas de orifício diferentes determinou-se coeficientes angulares da reta mencionada, constatando-se uma diferença percentual entre eles inferior a dois porcento.

PROPOSIÇÃO DO PROBLEMA

Ejetores. Aspiradores de ar comprimido pertencem a uma classe genérica de aparelhos denominada de EJETORES, cujo funcionamento baseia-se na transferência de quantidade de movimento entre um escoamento primário (fluído motor) e um escoamento secundário (fluído movido), através de sua mistura.

A fig. 1 apresenta um ejetor na qual um fluído motor é admitido no expansor e, com velocidade elevada, lançado na câmara de mistura através da câmara de aspiração. Como conseqüência da redução de pressão nesta câmara, fluido é aspirado do escoamento secundário e misturado com o fluído motor na câmara de mistura. A jusante desta o difusor decelera o escoamento da mistura, dirigindo-os para a atmosfera ou conduto de jusante.

Este trabalho apresenta a solução e os resultados obtidos no projeto desenvolvido para a medida da vazão de alimentação (primária) e da vazão aspirada (secundária) dum ejetor.

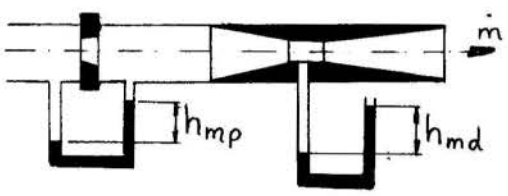

fig. 1 Sistema de Calibração

Diretrizes do projeto. A preocupação básica do projeto foi de evitar a influência dos equipamentos de medida de vazão no escoamento, de tal modo que os parâmetros determinados em ensaio correspondessem aos verificáveis durante a operação do aspirador.

Um primeiro medidor de vazão foi obtido a partir da própria configuração do aspirador, que, tomada a fig. 1 como referência, assemelha-se a um tubo de Venturi.

A vazão de saída do aparelho foi medida com o próprio difusor, empregado como medidor de vazão. Sendo aquela a soma das vazões primária e secundária, restava apenas determinar uma destas para, com a equação da continuidade, obter a outra incógnita.

Sendo a aspiração dos aparelhos conectada diretamente à atmosfera, optou-se pela medida da vazão de alimentação por meio de placa de orifício.

Devido à faixa de vazões abrangida pelos aspiradores, os difusores foram calculados e calibrados, não podendo ser especificados a partir de configurações normalisadas e que dispensam calibração. Este procedimento pôde ser aplicado apenas a duas placas de orifício escolhidas de tal modo a cobrir tôda a faixa estimada de vazões.

MEDIDORES DEPRIMÓGENOS DE VAZÃO

Um medidor deprimógeno de vazão caracteriza-se por associar a perda de carga imposta ao escoamento por uma restrição à vazão que o atravessa. Pela iteração entre restrição e escoamento , a vazão é convertida em outra grandeza física de fácil mensuração, no caso a pressão diferencial relativa à perda de carga (Δp). Um elemento externo é usado para a medida desta pressão cujo valor é lido diretamente ou convertido em sinal para processamento ou transmissão.

A equação de trabalho genérica para um medidor deprimógeno operando com fluído compressível é da forma :

$$\dot{m} = 0{,}0655\ \alpha\ \varepsilon\ D^2 \left(\frac{\rho\ p_1}{T_1\ z} \right)^{1/2} \qquad (1)$$

onde o índice 1 indica condições a montante do medidor.

O coeficiente de vazão (α) é um parâmetro indicativo da relação entre a vazão real incompressível e a teórica no medidor. O coeficiente de expansão (ε) corrige os efeitos de compressibilidade do escoamento. Em escoamentos subsônicos verifica-se que :

$$\alpha = \alpha\ (\beta, R_e) \qquad (2)$$

$$\varepsilon = \varepsilon\ (\beta, k, p_1, \Delta p) \qquad (3)$$

sendo β denominado coeficiente geométrico, exprimindo a razão entre o diâmetro da restrição ao escoamento (garganta) e o diâmetro do conduto.

$$\beta = \frac{D_o}{D} \qquad (4)$$

SISTEMA DE CALIBRAÇÃO

Para a calibração dos medidores dispunha-se de dois reservatórios interligados perfazendo um volume de 0,6 m^3. Tal disponibilidade revelou-se insuficiente para a calibração dentro da faixa de vazões necessária.

As alternativas para a calibração correta dos medidores seriam ampliar o volume disponível ou então pesquisar uma sistemática que, a partir da calibração correta na faixa permitida pelos tanques, pudesse ser estendida a vazões maiores.

A primeira simplificação aplicada ao sistema foi a admissão de escoamento isotérmico nos condutos. Tal aproximação pode ser feita sem sacrifício da precisão requerida para aplicações industriais [1].

O cálculo das placas de orifício foi efetuado admitida uma pressão diferencial máxima de 9000 Pa. Tendo a calibração do ejetor sido feita com saída para a atmosfera, a pressão a montante do mesmo atinge no máximo dez por cento acima da pressão atmosférica. Desprezada esta variação, introduz-se um erro de cêrca de três por cento no cálculo da vazão mássica expressa por (1), nas condições específicas de projeto.

No tangente aos efeitos de compressibilidade, verifica-se que, para as condições de operação dos aspiradores, o fator de compressibilidade é praticamente igual à unidade.

Delmée [2], apresenta uma equação empírica para o coeficiente de expansão de placas de orifício para tomadas em flange :

$$\varepsilon = 1 - (0{,}41 + 0{,}35\ \beta^4) \left(\frac{\Delta p}{p_1} \right) \frac{1}{k} \qquad (5)$$

onde k representa a constante adiabática

Nas condições de operação do sistema verifica-se que a maior variação do coeficiente de expansão alcança dois por cento. Além disso verifica-se ser o coeficiente de vazão inversamente proporcional ao de expansão, o que induz a resultados conservativos para o coeficiente de interesse, quando desprezada a compressibilidade.

Impostas todas as simplificações , a equação (1) pode ser escrita na forma:

$$\dot{m} = \lambda \sqrt{h_m} \qquad (6)$$

sendo λ uma constante e h_m a altura da coluna manométrica.

De (6) tem-se que para a placa de orifício:

$$\dot{m}_o = \lambda \sqrt{h_{mo}} \qquad (7)$$

e para o difusor :

$$\dot{m}_d = \lambda \sqrt{h_{md}} \qquad (8)$$

Durante a calibração do medidor, é evidente que a vazão em massa na placa de orifício deve ser igual à vazão através do difusor. Igualando as equações (7) e (8) :

$$h_{md} = C\ h_{mo} \qquad (9)$$

De (9) conclue-se que a calibração desejada para o difusor pode ficar restrita à pesquisa da constante de proporcionalidade entre as colunas manométricas da placa de orifício e do próprio difusor.

Sendo o volume disponível para armazenamento de ar reconhecidamente insuficiente, era de se esperar que durante o processo de calibração ocorressem problemas com relação às constantes C . Para vazões baixas o sufi-

ciente para não afetar as condições de pressão interna (e consequentemente a vazão de alimentação dos reservatórios), a linearidade expressa pela equação (9) seria mantida. Vazões acima da limite conduziriam a uma redução da pressão interna devido ao fato de o compressor não conseguir supri-la. Neste caso, a linearidade de (9) seria sacrificada.

RESULTADOS OBTIDOS

A calibração dos ejetores foi realizada a partir de medições com duas placas de orifício (ou diafragmas) de dimensões diferentes. Os resultados experimentais estão expressos nas figuras 2. e 3.

No trecho inicial das curvas, correspondente às menores vazões, confirma-se a esperada linearidade entre as colunas manométricas. Vazões acima da limite do compressor apresentam valores para a coluna manométrica que superam o esperado (indicado pela reta).

A divergência entre a coluna manométrica do difusor e da placa de orifício apresenta-se coerente com a condição de operação do sistema, onde o difusor foi locado a jusante da placa de orifício. Quando as vazões no sistema de medição se tornam significativas com relação ao volume dos reservatórios, o regime de escoamento deixa de ser permanente. No regime transitório que se estabelece, ocorrem significativas reduções da vazão em massa no difusor, correspondentes à redução de pressão nos reservatórios. Este fato é verificado pelo desvio dos resultados com relação ao comportamento linear esperado.

Será apresentada inicialmente uma abordagem genérica do equacionamento pertinente, para então serem expostos os valores numéricos correspondentes a cada caso sob forma de tabela.

Fazendo-se a regressão linear dos pontos das figuras 2. e 3., obtem-se as constantes de proporcionalidade C da equação (9), cujas retas correspondentes estão também indicadas nas figuras.

Tendo sido usadas placas de orifício diferentes para o ensaio dos dois ejetores, obteve-se, evidentemente, resultados diferentes das medidas efetuadas. Tomando-se as condições médias de escoamento, tem-se, então, duas equações diferentes de trabalho para cada placa de orifício. Estas equações serão na forma :

$$\dot{m}^{i}_{oj} = K^{i}_{j} \sqrt{h_{mo}} \qquad (10)$$

onde $i \equiv$ diafragma usado
$j \equiv$ ejetor ensaiado

A diferença percentual entre os dois valores da contante K para o mesmo ejetor é expressa por ΔK , e que corresponde à diferença percentual entre as respectivas vazões mássicas.

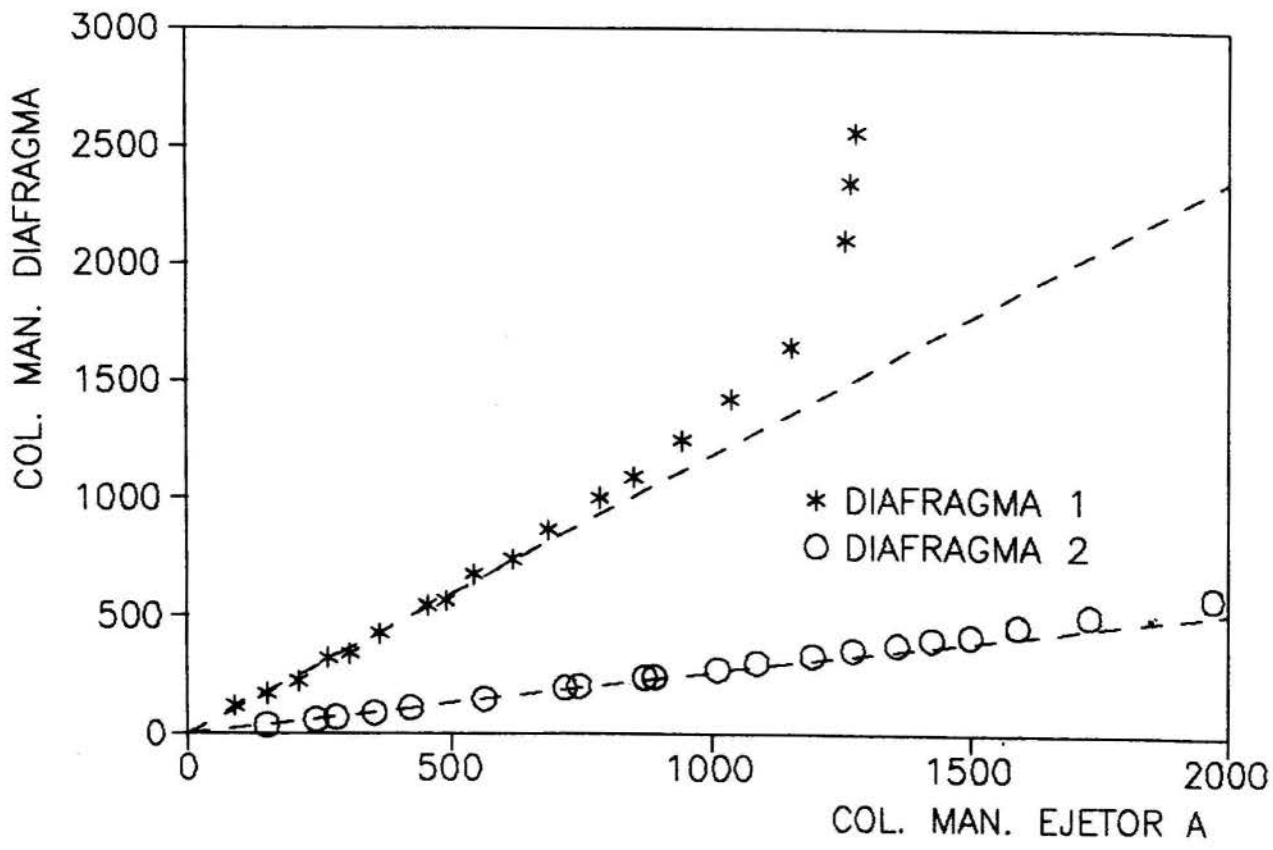

fig. 2 Ensaio do Ejetor B

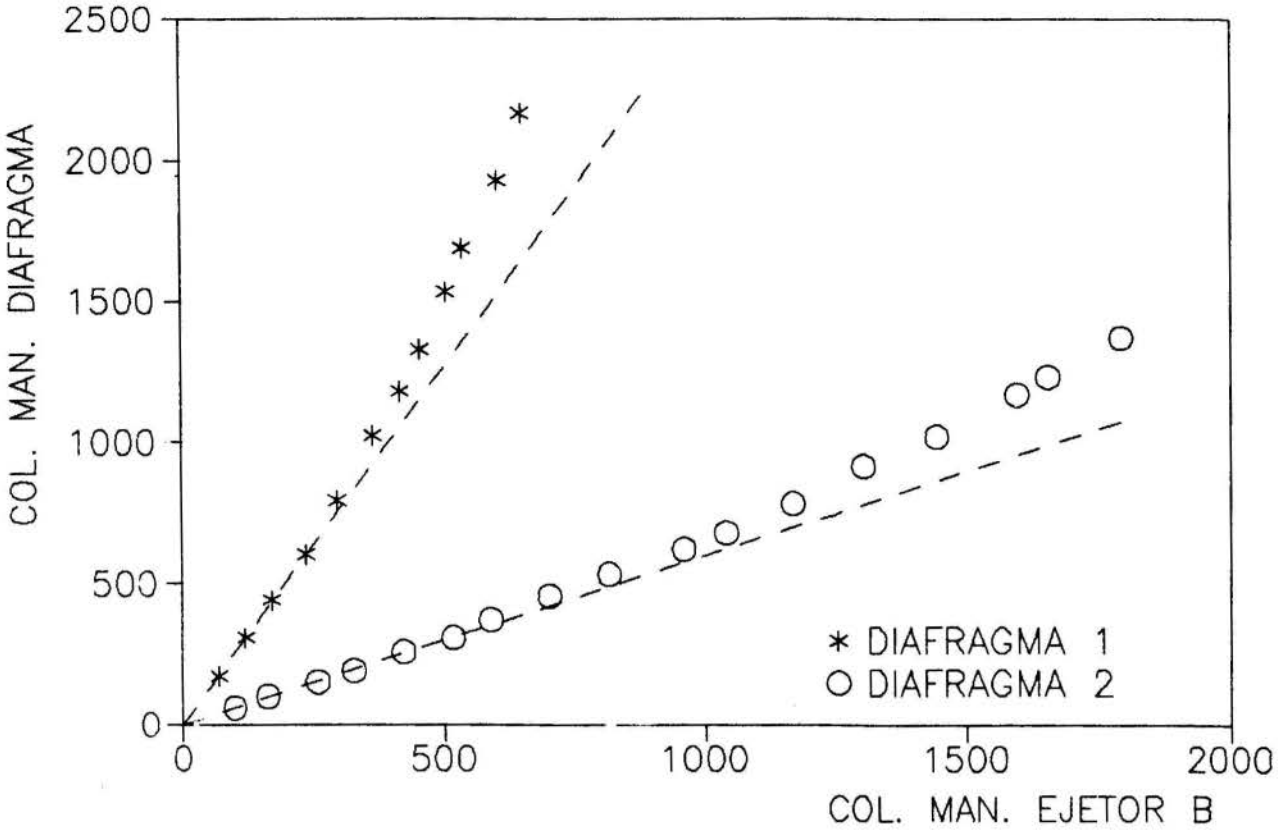

fig. 3 Ensaio do Ejetor B

Pode-se ainda calcular as mesmas vazões mássicas a partir das equações para os diafragmas, (7), (8) e (9):

$$\frac{\lambda_o}{\lambda_d} = \sqrt{C} \qquad (11)$$

Com (11) em (9):

$$\dot{m}_d = \frac{\lambda_o}{\sqrt{C}} \sqrt{h_{mo}} \qquad (12)$$

Na tabela 2:

$$\frac{\lambda_o}{\sqrt{C}} = K_d \qquad (13)$$

A relação entre as duas vazões mássicas calculadas para cada diafragma, igual em valor numérico à relação entre os coeficientes K_d é expressa por ΔK_d.

Tabela 1. Dimensões

Ejetores	Diâmetro de Entrada	β
EA	42 mm	0,38
EB	42 mm	0,30

Os diafragmas usados serão denominados D1 e D2.

Tabela 2. Resultados

Composição de ensaio	D1/EA	D2/EA	D1/EB	D2/EB
C	1,18	0,26	2,53	0,60
K ($\times 10^{-4}$)	0,167	0,166	8,40	8,37
ΔK (%)	0,6		0,4	
K_d ($\times 10^{-2}$)	1,06		1,08	
ΔK_d (%)	2			

CONCLUSÃO

Para as equações de trabalho das placas de orifício o emprego de valores médios do escoamento acarretou em variação máxima de 0,6 por cento, inferior à precisão admitida para esses elementos.

Na calibração do ejetor obteve-se uma diferença de apenas dois por cento para duas equações de trabalho, cada uma determinada por placas de orifício diferentes e amplas faixas de vazão. Identificado o trecho linear das curvas $h_{md} \times h_{mo}$, pôde-se, através do direcionamento de um número suficiente de ensaios para esta faixa, aplicar métodos estatísticos para obtenção das curvas melhor ajustadas.

Tendo sido as placas de orifício definidas dimensionalmente e construídas segundo normas técnicas usualmente aceitas [1], [2], pode-se considerar sua resposta como padrão de referência para a calibração dos ejetores. A menos de efeitos de compressibilidade e número de Reynolds, a razão entre as colunas manométricas de ambos os aparelhos deve ter um comportamento linear em regime permanente, conforme verificado na prática da Mecânica dos Fluidos e confirmado no trabalho. Eventuais desvios de linearidade podem ser atribuídos apenas ao regime transitório.

Com as medidas sendo feitas em equipamentos primários, manômetros de líquido, cuja precisão corresponde à incerteza de leitura dos valores das colunas manométrícas (escala milimetrada), os erros introduzidos por estes equipamentos são de reduzido valor.

Os resultados foram considerados suficientes para o processo de nacionalização dos aspiradores, dispensando-se a realização de ensaios posteriores.

Confirmou-se também a esperada não influência da compressibilidade no escoamento, alcançando- se um número de Mach máximo de 0,05.

BIBLIOGRAFIA

[1] Norma DIN 1952, "Durchflußmessung mit Blenden, Düsen und Venturirohren in voll durchströmten Rohren mit Kreisquerschnitt", Beuth Verlag, Berlin, Julho 1982.

[2] Norma ISO R541 "Measurement of Fluid Flow by Means of Orifice Plates and Nozzles", 1. edição, International Organization for Standardization, 1967

[3] Delmée, G.J., "Manual de Medição de Vazão", Editora Edgard Blücher Ltda., São Paulo, 1983.

[4] Levin, L., "Formulaire des Conduites Forcées, Oleoducts et Conduits d'Aération", Dunod, Paris, 1968.

[5] Lauria, J.C., "Projeto de Medidor de Vazão Deprimógeno, com a Calibração de Ejetores utilizados em Aspiradores Industriais de Ar Comprimido (Relatório Técnico)", IMT-CP, S. Caetano do Sul, 1986.

[6] Hill, B.J., "Two-Dimensional Analysis of Flow in Jet Pumps", Journal of the Hydraulics Division, ASCE, Vol. 99, pp. 1009-1026, Jul. 1976

SUMMARY

From results achieved in designing a measurement system to evaluate the performance characteristics of ejetors, the present work discusses a solution for gauging this kind of system in subsonic compressible flow when the avaiable amount of air is restricted to small values. The ejector was treated as a Venturi tube and was gauged by comparing the ratio of its manometer reading to the corresponding one of a orifice plate.

III ENCIT – Itapema, SC (Dezembro 1990)

ARRASTAMENTO DE GAS CIRCUNDANTE OBSERVADO COM UMA SONDA DE ENTALPIA

Aruy Marotta e Alfredo Gonçalves Cunha
Universidade Estadual de Campinas - UNICAMP
Instituto de Física "Gleb Wataghin"
13.081 - Campinas, SP.

RESUMO

Este trabalho apresenta os resultados obtidos com uma sonda de entalpia construída para a medida dos perfis de temperatura e velocidade num jato de plasma de ar. São analisados alguns dos fatores que influenciam na determinação da velocidade. O fluxo de massa mostra a presença de um forte arrastamento de ar, apresentando duas regiões distintas: uma mais próxima ao bocal, com rápido crescimento do arrastamento, e a outra, mais afastada, com um crescimento mais suave. Mostramos que o fluxo de energia pode ser utilizado para a calibração do sistema.

INTRODUÇÃO

Neste trabalho [1] construiu-se uma sonda de entalpia ou sonda calorimétrica, que permitiu determinar os perfis de temperatura, entalpia, pressão e velocidade em tres seções ao longo do jato de um maçarico de plasma não-transferido à ar comprimido, com arco elétrico estabilizado pelo fluxo em vórtice do gás. Através das integrais de fluxo de massa, calculadas para os tres planos, obteve-se a massa de ar ambiente que é arrastada pela turbulência do jato, tendo como consequência, o aparente aumento de massa de gás que flue do gerador . Esse cálculo explica, qualitativamente, a forte queda na temperatura média do plasma, bem como a observada estabilidade espacial do jato de plasma no eixo do maçarico. Foram, também, calculadas as integrais do fluxo de energia.

O grande número de medidas realizadas exigiu que o maçarico operasse de forma estável durante, pelo menos, uma dezena de horas. Esse problema foi resolvido através da diminuição da erosão do catodo, após o que foi possível operar o maçarico até 50 horas sem a troca do catodo [1-3]. O mesmo se pode afirmar da sonda, que resistiu bem às severas condições do jato de plasma, durante 9 horas de medidas.

A sonda de entalpia [4-7] é uma técnica intromissiva, exercendo certa perturbação nas condições locais do escoamento. Entretanto, sendo construída de pequenas dimensões, tem grandes vantagens quando comparada com outras técnicas, pois, além de permitir medidas locais, simultaneamente, de vários parâmetros importantes (temperatura, pressão, velocidade, composição), é de simples construção e de fácil interpretação dos resultados, sendo também mais adequada para o uso em ambientes industrais. Um outro fator positivo, é a capacidade da sonda de entalpia de efetuar a medida da temperatura cinética das partículas pesadas e não da temperatura eletrônica, que é o que se mede usualmente em espectroscopia atômica. A medida da temperatura das partículas pesadas é importante, pois são estas que contribuem, preponderantemente, para a entalpia dos plasmas térmicos. Como se sabe [6], abaixo de 7000K, as condições para o Equilíbrio Termodinâmico Local (ETL) nem sempre são satisfeitas e a medida da temperatura do plasma térmico por espectroscopia atômica incorrerá em êrro ao sobreestimar a temperatura do plasma. Isso se deve ao fato de que a temperatura dos elétrons é, geralmente, mais alta do que a das partículas pesadas, uma vez que aqueles recebem diretamente a energia do campo elétrico e, por choques, transmitem parte dessa energia às partículas pesadas.

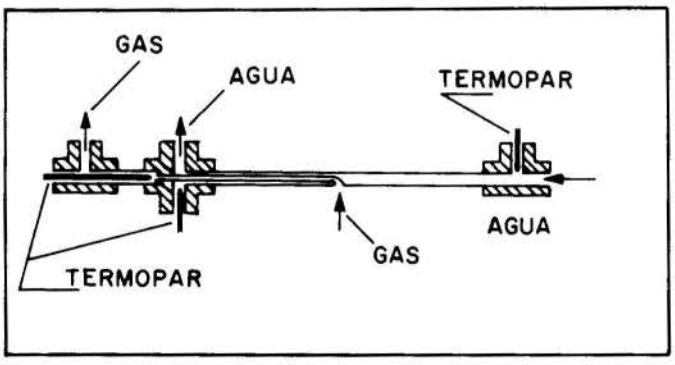

Fig. 1. Sonda de Entalpia.

TEORIA

A sonda de entalpia foi desenvolvida por Grey [4-7] e aplicada, pela primeira vez, ao argônio, ar e outros gases, na faixa de 2000 a 25000K. A versão original de Grey era coaxial com tres tubos, apresentando a desvantagem da complexidade na construção. Na Fig. 1 vemos a sonda por nós construida, contendo apenas dois tubos concêntricos. A sonda funciona como um calorímetro em que uma amostra de gás é absorvida do fluxo de plasma pelo tubo interno da sonda, e este transfere calor para a água de refrigeração, circulando na região anular limitada pelos tubos interno e externo. O tubo externo, em contacto com o plasma, recebe deste calor. São feitas medidas da elevação da temperatura da água, da temperatura do gás e das vazões de água e gás. O calor recebido pela água, do fluxo externo do plasma, deve ser subtraído do calor total recebido pela água. A medida é, então, realizada duas vezes, uma com fluxo de gás e outra, sem fluxo de gás.

A fórmula que permite calcular a entalpia do gás na entrada da sonda (entalpia do plasma) é dada pelo balanço térmico de energia:

$$\dot{m}_g (h_{1g} - h_{2g}) = (\dot{m}_a c_{pa} \Delta T_a)_{fluxo} - (\dot{m}_a c_{pa} \Delta T_a)_{não\text{-}fluxo} \qquad (1)$$

onde

$\dot{m}_g$ – fluxo de massa de gás
$\dot{m}_a$ – fluxo de massa de água
h_{1g} – entalpia desconhecida do plasma
h_{2g} – entalpia do gás na saída da sonda
ΔT_a – elevação da temperatura da água
c_{pa} – calor específico da água.

Ao ser realizada a medida nas condições de não-fluxo mede-se, também, a pressão dinâmica do plasma na entrada da sonda. A pressão estática no interior do jato foi considerada igual à pressão ambiente. A temperatura de estagnação do plasma, na entrada da sonda, foi obtida da Ref. [8] à partir da entalpia medida pela sonda e da pressão estática. O conhecimento da pressão dinâmica permite obter-se a velocidade do plasma na direção z (eixo do jato):

$$\overline{\Delta p} = \overline{p - p_o} = \frac{\overline{\rho v^2}}{2} \cong \frac{\rho v^2}{2} \quad , \tag{2}$$

onde a barra representa o valor médio integrado no intervalo de tempo em que é realizada a medida, p e p_o são a pressão total e estática, respectivamente, ρ é a densidade e v a velocidade. Em (2) consideramos desprezível a turbulência em ρ, isto é, $\overline{\rho} \cong \rho$. Como $v = \overline{v} + v'$, sendo $\overline{v}$ a velocidade média em z e v' a componente turbulenta da velocidade em z, para que a aproximação na Eq. 2 seja válida, é necessário que o nível de turbulência $\varepsilon = \sqrt{\overline{v'^2}/\overline{v}^2}$ seja também desprezível. A relação entre v e $\overline{v}$ pode ser escrita em função de ε:

$$v = \overline{v}\sqrt{1+\varepsilon^2} \tag{3}$$

Assim, ao supormos em (2) $v \cong \overline{v}$ estamos, na realidade, superestimando valor real da velocidade média que é $\overline{v}$ e não v, supondo que a medida de $\overline{\Delta p}$ esteja correta, o que não é verdade, pois a rotação do jato e a turbulência nas componentes transversais da velocidade (ε_x e ε_y) tem por efeito produzir uma depressão no interior do jato [9]. Por essa razão, a pressão estática no interior do jato deve ser menor do que a pressão ambiente. Como admitimos que a pressão estática no interior é a mesma que a externa, conclui-se que o valor de $\overline{\Delta p}$ está sendo subestimado. Assim os dois efeitos, o de desprezar a turbulência ε_z e o de não levar em conta a vorticidade e ε_x e ε_y tem efeitos opostos na medida da velocidade e o valor por nós medido da velocidade através de (2) pode estar próximo do valor real [9]. Para o cálculo da velocidade, a densidade foi obtida da Ref. [8], em função da temperatura e da pressão p_o.

O plasma será considerado incompressível, uma vez que temos $M \cong 0{,}3$, sendo M o número de Mach.

A influência da viscosidade na medida da velocidade é dada pela Ref. [6]:

$$p - p_o = \frac{1}{2}\rho v^2\left(1 + \frac{4}{Re + 0{,}457\sqrt{Re}}\right) = \frac{1}{2}\rho v^2 C, \tag{4}$$

onde, calculando C para $T \cong 3500K$, $p \cong 1$ atm, $v \cong 300m/s$, $\rho = 0{,}092\ kg/m^3$, $\mu = 1{,}707 \times 10^{-4}\ Ns/m^2$ e $D_1 = 3{,}85 \times 10^{-3}m$, obtem-se $C \cong 1{,}03$, sendo D_1 o diâmetro externo da sonda. Portanto, os efeitos devidos à viscosidade podem ser desprezados no cálculo da velocidade.

Grey [5] estimou a sensibilidade em função da geometria e demais parâmetros da sonda, obtendo:

$$\sigma \cong k\left(\frac{d_2^3}{D_1}\right)\left(\frac{1}{L}\right)\left(\frac{s}{\dot{m}}\right)\left(\frac{P\Delta P}{T^{3/2}}\right) \quad , \tag{5}$$

onde,

D_1 - diâmetro externo da sonda
d_2 - diâmetro interno do tubo de gás da sonda
L - comprimento exposto da sonda
$\dot{m}/s$ - densidade do plasma nas vizinhanças da sonda
T - temperatura do plasma
p - pressão do plasma
Δp - perda de pressão no tubo interno de gás.

Da fórmula (5), com o objetivo de otimizar a sonda, devemos escolher o maior diâmetro possível para o tubo interno (d_2) e o menor possível para o diâmetro externo (D_1). Por isso, os tubos devem ter paredes finas.

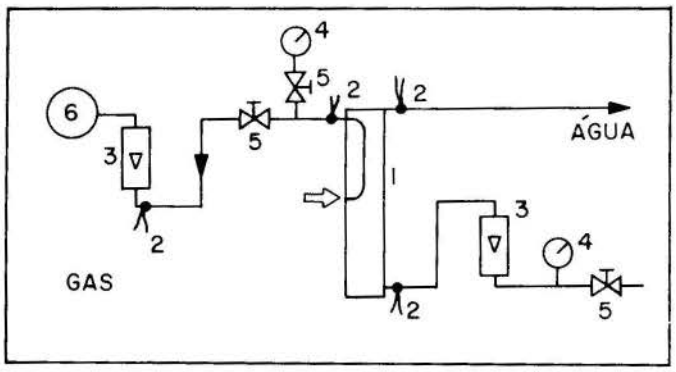

Fig. 2. Esquema da instrumentação. 1- sonda de entalpia; 2- termopar; 3- rotâmetro; 4- manômetro; 5- válvula; 6- bomba de vácuo.

A sensibilidade aumenta com o aumento da vazão de gás no tubo interno e diminuição da vazão da água. A sensibilidade é máxima quanto maior for a transferência de calor do tubo interno para a água. O limite de velocidade do gás no tubo interno é a velocidade local do plasma. O aumento dessa velocidade acima desse limite resulta num valor de entalpia sobreestimado.

À partir das medidas de temperatura e velocidade é possível calcular os fluxos de massa e energia que atravessam um plano perpendicular ao eixo do jato, pelas fórmulas:

$$G_z = \int_0^R \rho v 2\pi r dr, \tag{6}$$

para o fluxo de massa e

$$P_z = \int_0^R \rho v h 2\pi r dr \ , \tag{7}$$

para o fluxo de energia, onde R é o raio do jato.

Os cálculos dos fluxos de massa e energia, assim como da quantidade de movimento e do momento angular possibilitam obter-se uma visão mais profunda da dinâmica do jato. Os jatos com vorticidade se caracterizam pela maior capacidade de arraste, maior transferência de ca

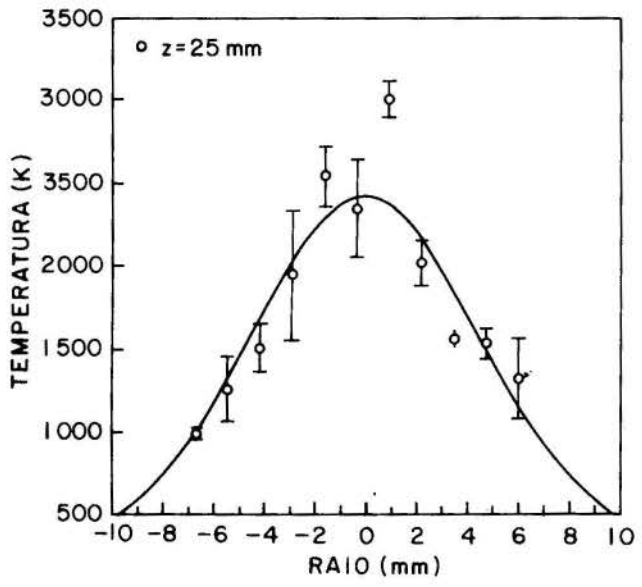

Fig. 3. Perfil de temperatura para z = 25mm.

lor, possuem um ângulo de abertura maior, têm menor alcance, do que os jatos sem vorticidade [9,10]. Além disso, a pressão estática apresenta gradiente radial sendo menor do que a pressão ambiente.

Uma das características mais importantes dos jatos é a sua capacidade de arraste, isto é, do aumento de sua massa às expensas do gás circundante. A característica do arraste é dada pelo parâmetro:

$$\Delta G = (G_z - G)/G \quad , \tag{8}$$

onde G_z é calculado por (6) e G é a massa de gás que sai pelo bocal. O estudo do arraste, em função da distância, e grau de vorticidade, é apresentado em [10,11], para fluxo de gás isotérmico . No nosso caso, além de o gás estar ionizado (plasma), o fluxo apresenta grande inhomogeidade. Entretanto, como veremos, certas características dos fluxos isotérmicos parecem prevalecer para o jato de plasma. No jato sem vorticidade, o arraste varia linearmente com a distância e é dado por

$$\Delta G = 0{,}32 \, \frac{z}{d} \sqrt{\frac{\rho_1}{\rho_2}} \quad , \tag{9}$$

sendo ρ_1 e ρ_2 as densidades do gás do jato e do gás exterior, respectivamente.

Ao contrário do jato sem vórtice, o jato com vórtice apresenta duas regiões distintas de variação de ΔG com z/d. A primeira região, imediatamente após o bocal, apresenta rápido aumento de ΔG com z/d e não depende da densidade do gás ambiente. Nessa região, a fórmula que se aplica é [10,11]

$$\Delta G = 0{,}5\,\Theta + 0{,}207\,(1+2\Theta)\,\frac{z}{d} \quad , \tag{10}$$

onde Θ é o parâmetro de vorticidade, que é dado por $\Theta = M/KR$, sendo $M = \int_0^R \rho v r u_\phi 2\pi r dr$, o momento angular e $K = \int_0^R \rho(v^2+p_o)2\pi r dr$ a quantidade de movimento do jato, R o raio do bocal, u_ϕ a componente tangencial da velocidade e v a componente axial.

Na segunda região, mais afastada do bocal, o arraste de gás cresce mais lentamente que na primeira região, e é dado pela fórmula:

$$\Delta G = \left(a\,\frac{z}{d} + \frac{k\Theta}{2}\right)\sqrt{\frac{\rho_1}{\rho_2}} \quad , \tag{11}$$

onde k = 4,4 e a = 0,32.

Para procedermos à uma estimativa da vazão de água necessária para a refrigeração da sonda, faz-se necessário calcular a potência térmica recebida pela sonda do fluxo de plasma na qual ela se encontra mergulhada. Medidas feitas por Grey [7] mostraram que menos de 0,5% da energia do plasma é perdida por radiação. Assim, o cálculo se restringirá à convecção térmica para o escoamento cruzado com gases. A fórmula utilizada é a dada em [12]

$$Nu = CRe^n Pr^{1/3} \quad , \tag{12}$$

onde as constantes C e n são dadas na mesma referência, pag. 269 e os números de Nusselt, Reynolds e Prandtl são calculados na temperatura de película $T_f = (T_p+T_\infty)/2$, sendo T_p a temperatura da parede e T_∞ a temperatura do plasma. O diâmetro utilizado é D_1, diâmetro externo da sonda. Os cálculos mostram que a potência térmica incidente na sonda é praticamente independente da temperatura da parede em virtude de $T_\infty >> T_p$. Considerando T_p = 150°C, T_∞ = 4027°C, Re(plasma) = 2291, Re(água) = 8310 (transporte bifásico), obtém-se uma potência térmica de 796W. Nos cálculos consideramos que o calor penetra uniformemente no cilindro, isto é, ao longo de toda a sua superfície externa $\pi D_1 L$. Para fazermos essa suposição , tomamos por base o gráfico apresentado na pag. 269 de [12]. Este cálculo é estimativo, uma vez que a fórmula (12) não leva em conta efeitos de recombinação nas proximidades da sonda.

CONDIÇÕES EXPERIMENTAIS

O maçarico de plasma. Foi utilizado neste trabalho, um maçarico de plasma à arco elétrico com estabilização em vórtice e funcionando à ar comprimido. Maiores detalhes sobre esse equipamento estão descritos em outro trabalho desta Conferência [2]. Para se obter as características médias do fluxo de plasma na saída do maçarico, medem-se as perdas térmicas para os eletrodos através da água de refrigeração, isto é $P_e = \Sigma \dot{m}_{ai} c_{pa} \Delta T_{ai}$, sendo $\dot{m}_{ai}$ a vazão de água do catodo e anodo e ΔT_{ai} a elevação de temperatura da água. A eficiência, então, é obtida por $\eta = (P-P_e)/P$, onde P = UI é a potência elétrica fornecida, sendo U a tensão e I a corrente. Sabendo-se a eficiência, podemos calcular a entalpia média $\bar{h}_2$ do fluxo de plasma na saída do canal pela fórmula $\eta = \Delta\bar{h}G/P$, onde $\Delta\bar{h} = \bar{h}_2 - h_1$ é a elevação da entalpia do gás e G é a vazão de gás. O conhecimento de $\bar{h}_2$ permite obter, de tabelas, a temperatura média do plasma na saída do maça

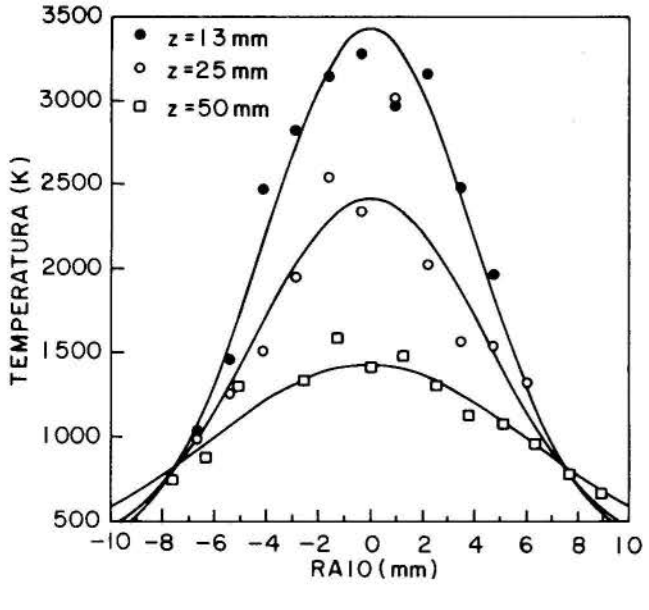

Fig. 4. Perfis de Temperatura

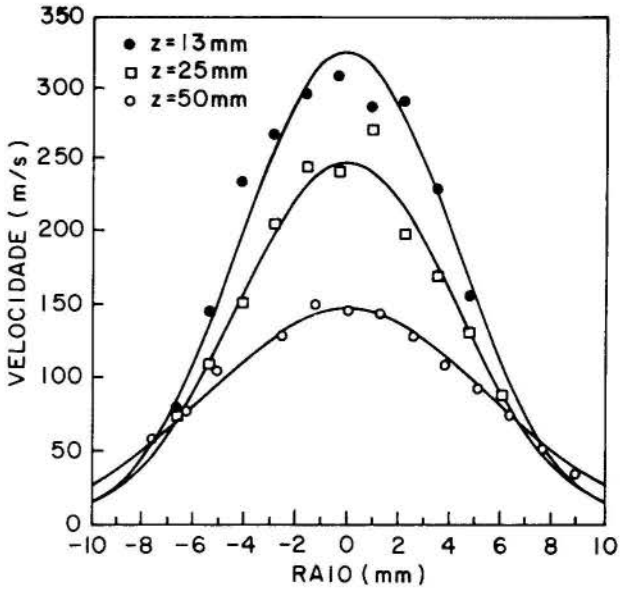

Fig. 5. Perfis de velocidade

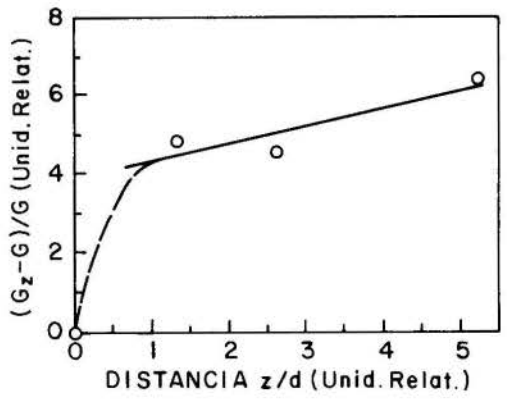

Fig. 6. Arrastamento de massa.

rico. A velocidade média do gás obtém-se da fórmula $G = \bar{\rho}_2 \bar{v}_2 A$, sendo $\bar{\rho}_2$ a densidade do gás na saída e A a área do canal. As medidas com a sonda de entalpia, que descrevemos abaixo, foram sempre feitas nas seguintes condições : diâmetro do anodo - 9,52mm, comprimento do anodo - 120mm, potência elétrica - 21,6kW, tensão - 230V, corrente-94A, vazão de gás-$1{,}613 \times 10^{-3}$kg/s (74,9 Nℓ/min), eficiência $\eta = 61\%$, potência térmica - 13,18kW. Os parâmetros calculados do fluxo de plasma, baseados nos dados acima, na saída do canal, são os seguintes (em valores médios) : $\bar{h}_2 = 8600$kJ/kg, $\bar{T}_2 = 4340$ K, $\bar{v}_2 = 349$m/s, $\bar{M}_2 = 0{,}26$, $\bar{p}_2 = 29{,}6$ mmHg, $\bar{p}_T = 736$ mmHg, onde h,T,V,M,p e p_T são, respectivamente, entalpia, temperatura, velocidade, número de Mach, pressão dinâmica e pressão total. Considerou-se que a pressão estática no laboratório era $\bar{p}_o = 706$mmHg, a densidade do ar, nas condições acima, $\bar{\rho}_o = 6{,}4 \times 10^{-2}$ kg/m^3, a velocidade do som $\bar{a}_2 = 1340$m/s e a constante adiabática $\bar{\gamma}_2 = 1{,}234$. A diferença entre a temperatura real e a de estagnação é $\bar{T}_{o2} - \bar{T}_2 = 34$K, sendo portanto, desprezível.

A sonda de entalpia. A sonda de entalpia foi construída de acordo com a Fig. 1. Suas características são as seguintes:

diâmetro externo da sonda	D_1	= 3,94 mm
diâmetro interno do tubo de água	D_2	= 3,85 mm
parede do tubo de água	ΔR	= 0,18 mm
diâmetro externo do tubo de gás	d_1	= 2,10 mm
diâmetro interno do tubo de gás	d_2	= 1,67 mm
parede do tubo de gás	Δr	= 0,22 mm
comprimento total da sonda	l	= 20 cm
comprimento da sonda exposto ao plasma	L	≅ 20 mm

Os tubos de cobre usados foram os encontrados normalmente no mercado. Suas dimensões originais eram $D_1 = 4{,}76$mm, $D_2 = 3{,}50$mm, $\Delta R = 0{,}63$mm e $d_1 = 2{,}77$mm, $d_2 = 1{,}67$mm e $\Delta r = 0{,}55$mm. A diminuição das dimensões foi obtida por corrosão química com hipoclorito de ferro (normalmente usado na confecção de circuitos impressos). O tubo de gás foi soldado ao tubo de água com solda prata.

Os termopares do tipo J(ferro-constantan), cuja sensibilidade é 0,05m V/^{o}C, foram envernizados com verniz isolante de transformador afim de evitar a condução elétrica através da água de refrigeração, uma vez que não usamos água deionizada. Como referência, usamos um banho de água destilada e gelo. Para a leitura da temperatura utilizamos um milivoltímetro digital de 4 1/2 dígitos com fundo de escala de 199,99mV, o que proporciona uma precisão na temperatura de ± 0,2^{o}C. Os termopares foram individualmente calibrados.

A refrigeração da sonda é feita em água à 14^{o}C e à pressão de 4 atm, fornecida pelo sistema, em circuito fechado, de refrigeração do prédio onde está instalado o laboratório. O sistema de refrigeração da sonda é mostrado na Fig. 2.

O sistema de amostragem do gás é apresentado, também, na Fig. 2. O gás é aspirado pelo tubo interno da sonda, passa pelo termopar e pelo rotâmetro. Uma válvula, situada antes do rotâmetro, ao ser fechada, permite medir-se a pressão dinâmica do plasma num manômetro.

RESULTADOS E DISCUSSÕES

As medidas foram feitas em três planos normais ao eixo do jato de plasma, distantes da saída do canal em z = 13mm, z = 25mm, z = 50mm. Em cada plano, foram levantados de 10 a 14 pontos, distantes um do outro de 1,27mm. Em cada ponto, foram feitas três medidas, na situação de fluxo, e três, na situação de não-fluxo. O total de medidas, em cada ponto, leva 12min para ser realizado e o tempo total por cada perfil leva cerca de 2 horas para ser obtido, pois é necessário que se espere num certo tempo para que se estabilize a temperatura na sonda. A sonda atravessa o plasma, fazendo com que o orifício de entrada do gás passe pelo eixo do jato de plasma. Na Tabela 1 apresentamos uma amostra dos resultados obtidos para z = 13mm, x = 0,31mm, afim de dar uma idéia das temperaturas e vazões envolvidas na experiência. Na Fig. 3 é apresentado o perfil de temperatura com as barras de erro (desvio padrão para três medidas), medido para z = 25mm. Os três perfis de temperatura e velocidade são mostrados, respectivamente nas Figs. 4 e 5. O ajuste aos dados experimentais foi realizado usando as funções

$$T(r) = T_o \exp\left[-ar^2\right] + T_a \quad \text{e}$$
$$v(r) = v_o \exp\left[-br^2\right], \qquad (13)$$

respectivamente, para a temperatura e velocidade, sendo $T_a = 300$K a temperatura ambiente e o centro r = 0 foi tomado coincidindo com o eixo do maçarico.

Tabela 1. Amostra de dados obtidos (z=13mm, r=0,31mm)

		c/fluxo	s/fluxo
$\dot{Q}_a$	(ℓ/min)	0,500 ± 0,025	0,500 ± 0,025
$\dot{Q}_g$	(ℓ/h)	50,0 ± 5,0	---
T_{a1}	(^{o}C)	13,8 ± 0,2	13,8 ± 0,2
T_{a2}	(^{o}C)	47,1 ± 0,2	43,3 ± 0,2
T_{g3}	(^{o}C)	52,3 ± 0,2	---
T_{rot}	(^{o}C)	21,8 ± 0,2	---
P_{rot}	(mm$H_2$0)	370,0 ± 4,0	470,0 ± 4,0

O arraste de massa ΔG, apresentado na Fig. 6, foi calculado pela fórmula (8) onde $G = 1{,}63 \times 10^{-3}$ Kg/s. Como vemos, o comportamento é semelhante ao apresentado pelo fluxo isotérmico [10,11], tendo duas regiões características, a primeira, com um crescimento rápido do arraste e a segunda, mais suave. Devido à insuficiência de dados, não é possível especificar exatamente os limites da primeira região. Na Fig. 7 vemos o comportamento da velocidade e temperatura axiais e na Fig. 8, da temperatura média. Para os pontos z = 13, 25, 50mm calculamos inicialmente, a entalpia média $H_z = P_z/C_z$ e desta, da tabela [8], a temperatura. Para $\bar{z} = 0$, a temperatura foi calculada pelo balanço térmico do maçarico. Como vemos, há uma grande queda da temperatura média na região $0 < z < 10$mm, caindo menos rapidamente para $z > 10$mm. Esse comportamento da temperatura está em acordo com o comportamento do arraste (Fig.6) que apresenta, também, duas regiões características, mostando que o arraste tem por efeito um forte resfriamento do jato de plasma. O ajuste aos pontos experimentais da Fig. 6 dá, para a segunda região $z > 10$mm, a reta:

$$\Delta G = 3{,}833 + 0{,}463z/d. \qquad (14)$$

Comparando esta fórmula com a fórmula (11) obtém-se $a \cong 2$ e $k\theta \cong 33$, sendo $\rho_1 = 6{,}4\times10^{-2}$ kg/m^3 (para T = 4340K) e $\rho_2 = 1{,}18$ kg/m^3.

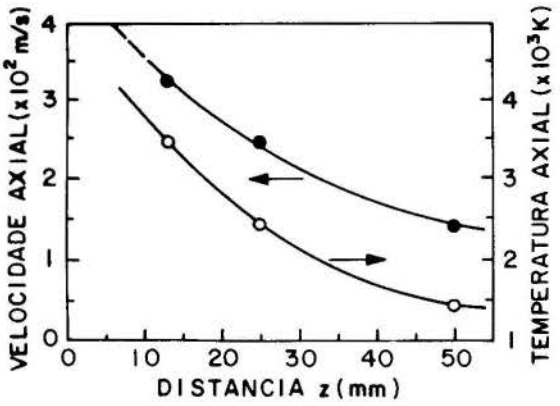

Fig. 7. Velocidade e temperatura axiais.

O balanço de energia P_z/P é apresentado na Fig. 9. Esse gráfico mostra um déficit de energia para z>25mm da ordem de 20%. Esse gráfico serve para se ter uma idéia geral da precisão da experiência, podendo servir para a calibração do sistema. Uma possível explicação para o déficit de energia é que o jato de plasma tem uma extensão radial em termos de energia maior do que os limites de integração usadas no cálculo. Tendo em vista o alto nível de arraste, esse erro de 20% é suficientemente pequeno para validar os resultados obtidos.

CONCLUSÕES

Foram feitas medidas dos perfis de temperatura e velocidade, utilizando uma sonda de entalpia, ao longo do jato de ar de um maçarico de plasma com vórtice. A análise mostrou que, para efeito da determinação da velocidade, o jato pode ser considerado incompressível. Verificou-se, também, que os efeitos de turbulência e viscosidade podem ser considerados desprezíveis para a obtenção da velocidade. Devido à alta temperatura do plasma, a potência térmica incidente na sonda, praticamente não depende da temperatura de parede para um modelo onde não se consideram efeitos de recombinação na camada limite. O cálculo do arraste de gás mostrou que o comportamento do jato de plasma em vórtice, que é fortemente inhomogêneo, tem certa semelhança com o jato isotérmico com vorticidade, apresentando duas regiões distintas no arraste, uma próxima ao bocal, com forte crescimento do arraste, e outra mais afastada, com crescimento do arraste mais lento com a distância ao bocal. Esse resultado se reproduz na medida da temperatura média que cai rapidamente na primeira região. O fluxo de energia relativo mostra a presença de um déficit de 20%. Esse erro, entretanto, é suficientemente pequeno para não invalidar os resultados obtidos.

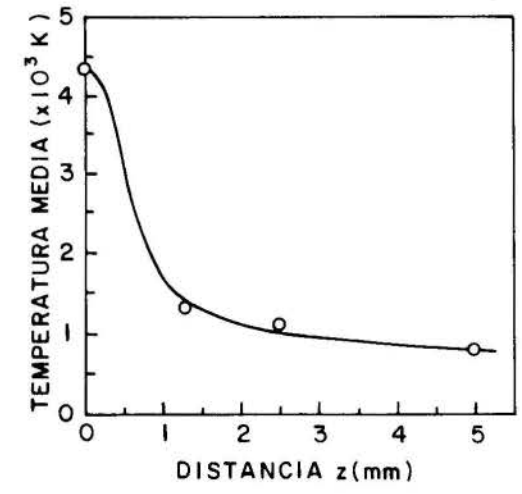

Fig. 8. Temperatura média.

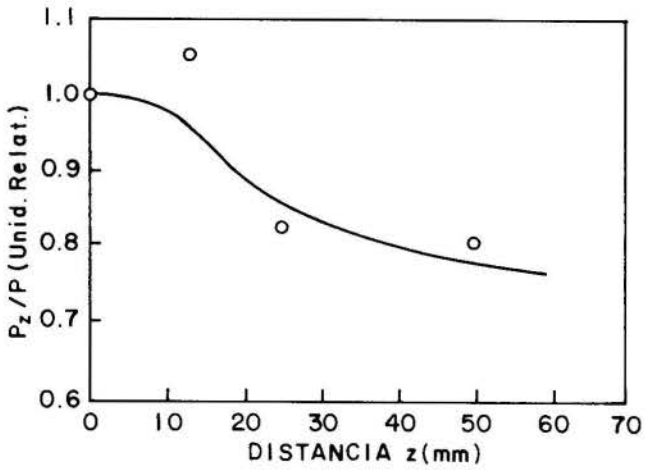

Fig. 9. Balanço de energia.

Agradecimentos

Agradecemos ao Prof. Dr. Daltro Garcia Pinatti da FTI/CEMAR e UNICAMP/IFGW pelo fornecimento do zircônio. Agradecemos ao Dr. Solonenko, O.P., pesquisador do Instituto de Termofísica da Academia de Ciências da URSS, Seção Siberiana, em Novosibirsk e ao Prof. Dr. Kamal Abdel Radi Ismail, da Faculdade de Engenharia Mecânica da UNICAMP pelas valiosas discussões. Agradecemos o suporte do CNPq, FAPESP, FINEP e UNICAMP.

REFERÊNCIAS

[1] Cunha, A.G. "Desenvolvimento de uma Sonda de Entalpia e Aplicação ao Maçarico de Plasma", Tese de Mestrado, 1988, UNICAMP.

[2] Marotta, A. "Potência Térmica Dissipada no Catodo de um Maçarico de Plasma de Ar" II Encontro Nacional de Ciências Térmicas, 10-12/12/90, Itapema, SC, Brasil.

[3] Cunha, A.G. e Marotta, A. "Low Erosion Rate of Zirconium Cathode in a Plasma Torch" 16th IEEE Internacional Conference on Plasma Science, 22-24/05/89, Buffalo, N.Y., USA, pp.66-7.

[4] Grey, J., Jacobs, P.F. and Sherman, M.P. "Calorimetric Probe for the Measurement of Extremely High Temperatures", Rev. Sci. Instr. 33,738-41 (1962).

[5] Grey, J. "Sensitivity Analysis for the Calorimetric Probe", Rev. Sci. Instr, 34, 857-59 (1963).

[6] Dresvin, S.V. editor. "Physics and Technology of Low Temperature Plasmas" The Iowa State University Press/AMES, 1977.

[7] Grey, J. "Probe Measurements in High Temperature Gases and Dense Plasmas", in "Temperature Measurements", Addison Wesley, 337-48, 1978.

[8] Vargaftik, N.B. "Tabelas de Propriedades Termofísicas de Gases e Líquidos". 2ª edição, Editora Nauka, Moscou, 1972.

[9] Abramovitch, G.N, Kracheninikov, S.I., Sekundov, A. N. e Smirnova, I.P. "Mistura Turbulenta de Fluxos Gasosos", Moscou, Nauka, 1974.

[10] Akhmedov, R.B., Balagula, T.B., Rachidov, F.K. e Sakaiev, A.I. "Aerodinâmica do jato em vórtice", Moscou, Energia, 1977.

[11] Maier P. "Untersuchung isothermen drallbehafteter Freistrahlen". Forsch. Ing., Nº 5, 133-64, 1968.

[12] Holman, J.P. "Transferência de Calor". McGraw-Hill, São Paulo, 1963.

ABSTRACT

This work gives some results for the profiles of temperature and velocity along a vortex plasma jet of an air plasma generator. The measurements were made using an enthalpy probe. Some factors influencing the measurement of the velocity were analysed. We calculated the mass and energy fluxes. From the mass flux , we concluded that a strong entrainment of the surrounding gas takes place along the air plasma jet. We notice clearly, the existence of two regions, the first , very close to the exit of the nozzle, with a very rapid increase in the entrainment with distance, the second region, somewhat downstream, shows a moderate increase in the entrainment. We conclude that the energy flux can be used for calibration of the system.

III ENCIT – Itapema, SC (Dezembro 1990)

NOISE AND SENSITIVITY ANALYSIS IN ELECTRICALLY COMPENSATED PYRANOMETERS

Lutero C. de Lima
Marcus A.V. Duarte
DEM-UFU
38.400 - Uberlândia - MG - Brazil

SUMMARY

In this study an analysis is showed of the electronic self-generated noise, the signal-to-noise ratio and sensitivity for electrically compensated pyranometers. The most significant conclusion from this study is that the source of self-generated noise in these instruments is due to the resistive relation between the sensors.

INTRODUCTION

Radiometers and/or absolute solarimeters of electrical compensation and of substitution such, for example, the Angström pyrheliometer, the Active Cavity Radiometer from Wilson, the Kendall radiometer and the electrical compensated pyranometers developed by Lobo and Beljo [1] and Lima and Lobo [2] are instruments which, having two absolutely equal sensors, one that receives the falling solar radiation and the other upon which the proportional electric energy is dissipated by Joulean effect, at their great majority use to be operated through negative feedback electric-eletronic servomechanism. The hot wire and hot film anemometers also operate through this principle. The instruments, product of this study, are two solarimeters which combine the property of self-adjust from the Callendar pyranometer, with the electrical compensation from the Angström radiometer. The thermoresistive sensor elements, absorber of the falling radiation and the from compensation, are maintained at the same temperature by an electronic circuit of feedback control which, heats preferentially the element not absorber from the solar energy (see Fig. 1).

In the present study a detailed theoretical analysis of the electronic noise, sensitivity and of the relation signal/noise from the two solarimeters is made in order to understand the influence of self-generated electronic noise at the voltage output of this kind of instrument.

NOISE ANALYSIS

In the present pyranometers, whose general scheme is shown in the figure 1, the electrical output indicates not only the falling radiation upon the solar sensor R_s but also irregular fluctuation of the output voltage which are caused by the electronic noise of the various parts of the instrument. The electronic noise covers the whole frequency range and disturbs the solar radiation measurements. The noise analysis that is to be shown here follows the same procedure proposed by Freymuth [3] for the study of noise in hotwire anemometry.

The noise is associated with the following: (1) the compensative R_c and solar R_s sensors as part of a nearly balanced Wheatstone bridge; (2) the bridge; and (3) the power and voltage amplifiers.

It is well known that a resistor R at temperature T produces within a small frequency range Δf, say 0.5 Hz, the following mean-squared thermal noise voltage (Johnson noise)

$$\bar{e}_R^2 = 4KTR\Delta f \qquad (1)$$

being K the Boltzmann's constant.

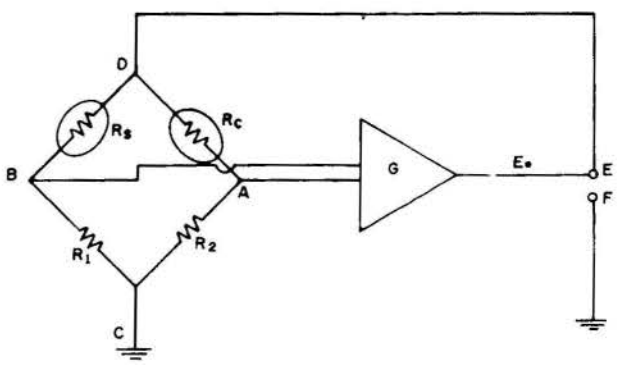

Fig. 1 - Pyranometer's general scheme

Consider the noise at the bridge diagonal AB which is generated by the various resistors and sensors of the bridge. The bridge is composed of the sensors R_s and R_c and resistors R_1 and R_2. R_1 and R_2 are maintained at ambient temperature T_o, while the two sensors are maintained at the temperature $T = T_o + \Delta T$ depending upon the falling radiation. The compensative sensor is maintained at the same temperature of the solar sensor, through the automatic bridge rebalancing. The ratio between R_c and R_2 and R_s and R_1 is defined as m, that is $R_c/R_2 = R_s/R_1 = m$ and between R_s and R_c and R_2 and R_1 is defined as n, that is $R_s/R_c = R_2/R_1 = n$. In this study m was assumed to be nearly unity.

The mean square value of the bridge noise is, considering e_{AC} and e_{BC} uncorrelated,

$$\bar{e}_B^2 = \bar{e}_{AC}^2 + \bar{e}_{BD}^2 \qquad (2)$$

being

$$\bar{e}_{AC}^2 = 4KT_oR_2\Delta f\left(\frac{R_c}{R_c+R_2}\right)^2 + 4KTR_c\Delta f\left(\frac{R_2}{R_c+R_2}\right)^2 \quad (3)$$

Observing that $R_2 \approx R_c$ and $T=T_o+\Delta T$, we obtain

$$\bar{e}_{AC}^2 = 4KT_oR_2\Delta f\frac{2+\Delta T/T_o}{4} \quad (4)$$

In the same way and after some algebraic manipulations

$$\bar{e}_{BD}^2 = 4KT_oR_2\Delta f\ \frac{2n}{4} \quad (5)$$

Therefore the total noise for the bridge is

$$\bar{e}_B^2 = 4KT_oR_c\Delta f\ \frac{2(1+n)+\Delta T/T_o}{4} \quad (6)$$

The noise in the amplifier can be represented as the noise of an equivalent resistor R_{eq} at the ambient temperature, that is

$$\bar{e}_a^2 = 4KT_oR_{eq}\Delta f \quad (7)$$

The total equivalent noise at the input of the amplifier is the sum of the bridge and the amplifier noises

$$\bar{e}_t^2 = 4KT_o\Delta f\left\{R_{eq}+R_c\frac{2(1+n)+\Delta T/T_o}{4}\right\} \quad (8)$$

Let us consider what effect the noise of the amplifier input has on the output EF of the self compensated pyranometer. To obtain the signal-to-noise ratio, let us consider, in addition, the effect of a small given radiation signal ΔH on the output of this instrument.

For the case where the bridge arms are not equal the basic equations for the compensative sensor, bridge and amplifier are:

$$\frac{E_o^2R_c}{(R_c+R_2)^2} = \frac{U(H)A}{R_a\beta}(R_c-R_a) + \frac{C}{R_a\beta}\frac{dR_c}{dt} \quad (9)$$

$$e = E_o(R_c-R_2)/[2(R_c+R_2)] \quad (10)$$

$$E_o = Ge_b + Ge + Ge_t \quad (11)$$

As already defined elsewhere[2], H is the radiation falling on the solar sensor, U(H) is the global heat transfer coefficient that mainly depends on radiation, β the temperature coefficient of the sensor resistance R_c, C is the sensor mass heat capacity, G the amplifier gain, E_o is the output voltage of the amplifier, e the input voltage, e_b is the input voltage of the amplifier with inputs grounded, e_t is the equivalent total noise of the bridge (including sensors) and the amplifier occuring at the amplifier input, and R_a is the resistance of the sensor at room temperature.

We are specially interested in the equations for the small deviations ΔE_o, Δe, and ΔR_c of the static values. To obtain them, eqs. (9)-(11) must be developed around their static values in a Taylor series, not considering terms greater than second order. Consequently, we obtain for the deviations ΔE_o, Δe, ΔR_c and ΔH the following equation system:

$$\frac{2E_oR_c}{(R_c+R_2)^2}\Delta E_o - \left[\frac{E_o^2(R_c-R_2)}{(R_c+R_2)^3} - \frac{U(H)A}{R_a\beta}\right]\Delta R_c - \frac{(R_c-R_a)A}{R_a\beta}\cdot\frac{dU(H)\Delta H}{dH} = \frac{C}{R_a}\frac{d\Delta R_c}{dt} \quad (12)$$

$$\Delta e = \frac{(R_c-R_2)\Delta E_o}{2(R_c+R_2)} - \frac{E_oR_2\Delta R_c}{(R_c+R_2)^2} \quad (13)$$

and neglecting e_b

$$\Delta E_o = G\Delta e + Ge_t \quad (14)$$

Through equation (13) and considering $R_c \approx R_2$, we obtain

$$\Delta R_c = \frac{(R_c-R_2)\Delta E_o}{E_o} - \frac{4R_2\Delta e}{E_o} \quad (15)$$

using the abbreviations

$$r = \frac{E_o^2(R_c-R_2)}{(R_c+R_2)^3} - \frac{U(H)A}{R_a\beta} \quad \text{and} \quad M = \frac{C}{R_a\beta r}$$

and introducing into the equation (12) we have

$$\Delta R_c + \frac{Md\Delta R_c}{dt} = \frac{2E_oR_c\Delta E_o}{r(R_c+R_2)^2G} - \frac{(R_c-R_a)A}{rR_a\beta}\frac{dU(H)}{dH}\Delta H \quad (16)$$

Solving equations (13)-(16) for ΔE_o we obtain

$$\Delta E_o = \frac{8rR_cR_2G}{E_o^2[1-2rR_c(R_c-R_2)/E_o^2]}\cdot\left(e_t + \frac{Mde_t}{dt}\right) + \frac{2R_c(R_c-R_a)AG}{E_oR_a\beta[1-2rR_c(R_c-R_2)/E_o^2]}\cdot\frac{dU(H)}{dH}\Delta H \quad (17)$$

Since $R_c \cong R_2$, we obtain

$$\Delta E_o = \frac{8rR_cR_2G}{E_o^2}\cdot\left(e_t + \frac{Mde_t}{dt}\right) + \frac{2R_c(R_c-R_a)AG}{E_oR_a\beta}\cdot\frac{dU(H)}{dH}. \quad (18)$$

Equation (18) shows that the signal ΔE_o is composed of a noise voltage and a radiation voltage. Considering the noise voltage as frequency w dependent we obtain the following for the noise and radiation voltages, respectively

$$\Delta E_N = \frac{8rR_cR_2G}{E_o^2}\cdot(1+w^2M^2)^{1/2}e_t \quad (19)$$

as $w^2M^2 \gg 1$

$$\Delta E_N = \frac{8rR_cR_2G.wMe_t}{E_o^2} \quad (19a)$$

$$\Delta E_H = \frac{2R_c(R_c-R_a)AG}{E_oR_a\beta} \cdot \frac{dU(H)}{dH} \cdot \Delta H \quad (19b)$$

The signal to noise ratio is

$$SNR = \frac{\Delta E_H}{\Delta E_N} = \frac{E_o(R_c-R_a)A.(dU/dH)\Delta H}{4R_a\beta rR_2wMe_t} \quad (20)$$

Using equation (8), for a steady-state operation, the SNR turns

$$SNR = \quad (21)$$

$$= \frac{E_o(R_c-P_a)A(dU/dH)\Delta H}{4R_a\beta rR_2wM\left[4KT_o\Delta f\{R_{eq}+R_c/4(2(1+n)+T/T_o)\}\right]^{1/2}}$$

SENSITIVITY ANALYSIS

To better understand the role of different variables in the instruments output voltage, a sensitivity analysis has been carried out. This also provides valuable information on the tolerance needed to be maintained during sensor design. The pyranometers output voltage at steady-state operation, as defined previously, is

$$E_o = (R_c+R_2).\left[\frac{U(H)A.(R_c-R_a)}{R_a\beta}\right]^{1/2} \quad (22)$$

The sensitivity of a parameter Z with respect to another parameter X is defined by [5] as

$$S_X^Z = \frac{X\partial Z}{Z\partial X} \quad (23)$$

Using equation (23), the sensitivities of the output voltage E_o relative to different sensor parameters can be obtained as following:

$$S_{U(H)}^{E_o} = 0.5 \quad (24)$$

$$S_A^{E_o} = 0.5 \quad (25)$$

$$S_{R_c}^{E_o} = 3.7 \quad (26)$$

The experimental values used for the determination of the above sensitivities were taken from elsewhere [2].

DISCUSSION OF THEORETICAL RESULTS

Equation (8) which describes the total noise at the input of the amplifier shows that e_t increases with n and that for low bridge noise it is necessary to keep nm small. Often nm is made equal to 1, although in this study one of our instruments was assumed with nm equal approximately to 100 and the second one equal to approximately 1. Looking at equations (6) and (8) we see that the resistance R_c for the compensative sensor and the overheat ratio $\Delta T/T_o$ also play significant role for the noise increase. In this moment, we see that there is a limit for the values of R_c and the overheat ratio in order that the output voltage E_o be maintained at a secure value, i.e. a value with which the signal-to-noise ratio be significant.

Examination of equation (21) that describes the signal-to-noise ratio indicates that the SNR decreases with the product of heat capacity of the compensative sensor and the frequency. On the same way analogy we see that the SNR also decreases with the increase in the values of R_c, n and overheat ratio $\Delta T/T_o$. It is worth noting that contrary to some researchers [3,4] the equation for the SNR attained in this study indicates that the noise increases with the increase in the overheat ratio. As it will be shown later the parameters that contribute significantly for the increasing of the SNR value are the output voltage E_o that is related to the amplifier gain G, the value of R_c and the value of the surface that receives the falling radiation It must be stressed that there is technical limitation for the manufacture from sensors, with restriction to the values of R_c and A. Although not highlighted by others studies in the literature to the opinion of the present authors the term that most influence the SNR of a self compensated pyranometer is the relation n, i.e., the relation between R_1/R_2 and R_s/R_c, as demonstrated by equation (21).

Equation (23) shows that the output voltage E_o of the present instrument is most sensitive to variation in the resistance value of the compensative sensor R_c, however R_c can not be increased indefinitely because of technical limitation in its manufacture. Although for this study the sensors were made of platinum fused upon pyrex substrate the range of material used for sensing elements is great. For the most of the resistance-temperature applications, the sensitivity depends on the product of resistivity and thermal coefficient of resistance defining by this way the sensing element electrical resistance. Tabulated data in the literature indicate that there are very interesting elements such bismuth, antimony and zirconium showing values of that product greater than most metallic elements.

CONCLUSION

In this study a detailed theoretical analysis of the self generated electronic noise, the signal-to-noise and sensitivity is made, for electrically compensated pyranometers. The most significant conclusion is that the greatest source of self generated electronic noise in this kind of instrument is due to the resistive relation n between the sensors, that is how much one sensor has resistance greater than the other and that at an unitary resistive relation the instrument accuses the minimal level of self generated electronic noise. A sensitivity analysis also accused that the voltage output of these pyranometers is most sensitive to variation in the resistance value of the compensative sensor.

REFERENCES

[1] Lobo, P.C. and Belo, F.A., "Experimental Validation of a Loss Compensated Radiometer", Proc. ASME Solar Energy Division 5th Annual Technical Conference, New York, USA, 1983.

[2] Lima, L.C. and Lobo, P.C., "An Electrical Compensated Pyranometer with Plane Sensors, First World Conference on Experimental Heat Transfer, Fluid Mechanics, and Thermodynamics, Dubrovnik, Yugoslavia, Sept.,1988.

[3] Freymuth, Peter, "Noise in Hot-Wire Anemometers", The Review of Scientific Instruments, Vol. 39(4), pp. 550-557, 1968.

[4] Kidron, I., "The Signal-to-Noise Ratios of Constant-Current and Constant-Temperature Hot-Wire Anemometers", IEEE Transactions on Instrumentation and Measurements, Vol. IM-16, nº 1, pp. 68-73, March, 1967.

[5] NG, K.T., Batchman, T.E., Pavlica, S. and Veasey, D.L., "Noise and Sensitivity Analysis for Miniature E-Field Probes", IEEE Transactions on Instrumentation and Measurement, Vol. 38, nº 1, pp. 27-31, February, 1989.

III ENCIT – Itapema, SC (Dezembro 1990)

TERMOPILHAS PRETO/BRANCO DE FILMES FINOS E APLICAÇÃO EM PIRANÔMETROS

João Francisco Escobedo*, Gilberto Lage** e Antonio A. Martins*
*Dep. de Biofísica - IB - UNESP - 18610 - Botucatu(SP)
**Dep. de Ciências Exatas - ESAL - 37200 - Lavras(MG)

RESUMO

Dois tipos de termopilhas preto/branco foram elaboradas por técnicas de filmes finos e testadas em vários piranômetros. Na calibração dos piranômetros, obtivemos sensibilidade de $7{,}7.10^{-6}$ Vm^2/W à $54{,}56.10^{-6}$ Vm^2/W com desvios aproximados desde 0,2 % à 0,7% em relação aos piranômetros Eppley e Middleton, e constantes de tempo de 0,85 s à 9,8 s. Curvas de insolação global, foram registradas com os piranômetros.

INTRODUÇÃO

Termopilhas de filmes finos obtidas por "evaporação de metais" ou "Sputtering", vem sendo estudadas desde a década de 30 por muitos pesquisadores. A literatura mostra que os trabalhos pioneiros foram apresentados por L. HARRIS; W.BUSSEN; MOLL e H.C. BURGER; STOCKFLETH; SCHWARZ e BROWN /1/2/. Posteriormente, BAKER /3/; L.P. BOIVIN e SMITH /4/, entre outros colaboraram no desenvolvimento da técnica realizando importantes aplicações dentro da radiometria solar. No Brasil, o processo foi introduzido por ESCOBEDO/5/ em 1986, que através de um método simples obteve vários tipos de termopilhas. Dando sequência ao desenvolvimento tecnológico deste sensor, bem como da sua aplicabilidade dentro da radiometria solar, neste trabalho apresentaremos resultados obtidos com piranômetros em suas características operacionais de constante de tempo, sensibilidade de resposta e linearidade, para várias termopilhas de filmes finos.

TEORIA E SELEÇÃO DE PARÂMETROS

A performance de uma termopilha pode ser calculada em dois estágios. No primeiro (efeito primário) o aumento da temperatura produzido pela radiação é calculado em função dos parâmetros térmicos como a capacidade e condutividade térmica. No segundo estágio (efeito secundário), o aumento de temperatura é utilizado para calcular a característica do sinal de saída representado pela responsividade ou sensibilidade de resposta. Um modelo para este cálculo é mostrado na Figura (1).

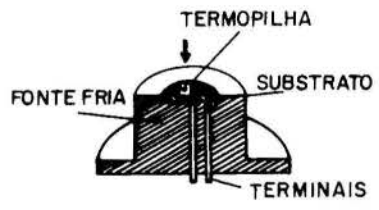

FIGURA 1: A termopilha em contacto com a fonte fria.

A termopilha é representada por um disco que está em contacto com uma fonte fria através da sua base inferior. O sensor possui uma capacidade térmica H em Joule por grau Kelvin (J/K) e uma condutância térmica K em Watts por grau Kelvin (W/K) para a fonte fria na temperatura T_A (temperatura ambiente). A fonte fria possui uma capacidade térmica elevada quando comparada com a da termopilha, de maneira que, quando exposta ao fluxo de radiação, sua temperatura permaneça constante.

Quando um fluxo de radiação $\phi(\omega)$ incide no absorvedor, o aumento de temperatura provocado ΔT pode ser calculado através do balanço de energia. Ou seja:

$$H \frac{d(\Delta T)}{dt} + K.\Delta T = \phi \qquad (1)$$

onde:

$H \frac{d(\Delta T)}{dt} = m.c_p. \frac{d(\Delta T)}{dt}$ = taxa de calor absorvida; m = massa da termopilha; c_p = calor específico do substrato; $K\Delta T$ = calor perdido através da condução térmica entre o detector e a fonte fria. Como a temperatura de operação da termopilha é muito próxima da temperatura ambiente, a perda por irradiação pode ser desprezada. Assumindo a potência radiante ser uma função periódica do tipo: $\phi = \phi_o.e^{j\omega t}$, onde:

ϕ_o = amplitude da radiação senoidal e $\omega = 2\pi f$

Temos para a equação diferencial linear (1), que:

$$H \frac{d(\Delta T)}{dt} + K\Delta T = \phi_o.e^{j\omega t} \qquad (2)$$

cuja solução é dada por:

$$\Delta T = \Delta T_o \cdot e^{-(K/H)t} + \frac{\phi_o.e^{j\omega t}}{(K + j\omega H)} \qquad (3)$$

O primeiro termo da equação é a parte transiente do aquecimento da termopilha, e quando o tempo aumenta, este termo decresce exponencialmente, tendendo a zero. Assim ele pode ser eliminado sem nenhuma perda generalizada na variação da temperatura ΔT. Assumindo que ε é a emissividade do absorvedor, podemos escrever que a variação de temperatura ΔT devido a um fluxo de radiação incidente na termopilha é:

$$\Delta T = \frac{\varepsilon.\phi_o.e^{j\omega t}}{K + j\omega H} \qquad (4)$$

tomando o módulo da expressão (4), temos que:

$$\Delta T = \frac{\varepsilon.\phi_o}{K\{1 + \omega^2(H/K)^2\}^{1/2}} \qquad (5)$$

A relação (H/K) possui dimensão de tempo e é denominada constante de tempo (τ). Como 1/e é igual aproximadamente a 0,368, a constante de tempo fica definida como o tempo necessário para a milivoltagem gerada na termopilha alcance 0,632 vezes o seu valor de equilíbrio. Este parâmetro determina para o sensor ou o instrumento que dele faz uso, a velocidade de resposta. Se a condutância térmica (K) for elevada, a termopilha responderá rapidamente (constante de tempo baixa). Se

contudo, a termopilha possuir grande capacidade térmica (H), sua resposta temporal será lenta (constante de tempo elevada). Assim, a constante de tempo é dada por:

$$\tau = H/K \qquad (6)$$

e a equação (5) pode ser escrita, como:

$$\Delta T = \frac{\varepsilon.\phi_o}{K\{1 + \omega^2\tau^2\}^{1/2}} \qquad (7)$$

Se N for o número de termopares e α constante termoelétrica (V/^oC) dos metais da termopilha, de acordo com o princípio de Seebeck, temos que o sinal de tensão produzido, é proporcional à variação de temperatura ΔT, e é dado por:

$$\Delta V = N \alpha \Delta T \qquad (8)$$

Substituindo (7) em (8), temos que:

$$\Delta V = \frac{N.\varepsilon.\alpha.\phi_o}{K\{1 + \omega^2\tau^2\}^{1/2}} \qquad (9)$$

A relação $\Delta V/\phi_o$ (VW^{-1}) é denominada: responsividade (R) e define para a termopilha a amplitude do sinal gerado em Volts por Watts de potência radiante incidente. Para frequência de resposta muito baixa, o produto $\omega^2.\tau^2$ é muito menor que 1, ou seja $\omega^2.\tau^2 << 1$, de forma que a equação (9) pode ser expressa aproximadamente por:

$$R = \frac{N.\alpha.\varepsilon.}{K} \qquad (10)$$

Uma pequena condutância térmica, e elevados valores do número de termopares, constante termoelétrica e emissividade, geram alta responsividade.

Nestas condições, a equação (6) nos mostra que temos uma limitação prática na performance do detector, pois ele terá uma constante de tempo elevada. Relacionando-se as equações (10) e (6), através de K, temos a responsividade em função da constante de tempo, por:

$$R = \frac{N.\alpha.\varepsilon.}{H} \cdot \tau \qquad (11)$$

que mostra a dependência de proporcionalidade entre estes dois parâmetros operacionais.

De acordo com as equações (6) e (10) a escolha para uma determinada aplicação, consiste basicamente em selecionar adequadamente o número de termopares, tipos de metais, capacidade e condutividade térmica do absorvedor. Para alguns tipos de aplicações é interessante termos responsividade elevada e baixa constante de tempo, como é o caso, por exemplo dos radiômetros de lasers e outros o contrário, como os radiômetros solares. Nosso interesse, continua sendo as termopilhas para uso na radiometria solar e o método de filmes finos permite a construção de termopilhas selecionando os parâmetros já citados. O número de termopares (N) em trabalhos anteriores pelo método de filmes finos, já obtivemos termopilhas com 36 e 60 termopares sem grandes dificuldades técnicas. Considerando que estes números proporcionam grande amplificação do sinal elétrico, mesmo que a constante termoelétrica do par metálico seja baixa, mantivemos o número 36 neste estudo.

Constante Termoelétrica (α): A seleção dos dois metais é feita pelo alto valor da constante termoelétrica, no entanto, dois pontos devem ser levados em consideração nesta escolha: os metais não devem mudar suas características após serem evaporados, e devem ainda serem resistentes a contactos mecânicos de modo a suportar as cargas das tintas absorvedora/refletora. Dos pares metálicos estudados e citados na literatura inclusive já testados por nós em pesquisas anteriores, o Bismuto/Antimônio cujo α= 109 $\mu V/^oC$ é o que preenche todos os requisitos, e portanto, continuamos com o mesmo.

Capacidade Térmica (H): A seleção do substrato, onde é depositado a bateria de termopares, parece ser o parâmetro mais importante nesta otimização, pois praticamente define as características desejadas da alta responsividade e velocidade de resposta. Este parâmetro deve ser baixo, quer seja pela massa ou calor específico do componente, ou então pelos dois: Para chegar a escolha, foi necessário testes preliminares com vários tipos de substratos como: vidro, acrílico, alumínio anodizado, alumínio com revestimento de óxidos de silício, que além de satisfazerem as condições anteriormente citadas, possuem superfícies polidas e apropriadas para depósitos de filmes finos. Outra característica importante testada nos substratos, foi a condutividade térmica, ou seja, não acumulam calor entre medidas. Este aspecto é fundamental para que a termopilha responda linearmente após horas de medições como nos radiômetros solares. Após os resultados, optamos pelo vidro e acrílico, que apresentaram valores de constante de tempo e responsividade aproximadas às termopilhas preto/branco importadas. Mantivemos, o substrato kapton neste estudo, considerando os bons resultados com ele já obtidos em estudos anteriores.

Condutância Térmica (K): quanto maior, mais rápida é a resposta da termopilha. Para este componente (extrator de calor), nós optamos pelo alumínio que além de leve, barato e fácil usinagem, é bom condutor térmico. No entanto, a configuração é o mais importante. Para se atingir um ótimo nessa construção, foi necessário alguns testes preliminares com vários extratores de calor para cada tipo de termopilha. Com esta técnica, foi possível reduzir em 50% os valores das constantes de tempo das termopilhas, sem causar perda na sensibilidade.

TERMOPILHAS

As Figuras (2) a (4) mostram as termopilhas construidas e submetidas nos testes experimentais neste trabalho. Elas foram obtidas através de processo fotográfico e filmes finos conforme descrito em /5/.

A Figura (2) mostra duas termopilhas estrela 36 termopares em kapton. (A espessura do kapton é de 25 μm, a espessura dos filmes finos de 3000 Å, e as resistências elétricas de 10,8 KΩ e 13,7 KΩ, respectivamente).

FIGURA 2: Termopilhas estrela 36 termopares em kapton. Termopilhas 1 e 2.

A Figura (3) mostra duas termopilhas disco-concêntrico 36 termopares. A da esquerda em kapton e da direita em vidro. (A espessura do vidro 0,5 mm e as resistências elétricas são 3,0 KΩ e 9,0 KΩ).

FIGURA 3: Termopilhas disco-concêntrico em kapton e vidro. Termopilhas 3 e 4.

A Figura (4) mostra uma termopilha estrela 36 em acrílico. (A espessura do acrílico é de 1 mm e a resistência elétrica de 11,4 KΩ).

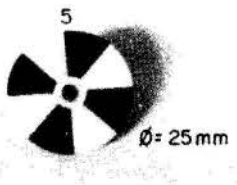

FIGURA 4: Termopilha estrela 36 termopares em acrílico. Termopilha 5.

As tintas preta e branca utilizadas no absorvedor das termopilhas são de boa qualidade ótica e térmica, de marca Colorgin. (Preto fosco 400 e branco geladeira). Testes espectrofotométricos da absortividade e refletividade já realizados após um ano de uso (descontínuo), mostraram que não houve mudanças nestes dois parâmetros na faixa espectral de 0,3 à 2,5 μm.

PIRANÔMETROS

Para a realização dos testes experimentais com as termopilhas já descritas, projetamos 3 piranômetros, como podem ser vistos na Figura 5.

Do ponto de vista tecnológico, os componentes que mais encarecem o piranômetro, são a termopilha e a cúpula, os demais, tais como corpo principal, nível de bôlha, conector elétrico, componentes de vedação e parafusos, comparados ao custo do aparelho, são relativamente baratos. Alguns desses componentes já com controle de qualidade podem ser encontrados comercialmente no país, enquanto outros podem ser usinados em oficinas de mecânica fina sem grandes dificuldades.

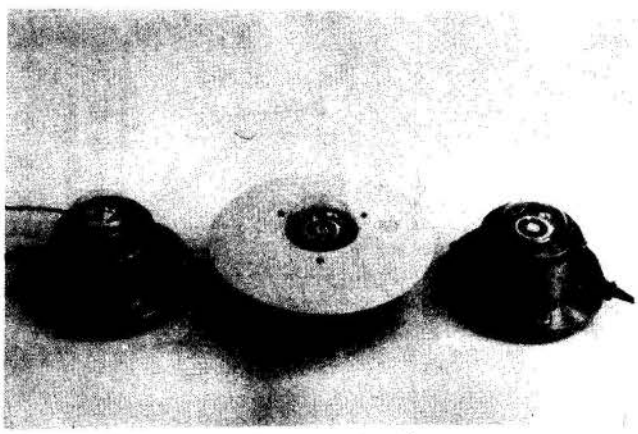

FIGURA 5: Fotografia dos Piranômetros.

É importante esclarecer que todos os componentes são importantes para o bom desempenho do piranômetro, um deles mal construido pode afetar consideravelmente a performance do instrumento. Como é um conjunto de características que classifica estes instrumentos de medidas, é fundamental que a construção seja equilibrada não só em termos das suas propriedades operacionais, como também em termos mecânicos e óticos, no sentido de minimizar os efeitos externos e intrínsicos que o piranômetro possui, como por exemplo, os efeitos de temperatura ambiente e cosseno, que interferem sistematicamente na linearidade do equipamento.

Considerando que não temos tecnologia desenvolvida para elaboração de cúpulas, e as termopilhas são objeto deste estudo para completar a construção dos instrumentos e realizar os testes com os piranômetros, achamos por bem utilizar cúpula de vidro comum, obtidas à partir de lâmpada comercial, visto que em experimentos anteriores já mostraram bons resultados /6/. Os critérios adotados para a seleção das mesmas foram o da transmitividade, homogeneidade e esferocidade da sua superfície. Testes espectrofotométricos com as cúpulas, garantem uma transmitividade de 95% na faixa do visível até 85% no infravermelho (2,5 μm). A resposta cosseno avaliada em um dos piranômetros construido (erro produzido pela resposta em função do ângulo de incidência), apresentou desvio de 2% para ângulo zenital de 70°. Para ângulos maiores que 80° o desvio é consideravelmente mais elevado.

A Figura (6) mostra uma fotografia de cúpula antes da montagem no aparelho.

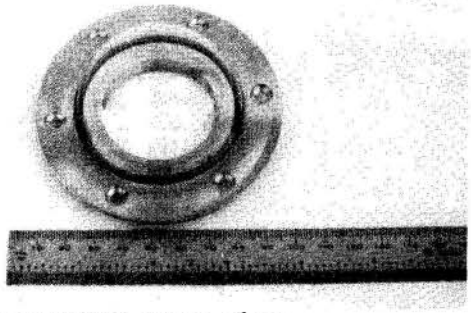

FIGURA 6: Fotografia de uma cúpula.

Os piranômetros foram construidos integralmente em aço inoxidável. O corpo principal é composto por uma base na forma disco ϕ = 15 cm e espessura e = 1 cm, acoplado através de solda tig à um tubo cilíndrico (altura = 4 cm, $\phi_{externo}$ = 9 cm e $\phi_{interno}$ = 8 cm). Neste componente, a base de rosca e vedação por o'ring, está instalado um conector elétrico de marca comercial MELRO. Uma tampa superior fecha o piranômetro com a cúpula fixada em sulco através de o'ring e cola resistente à umidade. A fixação da tampa superior no corpo principal é feita através de parafusos e a vedação por o'ring. Nestes acoplamentos, tomou-se cuidado especial com o nivelamento dos componentes e posicionamento da termopilha quanto à horizontalidade, centramento em relação ao corpo principal e à cúpula, respectivamente. Como as termopilhas são de diâmetros diferentes e os piranômetros somente 3, foi necessário construir várias tampas superiores adicionais, uma para cada diâmetro, a fim de que todas as termopilhas fosse testadas nos mesmos corpos principais.

CALIBRAÇÃO

Os piranômetros estão sendo submetidos a testes experimentais com luz natural desde junho de 1989 até o presente momento. Na ausência de um radiômetro absoluto, os instrumentos utilizados como referência na calibração dos nossos piranômetros são: um piranômetro Eppley PSP com sensibilidade de resposta igual à $9{,}48.10^{-6}$ Vm^2/W e um piranômetro Middleton $16{,}4.10^{-6}$ Vm^2/W. Ambos são instrumentos de medidas secundários e dos dois, o Eppley é o mais preciso, pois é de 1ª classe, o outro é de segunda classe, porém confiável, de acordo com a Organização Mundial de Meteorologia (O.M.M.). Portanto, as medidas de calibração são relativas e sujeitas aos erros dos dois piranômetros.

A constante de tempo, bem como a sensibilidade ou constante de calibração dos piranômetros, foram obtidas conforme a metodologia já descrita em /5/. Utilizamos um registrador potenciométrico de dois canais na obtenção das constantes de tempo e curvas de insolação global e dois multímetros 4 1/2 dígitos nas calibrações da sensibilidade.

CONSTANTE DE TEMPO, SENSIBILIDADE E LINEARIDADE

As Figuras de (7) a (11) mostram os resultados obtidos com os piranômetros em termos da curva de resposta, sensibilidade e Insolação Global para cada termopilha descrita. A Figura 7 a,b,c, mostra os resultados da termopilha (1) - estrela 36 em kapton (ϕ = 32 mm); a Figura 8 a,b,c, para a termopilha (2) - estrela 36 em kapton (ϕ = 25 mm); Figura 9 a,b,c, para a termopilha (3) - disco-concêntrico 36 em kapton (ϕ = 32 mm); Figura 10 a,b,c, para a termopilha (4) - disco-concêntrico 36 em vidro (ϕ = 22 mm) e a Figura 11 a,b,c, pa

ra a termopilha (5) - estrela 36 em acrílico (ϕ = 25 mm).

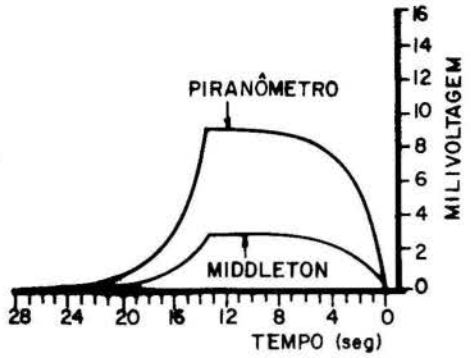

7a

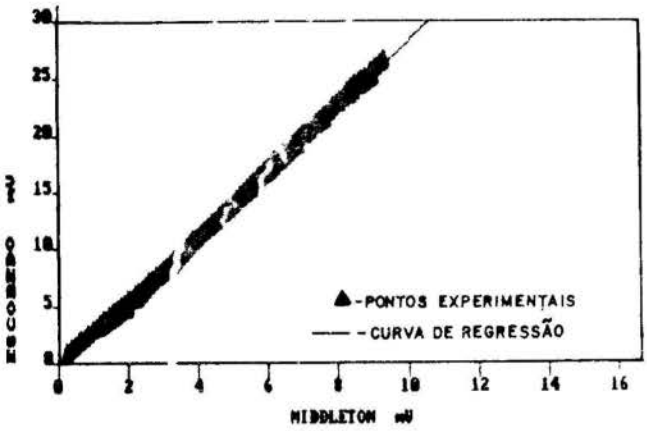

7b

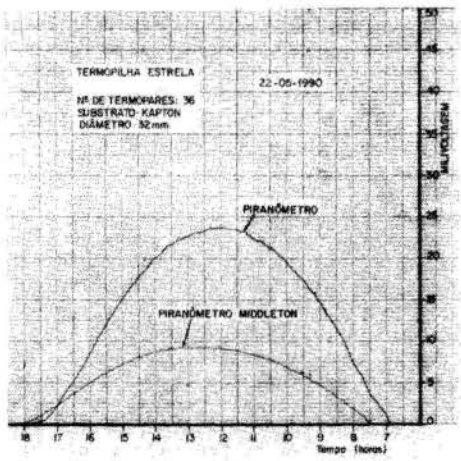

7c

FIGURA 7: Dados obtidos do piranômetro com termopilha 1. 7a. Curva de tempo de resposta; 7b. Calibração; 7c. Insolação Global.

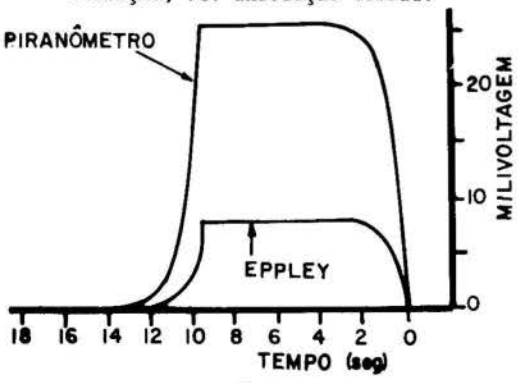

8a

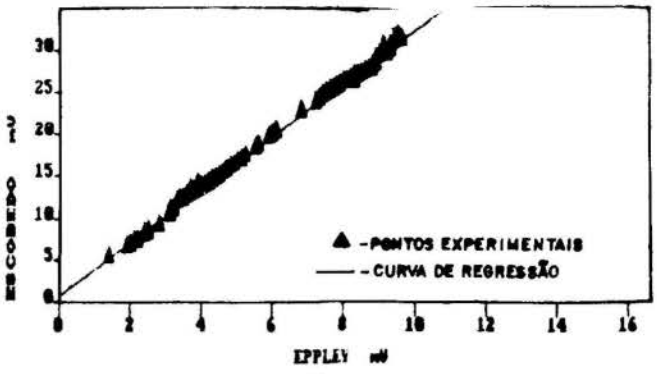

8b

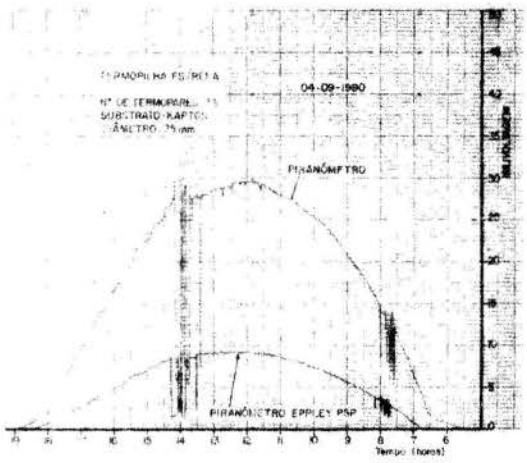

8c

FIGURA 8: Dados obtidos do piranômetro com termopilha 2. 8a. Curva de tempo de resposta; 8b. Calibração; 8c. Insolação Global.

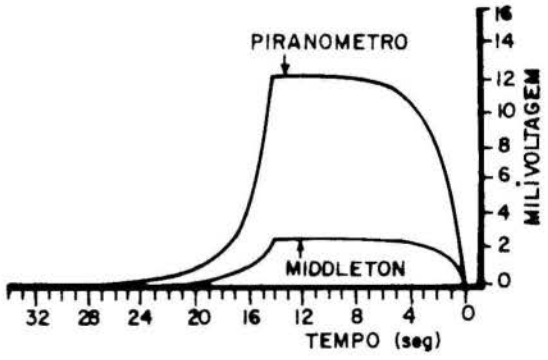

9a

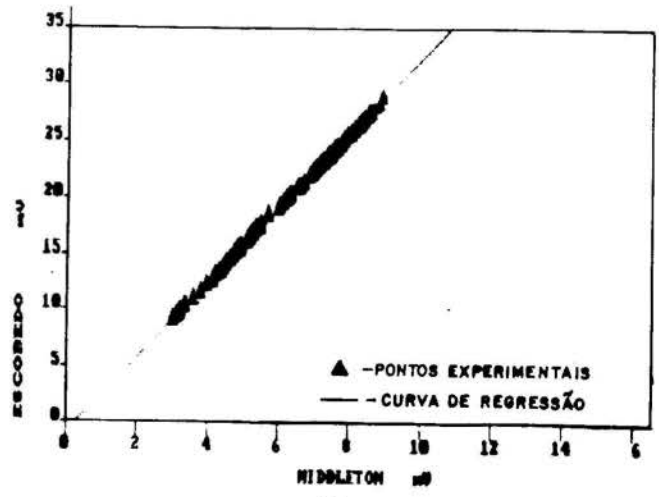

9b

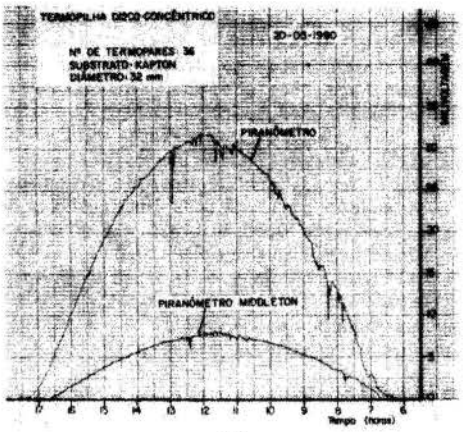

9c

FIGURA 9: Dados obtidos do piranômetro com termopilha 3. 9a. Curva de tempo de resposta; 9b. Calibração; 9c. Insolação Global.

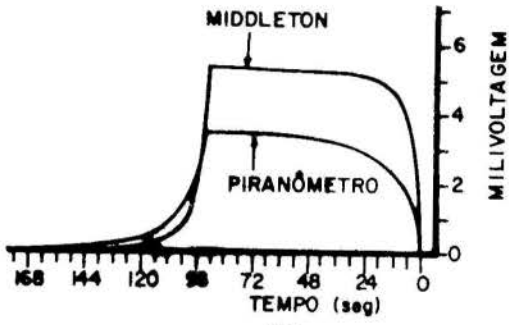

10a

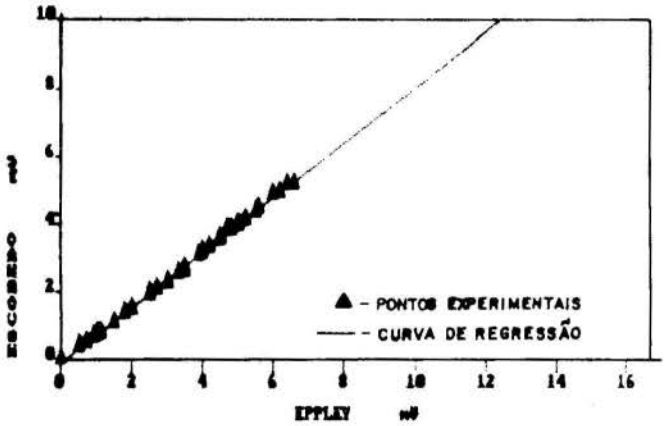

10b

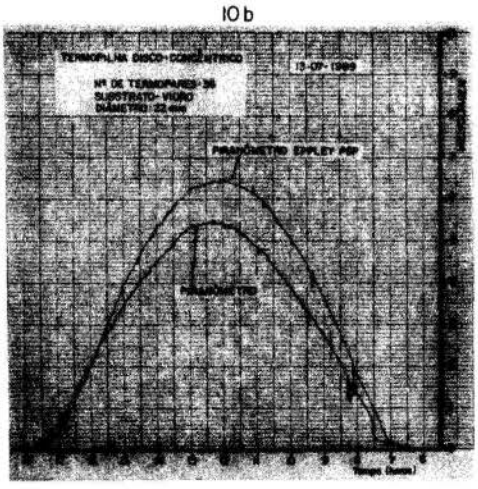

10c

FIGURA 10: Dados obtidos do piranômetro com termopilha 4. 9a. Curva de tempo de resposta; 9b. Calibração; 9c. Insolação Global.

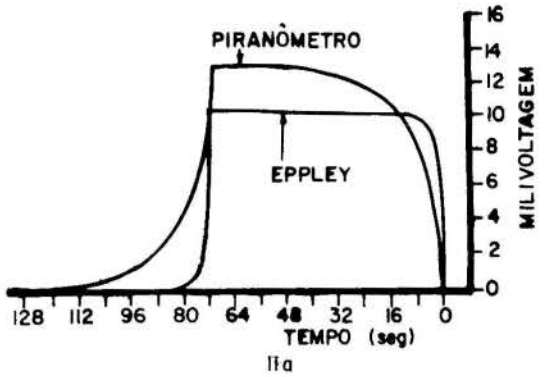

11a

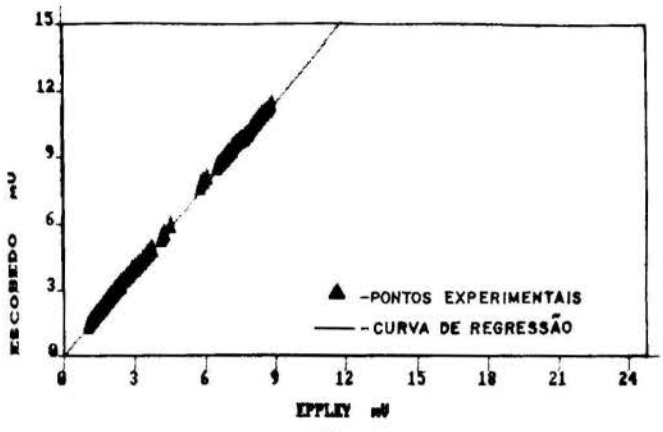

11b

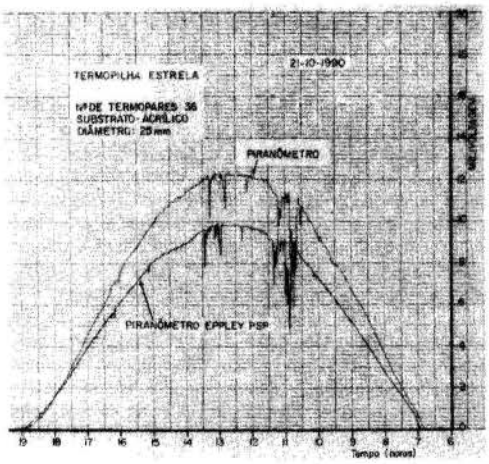

11c

FIGURA 11: Dados obtidos do piranômetro com termopilha 5. 11a. Curva de tempo de resposta; 11b. Calibração; 11c. Insolação Global.

Os resultados obtidos da calibração com seus respectivos testes estatísticos de regressão linear; coeficiente de regressão (b) e seu desvio de regressão (s_b), coeficiente de determinação (r^2) e o teste t a nível de 1%, estão apresentados na Tabela I.

TERMOPILHAS	Nº DE PONTOS	$b \pm s_b$	r^2	$t(p>0,01)$
1	185	2,888 ± 0,008	0,9987	382,32
2	80	3,119 ± 0,012	0,9975	170,19
3	71	3,327 ± 0,009	0,9996	395,12
4	40	0,815 ± 0,005	0,9987	165,16
5	120	1,272 ± 0,002	0,9998	778,56

TABELA I: Resultados dos ajustes das regressões lineares e seus respectivos testes estatísticos.

Os coeficientes de regressão da Tabela I, indicam quantas unidades de variação dos piranômetros em testes, representam em cada unidade de variação no padrão. Assim sendo, podemos calcular as constantes de calibração dos nossos piranômetros através do produto da constante de calibração conhecida dos piranômetros de referências pelos respectivos coeficientes de regressão. Como exemplo, tomamos o caso da termopilha (1) cujo b = 2,888, e calibrado pelo Middleton de $K = 16{,}40.10^{-6}$ Vm^2/W. Desta forma a constante do piranômetro (K_1) é igual a:

$$K_1 = 2{,}888 \times 16{,}40.10^{-6}\ Vm^2/W = 47{,}36.10^{-6}\ Vm^2/W$$

ou ainda:

$$K_1 = 47{,}36.10^{-6}\ Vm^2/W \pm 0{,}13$$ em relação ao Middleton.

O quadro II mostra os resultados de constante de tempo τ (tempo em que a milivoltagem atingiu 63,3% do tempo de equilíbrio das Figuras 7a.; 8a.; 9a.; 10a. e 11a.), constante de calibração de cada piranômetro e desvios.

PIRANÔMETROS	1	2	3	4	5
τ (s)	3,6	0,85	3,2	9,8	5,2
$K(10^{-6} Vm^2/W)$	47,36	29,57	54,56	7,73	12,06
$\pm s_k$	0,13 (M)	0,11 (E)	0,15 (M)	0,05 (E)	0,02 (E)

TABELA II: Resultados da constante de tempo, sensibilidades e desvios de linearidade, relativos ao piranômetro Eppley (E) e ao piranômetro Middleton (M).

Comparando os resultados obtidos com os piranômetros em suas características operacionais com piranômetros importados que utilizam a termopilha como sensor, citados na literatura /7/8/, observamos que os piranômetros com termopilhas em kapton atingiram valores extremos na sensibilidade de resposta e constante de tempo. O tipo disco-concêntrico atingiu uma constante de calibração $K = 54{,}56.10^{-6}$ Vm^2/W e o estrela 36 (ϕ = 25 mm) 0,85 s para constante de tempo. Esses valores são altamente significativos dentro da radiometria solar, pois piranômetros importados não possuem sensibilidade tão elevada e tão pouco uma velocidade de resposta tão pequena. Piranômetro com termopilha em acrílico, apresentou características semelhantes ao do Eppley preto/branco, enquanto que da termopilha em vidro, apenas aceitável. De uma forma geral todos os resultados foram considerados bons e se enquadram dentro dos limites estabelecidos pela Organização Mundial de Meteorologia.

A amostragem das curvas de insolação global obtidas por cada piranômetro em testes de campo, mostram um real desempenho dos instrumentos, acompanhando perfeitamento os piranômetros de referências (Eppley e Middleton) nas mais diversas situações de insolação. Estes fatos nos incentivam a encaminhar tais piranômetros para testes mais rigorosos no Instituto Nacional de Meteorologia (INAMET) em Brasilia, a fim de corroborar os resultados já obtidos e classificar os instrumentos dentro dos padrões da O.M.M.

No estágio em que se encontra este desenvolvimento tecnológico, é prematuro fazer análise de custo do instrumento, no entanto, sem levar em consideração a produção em série e computando apenas a elaboração da termopilha, do instrumento e dos materiais, estimamos ser da ordem de US$ 300.00 por unidade.

CONCLUSÕES

Termopilhas de filmes finos obtidos por evaporação de metais testados como sensor de radiação em piranômetros, apresentaram resultados em suas características operacionais de sensibilidade de resposta e constante de tempo, similares às dos piranômetros importados. Dos três substratos testados como absorvedor de radiação: kapton, acrílico e vidro, mais uma vez o kapton apresentou melhor desempenho, enquanto o acrílico satisfatório. Piranômetros com termopilhas em kapton apresentaram altas sensibilidades de resposta: $29{,}6.10^{-6}$ Vm^2/W à $54{,}6.10^{-6}$ Vm^2/W, com desvios da ordem de 0,3 % a 0,4% em relação aos piranômetros Middleton e Eppley, e constante de tempo de 0,85 s à 3,6 s. Piranômetro com termopilha em acrílico, apresentou $12{,}1.10^{-6}$ Vm^2/W para a sensibilidade com desvio de 0,2% em relação ao Eppley e constante de tempo de 5,2 s. Os resultados dos ajustes das regressões se mostraram significativos e expressaram um alto grau de fidedignidade.

BIBLIOGRAFIA

1) HARRIS, L. Rapid Response Thermopiles. Journal of Optical Society of America. Vol. 36, nº 10. 1946.

2) DERENIAK, E.L.; CROWE, D.G. Optical Radiation Detectors. John Wiley & Sous. 1984.

3) BUDDE, W. Optical Radiation Measurements. Academic Press. 1983.

4) BOIVIN, L.P. & SMITH, T.C. Electrically Calibrated Radiometer Using a Thin Film Thermopile. Applied Optics. 17. 1977.

5) ESCOBEDO, J.F.; PASSOS, E.F. e VIEIRA, A.C. Construção de Termopilhas para Radiômetros Solares d Lasers. Anais do II ENCIT. 113-116. 1988.

6) ESCOBEDO, J.F.; ZILO, S.C. e LAGE, G. Solarímetro Simples e de Baixo Custo para Equipar Estações Meteorológicas do Brasil. Anais da 42ª Reunião Anual da SBPC, p. 284-287. 1990.

7) ROBINSON, N. Solar Radiation, Elsevier, London, 1966.

8) COULSON, K.L. Solar Terrestrial Radiation, London, Ap. Cap. 4, pp. 85-141. 1975.

ABSTRACT

Two types of black and white thermopiles, were elaborated by thin films techniques and tested in several pyranometers. During the calibration of the pyranometers, it was obtained sensibilities response from $7{,}70.10^{-6}$ Vm^2/W to $54{,}56.10^{-6}$ Vm^2/W with the desviations from 0,2% to 0,7% in relation to Eppley and Middleton pyranometers, and time constants from 0,85 s to 9,8 s. Insolation global curves were registrade with the pyranometers.

AGRADECIMENTOS

À FAPESP e FUNDUNESP pelo financiamento do projeto, à Neisa Jovencio Narcizo, Dorival de Pieri, Vinicius S. Barbim e S.G. Manuel, pela colaboração prestada.

III ENCIT – Itapema, SC (Dezembro 1990)

PROTÓTIPO DE UM SISTEMA DE MEDIÇÃO DA TRANSPIRAÇÃO DA CANA DE AÇÚCAR POR BALANCO TÉRMICO

DULCÍDIO S. MANGUEIRA
Aluno de Mestrado em Engenharia Mecânica - UFPb

ALAIN PASSERAT DE SILANS
Professor Adjunto IV
UFPb - João Pessoa

RESUMO

Apresenta-se o princípio de funcionamento e os trabalhos dos testes experimentais de um protótipo de um aparelho destinado a medir o fluxo de seiva numa planta. Os experimentos foram efetuados em cana de açúcar. Um segmento da cana foi aquecido e o fluxo de seiva determinado por aplicação do balanço energético.

INTRODUÇÃO

A otimização dos sistemas de irrigação passa por uma estimativa precisa da transpiração das plantas. Estudos atuais [1] procuram estabelecer modelos complexos da transferência da água do solo para a planta e da planta para a atmosfera. O controle do consumo da planta quando in loco é imprescendível para a calibração destes modelos. Tendo em vista que os métodos de determinação direta da transpiração in loco não se aplicam em escala de tempo reduzida e para uma única planta, desenvolveu-se no Laboratório de Hidraúlica do Centro de Tecnologia da UFPb em João Pessoa um aparelho cuja finalidade é medir o fluxo de seiva, o qual é idêntico a transpiração nas horas onde a planta não acumula água nos seus tecidos [2], isto é, cedo pela manhã antes de se iniciar o processo de transpiração por abertura estomatal. Baseia-se o aparelho na aplicação do balanço de energia a um segmento do caule da planta e aquecido por uma resistência elétrica. Ao conhecimento dos autores, o método foi proposto recentemente por Valancogne et al. [5] e aplicado a pés de maçã e por Sakuratani [3,4] em pés de cana de açúcar. Em ambos os trabalhos, a transpiração foi medida em lisímetros instalados em casa de vegetação, isto é, em condições ambientais artificiais e controladas. Não fazem estes autores menção nenhuma a repartição dos diversos fluxos de calor envolvidos, nem sequer a ordem de grandeza das diferenças de temperaturas.

Neste trabalho apresenta-se os fundamentos teóricos do método, os detalhes construtivos do protótipo e a análise dos testes realizados com o mesmo exposto a condições atmosféricas naturais. O protótipo foi construido e testado para medir o consumo de água de uma cana de açucar.

Desenvolvimento Teórico

Na figura 1, apresenta-se esquematicamente o aparelho. Aplicando a equação do balanço de energia ao volume AA' BB', encontra-se a seguinte equação:

$$q = q_f + q_e + q_s + \Gamma \qquad (1)$$

onde: q representa o fluxo de calor condutivo radial que penetra no volume AA' BB' através da superfície externa. [watts]

q_e e q_s representam respectivamente o fluxo de calor condutivo que entra pela seção transversal AA' e que sai pela seção BB' [watts]

q_f representa o fluxo de calor transportado pela seiva entre as seções AA'e BB' [watts]

Γ é a quantidade de calor armazenada no volume de controle por unidade de tempo [watts]. Em regime permanente $\Gamma = 0$.

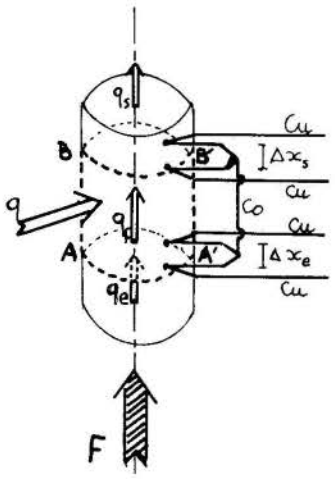

Fig. - 1 - Representação esquemática

Exprimindo separadamente estes fluxos, encontra-se:

a) Para o fluxo de calor condutivo radial

$$q = Q - q_l$$

onde:. Q é o fluxo de calor aplicado pela resistência elétrica.

. q_l é o fluxo de calor perdido lateralmente através do isolante. (ver fig. 2)

$$q_l = \frac{2\,\pi\,kl\,(T_r - T_i)}{Ln\,(r_i/r_o)} \qquad (2)$$

com k a condutividade térmica do isolante, T_r a temperatura da resistência e T_i a temperatura medida dentro do isolante distante do eixo da cana de açúcar de r_i.

b) Para os fluxos de calor condutivos longitudinais

$$q_e = \frac{\lambda A_e (T_e - T'_e)}{\Delta x_e} \quad e \quad q_s = \frac{\lambda A_s (T_s - T_s')}{\Delta x_s} \qquad (3)$$

Onde:

. T_e' e T_s' são as temperaturas medidas as distâncias Δx_e e Δx_s respectivamente das seções AA' e BB'. (No nosso experimento $\Delta x_s = \Delta x_e = 2mm$.).

. λ é a condutividade térmica da cana de açúcar. Sakuratani [3,4] estimou a condutividade térmica da cana de açúcar a partir da combinação das condutividades térmicas da água, da celulose e do ar que compõem os tecidos celulares de uma seção transversal da cana de açúcar. Encontrou valores variando entre 0.52 e 0.58 $WM^{-1}{}^{o}C^{-1}$ com média de 0,54 $WM^{-1}\ {}^{o}C^{-1}$. Já Valancogne [5] determinou a condutividade térmica λ considerando desprezíveis as perdas radiais e aplicando o balanço de energia numa hora em que o fluxo F é nulo, porém realizou esta experiência em pés de maçã. No nosso caso, como explicado mais adiante, aplicaremos o método proposto por Valancogne.

. Para determinar o fluxo de calor transportado pela seiva, aplica-se a primeira Lei da Termodinâmica entre as seções AA' e BB' e considerando o fluido incompressível [6], encontra-se:

$$qf = \eta F \cdot C\ (T_s - T_e) \qquad (4)$$

onde:

. F é o fluxo de seiva $[m^3/s]$
. C é o calor específico (4.18 KJ/Kg°C)
. η é a massa específica (η = 1000 Kg/m^3)

Combinando as equações (2), (3) e (4) na equação (1) deduz-se a equação (5), a qual permite calcular o fluxo de seiva a partir das medições das diferenças de temperaturas: $(T_e - T'_e)$; $(T_s - T_s')$; $(T_s - T_e)$; $(T_r - T_i)$.

$$F = \frac{Q - \frac{\lambda A_e (T_e - T'_e)}{\Delta x_e} - \frac{\lambda A_s (T_s - T_s')}{\Delta x_s} - \frac{2\P k l\ (T_r - T_i)}{Ln(r_i/ro)}}{\eta C\ (T_s - T_s)} \qquad (5)$$

No estabelecimento desta equação foi desprezada a influência sobre o fluxo F dos gradientes de temperatura.

MATERIAL E MÉTODO

A seguir, apresenta-se a descrição do sistema experimental composto de três partes: O aparelho em si, o sistema de aquisição dos dados experimentais e o sistema de controle.

O aparelho em si. É composto de uma resistência elétrica de fio de constantan (d = 0,25 mm.) repartido em duas camadas de espiras colocadas sobre uma fita crepe a qual garante aderência ao tronco ao mesmo tempo em que um mínimo de elasticidade necessário ao acompanhamento do crescimento do caule da cana de açúcar. (fig.2b). A resistência (86,6 ohms) apresenta uma repartição uniforme das espiras suficientes próximas umas das outras para assegurar uma temperatura constante ao longo do contorno de uma seção transversal. Envolve a resistência assim constituida uma camada de fita poliéster que garante a impermeabilização do sistema. Este conjunto é encaixado num isolante cilíndrico de isopor (fig. 2a). As diferenças de temperatura $(T_e - T'_e)$; $(T_s - T_s')$ e $(T_s - T_e)$ são medidas por termopares Cu-Co em paralelo, como esquematizado na figura (1). Os diâmetros dos fios de cobre e de constantan são de 0,25 mm.

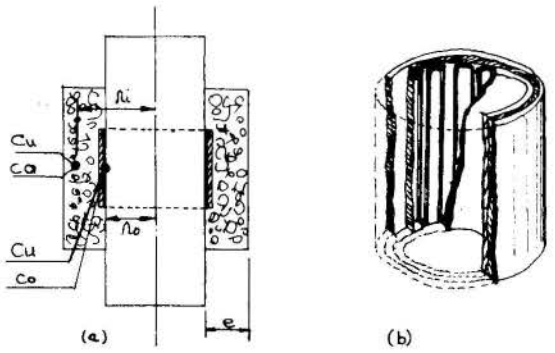

Fig. 2 - Detalhes do protótipo

O sistema de aquisição de dados. As saídas dos termopares em paralelo (Cu-Cu) são ligadas através de um fio blindado a uma placa de aquisição de dados 12 bits - 16 canais, instalada em microcomputador compátivel com IBM - PC - XT. Para evitar ruídos, as blindagens dos fios foram aterradas e as soldas entre fios de cobre do termopar e os fios de transmissão do sinal são mantidas a temperatura constante de 0°C durante toda experimentação em garrafa térmica. Da mesma forma, termopares Cu-Co foram instalados por baixo da resistência elétrica fornecendo a temperatura T_r e outro dentro do isolante a uma distância r_i do eixo da cana de açúcar (r_i = 3,3 cm para os dois isolantes utilizados). A placa de aquisição de dados é programável e gravou os dados de temperatura em disquete com intervalo sempre em torno de uma hora.

O sistema de controle: É constituído de medições anexas, as quais permitem verificar e ilustrar o correto funcionamento do aparelho. São estas: medições da temperatura ambiente e da radiaçao solar, feitas na área de experimentação.

Para controlar o volume efetivamente consumido pela planta e através deste verificar a validade do aparelho, dez pés de cana de açúcar foram plantados em um lisímetro de nível freático constante. A altura do nível do lençol freático é mantida constante por um recipiente de Mariotte, equipado de um visor que permite medir o volume consumido pelas plantas. Dentro do lisímetro, após ter introduzido cuidadosamente o solo, enriquecido por adubo orgânico em camadas homogêneas, foi implantado a 20 cm. de profundidade um tensiômetro com a leitura do qual se regulou o nível do lençol freático de modo a garantir perfeita alimentação das plantas. O lisímetro foi a seguir coberto por uma folha de plástico de modo a impedir toda evaporação pelo solo, deixando apenas as plantas transpirarem.

O protocolo experimental foi estabelecido considerando um estudo minucioso inicial da precisão da medição no sistema de Mariotte em função do efeito da temperatura ambiental e a pré-avaliação do tempo de resposta do aparelho [6]. As medições foram de um modo geral, efetuadas entre 6h 30 e 18h 30 com uma frequência de uma hora. Já o consumo do lisímetro era

lido apenas duas vezes ao dia no início e no final da experimentação. Dois períodos de medições foram efetuados nestes testes, correspondendo a dois tipos de isolantes: Com o isolante 1 de espessura e = 5,3 cm, nos dias 05, 08, 21, 22 e 23/03/90; com o isolante 2 de espessura e = 3 cm; nos dias 30/03/90, 03/04/90 e 10/04/90. Também com cada um dos isolantes uma medição noturna foi efetuada para avaliar o comportamento do aparelho em presença de fluxo de seiva muito baixo a nulo. Com o aparelho provido do isolante 2 foi realizado um teste com o intuito de determinar a condutividade térmica da cana de açúcar. Para isto, a cana de açúcar foi cortada e isolada termicamente as suas extremidades. Deste modo, durante algumas horas, antes que se inicia um processo de termomigração levando a cana de açucar a secar, garantiu-se a existência de um fluxo nulo, o qual se observa quando os calores calculados q_e e q_s são iguais. Utilizando a equação (5), encontrou-se o valor 0,62 $Wm^{-1}\,{}^oC^{-1}$ para a condutividade térmica λ da cana, valor este próximo aos valores encontrados por Sakuratani [4].

RESULTADOS

Na figura (3) são plotados os valores de fluxo de seiva (l/h) em função das horas para dois dias de experimentação. Em ambos dias foi utilizado o isolante 1. Nota-se uma diferença sensível no comportamento das curvas no início do dia. No caso (1), dia 22/03/90, propositalmente a resistência elétrica foi deixada ligada a noite toda. Em outros dias, tais como no caso (2) apresentado na figura, a resistência elétrica era ligada em torno de 5 horas da manhã. O valor elevado obtido as 6h 30 da manhã no caso (2) se deve ao valor muito pequeno de $(T_s - T_e)$ o qual na equação (5) aparece ao denominador. Este valor não reflete a realidade, pois a distribuição de temperatura não se encontra ainda estabelecida uma hora após ligar a resistência em caso de baixos fluxos de seiva (de madrugada). Este fato encontra-se ilustrado na curva da fig. 4, na qual se nota que entre 8 e 9 horas da manhã precisou-se de 40 minutos com o isolante 1 e 50 minutos com o isolante 2 para se atingir o patamar para os valores de $(T_s - T_e)$, indicando assim o regime estabelecido. Desta forma no cálculo do valor medido para a transpiração da planta, o primeiro valor será omitido quando obtido antes de 1h 30 após ter ligado a resistência.

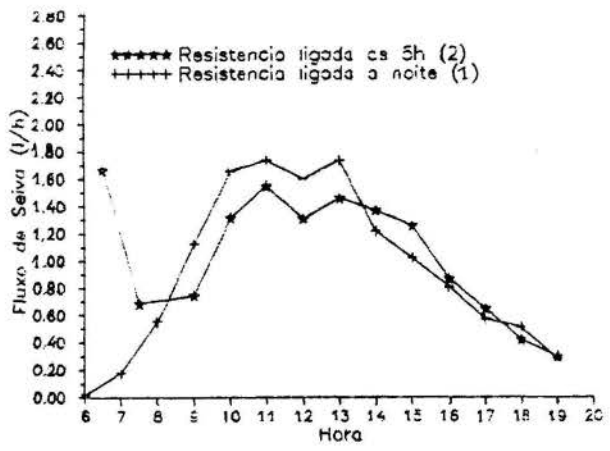

Fig. 3 - Evolução Comparativa do Fluxo de Seiva Medido

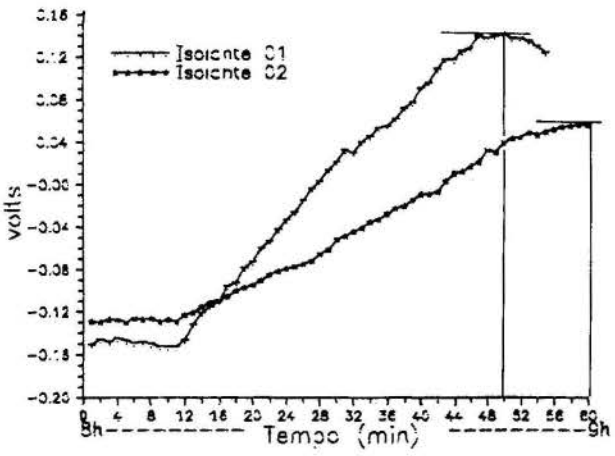

Fig. 4 - Tempo de resposta do sistema com dois isolantes diferentes

Na figura (5) compara-se para dois dias típicos a evolução diurna do fluxo de seiva com a evolução da radiação solar global. No dia 22/03/90 o aparelho estava equipado com o isolante 1. Nota-se uma evolução comparável do fluxo de seiva com a radiação solar, com uma ligeira defasagem do pico para direita, o que era de se esperar. A diminuição do fluxo da seiva entre 11 horas e 13 horas em relação a curva de radiação solar é um fenômeno clássico da cana de açúcar como analisado por Sakuratani [4]. Quanto menor é a proporção de radiação difusa em relação a radiação global, menor será proporcionalmente a transpiração da cana de açúcar, pois esta tende a fechar seus estômatos à radiação direta. No experimento do dia 22/03/90, o céu estava limpo e nestas condições, no local da experimentação entre 11 e 12 horas a cana está diretamente exposta aos raios solares. No dia 10/04/90 cujos resultados são apresentados na mesma fig. 5, a evolução do fluxo da seiva não acompanha tão bem quanto no outro dia a evolução da radiação solar. Nesta época (mês de abril) frequentes chuvas acompanhadas então de uma umidade relativa elevada ocorrerão, amortecendo deste modo a evaporação.

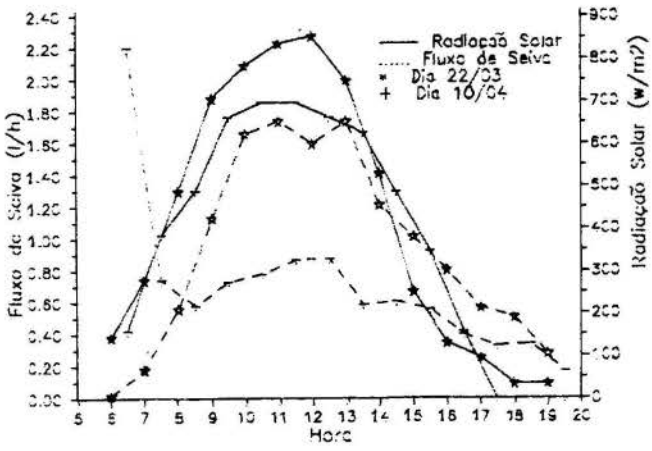

Fig. 5 - Evolução comparada entre o fluxo de seiva e a radiação solar.

Na tabela 1 a seguir, estão consignados os valores de fluxo de seiva medidos entre 7 horas da manhã e 7 horas da noite pelo aparelho e a variação do

volume de água no sistema de Mariotte.

O valor do fluxo de seiva realmente medido foi multiplicado por 10 para ser comparado com o valor consumido indicado pelo visor, tendo em vista que no lisímetro 10 unidades tinham sido plantadas. Este valor deve ser considerado como valor aproximado, pois cada cana sofreu desenvolvimento diferente. Assim por exemplo, notou-se que durante o período de medição três pés de cana mais novos cresceram mais do que os demais. No dia 30/03/90 por falha do sistema de aquisição de dados, não foi possível calcular o fluxo de seiva. Nos dias 21/03/90 e 03/04/90 o valor indicado pelo visor encontra-se inferior ao valor real devido ao fato de se ter encontrado no lisímetro água proveniente de precipitação noturna a qual foi transpirada pela planta mas não registrada no visor.

Nestes dias o segundo valor aparecendo na tabela 1 corresponde ao valor registrado corrigido do volume precipitado o qual foi medido no local através de um pluviômetro tipo Ville de Paris. (1,2 mm. na noite do dia 20 a 21 e 3,0 mm. na noite do dia 2 a 3).

Tabela 1 Resultados diurnos

ISOLANTE 1		
DATA	Variação no lisímetro 1.	Vol. Medido 1.
05.03.90	7,63	5,9
08.03.90	10,34	4,5
21.03.90	5,91-7,0	12,3
22.03.90	7,4	13,0
23.03.90	6,9	12,3
ISOLANTE 2		
DATA	Variação no lisímetro 1.	Vol. Medido 1.
30.03.90	-	-
03.04.90	4,43-7,15	8,42
10.04.90	8,87	7,60

Nos dias 5/03/90 e 8/03/90, os valores medidos pelo aparelho são pequenos. Uma análise pormenorizada dos resultados mostra que nestes dias os valores de fluxo de calor condutivo longitudinal foram muitos elevados, conduzindo a estimar baixos valores do fluxo de calor transportado pela seiva. Como o aparelho foi instalado no dia 4/03/90, acredita-se que este fato deve ser atribuído a necessidade dos tecidos da cana de açúcar se acomodarem em torno dos termopares para efetuar uma medição correta, tal como foi observado nos outros dias.

Os valores de fluxos apresentados na tabela 1 foram calculados considerando a condutividade térmica da cana de açúcar igual a 0,62 $WM^{-1}{}^{o}C^{-1}$. É interessante avaliar o efeito da estimação deste valor sobre os resultados de fluxos. Para isto cálculos foram efetuados para vários valores plausíveis de λ nos dias 22/03/90 e 03/04/90, levando ao seguintes resultados: (tabela 2)

Tab.2 - Consumo diário para vários valores da condutividade térmica

λ	0,52	0,54	0,56	0,58	0,60	0,62	0,64
22/3/90	14,2	14,0	13,7	13,5	13,3	13,0	12,8
03/4/90	9,8	9,6	9,5	9,3	9,2	9,0	8,9

Estes valores mostram que o cálculo do fluxo não é muito sensível ao valor de λ (erro máximo da ordem de 10%).

Da mesma forma, os termopares representam uma ponta quente de 0,6 mm. de diâmetro. Embora estas foram enfiadas na cana de açúcar após tê-la perfurada com gabarito (distância 2 mm.), pode se considerar uma imprecisão de $\pm$ 0,25 mm. sobre os valores de Δx_e e Δx_s. Considerando uma condutividade térmica de λ = 0,62 $WM^{-1}{}^{o}C^{-1}$, foram calculados os valores de fluxos para vários valores de Δx_s e Δx_e ($\Delta x_s = \Delta x_e$), levando aos seguintes resultados: (tab. 3)

Tab. 3 - Consumo diário para vários valores de Δx

Δx (mm)	1,5	1,75	2,0	2,25	2,5
22/03/90	10,6	12,0	13,0	13,8	14,5
03/04/90	7,5	8,4	9,0	9,5	9,9

Desta vez, o valor do fluxo é muito sensível a precisão na instalação dos termopares. Os resultados apresentados com o isolante 1 são coerentes. A discrepância que existe em relação aos valores medidos no lisímetro podem ser explicados pelo erro inerente a posição dos termopares, assim como ao fato que se considera que 10 pés de cana de açúcar transpiram em igual quantidade. As discrepâncias que existem entre os valores apresentados pelo isolante 1 e pelo isolante 2 são explicáveis então pela reinstalação necessária do sistema.

A sensibilidade do aparelho pode ser avaliada considerando a repartição dos vários fluxos de calor envolvidos. Maior é o fluxo convectivo em relação aos demais, mais sensível é o aparelho. A título de exemplo, apresenta-se na tabela 4 a repartição percentual dos fluxos de calor para alguns dias típicos.

Tabela 4 - Repartição Percentual dos Fluxos de Calor (%)

ISOLANTE 1

DIA	22/03/90			23/03/90		
HORA	q_λ	q_1	q_f	q_λ	q_1	q_f
07:00	44,4	35,7	19,9	40,9	43,1	16,0
08:00	12,8	23,2	36,0	13,2	37,3	49,5
09:00	21,4	17,6	61,0	5,4	20,3	74,3
10:00	21,4	13,3	65,3	16,0	17,9	66,1
11:00	23,0	15,6	61,4	16,7	22,7	60,0
12:00	21,0	16,3	62,7	12,5	16,3	71,2
13:00	16,4	17,6	66,0	12,8	22,2	65,0
14:00	21,4	22,4	56,2	11,6	19,9	68,5
15:00	20,6	25,7	53,7	13,2	24,0	62,8
16:00	20,6	24,5	54,9	21,4	24,5	54,1
17:00	30,0	30,6	39,4	32,3	35,8	31,9
18:00	35,4	36,2	28,4	54,9	40,9	4,2

ISOLANTE 2

DIA	03/04/90			10/04/90		
HORA	q_λ	q_1	q_f	q_λ	q_1	q_f
07:30	46,7	22,5	30,8	49,5	22,0	28,5
08:30	27,2	24,3	48,5	35,2	23,2	41,6
09:30	24,9	21,0	54,1	15,2	18,2	66,6
10:30	12,5	10,5	77,0	19,9	12,0	68,1
11:30	14,0	12,6	73,4	18,2	12,6	69,2
12:30	9,7	10,8	79,5	21,9	16,2	61,9
13:30	12,5	14,4	71,1	34,3	17,4	48,3
14:30	18,3	19,1	62,6	29,6	19,0	51,4
15:30	17,5	23,0	59,5	30,6	20,8	48,6
16:30	25,3	26,3	48,1	37,3	28,4	34,3
17:30	42,1	34,2	23,7	44,9	34,8	20,3
18:30	46,0	37,3	16,7	47,5	36,9	15,6

O fluxo de calor perdido lateralmente varia em torno de 20%. Muito mais elevado de manhã e ao anoitecer, passa para o mínimo em torno de meio dia quando a temperatura ambiente é máxima e a temperatura da resistência elétrica é mínima. Nos nossos experimentos não se notam diminuição sensível desta perda com o isolante mais espesso. O fluxo de calor de condução longitudinal apresenta variações muito superiores durante o dia. É máximo quando o fluxo de seiva é mínimo e mínimo quando o fluxo da seiva é máximo. O fluxo de calor médio transportado pela seiva durante o dia representa nos nossos experimentos em torno de 50% com o isolante 1 ou com o isolante 2. Este valor elevado explica a sensibilidade do aparelho que se traduz por um acompanhamento muito bom da evolução da radiação solar como já mencionado. A máxima temperatura da resistência elétrica, aplicando nela um fluxo de 1 watt foi de 52° C. Já a máxima diferença de temperatura (T_s - T_e) obtida durante o dia sempre oscilou em torno de 7° C. Ao longo de todo o experimento, nenhum efeito nocivo ao desenvolvimento da planta foi observado devido a presença do aparelho.

CONCLUSÕES

Este trabalho demostra a viabilidade técnica do método para medir o fluxo de seiva e consequentemente determinar a transpiração ou o consumo de água da mesma. Nestes testes não foram notadas diferenças sensíveis entre dois tipos de isolante utilizados, porém seria conveniente uma otimização do mesmo de modo a aumentar a percentagem do fluxo de calor transportado pela seiva em relação ao fluxo aplicado pela resistência. Tendo em vista o alto valor da temperatura máxima atingida pela resistência, não parece conveniente procurar aumentar o fluxo de calor aplicado na resistência de constantan. É imprescindível procurar diminuir o tempo de acomodação da cana de açúcar em torno dos sensores de temperatura minimizando-os e instalando-os em agulha hipodérmica por exemplo. Do mesmo modo, é conveniente procurar diminuir o tempo de resposta do aparelho. É indispensável procurar reduzir o tamanho da ponta quente dos termopare, assim como, a precisão na sua instalação.

Referências Bibliográficas

[1] Katerji M. e M. Hallaire "Les grandeurs de référence utilisables dans l'étude de l'alimentation em eau des cultures", Agronomie, 1984, Vol 4, nº 10 pp. 999 - 1008.

[2] Shimshi, D. "Water Status in Plants - Methodes of Measuring" in "Arid Zone Irrigation" B. Yaron, E. Danforsand Y. Vaadia Ed. Springer - Verlag Berlin N. York 1973, pp 249-263.

[3] Sakuratani T. "A Heat Balance method for measuring water flux in the stem of intact plant". J. A. Agr. Met., 37, pp 9-17, 1981.

[4] Sakuratani T. and J. ADE "A heat balance method for measuring water flow rate in stems of intact plants and its aplication to sugar-cane plant". J. A. R. Q. 19(2), pp 92-97, 1983.

[5] Valancogne C. and V. Nasr "Measuring sap flows in the stem of small trees by the heat balance method". Hortscience ASHE 1988.

[6] Mangueira D.S "Desenvolvimento de um sistema de medição de fluxo de seiva por balanço térmico" - Tese de Mestrado UFPb 1990 no prelo.

Sumary

In this paper are described system's embasement and tests results for measuring sap flow in stem of intact plant, Experiments were conducted in sugarcane plant. A portion of the stem was heated by an electrical resistance and the sap flux calculated by the heat balance aplication.

III ENCIT – Itapema, SC (Dezembro 1990)

FLOW OF A THIRD GRADE FLUID PAST A PLATE WITH SUCTION

C. E. Maneschy
Mechanical Engineering Department
Pontifícia Universidade Católica
22453 - Rio de Janeiro - RJ - Brazil

Vânia Regina Velloso
Mechanical Engineering Department
FUNREI
36300 - S.J. del Rei - MG - Brazil

ABSTRACT

In this paper the flow of an incompressible fluid of third grade past a plate with suction is investigated. The effects of the non-Newtonian nature of fluid on the velocity profile for different non-Newtonian viscosity coefficients and different suction rates are studied. It is observed from the numerical solution for the governing equation that, as in the Newtonian case, the steady asymptotic solution is not possible in the case of injection at the plate surface.

1 - INTRODUCTION

The steady asymptotic solution for an incompressible Newtonian fluid past an infinite plate subject to suction at its surface was first found by Griffith and Meredith (cf. Schlichting[1]). Kaloni[2] analysed some variations of the above boundary layer problem assuming the fluid to be viscoelastic. In recent years, interest in boundary layer flows of non-Newtonian fluids has increased. Amongst the many models which have been used to describe the non-Newtonian characteristic of certain fluids, the one developed by Truesdell and Noll[3] has received special attention. Rajagopal[4-6] established the solutions for several flows of second order fluids using the constitutive equation derived in this model.

The understanding of fluid mechanics in boundary layer flows with fluid injection or suction is of importance in many engineering problems such as in the design of thrust bearing[8] and the inlet region of a channel[8].

This paper investigates the boundary layer flow of a homogeneous incompressible non-Newtonian fluid of grade three, past an infinite plate with suction. The stress in such a fluid is related to the motion in the following manner[9]

$$\mathbf{T} = -p\mathbf{I} + \mu\mathbf{A}_1 + \alpha_1\mathbf{A}_2 + \alpha_2\mathbf{A}_1^2 + \beta_1(\text{tr } \mathbf{A}_1^2)\mathbf{A}_1 \qquad (1)$$

where p is the pressure, μ the Newtonian coefficient of viscosity, α_1 and α_2 material moduli which are usually refered as the normal stress coefficients, and β_1 the non-Newtonian viscosity. This parameter takes into account the dependence of the fluid viscosity on the deformation rate. The kinematical tensors $\mathbf{A}_1$ and $\mathbf{A}_2$ are defined as

$$\mathbf{A}_1 = \text{grad } \mathbf{v} + (\text{grad } \mathbf{v})^T \qquad (2)$$

$$\mathbf{A}_2 = \frac{d}{dt}\mathbf{A}_1 + \mathbf{A}_1(\text{grad } \mathbf{v}) + (\text{grad } \mathbf{v})^T\mathbf{A}_1 \qquad (3)$$

where $\mathbf{v}$ denotes the velocity and $\frac{d}{dt}$ the material time derivative.

The thermodynamics of a second order fluid modeled by Equation (1) for $\beta_1 = 0$, has been studied by Fosdick and Rajagopal[10]. They have shown that fluids with negative material moduli ($\alpha_1 < 0$) exhibit anomalous behavior not to be expected of any fluid of rheological interest. We will restrict ourselves to this points of view and consider in this paper only positive values of α_1.

2 - THEORETICAL ANALYSIS

Substituting Equation (1) into the balance of linear momentum

$$\rho\frac{d\mathbf{v}}{dt} = \text{div } \mathbf{T} + \rho\mathbf{b} \qquad (4)$$

gives, in the absence of body forces,

$$\begin{aligned}\rho\frac{d\mathbf{v}}{dt} = &-\text{grad } \mathbf{p} + \mu\text{div } \mathbf{A}_1 + \alpha_1\text{div } \mathbf{A}_2 + \\ &+ \alpha_2\text{div } \mathbf{A}_1^2 + \beta_1\text{div } [(\text{tr } \mathbf{A}_1^2)\mathbf{A}_1]\end{aligned} \qquad (5)$$

We shall seek a velocity field of the form

$$u = u(y), \quad v = v(y) \quad \text{and} \quad w = 0 \qquad (6)$$

where u, v and w are the velocity components in the x, y and z directions, respectively. Using the fact that the fluid can undergo only isochoric motion (incompressibility constraint), i.e.

$$\text{div } \mathbf{v} = 0 \qquad (7)$$

we find that v = constant

If suction at the plate surface is considered, then

$$v = -V_s \quad (V_s > 0) \qquad (8)$$

where V_s is the constant suction velocity.

With the velocity components given by Equations (8) and (6), one finds the following

$$\mathbf{A}_1 = \begin{bmatrix} 0 & \frac{du}{dy} & 0 \\ \frac{du}{dy} & 0 & 0 \\ 0 & 0 & 0 \end{bmatrix}$$

$$\mathbf{A}_1^2 = \begin{bmatrix} \left(\frac{du}{dy}\right)^2 & 0 & 0 \\ 0 & \left(\frac{du}{dy}\right)^2 & 0 \\ 0 & 0 & 0 \end{bmatrix}; \qquad \text{tr } \mathbf{A}_1^2 = 2\left(\frac{du}{dy}\right)^2$$

$$\mathbf{A}_2 = \begin{bmatrix} 0 & -V_s\frac{d^2u}{dy^2} & 0 \\ -V_s\frac{d^2u}{dy^2} & 2\left(\frac{du}{dy}\right)^2 & 0 \\ 0 & 0 & 0 \end{bmatrix}$$

If these, in turn, are substituted into equation (5), the following equations of motion are obtained

$$-\rho V_s\frac{du}{dy} = -\frac{\partial p}{\partial x} + \left[\mu + 6\beta_1\left(\frac{du}{dy}\right)^2\right]\frac{d^2u}{dy^2} - \alpha_1 V_s\frac{d^3u}{dy^3} \quad (9)$$

$$0 = -\frac{\partial p}{\partial y} + (2\alpha_1 + \alpha_2)\frac{d}{dy}\left[\left(\frac{du}{dy}\right)^2\right] \quad (10)$$

$$0 = -\frac{\partial p}{\partial z} \quad (11)$$

Let

$$\overline{p} = p - (2\alpha_1 + \alpha_2)\left(\frac{du}{dy}\right)^2 \quad (12)$$

then the equations of motion above reduce to

$$-\rho V_s\frac{du}{dy} = -\frac{\partial \overline{p}}{\partial x} + \left[\mu + 6\beta_1\left(\frac{du}{dy}\right)^2\right]\frac{d^2u}{dy^2} - \alpha_1 V_s\frac{d^3u}{dy^3} \quad (13)$$

$$\frac{\partial \overline{p}}{\partial y} = \frac{\partial \overline{p}}{\partial z} = 0 \quad (14)$$

From these equations of motion one can conclude that $\frac{\partial \overline{p}}{\partial x}$ is, at most, a constant. Futhermore, if one recalls that far away from the plate the stream velocity is constant, then $\frac{\partial \overline{p}}{\partial x} = 0$. Thus $\overline{p}$ is constant throughout the flow, while the pressure p depends on the velocity profile $u(y)$ and the material moduli α_1 and α_2 according to Equation (12).

The governing differential equation for the boundary value problem being analysed takes the following final form

$$\alpha_1 V_s\frac{d^3u}{dy^3} - \left[\mu + 6\beta_1\left(\frac{du}{dy}\right)^2\right]\frac{d^2u}{dy^2} - \rho V_s\frac{du}{dy} = 0 \quad (15)$$

subjected to the boundary conditions

$$\begin{aligned} &u(0) = 0 \\ &u(y) \to U_\infty \quad \text{as} \quad y \to \infty \\ &\frac{du}{dy} \to 0 \quad \text{as} \quad y \to \infty \end{aligned} \quad (16)$$

where U_∞ is the uniform stream velocity. As it can be seen from this equation, the velocity field is independent of the normal stress coefficient α_2.

3 - NUMERICAL SOLUTION

To make the equation of motion (15) dimensionless, the following quantities are defined

$$\overline{u} = \frac{u}{U_\infty} \quad ; \quad \overline{y} = \frac{y}{L} \quad (17)$$

where L is the characteristic length of the plate.

Substitution of (17) into (15) yields after a straightforward manipulation

$$\frac{d^3\overline{u}}{d\overline{y}^3} - \left[\gamma^* + \epsilon^*\left(\frac{d\overline{u}}{d\overline{y}}\right)^2\right]\frac{d^2\overline{u}}{d\overline{y}^2} - \delta^*\frac{d\overline{u}}{d\overline{y}} = 0 \quad (18)$$

$$\begin{aligned} &\overline{u}(0) = 0 \\ &\overline{u}(\overline{y}) \to 1 \quad as \quad \overline{y} \to \infty \\ &\frac{d\overline{u}}{d\overline{y}} \to 0 \quad as \quad \overline{y} \to \infty \end{aligned} \quad (19)$$

with the independent parameters of the equation (18) given as follows

$$\delta^* = \frac{\rho L^2}{\alpha_1} \quad (20)$$

$$\gamma^* = \frac{\mu L}{\alpha_1 V_s} = \frac{1}{c}\frac{\mu L}{\alpha_1 U_\infty} \quad (21)$$

$$\epsilon^* = \frac{6\beta_1 U_\infty^2}{\alpha_1 L} = \frac{\epsilon}{c} \quad (22)$$

The parameters c and ϵ in the equations above are given by

$$c = \frac{V_s}{U_\infty} \quad (23)$$

$$\epsilon = \frac{6\beta_1 U_\infty}{\alpha_1 L} \quad (24)$$

and were artificially introduced in the governing equation in order to see their effects on the final solution.

For all the cases discussed in this paper, we assumed

$$\delta^* = 1.0 \quad , \quad \frac{\mu L}{\alpha_1 U_\infty} = 0.01 \quad (25)$$

Different values for the dimensionless parameters ϵ and c were assumed in order to evaluate the effects of the non-Newtonian viscosity and the suction rate on the solution.

The boundary value problem given by Equations (18) and (19) was converted into an equivalente initial value problem in order to use the Runge-Kutta method in the search for the solution. The Newton-Raphson technique was used to satisfy the boundary condition at the infinity. The results obtained from the solution of those equations are discussed in the next section.

4 - DISCUSSION OF THE RESULTS

Analytical solutions to equation (18) for fluids of grade two ($\beta_1 = 0$), have been presented in [10]. To check the numerical accuracy of our results, we have compared our solution to those found in Rajagopal's work for the case of suction or blowing at the plate surface. These solutions are shown in Table 1 for the case of suction at the plate. It can be seen from that table that the agreement is very good.

Table 2 gives the initial slope of the solution, $\frac{d^2\overline{u}}{d\overline{y}^2}(0)$, for different non-Newtonian viscosities. The effect of suction on the solution is also included.

Figure 1 shows the variation of $\frac{d\overline{u}}{d\overline{y}}$ with respect to $\overline{y}$ for different non-Newtonian viscosities. Figure 2 shows the effect of the suction rate on $\frac{d\overline{u}}{d\overline{y}}$ for $\epsilon = 10^{-2}$. It is observed that an increase in the non-Newtonian viscosity would decrease the value of the initial slope of the solution while an increase in the suction rate would increase $\frac{d\overline{u}}{d\overline{y}}(0)$. In order to see these effects on the dimensionless velocity profiles u/U_∞ we have presented Figs. 3 and 4. Figure 3 indicates that the velocity

in the boundary layer decreases with larger values of the non-Newtonian viscosity. From Fig. 4 one can see that the velocity in the boundary layer decreases if smaller values of the suction rate are considered.

It should be mentioned that only positive values of the non-Newtonian viscosity (β_1), were assumed to plot the solution. For negative non-Newtonian viscosities the solution is similar to the one shown in the graphs.

Finally, it is interesting to point out that the solution corresponding to the case of blowing at the plate could be found by assuming negative values of the vertical velocity component, V_s. This was also investigated in this work and it was found that for $\beta_1 > 0$, asymptotic solutions were not possible for all non-Newtonian viscosity and blowing rates assumed. These results are similar to those found in classical fluid mechanics, since for Newtonian viscous fluid no steady asymptotic solution is possible in the case of blowing at the plate surface. However, if negative non-Newtonian viscosity is assumed, an asymptotic solution is determined. This result is in accordance with that found in reference[10] for second grade fluids.

Table 1 - Velocity distribution for fluid of grade two

$\overline{y}$	*Present work* ($\overline{u}$)	*Rajagopal's work* ($\overline{u}$)
0.2	0.181	0.172
1.0	0.635	0.642
2.0	0.864	0.860
3.0	0.951	0.952
∞	1.000	1.000

Table 2 - $\frac{d^2\overline{u}}{d\overline{y}^2}(0)$ for various ϵ's and c's

$c = 10^{-3}$	$c = 10^{-2}$	$c = 10^{-1}$
-0.543×10^{0}	-0.284×10^{-2}	-0.137×10^{-3}
-0.545×10^{0}	-0.287×10^{-2}	-0.139×10^{-3}
-0.561×10^{0}	-0.315×10^{-2}	-0.145×10^{-3}
-0.714×10^{0}	-0.562×10^{-2}	-0.178×10^{-3}

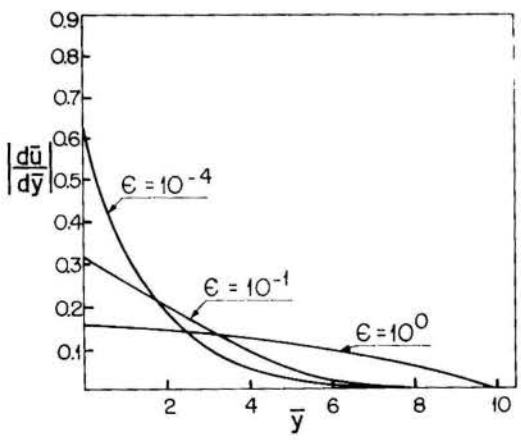

Figure 1 - $|\frac{d\overline{u}}{d\overline{y}}|$ vs $\overline{y}$ for $c = 10^{-2}$

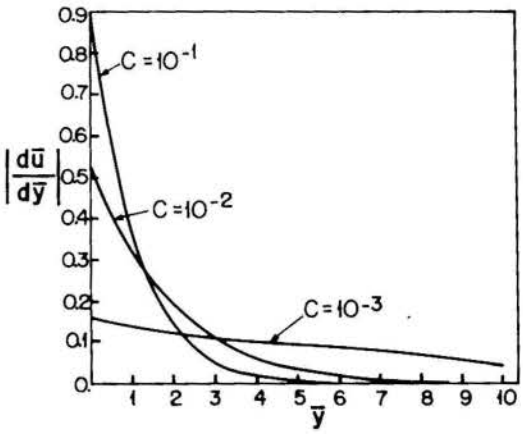

Figure 2 - $|\frac{d\overline{u}}{d\overline{y}}|$ vs $\overline{y}$ for $\epsilon = 10^{-2}$

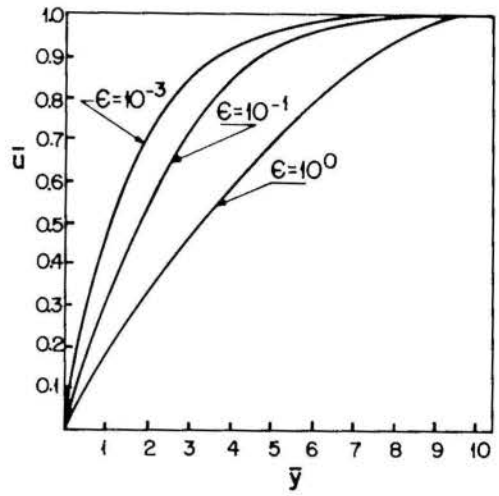

Figure 3 - Effect of the non-Newtonian viscosity on $\overline{u}$ for $c = 10^{-2}$

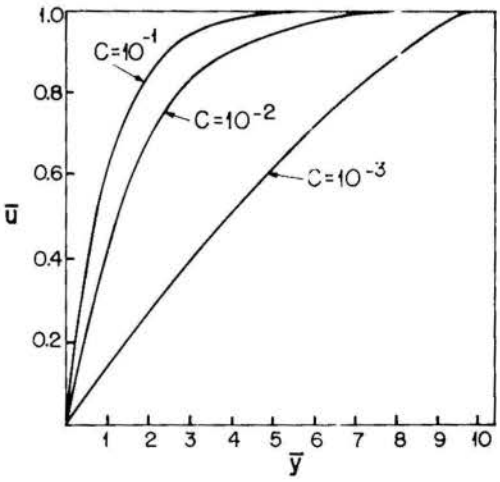

Figure 4 - Effect of the suction rate on $\overline{u}$ for $\epsilon = 10^{-2}$

5 - CONCLUSIONS

In this paper the flow of a third grade fluid past a porous plate was investigated. The velocity profile obtained in the case of suction at the plate surface is similar to the one that would be found had the fluid be assumed Newtonian. Also, as in the Newtonian case, no solution is obtained for positive non-Newtonian viscosity if blowing at the plate surface is con-

sidered. The analysis also reveals that for $\beta_1 < 0$, the elastic elements in the fluid prevents augmentation of boundary layer thickness due to blowing and enables the flow to reach a steady asymptotic state.

REFERENCES

[1] SCHLICHTING H., *Boundary layer theory*, New York: Mc Graw Hill Book Company, Inc., (1960).

[2] KALONI P. N., *Fluctuating flow of an elastico-viscous fluid past a porous flat plate*, Physics of Fluids **10**, 1344 (1966).

[3] TRUSDELL C., NOLL W., *Non-Linear field theories of mechanics*, Handbuch der Physick III/3, Berlin, Springer, (1965).

[4] RAJAGOPAL K. R., *On a class of exact solutions to the equations of motion of a second grade fluid*, Intl. J. Eng. Sci. **19**, 1014 (1981).

[5] RAJAGOPAL K. R., GUPTA A. S., *Flow and stability of a second grade fluid between two parallel plates rotating around non-coincident axes*, Intl. J. Eng. Sci. **19**, 1401 (1981).

[6] FOSDICK R. I., RAJAGOPAL K. R., *Anomalous feature in the model of second order fluids*, Arch. Rational Mech. Analysis **70**, 145 (1979).

[7] SACHETI N. C., BHATT B. S., *Steady laminar flow of a non-Newtonian fluid with suction or injection and heat transfer through porous parallel discs*, Z. angew. Math. Phys. **55**, 43 (1975).

[8] MISHRA S. P., PONDA T. C., *Effect of injection of the flow of second order fluid in the inlet region of a channel*, Acta Mech. **32**, 11 (1979).

[9] TANNER R.I., *Engineering rheology*, New York: Oxford University Press, (1985).

[10] RAJAGOPAL K. R., GUPTA A. S., *An exact solution for the flow of a non-Newtonian fluid past an infinite porous plate*, Acta Mech. **19**, 158 (1984).

III ENCIT – Itapema, SC (Dezembro 1990)

NON-NEWTONIAN FLOW OF A FALLING FILM AROUND A HORIZONTAL CYLINDER

P. R. Souza Mendes and M. F. Naccache
Department of Mechanical Engineering
Pontifícia Universidade Católica – RJ
Rio de Janeiro, RJ 22453 – BRAZIL

ABSTRACT

A theoretical investigation of the motion of a layer of a viscoelastic fluid around a horizontal cylinder is reported in this paper. The layer has initially a uniform thickness, and, at some instant of time, it starts to flow due to the presence of a gravity field. The result sought is the film thickness as a function of time and angular position. The mass- and momentum-conservation principles are employed in conjunction with the Maxwell constitutive equation. The results are compared with the ones for a Newtonian fluid, and the elastic fluid behavior is shown to change dramatically the flow.

INTRODUCTION

Pursuing further the study of the fluid mechanics involved in coating processes of electrical wires [1], the present paper deals with the flow of a thin layer of non-Newtonian fluid around a horizontal cylinder due to gravity.

The analysis of such a motion is of industrial interest since, when horizontal wire coating is employed, the gravity effect causes the liquid coating material previously deposited to flow down around the wire before solidification in the oven. This causes an eccentric layer of deposited material, which is highly undesirable.

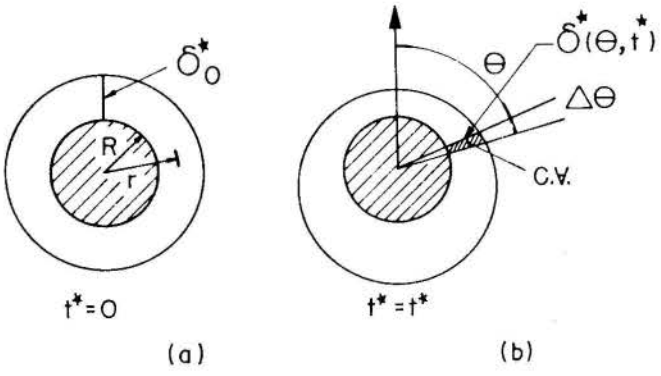

Figure 1. The problem under analysis.

Therefore, prediction of the fluid motion around the wire is necessary to control the eccentricity of the deposited layer of electrical insulation.

The coating material employed in this application is generally a varnish, which consists of a solution of a synthetic resin in drying oil [2]. This polymeric solution displays a viscoelastic behavior, and the Newtonian model for the stress field is not applicable.

The present research is concerned with a qualitative analysis of viscoelastic effects on the flow of the fluid layer. In this connection, the Maxwell model [3] was selected as the constitutive relation for stress. This choice was made with basis on the simplicity of this model.

The motion under study is represented in Fig. 1. At time $t^* = 0$, a fluid layer of uniform thickness δ_0^* is deposited around a horizontal cylinder (or wire), and a gravity field $\vec{g}$ directed downward is switched on (Fig. 1a). At some later time t^*, the flow has moved downward due to gravity (Fig. 1b). In this configuration, surface tension effects are important, and, due to motion, viscoelastic forces also arise. For the sought-for application, the film thickness is typically very small, generally of the order of 1 or 2% of the wire radius.

THE ANALYSIS

The solution of the present problem is obtained by following the same path as the one described in [1], with the appropriate adaptations for the non-Newtonian behavior. For completeness, however, the whole theory and procedure employed in the present paper is described in what follows, in spite of some superpositions with the description contained in [1].

The principles of mass and θ-momentum conservation are evoked, and applied to the deformable control volume shown at some instant t^* in Fig. 2.

In this two-dimensional analysis, the fluid density ρ is assumed to be invariant. The velocity field is given by $\vec{u} = u^*\hat{e}_r + v^*\hat{e}_\theta$. V^* stands for the the velocity component v^* evaluated at the interface, i.e.,

$$V^*(\theta, t^*) \equiv v^*(R + \delta^*, \theta, t^*) \qquad (1)$$

where $\delta^*(\theta, t^*)$ is the film thickness, measured in the radial direction, at some instant and θ location.

There exists a pressure difference Δp^* across the interface, due to the surface tension. Since the present study is focused on very thin films ($\delta^* << R$), the curvature radius of the interface is nearly constant and close to $R + \delta_0^*$ ([4],[5]), where δ_0^* is the initial (and uniform along θ) film thickness. Therefore, if σ is the surface tension,

$$\Delta p^* = \frac{\sigma}{R + \delta_0^*} \qquad (2)$$

Conservation of mass . The continuity equation for the control volume shown in Fig. 2 is ($\hat{n}$ is the unitary vector normal

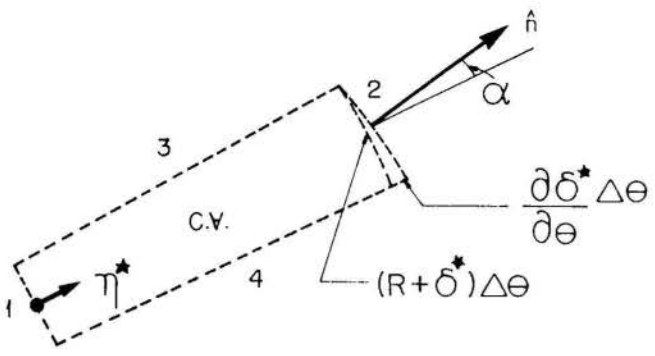

Figure 2. The control volume.

to the control surface):

$$0 = \int_{CS} \vec{u}\cdot\hat{n}\,dA = \int_1 \vec{u}\cdot\hat{n}\,dA + \int_2 \vec{u}\cdot\hat{n}\,dA + \int_3 \vec{u}\cdot\hat{n}\,dA + \int_4 \vec{u}\cdot\hat{n}\,dA \tag{3}$$

At surface 1, $\vec{u} = 0$, and hence $\int_1 \vec{u}\cdot\hat{n}\,dA = 0$. At surface 2,

$$\vec{u} = \frac{d\delta^*}{dt^*}\hat{e}_r + V^*\hat{e}_\theta \quad \text{and} \quad \hat{n} = \cos\alpha\,\hat{e}_r - \sin\alpha\,\hat{e}_\theta. \tag{4}$$

Then, at surface 2,

$$\vec{u}\cdot\hat{n} = \left(\frac{d\delta^*}{dt^*} - V^*\tan\alpha\right)\cos\alpha. \tag{5}$$

Now it is observed that

$$\tan\alpha = \frac{1}{R+\delta^*}\frac{\partial\delta^*}{\partial\theta} \quad \text{and} \quad \frac{d\delta^*}{dt^*} = \frac{\partial\delta^*}{\partial t^*} + \frac{V^*}{R+\delta^*}\frac{\partial\delta^*}{\partial\theta} \tag{6}$$

Substituting the above equations into eq. (5), the dot product $\vec{u}\cdot\hat{n}$ becomes simply equal to $\frac{\partial\delta^*}{\partial t^*}\cos\alpha$, and

$$\int_2 \vec{u}\cdot\hat{n}\,dA = \frac{\partial\delta^*}{\partial t^*}(R+\delta^*)\,\Delta\theta, \tag{7}$$

where, assuming a unitary length along the third direction, dA was replaced by $(R+\delta^*)d\theta/\cos\alpha$.

It can be seen that

$$\int_3 \vec{u}\cdot\hat{n}\,dA + \int_4 \vec{u}\cdot\hat{n}\,dA = \frac{\partial}{\partial\theta}\left[\int_0^{\delta^*} v^*\,d\eta^*\right]\Delta\theta \tag{8}$$

where $\eta^* \equiv r - R$.

Now, eqs. (7) and (8) are plugged into the continuity equation (eq. (3)), yielding

$$0 = \left(1+\frac{\delta^*}{R}\right)\frac{\partial\delta^*}{\partial t^*} + \frac{1}{R}\frac{\partial}{\partial\theta}\left[\delta^* V^*\int_0^1 v\,d\eta\right] \tag{9}$$

where $\eta \equiv \eta^*/\delta^*$ and $v \equiv v^*/V^*$.

An appropriate dimensionless version of eq. (9) is

$$0 = (1+\delta)\frac{\partial\delta}{\partial t} + \frac{\partial}{\partial\theta}\left[V\delta\int_0^1 v\,d\eta\right] \tag{10}$$

where

$$\delta \equiv \frac{\delta^*}{R}, \qquad t \equiv t^*\sqrt{\frac{g}{R}}, \qquad \text{and} \qquad V \equiv \frac{V^*}{\sqrt{gR}}, \tag{11}$$

g being the acceleration due to gravity.

Conservation of linear momentum. In the θ-direction, the principle of conservation of momentum gives, when applied to the control volume shown in Fig. 2,

$$F_c + F_e = \int_{C\forall}\frac{\partial(\rho v^*)}{\partial t^*}d\forall + \int_{CS} v^*\rho\vec{u}\cdot\hat{n}\,dA. \tag{12}$$

The contact forces F_c are due to the shear stress ($\sigma^*_{r\theta} \equiv \tau^*_{r\theta}$) at surface 1 and to the normal stress $\sigma^*_{\theta\theta}$ acting on surfaces 3 and 4. The contribution of fluid motion to normal stresses is generally very small ($\tau^*_{\theta\theta} \simeq 0$, or $\sigma^*_{\theta\theta} \simeq -\Delta p^*$), and it is common practice to neglect this effect in engineering analyses. For the present flow geometry and a Newtonian fluid, this hypothesis has been tested for a few cases. The results of these tests indicated that this simplifying assumption is also reasonable for the present flow. Therefore, the following expression has been used for the contact forces F_c:

$$F_c = -\tau^*_w R\Delta\theta - \Delta p^*\frac{\partial\delta^*}{\partial\theta}\Delta\theta, \tag{13}$$

where Δp^* is given by eq. (2). It is observed from eq. (13) that the surface tension effect depends directly on the thickness gradient along θ, the derivative $\partial\delta^*/\partial\theta$.

The shear stress at the wall τ^*_w is evaluated from the linear viscoelastic constitutive relation, in conjunction with the modulus of relaxation of the Maxwell fluid [6]:

$$\boldsymbol{\tau}^* = \int_{-\infty}^{t^*}\frac{\mu}{\lambda^*}\exp\left(-\frac{t^*-t^{*\prime}}{\lambda^*}\right)\dot{\boldsymbol{\gamma}}^*\,dt^{*\prime} \tag{14a}$$

where $\boldsymbol{\tau}^*$ is the deviatoric stress tensor; μ is the fluid viscosity; λ^* is the relaxation time; and $\dot{\boldsymbol{\gamma}}^*$ is the first Rivlin-Ericksen tensor. Observing that $\dot{\gamma}^*_{r\theta} = (V^*/\delta^*)\partial v/\partial\eta$ and that τ^*_w is the magnitude of the $r\theta$ component of $\boldsymbol{\tau}^*$ evaluated at the wall, one gets, after a nondimensionalization,

$$\tau_w(\theta,t) = \frac{1}{\lambda Re}\int_0^t \exp\left(-\frac{t-t'}{\lambda}\right)\frac{V}{\delta}\left.\frac{\partial v}{\partial\eta}\right]_{\eta=0} dt' \tag{14b}$$

where $\tau_w \equiv \tau^*_w/\rho gR$, $Re \equiv \rho R\sqrt{gR}/\mu$ is the Reynolds number, and $\lambda \equiv \lambda^*/\sqrt{R/g}$ is the Deborah number.

The external forces F_e are due to gravity, and hence given by

$$F_e = \int_0^{\delta^*}\rho g\sin\theta(R+\eta^*)\,d\theta\,d\eta^* = \rho g\sin\theta\left(R\delta^* + \frac{\delta^{*2}}{2}\right)\Delta\theta. \tag{15}$$

The first term on the right-hand side of eq. (12) may be written as

$$\int_{C\forall}\frac{\partial(\rho v^*)}{\partial t^*}d\forall = \rho\Delta\theta\int_0^{\delta^*}\frac{\partial v^*}{\partial t^*}(R+\eta^*)d\eta^* = \rho gR^2\delta\Delta\theta\int_0^1\frac{\partial(vV)}{\partial t}(1+\delta\eta)d\eta \tag{16}$$

If the same reasoning employed to obtain the mass conservation equation (eq. (10)) is followed while working on the right-most term of eq. (12), the expression below is obtained with no particular difficulty:

$$\int_{CS} v^* \rho \vec{u} \cdot \hat{n}\, dA =$$

$$= \rho V^* \frac{\partial \delta^*}{\partial t^*} R(1+\delta)\Delta\theta + \frac{\partial}{\partial \theta}\left[\delta^* V^{*2} \int_0^1 v^2 d\eta\right] \rho \Delta\theta \tag{17}$$

Now eqs. (2), (9), (12), (13), (15), (16) and (17) are combined, yielding, after some algebra, the following dimensionless equation:

$$-\delta\tau_w - \left(\frac{1}{S(1+\delta_0)}\right)\delta\frac{\partial\delta}{\partial\theta} + \sin\theta\left(1+\frac{\delta}{2}\right)\delta^2 =$$

$$\delta^2 \int_0^1 \frac{\partial(vV)}{\partial t}(1+\delta\eta)d\eta + \delta\frac{\partial}{\partial\theta}\left[\delta V^2 \int_0^1 v^2 d\eta\right] \tag{18}$$

$$-\delta V \frac{\partial}{\partial\theta}\left[\delta V \int_0^1 v\, d\eta\right]$$

where $S \equiv \rho g R^2/\sigma$.

Eqs. (10) and (18) are subjected to the following initial conditions:

$$V(\theta,0) = 0; \qquad \text{and} \qquad \delta(\theta,0) = \delta_0 \tag{19}$$

The boundary conditions are:

$$V(0,t) = V(\pi,t) = 0; \qquad \text{and} \qquad \frac{\partial\delta}{\partial\theta}(0,t) = \frac{\partial\delta}{\partial\theta}(\pi,t) = 0 \tag{20}$$

Evaluation of the Integral Terms. Further inspection upon eqs. (10), (14b) and (18) shows that there are four terms where the tangential component $v \equiv v^*/V^*$ of the velocity appears, three of them involving integrals, and the fourth involving a derivative evaluated at the wall. It is clear that the evaluation of these terms require the knowledge of the function $v^*(\eta,\theta,t)$.

In the present work, a linear profile of the form $v = a\eta + b$ was adopted. It is worth noting that this assumption is quite reasonable when $\delta << 1$, since any continuous function can be approximated by a straight line in such a small interval.

Using the facts that, at $\eta = 0$, $v = 0$, and at $\eta = 1$, $v = 1$, it is straightforward to obtain $v = \eta$. This profile is used in the four terms mentioned above, and the following results are obtained:

$$\int_0^1 v\, d\eta = \frac{1}{2}; \qquad \int_0^1 v^2\, d\eta = \frac{1}{3}; \qquad \left.\frac{\partial v}{\partial\eta}\right]_{\eta=0} = 1$$

$$\text{and} \qquad \int_0^1 \frac{\partial(vV)}{\partial t}(1+\delta\eta)d\eta = \left(\frac{\partial V}{\partial t} - \frac{V}{\delta}\frac{\partial\delta}{\partial t}\right)\left(\frac{1}{2}+\frac{\delta}{3}\right) \tag{21}$$

With the above results, the final form of the governing equations can be obtained:

$$(1+\delta)\frac{\partial\delta}{\partial t} + \frac{1}{2}\frac{\partial(V\delta)}{\partial\theta} = 0 \tag{22}$$

and

$$V\left(\frac{1}{2}+\frac{\delta}{3}\right)\delta\frac{\partial\delta}{\partial t} - \left\{\left(\frac{1}{S(1+\delta_0)}\right) - \frac{V^2}{6}\right\}\delta\frac{\partial\delta}{\partial\theta}$$

$$-\delta^2\left(\frac{1}{2}+\frac{\delta}{3}\right)\frac{\partial V}{\partial t} - \frac{V\delta^2}{6}\frac{\partial V}{\partial\theta} = \delta\tau_w - \sin\theta\left(1+\frac{\delta}{2}\right)\delta^2 \tag{23}$$

The problem under study is governed by the above partial differential equations for δ and V, together with the initial and boundary conditions given in eqs. (19) and (20). The dimensionless shear stress τ_w that appears in eq. (23) is given by eq. (14b).

It can be seen that the parameters that influence this physical situation are S, Re, λ and the dimensionless initial film thickness δ_0. S is the ratio between gravity forces and forces due to surface tension; the modified Reynolds number Re compares gravity forces with viscous forces; and the Deborah number λ is the ratio between a characteristic time of the fluid and a characteristic time of the flow. The characteristic time of the fluid, i.e., the relaxation time, gives the order of magnitude of the time duration of the fluid's "memory."

METHOD OF SOLUTION

It can be observed that eqs. (22) and (23) form a non-linear system of partial diferential equations. Since no discontinuities are expected in the sought-for solution, a finite-difference scheme is, in principle, appropriate for the integration of the governing equations. In the present work, the Crank-Nicolson implicit scheme was employed to generate the algebraic discretization equations, which were solved with the aid of the Thomas algorithm together with an iterative scheme.

This iterative scheme consisted basically of, for a given instant of time, (i) assuming initial guesses for δ and V; (ii) solving the set of algebraic equations generated from eq. (22) using the Thomas algorithm and the initial guesses for δ; (iii) solving the set of algebraic equations generated from eq. (23) using the Thomas algorithm and the present values of V; (iv) going back to step (ii), but now using the present values of δ; (v) proceeding in this manner until convergence is achieved. The initial guesses mentioned above were just the values at the previous time step. Convergence was typically achieved in three to four iterations.

Due to symmetry, the solution domain in θ is from 0 to π. The grid employed was uniform, with 33 nodal points in θ and time steps varying from case to case in the range 0.01–1, depending upon the Reynolds number Re and on the Deborah number λ.

The numerical evaluation of the hereditary integral that appears in the expression for τ_w (eq. (14b)) is rather straightforward. At $t = 0$, $\tau_w = 0$. At $t + \Delta t$,

$$\tau_w(\theta, t+\Delta t) = \tau_w(\theta,t) + \frac{1}{\lambda Re}\int_t^{t+\Delta t} \exp\left(-\frac{t-t'}{\lambda}\right)\frac{V}{\delta}\, dt' \tag{24}$$

The integral in the above equation may be transformed at each time step, via the trapezoidal rule of numerical integration, into an algebraic expression involving V and δ evaluated at t and $t+\Delta t$. This expression is employed recursively to evaluate $\tau_w(\theta, t+\Delta t)$.

RESULTS AND DISCUSSION

Attention will now be turned to the results obtained with the just described analysis. All results reported in the present paper pertain to $\delta_0 = 0.02$ and $S = 0.2$; the investigation was focused on the effects of the Deborah number λ and Reynolds number Re.

Fig. 3 shows the variation of the film thickness δ with the angular position θ, for the case of $Re = 50$ and $\lambda = 100$. Comparing this figure with Fig. (3) of [1], it is seen that the viscoelastic behavior of the fluid plays an important role on the flow.

At instant $t = 0$, the film thickness is uniform and equal to its initial value δ_0. As time ellapses, the fluid falls around the cylinder due to gravity, and therefore the film thickness at the upper region diminishes, whereas at the lower region the thickness increases.

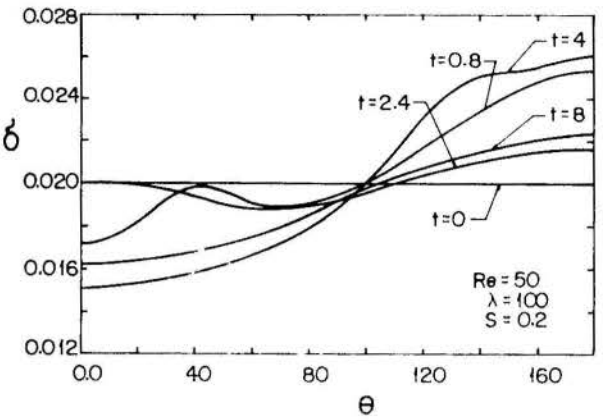

Figure 3. Film thickness versus angle for various times.

However, once a thickness gradient in the θ direction is established, a force due to surface tension appears, and acts to balance the gravity effect. Furthermore, the viscoelastic force is also present to influence the fluid motion. In contrast to what was observed for the Newtonian fluid [1] in this Re range, the fluid acquires an oscillatory motion, which makes the free surface to become wavy in the θ direction.

The behavior of the tangential velocity at the interface is illustrated in Fig. 4 for the same case shown in Fig. 3. It can

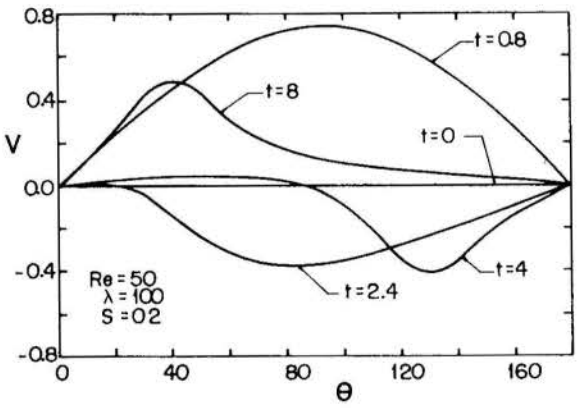

Figure 4. Tangential velocity versus angle for various times.

be seen that the fluid accelerates very fast at the onset of the motion, when the only force acting on it is gravity. Soon the surface tension and viscoelastic effects become important, and the velocity distribution $V(\theta, t)$ reaches high positive values at some early instant of time and then starts to oscillate with smaller magnitudes and changing sign periodically. Moreover, the velocity of maximum magnitude occurs at different θ locations for different times, and with different magnitudes.

Figs. 5, 6 and 7 show the variation of the film thickness at $\theta = 0°$ with time, for different values of the modified Reynolds number Re. From its definition, it can be seen that low values of Re indicate high fluid viscosity, and vice-versa, for a given cylinder radius and gravity field. Figs. 5, 6 and 7 differ in the values of the Deborah number, which is equal to 1, 100 and 10^5 respectively.

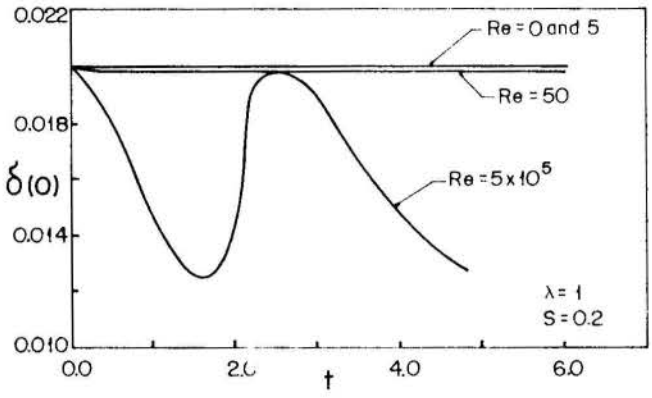

Figure 5. Film thickness at $\theta = 0°$ versus time for various Re's.

It is observed in these figures that, independently of the value of the Deborah number, for infinite fluid viscosity ($Re = 0$), the fluid flows at infinitely small velocity, and no change in thickness is observed.

At the other extreme, when $\lambda Re \mapsto \infty$, there is also no dependence on λ. This is illustrated by comparing the curves for $Re = 5 \times 10^5$ of Figs. 5, 6 and 7 with one another. It is seen that the curve in Fig. 6 ($\lambda Re = 5 \times 10^7$) is identical to the curve in Fig. 7 ($\lambda Re = 5 \times 10^{10}$). Moreover, the curve for $Re = 50$ in Fig 7 ($\lambda Re = 5 \times 10^6$) also coincides with these curves. The curve in Fig. 5 ($\lambda Re = 5 \times 10^5$), however, is not identical to the other three mentioned above, although very close.

An inspection upon eq. (14b) may explain this trend. When the term $\frac{1}{\lambda Re}$ in this equation is small enough to neutralize

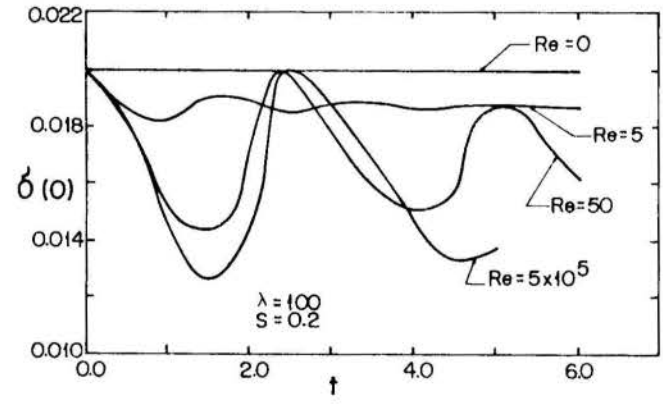

Figure 6. Film thickness at $\theta = 0°$ versus time for various Re's.

the effect of the memory term $\int_0^t \exp\left(-\frac{t-t'}{\lambda}\right) \frac{V}{\delta}\, dt'$, then the parameter λ alone becomes unimportant. This is true because this integral term is the only other term (besides $1/\lambda Re$) where λ appears.

Therefore, when $\lambda Re \mapsto \infty$, an undamped oscillation may be observed in two different situations. The first is the extreme case of zero fluid viscosity ($Re = \infty$), where no viscous damping for the fluid kinetic energy is available. This behavior is the same observed for the Newtonian fluid [1], as expected. However, even when the fluid displays a finite viscosity, an undamped oscillation may be observed, when $\lambda \mapsto \infty$. This is due to the extremely large elastic energy storage effect, which maintains the constant amplitude oscillation. The viscous energy dissipation becomes negligible in this case.

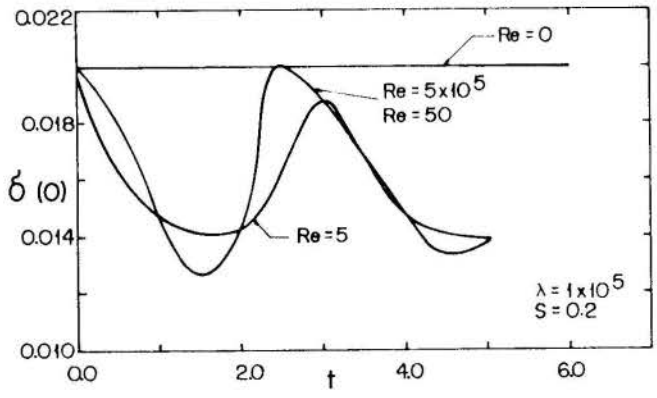

Figure 7. Film thickness at $\theta = 0°$ versus time for various Re's.

In the cases of Reynolds number values away from the two extremes discussed above, the Deborah number becomes important. For $\lambda = 1$ (Fig. 5), the curves for $Re = 0$ and 5 are coincident and horizontal, indicating that there is no motion. The curve for $Re = 50$ is essentially coincident with the previous ones, showing that in this case the viscosity is still high when compared with the elastic effect, preventing the fluid to flow. Only the curve for $Re = 5 \times 10^5$ displays fuid motion, which is oscillatory with almost no damping due to the low fluid viscosity, as discussed in the previous paragraph.

For $\lambda = 100$ (Fig. 6), the situation is quite different. When $Re = 5$ there is already fluid motion, and displays a strongly damped oscillation, which dies away fast. When $Re = 50$, the oscillatory motion has a wider amplitude and lasts longer, although viscous damping effects are still present. When $Re = 5 \times 10^5$, the film thickness oscillates with no damping.

For $\lambda = 10^5$ (Fig. 7), when Re is as low as 5 there is already a strong oscillatory motion with a very mild viscous damping, due to the prevailing elastic effect. When $Re = 50$, no viscous effects are detected, and the motion is purely elastic.

One might suspect at this point that the product λRe could correlate the results instead of Re and λ separately, as is the case for the extreme situations of $\lambda Re \mapsto 0$ and $\lambda Re \mapsto \infty$. However, a comparison between the curve for $Re = 5 \times 10^5$ in Fig. 5 and the curve for $Re = 5$ in Fig. 7 shows that this is not true. For both curves, $\lambda Re = 5 \times 10^5$, but they are clearly different from each other.

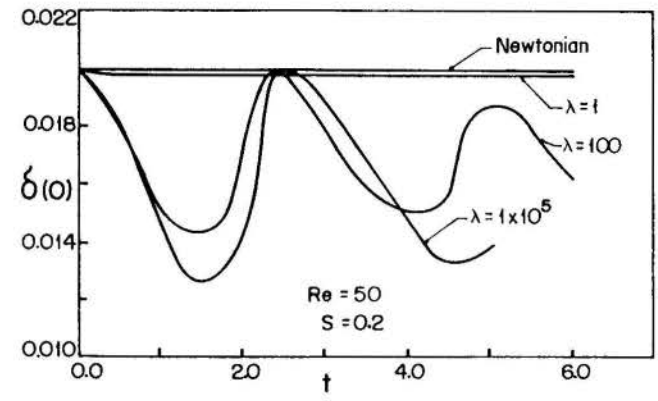

Figure 8. Film thickness at $\theta = 0°$ versus time for various λ's.

The effect of the fluid elasticity on the present flow is further emphasized with the aid of Fig. 8. In this figure, which pertains to a fixed fluid viscosity ($Re = 50$), it can be seen that the elasticity effect is dramatic. For $\lambda = 1$, departure from the Newtonian behavior is nearly negligible. As λ increases, however, the flow changes completely, with damped oscillation for $\lambda = 100$ and an oscillation with no noticeable viscous effect for $\lambda = 10^5$.

FINAL REMARKS

The purpose of the present paper is to report some progresses of the research presented in [1]. Here the study was aimed at analyzing, at least qualitatively, the effects of a non-Newtonian fluid behavior on the flow of a thin film around a horizontal cylinder (wire).

Inasmuch as the Maxwell model has been chosen to describe the fluid behavior, some limitations were imposed to the analysis. No shear thinning effects are predicted with this model. Another nonlinear effect which cannot be predicted via the Maxwell model and which may be of importance in the present case is related to normal stress differences.

REFERENCES

[1] P. R. Souza Mendes, 1989, "Gravity-driven motion of a fluid layer around a cylinder," *Revista Brasileira de Ciências Mecânicas* **11**, in print.

[2] F. Rodriguez, 1989, "Principles of Polymer Systems," *Hemisphere*, New York, 3rd edition.

[3] R. B. Bird, R. C. Armstrong and O. Hassager, 1987, "Dynamics of Polymeric Liquids," *Wiley*, New York, 2nd edition, vol. 1.

[4] A. Markovitz, B. B. Mikic and A. E. Bergles, 1972, "Condensation on a downward-facing horizontal rippled surface," *J. Heat Transfer* **94**, pp. 315–320.

[5] R. Krupiczka, 1985, "Effect of surface tension on laminar film condensation on a horizontal film," in *Chem. Eng. Process.* **19**, pp. 199–203.

[6] R. I. Tanner, 1985, "Engineering Reology," *Oxford Eng. Sci. Series*, Oxford.

III ENCIT – Itapema, SC (Dezembro 1990)

ANÁLISE DE MANCAIS ESFÉRICOS RANHURADOS VIA DIFERENÇAS FINITAS

M.V. DUARTE
C.R. RIBEIRO
DEPART.ENGENHARIA MECÂNICA/UFU
38400 – UBERLÂNDIA/MG

RESUMO

Este trabalho apresenta um método de diferenças finitas para se obter a solução do escoamento do filme fluido em um mancal esférico ranhurado. O problema é analisado para uma configuração arbitrária dos centros das duas esferas. São examinados os efeitos dos parâmetros do mancal sobre a capacidade de carga. É apresentado um estudo linearizado da estabilidade dinâmica de um rotor rígido.

1- INTRODUÇÃO

Os mancais esféricos ranhurados são amplamente utilizados como mancais de encosto em várias aplicações industriais de alta rotação, por apresentarem elevada rigidez radial e capacidade de evitar movimentos de precessão.

Dentre os métodos analíticos que prevêm o comportamento estático destes mancais destacam-se a teoria unidimensional [1], teoria que admite número infinito de ranhuras [2] e método da perturbação[3]. A utilização destes métodos, além de suas restrições intrínsecas exige o conhecimento de técnicas sofisticadas. Por exemplo, Murata [3], que apresenta o modelo mais realítico dos citados, restringe-se a mancais centrados, utiliza transformação conforme, projeção estereográfica, distribuição de linhas de fontes e vórtices, integração numérica no plano complexo, procedimentos iterativos, etc...

Neste trabalho apresentar-se-á a aplicação do método de diferenças finitas no estudo de mancais ranhurados discretizando-se a equação de Reynolds e condições de contorno diretamente sobre a superfície curva. É uma técnica simples que permite obter a influência dos diversos parâmetros do mancal na capacidade de carga e os coeficientes de rigidez e amortecimento para posições genéricas do eixo. Apresenta- se ainda um estudo comparativo com os resultados obtidos por Bootsma [2] e Murata [3] e um estudo de estabilidade dinâmica para rotores rígidos centrados.

2- EQUAÇÕES BÁSICAS

A figura 1 apresenta um mancal esférico ranhurado helicoidalmente onde o elemento ranhurado gira com velocidade angular constante ω em torno do eixo vertical. As ranhuras são cortadas regularmente desde o plano horizontal $\theta = \theta_1$ (usualmente $\pi/2$) até $\theta = \theta_2$ com inclinação constante β em relação aos círculos latidudinais.

Admitindo fluido Newtoniano incompressível e escoamento isotérmico, a equação de Reynolds em coordenadas esféricas é dada por:

$$\frac{\partial}{\partial\theta}\left(h^3 \operatorname{sen}\theta \frac{\partial p}{\partial\theta}\right) + \frac{1}{\operatorname{sen}\theta}\frac{\partial}{\partial\phi}\left(h^3\frac{\partial p}{\partial\phi}\right) = 6\mu\omega R^2 \operatorname{sen}\theta \frac{\partial h}{\partial\phi} \quad (1)$$

onde p é a pressão hidrodinâmica, R o raio da calota, μ a viscosidade e h a espessura do filme lubrificante.

$$h = c_{L,G} + e_x \operatorname{sen}\theta\cos\phi + e_y \operatorname{sen}\theta\operatorname{sen}\phi + e_z\cos\theta \quad (2)$$

onde o índice L refere-se à região lisa , G à região ranhurada e c é a folga radial.

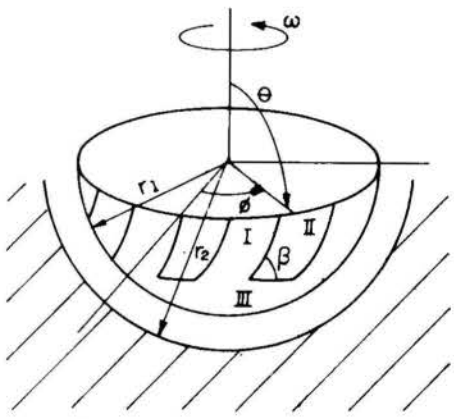

Fig. 1- Configuração do Mancal

Como condições de contorno admite-se (a) pressão constante na periferia externa do mancal e (b) conservação do fluxo de massa na passagem do fluido pelas fronteiras que separam as regiões lisas das ranhuradas. As velocidades médias nas direções θ e ϕ são dadas por:

$$\bar{v}_\theta = \frac{1}{h}\int_0^h v_\theta d\xi = -\frac{1}{12\mu}\frac{\partial p}{\partial\theta}\frac{h^2}{R} \quad (3)$$

$$\bar{v}_\phi = \frac{1}{h}\int_0^h v_\phi d\xi = -\frac{1}{12\mu\operatorname{sen}\theta}\frac{\partial p}{\partial\phi}\frac{h^2}{R} + \frac{\omega R}{2}\operatorname{sen}\theta \quad (4)$$

As equações (1), (3) e (4) estão expressas em relação a um referencial inercial. Como as ranhuras giram com velocidade ω, a condição (b) deve ser expressa em relação ao referencial móvel, onde:

$$(\bar{v}_\theta)_{rel} = \bar{v}_\theta \qquad (5)$$

$$(\bar{v}_\phi)_{rel} = \bar{v}_\phi - \omega R \operatorname{sen}\theta \qquad (6)$$

O fluxo através de uma fronteira cuja normal faz um ângulo α em relação ao círculo latidudinal é dado por:

$$q_n = h\left[(\bar{v}_\theta)_{rel}\operatorname{sen}\alpha + (\bar{v}_\phi)_{rel}\cos\alpha\right]$$

$$q_n = -\frac{h}{12\mu R}\left(\frac{\partial p}{\partial\theta}\cos\alpha + \frac{\partial p}{\partial\phi}\frac{\operatorname{sen}\alpha}{\operatorname{sen}\theta}\right) - \omega R h\frac{\operatorname{sen}\theta\operatorname{sen}\alpha}{2} \qquad (7)$$

A condição (b) exige que q_n se conserve ao atravessar as descontinuidades que separam as regiões lisas das ranhuradas, onde α é igual a β entre I e II (fig. 1) e igual a 90 graus entre II e III.

3- MODELO NUMÉRICO

Expressando as equações (1) e (7) em forma adimensional resulta:

$$\frac{\partial}{\partial\theta}\left(H^3\operatorname{sen}\theta\frac{\partial P}{\partial\theta}\right) + \frac{1}{\operatorname{sen}\theta}\frac{\partial}{\partial\phi}\left(H^3\frac{\partial P}{\partial\phi}\right) = \operatorname{sen}\theta\frac{\partial h}{\partial\phi} \qquad (8)$$

$$Q_n = -\frac{H^3}{12}\left(\frac{\partial P}{\partial\theta}\cos\alpha + \frac{\partial P}{\partial\phi}\frac{\operatorname{sen}\alpha}{\operatorname{sen}\theta}\right) - H\frac{\operatorname{sen}\theta\operatorname{sen}\alpha}{2} \qquad (9)$$

onde $H = \frac{h}{c_L}$, $\quad P = \frac{p c_L^2}{\mu\omega R^2}$, $\quad Q_n = \frac{q_n}{\omega R c_L}$

Utilizando o modelo clássico de diferenças finitas centradas (fig. 2), aproximando-se P parabolicamente tem-se

$$\frac{\partial P}{\partial\theta} = f(P_N, P_O, P_S) \qquad \frac{\partial P}{\partial\phi} = \frac{P_W - P_E}{2\Delta\phi}$$

$$\frac{\partial^2 P}{\partial\theta^2} = f(P_N, P_O, P_S) \qquad \frac{\partial^2 P}{\partial\phi^2} = \frac{P_W + P_E - 2P_O}{\Delta\phi} \qquad (10)$$

de maneira que (9) se resume a:

$$C_O P_O + C_N P_N + C_S P_S + C_W P_W + C_E P_E = B_O \qquad (11)$$

onde:

$$C_O = -2\left(\frac{A_1}{DTA\cdot DTP} + \frac{A_2(DTA - DTP)}{2\cdot DTA\cdot DTP} + \frac{A_4}{DF12}\right)$$

$$C_S = \frac{2A_1}{DT\cdot DTP} + \frac{A_2 DTA}{DTP\cdot DT}$$

$$C_L = \frac{A_3}{2DFI} + \frac{A_4}{DF12}$$

$$C_N = \frac{2A_1}{DT\cdot DTA} - \frac{A_2 DTP}{DTA\cdot DT}$$

$$A_1 = H^3\operatorname{sen}^2\theta$$

$$A_2 = 3H^2\cdot\frac{\partial H}{\partial\theta}\cdot\operatorname{sen}^2\theta + H^3\cos\theta\cdot\operatorname{sen}\theta$$

$$A_3 = 3H^2\cdot\frac{\partial H}{\partial\phi}$$

$$A_4 = H^3$$

$$B = 6\operatorname{sen}^2\theta\cdot\frac{\partial H}{\partial\phi}$$

$$DTA = \theta_i - \theta_{i-1}$$

$$DTP = \theta_{i+1} - \theta_i$$

$$DT = DTA + DTP$$

$$DF2 = \Delta\phi^2$$

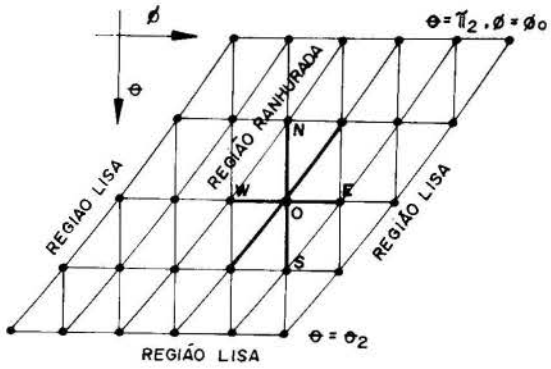

Fig.2 - Malha de diferenças finitas utilizada.

Quando o ponto O da figura 2 pertencer à fronteira, a igualdade dos fluxos Qn (eq. 9) nos dois lados da fronteira leva a uma equação discretizada do tipo da equação (11), ou seja, a obtenção do campo de pressão obedece a um padrão único.

Numéricamente o campo de pressão é obtido por relaxação sucessiva (SOR) da equação (11), ou seja a partir de uma estimativa inicial (usualmente nula) o valor de Po na iteração k+1 é obtido a partir do valor da iteração k através da equação:

$$P_O^{(k+1)} = P_O^k - \frac{W\cdot(P_O C_O + \ldots + P_W C_W - B_O)^k}{C_O} \qquad (12)$$

4- RESULTADOS OBTIDOS

Os resultados obtidos usando o modelo adotado neste trabalho (diferenças finitas) são apresentados nas figuras (3), (4) e (5). Nestas figuras plotou-se a força de sustencão do mancal para diversas configurações geométricas, onde: N é o número de ranhuras, β é o ângulo de hélice , Γ é a razão entre as espessuras do filme (C_a/C_L) e F_s a força de sustentação dada por:

$$F_s = \frac{W \cdot C_L^2}{\mu \omega R^4} \qquad (13)$$

onde:

W é a carga (N) atuando sobre o mancal

Em todos as figuras a hélice se desenvolve até a latitude de θ = 150 graus e a largura da ranhura foi mantida igual a da região lisa que,Segundo Murata [3], é a configuração que maximiza a sustentação.

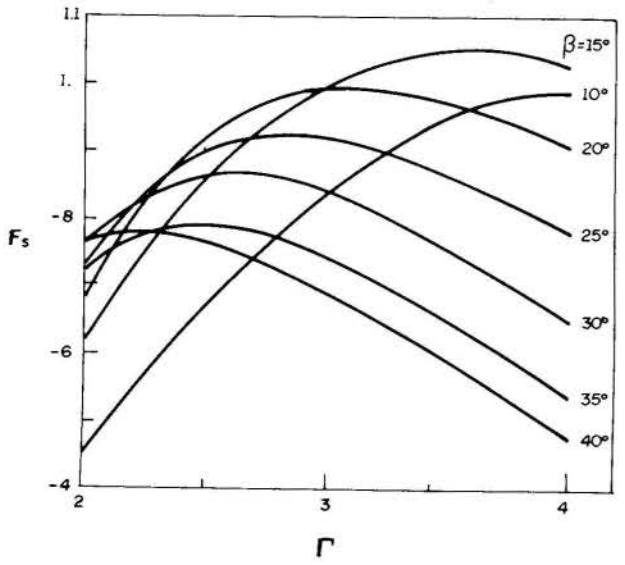

Fig. 3 - Influência do ângulo β e a razão Γ sobre a força de sustentação para N = 5.

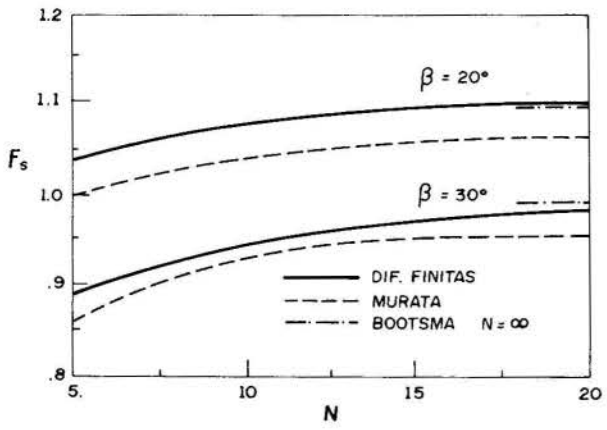

Fig. 4 - Influência do número de ranhuras sobre a força de sustentação para Γ = 3.

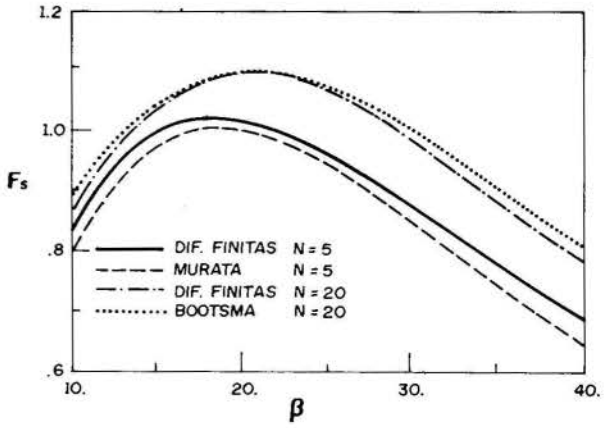

Fig. 5 - Influência do ângulo β e o do número de ranhuras na força de sustentação para Γ = 3.

Para fins comparativos apresenta-se nas Figs. 4 e 5 alguns resultados de Bootsma [2] (N=∞) e de Murata [3], onde observa-se boa correlação com o modelo atual. Quando N → ∞ a Fig.4 mostra que o método das diferenças finitas apresenta melhores resultados do que os de Murata em relação aos de Bootsma.

As pequenas diferenças observadas na Fig. 5 entre o modelo atual e o de Bootsma ocorrem para valores de β longe da faixa ideal de utilização, que , como mostram as Figs. 3 e 5 situa-se em torno de 20 graus. Para valores de β maiores do que 40^0 a distorção da malha de diferenças finitas introduz erros no cálculo do campo de pressão.

5 - ANÁLISE DE ESTABILIDADE

Para se ter uma idéia a respeito do nível de estabilidade proporcionada pela utilização de mancais esféricos ranhurados,uma ánalise simplificada será apresentada, adotando-se as seguintes hipóteses:

i - Os momentos de massa do rotor serão desprezados;

ii - O sistema será modelado com 3 graus de liberdade(rotor com rigidez infinita);

iii- Os efeitos giroscópicos serão desprezados;

iv - O eixo do rotor é coincidente com o eixo z do mancal;

v - Os deslocamentos do eixo são pequenos;

As 3 primeiras hipóteses foram admitidas visto que estamos interessados na influência do mancal na estabilidade do sistema, além do mais, a sua aplicação torna os resultados genéricos. A hipótese iv é adotada por ser a posição usual eixo/mancal em aplicações industriais. A hipótese v é adotada tendo em vista a linearização dos coeficientes de rigidez e amortecimento do mancal.

Sob estas hipóteses a equação diferencial homogênea do movimento do sistema, na forma matricial, é dada por:

$$M\ddot{X} + C\dot{X} + KX = \emptyset \qquad (14)$$

onde:

M = mr[I] é a matriz, simétrica, de inércia

mr é a massa do rotor

I é a matriz identidade

C é a matriz, assimétrica, de amotecimento viscoso

K é a matriz, assimétrica, de rigidez

X é o vetor das coordenadas generalizadas

Na forma adimensional, (14) pode ser escrita:

$$Ma\ddot{X} + wCa\dot{X} + w^2KaX = \emptyset \qquad (15)$$

onde:

$$Ma = \frac{wc^3}{\mu r^4} M;$$

$$Ca = \frac{c^3}{\mu r^4} C;$$

$$Ka = \frac{c^3}{\mu w r^4} K;$$

Reduzindo a ordem de (4) , tem-se:

$$\dot{AY} + BY = \emptyset \qquad (16)$$

onde:

$$A = \begin{bmatrix} Ma & \emptyset \\ \emptyset & -w^2Ka \end{bmatrix}$$

$$B = \begin{bmatrix} wCa & w^2Ka \\ w^2Ka & \emptyset \end{bmatrix} \qquad e \qquad Y = \begin{bmatrix} \dot{X} \\ X \end{bmatrix}$$

Admitindo pequenas pertubações, os coeficientes de rigidez e amorteciemnto linearizados são dados por:

$$K_{ij} = \frac{\partial F_j}{\partial X_i} \qquad i,j = 1,2,3 \qquad (17)$$

$$C_{ij} = \frac{\partial F_j}{\partial \dot{X}_i} \qquad i,j = 1,2,3 \qquad (18)$$

onde Fj é a força de sustentação na direção j.

O sistema é considerado instável caso algum dos seus autovalores tenha a parte real positiva. Numéricamente as equações (17) e (18) são calculadas pelo método das diferencas finitas centradas. Os resultados assim obtidos mostraram-se concordantes com os obtidos por Miyake [4].

A Fig. 6 mostra a região de estabilidade do sistema num gráfico de (ma/w) versus o deslocamento adimensional za =z/c_L do centro do rotor. Devido a ampla faixa de valores existente para ma/ω, optou-se por plotar dB versus za, onde:

$$dB = 20 \cdot \log\left(\frac{ma/\omega}{Ref} \right) \qquad (19)$$

onde Ref = 1 rad/s.

Admitindo-se que o mancal sustenta toda a carga do rotor a massa equivalente ma' é dada por:

$$ma'/\omega = \omega \cdot c_L F_s / g \qquad (20)$$

onde g é a aceleração da gravidade:

A Força de sustentação adimensional, (dB), em função de za é representada na Fig. 6 para análise. Uma vez que a ordem de grandeza usual de $\omega c_L / g$ é de aproximadamente -30 dB, observa-se da figura que os mancais esféricos ranhurados serão sempre estáveis, admitindo-se as hipóteses citadas anteriormente.

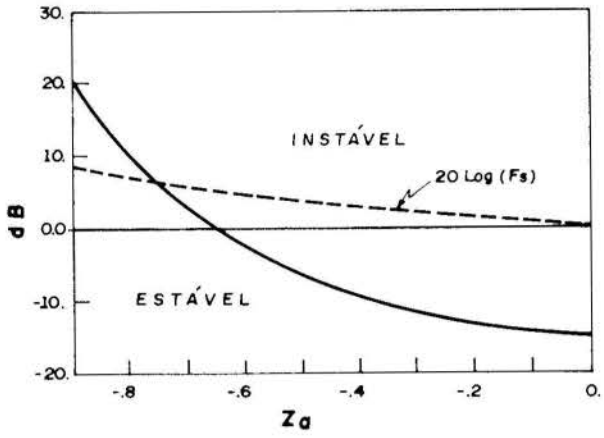

Fig. 6 - Curva de estabilidade para $\beta = 20^\circ$, $\Gamma = 3$ e N = 5.

6 - CONCLUSÕES

O método das diferenças finitas mostrou-se uma ferramenta robusta para o cálculo do campo de pressão em mancais esféricos ranhurados. A principal vantagem do método é o fato de poder ser aplicado para posições genéricas do eixo sem maiores dificuldades. A degeneração da malha de diferenças finitas, e consequentemente dos resultados, que ocorre para ângulos β maiores que 40 graus não limita o método, visto que os valores ideais para o ângulo β se situam em torno de 20 graus.

A análise de estabilidade, apesar de simplificada, demonstra o alto grau de estabilidade proporcionada pela utilização deste tipo de mancal.

7 - ABSTRACT

This paper is concerned with a finite difference method of obtainimg the solution for the flow of fluid film of spherical espiral groove bearing. The problem is analyzed for a arbitrary offset of centers of two spheres. Effects of bearing parameters on the load capacity are examined. A linearized study of dynamic stability for a infinitly rigid rotor is presented.

8 - BIBLIOGRAFIA

[1] Muijderman, E. A., "Spiral Groove Bearings", Philips Tech. Libr., 1966.

[2] Bootsma, J., "Spherical and Conical Spiral Groove Part I : Theory", ASME Journal of Lubrication Technology, Vol. 97, No. 2, pp. 236-242, Apr. 1975

[3] Murata, S., Miyake, Y., "Exact Two-Dimensional theory of Spherical Spiral Groove Bearings", Trans. ASME, Vol. 102, pp. 430-438, October 1980.

[4] Miyake, Y., Kawabata, N., Tominga, A. and Murata, S., "Two-Dimensional Analysis of Stiffnes and Damping Factor of Spiral Groove Spherical Bearings", Bulletin of JSME, Vol. 25 No. 202, pp. 663-670, April 1982.

III ENCIT — Itapema, SC (Dezembro 1990)

EFEITO DA CAVITAÇÃO NO CARREGAMENTO DINÂMICO DE MANCAIS RADIAIS TURBULENTOS

A.L. MANKE, A.T. PRATA E R.T.S. FERREIRA

Departamento de Engenharia Mecânica
Universidade Federal de Santa Catarina
Cx.Postal 476 - Florianópolis - SC - 88049

RESUMO

O carregamento dinâmico de mancais radiais finitos é investigado numericamente. A equação de Reynolds é integrada via o método dos volumes finitos, e especial atenção é devotada ao cálculo da fronteira de cavitação. A utilização de uma transformação de coordenadas mapeia o filme de óleo em um domínio retangular permitindo que a fronteira de cavitação seja avaliada com precisão. Resultados para uma carga constante subitamente aplicada no eixo são apresentados e comparados com aqueles obtidos quando se considera a aproximação de mancal curto.

INTRODUÇÃO

A análise do carregamento dinâmico de mancais radiais é de grande importância industrial. Inúmeras são as aplicações em engenharia onde sistemas rotativos são submetidos a carregamentos cuja orientação e intensidade variam com o tempo. A análise de sistemas rotativos à luz de carregamentos dinâmicos permite ainda que efeitos de instabilidade possam ser considerados. Desde o trabalho pioneiro de Newkirk e Taylor [1], onde a instabilidade de mancais foi identificada como um problema hidrodinâmico, diversos trabalhos tratando de carregamento dinâmico de mancais radiais tem sido publicados. Para uma revisão destes trabalhos menção é feita a Prata et al. [2] e Hashimoto et al. [3], bem como às referências lá citadas.

Na grande maioria dos trabalhos encontrados na literatura, verifica-se que o carregamento dinâmico é tratado à luz de duas simplificações. A primeira diz respeito às aproximações simplificativas referentes à fronteira de cavitação, e a segunda se refere ao tratamento laminar dado ao escoamento do lubrificante. Com o presente aumento de tamanho e velocidades dos sistemas rotativos, bem como a utilização de fluidos lubrificantes com viscosidades cada vez menores, tem sido crescente o número de mancais que operaram em regime turbulento. No presente artigo, especial atenção é dedicada tanto ao tratamento da fronteira de cavitação como à importância que alterações entre regime laminar e turbulento têm no desempenho de mancais radiais.

O objetivo do presente trabalho é apresentar uma nova metodologia que permita a análise de carregamentos dinâmicos de mancais radiais considerando efeitos de cavitação em regimes laminares e turbulentos. A metodologia apresentada é então aplicada para verificar a validade da aproximação de mancais curtos nas características dinâmicas de mancais radiais. Neste contexto o presente trabalho testa e estende os resultados recentemente apresentados em [4]. Uma revisão da literatura indica que até então não há trabalho algum que trate do carregamento dinâmico de mancais radiais finitos operando em regime turbulento, onde a equação de Reynolds é resolvida sem aproximações.

ANÁLISE

Formulação do Problema. A geometria do problema a ser investigado é apresentada na Fig. 1. Para esta situação, a equação de Reynolds considerando regime turbulento e dependente do tempo, pode ser escrita como,

$$\frac{1}{R}\frac{\partial}{\partial\theta}\left(\frac{1}{G_\theta}\frac{h^3}{\mu}\frac{1}{R}\frac{\partial p}{\partial\theta}\right)+\frac{\partial}{\partial y}\left(\frac{1}{G_y}\frac{h^3}{\mu}\frac{\partial p}{\partial y}\right)=\frac{\omega}{2}\frac{\partial h}{\partial\theta}+\frac{\partial h}{\partial t} \qquad (1)$$

onde h é a espessura do filme de óleo dada por $h = c(1 + \varepsilon \cos\theta)$, e G_θ e G_y são coeficientes de turbulência conforme apresentados em [5,6],

$$G_\theta = 12(a_\theta + b_\theta\,\varepsilon\cos\theta)\,,\quad G_y = 12(a_y + b_y\varepsilon\cos\theta) \qquad (2)$$

onde

$$a_\theta = 1 + 0{,}00069\,Re^{0{,}95},\quad b_\theta = 0{,}00066\,Re^{0{,}95}$$
$$a_y = 1 + 0{,}00069\,Re^{0{,}88},\quad b_y = 0{,}00061\,Re^{0{,}88} \qquad (3)$$

$$Re = \rho c R\omega/\mu$$

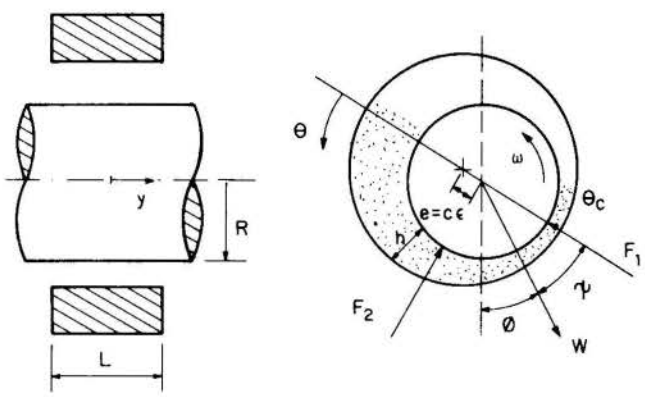

Fig. 1 - Geometria do problema.

A equação (1) é aplicável tanto para escoamentos laminares como turbulentos. À medida em que $Re \to 0$, G_θ, $G_y \to 12$ conforme requerido para escoamento laminar.

Uma das dificuldades associadas à solução da equação anterior está na determinação do ângulo $\theta_c(y)$ onde ocorre a cavitação do filme de óleo. Ao longo da fronteira de cavitação o óleo passa a escoar em estrias e o filme perde sua continuidade, não mais sendo capaz de sustentar forças hidrodinâmicas. Do ponto de vista matemático este é um problema de fronteira livre, que apresenta a dificuldade adicional de requerer a determinação do domínio de solução à medida em que a solução é procurada. A fim de lidar com esta classe de problema não linear de fronteira livre, o domínio de solução será transformado em um domínio retangular adotando o mesmo procedimento in-

troduzido em [7]. Este procedimento consiste em definir-se um novo sistema de coordenadas dado por

$$\eta = \theta/[\pi + \alpha(\xi)] \quad e \quad \xi = y/R \tag{4}$$

O ponto chave desta transformação é que a coordenada η varia de 0 a 1 para todos os valores de ξ, e o desconhecimento do domínio de solução fica agora embutido na equação diferencial do problema.

Em termos adimensionais, e utilizando as coordenadas η,ξ a equação (1) pode então ser escrita como,

$$\frac{\partial}{\partial\xi}\left[\frac{H^{3/2}}{G_\xi}\frac{\partial P}{\partial\xi}\right] + \frac{1}{(\pi+\alpha)^2}\frac{\partial}{\partial\eta}\left[\frac{H^3}{G_\eta}\frac{\partial}{\partial\eta}(H^{-3/2}P)\right] =$$

$$= 2\,\dot{\varepsilon}\cos[\eta(\pi+\alpha)] + 2\,\varepsilon\,\dot{\psi}\,\mathrm{sen}[\eta(\pi+\alpha)] +$$

$$\varepsilon(2\,\omega_L - 1)\,\mathrm{sen}\,[\eta(\pi+\alpha)] \tag{5}$$

onde G_ξ e G_η correspondem a G_Y e G_θ, respectivamente, e, as seguintes adimensionalizações foram adotadas,

$$P = pc^2H^{3/2}/6\mu\omega R^2\ ,\ H = h/c\ ,\ \omega_L = [d\phi/dt]/\omega$$

$$\dot{\varepsilon} = d\varepsilon/d\tau\ ,\ \dot{\psi} = d\psi/d\tau\ ,\ \tau = \omega t \tag{6}$$

Note-se que por simplicidade, a fronteira de cavitação $\alpha(\xi)$ foi simplesmente escrita como α. Para a determinação de α é necessário que se conheça o campo de P que por sua vez requer α para sua determinação. Em seção subseqüente será apresentada a metodologia utilizada para o cálculo de α.

As condições de contorno associadas à equação (5) são,

$$\eta = 0 \rightarrow P = 0\ ,\ \eta = 1 \rightarrow P = \partial P/\partial\eta = 0$$

$$\xi = 0 \rightarrow \partial P/\partial\xi = 0\ ,\quad \xi = L/2R \rightarrow P = 0 \tag{7}$$

Discretização da Equação de Reynolds. A integração da equação (5) é realizada numericamente através do método de volumes finitos. Para tal fim o domínio de solução é dividido em pequenos volumes de controle e em seguida a equação diferencial é integrada ao longo de cada um desses volumes de controle. Nesta integração as derivadas são aproximadas por diferenças centrais. Tem-se então, uma equação algébrica para cada volume de controle. Reportando-se à Fig. 2, onde é apresentado um volume de controle típico no domínio de solução, as equações algébricas são da seguinte forma,

$$a_P P_P = a_L P_L + a_0 P_0 + a_N P_N + a_S P_S + S \tag{8}$$

onde

$$a_L = a_{L1} + a_{L2}\ ,\quad a_0 = a_{01} - a_{02}$$

$$a_{L1} = G_\eta\Big|_\ell \frac{(1+\varepsilon\cos\theta_\ell)^{3/2}}{(\delta\eta)_\ell}\,\frac{\Delta\xi}{(\pi+\alpha)^2}$$

$$a_{L2} = \frac{3}{4}\,G_\eta\Big|_\ell\,(1+\varepsilon\cos\theta_\ell)^{1/2}\varepsilon\ \mathrm{sen}\ \theta_\ell\,\frac{\Delta\xi}{(\pi+\alpha)}$$

$$a_{01} = G_\eta\Big|_o \frac{(1+\varepsilon\cos\theta_o)^{3/2}}{(\delta\eta)_o}\,\frac{\Delta\xi}{(\pi+\alpha)^2}$$

$$a_{02} = \frac{3}{4}\,G_\eta\Big|_o (1+\varepsilon\cos\theta_o)^{1/2}\varepsilon\ \mathrm{sen}\,\theta_o\,\frac{\Delta\xi}{(\pi+\alpha)}$$

$$a_N = G_\xi\Big|_P \frac{(1+\varepsilon\cos\theta_P)^{3/2}}{(\delta\xi)_n}\,\Delta\eta$$

$$a_S = G_\xi\Big|_P \frac{(1+\varepsilon\cos\theta_P)^{3/2}}{(\delta\xi)_s}\,\Delta\eta \tag{9}$$

$$a_P = a_{L1} - a_{L2} + a_{01} + a_{02} + a_N + a_S$$

$$S = -[2\,\varepsilon\dot{\varepsilon}\cos\theta + 2\,\varepsilon\dot{\psi}\,\mathrm{sen}\theta + \varepsilon\,(2\omega_L - 1)\,\mathrm{sen}\theta]\Big|_P\,\Delta\eta\Delta\xi$$

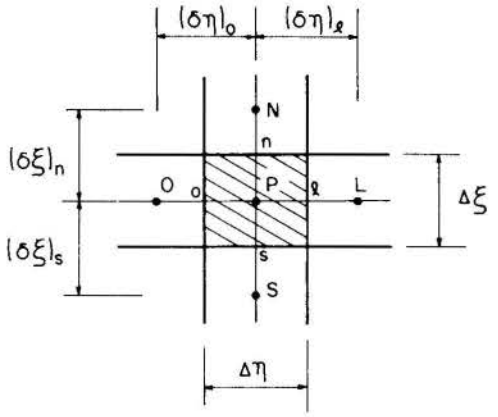

Fig. 2 - Volume de controle típico no domínio de solução.

O conjunto das equações algébricas associadas a cada volume de controle, juntamente com as condições de contorno, é resolvido iterativamente utilizando-se o método da linha-por-linha. Obtém-se desta forma, o campo de pressão P.

Determinação da Fronteira de Cavitação. Na determinação do campo de pressão conforme discutido anteriormente é necessário o conhecimento da fronteira de cavitação α. No presente estudo a localização da fronteira de cavitação será feita estendendo-se para carregamento dinâmico o método sugerido em [7] para carregamentos estáticos. A essência do método consiste em impor continuidade do filme de óleo para cada volume de controle adjacente à fronteira de cavitação. Para facilitar tal desenvolvimento a Fig. 3 foi preparada. Nesta figura vê-se um volume de controle típico adjacente à fronteira de cavitação. Nas direções η e ξ, o escoamento de óleo é dado por, respectivamente,

$$q_\eta = -\frac{h^3}{12\mu R(\pi+\alpha)}\frac{\partial p}{\partial\eta} + \frac{Uh}{2}\ ,\quad q_\xi = -\frac{h^3}{12\mu R}\frac{\partial p}{\partial\xi} \tag{10}$$

Definindo-se a vazão de óleo adimensional por $Q = 2q/cU$, a conservação de massa no volume de controle da Fig. 3 expressa em termos algébricos, requer que,

$$Q_1\Delta\xi + Q_2(\pi+\alpha)\Delta\eta = Q_3(\pi+\alpha)\Delta\eta + Q_4\Delta\xi +$$

$$+ Q_5(\pi+\alpha)\Delta\eta\Delta\xi + Q_6\Delta\eta\Delta\xi \tag{11}$$

onde,

$$Q_1 = A_o - G_\eta\Big|_o A_o^{1/2}\left[\frac{A_o}{(\pi+\alpha)}\frac{\partial P}{\partial\eta}\Big|_o + \frac{3}{2}\,B_o P\Big|_o\right]$$

$$Q_2 = -G_\xi\Big|_s A_s^{3/2}\frac{\partial P}{\partial \xi}\Big|_s \quad , \quad Q_3 = -G_\xi\Big|_n A_n^{3/2}\frac{\partial P}{\partial \xi}\Big|_n$$

$$Q_4 = 1 - \varepsilon\cos\alpha \quad , \quad Q_6 = 2A_P\dot{\alpha} \tag{12}$$

$$Q_5 = 2[\dot{\varepsilon}\cos\theta_P + \varepsilon(\omega_L+\dot{\psi})\operatorname{sen}\theta_P]$$

$$A_* = 1 + \varepsilon\cos\theta_* \quad , \quad B_* = \varepsilon\operatorname{sen}\theta_* \tag{13}$$

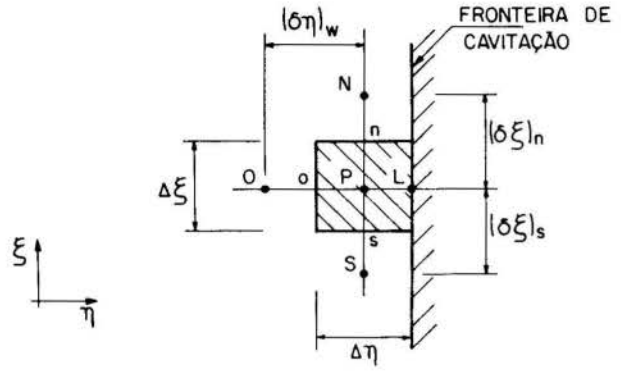

Fig. 3 - Volume de controle típico adjacente à fronteira de cavitação.

Ao escrever as expressões para o escoamento do filme de óleo cruzando cada face do volume de controle da Fig. 3, as derivadas da pressão que aparecem na equação (10) foram aproximadas por diferenças centrais. Adicionalmente, na expressão para Q_1, a pressão $P|_o$ foi numericamente aproximada tirando-se uma média entre P_P e P_O. A expressão para Q_4, que representa o óleo que cruza a fronteira de cavitação, tem embutida em si as condições $P = \partial P/\partial\eta = 0$. As vazões de óleo Q_5 e Q_6 representam, respectivamente, as parcelas referentes ao filme espremido e à pseudo vazão associada ao fato da fronteira de cavitação α estar variando com o tempo e desta forma estar incorporando ou eliminando óleo em um determinado instante. Note-se que em virtude do carregamento ser dinâmico, os volumes de controle estão variando de tamanho com o tempo. Tal variação está embutida na equação (11) uma vez que a malha computacional foi imobilizada pela transformação de coordenadas dada por (4).

A fim de se obter a fronteira de cavitação, é preciso que a equação (11) seja rearranjada de maneira que α apareça explicitamente. Desta forma, por conveniência computacional, a equação (11) é reescrita como,

$$\dot{\alpha} = \frac{\alpha^{\tau+\Delta\tau} - \alpha^\tau}{\Delta\tau} = \frac{D(\alpha^\tau)/\Delta\xi + \varepsilon\cos\alpha^{\tau+\Delta\tau} - 1}{2A_P\,\Delta\eta} \tag{14}$$

onde

$$D(\alpha^\tau) = Q_1\Delta\xi + Q_2(\pi+\alpha)\Delta\eta - Q_3(\pi+\alpha)\Delta\eta + \\ - Q_5(\pi+\alpha)\Delta\eta\Delta\xi \tag{15}$$

Note-se que na equação (14) utilizou-se um esquema semi-implícito, uma vez que os termos contendo α que aparecem na expressão de $D(\alpha)$ são avaliados no tempo τ ao passo que para o segundo termo no numerador do lado direito da equação (14) α é avaliado no tempo $\tau+\Delta\tau$. Fazendo agora,

$$\cos\alpha^{\tau+\Delta\tau} = \cos(\alpha^\tau + \dot{\alpha}\Delta\tau) \\ = \cos\alpha^\tau\cos(\dot{\alpha}\Delta\tau) - \operatorname{sen}\alpha^\tau\operatorname{sen}(\dot{\alpha}\Delta\tau) \tag{16}$$

e aproximando $\cos(\dot{\alpha}\Delta\tau)$ e $\operatorname{sen}(\dot{\alpha}\Delta\tau)$ por série de Taylor, tem-se, para pequenos valores de $\Delta\tau$,

$$\cos(\dot{\alpha}\Delta\tau) \doteq 1 - (\dot{\alpha}\Delta\tau)^2/2 \doteq 1 \\ \operatorname{sen}(\dot{\alpha}\Delta\tau) \doteq \dot{\alpha}\Delta\tau - (\dot{\alpha}\Delta\tau)^3/6 \doteq \dot{\alpha}\Delta\tau \tag{17}$$

Substituindo as expressões (17) na equação (16) obtêm-se,

$$\cos\alpha^{\tau+\Delta\tau} \doteq \cos\alpha^\tau - \dot{\alpha}\Delta\tau\operatorname{sen}\alpha^\tau \tag{18}$$

Combinando agora as equações (14) e (18), e isolando-se $\alpha^{\tau+\Delta\tau}$ chega-se à seguinte equação,

$$\alpha^{\tau+\Delta\tau} = \alpha^\tau + \left[\frac{D(\alpha^\tau)/\Delta\xi + \varepsilon\cos\alpha^\tau - 1}{2A_P\Delta\eta + \varepsilon\operatorname{sen}\alpha^\tau\Delta\tau}\right]\Delta\tau \tag{19}$$

Conhecido o valor de α em um instante τ, a equação (19) permite que o valor de α em um instante seguinte seja determinado.

O problema hidrodinâmico está agora completamente caracterizado. O próximo passo é determinar a posição do eixo ao longo da trajetória descrita pelo seu movimento. O conhecimento da posição do eixo fornecida pela variável ε, bem como das velocidades $\dot{\varepsilon}$ e $\dot{\psi}$, é requerido na equação de Reynolds para determinação do campo de pressão a cada instante.

Cálculo da Órbita do Eixo. A partir de um balanço entre a carga e as forças hidrodinâmicas nas direções ao longo e normal à linha que passa pelos centros do mancal e do eixo, as equações do movimento para um rotor rígido podem ser escritas de forma adimensional como,

$$\alpha\cos\psi - \beta F_1 = \ddot{\varepsilon} - \varepsilon\dot{\psi}^2 \\ \beta F_2 - \alpha\operatorname{sen}\psi = \varepsilon\ddot{\psi} + 2\dot{\varepsilon}\dot{\psi} \tag{20}$$

onde

$$\alpha = \frac{1}{G} \quad , \quad \beta = \frac{3}{\Delta G(L/D)} \quad , \quad G = \frac{\omega^2 c}{g} \quad , \quad \Delta = \frac{c^2 W}{\mu\omega R^3 L} \tag{21}$$

As forças F_1 e F_2 que aparecem nas equações (20) são as componentes da força hidrodinâmica ao longo e normal à linha de centros, respectivamente, conforme mostrado na Fig. 1. Estas forças são calculadas a partir da integração do campo de pressão de acordo com as expressões abaixo,

$$F_1 = -\int_0^{L/R}\int_0^1 \frac{P}{H^{3/2}}\cos[(\pi+\alpha)\eta]\,d\eta d\xi \\ F_2 = \int_0^{L/R}\int_0^1 \frac{P}{H^{3/2}}\operatorname{sen}[(\pi+\alpha)\eta]\,d\eta d\xi \tag{22}$$

Os termos do lado direito das equações (20) representam as quatro acelerações a que pode estar sujeito o eixo, ou seja, aceleração radial, centrífuga, angular e de Coriolis.

Conhecidas as forças hidrodinâmicas F_1 e F_2 a que está submetido o eixo em um determinado instante, bem como sua localização expressa por ε e ψ e suas velocidades e acelerações, a equação (20) permite que a localização do eixo e suas velocidades e acelerações possam ser determinadas em um instante seguinte. A integração das equações (20) foi realizada marchando-se no tempo em intervalos $\Delta\tau$, através de um método Runge-Kutta de 4ª ordem [9].

Aproximação Analítica para Mancal Curto. Para mancais cujo comprimento L é consideravelmente menor do que o raio R, as variações da pressão ao longo de θ podem ser desconsideradas na equação de Reynolds e a equação (5) pode então ser escrita como,

$$\frac{\partial^2 P}{\partial \xi^2} = \frac{G_\xi}{H^{3/2}} [2\,\dot{\varepsilon}\cos(\pi\eta) + (2\,\psi - 1)\,\varepsilon\,\mathrm{sen}(\pi\eta)] \qquad (23)$$

Na equação anterior fez-se por simplicidade $\omega_L = 0$ e assumiu-se a condição de meio Sommerfeld, ou seja, $\alpha = 0$.

A integração analítica da equação (23) fornece,

$$P = \frac{G_\xi}{2H^{3/2}} [2\,\dot{\varepsilon}\cos(\pi\eta) + (2\,\psi - 1)\,\varepsilon\,\mathrm{sen}(\pi\eta)](\xi^2 - \frac{L}{R}\,\xi) \qquad (24)$$

A partir do campo de pressão anterior, as forças hidrodinâmicas ao longo da linha de centros e normal a esta, calculadas a partir das equações (22) podem ser expressas por,

$$F_1 = \frac{1}{12}\left(\frac{L}{R}\right)^3 [(1-2\dot{\psi})[\frac{2\varepsilon^2}{(1-\varepsilon^2)^2}\,c_\xi + [\frac{2}{(1-\varepsilon^2)} - \frac{1}{\varepsilon}\ln\frac{(1+\varepsilon)}{(1-\varepsilon)}]\,b_\xi] + \pi\dot{\varepsilon}[\frac{(1+2\varepsilon^2)}{(1-\varepsilon^2)^{5/2}}\,c_\xi + \frac{2}{\varepsilon^2}\,b_\xi - \frac{(4\varepsilon^4 - 6\varepsilon^2 + 2)}{\varepsilon^2(1-\varepsilon^2)^{5/2}}\,b_\xi]] \qquad (25)$$

$$F_2 = \frac{1}{12}\left(\frac{L}{R}\right)^3 [(1-2\dot{\psi})\pi[\frac{\varepsilon}{2(1-\varepsilon^2)^{3/2}}c_\xi + \frac{(1-\varepsilon^2)^{1/2}}{\varepsilon(1-\varepsilon^2)}\,b_\xi - \frac{1}{\varepsilon}\,b_\xi] + 2\dot{\varepsilon}[\frac{2\varepsilon}{(1-\varepsilon^2)^2}\,c_\xi + \frac{2}{\varepsilon(1-\varepsilon^2)}\,b_\xi - \frac{1}{\varepsilon^2}\ln\frac{(1+\varepsilon)}{(1-\varepsilon)}\,b_\xi]] \qquad (26)$$

onde $c_\xi = a_\xi - b_\xi$.

As expressões anteriores para F_1 e F_2 correspondem àquelas para F_ξ e F_ϕ obtidas em [4] (a menos de alguns erros tipográficos encontrados naquele trabalho). Neste sentido as hipóteses anteriores de $\omega_L = \alpha = 0$ se justificam por terem sido também adotadas em [4]. Conforme mencionado na Introdução do presente trabalho, pretende-se aqui testar e estender os resultados de [4].

Adotando-se a aproximação de mancal curto, as expressões analíticas para F_1 e F_2 podem ser diretamente utilizadas nas equações (20) para o cálculo da órbita do eixo.

METODOLOGIA DE SOLUÇÃO

Tendo apresentado as equações que descrevem o carregamento dinâmico de mancais radiais, a atenção será agora voltada para a metodologia de solução utilizada no presente trabalho. Inicialmente deve-se considerar que o procedimento de cálculo envolve duas etapas distintas: a) determinação das forças hidrodinâmicas que atuam no eixo para uma dada posição e velocidade do eixo; b) determinação da posição e velocidade do eixo em função das forças hidrodinâmicas. Conforme discutido anteriormente, a primeira etapa envolve a solução da equação de Reynolds enquanto que a segunda requer a solução das equações do movimento. O aspecto a ser agora considerado se refere à interação entre o problema hidrodinâmico e a dinâmica do movimento.

Como o problema é dependente do tempo, deve-se partir de uma posição inicial em $\tau = \tau_0$. No presente trabalho tomou-se como condição inicial aquela em que o eixo está centrado no mancal sem suportar carga alguma, e desta forma em $\tau = \tau_0$ tem-se $\varepsilon = \psi = \dot{\varepsilon} = \dot{\psi} = 0$. Para $\tau > \tau_0$ uma carga é subitamente aplicada ao eixo. Logo que a carga é aplicada, as forças hidrodinâmicas são nulas e as equações (20) são então resolvidas para $F_1 = F_2 = 0$ fornecendo a posição e velocidade do eixo para o primeiro intervalo de tempo $\Delta\tau$. Tem-se então os valores de ε, ψ, $\dot{\varepsilon}$ e $\dot{\psi}$ para o tempo igual a $\tau_0 + \Delta\tau$. A partir destes valores o campo de pressão é calculado fornecendo então os valores de F_1 e F_2. Com F_1 e F_2 em $\tau_0+\Delta\tau$, retorna-se às equações (20) e obtém-se novos valores de ε, ψ, $\dot{\varepsilon}$ e $\dot{\psi}$ para o intervalo $\Delta\tau$ seguinte. A equação da pressão é então revisitada para que se obtenha os novos valores de F_1 e F_2. O procedimento anterior é então repetido sucessivamente e desta forma avança-se no tempo até que a solução seja descontinuada.

Na determinação do campo de pressão é necessário o conhecimento da fronteira de cavitação $\alpha(\xi)$. Como a determinação de $\alpha(\xi)$ requer o conhecimento do campo de pressão, interações se fazem necessárias. Assim, para o cálculo do campo de pressão no instante $\tau+\Delta\tau$, utiliza-se como primeira aproximação os valores de $\alpha(\xi)$ do instante τ. Com as pressões em $\tau+\Delta\tau$ os valores de $\alpha(\xi)$ são recalculados, e estes valores são então usados para a determinação de um campo de pressão corrigido em $\tau+\Delta\tau$. Novamente este campo de pressão é utilizado para atualizar $\alpha(\xi)$, e este procedimento iterativo é repetido até que o campo de pressão e os valores de $\alpha(\xi)$ não mais se alterem.

Em virtude das não linearidades associadas à determinação do campo de pressão e ao cálculo da fronteira de cavitação, a utilização de fatores de subrelaxação se faz necessária. Para a pressão empregou-se um fator de 0,95 enquanto que para α o fator utilizado foi 0,90.

RESULTADOS E DISCUSSÕES

A Figura 4 apresenta uma comparação entre a órbita do eixo para um carregamento constante subitamente aplicado no instante $\tau=0$, utilizando-se duas malhas distintas. Como o objetivo nesta figura era avaliar a influência da malha, por simplicidade, $\alpha=0$. A linha tracejada corresponde a uma malha com 20x11 (ηxξ) pontos nodais (220 pontos) e a linha cheia apresenta os resultados obtidos com uma malha de 40x21 (ηxξ) pontos nodais (840 pontos). O mancal da Fig. 4 possui as características associadas ao Caso 1, conforme apresentado na Tabela 1.

Tabela 1 - Casos Investigados

Caso	R[cm]	L[cm]	L/D	c[μm]	μ[Pa.s]	RPM	W[N]
1	7	3,5	1/4	250	0,02	3000	21439,8
2	3,5	3,5	1/2	250	0,001	3000	26,5
3	3,5	3,5	1/2	250	0,001	5000	26,5
4	3,5	3,5	1/2	250	0,001	4900	26,5

Em ambas as situações investigadas na Fig. 1 o intervalo de tempo utilizado foi $\Delta\tau=0,05$ ($=1,6 \times 10^{-4}$s). O tempo computacional para o mancal atingir a posição de equilíbrio ($\varepsilon=0,5$ e $\psi=0,94412$ rad) foi de 2,60 min e 29,42 min para as malhas com 20x11 pontos e 40x21 pontos, respectivamente. Considerando o compromisso entre precisão da solução e tempo computacional, para os demais casos, far-se-á uso da malha com 20x11 pontos. Para um estudo mais elaborado da malha, bem como avaliação do Runge-Kutta no cálculo da órbita do eixo, e de diferentes metodologias de solução envolvendo formas diversas de se calcular a fronteira de cavitação, referência se faz a [9].

A Fig. 5 apresenta uma comparação entre a aproximação de mancal curto (linha tracejada) e a solução para mancal finito (linha cheia) considerando a mesma situação investigada na Fig. 4. Observa-se da figura que, pela aproximação de mancal curto o eixo busca a posição de equilíbrio descrevendo uma espiral mais fechada do que quando se utiliza a solução para mancais finitos. Tal fato foi também verificado em [4]. A fim de mostrar a influência da fronteira de cavitação na órbita do mancal, a Fig. 6 foi preparada. A linha cheia representa a órbita do eixo quando $\alpha \neq 0$ e para a linha tracejada fez-se $\alpha = 0$. Nota-se da figura, a exemplo do que foi observado em [10], que na presença de cavitação o eixo procura sua posição de equilíbrio através de uma espiral mais fechada. Em [10] resultados semelhantes são plotados em um dia

grama ε versus τ e vê-se que para $\alpha \neq 0$ o eixo busca o equilíbrio através de um movimento oscilatório mais amortecido do que aquele correspondente a $\alpha = 0$.

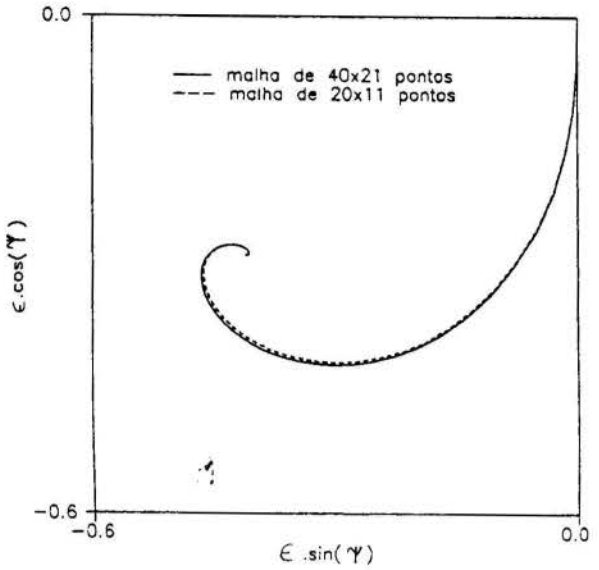

Fig. 4 - Comparação entre a órbita do eixo para situação laminar, mancal finito com α=0, para duas malhas distintas; caso 1.

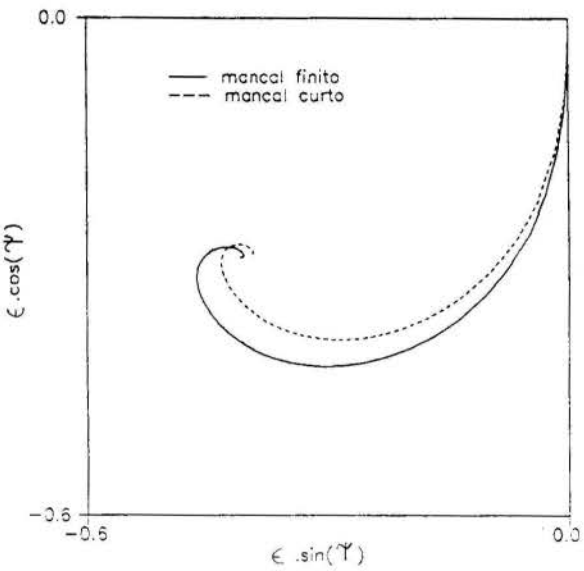

Fig. 5 - Comparação entre mancal curto e mancal finito; escoamento laminar; caso 1.

Uma comparação entre a órbita do eixo calculada a partir dos modelos para escoamento laminar e turbulento pode ser realizada ao analisar-se as Figs. 7 e 8 conjuntamente. Verifica-se que enquanto na Fig. 7 o eixo encontra uma posição de equilíbrio, na Fig. 8 o eixo não consegue encontrar o equilíbrio caracterizando uma situação instável. Tanto a Fig. 7 como a Fig. 8 representam a mesma situação física e a comparação entre ambas evidencia as diferenças entre os dois modelos. A extrapolação de modelos laminares para escoamentos que já seriam turbulentos pode gerar resultados significativamente incorretos.

A validade da aproximação de mancais curtos será agora verificada para o caso 4 da Tabela 1. Para tal fim as Figs. 9 e 10 foram preparadas. Conforme observado nestas figuras, a aproximação de mancal curto prevê que o eixo atingirá uma posição de equilíbrio ao passo que o modelo completo mostra que esta é uma situação instável. Note-se da Fig. 10 que o eixo busca demoradamente o equilíbrio, mas a cada volta da espiral, este se afasta dela e desta forma irá acabar atingindo o mancal.

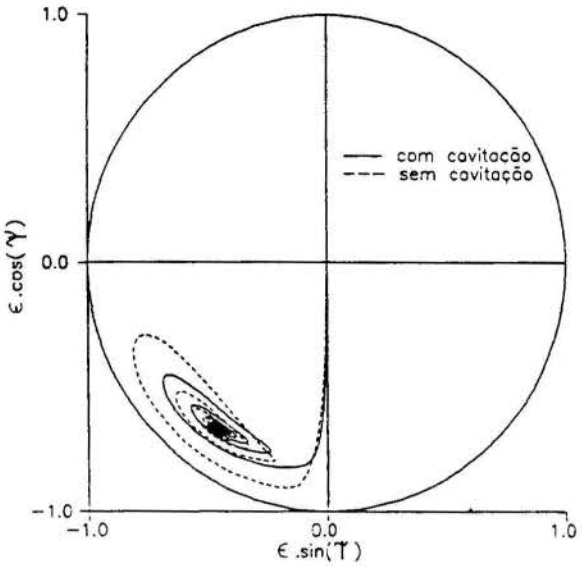

Fig. 6 - Comparação entre mancal finito com e sem cavitação; escoamento laminar; caso 2.

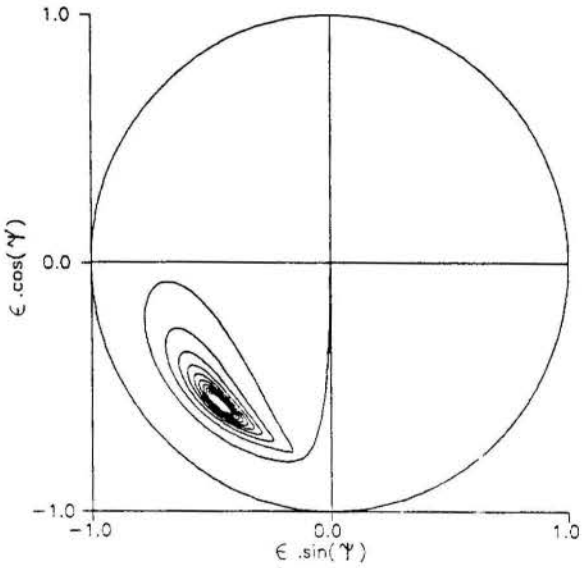

Fig. 7 - Órbita do eixo para mancal finito com cavitação em escoamento laminar; caso 3.

CONCLUSÕES

O presente trabalho apresenta uma metodologia em volumes finitos para o cálculo de carregamento dinâmico de mancais radiais. Considera-se tanto escoamento laminar como turbulento, e é dada ênfase especial no cálculo da fronteira na qual o filme de óleo cavita. Adicionalmente, são apresentadas as expressões associadas a mancais curtos. A trajetória do eixo no regime não permanente é obtida através das equações da dinâmica do rotor, e tais equações são resolvidas pelo método de Runge-Kutta.

A metodologia apresentada é empregada no cálculo das órbitas de um eixo quando submetido a uma carga constante, a partir de uma situação sem carga. Os gráficos mostram que ignorar os efeitos de turbulência e cavitação podem alterar significativamente os resultados. Da mesma forma, o emprego da aproximação de mancais curtos pode conduzir a grandes desvios nos resultados. Em geral, a inclusão dos efeitos de cavitação tendem a tornar o eixo mais estável uma vez que há um aumento do filme de

óleo já que este não se limita à região compreendida entre 0 e π radianos. A turbulência torna o mancal mais instável.

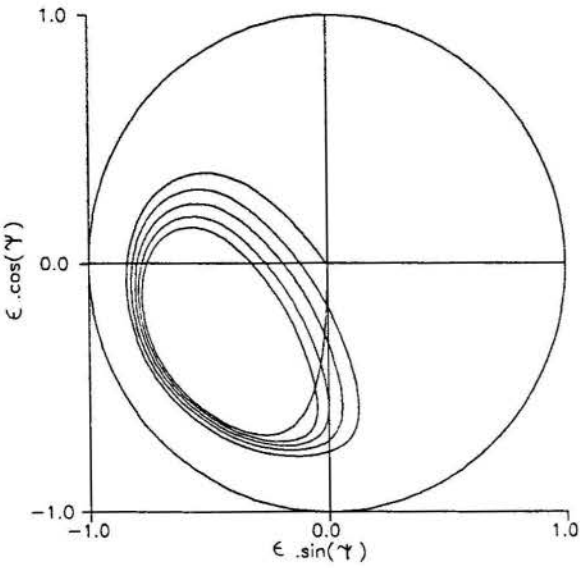

Fig. 8 - Órbita do eixo para mancal finito com cavitação em escoamento turbulento; caso 3.

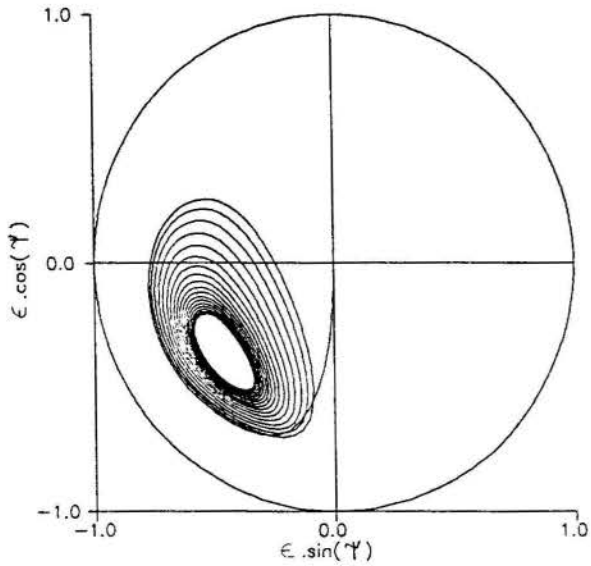

Fig. 9 - Órbita do eixo para mancal curto com cavitação em escoamento turbulento; caso 4.

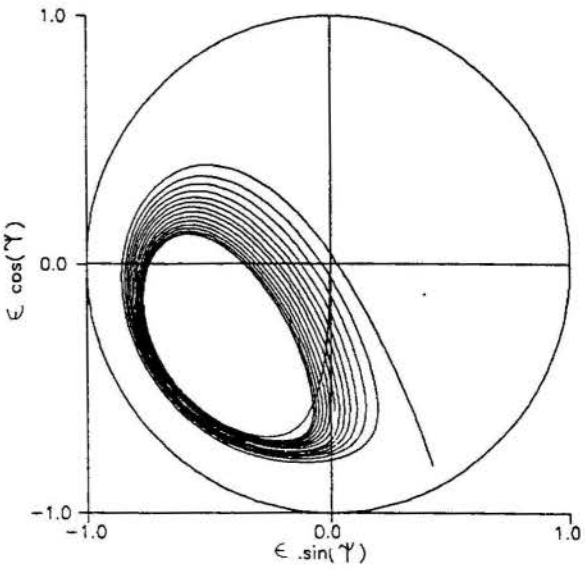

Fig. 10 - Órbita do eixo para mancal finito em escoamento turbulento; caso 4.

REFERÊNCIAS

[1] Newkirk, B.L., and Taylor, H.D., "Shaft Whipping Due to Oil Action in Journal Bearings," Gen.Electr. Rev.,Vol. 28, pp. 985-988, 1925.

[2] Prata, A.T., Ferreira, R.T.S., Lilie, D.E.B., e Bortoli, M.G.D., "Carregamento Dinâmico de Mancais Radiais: Análise pelo Método dos Volumes Finitos com Coordenadas Adaptadas às Fronteiras, "Anais do IX Congresso Brasileiro de Engenharia Mecânica, Florianópolis, SC, Vol. II, pp. 717-720, 1987.

[3] Hashimoto, H., Wada, S., and Sumitomo, M., "The Effects of Fluid Inertia Forces on the Dynamic Behavior of Short Journal Bearing in Superlaminar Flow Regime", Journal of Tribology, Vol. 110, pp. 539-547, 1988.

[4] Hashimoto, H., Wada, S., and Ito, I.I., "An Application of Short Bearing Theory to Dynamic Characteristic Problems of Turbulent Journal Bearings," Journal of Tribology, Vol. 109, pp.307-314, 1987.

[5] Hashimoto, H., and Wada, S., "An Influence of Inertia Forces on Stability of Turbulent Journal Bearings," Bulletin of JSME, Vol. 25. nº 202, pp. 653-662, 1982.

[6] Ng, C.W., and Pan, C.H.T., "A Linearized Turbulent Theory," ASME Journal of Basic Engineering, Vol. 87, pp. 675-688, 1965.

[7] Prata, A.T., and Ferreira, R.T.S., "The Accuracy of Short Bearing Theory in Presence of Cavitation," Journal of Tribology, to appear.

[8] Patankar, S.V., "Numerical Heat Transfer and Fluid Flow," Hemisphere Publishing Corporation, New York, 1980.

[9] Manke, A.L., "Desempenho de Sistemas de Mancais Radiais para Compressores Alternativos de Refrigeração", Dissertação de Mestrado em andamento, UFSC.

[10] Prata, A.T., Ferreira, R.T.S., Lilie, D.E.B. and Bortoli, M.G.D., "Dynamically Loaded Journal Bearings: Finite Volume Method Analysis," Proceedings of the 1988 International Compressor Engineering Conference at Purdue, Vol. I, pp.34-41, West Lafayette, IN, July, 1988.

ABSTRACT

The dynamically loaded journal bearings are investigated numerically. The Reynolds equation that describes the hydrodynamic pressure is integrated via the finite volume method, and special attention is devoted to the calculation of the cavitation boundary. The oil film is mapped into a rectangular domain using nonorthogonal coordinates, which allows the cavitation boundary to be precisely predicted. Results for a constant load suddenly applied on the journal are presented and compared with those for the short bearing approximation. Situations predicted as stable through the short bearing theory are shown to be unstable under the finite cavitating model.

III ENCIT – Itapema, SC (Dezembro 1990)

ASPECTOS TECNOLÓGICOS DA LUBRIFICAÇÃO DE MANCAIS AEROSTÁTICOS COM RESTRITORES FLEXÍVEIS

B. de M. Purquerio, Silvio A. Martinelli
USP - Escola de Engenharia de São Carlos
Av. Dr. Carlos Botelho, 1465
13560 - São Carlos, SP - Brasil

SUMÁRIO

Trata-se de uma revisão dos compensadores flexíveis para mancais aerostáticos, enfatizando o compensador flexível metálico. Este último, com novo projeto e dimensões otimizados utiliza elementos (restritores) metálicos que sensoriam a pressão de alimentação do mancal e, consequentemente, aumentam ou diminuem o escoamento através dos orifícios de alimentação. O desempenho do restritor foi observado através das caracte rísticas de capacidade de carga e da espessura do filme de ar lubrificante para várias condições de operação.

1- INTRODUÇÃO

Os mancais aerostáticos possuem diversas vantagens que são:

- baixo atrito;
- capacidade de operar a altas rotações;
- grande precisão de giro;
- desgaste muito baixo ou nulo;
- capacidade de operar em temperaturas altas e baixas;
- baixo ruído;
- o ar pode escapar para o ambiente sem perigo de contaminação;
- pode operar a baixas rotações, sem falha na lubrificação.

Dadas as vantagens acima, os mancais aerostáticos seriam preferíveis em diversas aplicações na indústria, se não fosse pela sua baixa rigidez e comparativamente baixa capacidade de carga.

A rigidez de um mancal é o parâmetro que relaciona a variação na folga do mancal respectivo, e essa rigidez depende essencialmente do método de controle de vazão para o mancal, ou seja, do método de compensação.

A fim de se aumentar a rigidez do mancal aerostático sem, entretanto, manter folgas muito reduzidas (que exigem qualidade de fabricação elevada), são propostos compensadores flexíveis que podem regular a vazão de alimentação do mancal em função da carga aplicada.

2 - RESTRITORES FLEXÍVEIS

LAUB (1960) propôs como método de compensação, o orifício elástico cuja variação do diâmetro em função da variação da carga no mancal controla a pressão no interior do mancal. Esses elementos flexíveis eram construídos de borracha. Nessa direção, NUNN e PAYTON (1969) propuseram elementos de borracha de forma tubular. Ambos foram abandonados em vista de suas dimensões reduzidas, inviáveis, posto que os elastômeros podem variar suas propriedades em se tratando de pequenas dimensões.

À luz desse fato, AL BENDER (1976) desenvolveu o restritor Flexível de Elementos Cônico, com as dimensões do elastômero (borracha de silicone) relativamente maiores.

O compensador flexível de elemento cônico foi testado por PURQUÉRIO (1979), mostrando resultados satisfatórios em termos de se aumentar a rigidez dos mancais aerostáticos. Contudo, a sua utilização não foi atraente devido as suas dimensões serem relativamente grandes.

DUDUCH (1988) otimizou o projeto do mesmo, solucionando os problemas inerentes a sua fabricação, tornando-o compacto e prático. O restritor foi construído na forma de cartucho, tornando a sua inserção nos mancais bastante simplificada, através de roscas.

Este trabalho visa otimizar o projeto e a construção de um novo restritor flexível metálico, com dimensões relativamente pequenas, fácil utilização e custo baixo, que, com seu elemento flexível metálico, terá inúmeras vantagens sobre os de borracha, particularmente no que se refere a homogeneidade do material, a vida mais longa e, uma maior resistência a ambientes severos tais como temperaturas altas e baixas, radiação e produtos químicos.

3 - ANÁLISE DA RIGIDEZ E DA CAPACIDADE DE CARGA

Os ensaios do compensador flexível em estudo foram efetuados em um mancal aerostático axial circular com alimentação central. Portanto, uma introdução a esse tipo particular de mancal aerostático torna-se aqui necessária, após uma análise do escoamento de um fluido incompressível entre placas paralelas.

3.1 - Escoamento Viscoso Incompressível Laminar Entre Placas Planas e Paralelas. A figura 1 ilustra o escoamento entre duas placas planas e paralelas. Admite-se que a pressão varia em apenas uma direção e que as placas são infinitas e se mantém paralelas a uma distância h. Como h é constante e não há variação de pressão através da película, o escoamento é predominante na direção x, e a velocidade na direção y é desprezada, ou seja, v=0.

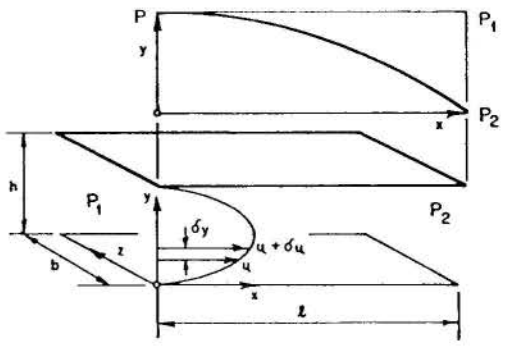

Fig. 1 - Escoamento entre duas placas planas e paralelas.

A equação do movimento na direção x é dada por:

$$u = \frac{1}{2\mu} \frac{dp}{dx} (y^2 - hy) \quad (1)$$

O perfil da velocidade na direção x é, portanto, parabólico e a equação fornece a velocidade do fluido em qualquer posição através do filme lubrificante.

A vazão em massa entre as placas de largura b é dada por:

$$\dot{m} = \rho\, b \int_0^h \mu\, dy \quad (2)$$

Assim, tem-se:

$$\dot{m} = -\frac{\rho\, b\, h^3}{12\,\mu} \cdot \frac{dp}{dx} \quad (3)$$

ou,

$$\frac{dp}{dx} = -\frac{12\,\mu\,\dot{m}}{\rho . b . h^3} \quad (4)$$

Essa equação relaciona a vazão em massa, o gradiente de pressão e as características da película lubrificante, na direção do escoamento.

3.2 - Modelagem de Mancais Aerostáticos Axiais Circulares com Alimentação Central. O escoamento em um mancal circular com vazão radial pode ser modelado de maneira semelhante ao das placas paralelas. A direção da variação de pressão, x, transforma-se na direção radial r, e a largura da seção considerada nas placas, b, é substituída pelo perímetro $2\pi r$ (fig.2). Assim, a equação 4, é modificada para expressar o gradiente de pressão radial em função da vazão do mancal

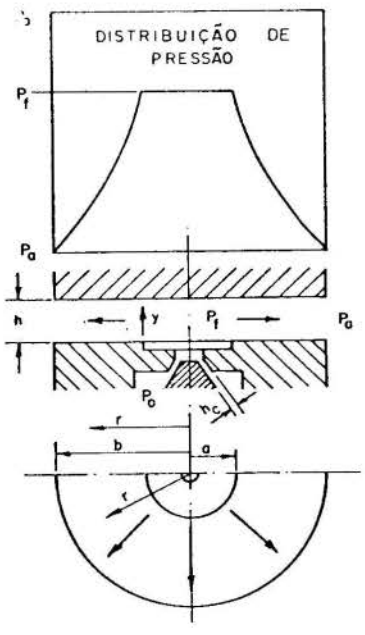

Fig. 2 - Esquema do mancal aerostático circular com alimentação central

axial, das características do fluido e da folga axial h, ou seja

$$\frac{dp}{dr} = \frac{6\,\mu\,\dot{m}}{\pi\,\rho\,r\,h^3} \quad (5)$$

A vazão em massa para este tipo de mancal, é dada por:

$$\dot{m} = \frac{(Pf^2 - Pa^2)\,\pi .\, h^3}{12\,\mu\,RT\,\ell n\,(b/a)} \quad (6)$$

onde, pode-se notar, a vazão é proporcional ao cubo da folga do mancal.

3.3 - Capacidade de Carga do Mancal. A carga total do mancal, W, pode ser obtida como uma função de Kg, da seguinte maneira:

$$W = Kg\,(P_0 - Pa)\,\frac{\pi\,(b^2 - a^2)}{\ell n\,(b/a)} \quad (7)$$

onde $Kg = \frac{Pf - Pa}{P_0 - Pa}$ é o coeficiente de pressão efetiva

Da mesma forma, a rigidez é dada por:

$$K = \frac{dw}{dh} = \frac{(P_0 - Pa)\,\pi\,(b^2 - a^2)}{\ell n\,(b/a)} \cdot \frac{dKg}{dh} \quad (8)$$

Uma expressão alternativa simplificada para a capacidade de carga do mancal pode ser obtida assumindo-se uma queda de pressão linear desde a entrada da alimentação até as bordas do mancal. A expressão resultante para a carga será:

$$W = Kg \cdot \pi\,(P_0 - Pa)\,(b^2 - a^2), \quad (9)$$

e, para a rigidez,

$$K = \frac{dw}{dh} = \pi\,(P_0 - Pa)\,(b^2 - a^2)\,\frac{dKg}{dh} \quad (10)$$

3.4 - Rigidez do Mancal. Nos mancais aerostáticos, a relação entre a carga e a espessura do filme lubrificante não é linear. Portanto, na análise desses mancais, torna-se necessário considerar a sua rigidez, ou seja, a variação da capacidade de carga com a espessura do filme. Supondo então, que um mancal esteja operando com uma espessura de filme h, sob uma carga aplicada W, então se esta carga é aumentada para um valor W + ΔW, a espessura do filme será reduzida para um valor h - Δh (fig.3). Inversamente se o carregamento no mancal foi reduzido para um valor W - ΔW, a espessura do filme tenderá a aumentar para um valor h + Δh

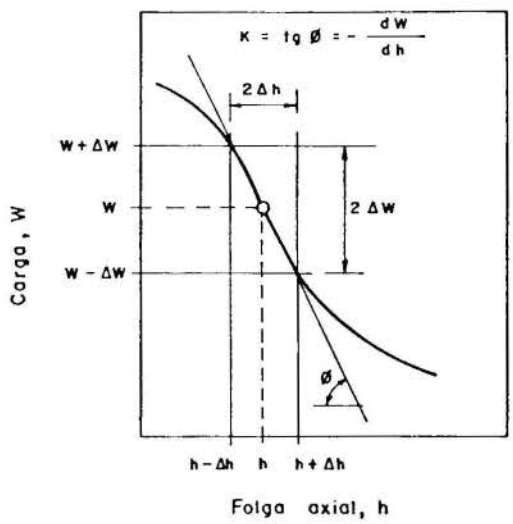

Fig. 3 - Carga em função da espessura do filme (folga axial)

A forma da curva W + h é típica para todos os mancais aerostáticos axiais, e a rigidez é definida por:

$$K = tg\,\emptyset = -\frac{dw}{dh} \quad (11)$$

A variação da carga, com a consequente variação da espessura do filme, denota uma região onde a curva tem uma maior inclinação. O ponto de maior inclinação na curva W x h, é o ponto de operação de rigidez máxima do mancal axial.

4 - MANCAIS, RESTRITORES E BANCO DE ENSAIOS

4.1 - Restritor com Elemento Flexível Metálico. O restritor flexível com elemento metálico cônico é ilustrado na fig. 4. A unidade tem simetria axial. O elemento flexível metálico 1, é montado, juntamente com o assento cônico 2, no mancal axial 4, através de um ajuste deslizante. Ambos os componentes são fixados sob o aperto da porca de fixação 3. Esses três elementos constituem o "cartucho" do atual compensador flexível em estudo experimental, objeto do presente trabalho.

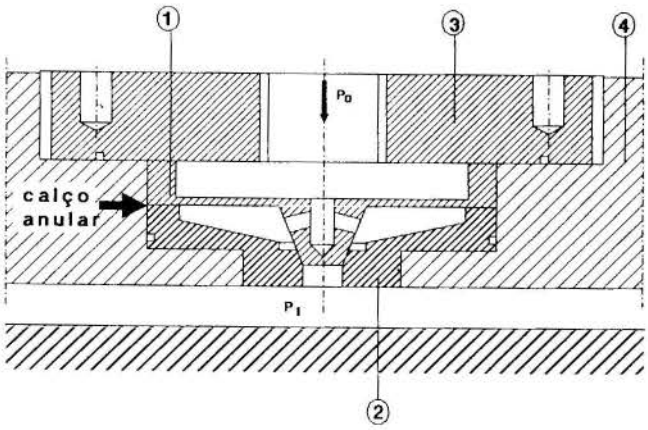

Fig. 4 - Restritor com elemento flexível metálico.

Na fig. 4, o elemento flexível e o assento cônico estão montados com interferência, ou seja, sem folga no ânulo cônico de passagem de ar. A abertura para a passagem de ar é feita através da colocação, durante a montagem, de calços de regulagem de espessura definida, entre o elemento cônico, assegurando assim o escoamento de ar através do restritor. Os elementos 2 e 3 são selados com anéis de borracha do tipo "O".

O presente restritor com elementos metálicos, apresenta vantagens com relação às versões anteriores (com elemento cônico de borracha) por ter somente três componentes no "cartucho". As versões anteriores possuem cinco ou mais componentes, além dos calços de regulagem.

4.2 - Regulagem da folga. Para se obter diferentes folgas no restritor flexível, são utilizados calços anulares de diferentes espessuras, inseridos entre as superfícies do elemento elástico cônico e do assento cônico, na posição indicada pela seta na ilustração do restritor na fig. 4. Os calços anulares montados dessa maneira, garantem a separação, na vertical, do elemento flexível 1 e assento cônico 2, de uma distância igual a espessura, e, do calço. O elemento flexível 1 e o assento cônico 2 permanecem concêntricos, pois ambos são guiados pelo mesmo furo no mancal 4. A folga, h_c , do restritor - separação entre as duas superfícies cônicas - pode ser então calculada conhecendo-se o ângulo de conicidade do elemento flexível, que no presente caso é de 30^0.

4.3 - Funcionamento. O ar proveniente do sistema de alimentação a pressão, P_0, é introduzido no restritor através da entrada na tampa 3 (ver fig. 4). Esse ar se escoa através de 4 orifícios existentes na superfície cônica do elemento flexível que se comunicam com a entrada de ar. O ar passa então pela folga , h_c , entre as superfícies cônicas, e, através do furo existente na superfície do mancal, passa para a folga do mancal formando o filme lubrificante a uma pressão P_f.

O mecanismo pelo qual a unidade de restrição aumenta a rigidez do mancal é o seguinte: a capacidade de carga do mancal é essencialmente dependente da pressão, P_f, no furo de entrada à superfície do mancal. Existe, todavia, uma muito pequena dependência da espessura do filme porque o escoamento entre as superfícies do mancal não é puramente laminar. Iniciando com uma carga elevada, o escoamento no restritor será pequeno, P_f será aproximadamente igual a pressão de alimentação, P_0 , e a deformação do elemento cônico-flexível será pequena. À medida que a carga é reduzida, P_f cai proporcionalmente e o elemento cônico flexível se distende restringindo o escoamento, evitando o aumento da espessura do filme lubrificante. Com a diminuição da carga não há um aumento de vazão, havendo portanto, um aumento da rigidez do mancal.

4.4 - Banco de Ensaios. O banco de ensaios é como esquematizado na fig. 5. Projetado para ensaio do mancal de escora (I), fig. 5.

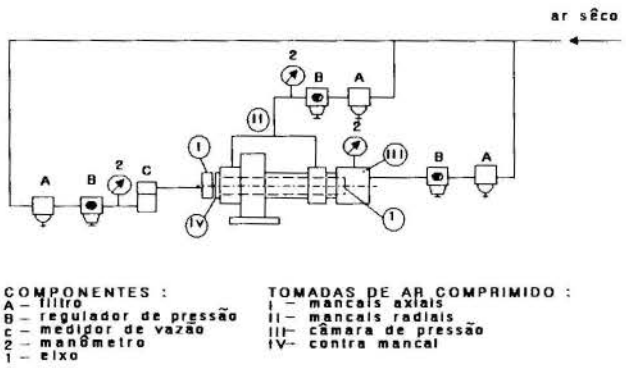

COMPONENTES :
A - filtro
B - regulador de pressão
C - medidor de vazão
2 - manômetro
1 - eixo

TOMADAS DE AR COMPRIMIDO :
I - mancais axiais
II - mancais radiais
III - câmara de pressão
IV - contra mancal

Fig. 5 - Banco de Ensaios.

A variação da carga sobre o mancal faz-se através da variação da pressão na câmara de pressão (III).

No mancal axial (I) é montado o restritor flexível através de três parafusos cuja ajustagem assegura o paralelismo entre o mancal (I) e o contra-mancal (IV). O restritor flexível é montado no mancal (I) e através do qual o ar entra para suas superfícies. O contra-mancal está fixado no eixo (1) sustentado por mancais aerostáticos alimentados pela tomada de ar (II). A outra extremidade do eixo se comunica com a câmara de pressão (III), formando assim um cilindro pneumático. A câmara (III) aplica uma pressão sobre o eixo, medida através do manômetro (2). A carga W que é aplicada no mancal (I) é então a pressão medida em (2) multiplicada pela área da seção do eixo. O deslocamento (e consequentemente a variação da folga h) do eixo e contra-mancal é medida através de três relógios comparadores micrométricos instalados em três furos executados no mancal (I).

5 - ENSAIOS E RESULTADOS

Com os resultados dos ensaios, construiram-se as curvas de capacidade de carga em função da folga axial, para cada pressão de alimentação utilizada, como as que ilustram a fig. 6, para s = 0,39 mm.

Na análise dessas curvas nota-se que quanto maior for a pressão de alimentação, tanto maior será a ca

pacidade de carga, para uma mesma folga de projeto.

Verifica-se também a existência de diferenças de comportamento dessas curvas, relativamente ao gradiente de inclinação, devido ao controle do restritor flexível do mancal, que compensa a variação da folga axial do mesmo em função da variação da pressão de alimentação (carga).

Considerando-se uma das curvas da fig. 6, como por exemplo a curva $P_0 = 4{,}14$ bar, que também é reproduzida na fig. 7, pode-se notar que a folga decresce normalmente com o aumento da carga até um determinado valor ($h \cong 8\mu m$, $W = 650$ N). Esse ponto localiza-se na fig. 7, na região 1. Nesse ponto a pressão P_f, no filme de ar do mancal, é maior e a diferença de pressão $\Delta p = P_0 - P_f$, é proporcionalmente menor do que no início do carregamento. Assim sendo, o restritor se deflete, aumentando a vazão de ar através dele e consequentemente através da folga do mancal, resultando no estabelecimento da folga $h \cong 4\mu m$ para $W = 880$ N. Esse ponto é localizado na região 2 da fig. 7.

Verifica-se portanto que entre as duas regiões da fig. 7, a curva apresenta um gradiente de inclinação, significando um aumento na rigidez do mancal. Isso ocorre no entorno da folga $h = 6\ \mu m$. Esse gradiente de inclinação é significativamente maior nesse trecho.

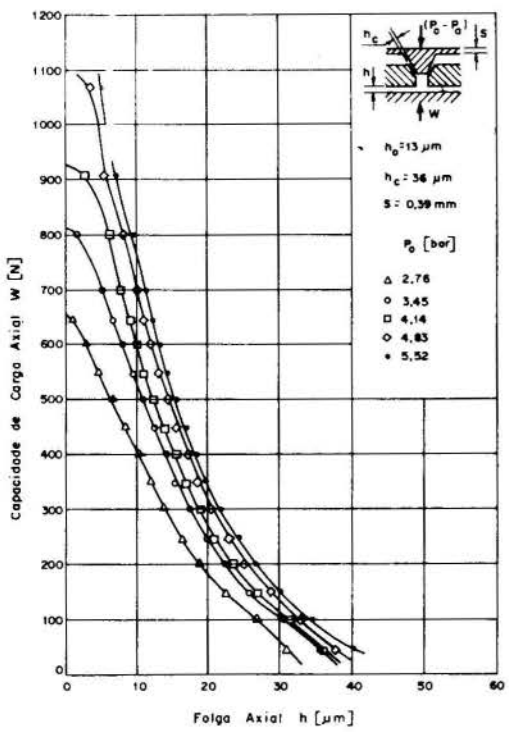

Fig. 6 - Capacidade de carga x folga axial do mancal para $h_c = 36\ \mu m$

A curva de capacidade de carga x folga axial do mancal seria equivalente a uma "curva dupla" conforme ilustra a fig. 7. No início do carregamento, a variação da folga com a carga ocorre segundo a curva 1 para uma folga no restritor $h_c = h_{c_1}$. Se não houvesse o controle flexível, essa curva teria um comportamento como mostra o trecho 1a (tracejado). Com o aumento da carga, o elemento flexível do restritor aumenta a vazão (mudando a folga de h_{c_1} até h_{c_2}), para contrabalançar uma pressão de carregamento maior no mancal, com o consequente aumento de inclinação da curva (trecho 3). A variação da folga axial com a carga passa então a ser descrita segundo a curva 2. Analogamente, o trecho 2a seria o comportamento do mancal se $h_c = h_{c_2}$ e constante, desde o início.

O trecho 3 mostrado na fig. 7, entre as regiões 1 e 2, representa a transição entre as "duas curvas". É neste trecho que o restritor flexível atua, controlando a vazão e corrigindo a folga, fazendo com que a rigidez apresente uma tendência ao infinito.

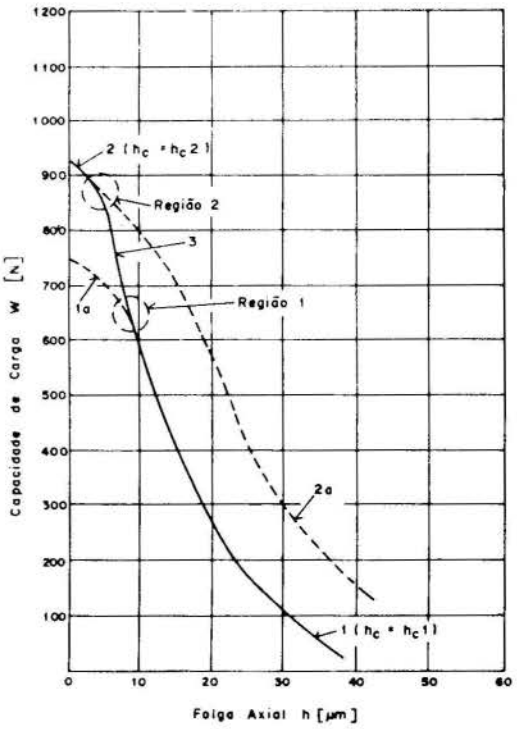

Fig. 7 - Comportamento do restritor flexível.

6 - CONCLUSÃO

Os mancais aerostáticos equipados com restritor flexível reunem alta rigidez, alta capacidade de carga e uma folga operacional grande aliadas ao baixo custo de fabricação. Contempla-se ainda a simplicidade e as dimensões reduzidas do compensador flexível metálico que o tornam atraente à utilização em mancais relativamente pequenos. Em muitas situações, como nas aplicações em máquinas ferramentas, onde a utilização de mancais aerostáticos é reduzida, devido ao seu elevado custo e características pobres de rigidez poderá agora tornar idealmente adequada para estas instalações.

7 - REFERÊNCIAS

[1] - AL BENDER, F.F.M. Investigation of a flexible compensator. M.Sc. Tribology Dissertation, Leeds, the University, 1976.

[2] - DUDUCH, J.G. Otimização de um restritor flexível para mancais aerostáticos axiais. Dissertação de Mestrado, São Carlos, EESC-USP, 1988.

[3] - LAUB, J.H. Elastic orifices for gas bearings. ASME - Journal of Basic Engineering, 82: p. 980 -982, 1960.

[4] - NUNN, M.C. and PAYTON, R.A. The influence of component flexibility on the performance of the externally pressurized air bearing. M.Sc. Tribology Dissertation, Leeds, the University, England, 1969.

[5] - PURQUÉRIO, B.M. Development of a flexible compensator for externally pressurized air bearing. M.Sc. Tribology Dissertation, Leeds, the University, 1979.

[6] - DUDUCH, J.G.; PURQUERIO, B.M. Otimização de um compensador flexível para mancais aerostáticos. Congresso Brasileiro de Engenharia Mecânica, 8, S.J. Campos - SP, dez. 1985 - Anais p. 753-758.

[7] - POWELL, J.W. Design of aerostatic bearings. London, The Machinary Publishing, 1970. 280 p.

[8] - NASA. Elastic orifices for gas bearing technology. Utilization Report, SP-5029, 1965.

[9] - PURQUERIO, B.M. Desenvolvimento de um compensador flexível para mancais aerostáticos. Congresso Brasileiro de Engenharia Mecânica, 7, Uberlândia, dez. 1983 - Anais. p. 161-170.

SUMARY

A review of the flexible compensators for aerostatic bearings, with enphasis to the metalic flexible compensator was carried out. The later, with a new design and optimized dimensions employs metalic elements which regulate the feed pressure in the bearing and, consequently increase the flow through the feed holes. The performance of the restrictor was measured by means of the load carriyng capacity and film thickness for many operation conditions.

III ENCIT – Itapema, SC (Dezembro 1990)

TRANSFERÊNCIA DE GASES EM SUPERFÍCIES LÍQUIDAS ALTAMENTE AGITADAS

HARRY EDMAR SCHULZ
Departamento de Hidráulica e Saneamento da
Escola de Engenharia de São Carlos, Universidade de São Paulo
Av. Dr. Carlos Botelho, 1465, CEP. 13.560 - S. Carlos - SP, BR

RESUMO

A absorção de gases por líquidos é analisada para uma situação na qual a difusividade molecular do gás no líquido não é um parâmetro relevante. Esta abordagem foi feita com vistas à aplicação para sistemas muito agitados. Experimentos de diferentes autores mostram comportamentos que sugerem que a formulação proposta pode ser encarada como um caso limite para o qual a razão entre dois coeficientes de troca de massa tende ao aumentar a agitação do líquido

INTRODUÇÃO

A busca de uma relação para descrever transferência de gases através de superfícies líquidas produziu uma discussão intensa acerca do valor do expoente da difusividade molecular que surge na expressão que relaciona o coeficiente de absorção do gás e a difusividade molecular. O cerne desta discussão gira em torno das previsões feitas pela teoria dos dois filmes e pelas teorias de penetração renovação superficial, gerando uma série de modelos que visam unificar as duas tendências. Pouca atenção foi dada às observações de Kishinevsky e Serebriansky (1955), que sugerem que a transferência de gases em sistemas líquidos altamente agitados tendem a seguir leis diferentes daquelas para sistemas líquidos pouco agitados e que a difusividade molecular é irrelevante nos primeiros.

A abordagem ora apresentada adota um ponto de vista molecular para estudar o fenômeno.

É aceito que a transferência de gases através de uma interface gás-líquido pode ser expressa por um coeficiente global, o qual traz informações sobre a fase líquida e a fase gasosa, na forma:

$$1/K_L = 1/k_L + 1/\bar{H}k_g \qquad (1)$$

K_L é o coeficiente global de transferência, k_L e k_g são os coeficientes de transferência para a fase líquida e a fase gasosa e $\bar{H}$ é a constante da lei de Henry para o gás selecionado. A ordem de grandeza relativa de k_L e $\bar{H}k_g$ determina se a transferência é controlada na fase líquida ou na fase gasosa. Uma revisão dos estudos em transferência de gases em superfícies líquidas encontradas na literatura levantou a questão dos limites de validade de certos métodos e modelos, e da necessidade de uma classificação das metodologias em relação às condições de estudo. Algumas das conclusões encontradas são

1 - A relação k_g/k_L depende das condições hidrodinâmicas em um dado processo. Parece, baseado nas tendências observadas, que k_g/k_L decresce em aumentando o nível de agitação do sistema (medido a partir de um número de Reynolds ou pela potência imposta, por exemplo). (Munz e Roberts (1984)).

2 - Para gases pouco solúveis sendo absorvidos em sistemas "normalmente" agitados o coeficiente de transferência global depende da difusividade molecular do gás no líquido, segundo uma lei exponencial. (Lewis & Whitman (1924), Dankwerts (1951)).

3 - Para sistemas altamente agitados, o coeficiente de transferência global não depende da difusividade molecular do gás no líquido (Kishinevsky (1955) e Kishinevsky e Serebriansky (1955)).

4 - Para dois gases sendo transferidos através de uma interface gás-líquido, vale a relação K_{L1}/K_{L2} = constante e, ainda, se o modelo de difusividade de Einstein for utilizado, esta relação pode ser expressa como $K_{L1}/K_{L2} = R_2/R_1$, onde R_i são os raios moleculares dos gases (Tsivoglou et alii (1965), Rainwater & Holley (1983)).

5 - A superfície do líquido pode ser admitida como "instantaneamente saturada" em processos de absorção de gases pouco solúveis. Esta conclusão pode ser baseada, por exemplo, no pequeno tempo (ordem de 10^{-7} segundos) que a camada superficial de água necessita para se saturar de oxigênio. (Holley (1977)).

DESCRIÇÃO DO PROBLEMA

As observações acima sugerem que, em aumentando a agitação, o processo de transferência de gases pode evoluir de uma situação controlada pela fase líquida para uma situação controlada pela fase gasosa ou, pelo menos, que exibe tal tendência. Além disso, enquanto é aceito que para sistemas "normalmente agitados" o coeficiente global de transferência é uma função da difusividade molecular do gás no líquido (embora exista alguma controvérsia acerca do valor do expoente da difusividade na "lei exponencial" proposta), para sistemas altamente agitados este tipo de dependência deixa de existir. Esses dois resultados parecem complementares. Contudo, para gases pouco solúveis em processos de absorção, se se aceita que a superfície líquida pode ser instantaneamente saturada, então a complementaridade anterior é perdida. Não é possível, neste caso, afirmar que os processos de absorção em agitação intensa são controlados pela fase gasosa, porque a saturação instantânea da superfície implica em difusividade infinita do gás na fase gasosa e é impossível controlar qualquer processo com uma difusividade infinita.

Adicionalmente, o resultado K_{L1}/K_{L2} = constante é

largamente utilizado sem um estabelecimento claro dos seus limites de validade, em considerando a agitação do líquido. Substituindo a equação 1 neste resultado, tem-se:

$$1/k_{L1} + 1/(H_1\, k_{g1}) = \text{Constante}.[1/k_{L2} + 1/H_2 k_{g2})] \quad (2)$$

Ou

$$IJ = \frac{(k_{g2}/k_{L2}) + 1/H_2}{(k_{g1}/k_{L1}) + 1/H_1} \cdot \frac{k_{g1}}{k_{g2}} \quad (3)$$

IJ é uma constante e os índices 1 e 2 estão relacionados com os dois gases em questão.

A equação 3 deve ser válida para os mais diversos equipamentos, uma vez que a expressão K_{L1}/K_{L2} = constante não considera qualquer tipo de geometria. k_{gi}/k_{Li} são dependentes das condições hidrodinâmicas e como conseqüência, a relação k_{gi}/k_{gj} deve levar em conta essas variações para manter constante o produto indicado. Os dados existentes atualmente, contudo não permitem verificar a equação 3.

O objetivo do presente artigo é estudar variações do coeficiente global de transferência e as ramificações dessas variações na dependência para com a difusividade molecular em diferentes niveis de agitação.

DESENVOLVIMENTOS ANALÍTICOS

Algumas equações para transferência de gases em superfícies líquidas altamente agitadas foram obtidas por Schulz (1990) considerando que a difusividade molecular não é relevante nessas situações. As Figuras 1 e 2 representam a região interfacial adotando um ponto de vista molecular, mostrando que é difícil definir uma "superfície" para o líquido. A Figura 1 mostra uma situação na qual é permitido ao gás difundir ao longo de uma distância no líquido, o que corresponde ao caso em que o "efeito inibidor" da superfície dificulta a ação dos turbilhões junto a ela. A Figura 2 mostra uma situação na qual os turbilhões atingem a superfície carregando volumes de líquido saturado com gás.

Os desenvolvimentos consideram, primeiramente, uma situação simplificada na qual a aproximação usual de uma superfície plana para a interface gás-líquido é feita (Figura 3). Neste desenvolvimentos foi considerada uma única célula de circulação. As conclusões, contudo, podem ser estendidas para todo o volume.

Uma vez que a difusão não é considerada, desenvolveu-se um primeiro modelo para a absorção muito simples. Uma região junto à superfície é admitida instantaneamente saturada e a introdução desta região saturada no volume de líquido é governada pelo movimento do líquido na superfície. Tem-se, então, seguindo o esquema da Figura 4, as expressões desenvolvidas abaixo:

O número de moléculas de gás que entra no volume de líquido, N_s, pode ser expresso por:

$$N_s = (n_{sat} - n).\text{Volume da camada saturada}$$

onde n é a densidade volumétrica de moléculas no líquido, sendo n_{sat} a condição de saturação. A taxa de transferência de massa ($\dot{M}$) é obtida multiplicando N_s pela massa molecular e dividindo o resultado pelo tempo médio de contato entre a fase líquida e a fase gasosa ($T \sim L/V$). (Grandezas definidas nas Figuras 3 e 4).

$$\dot{M} = (C_s - C) \cdot A_c \cdot \delta/T \quad (4)$$

C é a concentração do gás no líquido, com um valor de saturação C_s. Exprimindo $\dot{M} = d[C.(A_c.H)]/dt$, tem-se, finalmente,

$$dC/dt = (C_s - C).K_L/H \quad (5)$$

onde o coeficiente global de tranferência é expresso como $K_L = \delta/T \simeq \delta V/L$.

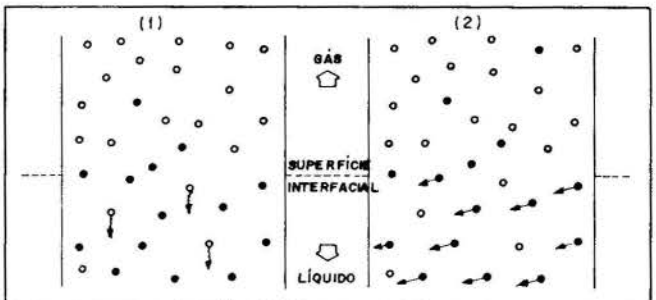

FIGURAS 1 e 2 : A REGIÃO INTERFACIAL A PARTIR DE UM PONTO DE VISTA MOLECULAR. 1 - DIFUSÃO DAS MOLÉCULAS DE GÁS, 2-TRANSPORTE DAS MOLÉCULAS DE GÁS DEVIDO AO MOVIMENTO PREFERENCIAL DO LÍQUIDO

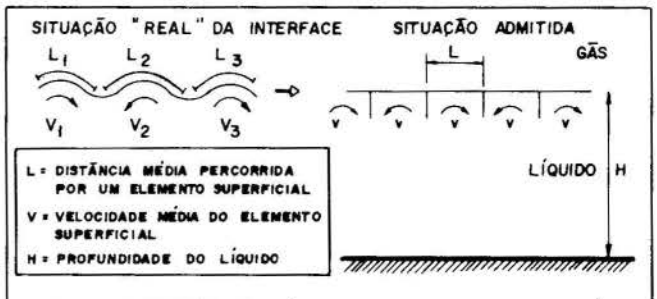

FIGURA 3 : SUPERFÍCIE DO LÍQUIDO CONSIDERADA PLANA. A ÁREA SUPERFICIAL DAS CÉLULAS DE CIRCULAÇÃO PODE SER EXPRESSA POR $Ac \propto L^2$, ISTO É, $Ac = w L^2$, ONDE w É UMA CONSTANTE

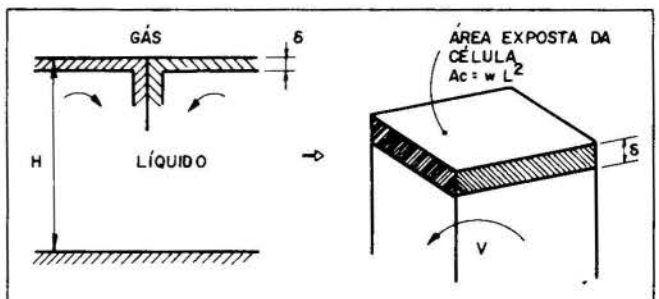

FIGURA 4 : ESQUEMATIZAÇÃO DA REGIÃO INTERFACIAL

A ordem de grandeza do comprimento δ pode ser obtida de resultados experimentais. Como uma primeira avaliação, para o caso de absorção de oxigênio pela água, os dados de Rainwater e Holley (1983) foram utilizados. O tempo de contato foi admitido ser da ordem de 1 segundo. Isto conduziu a valores entre 0,001 m e 0,0001 m para a espessura δ. Resultados para flutuações de concentração de oxigênio próximo à superfície da água obtidos por Lee e Luck (1982) mostram picos de concentração próximos à saturação até uma distância da superfície da ordem de 0,0001 m, indicando que os valores sugeridos são razoáveis. Deve ser enfatizado que os experimentos mencionados podem não corresponder a uma situação de agitação intensa. Porém, a despeito deste fato, a semelhança numérica atingida sugere que o modelo está razoavelmente bem relacionado com a situação física.

A equação $K_L = \delta/T$, contudo, não fornece uma relação útil para verificar resultados ou tendências experimentais e relacioná-las com parâmetros físicos conhecidos. Ao invés disso, um novo parâmetro (δ) é definido, o qual necessita ser estimado. Para obter informações que

envolvem parâmetros físicos úteis, uma nova simplificação sobre a região interfacial foi feita, na qual, ao invés de considerar uma região volumétrica instantaneamente saturada, foi admitido que apenas a superfície do líquido pode obsorver o gás. Esta absorção pode ocorrer seguindo uma equação de primeira ordem:

$$dN^*/dt = S(N^*_{sat} - N^*) \qquad (6)$$

N^* é o número de moléculas por unidade de área, sendo N^*_{sat} a condição de saturação, e S é uma constante. A integração com a condição $N^*(t = 0) = N^*_0$ produz:

$$N^*(t) = N^*_{sat} - (N^*_{sat} - N^*_0).\exp(-St) \qquad (7)$$

O tempo médio de exposição à atmosfera de um elemento de líquido que atinge a superfície é L/V. O número de moléculas adicionadas a este elemento de superfície, por unidade de área, é:

$$N^*_{adic} = N^*(t = L/V) - N^*_0 \quad \text{ou}$$

$$N^*_{adic} = (N^*_{sat} - N^*_0) \cdot [1 - \exp(-SL/V)] \qquad (8)$$

Para obter o número de moléculas que é incorporado ao volume de líquido por unidade de tempo ($\dot{N}$), a equação 8 é multiplicada pela área exposta da célula (wL^2) e dividida pelo tempo médio de exposição (L/V), fornecendo:

$$\dot{N} = G \cdot (N^*_{sat} - N^*_0) \cdot [1 - \exp(-SL/V)]\, wLV \qquad (9)$$

A constante de proporcionalidade G é utilizada, ao invés de uma igualdade imediata, porque é sabido que não apenas a "lâmina superficial" esta saturada (no presente caso, uma tendência assintótica). De $K_L = \delta/T$ e de resultados experimentais foi anteriormente concluído que uma região com espessura da ordem de 0,0001 m a 0,001 m pode estar saturada. Se é admitido que a "lâmina superficial" tem uma espessura de aproximadamente um diâmetro molecular, a constante de proporcionalidade deve ser da ordem de 10^6 a 10^7.

Para obter uma expressão envolvendo a concentração do gás no líquido, foi necessário relacionar N^* com a densidade volumétrica de moléculas, n. Para esta operação dois parâmetros foram definidos: vm, a fração de volume ocupado pelas moléculas e am, a fração de área ocupada pelas moléculas em uma superfície paralela à interface ar-água.

Baseado no esquema da Figura 5, é possível dizer que a área média ocupada pelas moléculas em uma superfície paralela à interface é uma função da posição da superfície no eixo z. Seja a(z) a função que descreve esta variação.

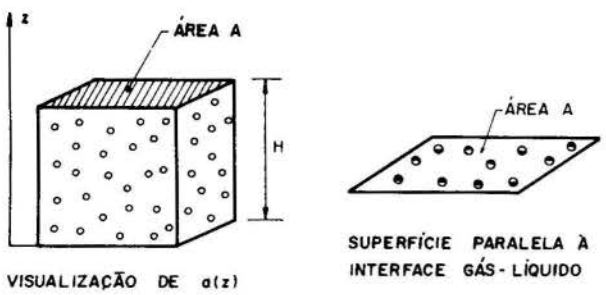

FIGURA 5 : VOLUME DE LÍQUIDO E SUPERFÍCIE UTILIZADOS PARA A ANÁLISE QUE CONDUZ À EXPRESSÃO 10

É possível escrever:

$$am = \frac{1}{H} \int_0^H a(z)\, dz = \frac{1}{A\,H} \int_0^H A.a(z)\, dz = vm \qquad (10)$$

Empregando, agora, o esquema da Figura 6 para avaliar o número médio de moléculas interceptado pela superfície (N).

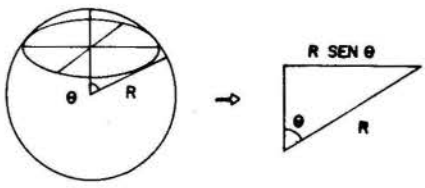

FIGURA 6 : ESQUEMA SEGUIDO PARA AVALIAR A ÁREA OCUPADA PELAS MOLÉCULAS

A área ocupada pelas moléculas (Am) é

$$Am = \sum_1^N \pi R^2 \sin^2(\theta_i) = \pi R^2 \cdot N \sin^2 \theta_{eq} \qquad (11)$$

$$\text{onde } \sin^2 \theta_{eq} = (1/N) \sum_1^N \text{sen}^2(\theta_i) \qquad (12)$$

$\sin^2(\theta_{eq})$ pode ser avaliado considerando que θ_i são uniformemente distribuídos entre $-\pi/2$ e $\pi/2$ e que N é um número grande, de forma que o cálculo integral pode ser utilizado. Este procedimento conduz a:

$$\sin^2(\theta_{eq}) = 1/2 \quad \text{e} \quad Am = \pi R^2\, N/2 \qquad (13)$$

Lembrando que:

$$Am = am.A = vm.A = (4\pi R^3 n/3).A$$

Então:

$$N = 8RnA/3 \quad \text{e} \quad N^* = 8Rn/3 \qquad (14)$$

O uso da equação 14 na equação 9 produz:

$$\dot{N} = \frac{8w\ RLVG}{3} [1 - \exp(-SL/V)]\, [n_{sat} - n] \qquad (15)$$

A descarga de massa é obtida da equação 15 multiplicando-a pela massa molecular do gás. Finalmente, este fluxo de massa pode ser aproximado por d(C.Volume)/dt, levando a:

$$dC/dt = \frac{8\,R\,V\,G}{3\,L\,H} [1 - \exp(-SL/V)]\, [C_s - C] \qquad (16)$$

Da equação 16 segue:

$$K_L = \frac{8\,R\,V\,G}{3\,L} [1 - \exp(-SL/V)] \qquad (17)$$

ANÁLISE DO COMPORTAMENTO PREVISTO

Se S é grande, é possível admitir que a superfície está instantaneamente saturada com o gás, e a equação 20 é reduzida para:

$$K_L = 8\,R\,V\,G/3L \qquad (18)$$

Definindo $\gamma = 8RG/3$ e $x = V/L$ e graficando K_L

das equações 17 e 18 em relação a x , obtém-se o gráfico da Figura 7.

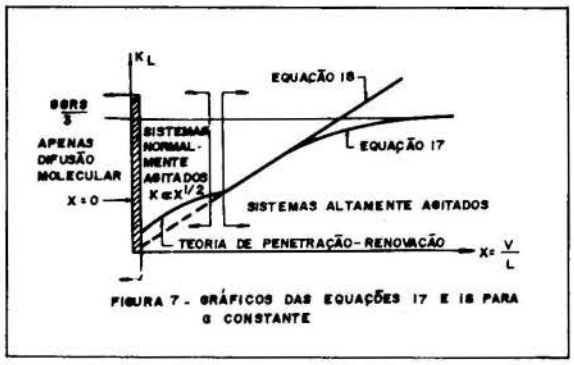

FIGURA 7 - GRÁFICOS DAS EQUAÇÕES 17 E 18 PARA G CONSTANTE

Nesta Figura, x é uma medida do inverso do tempo de exposição do elemento líquido à fase gasosa. Como não se espera que os presentes desenvolvimentos se apliquem para os sistemas menos agitados, a teoria da penetração de Higbie foi utilizada para completar o gráfico. Desta teoria $K_L \alpha x^{1/2}$.

Para dois gases diferentes sendo absorvidos pelo mesmo líquido, sujeitos às mesmas condições de agitação, tem-se:

$$\frac{K_{L1}}{K_{L2}} = \frac{R_1}{R_2} \quad \frac{\{1 - \exp(-S_1 L/V)\}}{\{1 - \exp(-S_2 L/V)\}} \qquad (19)$$

Para altos valores de S_1 e S_2 (superfície instantaneamente saturada), segue que:

$$K_{L1}/K_{L2} = R_1/R_2 \qquad (20)$$

Este resultado mostra que, para sistemas altamente agitados, uma relação limite entre os coeficientes de transferência de massa e raios moleculares é obtida, que é diferente daquela mencionada na introdução deste artigo e largamente utilizada na literatura. Para esta última é aceito que (ver Tsivoglou et alii (1965)):

$$K_{L1}/K_{L2} = R_2/R_1 \qquad (21)$$

Esta relação é razoavelmente verificada para volumes de líquido que podem ser ditos "normalmente agitados". (Ver Rainwater e Holley (1983), por exemplo).

As equações 20 e 21 sugerem que se sistemas normalmente agitados apresentam determinada tendência, então os sistemas altamente agitados apresentarão comportamento inverso.

A equação 20 foi obtida para uma situação de saturação instantânea da superfície (S muito alto). Se S tem um valor limitado, a Figura 7 mostra que é possível obter:

$$K_{L1}/K_{L2} = S_1 R_1/S_2 R_2 \qquad (22)$$

S_i são medidas das "taxas de fixação" das moléculas de gás na superfície do líquido e envolvem todas as possíveis interações entre as moléculas de gás e de líquido na região interfacial. Se S_i são dependentes dos raios moleculares, uma equação tão simples quanto a equação 20 pode não ser obtida.

Da Figura 3 também se conclui que a área superficial média pode ser maior que a sua projeção horizontal e que este valor de área pode ser uma função do nível de agitação. Portanto, nesses casos, a "constante" G deve aparecer explicitamente na Figura 7.

COMPARAÇÕES COM RESULTADOS EXPERIMENTAIS DE DIFERENTES FONTES

O comportamento dos dados experimentais de diferentes autores foi analisado de forma a avaliar os resultados apresentados aqui.

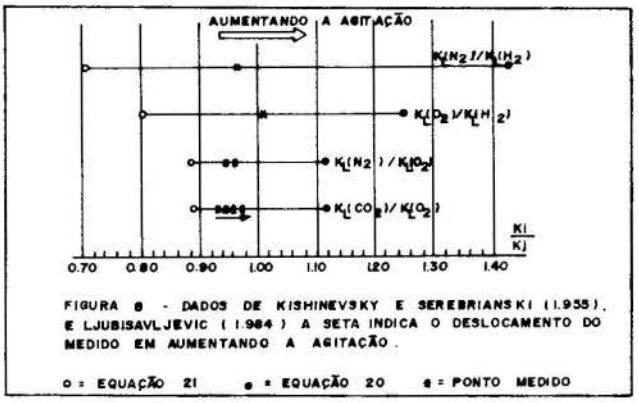

FIGURA 8 - DADOS DE KISHINEVSKY E SEREBRIANSKI (1.955), E LJUBISAVLJEVIC (1.984) A SETA INDICA O DESLOCAMENTO DO MEDIDO EM AUMENTANDO A AGITAÇÃO.

o = EQUAÇÃO 21 • = EQUAÇÃO 20 ⊛ = PONTO MEDIDO

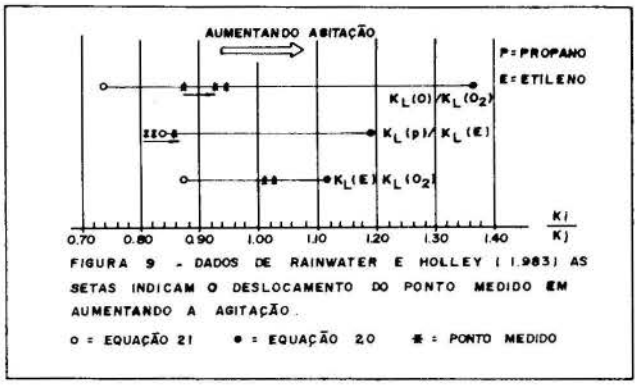

FIGURA 9 - DADOS DE RAINWATER E HOLLEY (1.983) AS SETAS INDICAM O DESLOCAMENTO DO PONTO MEDIDO EM AUMENTANDO A AGITAÇÃO.

o = EQUAÇÃO 21 • = EQUAÇÃO 20 ⊛ = PONTO MEDIDO

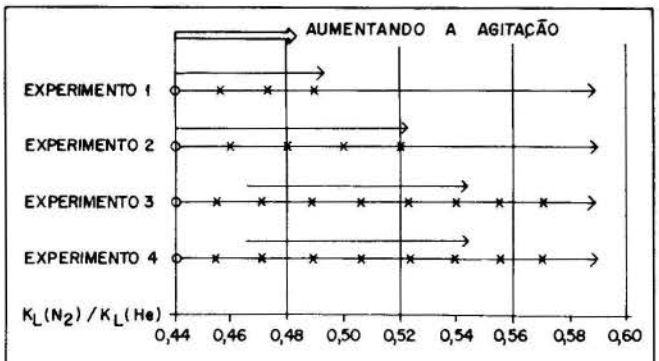

FIGURA 10 - DADOS DE DOBBINS (1962). AS SETAS INDICAM O DESLOCAMENTO DO PONTO MEDIDO (x) EM AUMENTANDO A AGITAÇÃO O VALOR INICIAL 0,44 FOI OBTIDO DOS PRÓPRIOS DADOS

As Figuras 8, 9 e 10 fornecem informações de 4 fontes: Kishinevsky e Serebriansky(1955), Ljubisavljevic (1984), Rainwater e Holley(1983) e Dobbins(1962). Em todas as figuras observa-se o deslocamento do ponto medido no sentido previsto pela formulação apresentada aqui. Os dados mostram que há a tendência à fuga da relação 21, com sentido na direção da relação 20. Entretanto, em nenhum dos casos se atingiu o valor final previsto por esta última relação. De fato é difícil afirmar se este valor é obtido uma vez que não se sabe se é possível atingir fisicamente o nível de agitação necessário para tal.

A Figura 11 apresenta dados obtidos por Barbosa (1989), mostrando, também, um desvio no sentido aqui sugerido.

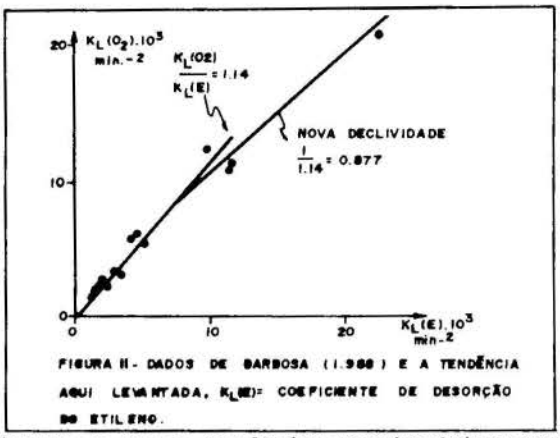

FIGURA 11 - DADOS DE BARBOSA (1.988) E A TENDÊNCIA AQUI LEVANTADA, $K_L(E)$= COEFICIENTE DE DESORÇÃO DO ETILENO.

Observa-se que os resultados experimentais apresentam comportamentos que sugerem que a presente formulação pode ser encarada como um caso limite para o qual a razão entre dois coeficientes de troca de massa tende ao aumentar a agitação do líquido.

CONCLUSÕES

A partir das equações propostas e da análise dos dados experimentais de diferentes fontes, foi possível mostrar que a relação entre dois coeficientes de transferência de massa em interfaces depende do nível de agitação do líquido.Esta evidência conduz às seguintes conclusões:

1 - A equação 2 não é incondicionalmente válida. Como uma extensão, o parâmetro IJ da equação 3, sugerida aqui, varia em variando o nível de agitação do líquido.

2 - A evolução da relação entre dois coeficientes globais de transferência segue tendências inversas nos casos de sistemas pouco agitados e altamente agitados.

O valor final da equação 20 pode não ser atingido porque pode implicar em um nível de agitação fisicamente inatingível. A tendência a este valor, contudo, foi verificada.

3 - A condição de superfície instantaneamente saturada foi utilizada na análise do problema. Parece que esta condição pode ser utilizada para gases pouco solúveis para todos os níveis de agitação e que as variações no comportamento de K_{L1}/K_{L2} podem ser relacionados com uma evolução na dependência para com a difusividade molecular.

4 - A equação 22 sugere que outras tendências podem também ser obtidas para sistemas líquidos altamente agitados.

AGRADECIMENTOS

Ao Centro de Recursos Hídricos e Ecologia Aplicada (CRHEA-SHS-EESC-USP) pelo apoio cedido para a pesquisa que originou o presente artigo.

Ao CNPq, pelo financiamento da pesquisa.

REFERÊNCIAS BIBLIOGRÁFICAS

[1] Barbosa, A.R. Jr., "Desenvolvimento de Metodologia para a Determinação do Coeficiente de Reaeração dos Escoamentos Naturais da Água com o Emprego de Traçador Gasoso". Dissertação de Mestrado. Escola de Engenharia de São Carlos, Universidade de São Paulo, São Carlos, SP, Brasil, 1989.

[2] Dankwerts, P.V., "Significance of Liquid-Films Coefficients in Gas Absorption. Industrial and Engineering Chemistry, vol. 46, nº 6, pp. 61-96,1951.

[3] Dobbins, W.E., "Mechanism of Gas Absorption by Turbulent Liquids". International Conference of Water Pollution Research, Proceedings, pp. 61-96, Pergamon Press, London, 1962.

[4] Holley, E.R., "Oxygen Transfer at the Air-Water Interface", Research Report, University of Illinois at Urbana-Champaign, 1977.

[5] Kishinevsky, M. Kh, "Two Approaches to the Theoretical Analysis of Absorption Processes". Jour. Appl. Chemistry, U.S.S.R., nº 28, pp. 881-886, 1955.

[6] Kishinevsky, M. Kh. and Serebriansky, V.T., "The Mechanism of Mass Transfer at the Gas-Liquid Interface with Vigorous Stirring". Jour. Appl. Chemistry, U.S.S.R., nº 29, pp. 29-33, 1955.

[7] Lewis, W.K. and Whitman, W.G., "Principles of Gas Absorption". Industrial and Engineering Chemistry, vol. 16, nº 12, pp. 1215-1220, 1924.

[8] Ljubisavljevic, D., "Carbon Dioxide Desorption from the Activated Sludge at the Waste Water Treatment Plants". In Brutsaert, W. and Jirka, G.H., ed. Gas Transfer at Water Surfaces, D. Reidel Publishing Company, Dordrecht, 1984.

[9] Munz, C. and Roberts, P.V., "The Ratio of Gas-Phase to Liquid-Phase Mass Transfer Coefficients in Gas-Liquid Contacting Processes". In Brutsaert, W. and Jirka, G.H., ed. Gas Transfer at Water Surfaces, D. Reidel Publishing Company, Dordrecht, 1984.

[10] Rainwater, K.A. and Holley, E.R., "Laboratory Studies on the Hydrocarbon Gas Tracer Technique for Reaeration Measurement". Technical Report, Center for Research in Water Resources, Bureau of Engineering Research, nº 189, Austin, 1983.

[11] Schulz, H.E., "Investigação do Mecanismo de Reoxigenação da Água em Escoamento e sua Correlação com o Nível de Turbulência junto à Superfície". Tese de Doutorado, Escola de Engenharia de São Carlos, Universidade de São Paulo, São Carlos, SP, 1990.

[12] Schulz, H.E.; Bicudo, J.R.; Barbosa Jr., A.R.; Giorgetti, M.F., "Some Important Parameters on The Turbulent Reaeration of Water: An Analytical Approach and Experimental Results". Artigo aceito para o "2nd International Symposium on Gas Transfer at Water Surfaces", Minneapolis, Minnesota, E.U.A., 1990.

[13] Tsivoglou, E.C.; O'Connell, R.L.; Walter, C.M.; Godsil, P.J. and Logsdon, G.S., "Tracer Measurements of Atmospheric Reaeration - I. Laboratory Studies". Journal of Water Pollution Control Federation, vol. 37, nº 10, pp. 1343-1362, 1965.

[14] Lee, Y.H. and Luck, S., "Characterization of Concentration Boundary Layer in Oxygen Absorption". Ind. Eng. Chem. Fundam., vol. 21, nº 4, pp. 128-434, 1982.

ABSTRACT

The absorption of gases by liquids is analysed for a situation in which molecular diffusivity is not a relevant parameter. Experimental data of different sources show that the suggested formulation can be viewed as a limiting case for gas transfer at higly agitated liquid surfaces.

III ENCIT — Itapema, SC (Dezembro 1990)

DESENVOLVIMENTOS COMPARATIVOS PARA A QUANTIFICAÇÃO DOS COEFICIENTES DE TROCA DE MASSA EM INTERFACES SÓLIDO-LÍQUIDO E LÍQUIDO-GAS

HARRY EDMAR SCHULZ
Departamento de Hidráulica e Saneamento da
Escola de Engenharia de São Carlos, Universidade de São Paulo
Av. Dr. Carlos Botelho, 1465, CEP. 13560 - S. Carlos - SP, BR

RESUMO

Os fenômenos de absorção de gases por líquidos e de dissolução de sólidos são analisados concomitantemente, buscando relações que permitam avaliar os coeficientes de transferência de massa de ambos os processos. Partiu-se da teoria estatística da turbulência, utilizando os modelos de misturadores isotrópicos. As conclusões acerca das variáveis envolvidas nos processos de troca entre gases e líquidos foram estendidas para as trocas entre sólidos e líquidos. Os resultados experimentais mostraram que as aproximações feitas conduzem a boas previsões.

INTRODUÇÃO

Os coeficientes de transferência de massa em interfaces (das quais pelo menos uma se encontra em um estado de agitação turbulenta) têm sido quantificados, historicamente, a partir de medidas diretas e de análises dimensionais feitas sobre os conjuntos de dados obtidos. As correlações mostram-se, via de regra, muito boas, e garantem, em vista disto, boas previsões acerca da quantidade de massa transferida.

Contudo esta forma de abordar o problema considera grandezas admitidas importantes "a priori", como uma escala de velocidade conveniente, uma escala geométrica conveniente e grandezas associadas ao meio fluido e ao elemento transferido na interface. Embora a boa resposta obtida a partir dos adimensionais assim construídos justifique por si só este procedimento, diferentes conjuntos de adimensionais podem ser construídos e correlacionados de forma a se manter uma boa previsão. Isto mostra que os fenômenos associados à turbulência ainda não são suficientemente conhecidos e que mais desenvolvimentos são necessários para obter informações acerca de quais grandezas devem ser admitidas importantes em processos de transferência em interfaces limitantes de meios turbulentos.

O presente trabalho apresenta as principais conclusões às quais se chegou acerca desta questão, partindo das equações para misturadores turbulentos isotrópicos de Corrsin (1964), as quais se baseiam na teoria estatística da turbulência.

ABSORÇÃO DE GASES

É geralmente aceito que a absorção de gases por corpos de líquido que não possuem misturadores ou outras fontes que não seja a atmosfera, segue a expressão:

$$dC/dt = (K_L/H)\ (C_s - C) \qquad (1)$$

K_L é o coeficiente de transferência de massa e H é a relação entre o volume de líquido e a área exposta à atmosfera, C é a concentração de gás no meio líquido e C_s é a concentração de saturação.

K_L é uma grandeza que depende do gás a ser dissolvido, do líquido solvente e das condições de agitação do sistema. Para sistemas líquidos agitados K_L deve poder ser expresso como função de grandezas que "descrevem" o movimento turbulento do meio. Schulz (1985, 1989 1990a), para analisar a absorção de gases por um volume de líquido em agitação turbulenta e com uma superfície exposta à atmosfera (ou a um ambiente gasoso), partiu do seguinte modelo físico:

i - A concentração do gás junto à superfície do líquido iguala a concentração de saturação. Esta hipótese é largamente utilizada na literatura.

ii - A concentração de gás abaixo da superfície (ultrapassando a camada limite de concentração) é homogênea. Também esta hipótese é encontrada e justificada na literatura. Schulz (1985) efetuou experimentos que a comprovam para oxigênio sendo absorvido pela água.

iii - A turbulência em uma região junto à superfície é considerada isotrópica. Esta é uma hipótese ousada e, a rigor, não se verifica, embora já tenha sido utilizada anteriormente por O'Connor e Dobbins (1958).

iv - A entrada de gás no líquido se faz através de elementos de líquido que se saturam e são incorporados no meio. A entrada assume, portanto, um caráter "discreto".

v - Entre a superfície e o meio há uma região em que a concentração de gás não iguala nem a concentração de saturação e nem aquela existente no meio. A partir da consideração iv admitiu-se que há um campo de flutuação de concentração homogêneo nesta região e que esta flutuação pode ser tratada considerando uma intermitência entre a concentração de saturação e a concentração do meio. (Figura 1).

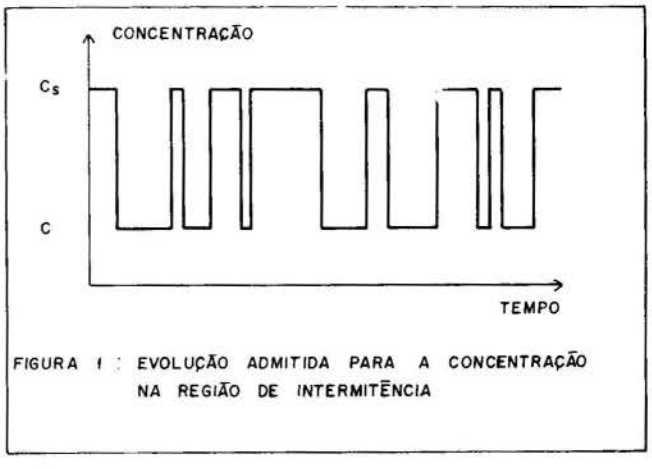

FIGURA 1 : EVOLUÇÃO ADMITIDA PARA A CONCENTRAÇÃO NA REGIÃO DE INTERMITÊNCIA

vi - A turbulência é estacionária ao longo do processo, isto é, mantém-se constante o nível de agitação do líquido.

Uma descrição detalhada das hipóteses e das suas conseqüências na construção do modelo matemático para absorção de gases é apresentada em Schulz e Giorgetti (1990).

Nos trabalhos acerca de misturadores isotrópicos, Corrsin (1958, 1964) define algumas das grandezas que foram utilizadas no modelo físico acima descrito. Essas grandezas são:

$$L_s(r, t) = \int_0^\infty g\,(r, t)\,dr \qquad (2)$$

$$I_s = c'^2/c_0'^2 \qquad (3)$$

$$I_s = \exp\,(-K_s.t) \qquad (4)$$

L_s é denominado de escala de segregação e é uma medida das "manchas não misturadas" de solvente em um soluto. $g(r, t)$ é a função de correlação instantânea para as flutuações de concentração entre dois pontos no meio líquido separados entre si por uma distância r. I_s é denominado de grau de segregação e é uma medida relativa entre a média dos quadrados das flutuações em um instante t (c'^2) e o seu valor inicial ($c_0'^2$). A expressão 4 mostra um decréscimo exponencial de I_s, associado a um parâmetro K_s, que expressa a "eficiência" do processo de mistura (no sentido de este ser mais ou menos demorado). K_s depende das condições turbulentas do meio.

A formulação para turbulência isotrópica fornece, para termos de inércia desprezíveis (correspondendo às menores taxas de dissipação de energia), a relação (ver Schulz (1985)):

$$I_s = \exp\,(-2\dot{u}t/5u'^2\rho)$$
$$K_s = 2\dot{u}/5u'^2\rho \qquad (5)$$

$\dot{u}$ é a potência dissipada por unidade de volume. u' é denominado de intensidade turbulenta, sendo a raiz quadrada da média dos quadrados das flutuações de velocidade, e ρ é a massa específica do líquido.

Corrsin (1964), utilizando conclusões acerca dos espectros de flutuações propostas por Batchelor (1958) obteve, para grandes números de Schmidt (Sc>>1), Peclet e Reynolds (correspondendo às maiores dissipações de energia), a relação:

$$\frac{1}{K_s} = \frac{1}{2}\left\{3\left[\frac{5}{\pi}\right]^{2/3}\left[\frac{\rho L_s^2}{\dot{u}}\right]^{1/3} + \left[\frac{\rho\nu}{\dot{u}}\right]^{1/2} \text{Ln Sc}\right\} \qquad (6)$$

ν é a viscosidade cinemática do liquido.

Em uma série de trabalhos, Schulz (1985, 1989, 1990a) e Schulz e Giorgetti (1986, 1990), aplicando as conclusões de Corrsin ao modelo físico para absorção de gases acima exposto, obtiveram os seguintes resultados:

i - $I_s = (C_s - C)^2/(C_s - C_0)^2$ (7)

C_0 e a concentração inicial de gás no líquido.

ii - $g(r, t) = g(r)$ e K_s é constante para o modelo físico adotado, apesar de C variar com o tempo.

iii - $C(t) = C_s - (C_s - C_0)\exp\,(-\varkappa\, K_s\, t/2H)$ (8)

$\varkappa$ é uma constante

$K_L = \varkappa K_s/2$

iv - Para baixas agitações (pequenas taxas de dissipação de energia) vale:

$$K_L = \gamma\,\nu^{7/2}\int_0^\infty k^6\exp\,(-\beta\nu k^2)\,dk \qquad (9)$$

γ e β são constantes e k é o número de ondas, utilizado no espectro de turbulência.

A potência dissipada não aparece, para líquidos pouco agitados, como um parâmetro relevante na avaliação do coeficiente de troca de massa. A distribuição da energia sobre os diferentes números de onda, contudo, é importante, como mostra a expressão 9.

v - Para altas agitações (altas taxas de dissipação de energia) vale:

$$K_L = \varkappa D^{1/2}/\left\{3\left[\frac{5}{\pi}\right]^{2/3}\left[\frac{\rho L_s^2}{\dot{u}}\right]^{1/3} + \left[\frac{\rho\nu}{\dot{u}}\right]^{1/2}\text{Ln Sc}\right\} \qquad (10)$$

D é a difusividade molecular do gás no líquido.

Três análises para a evolução de K_L em relação à dissipação de energia foram feitas. Considerou-se, em primeiro lugar, que a escala de segregação L_s não varia em modificando o nível de agitação do meio. Isto produziu a evolução da Figura 2.

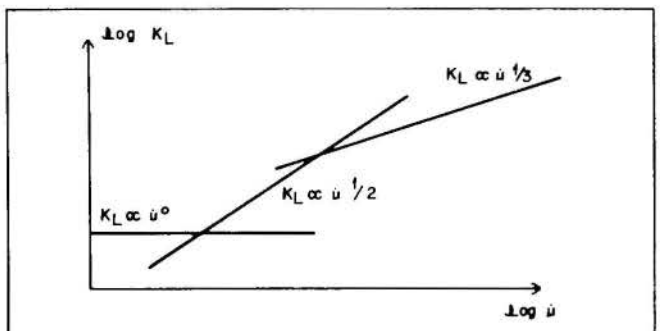

FIGURA 2 : VARIAÇÃO DE K_L COM $\dot{u}$ CONSIDERANDO L_s CONSTANTE

Posteriormente analisou-se a ordem de grandeza das parcelas do denominador da equação 10, que mostrou que apenas para valores de $\dot{u}$ muito pequenos a segunda parcela passa a ser relevante (para L_s da ordem de grandeza maior ou igual a 10^{-3} m). Esses valores mostraram-se bem abaixo daqueles atingidos nos experimentos relatados por diferentes autores (ver Roberts e Dändliker (1983) por exemplo), o que sugere que se possa abandonar a segunda parcela para as maiores agitações. Desta forma tem-se:

$$K_L = \varkappa D^{1/2}/\left\{3\left[\frac{5}{\pi}\right]^{2/3}\left[\frac{\rho L_s^2}{\dot{u}}\right]^{1/3}\right\} \qquad (11)$$

O comportamento de L_s em relação à dissipação de energia foi estudado a partir da hipótese de proporcionalidade desta escala com a escala dos turbilhões existentes no meio. Segundo Hinze (1959), para a maior parte do espectro de turbulência, a escala dos turbilhões é proporcional à potência -1/4 da taxa de dissipação de energia, o que induz, de imediato, a:

$$L_s \propto \dot{u}^{-1/4} \qquad (12)$$

Esta forma de variação produz como resultado

$$K_L \propto \dot{u}^{1/2} \qquad (13)$$

Se, por outro lado, L_s puder ser admitido constante (uma situação talvez possível para baixas agitações. Como exemplo, um escoamento laminar em um tubo permite variação na potência dissipada sem haver variação da escala de comprimento associada ao escoamento, que envolve

as dimensões do tubo) então tem-se:

$$K_L \alpha \dot{u}^{1/3} \quad (14)$$

A Figura 3 apresenta a forma de evolução em relação à dissipação de energia obtida com a segunda análise.

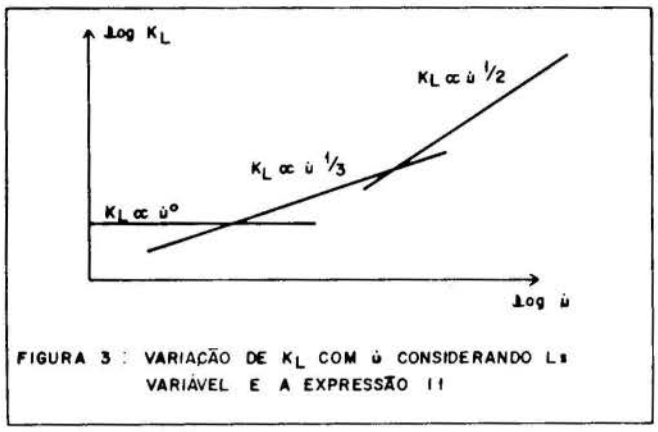

FIGURA 3 : VARIAÇÃO DE K_L COM $\dot{u}$ CONSIDERANDO Ls VARIÁVEL E A EXPRESSÃO 11

Finalmente, utilizando a equação 10 na forma integral e a proporcionalidade indicada na expressão 12, tem-se, para qualquer faixa de agitação:

$$K_L \alpha \dot{u}^{1/2}$$

A Figura 4 mostra o comportamento esperado para este tipo de evolução.

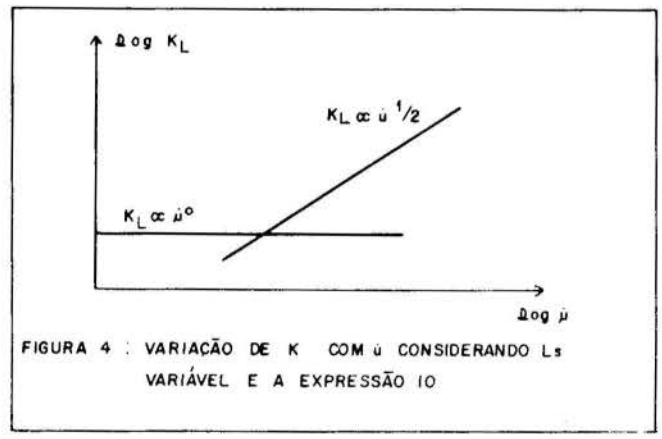

FIGURA 4 : VARIAÇÃO DE K_L COM $\dot{u}$ CONSIDERANDO Ls VARIÁVEL E A EXPRESSÃO 10

DISSOLUÇÃO DE SÓLIDOS

Para quantificar o processo de dissolução de sólidos admitiu-se uma situação de dissolução unidimensional. Esta abordagem foi preferida devido a sua modelação matemática simples e devido a facilidade de reprodução experimental. Para um sólido dissolvendo ao longo de apenas uma dimensão, pode-se escrever:

$$dh/dt = -v$$

$$M/M_0 = 1 - vt/ho$$

M e h são, respectivamente, a massa e a espessura instantâneas do sólido, sendo Mo e ho as suas massa e espessura iniciais. t é a variável tempo e v é o parâmetro que descreve a dissolução, denominado de velocidade de desgaste, constante de reação, ou velocidade de reação.

Procurou-se associar v com as grandezas que "descrevem" o escoamento turbulento utilizadas no problema de absorção de gases. A potência dissipada por unidade de volume ($\dot{u}$) e a escala do turbilhão (volume = $\forall$) estão simplesmente relacionadas, como segue:

$$\dot{U} = \dot{u} . \forall \quad (15)$$

$$d\dot{U} = \dot{u}\, d\forall + \forall\, d\dot{u} \quad (16)$$

$\dot{U}$ é a potência total dissipada no turbilhão.

O problema consiste em encontrar uma função $\phi = \phi(\dot{u}, \forall, v)$ que relacione de forma conveniente as variáveis em questão. Schulz (1990a, b) sugeriu para $d\phi$ a forma:

$$d\phi = \tau v^{\beta} \dot{u}\, d\forall + v^{\delta} \forall\, d\dot{u} \quad (17)$$

(τ, β e δ são constantes)

porque é suficientemente próxima de uma equação com sentido físico claro (equação 16) e porque permite ajustar a importância relativa de cada parcela e a influência de v nas mesmas. Como K_L para a absorção de gases foi relacionado com a taxa de dissipação de energia e com a escala de segregação (posteriormente associada à escala dos turbilhões), espera-se também aqui uma relação desse tipo. Por exemplo, como a expressão 17 envolve $d\dot{u}$, espera-se que:

$$\dot{u} = \dot{u}(\forall, v) \quad (18)$$

$$d\dot{u} = (\partial\dot{u}/\partial\forall)\, d\forall + (\partial\dot{u}/\partial v)\, dv \quad (19)$$

As expressões 17 e 19 não definem ϕ nem permitem obter relaçoes utilizáveis para v, uma vez que existem três constantes a serem determinadas. Para diminuir esse número de "graus de liberdade" e associar ϕ com grandezas físicas de sentido claro, Schulz (1990a, b) analisou o escoamento de um turbilhão em um meio fluido, associando este escoamento àquele que ocorre no interior de um tubo. Para uma situação de escoamento no qual o "fator de atrito" pode ser considerado constante, as seguintes equações foram obtidas:

$$d\psi = (4/3)\dot{u}\, d\forall + \forall\, d\dot{u} \quad (20)$$

$$d\psi = \dot{U}\, d\{\mathrm{Ln}[\textstyle\int_{\forall} V^3\, d\forall]\} \quad (21)$$

ψ é denominado Função Dissipação

V é a velocidade do turbilhão.

Se, por outro lado, se admitir uma variação do fator de atrito similar àquela que ocorre para escoamentos laminares, isto é, se houver uma relação de proporcionalidade inversa entre o número de Reynolds associado ao turbilhão e o fator de atrito tem-se:

$$d\psi = (5/3)\, \dot{u}\, d\forall + \forall\, d\dot{u} \quad (22)$$

$$d\psi = \dot{U}\, d\{\mathrm{Ln}[\textstyle\int_{\forall} V^2\, d\forall]\} \quad (23)$$

As informações geradas com esse tipo de análise podem ser incorporadas na equação 17. Para que não se perca o peso relativo das parcelas do segundo membro é necessário que os expoentes de v sejam iguais, isto é, que $\beta = \delta$. Das equações 20 ou 22 tem-se:

$$d\phi = \tau v^{\beta}\, \dot{u}\, d\forall + v^{\beta} \forall\, d\dot{u} \quad (24)$$

$$d\phi = v^{\beta}\, d\psi \quad (25)$$

$d\phi$ passa a ser definido ou pela expressão 21 ou pela expressão 23. Ambas envolvem apenas grandezas com significado físico estabelecido. τ pode assumir os valores 4/3 ou 5/3, de acordo com a definição de $d\phi$ utilizada. Schulz (1990a, b) utilizou, em sua análise, somente a definição 21.

A união das expressões 17, 19 e 24 produz:

$$d\phi = \tau v^{\beta}\, \dot{u}\, d\forall + v^{\beta} \forall (\partial\dot{u}/\partial\forall)\, d\forall + v^{\beta} \forall (\partial\dot{u}/\partial v)\, dv \quad (26)$$

Para obter uma relação entre v, $\dot{u}$ e $\forall$, avaliou-se $[d\phi/dv]_{\forall}$, $[d\phi/d\forall]_{v}$ e as derivadas segundas $\partial^2\phi/\partial v\,\partial\forall$ e $\partial^2\phi/\partial\forall\,\partial v$. As derivadas segundas devem ser iguais, o que leva ao resultado:

$$(\tau - 1)v\,(\partial\dot{u}/\partial v) + \beta\forall(\partial\dot{u}/\partial\forall) + \tau\beta\dot{u} = 0 \qquad (27)$$

O índice colocado após o colchete indica que a variável do índice permaneceu inalterada na operação.

Esta expressão é resolvida substituindo $\dot{u}$ pelo produto $V(v).W(\forall)$, dividindo o resultado obtido por esse produto e separando as variáveis que são função de v e $\forall$. Isto produz:

$$(\tau - 1)\,(v/V)\,(dV/dv) = -\tau\beta - \beta\,(\forall/W)\,(dW/d\forall) = \sigma \qquad (28)$$

σ é uma constante.

A integração das equações 28 resulta em:

$$\dot{u} = a.v^{[\sigma/(\tau - 1)]}\,.\,\forall^{-[(\sigma+\tau\beta)/\beta]},\quad a = \text{constante} \qquad (29)$$

Davies (1972) descreve uma análise dimensional associada a processos de transferência e relata experimentos nos quais a escala do turbilhão mostrou não ser um parâmetro de relevância nos processos. Para que esta observação seja utilizada na presente análise é preciso que o expoente de $\forall$ se anule em 29. Isto leva a:

$$\dot{u} = a.v^{-\beta\tau/(\tau - 1)} \quad e \quad v = b.\dot{u}^{-(\tau - 1)/\beta\tau} \qquad (30)$$

Utilizando a definição 21 tem-se:

$$v = b.\dot{u}^{-1/4\,\beta},\quad b = \text{constante} \qquad (31)$$

Utilizando a definição 23 resulta:

$$v = b.\dot{u}^{-2/5\,\beta} \qquad (32)$$

A partir de considerações acerca das escalas de comprimento e de velocidade dos turbilhões existentes no meio e das equações de transferência de massa em camadas-limite, Schulz (1990 a,b) obteve o valor $\beta = -1$ para a situação de maiores agitações do meio líquido (maiores dissipações de energia). Frisa-se novamente que Schulz trabalhou apenas com a equação 31 (definição 21). Este valor conduz, evidentemente, a:

$$v = b.\dot{u}^{1/4} \qquad (33)$$

ANÁLISE CONJUNTA DOS PROCESSOS DE TROCA DE MASSA

As equações 13 e 33, que, segundo a análise efetuada, parecem ser válidas para a situação de maior agitação do meio líquido, conduzem à tendência:

$$K_L/v \alpha\, \dot{u}^{1/4} \qquad (34)$$

Nenhuma observação foi feita quanto à geometria do corpo líquido no qual estão sendo efetuados os processos de troca. Em havendo influência desta geometria, ela deve ser introduzida na "constante" de proporcionalidade que surge da expressão 34.

VERIFICAÇÕES EXPERIMENTAIS DAS TENDÊNCIAS SUGERIDAS

Bicudo (1988) obteve relações empíricas para K_L/v em experimentos de absorção de oxigênio pela água e dissolução de ácido benzóico, as quais apresentou na forma:

$$K_L/v = 2.100{,}65\ V^{1{,}08}$$

$$K_L/v = 9{,}279\ Re^{1{,}01}$$

V é a velocidade média de escoamento em um canal e Re é o número de Reynolds associado a este escoamento. Utilizando a equação de Darcy-Weisbach na forma $\dot{U} = \rho g Q f L V^2/8Rg$, onde Q é a vazão veiculada no canal e R é o raio hidráulico do mesmo, sendo f o fator de atrito do escoamento e ρ a massa específica do líquido, pode-se obter alguma informação da variação de K_L/v em relação à taxa de dissipação de energia.

Admitiu-se turbulência desenvolvida, de forma que o fator de atrito foi considerado constante. Esta abordagem permitiu obter as seguintes relações de proporcionalidade:

$$K_L/v \alpha\, \dot{u}^{0{,}360} \quad e \quad K_L/v \alpha\, \dot{u}^{0{,}337}$$

Barbosa (1989) avaliou experimentalmente o coeficiente de absorção de oxigênio pela água em um tanque de agitação hidrodinâmica com um volume de aproximadamente 100 ℓ, no qual a turbulência era provocada pela rotação regulável de uma hélice. O mesmo equipamento foi utilizado por Schulz (1990a) para avaliar a velocidade de desgaste de ácido oxálico dihidratado, o qual foi colocado junto à superfície da água. Os resultados obtidos foram analisados em conjunto, conduzindo à tendência:

$$K_L/v \alpha\, \dot{u}^{0{,}292}$$

Schulz (1990a) realizou experimentos de absorção de oxigênio e de dissolução de ácido oxálico dihidratado em água em um canal de recirculação cujas dimensões foram:

Comprimento: 20,0 m
Largura da seção transversal: 0,35 m
Profundidade média da lâmina de água: 0,175 m

A agitação turbulenta foi produzida através da vazão induzida no canal e da introdução de rugosidade artificial no fundo do mesmo. Tanto a vazão como a rugosidade foram variados ao longo dos experimentos, conduzindo a quinze combinações distintas e igual número de valores para a taxa de dissipação de energia (potência dissipada). A vazão variou de $16{,}91.10^{-3}$ m³/s a $29{,}13.10^{-3}$ m³/s, enquanto o diâmetro de rugosidade artificial introduzida (foi utilizada areia previamente peneirada) variou de $0{,}97.10^{-3}$ m a $9{,}5.10^{-3}$ m. Foram realizados dezessete experimentos de reoxigenação e 70 experimentos de dissolução. Para a dissolução do ácido oxálico, o mesmo foi colocado junto à superfície da água, abaixo desta, para ficar sujeito ao mesmo nível de agitação que é o responsável pela reoxigenação da água. Os resultados dos experimentos de reoxigenação foram lançados em gráfico contra os valores calculados a partir de uma equação de melhor ajuste da forma:

$$K_L \alpha\, \dot{u}^{a}\, x^{b} \qquad (35)$$

(x é o diâmetro da areia utilizada na rugosidade) e são apresentados na Figura 5.

Verifica-se que o expoente $0{,}49 \pm 0{,}10$ obtido para a potência dissipada por unidade de volume é muito próximo do valor 0,5 previsto na expressão 13.

Os valores médios da dissolução de ácido oxálico para cada situação de dissipação de energia foram lançados em gráfico contra os valores calculados a partir de uma equação de melhor ajuste da forma:

$$v \alpha\, \dot{u}^{c}\, x^{d} \qquad (36)$$

e são apresentados na Figura 6.

Verifica-se que o expoente $0{,}246 \pm 0{,}019$ obtido para a potência dissipada por unidade de volume é muito próximo do valor 0,25 previsto na expressão 34.

Observa-se, também, que tanto o coeficiente de ab-

sorção de oxigênio como a velocidade de desgaste do ácido oxálico diminuem com o aumento da rugosidade, em se mantendo a mesma taxa de dissipação de energia. Este comportamento semelhante é esperado, uma vez que ambos os processos de transferência de massa ocorrem sob as mesmas condições experimentais. Adicionalmente, a influência da variação na geometria foi equacionada a partir de uma função multiplicativa, como comentado no ítem "análise conjunta dos processos de troca de massa".

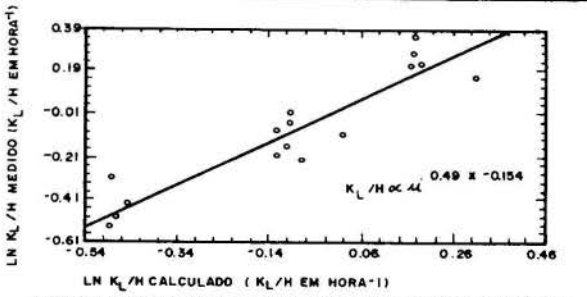

FIGURA 5 - AJUSTE OBTIDO PARA OS EXPERIMENTOS DE ABSORÇÃO DE OXIGÊNIO

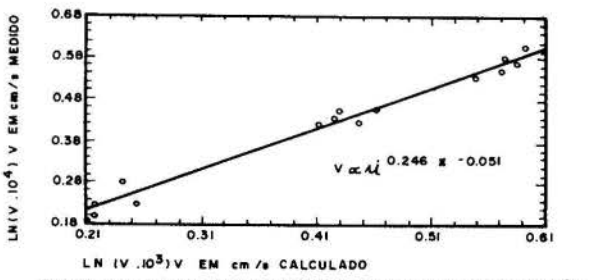

FIGURA 6 - AJUSTE OBTIDO PARA OS EXPERIMENTOS DE DISSOLUÇÃO DE ÁCIDO OXÁLICO

FIGURAS 5 E 6 - EXPRESSÕES OBTIDAS E DADOS EXPERIMENTAIS QUE COMPROVAM AS TENDÊNCIAS DAS EQUAÇÕES 13, 33, 34.

A partir dos resultados das Figuras 5 e 6, conclue-se que a relação K/v comporta-se, para os experimentos executados no canal de recirculação, na forma:

$$K_L/v \propto u^{0,244}$$

Novamente observa-se a boa concordância com a tendência prevista na expressão 34.

CONCLUSÕES

Processos de absorção de gases em interfaces gás-líquido e processos de dissolução que ocorrem em interfaces sólido-líquido foram estudados visando estabelecer a sua relação de dependência para com a dissipação de energia que ocorre no meio líquido. Para a absorção de gases foi considerado um modelo físico no qual uma região de alta flutuação de concentração de gás dissolvido foi definida e denominada "região de intermitência" para a concentração. A utilização das conclusões de Corrsin para misturadores isotrópicos nesta região de intermitência permitiu estabelecer uma relação de dependência para o coeficiente de absorção de gases na forma:

$$K_L \propto u^n$$

onde n pode assumir os valores 0, 1/3 e 1/2. O valor 1/2 foi observado experimentalmente.

A informação de que o coeficiente de absorção de gases está associado à taxa de dissipação de energia foi utilizada para modelar o fenômeno de dissolução de sólidos, produzindo para o parâmetro que quantifica a dissolução, a expressão:

$$v \propto u^{1/4}$$

Para a relação entre os dois coeficientes de troca de massa, sujeitos às mesmas condições de agitação, obte-se:

$$K_L/v \propto u^{1/4}$$

Todas as tendências aqui apresentadas foram observadas experimentalmente, sugerindo a validade dos desenvolvimentos propostos.

AGRADECIMENTOS

- Ao Centro de Recursos Hídricos e Ecologia Aplicada (CRHEA-SHS-EESC-USP) pelo espaço físico cedido.
- Ao CNPq, pelo financiamento da pesquisa.

REFERÊNCIAS BIBLIOGRÁFICAS

[1] Barbosa, A.R., Jr., "Desenvolvimento de Metodologia para a Determinação do Coeficiente de Reaeração dos Escoamentos Naturais da Água com o Emprego de Traçador Gasoso". Dissertação de Mestrado, Escola de Engenharia de São Carlos, Universidade de São Paulo, São Carlos, SP, Brasil, 1989.

[2] Batchelor, G.K., "Small-Scale Variation of Convected Quantities Like Temperature in Turbulent Fluid". Journal of Fluid Mechanics, 5, pp.113-133, 1958.

[3] Bicudo, J.R.P.W., "The Measurement of Reaeration in Streams". PhD Thesis, University of Newcastle, England, 1988.

[4] Corrsin, S., "Simple Theory of an Idealized Turbulent Mixer". A.I.Ch.E.Journal, vol. 3, nº 3, pp. 329-330, 1958.

[5] Corrsin, S., "The Isotropic Turbulent Mixer. Part II Arbitrary Schmidt Number". A.I.Ch.E.Journal, vol.10, nº 6, pp. 870-877, 1964.

[6] O'Connor, D.J. and Dobbins, N.E., "Mechanism of Reaeration in Natural Streams". ASCE Transactions, nº 123, pp. 641-684, 1958.

[7] Schulz, H.E., "Investigação do Mecanismo de Reoxigenação da Água em Escoamento e sua Correlação com o Nível de turbulência junto à Superfície". Dissertação de Mestrado. Escola de Engenharia de São Carlos, Universidade de São Paulo, São Carlos, SP, Brasil, 1985.

[8] Schulz, H.E., "Modelos Matemáticos para Reoxigenação em Canais de Pequeno Porte com Base na Teoria Estatística da Turbulência". Anais do 4º Simpósio Luso-Brasileiro de Hidráulica e Recursos Hídricos, vol. II, pp. 618-631, Lisboa, Portugal, 1989.

[9] Schulz, H.E., "Investigação do Mecanismo de Reoxigenação da Água em Escoamento e sua Correlação com o Nível de Turbulência junto à Superfície". Tese de Doutorado. Escola de Engenharia de São Carlos, Universidade de São Paulo, São Carlos, SP,Brasil,1990a.

[10] Schulz, H.E., "Busca de uma Formulação Unificada para o Problema de Transferência de Grandezas Físicas em Escoamentos Turbulentos". Artigo enviado para o III Encontro Nacional de Ciências Térmicas, Itapema, SC, Brasil, 1990b.

[11] Schulz, H.E. and Giorgetti,M.F.,"Um Modelo de Transferência de Oxigênio na Interface Ar-Água a partir da Teoria Estatística da Turbulência. Anais do II

Congresso Latinoamericano de Transferência de Calor e Materia, pp. 436-451, S.Paulo,SP,Brasil,1986

[12] Schulz, H.E. and Giorgetti, M.F., "On the Soluble Solid Floating Probe Method for the Indirect Determination of Gas-Transfer Coefficients". Artigo aceito para o "2nd International Symposium on Gas Transfer at Water Surfaces", Minneapolis, Minnesota, E.U.A., 1990.

[13] Roberts, P.V. and Dandliker, P.V., "Mass Transfer of Volatile Organic Contaminants from Aqueous Solutions to the Atmosphere During Surface Aeration", Env. Sci. and Tech., vol. 17, nº 8, pp. 484-489, 1983.

[14] Hinze, J.O., "Turbulence", McGraw-Hill. New York, 1959.

[15] Davies, J.T., "Turbulence Phenomena". Academic Press. New York, 1972.

ABSTRACT

The phenomena of gas absorption and solid dilution by liquids were studied to obtain equations for the mass-transfer coefficients. The statistical theory of turbulence applied to isotropic mixing was used. The conclusions about the parameters involved in the mass-transfer processes between gases and liquids were extended to the case of exchange between solids and liquids. The theoretical predictions are found to be in good agreement with the experimental data.

III ENCIT – Itapema, SC (Dezembro 1990)

EVAPORAÇÃO CONVECTIVA EM UM DUTO CONTENDO UM MEIO POROSO SATURADO

S.T. SEBBEN e A.T. PRATA

Deptº de Engenharia Mecânica
Universidade Federal de Santa Catarina
C.P. 476 - Florianópolis, SC - 88049

RESUMO

O presente trabalho é um estudo da transferência isotérmica de massa em um duto contendo um meio poroso saturado. Para a descrição do escoamento levou-se em consideração efeitos de inércia, atrito com as paredes sólidas e porosidade variável. No trabalho são apresentados perfis de conteúdo de umidade e quantidade de massa evaporada. Os resultados obtidos mostraram que a saturação do fluido ocorre de forma mais lenta junto à parede, muito embora as velocidades mais altas do escoamento ocorram nesta região. Também é mostrado que o número de Sherwood aumenta com o aumento da vazão do fluido no duto.

INTRODUÇÃO

A importância de estudos na área de transferência de calor e massa em meios porosos é devida ao grande número de aplicações industriais relacionadas com tais fenômenos. Algumas das aplicações que envolvem a transferência de calor e massa em meios porosos incluem trocadores de calor com matriz sólida, sistemas de estocagem térmica, sistemas geotérmicos, secagem de grãos etc.

A geometria de um meio poroso é bastante complexa, de forma que a modelagem do escoamento torna-se complicada e particular para cada meio em questão. Grande parte dos trabalhos encontrados nesta área usa a Lei de Darcy para a descrição do escoamento. O modelo clássico de Darcy relaciona a queda de pressão com a velocidade em um meio não limitado por fronteiras sólidas [1]. Este modelo, no entanto, não computa alguns dos efeitos que são característicos em escoamentos através de meios porosos, como por exemplo: os efeitos de inércia, a condição de não deslizamento em uma fronteira sólida e a variação espacial da porosidade. A consideração da variação da porosidade no meio altera significativamente o perfil de velocidade e dá origem ao importante efeito de canal.

No que se refere ao fenômeno conjugado da transferência de calor e massa em meios porosos, os trabalhos científicos disponíveis são poucos. Aplicações práticas deste tipo de problema podem ser encontradas em processos de secagem de grãos ou em problemas que envolvem transferência de calor em solos. Em [2] foi estudado a transferência conjunta de calor e massa em um canal contendo um meio poroso saturado. Neste trabalho foram desenvolvidas equações para o fluido e para a matriz sólida. Os autores utilizaram as simplificações baseadas na lei de Darcy para a descrição do escoamento. Tais simplificações não computam o efeito canal junto à parede.

Estudos relativos ao transporte de massa através de um leito compactado constituído por partículas esféricas foram realizados recentemente por A. Pesaran e A. F. Mills, [3]. Neste estudo foram investigados os mecanismos de difusão de massa através de partículas de sílica gel. A sílica gel é bastante utilizada em processos industriais de secagem. Os mesmos autores realizaram um estudo experimental sobre o transporte de massa em um leito de sílica gel, [4].

Princípios gerais sobre a metodologia e a teoria de secagem de grãos são encontrados na literatura em [5]. Os autores preocuparam-se com o estudo de grãos de cereais, sendo que os princípios apresentados podem ser utilizados para analisar o processo de secagem de outros produtos.

O presente trabalho investiga numericamente o fenômeno da transferência de massa em um duto contendo um leito de esferas compactadas. O fluido é uma mistura de ar e vapor d'água e, desta forma, ao escoar pela matriz sólida tem o seu conteúdo de umidade aumentado pela evaporação da água presente na superfície das partículas. No presente estudo, o processo de transferência de massa ocorre de forma isotérmica, de modo que a equação da massa encontra-se desacoplada da equação da energia. No modelo utilizado para a descrição do escoamento foram computados os efeitos de inércia, a condição de não deslizamento e a variação espacial da porosidade da matriz. No trabalho são apresentados perfis de conteúdo de umidade, quantidade de massa evaporada e desenvolvimento do número de Sherwood. O número de Sherwood é definido de forma a representar a taxa de transferência de massa entre as partículas sólidas e o fluido.

FORMULAÇÃO DO PROBLEMA

O problema a ser investigado trata da transferência isotérmica de massa em um duto contendo um meio poroso constituído por partículas esféricas. O modelo clássico de Darcy para a descrição do escoamento é modificado para computar os efeitos de inércia, condição de não deslizamento nas fronteiras sólidas e atrito. São também incluídos efeitos causados pela porosidade variável da matriz sólida.

O meio poroso está confinado entre duas placas paralelas isoladas e impermeáveis ao fluxo de vapor d'água. As placas encontram-se separadas por uma distância 2H.

Para o problema hidrodinâmico considerou-se o perfil de velocidade plenamente desenvolvido na entrada do duto, de forma que o campo de velocidade é função unicamente da coordenada normal as fronteiras sólidas. Tal consideração é assumida por diversos autores que publicam nesta área, como por exemplo [6-8]. No presente trabalho, o problema hidrodinâmico será discutido com brevidade. Tal problema já foi discutido com detalhes pelos autores em [9,10]. Tratando-se o fluido e o meio poroso como um contínuo, a equação do movimento é dada por,

$$0 = -(1/\rho)dp/dx + (\nu/\varepsilon)d^2u/dy^2 - \nu u/K - Au^2 \qquad (1)$$

onde x e y são as coordenadas longitudinal e transversal, respectivamente, u é a velocidade na direção de x, e p é a pressão; a porosidade do meio é representada por ε, ρ é a massa específica e ν é a viscosidade dinâmica do fluido. A origem do sistema de coordenadas se encontra na parede do duto.

As expressões para a permeabilidade do meio, K, e o parâmetro A do termo de inércia foram obtidas de [11]. A porosidade ε é obtida de [6,8,12]. Suas relações funcionais são dadas por,

$$K = d^2\varepsilon^3/[150(1-\varepsilon)^2] \qquad (2)$$

$$A = 1{,}75(1-\varepsilon)/(d\varepsilon^2) \tag{3}$$

$$\varepsilon = \varepsilon_\infty(1 + \lambda_1 e^{-\lambda_2 y/d}) \tag{4}$$

onde d é o diâmetro das esferas, $\varepsilon_\infty = 0{,}37$ [6], $\lambda_2 = 6$, e o valor da constante λ_1 é escolhido de modo que a porosidade seja igual à unidade nas paredes [12].

Para o problema da transferência de massa o fluido em consideração é uma mistura de ar seco e vapor d'água, e as partículas que constituem o meio poroso estão saturadas de água. Desta forma, o ar ao escoar pela matriz sólida tem seu conteúdo de umidade aumentado pela evaporação da água presente nas partículas.

Para uma situação isotérmica, a equação do balanço de massa está desacoplada da equação da energia, bastando para sua solução que se conheça a temperatura do sistema. Desta forma, um balanço de massa no sistema requer que,

$$u\frac{\partial w}{\partial x} = \frac{\partial}{\partial y}\left(D_{ef}\frac{\partial w}{\partial y}\right) + \frac{6}{d}(1-\varepsilon)\,k_{fp}\,(w_s - w) \tag{5}$$

onde w é a fração mássica do vapor d'água no ar, D_{ef} é a difusividade efetiva do vapor d'água no ar, k_{fp} é o coeficiente de transferência de massa entre o fluido e as partículas e w_s é a fração mássica do vapor d'água na superfície das partículas, ou seja, na temperatura de saturação. O vapor d'água na superfície das partículas está em equilíbrio termodinâmico com a água líquida e, assim sendo, seu estado é de saturação.

Para um meio de partículas não porosas, a relação entre o coeficiente de difusão efetivo D_{ef}, e o coeficiente de difusão molecular, D_f, é dada por [13]:

$$D_{ef} = \varepsilon D_f \tag{6}$$

Para completar a formulação do problema, apresenta-se a seguir as condições de contorno. Na equação do movimento, assume-se velocidade zero na parede e gradiente de velocidade zero na linha de simetria. Para o problema da transferência de massa, as paredes do duto são impermeáveis ao fluxo de vapor d'água e, pela simetria, o fluxo na linha central do sistema é zero.

Para a coordenada x o problema é parabólico, sendo necessário que se conheça somente as condições iniciais do fluido na entrada do sistema.

METODOLOGIA DE SOLUÇÃO

Dois métodos computacionais são empregados na solução das equações adimensionalizadas. Em uma primeira etapa, calcula-se numericamente a equação hidrodinâmica por volumes finitos. Devido à simplicidade deste método, o procedimento de solução desta equação é exposto de maneira sucinta. Para maiores detalhes reportar às referências [9,10]. Para a equação da conservação do conteúdo de umidade do fluido, utilizou-se o método implícito das Caixas de Keller [14].

As definições usadas para a adimensionalização das variáveis são as seguintes,

$$Y = y/H\ ,\quad X = x/HSc\ ,\quad D = d/H$$
$$U = uH/\nu B\ ,\quad \psi = (w - w_s)/(w_e - w_s) \tag{7}$$

As equações do movimento (1) e da massa (5) em sua forma adimensional ficam, respectivamente,

$$U + BC_1U^2 = C_2 + \frac{C_2}{\varepsilon}\,\frac{d}{dy}\left[\frac{dU}{dy}\right] \tag{8}$$

$$BU\,\frac{\partial\psi}{\partial X} = \frac{\partial}{\partial y}\left[\varepsilon\frac{\partial\psi}{\partial y}\right] - \frac{6}{D^2}\,Sh_{fp}\,(1-\varepsilon)\,\psi \tag{9}$$

onde B, C_1 e C_2 são dados por,

$$B = -\frac{dP}{dx}\,\frac{H^3}{\rho\nu^2} \tag{10}$$

$$C_1 = 1{,}75D/[150(1-\varepsilon)],\quad C_2 = D^2\varepsilon^3/[150(1-\varepsilon)^2]$$

Inclue-se também nas adimensionalizações o número de Sherwood local da transferência de massa entre o fluido e as partículas, Sh_{fp}.

$$Sh_{fp} = \frac{k_{fp}\,d}{D_f} \tag{11}$$

Para expressar o número de Sherwood local, valeu-se da analogia entre a transferência de calor e de massa [13]. Em termos dos números adimensionais de Schmidt ($Sc = \nu/D_f$) e de Reynolds ($Re_p = \rho ud/\nu$), tem-se:

$$Sh_{fp} = 2 + 1{,}1\ Sc^{1/3}\ Re_p^{0{,}6} \tag{12}$$

À medida que o número de Reynolds diminui, o número de Sherwood decresce a um valor limite correspondente ao transporte difusivo entre o fluido e as partículas do meio.

As equações (8) e (9) são independentes e podem ser resolvidas separadamente. Em uma primeira etapa a equação do movimento é resolvida fornecendo o campo de velocidade; em seguida, resolve-se a equação da massa e obtém-se o campo de conteúdo de umidade.

Conforme foi discutido na secção anterior, a metodologia de solução para o problema hidrodinâmico é discutida de maneira sucinta. O procedimento de solução consiste basicamente na discretização dos termos pelo método dos volumes finitos. A equação algébrica resultante é resolvida através do algorítmo TDMA (Tri-Diagonal Matrix Algorithm), [15]. Utilizou-se uma malha variável com 500 pontos nodais na direção perpendicular ao escoamento. Os pontos foram concentrados na região próxima as paredes do duto, com o objetivo de se observar o importante "efeito canal" causado pela porosidade variável do meio.

Para a solução da equação do transporte de massa, utilizou-se o método implícito das Caixas de Keller[14].

A idéia básica do método é reduzir as equações governantes em um sistema de primeira ordem. Em seguida, escreve-se as equações resultantes usando-se diferenças centrais para os termos de derivada e médias aritméticas para os demais parâmetros. Após, o método requer que se linearize as equações, caso as mesmas sejam não lineares, e que estas sejam escritas na forma de uma matriz tridiagonal. Finalmente, resolve-se o sistema linear pelo método da eliminação por blocos.

A equação da massa é resolvida para fornecer o perfil de conteúdo de umidade a cada posição X. A malha em X é não uniforme, sendo mais refinada na entrada do duto.

RESULTADOS E DISCUSSÕES

A Fig. 1 mostra o perfil de velocidade característico do meio poroso. Este perfil, bastante alterado com relação ao perfil uniforme de Darcy, surge devido a inclusão da variação da porosidade na equação. Observa-se na Fig. 1 que na região próxima à parede, há a formação de um canal preferencial de escoamento de fluido, que opta por uma região de menor resistência. Este efeito é denominado de "efeito canal". Tal efeito já foi discutido com detalhes pelos autores em [9,10].

Perfis de conteúdo de umidade ao longo das coordenadas perpendicular e paralela ao escoamento são apresentados para dois valores do parâmetro B, $B = 10^5$ e $B = 10^7$, e para uma única relação entre o diâmetro da partícula e a distância H,D = 0,1. Também para estes valores plotou-se a quantidade local de massa evaporada em várias posições X.

As Figs. 2(a) e 2(b) apresentam, respectivamente, para $B = 10^5$ e $B = 10^7$, a variação do conteúdo de umidade ψ ao longo do duto para as posições Y = 0 (parede do duto) e Y = 1 (centro do duto). Conforme observado nas Figuras, ψ diminui ao longo de X, tanto para Y = 0 como para Y = 1, em virtude do crescimento de w em direção a w_s, o que reflete o ganho de umidade com a evaporação.

Outro fato evidenciado nas Figs. 2(a) e 2(b) é o decréscimo mais lento de ψ para a posição Y = 0, o que será racionalizado a seguir. Nesta posição a taxa de massa evaporada é zero. Vale notar que na parede a porosidade do meio, ε, é igual a unidade, significando a não existência de uma área evaporativa. O transporte de

massa por convecção em Y = 0 também é nulo, uma vez que a velocidade é zero na parede. Desta forma, o ganho de umidade nesta posição é devido unicamente à difusão de massa. Tal fato explica o decréscimo mais lento de ψ para Y = 0.

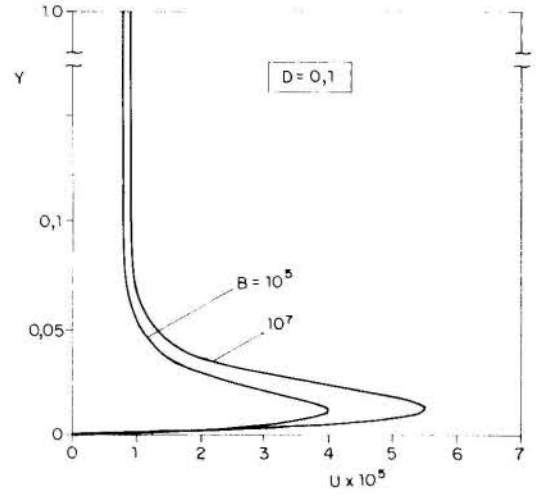

Fig. 1 - Perfil característico do meio poroso.

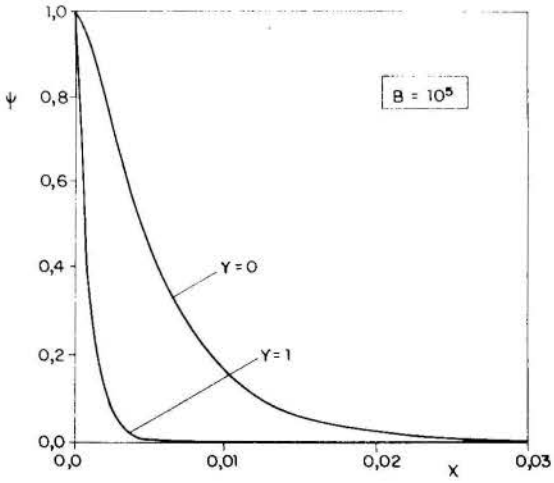

(a)

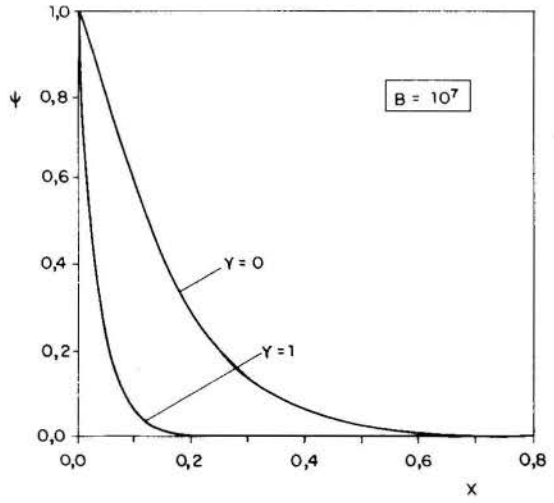

(b)

Fig. 2 - Desenvolvimento do conteúdo de umidade ψ ao longo de X para: (a) B = 10^5, (b) B = 10^7.

Comparando-se as Figs. 2(a) e 2(b), observa-se que o fluido atinge o conteúdo de umidade de saturação em uma posição X mais avançada no duto para o valor B = 10^7. A este valor está associada uma vazão de fluido mais elevada do que aquela para o valor B = 10^5. Esta vazão mais elevada requer uma quantidade de massa evaporada maior para se tornar saturada. Desta forma, à medida que B aumenta, aumentam os valores de X correspondentes à posição na qual o fluido satura.

Nas Figs. 3(a) e 3(b) estão apresentados perfis do conteúdo de umidade ψ ao longo da coordenada Y, para várias posições X no duto e para B = 10^5 e B = 10^7, respectivamente. Nestas Figuras observa-se que, à medida que se avança no duto, o fluido nas posições fora da região do canal atinge a saturação, ψ = 0, mais rapidamente do que o fluido que se encontra junto à parede. Na região do canal a velocidade do escoamento é mais elevada devido ao efeito da porosidade (esta região extende-se a uma altura em torno de 0,05<Y<0,1). Como conseqüência tem-se uma alta vazão de fluido que necessita de uma quantidade grande de massa para ter o seu conteúdo de umidade aumentado. Já para a região fora do canal, onde a vazão é mais baixa, o fluido atinge o conteúdo de umidade de saturação, w_s, mais rápido. Também pelas Figuras confirma-se o resultado que para B = 10^7 o fluido torna-se saturado em uma posição X mais avançada do duto. Em um processo de secagem de grãos, este resultado equivale a dizer que vazões maiores de fluido secam maiores quantidades de grãos, uma vez que o fluido satura em uma posição mais distante da entrada do duto.

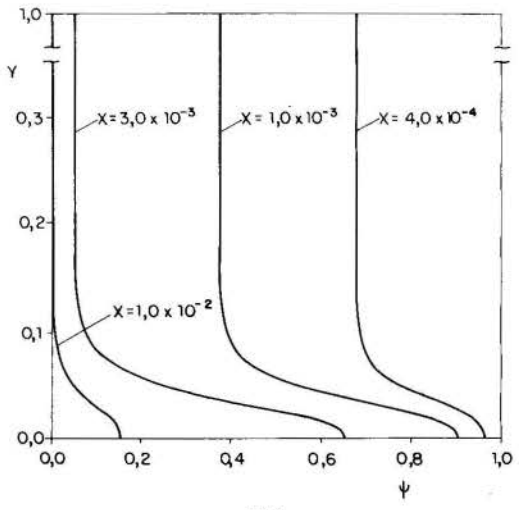

(a)

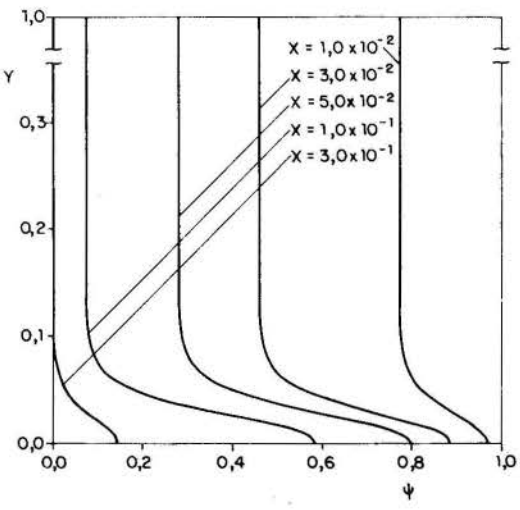

Fig. 3 - Perfis do conteúdo de umidade ψ para: (a) B = 10^5 , (b) B = 10^7.

A fim de explorar fisicamente as curvas representativas do conteúdo de massa evaporado, deve-se notar que o termo de geração de massa da equação (9) é proporcional à área efetiva de evaporação representada por $6(1 - \varepsilon)/D^2$, à velocidade do fluido que está embutida no

número de Sherwood, Sh_{fp}, e ao conteúdo de umidade do fluido, ψ. Para a compreensão deste termo, discutir-se-á, primeiramente a Fig. 4.

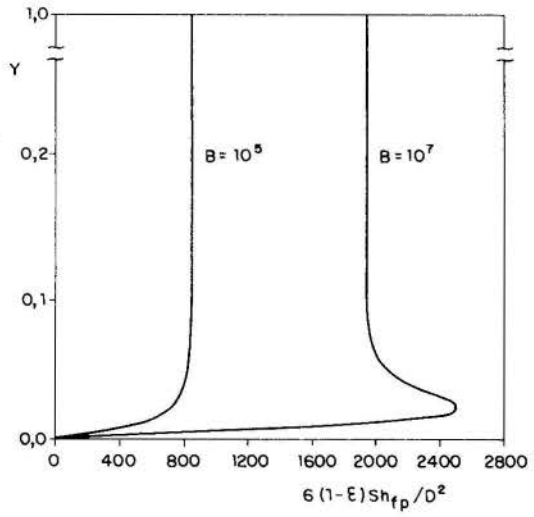

Fig. 4 - Comportamento do produto entre a área evaporativa e a velocidade do fluido.

A Fig. 4 mostra a relação do produto entre a área evaporativa e a velocidade do fluido com a coordenada Y. Conforme pode-se observar, a grandeza $[6(1 - \varepsilon)/D^2]Sh_{fp}$ cresce monotonicamente com Y para $B = 10^5$, indicando que o aumento da área evaporativa com Y se sobrepõe às altas velocidades encontradas na região do canal. O mesmo comportamento não é observado para a curva de $B = 10^7$. Neste caso, as altas velocidades correspondentes a vazão maior de fluido se sobrepõe ao fato da pequena área evaporativa existente na região do canal.

Nas Figs. 5(a) e 5(b) plotou-se a massa local evaporada, tendo como parâmetro de curva a coordenada X. Esta massa está adimensionalizada de forma a representar exatamente o termo de geração que aparece na equação (9).

Para uma dada posição Y, todas as curvas apresentadas nas Figs. 5(a) e 5(b) possuem os mesmos valores de $[6(1 - \varepsilon)/D^2]Sh_{fp}$, uma vez que ε e Sh_{fp} não variam com X. Sendo assim, o que distingue as curvas destas Figuras é unicamente o conteúdo de umidade ψ. Note-se que tanto para $B = 10^5$ como 10^7, quanto maior a variação de ψ com Y para um determinado X (ver Fig. 3), mais acentuada é a variação do termo de geração com Y. Vale notar que a maior variação de ψ com Y se encontra junto à parede do duto. No entanto, a porosidade nesta região é igual a unidade, e o termo de geração de massa é nulo.

Junto à entrada do duto ($X = 1{,}0 \times 10^{-5}$), tanto para $B = 10^5$ como para $B = 10^7$, como ψ é virtualmente constante e próximo da unidade, uma vez que $w \cong w_e$, as curvas da Fig. 5 são bastante semelhantes às curvas de $[6(1 - \varepsilon)/D^2]Sh_{fp}$ em função de Y, mostradas na Fig. 4.

À medida que se avança no duto, o fluido tem o seu conteúdo de umidade aumentado e o termo de geração diminui até atingir o valor zero para todas as posições Y, quando então não existem mais gradientes de umidade.

A Fig. 5(b) mostra valores de geração de massa maiores em relação à Fig. 5 (a), uma vez que o escoamento do fluido se dá a velocidades mais altas (B é maior), e portanto, a quantidade de massa evaporada é elevada.

A seguir será apresentado o desenvolvimento do número de Sherwood ao longo de X para vários valores de B. Para o cálculo do número de Sherwood representativo da transferência de massa entre as partículas e o fluido, definiu-se a seguinte expressão,

$$Sh_m = \frac{2H\bar{k}_{fp}}{D_f}$$

onde D_f é a difusividade molecular do vapor d'água no ar e $\bar{k}_{fp}$ é o coeficiente médio de transferência de massa entre o fluido e a matriz sólida. A definição de $\bar{k}_{fp}$ é obtida através de um balanço material feito em um volume de controle genérico, assumindo-se constantes os parâmetros do termo que representa a taxa de evaporação d'água.

O número de Sherwood, assim definido, será doravante denominado de Sherwood da matriz, e está representado na Fig. 6.

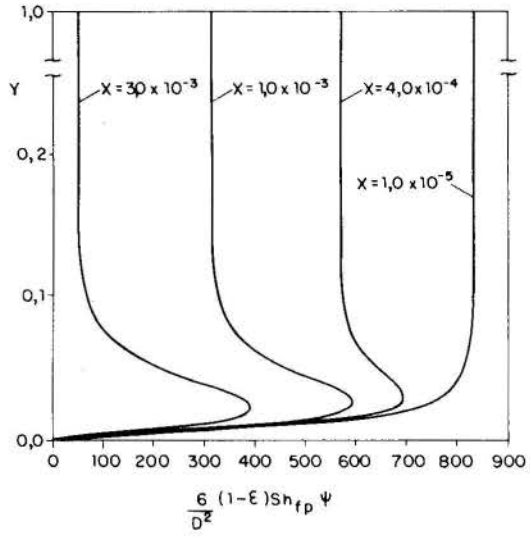

(a)

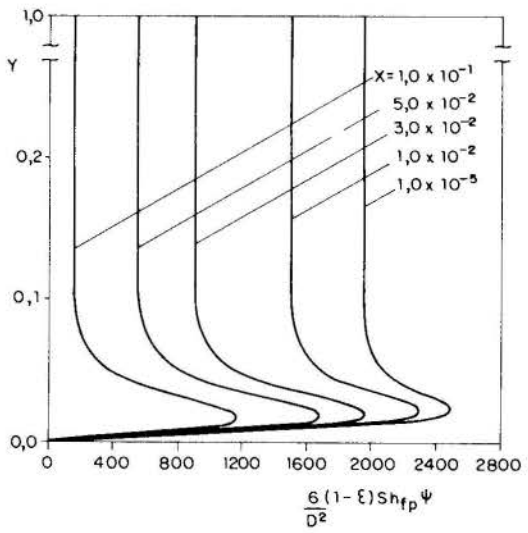

(b)

Fig. 5 - Geração local de massa para várias posições X do duto e para: (a) $B = 10^5$, (b) $B = 10^7$.

Conforme observado na Fig. 6, à medida que B aumenta os valores de Sh_m também aumentam. Tal fato era esperado, uma vez que velocidades maiores intensificam o processo de evaporação levando a valores mais elevados do número de Sherwood da matriz. Observa-se também pela Fig. 6 que para os primeiros estágios, onde as taxas de transferência de massa são elevadas, Sh_m varia pouco com X. O número de Sherwood decresce, então, bruscamente e atinge um valor limite correspondente ao da região plena

mente desenvolvida. Esta região é mais afastada da entrada do duto para valores de B maiores, conforme já foi comentado em figuras anteriores.

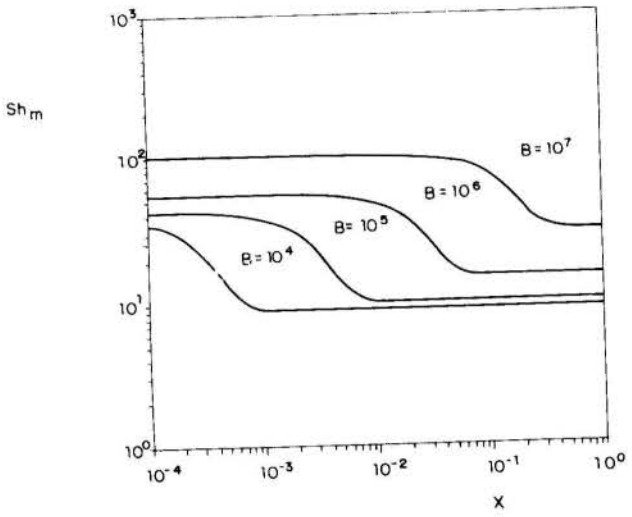

Fig. 6 - Variação do número de Sherwood da matriz ao longo do escoamento.

CONCLUSÃO

Neste trabalho foi investigado o problema isotérmico da transferência de massa em um duto contendo um leito de esferas. O fluido era uma mistura de ar e vapor d'água que ao escoar pela matriz sólida tinha o seu conteúdo de umidade aumentado pela evaporação d'água presente nas partículas. Na modelagem do escoamento foram computados efeitos de inércia, atrito e porosidade variável. Da análise dos resultados observou-se que a saturação do fluido ocorre mais lentamente junto à parede, muito embora nesta região tenham-se as velocidades mais elevadas, o que favorece o processo de evaporação. Isto ocorre porque nesta região a vazão de fluido é maior, necessitando de uma quantidade de massa d'água maior para ter o seu conteúdo de umidade aumentado. Observou-se também que o número de Sherwood da matriz cresce com o aumento do parâmetro B, significando que a transferência de massa á maior para vazões mais elevadas.

REFERÊNCIAS

[1] H. Darcy, "Les Fontaines Publiques de la Ville de Dijon", Dalmont, Paris, 1856.

[2] B. Wei and W. Chonggi, "Heat Transfer for Laminar Flow Through a Porous Channel with moisture Vaporisation", ASME WINTER ANNUAL MEETING, 1988.

[3] A.A. Pesaran and A.F. Mills, "Moisture Transport in Silica Gel Packed Beds - Theoretical Study", Int. J. Heat Mass Transfer, Vol. 30, N, 6, pp. 1037-1049, 1049, 1987.

[4] A.A. Pesaran and A.F. Mills, "Moisture Transport in Silica Gel Packed Beds - Experimental Study", Int. J. Heat Mass Transfer, Vol. 30, N, 6, pp. 1051-1060, 1987.

[5] Brooker, Bakker - Arkema and Hall, "Drying Cereal Grains", The Avi Publishing Company, Inc., 1974.

[6] D. Poulikakos and K. Renken, "Forced Convection in a Channel Filled with Porous Medium, Including the Effects of Flow Inercia, Variable Porosity, and Brinkman Friction", Journal of Heat Transfer, Vol. 109, pp. 880-888, 1987.

[7] K. Vafai and C.L. Tien, "Boundary and Inertia Effects on Flow and Heat Transfer in Porous Media", Int. J. Heat Mass Transfer, Vol. 24, pp.195-203, 1984.

[8] K. Vafai, "Convective Flow and Heat Transfer in Variable-Porosity Media", Journal Fluid Mechanics, Vol. 147, pp. 233-259, 1984.

[9] S.T. Sebben e A.T. Prata, "Transferência Convectiva de Calor em um Canal Preenchido com Esferas Compactadas", X COBEM, RJ, Vol.I, pp. 399-402, 1989.

[10] S.T. Sebben, "Transferência Convectiva de Calor e Massa em um Duto Preenchido com Esferas Compactadas", Dissertação de Mestrado, Universidade Federal de Santa Catarina, 1990.

[11] S. Ergun. "Fluid Flow Through Packed Columns", Chemical Engineering Progress, Vol. 48, pp.89-94, 1952.

[12] M.L. Hunt and C.L. Tien. "Non-Darcian Convection in Cylindrical Packed Beds" Journal of Heat Transfer, Vol.110, pp.378-384, 1988.

[13] N. Wakao and S. Kaguei, "Heat and Mass Transfer in Packed Beds", Gordon and Breach Publishers Inc., New York, 1982.

[14] T. Cebeci and P. Bradshaw. "Physical and Computational Aspects of Convective Heat Transfer", Springer-Verlag, New York, 1984.

[15] S.V. Patankar "Numerical Heat Transfer", Hemisphere Publishing Co., New York, 1980.

ABSTRACT

The present work investigates the mass transfer in a channel filled with a saturated porous medium. In the present formulation the problem is considered as being isothermal. The problem is modeled by a modified Darcy's law to compute flow inertia, no-slip condition on a solid boundary and spacial variation of porosity. The results are presented in terms of dimensionless moisture content and Sherwood number. It was shown that the saturation of the fluid near the walls is more difficult to occur, even though the higher velocities of the flow are located in this region. It's also observed that the Sherwood number increases as the channel flow rate increases.

III ENCIT – Itapema, SC (Dezembro 1990)

RATE OF EVAPORATION OF WATER IN A SPOUTED BED DRYER: THE EFFECT OF THE RATIO D_c/d, THE TEMPERATURE OF THE DRYING AIR AND THE RATIO Q/Q_{ms} (CONTINUOUS FEED)

JACQUELINE A. MORRIS e JOSÉ T. FREIRE
Universidade Federal de São Carlos
PPG-EQ - Cx. Postal 676
13560 - São Carlos-SP - Brazil

SUMMARY

In this work, the evaporation of water in a spouted bed dryer is analyzed with respect to three variables; T_{in}; D_c/d and Q/Q_{ms}. It was found that D_c/d and T_{in} are significant at 1 %, and a linear regression was performed for these variables. Tests were conducted with a yeast paste, to verify the behaviour of the dryer. It was noted that Q/Q_{ms} is important for the functioning of the bed as a dryer or as a particle coater.

INTRODUCTION

In view of the ever growing use of the spouted bed with inert particles as a dryer for pastes and suspensions, and the lack of information on the importance of the parameters in this process, the authors of this work decided to study the effect of a few of these variables on the evaporative capacity of a spouted bed dryer with inert particles.

The spouted bed has been used as a dryer since its discovery in 1955 by Mathur and Gishler [1]. However, the main emphasis on research in spouted beds has been for the immediate application of the process, such as the development of dryers for a specific paste, such as bovine blood, by Pham [2] and Ré [3]. Little research has been done in the more general field, in the sense of the studying the parameters of the process, with the aim of optimizing the drying process.

This work studied the effect of three parameters, the inlet air temperature, T_{in}; the surface area of the bed, in terms of D_c/d, the ratio of the diameter of the bed surface to the diameter of the inlet air orifice; and the flow rate of the entering air, in terms of Q/Q_{ms}, the ratio of the air flow to the air flow rate at minimum spouting. These parameters were chosen out of the myriad which affect the process because they were believed to be important, and for their ease in measurement.

After the experiment with water was concluded, tests were conducted with a solution of yeast, to verify the behavior of the dryer in the case of an actual paste.

MATERIAL AND METHODS

The spouted bed used consisted of a conical base with a 60° angle, followed by a cylindrical section with a diameter of 50 cm, and a height of 40 cm. The diameter of the inlet air orifice was 5 cm, and hence the maximum ratio of D_c/d that could be achieved was 10. Glass beads were used as the inert particle, with a diameter of 1.85×10^{-3} m and a density of 2500 kg/m^3. The liquid (water or yeast paste) was sprayed onto the bed from the top by a twin fluid nozzle. The air flow was provided by a 7.5 HP blower, and was heated by electrical resistances before entering the bed. The air temperature was measured by copper-constantan thermocouples at the air inlet and at the top (outlet) of the bed. Screens were couplet to the bed at the inlet and outlet, to support the bed, and to prevent the particles from being entrained. A cyclone was provided, to collect the powder formed during the paste drying, and a wet and dry bulb psycrometer was placed at the gas outlet to measure the humidity of the outlet air. A schematic of the equipment is shown in Figure 1.

Table 1 shows the levels of the parameters studied in the tests with water. A 3^3 factorial design was used, as described by Davies [4]

Table 1. The parameters used in the experiment with water and their levels

T_{in} (°C)	100,	120,	140
D_c/d	4.2,	6.2,	8.2
Q/Q_{ms}	1.2,	1.3,	1.4

Table 2 shows the levels of the parameters studied in the tests with yeast. A 3^3 factorial design was also used, with the factors studied being the concentration of the solution, C; the inlet air temperature, T_{in}; and the outlet air temperature, T_{out}. These factors were chosen because they were believed to be important for the drying of yeast paste, from Zanon [5] and Hadzismajlovic [6].

Table 2. Factors used for the experiment with yeast as feed, and their levels

T_{in} (°C)	100,	120,	140
T_{out} (°C)	60,	70,	80
C (%)	10,	15,	20

The yeast powder obtained underwent the following analyses: viability, by microscopic counting, after staining with methylene blue, following the procedure of Lee et alii [7] and protein solubility.

RESULTS AND DISCUSSION

Evaporative Tests With Water. The results of the experiments with water are shown in Table 3. An analysis of variance was carried out, according to Davies [4]. The results are shown in Table 4. The factors T_e and D_c/d are significant at 1 %, with Q/Q_{ms} insignificant at 10 %, which agrees with the data collected by Ré [3], which showed that the factor Q/Q_{ms} has no influence on the maximum feed rate at values between 1.2 and 1.5.

A linear regression was performed on the data, using a program created by Volk [8] which uses the method of all possible regressions, and the resulting 2 variable equation, in T_e and D_c/d, equation (1), has a coefficient of regression of 0.8926, compared with the three variable

equation, which gave a regression coefficient of 0.8983. A "t" test to compare the two equations gave a value of 4.5356, with a probability of error in chosing the two variable equation over the three variable equation of 0.0001

$$W = -5.8 + 0.04\ T_e + 0.76\ D_c/d \qquad (1)$$

Table 3. Results of the experiments with water as feed (maximum feed rate, l/h)

D_c/d		4.2	6.2	8.2
Q/Q_{ms}		1.2 1.3 1.4	1.2 1.3 1.4	1.2 1.3 1.4
T_{in}	100	2.4 2.4 1.5	1.5 3.9 2.4	3.9 4.8 4.8
	120	2.4 2.4 2.4	3.9 2.4 2.4	4.8 4.8 6.3
	140	2.4 3.9 2.4	3.9 3.9 3.9	6.3 6.3 7.5

Table 4. Analysis of variance for water data

Source of Variation	Sum of Squares	Degrees of Freedom	Mean Sum	F (calculated)
T_{in}	9.62	2	4.81	10.87
D_c/d	45.74	2	22.87	51.68
Q/Q_{ms}	0.62	2	0.31	1.43
$T_{in} \times D_c/d$	1.58	4	0.40	1.12
$T_{in} \times Q/Q_{ms}$	2.24	4	0.56	1.27
$D_c/d \times Q/Q_{ms}$	3.08	4	0.77	1.74
Error=$T_{in} \times D_c/d \times Q/Q_{ms}$	3.54	8	0.44	

It is improbable that the factor Q/Q_{ms} has little effect on the rate of evaporation of water in the spouted bed dryer. More likely is that the range of values studied was too small, but the capacity of the blower limited exploration of this factor at higher values. Considering Table 4, the parameter D_c/d has a very large F value, which emphasizes its importance in the process, also seen in the value of the coefficient of regression for the equation with only this variable, equal to 0.79.

$$W = -1 + 0.76\ D_c/d \qquad (2)$$

The parameter T_{in} is important, as intuition suggests, but its effect is not very large when compared to the effect of D_c/d.

Figure 2 shows some typical results of the evaporation. Equation (1) is included, and it can be seen that within experimental error, the fitted equation corresponds reasonably well to the data points. The strong effect of D_c/d can also be seen.

Tests With Yeast Paste. The results of some of the drying tests with yeast as feed are shown in Table 5. The solution was seen to have behaviour which differed substantially from the behaviour of the pastes studied earlier. The paste became very sticky during drying, causing the particles to agglomerate, which caused the spouting to stop. This seemed to occur at a solids concentration of between 25 and 30 %. Owing to this behaviour, the drying process was unreproducible, since the spouting was different every time the experiment was repeated. It also resulted in the loss of many data points, when the spouting stopped after a few minutes. This made the analysis of the results difficult, and the graph of the results (Figure 3) shows a large scatter of points, from which it is impossible to draw any conclusions.

However, experiments were carried out in which the process was left functioning for up to 6 hours, and these results (Table 6) show that this spouted bed can function as a dryer, which occurred with an air feed rate of 273.0 m^3/s, or as a coater of particles, since for an air feed rate of 193.2 m^3/s, the inert particles

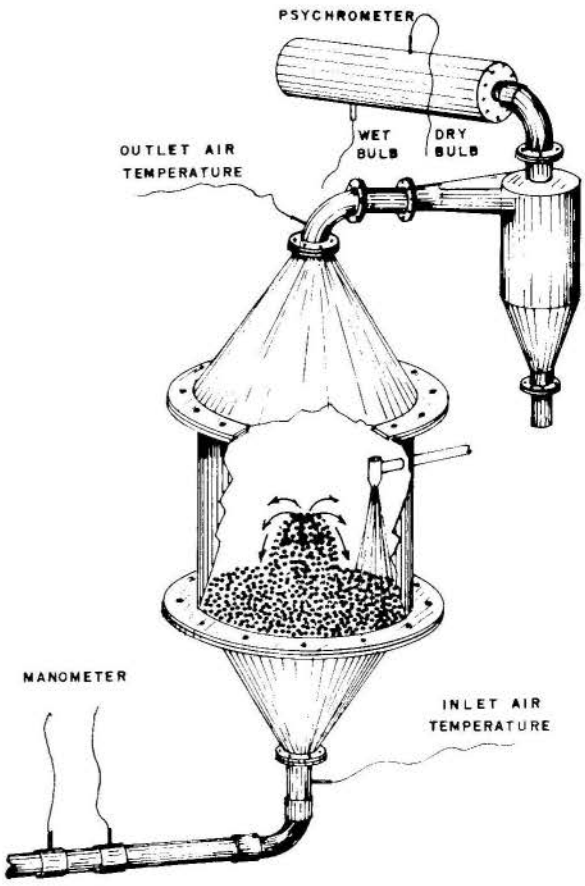

Figure 1 - Schematic of the spouted bed dryer used

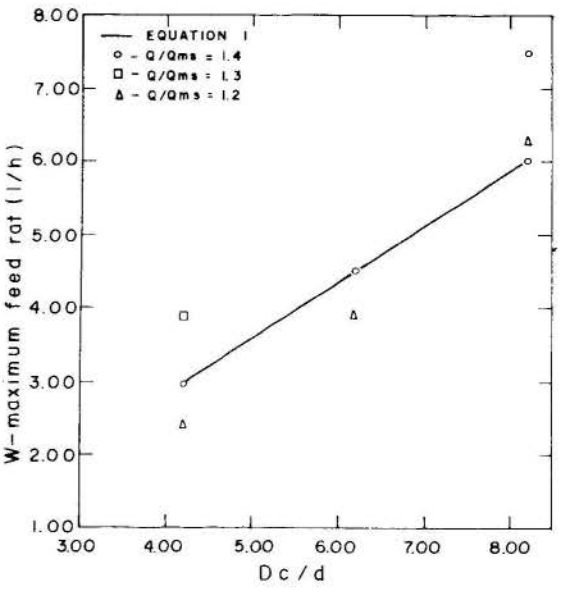

Figure 2 - Typical results of the evaporation tests; T_{in} = 140 °C, Q/Q_{ms} = 1.2-1.4

became coated with a hard resistant layer of yeast, approximately 0.5×10^{-3} m thick.

Table 5. Results of the experiments with yeast as feed (% of soluble protein)

T_{in} (°C)		100	120	140	100	120	140	100	120	140
T_{out} (°C)	60	47,53	53,42		41,87					
	70	39,70	52,22	46,99	57,03	34,38		24,54		
	80	38,42	54,85	36,38	45,00	33,00		26,87	24,13	

CONCLUSIONS

From this work, the following conclusions can be drawn:

1. The factor D_c/d is significant in the drying of pastes in a spouted bed of inert particles, with a F value of 51.68, significant at 1 %.

2. The factor T_{in} is also important, as intuition suggests, significant at 1 % with an F value of 10.87.

3. These two factors, D_c/d and T_{in}, can be combined in a fitted equation to predict the maximum feed rate of water (or paste) for the equipment studied and over the range of the parameters studied.

4. The parameter Q/Q_{ms} has no effect on the maximum feed rate in the range of values studied, further studies must be carried out for values of Q/Q_{ms} larger than 1.5, since it is probable that this parameter affects the maximum feed rate at higher values.

5. The equipment studied is feasible as a paste dryer, and, depending on the operating conditions, as a particle coater.

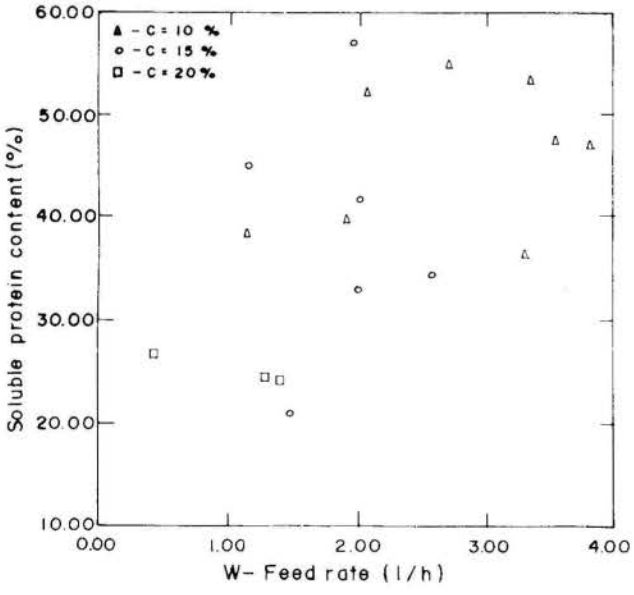

Figure 3. Typical results of the yeast drying experiments. D_c = 38.4 cm

Table 6. Results of two distinct runs with yeast paste in the spouted bed equipment. a) drying; b) Particle coating

(a) D_c = 31 cm; W = 2,5 l/h; Q = 376 m^3/s						
Run Time	Tin (°C)	Tout (°C)	Tdb (°C)	Twb (°C)	Powder Produced	
00:00:00	88.17	72.03	34.19	65.04	0-1hr	54.19g
00:15:00	97.00	58.21	36.09	57.76	1-2	56.04g
00:30:00	97.00	58.21	37.51	60.03	2-3	57.26g
00:45:00	99.77	60.49	37.75	59.35	3-4	50.76g
01:00:00	98.49	59.81	37.75	58.67	4-4:26	23.00g
01:15:30	98.49	62.31	37.75	59.35		
01:30:00	99.35	60.94	37.99	58.90		
02:00:00	99.35	62.08	39.89	59.35		
02:46:05	100.41	54.34	40.37	59.35		
03:00:00	100.41	58.21	39.89	58.44		
04:00:00	101.27	61.63	40.13	59.12		
04:26:00						
(b) D_c = 31 cm; W = 2.5 l/h; Q = 193.2 m^3/s						
Run Time	Tin (°C)	Tout (°C)	Tdb (°C)	Twb (°C)	Powder Produced	
00:00:00	98.28	86.24	45.12	78.66	0-1hr	20.65g
00:15:00	97.21	54.12	38.47	51.61	1-2	18.31g
00:29:45	100.91	54.57	38.70	52.07	2-3	18.02g
00:45:20	102.33	54.12	38.70	52.07	3-4	23.35g
01:00:00	102.76	54.34	38.70	52.07	4-5	21.56g
01:32:15	105.32	55.03	39.18	52.75	5-6	19.58g
02:01:30	102.12	54.12	38.47	51.39	6-7	29.61g
02:30:30	100.84	57.08	39.42	54.12	7-7:50	31.70g
03:00:00	99.77	55.48	39.18	53.21		
03:32:00	98.92	56.39	39.18	53.66		
04:01:45	97.85	58.67	39.66	56.17		
05:00:00	99.13	60.72	39.66	57.76		
05:30:30	100.41	61.85	40.61	57.99		
06:00:00	101.05	61.17	41.08	58.44		
06:30:35	101.05	60.94	40.84	57.99		
07:00:00	100.84	61.85	40.61	58.21		
07:29:00	101.48	61.40	40.84	58.90		
07:44:10	101.27	62.54	41.08	59.58		

ACKNOWLEDGMENTS

The authors would like to acknolewdege FINEP, processes nº 4.3.89.0194.00 for the financial support provided, which enabled this research to be carried out.

REFERENCES

[1] Mathur, K.B. and Gishler, P.E., "A technique for Contacting Gases with Coarse Solid Particles", AIChE J., Vol. 1, pp. 157-164, 1955.

[2] Pham, Q.T., "Behaviour of a Conical Spouted-Bed Dryer for Animal Blood", Can.J.Chem.Eng., Vol. 61, pp. 426-434, 1983.

[3] Rê, M.I., "Drying of Animal Blood in a Spouted Bed", (in portuguese), MSc. Thesis, Federal University of São Carlos, São Carlos, SP, Brazil, 1986.

[4] Davies, O.L., "The Design and Analysis of Industrial Experiments, 2nd Ed., Longman, New York, 1978.

[5] Zanon, C.J., "The Spouted Bed as a Dryer for Pastes and Similars", (in portuguese), Research Project Report, Federal University of São Carlos, São Carlos, SP, Brazil, 1989.

[6] Hadzismajlovic, Dz.E. et al., in "Fluidization V", Ed. J.R. Grace et al, AIChE, New York, pp. 277-284, 1989.

[7] Lee, S.S., Robinson, F.M. and Wang, H.Y., "Rapid Determination of Yeast Viability", Biotechnology and Bioengineering Symp., Vol. 11, pp. 641-649, 1981.

[8] Volk, W., "Calculator Solution to a Three Variable Problem", Chemical Engineering, Vol. 86, n. 27, pp. 93-98, dec.17, 1979.

III ENCIT – Itapema, SC (Dezembro 1990)

DETERMINACION EXPERIMENTAL DE COEFICIENTES DE TRANSFERENCIA DE CALOR EN UN SECADOR ROTATORIO DIRECTO

Pedro I. Alvarez y Alejandro Reyes S.
Departamento de Ingeniería Química
Universidad de Santiago de Chile
Casilla 10233, Santiago, Chile

RESUMEN

Se presenta una metodología experimental para la determinación de coeficientes volumétricos de transferencia de calor durante el secado de materiales particulados de origen vegetal. El equipo experimental es un secador rotatorio directo de flujo paralelo de 0,3 m de diámetro y 3 m de longitud. Los resultados experimentales de los coeficientes de transferencia de calor fueron menores que los calculados por las típicas correlaciones informadas por la bibliografía. Esto confirma la necesidad de obtener mayor información experimental, con el fin de desarrollar correlaciones más específicas.

INTRODUCCION

Aunque el uso de los secadores rotatorios es amplio en los procesos industriales, existe poca información cuantitativa conocida y disponible acerca de los factores que influyen en la operación y diseño de este tipo de equipos, haciendo difícil al ingeniero de procesos estimar precisamente el tamaño del equipo o las condiciones bajo las cuales podría operar más eficientemente. Debido a sus amplias aplicaciones una gran variedad de secadores han sido desarrollados, no obstante en todos ellos el principio de operación es el mismo. En Chile se secan más de 2.000.000 de toneladas de concentrados de cobre y molibdeno, y 1.000.000 de toneladas de harinas de pescado, siendo de gran impacto en la economía del proceso un estudio más completo de la eficiencia energética del proceso de secado. La eficiencia del equipo está fuertemente afectada por la transferencia de calor desde el gas a las partículas y por el tiempo de retención de éstas en el cilindro rotatorio. Aunque los clásicos resultados empíricos de Friedman y Marshall |1,2| son útiles en el dimensionamiento de los equipos, las investigaciones en los últimos años se han orientado a prescindir de los parámetros empíricos globales en la formulación del estudio de la dinámica del secador, usando en lo posible los principios de transferencia de momentum, calor y materia entre el sólido y el gas, con el fin de obtener los perfiles de humedad y temperatura de las corrientes, permitiendo mejorar la eficiencia del proceso de secado, principalmente en aquellos casos en que la calidad final del sólido está afectada por los niveles de temperatura en el interior del secador; sus cambios de calidad con las condiciones de operación, fijan el tiempo de secado o de retención en el secador.

En un trabajo previo, Alvarez et al.|3| formularon un modelo computacional de un secador rotatorio de calentamiento directo operado en flujo paralelo, considerando el efecto de la cinética del secado y las condiciones de entrada del aire, en los perfiles de temperatura y humedad del sólido y el gas a lo largo del secador. En este modelo se incorporaron como una primera aproximación, las típicas correlaciones empíricas para el tiempo de retención y el coeficiente global de transferencia de calor obtenidas en los trabajos de Friedman y Marshall |2,3|.

La estimación del tiempo de retención es difícil de obtener debido a la compleja interacción de factores como carga de sólidos, número y geometría de los elevadores, pendiente y velocidad de rotación del cilindro, diámetro y longitud del secador, propiedades físicas del material y velocidad del gas. El efecto de cada uno de estos factores ha sido discutido extensamente en la literatura por Williams-Gardner |4|, Perry |5|, entre otros.

Modelos teóricos para el tiempo de retención han sido desarrollados con el fin de introducir parámetros o variables básicas del sistema, los cuales emplean el concepto de "cascada", definido como el camino recorrido por la partícula desde el comienzo de su caída desde el elevador hasta el regreso a su posición original. Para su análisis los conceptos fluidodinámicos de la interacción fluido-partícula son muy importantes. No obstante, estos modelos más complejos y generales, incluyen coeficientes que deben ser determinados por las condiciones experimentales y la geometría de los elevadores.

Por otro lado, la determinación del tiempo de retención está íntimamente relacionada con el proceso de secado, el cual es realizado por la simultánea transferencia de calor y materia entre el material y el gas caliente. Es una aproximación vigente y frecuente, expresar la velocidad de transferencia de calor Q entre el sólido y el gas en la forma:

$$Q = (U\,a)\,AL\,(\Delta T)_m \qquad (1)$$

McCormick |6|, basado en los pioneros trabajos de Miller et al.|7|, Friedman y Marshall |2,3|, y Saeman y Mitchel |8|, derivaron la siguiente relación:

$$Ua = K\,G^n/D \qquad (2)$$

donde K es una constante ajustada empíricamente, la cual se ha observado que depende de parámetros del sistema como la retención de sólidos, velocidad de rotación, número y geometría de los elevadores. La potencia "n" aparece como uno de los puntos de controversia en la interpretación de trabajos experimentales. Valores usuales de K y n son 237 y 0.67, respectivamente, en unidades SI.

Kuramae y Tanaka |9|, Hirosue y Shinohara |10| usaron una aproximación teórica para deducir relaciones para coeficientes volumétricos de transferencia de calor, a partir de coeficientes individuales de transferencia de calor. Porter |11| y Turner |12| fueron los primeros en analizar los mecanismos cíclicos de transferencia de calor que ocurren durante períodos alternativos de caída y deslizamiento de las partículas individuales a lo largo del secador. Una aproximación teórica al análisis de la transferencia de calor requiere de un detallado examen del modelo de cascada del sólido, con la interacción sólido-gas muy bien definida.

En el proceso de secado en el secador rotatorio, la dinámica de la transferencia de masa no puede ser aislada, ya que la remoción de humedad depende de la transferencia de calor. Myklestad |13| desarrolló un procedimiento para predecir los perfiles de humedad del sólido a lo largo del secador suponiendo que la temperatura del gas varía linealmente con la humedad del sólido. De experiencias de secado efectuadas con arenas, encontró que el coeficiente volumétrico de transferencia de calor variaba con la potencia 0.8 de la velocidad del gas. Una aproximación más fundamental usada por Sharples et al. |14| requirió la solución simultánea de ecuaciones diferenciales para los balances de masa y energía. En el trabajo de Alvarez et al. |3| se muestra el efecto que tiene la velocidad de transferencia de calor a través del coeficiente volumétrico (Ua) y los diferentes mecanismos de transferencia de masa, en los perfiles de temperatura y humedad a lo largo del secador. Estos efectos son particularmente muy notorios cuando se trabaja a altas temperaturas de gas, en flujo paralelo de gas y sólido, principalmente en los perfiles de temperatura del sólido.

Formulación matemática del modelo dinámico en el secador rotatorio directo. La descripción de la transferencia simultánea de calor y materia se obtiene a través de la aplicación de los balances de masa y energía a un elemento diferencia de longitud de secador considerando nulas las pérdidas de calor, las cuales pueden resumirse como:

$$\frac{dX}{dz} = -\frac{N}{z}\,\Theta \qquad (3)$$

$$\frac{dY}{dz} = \frac{S_s\,N}{G_s\,z}\,\Theta \qquad (4)$$

$$\frac{dT_G}{dz} = \frac{1}{C_h\,G_s}\left|-(Ua)A\,(T_G-T_s) - (T_G-T_s)C_a S_s \frac{N}{z}\,\Theta\right| \qquad (5)$$

$$\frac{dT_s}{dz} = \frac{1}{C_{sh} S_s}\left|(Ua)A\,(T_G-T_s)-\lambda_s S_s \frac{N}{z}\,\Theta\right| \qquad (6)$$

Puede verse en las ecuaciones (5) y (6) la dependencia directa de Ua en los perfiles de temperatura del gas y sólidos, respectivamente. De aquí la importanci que tiene su estudio y determinación experimental,par materiales que presentan una gran variedad de forma y tamaño, de estructura compleja como son los materiale particulados de origen vegetal y marino.

Objetivo del trabajo. En este trabajo, se presenta una metodología experimental para obtener datos experimentales del secado de productos de origen marino y vegetal (harinas) en un secador rotatorio directo, con el objetivo de obtener parámetros característicos del proceso, en particular el coeficiente de transferencia de calor entre el gas y el sólido. La mayoría de los datos disponibles en la bibliografía han sido obtenidos con arena y otros productos similares en unidades de escala laboratorio.

MATERIALES Y METODOS EXPERIMENTALES

El material usado es un producto base soya con 52% de proteína, de dos tipos: "harina de soya" con densidad de sólido seco de 1220 Kg/m^3 y una distribución de tamaños entre 0.5 mm y 2.0 mm; "extender de soya" (carne vegetal) con una densidad de sólido seco de 840 Kg/m^3 y un tamaño entre 5.0 mm y 9.0 mm, generando un 10% en finos a su paso por el secador.

El equipo experimental es un secador rotatorio directo de 3 m de longitud y 0.3 m de diámetro (Figura 1) operando en flujo paralelo, fabricado en acero inoxidable, revestido en lana de vidrio como aislante. En su interior está provisto de tres tipos de elevadores radiales de 1 m de longitud cada uno: planos; con un ángulo de 45°; y un ángulo de 90°. La velocidad de giro del cilindro puede regularse por un sistema de poleas en valores de 5, 10 y 15 rpm. La inclinación puede ser modificada con una gata mecánica en un rango de 0 a 0.074 m/m. Una cámara de combustión de 0.8 m de longitud y 0.5 m de diámetro, provista de tres quemadores de gas licuado permite calentar el aire que ingresa por dos tomas de 0.102 m de diámetro, succionada por un ventilador, regulando el flujo mediante válvulas de mariposa. Un controlador automático regula la temperatura de entrada del aire. El sólido es cargado en una tolva y por medio de una vibradora se alimenta a un tornillo de velocidad variable, que lo transporta al interior del secador. Una válvula mariposa instalada en la descarga del secador impide la succión del aire y facilita la descarga del sólido. Las partículas finas arrastradas por el aire son recolectadas mediante un ciclón.

El equipo experimental consta de 2 vainas deslizables por el eje central del secador, permitiendo la toma de muestras para las mediciones de humedad del sólido y el registro instantáneo de las temperaturas del sólido y el gas, mediante termocuplas de Fe-Constantan. Fueron seleccionadas 6 posiciones en el secador para las medidas locales, ubicadas cada 0.3 m desde la entrada.

Para cada una de las experiencias la velocidad de rotación del cilindro fue de 10 rpm y una pendiente de 0.012.

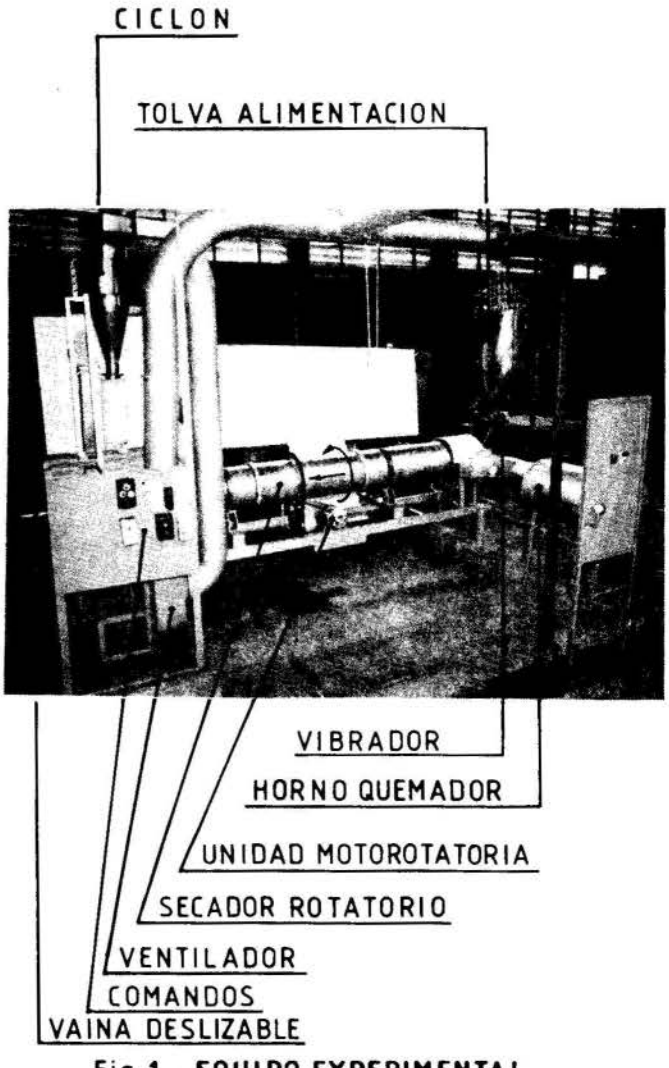

Fig. 1.- EQUIPO EXPERIMENTAL

Tabla 1. Condiciones de operación usadas en las experiencias y resultados experimentales de coeficientes volumétricos de transferencia de calor.

Corrida	Producto	G_s	S_s	T_G	X_o	Ua,global Aire	Ua,global Sólido	Ua* Aire	Ua* Sólido
1	HARINA	0.47	0.23	105	0.22	413	407	424	418
2	HARINA	0.43	0.24	137	0.27	367	338	398	366
3	HARINA	0.46	0.26	175	0.22	375	347	390	360
4	HARINA	0.82	0.17	100	0.34	586	523	579	530
5	HARINA	0.81	0.23	141	0.29	662	664	662	647
6	HARINA	0.84	0.27	178	0.31	473	453	516	493
7	EXTENDER	0.45	0.16	110	0.29	483	431	471	433
8	EXTENDER	0.45	0.17	135	0.31	368	325	387	349
9	EXTENDER	0.47	0.18	170	0.31	394	364	425	393
10	EXTENDER	0.83	0.16	107	0.38	510	499	530	518
11	EXTENDER	0.85	0.14	130	0.38	532	496	556	518
12	EXTENDER	0.86	0.16	165	0.39	528	452	526	448

RESULTADOS Y DISCUSION

En la Tabla 1 se muestran los valores experimentales de las variables de operación fijadas para este estudio. En la Fig. 2 se muestran los perfiles experimentales de temperatura del aire y el sólido, para la corrida 3. En la Fig. 3 se muestran los perfiles axiales de humedad del sólido para las corridas 1, 2 y 3. Similares resultados se obtuvieron para todas las demás experiencias.

Por observación visual se apreció que el alzamiento del sólido (cortina de sólido) no era uniforme en los tramos del secador provisto de elevadores planos (zona de entrada). Debido a la cercanía del horno con la sección de entrada del sólido se produjo un fuerte calentamiento de la alimentación por conducción, convección y radiación, produciéndose en la entrada una gran disminución de la humedad, en relación a la humedad en la tolva de alimentación. Debido a estos factores, los coeficientes de transferencia de calor fueron calculados a partir de la posición distante 0.9 m de la entrada. Las ecuaciones de cálculo del coeficiente local de transferencia de calor fueron planteadas para longitudes de secador de 0.30 m, tomando en cuenta el calor cedido por el gas (ec. 7) y el calor absorbido por el sólido, despreciando el aumento de calor sensible (ec. 8):

$$Ua = \frac{G_s C_{sh} \Delta T_G}{z\ (\Delta T)_{ML}} \qquad (7)$$

$$Ua = \frac{S_s \lambda_s \Delta X}{z (\Delta T)_{ML}} \qquad (8)$$

Los valores globales informados en la Tabla 1 fueron calculados según la relación propuesta por Friedman y Marshall [3] :

$$Ua^* = \frac{\Sigma\ Ua\ (\Delta T)_{ML}}{\Sigma\ (\Delta T)_{ML}} \qquad (9)$$

Los coeficientes globales de la Tabla 1 fueron calculados para todo el secador con una longitud de 2.10 m.

Aunque los resultados experimentales no permiten extraer conclusiones claras del efecto de las variables, puede notarse que los valores cambian sin una tendencia definida con el cambio de la temperatura de entrada del aire y del flujo de sólido. Sin embargo, al aumento del flujo gaseoso, trae como consecuencia un aumento del coeficiente Ua, concordando con resultados de la literatura. Por otro lado, los valores más altos del coeficiente por el lado del gas son lógicos y es atribuido a que incluyen las pérdidas de calor. Mayores y mejores conclusiones deben ser extraídas con un conjunto de experiencias cambiando significativamente las variables más importantes.

Para flujos promedios de aire dados por 0.46 Kg/m^{2}s y 0.84 Kg/m^{2}s, la ec. (1) predice para el coeficiente de transferencia de calor, valores de 470 J/m^{3}s °K y 70 J/m^{3}s °K, respectivamente. Puede notarse que

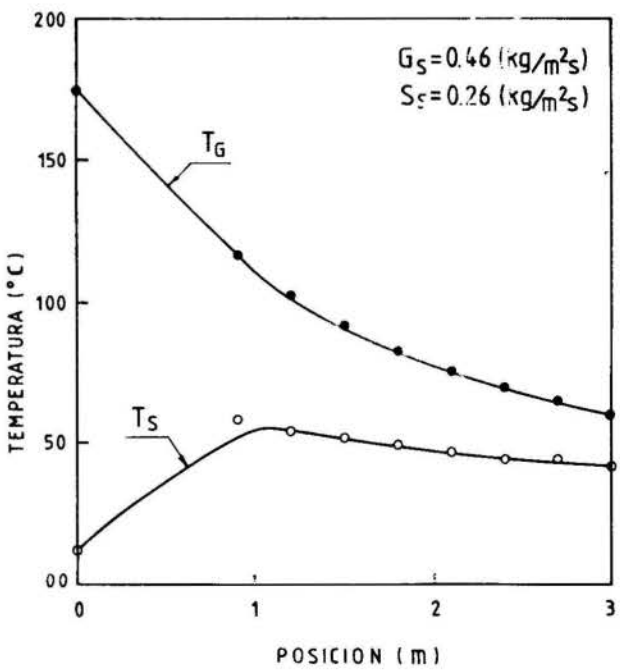

Fig. 2.- PERFILES EXPERIMENTALES DE TEMPERATURA EN EL SECADOR. CORRIDA 3.

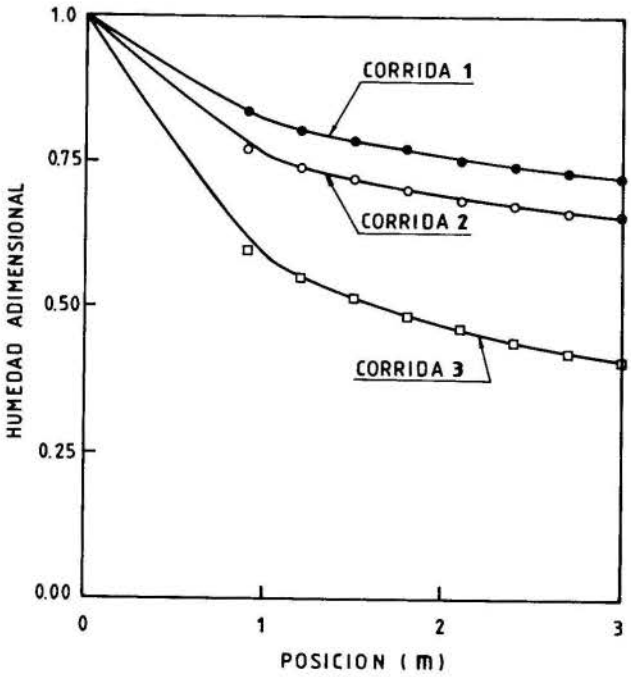

Fig.3.- PERFILES EXPERIMENTALES DE HUMEDAD DEL SOLIDO EN EL SECADOR.

NOMENCLATURA

A	: Sección transversal del secador, m^2
D	: Diámetro del secador, m
G	: Flujo de gas, Kg/m^2s
G_S	: Flujo de gas seco, Kg/m^2s
L	: Longitud total del secador, m
N	: Velocidad de secado, $dX/d\Theta$
Q	: Velocidad de transferencia de calor entre el sólido y el gas, J/s
S_S	: Flujo de sólido seco, Kg/m^2s
T_G	: Temperatura del gas, °C
T_S	: Temperatura del sólido, °C
$(\Delta T)_{ML}$	: Diferencia de temperatura media logarítmica entre el gas y el sólido, °C
Ua	: Coeficiente volumétrico de transferencia de calor, J/m^3s °K
X	: Humedad del sólido, base seca
X_o	: Humedad inicial del sólido, base seca
z	: posición axial, m
Θ	: Tiempo de retención, s
λ_S	: Calor latente de vaporización del agua, J/Kg

AGRADECIMIENTOS

Los autores agradecen el apoyo financiero prestado por el Fondo Nacional de Desarrollo Científico y Tecnológico a través del Proyecto 89-0753, y por la Dirección de Investigaciones de la Universidad de Santiago de Chile.

REFERENCIAS

|1| Alvarez, P.I., P. Legues y L. López, "Simulación Computacional de Secadores Rotatorios Directos: Efecto de la Cinética de Secado", III Congreso Latinoamericano de Transferencia de Calor y Materia, p. 648, Guanajuato, México, 1988.

|2| Friedman, S.J. y W.K. Marshall, "Studies in Rotary Drying. I: Holdup and Dusting", Chem. Eng. Prog., 45, 482, 1949.

|3| Friedman, S.J. y W.K. Marshall, "Studies in Rotary Drying. II: Heat and Mass Transfer", Chem. Eng. Prog., 1949, 45, 573, 1949.

|4| Williams-Gardner, A., "Industrial Drying", Leonard Hill, London, 1971.

|5| Perry, J.H., "Chemical Engineer's Handbook", 5a. ed., Mc Graw-Hill, 1975.

|6| McCormick, P.Y., "Gas Velocity Effects on Heat Transfer in Direct Heat Rotary Dryers", Chem. Eng. Prog. 58(6), 57, 1962.

|7| Miller, C.D., B.A. Smith, and W.H. Schuette, "Factors Influencing the Operation of Rotary Dryers", Trans. AICHE, 38, 841, 1942.

|8| Saeman, W.C., and T.R. Mitchell, "Analysis of Rotary Dryer and Cooler Performance", Chem. Eng. Prog., 50(9), 467, 1954.

|9| Kuramae, M., y T. Tanaka, "Analysis of Volumetric Heat Transfer Coefficient for a Rotary Dryer", Heat Transfer, Jpn, Res. 6(1), 66, 1977.

|10| Hirosue, H., y H. Shinohara, "Volumetric Heat Transfer Coefficient and Pressure Drop in Rotary Dryers and Coolers", Proc. 1st. Int. Symp. on Drying (McGill Univ., Montreal), A.S. Mujumdar, ed., Science Press, Princeton, NJ, 1978.

|11| Porter, S.J., "The Desing of Rotary Dryers and Coolers". Trans. Inst. Chem. Eng., 41, 272, 1963.

|12| Turner, G.A., "The Thermal History of a Granule in a Rotary Cooler", Can. J. Chem. Eng., 44, 13, 1966.

|13| Myklestad, O., "Heat and Mass Transfer in Rotary Dryers", Chem. Eng. Prog. Symp. Ser., 59(41), 129, 1963.

SUMMARY

The present investigation about the drying of particulate materials of vegetal origin was aimed at the acquisition of the volumetric coefficients of heat transfer between the gas and the solid, and was carried out in a direct rotatory drier with parallel flows, 0.3 m diameter and 3 m length.

The technique consisted in measuring the temperature of the flows and the moisture of the solids at positions given by 0.3 m increments along the axis of the drier. In the course of the investigation the entrance temperature of the gas and the flow rates of the gas and solids were changed. The solids were soya-based (meal and extender) and varied in size between 0.5 mm and 9.0 mm.

The experimental values for the heat transfer coefficients were lower than those obtained by typical correlation found in the literature. This confirms the need to obtain better experimental information about the drying of animal and vegetal materials, to lead to the development of more precise correlations.

III ENCIT – Itapema, SC (Dezembro 1990)

SECADOR ROTATÓRIO COM RECHEIO DE INERTES: II- ESTUDOS INICIAIS DE SECAGEM DE MELAÇO DE CANA-DE-AÇÚCAR

CLÁUDIA M. ÁLVARES[1], MAURO M. BURJAILI[2], JOSÉ ROBERTO D. FINZER[2]
[1]Deptº Engenharia Mecânica , [2]Deptº Engenharia Química
Universidade Federal de Uberlândia - Campus Santa Mônica
38400 - Uberlândia - MG - Brasil

RESUMO

Um secador de bandejas foi utilizado para estudar a secagem de melaço de cana-de-açúcar. Os resultados obtidos induziram a expectativa de que dispositivos que conseguissem eliminar continuamente uma casca endurecida, que se formava sobre a superfície do material, poderiam reduzir o tempo de secagem. Com base neste princípio utilizaram-se dois secadores rotatórios com recheio de inertes em escalas diferentes: o primeiro comprovou ser possível utilizar o equipamento para produção de melaço em pó; o segundo permitiu quantificar a capacidade do secador.

INTRODUÇÃO

Os equipamentos tradicionais de secagem de materiais fluidos mais destacados são os secadores por atomização e os de cilindro rotativo, onde a secagem ocorre na superfície cilíndrica externa [1]. A técnica de utilização de câmaras de secagem contendo corpos inertes, que servem de suporte para o material viscoso a ser desidratado, constitui o avanço mais recente na tecnologia de secagem de materiais pastosos [2]. A utilização de leitos de jorro contendo inertes tem sido objeto de muitas pesquisas de secagem de soluções e pastas [3, 4 e 5]. Neste secador, o movimento dos sólidos é promovido pela ação do ar de secagem. O secador de leito vibro-fluidizado possibilita o movimento dos sólidos por efeitos vibracionais impostos ao leito , restringindo assim o consumo de ar [6]. O secador rotatório com recheio de inertes promove o movimento dos sólidos pelo movimento de rotação de um cilindro horizontal de secagem [7].

O secador rotatório com recheio de inertes é um equipamento utilizado para a secagem de soluções, suspensões e pastas. A agitação dos inertes é promovida pela rotação de um cilindro horizontal e pela ação de aletas longitudinais dispostas em sua superfície interna [7]. No trabalho que antecede o atual, descreve-se a dinâmica das partículas no interior do cilindro rotatório e mostram-se os resultados de ensaios de secagem de pasta de leite de soja em operação contínua com escoamento concorrente.

No presente trabalho relatam-se os estudos referentes à secagem de melaço de cana-de-açúcar, que é o resíduo da operação de cristalização da sacarose nas usinas açucareiras, quando não mais se viabiliza economicamente cristalizar a sacarose contida nele [8].

Estudos Iniciais de Secagem de Melaço de Cana-de-Açúcar

Para estudar o comportamento do melaço de cana-de-açúcar, quando submetido à secagem com aquecimento direto, realizaram-se ensaios utilizando-se um secador de bandejas. Neste equipamento o ar de secagem escoava sobre a superfície livre do melaço disposto sobre placas de vidro em camadas com espessuras iniciais variando de 0.18 a 2.34 cm. As curvas de secagem obtidas são indicadas na Fig. 1, sendo a ordenada a relação de umidade X/Xo e a abscissa o tempo de secagem , t. O conteúdo de umidade em um tempo qualquer é denotado por X, kg H_2O/kg de melaço seco, e Xo refere-se à condição inicial, sendo igual a 0.33 kg H_2O/kg de melaço seco. As condições do ar foram: taxa mássica de 0.11 kg/min e temperatura de 80°C.

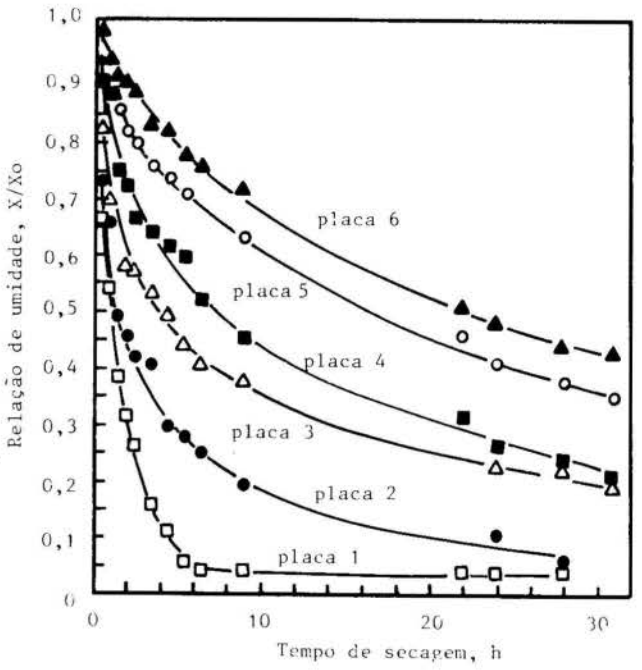

Fig. 1 Curvas de secagem de melaço disposto em camadas de espessura variável. Condições de operação: Taxa mássica e temperatura ar de secagem:0,11kg/min e 80°C; conteúdo inicial de umidade de melaço, Xo = 0,33 kg H_2O / kg de melaço seco; espessuras iniciais das camadas(cm) nas placas: 1(0,18cm); 2(0,34); 3(0.72) ; 4(0,91) ; 5(1,32); 6(2,34).

Analisando as curvas da Fig. 1, verifica-se que a relação de umidade X/Xo = 0,16 (5% de água, base úmida) é obtida após 3.7 horas de secagem, quando a espessura inicial do melaço é de 0,18 cm. O melaço com conteúdo de umidade inferior a 5% (base úmida) comporta-se como um sólido, sendo suscetível à transformação em pó. Partindo-se de camadas de melaço mais espessas, por exemplo, de 0,34 e 0,72 cm, para atingir o conteúdo de umidade anterior, o tempo de secagem aumenta para 13 e 36 horas, respectivamente. Verifica-se que um aumento em 89% na espessura da camada inicial, resultou em um aumento de 251% no tempo de secagem, o que inviabiliza a secagem de melaço em camadas espessas.

Acompanhando o comportamento do melaço durante a secagem, observou-se que sobre as camadas do mesmo for

mava-se uma casca endurecida ("case hardening"), enquanto, nos estágios iniciais de secagem, o material abaixo da mesma permanecia em estado pastoso. Ao se atritar um raspador sobre a casca endurecida de melaço, surgia um pó de coloração amarela, enquanto a camada pastosa sobre a placa de vidro conservava a cor marrom original.

Os inconvenientes da utilização de um secador de bandejas na secagem de melaço de cana são fundamentalmente operacionais, destacando-se a necessidade do emprego de uma câmara climatizada para moagem do melaço desidratado, devido à elevada higrospicidade do mesmo e à dificuldade da retirada do melaço das bandejas.

Os resultados anteriores induziram a expectativa de que dispositivos que conseguissem eliminar continuamente a casca endurecida de melaço poderiam atuar no sentido de reduzir o tempo de secagem do melaço de cana, por possibilitar o contato permanente de um filme renovável de material com o ar de secagem. O secador rotatório com recheio de inertes é um equipamento que atua no sentido de retirar gradativamente a casca endurecida que se forma sobre os inertes, devido ao atrito entre partícula-partícula, partícula-aleta e partícula-parede.

Os ensaios de secagem foram realizados no secador rotatório com recheio de inertes em escala reduzida [7] e em escala ampliada.

SECAGEM COM ALIMENTAÇÃO CONTÍNUA E INTERMITENTE DE MELAÇO - SECADOR EM ESCALA REDUZIDA

Para estudar o desempenho do secador rotatório com recheio de inertes (SRRI) a alimentação de melaço foi efetuada de duas maneiras: contínua e intermitente. O secador de 15 cm de diâmetro e 30 cm de comprimento continha 1600 g de esferas de vidro com diâmetro de 1 cm, girava a 40 rpm. No interior do cilindro de secagem foram dispostas quatro aletas de 5 cm de altura. As condições de operação do ar de secagem foram: temperatura de 80°C e velocidade de 97 cm/s (0,9 kg/min), referida à área da seção transversal do secador. O melaço cujo conteúdo de umidade inicial era de 26 % (bu) foi alimentado na entrada do secador por intermédio de uma bomba peristáltica.

Alimentação Contínua. Depois de 30 minutos de operação, à taxa de alimentação de melaço de 190 g/h, surgiram as primeiras frações de melaço seco, com coloração amarela, que foram coletadas por um ciclone. Devido à baixa produção de pó observada, após 60 minutos de operação, o SRRI foi desmontado para inspeção. Observou-se que as esferas de vidro encontravam-se completamente revestidas com melaço e que este ocupava, também, grande parte do volume do cilindro. Isto impedia a circulação efetiva das esferas e, possívelmente, o desprendimento do produto parcialmente seco que as revestia, comprometendo, assim, a produção de pó.

Evidentemente, a vazão de melaço tinha excedido a capacidade do secador. Contudo, este ensaio inicial confirmou a hipótese de que a remoção contínua da casca endurecida, que se formava à medida que o melaço perdia umidade, facilitava a secagem do mesmo.

Alimentação Intermitente. Na operação do SRRI, com alimentação intermitente, para evitar que a capacidade do secador fosse excedida, utilizou-se o seguinte procedimento. No decorrer da operação do secador o atrito e os choques entre as esferas de vidro e o corpo do secador geravam um ruído, cuja intensidade aumentava à medida que a espessura da camada de melaço sobre as esferas reduzia-se. Quando a intensidade do ruído tornava-se constante, mas não alta como na operação do secador livre de melaço, efetuava-se a alimentação utilizando a bomba peristáltica. A alimentação era efetuada até praticamente cessar todo o ruído, após o que repetia-se a etapa anterior.

Esta metodologia induziu a realização da alimentação contínua de melaço entre 5 e 7 minutos com interrupção da mesma por aproximadamente 10 minutos. Durante as interrupções do ensaio, inspeções realizadas no interior do secador indicaram a existência de melaço revestindo tanto as esferas, em cerca de 10% da superfície externa, quanto as paredes internas do compartimento. O melaço apresentava uma coloração amarela característica do produto em pó, o que sugeria que a capacidade do aparelho não havia sido ultrapassada. O presente estudo permitiu estimar a capacidade do SRRI em escala reduzida, o que correspondeu a uma produção em torno de 14 g/h de melaço seco com um conteúdo de umidade de 5% (b u).

Na realidade a produção de melaço em pó era superior à supracitada, considerando-se as perdas do produto pelas folgas nas conexões do cilindro rotatório com as tubulações a montante e a jusante do secador, além do efeito de arraste pelo ar de secagem que abandonava o topo do separador ciclone.

O presente estudo confirmou, portanto, a possibilidade da utilização de um SRRI para produzir melaço em pó em uma única etapa de processamento (com secagem e moagem simultâneas). Entretanto, o modelo disponível em escala reduzida, além de propiciar baixa produção e perdas de produto, ainda contaminava o mesmo com graxa oriunda dos rolamentos da conexão da parte fixa e móvel do equipamento, inviabilizando a realização de testes de análise sensorial e comprometendo índices como os de eficiência térmica.

SECAGEM COM ALIMENTAÇÃO INTERMITENTE DE MELAÇO - SECADOR EM ESCALA AMPLIADA

Um SRRI, em escala ampliada (diâmetro de 25 cm e comprimento de 65 cm), foi projetado com o objetivo de se eliminarem os problemas verificados nos ensaios de secagem com o modelo em escala reduzida e de se determinarem as melhores alternativas operacionais para quantificar a capacidade máxima de processamento do melaço de cana. As principais inovações realizadas nesta nova unidade foram: a) utilização de dois conjuntos com anéis duplos de politetrafluoretileno ("Teflon") nas extremidades do SRRI, com a função de permitir a rotação do SRRI, acoplando a parte móvel à fixa da instalação, evitando fugas do ar de secagem. Um dos anéis foi fixado ao cilindro rotatório e o outro na seção fixa da instalação. Na operação do SRRI a face de um anel desliza sobre a face estacionária do outro, promovendo assim a vedação; b) instalação de dois conjuntos de aletas (com 10 cm de altura) nas paredes internas do SRRI defasados de 30°. Cada conjunto foi constituído por seis aletas estando uma delas ligeiramente inclinada em relação à horizontal para promover o escoamento dos inertes do leito na direção longitudinal; c) utilização de esferas de aço inoxidável, exercendo a função de inertes do SRRI.

As condições de operação foram as seguintes: a) ar de secagem, temperatura de 80°C e velocidade de 1,9 m/s (5,1 kg/min) referida à seção transversal do secador; b) melaço, conteúdo de umidade 0,33 kg H_2O/kg de melaço seco; c) rotação do cilindro, 24 rpm.

Alimentação por um Período de Tempo Fixo. Os ensaios de secagem foram realizados mantendo-se uma alimentação contínua de melaço por 20 a 30 minutos, em ciclos de operação do secador de 60 minutos, à temperatura de 80°C para facilitar o escoamento do mesmo pela bomba peristáltica.

As taxas de alimentação de melaço foram: 180 g/h (alimentação por 20 minutos), 240 g/h (30 minutos) e 300 g/h (30 minutos).

A carga de inertes era de 32 kg, sendo o diâmetro médio das esferas de 1,7 cm.

Os resultados dos ensaios são mostrados na Fig.2, onde a ordenada representa a produção de melaço desidratado (umidade de 5%, bu) e a abscissa o tempo de secagem. Convem ressaltar que no SRRI em escala ampliada, uma fração grossa (correspondendo a 14% de produto desidratado) era coletada entre a saída do secador e o ciclone. Além disso, observou-se a ocorrência de perdas de produto desidratado (fração muito fina, correspondendo a cerca de 17% da produção) na saída de ar do ciclone.

Para a operação à taxa de alimentação de 300 g/h, verificou-se, depois de 7 horas de secagem, a existência de um excessivo acúmulo de melaço úmido na região

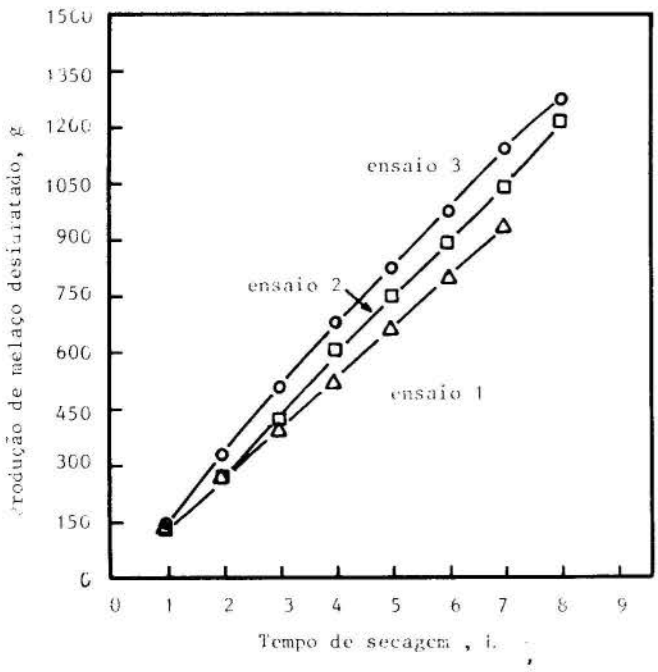

Fig. 2 Produção de melaço em pó (com alimentação por um período de tempo fixo) em função do tempo de secagem. Condições de operação: velocidade e temperatura do ar, 1,9 m/s e 80°C; conteúdo inicial de umidade , temperatura e taxas de alimentação do melaço, 0,33 kg H_2O/kg de melaço seco, 80°C e 180 g/h (ensaio 1), 240 g/h (ensaio 2), 300 g/h (ensaio 3); rotação do SRII , 24 rpm.

do leito próxima à tubulação de alimentação de melaço. Isto indicou que a capacidade do secador havia sido ultrapassada e, caso a operação continuasse, deveria ocorrer inundação do secador com a matéria prima. A análise da Fig. 2 (ensaio 3) mostra que isto já começava a se delinear nas duas últimas horas de secagem, onde o coeficiente angular da curva apresenta uma ligeira redução, correspondendo a um decréscimo na produção devido ao acúmulo de melaço no leito de secagem.

No ensaio 1 as inspeções no leito, entre ciclos sucessivos, mostraram a ausência de melaço sobre as esferas. Isto indicou que a capacidade do SRRI não tinha sido atingida.

Quando a alimentação foi de 240 g/h (ensaio 2) , ao final de cada ciclo, pouco melaço desidratado permanecia sobre as esferas. Apenas nas proximidades do local de alimentação havia um pouco de melaço úmido. Isto sugeriu que, caso a taxa de alimentação fosse aumentada, o comportamento do SRRI tenderia ao referido no ensaio 3. Portanto, uma taxa de alimentação de 240 g/h corresponde à capacidade do SRRI, que foi de 153 g/h.

Convem ressaltar que a produção de melaço em pó variava no decorrer de cada ciclo de secagem, e que durante a alimentação do melaço este retardava a geração e o desprendimento do material desidratado, caracterizando assim um tempo morto de produção. Isto induziu a expectativa de que a adição de melaço, de uma só vez, em toda a extensão do secador, reduziria o tempo de alimentação e, portanto, o tempo morto de produção, aumentando, consequentemente, a capacidade do SRRI.

Alimentação em Cargas. A carga de inertes foi aumentada para 54kg(o diâmetro médio das esferas passou para 1,9cm devido à adição de esferas maiores à carga anterior), ocupando metade do volume do secador, para possibilitar uma maior área de exposiçao do filme de melaço ao ar de secagem. Apesar deste parâmetro ser suscetível à otimização, no presente trabalho a carga citada foi considerada como sendo a de operação.

Para estudar o efeito, sobre a capacidade do secador, da alimentação do melaço de cana em toda a sua extensão longitudinal, a distribuição da matéria prima sobre os inertes foi efetuada através de duas janelas centrais de inspeção dispostas na carcaça do secador. Como não se realizou o bombeamento do melaço, o efeito da viscosidade deixou de ser relevante, possibilitando que o mesmo fosse alimentado à temperatura ambiente.

Depois de ser efetuada a alimentação, o soprador, o motor do SRRI e o sistema de aquecimento eram acionados e, após algumas rotações do SRRI, toda a massa de inertes ficava revestida por um filme de melaço. Isto possibilitava um bom contato do mesmo com o ar de secagem. Após 60 min de operação uma nova carga era adicionada no secador e repetia-se o ciclo.

Realizaram-se ensaios de secagem com cargas de melaço de 480, 550 e 593 g/h. Nos ensaios relativos às cargas de 480 e 550 g/h inspeções realizadas no interior do secador, ao final dos ciclos, mostraram que o mesmo encontrava-se limpo, sem acúmulo de material sobre as esferas, aletas e paredes do SRRI, o que indicava que a capacidade do secador não havia sido alcançada.

Os resultados experimentais do ensaio relativo à carga de 593 g/h são indicados na Fig. 3, onde cada curva refere-se a um ciclo de 60 minutos de operação. As curvas representativas dos ciclos de 1 a 4 indicam que a produção horária média de pó manteve-se constante, em torno de 340 g/h (fração fina coletada pelo ciclone com umidade de cerca de 5%, b.u.). Computando-se a parcela grossa coletada no sedimentador, a produção total de pó é de 397 g/h, não se considerando as perdas no ciclone, que foram de aproximadamente 17%.

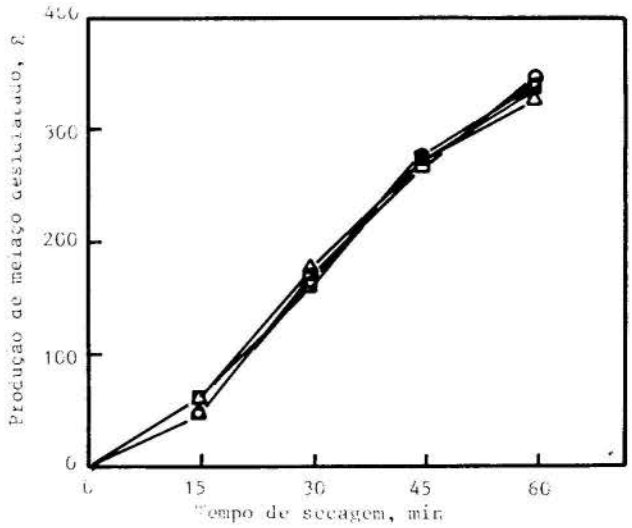

Fig. 3 Secagem de melaço em cargas, em função do tempo de secagem. Condições de operação: velocidade e temperatura do ar, 1,9 m/s e 80°C; conteúdo inicial de umidade, temperatura e taxa mássica de alimentação do melaço, 0,33 kg H_2O/kg de melaço seco, ambiente e 593 g/h ; rotação de SRRI , 24 rpm.

As inspeções realizadas no interior do secador , no final de cada ciclo, para o ensaio relativo à carga de 593 g/h, indicaram a existência de material úmido sobre algumas esferas. Para garantir uma produção constante de melaço desidratado, sem tendência à inundação do SRRI, ao operá-lo por um período prolongado, a carga de 593 g/h foi considerada como sendo a máxima de operação.

Comparando-se esta capacidade (593 g/h) com a quantificada na seção anterior (240 g/h) verificava-se um acréscimo de 147% na capacidade do SRRI. Como o aumento da carga de inertes foi de apenas 69%, desprezando-se outros efeitos, conclui-se que a influência da alimentação do melaço ao longo do corpo do secador possibilitou um aumento de produção, confirmando, assim, a hipótese indicada anteriormente.

CONCLUSÕES

O secador rotatório com recheio de inertes(SRRI) é adequado à secagem de melaço de cana-de-açúcar por possibilitar o contato permanente de um filme renovável de material úmido com o ar de secagem, produzindo melaço em pó em uma única etapa de processamento (com secagem e moagem simultâneas).

A alimentação do melaço no SRRI por cargas ao longo do secador possibilitou uma maior produção de pó do que na operação com alimentação intermitente na entrada do secador.

A capacidade máxima do SRRI foi quantificada em 593 g/h de melaço de cana-de-açúcar alimentado no secador à temperatura ambiente.

REFERÊNCIAS

[1] Van Arsdel, W.B., "Food Dehydratation" , AVI Publishing, Westport, USA,1963.

[2] Mrowiec, M., Ciesielczyk, W., "Fluidized - Bed Dryers for Paste Materials", International Chemical Engineering, Vol. 17, N. 2, pp. 373-379, New York, USA, 1977.

[3] Phan, O.T., "Behaviours of a Conical Spouted - Bed Dryer for Animal Blood", The Canadian Journal of Chemical Engineering, Vol. 61, N. 3, pp. 426-434 , Ottawa, Canadá, 1983.

[4] Ré, M.I., Freire, J.T.,"Secagem de sangue Animal em Leito de Jorro", Anais do XIV Encontro sobre Escoamento em Meios Porosos , pp. 187-198, Campinas, Brasil, 1986.

[5] Hufenuesser, M., Kachan, G.C., "Estudo da Viabilidade de Desidratação de Purê de Banana em Secador Tipo Jorro", Ciência e Tecnologia de Alimentos , Vol. 6, N.1, pp. 31-41, Campinas, Brasil, 1986.

[6] Novy, M.G. e Kieckbusch, T.G., "Secagem de Alimentos líquidos em leito vibro-fluidizado contendo inertes: Estudos Preliminares", Anais do XV Encontro sobre Escoamento em Meios Porosos, pp. 430 - 440, Uberlândia, Brasil, 1987.

[7] Burjaili, M.M., Limaverde, J.R., Finzer , J.R.D., "Secador Rotatório com Recheio de Inertes: I- Desempenho Preliminar do Equipamento", XV Encontro sobre Escoamento em Meios Porosos, pp. 493-499 , Uberlândia, Brasil, 1987.

[8] Hugot, E., "Manual da Engenharia Açucareira", Vol. I, Editora Mestre Jou, São Paulo, Brasil, 1977.

SUMMARY

A tray drayer was utilized to study sugar cane molasses drying. The results showed that the drying time could be reduced by the utilization of a procedure which could eliminate, continuously, the case hardening formed over the surface of the material. Based on that principle two laboratory rotatory dryers, filled with inert bed were utilized: the first one (small) showed qualitatively the drying efficiency, and the second one (large) showed quantitatively the drying capacity.

III ENCIT – Itapema, SC (Dezembro 1990)

CURVAS CARACTERÍSTICAS DE SECAGEM PARA LEITOS VIBRO-JORRADOS COM AQUECIMENTO DIRETO E INDIRETO

JOSÉ ROBERTO DELALIBERA FINZER[1] E THEO GUENTER KIECKBUSCH[2]
[1]UNICAMP/DEA-Departamento de Engenharia Química/UFU
Campus Santa Mônica-38400-Uberlândia, MG - Brasil
[2]UNICAMP - Departamento de Engenharia de Alimentos
Cidade Universitária - 13081 - Campinas,SP - Brasil

RESUMO

Um secador de leito vibro-jorrado foi ensaiado com dois sistemas de aquecimento: 1) direto, usando cubos de batata e 2) indireto , com um leito de grãos de soja. As curvas características de Fornell foram ajustadas aos dados de secagem operando em secador de leito estático e vibro-jorrado. Inspirado na técnica usada por Fornell, obtém-se uma curva característica de secagem para grãos de soja, operando em leito vibro-jorrado com aquecimento indireto. Estes modelos correlacionaram com sucesso os resultados da secagem da batata e da soja.

INTRODUÇÃO

O secador de leito vibro-jorrado, (LVJ), é um equipamento que submete um leito de partículas a uma vibração mecânica, que induz os sólidos a um movimento ascendente por um tubo central, semelhante a um leito de jorro convencional. Entretanto o movimento dos sólidos se processa com velocidade do ar de secagem inferior à velocidade mínima de jorro. Quando os sólidos apresentam elasticidade reduzida, o movimento no LVJ é mais intenso ao operar sem o tubo interno. Nos trabalhos que antecederam o atual, mostrou-se que existe uma frequência de vibração ótima, associada a uma condição de ressonância, na qual a circulação das partículas no leito é máxima [1], avaliou-se a uniformidade de temperatura e umidade do leito, na secagem de cubos de batata [2] e verificou-se a economia de energia na secagem de grãos de soja em LVJ comparado com a operação em leito estático [3].

A Fig. 1, denota o comportamento do LVJ, formado por esferas de sagú, em função da velocidade do ar [4], e dois regimes de escoamento de sólidos são observados. O regime de escoamento I, em fase densa é típico de baixas velocidades do ar de secagem. O regime II , em fase diluída, é associado a velocidades do ar inferiores à mínima de jorro (U_{mj}). Operando-se com velocidades do ar compreendidas entre esses intervalos não ocorre escoamento dos sólidos.

CURVAS CARACTERÍSTICAS DE SECAGEM - MODELO DE FORNELL

Estudando curvas de secagem obtidas com diferentes condições de ar de secagem, Van Meel, em 1958, observou que dividindo-se n (taxa de evaporação da água em kg H_2O/kg ss.h) por n_1 (taxa de evaporação no período de taxa constante),obtinha-se uma função única do conteúdo de umidade, mais precisamente:

$$\frac{n}{n_1} = n/\left[\frac{A}{W}\frac{h}{\Delta H_v}(T_\infty - T_{bu})\right] = f'(X^0) \qquad (1)$$

onde: $X^0 = (X - X_{eq})/(X_o - X_{eq})$; sendo X o conteúdo de umidade médio do sólido, kg H_2O/kg de sólido seco ; X_o é a umidade inicial e X_{eq} a de equilíbrio; A/W é a área de secagem específica (m^2/kg ss); h o coeficiente convectivo de transferência de calor; ΔH_v é o calor latente de vaporização da água livre; T_∞ e T_{bu}, são as temperaturas do ar de secagem, de alimentação e de bulbo úmido. No período de taxa constante, esta última é a temperatura do sólido.

Usando-se esta modelagem, diversas curvas de taxas de secagem (n) em função da umidade adimensional dos sólidos (X^0), transformam-se em uma única curva característica de secagem.

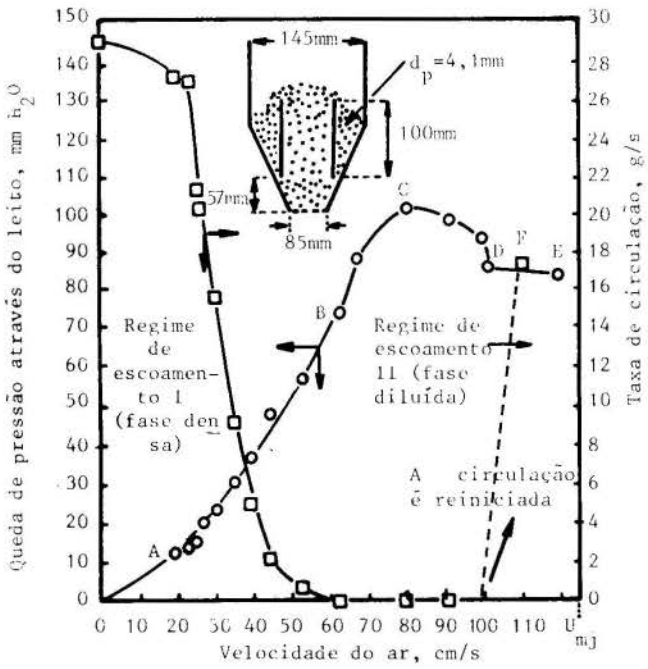

Fig. 1 Queda de pressão no leito e taxa de circulação de esferas de sagú de 4,1 mm de diâmetro. Condições de vibração: amplitude = 4 mm e frequência = 11,8 Hz.

A Eq. (1) apresenta uso limitado na secagem de materiais biológicos, pois com eles o primeiro período de secagem geralmente não é observado. Para contornar essa situação, Fornell [5], definiu uma taxa fictícia de secagem para materiais biológicos, no primeiro período de secagem e manteve ΔH_v constante durante o primeiro período fictício de secagem.

Complementando o modelo Loncin [6], demonstrou , que a razão, $h/\Delta H_v$ é proporcional a raiz quadrada da velocidade do ar de secagem, para corpos em forma de lâminas.

O modelo final é expresso pela Eq. (2):

$$\frac{n}{(T_\infty - T_{bu})v^{0,5}} = K\frac{A}{W}f'(X) = f(X) \qquad (2)$$

Fornell [5], observou uma boa superposição das curvas de taxa de secagem, usando o modelo expresso pela Eq. (2), para cubos de maçã, cenoura, batata e beterraba, em camadas delgadas dispostas sobre uma bandeja.

Entre outros métodos generalizados, o de Brunello foi aplicado com êxito em alimentos contendo uma película protetora [7]. O método de Fornell, entretanto, é mais geral.

APLICABILIDADE DO MODELO DE FORNELL

Na secagem da maioria dos vegetais, ricos em água, ocorrem contrações e deformações que são independentes das condições do ar de secagem (temperatura e velocidade) e geralmente são diretamente proporcionais ao conteúdo de água [2]. Isto faz com que estes fenômenos sejam englobados pelo modelo de Fornell, através da função f(X), da Eq. (2).

No modelo de Fornell, expresso pela Eq. (2), a temperatura do ar T_∞ é constante para uma câmara delgada, mas a temperatura dos sólidos, T_s, é maior do que T_{bu}, nos períodos de taxa de secagem decrescente. Portanto a parcela de diferença de temperatura é melhor representada por $(T_\infty - T_s) = (T_\infty - g'(X).T_{bu})$, pois a temperatura dos sólidos depende do conteúdo de umidade. Entretanto, representando a diferença de temperatura pela Eq. (3).

$$(T_\infty - g'(X) \cdot T_{bu}) = g(X).[T_\infty - T_{bu}] \qquad (3)$$

e explicitando a função g(X), tem-se:

$$g(X) = \left[\frac{T_\infty}{T_\infty - T_{bu}} - g'(X)\,\frac{T_{bu}}{T_\infty - T_{bu}}\right] \qquad (4)$$

Para um intervalo de temperatura do ar de secagem, com condições psicrométricas usuais em secagem de vegetais ricos em água, pode-se calcular as razões $T_\infty/(T_\infty - T_{bu})$; $T_{bu}/(T_\infty - T_{bu})$, para cada condição de secagem, assim como as médias destas razões.

Usando o segundo membro da Eq. (3) com g(X) estimado à partir das médias das razões de temperatura e admitindo um aumento considerável da temperatura do sólido, relativo a T_{bu}, o erro cometido não é significativo. Isto explica a aplicabilidade do modelo de Fornell, nas situações em que os sólidos apresentam comportamento higroscópico no início da secagem, uma vez que g(X) fica incluído em f(X) da Eq. (2).

Em sistemas nos quais a temperatura do ar varia ao longo do secador (camadas espessas), a análise é mais complicada. Por simplificação vamos assumir uma carga de sólidos constante e que a vazão de ar de operação seja alta, para que não ocorra saturação do ar na saída. No período fictício da secagem constante a taxa será dada por uma parcela da Eq. (2) adaptada:

$$n_1 = \frac{A}{W}\, Kv^{0,5}\, "\Delta T" \qquad (5)$$

onde "ΔT" representa uma média das diferenças de temperaturas entre o ar e o sólido ao longo do leito.

Quando o conteúdo de umidade dos sólidos for alto, a temperatura das partículas se aproximará de T_{bu}, enquanto a temperatura do ar reduzirá exponencialmente ao longo do leito. O "ΔT" será a média logarítmica das diferenças de temperaturas na entrada e na saída do ar.

Quando a secagem for dificultada pela resistência interna à transferência de massa, a temperatura média dos sólidos no leito se elevará, enquanto a variação de temperatura do ar no leito será menos pronunciada do que no período descrito acima. Isto faz com que ocorra diminuição na média logarítmica das diferenças de temperaturas. Para uma mesma vazão de ar é provável que "ΔT" seja uma função do conteúdo de umidade médio do leito, X.

O efeito da vazão do ar é mais complicado, pois ela também altera a variação de temperatura do ar ao longo do leito e portanto, indiretamente, o potencial para transferência de calor e massa. A forma da função da velocidade deve ser ainda caracterizada pela aplicação dos modelos físico-matemáticos mas em princípio, por simplificação, este trabalho mantém o expoente 0,5 da velocidade do ar.

Estas considerações mostram que o parâmetro mais influenciado pela operação em camada espessa é "ΔT".

Se a média logarítmica das diferenças de temperaturas entre o ar e o leito, pudesse ser expressa, com uma aproximação, pelo produto de uma função de X multiplicada por $(T_\infty - T_{bu})$, para uma carga constante de sólidos, como na análise da camada delgada anterior, a Eq. (2) poderia ser usada para obter curvas generalizadas de secagem de leitos profundos, pois a função de X estaria incluída no segundo membro da equação. O presente trabalho procura demonstrar experimentalmente esta hipótese, usando resultados de secagem em camada espessa, operando em LE e LVJ.

SECAGEM EM LEITO ESTÁTICO E VIBRO-JORRADO - AQUECIMENTO DIRETO

Para testar a aplicabilidade do modelo de Fornell, para leitos espessos, foram realizados ensaios de secagem de cubos de batata com arestas iniciais de 10 mm, operando em LE e LVJ (regime de escoamento II). O secador de LE era constituído por um tubo de "plexiglass" com 145 mm de diâmetro, o mesmo da seção cilíndrica do secador de LVJ.

A carga do leito era 30,3 kg/m^2 e seu conteúdo de umidade inicial era 5,3 kg H_2O/kg ss, e as umidades de equilíbrio foram obtidas de Krischer [8]. Inicialmente verificou-se o efeito de diferentes temperaturas do ar, que foram fixadas em 50, 60 e 70°C (T_{bu} = 23,2; 25,7 e 28,0, respectivamente). A vazão mássica do ar era 1,3 kg/min, o que correspondeu as velocidades de 1,30; 1,34 e 1,38 m/s, referidas à seção transversal da região cilíndrica do secador. Os resultados dos ensaios de secagem são mostrados na Fig. 2. No caso de secagem em LVJ, as condições de vibração eram, amplitude 4 mm e frequência 12,5 - 13.0 Hz. O método experimental e medidores utilizados(com suas precisões) são denotados em Finzer [4].

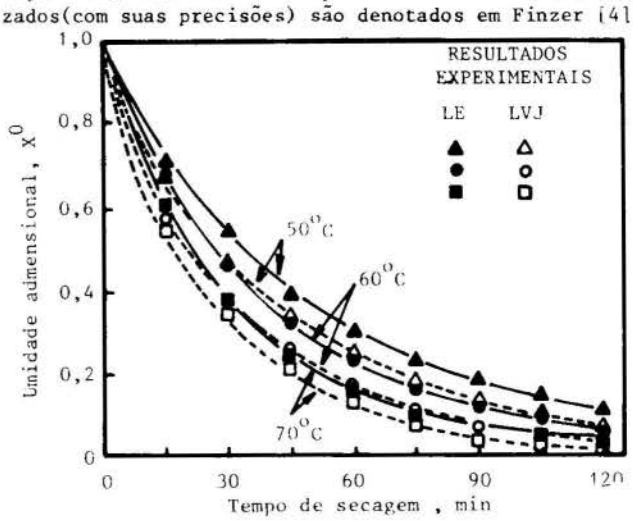

Fig. 2 Curvas de secagem de cubos de batata de 10 mm de aresta. Condições de operação: vazão de ar = 1,3 kg/min; carga = 30,3 kg/min; X_o = 5,3 kg H_2O/kg bs; amplitude e frequência de vibração, 4 mm e 12 a 14 Hz. As linhas contínuas e tracejadas são simuladas.

Os resultados da aplicação do modelo em estudo são mostrados na Fig. 3. A curva que representa a operação em LVJ se situa acima da curva da operação em LE. Este comportamento mostra o efeito da operação em LVJ, que promove o movimento permanente dos cubos de batata no leito, eliminando a aderência entre partículas e partículas-parede, expondo a totalidade da superfície das partículas ao ar de secagem.

Os pontos experimentais da Figura 3 foram correlacionados por equações, que integradas tornam a resgatar relações de X como função do tempo. Substituindo os parâmetros, observou-se um excelente ajuste com pontos experimentais, como se pode observar para a secagem de cubos de 10 mm de aresta , locadas na Figura 2.

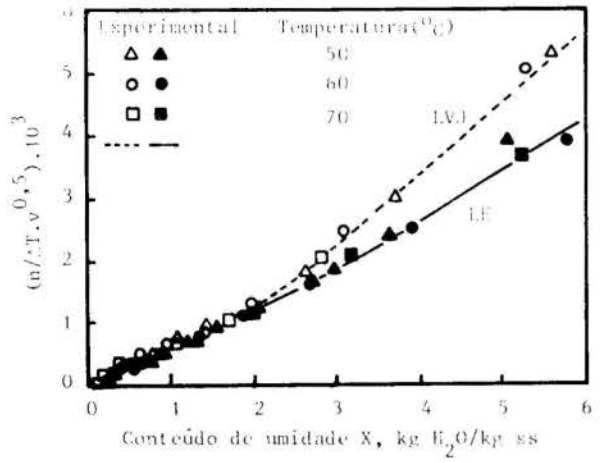

Fig. 3 Curvas generalizadas de secagem de cubos de batata com aresta inicial de 10 mm; n(kg H_2O/kg batata seca.min), $\Delta T(^oC)$, v(m/s). Condições de operação: vazão de ar = 1,30 kg/min; carga = 30,3 kg/m²; amplitude e frequência de vibração, 4 mm e 12 a 14 Hz.

SECAGEM EM LVJ, AQUECIMENTO INDIRETO

Na presente pesquisa, uma sequência natural no desenvolvimento do secador de LVJ, foi adaptá-lo para trabalhar com aquecimento indireto. Para tanto utilizou-se grãos de soja e o aquecimento foi realizado por meio de uma resistência elétrica envolta no tubo central ("draft tube") do secador [4].

Os resultados de ensaios de secagem são indicados na Fig. 4 pelos símbolos geométricos, onde também são denotadas as condições de operação, que correspondem ao regime de escoamento I (em fase densa).

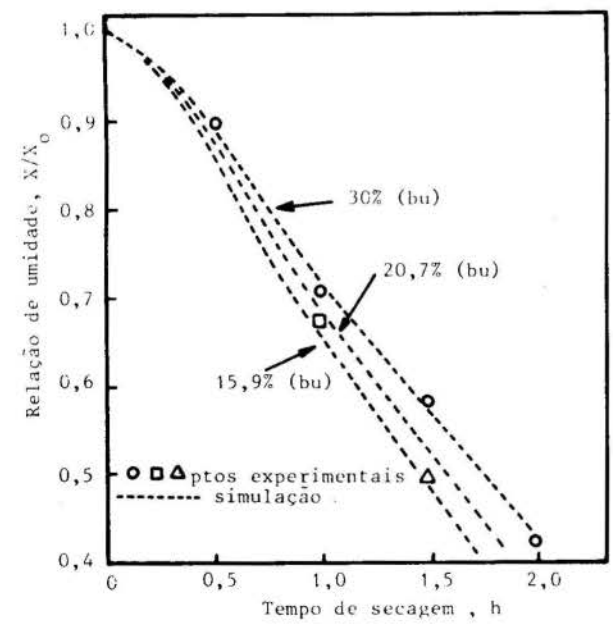

Fig. 4 Simulação de curvas de secagem em LVJ, com aquecimento indireto do leito, para conteúdos de umidade iniciais dos grãos de soja: 30,0; 20.7 e 15,9% (bu) , carga inicial de sólidos no leito = 182 kg/m², Tar = ambiente, v_{ar} = 15 cm/s, A = 4 mm, f = 12 a 17 Hz, potência fornecida ao leito = 266 watts.

TRANSFERÊNCIA DE CALOR POR CONDUÇÃO

Quando partículas de um material úmido são colocadas em um recipiente que recebe energia de um aquecedor submerso no leito, a taxa de secagem é dada pela Eq. (6), adaptada [9].

$$R_m = \frac{(X_o - X)\, W_s}{A_h\, t} = \frac{(h_{ef})_m\, (T_h - T_s)_m}{\Delta H_m} \qquad (6)$$

onde: R_m é a taxa de secagem global média, kg H_2O/m^2 s, de todo o intervalo de secagem, ou seja, do conteúdo de umidade X_o até X; W_s é a massa de sólidos secos, kg ; $(h_{ef})_m$ é o coeficiente efetivo médio de transferência de calor, $W/m^2.K$. Este coeficiente é um valor médio para a secagem dos sólidos de X_o até X. Variando o intervalo de conteúdo de umidade, $(h_{ef})_m$ também varia, pois este coeficiente é muito dependente das condições do sólido; $(Th - Ts)_m$ é uma média das diferenças de temperatura para todo o leito durante a secagem (K); ΔH_m é a variação de entalpia específica requerida para evaporar a água, J/kg.

Esta equação relaciona corretamente o tempo total necessário para se secar o produto de X_o até X. Sua utilização na forma como está, entretanto, é limitada, pois $(h_{ef})_m$ e $(Th - Ts)_m$ devem ser conhecidos ("a priori") para cada situação.

SIMULAÇÃO DA CINÉTICA DE SECAGEM EM LVJ

Na análise a seguir, verifica-se a possibilidade de expressar os parâmetros de operação, $(h_{ef})_m$, $(Th - Ts)_m$ e ΔH_m, contidos na Eq. 6, em função do conteúdo de umidade dos sólidos e conseguir uma equação característica de secagem para grãos de soja em LVJ, inspirado na técnica usada por Fornell.

A diferença de temperatura $(Th - Ts)_m$ em secadores que contém o tubo interno é função da geração de calor Q e da temperatura média dos grãos de soja. Esta última, em uma posição do leito, depende do conteúdo de umidade médio dos sólidos, que pode ser expresso pelo adimensional (X/X_o).

Por outro lado, a taxa de circulação dos grãos de soja no LVJ, em um dado instante, depende do conteúdo de umidade inicial dos mesmos, e isto afeta diretamente a temperatura do leito nas imediações do aquecedor e também o coeficiente efetivo médio de transferência de calor.

Portanto, para a instalação ensaiada, a diferença de temperatura é bem representada pela Eq. (7).

$$(T_h - T_s)_m = f(Q)\; g(X/X_o)\; h(X_o) \qquad (7)$$

onde as funções: $f(Q)$, $g(X/X_o)$ e $h(X_o)$, representam os efeitos: da transferência de calor para o leito, do conteúdo de umidade médio e inicial dos grãos de soja.

Substituindo a Eq. (7) na Eq. (6) vem:

$$\frac{(X_o - X)\, W_s}{A_h\, t} = \frac{(h_{ef})_m\, f(Q)\; g(X/X_o)\; h(X_o)}{\Delta H_m} \qquad (8)$$

Como $(h_{ef})_m$ depende principalmente do conteúdo de umidade inicial e final dos sólidos no leito , podemos quantificá-lo pela Eq. (9).

$$(h_{ef})_m = g'(X/X_o).\; h'(X_o) \qquad (9)$$

O mesmo raciocínio se aplica a entalpia de evaporação da água:

$$\Delta H_m = g''(X/X_o)\; .\; h''(X_o) \qquad (10)$$

Substituindo as Eq. (9) e (10) na Eq. (8) e englobando as funções dos conteúdos de umidade tem-se:

$$\frac{(X_o - X)\, W_s}{A_h\, t} = f(Q)\; G'(X/X_o)\; H(X_o) \qquad (11)$$

Considerando constante a transferência de calor em um equipamento com dimensões fixas, pode-se representar $f(Q)$ e A_h por K, de onde:

$$\frac{(X_o - X)\, W_s}{t\, H(X_o)} = K\; G'(X/X_o) = G(X/X_o) \qquad (12)$$

Para um mesmo (X/X_o), independente da umidade inicial do sólido, ter-se-á valores idênticos para o grupamento expresso pelo primeiro membro da Eq. (12). A equação indica que existe uma função $H(X_o)$, que agrupa os pontos experimentais, expressos pelo primeiro membro da equação, entorno de uma única curva. A forma da função $H(X_o)$ deve ser pesquisada para situações específicas. Por simplificação foi experimentada uma função de potência, ou seja:

$$H(X_o) = X_o^{\,n} \qquad (13)$$

onde: n é um parâmetro de ajuste que deve satisfazer a Eq. (12). Substituindo $H(X_o)$ nesta equação, tem-se:

$$\left[\frac{X_o - X}{t}\right] \cdot \frac{W_s}{X_o^{\,n}} = G(X/X_o) \qquad (14)$$

Esta equação é dimensional, nos cálculos realizados W_s foi expresso em gramas e t em minutos.

O valor de n que melhor agrupou os resultados experimentais da Fig. 4 foi 0,55. Os resultados são indicados na Fig. 5.

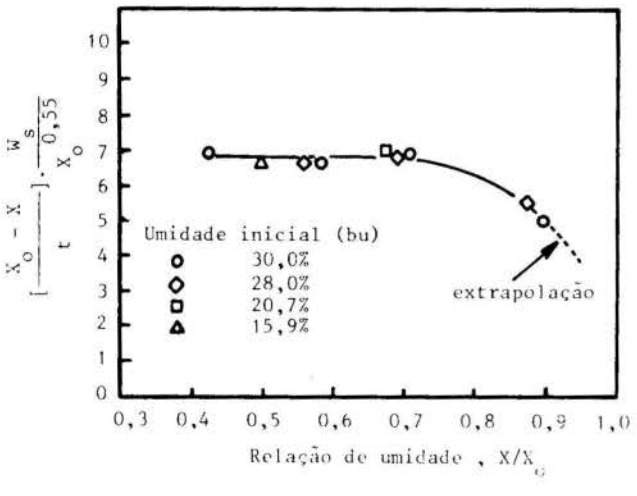

Fig. 5 Curva característica de secagem de grãos de soja em LVJ, com aquecimento indireto do leito. Condições de operação: T_{ar} = ambiente; v_{ar} = 15 cm/s; A = 4 mm; f = 12 a 17 Hz; potência = 266 watts; carga = 170 a 182 kg/m²; umidade média inicial dos sólidos de 15,9 a 30% (bu).

A Fig. 5 confirma a tendência de agrupamento dos pontos experimentais em torno de uma única curva característica de secagem. O maior número de pontos experimentais concentra-se em um trecho de curva no qual o coeficiente angular é igual a zero. Apenas os pontos experimentais associados ao período inicial de indução, se afastam do valor de 6,81, média aritmética dos demais. Neste período inicial, parte do calor dissipado é utilizado para aquecer os sólidos, o próprio tubo aquecedor central e o vaso de secagem.

Utilizando a curva característica de secagem em LVJ, Fig. 5, foram simuladas as curvas de secagem para as seguintes umidades iniciais médias dos grãos de soja: 30,0; 20,7 e 15,9 (bu). Os resultados são locados na Fig. 4. Na mesma figura são indicados os pontos experimentais, relativos as mesmas umidades iniciais dos grãos de soja das curvas simuladas.

A Fig. 4 indica que o uso da curva característica de secagem possibilita a reprodução dos pontos experimentais como um desvio inferior a 3%. Admitido um desvio desta ordem de grandeza, o modelo proposto se mostra eficiente na simulação de curvas de secagem em LVJ, partindo-se de alimentações com conteúdos de umidade diferentes e operando com aquecimento indireto do leito, desde que os parâmetros geométricos e operacionais sejam mantidos constantes.

CONCLUSÕES

A simulação de curvas de secagem, para leitos espessos de cubos de batata em LE e LVJ, ao invés de camadas delgadas conforme proposição original do modelo de Fornell, denotou um bom ajuste aos pontos experimentais ao variar a temperatura do ar de secagem.

O modelo desenvolvido, para a operação em LVJ com aquecimento indireto do leito de secagem, conduziu a uma única curva característica de secagem de grãos de soja. A curva característica pode ser utilizada para simular a cinética de secagem de grãos de soja com conteúdos iniciais de umidade no intervalo de 16 a 30% (bu).

REFERÊNCIAS

[1] Finzer, J.R.D. e Kieckbusch, T.G., "Desenvolvimento de um Secador de Leito Vibro-Jorrado. I- Estudo da dinâmica do leito", Anais do XIV Encontro sobre Escoamento em Meios Porosos, p. 314-352, Campinas, Brasil, 1986.

[2] Finzer, J.R.D. e Kieckbusch, T.G., "Desenvolvimento de um Secador de Leito Vibro-Jorrado. II- Cinética de secagem de cubos de batata", Anais do XV Encontro sobre Escoamento em Meios Porosos, V. II, p. 416-429, Uberlândia, Brasil, 1987.

[3] Finzer, J.R.D. e Kieckbusch, T.G., "Secagem de grãos de Soja em Leito Vibro-Jorrado com Aquecimento Indireto", Anais do XVII Encontro sobre Escoamento em Meios Porosos, em impressão, São Carlos, Brasil, 1989.

[4] Finzer, J.R.D., "Desenvolvimento de um Secador de Leito Vibro-Jorrado", Tese de Doutorado, UNICAMP, Campinas, Brasil, 1989.

[5] Fornell, A.; Bimbenet, J.J. and Almin, Y. "Experimental Study and Modelization for air Drying of Vegetable Products", Lebensmittel - Wissenschaft & Technologie, Vol. 13, pp. 96-100, 1980.

[6] Loncin, M., "Genie Industriel Alimentaire - Aspects Fondamentaux", Masson, Paris, 1976.

[7] Ogihara, L.A. "Determinação de Parâmetros de Secagem de Milho Verde e Ensaios de Aramazenamento", Tese de Mestrado, UNICAMP, Campinas, Brasil, 1989.

[8] Krischer, O. "Die Wissenschaftlichen Grundlagen der Trochnungstechnik", Springer-Verlag, Berlin, 1956.

[9] Nonhebel, G. and Moss, A. "Drying of Solids in the Chemical Industry", Butterworths, London, 1971.

SUMMARY

A vibro-spouted bed dryer was tested with two heating systems: 1) direct heating, using dices of potato and 2) indirect heating, applied to a bed of soya beans. Fornell's characteristic drying curves were fitted to the drying data of potatoes dices in static bed and in vibrated spouted bed dryers. Inspired in Fornell's technique, another characteristic curve was derived for soya beans drying in the vibro-spouted bed with indirect heating. Theses models correlated the drying results for potatoes and soya beans with sucess.

III ENCIT – Itapema, SC (Dezembro 1990)

LEI DA INTERFACE EM ESCOAMENTOS TURBULENTOS E ESTRATIFICADOS DE LÍQUIDO-GÁS

ELOI FERNÁNDEZ Y FERNÁNDEZ
CARLOS VALOIS MACIEL BRAGA

Departamento de Engenharia Mecânica
Pontifícia Universidade Católica do Rio de Janeiro
22.453 - Rio de Janeiro - R.J. - Brasil

RESUMO

A partir de considerações teóricas baseadas nas equações do movimento na vizinhança da interface, obtém-se o campo de velocidade principal e a distribuição da difusividade turbulenta para escoamentos turbulentos e estratificados de líquido-gás. A lei da interface mostra que a tensão cisalhante interfacial exerce uma forte influência na difusividade de momentum na vizinhança da interface. As comparações com resultados experimentais são consideradas excelentes.

INTRODUÇÃO

Os modelos semi-empíricos para a determinação da transferência de calor entre um gás e uma superfície sólida, associados a escoamentos bifásicos (líquido-gás) estratificados, exigem o prévio conhecimento da distribuição da velocidade e da difusividade turbulenta na região da interface líquido-gás. Uma revisão da literatura mostra, de uma forma geral, deficiência de resultados em tal região de escoamentos turbulentos. Isto é devido às dificuldades de caráter experimental de medir-se parâmetros típicos de turbulência em pontos próximos à região da interface. Além da interface mover-se e deformar-se continuamente, qualquer sensor posicionado junto à mesma provoca sérios distúrbios em sua estrutura.

Stephan [1] apresenta diversas inconsistências existentes nos modelos analíticos, pois estes não consideram variações da difusividade turbulenta na região próxima à interface. Tais inconsistências baseiam-se, principalmente, nas propostas de Levich [2] quanto à inexistência de tensão de cisalhamento na interface líquido-gás, ainda que, posteriormente, proponha a utilização de fatores empíricos para a correlação da mesma. Naturalmente, tal procedimento não é adequado quando se visa um equacionamento fundamental do problema físico que ocorre na região de separação entre as fases (líquido-gás).

Por outro lado, Yüksel e Schlünder [3] mostram que para a determinação correta da transferência de calor e massa na interface é necessário levar-se em consideração a variação difusividade turbulenta nesta região.

Nezu e Rodi [4] constataram experimentalmente, em escoamentos através de canais abertos, que a distribuição do campo de velocidades junto à região da interface apresenta um comportamento bem distinto daquele obtido quando se considera um perfil logarítmico de velocidades. Howe et al. [5] analisaram os campos de velocidade e temperatura em ambos os fluidos do escoamento estratificado. A conclusão apresentada pelos autores é que o mecanismo de transferência da quantidade de movimento sofre influência da "rugosidade" da interface. Contrariamente, o mecanismo do qual depende a transferência de calor não é influenciado por tal "rugosidade". Mais recentemente, Rashidi e Banerjee [6], investigaram a estrutura turbulenta em escoamentos horizontais de líquidos sobre uma placa e possuindo uma superfície livre em contato com o ar ambiente. Em [6] foi adotada a técnica de visualização do escoamento através de pequenas bolhas de oxigênio sendo "acompanhadas" por uma câmara de vídeo de alta velocidade. Observa-se que o campo principal de velocidades é bem representado pelo perfil logarítmico. Entretanto, não foi possível analisar-se a região da interface através de tal técnica. Também experimentalmente, Fabre et al. [7] determinaram o perfil de velocidades na direção principal do escoamento, inclusive junto à interface. Os resultados comprovam o desvio do campo de velocidades em relação à lei logarítmica na região de separação das duas fases em escoamentos estratificados, através de um canal de seção retangular. Obviamente, tal fato induz alterações sensíveis na tensão de cisalhamento em tal região em relação aos resultados obtidos com a hipótese do perfil logarítmico.

Mudawwar e El-Masri [8] realizaram recentemente um levantamento dos modelos existentes. Chen [13] analisou a condensação de um filme turbulento utilizando a teoria de comprimento de mistura e, também, o modelo de Levich [2]. Nestes trabalhos é assumido que a difusividade turbulenta varia com o quadrado da distância da interface na região próxima à mesma. Contrariamente, experimentos realizados por Ueda et al [9], analisando a interface gás-líquido em um canal aberto, indicaram que a difusividade turbulenta varia com o cubo da distância da interface. A maior parte destes estudos combinam a equação de Van Driest para difusividade turbulenta com o modelo de Levich [2] para o amortecimento da turbulência na região próxima da interface.

Lam e Banerjee [10] simularam numericamente um escoamento turbulento sobre uma parede sólida, possuindo uma superfície livre na qual não há tensão de cisalhamento. Os resultados de [10] mostram que a lei logarítmica prevalece para a interface. Tal resultado é contrário à argumentação de Levich que prevê a formação de uma sub-camada viscosa junto à interface quando não ocorre tensão de cisalhamento interfacial.

O objetivo do presente trabalho é apresentar o desenvolvimento de um modelo analítico para a distribuição da velocidade média e, também, para a difusividade turbulenta na região próxima da superfície livre de um escoamento turbulento bifásico estratificado(líquido-gás). A análise proposta utiliza as equações de conservação de massa e momentum na obtenção do modelo analítico para a velocidade e a difusividade turbulenta, de forma oposta aos modelos existentes de caráter semi-empírico. Outra consideração relevante adotada no modelo ora proposto é não assumir como nula a tensão de cisalhamento na interface. Os modelos analíticos disponíveis na literatura assumem tal tensão como sendo nula. Assim, através do presente modelo, pode-se obter a influência da tensão de cisalhamento da interface tanto no campo de velocidade na direção principal, quanto na distribuição da difusividade turbulenta, em ambas as fases do escoamento, na região próxima da interface. O presente trabalho, ao contrário de Fernández et al. [14], considera a flutuação de velocidade na interface devido à turbulência do escoamento.

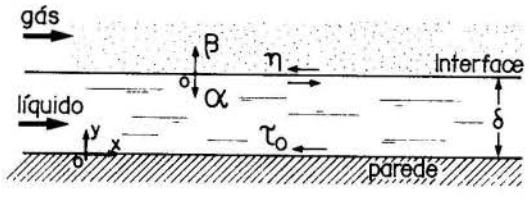

Fig. 1 – Diagrama esquemático do escoamento estratificado líquido-gás

A "lei da interface" proposta é diretamente aplicável na determinação da transferência de calor e massa em escoamentos turbulentos estratificados (líquido/gás).

ANÁLISE TEÓRICA

A Figura 1 apresenta o problema físico, bem como o sistema de coordenadas adotado no presente trabalho.

Equação do Momentum. A equação do momentum (média no tempo) na direção x é [11]

$$U\,U_x + V\,U_y + W U_z + P_x/\rho = \nu[U_{xx} + U_{yy} + U_{zz}] -$$

$$-(\overline{u\,u})_x - (\overline{u\,v})_y - (\overline{u\,w})_z + g\,I \qquad (1)$$

onde U, V e W são as velocidades médias nas direções x, y e z, repectivamente. As flutuações turbulentas da velocidade são expressas, analogamente, por u, v e w. P, ρ e ν representam a pressão, a densidade e a viscosidade cinemática, respectivamente. A aceleração da gravidade é "g" e a inclinação do escoamento (I) é dada por $I = sen\theta$. Ainda referindo-se à equação 1, os índices x, y e z indicam as derivadas em cada uma das respectivas direções.

Considerando-se o escoamento como sendo bi-dimensional, os termos WU_z e U_{zz} são nulos. Conforme sugerido em [11], por simetria, pode-se assumir que o termo $(\overline{uw})_z$ é desprezível. Devido ao fato da equação do momentum ser aplicada junto da interface ou da parede e, levando-se em conta as hipóteses de camada limite, pode-se desprezar, também, os termos U_{xx} e $(\overline{u\,u})_x$. Junto da interface e da parede, a hipótese de escoamento de Couette [11] implica em $U = U(y)$. Assim, a equação (1) reduz-se a

$$V\,U_y + P_x/\rho - g\,I = \nu\,U_{yy} - (\overline{u\,v})_y \qquad (2)$$

De forma semelhante, a equação de conservação do momentum na direção y fornece

$$P_y/\rho = -(\overline{v\,v})_y \qquad (3)$$

As componentes da velocidade, bem como as flutuações u, v e w devem satisfazer a equação da continuidade. Logo,

$$U_x + V_y + W_z = 0 \qquad (4)$$

$$(u)_x + (v)_y + (w)_z = 0 \qquad (5)$$

A análise da equação (4), conjuntamente com a hipótese de Couette, mostra que $V \neq V(y)$.

Na região próxima da parede, assim como junto à interface, as velocidades podem ser expressas através de séries de Taylor:

$$S = \sum S_n\,r^n \qquad (6)$$

onde:

$$S_n = (1/n!)(\partial^n\,S/\partial r^n)_{r=0} \qquad (7)$$

Utilizando-se a condição de não deslizamento na parede tem-se $(u)_w = (v)_w = (w)_w = U_w = 0$. Conclui-se, ainda, através da equação (5), que $(v)_1 = 0$. Assim, a tensão turbulenta junto à parede pode ser dada por:

$$S = u,\,v,\,w,\,U\;or V; \qquad r = y, \alpha\;or\;\beta$$

$$(\overline{u\,v}) = [\overline{(u)_1(v)_2}]y^3 + \{[\overline{(u)_1(v)_3}] + [\overline{(u)_2(v)_2}]\}y^4 + \cdots (8)$$

Tien e Wassan [12], utilizando tal metodologia, obtiveram expressões similares para escoamento turbulento através de canais.

Hipóteses. Por diferentes razões, no passado, modelos de superfícies lisas tem sido empregadas para predizer o transporte de massa, momentum e energia através de filmes líquidos [8]. A hipótese de superfície lisa somente pode ser justificada quando ocorre a presença de ondas longas que prevalecem em certas faixas do escoamento laminar ou turbulento. Na transição entre os regimes de escoamento ondulatório laminar e turbulento, os modelos de turbulência devem levar em conta o comportamento dinâmico das ondas. Neste trabalho será utilizada a hipótese de superfície lisa. A mesma hipótese foi empregada por Lam e Banerjee [10]. Ela é bastante realística para os casos de altos valores de tensão superficial entre as duas fases.

Na interface, é possível utilizar-se duas diferentes hipóteses para a flutuação na velocidade em tal região. As flutuações na direção principal do escoamento (u_i) e na direção transversal (w_i) foram assumidas nulas por Fernandes et al [14]. No presente trabalho a flutuação u_i é admitida como não nula. A velocidade principal na interface é diferente de zero fazendo com que a flutuação local deva possuir um valor finito não nulo. Neste caso a tensão cisalhante interfacial tem um peso importante porque a mesma afeta a intensidade turbulenta na vizinhança da interface. Lam e Barnejee [10] mostraram que essas flutuações são da ordem da velocidade de atrito $u^* = (\tau_o/\rho_l)^{1/2}$. Então, $v_i = w_i = 0$ e $u_i \neq 0$; assumindo ainda que $(u_i)_x = 0$, a equação da continuidade confirma que $v_1 = 0$. A tensão de cisalhamento na vizinhança da interface é

$$(\overline{u\,v}) = [\overline{(u)_0(v)_2}]r^2 + \{[\overline{(u)_0(v)_3}] + [\overline{(u)_1(v)_2}]\}r^3 +$$

$$\{[\overline{(u)_0(v_4)}] + \overline{(u)_1(v)_3}] + [\overline{(u_2)(v_2)}]\}r^4 + \ldots \qquad (9)$$

onde $r = \alpha$ ou β.

A equação do movimento é usada para estabelecer as relações existentes, na região da parede ou da interface, entre a distribuição da velocidade e da tensão de cisalhamento.

Fase Líquida. Na fase líquida, na vizinhança da interface a equação do momentum fica:

$$-V_{il}(U_\ell)_\alpha = -\nu_\ell(U_\ell)_{\alpha\alpha} + (\overline{u\,v})_\alpha + g\,I - P_x/\rho_\ell \qquad (10)$$

onde $\alpha = \delta - y$; U_ℓ é a velocidade principal no líquido e V_{il} é a velocidade transversal na fase líquida, independente de y (na interface). Na interface, as seguintes condições são aplicadas:

$$U_\ell(\alpha = 0) = U_v(\beta = 0) = U_i \qquad (11)$$

$$\tau_i = -\mu_\ell(U_\ell)_1 = \mu_v(U_v)_1 \qquad (12)$$

$$\rho_\ell V_{il} = -\rho_v\,V_{iv} \qquad (13)$$

O gradiente de pressão na fase líquida, que é o mesmo da fase gás, pode ser dado por:

$$(P_v)_x = (P_\ell)_x = -[\tau_i/(2\delta_0)] - \rho_v U_v(U_v)_x \qquad (14)$$

Uma manipulação apropriada das equações (6), (10) a (14), resulta:

$$(\overline{u\,v})_\ell = \{2\nu_\ell U_{2\ell} + \tau_i[(\mu_\ell)^{-1}(V_{il}) - (2\rho_\ell\delta_0)^{-1}] -$$

$$-gI - \rho_v U_v(U_v)_x\}(\alpha) + \{3\nu_\ell U_{3\ell} - V_{il}U_{2l}\}(\alpha)^2 +$$

$$+\{4\nu_\ell U_{4\ell} - V_{il}U_{3\ell}\}(\alpha)^3 + \{5\nu_\ell U_{5\ell} - V_{i\ell}U_{4\ell}\}(\alpha)^4 + \ldots \qquad (15)$$

Uma comparação entre as equações (9) e (15) implica que o coeficiente do primeiro termo do membro direito da equação (15) deve ser nulo. Por este caminho o coeficiente $U_{2\,\ell}$ é determinado.

A velocidade principal, U_ℓ, e a tensão cisalhante turbulenta, $(\overline{u\,v})_\ell$, na vizinhança da interface pode ser expressa em termos das quantidades adimensionais, como:

$$U_\ell^+ = U_i^+ - \tau_i^+\{1 - (\alpha/4\delta_0)\}(\alpha^+)$$

$$+0.5\{g^+I - \tau_i^+V_{i\ell}^+[1 - (\alpha/6\delta_o)] + \rho^+U_v^+(U_v^+)_x\}(\alpha^+)^2 +$$

$$+(U_{3\ell}^+(\alpha^+)^3 + U_{4\ell}^+(\alpha^+)^4 + \ldots \qquad (16)$$

e

$$(\overline{u\,v})_\ell^+ = \{3U_{3\ell}^+ - [(V_{il}^+)/2][g^+I - \tau_i^+(V_{il}^+ - (1/2\delta_0^+))] +$$

$$+\rho^+U_v^+(U_v^+)_x]\}(\alpha^+)^2 + [4U_{4\ell}^+ - V_{il}^+U_{3\ell}^+](\alpha^+)^3 + \ldots \qquad (17)$$

onde

$$\alpha^+ = (\alpha U^*/\nu_\ell) \qquad U^+ = U/U^*$$
$$\beta^+ = (\beta U^*/\nu_\ell) \qquad g^+ = [g\nu_\ell/(U^*)^3]$$
$$V_i^+ = V_i/U^* \qquad \tau_i^+ = \tau_i/\tau_o \qquad (18)$$
$$\rho^+ = \rho_v/\rho_\ell \qquad \mu^+ = \mu_v/\mu_\ell$$
$$\nu^+ = \nu_v/\nu_\ell \qquad (\overline{u\,v})^+ = (\overline{u\,v})/(U^*)^2$$

Neste momento, algumas aproximações podem ser realizadas. Primeiro, os termos $\alpha/4\delta_o$ e $\alpha/6\delta_o$ na equação (16) são pequenos comparados com a unidade e podem ser negligenciados. Segundo, as expressões em série de U^+ podem ser truncadas após o quarto termo da ordem. Ambas hipóteses são legítimas desde que α^+ seja limitada a uma faixa na vizinhança da interface, onde os termos das derivadas de mais alta ordem da velocidade principal são extremamente pequenos. A equação (16) pode, então, ser re-escrita:

$$U_\ell^+ = U_i^+ - \tau_i^+(\alpha^+) +$$
$$+0.5\{g^+ I - \tau_i^+ V_{il}^+ + \rho^+ U_v^+ (U_v^+)_x\}(\alpha^+)^2 +$$
$$+U_{3\ell}^+(\alpha^+)^3 + U_{4\ell}^+(\alpha^+)^4 + \ldots \qquad (19)$$

Fase Gás. Na fase do gás, na vizinhança da interface, a equação do momentum é

$$V_{iv}(U_v)_\beta = \nu_v(U_v)_{\beta\beta} - (\overline{u\,v})_\beta + gI - P_x/\rho_v \qquad (20)$$

onde $\beta = y - \delta$. U_v é a velocidade principal da fase gás e $V_{i\ell}$ é a velocidade transversal na fase gás independente de β. Na interface, as condições das equações (11) a (13) são aplicadas.

Combinando as equações (6), (11) a (14) e (20), obtém-se

$$(\overline{u\,v})_v = \{2\nu_v U_{2v} + \tau_i[(\mu_v)^{-1}(V_{iv}) - (2\rho_v\delta_0)^{-1}] +$$
$$+gI + U_v(U_v)_x\}(\beta) + \{3\nu_v U_{3v} - V_{iv}U_{2v}\}(\beta)^2 +$$
$$\{4\nu_v U_{4v} - V_{iv}U_{3v}\}(\beta)^3 + \{5\nu_v U_{5v} - V_{iv}U_{4v}\}(\beta)^4 + \ldots \qquad (21)$$

Os coeficientes U_{2v} e U_{3v} são determinados de maneira similar à fase líquida. A velocidade principal e a tensão cisilhante turbulenta na vizinhança da interface na fase gás podem ser expressas em termos das quantidades adimensionais, com as mesmas hipóteses da fase líquida.

$$U_v^+ = U_i^+ + [\tau_i^+/\mu^+](\beta^+) -$$
$$-(1/2\nu^+)\{g^+ I - [(\tau_i^+ V_{iv}^+)/\mu^+] + U_v^+(U_v^+)_x\}(\beta^+)^2 +$$
$$+U_{3v}^+(\beta^+)^3 + U_{4v}^+(\beta^+)^4 + \ldots \qquad (22)$$

e

$$(\overline{u\,v})_v^+ = \{3\nu^+ U_{3v}^+ - [(V_{iv}^+)^2/6(\nu^+)^2]|(\tau_i^+/\mu^+)(V_{iv}^+ -$$
$$-\nu^+/2\delta_o^+) - g^+ I - U_v^+(U_v^+)_x|\}(\beta^+)^2 +$$
$$+[4\nu^+ U_{4v}^+ - V_{iv}^+ U_{3v}^+](\beta^+)^3 + \ldots \qquad (23)$$

RESULTADOS PARA CANAIS ABERTOS

Nezu e Rodi [4], como Fabre et al. [7], confirmaram que a região na vizinhança da parede é governada pela viscosidade cinemática, ν, e a velocidade de atrito, U^*. Essas características são normalmente as mesmas daquelas observadas em escoamentos de canais fechados de uma única fase. Na parte afastada da parede, i.e., na região totalmente turbulenta, o perfil logarítmico é aplicável.

Por outro lado, a região na vizinhança da interface é governada pelos mesmos parâmetros da região da parede, mais a tensão cisalhante na interface.

Os perfis de velocidade de logarítmico são normalizados com os parâmetros da parede e representados pelas seguintes equações:

$$[U_\ell^+]_2 = k\,ln(\delta^+ - \alpha^+) + C \qquad (24)$$

$$[U_v^+]_2 = (U^+)_i + k_o\,\ell n(\beta^+) + C_o \qquad (25)$$

$$k_o = k[\tau_i^+/\rho^+]^{1/2} \qquad (26)$$

$$C_o = (\tau_i^+/\rho^+)^{1/2}\{C - k\,ln[\mu^+(\rho^+\tau_i^+)^{1/2}]\} \qquad (27)$$

O subscrito 2 nas eqs. (24) e (25) indicam a região logarítmica. Existem algumas discussões sobre quais os melhores valores para k e C, mas, em geral, tais parâmetros são muito próximos dos valores para escoamentos em tubos. Dados experimentais de Mezu e Rodi [4] foram melhor fitados com $k = 2{,}43$ e $C = 5{,}29$. Gayral et al. [12] encontraram para escoamentos de água-ar as constantes $k = 2{,}5$ e $C = 5{,}5$. Medidas de velocidade também foram realizadas por Ueda et al [9]. Eles encontraram $k = 2{,}5$ e $C = 5{,}75$, o qual é ligeiramente superior a $C = 5{,}5$ para escoamentos com altos números de Reynolds em tubos. Lam e Banerjee [10] obtiveram $C = 5{,}1$ em suas simulações numéricas. No presente trabalho, as constantes foram tomadas como sendo $k = 2{,}5$ e $C = 5{,}75$, para ambas as fases.

Desde que os dados experimentais disponíveis são sem mudança de fase, as comparações são realizadas para escoamento em canal horizontal adiabático com água e ar como fluidos de trabalho.

Com esta hipótese ($V_i = 0$) as equações para velocidade e tensão cisalhante turbulenta, na vizinhança da interface, para ambas as fases, são:

$$[U_\ell^+]_1 = U_i^+ - \tau_i^+(\alpha^+) + [g^+ I/2](\alpha^+)^2 + U_{3\ell}^+(\alpha^+)^3 +$$
$$+U_{4\ell}^+(\alpha^+)^4 + \ldots \qquad (28)$$

$$[(\overline{u\,v})_\ell^+]_1 = 3U_{3\ell}^+(\alpha^+)^2 + 4U_{4\ell}^+(\alpha^+)^3 \qquad (29)$$

$$[U_v^+]_1 = U_i^+ + [\tau_i^+/\mu^+](\beta^+) - (g^+ I/2\nu^+)(\beta^+)^2 +$$
$$+U_{3v}^+(\beta^+)^3 + U_{4v}^+(\beta^+)^4 + \ldots \qquad (30)$$

$$[(\overline{u\,v})_v^+]_1 = 3\nu^+ U_{3v}^+(\beta^+)^2 + 4\nu^+ U_{4v}^+(\beta^+)^3 + \ldots \qquad (31)$$

onde o subscrito 1 nas equações acima indicam a região próxima da interface.

Os perfis na vizinhança da parede são obtidos de forma similar. Neste caso a velocidade principal e a tensão cisalhante turbulenta são

$$U_w^+ = y^+ - (g^+ I/2)(y^+)^2 + U_{4w}^+(y^+)^4 + U_{5w}^+(y^+)^5 \qquad (32)$$

$$(\overline{u\,v})_w^+ = 4U_{4w}^+(y^+)^3 + 5U_{5w}^+(y^+)^4 \qquad (33)$$

onde o subscrito w indica a região na vizinhança da parede.

Para calcular os coeficientes U_{4w}^+ e U_{5w}^+ e o ponto y_t^+ no qual ocorre uma suave e contínua transição para o perfil logarítmico, o valor de U_t^+ e suas primeira e segunda derivadas com relação a y^+ são comparadas com os valores obtidos da equação (24). Para a fase líquida, o ponto de transição α_t e os coeficientes $U_{3\ell}^+$ e $U_{4\ell}^+$ são determinados pelas condições de U_ℓ^+ e as três primeiras derivadas com relação a α coincidirem com o perfil logarítmico. Esse procedimento permite a obtenção do valor de U_i^+ e similarmente, na fase gás β_t, U_{3v}^+ e U_{4v}^+ são encontradas pelas concordâncias de U_v^+ e suas duas primeiras derivadas com o perfil logarítmico.

Se o conceito de auto-similaridade aplica-se às regiões da parede e da interface, então os coeficientes determinados acima são universais. A velocidade principal é uma função única da coordenada transversal.

A Tabela 1 mostra um sumário dos parâmetros principais os quais foram calculados para as regiões da parede e interface. Esses resultados correspondem aos dados experimentais de Fabre et al [7], os quais foram obtidos para um escoamento de água-ar em canal retangular levemente inclinado em relação à posição horizontal. O número de Reynolds do gás é

Tabela 1 – Parâmetros para as leis da interface e parede, $\tau_i^+ = 0.103$ e $g^+ I/2 = 5.46 \times 10^{-4}$.

	U_i^+	α_t^+	$U_{3\ell}^+$	$U_{4\ell}^+$
interface líquido	29,4	267	$-0,14 \times 10^{-5}$	$0,13 \times 10^{-8}$
		β_t^+	U_{3v}^+	U_{4v}^+
interface gás		48	$-0,19 \times 10^{-2}$	$0,19 \times 10^{-4}$
		y_t^+	U_{4w}^+	U_{5w}^+
parede		20	$-0,98 \times 10^{-4}$	$0,29 \times 10^{-5}$

$Re_v = 33350$, e o número de Reynolds da água $Re_\ell = 14600$ e a espessura adimensional de líquido é $\delta^+ = 812$.

As Figuras 2 e 3 apresentam a comparação da lei da interface para a distribuição da velocidade principal nas fases gasosa e líquida, respectivamente, proposta no presente trabalho com os dados experimentais de Fabre [7]. Constata-se, através da Figura 3, que a velocidade principal U_1^+ (fase líquida) afasta-se significativamente do perfil logarítmico junto à superfície sólida. Tanto para o escoamento do gás (Fig. 2), como para o escoamento do líquido, verifica-se uma excelente concordância entre os pontos experimentais disponíveis e a teoria proposta.

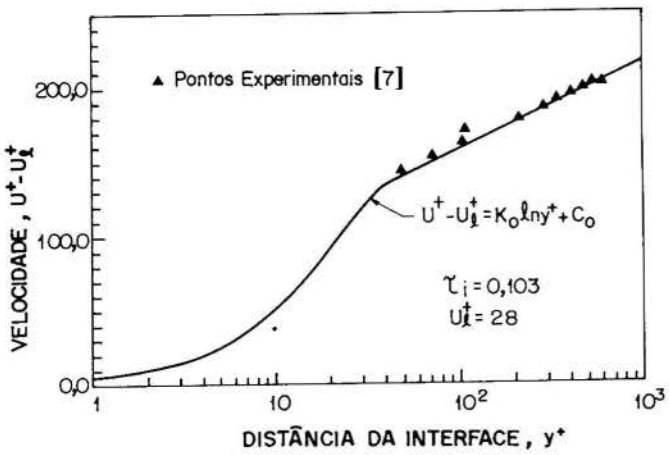

Fig. 2 – Distribuição da velocidade junto à interface para a fase gasosa

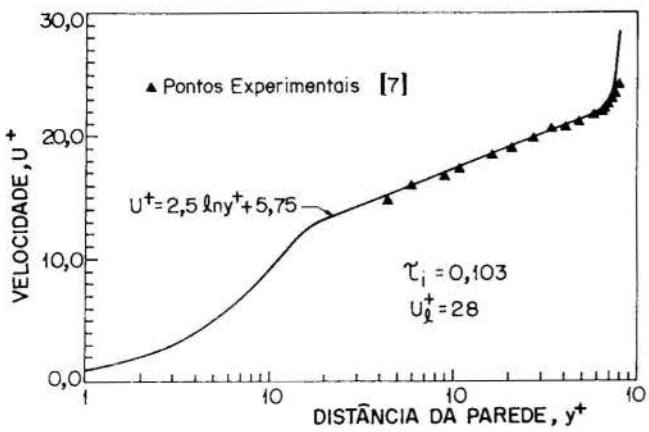

Fig. 3 – Distribuição da velocidade na fase líquida

A Figura 4 apresenta a velocidade principal do líquido na região próxima da interface. Não há dados experimentais para comparações em tal região. Constata-se que a velocidade na interface determinada pelo presente modelo é: $U_i^+ = 28$.

A Figura 5 mostra três perfis de velocidade principal e, também, os correspondentes pontos de transição do escoamento da fase líquida para três diferentes tensões de cisalhamento na interface.

Conforme pode-se verificar através da Figura 5, a tensão de cisalhamento interfacial tem forte influência sobre a forma dos perfis e a localização dos pontos de transição. O modelo prevê que os pontos de transição ocorrem em torno de $y_t^+ = 20$,

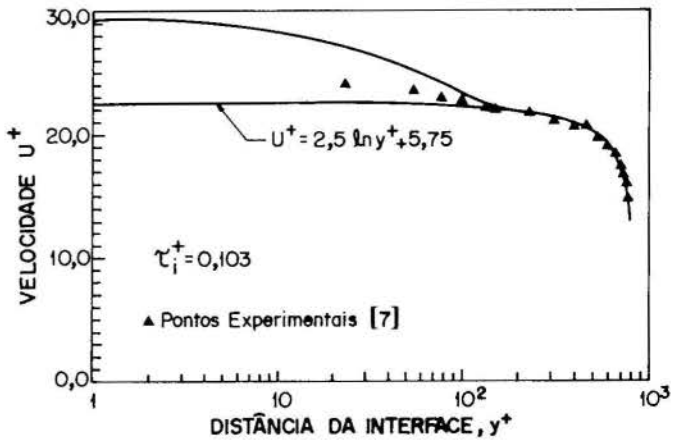

Fig. 4 – Distribuição da velocidade na fase líquida na região próxima da interface

na região junto à parede. Entretanto, na região da interface o ponto de transição não é fixo mas, sim uma função da relação entre a tensão de cisalhamento na interface e na parede. Um elevado valor da tensão na interface provoca um maior afastamento do ponto de transição da região de separação das fases. A espessura da sub-camada viscosa na interface aumenta sensivelmente com o crescimento da tensão de cisalhamento interfacial. Para escoamentos de filmes finos associados a elevadas tensões na interface é possível que todo o filme esteja sob influência do fenômeno interfacial. Assim, neste caso, não ocorreria o perfil logarítmico de velocidade em nenhuma região do filme.

Ueda et al. [9] obtiveram experimentalmente a distribuição da viscosidade turbulenta junto à interface em escoamentos com a superfície livre. Os autores [9] nada mencionam sobre a tensão de cisalhamento nas interfaces. No entanto, é possível comparar-se os resultados do presente trabalho com os da referência [9] em termos da difusividade turbulenta. Assim, obtém-se a seguinte expressão para a difusividade turbulenta

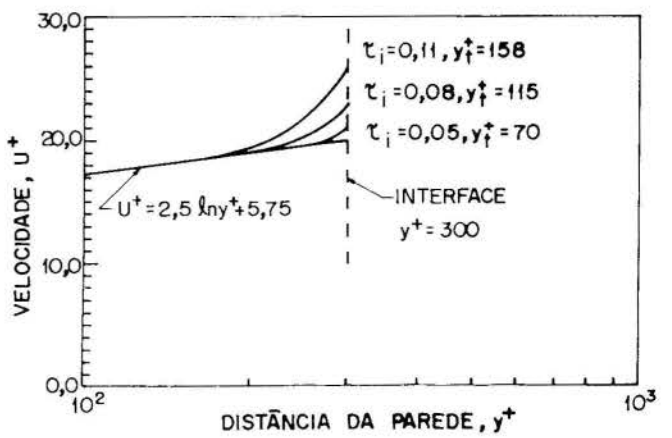

Fig. 5 – Distribuição da velocidade no líquido para diferentes valores da tensão de cisalhamento na interface

perto da superfície livre:

$$(\varepsilon_m/\nu)_\ell = 4.331 \times 10^4 (\alpha^+)^3 \qquad (34)$$

para $(\alpha^+) \to 0$.

A equação (34), que é baseada no modelo teórico apresentado em [9], possui ótima concordância com os resultados experimentais do mesmo trabalho. A lei da interface fornece a seguinte relação para a difusividade turbulenta:

$$\frac{\varepsilon_m}{\nu} = \frac{3U_{3\ell}^+(\alpha^+)^2 + 4U_{4\ell}^+(\alpha^+)^3}{-\tau_i^+ + g^+ I(\alpha^+) + 3U_{3\ell}^+(\alpha^+)^2 + 4U_{4\ell}^+(\alpha^+)^3} \qquad (35)$$

Quando $(\alpha^+) \to 0$ a equação (35) reduz-se a

$$\frac{\varepsilon_m}{\nu} = \frac{-3U_{3\ell}^+}{\tau_i^+}(\alpha^+)^2 \qquad (36)$$

A distribuição da difusividade turbulenta, para diversos valores da tensão de cisalhamento na interface, é mostrada na Figura 6. Conforme já mencionado, verifica-se nesta figura a forte influência de τ_i^+. A Figura 6 apresenta também a equação (34) que representa os resultados experimentais de Ueda et al. [9]. Na realidade, tais resultados [9] referem-se à região $7 < \alpha^+ < 100$. Portanto, a referida curva da Figura 6 possui uma extrapolação até $\alpha^+ = 0{,}1$.

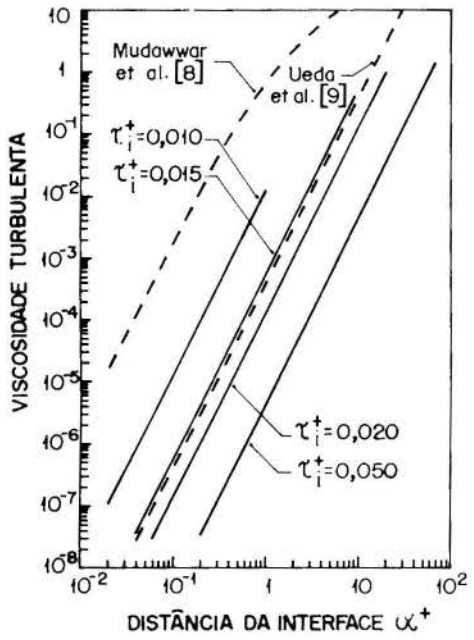

Fig. 6 – Distribuição da difusividade turbulenta na região da interface

Os resultados do modelo de Mudawwar et al. [8] também são mostrados na Figura 6. Tal modelo assume variação da difusividade turbulenta ao longo de todo o filme de líquido. Aceitando-se que a turbulência junto à interface é um fenômeno local, pode-se aplicar o modelo de [8] aos dados experimentais de Ueda [9] que são relativos a canais abertos.

Considerando o presente modelo e a simulação numérica de Lam e Banerjee [10], é possível analisar-se qualitativamente a turbulência na região da interface, no caso em que se assume as flutuações de velocidade transversais ao escoamento principal como sendo nulas ($v_i = 0$).

Não se tem conhecimento de resultados experimentais para o comportamento hidrodinâmico de regiões interfaciais quando ocorre condensação.

A Figura 7 apresenta o perfil de velocidade e a localização do ponto de transição em escoamentos de líquidos para duas diferentes taxas de condensação (V_{il}^+).

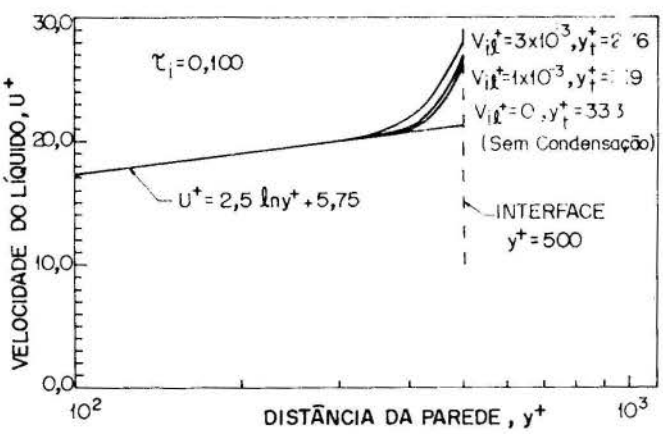

Fig. 7 – Perfis da velocidade para diferentes taxas de condensação

Verifica-se que a influência da transferência da massa (vapor para líquido) no movimento do fluido junto à região da interface é muito pequena. Com o aumento da taxa de condensação, o ponto de transição afasta-se da interface, o que acarreta no crescimento da tensão de cisalhamento na interface.

CONCLUSÕES

A presente proposta da lei da interface para escoamentos bifásicos estratificados apresenta escelente concordância com resultados experimentais obtidos em canais horizontais com escoamentos de água e ar. Em contraste com modelos anteriores, o presente modelo satisfaz as equações do movimento na região da interface.

A tensão de cisalhamento interfacial influi no perfil de velocidades e na difusividade turbulenta em ambas as fases, especificamente na região vizinha da interface. A espessura da sub-camada viscosa aumenta substancialmente com o acréscimo da tensão interfacial. A teoria prevê que, quando tal tensão é nula, a referida sub-camada não se forma. A presente lei da interface mostra que, a difusividade turbulenta varia com o quadrado da distância da interface.

Para a determinação da transferência de calor e massa em escoamentos estratificados, é proposto o emprego da presente lei para determinar-se as distribuições da velocidade principal do escoamento e da difusividade turbulenta, ambas na fase líquida. A comparação dos resultados, assim obtidos, para a transferência de calor e massa com os já disponíveis na literatura podem ser úteis na complementação da comprovação da lei da interface apresentada no presente trabalho.

REFERÊNCIAS

[1] Stephan, K., Warmeübergang beim Kondensieren und beim Sieden (Heat Transfer in Condensation and Boiling), Springer Berlin, 1988.

[2] Levich, V.G., Physicochemical Hydrodynamics, Prentice-Hall, Englewood Cliffs, NJ, 1962.

[3] Yüksel, M.L., and Schlünder, E.U., "Heat and mass transfer in nonisothermal absorption of gases in falling liquid films", Wärme-und Stoffübertragung, vol. 22, pp. 209–217, 1988.

[4] Nezu, I., and Rodi, W., "Open channel flow measurements with laser doppler anemometer", Journal of Hydraulic Eng. vol. 12, pp. 335–355, 1986.

[5] Howe, B.M., Chambers, A.J., Klotz, S.P., Cheung, T.K., and Street, R.L., "Comparison of profiles and fluxes of heat and momentum above and below an air-water interface", Journal of Heat Transfer, vol. 104, pp. 34–3 , 1982.

[6] Rashidi, M., and Banerjee, S., "Turbulen e structure in free-surface channel flows", The Physics of Fluids, vol. 31, pp. 2491–2503, 1987.

[7] Fabre, J., Masbernat, L., and Suzanne, C., "New results on the structure of stratified gas-liquid flow", Advances in Two-Phase Flow and Heat Transfer – Fundamentals and Applications, vol. 1, eds. S. Kakac and M. Ishii, Martinus Nijhoff Publ., pp. 135–154, 1983.

[8] Mudawwar, I.A., and El-Masri, M.A., "Momentum and heat transfer across freely-falling turbulen liquid film", Int. Journal of Multiphase Flow, vol 12, pp. 771–790, 1986.

[9] Ueda, H., Möller, R., Komori, S., and Mizushina, T., "Eddy diffusivity near the free surface of open channel flow", Int. Journal Heat Mass Transfer vol. 20, pp. 1127–1136, 1977.

[10] Lam, K., and Banerjee, S., "Investigation of turbulent flow bounded by a wall and a free surface", ASME Winter Annual Meeting, Chicago, IL, November 27–December 2, 1988.

[11] Kays, W.M., and Crawford, M.E., Convective Heat and Mass Transfer, McGraw Hill, ch. 4, 1980.

[12] Gayral, L., Masbernat, L., and Suzanne, C., "Mean velocities and Reynolds stress in co-current gas-liquid stratified channel flow", Two-Phase Momentum Heat and Mass Transfer; vol. 2; eds. F. Durst, G. Tsiklavri and N. Afgan; Hemisphere, pp. 921–931, 1979.

[13] Chen, S. J., "Turbulent Film Condensation on a Vertical Plate", Proceedings of the 8th International Heat Transfer Conference, San Francisco, 1986.
C. L. Tien, V. P. Carey and J. K. Ferrell, vol. 4, pp. 1601-1606, Hemisphere, Washington D.C. (1986).

[14] Fernández, E. F. y, Flix, M. J. and Tien, C. L., "Law of the interface for stratified turbulent gas-liquid flows",

submetido ao 9th International Heat Transfer Conference, 1990.

ABSTRACT

Theoretical considerations based on the equations of motion near the interface yield mean velocity and eddy diffusivity distributions for stratified turbulent gas-liquid flows. This novel "law of the interface" shows that the interfacial shear stress has a strong influence on the momentum diffusivity close to the interface. The agreement with experimental data is very good.

III ENCIT – Itapema, SC (Dezembro 1990)

VORTICAL MIXING AND HEAT TRANSFER IN LIQUID SPRAYS

ROGER H. RANGEL
Department of Mechanical Engineering
University of California
Irvine, California 92717, USA

SUMMARY

This paper examines vortical mixing and heat transfer in spray systems. The interaction between a vortical flow field with the process of molecular diffusion of species and energy is investigated. Transient heating and phase change are possible in the condensed phase. Of interest are the effect of the vortical field and other aspects of the fluid mechanics on the rates of entrainment, vaporization and mixing. The liquid spray is represented by a number of droplet groups which are followed in a Lagrangian manner, accounting for transient heating and vaporization. The scalar fields of temperature and fuel mass fraction in the gas phase are obtained by finite-differences with the droplets acting as point sources of mass and sinks of energy.

INTRODUCTION

Vortical flows occur naturally or are induced in most energy applications involving turbulent mixing of two or more species. Thus, many propulsion systems involving separate injection of the reactants, typically rely on the formation of a vortical field to enhance the rates of mixing and heat and mass transfer. The existence of coherent structures in turbulent flows, particularly in turbulent mixing layers, was observed and described in the experiments of Brown and Roshko [1] and Browand and Weidman [2]. Over the past fifteen years, an increasing number of studies focusing on the behavior of these coherent structures, their effects on the flow field, and their interaction with the scalar fields have appeared. A few examples are the works of Christiansen and Zabusky [3], Acton [4], Ho and Huang [5], and Corcos and Sherman [6]. A very complete overview of the current status of research on the interaction of particles with shear layers has been given recently by Crowe *et al.* [7]. An investigation of the effect of large-scale vortex structures on particle dispersion was performed by Crowe *et al* [8], who introduced a time scaling ratio, the Stokes number, to quantify the effect of the large-scale structures on the dispersion of particles.

The behavior of a group of droplets in a turbulent flow field generally depends on the concentration of the droplets and on the size of the droplets as compared with the scale of the turbulence [9]. At high droplet concentrations, the turbulence may be completely damped. Also, droplet agglomeration and collision can occur. At low concentrations, each particle may be considered isolated except for the indirect interaction which occurs if high vaporization rates exist. Theoretical studies of particle-turbulence interaction were performed by Tchen [10], Corrsin and Lumley [11], and Friedlander [12]. Some theoretical modeling of droplet containing eddies has been conducted by Bellan and Harstad [13]. In their work, the behavior of a cluster of droplets inside an already existing eddy is modeled in a global manner. The droplet cluster is embedded into a cylindrical vortex which is infinite in the longitudinal direction. Since the droplet cluster is assumed to be within the eddy at the begining of the calculation, no information can be inferred as to whether or not the droplets are entrained during the formation of the eddy and what mechanisms control this rate of entrainment. Those studies do provide interesting information on the subsequent behavior of the droplet cluster. In most cases it is shown that the droplets tend to form a shell near the outer rim of the vortex due to action of the centrifugal force.

The above studies have not considered heat transfer effects (in the gas or in the particles) during the vortical mixing of particles. Neither have the effects of droplet vaporization been considered to any significant extent. In this work, the interaction between the fluid mechanics and the mixing of a two-phase flow, including vaporization of the condensed phase, will be examined with the objective of determining the conditions that lead to a more efficient entrainment and mixing.

The configuration chosen for this investigation is one in which liquid spray is introduced into a gaseous shearing flow. The conditions under which the shearing flow can evolve into a number of large-scale vortical structures may be controlled, and the behavior of the spray, in terms of its spacial distribution, entrainment rates, and local and overall mixing, can be investigated so that the important controlling parameters are identified. The configuration studied corresponds to the temporal growth of a periodic shear layer.

LIQUID SPRAY

The Lagrangian equations governing the momentum dynamics of a droplet in a certain droplet group are the equations for the trajectory and the momentum exchange with the gas phase:

$$\frac{d\mathbf{x}}{dt} = \mathbf{v}, \qquad \frac{d\mathbf{v}}{dt} = \frac{C_D}{2}\frac{\rho\pi R^2}{m} v_{rel}(\mathbf{v}_g - \mathbf{v}) + \mathbf{g}. \tag{1}$$

where $\mathbf{x}$ and $\mathbf{v}$ are the droplet position and droplet velocity vectors, respectively. The gas velocity and density are $\mathbf{v}_g$ and ρ, respectively, and the absolute value of the droplet-gas relative velocity is v_{rel}. The droplet mass is m and the droplet radius is R. The drag coefficient is obtained from available numerical correlations or from experimental ones. The gravitational field $\mathbf{g}$ can play an important role, depending on the orientation, in modifying the rates of entrainment of the droplets by the vortical flow.

Recently, Nguyen *et al.* [14] compiled several droplet drag correlations for use in spray calculations. The drag coefficient is defined as:

$$C_D = \frac{D}{\frac{1}{2}\rho v_{rel}^2 \pi R^2} \tag{2}$$

where D is the magnitude of the drag force acting on the droplet. Most drag-coefficient correlations used in the spray literature account for a Reynolds-number effect and a vaporization effect through a dependence on the transfer number B. A common droplet correlation is that of Yuen and Chen [15], who experimentally showed that for low to moderate vaporization rates ($B = c_p(T_\infty - T_s)/h_{fg} \leq 3$) the drag coefficient of an evaporating droplet may be approximated by the standard drag curve for a solid sphere, provided the gas viscosity μ is evaluated at a reference temperature and the concentration obtained by using the 1/3-rule:

$$T_{ref} = T_s + \frac{1}{3}(T_\infty - T_s), \qquad Y_{F,ref} = Y_{Fs} + \frac{1}{3}(Y_{F\infty} - Y_{Fs}) \tag{3}$$

The solid sphere drag curve is approximated within 10% by the curve-fit formula [16]:

$$C_D = \frac{24}{Re} + \frac{6}{1 + Re^{0.5}} + 0.4 \tag{4}$$

in the range $0 \leq Re \leq 2 \times 10^5$.

For a vaporizing droplet there is also an equation governing the rate of change of the droplet mass:

$$\frac{4}{3}\pi\rho_\ell \frac{dR^3}{dt} = -\dot{m}, \tag{5}$$

Traditionally, the vaporization rate $\dot{m}$ is obtained from a quasi-steady analysis of the gas film around the droplet [17] as:

$$\dot{m} = 4\pi R\rho\mathcal{D}C_{Re}\ln(1 + B_{eff}), \tag{6}$$

In this expression, B_{eff} is an effective transfer number that takes into account the heat of vaporization and the heat conducted into the droplet [17,18]. The effective transfer number, B_{eff}, is defined by the mass fractions of fuel vapor at the droplet surface and in the surrounding air,

$$B_{eff} = \frac{Y_{Fs} - Y_{F\infty}}{1 - Y_{Fs}}. \tag{7}$$

An energy balance including the latent heat of vaporization, heat conduction into or out of the liquid, and conduction in the vapor phase, serves to determine B_{eff}. The convective correction C_{Re} appearing in the equation for the vaporization rate, modifies the spherically symmetric result to account for the convective effects. Several correlations are available for the convective correction, including the one suggested by Clift *et al.* [19]:

$$\begin{aligned} &Re \geq 1, \quad C_{Re} = 0.5\left(1 + (1 + RePr)^{1/3}Re^{0.077}\right), \\ &Re < 1, \qquad C_{Re} = 0.5\left(1 + (1 + RePr)^{1/3}\right). \end{aligned} \tag{8}$$

Recently, Abramzon and Sirignano [20] have proposed an expression for the vaporization rate that yields the logarithmic dependence on the transfer number for low Reynolds number, but which results in the more appropriate power-law dependence for high Reynolds number vaporization.

Since transient internal heating is considered, there is an equation for the conservation of energy inside the droplet. Employing a spherically symmetric model:

$$\frac{\partial T}{\partial t} = \alpha_{eff}\frac{1}{r^2}\frac{\partial}{\partial r}\left(r^2\frac{\partial T}{\partial r}\right), \tag{9}$$

where T is the liquid temperature and α_{eff} is an effective thermal diffusivity that takes into account the internal circulation in the droplet due to the convective gas flow surrounding it [20]:

$$\alpha_{eff} = \alpha\left\{1.86 + 0.86\ \tanh\left[2.245\log\left(\frac{Pe_\ell}{30}\right)\right]\right\}, \tag{10}$$

The energy conducted into the droplet is obtained from the definition of the effective transfer number as:

$$\dot{q}_\ell = \dot{m}\left[\frac{c_p(T_\infty - T_s)}{B_{eff}} - h_{fg}\right] \tag{11}$$

Other equations needed to complete the film model are the thermodynamic equilibrium equations relating the droplet surface temperature to the gas-phase fuel mass fraction at the surface.

THE FLOW FIELD

In the two-dimensional, inviscid case and assuming that the discrete phase has no effect on the continuous flow field [22], the only non-zero component of vorticity, ω_z, is convected by the flow field according to the equation:

$$\frac{D\omega_z}{Dt} = \frac{\partial\omega_z}{\partial t} + u\frac{\partial\omega_z}{\partial x} + v\frac{\partial\omega_z}{\partial y} = 0 \tag{12}$$

In order to solve these equations, one introduces a streamfunction, ψ, so that:

$$u = \frac{\partial\psi}{\partial y}, \qquad v = -\frac{\partial\psi}{\partial x} \tag{13}$$

The streamfunction satisfies the Poisson equation:

$$\nabla^2\psi = -\omega_z \tag{14}$$

The solution of Eq. (14) for the case in which vorticity is confined to an infinitesimally thin sheet of arbitrary shape [21], yields the velocity components at any point (x, y) as:

$$u(x,y) = -\frac{1}{2\pi}\int\frac{y - y'}{r^2}\gamma(s)ds \tag{15}$$

$$v(x,y) = \frac{1}{2\pi}\int\frac{x - x'}{d^2}\gamma(s)ds \tag{16}$$

where $\gamma(s)$ is the circulation per unit length (strength) of the vortex sheet at the point (x', y'), $r^2 = (x-x')^2 + (y-y')^2$, and s is a coordinate running along the vortex sheet. The integration is along the interface from $-\infty$ to $+\infty$. As we are interested in disturbances which are periodic in the horizontal direction, we need only consider the integration along one wavelength of the disturbance. Using complex notation with $z = x + iy$, Eqs. (15) and (16) become:

$$u(z) - iv(z) = \frac{i}{2}\int\gamma(s)\cot[\pi(z - z')]ds \tag{17}$$

where the integration is over one period of the disturbance (one unit of length). Separating Eq. (17) into its real and imaginary parts and approximating the continuous distribution of vorticity for the case of periodic disturbances of wavelength λ with a discrete distribution of vorticity with N line vortices per wavelength, the velocity field becomes:

$$u = -\frac{1}{2}\sum_{j=1}^{n}\frac{\Delta\Gamma_j\sinh 2\pi(y - y_j)}{\cosh 2\pi(y - y_j) - \cos 2\pi(x - x_j)} \tag{18}$$

$$v = \frac{1}{2\lambda}\sum_{j=1}^{n}\frac{\Delta\Gamma_j\sin 2\pi(x - x_j)}{\cosh 2\pi(y - y_j) - \cos 2\pi(x - x_j)} \tag{19}$$

where $\Delta\Gamma_j = \gamma_j\Delta s_j$ is the circulation associated with the segment of sheet Δs_j represented by vortex j.

Since the vorticity is simply convected by the flow field, the motion of the various vortex elements is obtained by integrating the equations

$$\frac{dx_i}{dt} = u_i, \qquad \frac{dy_i}{dt} = v_i \tag{20}$$

GAS-PHASE ENERGY AND SPECIES

In this one-way coupling approach, the effect of the droplets on the gas phase fluid dynamics is ignored. Future studies should remove this limitation. Consequently, the gas-phase scalar equations for conservation of energy and species can be solved once the flow velocity is known. Similarly, the droplet equations are solved with knowledge of the gas velocity. In this two-dimensional representation, the equations of conservation of energy and species in the gas phase are, assuming constant properties:

$$\frac{\partial\rho T}{\partial t} + \frac{\partial\rho uT}{\partial x} + \frac{\partial\rho vT}{\partial y} = \frac{1}{RePr}\frac{\partial^2 T}{\partial x^2} + \frac{1}{RePr}\frac{\partial^2 T}{\partial y^2} + S_{T,vap} \tag{21}$$

$$\frac{\partial\rho Y_i}{\partial t} + \frac{\partial\rho uY_i}{\partial x} + \frac{\partial\rho vY_i}{\partial y} = \frac{1}{ReSc}\frac{\partial^2 Y_i}{\partial x^2} + \frac{1}{ReSc}\frac{\partial^2 Y_i}{\partial y^2} + S_{Y_i,vap} \tag{22}$$

where the vaporization source term is given by:

$$S_{\phi,vap} = \sum_{j=1}^{N}\zeta_\phi\dot{m}_j\mathcal{N}\delta(\mathbf{r} - \mathbf{r}_j). \tag{23}$$

and where the delta functions are non-zero only at the locations of the droplets. The function ζ_ϕ generally depends on both gas and temperature properties. The solution procedure involves rewriting the governing equations in finite-difference form using a control-volume approach and solving a set of algebraic linearized equations [23].

RESULTS

We consider a sinusoidal disturbance and its first subharmonic, both of dimensionless amplitude 0.025, simultaneously imposed on the interface at $t = 0$. Since the vortices that define the interface are allowed to move closer to or farther away from each other, the initial

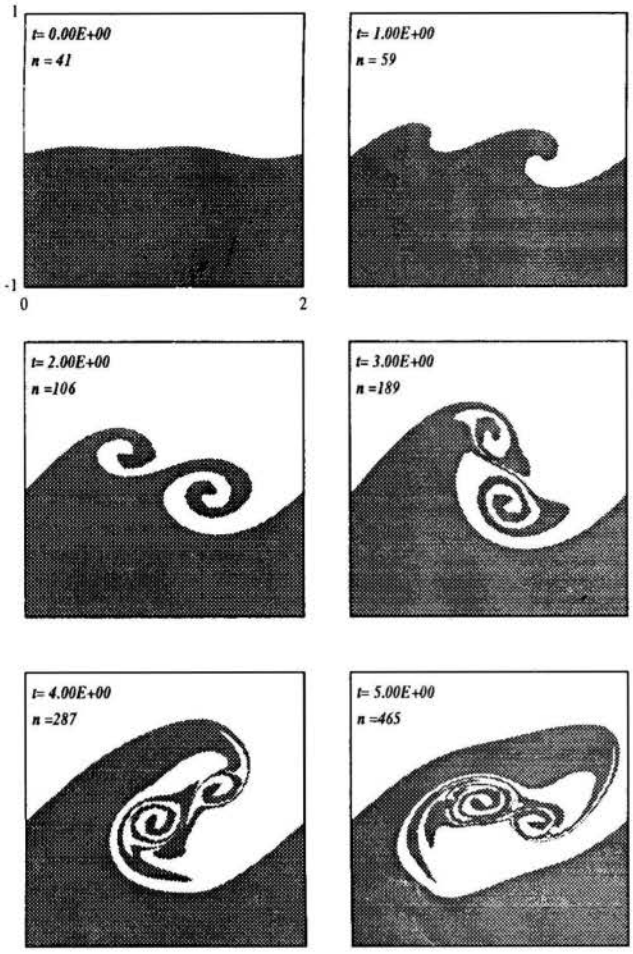

Fig. 1. Rollup and pairing of two vortical structures induced by the presence of the first subharmonic. The characteristic time is the wavelength divided by the velocity jump.

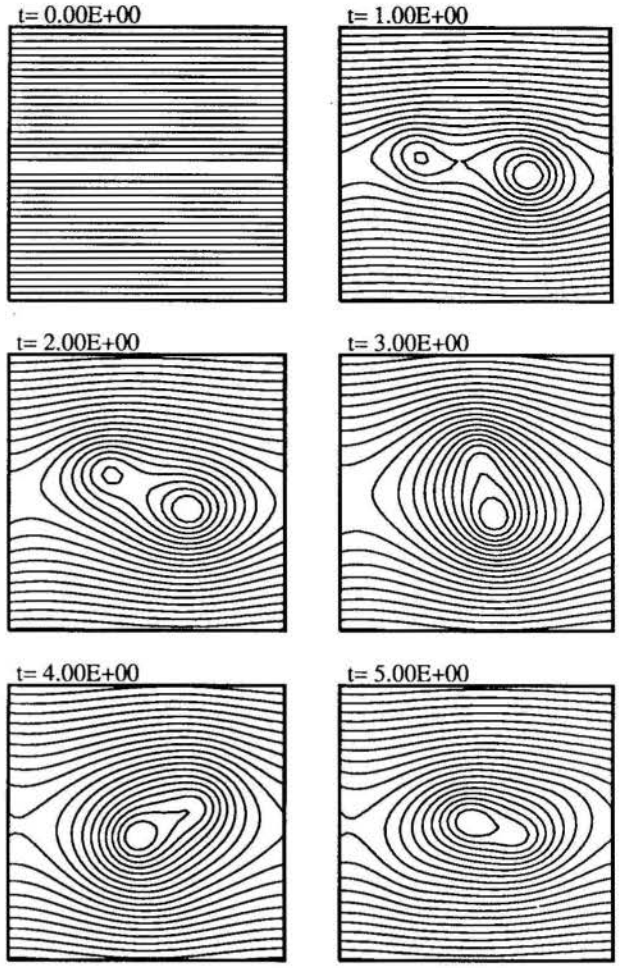

Fig. 2. Evolution of the gas-phase streamlines during the formation of two vortex structures from a vortex sheet, and their pairing induced by the first subharmonic.

resolution does not remain fixed in time. In order to prevent the resolution from deteriorating in regions where vorticity is being stretched, and in order to eliminate unnecessary calculations in regions where the vorticity agglomerates, addition of new vortices and combination of vortices is performed, accordingly. Whenever the separation between any two consecutive vortices decreases below a certain value (typically one half of the initial separation), these two vortices are combined and replaced by an equivalent single vortex.

We consider the formation and growth of two vortical structures in the presence of the fundamental and the first subharmonic and investigate the effect of the vortical structures on a few droplet streams initially located in the upper gas stream. Figure 1 shows the evolution of the interface separating the two gas streams (vortex sheet). It shows the formation of two large-scale vortical structures and their pairing induced by the first subharmonic. The number of vortex elements n is indicated at each time frame.

Figure 2 shows the gas-phase streamlines at various stages in the formation and pairing of two structures. Realize that the fluid particle paths are different from the streamlines in this unsteady flow. The steady state is reached after about 5 units of dimensionless time and after this time, the fluid particle paths and the streamlines coincide. While the fluid particle paths may cross the streamlines during the transient evolution, thus making entrainment possible, no entrainment of fluid particles occurs during steady state. Further entrainment is only possible by the process of continuous pairing.

Figures 3-6 present results for what we will consider the base-case calculation. Here the flow field corresponds to that of two vortical structures pairing under the effect of the first subharmonic. We consider three streams of 100 μm in diameter droplets of n-octane. The initial spacing between adjacent streams as well as the initial spacing between two adjacent drops in a stream is 2.5 cm. The Peclet number based on the disturbance wavelength and the velocity jump across the vortex sheet is 2500. The initial velocity of the droplets is that of the upper gas stream. The initial distance from the vortex sheet to the stream closest to it is 2 mm. In the base case calculation the inertia of the droplets is neglected so that the droplets move with the flow and the droplet paths coincide with the fluid particle paths. In Fig. 3, the contour lines of constant temperature are shown. Initially, the upper gas stream, which contains the droplets, is at 500 K while the lower one is at 1500 K. The droplet locations are indicated in Figs. 3 and 4 by the black circles. The size of the circles decreases as the droplets vaporize. The efficiency of the mixing process is better understood with the aid of Fig. 4 which shows the contour lines of constant mass fraction of the vaporized species. Initially, the mass fraction of the vaporizing species is zero. Since in the base-case calculation the droplets move as the gas particles, the only sensible measure of mixing is related to how well the gasified fuel is mixed with the initially fresh gas.

The droplet trajectories for droplets number 7, 10, 19, and 22 in the base-case calculation are shown in Fig. 5. With reference to the first frame of Fig. 3, the droplets are numbered from left to right starting with the stream closest to the initial vortex sheet. There are 12 droplets in each stream, thus, droplets 7 and 10 are in the stream closest to the vortex sheet, and droplets 19 and 22 are in the second stream, above droplets 7 and 10, respectively. In this case, in which the inertia of the droplets is neglected, these four droplets are entrained by the first vortex structure they encounter. The droplet temperature and size history are shown in Fig, 6. As this figure indicates, the droplets in the first stream are rapidly reached by the thermal diffusion wave propagating from the interface. These two droplets are heated up more rapidly independently of the formation of the structures. Droplets 19

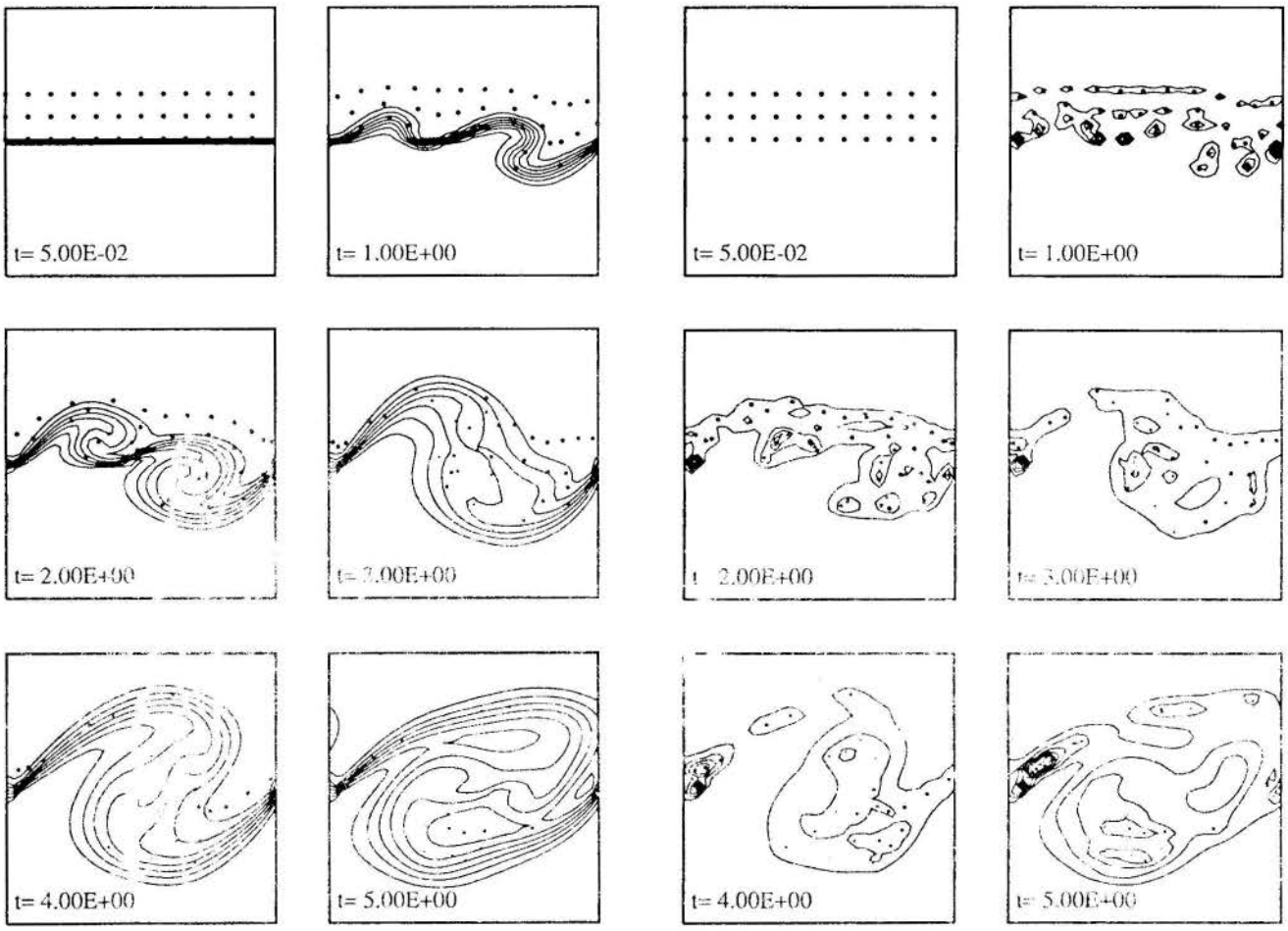

Fig. 3. Development of the gas-phase isotherms in the base-case calculation. Droplet size: 100 μm.

Fig. 4. Development of the gas-phase constant mass fraction contours in the base-case calculation. Droplet size: 100 μm. No inertia

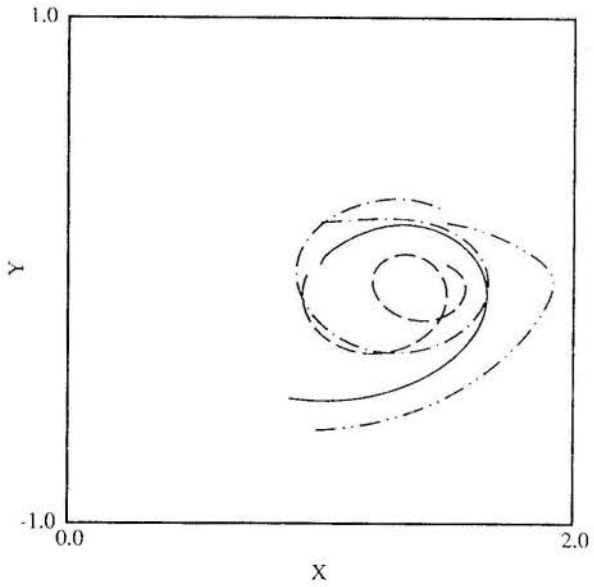

Fig. 5. Droplet trajectories of selected droplets without inertia.

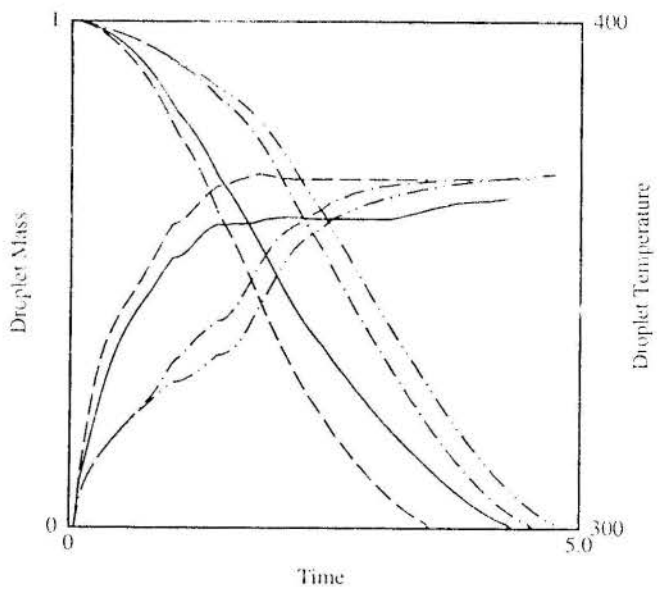

Fig. 6. Droplet size and surface temperature histories in the base case. No inertia.

and 22 rely on the formation of the vortex structures to reach the hot gas.

The results obtained by accounting for the inertia of the droplets are contained in Figs. 7-10. Figures 7 and 8 show the contour lines of constant gas temperature and constant mass fraction of the vaporizing species. The main feature observed in Figs. 7 and 8 is the fact that the droplets, on the average, tend to remain on the upper side of the shear layer. This is due to their inertia which makes them fairly insensitive to the changing gas velocity field. Figure 9 shows the paths of the same selected droplets of the base case. The droplets closest to the shear layer are entrained very easily. The droplets on the second droplet stream are not entrained by the first vortical structure, and by the time they reach the second structure (reentering on the left side of Fig. 9), that structure has already reached a quasi-steady state (closed streamlines). Thus, in order to proceed with the entrainment process, further pairing of vortical structures must occur. Since no other subharmonics are present in the initial disturbance, no further pairing occurs. Figure 10 shows the evolution of the droplet surface temperature and of the droplet mass versus time for the same selected droplets of Fig. 9. It is interesting to note that droplet number 7, represented by the solid line, which is entrained very easily, is exposed to the lower temperature fluid that is entrained with it. This droplet remains in the relatively cooler core of the structure. Other droplets that remain outside the core at exposed to higher temperatures.

CONCLUSIONS

This paper presents an investigation of the vortically-enhanced mixing of vaporizing sprays. This problem has applications in many engineering systems in which efficient mixing of a condensed substance within a carrier fluid is desired. Propulsion systems in which the fuel is injected in liquid form into an oxidizing air stream is an example of such applications. Further investigations should explore the conditions under which the entrainment is most or least efficient as a function of various controlling parameters such as droplet sizes, gas temperature, presence of subharmonics in the disturbance and so on. The two-way heat transfer coupling between the gas and the droplets should also be investigated.

REFERENCES

[1] Brown, G. L. and Roshko, A., On the Density Effects and Large Structure in Turbulent Mixing Layers, *J. Fluid Mech.*, **64**, 775-816, 1974.

[2] Browand, F. K. and Weidman, P. D., Large Scales in the Developing Mixing Layer, *J. Fluid Mech.*, **76**, 127-144, 1976.

[3] Christiansen, J. P. and Zabusky, N. J., Instability, Coalescence and Fision of Finite-Area Vortex Structures, *J. Fluid Mech.*, **61**, 219-243, 1973.

[4] Acton, E., The Modeling of Large-Scales Eddies in a Two-dimensional Shear Layer, *J. Fluid Mech.*, **76**, 561-592, 1976.

[5] Ho, C-M. and Huang, L-S., Subharmonics and Vortex Merging in Mixing Layers, *J. Fluid Mech.*, **119**, 443-473, 1982.

[6] Corcos, G. M. and Sherman, F. S., The Mixing Layer: Deterministic Models of a Turbulent Flow. Part 1. Introduction and the Two-dimensional Flow, *J. Fluid Mech.*, **139**, 29-65, 1984.

[7] Crowe, C. T., Chung, J. N., and Troutt, T. R., Particle Mixing in Free Shear Flows, *Prog. Energy Combust. Sci.*, **14**, 171-194, 1988.

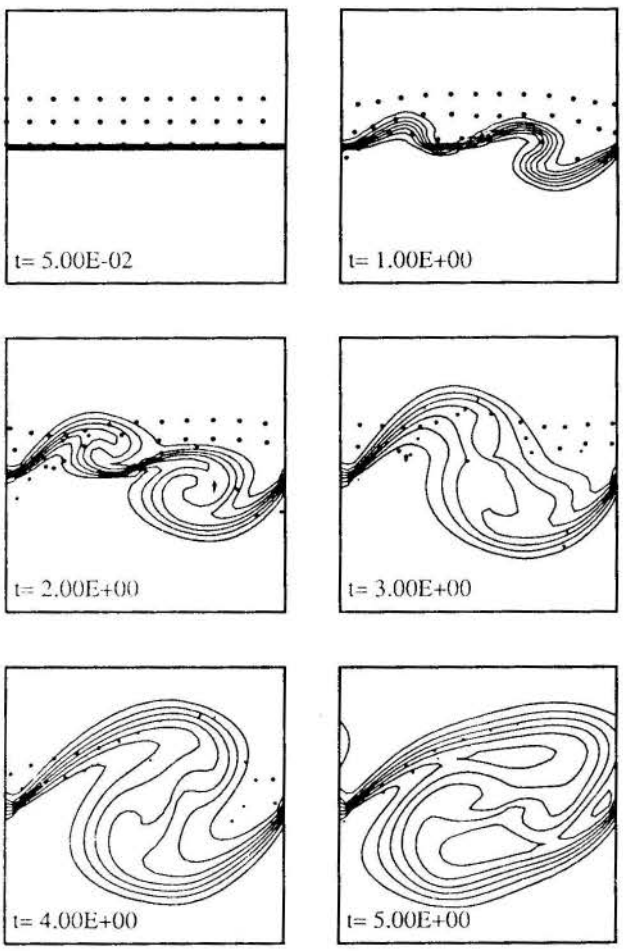

Fig. 7. Development of the gas-phase isotherms accounting for droplet inertia. Droplet size: 100 μm.

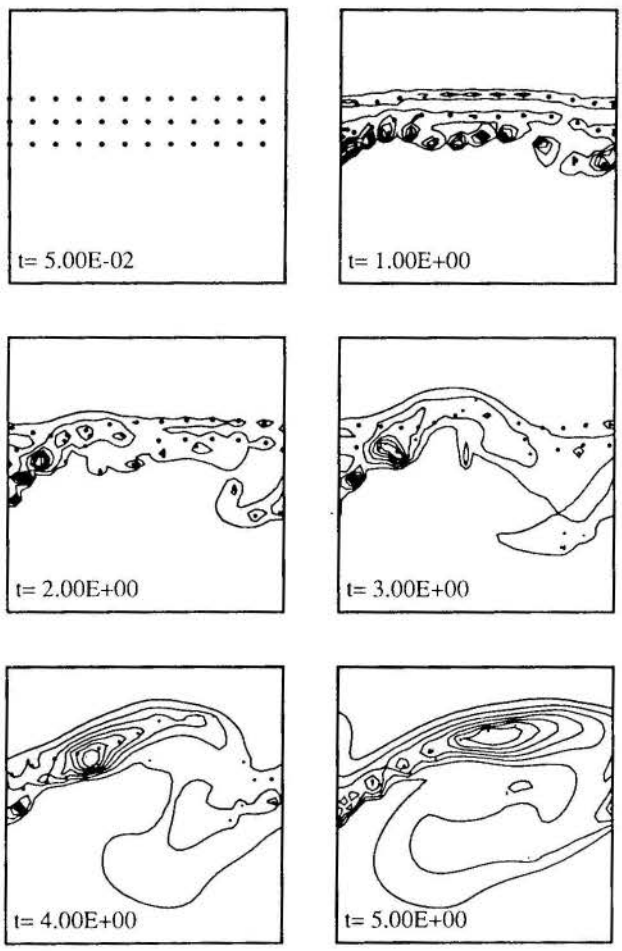

Fig. 8. Development of the gas-phase constant mass fraction contours accounting for droplet inertia. Droplet size: 100 μm.

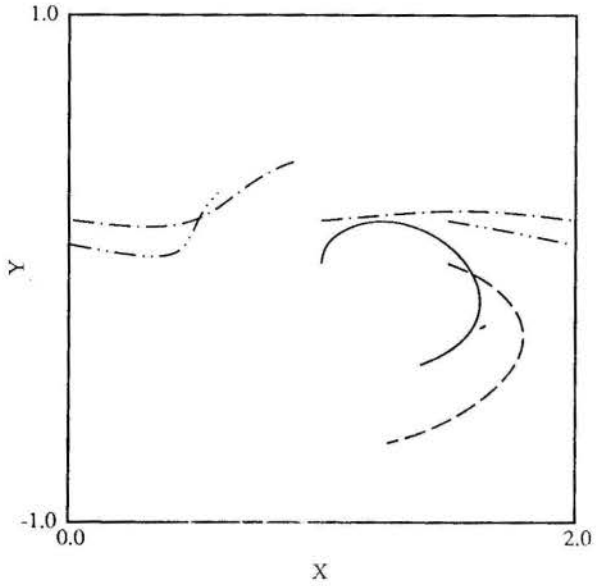

Fig. 9. Droplet trajectories of selected droplets with inertia.

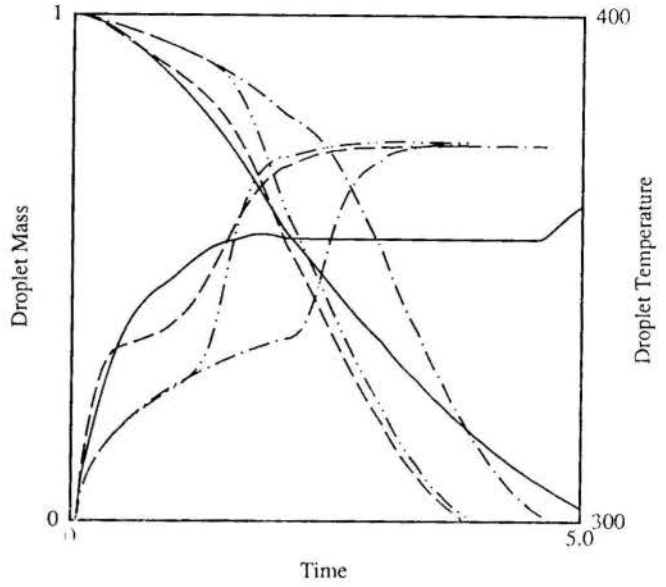

Fig. 10. Droplet size and surface temperature histories accounting for droplet inertia.

[8] Crowe, C. T., Gore, J. A., and Troutt, T. R., *Part. Sci. Technol J.*, **3**, 149, 1985.

[9] Hinze, J. O., *Turbulence*, McGraw-Hill, New York, 2nd Ed., 1975.

[10] Tchen, C. M., Mean Value and Correlation Problems Connected with the Motion of Small Particles Suspended in a Turbulent Fluid, Ph.D. Thesis, Delft, 1947.

[11] Corrsin, S. and Lumley J., *Appl. Sci. Research*, **6A**, 114, 1956.

[12] Friedlander, S. K., *AIChE Journal*, **3**, 381, 1957.

[13] Bellan, J. and Harstad, K., Some Aspects of Liquid Dispersion and Evaporation in Swirling Flows, Fall Meeting of the WSS/CI, Livermore, California, 1989.

[14] Nguyen, Q.-V., Rangel, R. H., and Dunn-Rankin, D., Measurement and Prediction of Trajectories for Vaporizing Droplet Pairs, Fall Meeting of the WSS/CI, Paper No. 89-62, Livermore, California, 1989.

[15] Yuen, M. C. and Chen, L. W., On Drag of Evaporating Liquid Droplets, *Combust. Sci. Techn.*, **14**, 144-154, 1976.

[16] White, F. M., *Viscous Fluid Flow*, McGraw-Hill, New York, 1974.

[17] Law, C. K., Recent Advances in Droplet Vaporization and Combustion, *Prog. Energy Combustion Science*, **8**, 169-199, 1983.

[18] Williams, F. A., Combustion Theory, Addison Wesley, 2nd Ed., 1985.

[19] Clift, R., Grace, J. R., and Weber, M. E., *Bubbles, Drops, and Particles*, Academic Press, 1978.

[20] Abramzon, B. and Sirignano, W. A., Droplet Vaporization Model for Spray Combustion Calculations. To appear in *Int. J. Heat Mass Transfer*, 1989.

[21] Batchelor, G. K., *An Introduction to Fluid Dynamics*, Cambridge University Press, 1970.

[22] Rangel, R. H. and Sirignano, W. A. The Dynamics of Vortex Pairing and Merging, *27th AIAA Aerospace Sciences Meeting*, Paper No. 89-0128, Reno, Nevada, 1989.

[23] Patankar, S. V., *Numerical Heat Transfer and Fluid Flow*, McGraw-Hill, 1980.

III ENCIT – Itapema, SC (Dezembro 1990)

MODELO BIFÁSICO PARA BOMBAS DE CIRCULAÇÃO DE REATORES NUCLEARES REFRIGERADOS A ÁGUA LEVE PRESSURIZADA

GILBERTO ALVES DOS SANTOS
Coordenadoria para Projetos Especiais - COPESP/RTS
ROBERTO LONGO FREITAS
Instituto de Pesquisas Energéticas e Nucleares - IPEN/RTS

RESUMO

O modelo bifásico das bombas de refrigeração do circuito primário de reatores nucleares a água leve pressurizada é um fator importante para a análise de um acidente por perda de refrigerante primário. As curvas homólogas estabelecem o desempenho completo do componente bomba, e são solicitadas como dados de entrada para os códigos termoidráulicos aplicáveis à análise de acidentes. Este trabalho propõe um modelo matemático capaz de descrever as curvas homólogas bifásicas considerando as condições geométricas e operacionais da bomba. Os resultados deste modelo são comparados com dados experimentais da literatura, apresentando uma concordância bastante satisfatória.

INTRODUÇÃO

No projeto dos sistemas de segurança e durante o processo de licenciamento de reatores nucleares a água leve pressurizada é dado grande importância para a refrigeração do núcleo quando de um acidente postulado de perda de refrigerante primário. A análise deste acidente inclui estudos sobre a vazão no núcleo e a sobrevelocidade da bomba no circuito quebrado, ambos dependentes das características das Bombas de Refrigeração do Reator (BRRs). Outros eventos, como por exemplo, partida de circuito primário inativo e parada de uma ou mais BRRs, também necessitam destas características de desempenho. A simulação destes eventos é normalmente realizada através de códigos computacionais termoidráulicos [1], tais como: CATHARE, DRUFAN-01/MOD2, THYDE/P2, RELAP4/MOD5, RELAP5/MOD1, RETRAN/02 e TRAC/PF1. Para a modelagem das BRRs, o usuário deve fornecer informações específicas do transiente operacional ou do acidente simulado, tais como, as condições nominais de operação e as curvas características das bombas. Estas curvas características representam o desempenho das BRRs e são expressas em termos de curvas homólogas e dos multiplicadores de degradação bifásicos, onde estes últimos são funções relacionando as curvas homólogas monofásicas e bifásicas.

O objetivo deste trabalho consiste no desenvolvimento de um modelo matemático para obtenção de curvas homólogas monofásicas e bifásicas de bombas de refrigeração de reatores nucleares refrigerados a água leve pressurizada. O modelo é baseado na equação de Euler para bombas e tem como parâmetros básicos as condições geométricas e operacionais das BRRs. Elaborou-se um programa computacional denominado CURVHOM (CURVas HOMólogas) capaz de fornecer as homólogas bifásicas e os multiplicadores de degradação bifásicos.

CURVAS HOMÓLOGAS

Normalmente, o desempenho completo das BRRs pode ser obtido relacionando a razão normalizada da vazão volumétrica ν e a velocidade de rotação α, para as diferentes zonas de operação. Assim o plano ν-α pode ser dividido em quatro quadrantes, a saber:

1° quadrante ($\nu \geq 0$ e $\alpha \geq 0$): Normal (N)
2° quadrante ($\nu < 0$ e $\alpha > 0$): Dissipação (D)
3° quadrante ($\nu \leq 0$ e $\alpha \leq 0$): Turbina (T)
4° quadrante ($\nu > 0$ e $\alpha < 0$): Reverso (R)

onde ν e α são definidos pelas seguintes expressões:

$$\nu = \frac{Q}{Q_r} \quad \text{e} \quad \alpha = \frac{\omega}{\omega_r} \tag{1}$$

sendo, Q = vazão volumétrica, ω = velocidade angular de rotação e o subscrito r denominando a condição nominal.

As curvas deste desempenho, no plano ν - α, são expressas pelas linhas constantes da altura manométrica normalizada h e do torque hidráulico normalizado β, onde h e β são definidos por:

$$h = \frac{H}{H_r} \qquad \beta = \frac{T \cdot \rho_r}{T_r \cdot \rho_m} \tag{2}$$

com ρ = massa específica, ρ_m = massa específica média da mistura bifásica, H = altura manométrica e T = torque hidráulico.

Para as curvas homólogas, os eixos da abscissa (X) e da ordenada (Y) são definidos da seguinte forma:

$$|\nu/\alpha| \leq 1, \qquad X = \frac{\nu}{\alpha} \qquad Y = \frac{h}{\alpha^2} \text{ ou } \frac{\beta}{\alpha^2} \tag{3}$$

$$|\alpha/\nu| < 1, \qquad X = \frac{\alpha}{\nu} \qquad Y = \frac{h}{\nu^2} \text{ ou } \frac{\beta}{\nu^2} \tag{4}$$

sendo que a nomenclatura das curvas homólogas é estabelecida pela identificação das três letras ($L_1L_2L_3$) que compõe o seu título, da seguintes forma:

L_1 { H - altura manométrica; B - torque hidráulico }

L_2 { A - denominador α; V - denominador ν }

L_3 { N - quadrante normal; D - quadrante dissipação; T - quadrante turbina; R - quadrante reverso }

Na simulação de um Acidente por Perda de Refrigerante Primário (APRP), pode-se postular a ruptura da tubulação na sucção ou na descarga das BRRs e, dependendo do arranjo da planta, uma bomba pode estar conectada em paralela com a bomba do circuito quebrado ou intacto. Estas bombas também estarão sujeitas ao escoamento avante e reverso, e necessitam da identificação das suas características nestas situações adversas. Devido a configuração dos projetos de reatores nucleares, torna-se difícil descrever as circunstâncias nas quais as BRRs seriam forçadas a operar no quarto quadrante, ou seja, vazão avante e velocidade de rotação reversa. Diante disso, o presente modelo não abrange o quadrante reverso.

MODELO BIFÁSICO PARA CURVAS HOMÓLOGAS

Quadrante Normal. Para o escoamento bifásico, admitiu-se que a altura manométrica é caracterizada pela ponderação do título mássico x nas alturas manométricas das fases líquida e vapor. Assim:

$$H^{bif} = (1 - x).\ H^{l} + x.\ H^{v} \qquad (5)$$

com, H^k dado pela equação de Euler para bombas, ou seja:

$$H^k\ .\ g = u_2^k.\ v_{u2}^k - u_1^k.\ v_{u1}^k \qquad k = l,v \qquad (6)$$

onde, u a velocidade circunferencial, H^{bif} a altura manométrica bifásica, subscrito k sendo fase líquida (l) ou vapor (v), e subscrito 1 e 2 sendo sucção e descarga.

Admitindo escoamento radial na entrada, as velocidades periféricas de v podem ser dadas por:

$$v_{u1}^k = 0 \qquad v_{u2}^k = u_2^k - \frac{v_{m2}^k}{tg\beta'_2} \qquad (7)$$

sendo β' o ângulo de inclinação da pá, e a componente meridiana v_m sendo dada por:

$$v_{m_1}^l = \frac{(1-x).\rho_{bif}.Q_{bif}}{(1-\alpha_{f1}).A_1.\rho_l} \qquad v_{m_i}^v = \frac{x.\rho_{bif}.Q_{bif}}{\alpha_{fi}.A_i.\rho_v} \qquad (8)$$

com Ai área de escoamento, αf fração de vazio e i=1 ou 2.

A massa específica bifásica pode ser dada por:

$$\rho_{bif_i} = (1 - \alpha_{fi}).\ \rho_l + \alpha_{fi}.\ \rho_v \qquad (9)$$

Admitindo um parâmetro a_i dado por:

$$a_i = \frac{\rho_v}{\rho_l}\ .\ \frac{\alpha_{fi}}{1 - \alpha_{fi}} \qquad (10)$$

e o título mássico:

$$x = \frac{1}{1 + \frac{\rho_l}{\rho_v}.\frac{1-\alpha_{fi}}{\alpha_{fi}}.\frac{1}{S_i}} \qquad (11)$$

onde Si é a velocidade de deslizamento entre fases, definida por:

$$S_i = \frac{v_{mi}^v}{v_{mi}^l} \qquad (12)$$

Podemos obter de (10) a (12) uma equação simplificada para o título mássico, ou seja:

$$x = \frac{a_i.S_i}{a_i.S_i + 1} \qquad (13)$$

Substituindo as equações (9) e (13) em (8), obtemos:

$$v_{mi}^l = \frac{1+a_i}{1+a_i.S_i}.\frac{Q_{bif}}{A_i} \qquad v_{mi}^v = S_i.\left(\frac{1+a_i}{1+a_i.S_i}\right).\frac{Q_{bif}}{A_i} \qquad (14)$$

Supondo que a velocidade circunferencial entregue a cada fase da mistura na entrada ou saída do impelidor seja dada por:

$$u_i^l = \frac{(1-\alpha_{fi}).\rho_l}{\rho_{bif}}.u_i \qquad u_i^v = \frac{\alpha_{fi}.\rho_v}{\rho_{bif}}.u_i \qquad (15)$$

e substituindo as equações (9) a (15) em (5), teremos:

$$H^{bif} = \left[\frac{1 + a_2^3.S_2}{(1+a_2.S_2).(1+a_2)^2}\right].\frac{\omega^2.r_2^2}{g} +$$

$$-\left[\frac{1 + a_2^2.S_2^2}{(1+a_2.S_2)^2}\right].\frac{\omega.Q^{bif}}{2\pi g.b_2.tg\beta'_2} \qquad (16)$$

com b = profundidade da pá do impelidor.

Assumindo os seguintes parâmetros adimensionais generalizados:

$$\alpha = \frac{\omega^{bif}}{\omega_r} \qquad \nu = \frac{Q^{bif}}{Q_r} \qquad h^{bif} = \frac{H^{bif}}{H_r} \qquad (17)$$

teremos para o quadrante normal:

$$h_{nor}^{bif} = \left[\frac{1 + a_2^3.S_2}{(1+a_2S_2).(1+a_2)^2}\right].\frac{\omega_r^2.r_2^2}{H_r.g}.\alpha^2 +$$

$$-\left[\frac{1 + a_2^2.S_2^2}{(1+a_2.S_2)^2}\right].\frac{\omega_r.Q_r}{2\pi g H_r}.\frac{1}{b_2 tg\beta'_2}.\alpha.\nu \qquad (18)$$

As perdas devidas aos atritos e turbulência no impelidor, mudanças bruscas de direção e transformação de velocidade em pressão, são consideradas supondo suas proporcionalidades ao quadrado da velocidade do escoamento e, portanto, ao parâmetro ν. Deste modo, admite-se um coeficiente de perda proporcional a ν^2 resultando em:

$$h^{bif} = C_1.\ D_2.\ \alpha^2 - C_2.\ C_3.\ E_2.\ \alpha\ .\ \nu - K_4.\ \nu^2 \qquad (19)$$

com

$$C_1 = \frac{\omega_r^2.r_2^2}{H_r.g} \qquad C_2 = \frac{\omega_r.Q_r}{2\pi.H_r.g} \qquad C_3 = \frac{1}{b_2.tg\beta'_2} \qquad (20)$$

$$D_2 = \frac{1 + a_2^3.S_2}{(1+a_2.S_2).(1+a_2)^2} \qquad E_2 = \frac{1 + a_2^2.S_2^2}{(1+a_2.S_2)^2} \qquad (21)$$

Para a condição nominal $\alpha=\nu=1$, a altura manométrica é uma função da fração de vazio α_f, onde a escolha deste parâmetro é realizada através de análise do comportamento mais conservativo dos coeficientes D2 e E2, ou seja, é escolhido aquele que produz a maior degradação na variação da fração de vazio. Deste modo, teremos:
curva HAN:

$$\frac{h}{\alpha^2} = 0{,}585.\left\{C_1.D_2 - C_2.C_3.E_2\left(\frac{\nu}{\alpha}\right) + \right.$$

$$\left. -\left[C_1.\ D_2 - C_2.C_3.E_2 - \frac{h_r^{nor}(\alpha_f)}{0{,}585}\right].\left(\frac{\nu}{\alpha}\right)^2\right\} \qquad (22)$$

curva HVN:

$$\frac{h}{\nu^2} = \eta.\left\{C_1.D_2.\left(\frac{\alpha}{\nu}\right)^2 - C_2.C_3.E_2.\left(\frac{\alpha}{\nu}\right) + \right.$$

$$\left. -\left[C_1.D_2 - C_2.C_3.E_2 - \frac{h_r^{nor}(\alpha_f)}{\eta}\right]\right\} \quad \text{com } \eta = \frac{\rho.g.Q.H}{\omega.T} \qquad (23)$$

onde as correções em ν=0 foram obtidas de Stepanoff [2].

Quadrante Dissipação. Admite-se que as componentes periféricas de v são dadas por:

$$v_{u1}^k = u_1^k + \frac{v_{m1}^k}{tg\beta'_1} \qquad v_{u2}^k = \frac{v_{m2}^k}{tg\alpha'_3} \qquad (24)$$

com α_3 ângulo de inclinação do difusor, e a equação de Euler para bombas podendo ser expressa por:

$$H^k\ .\ g = u_1^k.\ v_{u1}^k - u_2^k.\ v_{u2}^k \qquad k=l,v \qquad (25)$$

Fazendo as mesmas considerações, sobre as perdas, que são proporcionais à velocidade do escoamento, e as hipóteses adotadas para a condição nominal, teremos:
Curva HAD:

$$\frac{h}{\alpha^2} = C_4.D_1 - (C_7.E_1 - C_8.E_2).C_2.\left(\frac{\nu}{\alpha}\right) +$$

$$-\left[C_4.D_1 - (C_7.E_1 - C_8.E_2).C_2 - h(\alpha_f)^{dis}\right].\left(\frac{\nu}{\alpha}\right)^2 \qquad (26)$$

Curva HVD:

$$\frac{h}{\nu^2} = C_4.D_1.\left(\frac{\alpha}{\nu}\right)^2 - (C_7.E_1 - C_8.E_2).C_2.\left(\frac{\alpha}{\nu}\right) +$$

$$-\left[C_4.D_1 - (C_7.E_1 - C_8.E_2).C_2 - h(\alpha_f)^{dis}\right] \qquad (27)$$

com

$$C_4 = \frac{\omega_1^2.r_1^2}{H_1.g} \qquad C_7 = \frac{1}{b_1.tg\beta'_1} \qquad C_8 = \frac{1}{2.tg\alpha'_1} \qquad (28)$$

$$D_1 = \frac{1 + a_1^2.S_1}{(1+a_1.S_1).(1-a_1)^2} \qquad S_1 = \frac{1 + a_1'^2.S_1'^2}{(1+a_1.S_1)^2} \qquad (29)$$

Quadrante Turbina. Baseando no fato de que o escoamento é reverso no segundo e terceiro quadrantes, para o quadrante turbina supõe-se a mesma equação das fases (25) do quadrante dissipação onde

$$v_{ui}^k = u_i^k - \frac{v_{md}^k}{tg\beta'_i} \qquad k=i,v \qquad (30)$$

e v_{us}^k dado pela equação (24).

Aplicando o mesmo desenvolvimento feito ao quadrante dissipação, teremos:
Curva HAT:

$$\frac{h}{\alpha^2} = C_4.D_1 - (C_7.E_1 + C_8.E_2).C_2.\left(\frac{\nu}{\alpha}\right) +$$

$$-\left[\eta^2.C_4.D_1 - \eta.(C_7.E_1 + C_8.E_2).C_2 - h(\alpha_f)^{tur}\right].\left(\frac{\nu}{\alpha}\right)^2 \qquad (31)$$

Curva HVT:

$$\frac{h}{\nu^2} = C_4.D_1.\left(\frac{\alpha}{\nu}\right)^2 - (C_7.E_1 + C_8.E_2).C_2.\left(\frac{\alpha}{\nu}\right) +$$

$$-\left[\eta^2.C_4.D_1 - \eta.(C_7.E_1 + C_8.E_2).C_2 - h(\alpha_f)^{tur}\right] \qquad (32)$$

sendo que a correção dada no ponto nominal relacionando o quadrante normal (nor) e o turbina (tur), é dada por [2]:

$$H_{tur} = \frac{H_{nor}}{\eta^2} \qquad Q_{tur} = \frac{Q_{nor}}{\eta} \qquad (33)$$

MULTIPLICADOR DE DEGRADAÇÃO BIFÁSICO

Tendo em vista a dificuldade de se inserir as curvas homólogas bifásicas para cada valor de fração de vazio nos códigos computacionais, utiliza-se um multiplicador de degradação bifásico, que é uma função de ponderação, capaz de prever curvas homólogas com diferentes valores de fração de vazio. O multiplicador de degradação $M(\alpha_f)$ relaciona valores da curva homóloga de degradação $Y(\alpha_f)$ para fração de vazio α_f, a curva homóloga monofásica $Y^{mon}(X)$, $(X = \alpha/\nu)$, e a curva homóloga bifásica $Y_{min}^{bif}(X)$. Neste modelo $M(\alpha_f)$ dependerá dos valores assumidos para X. Uma vez estipulado este valor, podemos reproduzir Y^{bif} para qualquer valor de α_f. Ou seja:

$$Y^{bif}(\alpha_f) = Y^{mon}(X) - M(\alpha_f).\left[Y^{mon}(X) - Y^{bif}_{min}(X)\right] \qquad (34)$$

Em geral, os códigos computacionais termoidráulicos têm apresentado tabelas dos multiplicadores de degradação para valores de X=1,0 com $\alpha=\nu=0,5$, e aplicam estes valores para todos os quadrantes de qualquer bomba.

FRAÇÃO DE VAZIO NO IMPELIDOR

Para a resolução das curvas homologas bifásicas, verificou-se a necessidade do conhecimento da fração de vazio na saída (vazão avante) ou entrada (vazão reversa) do impelidor. O modelo adotado neste trabalho segue o mesmo tratamento que Hench e Johnston [3] utilizaram para resolver o problema de escoamento bifásico com bolhas em difusores e, em linhas gerais acompanha a filosofia desenvolvida por Furuya [4] e Zakem [5].

Supondo escoamento a bolhas no interior da bomba, a somatória das forças envolvidas pode ser expressa da seguinte forma:

$$\rho_v.V_v.\frac{dv}{dt} = \sum F_s \qquad (35)$$

sendo
V_v volume da bolha de vapor.
$\sum F_s$ força de pressão (F_p) + força centrifuga (F_{cf}) + força de Drag (F_D) + força de massa virtual (F_{mv}) + força devido a diferença de massa especifica entre as fases (F_y) + força de Bassel (F_B).
com

$$F_p = -\frac{\partial p}{\partial s}.V_v \qquad (36)$$

$$F_{cf} = \rho_v.V_v.r.\omega^2.\sin\beta'.\cos\gamma' \qquad (37)$$

$$F_D = C_D.\frac{1}{2}.\rho_l.(w_l - w_v).|w_l - w_v|.\pi.R_B^2 \qquad (38)$$

$$F_{mv} = -\frac{1}{2}.\rho_l.V_v.(a_v - a_l) \qquad (39)$$

sendo C_D= coeficiente de Drag, R_B = raio da bolha, e

$$a_k = \frac{dw_k}{dt} = \frac{\partial w_k}{\partial t} + w_k.\frac{\partial w_k}{\partial s} \qquad k=l,v \qquad (40)$$

De acordo com os estudos experimentais e teóricos realizados por Minemura e Murakami [6] em bombas centrífugas com escoamento bifásico, os termos F_y e F_B são muito pequenos comparados aos demais, podendo assim, serem desprezados na somatória das forças governantes. Desenvolvendo a expressão (35), teremos:

$$\left[\frac{\rho_l}{1-(1-S).\alpha_f}\right]^2\left\{1+\frac{1}{2(1-\alpha_f)}+\frac{S^2}{\alpha_f}\left[\frac{\rho_v}{\rho_l}.(1-\alpha_f)+\frac{1}{2}\right]\right\}.\frac{d\alpha_f}{ds} =$$

$$= -\frac{\rho_l}{A.\left[1-(1-S).\alpha_f\right]^2}\left\{\frac{3}{2}+\alpha_f-S^2\left[\frac{\rho_v}{\rho_l}.(1-\alpha_f)+\frac{1}{2}\right]\right\}.\frac{dA}{ds} +$$

$$+\left(1-\alpha_f\right).\left(\rho_l-\rho_v\right).r.\sin\beta'.\cos\gamma'.\left(\frac{A.\omega_r}{Q_r}\right)^2.\left(\frac{\alpha}{\nu}\right)^2 +$$

$$-\frac{3}{8}.\frac{C_D}{R_B}.\rho_l.\left[\frac{1-S}{1-(1-S).\alpha_f}\right].\left|\frac{1-S}{1-(1-S).\alpha_f}\right| \qquad (41)$$

e conforme Hench e Johnston [3], $\frac{C_D}{R_B}$ pode ser dado por:

$$\frac{C_D}{R_B} = \begin{cases} 109{,}843.(1-\alpha_f)^3 \ m^{-1} & \text{para } \alpha_f > 0{,}3 \\ 339{,}623 \ m^{-1} & \text{para } \alpha_f \leq 0{,}3 \end{cases}$$

e para $\alpha f > 0,3$ o termo de massa virtual da equação (41) pode ser desprezado. Portanto, conhecendo as condições geométricas do impelidor, ou seja, A_1, A_2, r_1, r_2, β_1, β_2, γ_1, γ_2, as funções de A(s), r(s), β'(s), γ'(s) e S(s), as condições nominais ω_r e Q_r, e admitindo valores de pressão e de α/ν, podemos considerar que a expressão (41) é uma equação diferencial ordinária, tendo como variável dependente a fração de vazio αf. Resolvendo-se esta equação, pode-se inferir a variação de αf ao longo de s (coordenada absoluta) e calcular as curvas homólogas bifásicas nos diferentes quadrantes.

RESULTADOS

O modelo do programa CURVHOM foi utilizado para simular o desempenho bifásico da bomba testada pela Combustion-Engineering (C-E) [7], para fração de vazio 0,4 e velocidade de deslizamento 3,0 e 5,0, onde apresentam resultados satisfatórios para o quadrante normal, conforme figura 1. Os multiplicadores de degradação bifásicos são comparados com as curvas do quadrante normal, figura 2, onde o modelo prevê desempenho distinto para cada quadrante, e é mais degradante para o quadrante normal. Ressalta-se que a C-E não apresenta resultados experimentais suficientes para comparações satisfatórias nos quadrantes dissipação e turbina, e que os dados experimentais da figura 2, são na verdade, ajustes realizados pela C-E com diversos valores de pressão. Diversas comparações experimentais e o desempenho teórico da evolução espacial da fração de vazio no interior da bomba, são apresentados detalhadamente por Dos Santos [8].

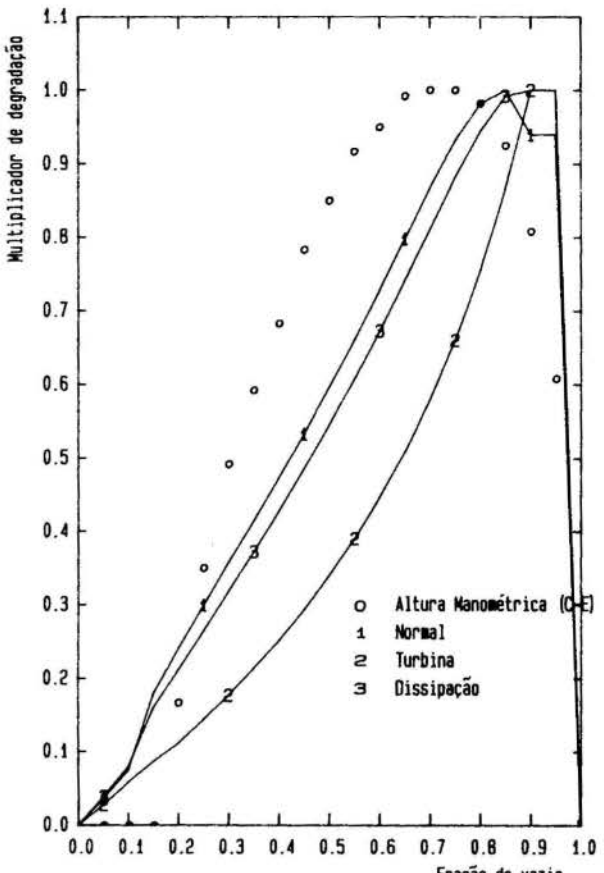

Fig. 2 Comparação entre multiplicador teórico e experimental

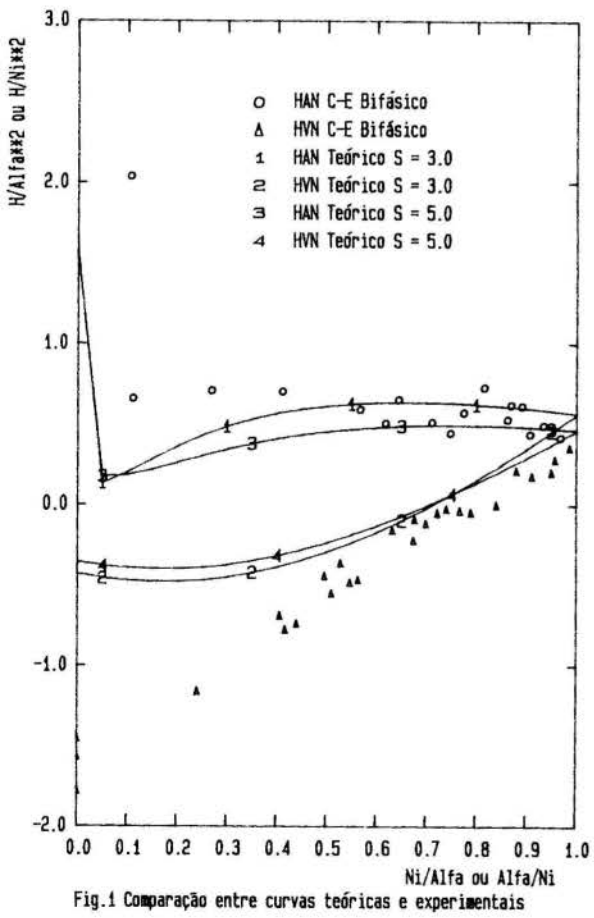

Fig.1 Comparação entre curvas teóricas e experimentais (Fração de vazio=0,40).

CONCLUSÃO

A análise de um acidente por perda de refrigerante primário em reatores nucleares refrigerados a água leve pressurizada envolve o desempenho das bombas de refrigeração de reatores. As características de desempenho destas bombas são dados de entrada solicitados pelos códigos computacionais termoidráulicos aplicáveis a este propósito, sob a forma de curvas homólogas. Neste contexto, elaborou-se um programa computacional denominado CURVHOM, baseado na equação Euler para bombas e modelos da evolução da fração de vazio ao longo do impelidor, para que possa ser avaliado e analizado com dados experimentais disponíveis. O modelo não dispõe de mecanismos que alterem o percurso realizado pelo fluido quando a bomba impõe funcionamento para condições fora de projeto. Contudo, este modelo quando aplicado à bomba testada pela C-E [7], revelou-se bastante satisfatório e com forte conservantismo para as condições fora de projeto, mesmo considerando o fato de grandes inconsistências encontradas nos dados experimentais.

REFERÊNCIAS BIBLIOGRÁFICAS

[1] Forge, A.; Pochard, R.; Porrachia, A.; Miro, J.; Sonnenburg, G.; Steinhoff, F. e Teschebdorff, V. "Comparison of thermal-hydraulic safety codes for PWR systems". London, Graham & Trotman, 1988.

[2] Stepanoff, A.J. "Centrifugal and axial flow pumps". New York, NY, J. Wiley, 1957.

[3] Hench, J.E. & Johnston, J.P. "Two-dimensional diffuser performance with subsonic, two-phase, air-water flow". J. Basic Eng., Trans. ASME, 94:(D1):105-21, 1972.

[4] Furuya, O. "An analytical model for prediction of two-phase (noncondensable) flow pump performance". J. Fluids Eng.,107(3):139-47, 1985.

[5] Zakem, S. "Analysis of gas accumulation and slip velocity in a rotating impeller". ASME century 2 emerging technology conference, held in San Francisco, 10-22 August, 1980. New York. 1980. p.167-73.

[6] Minemura, K. & Murakami, M. "A theoretical study on air bubble motion in a centrifugal pump impeller". J. Fluids Eng. 102(4):446-55, 1980.

[7] Kennedy, W.G.; Jacob, M.C.; Whitehouse, J.C.; Fishburn, J.D.; Kanupla, G.J. "Pump two-phase performance program". Palo Alto, CA, Eletric Power Research Inst., Sept. 1980 (EPRI-NP-1556 Vol. 1-8).

[8] Dos Santos, G.A. "Curvas homólogas monofásicas e bifásicas para bombas de refrigeração de reatores nucleares a água leve pressurizada". Dissertação de Mestrado, Instituto de Pesquisas Energéticas e Nucleares, São Paulo, SP, Brasil, 1990 (em defesa).

ABSTRACT

The two-phase coolant pump model of pressurized light water nuclear reactors is an important point for the loss of primary coolant accident analysis. The homologous curves set up the complete performance of the pump and are input for accidents analysis thermal-hydraulic codes. This work propose a mathematical model able to predict the two-phase homologous curves where it was incorporated geometric and operational pump condition. The results were compared with the experimental tests data from literature and it has showed a good agreement.

III ENCIT – Itapema, SC (Dezembro 1990)

ESCOMENTO ANULAR GÁS-LÍQUIDO EM DUTOS VERTICAIS COM LÍQUIDO ENTRANHADO NO NÚCLEO

E. Nogueira, N. C. L. Brum, e R. M. Cotta
Departamento de Engenharia Mecânica
EE/COPPE/UFRJ.

RESUMO

Propõe-se um modelo semi-analítico para o escoamento anular gás-líquido ascendente em um tubo circular, onde se usa, em ambos os meios, modelos algébricos de turbulência estabelecidos para escoamentos unifásicos, combinados com correlações empíricas para a determinação do fator de fricção interfacial. A integração direta das equações de momentum leva à determinação dos perfis de velocidade em cada uma das fases, o que possibilita a determinação de grandezas de interesse prático, tais como espessura média do filme líquido e gradiente de pressão axial. Os efeitos produzidos pelas gotículas de líquido dispersas no gás são levados em conta, de maneira aproximada, através de correlações empíricas especializadas. São efetuadas comparações com resultados experimentais, com o objetivo de demonstrar a consistência do modelo.

INTRODUÇÃO

Escoamentos bifásicos anulares gás-liquido ocorrem em diversos processos das indústrias química e nuclear e, devido a este fato, um razoável número de modelos semi-empíricos tem sido desenvolvidos para representá-los de forma aproximada [2,3,7,9,11,13]. Entretanto, uma das lacunas observadas na literatura disponível, é a inexistência de um modelo analítico que represente, com razoável precisão, os perfis de velocidade nos meios. Esta deficiência dos modelos disponíveis inibe o surgimento de modelos teóricos que representem satisfatoriamente o campo de temperatura em desenvolvimento e grandezas associadas à transferência de calor.
Neste trabalho desenvolvemos um modelo diferencial para escoamento bifásico anular desenvolvido e obtemos expressões explícitas para os perfis de velocidade no filme e no núcleo. Por conveniência, o modelo é apresentado em duas versões, ou seja, uma em que a fração de gotículas de líquido dispersas no núcleo gasoso é desprezada, e outra, generalização da primeira, em que esta fração é considerada("entrainment").

ANÁLISE

Considera-se escoamento desenvolvido, regime estacionário e propriedades constantes para os fluidos. As grandezas geométricas relevantes para a solução do problema são r_1, posição da interface, e r_2, coordenada da parede do duto. A equação de momentum na direção axial em termos das grandezas médias no tempo, é descrita por:

$$\frac{d}{dr}\left[r^n E_{mk} \frac{du_k(r)}{dr} \right] = \frac{r^n P_k}{\mu_k} ,$$

$$r_{k-1} < r < r_k \quad , \quad k = 1,2 \qquad (1.a,b)$$

onde o índice k identifica o fluido (1- gás, 2- líquido) e n representa a simetria do duto (1- axial, 2- plana).
Admitindo continuidade no perfil de velocidade e continuidade na tensão de cizalhamento na interface, temos as seguintes condições de contorno e interface:

$$\frac{du_1(r)}{dr} = 0 \quad , \text{ em } r = r_o = 0 \qquad (1.c)$$

$$u_1(r) = u_2(r) \quad , \text{ em } r = r_i \qquad (1.d)$$

$$\mu_1 E_{m1} \frac{du_1}{dr} = \mu_2 E_{m2} \frac{du_2}{dr} \quad , \text{ em } r = r_i \qquad (1.e)$$

$$u_2(r) = 0 \quad , \text{ em } r = r_2 \qquad (1.f)$$

Por integração direta das equações acima, obtemos expressões explícitas para as distribuições de velocidade, na forma:

$$u_1(R) = \frac{P_2 r_2^2}{(n+1)\mu_2} \left\{ \hat{\mu}\,\hat{P} \int_R^{\delta} \frac{R'\,dR'}{E_{m1}(R')} + \int_{\delta}^{1} \left[R' + \frac{(\hat{P}-1)\,\delta^{n+1}}{(R')^n} \right] \frac{dR'}{E_{m2}(R')} \right\} \qquad (2.a)$$

e,

$$u_2(R) = \frac{P_2 r_2^2}{(n+1)\mu_2} \left\{ \int_R^{1} \left[R' + \frac{(\hat{P}-1)\,\delta^{n+1}}{(R')^n} \right] \frac{dR'}{E_{m2}(R')} \right\} \qquad (2.b)$$

onde os diversos grupos adimensionais são dados por:

$$R = \frac{r}{r_2} \; , \; \delta = \frac{r_1}{r_2} \; , \; \hat{P} = \frac{P_1}{P_2} \; , \qquad (3.a\text{-}c)$$

$$\hat{\mu} = \frac{\mu_2}{\mu_1} \qquad (3.d)$$

$$E_{mk} = 1 + \frac{\varepsilon_{mk}(R, \mu_k)}{\upsilon_k} \qquad (3.e)$$

e onde,

$$P_k = - \left[\frac{dP}{dz} \pm \rho_k g \right] \qquad (3.f)$$

onde g é a aceleração da gravidade local, E_{mk} é a difusividade turbulenta do escoamento na fase k, μ_k é a viscosidade absoluta e υ_k é a viscosidade cinemática. Das expressões de velocidade obtém-se a distribuição de tensão no escoamento:

$$\tau_1(R) = \frac{P_2 r_2 \hat{P}}{n+1} R \; , \qquad 0 \le R \le \delta \qquad (4.a)$$

$$\tau_2(R) = \frac{r_2 P_2}{n+1} \left[R + \frac{\delta^{n+1}(\hat{P}-1)}{R^n} \right] ,$$

$$\delta \le R \le 1 \qquad (4.b)$$

e as velocidades médias são obtidas por intermédio de suas definições:

$$\bar{u}_k = \frac{\int_{r_{k-1}}^{r_k} r^n \, u_k(r) \, dr}{\int_{r_{k-1}}^{r_k} r^n \, dr} \; , \; k = 1,2 \qquad (5.a,b)$$

$$\bar{u} = \frac{\sum_{k=1}^{2} \int_{r_{k-1}}^{r_k} r^n \, u_k(r) \, dr}{\int_{r_o}^{r_2} r^n \, dr} \qquad (5.c)$$

No cálculo das vazões mássicas as áreas de escoamento dos fluidos (1) e (2) são obtidas através dos respectivos diâmetros hidráulicos,

$$A_1 = \frac{D_1 p_1}{4} \; , \; A_2 = A - A_1 \qquad (6.a,b)$$

onde,

$$\alpha_c = 1 - \frac{W_{LE}}{\rho_L \bar{u}_G A_1} \; ,$$

fração de vazio associada ao núcleo (8.b)

$$W_G = \rho_G \bar{u}_G \alpha_c A_1 \; ,$$

vazão de gás no núcleo (8.c)

$$\rho_c = \alpha_c \rho_G + (1-\alpha_c) \rho_L \; ,$$

densidade da mistura no núcleo (8.d)

$$\mu_c = \alpha_c \mu_G + (1-\alpha_c) \mu_L \; ,$$

viscosidade da mistura no núcleo (8.e)

$$D_1 = 2(2-n) \, r_1 \qquad (6.c)$$

e o perímetro p_1, em função do perímetro do tubo

$$p_1 = \delta^n \, p \qquad (6.d)$$

W_L, W_{LF} e W_{LE} são designados como sendo as vazões associadas ao líquido total, à fração de líquido contida no filme e à fração que se encontra dispersa no núcleo, respectivamente. Neste caso,

$$W_L = W_{LF} + W_{LE} \qquad (7.a)$$

$$Re_{LS} = \frac{4 W_L}{p \mu_L} \qquad (7.b)$$

O índice s ("superficial") aparece na definição do número de Reynolds acima para diferenciá-lo de dois outros números, também muito utilizados na literatura,

$$Re_{LF} = \frac{4 W_{LF}}{p \mu} \; , \qquad (7.c)$$

e

$$Re_L = \frac{\rho_L \bar{u}_L \bar{m}}{\mu_L} \simeq \frac{Re_{LF}}{4} \; , \qquad (7.d)$$

onde $\bar{m}$ é a espessura média do filme líquido. Outras grandezas de interesse são, então, definidas por:

$$E = \frac{W_{LE}}{W_L} \; ,$$

fração de líquido entranhado (8.a)

$$W_c = W_G + W_{LE} \; ,$$

vazão da mistura (8.f)

Para solução do problema proposto escolheu-se para cada uma das fases um modelo de difusividade turbulenta já bem testado em problemas unifásicos, segundo procedimento usual na literatura [2,3,7,11]. Definimos as seguintes grandezas adimensionais associadas aos meios (1) e (2):

$$y_k^+ = (\delta^{2-k} - R)\, r_2 \frac{\sqrt{\tau_k(r_k)/\rho_k}}{\nu_k} .$$

$$R_{k-1} < R < R_k \quad , \quad k = 1,2 \quad . \qquad (9.a,b)$$

$$u_k^+ = \frac{u_k(R) - u_k(R_k)}{\sqrt{\tau_k/\rho_k}} .$$

$$R_{k-1} < R < R_k \quad , \quad k = 1,2 \quad . \qquad (9.c,d)$$

Os modelos de difusividade turbulenta escolhidos são aqueles propostos por Deissler [1,3] e Reichardt [8]:

$$\frac{\varepsilon_{mk}}{\nu_k} = l^2 \mu_k^+(R)\, y_k^+ \left[1 - \exp(l^2 u_k^+(R)\, y_k^+)\right] .$$

$$\text{para } y_k^+ < 20 \qquad (10.a)$$

de acordo com expressão proposta por Deissler, onde $l^2 = 0.0154$, e

$$\frac{\varepsilon_{mk}}{\nu_k} = \frac{K_1'}{6} y_k^+ \left[1 + R\frac{r_2}{r_k}\right] \cdot$$

$$\left[1^2 + 2R^2\left(\frac{r_2}{r_k}\right)^2\right] , \quad \text{para } y_k^+ > 20 \qquad (10.b)$$

segundo a expressão obtida por Reichardt, onde $K_1' = 0.4$.

A solução do problema definido pelas equações (1.a-f) é segundo Sullivan[7], a solução do escoamento anular ideal. Este modelo para o escoamento água-ar, conduz a valores relativamente altos para vazão do ar. Sugere então a necessidade de um tratamento mais elaborado dos fenômenos que ocorrem na interface gás-líquido, levando-se em conta os efeitos de rugosidade interfacial, e presença de líquido entranhado no gás.

Com o intuito de simplificar a apresentação da análise, consideramos, inicialmente, a não ocorrência de gotículas no núcleo, ou seja,todo o líquido que entra no canal está na região anular. Neste caso, a única informação adicional a ser inserida no modelo seria uma correlação que levasse em conta a natureza irregular da interface e, como consequência, assumir descontinuidade de tensão de cizalhamento na interface, hipótese esta que é repassada para o modelo de turbulência. A correlação escolhida entre inúmeras existentes na literatura [6-11],é aquela sugerida por Whalley e Hewitt na forma apresentada na referência [14]. A escolha baseia-se nos bons resultados obtidos para tensão viscosa interfacial e espessura de filme,e também pela simplicidade da expressão.

Passamos, então, a explicitar as etapas para a solução do problema, considerando a hipótese de não-ocorrência de líquido entranhado:

ETAPA 1 - RELAÇÃO TRIANGULAR

a) Escolha dos modelos de difusividade turbulenta a serem utilizados. Para o caso de escoamento laminar no líquido, $E_{m2}=1$.

b) Estabelecimento dos dados de entrada: diâmetro do tubo (D), espessura média do filme ($m=r_1-r_2$), número de Reynolds associado ao filme ($Re_{LS}=4W_L/p\mu_L$) e propriedade dos meios ($\rho_L, \rho_G, \mu_L, \mu_G$).

c) Estima-se um valor para o gradiente de pressão (dp/dz) e calcula-se as tensões na parede e na interface (τ_w e τ_i, eqs. 4.a,b).

d) Determina-se, por integração numérica, o perfil de velocidade no filme, (eq.2.b).

e) Com o perfil obtido acima determina-se o número de Reynolds associado ao filme.

f) O valor do número de Reynolds é confrontado com o valor estipulado como dado de entrada. Caso a diferença seja menor que uma certa tolerância requerida passa-se à ETAPA 2; caso contrário, altera-se o gradiente de pressão até que esta condição seja atendida.

g) Estipula-se uma variação para o gradiente de pressão axial, determina-se um novo dp/dz, e voltamos ao ítem c. Por um processo de bisecção, obtemos um gradiente de pressão axial que satisfaça as condições de entrada.

ETAPA 2 - UTILIZAÇÃO DA CORRELAÇÃO PARA A TENSÃO INTERFACIAL

Através da equação:

$$f_i = \frac{2\tau_i}{\rho_G(\bar{u}_G - u_i)^2} \qquad (11.a)$$

e da correlação [14]

$$f_i = 0.079\, Re_{GS}^{-1/4} \cdot \left[1 + 24\left(\frac{\rho_L}{\rho_G}\right)^{1/3} \frac{\bar{m}}{D}\right] \qquad (11.b)$$

determina-se a velocidade média ($\bar{u}_G$) no ar. Ressalte-se que τ_i, a tensão na interface inicialmente utilizada, é obtida na ETAPA 1 (interface plana, sem rugosidades, e desprezando gradiente de pressão radial)

ETAPA 3 - DETERMINAÇÃO DO PERFIL DE VELOCIDADE NO GÁS.

a) Estipula-se um novo valor para a tensão interfacial ($\tau_i = \tau_i + \Delta\tau_i$)

b) Determina-se, por integração numérica, o perfil de velocidade no núcleo através da equação (2.a). A descontinuidade implícita no ítem a é introduzida por intermédio da expressão definida para E_{m2}, eq.(3.e).

c) Através do perfil obtido no ítem ânterior, determinamos a velocidade média por meio da eq. (5. a).
d) Comparamos a velocidade média calculada no ítem c com a velocidade média obtida na ETAPA 2. Quando a convergência é atingida para a tolerância requerida, assumimos os resultados obtidos como solução do problema; caso contrário, passamos ao ítem seguinte.
e) Determina-se um novo valor para a tensão de cizalhamento na interface($\tau_i = \tau_i + \Delta\tau_i$).

Volta-se ao ítem b e, através de uma rotina semelhante à citada no ítem g(ETAPA 1), obtemos uma tensão na interface que satisfaça o resultado determinado na ETAPA 2.
Caso o gradiente de pressão seja estipulado como dado de entrada ao invés da espessura média do filme, efetuamos a ETAPA 1 de maneira absolutamente equivalente, assumindo uma variação para a espessura do filme, até a obtenção da convergência.
Ressalte-se que as evidências experimentais [10,12] levam a crer que o número de Reynolds associado ao líquido (Re_{LS}) permite estimar a ocorrência, ou não, de gotas no núcleo. Para baixos Reynolds o fenômeno não ocorre, ou é desprezível [12,13].

A classificação "baixo Reynolds" é todavia, relativa, pois depende, como mostram os resultados apresentados no presente trabalho, do diâmetro do tubo.
Uma das limitações da abordagem acima descrita encontra-se, evidentemente, na hipótese de que todo o líquido encontra-se no filme. Como na maior parte dos ensaios experimentais disponíveis na literatura foi observada a presença de gotículas dispersas no gás, uma extensão natural do presente modelo é, portanto, a consideração da influência da fração de líquido entranhado.
Antes de apresentarmos o procedimento adotado para a solução do problema, considerando uma fração de gotículas entranhadas, torna-se necessário que enfatizemos alguns aspectos relacionados às grandezas definidas anteriormente: caso W_{LE}, a vazão associada às gotículas de líquido no núcleo, seja nula, $W_{LF} = W_L$. É importante observar que se assumirmos a igualdade acima ("no entrainment"), a espessura de filme adimensional experimental (correlações de Kosky(1971), Henstock e Hanratty(1976) e Kadambi(1985)) se mostrará, provavelmente, inferior ao valor da mesma grandeza determinada teóricamente, pois estamos assumindo mais líquido próximo à parede do que aquele que experimentalmente seria observado. Com base na desigualdade verificada, podemos nos aproximar do valor mais provável para a vazão do líquido confinado, o que por sua vez levará a um valor aproximado para a vazão de líquido no núcleo.
Passamos, então, a explicitar o procedimento iterativo adotado para solução do problema que considera gotículas entranhadas no núcleo gasoso do escoamento:
a) Determinação das grandezas relativas ao filme de acordo com o procedimento apresentado na ETAPA 1. Aqui, óbviamente, $Re_{LS} = Re_{LF}$
b) Determinação da espessura teórica através da expressão:

$$\bar{m}_{teor.} = \frac{\sqrt{\tau_w(Re_{LF})/\rho_L}}{\nu_L}$$

$$= \bar{m} \frac{\sqrt{\tau_w(Re_{LS})/\rho_L}}{\nu_L} \qquad (12)$$

onde $\tau_w(Re_{LS})$ é o valor da tensão de cizalhamento na parede, determinada no ítem a, quando $Re_{LS} = Re_{LF}$

c) Comparação entre $\bar{m}_{teo.}$ e $\bar{m}_{exp.}$, este obtido de:

$$\bar{m}_{exp} = \bar{m}^{+}_{exp} \left[\frac{\sqrt{\tau_w(Re_{LS})/\rho_L}}{\nu_L} \right]^{-1} \qquad (13.a)$$

onde,

$$\bar{m}^{+}_{exp} = 0.707\, Re_{LF}^{0.5} +$$

$$\left[1 + 7.835 \times 10^{-9} (Re_{LF})^{1.145} \right]^{0.1} \qquad (13.b)$$

Se $\bar{m}_{teo}$ estiver suficientemente próximo de $\bar{m}_{exp}$, dentro da tolerância especificada, segue-se da seguinte forma:

c.1) executase a ETAPA 2, definida anteriormente,

c.2) determina-se $W_{LE}, \alpha_c, W_G, \rho_c, \mu_c$;

c.3) faz-se $\rho_G = \rho_c$ e $\mu_G = \mu_c$;

c.4) executa-se a ETAPA 3, definida anteriormente,

Caso contrário, segue-se para o passo abaixo:

d) Especifica-se uma variação para o número de Reynolds associado ao filme (ΔRe_{LF}) e determina-se um novo valor para Re_{LF} ($Re_{LF} - \Delta Re_{LF}$), voltando-se ao ítem a.

Portanto, introduz-se ao formalismo anterior uma parcela de líquido disperso no gás que escoa no núcleo. Para a mistura gás-líquido utiliza-se o modelo homogêneo, assumindo-se uma dispersão uniforme de gotículas ao longo do raio e, além disso, admitindo-se velocidade relativa nula entre as gotículas de líquido e gás.

RESULTADOS E DISCUSSÃO

Foram obtidos resultados para gradiente de pressão axial, espessura de filme e perfis de velocidade, referentes a resultados experimentais apresentados na literatura [4,5,12,13]. Explorou-se uma ampla faixa de diâmetros de tubo (15,88, 31,75 e 50,8mm) e de vazões no filme. Comparou-se o modelo com resultados experimentais que praticamente não apresentaram gotículas de água no núcleo [14], mas também com aqueles que apresentavam uma parcela apreciável, de acordo com as demais referências.

Nas figuras 1-3 comparamos resultados obtidos pelo modelo que não considera gotículas no núcleo, com diferentes trabalhos experimentais [4,5,12]. Para todas as situações apresentadas na figura 1, não há ocorrência de gotas no núcleo de forma apreciável. Constatamos que, dentro da faixa de valores analisados, os resultados do modelo são muito próximos para o gradiente de pressão axial (a discrepância observada encontra-se dentro de uma faixa de 12% de desvio máximo). Na figura 2, para todas as situações analisadas, existe uma fração de gotículas do líquido dispersa no núcleo [12], que cresce com o aumento do número de Reynolds. Para Re_{LS} = 310, entretanto, dentro da faixa de vazão analisada, esta fração é ínfima, o que justifica a ótima concordância verificada. Para altos Reynolds, em que o "entrainment" não é desprezível, a discrepância é sempre maior que 30%. Observe-se que a contribuição gravitacional, devido ao líquido, não é desprezível frente ao gradiente de pressão relativamente baixo. Isto significa que ao considerarmos todo o líquido contido no filme, estamos adicionando ao gradiente de pressão total, uma parcela extra que, de fato, deveria ser desconsiderada quando da aplicação da relação triangular.

Na figura 3 apresentamos os perfis de velocidade, comparados com resultados experimentais [5,13], para um conjunto de vazões de água e ar para as situações em que o "entrainment" é desprezível (Re_{LS} = 153 e Re_{LS} = 253), e obtivemos uma razoável concordância entre os perfis teóricos e experimentais. Existe, entretanto, uma significativa discrepância quando a vazão no filme é relativamente elevada (Re_{LS} = 1010).

Uma das causas para esta diferença é o efeito de "laminarização do perfil", associado às gotículas no núcleo. Outra causa se relaciona ao modelo de turbulência escolhido para representar o escoamento no núcleo. O fato do perfil teórico, em todos as situações, ser mais "achatado",é uma evidência de que o modelo superestima o nível de turbulência no núcleo.

Os resultados apresentados através da figura 4 apresentam uma melhora acentuada, utilizando-se o modelo mais geral, principalmente na faixa de valores em que o "entrainment" é substancial, em relação ao modelo que assumia todo o líquido contido no filme (fig. 2). Além disso, os valores obtidos para espessura de filme, figura 5, e através do modelo generalizado, mostram-se em excelente concordância com os resultados experimentais. Também de grande interesse é notar que a consideração de gotículas entranhadas leva a melhores resultados para a determinação do perfil de velocidade no gás, como mostra a figura 6.

Neste caso, apesar de coerentemente a espessura de filme diminuir, a velocidade máxima aumentou, possivelmente devido à diminuição da área de escoamento disponível para o ar.

A vantagem significativa do modelo proposto é a de possibilitar a determinação dos perfis de velocidade com razoável precisão e em forma explícita, viabilizando estudos analíticos futuros para a transferência de calor em escoamento bifásicos.

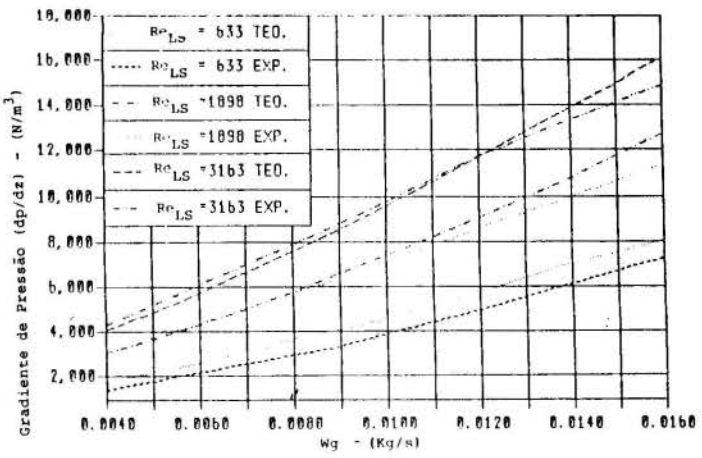

Figura 1 - Comparação teórico x experimental para gradiente de pressão. Resultados experimentais obtidos por Shearer e Nedderman (diâmetro do tubo = 15.88×10^{-3}m).

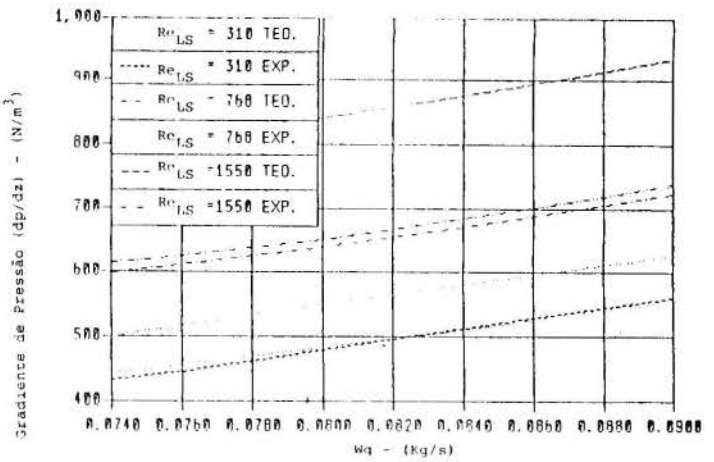

Figura 2 - Comparação teórico x experimental para gradiente de pressão. Resultados experimentais obtidos por Zuber, Dukler e Moalem-Maron (diâmetro do tubo = 0.8×10^{-3}m).

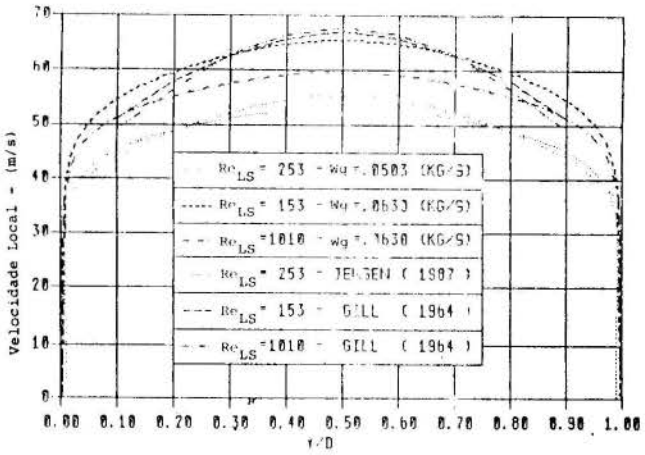

Figura 3 - Comparação teórico x experimental para perfis de velocidade. Resultados experimentais extraídos de Jensen e Gill et. al.

REFERÊNCIAS

[1] Deissler, R.G., "Analytical and Experimental Investigation of Adiabatic Turbulent Flow in Smooth Tubes", Naca TN 2138, 1950.

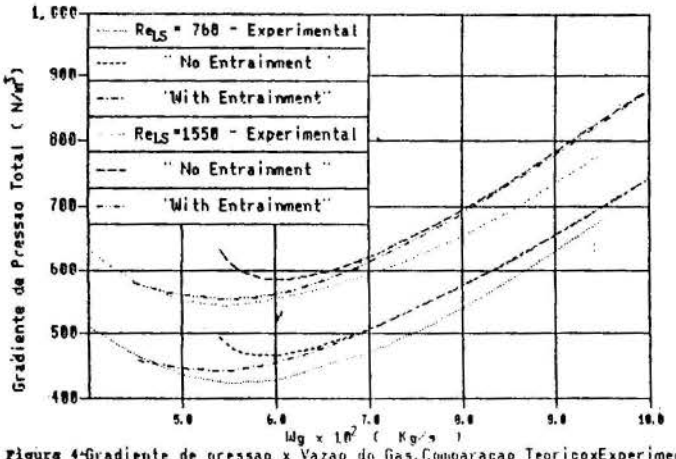

Figura 4-Gradiente de pressao x Vazao do Gas.Comparacao TeoricoxExperimental para hipotese de escoamento laminar no Filme.

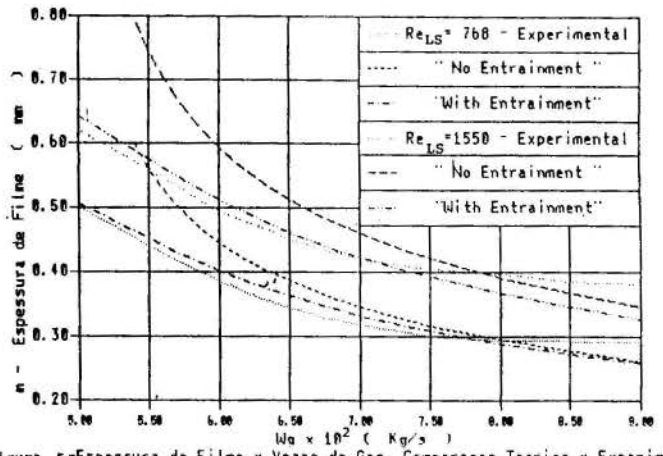

Figura 5-Espessura de Filme x Vazao do Gas. Comparacao Teorico x Experimental para hipotese de escoamento laminar no Filme.

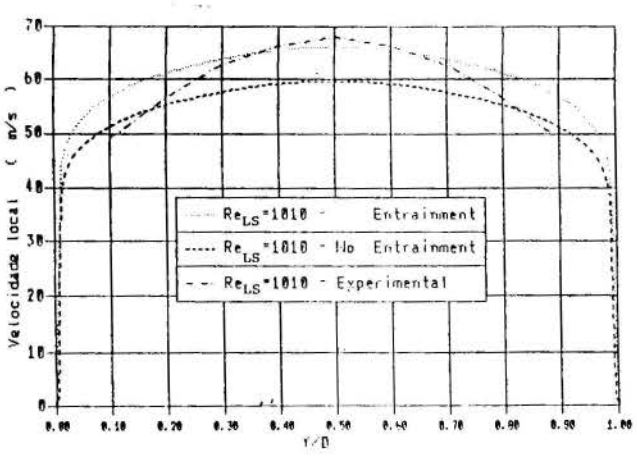

Figura 6 - Comparação entre perfil de velocidade experimental típico e perfis determinados através dos modelos teóricos [Wg =.061 (Kg/s)].

[2] Dukler, A. E. and O.P. Bergelin, "Characteristics of Flow in Falling Liquid Film". Chem. Eng. Progr., V.48, N.11, pp. 557-563, 1952

[3] Hewitt, G.F., "Analysis of Annular Two-Phase Flow: - Application of the Dukler Analysis to Vertical Upward Flow in a Tube". A.E.R.ER 3680 H.M.S.O., London, 1961.

[4] Shearer, C.J.and R.M. Nedderman, "Pressure Gradient and Liquid Film Thickness in Co-Current Upward Flow of Gas-Liquid Mixtures: Application to Film-Cooler Design", Chem. Eng. Science, V.20, pp. 671-683, 1964.

[5] Gill, L.E., G.F.Hewitt, P.M.C.Lacey,"Sampling Probe Studies of the Gas Core in Annular Two-Phase Flow II - Studies of the Effect of Flow Rater on Phase and Velocity Distribution", Chem. Eng. Science, V.19, pp. 665-682, 1964.

[6] Wallis, G.B., "One Dimensional Two-Phase Flow", McGraw-Hill, 1969.

[7] Sullivan, D.A., "Two-Phase Annular Flow in Pipes: Analytical Models", Thayer School of Engineering, Dartmont College, Hanover, N.H. 03755, 1970.

[8] Hewitt, G.F.and N.S. Hall-Taylor "Annular Two-Phase Flow", Pergamon Press, 1970.

[9] Wallis, G.B., "Annular Two-Phase Flow Part 2: Additional Effects". J. of Basic Eng. pp. 73-82, 1970.

[10] Henstonch, W.H.and T.J. Hanratti, "The Interfacial Drag and Height of the Wall Layer in Annular Flow". AICHE J. V.22, No. 6, pp. 990-999, 1976.

[11] Kadambi, V.,"Prediction of Pressure Drop and Void-Fraction in Annular Two-Phase Flow". Can. J. Chem. Eng., V.63, pp. 728-735, 1985.

[12] Zabaras, G., A.E. Dukler, and M.D. Maron, "Vertical Upward Cocurrent Gas-Liquid Annular Flow". AICHE J., V.32, No 5, pp. 829-834,1986.

[13 Jensen, M.K., "The Liquid Film and the Core Region Velocity Profiles in Annular Two-Phase Flow". Int. J. of Multi-Phase Flow, V.13, No.5, pp. 615-628, 1987

[14] Whalley, P.B., "Boiling Condensation and Gas-Liquid Flow", Clarendon Press, Oxford,1987.

ABSTRACT

A semi-analytical model is proposed for fully developed upward gas-liquid annular flow inside vertical circular tubes, by utilizing well-known turbulence algebraic models for single-phase flows, within both streams, combined with empirical correlations for the gas-liquid interface friction factor. Direct integration of the associated momentum equations provide the velocity distribution for each phase, as well as overall quantities of pratical interest such as liquid film thickness and pressure gradient. The effects of liquid droplets entrainment in the gas is approximately taken into account through specialized empirical correlations.Extensive comparisons with experimental results are made in order to demonstrate the consistency of the proposed model.

III ENCIT – Itapema, SC (Dezembro 1990)

ON MODELLING, MATHEMATICAL ANALYSIS AND NUMERICAL TREATMENT OF THREE-DIMENSIONAL TRANSIENT TWO-PHASE COOLANT FLOW IN ENGINEERING SYSTEMS

MAURIZIO BOTTONI*, WOLFGANG SENGPIEL**

* Visiting Scientist at Argonne National Laboratory, 9700 S. Cass Avenue, Argonne, IL 60439, USA;

** Kernforschungszentrum Karlsruhe, Institut für Reaktorentwicklung, Postfach 36 40, D 7500 Karlsruhe 1

SUMMARY

The conservation equations of mass, momentum and enthalpy and the entropy inequality, written for a two-phase flow in the local instantaneous form together with the respective jump conditions at the phase interfaces, are volume-averaged over Eulerian control cells yielding a system of coupled macroscopic governing equations for the separated phases suitable for the three-dimensional, transient numerical simulation of complex engineering systems. The equations for the separated phases are then combined to model the fluid mixture in the frame of a slip model. The state of the art of the numerical treatment of the discretized and linearized equations is presented with reference to solution methods of a resulting Poisson-equation for pressure and enthalpy distributions. The above algorithms have been implemented in the computer programmes BACCHUS-3D/TP and COMMIX-2. The application of these codes is reviewed with reference to the numerical simulation of sodium boiling experiments in bundle geometry and of forced and natural convection simulations in more complex geometrical configurations.

INTRODUCTION

Multiphase flow phenomena involve a widespread domain of technical applications ranging from the safety analysis of reactor cores under hypothetical accidents to pneumatic transport lines or optimization of combustion processes. Since the basic book by R.B. Bird, W. Stewart and E.N. Lightfoot [1] on transport phenomena has found wide distribution, the analytical treatment of the fundamental equations describing the conservation of mass, momentum and enthalpy has become the basic tool for the investigation of these processes, leading to computational codes which are in general less expensive to run than the operation of demonstration plants.

In the more restricted domain of two-phase flow, a state of the art of the ongoing research has been given in the well known monograph by M. Ishii [2] where the fundamental theory of thermo-fluid dynamic problems is presented in a self-consistent and mathematically rigorous treatment.

A more recent reference text on the thermohydraulics of two-phase systems is the book edited by J.M. Delhaye, M. Giot, M.L. Riethmüller [3], which is particularly oriented towards nuclear engineering applications. Among other significant results, it gives the conceptually important proof by J.M. Delhaye of equivalence of space-time and time-space averaging procedures. The theoretical importance of this result is matched by the practical circumstances which make experimental results independent of the particular technique used (sequence of time and space averaging) for recording mean-valued data.

Meanwhile, theoretical efforts do not concern only the derivation of macroscopic averaged equations, but also the modelling of terms describing the details of transport processes of mass, momentum and enthalpy between the phases, taking into account the physical characteristics of the phase boundary. The mathematical formulation of these terms is a particularly challenging task when turbulent exchange phenomena must be accounted for. A state of the art of this ongoing research has been presented recently in the monograph by D.A. Drew and R.T. Wood [4]. This reference gives also an overview of the constitutive equations used as a closure of the system of fundamental equations describing two-phase flow systems.

This article aims at giving an overview of i) the mathematical analysis involved in modelling a two-phase flow with the methodological approach of reference [4], ii) the numerical treatment of the discretized conservation equations, with particular reference to the algorithms used in the two codes COMMIX-2 [5] and BACCHUS-3D/TP [6], iii) recent work concerning application of the above codes in the frame of fast breeder reactor safety studies.

MATHEMATICAL BASIS OF TWO-PHASE FLOW MODELLING

In the following, a condensed representation must be given. A comprehensive overview of this subject with details concerning analytical deduction and physical meaning of equations and terms is presented in reference [9].

General form of instantaneous local equations and jump conditions

The canonical form of the equations for the flow of a pure compressible Newtonian fluid (or for the flow within the region consisting entirely of one phase in a multiphase mixture) is [7]

$$\frac{\partial(\rho\psi)}{\partial t} + \nabla \cdot (\rho\,\psi\,\mathbf{v} - \nabla) \cdot \mathbf{J} - \rho f = 0 \qquad (1)$$

where: ψ is the quantity conserved, J and f are its diffusive flux and source density, respectively.

Denoting n_k ($k = 1, 2$) a unit normal oriented from phase k outwards, and m the interfacial source of ψ, the jump conditions at the phase interface are

$$\left|\left| \left(\rho_k \psi_k (\mathbf{v}_k - \mathbf{v}_i) - \mathbf{J}_k \right) \cdot \mathbf{n}_k \right|\right| = m. \qquad (2)$$

The summation convention holds for the left hand side. The symbol [[ ]] denotes the jump across the phase interface.

We consider in the following the conservation equations for mass, momentum and enthalpy, which are used in the above mentioned codes and the entropy inequality which is used to check the consistency of the physical modelling [8]. The values of ψ, J, f and m for these equations are given in Table I.

Volume averaged conservation equations and jump conditions for the separated phases

For any scalar, vector or tensor field represented by a function f of time and of the spatial coordinate $\mathbf{x} = (x_1, x_2, x_3)$ we define the Eulerian volume average by

$$\langle f \rangle = \frac{1}{\Delta V} \int f(t, \mathbf{x})\, dV. \qquad (3)$$

Table I: Variables in generic conservation equations and jump conditions

Conservation Principle	ψ	$\mathbf{J}$	f	m
Mass	1	0	0	0
Momentum	$\mathbf{v}$	$\underline{\mathbf{T}}$	$\mathbf{g}$	$\mathbf{m}_i^{\sigma} = \sigma c \mathbf{n}$
Enthalpy	h	$-\mathbf{q}$	$1/\rho [\partial p/\partial t + \mathbf{v} \cdot \nabla p + (\underline{\tau} : \nabla \mathbf{v})] + r$	q_i
Entropy	s	$-\mathbf{q}/T$	r/T	$q_{si} \geq 0$

σ = surface tension [N/m]
c = mean curvature of the interface [1/m] (1/R, with radius of curvature R)
$\mathbf{n}$ = unit normal pointing out of a concave curvature
q_i = distributed heating source at the interface [W/m^2]
q_{si} = source of entropy at the interface [W/(m^2 K)]
r = specific heat source [W/kg]
$\underline{\mathbf{T}} = -p\underline{\mathbf{1}} + \underline{\tau}$ = stress tensor [N/m^2]
Subscript i refers to the phase interface

In the following all volume averages are denoted by overbars. Vectors are denoted by bold characters, tensors by bold underlined characters. For averaging the conservation equations of each phase over a control volume a phase indicator function X_k is defined with value 1 or 0 according to whether the point $\mathbf{x}$ considered lays within phase k or not.

An important property of the phase indicator function, which is used in the averaging process, is expressed by [9]

$$\frac{\partial X_k}{\partial t} + \mathbf{v}_i \cdot \nabla X_k = 0. \tag{4}$$

By means of the phase indicator function X_k one derives a generalization of the relation $\overline{\nabla f} = \nabla \bar{f}$, which holds only in absence of phase interfaces (i.e. within each phase). When both phases are present within a control volume, we define the phase averages of a scalar function f and of its gradient by:

$$\bar{f} = \overline{X_1 f + X_2 f}, \tag{5}$$

$$\overline{\nabla f} = \overline{X_1 \nabla f + X_2 \nabla f} = \overline{X_1 \nabla f} + \overline{X_2 \nabla f}. \tag{6}$$

It can be proved [4] that

$$\overline{\nabla f} = \nabla \overline{\left(X_1 f + X_2 f\right)} - \overline{\left(f \nabla X_1 + f \nabla X_2\right)} =$$

$$= \nabla \bar{f} - \overline{\left[\left[f\right]\right] \nabla X_k} \tag{7}$$

The corresponding relationships for a vector or tensor field $\mathbf{a}$ are (beyond the same definiton (5) with $f = \mathbf{a}$)

$$\overline{\nabla \cdot \mathbf{a}} = \overline{X_1 \nabla \cdot \mathbf{a} + X_2 \nabla \cdot \mathbf{a}} = \overline{X_1 \nabla \cdot \mathbf{a}} + \overline{X_2 \nabla \cdot \mathbf{a}}, \tag{8}$$

$$\overline{\nabla \cdot \underline{\mathbf{a}}} = \nabla \cdot \overline{\left(X_1 \underline{\mathbf{a}} + X_2 \underline{\mathbf{a}}\right)} - \overline{\left(\underline{\mathbf{a}} \cdot \nabla X_1 + \underline{\mathbf{a}} \cdot \nabla X_2\right)} =$$

$$= \nabla \cdot \bar{\underline{\mathbf{a}}} - \overline{\left[\left[\underline{\mathbf{a}}\right]\right] \cdot \nabla X_k} \tag{9}$$

The instantaneous values f(t, x) of physical quantities (scalar, vector or tensors) displaying time variations are considered as sum of a mean value $\bar{f}$ and of a turbulent fluctuation f'. Applying the volume-averaging procedure upon Eulerian cells, the following averaged forms of the governing equations are derived [9]:

Continuity equation

$$\frac{\partial}{\partial t}\left(\overline{\alpha_k}\ \overline{\rho_k^x}\right) + \nabla \cdot \left(\overline{\alpha_k}\ \overline{\rho_k^x}\ \overline{\mathbf{v}_k^{x,\rho}}\right) = \overline{\Gamma_k}; \tag{10}$$

Momentum equation

$$\frac{\partial}{\partial t}\left(\overline{\alpha_k}\ \overline{\rho_k^x}\ \overline{\mathbf{v}_k^{x,\rho}}\right) + \nabla \cdot \left(\overline{\alpha_k}\ \overline{\rho_k}\ \overline{\mathbf{v}_k^{x,\rho}}\ \overline{\mathbf{v}_k^{x,\rho}}\right) =$$

$$= \nabla \cdot \overline{\alpha_k}\left(\overline{\underline{\mathbf{T}}_k^x} + \overline{\underline{\mathbf{T}}_k^{Re}}\right) + \overline{\alpha_k}\ \overline{\rho_k^x}\ \mathbf{g} + \overline{\mathbf{v}_{ki}}\ \overline{\Gamma_k} + \overline{\mathbf{M}_k}; \tag{11}$$

Enthalpy equation

$$\frac{\partial}{\partial t}\left(\overline{\alpha_k}\ \overline{\rho_k^x}\ \overline{h_k^{x,\rho}}\right) + \nabla \cdot \left(\overline{\alpha_k}\ \overline{\rho_k^x}\ \overline{h_k^{x,\rho}}\ \overline{\mathbf{v}_k^{x,\rho}}\right) =$$

$$= -\nabla \cdot \overline{\alpha_k}\left(\overline{\mathbf{q}_k^x} + \overline{\mathbf{q}_k^{Re}}\right) + \overline{h_{ki}}\ \overline{\Gamma_k} +$$

$$+ \overline{\alpha_k}\left(\overline{\frac{\partial p_k^x}{\partial t}} + \overline{\mathbf{v}_k^{x,\rho}} \cdot \nabla \overline{p_k^x}\right) +$$

$$+ \overline{X_k\left(\frac{\partial p_k'}{\partial t} + \mathbf{v}_k \cdot \nabla p_k'\right)} + \overline{E_k} + \overline{\alpha_k}\ \overline{\underline{\mathbf{T}}_k^x} : \nabla \overline{\mathbf{v}_k^{x,\rho}} +$$

$$+ \overline{X_k \underline{\tau} : \nabla \mathbf{v}_k'} - \overline{X_k p \nabla \cdot \mathbf{v}_k'} + \overline{\alpha_k}\ \overline{\rho_k^x}\ \overline{r_k^{x,\rho}}; \tag{12}$$

Entropy inequality

$$\frac{\partial}{\partial t}\left(\overline{\alpha_k}\ \overline{\rho_k^x}\ \overline{s_k^{x,\rho}}\right) + \nabla \cdot \left(\overline{\alpha_k}\ \overline{\rho_k^x}\ \overline{\mathbf{v}_k^{x,\rho}}\ \overline{s_k^{x,\rho}}\right) -$$

$$- \nabla \cdot \overline{\alpha_k}\left(\overline{\boldsymbol{\Phi}_k^x} + \overline{\boldsymbol{\Phi}_k^{Re}}\right) - \overline{s_{ki}}\ \overline{\Gamma_k} - \overline{s_k} -$$

$$- \overline{\alpha_k}\ \overline{\rho_k^x}\ \overline{\sigma_k^{x,\rho}} = \overline{\Delta s_k} \geq 0, \tag{13}$$

with

$$\overline{\Delta s_k} = \overline{X_k \mathbf{q} \cdot \nabla\left(\frac{1}{T}\right)} + \overline{X_k \left|\frac{\underline{\tau}}{T} : \left(\overline{\mathbf{v}_k^{x,\rho}} + \mathbf{v}_k'\right)\right|} \tag{14}$$

The respective averaged jump conditions are:

(Mass)

$$\overline{\Gamma_1} + \overline{\Gamma_2} = 0; \tag{15}$$

(Momentum)

$$\mathbf{M}_1 + \mathbf{M}_2 + \overline{\mathbf{v}_{1i}}\ \overline{\Gamma_1} + \overline{\mathbf{v}_{2i}}\ \overline{\Gamma_2} = \tag{16}$$

$$= \overline{\left(\mathbf{n}_j \cdot \nabla X_j\right) m_i^{\sigma}} \quad (j = 1 \text{ or } 2);$$

(Enthalpy)

$$\sum_1^2{}_k \left(\overline{E_k} + \overline{h_{ki}}\ \overline{\Gamma_k} - \overline{p\,(\mathbf{v}_k - \mathbf{v}_i) \cdot \nabla X_k}\right) =$$

$$= \overline{\left(\mathbf{n}_j \cdot \nabla X_j\right) q_i}; \tag{17}$$

(Entropy)

$$\overline{s_1} + \overline{s_2} + \overline{s_{1i}}\ \overline{\Gamma_1} + \overline{s_{2i}}\ \overline{\Gamma_2} = \Delta s_i \geq 0 \tag{18}$$

In the above equations (10) - (18) we defined $\bar{\alpha}_k = \overline{X_k}$ and the following classes of averages:

i) Volume weighted averages

$$\overline{f_k^x} = \overline{X_k f} \;/\; \overline{\alpha_k} \tag{19}$$

for the set of variables

$$f = \left\{ \rho,\ \mathbf{q},\ \underline{\mathbf{T}},\ p\underline{\mathbf{I}},\ \frac{\underline{\mathbf{t}}}{T},\ \frac{\mathbf{q}}{T} \right\},$$

yielding the set of averages

$$\left\{ \overline{\rho_k^x},\ \overline{\mathbf{q}_k^x},\ \overline{\underline{\mathbf{T}}_k^x},\ \overline{\mathbf{p}_k^x},\ \overline{\underline{\mathbf{t}}_k^x},\ \overline{\Phi_k^x} \right\};$$

ii) Mass weighted averages

$$\overline{f_k^{x,\rho}} = \overline{X_k \rho f} \;/\; \overline{\alpha_k}\ \overline{\rho_k^x} \tag{20}$$

for the set of variables

$$f = \left\{ \mathbf{v},\ h,\ r,\ \frac{r}{T},\ s \right\},$$

yielding the set of averages

$$\left\{ \overline{\mathbf{v}_k^{x,\rho}},\ \overline{h_k^{x,\rho}},\ \overline{r_k^{x,\rho}},\ \overline{o_k^{x,\rho}},\ \overline{s_k^{x,\rho}} \right\};$$

iii) Averages over the interface between the phases

$$\overline{f_{ki}} = \overline{\rho f\,(\mathbf{v} - \mathbf{v}_i)\cdot\nabla X_k} \;/\; \overline{\Gamma_k}, \tag{21}$$

with

$$\overline{\Gamma_k} = \overline{\rho\,(\mathbf{v} - \mathbf{v}_i)\cdot\nabla X_k}, \tag{22}$$

for the set of variables

$$f = \left\{ \mathbf{v},\ h,\ s \right\},$$

yielding the set of averages

$$\left\{ \overline{\mathbf{v}_{ki}},\ \overline{h_{ki}},\ \overline{s_{ki}} \right\};$$

iv) Averages of diffusive fluxes

$$\overline{f_k} = \overline{f\cdot\nabla X_k} \tag{23}$$

for the set of variables

$$f = \left\{ -\underline{\mathbf{T}},\ \mathbf{q},\ \frac{\mathbf{q}}{T} \right\},$$

yielding the set of averages

$$\left\{ \overline{\mathbf{M}_k},\ \overline{E_k},\ \overline{s_k} \right\};$$

v) Averages of turbulent fluctuations

$$\overline{f_k^{Re}} = \overline{X_k \rho\, \mathbf{v}_k' f'} \;/\; \overline{\alpha_k} \tag{24}$$

for the set of variables

$$f = \left\{ -\mathbf{v}',\ h',\ -s' \right\},$$

yielding the set of averages

$$\left\{ \overline{\underline{\mathbf{T}}_k^{Re}},\ \overline{\mathbf{q}_k^{Re}},\ \overline{\Phi_k^{Re}} \right\}$$

Equations (10) - (18) are the basis for two-phase flow modelling of separated phases. Constitutive equations must be chosen for closing the system in dependence of the flow regime modelled, as reviewed in detail in reference [4].

Conservation equations for the fluid mixture

Conservation equations for the fluid mixture form the basis for modelling of two-phase flow in the frame of a slip model. They have been derived from the equations of separated phases in terms of slip velocity $\mathbf{v}_{Sl} = \overline{\mathbf{v}}_2^{x,\rho} - \overline{\mathbf{v}}_1^{x,\rho}$. Furthermore, for every physical quantity f_k we define a "phase shift" as difference between mean value for the phase and value for the mixture f_m (defined hereafter), i.e.: $\tilde{f}_k = \overline{f}_k - f_m$. The resulting conservation equations in terms of slip velocity are [9]:

Continuity equation

$$\frac{\partial \rho_m}{\partial t} + \nabla\cdot(\rho_m \mathbf{v}_m) = 0; \tag{25}$$

Momentum equation

$$\frac{\partial}{\partial t}(\rho_m \mathbf{v}_m) + \nabla\cdot\left[\rho_m \mathbf{v}_m \mathbf{v}_m + \frac{\overline{\alpha_1}\,\overline{\alpha_2}\,\overline{\rho_1^x}\,\overline{\rho_2^x}}{\rho_m}\mathbf{v}_{Sl}\mathbf{v}_{Sl}\right] =$$

$$= \nabla\cdot\left[\underline{\mathbf{t}}_m + \underline{\mathbf{T}}_m^{Re} + \frac{1}{\rho_m}\overline{\alpha_1}\,\overline{\alpha_2}\left(\overline{\rho_1^x} - \overline{\rho_2^x}\right)\times\right.$$

$$\left.\times\left(\overline{\underline{\mathbf{t}}_2^x} - \overline{\underline{\mathbf{t}}_1^x} + \overline{\underline{\mathbf{T}}_2^{Re}} - \overline{\underline{\mathbf{T}}_1^{Re}}\right)\right] + \rho_m \mathbf{g} +$$

$$+ \sum_1^2{}_k\left[\overline{\mathbf{v}_{ki}\,\Gamma_k} - \overline{\alpha_k}\,\nabla\overline{p_k^x} + \left(\overline{p_{ki}^x} - \overline{p_k^x}\right)\nabla\overline{\alpha_k} + \right.$$

$$\left. + \overline{p_k'\nabla X_k} - \overline{\underline{\mathbf{t}}_k'\cdot\nabla X_k} - \overline{\underline{\mathbf{t}}_{ki}'}\cdot\nabla\overline{\alpha_k}\right]; \tag{26}$$

Enthalpy equation

$$\frac{\partial}{\partial t}(\rho_m h_m) + \nabla\cdot(\rho_m h_m \mathbf{v}_m) +$$

$$+ \nabla\cdot\left[\frac{\overline{\alpha_1}\,\overline{\alpha_2}\,\overline{\rho_1^x}\,\overline{\rho_2^x}}{\rho_m}\left(\overline{h_2^{x,\rho}} - \overline{h_1^{x,\rho}}\right)\mathbf{v}_{Sl}\right] =$$

$$= -\nabla\cdot\left[\mathbf{q}_m + \overline{\overline{\mathbf{q}}}_m^{Re} + \frac{1}{\rho_m}\overline{\alpha_1}\,\overline{\alpha_2}\times\right.$$

$$\left.\times\left(\overline{\rho_1^x} - \overline{\rho_2^x}\right)\left(\overline{\mathbf{q}_2^x} - \overline{\mathbf{q}_1^x} + \overline{\overline{\mathbf{q}}}_2^{Re} - \overline{\overline{\mathbf{q}}}_1^{Re}\right)\right] +$$

$$+ \frac{\partial p_m}{\partial t} + \mathbf{v}_m\cdot\nabla p_m + \frac{\overline{\alpha_1}\,\overline{\alpha_2}}{\rho_m}\left(\overline{\rho_1^x} - \overline{\rho_2^x}\right)\mathbf{v}_{Sl}\cdot\nabla p_m +$$

$$+ \bar{\varepsilon} + D_m + \rho_m r_m + W_m +$$

$$+ \sum_1^2{}_k\left[-\frac{1}{2}\overline{v_{ki}^2\,\Gamma_k} + \frac{\overline{p_k^x}}{\overline{\rho_k^x}}\overline{\Gamma_k} + \right.$$

$$\left. + \overline{(\underline{\mathbf{T}}_k\cdot\mathbf{v}_k)\cdot\nabla X_k} + \overline{\alpha_k}\,\overline{\underline{\mathbf{T}}_k^x} : \nabla\overline{\mathbf{v}_k^{x,\rho}}\right]; \tag{27}$$

Entropy inequality

$$\frac{\partial}{\partial t}(\rho_m s_m) + \nabla\cdot(\rho_m s_m \mathbf{v}_m) +$$

$$+ \nabla\cdot\left[\frac{\overline{\alpha_1}\,\overline{\alpha_2}\,\overline{\rho_1^x}\,\overline{\rho_2^x}}{\rho_m}\left(\overline{s_2^{x,\rho}} - \overline{s_1^{x,\rho}}\right)\mathbf{v}_{Sl}\right] -$$

$$- \nabla\cdot\left[\Phi_m + \Phi_m^{Re} + \frac{\overline{\alpha_1}\,\overline{\alpha_2}}{\rho_m}\left(\overline{\rho_1^x} - \overline{\rho_2^x}\right)\times\right.$$

$$\left.\times\left(\overline{\Phi_2^x} - \overline{\Phi_1^x} + \overline{\Phi_2^{Re}} - \overline{\Phi_1^{Re}}\right)\right] -$$

$$- \rho_m o_m = \overline{\Delta s_1} + \overline{\Delta s_2} + \Delta s_i \geq 0. \tag{28}$$

In the above equations we used the following definitions of volume and mass weighted averages for the fluid mixture:

i) Volume weighted averages

$$f_m = \overline{\alpha_1}\ \overline{f_1} + \overline{\alpha_2}\ \overline{f_2^x} = \sum_1^2 {}_k\ \overline{X_k f} \qquad (29)$$

for the set of variables

$$\overline{f_k} = \left\{ \overline{\rho_k^x},\ \overline{p_k^x},\ \overline{D_k} = \frac{\overline{X_k\, \underline{\tau} : \nabla \mathbf{v}_k}}{\overline{\alpha_k}} \right\}$$

yielding the set of averages

$$\left\{ \rho_m,\ p_m \quad D_m \right\};$$

ii) Mass weighted averages

$$f_m = \frac{1}{\rho_m} \left(\overline{\alpha_1}\ \overline{\rho_1^x}\ \overline{f_1} + \overline{\alpha_2}\ \overline{\rho_2^x}\ \overline{f_2} \right) \qquad (30)$$

for the set of variables

$$\overline{f_k} = \left\{ \overline{\mathbf{v}_k^{x,\rho}},\ \overline{h_k^{x,\rho}},\ \overline{s_k^{x,\rho}},\ \overline{\omega_k^{x,\rho}},\ \overline{\underline{\tau}_k^x},\ \overline{r_k^{x,\rho}},\right.$$

$$\left. \overline{\underline{\mathbf{T}}_k^{Re}},\ \overline{\mathbf{q}_k^x},\ \overline{\hat{\mathbf{q}}_k^{Re}},\ \overline{\mathbf{d}_k^x},\ \overline{\Phi_k^{Re}} \right\},$$

yielding the set of averages

$$\left\{ \mathbf{v}_m,\ h_m,\ s_m,\ \omega_m,\ \underline{\tau}_m,\ r_m,\ \underline{\mathbf{T}}_m^{Re},\ \mathbf{q}_m,\ \hat{\mathbf{q}}_m^{Re},\ \Phi_m,\ \Phi_m^{Re} \right\}$$

Furthermore the following definitions have been used:

$$W_m = \sum_1^2 {}_k \left| \overline{X_k \left(\frac{\partial p_k}{\partial t} + \mathbf{v}_k \cdot \nabla p_k \right)} + \right.$$

$$\left. + \overline{\alpha_k} \left(\frac{\partial \tilde{p}_k}{\partial t} + \overline{\mathbf{v}_k^{x,\rho}} \cdot \nabla \tilde{p}_k \right) - \overline{X_k\ \rho_k \nabla \cdot \mathbf{v}_k} \right|, \qquad (31)$$

$$\bar{\varepsilon} = \sum_1^2 {}_k \left| \overline{\mathbf{q}_k \cdot \nabla X_k} - \overline{\left(\underline{\mathbf{T}}_k \cdot \mathbf{v}_k \right) \cdot \nabla X_k} + \left(\overline{h_k^{x,\rho}} - \frac{\overline{p_k^x}}{\overline{\rho_k^x}} \right) \overline{\Gamma_k} + \right.$$

$$\left. + \frac{1}{2}\ \overline{\rho\, v_k^2 \left(\mathbf{v}_k - \mathbf{v}_i \right) \cdot \nabla X_k} \right|. \qquad (32)$$

When two phases of a single component are in thermodynamic equilibrium with quality

$$x = \frac{h_m - \overline{h_1^{x,\rho}}}{\overline{h_2^{x,\rho}} - \overline{h_1^{x,\rho}}}, \qquad (33)$$

the above equations (25) - (28) are further simplified by means of the identity (see [9] for details)

$$\overline{\alpha_1}\ \overline{\alpha_2}\ \overline{\rho_1}\ \overline{\rho_2} = x\,(1-x)\,\rho_m^2. \qquad (34)$$

NUMERICAL TREATMENT OF GOVERNING EQUATIONS

Derivation of Poisson-like equations

Expressing the shear stress tensors in terms of velocity components and with suitable choice of a diffusion coefficient Γ_ψ and a source term S_ψ all above equation can be written in the generalized form [5]

$$\frac{\partial (\rho\psi)}{\partial t} + \nabla \cdot (\rho\, \psi\, \mathbf{v}) = \nabla \cdot \left(\Gamma_\psi\ \nabla \Psi \right) + S_\psi \qquad (35)$$

or

$$\frac{\partial (\rho\psi)}{\partial t} + \nabla \cdot J_\psi = S_\psi, \qquad (36)$$

with the definition of the total (convective plus diffusive) flux $J_\psi = \rho\psi\mathbf{v} - \Gamma_\psi\ \nabla\Psi$.

Let us consider a control cell around a node (i, j, k) and denote V_f the fluid volume in the cell and $A_{f,\,i\pm 1/2}$, $A_{f,\,j\pm 1/2}$, $A_{f,\,k\pm 1/2}$ the cross flow areas of the surfaces bounding the cell in the x, y, z directions, respectively. Integrating eq. (36) over the cell volume and applying the divergence theorem yields

$$\int_{V_f} \left| \partial(\rho\psi)/\partial t \right| dV + \int_{A_{f,\,i+1/2}} J_{\psi i}\, dA - \int_{A_{f,\,i-1/2}} J_{\psi i}\, dA +$$

$$+ \int_{A_{f,\,j+1/2}} J_{\psi j}\, dA - \int_{A_{f,\,j-1/2}} J_{\psi i}\, dA + \int_{A_{f,\,k+1/2}} J_{\psi k}\, dA -$$

$$- \int_{A_{f,\,k-1/2}} J_{\psi k}\, dA = \int_{V_f} S_\psi\, dV. \qquad (37)$$

The time dependent term can be discretized explicitly. Using the definitions of the mean values of the fluxes J_ψ's over the bounding surfaces and of mean values over the fluid volume V_f, the above equation is transformed into an algebraic equation for the seven unknowns ψ_β ($\beta = 0, 1, \ldots, 6$) at time t_{n+1}:

$$a_o \psi_o^{n+1} + \sum_{\beta=1}^{6} a_\beta \psi_\beta^{n+1} = b_o^{n+1}. \qquad (38)$$

Index o refers to the centre node (i, j, k) considered, while indices (1, 2), (3, 4), (5, 6) refer to the neigbouring nodes in the three coordinate directions. The right-hand side of eq. (38) collects all known terms at time level t_n and also terms at time level t_{n+1}.

Convective terms in eq. (37) are usually discretized with upwind differencing, which is however affected by numerical diffusion. The problem of minimizing the numerical diffusion has been tackeled in an advanced version (unpublished) of COMMIX-2 by introducing the QUICK interpolation scheme by Leonard [10] with the FRAM-filtering [11] of undesired wiggles.

Eq. (38) is formally identical with the equation which would be obtained by discretizing a Poisson equation. In case of the enthalpy equation $\psi = h$.

In case of the momentum equations, eq. (37) is actually combined with the continuity equation of the respective phase before being linearized to an algebraic equation. This process, the so called "pressure solution method" is equivalent, from an analytical viewpoint, to taking the divergence of the momentum equation written in vector form. It yields a Poisson-like equation for pressure ($\psi = p$). The analytical development involved is complex and cannot be explained here, but we refer to [5] where all details are given.

Solution of the Poisson equations

Both codes COMMIX and BACCHUS have several options for the numerical solution of the above Poisson-like equations for pressure and enthalpy. We distinguish between "Point" (cell by cell), "Line" and "Block" methods and between "iterative" and "direct" schemes, the latter being characterized by a fixed number of arithmetic operations performed for every solution. A "line" corresponds to all cells aligned along a coordinate direction, while a "block" contains all cells in plane perpendicular to one of the coordinate axes. Other definitions of blocks or lines are however possible.

i) Point methods. Of almost only historical interest is the Gauss-Seidel Point-SOR (Successive Over-Relaxation) iteration scheme given by

$$a_o \psi_o^r = b_o^{r-1} - a_1 \psi_1^r - a_3 \psi_3^r - a_5 \psi_5^r - a_2 \psi_2^{r-1} -$$

$$- a_4 \psi_4^{r-1} - a_6 \psi_6^{r-1}, \qquad (39)$$

were r is an iteration index. This method is easily implemented in the most general cases of definition domains with irregular shapes, but its convergence rate is usually poor. A substantial improvement of the convergence rate of the scheme is obtained by introducing a relaxation parameter ω and using the residuals

$$D_o^r = a_o \psi_o^r + \sum_{\beta = 1,3,5} a_\beta \psi_\beta^r + \sum_{\beta = 2,4,6} a_\beta \psi_\beta^{r-1} - b_o^{r-1} \qquad (40)$$

to update the dependent variable with a Newton-Raphson iteration

$$\psi_o^{r+1} = \psi_o^r - \omega \left(\partial \psi_o^r / \partial D_o^r \right) D_o^r = \psi_o^r - \frac{\omega D_o^r}{a_o} . \qquad (41)$$

The single-phase variant -1B of the code COMMIX has been provided with an advanced Conjugate Gradient algorithm for the pressure solution [12].

ii) Method of lines. The basic Alternating Direction Implicit (ADI) method is based on the concepts originally developed in the two-dimensional case by Peaceman and Rachford [13] and extended to three dimensions by Douglas [14]. These algorithms are not suitable however for vector computers. Recently astrophysicists developed an advanced algorithm [15] which is suitable for vectorization and allows gains in computational speed by a factor of ten with respect to the classical variants. We adapted this advanced variant to two-phase flow computations in the code BACCHUS (KfK interim report, yet unpublished).

iii) Direct and iterative block methods. The availability of large storage area in modern computers makes it now possible to solve, at least for problems with up to some ten-thousand computational cells, the system of eqs. (38) by means of direct methods. We have implemented in both COMMIX and BACCHUS codes the method of Doolittle [16] which uses a decomposition of the matrix of coefficients of equation (38) into a product of a lower triangular matrix **L** and an upper triangular matrix **U** so that the system can be written in matrix form

$$(\mathbf{LU})\ \{\psi\} = \{\mathbf{B}\}, \qquad (42)$$

where $\{\psi\}$ and $\{\mathbf{B}\}$ are the vectors of the unknowns and of the right side of eq. (38), respectively. Letting $\mathbf{U}\{\psi\} = \mathbf{Y}$, one has to solve first the system

$$(\mathbf{LY}) = \{\mathbf{B}\}, \qquad (43)$$

with respect to **Y**, and then the system

$$\mathbf{U}\ \{\psi\} = \mathbf{Y}, \qquad (44)$$

which yields the solution $\{\psi\} = \mathbf{U}^{-1}\,\mathbf{Y}$.

The computational time required to solve eq. (38) with the Doolittle method applied to the full domain, considered as a single block, is roughly proportional to the third power of the bandwith of the matrix of coefficients and requires a storage area which is proportional to the number of elements within the band of the matrix. For large problems both the storage requirement and the computing time become too large. For these cases we have developed options which consist in applying the Doolittle method to the planes perpendicular to one coordinate axis, then iterating over the planes. Choosing the planes perpendicular to the x-axis, the numerical scheme is expressed by the algorithm

$$a_o \psi_o^{r+1} + \sum_{\beta = 3}^{6} a_\beta \psi_\beta^{r+1} = b_o^r - a_1 \psi_1^r - a_2 \psi_2^r . \qquad (45)$$

APPLICATION OF THE ABOVE METHODOLOGY

Our experience in applying the methodology explained in the above sections, from both viewpoints of physical modelling and of numerical approach, has been gained with the development and verification, in team work, of the two computer programmes BACCHUS-3D/TP and COMMIX-2. In this section we summarize the validation work made for these two codes.

In the framework of safety analysis of LMFBRs the earlier Fast Breeder Reactor Project at KfK has sponsored the development of a computer programme describing the multi-dimensional thermal-hydraulic behaviour of a fuel rod bundle under nominal and accident conditions. The simulation of the coolant behaviour of a single phase flow up to boiling inception, in a three-dimensional approximation of the bundle geometry (the hexagonal rod array typical of LMFBRs), has been made with the code BACCHUS-3D/SP (Single Phase). This programme version has been documented from the theoretical viewpoint in 1983, in ref. [17], and its experimental verification has been published in ref. [18] in 1985. Unlike other programmes which describe the thermalhydraulic behaviour of LMFBR rod clusters with the so-called "subchannel-analysis" concept (triangular control cells), the programme BACCHUS relies upon the concept of volume porosities, surface permeabilities, distributed resistances and heat sources, typical of the "porous-body" model approach. The basic idea consists in grouping several subchannels to form a larger computational cell, within which the real geometrical configuration is smeared out.

The single-phase flow version of BACCHUS provided the basis and the initialization conditions for the development of the two-phase flow version of the code. At an early stage of the development two stand-alone variants became operational: the first was based on the Slip Model (SM) for the fluid mixture, which provides as a subcase the Homogeneous Equilibrium Model (HEM) if no slip between the phases is assumed; the second was based on five conservation equations for the separated phases, with only one enthalpy equation for the fluid mixture, referred to as Separated Phases Model (SPM). The state of development of these two variants of the code has been described in detail in reference [19]. An extensive verification of the SM version has been made with the numerical simulation of sodium boiling experiments in 37-pin bundle with a geometry typical of the SNR Mk-Ia core, run in the test section KNS-3 at KfK [20]. Results of this validation work have been presented in ref. [21].

Afterwards the slip model has been improved to allow for a smooth transition from the simulation of a bubbly flow to an annular flow through a slug flow regime. The so-called Improved Slip Model (ISM) has then been linked to the SPM into a combined programme with particular care paid to a consistent calculation of two-phase pressure drops in the transition between the flow regimes. The verification of the integrated code has been documented in ref. [22].

The BACCHUS programme belongs to the class of computer codes developed for rod-bundle thermal-hydraulic analysis for which a review was given by W.T. Sha in ref. [23]. The porous-body model approach has been formulated in general terms for engineering systems of arbitrary shape and complexity in the earlier references [24] and [25]. This modelling approach has been then followed in the COMMIX series of computer programmes, which describe steady state and transient three-dimensional fluid flows with heat transfer in nuclear reactor components and in multi-component systems.

It is beyond the scope of this review to make reference to all relevant validation work made in the frame of the COMMIX development. We just recall that the first operational code (Variant-1A) was documented in reference [26]. The version COMMIX-1B [27] which then followed includes substantial improvements in the turbulence modelling and, as mentioned, in the numerical solution [12].

Meanwhile the two-phase flow version, COMMIX-2 [5], had been developed at the Argonne National Laboratory on the basis of a slip model with a (not-yet operational) option for a model of separated phases. The validation of the slip model has been documented in ref. [28].

The most recent trend in reactor safety analysis aims at providing inherent coolant capabilities by means of passive natural convection heat removal. It thus implies the need for codes simulating flow behaviour in natural convection experiments within complex engineering systems. A recent verification of the COMMIX code in this domain has been documented in ref. [29].

REFERENCES

[1] Bird, R.B., Stewart, W.E., Lightfoot, E.N., "Transport Phenomena", John Wiley and Sons, 1960.

[2] Ishii, M., "Thermo-fluid Dynamic Theory of Two-Phase Flow", Eyrolles, Paris, 1975.

[3] Delhaye, D.M., Giot, M., Riethmuller, M.L., editors, "Thermohydraulics of Two-Phase Systems for Industrial Design and Nuclear Engineering", Hemisphere Publishing Corporation, 1981.

[4] Drew, D.A., Wood, R.T., "Overview and Taxonomy of Models and Methods", International Workshop on Two-Phase Flow Fundamentals, September 22 - 27, 1985, Minnesota University, Minneapolis, USA. DOE/ER/13056-1, 1986.

[5] Bottoni, M. et al., "COMMIX-2', A Three-Dimensional Transient Computer Program for Thermal-Hydraulic Analysis of Two-Phase Flows", NUREG/CR 4371, ANL-85-47 (September 1985).

[6] Bottoni, M., Dorr, B., Homann, Ch., "The Three-Dimensional Transient Two-Phase Flow Computer Programme BACCHUS-3D/TD", KfK 4760, in print.

[7] Hetsroni, G. (Editor), "Handbook of Multiphase Systems", McGraw-Hill, 1982.

[8] Arnold, G.S., Drew, D.A., Lahey, R.T. Jr., "An Assessment of Multiphase Flow Models Using the Second Law of Thermodynamics", Int. J. Multiphase Flow, 16, No. 3 (1990), 481-494.

[9] Bottoni, M., Sengpiel, W., "Review of Mathematical and Physical Basis of Two-Phase Flow Modelling", KfK 4759, in print.

[10] Leonard, B.P., " A Stable and Accurate Convective Modelling Procedure Based on Quadratic Upstream Interpolation", Comp. Methods Appl. Mech. Eng., 19 (1979), 59-98.

[11] Chapman, M., "FRAM-Non Linear Damping Algorithms for the Continuity Equation", J. Comp. Phys. 44 (1981), 84-103.

[12] King, J.B., Anghaie, S., Domanus, H., "Application of Conjugate Gradient Method to COMMIX-1B Three-Dimensional Momentum Equation", Int. Topl. Mtg. Advances in Reactor Physics, Mathematics and Computation, Paris, April 27-30, 1987.

[13] Peaceman, D.W., Rachford, H.H., "The Numerical Solution of Parabolic and Elliptic Differential Equations", J. Soc. Indust. Appl. Math. 3 (1955), 28 - 41.

[14] Douglas, J., "Alternating Direction Methods for Three Space Variables", Numerische Mathematik 4 (1962), 41-63.

[15] Messina, A., Londrillo, P., "A N-Body Code for Elliptical Galaxies", Super-computing in Astrophysics. Astronet Special Publication 88/1, Rome, 1988.

[16] Fox, L., "An Introduction to Numerical Linear Algebra" (Clarendon Press, Oxford, 1964).

[17] Bottoni, M., Dorr, B., Homann, Ch., Struwe, D., "BACCHUS-3D/SP; A Computer Programme for the Three-Dimensional Description of Sodium Single-Phase Flow in Bundle Geometry", Report KfK 3376 (July 1983).

[18] Bottoni, M., Dorr, B., Homann, Ch., Struwe, D., "BACCHUS 3D/SP, a Computer Programme to Describe Transient Three-Dimensional Single Phase Flow in LMFBR Rod Bundles", Nuclear Technology 71 (1985), 43-67.

[19] Bottoni, M., Dorr, B., Homann, Ch., Struwe, D., "State of Development of the Computer Programme BACCHUS-3D/TP for the Description of Transient Two-Phase Flow Conditions in LMFBR Fuel Pin Bundles", Nuclear Engineering and Design 100 (1987), 321-349.

[20] Huber, F., Kaiser, A., Mattes, Peppler, W., Till, W., "Loss of Flow Experiments in Sodium with an Electrically Heated 37-pin Bundle with Sinusoidal Axial Heat Flux Distribution". ANS/ENS Int. Topical Meeting on LMFBR Safety, and Related Design and Operational Aspects, Lyon, France, July 19-22, 1982.

[21] Bottoni, M., Dorr, B., Homann, Ch., Huber, F., Mattes, K., Peppler, F.W., Struwe, D.; "Experimental and Numerical Investigations of Sodium Boiling Experiments in Pin Bundle Geometry", Nuclear Technology, 89 (1990), 56-82.

[22] Bottoni, M., Dorr, B., Homann, Ch., "Flow Regime Dependent Modelling of Two-Phase Flows in 3D-Subassembly Geometry and its Experimental Validation", Proc. ANS/ENS Int. Conf., Snowbird, Utah, August 12-16, 1990.

[23] Sha, W.T., "An Overview on Rod-Bundle Thermal-Hydraulic Analysis", Nuclear Engineering and Design 62 (1980), 1-24.

[24] Sha, W.T., Domanus, H.M., Schmitt, R.C., Oras, J.J., Lin, E.I.H., Shah, V.L. "A New Approach for Rod-Bundle Thermal-Hydraulic Analysis", ENS/ANS Int. Topical Meeting on Nuclear Power Reactor Safety, Brussel, October 16-19, 1978.

[25] Sha, W.T., Chao, B.T., Soo, S.L., "Local Volume-Averaged Transport Equations for Multiphase Flow in Regions Containing Distributed Solid Structures", NUREG/CR-2354, ANL-81-69.

[26] Domanus, H.M., Schmidt, R.C., Sha, W.T., Shah, V.L., "COMMIX-1A: A Three-dimensional Transient Single-Phase Computer Program for Thermal Hydraulic Analysis of Single and Multicomponent Systems", NUREG/CR-2896, Vol. s I and II, 1983.

[27] Shah, V.L., et.al., "COMMIX-1B: A Three Dimensional Transient Single-Phase Computer Program for Thermal Hydraulic Analysis of Single and Multicomponent Systems," Vol. I: Equations and numerics; Vol. II: User's manual. ANL-85-42, NUREG/CR-4348, (Sept. 1985).

[28] Bottoni, M., Lyczkowski, R.W., Chi, H.N., Chien, T.H., Domanus, H.M., "Multidimensional Two-Phase Modeling with the COMMIX-2 Computer Program", Proc. 23rd AIChE/ASME National Heat Transfer Conference, Denver, Colorado, August 4-7, 1985.

[29] Lafortune, J.F., Meneley, D.A., "Natural Convection in a Vertical Cylinder: Comparison of COMMIX-1A Predictions with Experiment", Int. J. Heat Mass Transfer, 33 (1980), 435-445.

III ENCIT – Itapema, SC (Dezembro 1990)

VISUALIZAÇÃO DE UM ESCOAMENTO DE FREON 113 EM EBULIÇÃO SUB-RESFRIADA*

Júlio César Passos

Departamento de Engenharia Mecânica-UFRJ
C.P. 68.503-CT-Cidade Universitária
21.945 Rio de Janeiro - R.J.

Este trabalho apresenta os resultados da visualização, usando câmera rápida, de um escoamento de Freon-113, em cada um dos três regimes de ebulição e durante o fenômeno de *crise de ebulição*. A seção de teste é constituída de um duto vertical de seção transversal anular cuja parede do tubo interno é aquecida. Os testes foram realizados nas pressões de 0,15 e 0,30 MPa e nas faixas de valores de vazão mássica por unidade de tempo e de sub-resfriamento compreendidas, respectivamente, entre 146 e 611 kg/m^{2}s e entre 4,7 e 61,2°C.

INTRODUÇÃO

A determinação das várias configurações geométricas que pode assumir a interface líquido-vapor em um escoamento de um líquido em ebulição constitui um subsídio à formulação de novos modelos sobre os mecanismos de transferência de calor em ebulição. Em particular, estes estudos são relevantes quando o tipo de configuração é determinado em função da pressão (p), da vazão mássica por unidade de tempo (G), do sub-resfriamento do líquido (ΔT) ou do título de vapor (x_e), do nível de densidade de fluxo de calor (q_o), do regime de ebulição, etc.. A visualização cinematográfica, quando as paredes do duto são transparentes, permite uma descrição qualitativa das configurações presentes em um escoamento.

Vários autores, Delhaye [1], Collier [2], descrevem as principais configurações presentes em um escoamento bifásico. No caso particular de um líquido em ebulição no interior de dutos há interesse em classificar as configurações em função das condições de operação para as quais os valores de q sejam próximos dos valores que caracterizam a transição entre os regimes de ebulição nucleada (EN) e de ebulição em película (EP). Esta transição, chamada de *crise de ebulição*, é causada pela diminuição do coeficiente de troca de calor entre a parede aquecida e o fluido, Collier [2].

Mattson et al. [3] observaram que a *crise de ebulição* para o Freon-113 em escoamento, a alta pressão (pressão reduzida, p_r, compreendida entre 0,2 e 0,7), no interior de um duto horizontal de seção transversal retangular ocorre em presença de uma "camada limite de bolhas de vapor" (bolhas empilhadas que acabam por isolar a parede do líquido). Estes autores não constataram oscilações de velocidade na direção do escoamento nem mudança sensível, do ponto de vista macroscópico, entre as configurações imediatamente antes e depois da crise de ebulição.

Neste artigo, são apresentados os resultados da visualização cinematográfica de um escoamento de Freon-113, em ebulição no interior de um duto de seção transversal anular, nos três regimes de ebulição e durante a crise de ebulição.

DISPOSITIVO EXPERIMENTAL

Os experimentos foram realizados em um circuito de Freon-113, pressurizável até 1,0 MPa. A seção de teste é constituída de um tubo de Inconel (comprimento=107 mm, diâmetro externo=7 mm e espessura de parede=0,5 mm) soldado nas extremidades a dois tubos de cobre com diâmetro externo de 7 mm e espessura de parede de 1,5 mm, centrado, verticalmente, no interior de um tubo de Pyrex com diâmetro interno e comprimento medindo, respectivamente, 13 mm e 1067 mm. O tubo de Inconel é aquecido por efeito Joule e dispõe de seis termopares (TP) instalados, sobre uma mesma geratriz, na superfície interna, Figura 1. Os termopares são mantidos em contato com a parede interna do

* Este estudo foi realizado no *Groupe Phénomènes d'Interface* (GPI) da *Ecole Nationale Supérieure de Techniques Avancées* (ENSTA), 91120 Palaiseau-FRANÇA.

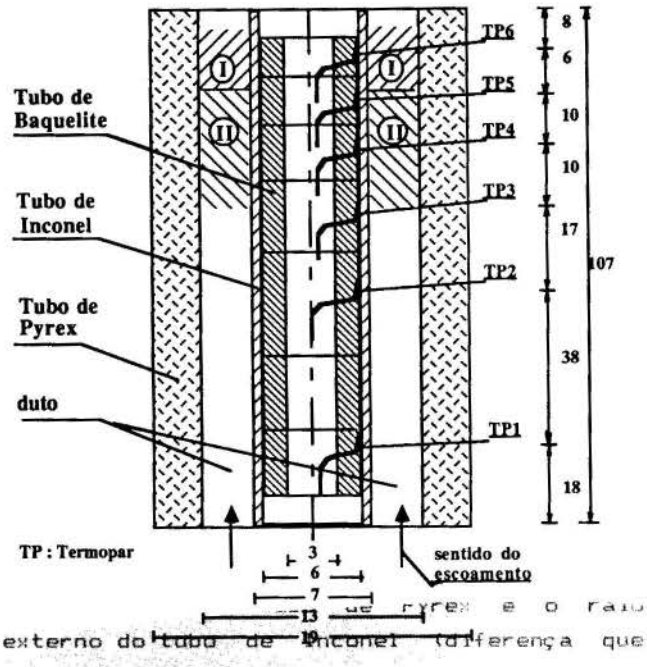

externo do tubo de Inconel (diferença que

Fig.1: Região aquecida da seção de teste.

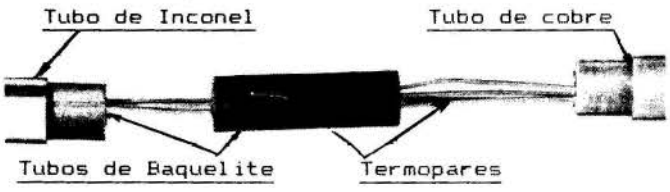

Fig.2: Detalhe de montagem dos termopares.

tubo de Inconel por meio de pequenos tubos de Baquelite, Figura 2.

Um dispositivo eletrônico, cujos detalhes de concepção e de fabricação podem ser obtidos em Gentile et al. [4], permite monitorar a corrente elétrica fornecida ao tubo, mediante o controle analógico (em *malha fechada*) do sinal fornecido por um termopar (o de nº 6, neste trabalho), permitindo, deste modo, operar o sistema no regime de ebulição de transição.

Para as filmagens, foi utilizada uma câmera rápida HYCAM, de prisma rotativo, capaz de fornecer até dez mil quadros por segundo.

Maiores detalhes do dispositivo experimental são fornecidos em [5].

PROCEDIMENTO EXPERIMENTAL E CONDIÇÃO DE TESTE

Durante a visualização, a região filmada foi iluminada pela parte posterior da seção de teste. A filmadora operou com velocidades compreendidas entre 500 e 4000 quadros por segundo, com ± 2,5% de incerteza.

Simultaneamente às filmagens, são realizadas medidas de temperatura e de q_e nas seguintes condições de teste: pressão de 0,15 MPa (p_r=0,044) e 0,30 MPa (p_r=0,088), vazão mássica por unidade de área compreendida entre 146 e 611 kg/m^{2}s e sub-resfriamento compreendido entre 4,7 e 61,2 °C.

RESULTADOS

Regime de ebulição nucleada. Na Figura 3, são apresentados quatro quadros selecionados de um filme realizado à velocidade de 1500 quadros por segundo. A região filmada corresponde à região I, indicada na Figura 1. As condições de teste são as seguintes: pressão de 0,30 MPa, G= 146 kg/m^{2}s, ΔT= 61,2 °C, x_e = 1% e q_e = 334 kW/m^2. O valor de q_e corresponde a 82% do valor crítico para o qual ocorre a *crise de ebulição*. Destaca-se, no instante inicial (referência para os quadros seguintes de cada sequência), a presença, no canto esquerdo superior da figura, de um bolsão de vapor, enquanto que do lado direito do tubo aquecido observam-se bolhas de vapor de dimensões menores. Nos dois quadros seguintes, cada lado do tubo aquecido é coberto por bolhas pequenas ou de dimensões comparáveis à diferença entre o raio interno do tubo de Pyrex e o raio externo do tubo de Inconel (diferença que será chamada de entreferro). Finalmente, à 142 ms, tem-se, praticamente, uma disposição simétrica, com relação ao eixo da seção de teste, das configurações já observadas em t=0 ms. As medidas de temperatura ao longo do tubo revelam, após correção da diferença de temperatura (= 5 °C) devido à espessura da parede, um superaquecimento médio da superfície do tubo em contato com o Freon de 20,5°C.

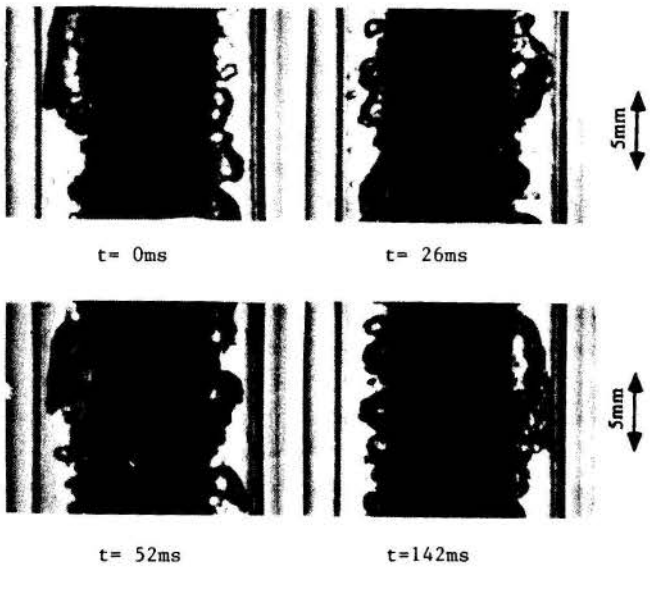

Fig. 3: Regime de ebulição nucleada (Câmera HYCAM, 1500 quadros/s).

Regime de ebulição em película. As condições de teste são indicadas sobre a Figura 4a, onde as temperaturas da superfície interna são mostradas em função da distância à entrada da região aquecida. Os termopares 5 e 6 acusam temperaturas médias próximas de 300 °C enquanto que na parte restante do tubo a temperatura média é de 67 °C. O título de vapor(**) calculado na seção de saída da região aquecida, x_e, é de - 6%. Dois quadros defasados de 20 ms, extraídos de um filme realizado a 1000 quadros/s, são apresentados na Figura 4b. A região observada compreende as regiões I e II. indicadas na Figura 1. Os dois quadros mostram configurações bem

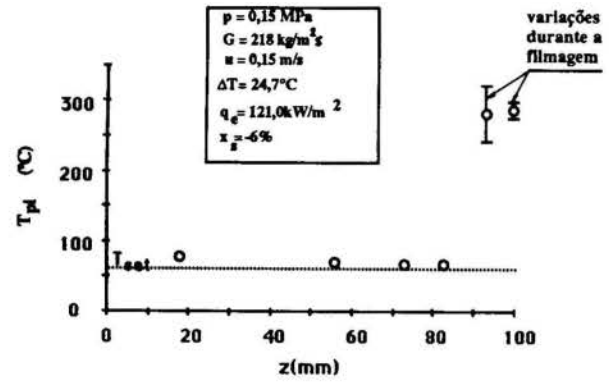

Fig.4a: Perfil de temperatura da superfície interna do tubo.

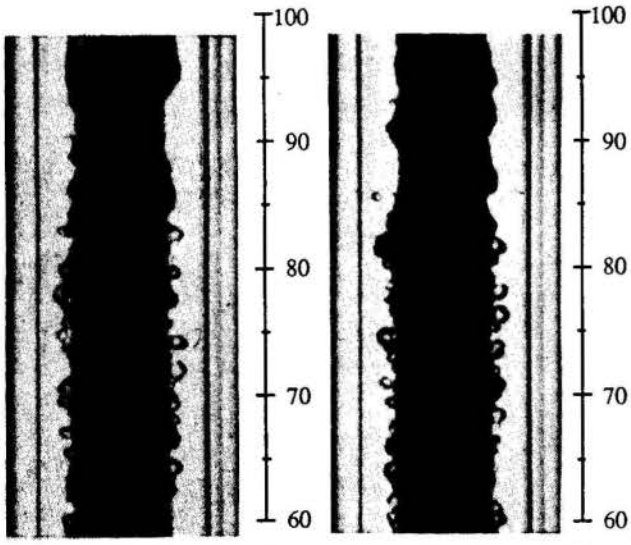

Fig.4b: Regime de ebu..ção nucleada, z<83 mm, Regime de ebulição em película, z > 83 mm. Câmera HYCAM, 1000 quadros/s.

**O título de vapor em um escoamento bifásico é calculado a partir do balanço de energia ao longo do duto, Collier [2]; e assume valores negativos quando a temperatura média do fluido, em uma seção do duto, encontra-se abaixo da temperatura de saturação. Não deve, pois, ser confundido com a definição clássica que considera o título igual à razão entre a massa de vapor e a massa total da mistura líquido-vapor, e que não pode ser calculada no caso de um escoamento.

distintas que confirmam as medidas de temperatura. Em z< 83 mm, a superfície do tubo aquecido é coberta por bolhas de vapor de pequenas dimensões (EN) e, em z>83 mm, por uma camada contínua de vapor (em escuro sobre a figura), (EP), cuja interface vapor-líquido (em claro) é marcada por instabilidades. Observa-se, em t=0 ms e 89<z<93 mm, do lado direito, que a camada de vapor é bastante fina enquanto que, para z>93 mm, a espessura máxima é de 1 mm.

A próxima visualização mostra um escoamento em que o fluido apresenta x_s = 8%. As condições de teste estão indicadas sobre as Figuras 5a e 5b que apresentam, respectivamente, q_e em função da temperatura indicada pelo TP6 e o perfil de temperatura ao longo do tubo. Dois quadros, extraídos de um filme realizado a 1500 quadros/s, são mostrados na Figura 6. Em t= 0 ms, observa-se a parede coberta por uma camada contínua de vapor, apresentando instabilidades na interface vapor-líquido, e bolhas dispersas no líquido. As bolhas interagem com a camada parietal de vapor e são criadas na parte

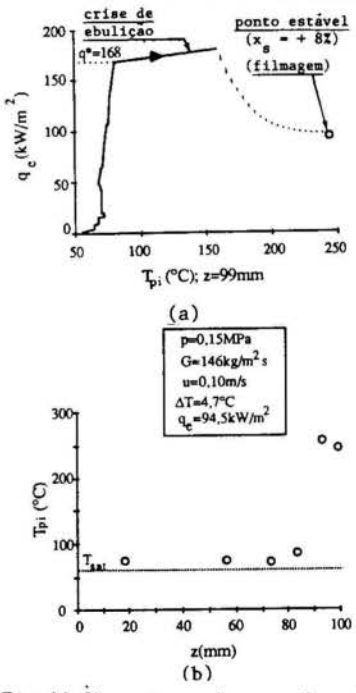

Fig.5: Condições durante a visualização.

t = 0ms t = 54ms

Fig.6: Regime de ebulição em película Câmera HYCAM, 1500 quadros/s.

inferior do tubo (não mostrada na figura), submetida, como indica o perfil de temperatura, Figura 5b, ao regime de EN. A análise do filme mostra as bolhas de vapor submetidas a flutuações de velocidade, devido às instabilidades da interface vapor-líquido, aceleradas, quando localizadas na esteira deixada pelo deslocamento de uma crista da interface, como aquela mostrada em t=54 ms, ou capturadas, por coalescência, pela camada de vapor.

Visualização da crise de ebulição. As condições de teste são as seguintes: pressão de 0,30 MPa, G= 584 kg/m^{2}s e ΔT= 60,2 °C. Nestas condições, a crise de ebulição ocorre quando q_e= 624,8 kW/m^2 e x_s= - 21%. O valor negativo para x_s, indicando condições de sub-resfriamento ao longo de toda a região aquecida, favorece a visualização da parede, pois a maior parte do entreferro é preenchida pela fase líquida.

Na Figura 7, são mostrados seis quadros ilustrando o fenômeno de crise de ebulição, com exceção do primeiro deles que ilustra as configurações presentes, imediatamente antes da crise. Observa-se, em t=0 ms e z> 85 mm, do lado esquerdo do tubo, uma bolha de vapor de forma alongada, medindo cerca de 10 mm, resultante da coalescência com outras bolhas que escapam da parede durante o seu movimento ascendente. A presença, na região superior do tubo aquecido, de bolhas de grande dimensão dificulta o acesso do líquido até a parede, permitindo que o fenômeno de crise de ebulição apareça nesta região.

O início da crise de ebulição, instante a partir do qual a temperatura local de parede aumenta continuamente, é marcado por configurações que apresentam a parede coberta, intermitentemente, por bolhas de grandes dimensões, como em t=2904 ms, e por uma camada de vapor quase contínua, em t= 2934 ms e z<83 mm. Em t=3304 ms, já não são distinguidas bolhas isoladas e 20 ms após, para z< 80 mm, o entreferro apresenta-se, praticamente, liberado de vapor. Em t=3384 ms e z> 84 mm, o processo de secagem a que está submetida a parede é ilustrado pela película de vapor que cobre a parede. A análise do filme, no trecho que corresponde a t>3284 ms, mostra um escoamento bastante instável, marcado por pulsações de velocidade das inclusões de vapor. Medidas de temperatura ao longo do tubo aquecido mostram que a crise de ebulição é detectada inicialmente pelo TP 6,

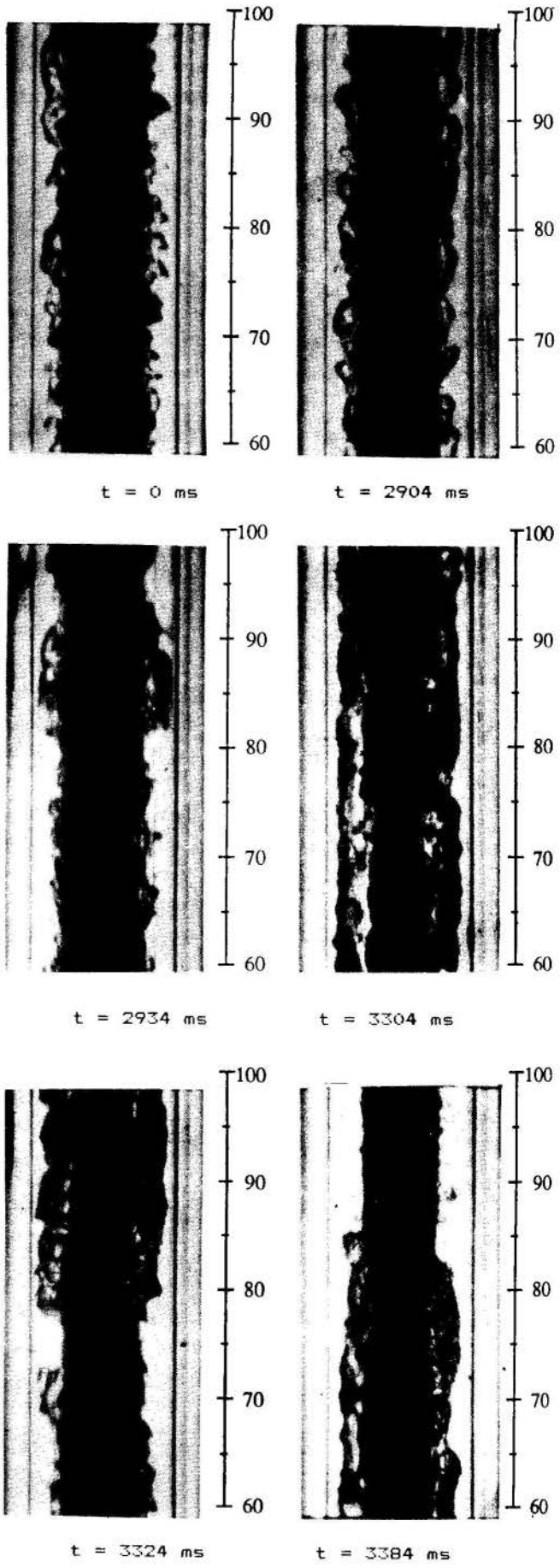

Fig.7: Visualização da *crise de ebulição* (Câmera HYCAM, 500 quadros/s).

propagando-se, em seguida, para a região inferior do tubo.

Os resultados que acabam de ser descritos diferem daqueles encontrados por Mattson et al. [3], a alta pressão. Neste estudo, a crise de ebulição parece ser consequência da evaporação de uma película líquida interposta entre a parede aquecida e uma grande bolha de vapor. Tais bolhas são observadas na Figura 3, para uma condição em que o valor de q_e é elevado, e na Figura 7, imediatamente antes da crise de ebulição.

Regime de ebulição de transição. Operando em malha fechada, foi possível visualizar o regime de ebulição de transição. Durante a filmagem, o sistema operou entre os pontos I e II, Figura 8a, e o título de vapor variou entre -11% e +7%. O termopar 6, cujo sinal foi controlado, indicou que a temperatura de parede diminuiu de 128 a 106°C durante a evolução de I a II, Figuras 8a e 8b. A visualização do escoamento é ilustrada por dois quadros, Figura 8c, defasados de 655 ms. Em t=0 ms, a maior parte do tubo é coberta por pequenas bolhas de vapor, EN, e apenas a região em que z>94 mm está sujeita ao regime de transição. Em t=655 ms, as bolhas de vapor apresentam maior volume e são comuns inclusões de vapor de forma alongada, como a observada em 60< z <70 mm ou como o bolsão de vapor em z >89 mm, do lado esquerdo do tubo.

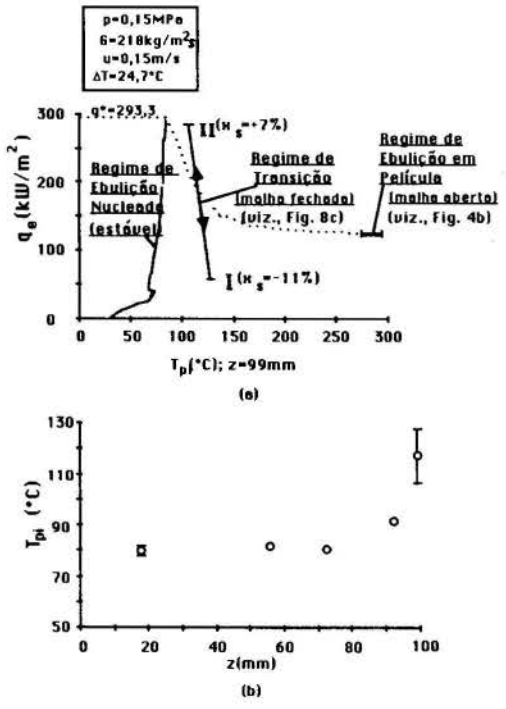

Fig.8a: Densidade de fluxo de calor em função da temperatura em z=99 mm.
b: Perfil de temperatura.

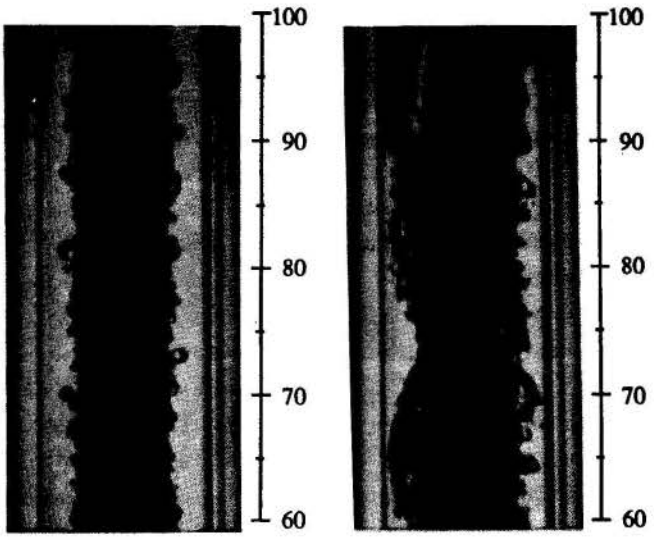

Fig.8c: Regime de transição (Câmera HYCAM, 1000 quadros/s).

A análise de outros quadros, entre 0 e 655ms, mostrou que o volume das inclusões de vapor aumenta gradativamente, à medida que o ponto de operação se desloca de I a II, Figura 8a. A interpretação deste resultado pode ser dada analisando a Figura 8a. Em t=0 ms, ponto I, a temperatura indicada pelo TP6 começa a diminuir. A fim de impedir que a região onde se encontra o termopar venha a operar no regime de EN, a corrente elétrica fornecida ao tubo é aumentada e o sistema passa a operar em II. Esta transição de I a II promove o aumento progressivo das dimensões das inclusões de vapor causando, por sua vez, o aumento da temperatura de parede. De forma a impedir a transição em direção ao regime de EP, a corrente elétrica é diminuída e o ponto de operação volta a ser I.

Um novo resultado é apresentado. Desta vez, o valor de G é aumentado e o ponto de operação se aproxima, com relação a uma curva análoga a que é apresentada na Figura 8a, do regime de EP. O perfil de temperatura e as condições de teste são apresentadas na Figura 9a. Dois quadros, extraídos de um filme realizado a 4000 quadros/s, são mostrados na Figura 9b. Observa-se a parede, do lado esquerdo, coberta por bolhas de vapor pequenas e médias enquanto, do lado direito, ela é coberta por uma camada contínua de vapor. As temperaturas em z>83 mm, Figura 9a, indicam nesta região do tubo o regime de EP ou o de transição, em concordância com o que se observa sobre a Figura 9b, do lado direito dos quadros. O que se observa do lado esquerdo, no entanto, não justifica este

nível tão elevado de temperatura já que as bolhas de vapor caracterizam um regime de EN. Este resultado foi obtido uma única vez durante este estudo e sugere a existência de gradientes de temperatura na direção azimutal. A análise do filme correspondente mostra que as bolhas de tamanho médio, observadas na Figura 9b, originam-se da ruptura da película de vapor que se estende, de forma assimétrica, até a parte inferior esquerda da região visualizada. Admite-se, como explicação do comportamento não simétrico da configuração, que tenha havido modificação das condições superficiais do lado esquerdo do tubo, devido a uma decomposição localizada do Freon, ocorrida provavelmente, em testes anteriores. Tal fato foi observado em [6], durante testes com Freon-113 em ebulição em película.

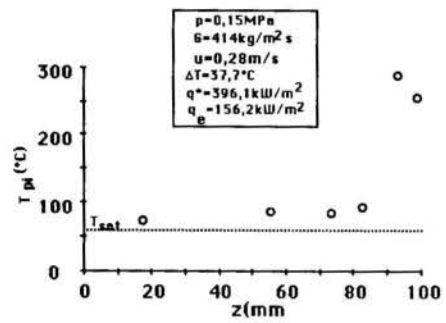

Fig.9a: Perfil de temperatura.

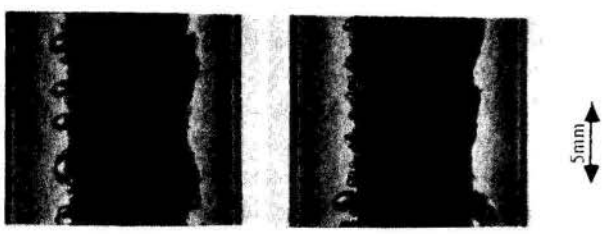

Fig.9b: Regime de transição (Câmera HYCAM, 4000 qudros/s).

CONCLUSÕES

Os resultados deste estudo de visualização revelam a presença de bolsões de vapor para condições de operação próximas da crise de ebulição, sugerindo como interpretação, que o mecanismo de crise de ebulição se deva à evaporação de uma película líquida entre a parede aquecida e o bolsão de vapor. Durante a crise de ebulição, observa-se, de forma intermitente que, após a passagem de grandes inclusões de vapor, a parede aquecida é coberta por uma película de vapor. Um resultado atípico da configuração no regime de transição mostra, em uma mesma seção do tubo, a coexistência de bolhas de um lado e de uma camada contínua de vapor do outro, permitindo supor a existência de gradientes de temperatura na direção azimutal.

AGRADECIMENTOS

Este estudo só foi possível devido às boas condições de trabalho encontradas no Centro de l'Yvette da ENSTA, FRANÇA, e ao apoio financeiro que o autor recebeu da UFRJ e através de uma bolsa de estudos concedida pela CAPES.

REFERENCIAS

[1] Delhaye, J. M., "Two Phase Flow Patterns, "Two-Phase Flow and Heat Transfer in the Power and Process Industries, Bergles et al., pp. 1-36, McGraw-Hill, 1981.

[2] Collier, J. G., "Convective Boiling and Condensation, "Ch. 1, 2nd ed., McGraw Hill, 1981.

[3] Mattson, R. J., Hammitt, F. J. and Tong, L. S., "A Photographic Study of the subcooled Flow Boiling Crisis in Freon-113," ASME-AIChE Heat Transfer Conference, Atlanta, Ga., August, paper 73-HT-39, pp. 1-8, 1973.

[4] Gentile, D., Llory, M. and Benejean, R., "Stabilization of Freon-113 Subcooled Boiling in Forced Convection, "Int. Com. Heat & Mass Transfer, Vol. 12, N° 5, pp. 521-529, 1985.

[5] Passos, J. C., "Etude Expérimentale de l'Ebullition d'un Liquide Sous-Saturè en Convection Forcée," Tese de Doutorado, Université Paris VI, França, setembro, 1989.

[6] Passos, J. C. and Gentile, .," An Experimental Investigation of Transition Boiling in Subcooled Freon 113 Forced Flow, "Transaction of ASME-Journal of Heat Transfer, aceito para publicação.

ABSTRACT

This work presents results of a photographic study, using a movie camara, operating between 500 and 4000 frames/sec, for a subcooled Freon-113 flow in three boiling regimes and, in particular, during the boiling crisis phenomenon. The test section is a circular vertical tube annulus in which the wall of the inside tube is heated. The observations include measurements of wall heated temperatures and heat flux density for different test conditions.

III ENCIT – Itapema, SC (Dezembro 1990)

THE EFFECT OF HEATER THERMAL PROPERTIES AND THICKNESS ON THE POOL BOILING CRITICAL HEAT FLUX

RICARDO D.M. CARVALHO AND ARTHUR E. BERGLES
Department of Mechanical Engineering,
Aeronautical Engineering & Mechanics
Rensselaer Polytechnic Institute
Troy, New York USA 12180–3590

SUMMARY

The present investigation reviews the current understanding of thermal conductance/capacitance effects on the CHF of thin heaters. The main issues are clearly established through direct comparison of models and respective data sets available in the literature. A criterion for obtaining CHF data free of such effects is developed. This criterion is then used to assess the soundness of existing CHF data and to discuss the simulation of electronic chips under saturated and subcooled conditions. Original data are presented.

INTRODUCTION

In laboratory experimentation, direct electrically heated tubes and strips are frequently used for simulation of indirectly heated industrial heaters or heat exchangers. When the former are used in investigations of the critical heat flux (CHF) phenomenon, the question arises as to how satisfactorily the simulation is accomplished. As early as 1960, it was already known that thin heaters exhibit CHF values lower than those of their counterparts of large mass [1]. In broad terms, the propagation of film boiling or the heater's physical destruction, after a local area of film boiling is established, depends on the heater geometry and properties. The thermal conductance and the thermal capacitance, which are functions of the heater thermal properties and thickness, are the relevant parameters in determining the temperature rise under a vapor patch (Fig. 1).

Industrial heaters have large mass, and a criterion is needed to ensure their proper simulation by electrically heated tubes and strips. Of particular interest to the present research project, a criterion is needed to ascertain the appropriateness of previous simulations of microelectronic chips by foil heaters [2]. Attempts at modelling the phenomena and developing such a criterion have been made [3,4,5,6], but the problem still remains unresolved.

The goals of the present work are two-fold:

(i) to provide guidance for the experimenter investigating the CHF phenomenon and to check whether existing correlations have been influenced by thermal conductance/capacitance effects (Part I);

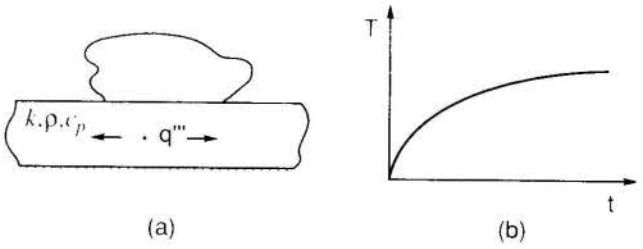

Fig. 1 (a) a vapor patch sitting on a thin heater surface and (b) the consequent temperature rise subsequent to dryout of the surface.

(ii) to discuss the simulation of electronic chips under saturated and subcooled conditions (Part II).

LITERATURE REVIEW

The CHF phenomenon has been studied extensively, both experimentally and theoretically. Bernath [1] and Ivey and Morris [7] reviewed CHF data to investigate the effect of geometry, diameter, thickness, material, and surface condition. Both authors concluded that the CHF from horizontal cylinders decreases as the thickness and diameter of the test sections are decreased. The data also indicated the occurrence of an asymptotic CHF for thick-walled cylinders. Carne [8] obtained data for the effects of diameter and wall thickness on the CHF of organic liquids boiling on horizontal cylinders. For cylinder diameters greater than 2.4 mm, a decrease in the CHF with decreasing wall thickness was also observed. Adams [9] studied the effect of heater diameter, surface tension, and multigravity on the CHF. Data were obtained for thick flat graphite heaters boiling on one side, which can be assumed uninfluenced by thermal conductance/capacitance effects. Cole and Shulman [10] presented CHF data for ribbon heaters of different thicknesses.

Lienhard and Dhir [11] developed hydrodynamic predictions for the CHF from horizontal cylinders, horizontal vertically oriented ribbons, and spheres, as a function of the corresponding characteristic length. These correlations represent the most complete set of hydrodynamic predictions, and are supposed uninfluenced by the heater thermal properties and thickness. Original data for the CHF of insulated and uninsulated ribbons were used. Park and Bergles [12] also studied the effects of size on the pool boiling CHF of vertically oriented ribbons boiling on one side. Data were presented and correlations were developed to predict the CHF as a function of both dimensionless height and width. These correlations, which do not allow for thermal conductance/capacitance effects on the data, can be applied to vertical heaters small in both directions – a geometry not investigated by previous authors.

There are relatively few papers in the literature dealing specifically with the effects of heater thermal properties and thickness on the CHF. Guglielmini and Nannei [6] obtained an extensive data set for the effect of wall thickness on the pool boiling CHF of horizontal cylinders. The thickness for which the CHF was 90% of the asymptotic value was correlated as a

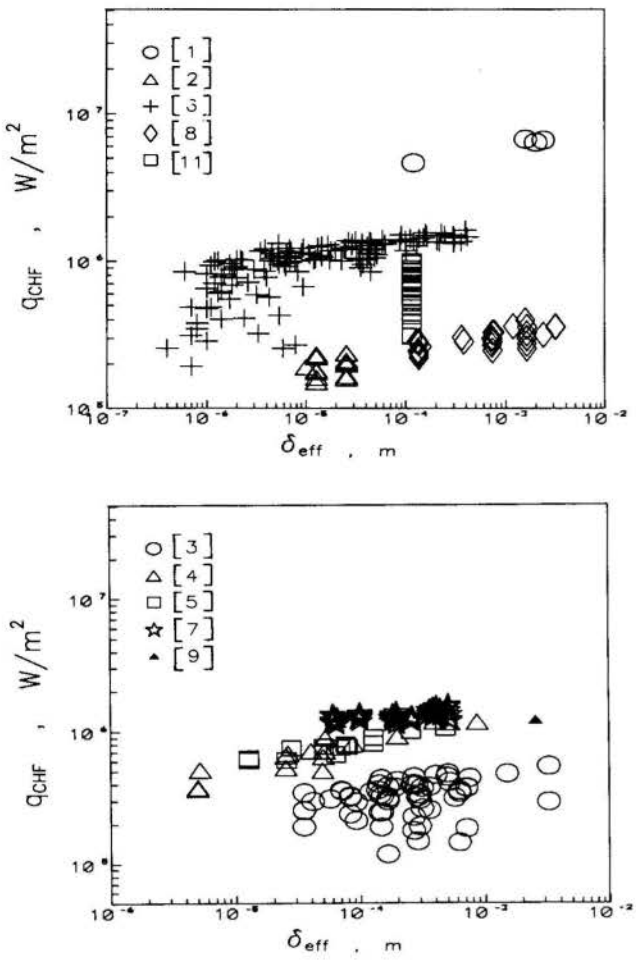

Fig. 2 Data sets for the CHF of thin heaters available in the literature.

function of the parameter $\sqrt{k\rho c_p}$. Carne and Charlesworth [3], Houchin and Lienhard [5], and Tachibana et al. [4] worked with substantially less extensive data sets to propose the only models available for the CHF of thin heaters. These models are not in agreement regarding the ultimate mechanism for the onset of the condition and, therefore, propose different correlating parameters.

Carne and Charlesworth believe that the thermal conductance ($k\delta$) is the parameter controlling the propagation of a local vapor patch and subsequent onset of the CHF condition. Tachibana et al. claim that the duration of a vapor patch, which would be one of the main factors determining the onset of the condition, is related to the thermal capacity per unit surface area ($\rho C_p \delta$). Houchin and Lienhard considered three different correlating parameters arising from different ways of modelling the phenomenon — $\rho C_p \delta$, $\rho C_p (T_{melt}-T_{sat})$, and $k\delta(T_{melt}-T_{sat})$. They concluded that the thermal capacity was the appropriate one for their own, rather limited data.

PART I : ANALYSIS OF DATA FROM THE LITERATURE

The main characteristics of the data sets used are listed in Table 1. The hydrodynamic predictions of Lienhard and Dhir [11] were used to calculate the hydrodynamic asymptotic CHF values for the geometries involved when applicable. These values represent expected CHF results for thick heaters, assuming that the correlations capture the essential features of the phenomenon and are uninfluenced by thermal conductance/capacitance effects. The experimental asymptotes are simply asymptotic CHF values inferred from the data sets themselves. However, because these data sets have only few points for thick heaters, the experimental asymptotes do not account for any scatter around a mean value.

Shown in Fig. 2 are the data sets listed in Table 1 (The data of Cole and Shulman [10] were not plotted because they were published in ratio form only.) The effective thickness δ_{eff} is the half thickness for uninsulated strips and the total thickness in the other cases. The data were grouped into two separate plots to avoid clustering. In all cases, there is a decrease in the CHF with decreasing thickness. The task at hand, therefore, is to identify which property, or combination of properties, governs the attainment of the asymptotic CHF, q''_{asy}, for different metals.

For a particular geometry, the arrangement of the data points for different metals on a $q''_{CHF} \times \delta$ plot was checked against values of k, ρc_p, $\sqrt{k\rho c_p}$, and a in an attempt to identify a systematic dependence on any of these parameters. As shown in Fig. 3 for the Houchin and Lienhard data set [5], the distribution of the CHF results for the various metals does not appear to be related to the values of the above parameters. The data seem to cluster around a common curve despite large variations in k, ρc_p, $\sqrt{k\rho c_p}$, and a.

The conclusions drawn for this and the other data sets are summarized in Table 2. In some cases, not enough data points were available so that a reliable check of the trends could be made. For data sets involving only one metal and/or only one value of the thickness, such a check could not be made at all. The results in Table 2, however, do indicate that none of the parameters above can be simply combined with the thickness to satisfactorily correlate data for the CHF of thin heaters. This testifies to the inappropriateness of previous interpretations and associated correlating parameters. A criterion for CHF data free of thermal conductance/capacitance effects was then sought in terms of the thickness only. The development of a such a criterion requires that reliable data be used. Moreover, the effects of geometry and fluid need to be taken into account.

In selecting data sets for further treatment, it was observed that the data of Guglielmini and Nannei [6] plotted substantially higher than the other authors' data. This was not simply due to a geometry effect, because the CHF values obtained exceeded the Lienhard and Dhir prediction for the CHF of horizontal cylinders [11] by as much as 50 percent. Besides, the

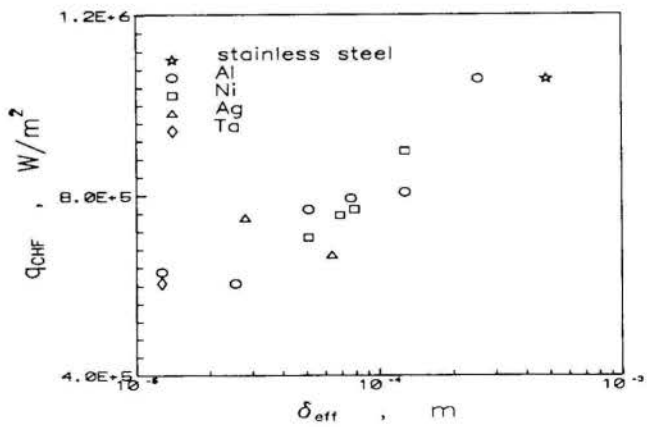

Fig. 3 The Houchin and Lienhard data set for the CHF of thin heaters [5].

Table 1 Data sets used in the present investigation

Data Set	Material(s)	Fluid(s)	Geometry	$q_{asy,hyd}$ [W/m²]	$q_{asy,exp}$ [W/m²]
Bernath [1]	Ni	subcool. water at 6.3 atm	vertical cylinder	–	6.57E6
Carne & Charlesworth [3]	inconel 600, monel 402 mild steel, BeCu, Cu	saturated n–propanol at 1 atm	hor., vert. orient., unins. strips	4.08E5	5.30E5
			hor., vert. orient., ins. strips	4.46E5	5.30E5
			hor., hor. orient., unins. strips	–	2.64E5
			hor., hor. orient., ins., up–facing strips	–	3.80E5
			hor., hor. orient., ins., down–facing strips	–	2.95E5
Tachibana et al [4]	Al, Ni, Pb, In, Mo, Cu, s. steel, phosphor bronze	sat. water at 1 atm	hor., vert. orient., unins. strips	9.95E5	1.17E6
Houchin & Lienhard [5]	Al, Ni, Ta, Ag, s. steel	sat. water at 1 atm	infin., hor., flat plate	1.26E6	1.10E6
Guglielmini & Nannei [6]	Zn, Sn, Ni, Cu	sat. water at 1 atm	horizontal cylinder	8.74E5	1.50E6[1] 1.45E6[2], 1.12E6[3]
Ivey & Morris [7]	s. steel, zircalloy	sat. water at 1 atm	horizontal cylinder	1.22E6	1.44E6
			hor., hor. orient., unins. strips	–	1.42E6
Carne [8]	steel	n–pentanol,	horizontal cylinder	–	3.30E5
		methyl ethyl ketone,		–	2.87E5
		n–butanol,		3.05E5	3.26E5
		toluene,		2.15E5	2.77E5
		acetone,		2.66E5	3.21E5
		n–propanol		3.56E5	3.59E5
Adams [9]	graphite	sat. water at 1 atm	hor., hor. orient., ins., up–facing strips	–	1.26E6
Cole & Shulman [10]	zirconium	toluene at 120 mmHg	hor., hor. orient., unins. strips	–	*
Lienhard & Dhir [11]	nichrome	acetone,	hor., vert. orient., unins. strips	variable	–
		benzene,	hor., vert. orient., ins. strips	variable	–
		methanol, isopropanol			
Park & Bergles [2]	nichrome, steel, constantan	sat. R–113 at 1 atm	hor., vert. orient., ins. strips	1.78E5	2.02E5

(1) Zn, Sn
(2) Ni
(3) Cu
(*) published in ratio form only

Table 2 The effect of thermal properties on the CHF of thin heaters

Data Set	k effect	ρc_p effect	$(k\rho c_p)^{0.5}$ effect	α effect
Carne & Charlesworth [3]	general. incr.	no	general. incr.	general. incr.
Tachibana et al [4]	no	not clear	not clear	no
Houchin & Lienhard [5]	no	no	no	no
Guglielmini & Nannei [6]	no	no	general	no
Ivey & Morris [7]	no	no	no	no

copper data exhibited a distinctively lower asymptote. This behavior was not acknowledged by the authors.

The aluminum data of Tachibana et al.[4] plotted exceedingly high, the effect being attributed to a surface chemistry phenomenon [12]. This effect, however, was not verified for the Houchin and Lienhard aluminum data [5].

Based on these considerations, the data of Guglielmini and Nannei [6] and the aluminum data of Tachibana et al. [4] were disregarded in the development of a criteria for δ_{asy}, the heater thickness for which the CHF is free of thermal conductance/capacitance effects.

In order to account for the effects of geometry and fluid, the remaining data were divided by the corresponding asymptotes. In so proceeding, data likely to have been affected by thermal conductance/capacitance effects and, even so, used to develop the only hydrodynamic predictions available for that particular geometry were disregarded. These include the Park and Bergles data for small heaters [2] (simulated electronic chips) and the Lienhard and Dhir data for ribbon heaters [11]. The latter were not explicitly used in the development of a criteria for δ_{asy}; however, they were still present through the hydrodynamic predictions for the CHF derived from them. Finally, as will be discussed later, the data set of Bernath [1] was not used because it involves subcooling.

As can be seen in Table 1, except for the Houchin and Lienhard data set [5] the asymptotes calculated from the hydrodynamic predictions are lower than the experimental ones. This could be an indication that the Lienhard and Dhir data for ribbon heaters were actually affected by thermal conductance/capacitance effects and/or the correlation does not capture all the basic aspects of the phenomenon. On the other hand, because the experimental asymptotes were inferred from a limited number of data points, they could have been overestimated. It was reasoned, then, that a criterion for δ_{asy} should be based on both asymptotes (Fig. 4).

The value for δ_{asy} based on the hydrodynamic predictions implies an underestimation of the thermal conductance/capacitance effects. A thicker heater would actually be necessary to approach the asymptotic CHF. On the other hand, the value for δ_{asy} based on the experimental asymptotes is affected by the uncertainty in the derivation of the asymptotes themselves. Due to the small number of data points available for thick heaters, these asymptotes could have been overestimated; the possibility also exists that they are still underestimated. Hence, as depicted in Fig. 4 the recommended value for δ_{asy}, δ_{eff}', as the arithmetic average of $\delta_{eff,1}$ and $\delta_{eff,2}$ should be viewed as a lower limit for the heater thickness in engineering experimentation. The value 0.90 for the ratio q''_{CHF}/q''_{asy} was arbitrarily taken as a practical cut-off for CHF data free of thermal conductance/capacitance effects.

A software package [13] that fits up to 196 different curves to paired data using least squares regression and a SAS computer code [14] were employed to determine the correlations $q''_{CHF}/q''_{asy} = f(\delta_{eff})$, Eqs. (1) and (2). Equation (1) was derived using geometries for which the Lienhard and Dhir hydrodynamic predictions [11] were applicable, and Eq. (2) was derived using the experimentally inferred asymptotes. As shown in Fig. 5, these expressions seem to reasonably correlate the data for purposes of establishing a practical criterion for the occurrence of conductance/capacitance effects based solely on the thickness.

The large scatter in the data for very small

$$\frac{q''_{CHF}}{q''_{asy,h}} = \frac{\delta_{eff}}{\left[9.330\times10^{-11}-0.145\ \delta_{eff}^{2}\ln\delta_{eff}\right]^{1/2}} \qquad \text{Eq.(1)}$$

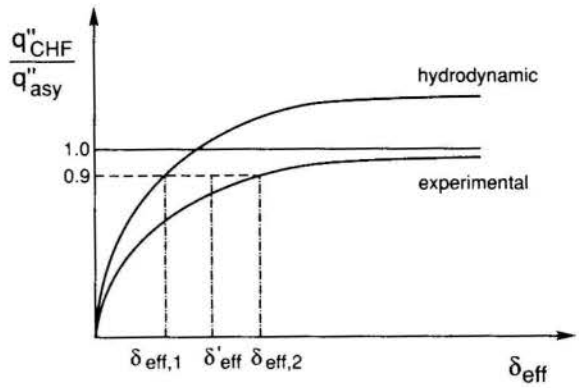

Fig. 4 Schematic of the procedure for determining δ'.

$$\frac{q''_{CHF}}{q''_{asy,e}} = \frac{\delta_{eff}}{\left[1.347\times10^{-10}-0.172\ \delta_{eff}^{2}\ln\delta_{eff}\right]^{1/2}} \qquad \text{Eq.(2)}$$

(δ_{eff} in meters)

thicknesses is thought to be associated with randomness of the nucleation process. Because the heater is very thin, the inception of the first vapor patches (which can occur for a range of heat fluxes) can cause the onset of the CHF condition.

For $q''_{CHF}/q''_{asy} = 0.90$, Eq. (1) yields $\delta_{eff,1} =$ 0.200 mm and Eq. (2) gives $\delta_{eff,2} = 0.768$ mm. The value for δ_{eff}' thus is 0.484 mm, or, approximately, 0.5 mm. It is believed that this result represents the best general criterion presently available to the experimenter for obtaining CHF data uninfluenced by the heater thermal properties and thickness. In addition, it can be used to assess the soundness of existing CHF data.

The difference in δ_{eff} as calculated from Eq. (1) and Eq. (2) is indicative of potential complications involving the Lienhard and Dhir hydrodynamic predictions for ribbon heaters [11]. These authors utilized 0.229-mm-thick nichrome foil heaters, which could have experienced an earlier CHF. The proposed correlations would thus be somewhat conservative.

The simulated microelectronic chips developed by Park and Bergles [2] used 25.4-μm-thick steel, 10-μm-thick constantan, and 12.7-μm-thick nichrome foil heaters. These values are considerably lower than the recommended value for δ_{eff}', 0.5 mm. Hence, these CHF data also could have been affected by thermal conductance/capacitance effects. A more appropriate simulation of microelectronic chips is discussed below.

As can be seen in Fig. 2, a major portion of the data falls below the 0.5-mm recommendation. This is due to the fact that electrical heating of 0.5-mm-thick heaters requires very high amperages for most metals.

PART II: THE SIMULATION OF MICROELECTRONIC CHIPS

EXPERIMENTAL APPARATUS AND PROCEDURE

The experimental apparatus and the test sections used in the present investigation have been discussed elsewhere [15]. Experiments were run in a pool of FC-72 at atmospheric pressure (B.P. 56°C) to determine the CHF of vertically oriented, 5 mm square heaters boiling on one side. In addition to experiments at saturated conditions, three different degrees of

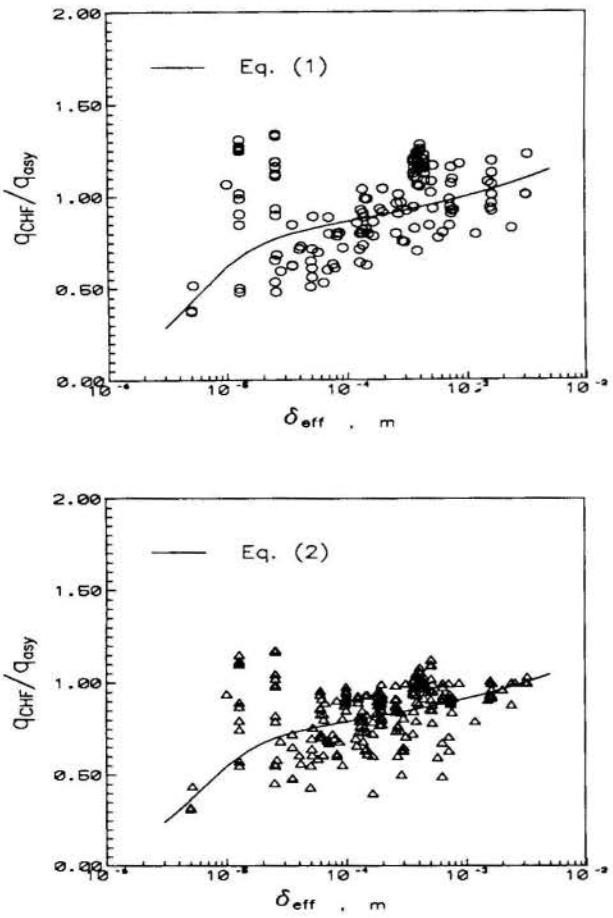

Fig. 5 (a) Eq. (1) and corresponding reduced data; adjusted R–square 0.7901. (b) Eq. (2) and corresponding reduced data; adjusted R–square 0.8128.

subcooling were also tested: 11°C, 21°C, and 31°C. The interested reader is directed to Ref. 15 for further details.

EXPERIMENTAL RESULTS AND DISCUSSION

In order to avoid the likelihood of thermal conductance/capacitance effects in the present study of the CHF from simulated microelectronic chips, a modification of the Park and Bergles design [2], termed guarded heat sink, was adopted [15]. In this case, a smooth copper block was bonded to the heat generating foil and a layer of epoxy was used to guard its sides. The CHF from this assembly was assumed uninfluenced by the heater thermal properties and thickness as would be the CHF from a thick, directly heated test section (Fig. 6). Moreover, electrical heating up to CHF was possible at relatively low amperages.

According to Gaertner [16], when boiling takes place on a heater of large mass, local areas of film boiling can exist stably on the surface. In the guarded heat sink design, no heat is generated in the copper block. If a dry patch is formed on the surface, the heat flow lines will be diverted to the surrounding wetted areas. A much more massive dry patch is required to cause burnout. This effect is enhanced by the fact that, contrary to a directly heated surface, the area underneath the vapor mass is less likely to experience a substantial increase in temperature. Therefore, even for moderate values of the copper block thickness, a satisfactory simulation should be accomplished.

In connection with the influence of subcooling on the CHF, Fig. 7 shows data obtained by the present authors for 25.4-μm-thick nichrome foil heaters and guarded heat sinks. It can be seen that whereas the CHF of nichrome foil heaters is only slightly affected by subcooling, the guarded heat sinks experimented a steady increase in the CHF. In order to explain these trends, it was assumed that in the range of interest the only effect of subcooling is to partially condense the vapor generated and add a necessary sensible heat transfer, $C_p(T_{sat}-T_b)$, to the total heat transfer [17]. The inception of a vapor patch now requires a higher heat flux; in addition, a higher heat flux is also needed to attain the necessary size for bubble departure. One would then think that the more the heater can tolerate local areas of film boiling, the more likely subcooling is to enhance the average CHF. In other words, subcooling will enhance the CHF as long as its beneficial effect is not overshadowed by thermal conductance/capacitance effects. In the case of a very thin heater, as the nichrome foil heaters used, the inception of even a small vapor patch is likely to trigger the CHF condition. This hypothesis becomes even more plausible when one considers the small heater size, 5 mm x 5 mm. Therefore, one should not expect a pronounced influence of subcooling on the CHF.

General guidelines are also needed for the recommended value of δ' under subcooled conditions. If it is assumed that the inception of a vapor patch is determined by the Leidenfrost point, subcooling is not likely to affect it for metal heaters. According to Baumeister and Simon [18], only for thermally insulating materials does subcooling affect the Leidenfrost point. Hence, for metal heaters under subcooled conditions the inception of vapor patches will be delayed because a higher heat flux is necessary to attain the same temperature levels existing under saturated conditions. The heater should then have an even larger mass in order to sustain local areas of film boiling. In other words, under subcooled conditions the heater should be thicker in order to yield CHF data free of thermal conductance/capacitance effects.

A linear relationship was found to describe the CHF of the guarded heat sinks as a function of subcooling in the range tested [15,17]. Furthermore, for a particular subcooling value the expected asymptotic dependence of the CHF on the thickness has been verified [1]. A linear dependence of δ' on subcooling is then suggested, but its development still requires further experimental work.

CONCLUSIONS

The present study investigated the effect of heater thermal properties and thickness on the CHF. The main conclusions are:

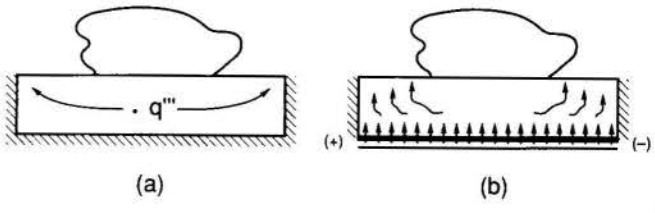

Fig. 6 Heat flow in a (a) thick, directly heated test section and in a (b) guarded heat sink.

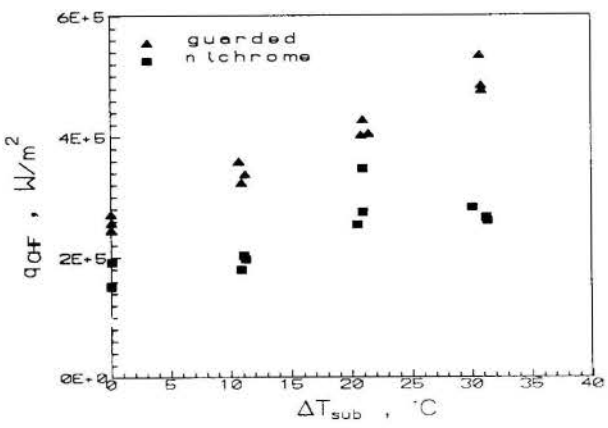

Fig. 7 The influence of subcooling on the CHF from 25.4–μm–thick nichrome foil heaters and guarded heat sinks (simulated electronic chips).

1. None of the parameters, k, ρc_p, $\sqrt{k\rho c_p}$, or a, succeeded in correlating CHF data of thin heaters on a q''_{CHF} x δ_{eff} plot. This is indicative of the inappropriateness of previous models.

2. The recommended value for δ_{asy},δ_{eff}', the heater thickness for which the CHF is 90% of the apparent asymptotic value, is 0.50 mm under saturated conditions. This thickness, however, could require a costly, high-amperage power supply for electrical heating.

3. Existing hydrodynamic CHF predictions available in the literature, as well as CHF data for simulated electronic chips, could have been influenced by thermal conductance/capacitance effects.

4. A simulation of electronic chips was developed which can be assumed free of such effects.

5. Under subcooled conditions, the recommended value for δ_{eff}' would be higher than that at saturation. However, the establishment of quantitative guidelines requires further experimental work.

ACKNOWLEDGEMENTS

The authors would like to express their appreciation to the 3M Industrial Chemical Products Division and to the IBM Data Systems Division for their support of this study. The first author gratefully acknowledges the scholarship support received from the Post-Graduate Education Federal Agency (CAPES-Brazil).

REFERENCES

[1] Bernath, L.A., "A Theory of Local Boiling Burnout and Its Application to Existing Data", Chem. Eng. Progr. Symposium Ser., No. 30, Vol. 56, pp. 95–116, 1960.

[2] Park, K.-A. and Bergles, A.E., "Effects of Size of Simulated Microelectronic Chips on Boiling and Critical Heat Flux", ASME Journal of Heat Transfer, Vol. 110, pp. 728–734, 1988.

[3] Carne, M. and Charlesworth, D.H., "Thermal Conduction Effects on the Critical Heat Flux in Pool Boiling", Chem. Eng. Progr. Symposium Ser., No. 64, Vol. 62, pp. 24–34, 1966.

[4] Tachibana, F., Akiyama, M. and Kawamura, H., "Non-Hydrodynamic Aspects of Pool Boiling Burnout", Journal of Nuclear Science and Technology, Vol. 4, pp. 121–130, 1967.

[5] Houchin, W.R. and Lienhard, J.H., "Boiling Burnout in Low Thermal Capacity Heaters", ASME Paper No. 66-WA/HT-40, 1966.

[6] Guglielmini, G. and Nannei, E., "On the Effect of Heating Wall Thickness on Pool Boiling Burnout", Int. J. Heat Mass Transfer, Vol. 19, pp. 1073–1075, 1973.

[7] Ivey, H.J. and Morris, D.J., "The Effect of Test Section Parameters on Saturation Pool Boiling Burnout at Atmospheric Pressure", Paper No. 160, A.I.Ch.E. 55th Annual Meeting, Chicago, 1962.

[8] Carne, M., "Some Effects of Test Section Geometry in Saturated Pool Boiling on the Critical Heat Flux for Some Organic Liquids and Liquid Mixtures", Chem. Eng. Progr. Symposium Ser., No. 59, Vol. 61, pp. 281–289, 1965.

[9] Adams, J.M., "A Study of the Critical Heat Flux in An Accelerating Pool Boiling System", Ph.D. Dissertation, University of Washington, Seattle, Washington (USA), 1962.

[10] Cole, R. and Shulman, H.L., "Critical Heat Flux Values at Sub-Atmospheric Pressures", Chemical Engineering Science, Vol. 21, pp. 723–724, 1966.

[11] Lienhard, J.H. and Dhir, V.K., "Hydrodynamic Prediction of Peak Pool Boiling Heat Fluxes from Finite Bodies", ASME Journal of Heat Transfer, Vol. 95, pp. 152–158, 1973.

[12] Costello, C.P. and Frea, W.J., "A Salient Nonhydrodynamic Effect on Pool Boiling Burnout of Small Semicylindrical Heaters" Chem. Eng. Progr. Symposium Ser., No. 57, Vol. 61, pp. 258–268, 1965.

[13] Hudson, J.C., "Exploratory Regression Using CFIT", 4198 Warbler Dr., Flint, MI 48504,USA, 1986.

[14] "The REG Procedure", SAS User's Guide : Statistics, Version 5 Edition, Chapter 31, 1985.

[15] Carvalho, R.D.M. and Bergles, A.E., "The Influence of Subcooling on the Pool Nucleate Boiling and Critical Heat Flux of Simulated Electronic Chips," Proceedings of the Ninth International Heat Transfer Conference, Jerusalem, Israel, August 1990, Vol. 2, pp. 289–294.

[16] Gaertner, R.F., "Photographic Study of Nucleate Pool Boiling on a Horizontal Surface", ASME Journal of Heat Transfer, Vol. 87, pp. 17–29, 1965.

[17] Elkassakgi, Y. and Lienhard, J.H., "Influences of Subcooling on Burnout of Horizontal Cylindrical Heaters", ASME Journal of Heat Transfer, Vol. 110, pp. 479–486, 1989.

[18] Baumeister, K.J. and Simon, F.F., "Leidenfrost Temperature–Its Correlation for Liquid Metals, Cryogens, Hydrocarbons, and Water", ASME Journal of Heat Transfer, Vol. 95, pp. 166–173, 1973.

III ENCIT – Itapema, SC (Dezembro 1990)

NUCLEATE POOL BOILING FROM A HORIZONTAL WIRE TO A VISCOELASTIC FLUID

ROBERT Y.Z. HU and JAMES P. HARTNETT
Energy Resources Center
University of Illinois at Chicago
Chicago, IL 60680-4348

SUMMARY

The nucleate pool boiling behavior of a viscoelastic aqueous solution of hydroxyethyl cellulose of 6 concentrations ranging from 500 to 5,000 wppm has been measured experimentally and compared with results for pure water. The conventional q" vs ΔT boiling curves were measured using a electrically heated horizontal platinum wire of diameter 0.0254 cm submerged in a saturated pool of liquid at atmospheric pressure. It was found that the water boiling data are in resonable agreement with established correlations. In the case of the polymer solutions the lowest concentration of 500 wppm gave results which were about the same as found for water. However at concentrations of 1,500 wppm and above, dramatically different behavior was observed. At lower heat flux values the magnitude of ΔT increased as q" increased, as anticipated. However at approximately 13 W/cm² a maximum ΔT was reached and as q" was increased above 13 W/cm² the value of ΔT decreased.

A series of photographs provided additional insight into the boiling process for all the solutions. It was observed that the bubbles are generally smaller and more spherical in the polymer solutions as compared with water. At medium to high heat flux values, coalescence of bubbles took place more frequently in water. When the maximum ΔT was reached in the boiling of the higher concentration Natrosol solutions (at approximately 13 W/cm²), a large population of fine spherical bubbles was suddenly generated on the heating surface (5 to 10 times more than in water case). This observed behavior is consistent with the measured boiling curve.

INTRODUCTION

The boiling heat transfer behavior of non-Newtonian fluids, particularly viscoelastic polymer solutions, is of special interest to the chemical, pharmaceutical and food industries. An understanding of the boiling performance of these fluids should lead to the development of more energy efficient processes and to better quality control of many processes in the cited industries.

Since early 1970, only a limited number of experimental studies of the boiling heat transfer performance on viscoelastic non-Newtonian fluids have been reported [1-9]. Unfortunately, the boiling data reported are not consistent. Most of the investigators [1,2,3,4,5], reported that for a given temperature difference the addition of a high molecular weight polymer such as polyacrylamide or polyethylene oxide to a solvent increases the heat flux in pool and flow boiling over the value for the solvent alone. However this finding is not conclusive since other studies [6,7,8,9] report contradictory experimental results. In short, these studies show large discrepancies and some contradictions in the observed boiling performance of aqueous polymer solutions. Most of the investigators did not report the rheological properties of the polymer solutions used, which further complicates the interpretation of the experimental findings.

EXPERIMENTAL METHOD

Apparatus. Figure 1 shows the schematic diagram of the pool boiling test set-up. The heat transfer studies were carried out on a platinum wire of diameter 0.0254 cm and 15.24 cm in length. The wire itself serves both as the main heat source and the wire temperature measuring device. The wire was placed horizontally inside a glass tank with dimensions of 10.2 cm W x 30.1 cm L x 27.3 cm H. The glass tank is placed on top of a specially made aluminum stand placed in another tank (a stainless steel tank with dimensions 30.5 cm W x 45.7 cm L x 40.6 cm H) equipped with two pyrex glass windows. The 24.1 cm x 24.1 cm windows are aligned and mounted on the outer tank for the purpose of viewing the experiment. The outer tank is filled with a clear transparent oil of high boiling point (274 °C) which is used as a constant temperature bath. The main heat source for the oil bath comes from four 1,000 W heating rods located horizontally under the inner glass tank. The oil bath temperature is regulated by two 30.5 cm x 30.5 cm heating pads, glued on the two windowless sides of the outer tank, and manually controlled by a variac. Each heating pad can deliver a maximum of 720 W of heat.

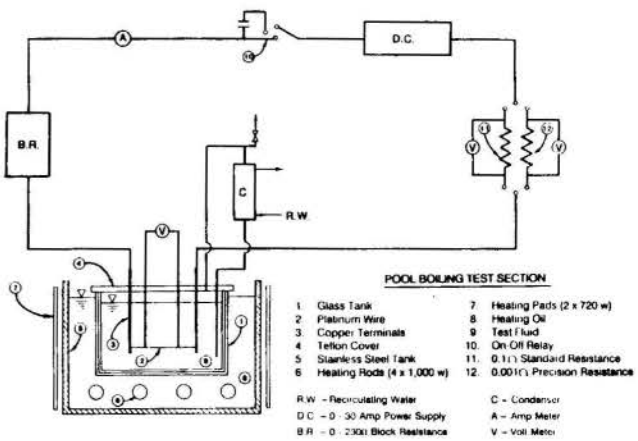

Fig. 1: Schematic diagram of pool boiling experiment.

The temperature of the oil is measured by a mercury thermometer. The whole system is insulated with 5.1 cm thick insulation boards with removable blocks covering the viewing windows. The main heaters are used mostly when calibrating the platinum wire, in which case the fluid temperature is raised incrementally from a value of 50°C to 100°C. They also are used to raise the temperature of the polymer solutions to near 100 °C. During the boiling experiments the oil bath temperature is controlled by the sidewall heating pads which is manually controlled by a variac.

The temperature of the fluid is measured by four copper-constantan thermocouples fitted in 0.32 cm diameter thermowells which extend from the cover of the boiling tank. The tips of the thermowells are bent 90° and filled with copper-oxide cement. The thermocouples can be raised or lowered by adjusting the thermocouple holders on the teflon cover of the boiling tank, thereby covering a large area in the fluid.

The power supply of the test wire is a 200 W autoranging direct current power supply (model 6023A by Hewlett Packard Co.). It is capable of delivering a fixed voltage ranging from 0 to 20 volts or a fixed amperage from 0 to 30 amps such that heat transfer under different values of heat flux can be studied. The detailed design of the system can be found in reference [10].

The photographic system used to study pool boiling is a high speed video camera with a motion analysis system (SP-2000 system by Eastman Kodak Company, U.S.A.) [11]. This system is capable of recording information at the rate of 60 to 12,000 frames per second in partial frames format (the full frame limit is 2,000 frames per second). After video recording the boiling processes at the desired frame speed (2,000 frames per second in this study), the recording can be played back on a frame by frame basis allowing the identification and measurement of the size, the number and the location of individual bubbles.

Test Fluids. A commercially available high molecular weight polymer was used in this study; a hydroxyethyl cellulose (250HHR Natrosol, Hercules Co.) [12] of six different concentrations ranging from 500 to 5,000 wppm. The method for preparing aqueous solutions of this polymer is described in detail in reference [10]. Deionized water was used as solvent in this study.

Procedures. The procedures followed in the pool boiling experiments can be described as follows:

Sequence 1: Pool boiling of water
- Step 1: Calibrate the platinum wire at 5 different temperature levels (at about 60, 70, 80, 90 and 100 °C).
- Step 2: Stabilize the water in the boiling tank at about 100 °C (without boiling taking place) for 1/2 to 1 hour.
- Step 3: A total of 12 different heat flux values ranging from 2.2 to 55 W/cm^2 are supplied to the test section. The temperature difference between the heating surface and the bulk fluid is measured for each heat flux. This process is repeated for several heat fluxes. On the conclusion of this sequence, the test section is cooled to room temperature and cleaned.

Sequence 2: Pool boiling of polymer solution
- Step 1: The steady shear viscosity of the fresh polymer solution is measured and the glass tank is filled with the polymer solution. The polymer solution is gradually heated to approximately 100 °C (without boiling taking place) and maintained for 1/2 to 1 hour.
- Step 2: Repeat Step 3 in Sequence 1. After the boiling experiments are completed for a given polymer concentration the steady shear viscosity is measured over a wide shear rate range.

Sequence 3: Pool boiling of water
Repeat Sequence 1 again.

Detailed photographic studies of water and of the 1,500 wppm Natrosol solution were carried out over a wide range of heat flux. From these photographs the bubble departure diameter and nucleation site density were measured.

RESULTS

Figures 2 present the apparent viscosity η vs the shear rate $\dot{\gamma}$ for representative concentrations of the 250 HHR Natrosol solutions. A decrease of the viscosity at the low shear rate range after boiling processes was observed for each and every concentration. At the higher shear rate range (i.e., above 100 sec^{-1}), the change in viscosity between the fresh solution and solution after boiling was not as large. This decrease in viscosity, especially at the low shear rate range, is caused by the severe bubble motion occurring during the boiling process which results in the rupture of some of the long-chained molecular bonds.

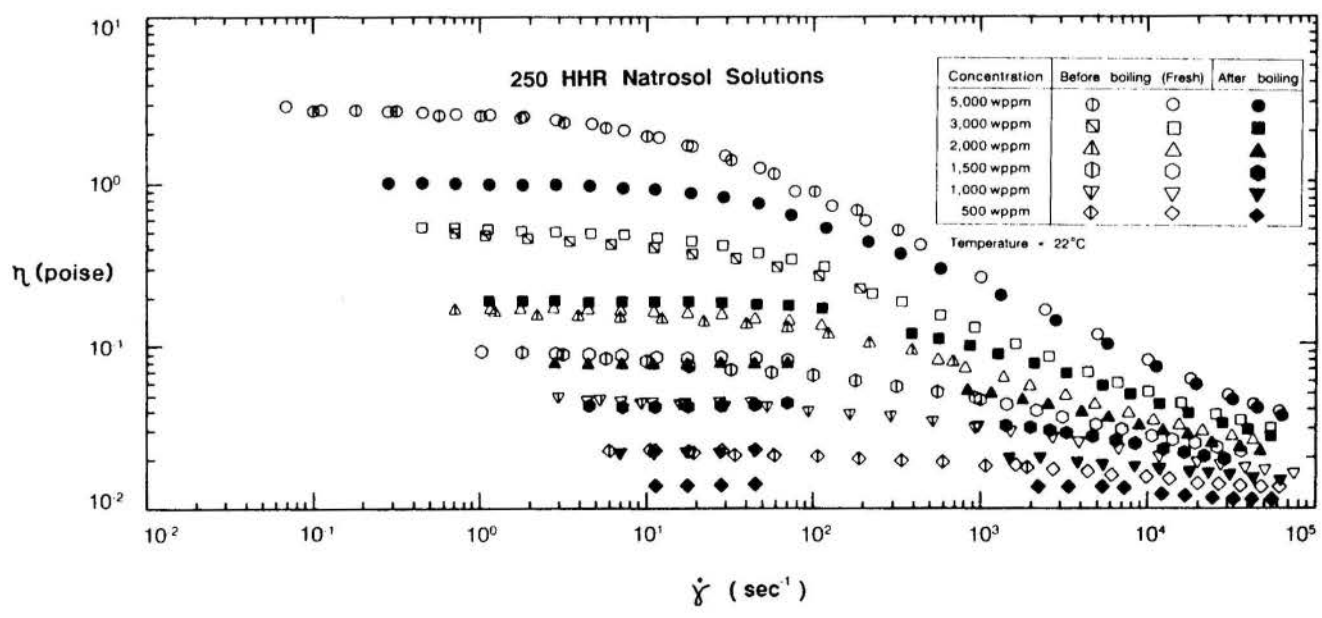

Fig. 2: Steady shear rate viscosity of 250HHR Natrosol solutions.

The surface tension as a function of temperature for the Natrosol solutions and water was also measured, as shown in Figure 3. The values of the surface tension of the Natrosol solutions are lower than those of water by about 10%. Except for the viscosity and surface tension, all other properties of the polymer solutions were assumed to be the same as those of pure water.

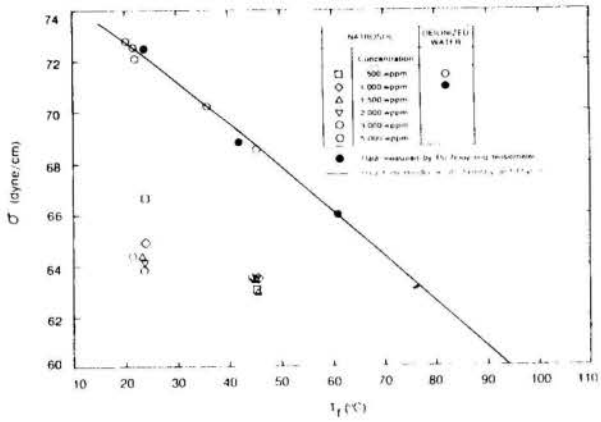

Fig. 3: Surface tension of various fluids at different temperature.

The conventional pool boiling curves of the heat flux q", as a function of the surface superheat temperature $\Delta T=T_w-T_{sat}$ were measured for water and for the 6 concentrations of hydroxyethyl cellulose. A typical set of heat transfer measurement is shown in Figure 4. The water data taken before and after the polymer solution are in very good agreement, demonstrating that the heating surface characteristics did not change during the experiments. Figure 5 shows the pool boiling data for the deionized water, with the odd number runs taken before the polymer solution boiling experiments and the even number runs taken after the polymer runs. In general, the reproducibility of the data is reasonably good and the measurements are in good agreement with Kutateladze's correlation [13], with Rohsenow's earlier correlation proposed in 1952 [14] and in fair agreement with Nishikawa's correlation [15]. However, the water data differ substantially from the later correlation proposed by Rohsenow in 1973 [16].

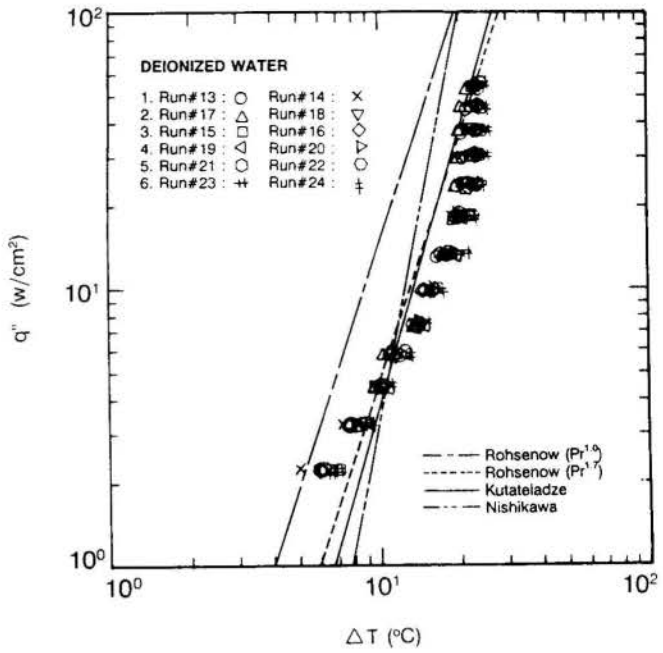

Fig. 5: Boiling data of deionized water.

The results for Natrosol are summarized on Figure 6, along with the measured results for deionized water. The lowest concentration of Natrosol, the 500 wppm solution, yielded results which were about the same as found for water. In the case of Natrosol concentrations above 1000 wppm dramatically different behavior was observed. In such cases, the boiling curves took on a completely new shape. At low heat fluxes the magnitude of ΔT increased as q" increased, as anticipated. However, at a heat flux of the order of 13 W/cm² a maximum ΔT was reached and at heat fluxes above this value an increase in q" was accompanied by a decrease in the value of ΔT. Thus the heat transfer performance of the higher concentration Natrosol solutions was superior to the boiling performance of deionized water over the range of q" from 13 W/cm² to 55 W/cm².

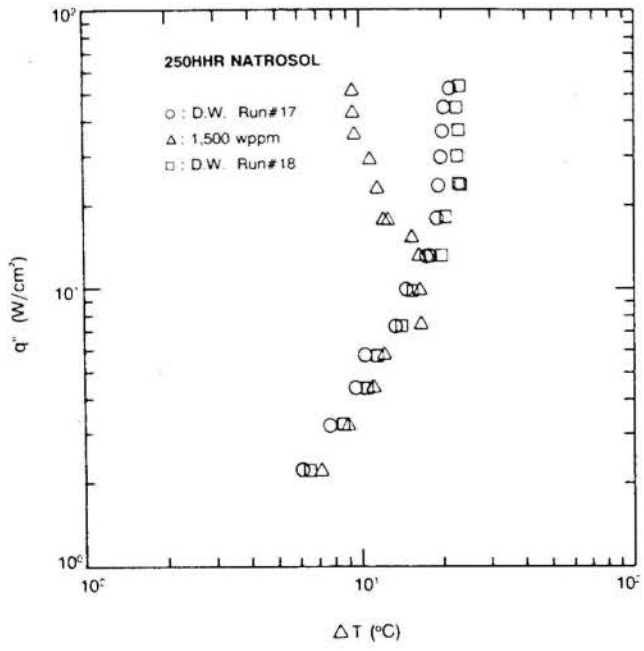

Fig. 4: Boiling data of the 1,500 wppm Natrosol solution.

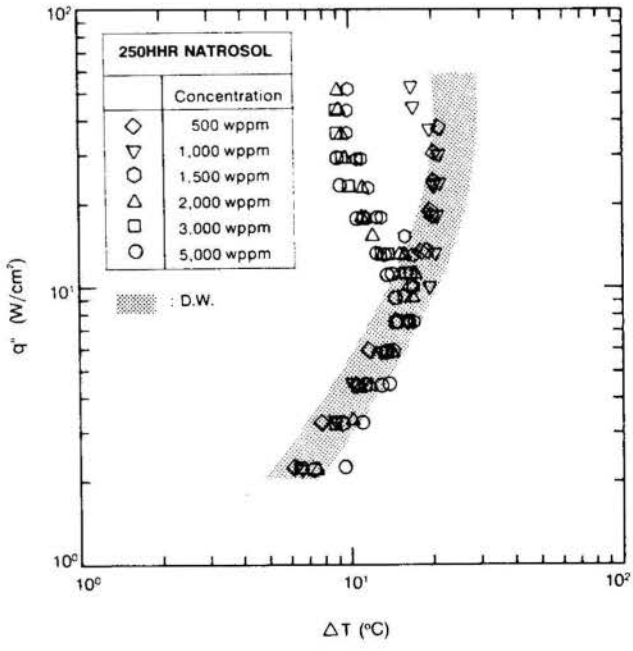

Fig. 6: Comparsion of boiling data for the Natrosol solutions and water.

Further support for these surprisihg findings was provided by a series of photographs taken through the viewing windows. Figure 7 shows two sets of photographs for the water and the Natrosol solution, taken at heat fluxes of approximately 13 W/cm^2, 18 W/cm^2 and 53 W/cm^2. It can be observed that the bubbles are generally smaller and more spherical for the Natrosol solutions. Furthermore, there are many more bubbles in the case of the Natrosol solution than in the water. This is particularly noticeable at the higher heat flux, which is associated with a ΔT value of 9.8°C for the Natrosol solution as compared with corresponding values of 21.3 °C for the deionized water. It is concluded that the observed improvement in heat transfer in the Natrosol solution is caused by the dramatic mixing which is associated with the very large population of very fine bubbles.

(1a) Deionized water,
q"=13.05 W/cm^2, ΔT=16.72 °C.

(1b) 1,500 wppm Natrosol solution,
q"=13.09 W/cm^2, ΔT=16.57 °C.

(2a) Deionized water,
q"=17.82 W/cm^2, ΔT=17.64 °C.

(2b) 1,500 wppm Natrosol solution,
q"=17.70 W/cm^2, ΔT=11.98 °C.

(3a) Deionized water,
q"=52.41 W/cm^2, ΔT=21.26 °C.

(3b) 1,500 wppm Natrosol solution,
q"=51.37 W/cm^2, ΔT=9.80 °C.

Fig. 7: Photograph of boiling liquids.

Figure 8 presents the measurements of bubble departure diameter D_d as a function of heat flux q". The departure diameter of water bubbles increase very slowly with an increase in heat flux. In fact, the increase is so small that the average departure diameter (about 0.20 cm) only varies ±10% over the heat flux range studied. In the case of the 1,500 wppm Natrosol solution, the bubble departure diameters at lower heat fluxes are about the same as for water but at higher heat fluxes the departure diameter of the Natrosol bubbles is much smaller than found for water. In general the 1,500 wppm Natrosol solution shows a distinct decrease of the bubble departure diameter with increasing heat flux q", in sharp contrast to the finding in the water case.

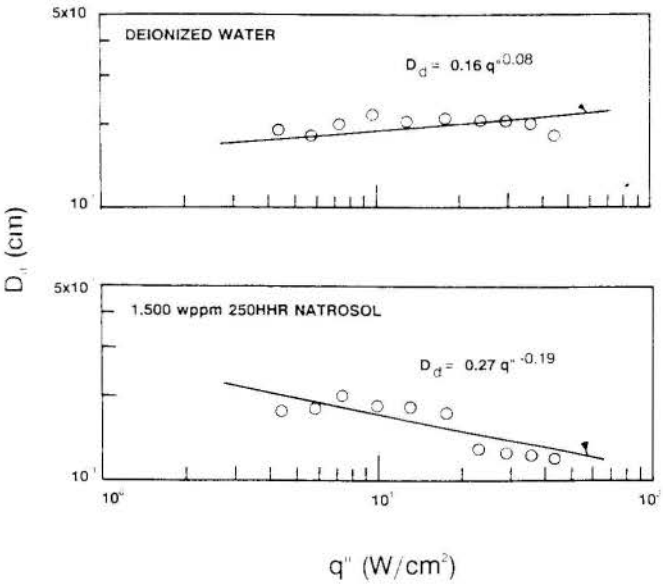

Fig. 8: The bubble departure diameter as a function of heat flux for different solutions.

Figure 9 presents the measurements of bubble nucleation site density N/A as a function of heat flux q". Compared with water data, the 1,500 wppm Natrosol solution showed distinctly different behavior, showing much higher bubble population at higher heat fluxes. This is consistent with the measured boiling curve for Natrosol. In particular, when the observed bubble population suddenly increased the corresponding measured heat transfer coefficient also increased.

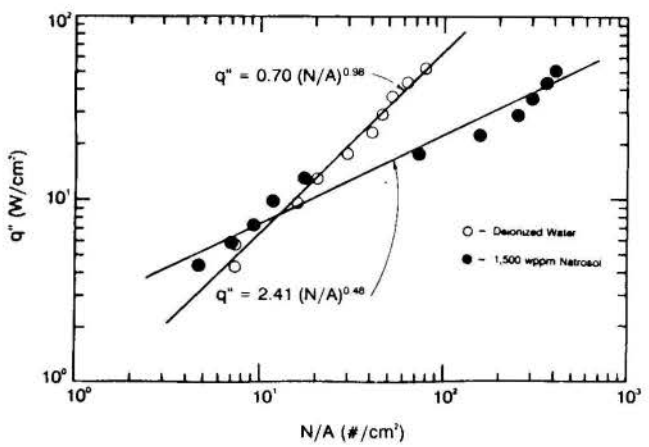

Fig. 9: Comparsion of q" vs N/A for different solutions.

CONCLUSION

Nishikawa's equation shows no effect of viscosity on boiling, while the correlation of Rohsenow and Kutateladze both show a decrease in heat transfer when the viscosity is increased. Noting that the Natrosol solutions have higher viscosity and better heat transfer performance than water, it is clear that viscosity is not responsible for the observed phenomena.

The surface tension of the Natrosol solution was found to be 10% lower than that of water, and this should yield some increase in the boiling performance; however, the observed difference in surface tension, if judged on the basis of Newtonian fluid boiling behavior, does not explain the observed results. More detailed investigation is necessary before an adequate explanation of the observed unusual behavior is possible.

ACKNOWLEDGEMENTS

The authors acknowledgement the financial support of the Division of Engineering of the Office of Basic Energy Sciences of the U.S. Department of Energy under its Grant No. 85ER13311. In addition, the authors wish to express their appreciation to Argonne National Laboratory for the use of high speed photographic system.

NOMENCLATURE

D_d	bubble departure diameter, (cm)
N/A	bubble nucleation site density, (#/cm²)
q"	heat flux, (W/cm²)
T_f	fluid temperature, (°C)
T_{sat}	saturation temperature of the fluid, (°C)
T_w	surface wall temperature, (°C)
ΔT	$-T_w-T_{sat}$, (°C)
η	steady shear (apparent) viscosity, (poise)
$\dot{\gamma}$	shear rate, (sec^{-1})
σ	surface tension of the fluids, (dyne/cm)

REFERENCES

[1] Kotchaphakdee, P. and William, M.C.: "Enhancement of nucleate pool boiling with polymer additives", Int. J. Heat Mass Transfer, vol. 13(6), pp. 835-848, 1970.

[2] Gannett, H.J. and William, M.C.: "Pool boiling in dilute non-aqueous polymer solutions", Int. J. Heat Mass Transfer, vol. 14, pp. 1001-1005, 1971.

[3] Papaioannou, A.T. and Koumoutsos, N.G.: "The effects of polymer additives on nucleate boiling", Proc. 7th Int. Heat Transfer Conf., vol. 4, pp. 67-72, Munich, West Germany, 1982.

[4] Wagle, A.K.: "Boiling heat transfer in viscoelastic fluids", Ph.D. thesis, Univ. of Delaware, Newark, 1972.

[5] Wei, H. and Maa, J.R.: "Enhancement of flow boiling heat transfer with polymer additives", Int. J. Heat Mass Transfer, vol. 25(3), pp. 431-434, 1982.

[6] Miaw, C.B.: "A study of heat transfer to dilute polymer solutions in nucleate pool boiling", Ph.D. thesis, Univ. of Michigan, Ann Arbor, 1978.

[7] Ulicny, J.C.: "Nucleate pool boiling in dilute polymer solutions", Ph.D. thesis, Univ. of Michigan, Ann Arbor, 1984.

[8] Yang, Y.M. and Maa, J.R.: "Effects of polymers additives on pool boiling phenomena", Lett. Heat Mass Transfer, vol. 9, pp. 237-244, 1982.

[9] Paul, D.D. and Abdel-Khalik, S.I.: "Nucleate boiling in drag-reducing polymer solutions", J. Rheol., vol. 27, No. 1, pp. 59-76, 1983.

[10] Robert Yie-Zu Hu: "Nucleate pool boiling from a horizontal wire in viscoelastic fluids", Ph.D. thesis, University of Illinois at Chicago, 1989.

[11] "Kodak SP-2000 Motion Analysis System Operation Manual", Spin Physic Division, Eastman Kodak Company, San Diego, CA, 1985.

[12] Davidson, R.C.: "Handbook of Water-Soluble Gums and Resins", McGraw-Hill, New York, 1980.

[13] Kutateladze, S.S.: "Fundamentals of Heat Transfer", Edward Arnold Ltd., London, 1963.

[14] Rohsenow, W.M.: "A method of correlating heat transfer data for surface boiling of liquids", Trans. ASME, vol. 74, No. 8, pp. 969-975, 1952.

[15] Nishikawa, K. and Fujita, Y.: "Correlation of nucleate boiling heat transfer based on bubble population density", Int. J. Heat Mass Transfer, vol. 20, pp. 233-245, 1977.

[16] Rohsenow, W.M.: "Boiling", in Handbook of Heat Transfer, section 13, McGraw-Hill, New York, 1973.

III ENCIT – Itapema, SC (Dezembro 1990)

ESTUDO DO COEFICIENTE DE INÉRCIA NO ESCOAMENTO NÃO-DARCIANO DE UM FLUIDO ATRAVÉS DE UM MEIO POROSO

SHEILA LOPES VIEIRA, CESAR COSTAPINTO SANTANA
Universidade Estadual de Campinas - Departamento de Engenharia de Petróleo
Caixa Postal 6122
13081 Campinas SP Brasil

RESUMO

Este trabalho consiste no estudo do escoamento de gases a altas velocidades através dos poros de rochas reservatório de petróleo. Neste caso, há um desvio da lei de Darcy devido às forças inerciais que não podem ser desprezadas. A análise deste escoamento é feita através da equação de Forchheimer que considera tanto as perdas viscosas quanto as inerciais. Por fim, propõe-se uma correlação para o coeficiente de inércia da equaçã de Forchheimer em função da permeabilidade e da porosidade da rocha para um sistema monofásico.

INTRODUÇÃO

Na engenharia de petróleo é necessário fazer-se a previsão da capacidade de produção de poços de gás com o objetivo de se estudar a viabilidade econômica dos investimentos a serem realizados em um campo produtor e, consequentemente, definir os contratos de venda do produto. Sendo assim, é fundamental conhecer-se o comportamento do gás ao escoar através dos poros da rocha.

Muitos estudos têm sido realizados com o intuito de se entender o escoamento de um fluido através de um meio poroso, que normalmente é descrito pela equação de Darcy:

$$-\nabla P = \frac{\mu v}{\kappa} \tag{1}$$

No entanto, sabe-se que a altas velocidades, a Eq.(1) é ineficiente para descrever tal escoamento, já que as perdas devido às forças inerciais tornam-se significativas frente às viscosas. Forchheimer[12] introduziu um termo adicional à equação de Darcy que representa o acréscimo na queda de pressão devido a essas forças inerciais:

$$-\nabla P = \frac{\mu v}{\kappa} + \beta \rho v^2 \tag{2}$$

onde a magnitude de β quantifica o desvio que se tem da lei de Darcy.

Na literatura, o coeficiente β é chamado de coeficiente de inércia, coeficiente não-darciano, fator de turbulência, coeficiente de velocidade; contudo, nem todos os autores aceitam estas denominações, já que, em se tratando de altas velocidades, muitas controvérsias têm surgido quanto ao mecanismo causador da queda de pressão adicional. Diferentes pontos de vista têm sido colocados:

- Green e Duwez[7] chamaram β de coeficiente de inércia e interpretaram-no como sendo uma medida da tortuosidade dos canais de fluxo, determinando a aceleração do fluido.
- Tek[8] se refere à equação generalizada de Darcy (Eq.2) como uma descrição do regime não-darciano. Completando esta idéia, Katz[9] justifica o uso do termo "escoamento turbulento" dizendo que o movimento extra do fluido é quem causa a queda de pressão adicional.
- Em contrapartida, Houpeurt[10] acredita que, na verdade, o escoamento não seja turbulento, mas que as perdas por energia cinética é que são as reponsáveis pelo desvio da lei de Darcy. Geertsma[3] continua o mesmo pensamento de Houpeurt quando diz que este desvio é resultado de acelerações e desacelerações convectivas das partículas do fluido nos seus caminhos através dos poros.
- Segundo Wright[13], à medida que a velocidade cresce, inicialmente, o desvio é causado por efeitos de inércia e, a seguir, por efeitos de turbulência quando se tem velocidades maiores. Ao escoamento que incorpora os efeitos laminar, inercial e de turbulência deu-se o nome de LIT.
- Firoozabadi[5] já analisa o problema sob outro aspecto: uma vez que existe uma função contínua entre a queda de pressão e a vazão, o termo "não-darciano" não está bem colocado porque dá a idéia de existirem dois mecanismos de fluxo diferentes. O mesmo raciocínio é válido quando o escoamento a baixas velocidades é dito "escoamento darciano", ou quando se tem altas velocidades e usa-se o termo "regime de inércia", já que o efeito de inércia está sempre presente. Continuando nesta linha de pensamento, Firoozabadi apresenta um conceito simples que é considerar o fluxo como sendo de baixa ou de alta velocidade para distinguir as condições em que o termo $(\beta \rho v^2)$ pode ser desprezado ou não. Segundo ele, um nome apropriado para β seria "coeficiente de velocidade".

No presente trabalho, optamos por chamar β de "coeficiente de inércia" já que o termo $(\beta \rho v^2)$ representa a queda de pressão adicional devido às forças inerciais quando estas se tornam significativas.

CORRELAÇÕES APRESENTADAS NA LITERATURA

Uma consideração dimensional da Eq.(2) mostra que a dimensão do coeficiente de viscosidade, κ, é $[L^2]$ e a do coeficiente de inércia, β, é $[L^{-1}]$. Uma vez que ambos têm dimensão de comprimento, espera-se que contribuam na caracterização da estrutura do meio poroso e que sejam independentes das propriedades do fluido.

Com o objetivo de correlacionar o coeficiente de inércia com as propriedades da rocha, Cooke[14] mediu β para diferentes amostras e obteve uma relação da forma:

$$\beta = \frac{b}{\kappa^a} \tag{3}$$

onde as constantes a e b dependem do diâmetro dos grãos de areia da rocha. Geertsma[3] propôs uma outra correlação para a predição de β usando, além de dados experimentais, uma análise dimensional:

$$\beta = \frac{0.005}{\phi^{5.5}\kappa^{0.5}} \tag{4}$$

Geertsma[3] modificou a equação acima para o caso de existir uma saturação de líquido :

$$\beta = \frac{0.005}{\phi^{5.5}\kappa^{0.5}}\left(\frac{1}{(1-S_w)^{5.5}\kappa_r^{0.5}}\right) \tag{5}$$

Noman[2] chegou à conclusão de que, para os dados de que dispunha, a melhor correlação seria a da forma:

$$log\beta = 2.4388 \quad log\left(\frac{\kappa}{\phi S_g}\right)^{-0.5} - 5.2846 \tag{6}$$

Noman acentua que o motivo desta forma de correlação ser a melhor está diretamente ligado ao fato de o parâmetro $(\kappa/\phi)^{0.5}$ ser uma boa estimativa do comprimento médio característico do meio poroso.

Evans[1], através de dados experimentais de um escoamento bifásico, chegou à relação:

$$\beta = \frac{1.891\ 10^{-5}}{\phi}\left(\frac{1}{(1-S_{wr})\kappa_g^{0.5}}\right)^{1.839} \tag{7}$$

sendo que os valores de β fornecidos por ela são bons e concordam razoavelmente bem com os obtidos experimentalmente para as rochas dentro da faixa de porosidade e permeabilidade para a qual a equação foi desenvolvida.

Na ausência de dados experimentais, qualquer uma das correlações acima pode ser usada para estimar o coeficiente de inércia, apesar de se saber da necessidade de desenvolver relações para cada tipo de rocha. A maior parte destas correlações foi desenvolvida para condições de escoamento monofásico, sendo que há uma grande falta de dados experimentais para o cálculo de β sob condições de escoamento multifásico.

REPRESENTAÇÃO MATEMÁTICA

Ao correlacionar dados obtidos experimentalmente para o escoamento linear de água a altas velocidades, Forchheimer chegou a uma relação representada pela Eq.(2.a):

$$-\frac{dP}{dL} = \frac{\mu v}{\kappa} + \beta\rho v^2$$

Desenvolvendo-se a Eq.(2.a) para gases e integrando-a com a consideração de μ, T e Z serem constantes, chega-se a:

$$\frac{(P_1^2 - P_2^2)M}{2ZRTL\left(\frac{W}{A}\right)\mu} = \frac{1}{\kappa} + \frac{\beta}{\mu}\left(\frac{W}{A}\right) \tag{8}$$

Um gráfico de $\left(\frac{(P_1^2-P_2^2)M}{2ZRTL\left(\frac{W}{A}\right)\mu}\right)$ vs $\left(\frac{W}{A\mu}\right)$ fornece uma linha reta com o coeficiente angular igual a β e coeficiente linear igual ao inverso da permeabilidade do meio poroso. Então, fazendo-se testes com várias vazões de gás escoando através de um meio poroso, e medindo-se a queda de pressão causada por este, pode-se inferir os parâmetros β e κ do mesmo.

Entretanto, em alguns casos, dados experimentais plotados segundo a Eq.(15) desviam-se do comportamento de linha reta. Este desvio é atribuído a dois fatores:

- Efeito de escorregamento do gás (também chamado de "efeito de Klinkenberg" ou "slip effect") que acontece a baixas pressões quando o caminho livre médio das moléculas fica da mesma ordem de grandeza que o diâmetro dos poros.

- Equação de Forchheimer não descreve bem o sistema, sendo necessário adicionar-se a ela um outro termo:

$$-\frac{dP}{dL} = \frac{\mu v}{\kappa} + \beta\rho v^2 + \gamma\rho^2 v^3 \tag{9}$$

onde γ é o segundo coeficiente de velocidade. No presente trabalho, este acréscimo do termo $(\gamma\rho^2 v^3)$ é desnecessário. Outros pesquisadores, como é o caso de Johnson e Taliaferro[11] optaram pela seguinte representação:

$$-\frac{dP}{dL} = \frac{\mu v}{\kappa} + \rho v^n \tag{10}$$

Neste estudo será analisada a equação de Forchheimer, tanto por sua simplicidade quanto por descrever bem o sistema.

PROCEDIMENTO EXPERIMENTAL

As Figuras 1e 2 mostram esquematicamente a montagem dos equipamentos utilizados neste estudo. O experimento con-

sistiu em injetar-se N_2 a diferentes vazões e medir-se a queda de pressão causada pela presença do meio poroso. A pressão máxima de entrada de N_2 na amostra era de 2 $10^6 Pa$ e a vazão estava compreendida numa faixa entre 5.6 $10^{-5} Nm^3/s$ a 7 $10^{-4} Nm^3/s$.

Os meios porosos utilizados eram 15 amostras de rochas provenientes do afloramento Rio Bonito e tinham o diâmetro de aproximadamente 3.8 cm e comprimento que variava entre 5 e 7 cm. A permeabilidade das amostras estava compreendida dentro de uma faixa de 4 10^{-14} a 5 $10^{-13} m^2$ e a porosidade ia de 13% a 30%.

Durante o experimento, a amostra ficava dentro de um compartimento ("Core-Holder") submetida a uma pressão de confinamento (63 $10^5 Pa$) que garantia que o escoamento fosse linear, impedindo vazamentos.

o N_2 era injetado no "Core-Holder" através de um capilar, sendo distribuído na face 1 da rocha através de sulcos existentes no equipamento. A tomada de pressão era feita na face 1, enquanto que na face 2 media-se a vazão volumétrica. O tempo de duração de cada teste era de aproximadamente 10 minutos.

Para algumas das amostras testadas, escoando N_2 a uma vazão de 7 $10^{-4} Nm^3/s$, houve um desvio significativo da lei de Darcy, da ordem de 50%.

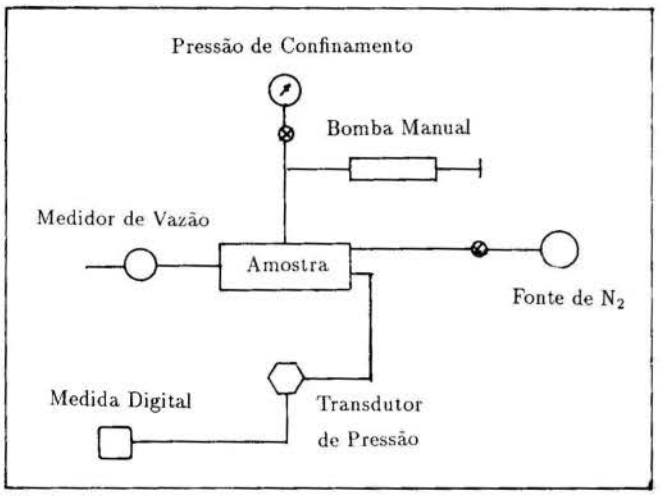

Fig.1 - Desenho esquemático da aparelhagem usada para o escoamento monofásico.

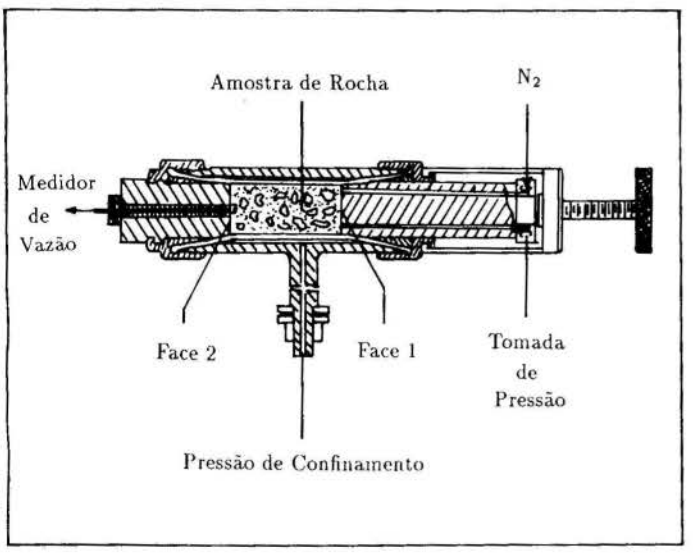

Fig.2 - Desenho esquemático da amostra dentro do Core-Holder

RESULTADOS EXPERIMENTAIS

Para cada uma das amostras, foram feitos dois gráficos: o primeiro, usando a equação de Darcy (Fig. 3) para ter-se certeza de que havia ocorrido um desvio em relação a ela; o segundo, usando a equação de Forchheimer para determinar-se os parâmetros β e κ da amostra (Fig.4).

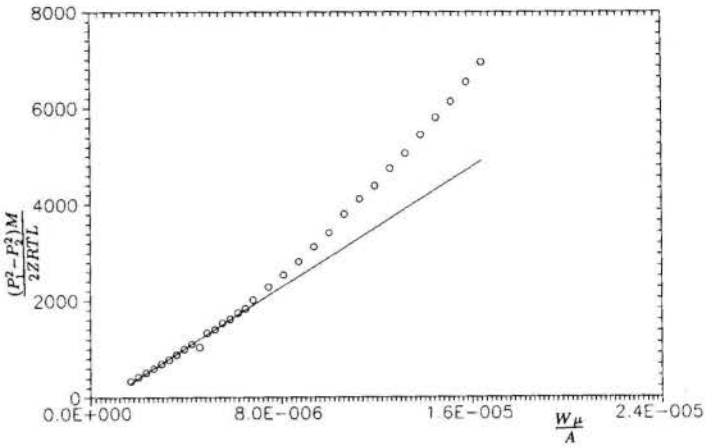

Fig.3 - Dados experimentais plotados segundo a equação de Darcy

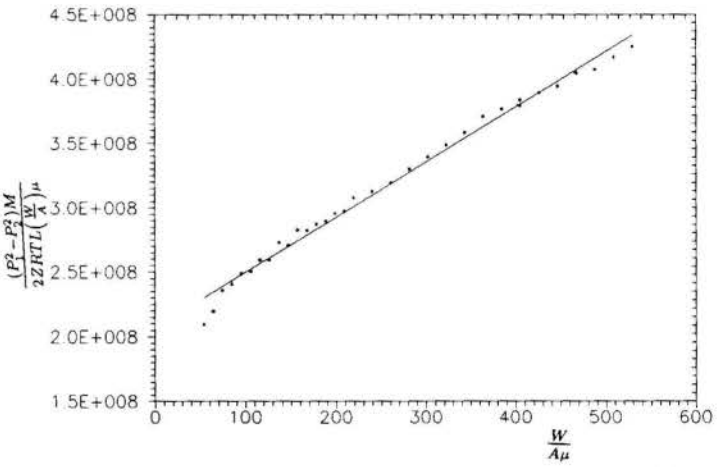

Fig.4 - Dados experimentais plotados segundo a equação de Forchheimer para o cálculo de β e κ.

Sabe-se que várias curvas podem ser obtidas, quando são plotados os dados experimentais de cada amostra conforme as figuras 2 e 3. Na tentativa de colapsar todos os pontos experimentais sobre uma mesma curva, definiu-se o número de Reynolds como:

$$Re = \frac{\beta \kappa \rho v}{\mu} = \frac{c\sqrt{\kappa}\rho v}{\mu} \qquad (11)$$

onde c é uma constante adimensional em que:

$$c = \beta\sqrt{\kappa} \tag{12}$$

A partir do desenvolvimento da equação de Forchheimer para gases e com as hipóteses de μ, Z e T serem constantes, tem-se:

$$\frac{(P_1^2 - P_2^2)M\kappa}{2ZRTL\left(\frac{W}{A}\right)\mu} = \frac{W\beta\kappa}{A\mu} + 1 \tag{13}$$

Em publicações anteriores, o primeiro termo da Eq.(20) é chamado de número de Darcy (Da), enquanto que o segundo é o número de Reynolds definido anteriormente. Logo,

$$Da = Re + 1 \tag{14}$$

$$H_F = \frac{Da}{Re} = 1 + \frac{1}{Re} \tag{15}$$

A Eq.(22) colapsa todas as curvas dos sistemas cujo escoamento é bem descrito pela equação de Forchheimer. Procedendo-se da mesma forma com a equação de Darcy, chega-se à Eq.(23):

$$H_D = \frac{1}{Re} \tag{16}$$

onde H_D e H_F são os fatores de atrito das equações de Darcy e de Forchheimer, respectivamente.

Plotando-se H vs Re (Fig.5), confirma-se que a equação de Forchheimer é ideal para descrever o escoamento em questão.

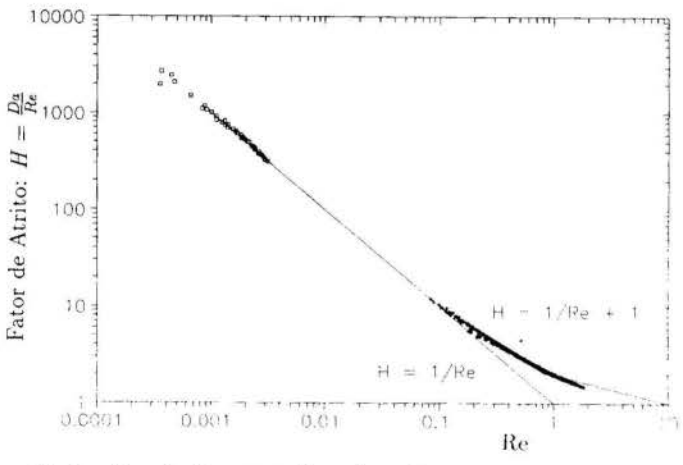

Fig.5 - Correlação para o fator de atrito.

Através da Fig.5, faixas de validade da lei de Darcy podem ser determinadas. Supondo-se que o erro máximo tolerado quando as perdas devido às forças inerciais são desprezadas seja de 5%, então:

$$E = \frac{H_F - H_D}{H_F} \leq 0.05 \tag{17}$$

$$Re \leq 0.053 \tag{18}$$

Sendo assim, para $Re \leq 0.05$ há predominância das forças viscosas no escoamento e a lei de Darcy pode ser usada com erro inferior a 5.3%. Este, segundo alguns autores, é o chamado "regime laminar". Para $Re \geq 0.1$, as forças inerciais passam a não ser mais desprezíveis, causando um erro superior a 11% quando se usa a equação de Darcy, ao invés da equação de Forchheimer. Este é o regime IT.

Uma das formas de analisar os valores de β e κ obtidos experimentalmente é calcular a constante adimensional, c, definida segundo a Eq.(19) e compará-la com correlações da literatura. Usando a relação desenvolvida por Geertsma, c é calculado como:

$$c = \frac{0.005}{\phi^{5.5}} \tag{19}$$

Segundo Evans,

$$c = \frac{1.891\ 10^{-5}}{\phi}\left(\frac{1}{(1 - S_{wr})\kappa_g^{0.5}}\right)^{1.839}\sqrt{\kappa} \tag{20}$$

em que $S_{wr} = 0$ e $\kappa_g = \kappa_\infty$ para um sistema monofásico.

Através da Fig.6, vê-se que os valores de c obtidos experimentalmente concordam com os valores determinados através de correlações propostas na literatura, apresentando resultados que estão compreendidos entre os valores calculados por Geertsma e Evans.

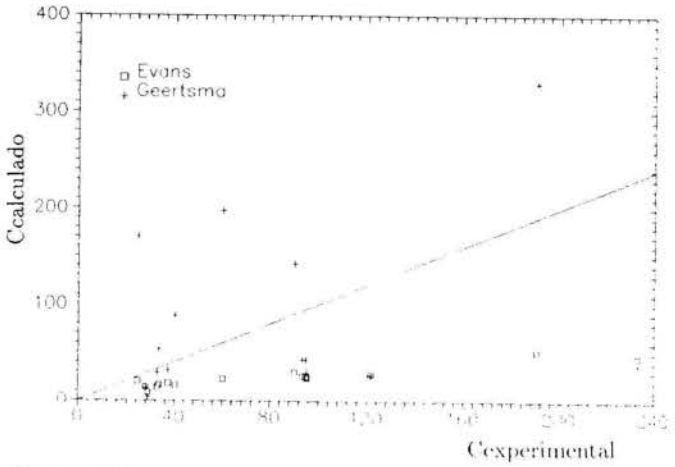

Fig.6 - Gráfico comparativo entre c experimental e c da literatura.

Correlacionando-se os valores experimentais de β em função da permeabilidade e da porosidade, chegou-se a uma relação da forma:

$$\beta = \frac{7.8206\ 10^{-9}}{\phi^{1.5}\kappa^{1.194}} \tag{21}$$

A Fig.7 compara a correlação desenvolvida acima com as apresentadas na literatura:

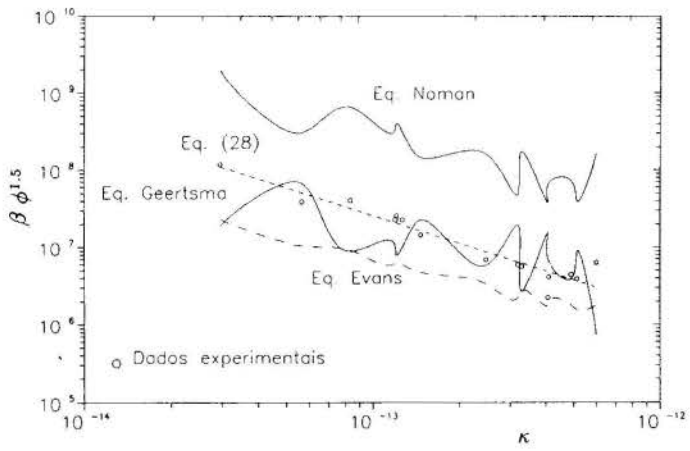

Fig.7 - Correlação entre $\beta\phi^{1.5}$ e κ.

Através da Fig.7, comprova-se que as correlações da literatura podem não dar uma boa estimativa para o coeficiente de inércia.

CONCLUSÕES

O coeficiente de inércia β foi medido experimentalmente para amostras do afloramento Rio Bonito sob condições de escoamento monofásico. A partir dos resultados obtidos, pode-se concluir:

- À medida em que κ e ϕ diminuem, atuando como agentes que dificultam o escoamento e, portanto, tornando os efeitos inerciais mais pronunciados, β aumenta.
- Contradizendo Noman, pode-se dizer que, para as amostras em questão, o parâmetro $\left(\frac{\kappa}{\phi}\right)^{0.5}$ não é uma boa estimativa do comprimento médio característico do meio poroso.
- Uma vez que β não é uma função somente de κ e de ϕ, mas também de outras propriedades da rocha, não existe uma única correlação possível entre β, κ e ϕ.
- Baseando-se em correlações da literatura, pode-se afirmar que o escoamento a altas velocidades é influenciado pela presença da fase líquida imóvel. Portanto, como continuidade deste trabalho serão incorporados resultados referentes ao escoamento bifásico não-darciano.

ABSTRACT

This article presents a study of high-velocity gas flow through the pores of petroleum reservoirs. When fluid velocities are large, inertial effects become significant and a modification of Darcy's law is necessary. This flow analysis is described by Forchheimer that considers viscous and inertial effects in his equation. A correlation is developed from this analysis to predict the inertial coefficient as a function of rock properties in a single-phase fluid flow.

NOMENCLATURA

A = Área da secção transversal, m^2
c = Constante adimensional da Eq.(20), $(= \beta\sqrt{\kappa})$
D = Constante não-darciana do skin aparente, $(m^3/d)^{-1}$
Da = Número de Darcy
H = Fator de atrito
h = Espessura da formação, m
L = Comprimento da amostra, m
M = Peso molecular, $kg/kgmol$
$m(p)$ = Pseudo-pressão do gás real, $Pa^2/(Pa\ s)$
P_1 = Pressão de injeção na amostra, Pa
P_2 = Pressão na saída da amostra, Pa
Q = Vazão volumétrica do gás, m^3/s (@ 15.9° C e 1 atm)
R = Constante universal dos gases, $Pa\ m^3/kgmolK$
Re = Número de Reynolds
r_e = Raio do reservatório de petróleo ou gás, m
r_w = Raio do poço, m
s = Fator de película
s' = Skin aparente ou fator de película dependente da vazão
S_g = Saturação de gás
S_{wr} = Saturação de líquido imóvel
T = Temperatura absoluta, K
v = Velocidade do fluido, m/s
W = Vazão mássica do gás, Kg/s
Z = Fator de compressibilidade do gás
β = Coeficiente de inércia, m^{-1}
γ = Segundo coeficiente de velocidade, m^3s/kg
κ = Permeabilidade absoluta do meio poroso, m^2
κ_g = Permeabilidade efetiva do gás, m^2
κ_r = Permeabilidade relativa
μ = Viscosidade do gás, $Pa\ s$
ν = Densidade do gás, (ar = 1.0)
ρ = Massa específica do gás, kg/m^3
ϕ = porosidade

BIBLIOGRAFIA

[1] Evans, R.D., Hudson, C.S. and Greenlee, J.E., "The Effect of an Immobile Liquid Saturation on the Non-Darcy Flow Coefficient in Porous Media", SPE Production Engineering,(Nov.1987), pp. 331 - 338.

[2] Noman, R., Shrimanker, N. and Archer, J.S., "Estimation of the Coefficient of Inertial Resistance in High-Rate Gas Wells", SPE - 14207, 10 pp.

[3] Geertsma, J., "Estimating the Coefficient of Inertial Resistance in Fluid Flow Through Porous Media", Society of Petroleum Engineers Journal, (Oct.1974), pp. 445 - 450.

[4] Energy Resources Conservation Board, "Theory and Practice of the Testing of Gas Wells", third edition, Calgary, Canada, 1975

[5] Firoozabadi, A. and Katz, D.L., "An Analysis of High-Velocity Gas Flow Through Porous Media", Journal of Petroleum Technology, (Feb. 1979), pp. 211 - 216.

[6] Amyx, J.W., Bass, D.M. and Whiting,R.L., "Petroleum Reservoir Engineering", McGraw-Hill Book Company, (1960), pp. 86 - 96.

[7] Green,L. and Duwez,P.,"Fluid Flow Through Porous Metals", J. Appl. Mech.,(Mar.1951) **18,39.**

[8] Tek,M.R.,"Development of Generalized Darcy Equation" Trans.,AIME , (1957) **210**, 376-377.

[9] Katz,D.L.,Cornell,D.Kobayashi,R.,Poettman,F.H.,Vary,J.A., Elenbaas,J.R. and Weinaug,C.F., "Handbook of Natural Gas Engineering", McGraw-Hill Book Company Inc., New York City, (1959)

[10] Houpeurt,A.,"On The Flow of Gases in Porous Media",Revue l'Institut Français du Petrole, (Nov.1959) **XVI**,1468

[11] Johnson,T.W. and Taliaferro,D.B.,"Flow of Air and Natural Gas Through Porous Media",Techinical Paper 592, USBM, (1938).

[12] Forchheimer,P.,"Wasserbewegung durch Boden, Zeitz ver deutsch Ing., (1901) **45**, 1731.

[13] Wright,D.E.,"Non-Linear Flow Through Granular Media", "J. Hydraulic Div." ASCE(1968) **94**, 851

[14] Cooke,C.E.Jr.,"Conductivity of Fracture Proppants in Multiple Layers" JPT, (Sept.1973) 1101-08, Trans-AIME, **255**

III ENCIT – Itapema, SC (Dezembro 1990)

CONVECÇÃO NATURAL NO INTERIOR DE UMA CAVIDADE POROSA IRREGULAR

JORGE I. LLAGOSTERA BELTRÁN
OSVAIR VIDAL TREVISAN
Departamento de Energia, FEM/UNICAMP
C.P. 6122 - CEP 13081 - Campinas - SP

RESUMO

A convecção natural no interior de uma cavidade porosa irregular aquecida em sua parede inferior foi analisada. A influência do número de Rayleigh modificado, na faixa de 0 a 1600, e dos parâmetros geométricos relevantes foi estudada por meio de simulações numéricas. Foram obtidos os valores locais e globais do número de Nusselt na parede aquecida para os diversos casos e caracterizados o escoamento e os campos de temperatura.

INTRODUÇÃO

O fenômeno da convecção em meios porosos vem sendo estudado crescentemente em função do desenvolvimento das tecnologias envolvendo energia geotérmica, processos térmicos de recuperação de petróleo, isolamentos térmicos de elevado desempenho em sistemas criogênicos e armazenamento de rejeitos nucleares em sítios geológicos considerados adequados. Os estudos realizados tem-se dirigido principalmente à análise da convecção natural em camadas horizontais aquecidas em sua região inferior e em camadas verticais submetidas a gradientes verticais de temperatura [1].

Trabalhos publicados recentemente referem-se a situações envolvendo convecção natural em cavidades porosas retangulares com paredes aquecidas ao longo de trechos limitados ou não [2], [3], [4].

Neste trabalho o objeto de estudo corresponde à análise da convecção natural no interior de uma cavidade porosa irregular, a qual pode ser descrita como uma cavidade retangular horizontal que apresenta uma depressão aquecida na base em uma de suas extremidades.

Constitui o objetivo do trabalho a análise do efeito das características geométricas da cavidade e dos parâmetros térmicos do problema sobre o escoamento e sobre as taxas de transferência de calor.

FORMULAÇÃO DO PROBLEMA

Foi estudado o fenômeno de convecção natural em um meio poroso saturado, correspondente a uma cavidade irregular representada na Figura 1. Todas as paredes da cavidade são impermeáveis. A parede quente (a) e a fria (b) são mantidas a temperaturas uniformes, sendo todas as demais adiabáticas.

O problema refere-se a um fluido incompressível, de propriedades constantes, escoando em regime permanente através de um meio poroso rígido, homogêneo e isotrópico. Os efeitos de empuxo decorrentes de diferenças de temperatura no fluido são considerados por meio da aproximação de Boussinesq.

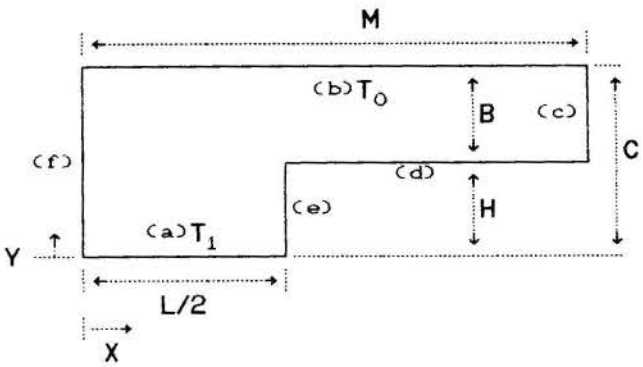

Figura 1. Esquema da cavidade porosa irregular.

Na formulação do problema foi assumida a aplicabilidade da Lei de Darcy, sendo desprezados os têrmos viscosos e os de inércia das equações de conservação da quantidade de movimento. Assume-se, também que em qualquer ponto do meio a matriz porosa e o fluido estão em equilíbrio térmico.

A partir das hipóteses expostas, as equações de conservação de massa e de quantidade de movimento podem ser resumidas em uma única equação envolvendo a função corrente (Ψ^*), definida por

$$u^* = \frac{\partial \Psi^*}{\partial Y} \quad , \quad v^* = -\frac{\partial \Psi^*}{\partial X}$$

onde u^* e v^* representam as componentes da velocidade média por unidade de volume do meio poroso. Foi efetuada a adimensionalização das grandezas envolvidas, sendo definidas as seguintes variáveis:

$$x = \frac{X}{L} \quad , \quad y = \frac{Y}{L} \quad , \quad \Psi = \frac{\Psi^*}{\alpha} \quad , \quad \theta = \frac{T - T_0}{T_1 - T_0}$$

Com o uso dessas variaveis a conservação da massa e da quantidade de movimento podem ser expressas por meio da equação (1), enquanto a equação (2) corresponde à conservação da energia.

$$\frac{\partial^2\Psi}{\partial x^2} + \frac{\partial^2\Psi}{\partial y^2} = \frac{Kg\beta\rho L(T_1 - T_0)}{\mu\alpha}\frac{\partial\theta}{\partial x} \qquad (1)$$

$$\frac{\partial\Psi}{\partial y}\frac{\partial\theta}{\partial x} - \frac{\partial\Psi}{\partial x}\frac{\partial\theta}{\partial y} = \left[\frac{\partial^2\theta}{\partial x^2} + \frac{\partial^2\theta}{\partial y^2}\right] \qquad (2)$$

Nessas equações, θ representa a temperatura de equilíbrio local, adimensionalizada, entre a matriz porosa e o fluido, enquanto α corresponde à difusividade térmica efetiva. A permeabilidade do meio poroso saturado é K, e g refere-se à aceleração da gravidade. Enquanto β representa o coeficiente isobárico de expansão térmica do fluido, ρ corresponde à sua massa específica e μ à sua viscosidade dinâmica.

As condições de contorno são representadas a seguir, de acordo com a Figura 1.

(a) $\Psi = 0 \quad \wedge \quad \theta = 1$ (3)

(b) $\Psi = 0 \quad \wedge \quad \theta = 0$ (4)

(c), (d), (e), (f) $\Psi = 0 \quad \wedge \quad \frac{\partial\theta}{\partial n} = 0$ (5)

onde n corresponde à direção normal à parede correspondente.

Analisando as expressões (1) a (5) podem ser definidos os seguintes parâmetros adimensionais relevantes:

Rayleigh modificado: $Ra = \frac{Kg\beta\rho L(T_1 - T_0)}{\mu\alpha}$

relações geométricas: $\frac{H}{L}$, $\frac{B}{L}$, $\frac{M}{L}$

Foram calculados, com base na dimensão L, o valor de Nusselt local e global em relação à parede quente (a) e o valor local para a parede fria (b), de acordo com as expressões (6) e (7), respectivamente.

(a) $Nu_x = -\left.\frac{\partial\theta}{\partial y}\right|_{y=0} \qquad Nu = 2\int_0^{1/2} -\left.\frac{\partial\theta}{\partial y}\right|_{y=0} dx$ (6)

(b) $Nu''_x = -\left.\frac{\partial\theta}{\partial y}\right|_{y=C/L}$ (7)

SOLUÇÃO NUMÉRICA

As equações diferenciais foram resolvidas numericamente por meio de programa computacional elaborado especificamente para domínios irregulares deste tipo [5]. A discretização das equações foi efetuada por meio de integração em volumes de controle finitos, e os fluxos convectivos nas fronteiras de cada volume de controle foram representados por meio do esquema da lei de potência, proposto por Patankar [6]. Foram definidas como objeto de estudo as situações em que a dimensão M é grande comparada com as demais, e em particular com a dimensão B, que define a espessura da camada horizontal. Por meio da análise de diversos casos concluiu-se pela adoção de M superior a 4B, de modo a contemplar essa premissa de trabalho. Em casos envolvendo números de Rayleigh elevados foram utilizados valores de M superiores a 5B.

Os sistemas de equações algébricas obtidos foram resolvidos utilizando-se o procedimento iterativo linha-a-linha, com alternância no sentido e direção de varredura, completando dessa forma um ciclo de quatro varreduras do domínio de cálculo. Em cada iteração foram realizados quatro ciclos para Ψ e quatro ciclos para θ, a fim de reduzir o número de iterações necessárias, como indicado na Tabela 1.

Em todos os casos estudados foram adotadas, como ponto de partida para o processo iterativo, distribuições nulas de temperatura e da função corrente, exceto quando assinalado em contrário.

Tabela 1. Análise do efeito do número de ciclos de varredura (B/L=H/L=0,25; Ra=200; grade: 62x42).

	Ciclos em (Ψ/θ)			
	(1/1)	(2/2)	(3/3)	(4/4)
Nusselt	5,8052	5,8056	5,8057	5,8057
ΔE_R (%)	0,335	0,327	0,325	0,324
Iterações	153	86	62	49
CPU (índice)	152	116	106	100

O processo iterativo foi interrompido somente depois que os valores de Ψ, θ e Nu tivessem satisfeito os seguintes critérios:

$$\Delta\xi_R = \frac{\sum_{i,j}|\xi_n - \xi_{n-1}|}{\sum_{i,j}|\xi_n|} < \delta \; ; \quad \Delta Nu_R = \frac{|Nu_n - Nu_{n-1}|}{|Nu_n|} < \delta$$

onde ξ representa Ψ e θ, e n corresponde à iteração mais recente. O valor de δ adotado neste trabalho foi 10^{-5}, considerado adequado para a determinação das taxas globais de transferência de calor e para a obtenção de resíduos suficientemente pequenos no balanço de energia. Esse resíduo foi avaliado de acordo com a expressões (8) e (9).

$$\Delta E_R = \frac{E_S - E_N}{E_S + E_N} \qquad (8)$$

$$E_S = \int_0^{1/2} -\left.\frac{\partial\theta}{\partial y}\right|_{y=0} dx \qquad E_N = \int_0^{M/L} -\left.\frac{\partial\theta}{\partial y}\right|_{y=C/L} dx \qquad (9)$$

A grade foi definida dividindo-se o domínio da Figura 1 em retângulos, representando os volumes de controle finitos. Os pontos discretos do domínio de cálculo foram alocados no centro de cada volume de controle. Em todo o contorno do domínio foram considerados volumes de controle com dimensão nula na direção normal ao contorno.

O efeito do refinamento da grade foi também analisado. A Tabela 2 ilustra a abordagem utilizada na análise. Na tabela o item "grade" refere-se à uma grade retangular que contém o domínio irregular. Os procedimentos de cálculo foram executados somente para os pontos da grade pertencentes ao domínio, indicados também na tabela.

Tabela 2. Análise do efeito do refinamento da grade (B/L=H/L=0,25; Ra=200).

Intervalo	Número de Volumes de Controle A	B	C	D	E
x ∈ [0 , 1/2]	15	20	25	30	40
x ∈ [1/2, 3/2]	30	40	50	60	80
y ∈ [0 , 1/4]	15	20	25	30	40
y ∈ [1/4, 1/2]	15	20	25	30	40
Grade	47x32	62x42	77x52	92x62	122x82
Pontos	900	1600	2500	3600	7200
Nusselt	5,753	5,806	5,832	5,846	5,861
ΔE$_R$ (%)	0,49	0,32	0,23	0,18	0,12
Iterações	31	49	74	107	197
CPU (índice)	17	44	100	211	746

A fim de verificar a possibilidade de melhor representar os gradientes de temperatura na região próxima às paredes, por meio da subdivisão dos volumes de controle que tem uma face na parede, foram analisados os casos apresentados na Tabela 3, onde "pontos" representa os nós da grade interiores ao domínio, para os quais Ψ e θ foram efetivamente calculados. A única parede em que não foi efetuada a subdivisão foi a definida por x = M/L (distante da região aquecida).

Tabela 3. Verificação do efeito da subdivisão dos volumes junto às paredes (B/L=H/L=0,25; Ra=200; grade: 62x42).

	Denominador da Subdivisão 1	2	3	4
Grade	62x42	64x45	66x48	68x51
Pontos	1600	1826	2064	2314
Nusselt	5,8057	5,8172	5,8202	5,8219
ΔE$_R$ (%)	0,324	0,249	0,226	0,214
Iterações	49	109	117	124
CPU (índice)	44	109	130	155

Pode ser observado na Tabela 3 que a subdivisão causou um aumento brusco no número de iterações necessário e, portanto, no tempo total necessário à obtenção da solução. Analisando graficamente a evolução do cálculo ao longo do processo iterativo, por meio da elaboração de curvas de nível em termos de Ψ, constatou-se que nos casos em que foi verificado o aumento do número de iterações, durante a evolução do processo iterativo de solução formaram-se zonas adicionais de recirculação que demandaram tempo adicional para serem desfeitas, e que não surgiram quando a grade utilizada não foi subdividida.

Em função dessas considerações optou-se pelo uso de grades não subdivididas nas paredes e com grau de refinamento similar ao da grade C, apresentada na Tabela 2, de modo que ao longo do comprimento aquecido houvessem ao menos 25 volumes de controle.

Em relação à estabilidade e convergência do processo de resolução os resultados foram bastante satisfatórios, não tendo sido necessário o uso de fatores de relaxação.

RESULTADOS E DISCUSSÃO

Inicialmente foi estudada a influência do número de Rayleigh (Ra), variando entre 0 e 1600, sobre as taxas locais e global de transferência de calor para as configurações geométricas dadas por B/L = H/L = 0,25 e 1,0.

O número de Nusselt Global, calculado na parede quente de acordo com a equação (6), foi dividido para todos os casos pelo parâmetro D. Esse parâmetro representa a taxa de transferência de calor na situação puramente difusiva. Os resultados estão representados na Figura 2, para as duas configurações geométricas citadas.

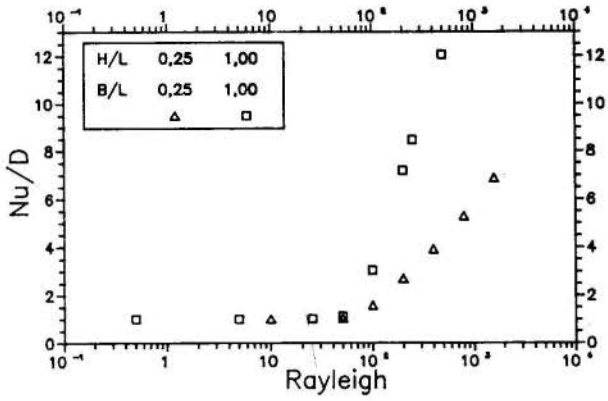

Figura 2. Efeito convectivo sobre as taxas globais de transferência de calor em função do número de Rayleigh (B/L=H/L=0,25 e B/L=H/L=1).

Por meio da Figura 2 pode-se observar o incremento da influência do efeito convectivo sobre a transferência de calor à medida em que Rayleigh aumenta, sendo que esse efeito,nos dois casos, passa a ser significativo no intervalo dado por 50< Ra <100.

Observa-se também que o efeito convectivo é mais acentuado para a geometria definida por B/L=H/L=1, situação em que a resistência térmica puramente difusiva é bem superior. Para as duas configurações, em todos os casos, observou-se a ocorrência de uma única zona de circulação (sentido horário). Nas Tabelas 4 e 5 são apresentados os resultados obtidos para essas configurações.

Tabela 4. Resultados para Nusselt Global (B/L=H/L=0,25).

Rayleigh	Nusselt	Ψ_{min}	ΔE$_R$ (%)
0	2,162	0,000	0,02
10	2,162	-0,058	-0,07
50	2,213	-0,471	-0,38
100	3,389	-2,519	-0,35
200	5,812	-5,628	-0,37
400	8,457	-9,256	-0,40
800	11,424	-13,874	-0,66
1600	14,867	-20,124	-1,11

Na Tabela 4 pode-se observar que para Ra=50 já é possível notar um pequeno efeito convectivo no valor de Nusselt Global, bem como na intensidade da circulação dada pelo valor do mínimo de Ψ. Para a geometria dada por B/L=H/L=1, de acordo com a Tabela 5, o mesmo fenômeno pode ser observado para Ra=25.

Pode-se também observar que para valores similares de Rayleigh, os casos referentes à geometria B/L=H/L=1 apresentam valores superiores de $|\Psi_{min}|$, o que é coerente com o efeito convectivo mais acentuado observado na Figura 2 para essa geometria.

Tabela 5. Resultados para Nusselt Global (B/L=H/L=1,0).

Rayleigh	Nusselt	Ψ_{min}	ΔE_R (%)
0,0	0,643	0,000	-0,08
0,5	0,643	-0,007	-0,09
5	0,643	-0,069	-0,22
25	0,650	-0,410	-0,82
50	0,717	-1,042	-1,58
100	1,952	-3,554	-0,87
200	4,615	-7,562	-0,34
250	5,431	-8,985	-0,29
500	7,740	-14,322	-0,40

Foi também analisado o efeito de H/L. Na Figura 3 são apresentados os resultados para o Nusselt Global para duas configurações geométricas dadas, respectivamente, por B/L=0,25 e B/L=1, mantendo-se em todos os casos Rayleigh = 200, para o qual o efeito convectivo é apreciável.

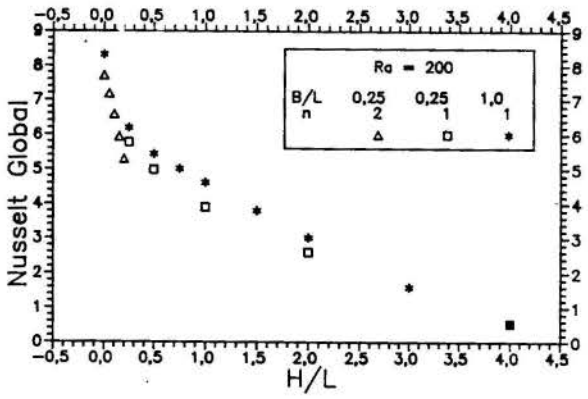

Figura 3. Taxas globais de transferência de calor em função de H/L (Ra=200).

Por meio da Figura 3 pode-se observar que os resultados obtidos, em têrmos de Nusselt Global, para as duas configurações tem uma distribuição similar e valores próximos. O efeito do aumento de H/L é a redução progressiva da transferência de calor, e a diminuição relativa da diferença entre os resultados para as duas configurações.

Para todos os casos em que B/L=1 foi obtida uma única célula de circulação (n=1), enquanto que para os casos onde B/L=0,25 observou-se a transição de duas células (n=2) para uma única célula (n=1) entre H/L=0,20 e H/L=0,25, acompanhada de um incremento no valor de Nusselt Global (Tabela 6).

É interessante observar que na transição de uma para duas células, o aumento de Nusselt é acompanhado de uma redução na vazão, indicada por $\Psi_{max} - \Psi_{min}$.

A Figura 4 apresenta os mapas de linhas de corrente e de isotermas para H/L=0,20 e H/L=0,25.

Tabela 6. Resultados para Nusselt Global em função de H/L (B/L=0,25 e Ra=200).

H/L	Nusselt	Ψ_{min}	Ψ_{max}	$\Psi_{max} - \Psi_{min}$
0,00	7,743	-3,286	2,154	5,440
0,05	7,175	-3,594	2,669	6,263
0,10	6,567	-3,818	2,675	6,493
0,15	5,928	-3,978	2,466	6,444
0,20	5,288	-4,065	2,053	6,118
0,25	5,769	-5,613	0,000	5,613
0,50	4,983	-6,239	0,000	6,239
1,00	3,904	-6,031	0,000	6,031
2,00	2,600	-4,910	0,000	4,910
4,00	0,533	-1,841	0,000	1,841

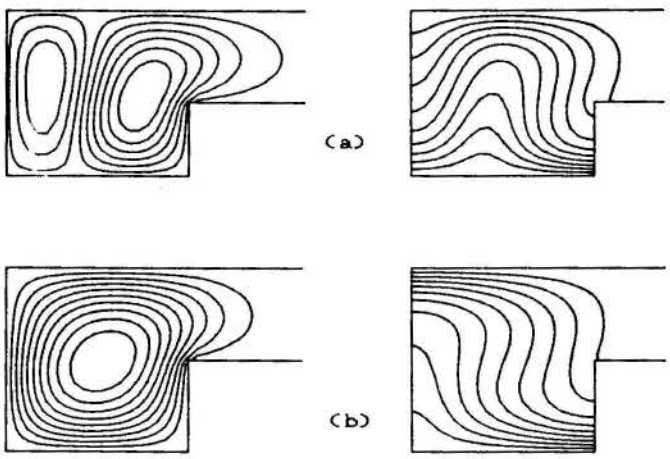

Figura 4. Mapas de linhas de corrente e de isotermas para H/L=0,20 (a) e H/L=0,25 (b), com B/L=0,25; Ra=200 e $\Delta\Psi=\Delta\theta=0,1$ da faixa.

A variação de Nusselt local na parede quente, apresentada na Figura 5, para alguns casos envolvendo B/L=0,25 e Ra=200, indica que o ponto de mínimo que ocorre nos casos que apresentaram duas células, desloca-se progressivamente para a esquerda com o aumento de H/L. O valor da taxa local de transferência de calor nesses pontos de mínimo mantém-se praticamente constante nos diversos casos com duas células. Esse fato corresponde ao progressivo alargamento da região inferior da célula da direita (circulação no sentido horário) com o aumento de H/L. Destaca-se também o comportamento qualitativamente distinto da curva obtida para H/L=0 em relação aos demais casos. Nessa situação observa-se variação acentuada de Nusselt local nas proximidades de x=0,5, correspondente ao final do trecho aquecido.

Nos casos que apresentaram uma única célula, as curvas são crescentes ao longo da parede quente. À medida em que H/L aumenta, a distribuição vai tornando-se cada vez mais uniforme. Com H/L=4,0 a distribuição de Nusselt local é basicamente uniforme, indicando que para valores maiores de H/L os resultados sofrerão pequenas alterações.

Para os mesmos casos abordados na Figura 5 são apresentadas as curvas de distribuição de Nusselt local ao longo da parede fria na Figura 6. Nos casos que apresentaram duas células as curvas apresentam pontos de máximo que decrescem com o incremento de H/L.

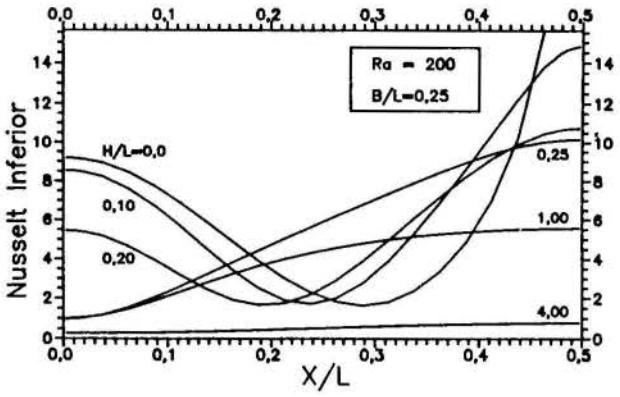

Figura 5. Distribuição de Nusselt local ao longo da parede quente (B/L=0,25 e Ra=200).

Para H/L=0 o máximo situa-se à direita dos pontos de máximo registrados para H/L=0,10 e para H/L=0,20, sendo que nestes dois casos o máximo ocorre quase que no mesmo local da parede fria (X/L ≅ 0,24). Pode-se também observar que em todos os casos o valor de Nusselt local é praticamente nulo para X/L > 1.

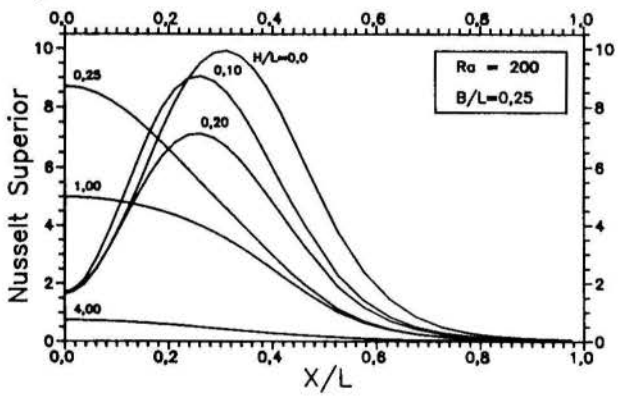

Figura 6. Distribuição de Nusselt local ao longo da parede fria (B/L=0,25 e Ra=200).

Com o objetivo de explorar o surgimento de diversas células em função do número de Rayleigh considerou-se interessante analisar dois conjuntos de casos com B/L=0,25. Na Figura 7 são apresentados os resultados obtidos para o Nusselt Global, dividido pela taxa obtida para a situação puramente difusiva, para H/L=0,10 e para H/L=0,20. Nessa figura podem ser observados os dois conjuntos de resultados e o correspondente número de células obtido para cada caso. De modo geral, as duas famílias de valores são bastante próximas, mas pode-se observar um efeito convectivo ligeiramente superior para H/L=0,20, confirmando tendência já observada por meio do gráfico da Figura 2. Pode ser observada, para os dois valores de H/L estudados, a passagem de uma para duas células e de duas para três células, com o incremento do número de Rayleigh. A ocorrência da alteração do número de células para H/L=0,10 verifica-se para valores inferiores de Rayleigh, em comparação à ocorrência correspondente aos casos para H/L=0,20.

É interessante observar que apesar da alteração do número de células o comportamento geral dos resultados para as taxas globais de transferência de calor não sofre mudanças significativas quanto à sua tendência de evolução em função do número de Rayleigh.

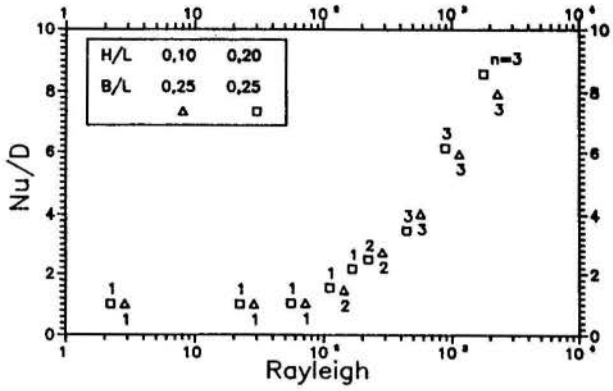

Figura 7. Efeito convectivo em função de Rayleigh, com B/L=0,25 para H/L=0,10 e 0,20.

Os mapas de linhas de corrente e de isotermas para um dos casos em que foram obtidas três células são apresentados na Figura 8.

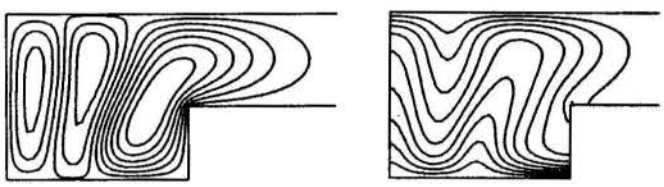

Figura 8. Mapas de linhas de corrente e de isotermas para H/L=0,20 com B/L=0,25; Ra=444 e $\Delta\Psi=\Delta\theta=0,1$ da faixa.

Estudando-se a variação de Nu/D em relação à evolução da faixa de variação de Ψ ($\Delta\Psi$) nos casos em que o efeito convectivo dado por Nu/D foi superior a 1,01 observou-se uma forte correlação entre os mesmos. Foi feita regressão linear, cujo resultado é apresentado na Figura 9.

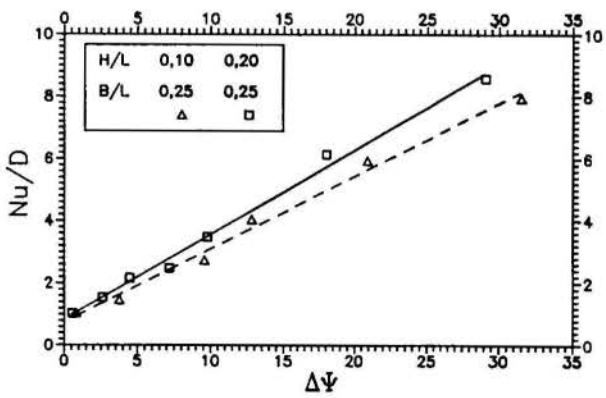

Figura 9. Efeito convectivo em função de $\Delta\Psi = \Psi_{max} - \Psi_{min}$, com B/L=0,25 para H/L=0,1 e 0,2.

Para H/L = 0,10 o coeficiente da regressão foi 0,235, e o coeficiente de correlação foi 0,994. Para H/L = 0,20 o coeficiente da regressão foi 0,272 e o coeficiente de correlação obtido foi 0,997. Esses resultados indicam uma intensa correlação linear entre o efeito convectivo na transferência de calor e a vazão representada adimensionalmente por $\Delta\Psi = \Psi_{max} - \Psi_{min}$.

Procurou-se também estudar o efeito do parâmetro B/L sobre as taxas de transferência de calor. Para tanto foram analisadas duas situações com Ra=200 , para os valores H/L=1 e H/L=0, e os resultados estão representados na Figura 10.

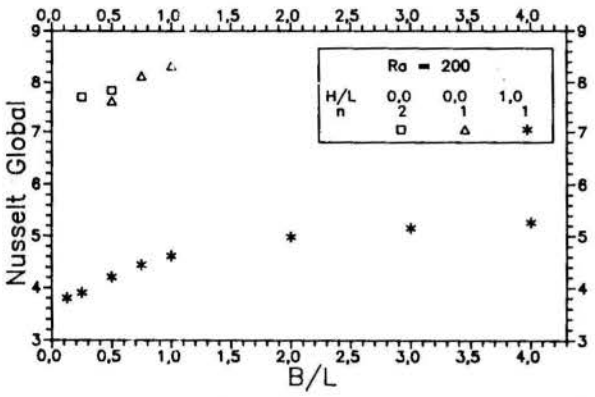

Figura 10. Nusselt global em função de B/L (Ra=200).

Para H/L=1 observa-se um aumento significativo de Nusselt Global em função de B/L para valores desse parâmetro entre 0,125 e 1,0, sendo que para valores superiores de B/L o efeito dos sucessivos incrementos torna-se progressivamente menos importante. Em todos os casos estudados com H/L=1 foram obtidas soluções com uma única célula de circulação no sentido horário.

Para H/L=0 o domínio corresponde a um retângulo com um trecho aquecido em sua parede inferior. Nestes casos foi observada, além do crescimento de Nussselt Global em função de B/L, a mudança de duas células para uma célula, com o aumento de B/L.

Verificou-se também a ocorrência de duas soluções diferentes, extensivamente testada e confirmada, para o caso com B/L=0,5, situado na transição de um modo de escoamento para o outro. Partindo de uma distribuição nula inicial para o campo de temperaturas e para o de velocidades, foi obtida a solução com duas células, e partindo-se de solução anterior, obtida para Ra=100, obteve-se a segunda solução, com uma única célula. Esses resultados que indicam duplicidade de soluções para um mesmo caso são detalhados na Tabela 7.

Tabela 7. Nusselt Global em função de B/L (H/L=0 e Ra=200).

B/L	Nu	Ψ_{min}	Ψ_{max}	ΔE_R (%)
0,25	7,743	-3,286	2,154	0,30
0,50	7,921	-5,568	3,039	0,95
0,50	7,692	-6,271	0,000	1,02
0,75	8,224	-7,956	0,000	1,40
1,00	8,430	-8,974	0,000	1,75

A solução com duas células apresentou Nusselt Global, e faixa de variação da função corrente Ψ, superiores ao da solução com uma célula, e os resíduos ΔE_R obtidos foram muito próximos. A possibilidade de ocorrência de múltiplas soluções em problemas de convecção natural em meios porosos foi demonstrada numericamente por Robillard e outros [3] para o caso de uma cavidade quadrada, com aquecimento na região central da parede inferior e o uso de perturbações iniciais adequadas. Os autores citados afirmam que em regime permanente várias soluções são possíveis envolvendo diferente número de células, e que o sentido de rotação dessas células pode ser revertido em alguns casos.

Em conclusão, neste trabalho foi analisado o efeito do incremento do número de Rayleigh modificado sobre o padrão de escoamento (unicelular ou multicelular) e sobre as taxas de transferência de calor em função dos parâmetros geométricos da cavidade, considerados aqui por meio de B/L e H/L. Procurou-se estudar o efeito específico dos parâmetros geométricos, mantendo-se constante o número de Rayleigh. A distribuição de Nusselt local foi analisada para as paredes quente e fria, observando-se as diferenças entre casos envolvendo escoamento unicelular e bicelular. Finalizando, mapas de linhas de corrente e de isotermas foram apresentados, permitindo a observação das distintas características dos diversos padrões celulares de escoamento.

REFERÊNCIAS

[1] BEJAN, A. Convective heat transfer in porous media. In: KAKAÇ, S.; SHAH, R.K.; AUNG, W., eds. **Handbook of single-phase convective heat transfer**. New York: Wiley, 1987.

[2] PRASAD, V.; KULACKI, F.A.; STONE, K. Free convection in a porous cavity with a finite wall heat source. In: FIGLIOLA, R.S.; CATTON, I., eds. **Natural convection in enclosures**. ASME HTD, v.63, p.91-98, 1986.

[3] ROBILLARD, L.; WANG, C.H.; VASSEUR, P. Multiple steady states in a confined porous medium with localized heating from below. **Numerical Heat Transfer**, v. 13, p. 91-110, 1988.

[4] TREVISAN, O.V.; BEJAN, A. Mass and heat transfer by high Rayleigh number convection in a porous medium heated from below. **Int. J. Heat Mass Transfer**, v. 30, p. 2341-2356, 1987.

[5] LLAGOSTERA B., J.I.; TREVISAN, O.V. Convecção forçada sobre uma cavidade porosa aberta. **Anais do X Congresso Brasileiro de Engenharia Mecânica**, v. I, p. 305-308, Rio de Janeiro, 1989.

[6] PATANKAR, S.V. **Numerical heat transfer and fluid flow**. New York: Hemisphere, 1980.

ABSTRACT

Natural convection flow induced by heating from below in a irregular porous cavity is investigated numerically. The influence of the modified Rayleigh number and geometric ratios on heat transfer and fluid flow is studied. Global and local Nusselt numbers on the heated surface are obtained for Rayleigh numbers covering the range 0 - 1600 and for several geometric ratios. The fluid flow and the temperature field are illustrated by contour maps.

III ENCIT – Itapema, SC (Dezembro 1990)

TRATAMENTO NUMÉRICO DA EQUAÇÃO DE DIFUSÃO-CONVECÇÃO PARA MODELO PADRÃO DE CINCO-POÇOS

R. L. A. Santos, A. C. F. Corrêa, O. A. Pedrosa Jr.
Universidade Estadual de Campinas - Departamento de Engenharia de Petróleo
Caixa Postal 6122
13081 Campinas SP Brasil

RESUMO

Este trabalho consiste no estudo de deslocamento miscível em reservatório desenvolvido por padrão de 5-poços. O tratamento numérico do problema é realizado por diferenças finitas, utilizando-se o esquema exponencial proposto por Patankar [1]. O método reduz a dispersão numérica e não apresenta oscilações encontradas quando se utiliza diferenciamento central ou esquema a montante. O procedimento descrito no artigo garante que o grau de convergência entre a solução numérica e a analítica é independente do mecanismo que rege o escoamento (convecção ou difusão). Objetivando-se minimizar efeitos de orientação de malha , implementou-se esquema de discretização por 9-pontos baseado na proposta apresentada por Bertiger & Padmanabhan [4]. Com este esquema, a solução numérica independe do ângulo entre a malha e a direção de escoamento.

INTRODUÇÃO

Considerando-se o problema de deslocamento miscível em reservatório de geometria bidimensional, desenvolvido por padrão de 5-poços, o tratamento numérico da equação de Difusão-Convecção com a aplicação da técnica padrão de discretização por diferenças finitas apresenta dificuldades, quando o processo convectivo é dominante (altos números de Peclet).

Dispersão numérica, instabilidades, oscilações e efeitos de orientação de malha são os problemas enfrentados. A aplicação do método de diferenciamento central pode resultar em soluções numéricas instáveis com oscilações, sendo geralmente empregado o método a montante para contornar tal problema. Desta forma, a aproximação de segunda ordem para o termo convectivo é substituída por uma aproximação de primeira ordem, causando a suavização artificial das frentes de concentração [1], [2], [3], o que pode ser minimizado com o refinamento do grid.

Este trabalho apresenta uma proposta de diferenças finitas que se baseia na obtenção da equação de diferenças a partir da solução analítica da equação de Difusão-Convecção para o problema unidimensional, resultando em esquema exponencial (Patankar [1]).

Para a geometria em questão, verificou-se que a simulação numérica baseada em esquemas de diferenças finitas por 5-pontos fornece respostas diferentes se a orientação dos eixos coordenados com relação à direção real de escoamento é alterada, malhas diagonal e paralela (fig 1). O erro de difusão numérica em sistemas multidimensionais, chamado de "falsa difusão", é rotacionalmente dependente da orientação do sistema de malha [1], [2]. Para contornar este efeito de orientação de malha será aplicado um esquema de 9-pontos baseado na proposta de Bertiger & Padmanabhan [4] para processos puramente convectivos.

Resultados apresentados demonstram a resposta do esquema proposto com relação à variação do número de Peclet e variação da orientação de malha.

EQUAÇÕES DIFERENCIAIS

O transporte de um traçador , conservativo e não reagente, por um fluido de densidade e viscosidade constantes através de um meio poroso, é dado pela equação de Difusão-Convecção [5] :

$$\frac{\partial(\phi C)}{\partial t} + \nabla.\mathbf{J} + \nabla.(\mathrm{u}C) + qCi = 0 \qquad (1)$$

$$\mathbf{J} = -\phi\mathcal{D}\nabla C \qquad (2)$$

sendo C a concentração do traçador no meio poroso, ϕ a porosidade, q o termo fonte/sorvedouro, u vetor velocidade intersticial, Ci a concentração de injeção, $\mathbf{J}$ vetor fluxo difusivo e $\mathcal{D}$ tensor coeficiente de dispersão.

O escoamento do traçador em solução considera dois fenômenos: a convecção, representada pelo terceiro termo da eq. (1), e a dispersão, representada pelo segundo termo. A dispersão hidrodinâmica está relacionada ao espalhamento do traçador em solução, incluindo dois processos: dispersão mecânica, resultante do movimento das partículas do fluido no meio poroso, e a difusão molecular devido aos gradientes de concentração através de superfícies perpendiculares à direção do escoamento. O efeito da difusão molecular é significativo somente em condições de baixas velocidades, podendo ser desprezada.

O coeficiente de dispersão é relacionado à velocidade intersticial por [5]:

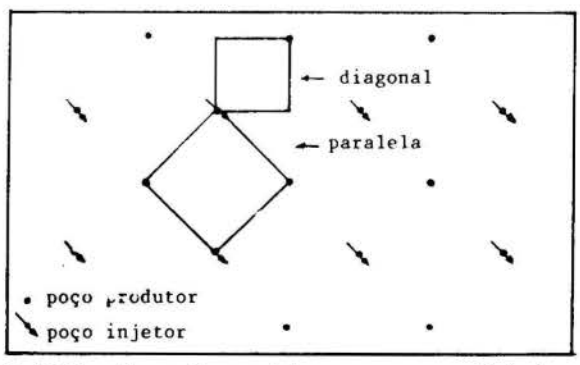

fig.1- Malhas diagonal e paralela para um reservatório desenvolvido por padrão de injeção 5-poços.

$$D_x = \frac{\alpha |u_x|}{\phi} \tag{3}$$

sendo α a dispersividade do meio, $|u_x|$ o módulo da velocidade em x e D_x o coeficiente de dispersão em x.

A convecção relaciona-se ao deslocamento do fluido causado por um gradiente de pressão. O campo de pressão em regime permanente é obtido pelo tratamento numérico da equação diferencial parabólica representativa do escoamento horizontal de um fluido incompressível, de viscosidade invariante com a pressão, através de meio poroso homogêneo e isotrópico, dada pelo Princípio de Conservação da Massa em combinação com a equação de Darcy:

$$\nabla^2 p = \frac{\phi \mu ct}{k} \frac{\partial p}{\partial t} + \frac{\mu}{k} q \tag{4}$$

onde p é pressão, μ viscosidade, ct coeficiente de compressibilidade, k permeabilidade e q termo fonte/sorvedouro.

TRATAMENTO NUMÉRICO

Equação de Pressão. Objetivando-se definir o campo de pressões para regime permanente, tratou-se numericamente a equação de fluxo (4) por diferenças finitas, utilizando-se a técnica de diferenciamento central para as derivadas espaciais e método implícito em relação ao tempo. Tal procedimento não implica em problemas numéricos por se tratar de uma equação parabólica.

O modelo tem geometria 1/4 do padrão de 5-poços, quadrado, malha regular e distribuição de bloco centrado. Não há escoamento através dos limites do meio poroso, aplicando-se a técnica da reflexão no tratamento das fronteiras. Nos blocos de injeção e produção foi utilizado conceito de raio equivalente desenvolvido por Peaceman [6].

Equação de Difusão-Convecção. Trabalhando-se com a forma integral da equação (1),temos:

$$\int_V \frac{\partial(\phi C)}{\partial t} dV + \int_V \nabla.\mathbf{J}\, dV + \int_V \nabla.\mathbf{u}C\, dV + \int_V qCi\, dV = 0 \tag{5}$$

onde V é o volume de controle . Aplicando-se o teorema da divergência, transforma-se a integral de volume em integral de superfície para os termos de fluxo convectivo e difusivo:

$$\begin{aligned} \int_V \frac{\partial(\phi C)}{\partial t} dV &+ \int_A (\mathbf{J}.\mathbf{n})\, dA + \\ \int_A (\mathbf{u}.\mathbf{n}) C\, dA &+ \int_V (qCi)\, dV = 0 \end{aligned} \tag{6}$$

onde A é a área do contorno do volume de controle e $\mathbf{n}$ o vetor unitário normal à superfície.

Considerando-se o volume de controle como o volume do bloco ij (ΔV_{ij}),por diferenças finitas temos:

-termo de acumulação:

$$\frac{\Delta V_{ij}\phi}{\Delta t} \Delta_t (C_{ij}) \tag{7}$$

-termo fonte:

$$qCi \Delta V_{ij} \tag{8}$$

-termo de Difusão+Convecção: A vazão total F (difusão + convecção) através da área de fronteira $A_{i+1/2}$ (fig 2) é:

$$F_{i+1/2} = \int_{A_{i+1/2}} (\mathbf{J}.\mathbf{n})\, dA + \int_{A_{i+1/2}} (\mathbf{u}.\mathbf{n}) C\, dA \tag{9}$$

substituindo-se (2) em (9)

$$F_{i+1/2} = \int_{A_{i+1/2}} -\phi(\mathcal{D}\nabla C.\mathbf{n}) + C(\mathbf{u}.\mathbf{n})\, dA \tag{10}$$

$$\begin{aligned} \nabla C &= \frac{\partial C}{\partial x}\hat{\mathbf{e}}_x + \frac{\partial C}{\partial y}\hat{\mathbf{e}}_y \\ \mathbf{u} &= u_x \hat{\mathbf{e}}_x + u_y \hat{\mathbf{e}}_y \\ dA &= \Delta z\, dy = h\, dy \end{aligned} \tag{11}$$

substituindo-se (11) em (10)

$$F_{i+1/2} = -\phi h \int_{A_{i+1/2}} D_x \frac{\partial C}{\partial x}\, dy + h \int_{A_{i+1/2}} u_x C\, dy \tag{12}$$

Considera-se que ($D_x \partial C/\partial x$) e ($u_x C$) sejam somente funções de x, ou então não variam ao longo da face $A_{i+1/2}$, e integra-se numericamente (12) pelo método de quadratura simples.

$$F_{i+1/2} = -\phi h \Delta y_j \left(D_x \frac{\partial C}{\partial x} \right)_{i+1/2} + \Delta y_j h (u_x C)_{i+1/2} \tag{13}$$

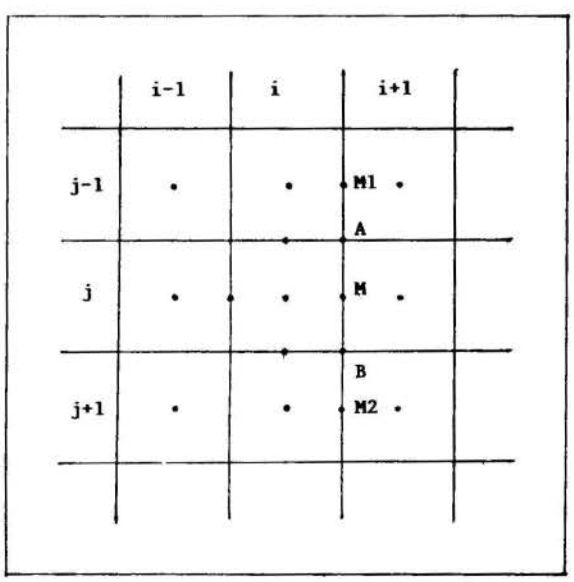

fig.2- Malha de blocos centrados.

A questão crucial do tratamento numérico para o termo convectivo está na aproximação para $C_{i+1/2}$, podendo-se utilizar os esquemas de diferenciamento central e o esquema a montante. Para os dois métodos, o termo difusivo é estimado por diferenciamento central. Tal procedimento é efetuado para as outras faces.

ESQUEMA EXPONENCIAL

O esquema proposto para o adequado tratamento dos termos convectivo e difusivo da equação de Difusão-Convecção é obtido através da solução analítica desta equação em 1 D (Patankar [1], Figueiredo [3]).

Considerando-se escoamento em regime permanente, a equação de Difusão-Convecção é dada por:

$$u_x \frac{dC}{dx} - \phi D_x \frac{d^2C}{dx^2} = 0 \tag{14}$$

Para condições de contorno tais como

$$\begin{aligned} C &= C_0 \quad \text{em } x = 0 \\ C &= C_L \quad \text{em } x = L \end{aligned} \tag{15}$$

A distribuição de concentração é dada por:

$$\frac{C - C_0}{C_L - C_0} = \frac{\exp(\mathrm{Pe}x/L) - 1}{\exp(\mathrm{Pe}) - 1} \tag{16}$$

onde o número de Peclet,(Pe), é definido por

$$\mathrm{Pe} = \frac{u_x L}{\phi D_x} = \frac{u_x L}{\alpha |u_x|} \tag{17}$$

Baseando-se na solução analítica equação (16), verifica-se que no limite Pe = 0 , tem-se o problema de pura difusão, e a variação de C em x é linear, quando então o esquema de diferença centrada é aceitável. Para altos valores de Pe, o valor da concentração na face se aproxima do valor de concentração na fronteira a montante, sendo o resultado obtido próximo ao do esquema a montante. Ainda para valores mais elevados de Pe, o gradiente é nulo na interface, o que significa ausência de difusão.

Obtendo-se a equação de diferenças diretamente da solução exata (16), o esquema resultante não estará sujeito às variações do número de Peclet. Utilizando-se o perfil de concentrações dado por (16) para obter expressões para $(\partial C/\partial x)$ e C nas faces, teremos como vazão total na face $i + 1/2$:

$$F_{i+1/2} = \Delta z \Delta y_j u_{x_{i+1/2}} \left(C_{ij} + \frac{C_{ij} - C_{i+1,j}}{\exp(\mathrm{Pe})_{i+1/2} - 1} \right) \tag{18}$$

Definindo-se $\mathrm{Pe}_{i+1/2}$ por:

$$\mathrm{Pe}_{i+1/2} = \frac{u_{i+1/2} \Delta x}{\alpha |u_{i+1/2}|} \tag{19}$$

Para $\Delta x = \Delta y$,

$$\begin{aligned} \mathrm{Pe}_{j+-1/2} &= \frac{u_{j+-1/2} \Delta y}{\alpha |u_{j+-1/2}|} \\ |\mathrm{Pe}_{i+-1/2}| &= |\mathrm{Pe}_{j+-1/2}| = \mathrm{Pe} \end{aligned} \tag{20}$$

Procedimento analógo é realizado para as demais faces, obtendo-se portanto a aproximação para o problema bidimensional.

De acordo com Figueiredo [3], as discretizações baseadas em equações geratrizes homogêneas (14) coincidem com as obtidas por equações geratrizes não homogêneas com a utilização de grade regular. Neste caso, a equação de Difusão-Convecção seria expressa por:

$$u_x \frac{dC}{dx} - \phi D_x \frac{d^2C}{dx^2} = K \tag{21}$$

sendo K uma constante representativa da soma dos termos fonte, fluxos convectivo e difusivo na direção cruzada ou quaisquer termos extras, segundo o autor.

EFEITO DE ORIENTAÇÃO DE MALHA

Falsa Difusão. Segundo Patankar [1], a chamada "falsa difusão" normalmente atribuída à ordem de acuidade do esquema de discretização, obtida por série de Taylor, é considerada existente somente em fenômenos multidimensionais, surgindo da simplificação ao se tratar o fluxo através de cada face como localmente unidimensional. É um fenômeno essencialmente associado ao ângulo entre a direção do escoamento e os eixos do grid.Tal fenômeno tende a ser minimizado quando se utiliza esquema que leva em consideração a natureza multidimensional do escoamento.

Esquema de 9-Pontos. A simetria da geometria em estudo permite o uso de duas malhas de diferentes orientações, diagonal e paralela (fig. 1).A malha diagonal representa 1/4 de um padrão de 5-poços, com linhas do grid a 45° em relação à linha que une os poços injetor e produtor, enquanto que a paralela representa 1/2 do padrão de injeção, com linhas do grid paralelas e perpendiculares às linhas injetor/produtor.

Esta possibilidade de variação na orientação da malha freqüentemente influencia os resultados da simulação numérica baseada no esquema de discretização de 5-pontos. Tal efeito de orientação pode ser verificado na localização dos contornos de concentração do traçador para os dois tipos de malha.

Com o objetivo de se considerar a natureza multidimensional do problema, como proposta de minimizar o efeito de orientação de malha, utiliza-se esquema de discretização de 9-pontos baseado no esquema desenvolvido por Bertiger & Padmanabhan [4].

A vazão total através da face $i + 1/2$ é dada pela equação (12):

$$\begin{aligned} F_{i+1/2} &= h \int_{A_{i+1/2}} \left(-\phi D_x \frac{\partial C}{\partial x} + u_x C \right) dy \\ &= h \int_{A_{i+1/2}} G_x \, dy \end{aligned} \tag{22}$$

Pelo esquema de 5-pontos, o fluxo total G_x é admitido constante na face $i+1/2$. Pelo esquema de 9-pontos proposto, a integração ao longo de $A_{i+1/2}$ é realizada por regra de Simpson:

$$F_{i+1/2} = h\int_{y_A}^{y_B} G_x\,dy$$
$$= \frac{h\Delta y_j}{6}\left[G_{x_A} + 4G_{x_M} + G_{x_B}\right] \qquad (23)$$

Os fluxos G_{x_A} e G_{x_B} podem ser obtidos por interpolação linear entre pontos vizinhos M_1 e M_2 (fig 2). Emprega-se o esquema exponencial para a definição dos fluxos. Procedimento análogo é realizado para as outras faces.

A equação resultante para o bloco ij terá termos das variáveis no bloco ij e seus oito vizinhos, enquanto que o esquema tradicional de 5-pontos envolve apenas os vizinhos alinhados com os eixos coordenados. O esquema em questão não permite o fluxo direto entre uma célula ij e suas vizinhas diagonais, apesar de considerar a contribuição destas sobre a célula ij quando se faz a interpolação de fluxos nas faces. De acordo com a referência [4], a formulação 5-pontos conduz a resultados que exageram o fluxo ao longo das linhas do grid por não considerar a contribuição diagonal.

Um problema sério que aparece neste esquema é verificado quando a concentração de traçador no bloco ij atinge valor da concentração de injeção . Pelo esquema proposto, os fluxos totais entre a célula ij e suas vizinhas na orientação dos eixos seriam nulos, mas não necessariamente os fluxos obtidos por interpolação. Esta situação pode forçar a injeção de traçador, assumindo um valor de concentração em ij superior ao de injeção. Por tal motivo, colocou-se controle de máxima concentração permitida, o que resultou em erro no balanço material considerado desprezível. Semelhante resultado foi verificado por Rocha [7], o qual adotou mesmo procedimento de controle, tendo como resposta erro no balanço material também considerado desprezível.

A utilização da regra de Simpson na integração tem como objetivo igualar o esquema em estudo ao esquema proposto por Yanosik & Mc Cracken [8] , o qual produz resultados bastante aceitáveis, quando aplicado à malha quadrada, meio isotrópico, fluxo monofásico e pequenos gradientes de pressão [7].

RESULTADOS OBTIDOS

Com o objetivo de se comparar a resposta do esquema proposto em relação aos esquemas tradicionais de diferenças finitas sob diferentes níveis relativos de convecção e difusão, simulou-se o transporte de traçador no modelo em questão, esquema 5-pontos, malha quadrada de orientação diagonal, refinamento de 10 blocos em x e 10 blocos em y, com a variação do número de Peclet.

Após a injeção da metade do volume poroso, plotou-se o perfil de concentração ao longo da linha que une o bloco injetor ao produtor, distância adimensionalizada (LD) em relação a $\sqrt{{L_x}^2 + {L_y}^2}$, sendo L_x e L_y dimensões do reservatório.

Para pequenos valores de Pe, obteve-se resposta com o esquema exponencial próxima da obtida com o diferenciamento central, considerado de maior precisão pela literatura para a condição de difusão predominante. Idêntico comportamento é reportado por Patankar [1] e Figueiredo [3]. Para tal situação, o esquema a montante apresenta resposta com maior dispersão numérica devido à ordem do erro de truncamento (fig 3). Com o aumento da razão convecção-difusão (Pe > 1), verifica-se o problema numérico de oscilações com a utilização de diferenças

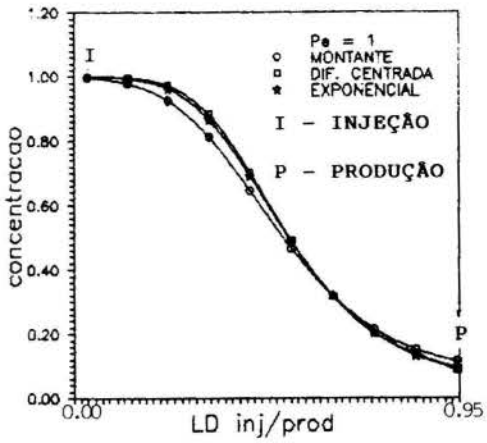

fig.3- Distribuição de concentração ao longo da linha bloco injetor-produtor após 1/2 volume poroso injetado. Distância adimensional LD. Comparação entre esquemas 5-pontos para baixo valor de Pe.

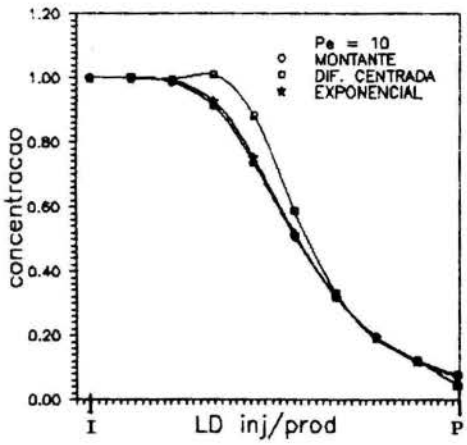

fig.4- Distribuição de concentração ao longo da linha bloco injetor-produtor. Comparação entre esquemas 5-pontos para alto valor de Pe.

centradas devido à instabilidade do método nesta condição de escoamento. As respostas apresentadas pelos esquemas a montante e exponencial não mostram tal deficiência, havendo elevado grau de coincidência nos resultados. Nesta situação, o esquema a montante é considerado eficiente na representação da distribuição de concentração no meio poroso (fig 4).

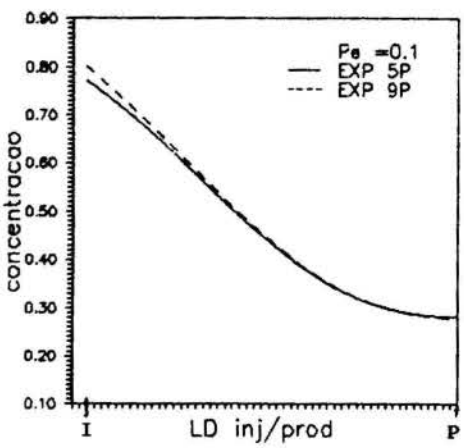

fig.5- Distribuição de concentração ao longo da linha bloco injetor-produtor. Comparação entre esquemas exponenciais 5 e 9-pontos para baixo valor de Pe.

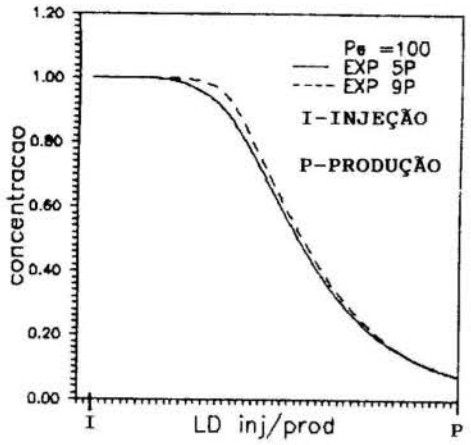

fig.6- Distribuição de concentração ao longo da linha bloco injetor-produtor. Comparação entre esquemas 5 e 9-pontos para alto valor de Pe.

Pelas figuras 5 e 6, compara-se o esquema exponencial por 5-pontos em relação ao 9-pontos. Tanto na condição difusiva quanto em regime convectivo, a distribuição de concentração obtida por 9-pontos é menos suave, sugerindo a minimização de dispersão numérica.

O efeito de orientação de malha para esquema de 5-pontos pode ser verificado na figura 7, representando os contornos de concentração obtidos nas malhas diagonal e paralela após a injeção da metade de volume poroso. Empregando-se o esquema proposto de 9-pontos, há melhora nos resultados (fig 8).

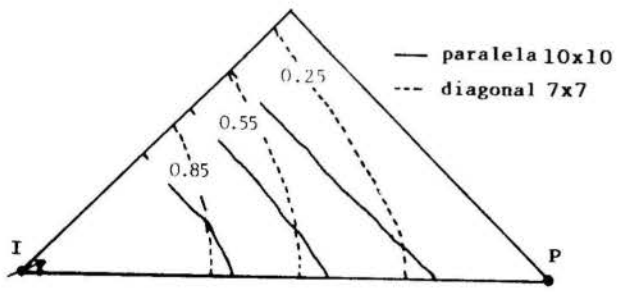

fig.7- Mapas de contorno de concentração após injeção de 0.5 volume poroso. Malhas diagonal e paralela. Esquema exponencial 5-pontos.

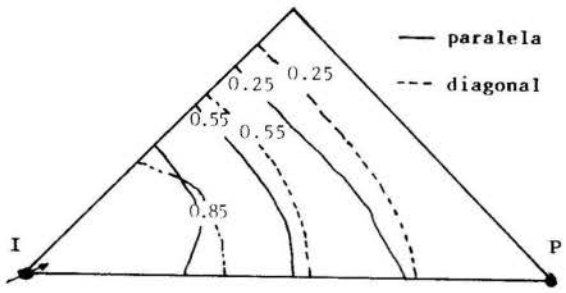

fig.8- Mapas de contorno de concentração. Malhas diagonal e paralela. Esquema exponencial 9-pontos.

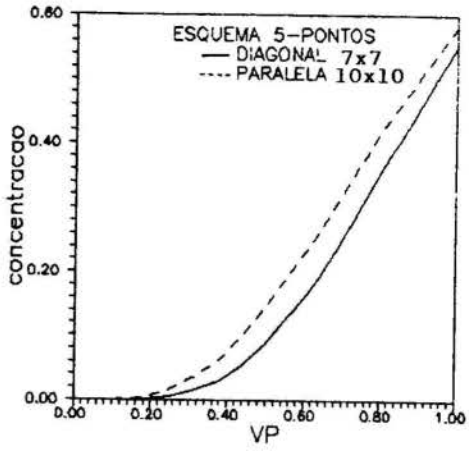

fig.9- Concentração efluente de traçador X volume poroso injetado. Malhas diagonal e paralela. Esquema exponencial 5-pontos.

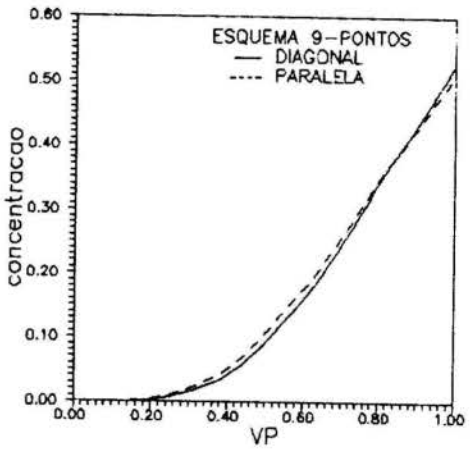

fig.10- Concentração efluente X volume poroso injetado. Esquema exponencial 9-pontos.

A resposta otimizada, obtida com a utilização do esquema de 9-pontos, também é verificada plotando-se a concentração efluente de traçador contra volume poroso injetado para as duas orientações de malha (figs 9 e 10).

CONCLUSÃO

Uma nova proposta de tratamento numérico por diferenças finitas para a equação de Difusão-Convecção em problema bidimensional foi apresentada para a simulação de deslocamento miscível em meios porosos. Foi demonstrado que a modelagem do escoamento com convecção predominante, através do esquema referido, não introduz as dificuldades numéricas normalmente encontradas por técnicas tradicionais, tais como oscilações e instabilidades, minimizando o grau de dispersão numérica e efeito de orientação de malha.

O esquema numérico foi comparado com outros usualmente utilizados, sendo comprovada a eficiência da proposta sob diferentes níveis de convecção e difusão.

BIBLIOGRAFIA

[1] Patankar,S. V.,"Numerical Heat Transfer and Fluid Flow", McGraw-Hill , New York.

[2] Patel,M. ,Cross,M. and Markatos,N. C. , "An Evaluation of Eleven Discretization Schemes for Predicting Elliptic Flow and Heat Transfer in Supersonic Jetst", International Journal of Heat and Mass Transfer , Vol. 30 , No. 9 , pp. 1907-1925 , 1987.

[3] Figueiredo,J. R. ,"Generalização e Aproximação do Esquema Discretizante de Allen para Equações de Transporte em Fluidos", Tese de Doutorado , Universidade Estadual de Campinas , 1988.

[4] Bertiger, W. I. and Padmanabhan, L. ,"Finite Difference Solutions to Grid Orientation Problems Using IMPES ", Society of Petroleum Engineers, SPE 12250 , 1983.

[5] Lake, L. W. , Pope , G. A. , Carey , G. F. and Sepehrnoori , K. ,"Isothermal , Multiphase , Multicomponent Fluid Flow in Permeable Media. Part I : Description and Mathematical Formulation.", IN SITU , Vol. 8, No. 1, pp. 1-40, 1984.

[6] Peaceman , D. W. ,"Interpretation of Well-Block Pressures in Numerical Reservoir Simulation ", Society of Petroleum Engineers, SPE 6893 , 1977.

[7] Rocha , P. S. M. V. ,"Efeitos de Orientação de Malha na Simulação Numérica de Reservatórios de Petróleo - Esquemas de Solução por Nove Pontos", Tese de Mestrado , Universidade Federal de Ouro Preto ,1987.

[8] Yanosik , J. L. and Mc Cracken , T. A. ," A Nine-Point , Finite-Difference Reservoir Simulation for Realistic Prediction of Adverse Mobility Ratio Displacements ",Society of Petroleum Engineers, SPE 5734 , 1976.

ABSTRACT

The paper describes new finite-difference techniques for numerical solution of the convection-dispersion equation for 2 D problem. Application of standard finite difference methods to this class of problems may lead to numerical dispersion, grid orientation effects and overshoot at the miscible front.The main purpose of this work is to present a method which reduces these difficulties in numerical simulation.A discretized equation obtained from the analytical solution of the 1 D convection-dispersion problem will be used to model the 2 D problem, resulting in a finite difference scheme of exponential order.The procedure described in the paper ensures that convergence of the finite difference solution to the exact solution of the differential system will not depend on the ratio of convection to diffusion rates (Peclet Number). In addition to that, 9-point scheme will be presented to model miscible displacement problems in order to minimize the grid orientation effects.

III ENCIT – Itapema, SC (Dezembro 1990)

SOLUÇÃO PERTURBATIVA DA CONVECÇÃO DUPLAMENTE DIFUSIVA SOBRE UM CILINDRO ENTERRADO

CARLOS A. CHAVES e OSVAIR V. TREVISAN

Faculdade de Engenharia Mecânica - UNICAMP
Cx. Postal 6122 - 13081 - Campinas - SP

RESUMO

Neste trabalho é apresentada uma solução do tipo perturbativa para o problema da convecção duplamente difusiva em torno de um cilindro aquecido enterrado em um meio poroso saturado. A solução válida nas proximidades do estado estagnante é desenvolvida tomando por base a perturbação do número de Rayleigh Ra e da razão de empuxo N. Os resultados obtidos em termos dos números de Nusselt e Sherwood são comparados com resultados obtidos numericamente a partir da forma completa das equações que regem o fenômeno para as condições Ra< 2 e -4<N<3 nas situações em que Le é de ordem O(1).

INTRODUÇÃO

A ocorrência de um diferencial de temperatura entre um cilindro enterrado e o meio que o circunda é comum em diversos processos naturais ou industriais. Exemplos dessa ocorrência são as tubulações de distribuição de vapor, as linhas de oleodutos onde o fluido é mantido aquecido para reduzir os custos de transporte e os cabos de energia elétrica em que se deseja uma dissipação controlada do calor gerado. A difusão pura e a convecção natural são os mecanismos envolvidos na transferência de calor nestes casos.

Na literatura encontramos alguns trabalhos sobre a resolução do problema análogo de transferência de calor na ausência de disseminação de componentes químicos.

Os primeiros trabalhos que trataram do assunto consideraram a transferência de calor num meio puramente condutivo [1,2] e algumas soluções analíticas estão disponíveis na literatura para cilindros e cabos em tais condições.

Mais recentemente Bau [3], avançando na linha do problema convectivo, apresentou soluções analíticas para a convecção natural em casos de números de Rayleigh baixos. No problema estudado, a convecção é induzida por um cilindro aquecido em meio poroso saturado e permeável, onde ambos, cilindro e solo, são mantidos a uma temperatura constante. O autor utilizou uma técnica de expansão por perturbação regular para o cálculo dos campos de escoamento e de temperatura obtendo soluções analíticas válidas para números de Rayleigh menores do que O(1).

Ficou então a necessidade de ampliar o campo de conhecimento sobre o problema de convecção duplamente difusiva. O presente trabalho é um estudo sobre a convecção natural promovida pela difusão dupla em meios porosos saturados através de soluções analíticas via expansão por perturbação. Além da análise matemática, os resultados obtidos por este tipo de solução são comparados também com resultados numéricos obtidos a partir da forma completa das equações que regem o fenômeno.

FORMULAÇÃO DO PROBLEMA

Consideramos o problema de um cilindro enterrado em um meio poroso saturado. O cilindro tem raio r1 e está enterrado a uma profundidade d da superfície superior do meio poroso. A parede externa do cilindro é mantida a uma temperatura Tw e a uma concentração Cw, constantes, enquanto a superfície superior do meio poroso é mantida a uma temperatura Ts e a uma concentração Cs, conforme a Figura 1. As hipóteses de regime permanente e parede impermeável também foram consideradas. Assumimos também a aproximação de Boussinesq para variações de densidade devido a mudanças tanto de temperatura quanto de concentração, além de considerarmos válida a Lei de Darcy para descrever o escoamento do fluido no meio poroso.

Nestas condições as equações governantes do fenômeno em regime permanente podem ser reduzidas a

Conservação de Massa

$$\nabla.\bar{V} = 0 \qquad (1)$$

Variação da Quantidade de Movimento

$$(\mu/K).\bar{V} = -[\nabla p - \rho\bar{g}] \qquad (2)$$

Conservação da Energia

$$(\bar{V}.\nabla)T = \alpha\,\nabla.(\nabla T) \qquad (3)$$

Conservação do Constituinte Químico

$$(\bar{V}.\nabla)C = D\,\nabla.(\nabla C) \qquad (4)$$

Onde o parâmetro α definido como a difusividade térmica efetiva, o termo D representa a difusividade do constituinte no meio poroso saturado pelo fluido.

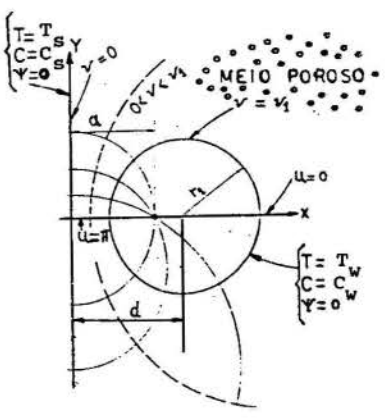

Figura 1 - O sistema de coordenadas (u,v)

A geometria bastante complexa do problema sugere a utilização de um sistema de coordenadas bipolares (u,v) para o encaminhamento de nossa solução analítica perturbativa. O nosso sistema é relacionado ao sistema de coordenadas cartesianas (x,y) pela fórmula:

$$x + i\,y = a\,\mathrm{cotgh}\,((v - i\,u)/2) \qquad (5)$$

Como relação de transformação entre os dois sistemas de coordenadas temos

$$x = (a\,\mathrm{senh}(v))/(\cosh(v)-\cos(u)) \qquad (6)$$

$$y = (a\,\mathrm{sen}(u))/(\cosh(v)-\cos(u)) \qquad (7)$$

$$z = z \qquad (8)$$

Com

$$-\pi \le u \le \pi$$
$$-\infty < v < \infty \qquad (9)$$

A profundidade d é dada por:

$$d = r1\,\cosh(v1) \qquad (10)$$

O fator de escala a por:

$$a = r1\,\mathrm{senh}(v1) \qquad (11)$$

Onde v1 é o valor de v sobre o cilindro.

Vamos utilizar a formulação função de corrente nas equações (1)-(4) que pode ser definida num sistema genérico de coordenadas como

$$Vu = 1/hv\ \partial\psi/\partial v \qquad (12)$$

$$Vv = -\,1/hu\ \partial\psi/\partial u \qquad (13)$$

Onde

$$hu = hv = a/(\cosh(v)-\cos(u)) \qquad (14)$$
$$hz = 1$$

Em termos da função de corrente ψ temos

$$\partial^2\psi/\partial u^2 + \partial^2\psi/\partial v^2 = (K\,a\,\rho_o\,g/\mu)\,[H(\beta\partial T/\partial u + \beta_c\,\partial C/\partial u) + G(\beta\partial T/\partial v + \beta_c\partial C/\partial v)] \qquad (15)$$

$$\partial^2 T/\partial u^2 + \partial^2 T/\partial v^2 = (1/\alpha)\ (\partial\psi/\partial v\ \partial T/\partial u - \partial\psi/\partial u\ \partial T/\partial v) \qquad (16)$$

$$\partial^2 C/\partial u^2 + \partial^2 C/\partial v^2 = (1/D)\ (\partial\psi/\partial v\ \partial C/\partial u - \partial\psi/\partial u\ \partial C/\partial v) \qquad (17)$$

onde

$$H = (1 - \cos(u)\,\cosh(v))/(\cosh(v)-\cos(u))^2 \qquad (18)$$

$$G = \mathrm{senh}(v)\,\mathrm{sen}(u)/(\cosh(v)-\cos(u))^2 \qquad (19)$$

VARIÁVEIS ADIMENSIONAIS

Para a reformulação adimensional das equações (15)-(17) são definidas as seguintes variáveis:

$$a^* = a/r1 = \mathrm{senh}(v1)$$
$$d^* = d/r1 = \cosh(v1)$$
$$T^* = (T-Ts)/(Tw-Ts) \qquad (20)$$
$$C^* = (C-Cs)/(Cw-Cs)$$
$$\psi^* = \psi/\alpha$$

As equações (15)-(17) em termos das variáveis adimensionais ficam:

$$\partial^2\psi^*/\partial u^2 + \partial^2\psi^*/\partial v^2 = a^*\,Ra\,[H\,\partial T^*/\partial u + G\ \partial T^*/\partial v) + N\,(H\,\partial C^*/\partial u + G\,\partial C^*/\partial v)] \qquad (21)$$

$$\partial^2 T^*/\partial u^2 + \partial^2 T^*/\partial v^2 = \partial\psi^*/\partial v\ \partial T^*/\partial u - \partial\psi^*/\partial u\ \partial T^*/\partial v \qquad (22)$$

$$\partial^2 C^*/\partial u^2 + \partial^2 C^*/\partial v^2 = Le\ (\partial\psi^*/\partial v\ \partial C^*/\partial u - \partial\psi^*/\partial u\ \partial C^*/\partial v) \qquad (23)$$

onde

$$Ra = (K\,g\,\beta\,\Delta T\,r1)\ /\ (\upsilon\,\alpha) \qquad (24)$$

$$\Delta T = Tw - Ts$$

$$N = \beta_c\,\Delta C\ /\ (\beta\,\Delta T) \qquad (25)$$

$$Le = \alpha/D \qquad (26)$$

O parâmetro N nos fornece a proporção entre as forças de empuxo térmica e as devidas ao gradiente de concentração, cuja combinação dirige o movimento do fluido. O valor de N pode ser positivo ou negativo, conforme as forças de empuxo sejam concordantes, ou adversas.

CONDIÇÕES DE CONTORNO

Em termos adimensionais no novo sistema de coordenadas (u,v) estabelecemos as seguintes condições de contorno conforme o domínio mostrado na Figura 1.

Simetria
$u = 0 \quad v1 < v \le 0 \quad \psi^* = 0 \quad \partial T^*/\partial v = \partial C^*/\partial v = 0$

Simetria
$u = \Pi \quad v1 < v < 0 \quad \psi^* = 0 \quad \partial T^*/\partial v = \partial C^*/\partial v = 0$

Superfície do cilindro impermeável
$v = v1 \quad 0 \le u \le \Pi \quad \psi^* = 0 \quad T^* = C^* = 1$

Superfície superior impermeável
$v = 0 \quad 0 \le u \le \Pi \quad \psi^* = T^* = C^* = 0 \qquad (27)$

NUSSELT E SHERWOOD NO SISTEMA DE COORDENADAS (u,v)

Definindo-se o número de Nusselt médio por

$$Nu = \left(\int_{-\pi}^{\pi} \partial T^*/\partial v\,\Big|_{v=v1}\,du\right) / Q_{condução} \qquad (28)$$

Para o cilindro temos

$$Nu_c = (v1/2\Pi) \int_{-\pi}^{\pi} \partial T^*/\partial v\,\Big|_{v=v1}\,du \qquad (29)$$

Para o número de Sherwood valem as mesmas relações trocando-se T por C. Assim para Sherwood médio no cilindro temos

$$Sh_c = (v1/2\Pi) \int_{-\pi}^{\pi} \partial C^*/\partial v \Big|_{v=v1} du \qquad (30)$$

EXPANSÃO POR PERTURBAÇÃO

O movimento convectivo é comandado pela combinação de dois mecanismos de empuxo: térmico e químico. Desta forma a perturbação sobre um estado estacionário pode ser originária de alterações no gradiente térmico e/ou no gradiente de concentração. Em termos da solução proposta, a perturbação deve ser considerada correspondentemente sobre dois parâmetros, representativos das duas forças de empuxo. Para ψ^*, T^*, C^*, Nu e Sh construimos uma solução por perturbação em torno dos parâmetros R e N na forma

$$\psi^* = \psi_0^* + R\,\psi_1^* + N\,\psi_2^* + R\,N\,\psi_3^* + R^2\,\psi_4^* + N^2\,\psi_5^* + R\,N^2\,\psi_6^* + R^2N\,\psi_7^* + R^2N^2\,\psi_8^* + \ldots \qquad (31)$$

$$\text{Onde } R = a^*\,Ra \qquad (32)$$

Expressões análogas teremos para T^*, C^*, Nu e Sh, trocando-se ψ^* por tais variáveis em (31).

As equações (21) a (23) mais as condições de contorno (27) podem ser resolvidas introduzindo-se a expansão (31) e demais respectivas para T^*, C^*, Nu e Sh, comparando-se os termos de mesma potência em n e obtendo-se assim para cada nível de aproximação um novo conjunto de equações diferenciais que conduzirá aos resultados apresentados pelas equações (33)-(37). As passagens não mostradas entre (31) e (33)-(37) foram omitidas por falta de espaço e que foram obtidas considerando-se números de Lewis próximos da unidade. Assim para números de de Lewis próximos da unidade, teremos agora R e (N+1) próximos de zero. O aparecimento de (N+1) próximo de zero era esperado por ser N=-1 um estado estacionário do problema, além de Ra = 0.

Assim para $Le \cong 1$ e R, $(N+1) \cong 0$ as expansões (31) e respectivas para T^*, C^*, Nu e Sh tomam a forma

$$\psi^* = R(1+N)\,\psi_1^* + R^2(1+N)^2\,\psi_4^* \qquad (33)$$

$$T^* = v/v1 + R(1+N)\,T_1^* + R^2(1+N)^2\,T_4^* \qquad (34)$$

$$C^* = v/v1 + R(1+N)\,C_1^* + R^2(1+N)^2\,C_4^* \qquad (35)$$

$$Nu = 1 + R(1+N)\,Nu_1 + R^2(1+N)^2\,Nu_4 \qquad (36)$$

$$Sh = 1 + R(1+N)\,Sh_1 + R^2(1+N)^2\,Sh_4 \qquad (37)$$

Onde ψ_1^*, ψ_4^*, T_1^*, T_4^*, C_1^* e C_4^* são soluções obtidas através dos seguintes sistemas

$$\partial^2\psi_1^*/\partial u^2 + \partial^2\psi_1^*/\partial v^2 = G/v1$$

$$\partial^2 T_1^*/\partial u^2 + \partial^2 T_1^*/\partial v^2 = -(1/v1)\,\partial\psi_1^*/\partial u$$

$$\partial^2 C_1^*/\partial u^2 + \partial^2 C_1^* = -(Le/v1)\,\partial\psi_1^*/\partial u \qquad (38)$$

$$\partial^2\psi_4^*/\partial u^2 + \partial^2\psi_4^*/\partial v^2 = G\,\partial T_1^*/\partial v + H\,\partial T_1^*/\partial u$$

$$\partial^2 T_4^*/\partial u^2 + \partial^2 T_4^*/\partial v^2 = -(1/v1)\,\partial\psi_4^*/\partial u + \partial\psi_1^*/\partial v\,\partial T_1^*/\partial u - \partial\psi_1^*/\partial u\,\partial T_1^*/\partial v$$

$$\partial^2 C_1^*/\partial u^2 + \partial^2 C_1^* = Le\,[-(1/v1)\,\partial\psi_4^*/\partial u + \partial\psi_1^*/\partial v\,\partial C_1^*/\partial u - \partial\psi_1^*/\partial u\,\partial C_1^*/\partial v] \qquad (39)$$

Para o cálculo dos sistemas (38) e (39), expandiremos as funções G e H em suas respectivas séries de Fourier:

$$G = \sum_{k=1}^{\infty} 2k\,e^{-kv}\,\text{sen}(ku) \qquad (40)$$

$$H = \sum_{k=1}^{\infty} (-2k)\,e^{-kv}\cos(ku) \qquad (41)$$

Verifica-se como conveniente o uso de série de Fourier-cossenos para T_n e C_n ($n \geq 1$) sendo que para ψ_n^* ($n \geq 1$) a série de Fourier-senos é a recomendada:

$$\psi_1^* = \sum_{n=1}^{00} f_{1,n}\,\text{sen}(nu) \qquad (42)$$

$$T_1^* = \sum_{n=0}^{00} g_{1,n}\cos(nu) \qquad (43)$$

$$C_1^* = \sum_{n=0}^{00} h_{1,n}\cos(nu) \qquad (44)$$

$$\psi_4^* = \sum_{n=1}^{00} f_{2,n}\,\text{sen}(nu) \qquad (45)$$

$$T_4^* = \sum_{n=0}^{00} g_{2,n}\cos(nu) \qquad (46)$$

$$C_4^* = \sum_{n=0}^{00} h_{2,n}\cos(nu) \qquad (47)$$

As expansões (42) a (47) consideradas com as condições de contorno

$$\psi_i^* = T_i^* = C_i^* = 0 \quad \text{em} \quad v=0 \quad i \geq 1$$
$$\psi_i^* = T_i^* = C_i^* = 0 \quad \text{em} \quad v=v1 \quad i \geq 1 \qquad (48)$$

nos permitem chegar a expressões analíticas para ψ, T e C dadas por

$$\psi^*(u,v) \cong R\,(1+N)\,[\,-(v/2v1).(\mathrm{sen}(u) + e^{-v})/(\cosh(v)-\cos(u)) + \sum_{n=1}^{\infty} e^{-nv1}\,\mathrm{senh}(nv)\,\mathrm{sen}(nu)/\mathrm{senh}(nv1)\,] \quad (49)$$

$$T^*(u,v) \cong v/v1 + R(1+N)\,\{\,-(1/64)\,(v/v1)\times \times(\cos(u) - e^{-v})/(\cosh(v)-\cos(u)) - (v/4v1^2)\times \times(v/2 - 0.5\,\mathrm{Ln}\,[\,2(\cosh(v) - \cos(u))\,] + \sum_{n=1}^{\infty} e^{-nv1}(1 + 1/(nv1) + 2\mathrm{cotgh}(nv1))\,\mathrm{senh}(nv)\times \times \cos(nu)(4\mathrm{senh}(nv1)) - (v/2v1)\sum_{n=1}^{\infty} e^{-nv1}\times \times \cosh(nv)\cos(nu)/(\mathrm{senh}(nv1))\,\}, \quad (50)$$

$$C^*(u,v) \cong v/v1 + R\,Le\,(1+N)\,\{-(1/64)\,(v/v1)\times \times (\cos(u) - e^{-v})/(\cosh(v)-\cos(u)) - (v/4v1^2)\times \times(v/2 - 0.5\,\mathrm{Ln}\,[\,2(\cosh(v) - \cos(u))\,] + \sum_{n=1}^{\infty} e^{-nv1}(1 + 1/(nv1) + 2\mathrm{cotgh}(nv1))\,\mathrm{senh}(nv)\times \times \cos(nu)(4\mathrm{senh}(nv1)) - (v/2v1)\sum_{n=1}^{\infty} e^{-nv1}\times \times \cosh(nv)\cos(nu)/(\mathrm{senh}(nv1))\,\} \quad (51)$$

Os números de Nusselt e Sherwood dados por

$$Nu = 1 + R^2/2\,(1+N)^2 \sum_{n=1}^{\infty} n \int_0^{v1} f_{1,n}\, g_{1,n}\, dv \quad (52)$$

$$Sh = 1 + R^2/2\,Le^2\,(1+N)^2 \sum_{n=1}^{\infty} n \int_0^{v1} f_{1,n}\, g_{1,n}\, dv \quad (53)$$

onde

$$f_{1,n} = (1 + 1/(nv1) + 2\mathrm{cotgh}(nv1))\,e^{-nv1}\times \times \mathrm{senh}(nv)/(4\mathrm{senh}(nv1)) - ve^{-nv1}\cosh(nv)/(2v1\times \times \mathrm{senh}(nv1)) - (v + 1/n)\,v\,e^{-nv}/(4v1^2) \quad (54)$$

$$g_{1,n} = e^{-nv1}\,\mathrm{senh}(nv)/\mathrm{senh}(nv1) - v\,e^{-nv}/v1 \quad (55)$$

Conforme o desenvolvimento, as expressões analíticas (49)-(53) são válidas para as condições:

$$R \cong 0\,, \quad (N+1) \cong 0 \quad e \quad Le \cong 1 \quad (56)$$

RESULTADOS E DISCUSSÕES

Para obtenção dos resultados aqui apresentados, foi utilizado uma rede de 900 elementos. Os campos de temperatura apresentados foram obtidos resolvendo-se a equação (50). Os resultados obtidos em termos dos números de Nusselt e Sherwood dados pelas equações (52) e (53) foram comparados com resultados obtidos numericamente por Chaves [4].

Na Figura 2 apresentamos para comparação os campos de temperatura ($T_0 + R\,T_1$) por perturbação (linha tracejada) e por simulação numérica (linha cheia). Podemos perceber claramente a boa concordância dos campos para o caso N=0 com Ra=Le=1. Nota-se neste cas de escoamento ascendente que as contribuições de primeira ordem T_1 e C_1 para as equacões (50) e (51) resultam em um aumento na temperatura e concentração sobre as soluções puramente difusivas no espaço entre o cilindro e a parede superior. Na região inferior do domínio os termos de primeira ordem produzem um decréscimo nas soluções de ordem zero.

Na região onde a convecção é predominante, as soluções se afastam indicando a menor precisão do método perturbativo nessa região. Pode-se perceber a região de presença da convecção situando-se entre o cilindro e a parede impermeável na geometria estudada.

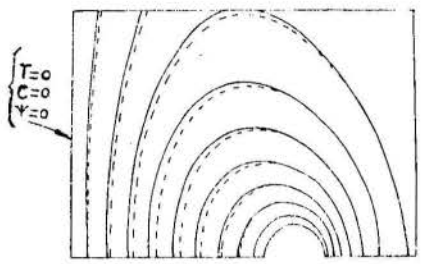

Figura 2 - Distribuição de Temperatura para N=0 Ra=Le=1
(- - - expansão —— simulação)

Na Figura 3 apresentamos conjuntamente os campos de temperatura para Ra=Le=1 nas situações N = -1.05 (linha tracejada) e N = -0.95 (linha cheia). O aspecto da inversão do escoamento em torno de N = -1 é aqui também verificado. Mesmo na presença de valores de Ra baixos o efeito da inversão se faz notar pela diferença relativa entre as curvas. Conforme a difusão da espécie química aumenta sua contribuição à força de empuxo do movimento, nas proximidades do ponto de inversão, o escoamento altera dramaticamente seu comportamento. Para N=-0.95 a difusão química se opõe fortemente ao movimento mas só para dominá-lo após -1.0, o que pode ser observado nas linhas para N=-1.05, quando a região de fluido quente e de maior concentração muda-se para o domínio inferior ao cilindro. Este efeito é trazido à solução perturbativa através dos termos de primeira ordem, que passam a contribuir negativamente sobre a solução difusiva na região sobre o cilindro e positivamente no domínio abaixo do cilindro. Na Figura 2 as curvas correspondentes à solução puramente difusiva situam-se coerentemente entre as curvas apresentadas para as duas soluções.

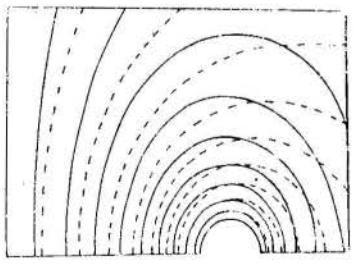

Figura 3 - Distribuição de Isotermas para Ra=Le=1
(- - - N=-1.05 —— -0.95)

A Figura 4 mostra o comportamento de Sherwood em função de Le. Dos resultados obtidos via perturbação, para uma variação menor que 1%, Le = 2 seria o limite de validade do método de perturbação caso os resultados do método numérico sejam tomados como referência.

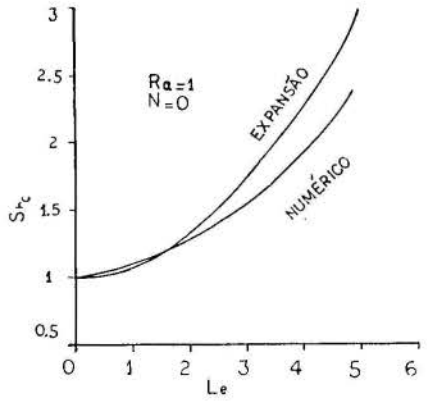

Figura 4 - Efeito do número de Lewis sobre a taxa de transferência de massa

A Figura 5 mostra uma comparação da solução perturbativa de segunda ordem com a solução numérica para Nu com Ra=Le=1. Na faixa estudada, o valor N=1 é um limite do método para uma diferença admissível de 2%. N=2 conduz a uma diferença < 5%. A análise das variações para Ra e N mostra um aumento relativamente suave da diferença com N. Tal fato não é observado nas variações com Le para a faixa de Ra, Le e N estudados. Esta figura também é ilustrativa do efeito introduzido no fenômeno pela presença de uma substância miscível. A geração de uma substância simultaneamente com a geração de calor em uma fonte pode afetar seriamente o comportamento do escoamento que penetra no meio poroso e consequentemente alterar de forma significativa as taxas de troca de calor e transferência de massa.

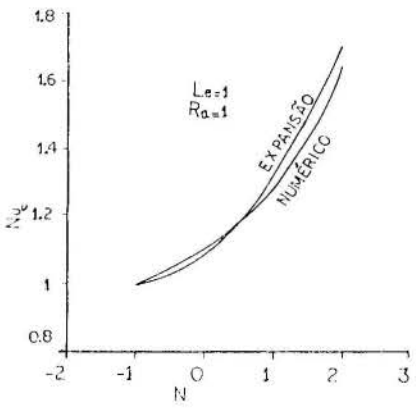

Figura 5 - Efeito da razão de empuxo sobre a taxa de troca de calor

Na Figura 6 apresentamos Sh em função de N para os casos Le = 1.1, 1.0 e 0.9. Esta figura reforça o carater quadrático de aproximações por perturbação adotadas. Conforme se depreende das equações, os ramos das parábolas da Figura se projetam simetricamente em relação ao eixo vertical passando por N=-1.

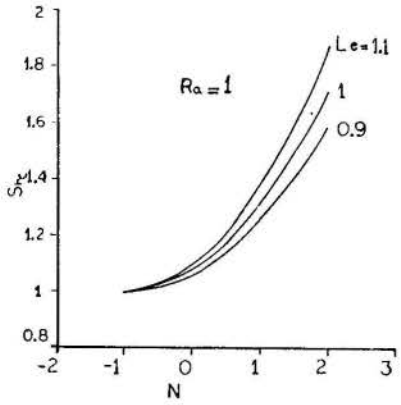

Figura 6 - Influência da razão de empuxo e da difusividade relativa sobre a taxa transferência de massa

Na Tabela 1 apresentamos os valores obtidos numericamente e por expansão perturbativa de Nu emfunção de N com Ra=Le=1, N variando entre -1 e 2.

Tabela 1. Comparação entre Sh analítico e numérico em função de N (Ra = 1 Le = 1)

N	Sh analítico	Sh numérico
-1	1.0	1.00
0	1.08	1.10
1	1.32	1.28
2	1.70	1.64

Na Tabela 2 apresentamos os resultados no caso de Nu em função de Ra com Le=1, N=0 e Ra variando entre 0.1 e 5.0. Para uma diferença máxima de 1%. o valor limite de Ra é 1. Ra = 2 já conduz a um desvio de 13% nos cálculos dos números de Nusselt e Sherwood.

Tabela 2. Comparação entre Nu analítico e numérico em função de Ra (N = 0 Le = 1.)

Ra	Nu analítico	Nu numérico
0.1	1.006	1.009
1.0	1.150	1.140
2.0	1.600	1.402
5.0	2.970	1.941

CONCLUSÕES

Apresenta-se o desenvolvimento de um estudo teórico sobre a convecção natural resultante de empuxos devidos ao calor e à diferença de concentração scbre um cilindro enterrado em um meio poroso. O objetivo foi o de estender a aplicação de soluções perturbativas, antes aplicadas à convecção natural puramente difusiva, ao problema em questão. A convecção duplamente difusiva depende normalmente de dois parâmetros, Ra e N, e a abordagem adotada emprega uma expansão dupla sobre estes parâmetros.

Os resultados apresentados são válidos nos regimes dominados pelo fenômeno difusivo. Ou seja, as faixas dos parâmetros principais para aplicação da solução se restringem àquelas em que as contribuições convectivas às distribuições de temperatura e concentração são relativamente pequenas se comparadas à contribuição puramente difusiva (Ra=0 ou Le=1 e N=-1). Este critério foi satisfeito em todos os casos estudados.

A verificação do campo de validade da análise perturbativa foi também realizada, através da comparação dos resultados com aqueles obtidos por simulação numérica. A comparação criteriosa realizada separadamente para cada parâmetro fundamental revela que a análise perturbativa produz resultados apropriados em faixas relativamente estreitas de Ra ($0<Ra<2$) e de Le ($0<Le<2$) sendo menos sensível à variação de N ($-4<N<3$) para desvios sempre menores que 5% em relação à solução numérica.

O desenolvimento das soluções apresentadas neste trabalho pelo o método da perturbação é relativamente exaustivo porém permitiu a obtenção de resultados exatos para a faixa de parâmetros Ra, Le e N onde os efeitos convectivos não estão presentes de forma dominante. O método de perturbação tem também o grande mérito de revelar relações importantes para T e C nas condições de estabelecimento do fenômeno.

Nomenclatura

a	fator de escala para coordenadas bipolares
C	concentração do constituinte químico
d	profundidade do cilindro superior à superfície
D	difusividade de massa do constituinte químico
g	aceleração da gravidade
G	função, definida na eq.(19)
H	função, definida na eq.(18)
K	permeabilidade do meio poroso
Le	número de Lewis, α/D
N	razão de empuxo, $(\beta_c \Delta C)/(\beta \Delta T)$
Nu	número de Nusselt médio
p	pressão
rl	raio do cilindro enterrado
Ra	número de Rayleigh modificado
Sh	número de Sherwood médio
T	temperatura
u,v	coordenadas bipolares
vl	valor da coordenada v sobre o cilindro
x,y	coordenadas cartesianas

Símbolos Gregos

α	difusividade térmica efetiva do meio poroso saturado
β	coeficiente de expansão térmica
β_c	coeficiente de dilatação química
ΔC	diferença de concentração, do cilindro à superfície superior
ΔT	diferença de temperatura, do cilindro à superfície superior
ρ	densidade da solução
ψ	função de corrente
∇	operador diferencial nabla

Índices

$( )^*$	variáveis adimensionais
$( )_w$	valores relativos ao cilindro
$( )_s$	valores relativos à superfície superior
$(\bar{\ })$	grandezas vetoriais

REFERÊNCIAS

[1] Di Felice,R.F. and Bau,H.H., Conductive Heat Transfer between eccentric cylinders with boundary conditions of the third kind, Trans. Am. Soc. Mech. Engrs, Series C, J. Heat Transfer 105, 678-680 (1983).

[2] Eckert,E.R.G. e Drake,R.M., Analysis of Heat and Mass Transfer, 92-102. Mc Graw Hill, New York (1972).

[3] Bau,H.H., Convective Heat Losses from a Pipe Buried in a Semi-Infinite Porous Medium, ASME/AICHE National Heat Transfer Conf.,Niagara Falls, (1984).

[4] Chaves,C.A., Convecção Natural Duplamente Difusiva em torno de um cilindro enterrado num meio poroso saturado, Tese de Doutorado a ser apresentada, UNICAMP - FEC

ABSTRACT

This paper presents a perturbative type solution to the problem of double diffusion natural convection around a cylinder buried in a saturated porous medium.

The solution, valid in the vicinity of the stagnant condition, is developed from perturbations introduced simultaneously Rayleigh number Ra and to the buoyancy ratio number N. The results, presented in terms of Nusselt and Sherwood numbers, are compared with numerical results obtained via simulations with the complete governing equations. The solution covers the range of $Ra<2$, $-4<N<3$ in conditions that Le is of O(1).

III ENCIT – Itapema, SC (Dezembro 1990)

MOISTURE MIGRATION NEAR A HEATED CYLINDER BOUNDED BY A MOIST SOIL

L.S. Damasceno-Ferreira* and A.T. Prata
Dept9 of Mechanical Engineering - UFSC
Cx.P. 476 - Florianópolis - SC

ABSTRACT

The moisture migration near a heated cylinder bounded by a moist soil is numerically investigated using two models. The first model is a parametric analysis where the properties of the soil is assumed to be constant. In the second model the properties dependence with temperature and moisture content are taken into account. The results for the two models are compared in order to verify the deviations associated to the constant property model.

INTRODUCTION

Heat and mass transfer in unsaturated porous media has been largely investigated due to its great importance in engineering. Examples include drying and humidification in chemical process, heat transfer from buried electrical cables and pipelines, heat pipe wicks, and geothermal energy production.

A detailed analysis of those processes is complicated due to several factors. The geometry of the porous and structure of the solid matrix are very complex, different phases coexist in the porous interstices, and the thermophysical properties which govern the transport of mass and heat are very dependent of temperature and moisture content.

The main motivation of the present work comes from the necessity of understanding the drying process that occurs around buried power cables. The passage of electrical current generates heat which needs to be dissipaded through the medium that envolves the cable; otherwise the cable could be damaged by superheating.

In designing those cables, the thermal resistivity of the soil is a very important parameter; its value increases rapidly as the moisture content decreases. The electrical current induces high temperatures at the cable surface creating a thermal gradient between the environment and the cable surface. Due to this gradient, moisture starts migrating away from the cable in the vapor phase. If this moisture is not returned to the cable by capillarity, total dryness of the soil can occur. Dry soil has high resistivity and no longer dissipates the heat generated by the cable. In turn, the cable surface temperature can reaches values not bearable by the insulating sheath.

Among the possible solution for this problem are the change in the cable insulation material and the increase in its thickness. However, these possibilities are economically infeasible. A pratical solution for the problem is the choice of a natural or artificial medium that is capable to either retain moisture or to dissipate heat at low moisture contents. This procedure has been routinely adopted in engineering practice.

The choice of the medium that should be employed to surround the cable has to be based on the thermophysical properties of the medium and on the understanding of the moisture migration in unsatureted soils.

For the moisture migration in soils, the model due to Philip and de Vries [1-3] has become the most accepted since its introduction in the late fifties. In that model, the heat and mass fluxes are related to the thermal and moisture gradients by macroscopic diffusivities. These diffusivities can be determined from three functionals which characterizes the soil: the dependance of the moisture potential, the hydraulic conductivity, and the effective thermal conductivity on the moisture content and temperature of the soil. Due to the complex shape of those functionals, expressions for calculation of the macroscopic diffusivities require constants and parameters that can only be determined experimentally and are very specific for each kind of soil. Therefore, a general understanding of the phenomena, which can be used as a guide for situations in which no specific solutions are available, is difficult to obtain.

Several authors have proposed theoretical expressions for the macroscopic diffusivities (eg.[4-6]), and recent works have demonstrated that reasonable to good agreement is obtained between theory and experiment [7-10]. The referenced works consider certain types of media and boundary condictions, and despite the valuable information encountered therein, the specificity of the situation investigated precludes a generalization of the results.

Motivated by the need to obtain a general understanding of heat and mass transfer in unsaturated porous media, Eckert and Faghri have proposed a parametric model [11-13]. Such model can be used for preliminary engineering analysis to obtain solutions for any kind of medium. The parametric model is obtained by proper simplifications of the conservation equations and their boundary conditions, especially by assuming the properties to be constant. As observed by Eckert and Faghri, a situation similar existed in the convective heat transfer field at the beginning of this century. At that time, a systematic understanding of heat transfer process was obtained only when W. Nusselt introduced a constant property model, and derived dimensionless relations expressing Nusselt numbers as functions of Reynolds and Prandtl numbers. Such relations are widely accepted today by the engineering community.

It is felt that such procedure can also be used to describe heat and mass transfer in porous medium, and is useful as a first aproximation to this problem. Mathematically, the parametric model can be seen as an asymptotic solution with variations of temperature and moisture content moving toward zero.

The main objective of the present work is to verify, for a given situation, the deviations associated to the parametric model when compared to a variable property model based on the Philip and de Vries theory. To this extent, numerical solutions obtained from the two models will be presented.

The comparison will be performed for two concentric and infinite cylinders filled with moist soil. The moisture migration is caused by thermal gradients between the cylinders walls. The results obtained herein are aimed to guide and to provide insights about the

* Presently, Assistant Professor of the Chemical Engineering Department, UFRGS, Porto Alegre-RS

engineering problem of heat dissipation around buried power cables

TRANSPORT EQUATIONS AND PROBLEM FORMULATION

The simultaneous transport of heat and moisture in moist soils is a very complex phenomenon. In the present work the following simplifications will be adopted: a) mass of water vapor present in the pores interstices is small compared to the mass of liquid water; b) water vapor and air are governed by the ideal gas law; c) gravity can be ignored; d) hysteresis effects are not present since heat and moisture are transfered only in one direction; e) the solid matrix is rigid, and no swollen effects occur; f) the porous medium is isotropic, and is treated as a continuum.

The geometry of the problem to be investigated is presented in Fig. 1.

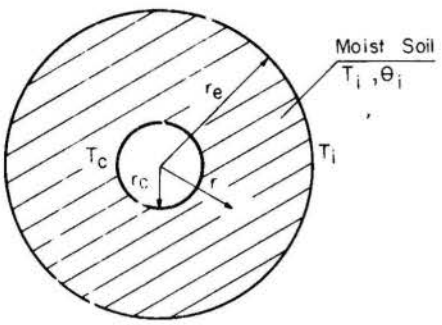

Fig. 1 - Problem geometry

Initially, the soil temperature and moisture content are T_i and θ_i, respectively. The temperature of the inner boundary, which from now on will be designated by cable (alluding to the problem that motiveted this work), is T_c. The outer temperature is kept constant and equal to the soil initial temperature T_i. Additionally, the cable and the outer boundary are impermeable to the liquid and vapor fluxes.

The transport of heat in a porous medium is governed by the following equation [14]

$$\frac{\partial}{\partial t}(CT) = \frac{1}{r}\frac{\partial}{\partial r}\left(r\,\lambda^*\,\frac{\partial T}{\partial r}\right)\ ,\quad \lambda^* = k^* + \rho h D_{TV} \tag{1}$$

where C is the volumetric heat capacity and k^* is the effective thermal conductivity for the hypothetical case of no moisture migration [15]; ρ is the density of the liquid, h is the latent heat of vaporization. D_{TV} is the vapor diffusivity associated to the thermal gradient and T is the temperature of the soil; t and r are, respectively, the temporal and spatial coordinates. In equation (1), the energy flux associated to the moisture migration has been neglected. Such term becomes important only for low moisture contents ($\theta \to 0$) as discussed in [16].

For the mass conservation in a porous medium the following equation can be written [14]

$$\frac{\partial \theta}{\partial t} = \frac{1}{r}\frac{\partial}{\partial r}\left[r(D_{\theta L} + D_{\theta V})\frac{\partial \theta}{\partial r}\right] + \frac{1}{r}\frac{\partial}{\partial r}\left(r\,D_{TV}\,\frac{\partial T}{\partial r}\right) \tag{2}$$

Where θ is the volumetric moisture content, $D_{\theta L}$ and $D_{\theta V}$ are, respectively, the liquid and vapor diffusivities associated to the moisture content. The second term on the right-hand side of equation (2) represents the vapor flux due to thermal gradient.

The initial and boundary conditions to be satisfied by equations (1) and (2) are,

$t = 0$; $T = T_i$ and $\theta = \theta_i$

$t > 0$; $r = r_c$; $T = T_c$ and

$$(D_{\theta L} + D_{\theta V})\frac{\partial \theta}{\partial r} + D_{TV}\frac{\partial T}{\partial r} = 0$$

$t > 0$; $r = r_e$; $T = T_i$ and

$$(D_{\theta L} + D_{\theta V})\frac{\partial \theta}{\partial r} + D_{TV}\frac{\partial T}{\partial r} = 0$$

At this point the formulation of the problem has been completed. Knowing how the properties $D_{\theta V}$, $D_{\theta L}$, D_{TV}, C and λ^* vary with temperature and moisture content, equations (1) and (2) together with the initial and boundary condition can be used to calculate $\theta(r,t)$ and $T(r,t)$

PARAMETRIC MODEL

The parametric model is obtained by assuming all the properties to be constant, that is, do not vary with θ and T. For the situation been investigated here, the moisture migration is due to the temperature difference ($T_c - T_i$) established between the cylinder boundaries. As this temperature difference decreases, the variations of the properties with θ and T become smaller, and the results obtained with the parametric model approach, asymptotically, those obtained using the variable property model. In this way, for situations where the properties are not known in details, the parametric model can furnish a first aproximation for the problem.

The following dimensionless variables will be used in the parametric model,

$$\alpha = (T-T_i)/(T_c-T_i)\ ,\quad \Omega = (\theta/\theta_i - 1)/Pn$$
$$R = r/r_e\ ,\quad \tau = D_\theta t/L^2 \tag{3}$$

where Pn is the Posnov number defined as

$$Pn = D_{TV}\,(T_c-T_i)/D_\theta\theta_i \tag{4}$$

For simplicity the sum of the liquid and vapor difusivities associated with the moisture gradient was represented by D_θ, that is, $D_\theta = D_{\theta L} + D_{\theta V}$.

With those variables, equations (1) and (2) take on, respectively, the following forms,

$$Lu\,\frac{\partial \alpha}{\partial \tau} = \frac{1}{R}\frac{\partial}{\partial R}\left(R\,\frac{\partial \alpha}{\partial R}\right) \tag{5}$$

$$\frac{\partial \Omega}{\partial \tau} = \frac{1}{R}\frac{\partial}{\partial R}\left(R\,\frac{\partial \Omega}{\partial k}\right) + \frac{1}{R}\frac{\partial}{\partial R}\left(R\,\frac{\partial \alpha}{\partial R}\right) \tag{6}$$

Where Lu is the Luikov number defined as,

$$Lu = D_\theta/\lambda \quad \text{in which} \quad \lambda = \lambda^*/C \tag{7}$$

The initial and boundary conditions associated to the parametric model are,

$\tau = 0$, $\alpha = \Omega = 0$

$\tau > 0$ and $R = r_c/r_e$, $\alpha = 1$ and

$$\partial\Omega/\partial R + \partial\alpha/\partial R = 0 \tag{8}$$

$\tau > 0$ and $R = 1$, $\alpha = 0$ and

$$\partial\Omega/\partial R + \partial\alpha/\partial R = 0$$

From the previous equations it can be seen that the parametric model is governed by only one dimensionless parameter, the Luikov number Lu. The Luikov number is the ratio between the isothermal diffusivity D_θ and the apparent thermal diffusivity λ. This number is related to the development of the moisture and temperature profiles as time passes. For low values of Lu the temperature profile develops earlier than the moisture content profile, and the mass transfer problem

can be decoupled from the thermal problem.

There is another dimensionless number embedded in the dimensionless moisture content Ω, the Posnov number Pn. The Posnov number relates the importance between the thermal and the moisture content gradients in the transport of mass in the porous medium. For high values of Pn, the transport of mass occurs, primarily, due to temperature gradients. On the contrary, for low values Pn, the transport of mass is associated to the gradient of moisture. Knowing the values of Lu and Pn, the distribution of θ/θ_i with R and τ can be determined.

SOLUTION METHODOLOGY

For both, the variable property model and the parametric model, the solution of the differential equations were obtained numerically using the control volume method [17].

In this method the solution domain is divided in small non-overlapping control volumes, and the differential equations are integrated over each one of these control volumes. The time integration is performed using a fully implicity finite difference scheme. From those integrations, a set of algebraic equations is generated. For the variable property model, the values of θ and T needed to determine D_θ, D_T, C, and λ, were that of the previous time step. As the solution proceeded on time, the time step was kept small enough to assure that the changes in the θ and T field from one instant to the other did not alter the properties. The set of algebraic equation for each instant were solved directly using the Thomas algorithm [17].

This methodology has been used routinely to solve transient heat conduction and parabolic fluid flow problems. For more details the reader is refered to [17].

Special attention was devoted to the selection of the number of control volumes used in the discretization of the differential equations. For all results to be presented, 80 nodal points have been used for the solution. The use of 120 nodal points yielded results that differ from those obtained with the 80 nodal points by less than 0.2%.

Aside from the accuracy tests involved with the mesh selection, additional tests were performed to select the time step. Depending on the initial moisture content and temperature difference between the walls a different value for the time increment was used. Representative values for Δt and $\Delta\tau$ were, respectively, 1×10^3s and 1×10^{-5}.

RESULTS AND DISCUSSIONS

The comparison between the two models will be performed for a sandy silt soil with porosity 0.517, and dry density of 1280 kg/m³. This medium was chosen because analytical expressions for all its properties are available in [18]. For all cases investigated, $r_c/r_e = 0.06$.

Results were obtained for four different initial moisture contents, θ_i = 0.026, 0.103, 0.155 and 0.206. These values of θ_i cover situations from dry soils where there is no continuity of the liquid phase (pendular state), to situations where the soil is wet and the liquid is mobile (funicular state). For each value of θ_i, two different values of the temperature difference between the cylinder boundaries were investigated, (T_c-T_i) = 1 and 10 °C. The initial temperature T_i was always kept at 35 °C.

For the parametric model, the value of Lu and Pn corresponding to each case were evaluated at θ_i and T_i. Table I presents the Lu and Pn values for each θ_i, (T_c-T_i) pair. As can be seen in the table there is a strong dependence of Lu and Pn with moisture content and temperature.

Figures 2 to 9 show results for the dimensionless moisture content $\Omega = (\theta/\theta_i - 1)/Pn$ as a function of $R = r/r_e$, having the time t as a curve parameter. Figs. 2 and 3 are for θ_i = 0.026, Figs. 4 and 5 for θ_i = 0.103, Figs. 6 and 7 for θ_i = 0.155, and Figs. 8 and 9 for θ_i = 0.206. In those figures, the solid line corresponds to the variable property model, and the dashed line corresponds the parametric model. In all figures two distinct regions can be identified. Near the cable surface, at R = 0.06, the moisture content θ is less than θ_i indicating that due to the heat provided by the cable occured moisture migration. Near the outer region, at R = 1, there is an acumulation of moisture and, therefore, θ is larger than θ_i.

TABLE I: POSNOV AND LUIKOV NUMBERS FOR EACH θ_i,(T_c-T_i) PAIR

θ_i	(T_c-T_i) = 1 °C		5 °C		10 °C	
	Pn	1/Lu	Pn	1/Lu	Pn	1/Lu
0.026	0.0217	81.85	0.108	81.85	0.217	81.85
0.103	0.191	426.0	0.956	426.0	1.91	426.0
0.155	0.0129	60.13	0.0645	60.13	0.129	60.13
0.206	0.00026	2.97	0.0013	2.97	0.0026	2.97

As can be seen in Figs. 2, 4, 6 and 8, for the case where ΔT = 1 °C, the results for the two models are very close, regardless of the initial moisture content. Particularly in Fig. 4, for θ_i = 0.103, it is noted a deviation relatively large at the cable surface for $t \to \infty$. In fact this deviation in Ω is amplified because of the presence of the Posnov number in the denominator of Ω. If the same deviation were computed in θ, instead of in Ω, the divergence between the two models would be 4,3%.

The cases where ΔT = 10 °C will now be discussed. As observed in the figures, for θ_i = 0.026 and 0.206 there is a very good agreement between the two models. The maximum deviation occurs at the cable surface for $t \to \infty$. For θ_i = 0.026 the maximum deviation in θ is 2,3%., whereas, for θ_i = 0.206 the maximum deviation in θ is 0,03%.

For intermediate values of θ_i, the deviation between the two models for larger values of time increases considerable as observed in the Figs. 5 and 7. To understand why such deviations occur, some facts about the medium under consideration should be pointed out. For low moisture contents up to values of θ equal to 0.13, $D_{\theta V} >> D_{\theta L}$. The moisture transport is then due to vapor movement because there is no continuity of the liquid phase (pendular state). When θ reaches the value of 0.14, the contact between the liquid bridges present in the pores interstices starts existing and the liquid starts moving due to moisture gradients. Around those values of θ, D_θ changes considerable. In turn, Pn and Lu also change considerable. Thus, assuming the properties to be constant in the range of the moisture content in which the state of the liquid in the medium changes from pendular to funicular can introduce considerable error in the analysis. That is the situation depicted in Figs. 5 and 7. It is worth nothing that theses aspects do not produce any significant deviation for the cases where θ_i = 0.026 and θ_i = 0.206. For those cases the liquid in the soil is either in the pendular or in the funicular state, and no change from one state to the other occur.

Focusing the attention again in Figs. 5 and 7, it is seen that the deviation between the two models becomes more accentuated near the cable surface where the efects of the thermal gradients are greater. In the case where θ_i = 0.103, Fig. 5, the parametric model predicts that the soil near the cable completely dries and that a drying front develops and propagates outward with increasing time. This was the only situation, for all cases investigated here, where such a behavior was observed.

For the case where θ_i = 0.155, Fig. 7, an abrupt change in the θ profiles for larger times can be noted at Ω around - 0.5, wich is the value that the liquid in the medium becomes mobile. Large deviations are then observed between the two models near the cabe surface.

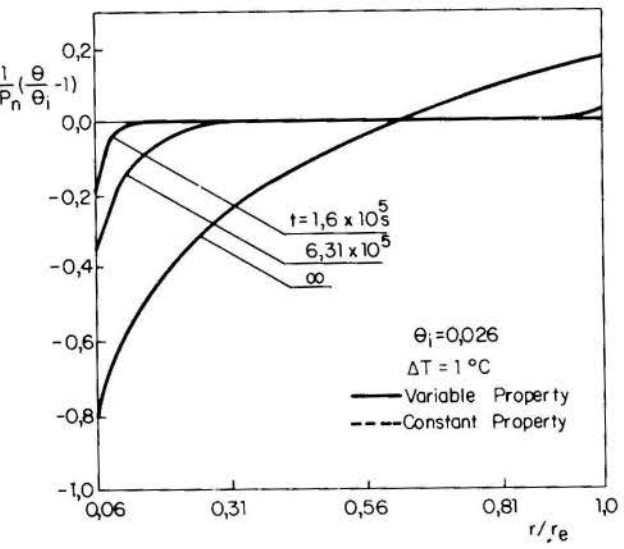

Fig. 2 - Moisture content as a function of position; θ_i = 0.026 and $\Delta T = 1^0C$

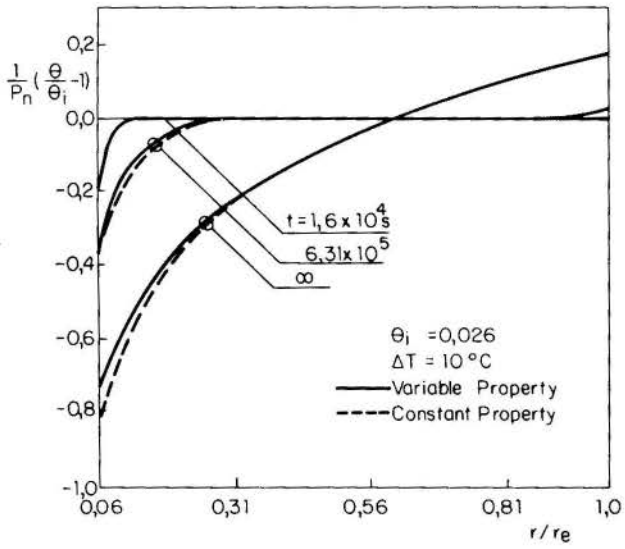

Fig. 3 - Moisture content as a function of position; θ_i = 0.026 and $\Delta T = 10^0C$

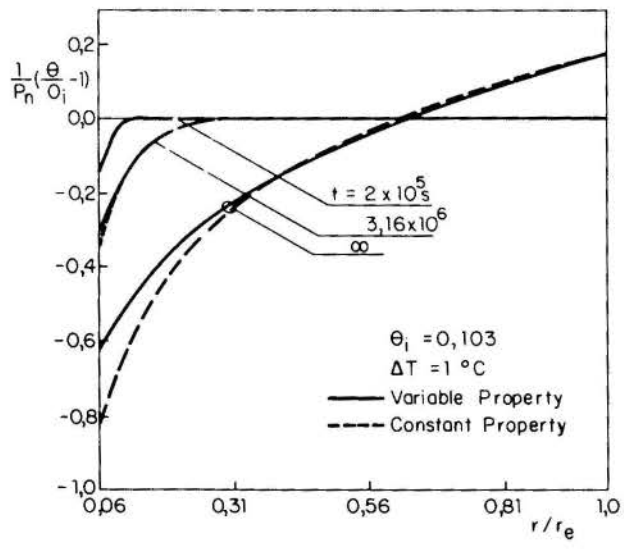

Fig. 4 - Moisture content as a function of position; θ_i = 0.103 and $\Delta T = 1^0C$

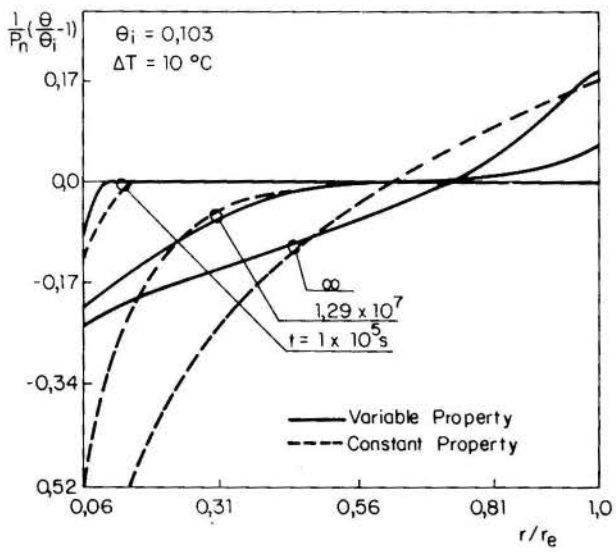

Fig. 5 - Moisture content as a function of position; θ_i = 0.103 and $\Delta T = 10^0C$

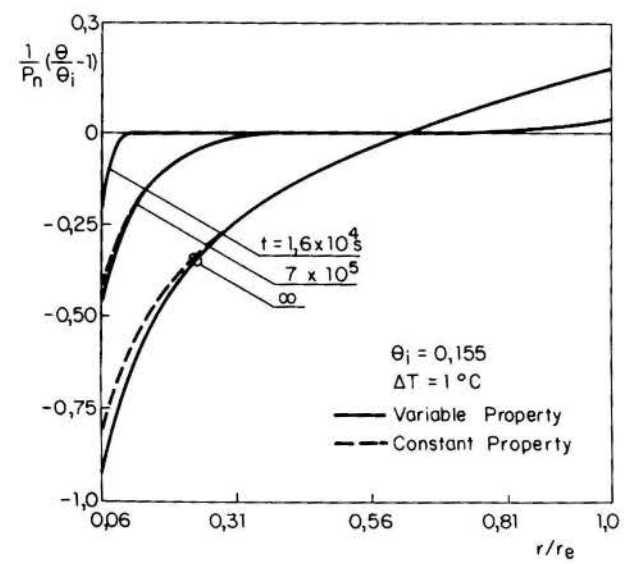

Fig. 6 - Moisture content as a function of position; θ_i = 0.155 and $\Delta T = 1^0C$

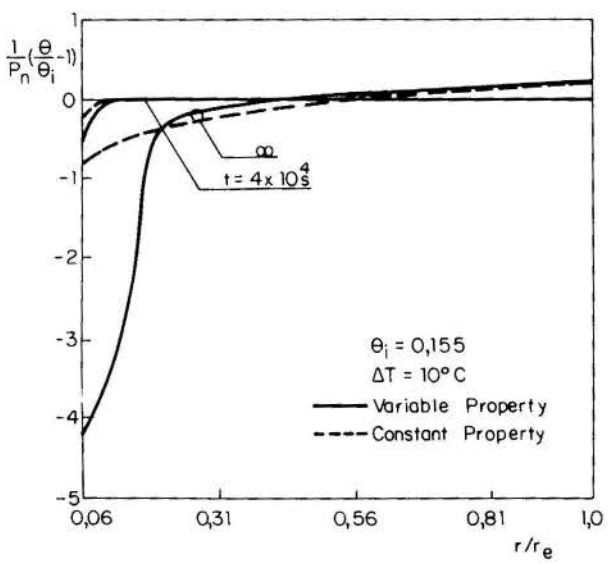

Fig. 7 - Moisture content as a function of position; θ_i = 0.155 and $\Delta T = 10^0C$

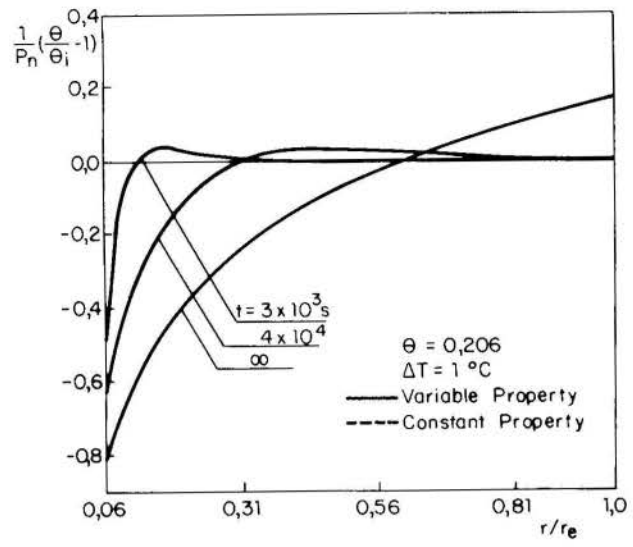

Fig. 8 - Moisture content as a function of position; θ_i = 0.206 and $\Delta T = 1^0C$

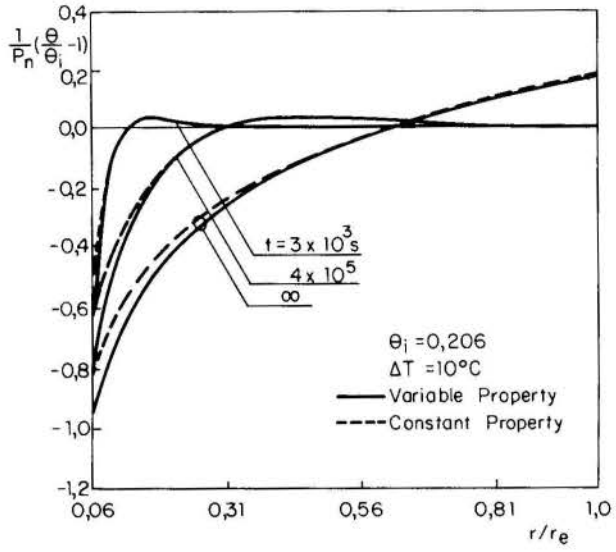

Fig. 9 - Moisture content as a function of position; θ_i = 0.206 and $\Delta T = 10^0C$

In general, it can then be said that for the range of parameters investigated here, it is allowed to recommend the parametric model for situations where the moisture content is either below or above the crictical moisture content of the medium, that is, the value of θ in which the liquid in the pores passes from pendular to funicular state.

Finally, an interesting aspect which is not related to the comparison between the two models will now be discussed. As can be noticed from Figs. 8 and 9, for θ_i = 0.206 occurs an increase in the soil moisture content near the cable surface for low values of time. This behavior is not observed for the others values of θ_i investigated, and will be explained next.

For θ_i = 0.206 the Luikov number is relatively high, and for earlier times the temperature is still developing. Since the vapor flux is essentially due to the temperature gradient, in this case the vapor flux originated from the evaporation of the liquid at the cable surface diminishes as R increases and the vapor is absorbed by condensation. This condensation causes an increase in the moisture content, which can be observed in Figs. 8 and 9 around the position R = 0.17. In turn, the values of θ in that region becomes greater than the initial moisture content θ_i.

CONCLUSIONS

An analysis of the moisture transport caused by thermal gradients between two impermeable boundaries in a cylindrical geometry has been conducted. For the analysis of the phenomenon, two models were employed. In the first model, due to Philip and de Vries, the variation of the thermophysical properties of the medium with temperature and moisture content is taken into account. For the second model, the properties are taken to be constant and the moisture migration is governed by two dimensionless parameters, the Luikov and the Posnov numbers. The main focus of the work was to verify the deviations associated to the constant property model, by comparing the results obtained from the two models.

The solution of the differential equations were obtained numerically via a finite difference scheme known as the control volume method.

A sandy silt soil was used as the porous medium. Four initial moisture contents were investigated, 0.026, 0.103, 0.155 and 0.206. These moisture contents cover situations from dry soils where there is no continuity of the liquid phase in the pores (pendular state), to situations where the soil is wet and the liquid is mobile (funicular state). For each moisture content, two values of the temperature difference between the cylinder walls were investigated, 1 and 10 ^{0}C.

In situations where the moisture content in the medium is either below or above the critical moisture content, that is, the value in which the liquid in the pores becomes mobile, the parametric model yielded good results. For the medium analysed here, this critical moisture content is around 0.14. However, around the critical moisture content there is a drastic change of the properties with moisture and the deviations associated with the constant property model increase substantially. Furthermore, as expected, the errors introduce by using the parametric model increase as the temperature gradients within the medium increase.

By the analysis of the results, it is allowed to recommend the parametric model for low temperature differences between the boundaries and/or for soils with very low or very high moisture content. For situations around the soil critical moisture content the parametric model should be imployed as a first approximation of the problem.

ACKNOWLEDGEMENTS

The authors acknowledge gratefully the financial support provided by Pirelli S.A. Cable Division - São Paulo, and CAPES - Brazilian Ministry for Education.

REFERENCES

[1] J.R. Philip and D.A. de Vries, "Moisture Movement in Porous Media Under Temperature Gradients", Trans. Am. Geophys. Union, pp. 222-232, Vol. 38, 1957.

[2] D.A. de Vries, "Simultaneous Transfer of Heat and Moisture in Porous Media", Trans. Am. Geophys. Union, pp. 909-916, Vol. 39, 1958.

[3] D.A. Vries, "The Theory of Heat and Moisture Transfer in Porous Media Revisited", Int. J. Heat Transf., pp. 1343-1349, Vol. 30, 1987.

[4] A.V. Luikov, "Heat and Mass Transfer in Capillary-Porous Bodies", Pergamon Press, Oxford, 1966.

[5] S. Whitaker, "Simultaneous Heat, Mass and Momentum Transfer in Porous Media: A Theory of Drying", Advances in Heat Transfer, Vol. 13, Academic Press, New York, 1977.

[6] J.W. Cary and S.A. Taylor, "Thermally Driven Liquid

and Vapor Phase Transfer of Water and Energy in Soil", Soil Sci. Soc. Am. Proc., Vol. 26, pp. 417-420, 1962.

[7] P. Crausse, G. Bacon and S. Bories, "Etude Fondamentate des Transferts Couples Chaleur - Masse en Milieu Poreux", Int. J. Heat Mass Transfer, pp. 991-1004, Vol. 24, 1981.

[8] R.J. Couvillion and J.G. Hartley, "Drying Front Movement Near Low - Intensity, Impermeable Underground Heat Sources", J. Heat Transfer, pp. 182-189, Vol. 108, 1986.

[9] W.A. Jury, "Simultaneous Transport of Heat and Moisture Through a Medium Sand", Ph.D. Thesis, University of Wisconsin, 1973.

[10] R.J. Preece and J.A. Hitchcock, "Simultaneous Diffusion of Heat and Moisture Through Isotropic Porous Media with Varying Physical Properties", 6th International Heat Transfer Conference, Toronto, pp. 2348-2353, 1978.

[11] E.R.G. Eckert and M. Faghri, "A General Analysis of Moisture Migration Caused by Temperature Differences in an Unsaturated Porous Medium", Int. J. Heat Mass Transfer, pp. 1613-1623, Vol.23, 1980.

[12] M. Faghri and E.R. Eckert, "Moisture Migration Caused by Periodic Temperature Fluctuations in an Unsaturated Porous Medium", Wärme-Stoffübertrag, pp. 217-223, Vol. 14, 1980.

[13] E.R.G. Eckert and M. Faghri "A parametric analysis of Moisture Migration in an Unsaturated Porous Slab Caused by Convective Heat and Mass Transfer", Wärme-Stoffübertrag, pp. 77-87, Vol. 20, 1986.

[14] L.S. Damasceno Ferreira, "Migração de Umidade Causada por Gradientes Térmicos entre Duas Fronteiras Impermeáveis Contendo um Meio Poroso Insaturado", M.Sc. Dissertation, Federal University of Santa Catarina, 1987.

[15] D.A. de Vries, "Heat Transfer in Soils", in Heat and Mass Transfer in Biosphere , pp. 5-28, Scripta, Washington, 1975.

[16] J.G. Hartley, "Coupled Heat and Moisture Transfer in Soils: A Review", Chapter 4 of Advances in Drying, edited by A.S. Mujumbar, Hemisphere, Washington, 1987.

[17] S.V. Patankar, "Numerical Heat Transfer and Fluid Flow", Hemisphere, Washington, 1980.

[18] J.G. Hartley, W. Black, R.A. Bush and M.A. Bush and M.A. Martin Jr., "Thermal Stability of Soils Adjacent to Underground Transmission Power Cables", Technical Report of Georgia Institute of Technology for EPRI, 1982.

III ENCIT – Itapema, SC (Dezembro 1990)

ESTUDO DOS PROCESSOS DE CONDENSAÇÃO-EVAPORAÇÃO NA CONDIÇÃO DE EQUILIBRIO HIGROTERMICO EM MEIOS POROSOS CONSOLIDADOS.

Fernandes, C. P. ; Philippi, P. C. ; Brincas, C. R. ; Pedrini, A.
Universidade Federal de Santa Catarina
Departamento de Engenharia Mecânica
Caixa Postal 476 Florianópolis - 88049 - S.C.

RESUMO

O presente artigo trata de uma análise experimental dos fenômenos físicos de condensação-evaporação de umidade em um meio poroso consolidado, um tipo de argamassa de cal e cimento. As isotermas de adsorção e dessorção são obtidas com o auxílio de soluções salinas saturadas. Faz-se, ainda, uma investigação da estrutura porosa da argamassa, através do método de porosimetria com injeção de mercúrio. Os resultados são analisados, visando uma caracterização do comportamento hídrico da argamassa, considerando-se sua estrutura porosa.

INTRODUÇÃO

Um bom conhecimento dos processos físicos, envolvendo a presença de umidade, que ocorrem no interior das estruturas porosas dos materiais que compõem as edificações é essencial para promover um uso racional de energia, incrementar a durabilidade dos materiais e para assegurar condições adequadas de higiene para os ocupantes da habitação.

Um fenômeno físico muito importante, é o de adsorção ou dessorção de umidade do ar ambiente pela estrutura porosa, conforme as condições higrotérmicas reinantes.

Dois tipos de água condensada, que coexistem em meios porosos, compõem o conteúdo de umidade para uma dada condição de equilíbrio higrotérmico : a água adsorvida fisicamente e a água capilar.

O volume de água condensada, para uma dada condição de equilíbrio higrotérmico está intimamente relacionado com a estrutura porosa do material (distribuições de volumes e superfícies de poros e topologia).

É interessante dessa maneira um conhecimento da estrutura porosa do material, que servirá de suporte de análise para a caracterização do seu comportamento hídrico.

Neste trabalho, as isotermas de adsorção e dessorção a 25°C, para uma argamassa de cal e cimento de uso bastante difundido para o revestimento de paredes externas, são obtidas com o uso de soluções salinas saturadas com corpo de fundo, que mantêm a umidade relativa constante para uma dada temperatura.

O uso dessas soluções apresenta duas vantagens, MEROUANI [2]:
- A umidade relativa mantida por uma dada solução varia pouco com a temperatura;
- desde que a solução se mantenha saturada não há variação de umidade relativa.

A estrutura porosa da argamassa é investigada com o auxílio do método de injeção de mercúrio para os poros com raio até 240 Å; os poros de raios menores que 240 Å são analisados através da isoterma experimental de adsorção conjugada ao modelo B.J.H. [3], [1], veja-se apêndice.

O modelo dito B.J.H. é classicamente utilizado para calcular as distribuições de volumes e superfícies de poros a partir da isoterma de adsorção.

A idéia de se obter a isoterma de adsorção a partir da estrutura porosa foi sugerida por DAIAN [1]. O modelo B.J.H. separa quantitativamente as parcelas de água adsorvida e água capilar que compõem o conteúdo de umidade total para uma dada condição de equilíbrio, e é um modelo não-histerético.

ISOTERMAS DE ADSORÇÃO - DESSORÇÃO

As isotermas de adsorção-dessorção descrevem as condições de equilíbrio entre ar úmido, água líquida e a matriz porosa do material.

O fenômeno físico de adsorção pura ocorre, dado que os materiais porosos têm a capacidade de capturar as moléculas de vapor de água: essas moléculas apresentam uma grande afinidade com a superfície dos poros. A água adsorvida consiste de camadas de moléculas que condensam sobre a superfície dos poros. Sua quantidade no equilíbrio é função da superfície específica do meio poroso, da afinidade entre o vapor de água e a matriz sólida e das condições higrotérmicas reinantes.

Em meios porosos, as isotermas de adsorção-dessorção são modificadas pela condensação capilar. A condensação capilar ocorre, quando a umidade relativa atende um valor mínimo h_* para um dado raio r de poro, descrito por:

$$h_* = \exp\left[\frac{-2\sigma M \cos\alpha}{\rho_l R T r}\right]$$

onde:

σ = tensão superficial [$N.m^{-1}$]
M = massa molecular [$Kg.mol^{-1}$]
α = ângulo de contacto
ρ_l = massa específica do líquido [$Kg.m^{-3}$]

R = constante dos gases [$J.mol^{-1}.K^{-1}$]
T = temperatura [K]

A água capilar representa uma fase contínua de líquido que preenche totalmente os poros do material. Existe uma descontinuidade de pressão na interface curva que separa a água capilar da fase gasosa.

A condensação capilar é a responsável pelo fenômeno de histerese que a isoterma de dessorção apresenta. Observando-se resultados experimentais de adsorção-dessorção, veja-se p.ex. a Fig.1, nota-se que para a mesma umidade relativa o volume de água condensado em dessorção é maior que em adsorção.
Isto significa que as condições de equilíbrio entre o ar úmido, água líquida e a matriz porosa são dependentes da história do processo.

A topologia (conectividade) e a não-uniformidade dos raios dos poros têm sido atribuídos como fatores principais para a ocorrência da histerese.

DESCRIÇÃO DAS AMOSTRAS

Foram utilizadas amostras de argamassa de cal e cimento confeccionadas na proporção em massa 8:2:1 (areia fina: cal: cimento) com adição de água representando cerca de 20% da massa total.

Os componentes da argamassa são misturados mecanicamente e a água adicionada dá uma plasticidade adequada à trabalhabilidade nos moldes. O período de cura é de 28 dias sendo que a desmoldagem é feita no 5º dia.

A reação química de carbonatação

$$Ca(OH)_2 + CO_2 \longrightarrow CaCO_3 + H_2O$$

ocorre com as amostras mantidas ao ar livre, decorrente da ação do CO_2 presente no ar sobre a cal.

Esta é uma reação que progride lentamente a partir da superfície em direção ao centro do material devido à difusão de gás carbônico. A velocidade de progressão da carbonatação é função da temperatura e umidade relativa do ar. Ela aumenta sensivelmente com a temperatura e atinge um máximo para a umidade relativa de 50%, [1]. Utilizou-se o indicador ácido-base fenolftaleína para o acompanhamento da região afetada pela carbonatação.

Para os ensaios de adsorção-dessorção foram usadas pequenas placas de argamassa (50 X 100 X 3 mm^3) extraídas de amostras cilíndricas (altura de 100 mm ediâmetro de 100mm), inicialmente confeccionadas, através de processo de serragem. As placas destinadas aos ensaios de adsorção-dessorção foram mantidas ao ar livre, por tempo suficiente tal que apresentassem todo o volume poroso carbonatado; o acompanhamento da carbonatação foi feito com o indicador fenolftaleína.

O padrão de massa seca utilizado neste trabalho é o de secagem em estufa com circulação forçada de ar à 75°C, na presença de sílica-gel, por tempo sufucientemente longo tal que não mais se observe variação de massa. Temperaturas mais elevadas não foram utilizadas, no intuito de se evitar a evaporação da água quimicamente adsorvida, presente na pasta de ligantes (cal, cimento e água).

As amostras de argamassa apresentam uma porosidade de 0,31 $\pm$ 0,03 cm^3/cm^3 e densidade aparente de 1,73 $\pm$ 0,05 g/cm^3.

DETERMINAÇÃO EXPERIMENTAL DAS ISOTERMAS DE ADSORÇÃO-DESSORÇÃO

As isotermas de adsorção-dessorção foram obtidas, para a argamassa em análise neste artigo, em dessecadores, contendo soluções salinas saturadas os quais são dispostos no interior de uma estufa com temperatura controlada.

Utilizou-se nove soluções abrangendo a faixa de 8 a 97% (KOH e K_2SO_4, respectivamente) de umidade relativa à temperatura de 25°C, em concordância com a norma francesa NF X 15-014.

A monitoração da temperatura da estufa é feita com termômetro vidro-mercúrio (resolução de 0,05°C) com o bulbo posicionado no seu centro geométrico. Com este termômetro, na posição citada, observa-se uma variação de $\pm$ 0,1°C.

As amostras destinadas ao ensaio de adsorção foram secadas, como descrito anteriormente, e colocadas em um dessecador grande, contendo sílica-gel, para o abaixamento de temperatura até 25°C, valor do teste.

As amostras para o ensaio de dessorção, após a determinação da massa seca, são imersas em água destilada à pressão atmosférica e temperatura de 25 $\pm$ 1°C para a saturação.

As amostras são então colocadas e mantidas nos dessecadores (que já estão em equilíbrio térmico com o ambiente interior da estufa, na temperatura do ensaio) até a obtenção da massa de equilíbrio.

O intervalo de tempo requerido para a obtenção dessa condição de equilíbrio varia em função do tipo de ensaio: para dessorção, de 4 a 5 semanas; para adsorção de 3 a 4 semanas.

As massas são medidas a cada 5 ou 7 dias, com balança digital (resolução 0,01g) até a sua estabilização. Um por vez, os dessecadores são retirados da estufa, e medida a massa da amostra. Haverá uma perturbação ligeira da umidade relativa do dessecador quando de sua abertura, e transferência de massa entre a amostra e o meio ambiente durante o intervalo de tempo necessário à pesagem.
No entanto, para a balança utilizada, e o pequeno intervalo de tempo de medição não é notada variação de massa.

Os resultados obtidos para as isotermas de adsorção e dessorção à temperatura de 25°C são mostrados na Fig.1.

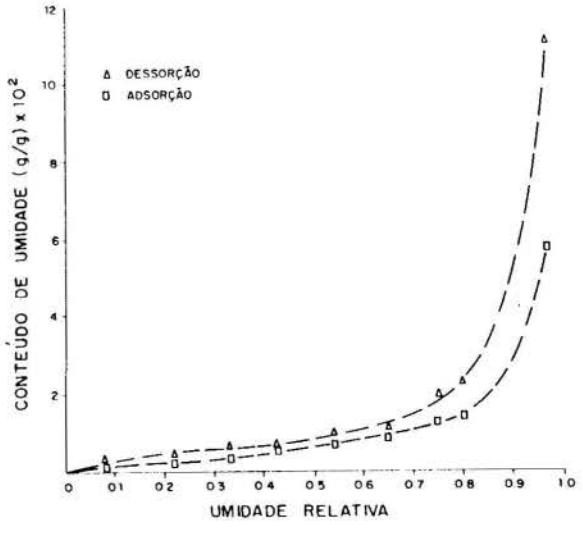

Fig.1 Pontos experimentais adsorção-dessorção.

Na Fig.2 mostra-se as contribuições da água adsorvida e capilar para o conteúdo total, em função da umidade relativa. Essas curvas foram obtidas com o uso do modelo B.J.H.[3], sendo que para a sua avaliação é necessário o conhecimento da estrutura porosa da argamassa, que será descrita a seguir.

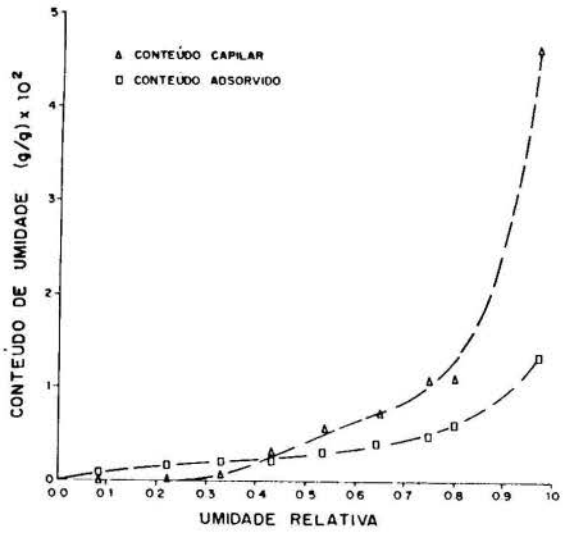

Fig.2 Separação dos conteúdos adsorvido e capilar.

ESTRUTURA POROSA

A estrutura porosa da argamassa de cal e cimento foi investigada com o uso do método de injeção de mercúrio. Como será visto, este é um método de fácil utilização, todavia apresenta problemas quanto à interpretação dos seus resultados.

A idéia básica consiste em injetar mercúrio, um fluido não molhante, no meio poroso previamente submetido a vácuo.

Considere-se um poro cilíndrico de raio r contendo mercúrio, Fig. 3. A lei de Laplace para a descontinuidade de pressão no menisco esférico convexo é

$$P_l - P_o = - \frac{2\,\sigma \cos\alpha}{r} \qquad (1)$$

onde, para o mercúrio é assumido [2]:

$\sigma = 0{,}480\ N.m^{-1}$; a tensão superficial
$\alpha = 140°$; o ângulo de contacto

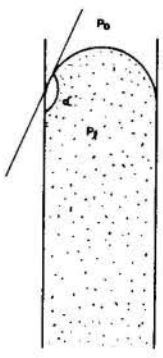

Fig.3 Poro cilíndrico contendo mercúrio .

Para a consecução do método, uma pequena amostra do material poroso, previamente submetida a vácuo, é colocada em uma câmara contendo mercúrio e sujeita passo a passo a incrementos de pressão. Devido à evacuação, é assumido $p_o = 0$.

Um incremento de pressão Δp_{li}, indicado diretamente pelo porosímetro, produz uma injeção de mercúrio de volume ΔV_i na amostra, atribuído ao preenchimento de uma classe de poros cilíndricos com raio equivalente r_i, dado por:

$$r_i = \frac{-2\,\sigma \cos\alpha}{P_{li}} \qquad (2)$$

Como o volume ΔV_i também é medido diretamente no porosímetro, pode-se através da Eq.(2) obter a distribuição de volume de poros em função de seus raios.

A superfície dos poros da classe em consideração, com a suposição que sejam cilíndricos, será:

$$\Delta S_i = \frac{2\Delta V_i}{r_i} \qquad (3)$$

Assim, acumulando-se os ΔS_i, obtém-se a distribuição de superfícies dos poros em função dos seus raios.

Considere-se agora uma formação de poros do tipo "com garganta", Fig. 4, que é uma das causas principais do aparecimento de histerese nas isotermas de adsorção-dessorção, como comentado anteriormente.

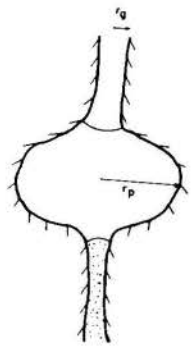

Fig. 4 Formação de poros "com garganta".

No método descrito, assume-se que os poros com mesmo raio vão sendo preenchidos independentemente da sua posição no meio poroso, quando este é submetido a incrementos de pressão. Inicialmente, para pressões baixas, são preenchidos os poros maiores, e com pressões mais elevadas os poros menores, consecutivamente.

Contudo em uma configuração como a apresentada na Fig. 4, o poro de raio r_p se preencherá apenas a uma pressão correspondente ao raio r_g ($r_g < r_p$), ou seja, o preenchimento do poro de raio r_p é condicionado ao da garganta de raio r_g.

Dessa maneira, o volume de mercúrio penetrado será atribuído de maneira errônea ao poro de raio equivalente r_g.

Portanto, a porosimetria com injeção de mercúrio sobreestima o volume dos poros menores em detrimento ao dos maiores.

Ainda, haverá sobreestimação da superfície dos poros, devido a divisão na Eq.(3) ser feita por um raio menor que o real.

MODO OPERACIONAL

Utilizou-se o porosímetro Aminco-Winlow do Departamento de Engenharia de Materiais da Universidade Federal de São Carlos (estado de São Paulo).

Com este porosímetro, consegue-se uma pressão máxima de 5.000 psi; a gama de raios de poros explorados variou de 240 Å até 1 μm.

Os poros com raios menores que 240 Å, inacessíveis a esse porosímetro, foram investigados com o uso da isoterma experimental de adsorção (isenta de histerese) conjugada ao modelo B.J.H., veja-se apêndice.

Nas Figs. 5 e 6 estão representadas a função distribuição e a função densidade de probabilidade para os volumes de poros. A função distribuição para a superfície dos poros é mostrada na Fig. 7.

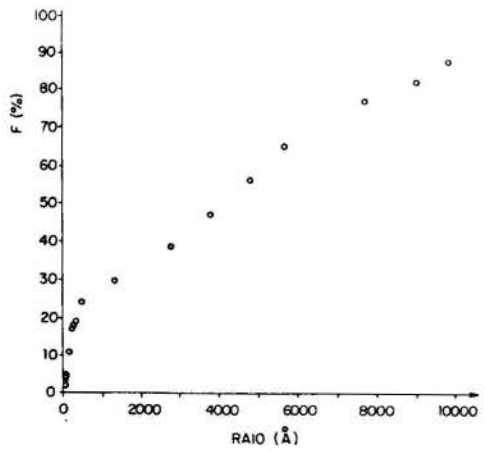

Fig.5 Função distribuição de volumes de poros

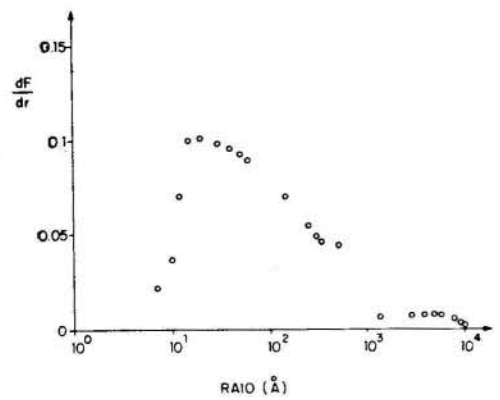

Fig.6 Função densidades de probabilidades para os volumes de poros .

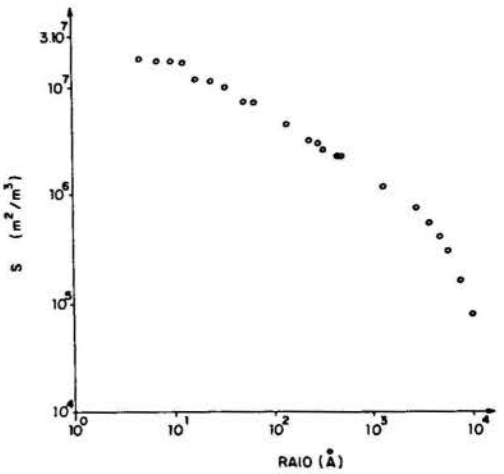

Fig.7 Repartição de superfícies de poros.

CONCLUSÕES

Pode-se observar da função densidade de probabilidades de volumes de poros, Fig. 6, que a argamassa apresenta uma gama de raios de poros bastante variada, com proporções de volume poroso apreciáveis contendo mesoporos (20 Å < raio < 500 Å) e macroporos (raio > 500 Å). Nota-se ainda da função densidade, uma alta concentração de poros com raios entre 10 e 100 Å. A despeito da sobrestimação do volume dos poros menores em detrimento aos maiores, inerente ao método de investigação adotado, essa dimensão (10-100 Å) é atribuida como sendo característica dos poros que compõem a pasta de ligantes (que agrega os grãos de areia). Para essa grande conçentração de volume poroso (entre 10Å e 100Å), aventa-se a hipótese de a água adsorvida predominar sobre a capilar: a interação entre as moléculas de água e a matriz sólida é muito supeior às forças de interação entre as moléculas, não havendo mobilidade no sentido de se constituir uma fase líquida.

Pode ser observado da Fig.1, uma fraca histerese até em torno de 50% de umidade relativa, devido possivelmente ao pequeno volume de água condensada capilarmente.

A condensação capilar começa para um valor de umidade relativa em torno de 33%, Fig.2, e a partir desse ponto começa a ocorrer um sensível crescimento no conteúdo de umidade, devido ao volume formado pelas ilhas de líquido.

A presença de poros com dimensões tais que permitam a ocorrência da condensação capilar a partir de valores médios de umidade relativa, implicando em um aumento sensível do conteúdo de umidade, confere à argamassa uma grande capacidade de retenção de água.

BIBLIOGRAFIA

[1] Daian, J.F., "Processus de Condensation et de Transfert d'Eau dans un Matériau Meso et Macroporeux. Étude Expérimentale du Mortier de Ciment", These Docteur Es-Sciences Physiques. Institut National Polytechnique de Grenoble, 1986.

[2] Merouani, L., "Phénomenes de Sorption et de Transfert d'Humidité des Matériaux du Bâtiment. Étude Experimentale Comparative d'un Mortier de Ciment et d'un Enduit de Façade", These Docteur 3e Cycle Institut National Polytechnique de Grenoble, 1987.

[3] Barret, E.P., Joyner, L.G., Halenda, P.P., "The Determination of Pore Volume and Area Distributions in Porous Substances. I. Computations from Nitrogen Isothermes" Journal of the American Chemical Society, Vol. 73, no. 1, pp. 373-380.

[4] Fernandes, C.P., "Estudo dos Processos de Condensação e Migração de Umidade em Meios Porosos Consolidados. Análise Experimental de uma Argamassa de Cal e Cimento", Dissertação de Mestrado, Universidade Fedaral de Santa Catarina, março de 1990.

APÊNDICE

Apresenta-se de maneira bastante condensada as idéias principais do modelo B.J.H. . Para tanto, supõe-se que o meio poroso é constituído de um feixe de poros cilíndricos sem interconexões. O meio é então submetido a um incremento Δh de umidade relativa passando de h para $h+\Delta h$. Quando isto ocorre, uma classe de poros de raios r a $r+\Delta r$ se preencherá com água capilar, que coexistirá com a camada de água previamente adsorvida de espessura e_a, Fig.8 .

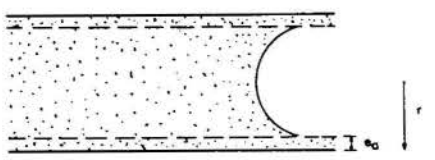

Fig.8 Poro preenchido com água capilar

O conteúdo de água condensada capilarmente, $\Delta\theta_{cap}$, será dado por :

$$\Delta\theta_{cap} = \frac{\Delta Sr}{2}\left[r - e_a\right]$$

onde, ΔSr é a superfície lateral dessa classe de poros .

Os poros com raio superior a essa classe, terão apenas um aumento na espessura da camada adsorvida, pois $h+\Delta h$ não é suficiente para provocar a condensação capilar, Fig.9 .

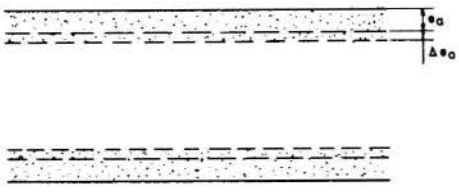

Fig.9 Aumento da espessura da camada adsorvida nos poros com raio superior a $r+\Delta r$.

O volume de água $\Delta\theta_{ads}$ associado ao acréscimo na camada adsorvida, Δe_a, será dado por :

$$\Delta\theta_{ads} = \Delta e_a \cdot S(r)$$

onde, $S(r)$ é a superfície acumulada dos poros com raio maior que r .

Portanto, o aumento de conteúdo total $\Delta\theta$ asssociado ao incremento Δh será :

$$\Delta\theta = \Delta\theta_{cap} + \Delta\theta_{ads} = \frac{\Delta Sr}{2}\left[r - e_a\right] + S(r).\Delta e_a$$

Para o cálculo das superfícies acumuladas de poros escreve-se a equação anterior na forma:

$$\Delta Sr = \frac{2}{r - e_a}\left[\Delta\theta - S(r)\,\Delta e_a\right]$$

Para tanto, partindo-se de um valor inicial de $S(r)$, faz-se o acúmulo dos valores ΔSr passo a passo.

Este acúmulo é feito para valores decrescentes de umidade relativa h, a partir de um ponto experimemtal da isoterma de adsorção (ou dessorção), bem próximo da saturação, caso isto seja possível, onde se assume $S(r) = 0$, o que significa volume de vazios nulo.

No caso deste trabalho, o maior valor de umidade relativa utilizado, 97% , dá um valor e conteúdo de equilíbrio na adsorção de 5,7% (em massa) que está longe da saturação (em torno de 18%) o que significa que não podemos admitir $S(r) = 0$ para $h = 0,97$.
Para contornar esse problema, fez-se uma estimativa inicial para $S(r)$ utilizando dados obtidos com o ensaio de porosimetria com injeção de mercúrio.

Resta ainda, para o cálculo das superfícies acumuladas de poros, avaliar a espessura da camada adsorvida e_a em função da umidade relativa, e o raio r de poro, para cada valor de h, que delimita os poros menores, capazes de conter água capilar levando em conta a existência da camada adsorvida, dos poros maiores que contém apenas água adsorvida.

No caso deste trabalho, a espessura e_a foi avaliada a partir do número de camadas adsorvidas, obtido através da equação BET, que é um modelo de adsorção pura, veja-se [2]. Os parâmetros desconhecidos da equação BET foram obtidos a partir da isoterma experimental de adsorção.

Finalmente, para o cálculo do raio r limite, para cada valor de h, como mencionado anteriomente, utilizou-se a equação do limite de condensação capilar levando em consideração a existência da camada adsorvida:

$$r = \frac{-2\,\sigma\,M}{\rho_l\,R\,T\,\ln h} + e_a(h)$$

Deve-se ter em mente que a equação anterior supõe uma geometria esférica para o menisco.

SUMMARY

This paper shows the results of an experimental work about the processes of evaporation and condensation over a consolidated porous medium surface. Lime mortar was chosen for this study. Sorption isotherms were obtained wing saturated salt solutions and mercury porosimetry was used to found the pore distribution function. The results were analysed taking the links between the porous structure and hydric behaviour into account .